ACHIEVEMENTS AND NEW FRONTIERS IN RESEARCH ORIENTED TO EARTHQUAKE FORECASTING

EDITED BY: Giovanni Martinelli, Antonella Peresan and Ying Li
PUBLISHED IN: Frontiers in Earth Science

frontiers Research Topics

Frontiers eBook Copyright Statement

The copyright in the text of individual articles in this eBook is the property of their respective authors or their respective institutions or funders. The copyright in graphics and images within each article may be subject to copyright of other parties. In both cases this is subject to a license granted to Frontiers.

The compilation of articles constituting this eBook is the property of Frontiers.

Each article within this eBook, and the eBook itself, are published under the most recent version of the Creative Commons CC-BY licence. The version current at the date of publication of this eBook is CC-BY 4.0. If the CC-BY licence is updated, the licence granted by Frontiers is automatically updated to the new version.

When exercising any right under the CC-BY licence, Frontiers must be attributed as the original publisher of the article or eBook, as applicable.

Authors have the responsibility of ensuring that any graphics or other materials which are the property of others may be included in the CC-BY licence, but this should be checked before relying on the CC-BY licence to reproduce those materials. Any copyright notices relating to those materials must be complied with.

Copyright and source acknowledgement notices may not be removed and must be displayed in any copy, derivative work or partial copy which includes the elements in question.

All copyright, and all rights therein, are protected by national and international copyright laws. The above represents a summary only. For further information please read Frontiers' Conditions for Website Use and Copyright Statement, and the applicable CC-BY licence.

ISSN 1664-8714
ISBN 978-2-88974-082-6
DOI 10.3389/978-2-88974-082-6

About Frontiers

Frontiers is more than just an open-access publisher of scholarly articles: it is a pioneering approach to the world of academia, radically improving the way scholarly research is managed. The grand vision of Frontiers is a world where all people have an equal opportunity to seek, share and generate knowledge. Frontiers provides immediate and permanent online open access to all its publications, but this alone is not enough to realize our grand goals.

Frontiers Journal Series

The Frontiers Journal Series is a multi-tier and interdisciplinary set of open-access, online journals, promising a paradigm shift from the current review, selection and dissemination processes in academic publishing. All Frontiers journals are driven by researchers for researchers; therefore, they constitute a service to the scholarly community. At the same time, the Frontiers Journal Series operates on a revolutionary invention, the tiered publishing system, initially addressing specific communities of scholars, and gradually climbing up to broader public understanding, thus serving the interests of the lay society, too.

Dedication to Quality

Each Frontiers article is a landmark of the highest quality, thanks to genuinely collaborative interactions between authors and review editors, who include some of the world's best academicians. Research must be certified by peers before entering a stream of knowledge that may eventually reach the public - and shape society; therefore, Frontiers only applies the most rigorous and unbiased reviews.
Frontiers revolutionizes research publishing by freely delivering the most outstanding research, evaluated with no bias from both the academic and social point of view. By applying the most advanced information technologies, Frontiers is catapulting scholarly publishing into a new generation.

What are Frontiers Research Topics?

Frontiers Research Topics are very popular trademarks of the Frontiers Journals Series: they are collections of at least ten articles, all centered on a particular subject. With their unique mix of varied contributions from Original Research to Review Articles, Frontiers Research Topics unify the most influential researchers, the latest key findings and historical advances in a hot research area! Find out more on how to host your own Frontiers Research Topic or contribute to one as an author by contacting the Frontiers Editorial Office: frontiersin.org/about/contact

ACHIEVEMENTS AND NEW FRONTIERS IN RESEARCH ORIENTED TO EARTHQUAKE FORECASTING

Topic Editors:
Giovanni Martinelli, National Institute of Geophysics and Volcanology, Section of Palermo, Italy
Antonella Peresan, Istituto Nazionale di Oceanografia e di Geofisica Sperimentale (Italy), Italy
Ying Li, Institute of Earthquake Forecasting, China Earthquake Administration, China

Cover Image Credit: Zhaofei Liu and Ying Li From the Institute of Earthquake Forecasting, China

Citation: Martinelli, G., Peresan, A., Li, Y., eds. (2022). Achievements and New Frontiers in Research Oriented to Earthquake Forecasting.
Lausanne: Frontiers Media SA. doi: 10.3389/978-2-88974-082-6

Table of Contents

05 ***Editorial: Achievements and New Frontiers in Research Oriented to Earthquake Forecasting***
Giovanni Martinelli, Antonella Peresan and Ying Li

08 ***Mechanical Mechanism of Fault Dislocation Based on* in situ *Stress State***
Haoyu Shi, Fuqiong Huang, Zhenkai Ma, Yongjian Wang, Jicheng Feng and Xu Gao

17 ***Structural Controls on Aftershock Distribution in Subduction Zones***
Simon Richards

27 ***Injection-Induced Seismic Risk Management Using Machine Learning Methodology – A Perspective Study***
Miao He, Qi Li and Xiaying Li

45 ***Statistical and Non-linear Dynamics Methods of Earthquake Forecast: Application in the Caucasus***
Tamaz Chelidze, Giorgi Melikadze, Tengiz Kiria, Tamar Jimsheladze and Gennady Kobzev

60 ***Earth's Outgoing Longwave Radiation Variability Prior to* M ≥*6.0 Earthquakes in the Taiwan Area During 2009–2019***
Ching-Chou Fu, Lou-Chuang Lee, Dimitar Ouzounov and Jyh-Cherng Jan

75 ***Spatial Distribution of Rn, CO_2, Hg, and H_2 Concentrations in Soil Gas Across a Thrust Fault in Xinjiang, China***
Yang Xiang, Xiaolong Sun, Dongying Liu, Long Yan, Bo Wang and Xiaoqi Gao

84 ***Revealing Short-Term Precursors of the Strong* M *> 7 Earthquakes in Southern California From the Simulated Stress–Strain State Patterns Exploiting Geomechanical Model and Seismic Catalog Data***
Valery G. Bondur, Mikhail B. Gokhberg, Igor A. Garagash and Dmitry A. Alekseev

99 ***"Bristle-State" Friction: Modeling Slip Initiation and Transient Frictional Evolution From High-Velocity Earthquake Rupture Experiments***
Seth Saltiel, Tushar Mittal, Jorge G. F. Crempien and Jaime Campos

109 ***Multi-Level Gas Monitoring: A New Approach in Earthquake Research***
Heiko Woith, Kyriaki Daskalopoulou, Martin Zimmer, Tomáš Fischer, Josef Vlček, Jakub Trubač, Jan-Erik Rosberg, Tomáš Vylita and Torsten Dahm

115 ***On the Long Range Clustering of Global Seismicity and its Correlation With Solar Activity: A New Perspective for Earthquake Forecasting***
Vito Marchitelli, Claudia Troise, Paolo Harabaglia, Barbara Valenzano and Giuseppe De Natale

123 ***Electric and Magnetic Recordings by Chieti CIEN Station During the Intense 2016–2017 Seismic Swarms in Central Italy***
Cristiano Fidani, Massimo Orsini, Giovanni Iezzi, Noemi Vicentini and Francesco Stoppa

142 ***The Method of the Minimum Area of Alarm for Earthquake Magnitude Prediction***
Valeri Gitis and Alexander Derendyaev

153 ***Influence of Lithosphere Rheology on Seismicity in an Intracontinental Rift: The Case of the Rhine Graben***
Denis Anikiev, Mauro Cacace, Judith Bott, Maria Laura Gomez Dacal and Magdalena Scheck-Wenderoth

172 ***Earthquake-Related Signals in Central Italy Detected by Hydrogeochemical and Satellite Techniques***
Giovanni Martinelli, Gianluca Facca, Nicola Genzano, Fabrizio Gherardi, Mariano Lisi, Lisa Pierotti and Valerio Tramutoli

182 ***Stress-Related Pre-Seismic Water Radon Concentration Variations in the Panjin Observation Well, China (1994–2020)***
Zhihua Zhou, Lei Tian, Jing Zhao, Haiyan Wang and Jianguang Liu

194 ***Global Seismic Noise Entropy***
Alexey Lyubushin

206 ***A Multiparametric Approach to Study the Preparation Phase of the 2019 M7.1 Ridgecrest (California, United States) Earthquake***
Angelo De Santis, Gianfranco Cianchini, Dedalo Marchetti, Alessandro Piscini, Dario Sabbagh, Loredana Perrone, Saioa Arquero Campuzano and Sedat Inan

221 ***Hydrogeological Earthquake Precursors: A Case Study From the Kamchatka Peninsula***
Galina Kopylova and Svetlana Boldina

228 ***Aftershock Rate Changes at Different Ocean Tide Heights***
P. N. Shebalin and A. A. Baranov

246 ***Characterizing the Foreshock, Main Shock, and Aftershock Sequences of the Recent Major Earthquakes in Southern Alaska, 2016–2018***
B. G. Bukchin, A. S. Fomochkina, V. G. Kossobokov and A. K. Nekrasova

258 ***Unified Scaling Law for Earthquakes: Space-Time Dependent Assessment in Friuli-Venezia Giulia Region***
Anastasia Nekrasova and Antonella Peresan

271 ***Precursor-Based Earthquake Prediction Research: Proposal for a Paradigm-Shifting Strategy***
Alexandru Szakács

280 ***Short-Term Seismic Precursor Anomalies of Hydrogen Concentration in Luojishan Hot Spring Bubbling Gas, Eastern Tibetan Plateau***
Xiaocheng Zhou, Yucong Yan, Wenya Fang, Wanli Wang, Hongyu Shi and Pengfei Li

292 ***New Possible Earthquake Precursor and Initial Area for Satellite Monitoring***
Atanas Vasilev, Milen Tsekov, Petar Petsinski, Konstantin Gerilowski, Violeta Slabakova, Dimitar Trukhchev, Emil Botev, Orlin Dimitrov, Nikolai Dobrev and Dimitar Parlichev

301 ***The Seismotectonic Significance of Geofluids in Italy***
Paola Vannoli, Giovanni Martinelli and Gianluca Valensise

327 ***Earthquake Shocks Around Delhi-NCR and the Adjoining Himalayan Front: A Seismotectonic Perspective***
Prosanta Kumar Khan, Sarada P. Mohanty, Partha P. Chakraborty and Rashmi Singh

342 ***Long Memory in Earthquake Time Series: The Case Study of the Geysers Geothermal Field***
S. Barani, L. Cristofaro, M. Taroni, L. A. Gil-Alaña and G. Ferretti

frontiers in Earth Science

EDITORIAL
published: 29 November 2021
doi: 10.3389/feart.2021.793911

Editorial: Achievements and New Frontiers in Research Oriented to Earthquake Forecasting

Giovanni Martinelli[1,2,3]*, *Antonella Peresan*[4] and *Ying Li*[5]

[1]Department of Palermo, INGV Istituto Nazionale di Geofisica e Vulcanologia, Palermo, Italy, [2]Northwest Institute of Eco-Environment and Resources, Chinese Academy of Sciences, Lanzhou, China, [3]Key Laboratory of Petroleum Resources, Gansu Province/Key Laboratory of Petroleum Resources Research, Institute of Geology and Geophysics, Chinese Academy of Sciences, Lanzhou, China, [4]National Institute of Oceanography and Applied Geophysics-OGS, Udine, Italy, [5]Institute of Earthquake Forecasting, China Earthquake Administration, Beijing, China

Keywords: earthquake preparation processes, stress field variations, earthquake source physics, earthquake forecasting, test site areas

Editorial on the Research Topic

Achievements and New Frontiers in Research Oriented to Earthquake Forecasting

Forecasting earthquakes is a challenging scientific task, due to the intrinsic complexity of the problem, as well as to the limited size and different accuracy of available observations. During the last decades increasing efforts have been devoted by geophysical research in an attempt to answer the following fundamental questions: 1) Which are the physical processes that take place in the Earth crust that are relevant for an earthquake to nucleate? 2) How can we observe, describe and model them statistically and physically? Although a clear univocal picture is still missing, a large amount of data and long-term observations accumulated over the time, as well as new methodological approaches, which eventually allow for development and verification of theoretical models.

Observations and physical models suggest that several processes in the Earth's lithosphere are predictable, but after substantial averaging and up to a limit. Accordingly, earthquake forecasting requires a holistic approach, and should be posed as an integrated, multi-scale process, narrowing down the magnitude range, territory, and time of expectation, all within the limits imposed by physics and data uncertainties. The understanding of governing laws, from long-term tectonic loading and slow nucleation to rapid rupture propagation, may contribute to estimate the stress state and temporal evolution of geophysical observables around seismically active areas. The use of preliminary time-independent information, such as seismotectonic setting of the study region, may be relevant to guide the search for different precursors (e.g., Crespi et al., 2020). Reducing space-time uncertainty of forecasts, however, it requires the use of additional, independent and reliable information, which can be provided by multi-disciplinary observations, "sampling" the system at different space-time scales.

A preliminary step toward earthquake forecasting is the identification of those parameters (physical, geological, seismological and chemical), whose space-time dynamics can be associated with the preparation process of crustal deformations that can be accompanied by earthquakes. Significant steps have been made towards assessing earthquake space-time correlations, clustering, and the emergence of seismicity patterns, showing the potential for reproducible and testable earthquake forecasting. Seismicity, however, is just one manifestation of Earth's complex dynamics prior to catastrophic earthquakes. Besides identified patterns and probabilistic models of earthquake occurrence, many newly available non seismological data collected on a global scale provide new opportunities for systematic analysis and model testing. A variety of geophysical and geochemical observables, ranging from ground-related deformation patterns (GPS, SAR, etc.) to pre-earthquake

OPEN ACCESS

Edited and reviewed by:
Carolina Lithgow-Bertelloni, UCLA Department of Earth, Planetary, and Space Sciences, United States

***Correspondence:**
Giovanni Martinelli
giovanni.martinelli15@gmail.com

Specialty section:
This article was submitted to Solid Earth Geophysics, a section of the journal Frontiers in Earth Science

Received: *12 October 2021*
Accepted: *01 November 2021*
Published: *29 November 2021*

Citation:
Martinelli G, Peresan A and Li Y (2021) Editorial: Achievements and New Frontiers in Research Oriented to Earthquake Forecasting. Front. Earth Sci. 9:793911. doi: 10.3389/feart.2021.793911

changes (be they geochemical, electromagnetic, hydrogeological or thermodynamic), recorded by ground based or by satellite based techniques may, be related to stress variations in the lithosphere prior to an eventual large earthquake.

What's new after decades of research? A renewed interest and attitude towards earthquake forecasting is testified by the increasing number of articles and special issues dedicated to this topic, also involving authors that so far were quite skeptical about such possibility. A wealth of new observables has been proposed, taking advantage from the large amount of data provided by new Earth observation systems and from increased computational power. However, resorting to the words by Richter (1964), efforts in converting such rather indefinite and elusive phenomena into precisely definable ones are still limited. Operational earthquake forecasting methods, in particular, should be testable and confirmed by evidence. It is indisputable that: "Only by careful recording and analysis of failures as well as successes can the eventual success of the total effort be evaluated and future directions charted" (Allen et al., 1976). The set of errors, namely the rates of failure and of the space-time extent of alarms, compared to those obtained in the same number of random guess trials permits evaluating the forecasting method effectiveness. As recalled by Freund et al. (2021), strong emphasis should be placed on continuous statistical testing of the relevance and confidence of the precursors, in order to assess and continue to improve the performance of the forecasts; according to the authors this became feasible in recent years thanks to new technological development in computing power and in big data management. However, while big data and current computational capabilities provide unprecedented opportunities for development and enhancing pattern recognition studies, "they open as well wide avenues for finding deceptive associations in inter- and *trans*-disciplinary data" (Kossobokov, 2022), thus stressing the need for rigorous statistical assessment of proposed precursors and related forecasts. With this Research Topic, we present the current state of the art in research on pre-earthquake processes, with a particular emphasis on:

1) Systematic analysis, physical interpretation and modeling of pre-earthquake processes (Shi et al.; Saltiel et al.; Anikiev et al.; Marchitelli et al.; Xiang et al.; Fu et al.);
2) Model validation and statistical assessment of proposed physical-based precursors (Gitis and Derendyaev; Kumar Khan et al.; Shebalin and Baranov);
3) Statistical methods and problems in earthquake forecast validation (Richards; Szakasz; Barani et al.);
4) Input data analysis and requirements for real-time model testing (Chelidze et al.)
5) Time-dependent seismic hazard assessment based on space-time characterization of earthquakes occurrence (Nekrasova and Peresan; Bukchin et al.);
6) Geophysical interpretation of non-seismological parameters linked to crustal deformation processes (Vasilev et al.; Fidani et al.; De Santis et al.);
7) Time series analysis of geophysical and geochemical parameters (Lyubushin);
8) Modeling of pressure fluctuation in deformating deep reservoirs etc. (He et al.);
9) Slow-slip geodetic precursors (Shi et al.);
10) Modeling of chemical and physical parameters fluctuations in faulted areas (Woith et al.; Vannoli et al.)
11) Spatial and temporal variation of geochemical and hydrogeological characteristics in seismic areas and their correlation to faults and to earthquake activity (Martinelli et al.; Kopylova and Boldina; Zhou et al. a; Zhou et al. b)

CONCLUSION

The papers in this Volume address the physical processes that occur in the Earth's crust prior to earthquake nucleation. Many newly available non seismological data collected on a worldwide scale, in addition to discovered patterns and probabilistic models of earthquake occurrence, present new opportunity for systematic study and model testing. A number of geophysical and geochemical measurements obtained by ground based or satellite based approaches, ranging from ground associated deformation patterns to pre seismic alterations, may be related to stress variations in the lithosphere before to an eventual big earthquake. We believe that an objective reappraisal of the proposed methods, along with state-of-the-art and novel observations, may contribute highlighting preferred research paths. The main goal of the Frontiers in Earth Sciences Research Topic on pre-earthquake observations, methods, and perspectives is to provide a current view of current knowledge of processes preceding earthquake occurrence, which can be used to set up earthquake forecasting experiments aimed at verifying their accuracy in large and small Test Site areas.

AUTHOR CONTRIBUTIONS

All authors listed have made a substantial, direct and intellectual contribution to the work, and approved it for publication.

REFERENCES

Allen, C. R., Edwards, W., Hall, W. J., Knopoff, L., Raleigh, C. B., Savit, C. H., et al. (1976). *Predicting Earthquakes: A Scientific and Technical Evaluationd with Implications for SocietyPanel on Earthquake Prediction of the Committee on Seismology, Assembly of Mathematical and Physical Sciences*. Washington, DC: National Research Council, US National Academy of Sciences.

Crespi, M., Kossobokov, V., Panza, G. F., and Peresan, A. (2020). Space-Time Precursory Features within Ground Velocities and Seismicity in North-Central Italy. *Pure Appl. Geophys.* 177, 369–386. doi:10.1007/s00024-019-02297-y

Freund, F., Ouillon, G., Scoville, J., and Sornette, D. (2021). Earthquake Precursors in the Light of Peroxy Defects Theory: Critical Review of Systematic

Observations. *Eur. Phys. J. Spec. Top.* 230, 7–46. doi:10.1140/epjst/e2020-000243-x

Kossobokov, V. (2022). "Hazard, Risks, and Prediction," in *Earthquakes and Sustainable Infrastructure* (Elsevier), 1–25. Chapter 1. doi:10.1016/B978-0-12-823503-4.00031-2

Richter, C. F. (1964). Discussion of Paper by V. I. Keylis-Borok and L. N. Malinovskaya, 'One Regularity in the Occurrence of strong Earthquakes'. *J. Geophys. Res.* 69 (14), 3025. doi:10.1029/jz069i014p03025

Conflict of Interest: The authors declare that the research was conducted in the absence of any commercial or financial relationships that could be construed as a potential conflict of interest.

Publisher's Note: All claims expressed in this article are solely those of the authors and do not necessarily represent those of their affiliated organizations, or those of the publisher, the editors and the reviewers. Any product that may be evaluated in this article, or claim that may be made by its manufacturer, is not guaranteed or endorsed by the publisher.

Copyright © 2021 Martinelli, Peresan and Li. This is an open-access article distributed under the terms of the Creative Commons Attribution License (CC BY). The use, distribution or reproduction in other forums is permitted, provided the original author(s) and the copyright owner(s) are credited and that the original publication in this journal is cited, in accordance with accepted academic practice. No use, distribution or reproduction is permitted which does not comply with these terms.

frontiers in Earth Science

ORIGINAL RESEARCH
published: 20 March 2020
doi: 10.3389/feart.2020.00052

Mechanical Mechanism of Fault Dislocation Based on *in situ* Stress State

Haoyu Shi[1,2], Fuqiong Huang[3], Zhenkai Ma[4], Yongjian Wang[1], Jicheng Feng[1] and Xu Gao[2]*

[1] North China Institute of Science and Technology, Beijing, China, [2] School of Resources and Safety Engineering, China University of Mining and Technology, Beijing, China, [3] China Earthquake Networks Center, Beijing, China, [4] School of Mining, Liaoning Technical University, Fuxin, China

Fault dislocation occurs under certain stress conditions. Based on the mechanical relationship between the direction of crustal stress and fault occurrence, three criteria – fault dislocation trend, fault strike dislocation trend, and dip dislocation trend – are put forward. According to these three criteria, the fault slip and the type of slip can be inferred. The parameters that have great influence on the characteristics of fault slip are fault dip angle, angle between horizontal principal stress and fault strike, depth, lateral pressure coefficient, internal friction angle, and cohesion of fault plane. Fault slip is more likely to occur in the environment of high deviation stress, low friction angle, and dip angle of about 40°. Fault rupture is a point-to-surface and deep-to-shallow process. When the criterion value of the local position of the fault is greater than 0, it will lead to the slip of the nearby fault. When the slip range of the fault extends to the surface, it will cause large earthquakes with large-scale surface rupture. The theoretical calculation is basically consistent with the numerical simulation results. According to the theory in this paper, the slip instability state of Longmen Mountain Fault Zone under different stress conditions is calculated, and the results show that when the lateral pressure coefficient is greater than 2.5, dislocation occurs in the deep part of the fault.

Keywords: fault dislocation, mechanics mechanism, dislocation criterion, *in situ* stress state, dislocation type

OPEN ACCESS

Edited by:
Giovanni Martinelli, National Institute of Geophysics and Volcanology, Section of Palermo, Italy

Reviewed by:
Bojing Zhu, National Astronomical Observatories (CAS), China
Antonello Piombo, University of Bologna, Italy

****Correspondence:***
Fuqiong Huang
hfqiong@seis.ac.cn

Specialty section:
This article was submitted to Structural Geology and Tectonics, a section of the journal Frontiers in Earth Science

Received: *07 December 2019*
Accepted: *13 February 2020*
Published: *20 March 2020*

Citation:
Shi H, Huang F, Ma Z, Wang Y, Feng J and Gao X (2020) Mechanical Mechanism of Fault Dislocation Based on in situ Stress State. Front. Earth Sci. 8:52. doi: 10.3389/feart.2020.00052

INTRODUCTION

How did the earthquake happen? What are the physical mechanisms of fault dislocation and fracture conduction and energy release? This is one of the pressing problems in seismology (Shearer, 2009; Lu et al., 2014). People have gone through a long process of understanding earthquakes; when earthquakes occur, they are often accompanied by fault slip or other phenomena. After the San Francisco earthquake in 1906, Lawson thought that the earthquake was caused by the sudden dislocation of the fault (Lawson and Reid, 1908). The theory of elastic rebound is put forward because of the fault dislocation under the action of in-situ stress (Reid, 1910; Liu, 2014). The coupling source theory is a hypothesis of source mechanics, which provides a theoretical basis for determining the initial fault dislocation position (Nakano, 1923). The theory of plate tectonics can explain that earthquakes are caused by the dislocation of plate margin faults (Le Pichon et al., 1973).

Seismic models based on fault activity have been proposed successively, such as the finite moving source model, the source model of double couple equivalent to fault dislocation (Haskell, 1964), the crack propagation model (Starr, 1928; Burridge and Knopoff, 1964), and the obstacle and convex body models (Das and Aki, 1977; Wyss et al., 1981), which describe the fault rupture process. Based on the butterfly plastic zone theory, Ma Nianjie et al. proposed a conjugate fault-seismic composite model, which partly explained the cause of earthquake (Ma et al., 2019a,b; Qiao et al., 2019).

A critical state of stress is a necessary condition for earthquake occurrence, such as the change of additional normal stress and shear stress caused by tidal action on fault plane (Li and Chen, 2018; Moncayo et al., 2019), which may lead to earthquake; the change of static Coulomb rupture stress caused by earthquake can affect the seismicity nearby (King et al., 1994; Stein, 1999; Wan et al., 2002). Coulomb stress explains the mechanical mechanism of fault dislocation to some extent, but it only pays attention to the stress increment part, ignoring the stress environment of the fault itself (Zhu and Miao, 2016). Under the continuous action of plate movement, faults will inevitably dislocate (Shi and Ma, 2018). In the Wenchuan earthquake, fault rupture propagation occurred (Chen and Li, 2018; Li et al., 2019). Experiments have suggested that earthquakes may be caused by dislocation due to overcoming fault friction under certain stress conditions (Zheng et al., 2019). According to the state of *in situ* stress and the occurrence of fault, the critical value of fault dislocation and the criterion value of fault dislocation type are calculated. By using the criterion of fault dislocation, whether fault dislocation occurs and the type of fault dislocation can be directly determined, and these criteria are applied to the judgment of fault dislocation of Longmenshan fault zone.

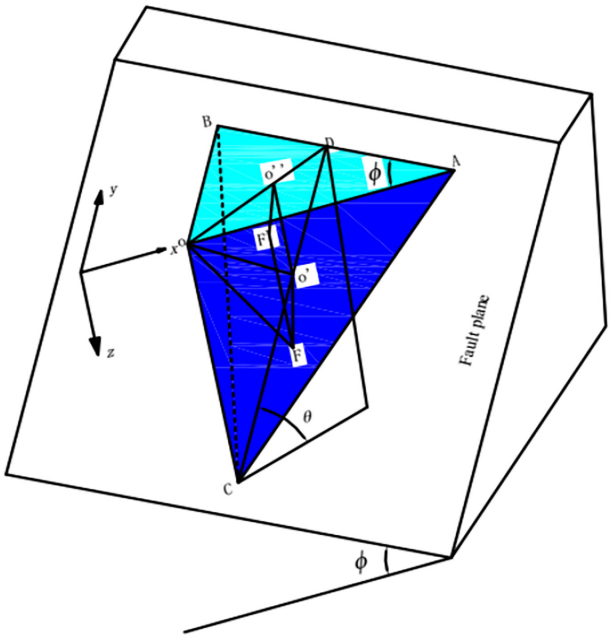

FIGURE 1 | Corresponding relationship between fault occurrence and principal stress direction. OA is the direction of maximum principal stress, OB is the direction of minimum principal stress, OC is the direction of vertical stress, of is the direction of resultant stress of OA and OB and OC acting on surface ABC, OO′ is the direction of normal resultant stress of three-dimensional stress acting on fault surface, O′F is the direction of tangential resultant stress of three-dimensional stress acting on fault surface, and O″F′ is the projection direction of O′F on the horizontal plane. The angle between the strike and horizontal principal stress direction of the fault slope is φ and the dip angle is θ; the maximum and minimum horizontal principal stress and vertical stress are σ_H, σ_h, and σ_v, respectively, and plane ABC is the unit plane on the fault plane.

MECHANICAL ANALYSIS OF FAULT DISLOCATION

We consider a planar fault surface (**Figure 1**). We adopt a coordinate system, and the direction of the maximum horizontal principal stress, the direction of the minimum horizontal principal stress, and the direction of the vertical stress represent the *x* axis, the *y* axis, and the *z* axis, respectively. The relationship between fault plane and *in situ* stress is shown in **Figure 1**.

Let the basic equation of the fault plane be:

$$ax + by + cz + d = 0 \tag{1}$$

When the dip of the fault plane is θ, it is the angle between the fault plane and the horizontal plane.

The horizontal equation passing through the origin is: $z = 0$.

Then,

$$\cos\theta = \frac{c}{\sqrt{a^2 + b^2 + c^2}} \tag{2}$$

Set the strike of fault plane to ϕ, when $z = 0$. That is to say, the equation of the line AB on the plane is:

$$y = -\tan\phi \cdot x \tag{3}$$

By calculating formulas (2) and (3), then formula (4):

$$\begin{cases} a = \tan\phi \\ b = 1 \\ c = \dfrac{1}{\cos\phi \cdot \tan\theta} \end{cases} \tag{4}$$

The plane equation of the fault plane can be obtained as follows:

$$\tan\phi \cdot x + y + \frac{1}{\cos\phi \cdot \tan\theta} \cdot z + d = 0 \tag{5}$$

$$\sqrt{a^2 + b^2 + c^2} = \frac{1}{\sin\theta \cdot \cos\phi}$$

The unit vector of line OO′ is:

$$\vec{e}_{OO'} = \left[(\sin\theta \cdot \sin\phi) \cdot i + \sin\theta \cdot \cos\phi \cdot j + \frac{1}{\cos\theta} \cdot k \right] \tag{6}$$

As can be seen from **Figure 1**, the normal vector of surface OBC is:

$$x = 0 \tag{7}$$

The normal vector of the surface OAC is:

$$y = 0 \tag{8}$$

The normal vector of the plane OAB is:

$$z = 0 \tag{9}$$

The angles between plane ABC and plane OBC, OAC, and OAB are a, β, and γ, respectively. According to formula (5):

$$\cos\alpha = \frac{a}{\sqrt{a^2+b^2+c^2}} = \tan\phi\cdot\sin\theta\cdot\cos\phi = \sin\theta\cdot\sin\phi \tag{10}$$

$$\cos\beta = \frac{b}{\sqrt{a^2+b^2+c^2}} = \sin\theta\cdot\cos\phi \tag{11}$$

$$\cos\gamma = \frac{\mathrm{c}}{\sqrt{a^2+b^2+c^2}} = \frac{\sin\theta\cdot\cos\phi}{\cos\phi\cdot\tan\theta} = \cos\theta \tag{12}$$

$$\text{Unit vector of line OA: } \vec{\mathrm{OA}} = i \tag{13}$$

$$\text{Unit vector of line OB: } \vec{\mathrm{OB}} = j \tag{14}$$

$$\text{Unit vector of line OC: } \vec{\mathrm{OC}} = k \tag{15}$$

The stress of three principal stresses acting on plane ABC is as follows:

$$\sigma_x = \sigma_\mathrm{H}\cdot\cos\alpha\cdot\vec{\mathrm{OA}} = \sigma_\mathrm{H}\cdot\sin\phi\cdot\sin\theta\cdot i \tag{16}$$

$$\sigma_y = \sigma_h\cdot\cos\beta\cdot\vec{\mathrm{OB}} = \sigma_h\cdot\cos\phi\cdot\sin\theta\cdot j \tag{17}$$

$$\sigma_z = \sigma_\mathrm{v}\cdot\cos\gamma\cdot\vec{OC} = \sigma_\mathrm{v}\cdot\cos\theta\cdot k \tag{18}$$

The resultant stress is:

$$\sigma_\mathrm{OF} = \sigma_\mathrm{H}\cdot\sin\phi\cdot\sin\theta\cdot i + \sigma_h\cdot\cos\phi\cdot\sin\theta\cdot j + \sigma_\mathrm{v}\cdot\cos\theta\cdot k \tag{19}$$

OF indicates the direction of the resultant stress, and the magnitude of the resultant stress is:

$$|\sigma_\mathrm{OF}| = \sqrt{(\sigma_\mathrm{H}\sin\phi\cdot\sin\theta)^2 + (\sigma_h\cos\phi\cdot\sin\theta)^2 + (\sigma_\mathrm{v}\cos\theta)^2} \tag{20}$$

Then, the angle between σ_OF and the normal vector of surface ABC is:

$$\varphi = \arccos\frac{\sigma_\mathrm{H}\sin\phi\cdot\sin\theta\cdot\tan\phi + \sigma_h\cos\phi\cdot\sin\theta + \sigma_\mathrm{v}\cos\theta\dfrac{1}{\cos\phi\cdot\tan\theta}}{\sqrt{\dfrac{1}{\cos\phi\cdot\sin\theta}}\sqrt{(\sigma_H\sin\phi\cdot\sin\theta)^2 + (\sigma_h\cos\phi\cdot\sin\theta)^2 + (\sigma_\mathrm{v}\cos\theta)^2}} \tag{21}$$

As shown in **Figure 1**, $\sigma_{\mathrm{OO}'}$ and $\sigma_{\mathrm{O}'\mathrm{F}}$ represent the normal stress component and tangential stress component of σ_OF in plane ABC, respectively:

$$|\sigma_{\mathrm{OO}'}| = |\sigma_\mathrm{OF}|\cdot\sin\varphi \tag{22}$$

$$\begin{aligned}\sigma_{\mathrm{OO}'} &= |\sigma_{\mathrm{OO}'}|\cdot\vec{e}_{\mathrm{OO}'} \\ &= \frac{|\sigma_\mathrm{OF}|\cdot\sin\varphi}{\sin\phi\cdot\cos\theta}\left[(\sin\phi\cdot\cos\theta\cdot\tan\phi)\cdot i + \sin\phi\cdot\cos\theta\cdot j + \frac{\sin\phi\cdot\cos\theta}{\cos\phi\cdot\tan\theta}\cdot k\right] \\ &= |\sigma_\mathrm{OF}|\cdot\sin\varphi\left(\tan\phi\cdot i + 1\cdot j + \frac{1}{\cos\phi\cdot\tan\theta}\cdot k\right)\end{aligned} \tag{23}$$

Because

$$\sigma_\mathrm{OF} = \sigma_{\mathrm{OO}'} + \sigma_{\mathrm{O}'\mathrm{F}} \tag{24}$$

Then, $\sigma_{\mathrm{O}'\mathrm{F}}$ can be obtained.

$$\begin{aligned}\sigma_{\mathrm{O}'\mathrm{F}} &= \sigma_\mathrm{OF} - \sigma_{\mathrm{OO}'} \\ &= (\sigma_\mathrm{H}\cdot\sin\phi\cdot\sin\theta - |\sigma_\mathrm{OF}|\cdot\sin\varphi\cdot\tan\phi)\cdot i \\ &\quad +(\sigma_h\cdot\cos\phi\cdot\sin\theta - |\sigma_\mathrm{OF}|\cdot\sin\varphi)\cdot j \\ &\quad +\left(\sigma_\mathrm{v}\cdot\cos\theta - \frac{|\sigma_\mathrm{OF}|\cdot\sin\varphi}{\cos\phi\cdot\tan\theta}\right)\cdot k\end{aligned} \tag{25}$$

Simplifying Eq. 25:

$$l = \sigma_\mathrm{H}\cdot\sin\phi\cdot\sin\theta - |\sigma_\mathrm{OF}|\cdot\sin\varphi\cdot\tan\phi \tag{26}$$

$$m = \sigma_h\cdot\cos\phi\cdot\sin\theta - |\sigma_\mathrm{OF}|\cdot\sin\varphi \tag{27}$$

$$n = \sigma_\mathrm{v}\cdot\cos\theta - \frac{|\sigma_\mathrm{OF}|\cdot\sin\varphi}{\cos\phi\cdot\tan\theta} \tag{28}$$

$$\sigma_{\mathrm{O}'\mathrm{F}} = l\cdot i + m\cdot j + n\cdot k \tag{29}$$

Whether a fault slips depends on the friction angle and cohesion of the fault plane, and the normal stress value of ABC on the fault plane is $|\sigma_{\mathrm{O}'\mathrm{O}}|$.

The tangential stress value σ_s is $|\sigma_{\mathrm{O}'\mathrm{F}}|$. The following relationships can be obtained:

$$f_1 = \sigma_s - \sigma_\mathrm{n}\cdot\tan\varphi - C \tag{30}$$

$$|\sigma_\mathrm{OF}| = \sqrt{(\sigma_\mathrm{H}\sin\phi\cdot\sin\theta)^2 + (\sigma_h\cos\phi\cdot\sin\theta)^2 + (\sigma_\mathrm{v}\cos\theta)^2} \tag{31}$$

$$|\sigma_{\mathrm{O}'\mathrm{O}}| = \sin\varphi\cdot\sqrt{(\sigma_\mathrm{H}\sin\phi\cdot\sin\theta)^2 + (\sigma_h\cos\phi\cdot\sin\theta)^2 + (\sigma_\mathrm{v}\cos\theta)^2} \tag{32}$$

$$|\sigma_{\mathrm{O}'\mathrm{F}}| = \cos\varphi\cdot\sqrt{(\sigma_\mathrm{H}\sin\phi\cdot\sin\theta)^2 + (\sigma_h\cos\phi\cdot\sin\theta)^2 + (\sigma_\mathrm{v}\cos\theta)^2} \tag{33}$$

In formula (30), C is the cohesion of fault plane. When $f_1 > 0$, the fault slips, and when $f_1 < 0$, the fault does not slip, so f_1 can be used as the criterion of strike slip.

In Eq. 29, n is the vertical component of $\sigma_{\mathrm{O}'\mathrm{F}}$, and the n value is related to the fault dislocation in the vertical direction; when $n > 0$, the fault has a downward slip trend. When $n = 0$, the fault has no vertical slip trend. When $n < 0$, the fault has an upward

slip trend. n can be used as a criterion for normal and reverse fault slip.

In order to judge the fault movement trend in horizontal direction, calculate the combined stress of $\sigma_{O'F}$ in the horizontal plane:

$$\sigma_{O''F'} = (l \cdot i + m \cdot j) \tag{34}$$

In order to obtain the relationship between direction and fault strike, rotating $\sigma_{O''F'}$ counterclockwise at φ, $\sigma'_{O''F}$.

$$\sigma'_{O''F'} = \left[(l \cdot \cos\phi + \mathrm{m} \cdot \sin\phi) \cdot i - (l \cdot \sin\phi - \mathrm{m} \cdot \cos\phi) \cdot j\right] \tag{35}$$

At this time, the vector i is consistent with the fault strike.

$$f_2 = l \cdot \cos\phi + \mathrm{m} \cdot \sin\phi \tag{36}$$

When $f_2 > 0$, fault sinistral slip. When $f_2 = 0$, the fault has no strike slip trend. When $f_2 < 0$, fault dextral dislocation. Therefore, f_2 can be used as the criterion of strike slip.

Then, when $f_1 \leq 0$, the fault is relatively stable, and when $f_1 > 0$, the fault is dislocation. The dislocation trend between faults can be judged by n value and f_2 value:

(1) When $n > 0, f_2 > 0$, the faults tend to move downward and leftward, that is, normal faults and leftward faults.
(2) When $n > 0$, $f_2 = 0$, there is a downward dislocation trend on the wall of the fault plane, i.e., normal fault-type dislocation.
(3) When $n > 0$, $f_2 < 0$, there is a downward and leftward dislocation trend on the wall of the fault plane, that is, normal fault and dextral dislocation.
(4) When $n = 0, f_2 > 0$, there is a right-lateral dislocation on the wall of the fault plane, i.e., left-lateral dislocation.
(5) When $n = 0, f_2 = 0$, there is no dislocation trend on the wall of the fault plane.
(6) When $n = 0$, $f_2 < 0$, there is a trend of left-lateral dislocation on the wall of the fault plane, that is, right-lateral dislocation.
(7) When $n < 0, f_2 > 0$, the faults tend to move upward and right, i.e., reverse faults and sinistral faults.
(8) When $n < 0, f_2 = 0$, the fault has upward dislocation trend, i.e., reverse fault type dislocation.
(9) When $n < 0, f_2 < 0$, the faults tend to move upward and left, i.e., reverse faults and right-handed faults.

INFLUENCING FACTORS OF FAULT DISLOCATION

There are many parameters affecting fault dislocation. As shown in **Figure 2**, fault dip angle, principal stress, fault strike angle, and depth are fixed parameters in a certain period of plate movement, while cohesion of fault plane has relatively little influence on fault plane slip. The influence of lateral pressure coefficient and internal friction angle is relatively large, and these two parameters are variable parameters, such as plate movement, long-range earthquake, tidal induction, and so on, which will cause minor changes in local geostress. For faults in critical state, such as f_1 value approaching 0, minor changes in geostress may prompt instantaneous slip of faults and cause earthquakes. Mining and mining activities cause a large amount of water to enter the fault, and the friction coefficient of the fault surface decreases, which leads to earthquakes.

As shown in **Figure 2A**, when the lateral pressure coefficient is 0.1, $f_1 > 0$, $n > 0$, and $f_2 < 0$, indicating that normal fault and right-lateral slip can occur at this time, when the lateral pressure coefficient is 0.1; when the lateral pressure coefficient is between 0.1 and 2.8, $f_1 < 0$, indicating that the fault does not slip; when the lateral pressure coefficient is greater than 2.8, $f_1 > 0$, $n < 0$, and $f_2 > 0$, indicating that the fault can produce both normal fault and left-lateral slip, thus indicating a high deviational stress environment. Faults are more prone to slip.

As shown in **Figure 2B**, when the dip angle of the fault is less than 24° or more than 56°, $f_1 < 0$ indicates that the fault does not slip; when the dip angle of the fault is between 24° and 56°, $f_1 > 0$, $n < 0$, and $f_2 > 0$, indicating that the fault can produce reverse fault and dextral dislocation, which indicates that the fault is more likely to slip at the dip angle of 40°.

As shown in **Figure 2C**, when the angle between the maximum horizontal principal stress and the fault is greater than 15°, $f_1 > 0$ and the fault plane slips, of which $n < 0$, indicating thrusting slip of the fault, while $f_2 > 0$ when the angle between the maximum horizontal principal stress and the fault is 15°–26°, 38°–52°, and 64°–78°, indicating right slip of hanging wall, i.e., thrusting and left-lateral slip, when the angle is 26°–38°, 52°–64°, and 78°–90°, $f_2 < 0$, indicating the fault. The hanging wall slips to the left, i.e., thrust and dextral slip.

As shown in **Figure 2D**, when the depth is greater than 1 km, $f_2 > 0$, $n < 0$, and $f_2 > 0$, indicating that thrusting and sinistral slip occur in faults, but the effect of depth on f_1 value is relatively small, which indicates the dispersion of focal depth.

As shown in **Figure 2E**, when the friction angle of the fault plane is less than 23°, $f_1 > 0$, $n < 0$, and $f_2 > 0$, indicating that thrust and sinistral slip occur on the fault. When the friction angle of the fault plane is greater than 23°, $f_1 < 0$, indicating that no slip occurs on the fault. It shows that the friction angle of the fault plane has a great influence on the slip of the fault.

As shown in **Figure 2F**, cohesion between fault planes is relatively small. When cohesion varies from 0 to 5.1 MPa, the variation range of f_1, n, and f_2 is relatively small, which indicates that the value has little influence on fault slip. Therefore, for deep faults, the effect of cohesion on fault plane can be neglected (Goodman, 1989).

According to f_1, n, and f_2, we can infer whether the fault is dislocated and its type. The parameters that have great influence on the characteristics of fault slip are fault

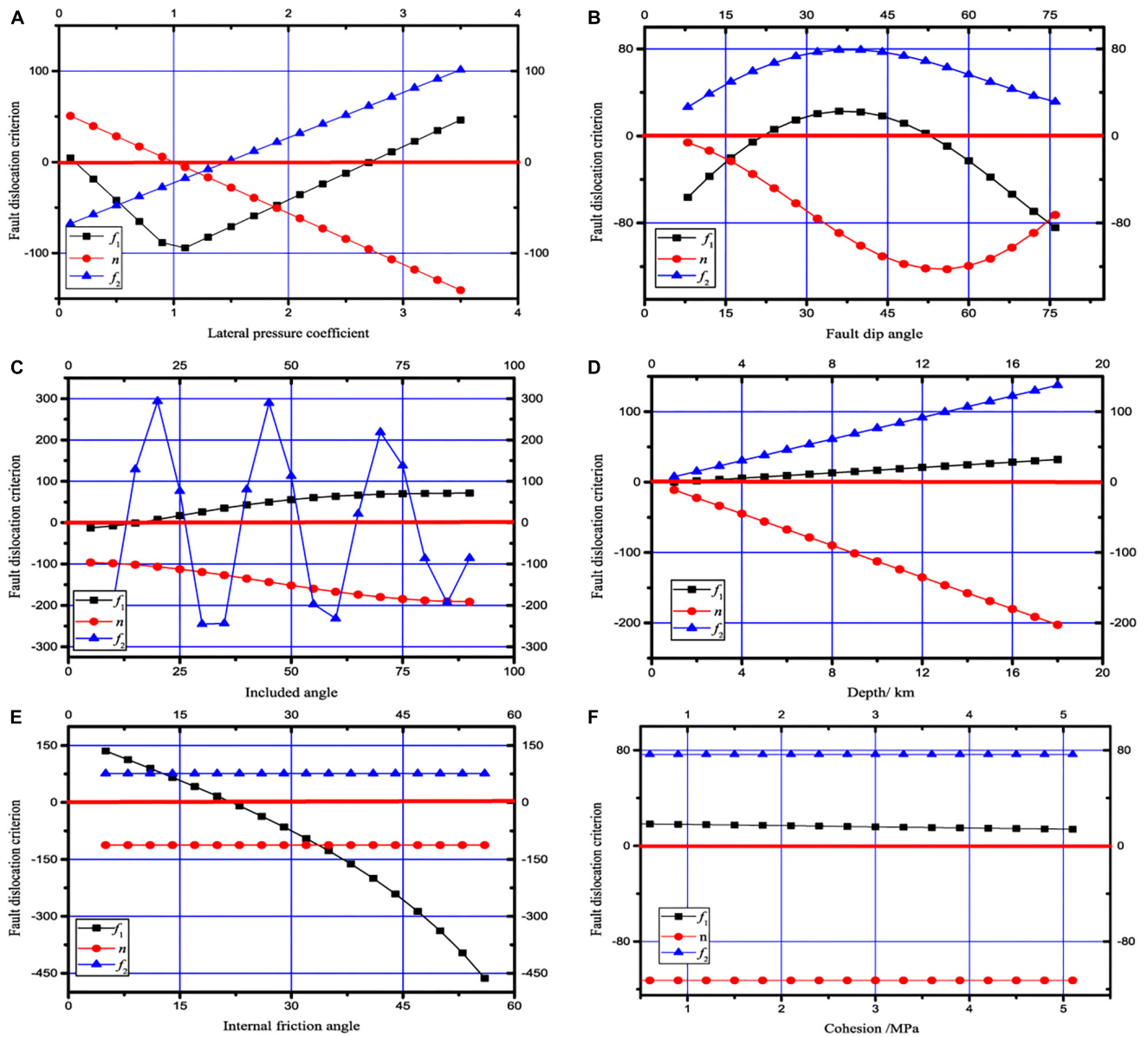

FIGURE 2 | Numeric diagram of fault slip criterion under different parameters. Given a set of data, the dip angle of the fault is $\theta = 45°$, the angle between the direction of principal stress σ_1 and the strike of the fault is $\varphi = 25°$ degrees, the depth $H = 10$ km, the lateral pressure coefficient is $\lambda = 3$, the friction angle in the fault plane is $\varphi = 20°$, the cohesion force is 2 MPa, $\sigma_3 = \gamma H$, and $\sigma_2 = 0.5\ (1 + \lambda)\ \sigma_3$. **(A)** Fault dislocation criterion under different lateral pressure coefficients, **(B)** fault dislocation criterion under different fault dip angles, **(C)** fault dislocation criterion under different included angles, **(D)** fault dislocation criterion under different depth, **(E)** fault dislocation criterion under different internal friction angles, **(F)** fault dislocation criterion under different cohesions.

dip angle, angle between horizontal principal stress and fault strike, depth, lateral pressure coefficient, internal friction angle, and cohesion of fault plane. Faults with dislocation generally have the following characteristics: firstly, in high deviational stress environment, if the lateral pressure coefficient is less than 0.1 or more than 2.8, but there is no fault dislocation in the area where the lateral pressure coefficient approaches 1; secondly, the fault is more prone to slip at the dip angle of 40°; thirdly, the fault surface with low friction angle is more prone to slip.

DISCUSSION

(1) Five groups of simulation schemes are designed. The occurrence and mechanical parameters of faults and the state of regional principal stress are shown in **Table 1**. The values of fault slip criteria f_1, n, and f_2 can be obtained by substituting the parameters into formulas (1)–(36) in turn. According to the theoretical calculation results, the faults in schemes 1 and 2 have not yet produced slip, while those in schemes 3–5 have slip, and

TABLE 1 | Summary of simulation schemes and calculation results.

Simulation schemes	Dip angle (°)	Included angle (°)	σ_1 (MPa)	σ_2 (MPa)	σ_3 (MPa)	Friction angle (°)	Cohesion (MPa)	f_1	n	f_2
1	54	45	405	250	270	20	1	−44.46	−22.07	178.99
2	54	45	540	400	270	20	1	−14.44	−57.64	230.83
3	54	45	675	450	270	20	1	17.92	−93.22	282.67
4	54	45	810	400	270	20	1	50.98	−128.80	334.51
5	54	45	540	300	270	17	1	6.99	−57.64	230.83

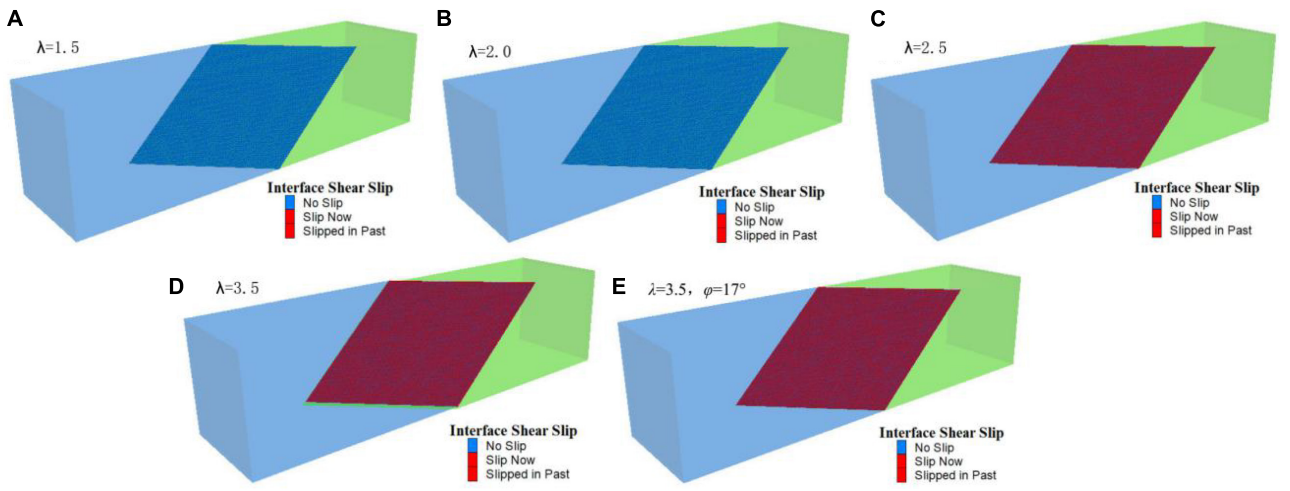

FIGURE 3 | Fault slip simulation under different schemes. The simulation scheme is listed in **Table 1**, and **(A)** shows that the fault of simulation scheme 1 has no dislocation, **(B)** shows that the fault of simulation scheme 2 has no dislocation, **(C)** shows that the fault of simulation scheme 3 has no dislocation, **(D)** shows that the fault of simulation scheme 4 has dislocation, **(E)** shows that the fault of simulation scheme 5 has dislocation.

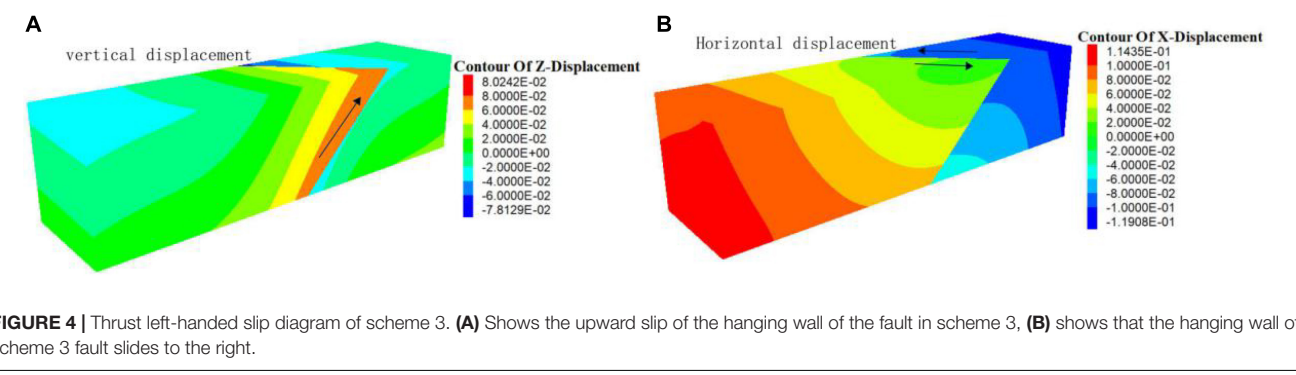

FIGURE 4 | Thrust left-handed slip diagram of scheme 3. **(A)** Shows the upward slip of the hanging wall of the fault in scheme 3, **(B)** shows that the hanging wall of scheme 3 fault slides to the right.

$n < 0$ and $f_2 > 0$. It can be judged that thrusting sinistral slip occurs in faults. The simulation results are basically consistent with the theoretical calculation criteria, as shown in **Figure 3**, and the slip trend of schemes 3–5 is consistent with the theoretical calculation results. As shown in **Figure 4**, the upper wall of the fault produces upward and right displacement, indicating that the fault has thrusting left-lateral dislocation (Liu and Song, 1999; Huang et al., 2017).

(2) Taking Longmenshan fault zone as an example, the vertical stress is calculated by γH, and γ is 27 KN/m^3. The *in situ* stress data are shown in **Table 2** (Chen et al., 2012; Qin et al., 2018); the lateral pressure coefficient is 1.0–5.0, the angle between maximum horizontal principal stress and fault strike is about 80°, the cohesion of Longmenshan fault zone is 2MPa, the internal friction angle is 20°, and the Longmenshan fault zone is a typical shovel thrust fault. The relationship between dip and depth is shown in **Figure 5**. The slip of faults under different lateral pressure coefficients can be calculated, as shown in **Figure 6**, when the lateral pressure coefficient is less than 2; no slip occurs on the fault plane. When

TABLE 2 | Stress measurement values of the Longmen mountain fault zone QQ (Chen et al., 2012; Qin et al., 2018).

Drilling number	Depth (m)	S_H (MPa)	S_V (MPa)	S_H/S_V
JY-1	178	11.26	4.73	2.38
JY-2	195	6.55	5.17	1.27
JY-3	193	15.91	5.11	3.11
PW-1	439	37.55	11.63	3.23
PW-1	323	33.12	8.56	3.87
KD-1	185	16.61	4.91	3.38
QQ-99	280	25.53	7.42	3.44
QQ-09	214	23.73	5.68	4.18
QQ-14	188	21.02	11.51	4.98
YX-02	733	28.04	19.81	1.42
YX-09	178	16.36	4.72	3.47

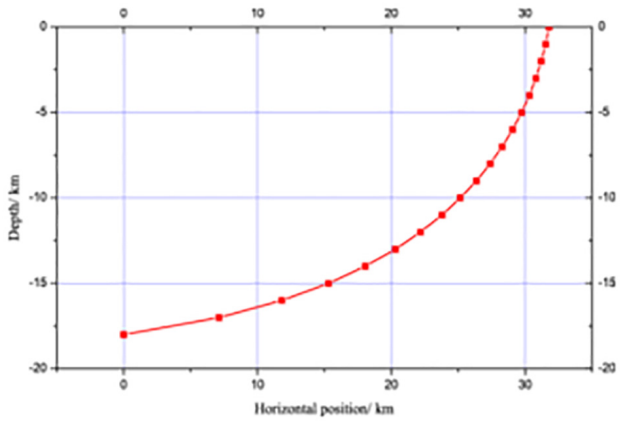

FIGURE 5 | Diagram of occurrence of Longmenshan fault.

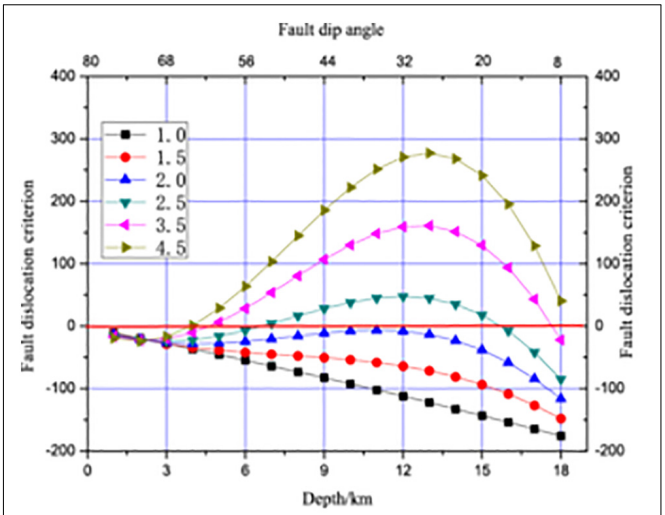

FIGURE 6 | f_1 value of Longmenshan fault zone under different side pressure coefficients.

the lateral pressure coefficient is greater than 2.5, slip occurs at the depth of 12 km. With the increase of the lateral pressure coefficient, the range of slip increases, but the shallow part of the fault is still locked. At this time, the values of n and f_2 are less than 0, which indicates that when the lateral pressure coefficient is greater than 2.5, the fault will undergo thrusting and dextral slip or earthquake. Therefore, when a small stress variable is applied to a fault in the critical state, the lateral pressure coefficient will change, and the fracture range of the fault will expand accordingly. It is possible for an earthquake to be triggered by a small stress change (Shi et al., 2019). The triggering stress includes dynamic and static (Ma, 2010). For example, plate movement and other tectonic processes can cause slow and stable changes in tectonic stress. Solid tidal force, reservoir water level change, celestial tidal force, and strong earthquake stress wave can cause dynamic stress changes (Huang and Ma, 2008).

(3) Fault rupture is a process from point to surface, from deep to shallow. When the slip criterion f_2 of a deep point of fault is greater than 0, the point will dislocate, which will lead to the increase or decrease of tangential stress around the point, and then the fault near the point will slip. When the fault slip range is small, it can cause small earthquakes. When the fault slip range extends to the surface, it can cause large earthquakes with large-scale surface rupture (Hu and Wang, 2008; Wang et al., 2012). When a fault dislocation occurs, it will inevitably lead to volume expansion, stress reduction, and energy release of local rock mass near the fault. The strain energy released may become the energy source of the earthquake. For example, the rupture process of Wenchuan earthquake is initiated by the NW-trending Xiaoyudong fault, which triggered the Beichuan-Yingxiu fault and the Pengguan fault, and resulted in the cascade rupture of the Beichuan-Yingxiu fault in NE direction (Qian and Han, 2010).

CONCLUSION

Fault dislocation occurs under a certain mechanical mechanism. According to the relationship between *in situ* stress and fault occurrence, three criteria are put forward in this paper, i.e., fault tendency dislocation trend criterion n, strike dislocation trend criterion f_1, and fault occurrence dislocation criterion f_1. According to these criteria, the stability of fault can be evaluated directly. If f_1 approaches zero, the fault has the risk of dislocation. Fault dislocation is usually a process from deep to shallow, which is characteristic of the fault rupture process of Wenchuan earthquake. Using the mechanical model in this paper, we can calculate the dislocation criteria of different depths of major faults and evaluate the stability of faults. For unstable faults, we should further

monitor the changes of *in situ* stress. However, our work in this measurement can be as a reference for enhancing the stress/strain monitoring network in both precision and density of observation station.

DATA AVAILABILITY STATEMENT

All datasets generated for this study are included in the article/supplementary material.

AUTHOR CONTRIBUTIONS

HS responsible for the writing of the manuscript. FH provides the writing ideas of the paper and gives guidance in the writing process. ZM assists in completing the graphic processing work. YW provided geological data and JF participated in the derivation of the formula. XG assists in data sorting.

FUNDING

The authors are grateful to the financial support provided by the Foundation of Basic Research of Central University (3142018022) and the National Natural Science Foundation of China (41274061 and 51804118).

ACKNOWLEDGMENTS

Thanks to the editor GM for his article organization, reviewers BZ and AP for their pertinent suggestions, and Professor Nianjie Ma of China University of Mining and Technology (Beijing) for his help in the writing process.

REFERENCES

Burridge, R., and Knopoff, L. (1964). Body force equivalents for seismic dislocations. *Bull. Seism. Soc. Am.* 54, 1875–1888.

Chen, Q. C., Feng, C. J., Meng, W., Qing, X. H., and An, Q. M. (2012). Analysis of in situ stress measurements at the northeastern section of the longmenshanfault zone after the 5.12 Wenchuan earthquake. *Chinese J. Geophys.* 55, 3923–3932.

Chen, Q. F., and Li, L. (2018). Deep deformation of the longmenshan fault zone related to the Wenchuan earthquake. *Chin. Sci. Bull.* 63, 1917–1933. doi: 10.1360/n972018-00362

Das, S., and Aki, K. (1977). Fault plane with barriers: a versatile earthquake model. *J. Geophys. Res.* 82, 5658–5670. doi: 10.1029/jb082i036p05658

Goodman, R. E. (1989). *Introduction to Rock Mechanics*, 2nd Edn, New York, NY: Wiley.

Haskell, N. A. (1964). Total energy and energy spectral density of elastic wave radiation from propagating faults. *Bul.l Seism. Soc. Am.* 54, 1811–1841.

Hu, Y., and Wang, K. (2008). Coseismic strengthening of the shallow portion of the subduction fault and its effects on wedge taper. *J. Geophys. Res.* 113: B12411.

Huang, F. Q., Li, M., Ma, Y. C., Han, Y. Y., Tian, L., Yan, W. (2017). Studies on earthquake precursorsin China: a review for recent 50 years. *Geod. Geodyn.* 8, 1–12. doi: 10.1016/j.geog.2016.12.002

Huang, Y. M., and Ma, S. L. (2008). Discussion on mechanism of earthquake triggering by stress. *Earthquake* 28, 95–102.

King, G. C. P., Stein, R. S., and Lin, J. (1994). Static stress ch anges and th e triggering of earth quakes. *Bull. Seism. Soc. Am.* 84, 935–953.

Lawson, A. C., and Reid, H. F. (1908). *The California Earthquake of April 18, 1906: Report of the State Earthquake Investigation Commission*. Washington, DC: Carnegie institution of Washington.

Le Pichon, X., Francheteau, J., and Bonnin, J. (1973). *Plate Tectonics. Developments in Geotectonics*. Amsterdam: Elsevier.

Li, Y. E., and Chen, X. Z. (2018). Earth tidal stress as an earthquake trigger prior to the Wenchuan earthquake, Sichuan, China (in Chinese). *Chin. Sci. Bull.* 63, 1962–1970. doi: 10.1360/n972018-00259

Li, C. Y., Li, X. N., and Wei, Z. Y. (2019). Fault geometries and structures associated with the rupture endpoints of the 2008 Mw 7.9 wenchuan earthquake eastern tibet plateau China. *Tectonics* 38, 2161–2184. doi: 10.1029/2018tc005425

Liu, J., and Song, H. Z. (1999). Estimation of earthquake risk for northern North China by numerical modeling. *Seismol. Geol.* 21, 221–228.

Liu, L. Q. (2014). Elastic rebound model: from the classic to the future. *Seismol. Geol.* 36, 825–832.

Lu, K. Q., Cao, Z. X., Hou, M. Y., Jiang, Z. H., Shen, R., Wang, Q., et al. (2014). On the mechanism of earthquake. *Acta Phys. Sin.* 63:219101.

Ma, J. (2010). Uncertainty of the earthquakes and earthquake mechanism and seismic triggering effect of instantaneous factors. *Chin. J. Nat.* 32, 311–313.

Ma, J., Zhao, Z. Q., Shi, H. Y., Guo, X. F., Qiao, J. Y., Ma, N. J. (2019a). Sources of seismic energy based on butterfly failure theory. *J. China Coal Soc.* 44, 1654–1665.

Ma, N. J., Ma, J., Zhao, Z. Q., Guo, X. F., Shi, H. Y., Qiao, J. Y. (2019b). Mechanical mechanism and evolution of X-shaped conjugate shear fracturesseism. *J. China Coal Soc.* 44, 1647–1653.

Moncayo, G. A., Monsalve, G., and Zuluaga, J. I. (2019). Tidal coulomb failure stresses in the northern andean intermediate depth seismic clusters: implications for a possible correlation between tides and seismicity. *Tectonophysics* 762, 61–68.

Nakano, H. (1923). Note on the nature of forces which give rise to the earthquake motions. *Seismol. Bull. Centr. Meteorol. Obs. Tokyo* 1, 92–120.

Qian, Q., and Han, Z. J. (2010). Determinationoftheinitialruptureofthe2008 Wenchuan MS8.0 earthquake form analysis of faultinteraction during the main shock process. *Earth Sci. Front.* 17, 84–92.

Qiao, J. Y., Ma, N. J., Ma, J., Zhao, Z. Q., Guo, X. F., Shi, H. Y. (2019). Conjugate shear fracture-seismic composite model based on structural stability of dynamic system. *J. China Coal Soc.* 44, 1637–1646.

Qin, X. H., Chen, Q. C., Meng, W., Tan, C. X., Zhang, C. Y., Feng, C. J. (2018). Evaluatingmeasured insitu stress state changes associated with earthquakes and its implications: a case study in the longmenshan fault zone. *J. Geomech.* 24, 309–320.

Reid, H. F. (1910). *Mechanics of the earthquake the California Earthquake of April 18 1906. Report of the State Investigation Commission*. Washington, DC: Carnegie Institution of Washington.

Shearer, P. M. (2009). *Introduction to Seismology*, 2nd Edn, New York: Cambridge University Press.

Shi, H. Y., and Ma, N. J. (2018). Geomorphic formation and crustal stress evolution mechanism in the Longmenshan fault zone and its adjacent regions. *Acta Seismol. Sin.* 40, 332–340.

Shi, H. Y., Ma, N. J., Shi, J. J., Li, N., and Ma, J. (2019). Simulation on energy release of fault rock mass triggered by stress incrementand discussion on seismogenesis: taking longmenshan fault zone as an example. *Acta Seismol. Sin.* 41, 502–511.

Starr, A. T. (1928). Slip in a crystal and rupture in a solid due to shear. *Proc. Amb. Philso. Soc.* 24, 489–500. doi: 10.1017/s0305004100014626

Stein, R. S. (1999). The role of stress transfer in earthquake occurrence. *Nature* 402, 605–609. doi: 10.1038/45144

Wan, Y. G., Wu, Z. L., Zhou, G. W., Huang, J., and Qin, L. X. (2002). Research on seismic stress triggering. *Acta Seismol. Sin.* 24, 533–551.

Wang, K., Hu, Y., and He, J. (2012). Deformation cycles of subduction earthquakes in a viscoelastic Earth. *Nature* 484, 327–332. doi: 10.1038/nature11032

Wyss, M., Johnston, A. C., and Klein, F. W. (1981). Multiple asperity model for earthquake prediction. *Nature* 289, 231–234. doi: 10.1038/289231a0

Zheng, L., Rivière, J., Yang, Q., Marpm, J., and Marone, C. (2019). On the mechanics of granular shear: the effect of normal stress and layerthickness on stick-slip properties. *Tectonophysics* 763, 86–99. doi: 10.1016/j.tecto.2019.04.010

Zhu, S. B., and Miao, M. (2016). On the study of earthquake triggering: solution to paradox that Coulomb stresses increase with frictional coefficients. *Chin. J. Geophys.* 59, 169–173.

Conflict of Interest: The authors declare that the research was conducted in the absence of any commercial or financial relationships that could be construed as a potential conflict of interest.

Copyright © 2020 Shi, Huang, Ma, Wang, Feng and Gao. This is an open-access article distributed under the terms of the Creative Commons Attribution License (CC BY). The use, distribution or reproduction in other forums is permitted, provided the original author(s) and the copyright owner(s) are credited and that the original publication in this journal is cited, in accordance with accepted academic practice. No use, distribution or reproduction is permitted which does not comply with these terms.

frontiers in Earth Science

ORIGINAL RESEARCH
published: 18 May 2020
doi: 10.3389/feart.2020.00151

Structural Controls on Aftershock Distribution in Subduction Zones

*Simon Richards**

Independent Research Geologist, Brisbane, QLD, Australia

The trench-parallel distribution of aftershocks generated after a major subduction-related earthquake does not conform to a fractal or normal distribution as expected but does appear to be spatially constrained by fractures on the subducting oceanic crust. Newly developed and very detailed 3D models of subducting plates (slabs) are combined with high-resolution topographic and bathymetric models of the crustal upper-plate and subducting lower-plate respectively to show how irregularities such as transform faults, spreading centers, fossil subduction zones and vertical tears form structural barriers to the spatial distribution of subduction zone aftershocks. When correctly constructed, slab models can now be used to better forecast the lateral (along-arc) extent of damaging aftershock swarms following large magnitude subduction-related earthquakes. Two earthquakes, [magnitude M_W 7.8 in Vanuatu, 7th October 2009 (UTC) and magnitude M_W 8.8 in southern Chile, 27th February 2010 (UTC)] were followed by hundreds of aftershocks, with many recording magnitudes over M_W 6.5. Closer examination of these aftershocks and their spatial distribution indicate that they were unexpectedly confined to discrete sections of the subducting plate. It is revealed here that lithospheric-scale structures including fossil oceanic transform faults represent crustal and lithosphere-scale fractures in the crust that terminates the lateral spread of aftershocks. This contrasts with the predicted decrease in aftershock size and number with increasing distance from the epicenter referred to as the Omori (power law) distribution. This hypothesis addresses the paradigm that oceanic crust is a single, semi-continuous and uniform section of crust where the lateral distribution of earthquakes is described in terms of uniform rock mechanics. Additional research on the M_W 9.0 earthquake in Japan [11th March 2011 (UTC)] and the M_W 8.0 earthquake in the eastern Solomon Islands [6th February 2013 (UTC)] supports the aforementioned hypothesis. Using new techniques to help define the location of sub-plate boundaries, it is now possible to generate aftershock probability maps for some of the most seismically active subduction margins around the world.

Keywords: subduction, tectonics, earthquakes, aftershocks, structural geology, Vanuatu, South America

OPEN ACCESS

Edited by:
Giovanni Martinelli, National Institute of Geophysics and Volcanology, Italy

Reviewed by:
Masanao Shinohara, The University of Tokyo, Japan
Federico Pasquaré Mariotto, University of Insubria, Italy

***Correspondence:**
Simon Richards
ausflats@gmail.com

Specialty section:
This article was submitted to Structural Geology and Tectonics, a section of the journal Frontiers in Earth Science

Received: *25 March 2020*
Accepted: *21 April 2020*
Published: *18 May 2020*

Citation:
Richards S (2020) Structural Controls on Aftershock Distribution in Subduction Zones. Front. Earth Sci. 8:151. doi: 10.3389/feart.2020.00151

INTRODUCTION

The impact of a large magnitude earthquakes ($M_W > 7.0$) and associated aftershocks can be devastating, for example, the 2011 Japan earthquake and Tsunami (Norio et al., 2011) or the Mw 7.0 earthquake in Haiti, 2010 (Hayes et al., 2010; Shan et al., 2011 and references therein]. Large earthquakes are always associated with a swarm of aftershocks with individual events attaining magnitudes almost as large as that of the original event and often over M_W 6.5. In many cases, these

aftershocks can be just as damaging as the primary event (Thorvald, 1997; Spencer et al., 2004). The spatial distribution of aftershocks around a single event means that areas often located hundreds of kilometers from the principal earthquake may be affected and the aftershocks may persist for over a month after the initial event. If the spatial extent of these aftershocks can be more accurately constrained and defined, then accurate forecasting and advanced warning systems can also be developed. This paper presents detailed evidence from two locations where large earthquakes have recently occurred: in the northern New Hebrides Trench near Vanuatu and near the city of Concepción in Southern Chile. The Vanuatu area was initially selected due to the abundance of structural and tectonic information in the area. In order to investigate the hypothesis at a global-scale, these two earthquakes are compared with four other historical earthquakes; (1) a magnitude M_W 8.3 earthquake in the Kuril Islands in November of 2006, (2) a magnitude M_W 8.0 earthquake in the western Aleutians in May of 1986, (3) the more recent Mw 9.0 earthquake in Japan [11th March 2011 (UTC)] and finally, (4) a Mw 8.0 earthquake in the eastern Solomon Islands [6th February 2008 (UTC)]. The earthquakes have been selected from subduction zones around the world in order to test the hypothesis in different subduction systems.

The following assessment of several large (Mw > 7.0), subduction-related earthquakes builds on existing evidence that the presence of geological irregularities such as seamounts or other bathymetric highs on the subducting plate typically focus the trigger point of a major subduction-related earthquake (Kelleher and McCann, 1976; Nishizawa et al., 2009; Das and Watts, 2009; Watts et al., 2010). Resent research by Sparkes et al. (2010) has shown that the northern limit of rupture propagation after the Mw 8.8 earthquake on the west coast of Chile (Maule, February, 2010) was terminated by the presence of the Juan Fernandez Ridge which is a bathymetric high on the subducting Nazca Oceanic Plate. Accordingly, bathymetric anomalies such as bathymetric highs appear to stop the lateral rupture propagation of aftershocks because they are areas where discernible changes in the strength, thickness and temperature of the subducting crust exist. Here evidence is presented to demonstrate that the lateral boundaries of the domain of rupture and subsequent aftershocks is not confined by bathymetric highs but appear to be very well-constrained to within major fracture zones in the subducting oceanic crust.

PLATE STRUCTURE

Transform faults are laterally extensive, vertical fractures that develop at oceanic spreading center and propagate from the surface of the crust to the base of the lithosphere (e.g., Abercrombie and Ekström, 2001). The fractures initially form at oceanic spreading centers (Wilson, 1965); however, due to divergent plate motion, these faults and the sections of oceanic crust that they separate essentially migrate away (perpendicular) from the spreading center. At the point where the oceanic crust moves beyond the limits of the spreading, the two adjacent sections of oceanic crust continue to migrate laterally but at the same velocity which in turn causes the fault to become mostly inactive and likely only accommodate very small amounts of displacement. At this point, the adjacent sections of oceanic crust are considered semi-coupled and seismicity is dramatically reduced. Another significant feature of these oceanic fractures is the high proportion of serpentinized crust that they may contain relative to adjacent oceanic crust (Rona et al., 1987) thereby making them mechanically very different to the adjacent oceanic crust (e.g., Lowrie et al., 1986; Behn et al., 2002; Kuna et al., 2019).

Both the oceanic crust and the fractures that they develop at the spreading center are subducted at convergent plate boundaries. Subduction zones exhibit complex geometries, variable plate convergent directions and most are arc-like in shape. In order to accommodate the subduction of generally flat oceanic crust into irregularly shaped subduction zones, the subducting plate must deform (e.g., Schellart and Lister, 2004). Recent mapping of subducting slabs in three dimensions has demonstrated that this deformation is accommodated by large- and small-scale displacements along existing zones of weakness such as oceanic fracture zones that, in some instances are interpreted to have developed into vertical tears of the subducting plate (Pesce, 1996; Burkett and Billen, 2010; Richards and Holm, 2013). Other features that can also sub-divide the oceanic crust into smaller segments may include fossil plate boundaries including subduction zones, spreading centers or strike-slip plate boundaries (Burkett and Billen, 2010). Regardless, these features all represent regions where the plate exhibits an existing break that extends from the surface to the base of the lithosphere.

In an attempt to better resolve how structures on the seafloor influence subduction zone morphologies and the distribution of earthquake aftershocks, a method of accurately defining the slab geometry has been developed. The methods and some results of this work are published in Richards et al. (2007). The same techniques have been used to construct accurate models of slab geometries presented in this paper. In subduction zone settings, earthquakes primarily occur at or near to the interface between the overriding and subducting plate but also within the subducting slab; this is the Wadati-Benioff zone. A 3-dimensional map of the slab can be developed by accurately mapping out the limits of the seismogenic zone (Richards et al., 2007). Variations in the dip and the strike of the Wadati-Benioff zone reflect variations in the geometry of the subducting plate. Results so far show that subducting slabs are not smooth sheets as often depicted, rather they are highly irregular, folded and often exhibit vertical and horizontal tears. Like folds and faults preserved in crustal rocks exposed at the Earth's surface, these variations in slab geometry reflect processes such as changes in the rate or angle of subduction, changes in the shape of the trench or even the arrival of buoyant oceanic or continental crust or, most importantly, the subduction of oceanic fracture zones (Richards et al., 2007; Billen, 2008).

RESULTS AND INTERPRETATION

The hypothesis presented here is that subducted oceanic crust is divided into sub-plates and that these boundaries (i.e., oceanic

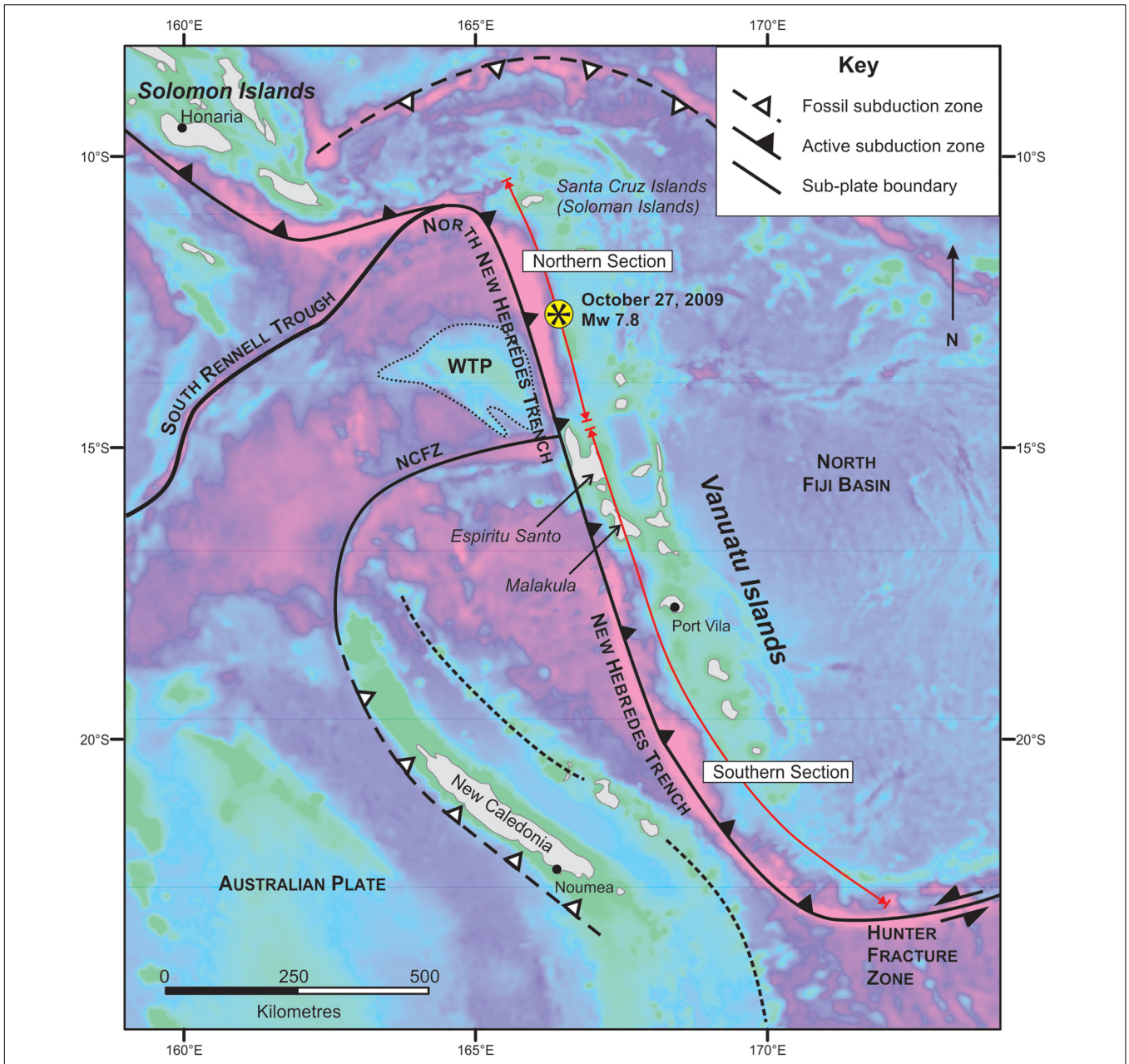

FIGURE 1 | Map of the southeastern Solomon Islands and the Vanuatu Arc showing the major tectonic features of the region as well as the location of the magnitude 7.8 earthquake in 2009. The subduction margin is divided into northern and southern sections by the major structures; the South Renell Trough and the New Hebrides Trench.

fractures) limit the distribution of aftershocks; this can be demonstrated for the magnitude M_W 7.8 earthquake in the central part of the northern New Hebrides Trench in October of 2009 (**Figure 1**; Cleveland et al., 2014). Oceanic crust entering the trench is extremely irregular and characterized by major structures including the West Torres Plateau and the South Renell Trough. The crust and associated subducted plate is segmented into two discrete sections, a northern and southern section separated by two prominent vertical tears (**Figure 2**). The principal vertical tear separating the two sections is the extinct New Caledonia Fracture Zone (NCFZ) or also referred to as the d'Entrecasteaux Ridge which is a strike-slip fault that formed the northern margin to the 48–25 Ma old New Caledonian arc (Schellart et al., 2002). The NE-trending fracture system is an ancient strike-slip plate margin that formed in response to NE-directed subduction of the Australian plate (**Figure 1**) below the New Caledonian Arc (Schellart, 2007). The southern limit to the southernmost slab section is the Hunter Fracture Zone. This is a curvi-planar ENE-trending left-lateral fault and series of connected spreading centers that formed during asymmetric

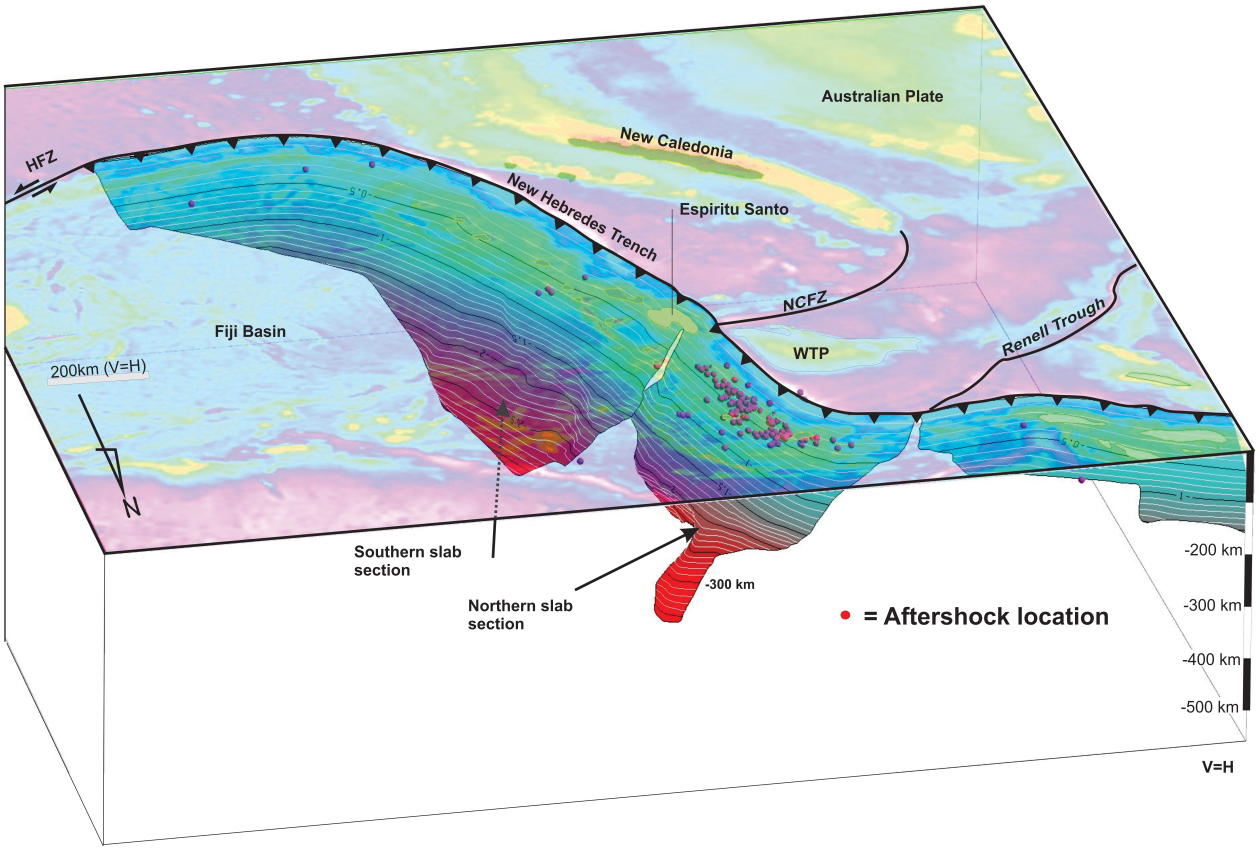

FIGURE 2 | Oblique view of the subducting Vanuatu Slab and adjacent seafloor viewed looking to the South East. Shown here is a 3D map of the subducted plate highlighting the shape of the slab but also the location of the sub-plate and respective slab boundaries as the two major slab tears located down-dip from the New Caledonia Fault Zone (NCFZ) and the Renell Trough. Aftershock seismicity is represented by the cluster of red spheres and is spatially limited to within the northern section of the subducting plate. The slab is shaded cyan to red to represent increasing depth of the subducted plate. HFZ, Hunter Fracture Zone.

rollback of the New Hebrides Trench (Schellart et al., 2002). Like the NCFZ, this fracture also extends to the base of the lithosphere. The second of the two slab sections is bound to the north by the Renell Trough (also spelled Rennell) and to the south by the subducted NCFZ. The geometry of the subducted slab is shown in detail to a depth of 500 km in **Figure 2**.

The magnitude M_W 7.8 earthquake on the 7th of October 2009 occurred approximately midway between the NCFZ and the Renell Trough where the oceanic crust entering the northern New Hebrides Trench is characterized by the prominent West Torres Plateau (**Figure 1**). The top of the plateau rises over 1,000 m above the adjacent seafloor and is impeding subduction there. This impeded subduction combined with the northeast-directed motion of the Australian plate is a likely trigger for the magnitude M_W 7.8 earthquake in 2009 and the three subsequent magnitude M_W 7 earthquakes in the same region. Seamounts and uncharacteristic seafloor structures have been shown in many studies, including Bilek et al. (2003), to act as a point of rupture in subduction zone earthquakes. Some 263 aftershocks (NEIC earthquake catalog $M_W > 4$) occurred within the 30 days after the first rupture in late October and all earthquakes are located within the interpreted upper and lower boundaries of the subducting plate. Aftershocks, however, continued for weeks after the main event and were limited in their southern extent by the Wharton Fossil Ridge, a major fracture in the subducting Indo-Australian plate. In the Vanuatu region, the swarm of aftershocks was confined to a well-defined zone that was limited to the north by the Renell Trough, a fossil spreading center (Larue et al., 1977), and to the south by the NCFZ (**Figures 2**, **5B**). Evidence presented here suggests that the two major lithospheric-scale fractures inherited by the subducting slab limited the lateral distribution of the aftershocks. In all cases presented, there are likely to be earthquakes that occur outside these zones as a result of dynamically triggered events away from the rupture zone (**Figure 5**), nevertheless, the bulk of the seismicity remains confined to domains that are limited in lateral extent by the presence of major structures on the subducting slab. Finally, some earthquakes may be triggered further from the rupture by processes such as viscoelastic relaxation but demonstrating whether or not such earthquakes are related to the initial rupture or part of a new event is difficult to demonstrate, especially in dynamic subduction zone settings. Furthermore, many of the earthquakes (aftershocks) occur in the upper plate and may be the result of rupture triggered by seismicity in the underlying

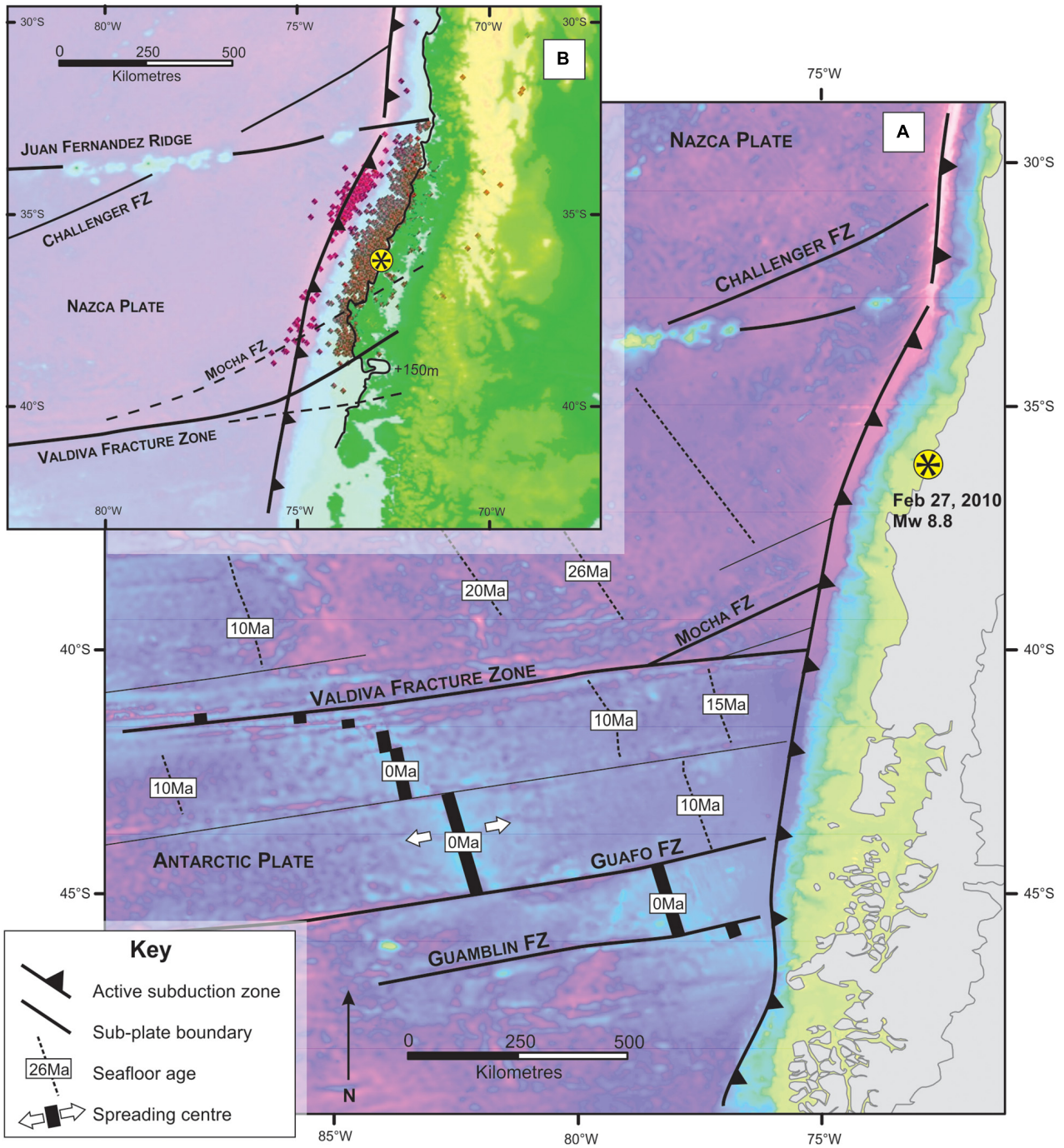

FIGURE 3 | (A) Map of southern Chile and the adjacent seafloor showing major structures including fault zones, spreading centers, the Juan Fernendez Ridge and associated lithospheric boundary and the Valdiva Fracture Zone. The location of the magnitude 8.8 earthquake in 2010 is also shown relative to geological and topographic features including aftershock distribution **(B)**. The southern limit of the aftershocks also corresponds with a dramatic change in the topography of the South American Continent as shown by the 150 m contour.

lower plate. Many variables do exist, however, the possibility that structures on the seafloor represent physical barriers to the lateral migration of aftershocks must be explored.

The same structural controls can be demonstrated for major earthquakes along the subduction margin of central and southern Chile. Here, the Nazca Slab is subducting to the ENE below the overriding South American continent (**Figure 3**). The Nazca oceanic plate is not unusual in that it contains a number of key geomorphologic and geological features that, after subduction, may form the nucleation point for the development

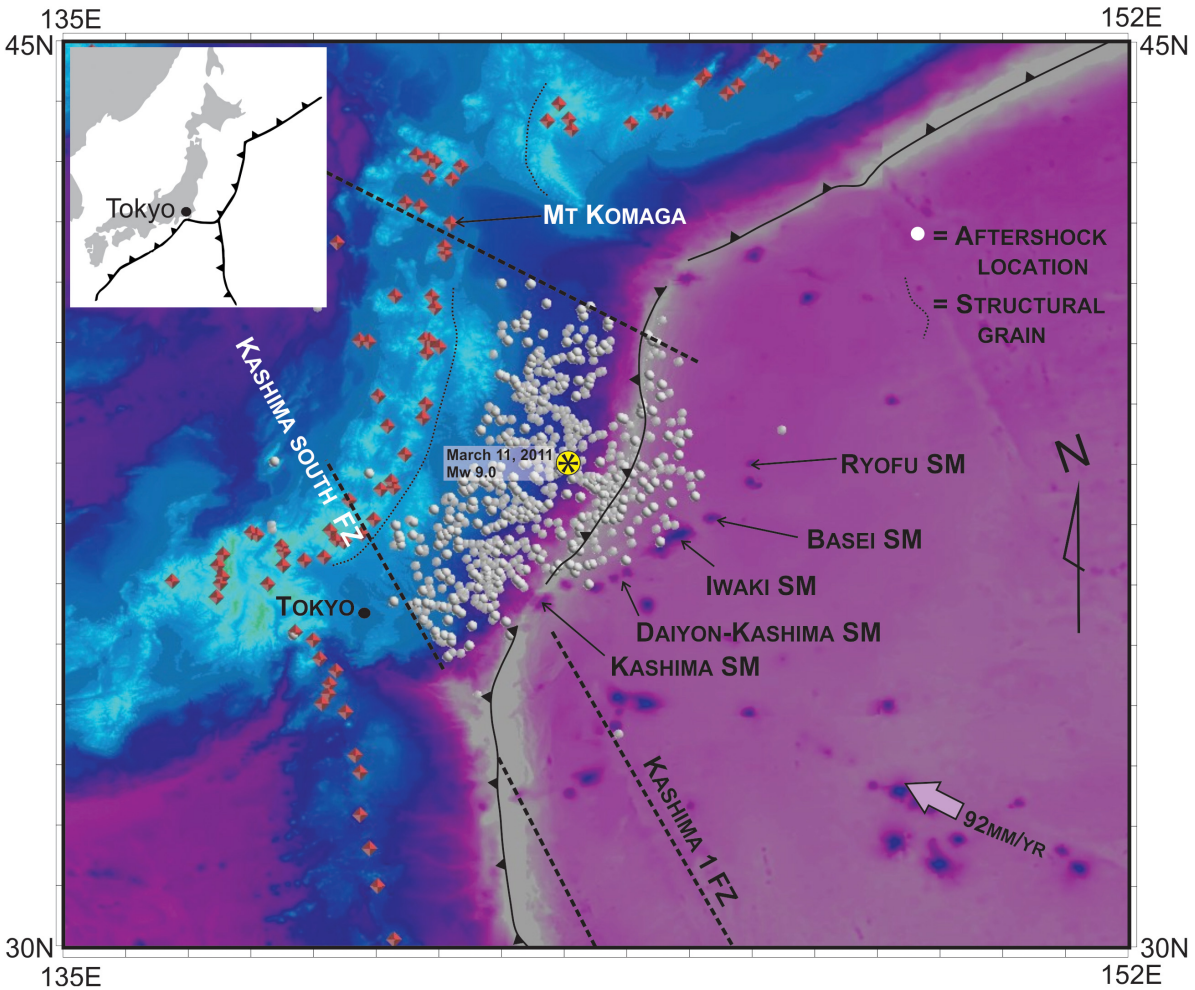

FIGURE 4 | Map showing the distribution of aftershocks following the Mw 9.0 earthquake in Japan on March 11, 2011. Aftershocks are shown as small white spheres superimposed onto a composite topographic and bathymetric map of the region surrounding the earthquake epicenter. The distribution of aftershocks is structurally controlled and does not gradually decrease in number and intensity with increasing distance from the principal Mw 9.0 epicenter. The eastern limit of aftershocks is controlled by the location of the Ryofu-Kashima seamount chain. Red points to the west of the earthquakes are volcanoes in the Japan Island arc chan.

of vertical tears. Major structures on the seafloor are illustrated in **Figure 3** and include the Valdiva and Mocha Fracture Zones, the Challenger Fracture Zone and the Juan Fernandez volcanic chain. Whether or not such features develop into tears after entering the mantle is dependant on the conditions operating at each location, nevertheless, these features do represent major structural breaks in the subducting plate. The research presented here focuses on the section of southern Chile in the vicinity of Bao Bao and Concepción approximately mid-way between the Challenger Fracture zone to the north and the Valdiva and Mocha Fracture Zones to the south. The magnitude M_W 8.8 earthquake occurred on the 27th of February in 2010 and was associated with over 1,370 aftershocks in the month following the main rupture with some of these aftershocks reaching magnitudes greater than M_W 6.5. The aftershocks were almost exclusively constrained to a section of the subducting plate between two major lithospheric-scale fracture systems.

The spatial distribution of aftershocks following the magnitude M_W 8.8 earthquake is limited to the north and south by two major fractures that are evident in bathymetric data. The two structural features on the Nazca Plate are the Juan Fernandez Ridge to the north and the Valdiva and Mocha fracture zones to the south. The latter two structures represent transform faults formed at the Nazca Ridge (**Figure 3**). The subducted Mocha fracture zone is also interpreted to be a vertical tear in the subducted Nazca Plate (Pesce, 1996). These two transforms divide the Nazca Plate into multiple sub-plates. The Juan Fernandez Ridge trends approximately east-west and enters the subduction zone near Santiago at 32° south (**Figure 3**). To the north of this ridge, the subducting slab is undergoing relatively shallow slab subduction but to the south, the oceanic crust is characterized by very few buoyant structures so the dip of the slab is ∼45°.

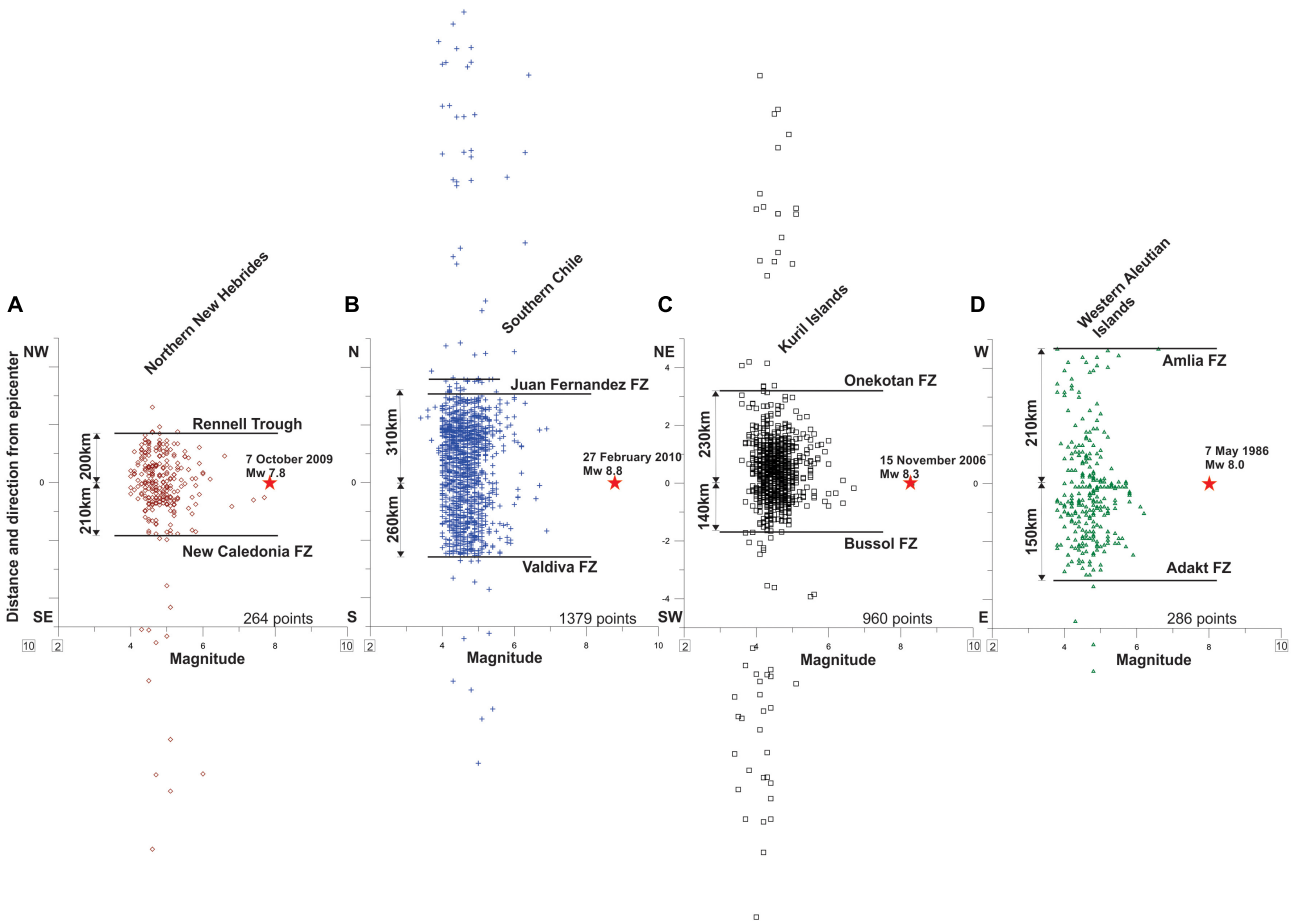

FIGURE 5 | Plot showing the lateral extent of aftershocks relative to magnitude after the main rupture event in four locations. **(A)** Shows the concentration of aftershocks limited to within the two sub-plate boundaries of the northern New Hebrides. **(B)** Shows the concentration of aftershocks between the accurately located Juan Fernandez and Valdiva fracture zones on the Nazca Plate. **(C)** shows the concentration of aftershocks in the Kuril Islands and **(D)** shows the distribution of aftershocks in the Aleutians. The distance and direction away from the main rupture event is also shown for each location.

To the north of the Juan Fernandez Ridge, for example, the Nazca slab exhibits a shallow angle of subduction. On the southern side of the ridge, the slab is dipping moderately at 45–50 degrees. A vertical zone of displacement or a developing vertical slab tear accommodates this change in slab dip. Thus, although the Juan Fernandez island chain is not specifically a transform fracture, its presence imposes a dramatic change in the slab structure, which in turn acts to develop the types of structures necessary for the termination of aftershock migration. Further south, the Nazca oceanic plate is characterized by the Valdiva Fracture Zone (VFZ) and the associated, but NE-trending Mocha Fracture Zone (MFZ) (**Figure 3**). The MFZ and VFZ separate older oceanic plate to the north from the younger oceanic plate to the south. The fracture offsets crust that differs in age by ∼12–15 million years (**Figure 3**). The fracture also separates colder, older and less buoyant oceanic crust to the north from the younger, hotter and more buoyant crust on the southern side of the VFZ. The Bao Bao/Concepción earthquake (Maule, Chile, February 2010 Mw 8.8; Pulido et al., 2010) occurred ˜400 km north of the VFZ and some 350 km south of the Juan Fernandez island chain (**Figure 3**). Over 1,300 aftershocks were tightly constrained to within these two fracture zones (**Figure 3**). As shown for Vanuatu, these major crustal and lithospheric fracture zones, which separate and decouple adjacent sub-plates, appear to limit to the lateral distribution of aftershock seismicity at shallow levels (<100 km) in active subduction zone systems.

Recent seismicity in Japan also demonstrates the structural control on aftershock distribution. The magnitude 9.0 (M_W) earthquake (11th March 2011 32 km depth) occurred in the upper crustal plate above the west-dipping subducted Pacific oceanic crust (e.g., Zhao et al., 2011; Huang and Zhao, 2013). The initial Mw 9.0 earthquake occurred at a depth of only 32 km, which should imply that structures exhibited by the seafloor have little influence on the distribution of aftershocks in the upper plate. However, a plot of aftershocks between 11th and 21st of March reveal a well-constrained distribution. The southern limit of the earthquakes is bound by the location of the Kashima South fracture zone on the Pacific Plate. The southeastern limit of aftershocks is the NE-trending chain of seamounts including Daiyon-Kashima, Basei, Futaba and Iwaki Seamounts, which

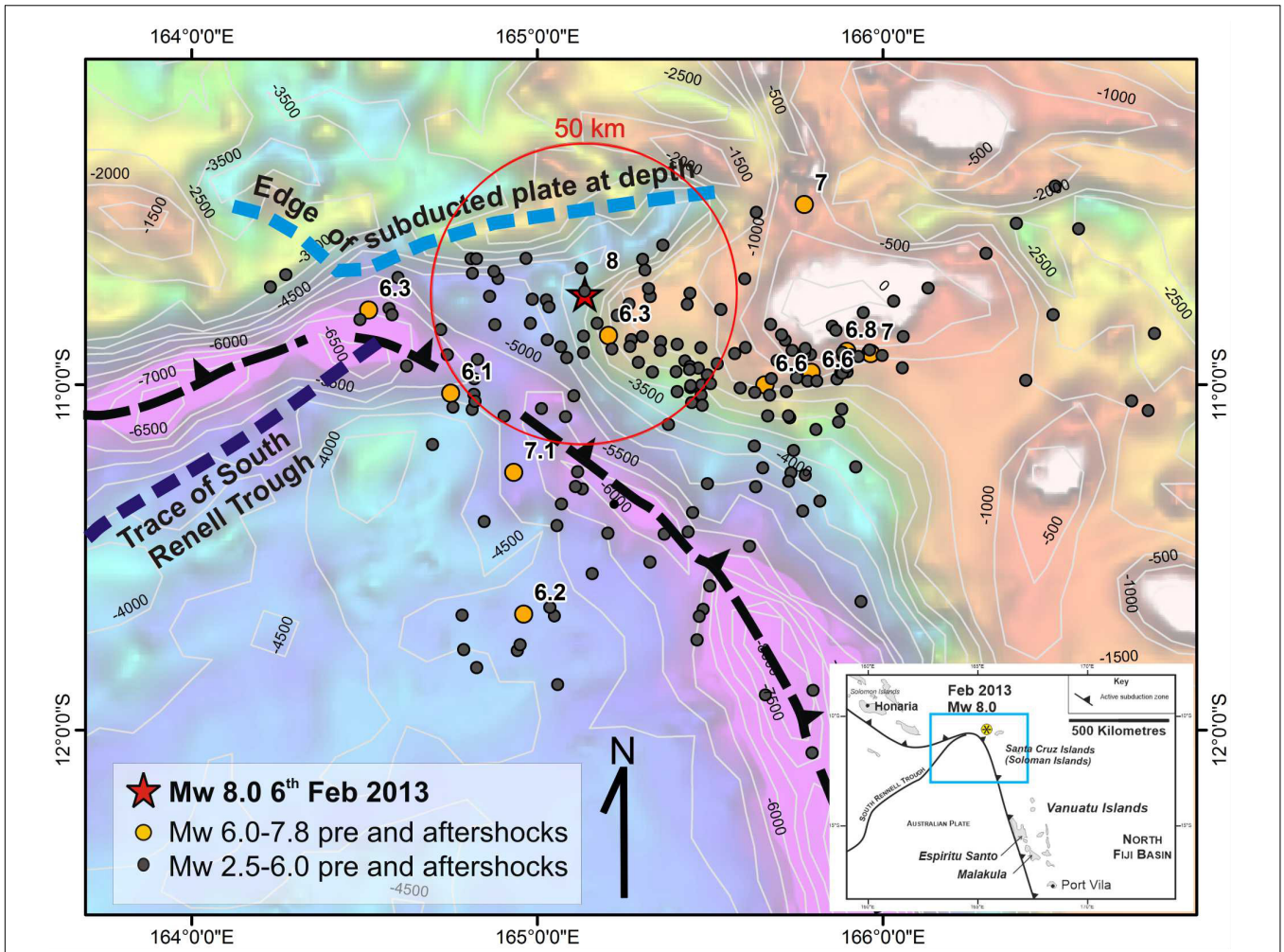

FIGURE 6 | Image showing the location of the Mw 8.0 earthquake in the eastern Solomon Islands on the 6th of February 2013. The main rupture and associated aftershocks represent a collation of seismic data from the USGS records spanning the time interval from the 3rd February 2013 to the 10th of February 2013 (UTC). Only 4 days of aftershocks are shown here, yet the clustering and the lack of aftershocks north of the principal Mw 8.0 epicenter is already apparent. The location of major structural features is shown. 500 m bathymetry contours are superimposed on color contoured ETOPO v1 bathymetric data. The northern limit of the subducted slab is highlighted for on the map as it would appear at the surface, however, the reader is directed to **Figure 2** for a 3D image of the slab surface.

supports the interpretations of Sparkes et al. (2010). The northern limit of aftershocks terminates abruptly, however, the seafloor the specific limiting the northern extent of the aftershocks is less defined. The orientation or strike of the northern limit (**Figure 4**) is exactly parallel to the direction of motion of the Pacific plate implying some structural control. Furthermore, the location of the northern boundary is coincident with the change in orientation of crustal structures between Hokkaido in the north and Honshu in the south. The limit of seismicity is also parallel to the geographic ridge and NW-trending line of volcanoes that includes the famous Mt Komaga-Dake and Mt Yokotsu-Dake which suggests a possible link between the limit of seismicity and a major crustal- to lithosphere-scale fracture there. As in the south, earthquakes here are distributed between the upper and lower plates so it is interpreted that the structure is likely to be an upper plate crustal structure developed as a consequence of NW-directed subduction of the Pacific plate. Further work on this area is required before conclusions on the aftershock distribution can be made.

The hypothesis was also tested for the magnitude M_W 8.3 earthquake in the Kuril Islands (15th of November, 2006; Lay et al., 2009). There, the seafloor is characterized by several oceanic structures, but the major earthquake occurred between the Onekotan Fracture zone to the North and the Bussol Fracture Zone to the south. The plot of distance vs. magnitude in **Figure 5C** shows that the primary M_W 8.3 earthquake occurred closer to the Bussol Fracture, however, of the 960 aftershocks that occurred for the 30 days after the main event, almost all were limited to within these two fractures. Similarly, for the magnitude M_W 8.0 earthquake in the western Aleutians on the 7th of May in 1986 (Hwang and Kanamori, 1986), only four of the 285 aftershocks occurred outside the limits of the two major bounding structures, the Amlia Fault Zone to the east and the Adak Fracture Zone to the west (**Figure 5D**).

The data presented in **Figure 5** also suggest that the size and location of the earthquake does not determine the distribution of the aftershocks. The aftershocks following the magnitude 8.0 earthquake in the Aleutian Islands were distributed over a lateral distance of 270 km while the less intense magnitude M_W 7.8 earthquake in the northern New Hebrides exhibited aftershocks over a distance of 440 km (**Figure 5**). Furthermore, the distribution of aftershocks is not symmetrically distributed about the initial rupture. Aftershocks from the Kuril Islands earthquake extended some 200 km to the northeast but only 120 km to the southwest (**Figure 5C**) implying that the identified sub-plate boundaries formed a barrier to the lateral migration of aftershocks.

Finally, preliminary data from the Mw 8.0 earthquake in the eastern Solomon Islands in February 2013 (Lay et al., 2013) reveal that the distribution of aftershocks is highly irregular but nevertheless constrained to the north by the northern limit of the subducting Australian plate. The point where the Renell trough enters the subduction zone, a major inverted, "V-shaped" tear has developed. The northern limit of the seismicity corresponds with the northern limit of this slab edge (**Figure 6**).

CONCLUSION

Although many examples of earthquakes with magnitudes greater than Mw 7.0 have occurred within subduction zone settings in recent history, not all can be presented here. The research presented is a test case of four major earthquakes where close examination of the seafloor structure and 3D slab geometry has assisted in recognizing major structural weaknesses in the subducting plate that also appears to limit the spatial distribution of aftershocks. Thus, four cases were presented where the lateral extent of aftershocks post-dating a major rupture event were limited by the presence of sub-plate boundaries including major transform faults and fossil plate boundaries. Some of these boundaries were identified as vertical tears in the adjacent subducted slab. Combining detailed maps of the seafloor adjacent to active subduction zones with accurate 3D models of subducted slabs may lead to the development of a global map of subduction zones highlighting domains of aftershock susceptibility following major earthquake events.

DATA AVAILABILITY STATEMENT

The raw data supporting the conclusions of this article will be made available by the author, upon reasonable request, to any qualified researcher.

AUTHOR CONTRIBUTIONS

The following research was carried out in full by SR. All results and interpretations were generated by SR. SR produced all figures and prepared all aspects of the manuscript.

REFERENCES

Abercrombie, R., and Ekström, G. (2001). Earthquake slip on oceanic transform faults. *Nature* 410, 74–77. doi: 10.1038/35065064

Behn, M. D., Lin, J., and Zuber, M. T. (2002). Evidence for weak oceanic transform faults. *Geophys. Res. Lett.* 29, 60–61.

Bilek, S., Schwartz, S., and DeShon, H. (2003). Control of seafloor roughness on earthquake rupture behavior. *Geology* 31, 455–458.

Billen, M. I. (2008). Modeling the dynamics of subducting slabs. *Annu. Rev. Earth Planet. Sci.* 36, 325–356. doi: 10.1073/pnas.1616216114

Burkett, E. R., and Billen, M. I. (2010). Three-dimensionality of slab detachment due to ridge-trench collision: laterally simultaneous boudinage versus tear propagation. *Geochem. Geophys. Geosyst.* 11:Q11012. doi: 10.1029/2010GC003286

Cleveland, K. M., Ammon, C., and Lay, T. (2014). Large earthquake processes in the Northern Vanuatu subduction zone. *J. Geophys. Res. Solid Earth* 119, 8866–8883.

Das, S., and Watts, A. B. (2009). "Effect of subducting seafloor topography on the rupture characteristics of great subduction zone earthquakes," in *Subduction Zone Geodynamics*, eds S. Lallemand, and F. Funiceillo, (Berlin: Springer-Verlag), 103–118.

Hayes, G., Briggs, R., Sladen, A., Fielding, E. J., Prentice, C., Hudnut, K. W., et al. (2010). Complex rupture during the 12 January 2010 Haiti earthquake. *Nat. Geosci.* 3, 800–805.

Huang, Z., and Zhao, D. (2013). Mechanism of the 2011 Tohoku-oki earthquake (Mw 9.0) and tsunami: insight from seismic tomography. *J. Asian Earth Sci.* 7, 160–168.

Hwang, L. J., and Kanamori, H. (1986). Source parameters of the May 7, 1986 andrean of Islands earthquake. *Geophys. Res. Lett.* 13, 1426–1429.

Kelleher, J., and McCann, W. (1976). Buoyant zones, great earthquakes, and some predictions. *J. Geophys. Res.* 81, 4885–4896.

Kuna, V. M., Nábělek, J. L., and Braunmiller, J. (2019). Mode of slip and crust–mantle interaction at oceanic transform faults. *Nat. Geosci.* 12, 138–142.

Larue, B., Daniel, J., Jouannic, C., and Recy, J. (1977). "The south renell trough: evidence for a fossil spreading zone," in *Proceedings of the International Symposium on the Geodynamics of the South-West Pacific* (Paris: Editions Technip), 51–61.

Lay, T., Kanamori, H., Ammon, A., Hutko, A., Furlong, K., and Rivera, L. (2009). The 2006–2007 Kuril Islands great earthquake sequence. *J. Geophys. Res. Solid Earth* 114:B11308.

Lay, T., Ye, L., Kanamori, H., Yamazaki, Y., Cheung, K. F., and Ammon, C. J. (2013). The February 6, 2013 Mw 8.0 Santa Cruz Islands earthquake and tsunami. *Tectonophysics* 608, 1109–1121.

Lowrie, A., Smoot, C., and Batiza, R. (1986). Are oceanic fracture zones locked and strong or weak? New evidence for volcanic activity and weakness. *Geology* 14, 242–245.

Nishizawa, A., Kaneda, K., Watanabe, N., and Oikawa, M. (2009). Seismic structure of the subducting seamounts on the trench axis: Erimo Seamount and Daiichi-Kashima Seamount, northern and southern ends of the Japan Trench. *Earth Planets Space* 61, e5–e8.

Norio, O., Ye, T., Kajitani, Y., Shi, P., and Tatano, H. (2011). The 2011 eastern Japan great earthquake disaster: overview and comments. *Int. J. Disaster Risk Sci.* 2, 34–42.

Pesce, A. H. (1996). "The Plio-Holocene magmatic arc between 36°-39°S: controls of the Benioff geometry," in *Proceedings of the Third ISAG Sr Malo (France), 17-19/9/1996*, St Malo.

Pulido, N., Sekiguchi, T., Shoji, G., Alba, J., Lazares, F., and Saito, T. (2010). *Earthquake Source Process and Strong Ground Motions of the 2010 Chile Mega-Earthquake*. Tsukuba: National Research Institute for Earth Science and Disaster Prevention.

Richards, S., and Holm, R. (2013). "Tectonic preconditioning and the formation of giant porphyry deposits," in *Tectonics, Metallogeny, and Discovery: the North American Cordillera and Similar Accretionary Settings*, Vol. 17, eds M. Colpron,

T. Bissig, B. G. Rusk, and J. F. H. Thompson, (Littleton, CO: SEG Special Publication), 265–276.

Richards, S., Lister, G., and Kennett, B. (2007). A slab in depth: three-dimensional geometry and evolution of the Indo-Australian plate. *Geochem. Geophys. Geosyst.* 8:Q12003.

Rona, P. A., Widenfalk, L., and Bostrom, K. (1987). Serpentinized ultramafics and hydrothermal activity at the Mid-Atlantic Ridge crest near 15^{O}N. *J. Geophys. Res.* 92, 1417–1427.

Schellart, W. P. (2007). Northeastward subduction followed by slab detachment to explain ophiolite obduction and late Miocene volcanism in Northland, New Zealand. *Terra Nova* 19, 211–218.

Schellart, W. P., and Lister, G. S. (2004). "Tectonic models for the formation of arc-shaped convergent zones and backarc basins," in *Orogenic Curvature: Integrating Paleomagnetic and Structural Analyses*, Vol. 383, eds A. J. Sussman, and A. B. Weil, (Boulder, CO: Geological Society of America Special Publications), 237–258.

Schellart, W. P., Lister, G. S., and Jessell, M. W. (2002). Analogue modeling of arc and backarc deformation in the New Hebrides arc and North Fiji Basin. *Geology* 30, 311–314.

Shan, J., Eguchi, R., and Jones, B. (2011). Haiti 2010 earthquake. *Photogr. Eng. Remote Sensing* 77, 995–996.

Sparkes, R., Tilmann, F., Hovius, N., and Hillier, J. K. (2010). Subducted seafloor relief stops rupture in South American great earthquakes: implications for rupture behavior in the 2010 Maule, Chile earthquake. *Earth Planet. Sci. Lett.* 298, 89–94.

Spencer, B. F. Jr., Ruiz-Sandoval, M. E., and Kurata, N. (2004). Smart sensing technology: opportunities and challenges. *Struct. Control Health Monitor.* 11, 349–368.

Thorvald, S. (1997). Architectural and engineering issues in disasters: the collapse-prone building. *Ren. Fail.* 19, 607–610. doi: 10.3109/08860229709109026

Watts, A. B., Koppers, A. A. P., and Robinson, D. P. (2010). Seamount subduction and earthquakes. *Oceanography* 23, 166–173.

Wilson, J. T. (1965). A new class of faults and their bearing on continental drift. *Nature* 207, 343–347.

Zhao, D., Huang, Z., Umino, N., Hasegawa, A., and Kanamori, H. (2011). Structural heterogeneity in the megathrust zone and mechanism of the 2011 Tohoku−oki earthquake (Mw 9.0). *Geophys. Res. Lett.* 38, 1–5.

Conflict of Interest: The author declares that the research was conducted in the absence of any commercial or financial relationships that could be construed as a potential conflict of interest.

Copyright © 2020 Richards. This is an open-access article distributed under the terms of the Creative Commons Attribution License (CC BY). The use, distribution or reproduction in other forums is permitted, provided the original author(s) and the copyright owner(s) are credited and that the original publication in this journal is cited, in accordance with accepted academic practice. No use, distribution or reproduction is permitted which does not comply with these terms.

frontiers in Earth Science

REVIEW
published: 22 June 2020
doi: 10.3389/feart.2020.00227

Injection-Induced Seismic Risk Management Using Machine Learning Methodology – A Perspective Study

Miao He[1,2], *Qi Li*[1,2]* *and Xiaying Li*[1,2]

[1] State Key Laboratory of Geomechanics and Geotechnical Engineering, Institute of Rock and Soil Mechanics, Chinese Academy of Sciences, Wuhan, China, [2] School of Engineering Science, University of Chinese Academy of Sciences, Beijing, China

Effective identification of induced seismicity and real-time management of seismic risks are hot topics due to increasing induced seismicity in areas related to energy exploitation. Existing decision-making tool for managing seismic risks, known as the traffic light system, is not robust enough. To meet the increasing needs for safe mining of energy at production sites, finding an advanced and efficient method to improve the traffic light system is essential. In recent years, machine learning, an advanced inductive and analytical method, has been widely used in seismology. In this context, research gaps associated with the identification and management of induced seismicity, as well as the current achievements of machine learning in addressing induced seismicity problems, are reviewed. A basic framework of using machine learning method to optimize the traffic light system in the industrial production process is first proposed. Then, its feasibility and rationality are demonstrated by similar cases. This framework may provide a reference for the development of a risk-based adaptive traffic light management system.

Keywords: induced seismicity, machine learning, discriminating earthquakes, managing seismic risk, traffic light system

OPEN ACCESS

Edited by:
Giovanni Martinelli, National Institute of Geophysics and Volcanology, Section of Palermo, Italy

Reviewed by:
Enrico Priolo, Istituto Nazionale di Oceanografia e di Geofisica Sperimentale (OGS), Italy
Ruishan Cheng, Central South University, China

***Correspondence:**
Qi Li
qli@whrsm.ac.cn

Specialty section:
This article was submitted to Solid Earth Geophysics, a section of the journal Frontiers in Earth Science

Received: *29 February 2020*
Accepted: *27 May 2020*
Published: *22 June 2020*

Citation:
He M, Li Q and Li X (2020) Injection-Induced Seismic Risk Management Using Machine Learning Methodology – A Perspective Study. Front. Earth Sci. 8:227. doi: 10.3389/feart.2020.00227

HIGHLIGHTS

- The progress and gaps in injection-induced seismicity are reviewed.
- The concepts and current challenges of traffic light systems are reviewed.
- The main methods of machine learning and their applications in induced seismicity are summarized.
- The basic framework for improving the traffic light system using machine learning method is proposed.
- The feasibility and rationality of the framework are demonstrated by similar cases.

Abbreviations: AE, acoustic emission; AI, artificial intelligence; AIC, Akaike information criterion; ANN, artificial neural network; ATLS, adaptive traffic light system; BPNN, back propagation neural network; CLVD, compensated linear vector dipole; CNY, Chinese Yuan; CO_2, carbon dioxide; DC, double-couple; EGS, enhanced geothermal system; ETAS, epidemic-type aftershock sequence; FLAC, fast Lagrangian analysis of continua; GPR, Gaussian process regression; Graviquakes, fluid removal from a stratigraphic reservoir that can cause normal faults-related earthquakes; ISO, isotropic; LSSVM, least square support vector machine; ML, machine learning; MT, moment tensor; PGV, peak ground velocity; RBF, radial basis function; RIS, reservoir-induced seismicity; RVM, relevance vector machine; SVM, support vector machine; THM, thermal-hydrological-mechanical; TLS, traffic light system; TOUGH, transport of unsaturated groundwater and heat; US, the United States.

INTRODUCTION

Earthquakes can cause the sudden release of elastic energy in the Earth. Generally, natural earthquakes are caused by crustal movements, and the majority of strong seismic events in the world are natural earthquakes and have tectonic origin. Unlike natural earthquakes, most induced seismic events are usually related to anthropogenic production activities. The mechanisms that account for induced seismicity include changes in the state of stress, pore pressure, volume, and applied forces or loads (McGarr et al., 2002). The earliest induced earthquake records can be traced back to the 1920s (Pratt and Johnson, 1926), and the most classic case of wastewater reinjection-induced seismicity occurred in Denver, Colorado, in the 1960s (Evans, 1966; Healy et al., 1968; Hsieh and Bredehoeft, 1981).

The potential of energy technologies to induce earthquakes is known (National Research Council, 2013), mainly including wastewater disposal (e.g., Pratt and Johnson, 1926; Davis and Frohlich, 1993; Currie et al., 2018), extraction and injection of natural gas (e.g., Grasso and Wittlinger, 1990; Herber and de Jager, 2014; Zbinden et al., 2017), geothermal energy exploitation (e.g., Majer and Peterson, 2007; Martínez-Garzón et al., 2016; Boyd et al., 2018), hydraulic fracturing (e.g., Rutqvist et al., 2015; Bao and Eaton, 2016; Ghofrani and Atkinson, 2016) and Carbon dioxide (CO_2) geological sequestration (Goertz-Allmann et al., 2014, 2017a,b). Frequently felt earthquakes ($3 \leq M < 4.5$) can create negative public sentiments and even hinder the smooth progress of industrial production. For instance, in the Basel Geothermal Field, Switzerland, enhanced geothermal system (EGS) exploitation projects induced a series of locally felt earthquake events. The damage claims in Basel amounted to more than $9 million, and these projects were temporarily suspended due to strong protests from the general public (Giardini, 2009). A similar case occurred in the Groningen gas field, the Netherlands. In the 28 years since the gas was extracted in 1991, there have been approximately 320 earthquakes with $M > 1.5$, including 3 $M \approx 3.5$ earthquakes. These growing seismic events have caused widespread building damage, social concern and political upheaval (Sintubin, 2018; Vlek, 2018, 2019a,b). Moderate magnitude earthquakes ($4.5 \leq M < 6$) may threaten public safety and cause heavy economic losses. For instance, in the Changning shale gas block, Sichuan Basin, China, a moderate intensity earthquake (M_L 5.7) occurred on 16 December 2018. In this event, 17 persons were injured, more than 390 houses were damaged, and 9 houses collapsed. The direct economic loss reached approximately 50 million CNY (Lei et al., 2019). Another famous induced earthquake is the M_W 5.5 Pohang earthquake. The earthquake occurred on 15 November 2017, in Heunghae, Pohang in the North Gyeongsang Province in South Korea (Kim et al., 2018). The earthquake injured 82 people, killed one and left about 1,500 homeless, moreover, it caused serious damage to infrastructure and more than 75 million US dollars (Ellsworth et al., 2019). More cases of human-induced seismicity can be found in some reports and papers (e.g., Gibson and Sandiford, 2013; Folger and Tiemann, 2017; Foulger et al., 2018). Therefore, managing the risks of induced seismicity is of great significance for the smooth progress of industrial production and the development of energy technology.

In recent years, due to the fossil energy crisis, more resources from deeper in the Earth are needed, and in turn, the induced seismicity becomes more prominent. Although the traffic light system (TLS) has been used to manage the risk of induced seismicity, there remain two unresolved problems at present: (1) the differences between natural and induced earthquakes cannot be completely distinguished; (2) the evolving risk of deep fluid injection-induced seismicity is still difficult to manage effectively and timely, especially in the post-injection phase after shut-in. To solve these two problems, many different types of data related to injection-induced seismicity are needed, including geological data, seismicity and operational parameters (Yang et al., 2017). Unfortunately, the characteristics of the induced seismicity and their relationships with the production parameters are usually hidden in these large and disorderly data, and we cannot extract effective information from the large amount of data merely by analytical or conventional methods.

The rapid development of computer science provides technical support for big data processing, especially machine learning techniques. Machine learning (ML) was proposed in the computational model theory of neural networks in the 1940s (McCulloch and Pitts, 1943). It is a computer algorithm that can automatically improve itself through experience (Mitchell, 1997), and also a transformation chain from data to decision. ML can use mathematical and statistical methods to determine the intrinsic regulation from various data. To date, it has evolved towards more advanced learning types that are closer to the human brain, such as deep learning (Hinton and Salakhutdinov, 2006), transfer learning (Pan and Yang, 2010) and deep reinforcement learning (Mnih et al., 2015). At the same time, ML has been widely used in many fields, especially in seismology, such as for the identification and prediction of earthquake events (e.g., Asim et al., 2016; DeVries et al., 2018; Lubbers et al., 2018; Rajguru et al., 2018; Corbi et al., 2019) and the classification of seismic remote sensing images (e.g., Afonso et al., 2016; Bialas et al., 2016; Frank et al., 2017), etc. However, the achievements in solving induced seismicity by using ML-based methods are rarely reported, especially in improving traffic light systems.

In this context, we attempt to propose a basic framework for improving current traffic light system that is, using machine learning method to build a proxy model. This model could well reflect the complex relationship between seismicity magnitude and operational parameters. The paper is organized as follows. The first section briefly reviews the research progress of induced earthquakes related to fluid injection, including the explanation of the mechanism, the discrimination of induced seismicity and the concept of the traffic light system. Then, the main methods of machine learning and their research achievements in induced seismicity are summarized and reviewed systematically. Finally, the basic framework of using machine learning method to optimize the traffic light system is elaborated.

REVIEW OF FLUID-INDUCED SEISMICITY

Fault reactivation induced by fluid injection in industrial activity is one of the main causes of seismicity (Ellsworth, 2013), and **Figure 1** displays this process. Identified factors affecting fault reactivation mainly include the rate and volume of fluid injection (Nicol et al., 2011), in-situ stress conditions (Rutqvist et al., 2010), type and occurrence of the fault (Macdonald et al., 2012), and physical and mechanical properties of host rocks (Figueiredo et al., 2015). Notably, the most relevant role is played by fault orientation versus dominant stress orientation. In this section, the research progress and gaps in induced seismicity related to industrial activities are reviewed briefly.

Mechanisms of Induced Seismicity

The Coulomb failure criterion based on Mohr-Coulomb theory is commonly used to explain the mechanism of induced seismicity (Healy et al., 1968) and can be defined as:

$$\Delta CFS = \Delta\tau - \mu\,\Delta\sigma' \tag{1}$$

where ΔCFS is Coulomb stress, $\Delta\tau$ is the shear stress change (MPa), μ is the friction coefficient on the fault, and $\Delta\sigma'$ is the effective normal stress change (MPa), which can be calculated according to the effective stress principle (Alcoverro, 2003):

$$\Delta\sigma' = \Delta\,(\sigma - P) \tag{2}$$

where σ is the normal stress (MPa) and P is the pore pressure (MPa).

In Eq. (1), when $\Delta CFS > 0$, the fault loses stability and fails; otherwise, it remains stable.

Based on different ways of fluid injection or extraction in industrial production, Doglioni (2018) further summarized four possible mechanisms, that is, fluid removal from a stratigraphic reservoir that can cause normal faults-related earthquakes (also called graviquakes), reinjection quakes, hydrofracturing quakes and load quakes, as shown in **Figure 2**. For a more detailed explanation of the mechanism of fluid-induced seismicity, please refer to Shapiro (2015).

It is worth noting, however, that the Coulomb failure criterion can only be used to simply evaluate whether a fault is reactivated, and cannot truly reflect the entire physical process of fault failure induced by industrial activities.

Discrimination of Natural and Induced Seismicity

The first step for reducing seismic hazard is to effectively identify induced seismicity among a large number of earthquake events. Davis and Frohlich (1993) first proposed analytical approaches to discriminate between induced and natural earthquakes in industrial activity based on a set of YES or NO criteria. The analytical approaches for differentiation mainly include physics-based probabilistic models, statistics-based seismicity models and source parameter approaches (Dahm et al., 2012). **Table 1** lists the basic information about these three discrimination methods, including theoretical bases, advantages, disadvantages, and application scopes.

Physics-Based Probabilistic Model

The physics-based model is used to understand the complicated relationship between fluid migration and seismic activity and reveal the physical processes of induced seismicity by using laboratory and in-situ measurements and numerical simulations (e.g., Guglielmi et al., 2015; Zbinden et al., 2017). In recent years, physics-based probabilistic models have been developed, taking into account physical and statistical-stochastic factors (Dahm et al., 2015).

This model can be used to quantify the probability of event rate change induced by stress changes. However, it is not suitable in case of insufficiently detailed data, such as production/exploitation data and rock parameters (e.g., Passarelli et al., 2012; Rinaldi and Nespoli, 2017).

Statistics-Based Seismicity Model

The statistics-based seismicity model directly uses the change in statistical parameters in an earthquake catalog to determine whether the rate of stress change caused by production exceeds the change in natural stress. It is worth mentioning that the changes in these parameters are likely related to human activities. The epidemic-type aftershock sequence (ETAS) model (Hainzl and Ogata, 2005) is often used to identify artificial factors in seismicity event statistics.

The ETAS model is a combination of a constant background activity rate and the behavior of aftershock sequences according to the Omori-Utsu law (Tokuji et al., 1995). The total occurrence rate can be calculated by the sum of Omori's law for aftershocks $\nu(t)$ and the background activity rate $\lambda(t)$ (Lei et al., 2017):

$$\left.\begin{aligned} \nu(t) &= K_0 \textstyle\sum_{t_i<t} \dfrac{e^{\alpha(M_i-M_c)}}{(t-t_i+\hat{c})^{\hat{p}}} \\ \lambda(t) &= \lambda_0(t) + \nu(t) \end{aligned}\right\} \tag{3}$$

where K_0 is a constant, α is a constant related to the magnitude dependence, M_i is the magnitude of the i-th earthquake, M_c is the estimated cut-off magnitude of completeness, $\hat{c}$ and $\hat{p}$ are constants for Omori's law.

When the background rate $\lambda(t) >> 50\%$ and the Omori's law aftershocks $\nu(t)$ are rare, the earthquake can be considered artificially induced (Lei et al., 2008, 2013, 2017, 2019). In recent years, improved statistical models have been proposed to forecast and discriminate induced seismicity in the space-time-magnitude domain (Gaucher et al., 2015; Zaliapin and Ben-Zion, 2016; Grigoli et al., 2017).

Statistics-based methods do not need to consider complex physical constraints, so their advantage is that few input data or detailed models are required.

Source Parameter Approach

The source parameter approach attempts to discriminate between induced and natural earthquakes by searching specific rupture processes. It is generally believed that the hypocentral locations of induced earthquakes are different in the range of human activities. The source mechanism solution obtained by moment

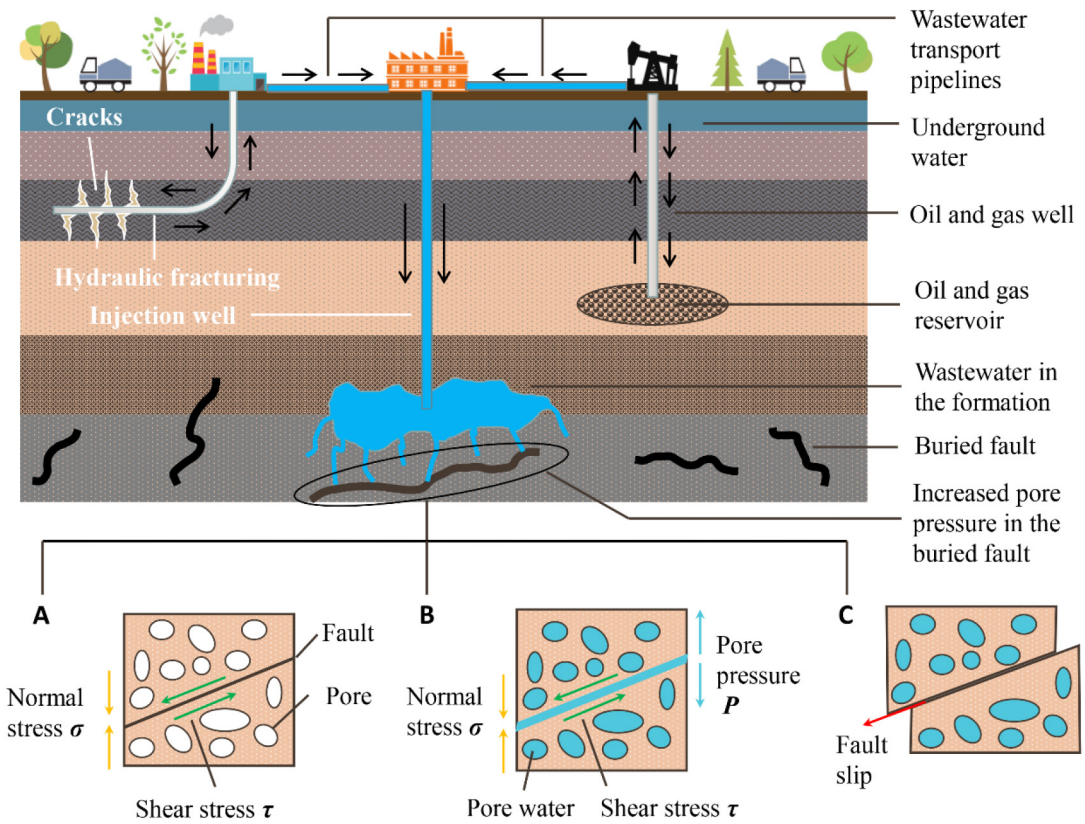

FIGURE 1 | The whole process of fault slip induced by fluid injection in industrial production. **(A)** Before fluid injection, the fault is closed under the pressure of normal stress on both sides. **(B)** With the continuous injection of fluid during the production process, the pores and cracks in the fault are gradually filled with fluid. **(C)** When pore pressure increases to a certain value, the fault slips because the effective normal stress on both sides is less than the shear stress; then, an earthquake is induced.

tensor (MT) inversion helps in understanding the orientation and type of fault and obtaining the subsurface stress field disturbance caused by fluid injection (Grigoli et al., 2017).

The moment tensor inversion is an important physical quantity describing different types of earthquakes. It consists of double-couple (DC) and non-DC components, where the non-DC includes isotropic (ISO) components and compensated linear vector dipole (CLVD) components (Gilbert, 1971):

$$MT = MT^{DC} + MT^{non\text{-}DC} = MT^{DC} + MT^{ISO} + MT^{CLVD} \quad (4)$$

where MT is the moment tensor, which can be inversed by $MT = (G_f^T G_f)^{-1} G_f^T \tilde{u}$, G_f is Green's function, and $\tilde{u}$ is the ground motion. When a high proportion of ISO and non-DC components occurs, an earthquake is likely to be induced because natural earthquakes are often characterized by a nearly pure DC source mechanism. This contrast provides an effective means to discriminate induced from natural seismicity (Cesca et al., 2012).

The moment tensor inversion is usually combined with other methods, such as waveform template matching (Skoumal et al., 2015), source spectra, and stress drop estimation (Clerc et al., 2016; Zhang et al., 2016). However, the source parameter approach requires high-quality data. If the structural model is not sufficiently accurate, a certain error appears in the analog waveform, and the results of waveform inversion may have significant deviations (Jechumtálová and Bulant, 2014).

It is worth noting that these three methods are often used in combination with detailed seismicity source parameters (Dahm et al., 2015). Some research cases and achievements in typical regions are given in **Table 2**.

Relationship Between Operational Parameters and Seismicity Magnitude

The operational parameters of fluid injection, such as wellhead pressure, total injection volume, injection rate and injection location, are the important factors affecting fault reactivation. Understanding the relation between reservoir engineering operations and corresponding seismic response is important towards the optimization of production and mitigating seismic hazard (Hofmann et al., 2018).

Some scholars have built analytical models based on statistical methods. For instance, Nicol et al. (2011) conducted statistical analysis of water injection data and seismic data from the 30 best reported seismicity sites. They found that the magnitude was positively correlated with the fluid injection, which could be expressed as $M = 0.3353 \ln \Delta V + 1.8061$, where M is the earthquake magnitude and ΔV is the water injection

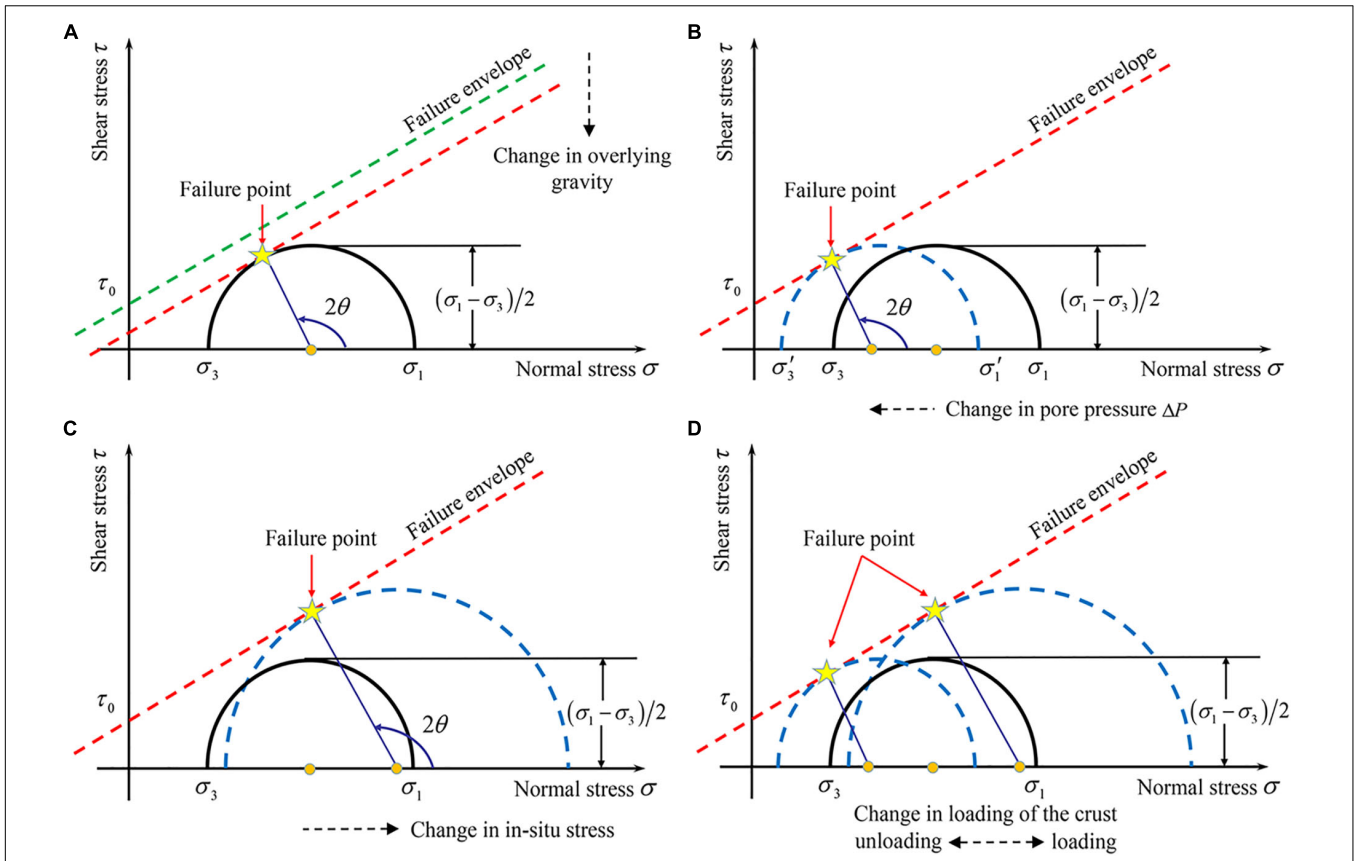

FIGURE 2 | Fault failure is induced by four possible mechanisms: **(A)** graviquakes, **(B)** reinjection quakes, **(C)** hydrofracturing quakes, **(D)** load quakes. The black solid Mohr circles represent the in-situ stress state of the fault before industrial production, while the blue dashed circles show the stress state after different changes. The red dotted lines mark the failure envelope in the safe state, and the red corresponds to the critical state. The fault is considered to fail when the Mohr circle is tangent to the envelope (as shown by the yellow star). [Modified from Doglioni (2018)] (This work is licensed under the CC BY-NC-ND license. http://creativecommons.org/licenses/by-nc-nd/4.0/).

TABLE 1 | Basic information of three different discrimination methods.

Methods	Theoretical basis	Advantage	Disadvantage	Application scope
Physics-based model	Coulomb failure criterion Rate-state seismicity model Background tectonic stress rate	This model can quantify the probability of an event rate change caused by the induced stress changes and investigate physical processes governing induced seismicity	This method can be difficult to apply because of the limited data availability and computational ability	This model is suitable for testing the occurrence of a single event and observed changes of event rate.
Statistics-based model	Seismic statistical model ETAS model	This method only requires less seismic catalog input data	This method does not take into account the physical mechanism that control induced seismicity	This method is suitable for short- and medium-term seismic activity patterns related to human activities, such as borehole fluid injections
Source parameter approach	Focal mechanism solution Specific rupture process of induced seismicity Background tectonic stress	This method not only allows us to understand the type of fault, but also reveals the specific motion of the fault before and after earthquake	This method is greatly affected by external uncertain factors such as anisotropic media and data quality, and its robustness is difficult to be guaranteed	This method is usually only applicable to some large seismic events of $M_L > 3$ non-DC terms.

volume. McGarr (2014) studied some earthquakes induced by unconventional oil and gas production in the central and eastern United States and found that the maximum magnitude seemed to be proportional to the total volume of the injected fluid but with an upper limit. Under some assumptions, which can be found in section 3 of McGarr (2014), the upper limit magnitude for a given fluid injection activity could be estimated as M_0 (max) = $G\Delta V$, where G is the shear modulus. Galis et al. (2017) analyzed

TABLE 2 | Discrimination of natural and induced seismicity in some typical regions.

Source	Seismogenic zone	Seismicity event	Discriminating method	Research result
Passarelli et al., 2012	Tjörnes Fracture Zone (Iceland)	1976.01.13 Kópasker earthquake (M 6.2)	Physics-based probabilistic model and Bayes' theorem	The probability of earthquake being triggered by a dike was approximately 60% to 90%
Cesca et al., 2012	Germany and adjacent areas (Central Europe)	1996.09.11 Teutschenthal earthquake (M_w 4.6) 1989.03.13 Völkershausen earthquake (M_w 4.9)	Full moment tensor inversion and decomposition (source parameter method)	The two events were induced by pillar burst and roof collapse in potash mines
Lei et al., 2013	Huangjiachang gas field (Sichuan Basin, China)	2009.01–2010.07 Hundreds of earthquakes ($> M$ 2)	Statistics-based seismicity model and mode analysis of injection rate and pressure	Seismic activity in this region was induced by water injection during natural gas production
Dahm et al., 2015	(1) Ekofisk oil field (North Sea) (2) Söhlingen gas field (Northern Germany) (3)Hydrocarbon reservoir (Northern Italy)	2001 Ekofisk earthquake in the North Sea (M_w 4.3) 2004 Rotenburg earthquake in Germany (M_w 4.4) 2012 Emilia earthquake In northern Italy (M_w 6.1)	Physics-based probabilistic model and source parameter approach	(1) The Ekofisk earthquake had a high probability of being triggered and induced by depletion (2) The Rotenburg earthquake was triggered with a probability of about 74% and induced with a probability of about 50% (3) The Emilia earthquake was probably entirely tectonic
Schoenball et al., 2015	Coso Geothermal Field (Eastern California, United States)	1981–2013 35,00 seismic events	Statistical analysis of space-time-magnitude	Distribution of nearest neighbor distances in a combined space-time-magnitude metric was able to identify induced seismicity
Skoumal et al., 2015	Northeastern Ohio (United States)	All Ohio earthquakes catalogued since the arrival of nearby EarthScope TA stations in 2011.11.06	Template matching	Template matching found the swarms that could identify induced seismicity due to natural earthquakes lacked swarminess
Zhang et al., 2016	Western Canadian Sedimentary Basin	2001.01.14—2015.06.13 9 seismic events ($> M_w$ 3)	Moment tensor solution and Static stress-drop value (source parameter method)	Focal depth could be the most robust parameter in this area, because focal depth of induced seismicities was significantly smaller than natural earthquakes
Albano et al., 2017	Emilia Romagna oil field (Northern Italy)	2011.07.17 Emilia-Romagna Earthquake (M_w 4.5) 2012.05.20 Emilia-Romagna Earthquake (M_w 5.9)	Physics-based poroelastic model	Anthropogenic activities only accounted for less than 10% in M_w 4.5 earthquake, so 2012 M_w 5.9 earthquake may be related to increased natural pressure
Lei et al., 2017	Shangluo shale gas site block and its environs (Sichuan Basin, China)	2014.12—2017.07 13 seismic events ($> M_w$ 3.5)	ETAS sequence model, hypocenter relocation, Focal mechanism solution and Coulomb failure stress numerical calculation	A series of seismicities with more than M_w 4.7 were induced by "short-term" injections for hydraulic fracturing at depths of 2.3~3 km
Lei et al., 2019	Changning shale gas block (Sichuan Basin, China)	2018.12.16 main shock in southwestern (M_L 5.7) 2019.01.03 mainshock in northeastern (M_L 5.3)	Hypocenter relocation, Moment tensor inversion, Pore overpressure analysis and Coulomb failure stress estimation	Both M_L 5.7 and 5.3 earthquakes were induced by nearby hydraulic fracturing, the pore overpressure to induce $M_w > 3.5$ events was ranged from 0.2 to 5.8 MPa

a scaling relation between the largest magnitude $M_0^{\max-arr}$ of self-arrested earthquakes and the injected volume ΔV with an analytical model $M_0^{\max-arr} \propto \Delta V^{3/2}$.

Numerical simulations are also used to predict the maximum seismic magnitude. Lei et al. (2017) studied the physical mechanisms of several moderate earthquake sequences in the Shangluo shale gas block and its environs (Sichuan Basin, China). They used the "TOUGH-FLAC" simulator to conduct coupled thermal-hydrological-mechanical (THM) analysis on the ΔCFS evolution patterns caused by hydraulic fracturing injection in this area. Based on it, a numerical model containing four layers of different mechanical and hydraulic properties was established, and the critical pressure at the injection wellhead that could cause fault failure was determined. Focusing on the different shale gas basins in North America, Amini and Eberhardt (2019) studied the effect of tectonic stress regime on the magnitude and

its distribution of induced seismicity associated with hydraulic fracturing. They used the 3D distinct-element method to simulate the fault slip under different stress regimes, and found that both the shear displacement magnitudes and the stress drop for the thrust and reverse fault case were much larger than those for the normal and strike-slip fault case.

Notably, the prediction accuracy of these analytical models is highly dependent on the input parameters (Eaton and Igonin, 2018), and the relationship between operational parameters and seismicity magnitude may not always be simple or straight. In addition, numerical simulations might have problems with calibration when proper parameters are difficult to select.

Traffic Light System for Safe Production

The traffic light system (TLS) is a powerful decision-making tool to manage industrial activities (Bommer et al., 2006). This system has been widely used to manage a risk associated with operation-related earthquakes, often using two or more thresholds to mitigate unexpected seismic hazards (Baisch et al., 2019; Wei et al., 2020). In this section, the application and limitations of TLS in induced seismicity are reviewed.

Working Mechanisms and Application Cases

A TLS consists of decision variables (e.g., peak ground acceleration, peak ground velocity, earthquake magnitude and other parameters) and thresholds (Mignan et al., 2017). When the earthquake magnitude or ground shaking exceed the threshold, the alert levels will be automatically activated and relevant actions must be taken (e.g., stopping operations, reducing injection rate or volume) (Braun et al., 2020).

The TLS is usually divided into three alert levels to provide feedback to manage operational measures or actions. **Figure 3** shows a workflow of the traffic light system. When the traffic light is green, conditions are normal, and production can continue as planned. When the light becomes orange, it means caution, and the operational parameters should be adjusted. However, if the light turns red, the production must be suspended.

At present, the model of predicting piecewise induced seismic activity rate$\lambda\left(t, M \geq M_0; \theta\right)$and the exceedance probability of risk assessment in TLS are as follows (Mignan et al., 2017):

$$\lambda\left(t, M \geq M_0; \theta\right) = \begin{cases} 10^{a_{fb}-b_s M_0}\,\dot{V}\left(t\right) & ; t \leq t_{shut-in} \\ 10^{a_{fb}-b_s M_0}\,\dot{V}\left(t_{shut-in}\right)\exp\left(-\frac{t-t_{shut-in}}{\tau_r}\right) & ; t > t_{shut-in} \end{cases} \quad (5)$$

$$\Pr\left(M \geq M_{saf}\right) = 1 - \exp\left\{-10^{a_{fb}-b_s M_{saf}}\left[V\left(t_{shut-in}\right) + \tau_r \dot{V}\left(t_{shut-in}\right)\right]\right\} = Y \quad (6)$$

where $V(t)$ is the cumulative injected fluid volume (m^3), $\dot{V}\left(t\right)$ is the injection flow rate (m^3/day), $\theta\left(a_{fb}, b_s, \tau_r\right)$ is a set of model parameters describing the underground characteristics, a_{fb} is the activation feedback in m^{-3}, b_s is the earthquake size ratio, τ_r is the mean relaxation time in days, M_0 is the minimum cut-off magnitude, $t_{shut-in}$ is the shut-in time (day), and M_{saf} is the given safety magnitude (i.e., threshold magnitude). Notably, Y represents the probability that the magnitude exceeds the threshold. Whenever the magnitude of an induced seismic event exceeds the threshold, $Y = 1$.

For different industrial activities, criteria for setting-up the TLS may be very different. Baisch et al. (2019) summarized some examples of existing TLS that correspond to different industrial activities taking place in Europe, North America and Australia, as shown in **Figure 4**. Notably, the wastewater disposal in the Cavone oil field is mainly used to enhance oil (or gas) production and to balance the loss of volume due to the primary production. It is within the production reservoir and is considered quite safe as regards induced seismicity (Styles et al., 2014).

Meanwhile, Baisch et al. (2019) investigated the different effects of TLS on seismic activity caused by fluid injection and gas production based on observation data from 12 fluid-injection operations in geothermal reservoirs and gas production in 26 gas fields. Their research showed that, for an earthquake of a given strength, the effect of TLS on short-term fluid injection induced seismicity was significantly better than that of gas production-induced seismicity.

Current Limitations

Remarkably, in TLS, the decision variables such as magnitude, PGV, and possibly other parameters are linked each other, and which decision variable to choose depends on how they contribute to the risk evaluation. When the appropriate reference variables for the decision are selected, their corresponding thresholds need to be further determined. Unfortunately, there are some challenges in determining the threshold effectively and timely.

Take the threshold magnitude as an example. Threshold magnitude is the transitional magnitude between different alert levels. The relationship between threshold magnitudes and operational parameters plays a vital role in TLS. However, the current definition of threshold magnitude M_{saf} in Eq. (6) is mainly chosen on the basis of expert judgment and regulation (Grigoli et al., 2017; Mignan et al., 2017), which lacks objectivity and cannot reflect the full range of possible scenarios. Magnitude thresholds enforced by different jurisdictions may vary significantly. It would further result in TLS not being flexible enough to adapt to evolving risks. Therefore, at present, one of the main limitations of classical TLS is that the threshold magnitudes for different stages are difficult to reappraisal accurately and timely, especially in the post-injection phase.

An important lesson about the limitation of classical TLS has recently come from the Pohang earthquake. Notably, Woo et al. (2019) used a variety of methods including the construction of a velocity model, to conduct earthquake detection, the determination of hypocenters, magnitudes, focal mechanisms and stress inversion, and a clustering analysis, to conduct a seismic analysis on the earthquakes occurring around the EGS site in the past 10 years. It is worth noting that all those investigations were important in order to improve the seismological interpretation, which was needed for an effective application of TLS. As part of the EGS project, a clear causal relationship between the origin of the M_W 5.5 Pohang earthquake and the injected fluid was discovered. That is, the earthquake initiated on the fault zone that was reactivated by fluid injection, representing a self-sustained rupture process that released a large

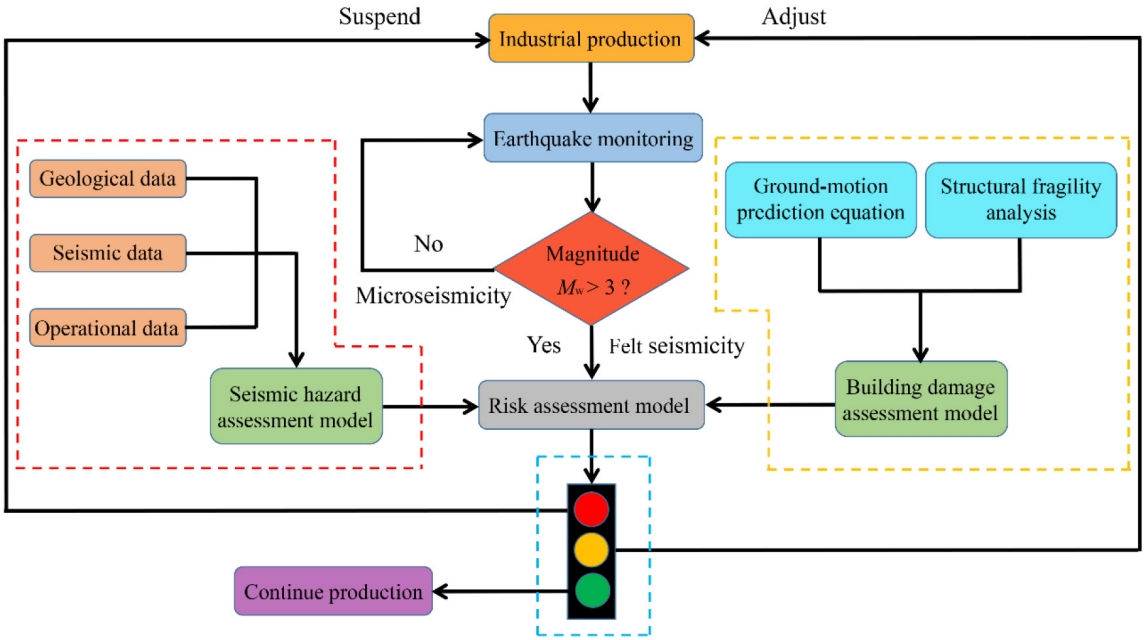

FIGURE 3 | A complete workflow of the traffic light system. The traffic light system needs to make decisions based on the results of the risk assessment model, which consists of a seismic assessment model and a building damage assessment model. The judgment basis for the former model is magnitude, while that for the latter model is ground motion.

amount of energy via tectonic loading rather than being a directly induced earthquake via fluid injection.

In the Pohang EGS project, the monitoring focus of classical TLS is the threshold magnitude. However, Ellsworth et al. (2019) and Lee et al. (2019) found that EGS stimulation could trigger large earthquakes that rupture beyond the stimulated volume, and the assumption that the maximum seismic magnitude was governed by the injection volume might no longer be true. It indicated that in addition to injection volume, more operational parameters should be considered in reappraising the threshold magnitude. Moreover, sufficient attention must be paid to post-injection seismicity after shut-in.

On the issue of post-injection earthquakes, Baisch et al. (2019) pointed out that the performance of TLS depends heavily on the prediction model that accounts for post-injection seismicity, so the post-injection phase must be considered in the design of TLS thresholds. The predicting model in Eq. (5) has the advantages of simplicity and stability, and can also consider the underground feedback in the post-injection phase. However, it assumes that the relationship between injection rate and overpressure is linear, and the fluid diffusion process at the post-injection phase is only represented by an exponential decay, which is different from the actual physical process (Mignan et al., 2017). In addition, the magnitude used in post-injection model does not change with time and cannot meet the real-time design of TLS thresholds in the post-injection phase.

Based on the 2017 Pohang earthquake experience, it is urgent to develop risk-based TLS based on the relationship between EGS and associated stimulus activities to adapt to evolving hazards. To this end, physical and statistical models of induced and triggered seismicity were also needed to further develop, as well as some advanced analyses. Machine learning methods may help us.

MACHINE LEARNING IN INDUCED SEISMICITY

Artificial intelligence (AI) is considered one of the most sophisticated technologies with research prospects and strategic value in the 21st century. The cornerstone of AI is machine learning, a simulation of the learning process of the human brain. ML has become a useful tool to study earthquakes in the field of earth science in recent years. In this section, the basic algorithms of ML and their application to induced seismicity are briefly reviewed.

Basic Algorithms of Machine Learning

According to the types of available datasets, ML can be roughly divided into supervised learning and unsupervised learning (Love, 2002). Supervised learning is the most basic type of ML. The goal of supervised learning is to train data from samples with known labels and finally gain generalization capabilities. Unsupervised learning can automatically find hidden structures in unlabelled data. Some information on supervised and unsupervised learning is introduced as follows.

Supervised Learning

The basic tasks of supervised learning are regression and classification. The algorithm models include but are not limited

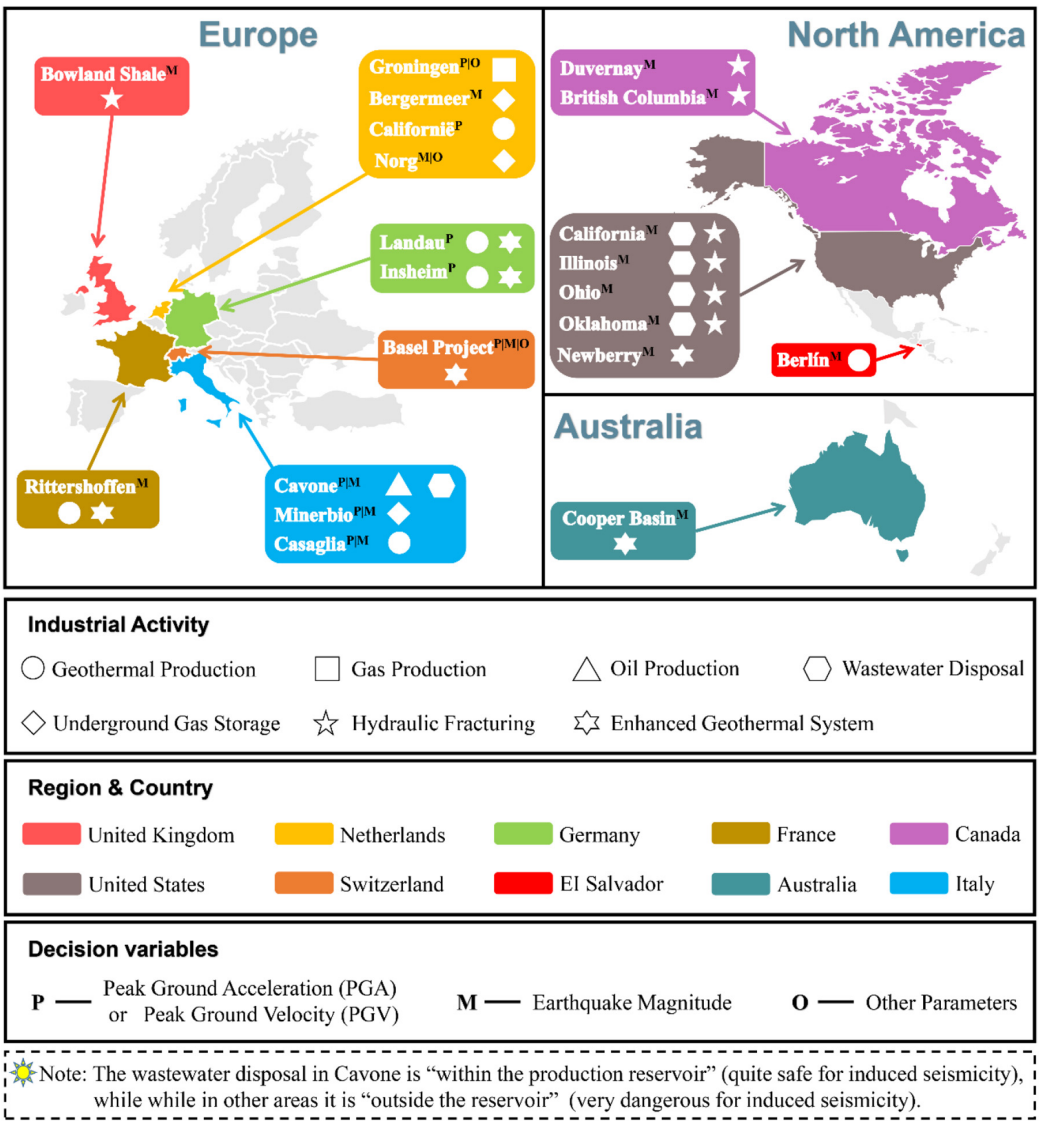

FIGURE 4 | Application cases of traffic light system (TLS) corresponding to different industrial activities in Europe, North America and Australia.

to linear regression, logistic regression, artificial neural networks (ANNs) and support vector machines (SVMs).

Linear regression is, as the definition implies, a regression algorithm (Franklin, 2005). The basic idea is to use a linear combination of features to approximate the predicted value:

$$y = \omega^T x + b \tag{7}$$

where y is a vector of predicted values, x is a matrix of features, ω is a matrix of optimizing coefficients, and b is a matrix of bias. The optimal values of ω and b can be determined by square loss:

$$f(\omega, b) = \arg\min \left(\omega^T x + b - y\right)^T \left(\omega^T x + b - y\right) \tag{8}$$

where $\arg\min f(x)$ stands for the argument of the minimum, that is to say, the set of points of the given argument for which the value of the given expression attains its minimum value.

Notably, linear regression sometimes leads to over-fitting, and adding a regularization coefficient $\tilde{\lambda}$ is an effective method to address the over-fitting problem (Cawley and Talbot, 2007; Aghajanyan, 2017).

Logistic regression is actually a classification algorithm that outputs predicted values in the range of 0 to 1, which is suitable for discrete labels. Although the logistic regression model is a non-linear model, it is still based on linear regression theory. The predicted value can be expressed as:

$$y = \text{sigmoid}\left(\omega^T x\right) \tag{9}$$

where $\text{sigmoid}(x) = \frac{1}{1+e^{-a_r x}}$, and a_r is the learning rate.

The ANNs are an abstraction and approximation of the biological nervous system. The purpose of ANNs is to simulate the learning function of biological neural networks (Rumelhart et al., 1986). An ANN is a network in which many logical units are organized according to different layers, and the variable of each layer is the output. Then, the variable acts as the input for the next layer. **Figure 5** shows an n-layer neural network. The first layer becomes the input layer, and the last layer is called the output layer. In addition, other layers are called hidden layers. There is an activation unit on each neuron that acts to turn the input into a specific output and a weight between different layers. Furthermore, the ANNs have a powerful non-linear adaptive information processing capability and can adapt sample data (Schmidhuber, 2015).

The core of SVMs is to find the one hyperplane with the largest margin out of many hyperplanes that divide the training set (Cortes and Vapnik, 1995). The mathematical representation is:

$$\begin{cases} \min\limits_{\omega,b} \frac{1}{2} ||\omega| |^2 \\ y_i \left(\omega^T \phi\left(x_i\right) + b\right) \geq 1, i = 1, 2, ..., m_f \end{cases} \tag{10}$$

where m_f is the number of features, $\phi(x)$ is the eigenvector after x mapping and $f(x) = \omega^T \phi(x) + b$ is the mathematical representation of the hyperplane.

The final performance of SVMs is directly determined by the kernel function (Crammer and Singer, 2002):

$$f(x) = sgn\left\{ \sum_{i=1}^{m_f} \alpha_{Li} Y_i \kappa(x, x_i) \right\} \tag{11}$$

where α_L is the Lagrange multiplier and $\kappa(x, x_i) = \phi^T(x_i)\phi(x)$ is the kernel. Commonly used kernel functions are shown in **Table 3**.

The linear function has the advantage of fewer parameters and fast speed but can be used only in the case of linear separability. Although the polynomial function can map a low-dimensional input space to a high-latitude feature space, its multiple parameters may make the computation complicated. In contrast, the radial basis function (RBF) has good performance in both large and small samples and requires fewer parameters than the polynomial function. Therefore, the RBF is widely used in SVMs.

Unsupervised Learning

The major task of unsupervised learning is data clustering. Clustering is one of the data mining techniques in which data are divided into groups of similar and dissimilar objects by using the intrinsic relations between data (Saroj and Kavita, 2016).

K-means clustering is the most basic clustering algorithm. The idea is to measure the similarity between different data objects by using the Euclidean distance. The similarity is inversely proportional to the Euclidean distance between different data objects. If the similarity between the data objects is greater, the Euclidean distance is smaller.

The local optimal solution of the K-means algorithm (y_i) is the minimum value of the sum of distances between all data points and their associated cluster centroids. It can be calculated as:

$$\begin{cases} y_i = \arg \min\limits_{\substack{1 \leq i \leq m_t \\ 1 \leq j \leq k}} \left|\left|x_i - u_j\right|\right| \\ u_j = \frac{1}{n_j} \sum\limits_{x \in C_j} x \end{cases} \tag{12}$$

where m_t is the total number of samples, k is the total number of clusters, C_j is the j-th cluster, u_j is the cluster centroid of C_j and n_j is the number of samples in C_j. The workflow of the K-means clustering algorithm is shown in **Figure 6**.

The K-means algorithm is very efficient when dealing with a large dataset. However, there are typically still two disadvantages: sensitivity to the initial value and ease of falling into a local optimal solution (Hung et al., 2013).

In short, these basic algorithms of ML do not have absolutely clear scopes of application. We should choose a relatively appropriate algorithm according to specific problems.

Applications of Machine Learning in Induced Seismicity

Incorporating novel ML into traditional seismological methods could provide great benefit. Kong et al. (2018) reviewed several current applications of ML in seismology, including earthquake detection and phase picking, real-time earthquake early warning, ground-motion prediction, seismic tomography and earthquake geodesy, etc. However, these applications are mainly focused on natural earthquakes. Since in the induced seismicity context one has to establish a causative connection between the human activities and detected seismicity, studying induced seismicity needs more data than studying natural earthquakes, especially operational data, which reflect the information of industrial activities. Unfortunately, some operational data are hardly available to the public. This is the main obstacle to applying ML to induced seismicity. For this reason, the current application of ML in induced seismicity is mainly focused on the laboratory study of mechanism, while the preliminary field applications are relatively rare.

Laboratory Study of the Mechanism

The seismogenic mechanism of induced seismicity is absolutely vital for managing induced seismicity, and laboratory rock testing is an important means to understand its mechanism. Energy stored in rocks is released in the form of elastic waves, which are called acoustic emissions (AEs), during micro-crack initiation, propagation and connection in the laboratory (Lei et al., 2003; Liu et al., 2019; Yue et al., 2019). The phenomena of micro-seismicity at the field scale and AEs in the laboratory are similar in nature (Sarout et al., 2017), and high-quality microseismic observations can effectively improve the statistical models that forecast expected seismic event magnitudes (Clarke et al., 2019). Therefore,

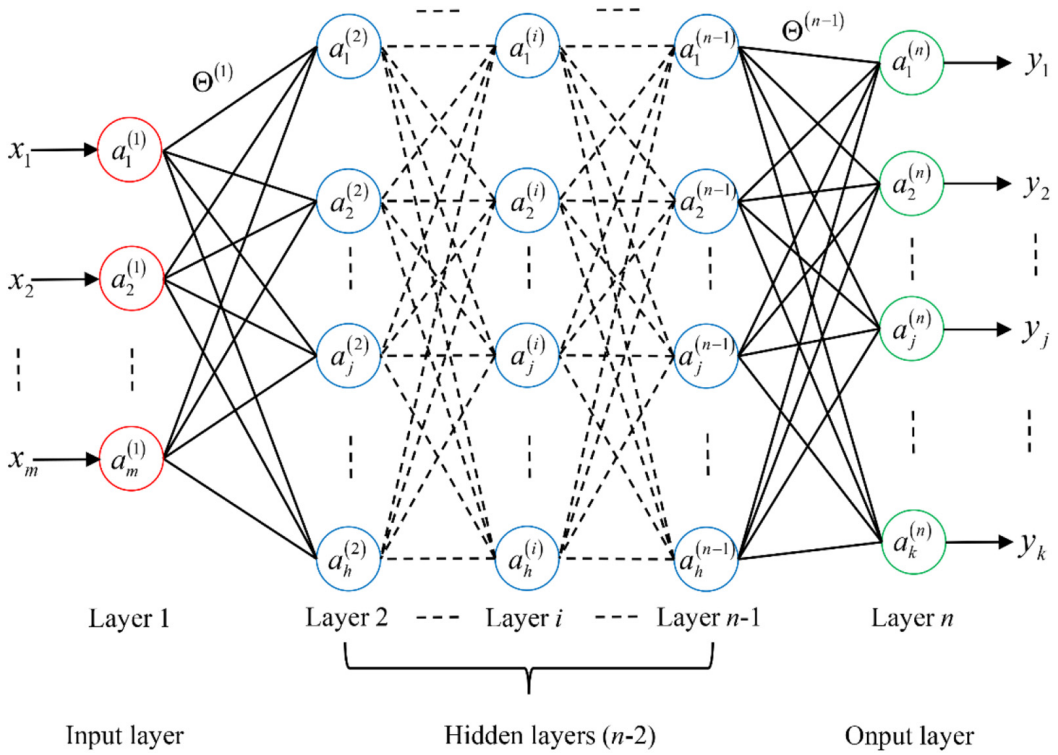

FIGURE 5 | Diagram of an *n*-layer neural network. In this neural network, *i* is the number of layers and *j* is the number of units in each layer. $x_1, x_2, \ldots, x_m$ represent input units, while $y_1, y_2, \ldots, y_k$ represent output units. $a_j^{(i)}$ represents the *j*-th activation unit in the *i*-layer, which is responsible for mapping the input of a neuron to the output. $\Theta^{(i)}$ represents the weight from the *i*-th layer to the *i*+1-th layer, whose function is to adjust the proportion of each input value before entering the activation function. Furthermore, we sometimes add a bias unit to each layer to reduce the error of the output value.

TABLE 3 | List of commonly used kernel functions.

Function name	Mathematical expression	Instruction
Linear function	$\kappa(x, x_i) = x^T x_i$	This function is mainly used in the case of linear separability, and its fewer parameters and fast speed are ideal for classification of linear separable data
Polynomial function	$\kappa(x, x_i) = (\gamma x^T x_i + c)$	This function can map a low-dimensional input space to a high-latitude feature space, but its multiple parameters may make the computation complicated
Radial basis function (RBF)	$\kappa(x, x_i) = exp\left(-\frac{\|x-x_i\|^2}{2\tilde{\sigma}^2}\right)$	This function can realize non-linear mapping. It has good performance in both large and small samples and needs fewer parameters than the polynomial function
Sigmoid function	$\kappa(x, x_i) = \tanh\left(\eta x^T, x_i + \hat{\theta}\right)$	This function is usually used to implement multi-layer neural networks

[a] *In the polynomial function,* $\gamma > 0$, $c \geq 0$, *and n is the degree of the polynomial. When* $\gamma = c = n = 1$, *we can obtain the linear function.* [b] *In the radial basis function,* $\tilde{\sigma}$ *is the width of the Gaussian kernel, and* $\tilde{\sigma} > 0$. [c] *In the sigmoid function, tanh(x) is the hyperbolic tangent function,* $\eta > 0$ *and* $\hat{\theta} < 0$.

the accurate identification and location of rock AE signals in the laboratory is of great significance for the study of induced seismicity.

Liu et al. (2015) used wavelet transform and ANNs to study the AE characteristics of different rock specimens during fracture under uniaxial compression. They created an efficient way to identify rock types and noise based on wavelet transform and ANNs. Rouet-Leduc et al. (2017) and Hulbert et al. (2018) applied the ML method to identify AE signals from fault shear experiments and AE signals before both slow and fast slip modes. It was found that ML could not only effectively identify AE signals that were previously considered to represent low-amplitude fault zones but also successfully predict the timing and duration of laboratory earthquakes. Rock fracture and blast events have similar waveform characteristics, and they are always mixed together. To effectively distinguish the AE signals of rocks from environmental noise and other signals, Zhou et al. (2018) proposed a new method based on signal complexity analysis and ML. This method did not seek waveform parameters of detected signals and could classify rock fracture and blast signals automatically based on the self-learning capacity of back propagation neural networks (BPNNs). On this basis, (Zhou et al., 2019a,b, 2020) further proposed an improved joint method based on discrete wavelet transform, modified energy ratio and Akaike information criterion (AIC) pickers, which effectively overcame

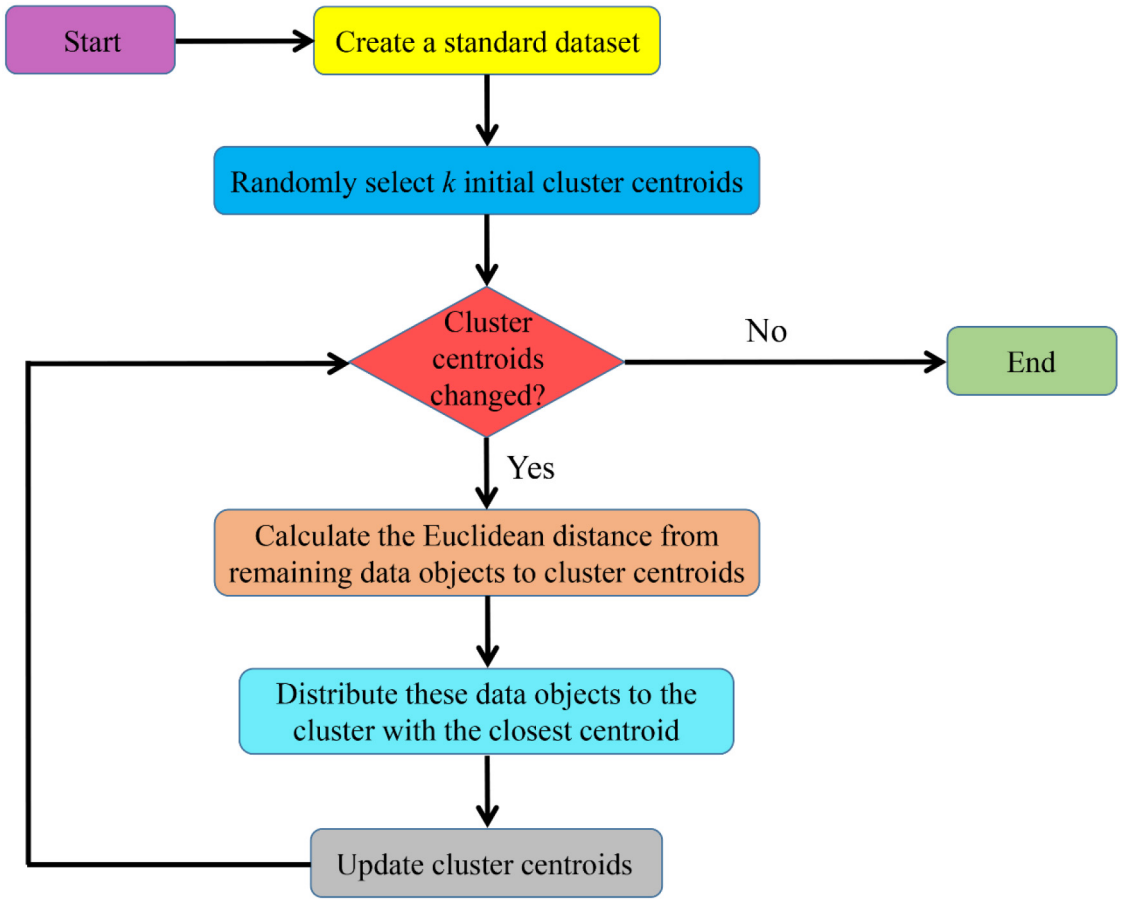

FIGURE 6 | The workflow of the K-means clustering algorithm. This algorithm needs to select *k* initial cluster centroids in advance. Then, the positions of cluster centroids are continuously updated according to the similarity between data objects and these positions. When updated cluster centroids no longer change or the objective function converges, the iteration ends, and the final result can be obtained.

the interference of spike noise and channel crosstalk and greatly improved the accuracy of automatic method for picking onset time of AE signals.

These results indicate that using ML method can capture more comprehensive and accurate rock fracture information at the laboratory scale, which can help us deepen understanding of the mechanism and further improve the physical and statistical models of induce seismicity.

Preliminary Exploration and Application in the Field

For seismicity induced by EGS exploitation, Holtzman et al. (2018) studied various small earthquake events in the Geysers geothermal field using the ML method, indicating that it could reveal the time-dependent spectral characteristics of seismicity signals and identify changes in the faulting process. In response to a large number of induced earthquakes in Oklahoma since 2009, Hincks et al. (2018) developed an advanced Bayesian network to model joint conditional dependencies among spatial, operational and seismic parameters, indicating that the injection depth was closely related to the release of the seismic moment. The model they proposed proved the feasibility and superiority of using ML to establish the mapping relationship between operational parameters and seismic information.

USING MACHINE LEARNING METHOD TO IMPROVE ADAPTIVE TRAFFIC LIGHT SYSTEM

The importance of TLS for managing induced seismic risks has been illustrated in section "Traffic Light System for Safe Production." One of the ways to improve TLS is to develop a risk-based adaptive TLS. The work of Mignan et al. (2017) has great reference value. They used statistical and actuarial approaches to improve the current prediction model (mentioned in section "Traffic Light System for Safe Production") of induced seismic activity, and further proposed an adaptive traffic light system (called ATLS) that can reflect the mapping relationship between earthquake magnitude and risk.

In this ATLS, the threshold magnitude is selected as the decision variable. They put forward a method to calculate the

threshold magnitude so that it can be updated in time with the change of the planned injection scheme.

$$M_{th}=\frac{1}{b_s}\log_{10}\left[Y-10^{a_{fb}-b_sM_{saf}}\tau_r\dot{V}\left(t_{shut-in}\right)\right]+M_{saf} \quad (13)$$

where M_{th} is the threshold magnitude in ATLS, and the meaning of other parameters can be found in Eq. (5) and Eq. (6).

Based on it, they then defined the ATLS as the operational threshold M_{th} at which the injection was stopped in order to meet the safety target, and thus obtained the following system of equations [for the meaning of the symbols, please see Eq. (5) and Eq. (6)]:

$$\begin{cases} 10^{a_{fb}-b_sM_{saf}}\left[V\left(t_{shut-in}\right)+\tau_r\dot{V}\left(t_{shut-in}\right)\right]\approx Y \\ 10^{a_{fb}-b_sM_{th}}V\left(t_{shut-in}\right)=1 \end{cases} \quad (14)$$

In Eq. (14), the first equation represents the situation of production safety. The probability that the magnitude exceeds the threshold is much less than 1 (i.e., $Y << 1$), and $M_{th}\approx M_{saf}$ can be obtained according to Eq. (13). The second equation represents the first time during the production process that the magnitude exceeds the threshold (i.e., $Y = 1$). At this point, the injection should be stopped immediately ($t = t_{shut-in}$, $\dot{V}\left(t_{shut-in}\right)=0$), and M_{th}=M_{saf} can be obtained according to Eq. (13). In particular, m_0 in Eq. (5) can be replaced by M_{th} to consider induced seismic activity in the post-injection phase.

The quantitative risk-based ATLS they proposed is a suite of simple closed-form expressions, with the advantages of high transparency and fast execution speed, which can provide the operator with the greatest chance of success. It is important to note, however, that the data set used to generate ATLS is relatively small (only data from 6 underground reservoir stimulation experiments were used for analysis), so its application scope needs further testing, although in principle its adoption would make any project in compliance with the safety threshold whatever the response of the underground.

The present study points the way for developing risk-based adaptive TLS and also illustrates that a large number of operational data are needed to improve TLS. In terms of big data processing, ML method is superior to traditional actuarial approach. Using ML methods to further improve the adaptive TLS has attractive potential.

Basic Framework

In order to solve the shortcomings of the ATLS proposed by Mignan et al. (2017), this section describes a basic framework for further improving the adaptive TLS by using ML method. Through the training and learning of a large number of samples, a proxy model that reflects the complex non-linear relationship between threshold magnitude and operating parameters can be obtained. The implementation process of the basic framework is shown in **Figure 7**.

The establishment of the proxy model requires sufficient geological, seismic and production data. Geological data include information such as geomechanical and hydraulic parameters, which can be obtained through geological exploration. Seismic data mainly contain waveform information that can be acquired by monitoring at nearby seismic stations. Production data can be divided into engineering data and operational data. The engineering data mainly include drilling information, such as drilling time, drilling position, drilling depth and the number of wells, while the operational data reflect the information about injection operational parameters, such as wellhead pressure, total injection amount, injection speed and injection position.

For a specific study region, the local geological data should be acquired in advance, which include geomechanical and hydraulic parameters. Next, we must collect seismicity wave data and the engineering dataset in this region over a relatively long period of time (e.g., 5 or 10 years) to ensure that the dataset is comparatively complete. It should be noted that the seismic wave data are mixtures of natural and induced earthquake information (i.e., unlabelled), while the engineering dataset contains some previously known drilling information (i.e., labeled). Then, the original data for earthquake events, including hypocentral location, focal mechanism solution and aftershock sequence type analysis, need to be pre-processed to obtain the seismic dataset. The seismic dataset and the engineering dataset are combined, and methods mentioned in section "Discrimination of Natural and Induced Seismicity" can be used to distinguish the induced seismic events, as shown in **Figure 7A**. There are some relations between induced seismicity data and engineering data. Finally, we can form a training dataset based on the relationship between the induced seismicity data and operational data. These data are taken as prior knowledge for ML. Since both induced seismicity data and operational data are labeled, we can use the supervised learning methods mentioned in section "Supervised Learning" to train this dataset and further fit a proxy model, as shown in **Figure 7B**.

Additionally, to ensure the generalization ability of the training model, over-fitting should be mitigated to the greatest extent. To improve the algorithms, we can divide the original dataset into three parts: training dataset, validation dataset and testing dataset before training. According to the performance of the training model on the cross-validation dataset and testing dataset, the generalization ability of this proxy model could be roughly determined (Santos et al., 2018).

Similar Cases

In this section, the theoretical feasibility of the basic framework will be demonstrated with some real cases. However, as mentioned in section "Applications of Machine Learning in Induced Seismicity," there is almost no public report on the use of ML for injection-induced seismic risk management. To overcome this difficulty, we select some similar cases that use ML to manage reservoir-induced seismicity (RIS). At present, the application of ML in reservoir induced earthquake is mainly reflected in the prediction of earthquake magnitude based on reservoir parameters, which is very similar to the real-time evaluation of threshold magnitude in TLS.

Samui and Kim (2013) used SVM and Gaussian process regression (GPR) models in ML to predict the magnitude of RIS based on reservoir properties. At first, they collected information from 30 worldwide historical cases of RIS into dataset. These data were taken as prior knowledge for SVM and

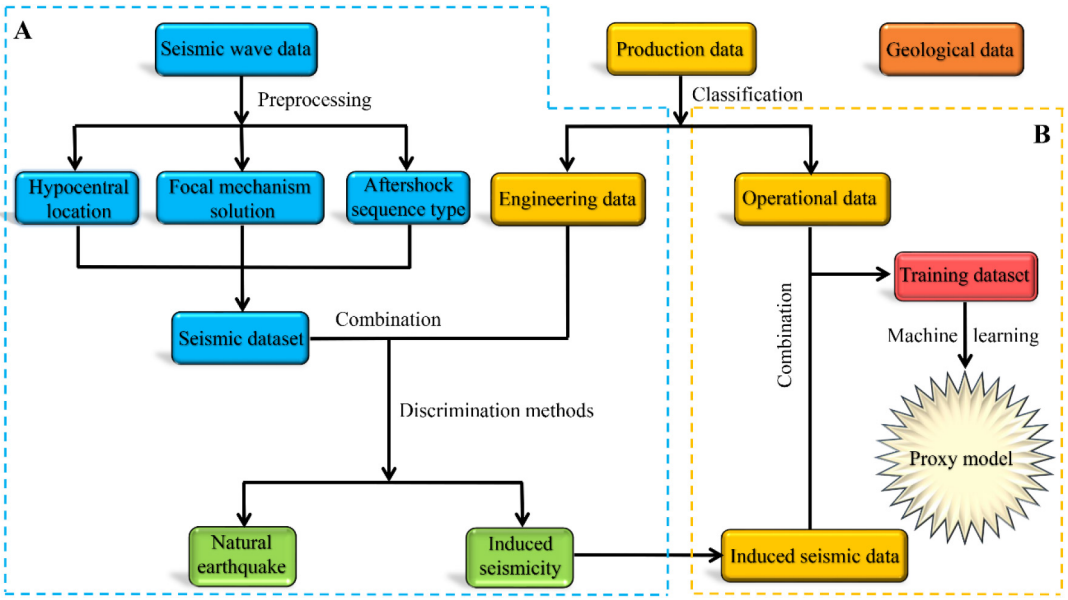

FIGURE 7 | Flowchart for using machine learning methods to improve the adaptive TLS. **(A)** Identify induced seismicity and **(B)** Determine the proxy model.

GPR models. Reservoir depth H_R, reservoir capacity V_R, reservoir surface S_R and earthquake magnitude M were suggested to be main influential factors of RIS. In that study, they used the comprehensive parameter E to characterize the three elements (i.e., H_R, V_R, S_R) of reservoir size, which could be expressed as $E = S_R H_R / V_R$ (Baoqi, 1990). These parameters could well reflect the internal and exterior causes of RIS. Then, to develop the SVM and GPR, they divided the dataset into two types: the training dataset (containing information about 24 reservoirs) and the testing dataset (containing information about 6 reservoirs). The comprehensive parameter E and the reservoir depth H_R were used as input variables, while the earthquake magnitude M was output. Finally, through learning process by SVM and GPR models, the complex mapping relationship between RIS magnitude and its influence factors was established, respectively. Thus the magnitude could be controlled by adjusting the input parameters in the relationship.

It is worth noting that the correlation coefficient (R) value is the criterion for determining the success of the learning process. The closer R is to 1, the more accurate the mapping relationship (overlearning needs to be excluded). For SVM model, the penalty coefficient $\tilde{C}$, the error insensitive zone $\tilde{\varepsilon}$ and the radial basis function width $\tilde{\sigma}$ should be determined. As for GPR model, the design values that need to be determined are the Gaussian noise and the radial basis function width $\tilde{\sigma}$.

Based on those studies, Samui and Kim (2014) further tested the feasibility of least square support vector machine (LSSVM) and relevance vector machine (RVM) in predicting RIS magnitude and compared the results with ANN and linear regression models. They found that the LSSVM and RVM models were more efficient and effective. Furthermore, Su (2008) also used the GPR model to predict the magnitude of RIS in western China. They considered more impact parameters in learning process, including reservoir depth, tectonic stress, lithologic character, activity background of seismicity, activity of fault, development degree of geology structure plane, connectivity between geology structure plane and reservoir water, and development degree of karst, etc. Their method has been applied to control RIS magnitude at the Three Gorges Reservoir in China. Although these achievements are limited to RIS, it provides ideas and confidence for using ML to manage the risk of injection-induced seismicity also for other kinds of activities.

Some Statements

(1) Decision variable: Since the basic framework is based on the results of Mignan et al. (2017), it takes the threshold magnitude as the decision variable for induced seismic risk control. If PGV or other parameters are selected as decision variables, they must be converted to the corresponding magnitude.

(2) Application scope: The operational parameters mentioned in the basic framework mainly involve some fluid injection information. Therefore, it is mainly applicable to injection-induced seismicity, including wastewater reinjection, hydraulic fracturing and geothermal energy exploitation, etc. Notably, for different activities, it is necessary to collect corresponding key parameters according to the characteristics of the activities and take these parameters as the prior knowledge for ML training. The combination of ML methods with specific TLS models implemented for different activities is very important.

(3) Post-injection phase: The basic framework can also consider the post-injection phase. To do this, we need to expand the time window to a period of time after shut-in and collect the data. Then, the data before and after shut-in are trained to establish their proxy models, respectively.

(4) Main challenges: The complete collection of relevant data is a major challenge, because some production data is hardly available to the public. In addition, the efficient processing of large amounts of data is also a problem faced by ML.

CONCLUSION

This paper provides an overview of current research progress of induced seismicity related to fluid injection, and proposes a basic framework of using ML method to improve the adaptive TLS. The implementation process of the framework has been described in detail, and its feasibility and rationality have also been demonstrated by some cases related to reservoir-induced seismicity.

The proposed framework uses the threshold magnitude as the decision variable and can also consider the post-injection phase after shut-in. Compared with the statistical and actuarial approaches, the proxy model based on ML training with a large amount of data can more comprehensively reflect the complex relationship between operational and seismic parameters. Moreover, it can be applied to various injection-induced earthquakes by collecting characteristic data of different activities. However, the complete collection of relevant data is the primary challenge.

We hope that this basic framework can provide valuable references for developing the risk-based adaptive TLS models in the future.

AUTHOR CONTRIBUTIONS

QL designed the research project. MH and XL wrote the manuscript. All authors performed the research, analyzed the results, and finally approved the manuscript.

FUNDING

This work was partially supported by the National Natural Science Foundation of China (Grant Nos. 41872210 and 41902297) and Open Research Fund of State Key Laboratory of Geomechanics and Geotechnical Engineering, Institute of Rock and Soil Mechanics, Chinese Academy of Sciences (Grant No. Z017006).

ACKNOWLEDGMENTS

We would like to thank all the reviewers for their insightful and constructive comments on the manuscript, as these comments led us to a real improvement of the current work.

REFERENCES

Afonso, L., Vidal, A., Kuroda, M., Falcao, A. X., and Papa, J. P. (2016). "learning to classify seismic images with deep optimum-path forest," in *Proceedings of the 2016 29th SIBGRAPI Conference on Graphics, Patterns and Images (SIBGRAPI)*, São Paulo.

Aghajanyan, A. (2017). "Softtarget regularization: an effective technique to reduce over-fitting in neural networks," in *Proceedings of the 2017 3rd IEEE International Conference on Cybernetics (CYBCONF)*, Piscataway, NJ.

Albano, M., Barba, S., Tarabusi, G., Saroli, M., and Stramondo, S. (2017). Discriminating between natural and anthropogenic earthquakes: insights from the Emilia Romagna (Italy) 2012 seismic sequence. *Sci. Rep.* 7:282. doi: 10.1038/s41598-017-00379-2

Alcoverro, J. (2003). The effective stress principle. *Math. Comput. Model.* 37, 457–467. doi: 10.1016/s0895-7177(03)00038-4

Amini, A., and Eberhardt, E. (2019). Influence of tectonic stress regime on the magnitude distribution of induced seismicity events related to hydraulic fracturing. *J. Petrol. Sci. Eng.* 182:106284. doi: 10.1016/j.petrol.2019.106284

Asim, K. M., Martínez-lvarez, F., Basit, A., and Iqbal, T. (2016). Earthquake magnitude prediction in Hindukush region using machine learning techniques. *Nat. Haz.* 85, 471–486. doi: 10.1007/s11069-016-2579-3

Baisch, S., Koch, C., and Muntendam-Bos, A. (2019). Traffic light systems: to what extent can induced seismicity be controlled? *Seismol. Res. Lett.* 90, 1145–1154. doi: 10.1785/0220180337

Bao, X., and Eaton, D. W. (2016). Fault activation by hydraulic fracturing in western Canada. *Science* 354, 1406–1409. doi: 10.1126/science.aag2583

Baoqi, C. (1990). Preliminary study on the prediction of reservoir earthquakes. *Gerlands Beiträge Zur Geophysik* 99, 407–424.

Bialas, J., Oommen, T., Rebbapragada, U., and Levin, E. (2016). Object-based classification of earthquake damage from high-resolution optical imagery using machine learning. *J. Appl. Remote Sens.* 10:e036025.

Bommer, J. J., Oates, S., Cepeda, J. M., Lindholm, C., Bird, J., Torres, R., et al. (2006). Control of hazard due to seismicity induced by a hot fractured rock geothermal project. *Eng. Geol.* 83, 287–306. doi: 10.1016/j.enggeo.2005.11.002

Boyd, O. S., Dreger, D. S., Gritto, R., and Garcia, J. (2018). analysis of seismic moment tensors and in-situ stress during enhanced geothermal system development at the geysers geothermal field, California. *Geophys. J. Intern.* 215, 1483–1500. doi: 10.1093/gji/ggy326

Braun, T., Danesi, S., and Morelli, A. (2020). Application of monitoring guidelines to induced seismicity in Italy. *J. Seismol.* doi: 10.1007/s10950-019-09901-7 [Epub ahead of print].

Cawley, G. C., and Talbot, N. L. (2007). Preventing over-fitting during model selection via Bayesian regularisation of the hyper-parameters. *J. Mach. Learn. Res.* 8, 841–861.

Cesca, S., Rohr, A., and Dahm, T. (2012). Discrimination of induced seismicity by full moment tensor inversion and decomposition. *J. Seismol.* 17, 147–163. doi: 10.1007/s10950-012-9305-8

Clarke, H., Verdon, J. P., Kettlety, T., Baird, A. F., and Kendall, J. M. (2019). Real-Time imaging, forecasting, and management of human-induced seismicity at preston new road, lancashire, England. *Seismol. Res. Lett.* 90, 1902–1915.

Clerc, F., Harrington, R. M., Liu, Y., and Gu, Y. J. (2016). Stress drop estimates and hypocenter relocations of induced seismicity near Crooked Lake, Alberta. *Geophysical Research Letters* 43, 6942–6951. doi: 10.1002/2016gl069800

Corbi, F., Sandri, L., Bedford, J., Funiciello, F., Brizzi, S., Rosenau, M., et al. (2019). Machine learning can predict the timing and size of analog earthquakes. *Geophys. Res. Lett.* 46, 1303–1311. doi: 10.1029/2018gl081251

Cortes, C., and Vapnik, V. (1995). Support-vector networks. *Mach. Learn.* 20, 273–297.

Crammer, K., and Singer, Y. (2002). On the algorithmic implementation of multiclass kernel–based vector machines. *J. Mach. Learn. Res.* 2, 265–292.

Currie, B. S., Free, J. C., Brudzinski, M. R., Leveridge, M., and Skoumal, R. J. (2018). Seismicity induced by wastewater injection in washington county, ohio: influence of preexisting structure, regional stress regime, and well operations. *J. Geophys. Res. Solid Earth* 123, 4123–4140. doi: 10.1002/2017jb015297

Dahm, T., Becker, D., Bischoff, M., Cesca, S., Dost, B., Fritschen, R., et al. (2012). Recommendation for the discrimination of human-related and natural seismicity. *J. Seismol.* 17, 197–202. doi: 10.1007/s10950-012-9295-6

Dahm, T., Cesca, S., Hainzl, S., Braun, T., and Krüger, F. (2015). Discrimination between induced, triggered, and natural earthquakes close to hydrocarbon reservoirs: a probabilistic approach based on the modeling of depletion-induced stress changes and seismological source parameters. *J. Geophys. Res. Solid Earth* 120, 2491–2509. doi: 10.1002/2014jb011778

Davis, S. D., and Frohlich, C. (1993). Did (or will) fluid injection cause earthquakes — Criteria for a rational assessment. *Seismol. Res. Lett.* 64, 207–224. doi: 10.1785/gssrl.64.3-4.207

DeVries, P. M. R., Viegas, F., Wattenberg, M., and Meade, B. J. (2018). Deep learning of aftershock patterns following? large earthquakes. *Nature* 560, 632–634. doi: 10.1038/s41586-018-0438-y

Doglioni, C. (2018). A classification of induced seismicity. *Geosci. Front.* 9, 1903–1909. doi: 10.1016/j.gsf.2017.11.015

Eaton, D. W., and Igonin, N. (2018). What controls the maximum magnitude of injection-induced earthquakes? *Lead. Edge* 37, 135–140. doi: 10.1190/tle37020135.1

Ellsworth, W. L. (2013). Injection-induced earthquakes. *Science* 341:1225942. doi: 10.1126/science.1225942

Ellsworth, W. L., Giardini, D., Townend, J., Ge, S., and Shimamoto, T. (2019). Triggering of the Pohang, Korea, Earthquake (Mw 5.5) by enhanced geothermal system stimulation. *Seismol. Res. Lett.* 90, 1844–1858.

Evans, D. M. (1966). The Denver area earthquakes and the rocky mountain arsenal disposal well. *Mount. Geol.* 3, 23–26.

Figueiredo, B., Tsang, C.-F., Rutqvist, J., Bensabat, J., and Niemi, A. (2015). Coupled hydro-mechanical processes and fault reactivation induced by CO2 Injection in a three-layer storage formation. *Intern. J. Greenhouse Gas Control* 39, 432–448. doi: 10.1016/j.ijggc.2015.06.008

Folger, P., and Tiemann, M. (2017). *Human-Induced Earthquakes From Deep-Well Injection: A Brief Overview*. Washington, DC: Congressional Research Service.

Foulger, G. R., Wilson, M. P., Gluyas, J. G., Julian, B. R., and Davies, R. J. (2018). Global review of human-induced earthquakes. *Earth Sci. Rev.* 178, 438–514. doi: 10.1016/j.earscirev.2017.07.008

Frank, J., Rebbapragada, U., Bialas, J., Oommen, T., and Havens, T. (2017). Effect of label noise on the machine-learned classification of earthquake damage. *Remote Sens.* 9:803. doi: 10.3390/rs9080803

Franklin, J. (2005). The elements of statistical learning data mining, inference, and prediction. *Math. Intellig.* 27, 83–85. doi: 10.1007/bf02985802

Galis, M., Ampuero, J. P., Mai, P. M., and Cappa, F. (2017). Induced seismicity provides insight into why earthquake ruptures stop. *Sci. Adv.* 3:7528.

Gaucher, E., Schoenball, M., Heidbach, O., Zang, A., Fokker, P. A., Van Wees, J. D., et al. (2015). Induced seismicity in geothermal reservoirs: a review of forecasting approaches. *Renew. Sustain. Energy Rev.* 52, 1473–1490. doi: 10.1016/j.rser.2015.08.026

Ghofrani, H., and Atkinson, G. M. (2016). A preliminary statistical model for hydraulic fracture-induced seismicity in the western canada sedimentary Basin. *Geophys. Res. Lett.* 43:10164.

Giardini, D. (2009). Geothermal quake risks must be faced. *Nature* 462, 848–849. doi: 10.1038/462848a

Gibson, G., and Sandiford, M. (2013). *Seismicity & Induced Earthquakes. Background Paper to NSW Chief Scientist and Engineer (OCSE)*. Melbourne: University of Melbourne.

Gilbert, F. (1971). Excitation of the normal modes of the earth by earthquake sources. *Geophys. J. Intern.* 22, 223–226. doi: 10.1111/j.1365-246x.1971.tb03593.x

Goertz-Allmann, B. P., Gibbons, S. J., Oye, V., Bauer, R., and Will, R. (2017a). Characterization of induced seismicity patterns derived from internal structure in event clusters. *J. Geophys. Res. Solid Earth* 122, 3875–3894. doi: 10.1002/2016jb013731

Goertz-Allmann, B. P., Oye, V., Gibbons, S. J., and Bauer, R. (2017b). Geomechanical monitoring of CO_2 storage reservoirs with microseismicity. *Energy Proc.* 114, 3937–3947. doi: 10.1016/j.egypro.2017.03.1525

Goertz-Allmann, B. P., Kühn, D., Oye, V., Bohloli, B., and Aker, E. (2014). Combining microseismic and geomechanical observations to interpret storage integrity at the in Salah CCS site. *Geophys. J. Intern.* 198, 447–461. doi: 10.1093/gji/ggu010

Grasso, J. R., and Wittlinger, G. (1990). Ten years of seismic monitoring over a gas field. *Bull. Seismol. Soc. Am.* 80, 450–473.

Grigoli, F., Cesca, S., Priolo, E., Rinaldi, A. P., Clinton, J. F., Stabile, T. A., et al. (2017). Current challenges in monitoring, discrimination, and management of induced seismicity related to underground industrial activities: a European perspective. *Rev. Geophys.* 55, 310–340. doi: 10.1002/2016rg000542

Guglielmi, Y., Cappa, F., Avouac, J. P., Henry, P., and Elsworth, D. (2015). Seismicity triggered by fluid injection-induced aseismic slip. *Science* 348, 1224–1226. doi: 10.1126/science.aab0476

Hainzl, S., and Ogata, Y. (2005). Detecting fluid signals in seismicity data through statistical earthquake modeling. *J. Geophys. Res.Solid Earth* 110: B05S07.

Healy, J. H., Rubey, W. W., Griggs, D. T., and Raleigh, C. B. (1968). the denver earthquakes. *Science* 161, 1301–1310. doi: 10.1126/science.161.3848.1301

Herber, R., and de Jager, J. (2014). Geoperspective oil and gas in the Netherlands – is there a future? *Nether. J. Geosci. Geol. Mijnb.* 89, 91–107. doi: 10.1017/s001677460000072x

Hincks, T., Aspinall, W., Cooke, R., and Gernon, T. (2018). Oklahoma's induced seismicity strongly linked to wastewater injection depth. *Science* 359, 1251–1255. doi: 10.1126/science.aap7911

Hinton, G. E., and Salakhutdinov, R. R. (2006). Reducing the dimensionality of data with neural networks. *Science* 313, 504–507. doi: 10.1126/science.1127647

Hofmann, H., Zimmermann, G., Zang, A., and Min, K. B. (2018). Cyclic soft stimulation (CSS): a new fluid injection protocol and traffic light system to mitigate seismic risks of hydraulic stimulation treatments. *Geotherm. Energy* 6:27.

Holtzman, B. K., Paté, A., Paisley, J., Waldhauser, F., and Repetto, D. (2018). Machine learning reveals cyclic changes in seismic source spectra in Geysers geothermal field. *Sci. Adv.* 4:eaao2929. doi: 10.1126/sciadv.aao2929

Hsieh, P. A., and Bredehoeft, J. D. (1981). A reservoir analysis of the denver earthquakes: a case of induced seismicity. *J. Geophys. Res. Solid Earth* 86, 903–920. doi: 10.1029/jb086ib02p00903

Hulbert, C., Rouet-Leduc, B., Johnson, P. A., Ren, C. X., Rivière, J., Bolton, D. C., et al. (2018). Similarity of fast and slow earthquakes illuminated by machine learning. *Nat. Geosci.* 12, 69–74. doi: 10.1038/s41561-018-0272-8

Hung, C.-H., Chiou, H.-M., and Yang, W.-N. (2013). Candidate groups search for K-harmonic means data clustering. *Appl. Math. Model.* 37, 10123–10128. doi: 10.1016/j.apm.2013.05.052

Jechumtálová, Z., and Bulant, P. (2014). Effects of 1-D versus 3-D velocity models on moment tensor inversion in the Dobrá Voda area in the Little Carpathians region, Slovakia. *J. Seismol.* 18, 511–531. doi: 10.1007/s10950-014-9423-6

Kim, H. S., Sun, C. G., and Cho, H. I. (2018). Geospatial assessment of the post-earthquake hazard of the 2017 Pohang earthquake considering seismic site effects. *ISPRS Intern. J. Geo Inform.* 7:375. doi: 10.3390/ijgi7090375

Kong, Q., Trugman, D. T., Ross, Z. E., Bianco, M. J., Meade, B. J., and Gerstoft, P. (2018). Machine learning in seismology: turning data into insights. *Seismol. Res. Lett.* 90, 3–14. doi: 10.1785/0220180259

Lee, K. K., Ellsworth, W. L., Giardini, D., Townend, J., Ge, S., Shimamoto, T., et al. (2019). Managing injection-induced seismic risks. *Science* 364, 730–732. doi: 10.1126/science.aax1878

Lei, X., Huang, D., Su, J., Jiang, G., Wang, X., Wang, H., et al. (2017). Fault reactivation and earthquakes with magnitudes of up to Mw4.7 induced by shale-gas hydraulic fracturing in Sichuan Basin, China. *Sci. Rep.* 7:7971.

Lei, X., Kusunose, K., Satoh, T., and Nishizawa, O. (2003). The hierarchical rupture process of a fault: an experimental study. *Phys. Earth Planet. Inter.* 137, 213–228. doi: 10.1016/s0031-9201(03)00016-5

Lei, X., Ma, S., Chen, W., Pang, C., Zeng, J., and Jiang, B. (2013). A detailed view of the injection-induced seismicity in a natural gas reservoir in Zigong, southwestern Sichuan Basin, China. *J. Geophys. Res. Solid Earth* 118, 4296–4311. doi: 10.1002/jgrb.50310

Lei, X., Wang, Z., and Su, J. (2019). The december 2018 ML5.7 and January 2019 ML5.3 earthquakes in South Sichuan basin induced by shale gas hydraulic fracturing. *Seismol. Res. Lett.* 90, 1099–1110. doi: 10.1785/0220190029

Lei, X., Yu, G., Ma, S., Wen, X., and Wang, Q. (2008). Earthquakes induced by water injection at 3 km depth within the Rongchang gas field, Chongqing, China. *J. Geophys. Res. Solid Earth* 113:B10310.

Liu, X., Liang, Z., Zhang, Y., Wu, X., and Liao, Z. (2015). Acoustic emission signal recognition of different rocks using wavelet transform and artificial neural network. *Shock Vibrat.* 2015, 1–14. doi: 10.1155/2015/846308

Liu, X., Liu, Q., Liu, B., and Liu, Q. (2019). Acoustic emission characteristics of pre-cracked specimens under biaxial compression. *J. Geophys. Eng.* 16, 1164–1177. doi: 10.1093/jge/gxz087

Love, B. C. (2002). Comparing supervised and unsupervised category learning. *Psychon. Bull. Rev.* 9, 829–835. doi: 10.3758/bf03196342

Lubbers, N., Bolton, D. C., Mohd-Yusof, J., Marone, C., Barros, K., and Johnson, P. A. (2018). Earthquake catalog-based machine learning identification of laboratory fault states and the effects of magnitude of completeness. *Geophys. Res. Lett.* 45, 269–213.

Macdonald, J., Backé, G., King, R., Holford, S., and Hillis, R. (2012). Geomechanical modelling of fault reactivation in the Ceduna Sub-basin, Bight Basin, Australia. *Geol. Soc. Lond. Spec. Public.* 367, 71–89. doi: 10.1144/sp367.6

Majer, E. L., and Peterson, J. E. (2007). The impact of injection on seismicity at the geysers, California geothermal field. *Intern. J. Rock Mech. Min. Sci.* 44, 1079–1090. doi: 10.1016/j.ijrmms.2007.07.023

Martínez-Garzón, P., Kwiatek, G., Bohnhoff, M., and Dresen, G. (2016). Impact of fluid injection on fracture reactivation at the geysers geothermal field. *J. Geophys. Res. Solid Earth* 121, 7432–7449. doi: 10.1002/2016jb013137

McCulloch, W. S., and Pitts, W. (1943). A logical calculus of the ideas immanent in nervous activity. *Bull. Math. Biophys.* 5, 115–133. doi: 10.1007/bf02478259

McGarr, A. (2014). Maximum magnitude earthquakes induced by fluid injection. *J. Geophys. Res. Solid Earth* 119, 1008–1019. doi: 10.1002/2013jb010597

McGarr, A., Simpson, D., and Seeber, L. (2002). 40 Case histories of induced and triggered seismicity. *Intern. Handb. Earthq. Eng. Seismol.* 81, 647–661. doi: 10.1016/s0074-6142(02)80243-1

Mignan, A., Broccardo, M., Wiemer, S., and Giardini, D. (2017). Induced seismicity closed-form traffic light system for actuarial decision-making during deep fluid injections. *Sci. Rep.* 7, 1–10.

Mitchell, T. M. (1997). Does machine learning really work? *AI Mag.* 18, 11–20.

Mnih, V., Kavukcuoglu, K., Silver, D., Rusu, A. A., Veness, J., Bellemare, M. G., et al. (2015). Human-level control through deep reinforcement learning. *Nature* 518, 529–533.

National Research Council (2013). *Induced Seismicity Potential In Energy Technologies*. Washington, DC: National Academies Press.

Nicol, A., Carne, R., Gerstenberger, M., and Christophersen, A. (2011). Induced seismicity and its implications for CO2 storage risk. *Energy Proc.* 4, 3699–3706. doi: 10.1016/j.egypro.2011.02.302

Pan, S. J., and Yang, Q. A. (2010). A survey on transfer learning. *IEEE Trans. Knowl. Data Eng.* 22, 1345–1359.

Passarelli, L., Maccaferri, F., Rivalta, E., Dahm, T., and Abebe Boku, E. (2012). A probabilistic approach for the classification of earthquakes as 'triggered' or 'not triggered'. *J. Seismol.* 17, 165–187. doi: 10.1007/s10950-012-9289-4

Pratt, W. E., and Johnson, D. W. (1926). Local Subsidence of the Goose Creek Oil Field. *J. Geol.* 34, 577–590. doi: 10.1086/623352

Rajguru, G., Bhadauria, Y. S., and Mukhopadhyay, S. (2018). "Estimation of earthquake source parameters using machine learning techniques," in *Proceedings of the International Conference on Computing, Communication and Networking Technologies, 9th IEEE*, New York, NY.

Rinaldi, A. P., and Nespoli, M. (2017). TOUGH2-seed: a coupled fluid flow and mechanical-stochastic approach to model injection-induced seismicity. *Comput. Geosci.* 108, 86–97. doi: 10.1016/j.cageo.2016.12.003

Rouet-Leduc, B., Hulbert, C., Lubbers, N., Barros, K., Humphreys, C. J., and Johnson, P. A. (2017). Machine learning predicts laboratory earthquakes. *Geophys. Res. Lett.* 44, 9276–9282. doi: 10.1002/2017gl074677

Rumelhart, D. E., Hinton, G. E., and Williams, R. J. (1986). Learning representations by back-propagating errors. *Nature* 323, 533–536. doi: 10.1038/323533a0

Rutqvist, J., Rinaldi, A. P., Cappa, F., and Moridis, G. J. (2015). Modeling of fault activation and seismicity by injection directly into a fault zone associated with hydraulic fracturing of shale-gas reservoirs. *J. Petrol. Sci. Eng.* 127, 377–386. doi: 10.1016/j.petrol.2015.01.019

Rutqvist, J., Vasco, D. W., and Myer, L. (2010). Coupled reservoir-geomechanical analysis of CO2 injection and ground deformations at In Salah, Algeria. *Intern. J. Greenhouse Gas Control* 4, 225–230. doi: 10.1016/j.ijggc.2009.10.017

Samui, P., and Kim, D. (2013). Determination of reservoir induced earthquake using support vector machine and gaussian process regression. *Appl. Geophys.* 10, 229–234. doi: 10.1007/s11770-013-0381-5

Samui, P., and Kim, D. (2014). Applicability of artificial intelligence to reservoir induced earthquakes. *Acta Geophys.* 62, 608–619. doi: 10.2478/s11600-014-0201-1

Santos, M. S., Soares, J. P., Abreu, P. H., Araujo, H., and Santos, J. (2018). "Cross-validation for imbalanced datasets: avoiding overoptimistic and overfitting approaches [research frontier]," in *Proceedings of the IEEE Computational Intelligence Magazine*, Piscataway, NJ.

Saroj, and Kavita (2016). Review: study on simple k mean and modified k mean clustering technique. *Intern. J. Comput. Sci. Eng. Technol.* 6, 279–281.

Sarout, J., Le Gonidec, Y., Ougier-Simonin, A., Schubnel, A., Guéguen, Y., and Dewhurst, D. N. (2017). Laboratory micro-seismic signature of shear faulting and fault slip in shale. *Phys. Earth Planet. Inter.* 264, 47–62. doi: 10.1016/j.pepi.2016.11.005

Schmidhuber, J. (2015). Deep learning in neural networks: an overview. *Neural Netw.* 61, 85–117. doi: 10.1016/j.neunet.2014.09.003

Schoenball, M., Davatzes, N. C., and Glen, J. M. G. (2015). Differentiating induced and natural seismicity using space-time-magnitude statistics applied to the Coso Geothermal field. *Geophys. Res. Lett.* 42, 6221–6228. doi: 10.1002/2015gl064772

Shapiro, S. A. (2015). *Fluid-Induced Seismicity*. Cambridge: Cambridge University Press.

Sintubin, M. (2018). The groningen case: when science becomes part of the problem, not the solution. *Seismol. Res. Lett.* 89, 2001–2007. doi: 10.1785/0220180203

Skoumal, R. J., Brudzinski, M. R., and Currie, B. S. (2015). Earthquakes induced by hydraulic fracturing in Poland township, Ohio. *Bull. Seismol. Soc. Am.* 105, 189–197. doi: 10.1785/0120140168

Styles, P., Gasparini, P., Huenges, E., Scandone, P., Lasocki, S., and Terlizzese, F. (2014). *Report on the Hydrocarbon Exploration and Seismicity in Emilia Region. International Commission on Hydrocarbon Exploration and Seismicity in the Emilia Region.* ICHESE Report, 1–213. Available online at: http://mappegis.regione.emilia-romagna.it/gstatico/documenti/ICHESE/ICHESE_Report.pdf

Su, G. (2008). "Reservoir-induced seismicity forecast based on gaussian process machine learning," in *Proceedings of Information Technology and Environmental System Sciences: ITESS 2008*, Jiaozuo.

Tokuji, U., Yosihiko, O., Ritsuko, S., and Matsu'ura (1995). The centenary of the Omori formula for a decay law of aftershock activity. *J. Phys. Earth* 43, 1–33. doi: 10.4294/jpe1952.43.1

Vlek, C. (2018). Induced earthquakes from long-term gas extraction in groningen, the netherlands: statistical analysis and prognosis for acceptable-risk regulation. *Risk Anal.* 38, 1455–1473. doi: 10.1111/risa.12967

Vlek, C. (2019a). Rise and reduction of induced earthquakes in the Groningen gas field, 1991–2018: statistical trends, social impacts, and policy change. *Environ. Earth Sci.* 78:59.

Vlek, C. (2019b). The groningen gasquakes: foreseeable surprises, complications of hard science, and the search for effective risk communication. *Seismol. Res. Lett.* 90, 1071–1077. doi: 10.1785/0220180368

Wei, X., Li, Q., Li, X., and Niu, Z. (2020). Traffic light detection method for underground CO_2Ć injection-induced seismicity. *Int. J. Geomech.* 20, 04019162–04019161. doi: 10.1061/(ASCE)GM.1943-5622.0001573

Woo, J. U., Kim, M., Sheen, D. H., Kang, T. S., Rhie, J., Grigoli, F., et al. (2019). An in-depth seismological analysis revealing a causal link between the 2017 MW 5.5 Pohang earthquake and EGS project. *J. Geophys. Res.Solid Earth* 124, 13060–13078. doi: 10.1029/2019jb018368

Yang, H., Liu, Y., Wei, M., Zhuang, J., and Zhou, S. (2017). Induced earthquakes in the development of unconventional energy resources. *Sci. China Earth Sci.* 60, 1632–1644. doi: 10.1007/s11430-017-9063-0

Yue, Y., Peng, S., Liu, Y., and Xu, J. (2019). Investigation of acoustic emission response and fracture morphology of rock hydraulic fracturing under true triaxial stress. *Acta Geophys.* 67, 1017–1024. doi: 10.1007/s11600-019-00299-x

Zaliapin, I., and Ben-Zion, Y. (2016). Discriminating characteristics of tectonic and human-induced seismicity. *Bull. Seismol. Soc. Am.* 106, 846–859. doi: 10.1785/0120150211

Zbinden, D., Rinaldi, A. P., Urpi, L., and Wiemer, S. (2017). On the physics-based processes behind production-induced seismicity in natural gas fields. *J. Geophys. Res. Solid Earth* 122, 3792–3812. doi: 10.1002/2017jb014003

Zhang, H., Eaton, D. W., Li, G., Liu, Y., and Harrington, R. M. (2016). Discriminating induced seismicity from natural earthquakes using moment tensors and source spectra. *J. Geophys. Res. Solid Earth* 121, 972–993. doi: 10.1002/2015jb012603

Zhou, Z., Cheng, R., Cai, X., Ma, D., and Jiang, C. (2018). Discrimination of rock fracture and blast events based on signal complexity and machine learning. *Shock Vibrat.* 2018, 1–10. doi: 10.1155/2018/9753028

Zhou, Z., Cheng, R., Chen, L., Zhou, J., and Cai, X. (2019a). An improved joint method for onset picking of acoustic emission signals with noise. *J. Cent. South Univ.* 26, 2878–2890. doi: 10.1007/s11771-019-4221-5

Zhou, Z., Cheng, R., Rui, Y., Zhou, J., and Wang, H. (2019b). An improved automatic picking method for arrival time of acoustic emission signals. *IEEE Access.* 7, 75568–75576. doi: 10.1109/access.2019.2921650

Zhou, Z., Cheng, R., Rui, Y., Zhou, J., Wang, H., Cai, X., et al. (2020). An improved onset time picking method for low SNR acoustic emission signals. *IEEE Access.* 8, 47756–47767. doi: 10.1109/access.2020.2977885

Conflict of Interest: The authors declare that the research was conducted in the absence of any commercial or financial relationships that could be construed as a potential conflict of interest.

Copyright © 2020 He, Li and Li. This is an open-access article distributed under the terms of the Creative Commons Attribution License (CC BY). The use, distribution or reproduction in other forums is permitted, provided the original author(s) and the copyright owner(s) are credited and that the original publication in this journal is cited, in accordance with accepted academic practice. No use, distribution or reproduction is permitted which does not comply with these terms.

frontiers in Earth Science

ORIGINAL RESEARCH
published: 29 June 2020
doi: 10.3389/feart.2020.00194

Statistical and Non-linear Dynamics Methods of Earthquake Forecast: Application in the Caucasus

Tamaz Chelidze, Giorgi Melikadze, Tengiz Kiria, Tamar Jimsheladze and Gennady Kobzev*

M. Nodia Institute of Geophysics, Tbilisi, Georgia

In 20th century, more than 10 strong earthquakes (EQs) of magnitudes 6,7 hit South Caucasus, causing thousands of casualties and gross economic losses. Thus, strong-EQ forecast is an actual problem for the region. In this direction, we developed a physical percolation model of fracture, which considers the final failure of solid as a termination of the prolonged process of destruction: generation and clustering of micro-cracks, till appearance—at some critical concentration—of the infinite cluster, marking the final failure. Percolation provides a model of preparation of an individual strong event (slip or EQ). The natural seismic process contains many such events: the appropriate model is a non-linear stick-slip model, which is a particular case of the general theory of the integrate-and-fire process. Non-linearity of the seismic process is in contradiction with a memoryless Poissonian approach to seismic hazard. The complexity theory offers a chance to improve strong EQs' forecast using analysis of hidden (non-linear) patterns in seismic time series, such as attractors in the phase space plot. For a regional forecast, we applied the Bayesian approach to assess the conditional probability expected in the next 5 years of strong EQs of magnitudes five and more. Later on, in addition to Bayesian probability assessment, we applied to seismic time series the pattern recognition technique, based on the assessment of the empirical risk function [generalized portrait (GP) method]: nowadays, this approach is known as the support vector machine (SVM) technique. The preliminary analysis shows that application of the GP technique allows predicting retrospectively 80% of M5 events in Caucasus. Besides long- and middle-term forecast studies, intensive work is under way on the short-term (next-day) EQ prediction also. Here, we present the results of multiparametrical (hydrodynamic and magnetic) monitoring carried out on the territory of Georgia. In order to assess the reliability of the precursors, we used the machine learning approach, namely, the algorithm of deep learning ADAM, which optimizes target function by a combination of optimization algorithm designed for neural networks and a method of stochastic gradient descent with momentum. Finally, we used the method of receiver operating characteristics (ROC) to assess the forecast quality of this binary classifier system. We show that the true positive rate statistical measure is preferable for the EQ forecast.

Keywords: Earthquake forecast, phase space portraits, water level in wells, magnetic variations, machine learning, receiver operating characteristic

OPEN ACCESS

Edited by:
Giovanni Martinelli, National Institute of Geophysics and Volcanology, Italy

Reviewed by:
Alexey Lyubushin, Institute of Physics of the Earth (RAS), Russia
Galina Kopylova, Geophysical Survey (RAS), Russia

****Correspondence:***
Tamaz Chelidze
tamaz.chelidze@gmail.com

Specialty section:
This article was submitted to Solid Earth Geophysics, a section of the journal Frontiers in Earth Science

Received: *01 April 2020*
Accepted: *14 May 2020*
Published: *29 June 2020*

Citation:
Chelidze T, Melikadze G, Kiria T, Jimsheladze T and Kobzev G (2020) Statistical and Non-linear Dynamics Methods of Earthquake Forecast: Application in the Caucasus. Front. Earth Sci. 8:194. doi: 10.3389/feart.2020.00194

INTRODUCTION

Caucasus is located in the central section of the Alpine-Himalayan belt, namely, at the junction of its European and Asian branches. The seismicity of the region is connected with the ongoing northward convergence of the Arabian and Eurasian plates, which began in post-Oligocene (Adamia et al., 2017): now the GPS velocities in South Caucasus with respect to Eurasia vary from 2–5 mm/year in the western part to 12–14 mm/year in the eastern part of the region (Reilinger et al., 2006). Due to this convergence, in the 20th century alone, more than 10 strong earthquakes (EQs) of magnitudes from 6 to 7 hit South Caucasus, causing thousands of casualties and gross economic losses. Thus, the problem of forecast/prediction of strong EQs is important for the region. The following solution to this problem seems to be rational: (i) developing appropriate theoretical models for fracture process of solids and their testing in numerical experiments; (ii) statistical/non-linear analysis of seismic catalogs/geophysical data aiming to forecast long- and middle-term periods of increased probability of strong (say $M \geq 5$) EQs, and lastly, (iii) operative forecast (short-time prediction) of the next impending strong event by monitoring geophysical fields, sensitive to tectonic strain variation (hydrodynamic and magnetic fields' variations).

The EQ forecast/prediction-oriented geophysical network in Georgia consists of seismic stations' network (from 1890), the network of water-level (WL) monitoring boreholes (from 1988), and the Tbilisi/Dusheti geomagnetic station (from 1840), which has operated systematically for a long time. The summary of results, obtained in Georgia in the framework of the Soviet Union program for EQ prediction, were published by Chelidze et al. (1995).

THEORETICAL MODELS

The general approach to developing a physical model of seismic activity can be divided into two main problems: (i) constructing the physical model of the sequence of events preceding the main rupture (a single strong EQ) and (ii) analyzing the complexity of the entire seismic catalog, considered as time series of EQs (following the stick-slip or integrate-and-fire model).

Physical Model of a Single Strong Event Preparation

In series of papers (Chelidze, 1986, 1987; Chelidze and Kolesnikov, 1984), we developed the physical model of the fracture process based on percolation theory (Sahimi, 1994; Stauffer and Aharony, 1994; Aharony and Stauffer, 2010; Saberi, 2015), which considers the final failure as a termination of the prolonged process of damage accumulation in disordered media (Charmet et al., 1990; Herrmann and Roux, 1990). The model considers the fracture process as generation/coalescence of elementary fractures (with increasing volumetric concentration x) and their clustering, till appearance, at some critical concentration x_c, of the infinite cluster (IC) of cracks (the major rupture), marking the final destruction of the material. For the random distribution of elementary cracks with a constant interaction length L, both percolation theory and laboratory experiments (Zhurkov et al., 1977) prove that transition from a diffuse fracture state to the appearance of the IC (main rupture) occurs at a critical value of damage N:

$$N^{-1/3} = k_e/L1 \quad (1)$$

where N is the number of elementary cracks in the unit volume, k_e is the proportionality constant, and L is the mean size of cracks. According to Chelidze (1987), the value of k_e varies in the range 2.5–7 with the mean value 4 and is quite stable for very different values of $N^{-1/3}$ and L (Zhurkov et al., 1977). Percolation fracture theory provides also a mathematical model of preparation of a single large-scale strong dynamic event (slip or EQ).

It is clear that generation and merging of elementary cracks are connected with the emission of energy due to redistribution of local stresses. The appearance of each new crack provokes seismic energy emission with effective amplitude, depending on the increment of the size of the existing clusters after addition of a new elementary crack (Chelidze and Kolesnikov, 1984). The emitted energy or conditional amplitude A of the event, generated by the appearance of a new elementary crack, is

$$A \approx A_0 \left\{ \left(\sum_{i=1}^{k+1} s_i \right)^2 - \sum_{i=1}^{k} s_i^2 \right\}^{1/2} \quad (2)$$

where A_0 is a conventional amplitude of the dynamic signal, due to nucleation of a (isolated) single defect, k is the number of clusters merged by addition of an elementary defect, and s_i is the number of sites in the ith cluster, formed by merging two clusters. Thus, the value of A depends on the increment of the size of the resulting cluster formed by the coalescence of cracks caused by the appearance of a new elementary crack.

The percolation model allows formulating several possible precursors of the main fracture (Chelidze, 1986, 1987), for example, some anomalies in the behavior of the so-called percolation functions at approaching the final fracture, such as (i) increased divergence of finite size of clusters s, in other words, a strong increase in the scatter of amplitude A at approaching the critical crack concentration x_c; (ii) a strong increase of the number of large pulses, and (iii) a decrease of the slope of magnitude–frequency relation. Many of these precursors of impending final failure are observed in laboratory acoustic emission as well as in seismic time series (STS) preceding strong EQ (Chelidze, 1986, 1987).

At the same time, it is clear that such a separate event—formation of a single major rupture—is only an isolated episode of the long-term seismic process, containing many strong events (EQs). Analysis of this process calls for development of different models, which consider the mechanism of generation of a continuous sequence of separate strong events.

Modeling the Pattern of a Seismic Process—Long Time Series of EQs

We know that a seismic process is a large-scale continuous stick-slip motion along the fault plane, generating a sequence

of dynamic events of different magnitudes: the approach was initiated in other works (Brace and Byerlee, 1966; Burridge and Knopoff, 1967; Ruina, 1983). Such a stick-slip motion is a particular case of the general theory of the non-linear integrate-and-fire process (Pikovsky et al., 2003). On the laboratory slider-spring model, we show that a weak regular forcing synchronized stick-slip with this impact, which confirms the complex (non-linear) nature of the seismic process (Chelidze et al., 2005; 2006, 2010; Chelidze and Lursmanashvili, 2003; Chelidze and Matcharashvili, 2013, 2015). Non-linear models of the seismic process founded on complexity theory are in contradiction with a memory-less purely Poissonian approach to seismic hazard assessment (SHA), where all EQs are considered as independent events (Cornell, 1968; McGuire, 1976; Bender and Perkins, 1987; Ogata, 1998).

In the next section, we show that the complexity theory offers a chance to improve methods of strong EQs' forecast using analysis of hidden (non-linear) patterns in STS, such as attractors in the phase space (PS) plot.

LONG-TERM AND MIDDLE-TERM EQ FORECAST [BAYESIAN APPROACH, SUPPORT VECTOR MACHINES (SVMs), AND PHASE SPACE PORTRAITS (PSPs)]

Bayesian Approach

Besides the standard SHA of Georgia, in 1990, the Georgian Institute of Geophysics carried out together with the Russian Institute of Physics of Earth pioneering investigations related to developing the Bayesian mathematical model of EQ forecast by analysis of *i* precursors (Sobolev et al., 1991), which was called the map of expected earthquakes (MEEQ). We used Bayes equation for assessing conditional probabilities of EQ occurrence $P(D_1|\,K)$ in a given spatial pixel:

$$P(D_1|K) = \frac{P(D_1)\prod_{i=1}^{n} P(K_i|D_1)}{P(D_1)\prod_{i=1}^{n} P(K_i|D_1) + P(D_2)\prod_{i=1}^{n} P(K_i|D_2)} \quad (3)$$

where D_1 and D_2 are correspondingly alarm and quiescence diagnoses, K_i is the *i*th precursor, $P(K_1|\,D_1)$ and $P(K_i|\,D_2)$ are correspondingly probabilities of successful prediction and false alarm using *n* predictors, $P(D_1)$ is the unconditional stationary probability of the occurrence of an EQ of $M \geq 5$ in a spatial cell examined, and $P(D_2) = 1 - P(D_1)$ is the unconditional stationary probability of the occurrence of an EQ of $M \geq 5$.

The compilation of MEEQ envisions three steps: (i) generation of the map of stationary conditional probability $P_{scp}(D_1)$ of a strong EQ of $M \geq 5$ in the region (Caucasus) for a full catalog; (ii) compilation of non-stationary conditional probability $P(D_1|\,K)$ of the occurrence of a strong EQ of $M \geq 5$ using the ensemble of several predictors for a given time interval; (iii) compilation of probability gain (effectivity), obtained by using previously mentioned predictive signs in the time and space domains.

The basis of calculations was the seismic catalog of Caucasus from 1962 to 1987 (Sobolev et al., 1991), which is considered as homogeneous (events of M2.5 were registered without omission). Unfortunately, the regional catalog after 1987 due to political turmoil is of less quality.

The map of stationary conditional probability $P_{scp}(D_1|\,K)$ was calculated in the following manner: each strong EQ was represented by its preparatory area S_p, where, according to existing models of focal processes, significant anomalies of geophysical fields are expected—namely, the preparation areas with a size that is an order of magnitude larger than the rupture size L of a given EQ. The area S_p of such a focal zone for an EQ of $M \geq 5$ was accepted as a circular area of radius $R = 10L$, where $L \approx 8$ km. Accordingly, the S_p of a single event $S_p = \pi R^2 = 5{,}400$ km^2. The unconditional stationary probability $P_{usp}(D_1)$ of the occurrence of an EQ of $M \geq 5$ in a given spatial cell (pixel) per year is calculated by averaging the data of 36 strong EQs occurring in the period 1962–1983, with clusters taken as a single event. The $P_{usp}(D_1)$ per 5 years per pixel turns out to be 0.09. The stationary conditional probability $P_{scp}(D_1|\,K)$ was calculated by the Bayes formula, using the stationary predictors—amplitudes of vertical displacements and existence of fault intersections in a given cell.

For the calculation of the non-stationary conditional probability $P(D_1|\,K)$ map, we used the following time series of (time-dependent) predictors in a given pixel: density of seismogenic faults k_s, slope of the magnitude–frequency relation γ, seismic activity rate γ (number of events N per unit time), emitted seismic energy E_{em}. Note that the value of seismogenic faults' density k_s was defined as a function of seismic energy, emitted jointly by faults and activated in the volume V in the time interval Δt. Predictors are calculated as deviations of their current values from the long-term (background) values, normalized to the mean square error of the averaged background value. The details of calculations of the magnitudes of predictors and their critical values, when the alarm period should be announced, are presented in the literature (Sobolev et al., 1991; Chelidze et al., 1995; Zavjalov, 2006).

We applied the Bayesian approach to assess conditional probability expected in the next 5 years of strong EQ of magnitudes five and larger. Specifically, the probability of alarm was calculated by the above Bayes equation, where $P(D_1|\,K)$ was considered as a time-variable probability. The probabilities of successful forecasts and false alarms as well as the mean alarm periods were estimated from the retrospective analysis of predictors' database and the regional catalog of strong EQs. The forecast was recognized as a successful one if the EQ preparation area, defined as the circle of radius $R = 10L$, where L is the half length of the EQ rupture, covers more than half of the pixel with a high value of conditional probability $P(D_1|\,K)$, namely, where the ratio of $P(D_1|\,K)$ to the stationary conditional probability $P_{scp}(D_1|\,K)$ is of the order of 2 or more. The 5 years' duration of the alarm period was adopted.

The efficiency or probability gain in the time and space domains (correspondingly J_t and J_s), obtained by application of abovementioned methodology, was calculated as

$$J_t = \frac{N_{pr}/T_{sa}}{N_{sum}/T_s}$$

where N_{pr} is the total number of predicted EQs and N_{sum} is the total number of EQs during summary observation period T_s; T_{sa} is the summary duration of alarms.

$$J_s = \frac{N_{pr}/S_{sa}}{N_{sum}/S_{obs}}$$

where S_{sa} is the summary area of alarms and S_{obs} is the summary area of observations.

The MEEQ compiled for the period 1988–1992 marks an anomaly in the epicentral areas of the Spitak (M6.9, December 1988) and Racha (M7, April 1991) EQs. The Spitak anomaly appears in the MEEQ alarm period beginning from 1986 to 1990. There was no anomaly in MEEQs of the Racha region till 1988, when a stable anomaly appears close to the epicentral area of impending EQ (Sobolev et al., 1991; Chelidze et al., 1995).

The foregoing methodology was further developed and applied to different seismo-active regions of the globe: Central Asia, South California, China, Western Turkey, and Greece (Zavjalov, 2006). In most cases, the probability gain J_t was 2.5 compared to random guess, and the mean area of alarm S_{sa} occupies only 30% of the total area S_{obs} with a seismic rate of one EQ per year.

Generalized Portrait (GP)—SVMs

Later on, Chelidze et al. (1995) used for a long-term forecast the pattern recognition technique (GP method), based on the assessment of the empirical risk function (Vapnik and Chervonenkis, 1974; Vapnik, 1984), in addition to Bayesian probability assessment. Nowadays, this approach is known as the SVM technique (Burges, 1998; Nello and Shawe-Taylor, 2000; Steinwart and Christmann, 2008; Theodoridis and Koutroumbas, 2009). The main point of the SVM technique is calculating the so-called Vapnik–Chervonenkis (VC) dimension. The VC measure divides the vector space (where the components of vectors are different EQ predictors) into two classes: EQ alarm and quietness. It is important that the method is not very demanding to the size of the data sample.

The GP technique can be briefly summed as follows: there is a sequence of situations which reflect the existence of some distribution density function $P(x)$. Variable x is a vector, which can have many components (features, symptoms, and predictors). These situations, represented by the corresponding set of predictors, can be linked to a definite class of events ω by some teaching algorithms in assumption that there exists the conditional probability $P(\omega|\ x)$. If $\omega = 0$, then vector x is attributed to the first class, and if $\omega \neq 0$, the situation belongs to the second class. Both $P(x)$ and $P(\omega|\ x)$ are unknown *a priori*: all that we know is that they really exist and that these probabilities reveal themselves in the (x, ω) pairs, obtained after n observations of the vector x and corresponding classifications ω: x_1, ω_1; x_2, ω_2; x_3, ω_3 … x_n, ω_n. From this correspondence set, one should derive a diagnostic rule, which guarantees the minimal number of errors in the used class a of a decision function. The quality F of the rule, which links ω and x as $\omega = F(x, a)$, is controlled by the risk function $I(F)$:

$$I(F) = \int(\omega - F(x, a))^2 * P(\omega|x)\, P(x)\, dx = \int q(z) P(\omega|x)\, P(x)\, dx \quad (4)$$

where the term $q(z) = [\omega - F(x, a)]^2$ is called the risk function. Each classification error increases the function $I(F)$, as in this case, the observed class and the predicted class do not coincide, which means that $z \neq 0$ and correspondingly $q(z) = 1$; on the contrary, if $z = 0$, i.e., the predicted class is correct, then $q(z) = 0$ and the risk function $I(F)$ does not increase. Thus, the pattern recognition problem is solved if a chosen risk function is optimal and the risk function $I(F)$ is minimal for a given $P(x|\ \omega)$. The diagnostic rule optimization rests on the analysis of the following features: (i) number of errors, (ii) complexity of rule, and (iii) length of the x, ω-sequence. The practical rule for the application of the GP method is that the dimensionality of the space of predictors d should be at least three times less than the length of the experimental x, ω-sequence l: $(l/d) > 3$. After this, we search for the simplest class of F-functions, which allows us to construct the optimal hyperplane, dividing the set of x-vectors into two classes. The term GP is attributed to the vector Q, which is normal to the dividing hyperplane. If perfect separation of classes is impossible, the most "naughty" x, ω-pair, which prevents division of classes, is to be excluded, then the next one, and so on, until the two classes are divided without overlapping by the distance R, which represents the width of the dividing strip between two classes. The ratio of the number of withdrawn vectors to the total number of vectors defines the level of diagnostic rule reliability.

The above methodology was applied to forecast periods of strong EQ of $M \geq 5$ in Caucasus. The catalog contained 53 events, occurring after 1971. The predictors used earlier in the Bayesian approach, namely, the density of seismogenic faults k_s, the slope of the magnitude–frequency relation γ, the seismic activity rate γ (number of events N per unit time), and the emitted seismic energy E_{em}, were used in the GP approach also. Actually, only 30 active periods before strong EQs were used as the experimental sequence, because considerable time is needed for the accumulation of averaged values of predictors. Most of the training procedures follow a scheme: 24 quarterly values of each predictive function during 6 years, preceding a strong EQ, were picked out. The first 12 values of these sub-predictors were attributed to the second class (quiet period) and the last 12 values to the first class (alarm periods); different schemes were also tested (Chelidze et al., 1995). The retrospective forecast was considered as a successful one if the last 12 quarterly values of the sub-predictor set were recognized as first-class objects. **Table 1** represents the results of the application of the GP technique to forecasting the periods of increased EQ hazard level in Caucasus.

The preliminary analysis shows that application of the GP technique with a predictor γ (the slope of magnitude–frequency relation) allows retrospectively forecasting 85% of periods with M5 events and 100% of calm periods without strong events in Caucasus (Chelidze et al., 1995; Zavjalov, 2006). Addition of a less informative predictor E_{em} (emitted seismic energy) spoils the total forecast quality by 11%.

TABLE 1 | Results of the application of the GP technique to forecasting the periods of increased EQ hazard level in caucasus using predictor γ or predictors γ and E_{em} jointly; n is the number of a given class situation—alarm or quietness.

Classes	Predictor γ			Predictors γ and E_{em}		
	n	Successes	Failures	n	Successes	Failures
Class 1—alarm	28	24 (85.7%)	4 (14.3%)	27	21 (74.2%)	6 (25.8%)
Class 2—quiet	31	31 (100%)	0 (0%)	28	25 (89.3%)	3 (10.7%)
Total	59	55 (93.2%)	4 (6.8%)	55	46 (81.9%)	9 (18.1%)

Middle-Term Forecast: PSPs

To obtain a middle-term forecast, we analyzed the number of seismic events in a sequential time window—a seismic rate (Sobolev, 2011). The seismic rate is widely used as a proxy of the strain rate in the Earth crust (Dieterich et al., 2000). We performed PS analysis of data sets obtained from the seismic catalog of Caucasus 1960–2011 (Chelidze et al., 2018). The representative magnitude for the period is M2. In this instrumental period, the two largest EQs, Spitak and Racha (M6.9–7), struck the region in 1988 and 1991 correspondingly. Three areas were selected: (i) Batumi area, in order to show the pattern of STS in a seismically (relatively) quiet region; (ii) Spitak; and (iii) Racha. We analyzed both original and declustered, by Riesenberg algorithm (Reasenberg and Matthews, 1988), STS using the catalog of Georgia (Tsereteli et al., 2016). The following parameters of STS were varied: (i) different epicentral areas, where STS were obtained; (ii) length of the time window for the rate count; (iii) year span (periods in the catalog); (iv) periods before and after strong events; and (iv) different magnitude thresholds (Chelidze et al., 2018). The PSPs were compiled using both original STS and STS smoothed by the Savitzky–Golay (SG) filter. The SG filter has the advantage over, for instance, the moving average filter, as the magnitude of the variations in the seismic rate data, i.e., the value of the local extremes, is preserved (Press et al., 2007). Trajectories on PSP plots are obtained by connecting the consecutive phase states in a clockwise direction, which corresponds to an increase in time. For plotting phase plots, we used either standard MATLAB scripts (seism_port or phase_portrait). Both approaches sometimes produce negative values of phase states, which means that the smoothed lagged values in a given window are smaller than in the previous ones. In the following, we only show results, compiled in the following way (Sobolev, 2011): on the X-axis are plotted the mean values of the number N of EQs per n days, and on the Y-axis is plotted a differential of N for the next 10 days, i.e., $(N_{i=10} - N_i) = dN$. The trajectories on PSP plots form a "noisy attractor" with a diffuse source area. Such attractors are common in biological systems (Molaie et al., 2013).

The PS plot analysis reveals some fine details of the seismic process dynamics related to strong EQ precursory/post-event patterns. The plots generally manifest two main features: a diffuse but still limited "source/basin" area, formed by background seismicity, and anomalous orbit-like deviations from the source area, which are related to foreshock and aftershock activity of strong EQs or to appearance of clusters.

In **Figure 1**, we present an example of application of the PS reconstruction method to EQ time series, which revealed nonlinear structures in the PSP for the circular area with radius $R = 200$ km of the strong Racha EQ (M7), which occurred in West Georgia at 9:12 UTC on 29 April 1991. The used catalog covers the time long before, during, and after the EQ occurrence. The dates on different trajectories mark strong EQ occurrences in the area. The most extended orbits reach the maximal deviations at lags dN equal to 10 or 20 days on the following dates: (i) 1976, August—during swarm of EQs within $R = 200$ km; (ii) 1991, May—close to the moment of the Racha EQ mainshock, M7.0; (iii) 1991, June—the moment of a strong Java aftershock of the Racha EQ (15 June 1991, M6.2); and (iv) 2009, October—the time of the Racha EQ on 8 September 2009, M6.0 (the late aftershock of the main 1991 Racha EQ).

The whole length of the most extended trajectory with the label 3 May 1991 is 133 days, from start to finish at the source cluster. The time from the moment when a significant deviation from the background seismicity ("noisy" basin) begins to that with the label 3 May 1991 is approximately half of the full orbit duration. We presume that this time is needed to form a "precursory" half orbit, lasting approximately 60 days. We presume that a strong deviation of the orbit from the source area is a precursor of the Racha 1991 event, due probably to foreshock (correlated) activity, not excluded fully by Reasenberg declustering. Indeed, Matcharashvili et al. (2016) showed that after Reasenberg declustering, many correlated events are still left in the catalog.

Similar PSPs were obtained for the Spitak EQ area (Chelidze et al., 2018): the PS orbit begins to deviate from the fuzzy source area approximately 60 days before the Spitak event. It is necessary to note that the long-deviating orbit for 1983 was obtained also in the quiet Batumi area due to the effect of a remote ($R \approx 500$ km) 1983 Erzurum EQ (Chelidze et al., 2018). However, in PSPs of Racha and Spitak test areas, there are no orbits connected with the 1983 Erzurum EQ, despite the comparable distance between the EQ and test areas. Probably, this is due to the directivity effect. We conclude that the strong EQ forecast using the PSP approach is promising for revealing deviations in the time domain 30–60 days before the strong event, though the location of impending event remains uncertain.

The results of PSP analysis are intriguing, but we still need many efforts to get definite conclusions: are they just PSPs, or are they real strange attractors obeying the model of deterministic chaos, like those proposed by Sobolev (2011)? The appearance of the strange attractor means that the state of system after some

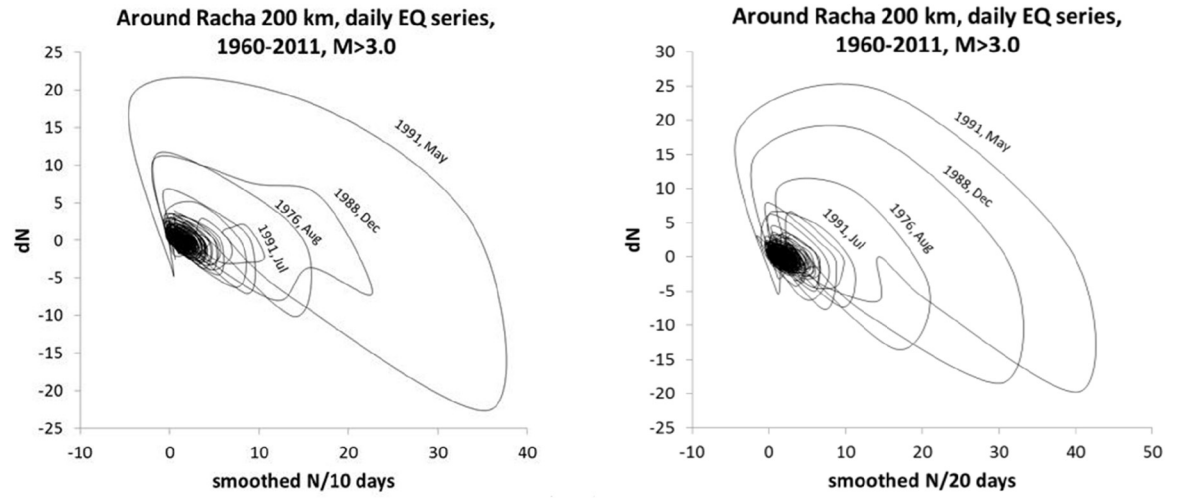

FIGURE 1 | Phase space portraits plotted for the number of EQs *N* smoothed by the Savitzky–Golay filter versus *dN* using the declustered catalog (10 and 20 days of smoothed EQ number with a 1-day step) for the area with *R* = 200 km around the Racha EQ epicenter. On the *X*-axis are plotted the mean values of the number *N* of EQs per *n* days, and on the *Y*-axis is plotted a differential of *N* for n days, i.e., $(N_{i=n} - N_i) = dN$ for *n* = 10 (left) and 20 (right) days. The dates on trajectories mark strong EQ occurrences.

delay repeats itself, i.e., the orbits attain the limit cycle. We cannot expect such regular behavior in a complicated extremely heterogeneous Earth system (see **Figure 1**), but still deviations of orbits from the source area seem to be informative for EQ source physics.

SHORT-TERM OPERATIONAL FORECAST

Networks, Devices, Data

Besides these statistical models, oriented to regional long- and middle-term forecast studies, intensive work is under way on the short-term EQ forecast/prediction also. The most systematic work in this direction in Georgia is connected with regular monitoring of WL in the network of deep wells, which began in 1988. Here, we present the results of multiparametrical (hydrodynamic and magnetic) monitoring carried out in 2017–2019 on the territory of Georgia.

In this paper, the WL monitoring data in deep wells' network in Georgia, operated by the M. Nodia Institute of Geophysics (**Figure 2**), are used. The WL monitoring network in Georgia includes several deep wells, drilled in a confined subartesian aquifer: Kobuleti, Akhalkalaki, Marneuli, Lagodekhi, Ajameti, Chvishi, Nokalakevi, and Oni (**Table 1** and **Figure 2**). The sampling rate at all these wells is 1/min (except Oni, where the sampling rate is 1/10 min). Measurements are done by sensors MPX5010 with a resolution at 1% of the scale (Freescale Semiconductors; [1]) and recorded by a datalogger XR5 SE-M (Pace Scientific; [2]) remotely thru a modem, Siemens MC-35i Terminal (Siemens) using program LogXR; the datalogger can acquire WL data for 30 days at the 1/min sampling rate. Variations of WL represent an integrated response of the aquifer to different periodic and quasi-periodic (tidal variation and atmosphere pressure) as well as to non-periodic influences, including generation of EQ-related strains in the Earth crust of the order of 0.1–0.001 microstrain. The atmosphere pressure factors (**Figure 3**) were subtracted from the summary WL variations.

Magnetic variations were recorded at the Dusheti Geophysical Observatory (latitude 42.052N, longitude 44.42E), by the fluxgate magnetometer FGE-95 (Japan), registering *x*, *y*, *z* components at a count rate of 1/s with accuracy of 0.1 nT. The data are representative for a whole territory of Georgia.

Machine Learning (ML) Methodology

Quantitative analysis of impacts of different components of endogenous and exogenous origins in the observed integral dynamics remains one of the main geophysical problems. Especially important, taking into account their possible prognostic value, is identifying the impact of non-periodic processes related to the EQ generation. We investigate the dynamics of regular and non-periodic components in the considered time series using special ML programs: ADAM and ROC (Diederik and Ba, 2014). The advances in ML allow teaching computers to learn from the observed data how to make decisions or predictions (Bottou and Bousquet, 2012; Diederik and Ba, 2014). In the last years, ML was successfully applied to the problem of laboratory stick-slip and slow EQ sequence prediction (Rouet-Leduc et al., 2017, 2019). We presume that other geophysical observations, sensitive to earth strain, also are promising for EQ prediction. Namely, we used the ML approach to make a short-term forecast (prediction) of

[1] www.freescale.com

[2] http://www.pace-sci.com/data-loggers-xr5.htm

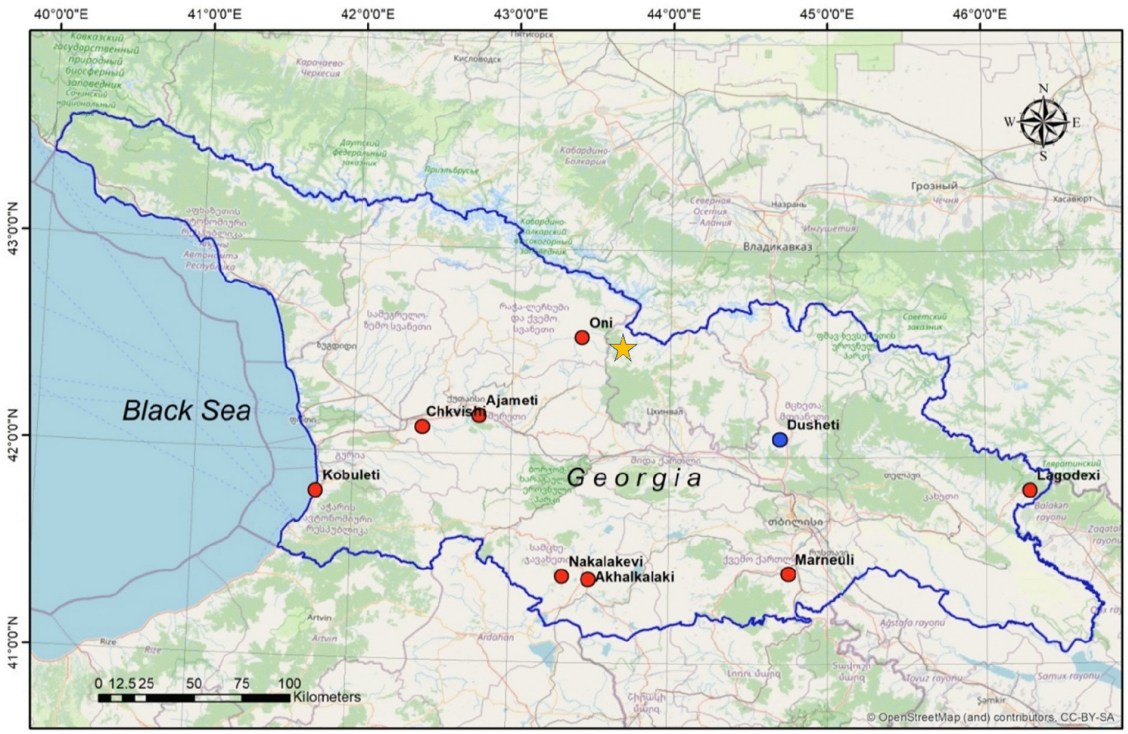

FIGURE 2 | Map of Georgia with location of the deep wells' network (red circles) for WL monitoring and the Dusheti Geomagnetic Observatory (blue circle). The star marks the location of the 1991 M7 Racha EQ.

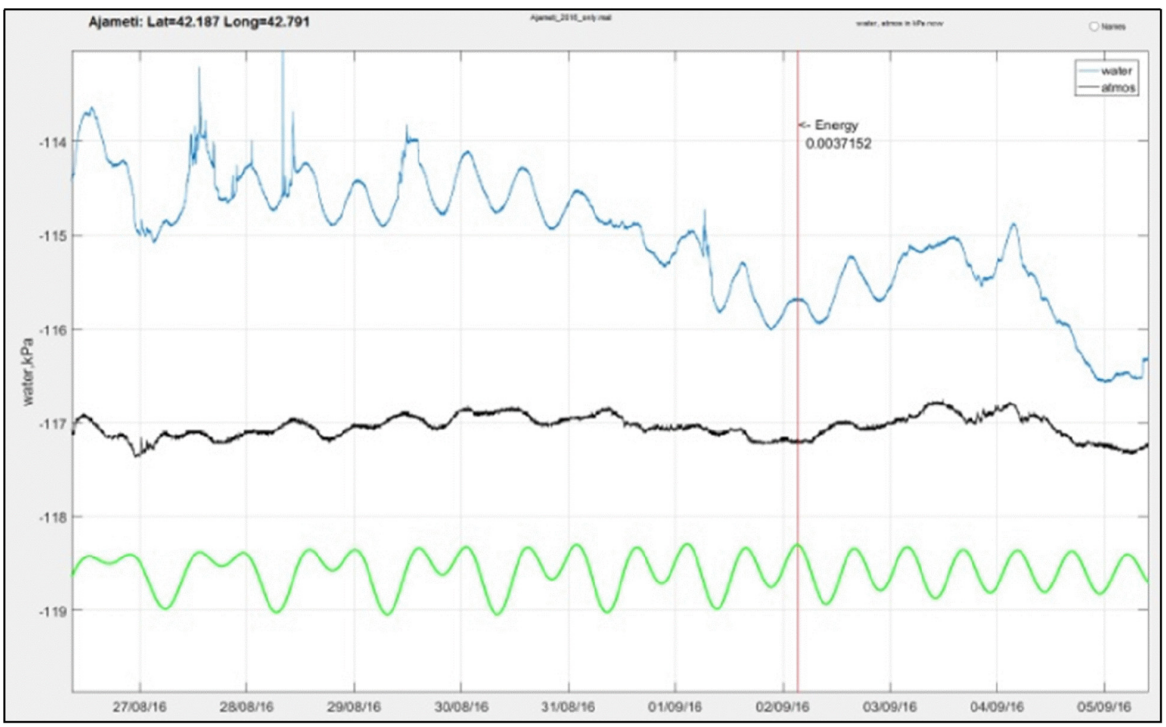

FIGURE 3 | Recording of WL (blue), barometric pressure (black), and computed tidal variations (green) in the Ajameti well before and after the 02/09/2016 Gagra EQ (M4), marked by the red line.

EQs of magnitudes M3–4 in Georgia and adjoining territories using as predictors the training geophysical monitoring data on WL in the deep wells' network and geomagnetic field. The choice of precursory signs of the impending EQ is founded on the theoretical models of tectonic/seismic process as well as on numerous field observations of pre-seismic anomalies. It is well known that underground water dynamics and, in particular, WL variations in the deep wells reflect anomalous pre-seismic hydraulic flows in the aquifer due to the impact of tectonic strain (King et al., 2000; Wang and Manga, 2009; Martinelli, 2015). We choose the interaction length R for EQs of M3–4 hydraulic precursors (R = 200 km) for a given well. Note, that there are different assessments of EQ precursory area. According to the widely used models, the anomalous precursory static strain area (Dobrovolsky et al., 1979) is of the order of 20–30 km for EQs of M3 and 50–70 km for M4. We presume that there are at least two mechanisms, which can explain the accepted long radius of action of hydraulic precursors (R = 200 km): (i) long-range fluid diffusion from the stressed source to the well due to poroelastic effects and (ii) the fast squirt-flow (Dvorkin et al., 1994) of pore water from the EQ source to the well, excited by foreshocks of the impending EQ – such signals can travel on a long distance (Chelidze et al., 2016). The small spikes in WL before EQ (**Figure 3**) can be explained by foreshock activity in the EQ source.

The geomagnetic field's variations are also recognized as possible tectonic strain-related signs of impending EQ (Stacey, 1964; Kopytenko et al., 1990; Pulinets and Boyarchuk, 2004). The physical mechanism of precursory magnetic anomaly can be the magnetostriction of rocks (Stacey, 1964), magnetic field induced by underground water flow (Jouniaux and Pozzi, 1995), and migration of positive holes (p-holes) or gases/fluids along the fault due to tectonic stress, leading to the appearance of magnetic field anomalies due to lithosphere–atmosphere–ionosphere coupling (De Santis et al., 2019). By the way, Kopytenko et al. (1990) detected geomagnetic anomalies in recordings of the Dusheti Geomagnetic Observatory in Georgia before the strong 1991 Racha (M7) and 1988 Spitak (M6.9) EQs.

Precisely, we analyzed WL in the wells, tidal variations (Tid1, Tid2, and Tid3), local magnetic field components (mv1, mv2, and mv3)—where numbers 1, 2, and 3 correspond to x, y, and z components of the variables—and hourly geomagnetic DST index (DST) data for the year 2019 (**Table 1**).

TABLE 2 | Locations and depths of wells in Georgia.

Location	Name	Depth of well, m	Interval of screen, m	Aquifers' lithology
Nakalakevi	Nak	600	255–367	fractured andesite–basalts
Kobuleti	Kblt	2,000	187–640	fractured andesite–basalts
Marneuli	Marn	3,505	1,235–1,600	fractured mergels
Chvishi	Tsk	3,675	3,250–3,675	fractured limestones
Akhalkalaki	Akh	1,400	100–1,400	fractured andesite–basalts
Ajameti	Ajmt	1,339	520–740	fractured limestones
Lagodekhi	Lgdx	800	255–367	fractured shales
Oni	Oni	255	70–250	fractured shale and basalts

The example of WL recording in the Ajameti well before the 02/09/2016 Gagra EQ and synchronous data on tidal variations and barometric pressure are presented in **Figure 3**. The small anomalous WL spikes before EQ are noticeable even visually.

In the **Table 3**, we present the values of WL with correction factors for each well with a 1-min count rate and synchronous tidal and geomagnetic data. In the last column of the table, the occurrences of EQs (Events) at a given day, hour, and minute on the distance of R = 200 km from the well are marked by 1 and their absence by 0.

For the analysis of observed data, we used the algorithm of deep learning ADAM (Kingma and Ba, 2014), which optimizes target function by the combination of the optimization algorithm designed for neural networks (Karpathy, 2017) and a method of stochastic gradient descent with momentum (Bottou and Bousquet, 2012). Our goal is to reveal the change in ML, using statistical characteristics of the time series of **Table 3**, which precede (here, by 1 day) the occurrence of a seismic event of M3–4; in other words, we consider the next-day EQ forecast problem. In order to apply the ML approach to 1-min observation data (**Table 3**), it is necessary to transform standard input files into somehow structured data, which permits finding hidden regularities and optimization of prediction. Namely, we calculate

TABLE 3 | One-minute values of predictors and correction factors: water level in the well, tidal variations' components, magnetic field components, geomagnetic DST index, and EQs.

Date	Water	Tid1	Tid2	Tid3	Mv1	Mv2	Mv3	DST	Event
1/11/2019 0:00	−130.175	−0.0211	−0.01516	−0.1135	−18.7	−25.1	105.0	−18	0
1/11/2019 0:01	−130.155	−0.02092	−0.01502	−0.11385	−18.7	−23.7	104.6	−18	0
1/11/2019 0:02	−130.155	−0.02075	−0.01488	−0.11418	−18.4	−23.2	104.8	−18	0
..	..	..	..	..	..	..	..	..	..
..	..	..	..	..	..	..	..	..	..
1/22/2019 18:35	−128.697	−0.01092	0.068955	−0.01541	19.3	43.3	203.1	6	1
..	..	..	..	..	..	..	..	..	..
..	..	..	..	..	..	..	..	..	..
12/31/2019 23:09	−134.191	−0.05563	−0.02369	−0.04903	29.0	3.7	196.1	−3	0

*Similar analysis of input data was carried out for other seven wells: the results are presented in **Tables 5**, **6**.*

for each observation data value (Water, Tid1, Tid2, Tid3, Mv1, Mv2, Mv3, and DST), presented in **Table 2** (at a minute count rate), with five statistical functions: Average, Var, SD, Min, and Max. As a result, we obtained **Table 4** with dimension 45 × 365 for the mentioned predictors. We also add the 46th column with values 0 or 1 which mark the occurrence (1) or absence (0) of a seismic event in the range M3–4 at the distance of 200 km from the well at a given minute of the year. The catalog used for compilation of the column was from www.emsc-csem.org.

As a result, we obtained 40 input and one output (target) data for ML. **Table 4** is constructed so that a specific day with 40 previously known statistical parameters corresponds to the value of the next day's event occurrence (0 or 1). We are looking for a functional connection of the previous precursory day data to the next-day seismic event. In other words, the next-day EQ forecast is produced on the basis of statistical analysis of five geophysical variables for the preceding days.

It was interesting to explore the forecasting potential used in ML statistical measures. In **Figure 4**, we present the weights of such measures, obtained in the process of ML on our 1-day input data for the Ajameti well. We see that in this case the leading factors are the maximal value of the *z*-component of tidal variation, then followed by, approximately with the same weights, the *x*-component of magnetic variation and the mean daily value of WL. In general, in all wells, we find six to seven measures, which have the largest weights. This conclusion could change if we include into the input data several preceding days, which we plan to do in the future. The recent paper of Zhang et al. (2019) indicated that the magnitude and phase shift of the tidal response changed significantly after the great Tohoku EQ, so we can expect that a similar effect can take place during EQ preparation.

In order to estimate the reliability of the precursors, we used the methodology of receiver operating characteristics (ROC), which is a standard technique for assessing the performance of a binary classifier system (Fawcett, 2006). We are looking for a binary classification (positive *p* or negative *n*) of data with four possible outcomes (diagnoses): if the prediction outcome is positive *p* and the actual value is also *p* (i.e., the event is correctly predicted), then the outcome is called a true positive (TP) with synonyms sensitivity, recall, and hit rate. If, on the contrary, the diagnosis is positive *p* and the actual value is *n*, then the prediction is false positive (FP) with the synonym fallout. Accordingly, when both the diagnosis and the actual value are *n*, the result is a true negative (TN), and when the prediction outcome is *n* while the actual value is *p*, the prediction is classified as a false negative (FN). Using these four diagnoses, the ROC program provides the possibility to calculate the following statistical measures:

Precision = $\frac{TP}{AV} = \frac{TP}{TP+FP}$; Recall = True positive rate (TPR) = $\frac{TP}{TP+FN}$; Accuracy = $\frac{TP+TN}{TP+FP+TN+FN}$

False positive rate (FPR) = $\frac{FP}{FP+TN}$; *F*-measure = *F*-score = $2\frac{\text{precision}*\text{recall}}{\text{precision}+\text{recall}}$ - the harmonic mean of precision and recall: the perfect value of the score is 1, and the worst one is 0.

TABLE 4 | Daily values of statistical measures for the complex of predicting fields presented in **Table 3**.

Date	Average of water	Average of Tid1	Average of Tid2	Average of Tid3	Average of mv1	Average of mv2	Average of mv3	Average of DST	Var of water	Var of Tid1	Var of Tid2	Var of Tid3	Var of mv1	Var of mv2	Var of mv3	Var of DST	SD of water	SD of Tid1	SD of Tid2	SD of Tid3	SD of mv1	SD of mv2	SD of mv3	SD of DST	Min of water	Min of Tid1	Min of Tid2	Min of Tid3	Min of mv1	Min of mv2	Min of mv3	Min of DST	Max of water	Max of Tid1	Max of Tid2	Max of Tid3	Max of mv1	Max of mv2	Max of mv3	Max of DST	Event
1-Jan	.	.	.	.	.	.	.	.	.	.	.	.	.	.	.	.	.	.	.	.	.	.	.	.	.	.	.	.	.	.	.	.	.	.	.	.	.	.	.	.	0
2-Jan	.	.	.	.	.	.	.	.	.	.	.	.	.	.	.	.	.	.	.	.	.	.	.	.	.	.	.	.	.	.	.	.	.	.	.	.	.	.	.	.	0
.	.	.	.	.	.	.	.	.	.	.	.	.	.	.	.	.	.	.	.	.	.	.	.	.	.	.	.	.	.	.	.	.	.	.	.	.	.	.	.	.	1
.	.	.	.	.	.	.	.	.	.	.	.	.	.	.	.	.	.	.	.	.	.	.	.	.	.	.	.	.	.	.	.	.	.	.	.	.	.	.	.	.	.
.	.	.	.	.	.	.	.	.	.	.	.	.	.	.	.	.	.	.	.	.	.	.	.	.	.	.	.	.	.	.	.	.	.	.	.	.	.	.	.	.	.
31-Dec	.	.	.	.	.	.	.	.	.	.	.	.	.	.	.	.	.	.	.	.	.	.	.	.	.	.	.	.	.	.	.	.	.	.	.	.	.	.	.	.	0

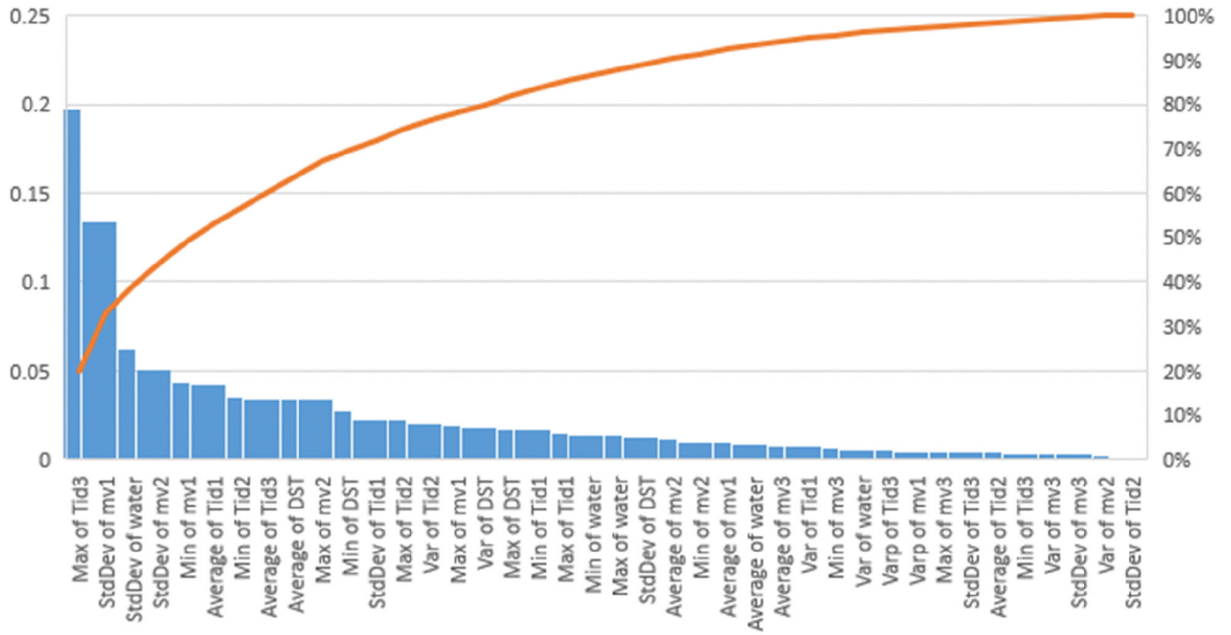

FIGURE 4 | The weights of different statistical measures, obtained in the process of machine learning using input data for the Ajameti well (blue columns). The red curve shows the cumulative percentage of separate weights.

The K-S statistic is a non-parametric test of the equality of continuous one-dimensional probability distributions that can be used to compare a sample with a reference Kolmogorov–Smirnov probability distribution.

Phi coefficient = (TP * TN - FP * FN)/sqrt[(TP + FP) * (TP + FN) * (TN + FP) * (TN + FN)], which is a correlation coefficient between the observed and predicted binary classifications; it returns a value between + 1 (a perfect prediction) and −1 (total disagreement between prediction and observation).

Lift = [TP/(TP + FP)]/[(TP + FN)/(TP + FP + TN + FN)], which is a measure of the performance of a model at predicting or classifying cases, measuring against a random choice model, i.e., how good it is at identifying the positive (1s) or negative (0s) instances of our dataset.

Kendall's tau coefficient and Spearman's rank correlation coefficient (rho) assess Pearson's correlation between the input values and target values with a difference that the first one works well in the case of linear relationships, whereas the second one is applicable even with non-linear relationships.

ROC AUCH (ROC convex hull) = ROC AUC (area under the ROC curve), which is a performance measure for the ROC classification problem at various thresholds settings. It tells how much the model is capable of distinguishing between classes 1 and 0. The higher the AUC, the better the model predicts 0 as 0 and 1 as 1.

ML Results

The sequence of resources created to generate the deep learning net for all wells (Deepnet) was as follows: Dataset ML_(well name)_2019: 365 instances, 40 fields (1 categorical, 40 numeric); Deepnet ML_(well name)_2019; auto structure suggestion; three hidden layers; ADAM; learning rate = 0.001; beta1 = 0.9; beta2 = 0.999; epsilon = 1e-08; missing values; and max. training time = 1,800. The only parameter which varies for different wells is the number of iterations (indicated for each well separately).

As an example, we show in detail the ML workflow for the 2019 Ajameti well (**Figure 5**); the number of iterations is 177. Analyzing results presented in **Figure 5**, we can conclude that the used technique allows next-day forecast (predicting) of 38 EQs (TP) from the total number of 44. Three predictions of event occurrence turn to be false—FP. Seven predictions of the quiet state failed (FN), and 299 of them correctly predicted quietness (TN).

According to **Table 5** wells allow forecast of next-day EQ with lesser omission. Note that the sum of all ROC values is less than 365, which means that some days' observations failed. **Table 6** contains values of different statistical measures, which we explained above. These data characterize in more detail the different aspects of ADAM algorithm forecasts.

According to the data presented in **Tables 5**, **6**, five wells (Ajameti, Akhalkalaki, Chvishi, Lagodekhi, and Oni) have good next-day joint EQ/quietness prognostic characteristics (ROC AUCH 0.97–0.81). At the same time, it is necessary to point that due to an overwhelming prevalence of quiet days, even the random prediction of the quiet state is highly successful, and this makes the success of joint prediction very high. We conclude that ROC measures, containing the TN value, increase the joint assessment (ROC AUCH) values. Consequently, the

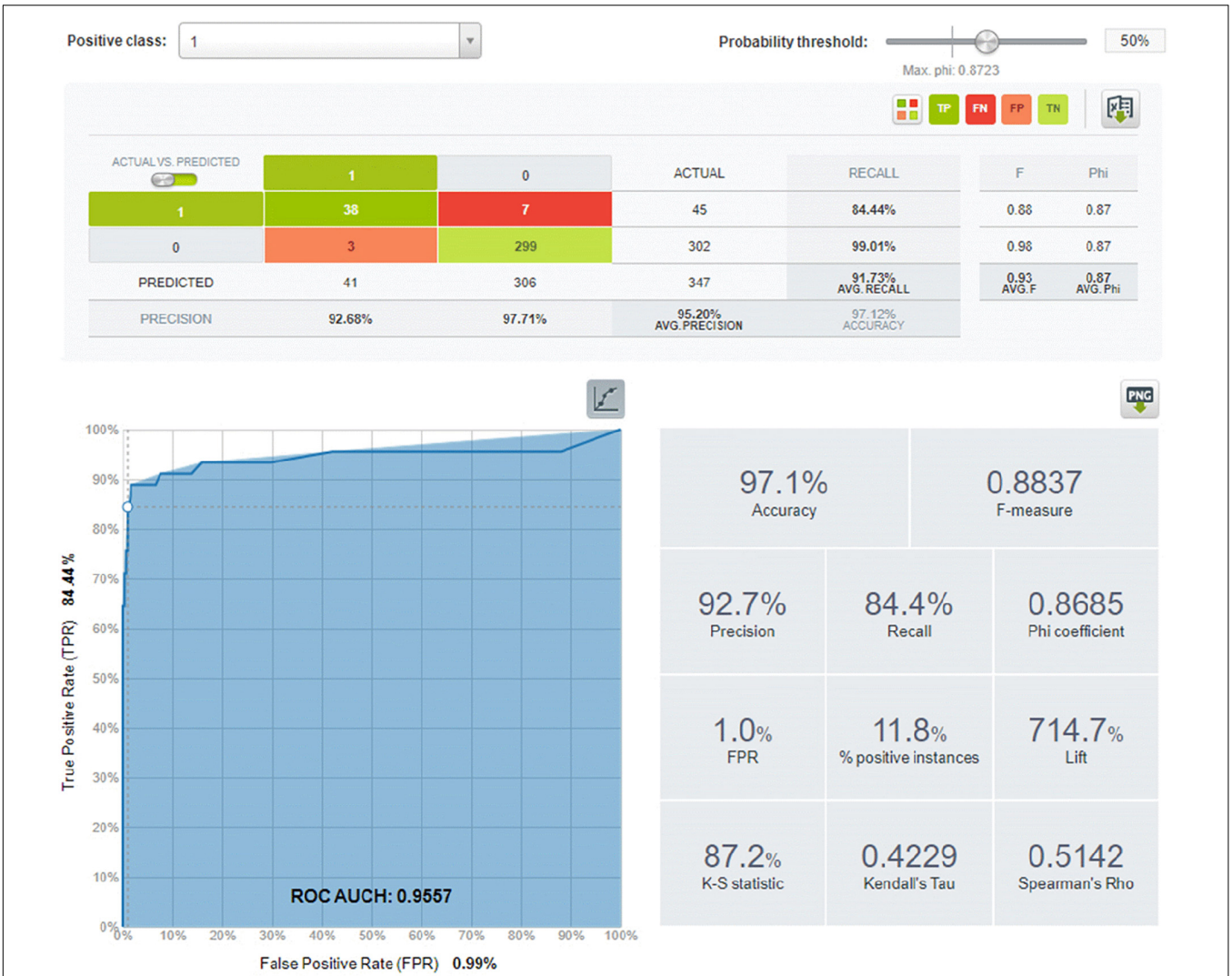

FIGURE 5 | Machine learning and ROC analysis results for 1-year data: next-day M3–4 EQ forecast results for the Ajameti well area (R = 200 km).

really important measures for the EQ-oriented prediction are "EQ-selective" measures, which do not include TN measures, such as TPR = Recall. In this case, the "best" wells seem to be Ajameti and Chvishi. Note that this conclusion is true only for the next-day forecast—we hope that taking into account input data for several forerunning event days instead of one day can improve the forecasting potential of the used ML algorithm. We cannot exclude also the possibility of different sensitivities of separate wells to pre-seismic deformations, affecting WL in wells.

It is interesting to note that calculated tidal variations reveal high forecasting potential (**Figure 3**): this can be explained by the indirect effect, the change of the local strain sensitivity of hydraulic properties (permeability and transmissivity) in an aquifer during EQ preparation. Such anomalies were observed by Zhang et al. (2019) after the Tohoku EQ: we presume that similar processes can take place on the preparatory stage of seismic event also.

Next-Day Forecast Testing on the Randomized Events Catalog

In order to assess the reliability of the ML results in the next-day EQ forecast, we distorted the sequence of EQs in

TABLE 5 | ROC values for different wells.

Name	TP	FP	FN	TN	Actual EQ number
Ajmt	38	3	7	299	45
Akh	3	0	41	317	44
Cvsh	25	2	5	232	30
Kbl	18	119	17	190	35
Marn	30	50	41	177	126
Lgdx	67	11	51	232	71
Nkl	19	92	16	234	35
Oni	2	0	56	240	58

TABLE 6 | Statistical measures of 1-day ROC predictions for different wells.

Stations	Accuracy, %	*F*-score	Precision, %	Recall, %	Phi coeff	FPR, %	% positive	Lift, %	K-S stat, %	Kendall tau	Spearman's rho	ROC AUCH	TPR, %
Ajmt	97	0.88	93	84	0.87	1.0	12	715	87	0.42	0.50	0.97	84
Akh	89	0.13	100	6.8	0.25	0.0	0.8	820	57	0.33	0.40	0.87	7.0
Cvsh	97	0.88	93	83	0.87	0.9	10	808	86	0.43	0.51	0.97	83
Kbl	60	0.21	13	51	0.08	38	40	129	27	0.10	0.12	0.66	51
Marn	70	0.40	38	43	0.19	22	27	157	21	0.14	0.17	0.64	42
Lgdx	83	0.68	86	57	0.60	4.5	22	263	64	0.51	0.62	0.89	57
Nkl	70	0.26	17	54	0.17	28	31	177	32	0.16	0.20	0.74	54
Oni	81	0.07	100	3.4	0.17	0.0	0.7	514	52	0.32	0.40	0.81	54

TABLE 7 | ROC values for the randomized EQ catalog—Ajameti well.

Name	TP	FP	FN	TN
Ajmt	0	0	44	303

the "Events" column in the **Table 4** in the following way: the dates of events (EQs) for the time t were displaced in time randomly to positions $t + 3$ or $t + 4$. After this, the ADAM algorithm was again used to check the forecast results on the same input data and the randomized EQ sequence.

The results of ML testing on the distorted EQ catalog of Ajameti well data, presented in **Tables 6**, **7** show that EQ forecast results are negative (TPR, Recall = 0.0%), in contrast to the original data results (**Figure 5** and **Tables 5**, **6**). This points to a high accuracy of prediction based on the original data (TPR, Recall = 84%). Namely, all ROC measures, predicting EQ occurrence, have zero values in **Tables 7**, **8** for randomized data; only quiet days are predicted more or less successfully even in the case of distorted data, which should be expected.

FUTURE WORK

Our short-term forecast analysis was restricted to solving the next-day prediction problem. At the same time, some anomalies are appreciable even visually several days before EQ without complicated analysis (**Figure 3**). The preliminary results of the quantitative (wavelet) analysis on our data show that the correlation between tidal variations and WL in some wells is broken several days before the local EQs of magnitudes M3–4, in both the amplitude and frequency spectra. We also fixed disturbances of wavelet patterns of magnetic variations in the same periods well before the seismic event. In the future, we are going to apply a detailed ML + ROC analysis to longer (say, several days) prediction intervals and longer series of input data (namely, observation data for dozens of years, prior to 2019), which can improve the results of short-term forecast, in particular, to solve the question on the different prognostic potentials of different wells. In addition, we tried to use a longer prediction interval (10 days) for the Marneuli well, but in this case, the TPR was only 14.5%, i.e., less than the next-day TPR forecast (42%), though the joint EQ/quietness forecast improved significantly (ROC AUCH increased from 42 to 81%). The small TPR effectiveness of the well can be explained by the low sensitivity of the well to EQ-related strains or by another effect, namely, that sometimes a shorter prediction time can be better than a longer one.

CONCLUSION

We applied several statistical methods to EQ forecast in Caucasus and Georgia and assessed their effectiveness:

TABLE 8 | Statistical measures of the next-day predictions for Ajameti well using randomized EQ catalog.

Station	Accuracy,%	*F*-score	Precision,%	Recall,%	Phi coeff	FPR,%	% positive	Lift,%	K-S stat,%	Kendall tau	Spearman rho	ROC AUCH
Ajmt	87	0.0	–	0.0	–	0.0	0.0	0.0	18	0.06	0.08	0.61

(i) Bayesian approach to assess conditional probability of expected strong EQs;
(ii) Pattern recognition technique, based on the assessment of the empirical risk function;
(iii) Non-linear PS plot analysis;
(iv) Machine Learning/Receiver Optimization Characteristic (ML/ROC) algorithms, which show that five wells (Ajameti, Akhalkalaki, Chvishi, Lagodekhi, and Oni) have a good next-day joint EQ/quiet prognostic characteristics (ROC AUCH 0.97–0.81). The other three wells show a less satisfactory result—from 64 to 73%. Our opinion is that due to an overwhelming prevalence of quiet days, even the random prediction of a quiet next-day state is highly successful, and this makes the success of joint EQ/quietness prediction very high due to the large value of the TN term.

Thus, we think that "EQ-aimed" measures, such as TPR = Recall, which do not include the TN measure, are really important for the EQ prediction-oriented studies. In this case, two from the eight wells show good ROC, namely, a high value of the TP EQ prediction (TPR, Recall) of the order of 84–83%; i.e., the next-day impending EQ was predicted from the previously observed data with above-indicated probability. Of course, we cannot exclude the possibility of different sensitivities of separate wells to EQ precursors (different strain sensitivities).

In order to assess the reliability of the ML results in the next-day EQ forecast, we distorted the sequence of EQs in the "Events" sequence and applied the same (ML/ROC) algorithm to the randomized catalog. The results of ML testing on the distorted EQ catalog of Ajameti well data show that EQ forecast results became negative (TPR, Recall = 0.0%), in contrast to the good results obtained for the original data (TPR, Recall = 84–83%).

There is a hope that extending the ML/ROC analysis to longer (say, several days) prediction intervals and longer time series of input data (namely, observation data for dozens of years, prior to 2019) can improve the results of short-term forecast.

DATA AVAILABILITY STATEMENT

The original contributions presented in the study are included in the article/supplementary material, further inquiries can be directed to the corresponding author.

AUTHOR CONTRIBUTIONS

TC contributed to the sections "Introduction," "Theoretical Models," "Long-Term and Middle-Term EQ Forecast [Bayesian Approach, Support Vector Machines (SVMs), and Phase Space Portraits (PSPs)]," "Machine Learning (ML) Methodology," "ML Results," and "Next-Day Forecast Testing on the Randomized Events Catalog." GM, GK, and TJ contributed to the sections "Networks, Devices, Data" and "Machine Learning (ML)

Methodology." TK contributed to the sections "Machine Learning (ML) Methodology," "ML Results," and "Next-Day Forecast Testing on the Randomized Events Catalog." All authors contributed to the article and approved the submitted version.

FUNDING

This work was supported by the Shota Rustaveli National Science Foundation of Georgia (SRNSFG) (FR17_633, study of geodynamical processes evolution and forecasting).

REFERENCES

Adamia, S. H., Alania, V., and Tsereteli, N. (2017). Postcollisional tectonics and seismicity of Georgia. *Geol. Soc. Am. Spec. Pap.* 525, 535–572. doi: 10.1130/2017.2525(17)

Aharony, A., and Stauffer, D. (2010). *Introduction to Percolatin Theory*. London: Taylor & Francis.

Bender, B., and Perkins, D. M. (1987). *Seisrisk III: A Computer Program for Seismic Hazard Estimation*. Washington, DC: United States Government Publishing Office.

Bottou, L., and Bousquet, O. (2012). "The tradeoffs of large scale learning," in *Optimization for Machine Learning*, eds S. Sra, S. Nowozin, and S. Wright (Cambridge: MIT Press), 351–368.

Brace, W. E., and Byerlee, I. D. (1966). Stick-slip as a mechanism for Earthquakes. *Science* 153, 990–992. doi: 10.1126/science.153.3739.990

Burges, C. (1998). A tutorial on support vector machines for pattern recognition. *Data Min. Knowl. Discov.* 2, 121–167.

Burridge, R., and Knopoff, L. (1967). Model and theoretical seismicity. *Bull. Seism. Soc. Am.* 57, 341–371.

Charmet, J. C., Roux, S., and Guyon, E. (eds) (1990). *Disorder and Fracture. NATO ASI Series*. Berlin: Springer-Verlag.

Chelidze, T. (1986). Percolation theory as a tool for imitation of fracture process in rocks. *PAGEOPH* 124, 731–748. doi: 10.1007/bf00879607

Chelidze, T. (1987). *Percolation Theory in Mechanics of Geomaterials*. Moscow: Nauka.

Chelidze, T., and Kolesnikov, Y. (1984). On the physical interpretation of transitional amplitude in percolation theory. *J.Phys. A* 17, L791–L793.

Chelidze, T., Kolesnikov, Y., and Matcharashvili, T. (2006). Seismological criticality concept and percolation model of fracture. *Geophys. J. Int.* 164, 125–136. doi: 10.1111/j.1365-246x.2005.02818.x

Chelidze, T., and Lursmanashvili, O. (2003). Electromagnetic and mechanical control of slip: laboratory experiments with slider system. *Nonlin. Proces. Geophys.* 20, 1–8.

Chelidze, T., Lursmanashvili, O., Matcharashvili, T., Varamashvili, N., Zhukova, N., and Mepharidze, E. (2010). "Triggering and synchronization of stick-slip: experiments on spring-slider system," in *Synchronization and Triggering: from Fracture to Earthquake Processes*, eds V. de Rubeis, Z. Czechowski, and R. Teisseyre (Berlin: Springer), 123–164. doi: 10.1007/978-3-642-12300-9_8

Chelidze, T., and Matcharashvili, T. (2013). "Triggering and synchronization of seismicity: laboratory and field data- a review," in *Earthquakes - Triggers, Environmental Impact and Potential Hazards*, ed. K. Konstantinou (Hauppauge, NY: Nova Science Pub.), 165–231.

Chelidze, T., and Matcharashvili, T. (2015). "Dynamical patterns in seismology," in *Recurrence Quantification Analysis: Theory and best practices*, eds C. Webber and N. Marwan (Cham: Springer), 291–335.

Chelidze, T., Matcharashvili, T., and Zhukova, N. (2018). "Phase space portraits of earthquake time series of caucasus: signatures of strong earthquake preparation," in *Complexity of Seismic Time Series*, eds T. Chelidze, F. Vallianatos, and L. Telesca (Amsterdam: Elsevier), doi: 10.1016/B978-0-12-813138-1.00001-8

Chelidze, T., Matcharshvili, T., Gogiashvili, J., Lursmanashvili, O., and Devidze, M. (2005). Phase synchronization of slip in laboratory slider system. *Nonlin. Process. Geophys.* 12, 163–170. doi: 10.5194/npg-12-163-2005

Chelidze, T., Shengelia, I., Zhukova, N., Matcharashvili, T., Melikadze, G., and Kobzev, G. (2016). *M9* Tohoku earthquake hydro- and seismic response in the caucasus and North Turkey. *Acta Geophys.* 64, 567–588. doi: 10.1515/acgeo-2016-0022

Chelidze, T., Sobolev, G., Kolesnikov, Y., and Zavjalov, A. (1995). seismic hazard and earthquake prediction research in georgia. *J. Georg. Geophys. Soc.* 1A, 7–39.

Cornell, C. A. (1968). Engineering seismic risk analysis. *Bull. Seismol. Soc. Am.* 58, 1583–1606.

De Santis, A., Marchetti, D., Pavón-Carrasco, F. J., Cianchini, G., Perrone, L., Abbattista, C., et al. (2019). Precursory worldwide signatures of earthquake occurrences on Swarm satellite data. *Sci Rep.* 9:20287. doi: 10.1038/s41598-019-56599-1

Diederik, K., and Ba, J. (2014). Adam: a method for stochastic optimization. *arXiv* [Preprint]. Available online at: https://arxiv.org/abs/1412.6980#:~{}:text=We%20introduce%20Adam%2C%20an%20algorithm,estimates%20of%20lower%2Dorder%20moments.&text=The%20method%20is%20also%20appropriate,noisy%20and%2For%20sparse%20gradients (accessed June 12, 2020).

Dieterich, J., Cayol, V., and Okubo, P. (2000). The use of earthquake rate changes as a stress meter at Kilauea volcano. *Nature* 408, 457–460. doi: 10.1038/35044054

Dobrovolsky, I., Zubkov, S., and Miachkin, V. (1979). Estimation of the size of earthquake preparation zones. *Pure Appl. Geophys.* 117, 1025–1044. doi: 10.1007/bf00876083

Dvorkin, J., Nolen-Hoeksema, R., and Nur, A. (1994). The Squirt-flow mechanism: Macroscopic description. *Geophysics* 59, 428–438. doi: 10.1190/1.1443605

Fawcett, T. (2006). An Introduction to ROC analysis. *Patt. Recogn. Lett.* 27, 861–874. doi: 10.1016/j.patrec.2005.10.010

Herrmann, H., and Roux, S. (eds) (1990). *Statistical Models For The Fracture Of Disordered Media*. Amsterdam: Elsevier.

Jouniaux, L., and Pozzi, J. (1995). Streaming potential and permeability of saturated sandstones under triaxial stress: - consequences for electrotelluric anomalies prior to earthquakes. *J. Geophys. Res.* 100, 10197–10209. doi: 10.1029/95jb00069

Karpathy, A. (2017). *A Peek at Trends in Machine learning*. Available online at: https://medium.com/@karpathy/a-peek-at-trends-in-machine-learning-ab8a1085a106 (accessed June 12, 2020).

King, C.-Y., Azuma, S., Ohno, M., Asai, Y., Asai, Y., He, P., et al. (2000). . In search of earthquake precursors in the water-level data of 16 closely clustered wells at Tono, Japan. *Geophys. J. Int.* 143, 469–477. doi: 10.1046/j.1365-246X.2000.01272.x

Kingma, D., and Ba, J. (2014). *Adam: A Method for Stochastic Optimization*. Available online at: http://arxiv.org/abs/1412.6980http://arxiv.org/abs/1412.6980 (accessed May 12, 2020).

Kopytenko, Y. A., Matiashvily, T. G., Voronov, P. M., Kopytenko, E. A., and Molchanov, O. A. (1990). *Discovering of Ultra-Low-Frequency Emissions Connected With Spitak Earthquake and Its Aftershock Activity With the Data of Geomagnetic Pulsations Observations*. IZMIRAN, Moscow: Dusheti and Vardzija, 27.

Martinelli, G. (2015). Hydrogeologic and geochemical precursors of earthquakes: an assessment for possible applications. *Bollettino di Geofisica Teorica ed Applicata*. 56, 83–94.

Matcharashvili, T., Chelidze, T., and Zhukova, N. (2016). Assessment of a ratio of the correlated and uncorrelated waiting times in the Southern California earthquake catalogue. *Phys. A* 449, 136–144.

McGuire, R. K. (1976). *Fortran Computer Program for Seismic Risk Analysis*. Reston, VA: U.S. Geological Survey.

Molaie, M., Jafari, S., Moradi, M. H., Sprott, J. C., and Golpayegan, S. (2013). A chaotic viewpoint on noise reduction from respiratory sounds. *Biomed. Signal Process. Control*. doi: 10.1016/j.bspc.2013.10.009

Nello, C., and Shawe-Taylor, J. (2000). *An Introduction to Support Vector Machines and other Kernel-Based Learning Methods*. Cambridge: Cambridge University Press.

Ogata, Y. (1998). Space-time point-process models for earthquake occurrences. *Ann. Instit. Statist. Math.* 50, 379–402. doi: 10.1023/a:1003403601725

Pikovsky, A., Rosenblum, M. G., and Kurths, J. (2003). *Synchronization: Universal Concept in Nonlinear Science*. Cambridge: CambridgeUniversity Press.

Press, W., Teukmolsky, S., Vetterling, W., and Flannery, B. (2007). *Numerical Recipes Art of Scientific computations*. Cambridge: Cambridge University Press.

Pulinets, S., and Boyarchuk, K. (2004). *Ionospheric Precursors of Earthquakes*. Berlin: Springer.

Reasenberg, P., and Matthews, M. (1988). Precursory seismic quiescence: a preliminary assessment of the hypothesis. *PAGEOPH* 126, 373–406. doi: 10.1007/BF00879004

Reilinger, R., McClusky, S., Vernant, P., Lawrence, S., Ergintav, S., Cakmak, R., et al. (2006). GPS constraints on continental deformation in the Africa-Arabia-Eurasia continental collision zone and implications for the dynamics of plate interactions. *J. Geoph. Res.* 111:B05411. doi: 10.1029/2005JB004051

Rouet-Leduc, B., Hulbert, C., and Johnson, P. (2019). Continuous chatter of the *Cascadia subduction* zone revealed by machine learning. *Nat. Geosci.* 12, 75–79. doi: 10.1038/s41561-018-0274-6

Rouet-Leduc, B., Hulbert, C., Lubbers, N., Barros, K., Humphreys, C., and Johnson, P. (2017). Machine learning predicts laboratory earthquakes. *Geophys. Res. Lett.* 44, 9276–9282. doi: 10.1002/2017GL074677

Ruina, A. (1983). Slip instability and state variable friction laws. *J. Geophys. Res.* 88B, 10359–10370. doi: 10.1029/jb088ib12p10359

Saberi, A. (2015). Recent advances in percolation theory and its applications. *Phys. Rep.* 578, 1–32. doi: 10.1016/j.physrep.2015.03.003

Sahimi, M. (1994). *Applications of Percolation Theory*. London: Taylor&Francis.

Sobolev, G. (2011). Seismicity dynamics and earthquake predictability. *Nat. Hazards Earth Syst. Sci.* 11, 445–458. doi: 10.5194/nhess-11-445-2011

Sobolev, G., Chelidze, T., Zavjalov, A., Slavina, L., and Nikoladze, V. (1991). Maps of Expected Earthquakes based on combination of parameters. *Tectonophysics* 193, 255–265. doi: 10.1016/0040-1951(91)90335-p

Stacey, F. D. (1964). The seismomagnetic effect. *Pure Appl. Geophys.* 58, 5–22. doi: 10.1007/bf00879136

Stauffer, D., and Aharony, A. (1994). *Introduction To Percolation Theory*. London: Taylor & Francis, 192.

Steinwart, I., and Christmann, A. (2008). *Support Vector Machines*. New York, NY: Springer.

Theodoridis, S., and Koutroumbas, K. (2009). *Pattern Recognition*, 4th Edn, Cambridge, MA: Academic Press.

Tsereteli, N., Varazanashvili, O., Kupradze, M., Kvavadze, N., and Gogoladze, Z. (2016). Seismic catalog for Georgia. *J. Georg. Geophys. Soc.* 19A, 66–74.

Vapnik, V., and Chervonenkis, A. (1974). *Pattern Recognition Theory, Statistical Learning Problems*. Moskva: Nauka Publisher.

Vapnik, V. (ed.) (1984). *Algorithms and Programs For Recovering Dependences*. Moscow: Nauka Publisher.

Wang, C. Y., and Manga, M. (2009). "Earthquakes and water," in *Encyclopedia of Complexity and Systems*, ed. R. A. Maiers (New York, NY: Springer), doi: 10.1007/978-3-642-27737-5_606-1

Zavjalov, A. (2006). *Middle-term Earthquake Prediction*. Moscow: Nauka Publisher.

Zhang, H., Shi, Z., Wang, G., Sun, X., Yan, R., and Liu, C. (2019). Large earthquake reshapes the groundwater flow system: insight from the water-level response to earth tides and atmospheric pressure in a deep well. *Water Resour. Res.* 55, 4207–4219. doi: 10.1029/2018WR024608

Zhurkov, S., Kuksenko, V., Petrov, V., Savelyev, V., and Sultanov, U. (1977). On the prognosis of fracture of rocks. *Sci. USSR Phys. Earth* 6, 1–18.

Conflict of Interest: The authors declare that the research was conducted in the absence of any commercial or financial relationships that could be construed as a potential conflict of interest.

Copyright © 2020 Chelidze, Melikadze, Kiria, Jimsheladze and Kobzev. This is an open-access article distributed under the terms of the Creative Commons Attribution License (CC BY). The use, distribution or reproduction in other forums is permitted, provided the original author(s) and the copyright owner(s) are credited and that the original publication in this journal is cited, in accordance with accepted academic practice. No use, distribution or reproduction is permitted which does not comply with these terms.

frontiers in Earth Science

ORIGINAL RESEARCH
published: 02 September 2020
doi: 10.3389/feart.2020.00364

Earth's Outgoing Longwave Radiation Variability Prior to $M \geq 6.0$ Earthquakes in the Taiwan Area During 2009–2019

Ching-Chou Fu[1], Lou-Chuang Lee[1], Dimitar Ouzounov[2] and Jyh-Cherng Jan[3]*

[1] Institute of Earth Sciences, Academia Sinica, Taipei, Taiwan, [2] Schmid College of Science and Technology, Physics, Computational Science and Engineering, Chapman University, Orange, CA, United States, [3] Marine Meteorology Center, Central Weather Bureau, Taipei, Taiwan

This paper proposes an analysis method, using the National Oceanic and Atmospheric Administration satellite data, to trace variations in outgoing longwave radiation (OLR) for finding the precursors of earthquakes. The significance of these observations is investigated using data sets of recent $M \geq 6.0$ earthquakes around the Taiwan area from 2009 to 2019. We suggest that the precursory signal could be an E_{Index} anomaly (EA) in the form of substantial thermal releases distributed near the epicenter. The consecutive appearances of OLR EAs are observed as precursors 2–15 days before significant earthquakes, and we refer to this as a pre-earthquake OLR E_{Index} anomaly (POEA). We interpret these thermal sources as possibly originating from electromagnetics together with gas emissions associated with pre-seismic processes. This study highlights the potential of OLR anomalous changes in earthquake precursor studies, at least in the Taiwan region.

Keywords: National Oceanic and Atmospheric Administration, outgoing longwave radiation, pre-earthquake OLR E_{Index} anomaly, earthquake precursor, Taiwan

OPEN ACCESS

Edited by:
Giovanni Martinelli, National Institute of Geophysics and Volcanology, Italy

Reviewed by:
Nicola Genzano, University of Basilicata, Italy
Marzieh Khalili, Shiraz University, Iran

****Correspondence:***
Ching-Chou Fu
ccfu@earth.sinica.edu.tw

Specialty section:
This article was submitted to Solid Earth Geophysics, a section of the journal Frontiers in Earth Science

Received: *07 June 2020*
Accepted: *07 August 2020*
Published: *02 September 2020*

Citation:
Fu C-C, Lee L-C, Ouzounov D and Jan J-C (2020) Earth's Outgoing Longwave Radiation Variability Prior to M ≥6.0 Earthquakes in the Taiwan Area During 2009–2019. Front. Earth Sci. 8:364. doi: 10.3389/feart.2020.00364

INTRODUCTION

Outgoing long-wave radiation (OLR) is energy emitted from Earth in the form of electromagnetic radiation, which passes out of the atmosphere and into space in the form of thermal radiation. The flux of energy transport by OLR can be measured by a satellite. OLR is primarily sensitive to near-surface and atmospheric temperatures, the humidity of the air, and the presence of clouds, which are related to the intensity of convective activity as well as the latitude and altitude dependence of the variability (Kane and Buriti, 1997; Ouzounov et al., 2007; Graham et al., 2011).

Analysis of the thermal anomaly phenomenon using satellite techniques for monitoring seismically active regions has been carried out since the 1980s (Gorny et al., 1988). Many studies have reported that thermal anomalous space-time transients were detected in the OLR or thermal infrared radiation (TIR) before and/or during the earthquake preparation stage (Tronin, 1996, 2000; Tramutoli et al., 2001, 2005, 2009, 2013; Di Bello et al., 2004; Ouzounov and Freund, 2004; Ouzounov et al., 2006, 2007; Pulinets et al., 2006; Genzano et al., 2007, 2009, 2010, 2015;

Pulinets and Dunajeck, 2007; Aliano et al., 2008a,b; Pergola et al., 2010; Xiong et al., 2010, 2013, 2015; Pulinets and Ouzounov, 2011; Jing et al., 2012; Lisi et al., 2015; Xiong and Shen, 2017; Khalili et al., 2019, 2020). The main mechanisms proposed for the temperature increase are (1) the emission of diffuse gases (e.g., radon and CO_2) leading to a local greenhouse effect or near-ground air ionization to release heat (Tronin, 2002; Pulinets et al., 2006; Tramutoli et al., 2009, 2013; Koll and Cronin, 2018) and (2) positive hole charge or the excitation of an electric field from the stressed rock resulting in infrared emission and energy flow (Ouzounov and Freund, 2004; Freund, 2007a,b; Freund et al., 2007).

Taiwan is located on the Pacific seismic belt, where earthquake activity is intense. Many large earthquakes have occurred in Taiwan and caused seismic disasters in the past hundred years as a result of the continuous collision between the Philippine Sea Plate and the Eurasian Plate at a rate of 82 mm/yr to the northwest (Yu et al., 1997). For example, the M_L7.3 Chi-Chi earthquake in 1999 killed more than 2400 people and had a substantial impact on Taiwan.

Identifying earthquake precursors has often been considered a useful method to mitigate seismic disasters. In the past few decades, a wide variety of earthquake precursors have been investigated for Taiwan, including gas and fluid geochemical changes (Liu et al., 1985; Song et al., 2003, 2006; Chyi et al., 2005; Fu et al., 2005, 2008, 2009, 2017a,b,c; Yang et al., 2005, 2006; Kuo et al., 2006, 2010; Walia et al., 2009, 2013; Kumar et al., 2015; Fu and Lee, 2018), gamma-ray monitoring (Fu et al., 2015, 2019), groundwater levels (Chia et al., 2001; Wang et al., 2001; Lai et al., 2010; Chen et al., 2013b, 2015c), borehole strain changes (Liu et al., 2009; Canitano et al., 2015, 2017; Hsu et al., 2015), seismicity changes (Chen et al., 2005, 2006; Wu and Chiao, 2006; Wu and Chen, 2007; Wu et al., 2008; Lin, 2009; Kawamura et al., 2014), tidal variations (Lin et al., 2003; Chen et al., 2012), GPS observations (Chen et al., 2013c, 2015b), lightning activity (Liu et al., 2015), geo-electromagnetic observations (Tsai et al., 2004, 2006; Yen et al., 2004, 2009; Chen et al., 2011, 2012, 2013a, 2015a,b), and seismo-ionospheric anomalies (Liu et al., 2000, 2001, 2004, 2006, 2010; Chen et al., 2004).

Previous studies have applied remote-sensing techniques to survey thermal anomalies in Taiwan (Wu et al., 2006; Liu et al., 2007; Pulinets and Ouzounov, 2011; Genzano et al., 2015; Chan and Chang, 2018; Chan et al., 2018, 2020). It is worth mentioning that a significant sequence of TIR anomalies was observed 2 weeks before the Chi-Chi earthquake and close to its epicenter. Previous studies have also proposed that the observed TIR anomalies were related to earthquakes with $M > 4$ that occurred around Taiwan from 1995 to 2002 (Genzano et al., 2015).

These studies provide the opportunity to explore OLR/TIR variations related to energy radiating from underground toward the atmosphere as a result of rock deformation and geodynamic processes in the Taiwan area. However, most of the above-referenced studies have been limited by a lack of sufficient earthquake events with OLR results ($M \geq 6$) to further investigate the potential of detecting significant earthquakes in Taiwan. Nevertheless, these potential precursory phenomena for Taiwan may provide an opportunity to better understand the physical and chemical processes before earthquakes, which would be crucial for exploring the theoretical mechanism of lithosphere–atmosphere–ionosphere coupling (LAIC) (Pulinets and Ouzounov, 2011; Kuo et al., 2011, 2014).

This paper aims to describe the characteristics of the OLR monitoring system, process the data, and systematically assess the feasibility of using the OLR method to find precursors prior to the $M \geq 6$ earthquakes that occurred over 2009–2019 around Taiwan (**Figure 1**). We also interpret the observed precursors of OLR and a possible pre-earthquake generation process by comparing the results with multiple observations.

MATERIALS AND METHODS

The OLR data used in this study are daily measurements from the Advanced Very-High-Resolution Radiometer (AVHRR) polar orbiters NOAA-18, obtained from the NOAA Climate Prediction Center website.[1] To compute the daily zonal OLR anomaly over the Taiwan area, we use a daily mean with a $1^\circ \times 1^\circ$ spatial resolution in both longitude and latitude, as shown in **Figure 2**.

Taiwan is located in the Pacific Ocean and has a subtropical climate, and it is frequently impacted by typhoons. Increasing sea surface temperatures can effectively increase the surface latent heat flux during the typhoon season, which means that the heavy precipitation and strong convective flow of a typhoon can induce a region of extreme negative OLR anomalies (Liebmann and Smith, 1996; Lee et al., 2006; Susskind et al., 2012; Hatchett, 2018). The latitude and altitude effects on OLR variations around the study area can be ignored, owing to the narrow latitude range and smooth topography, except in the Central Range of Taiwan. To acquire non-cloud satellite data at the time of a typhoon is difficult because of bad weather condition. In other words, the effect of the continuous presence of clouds during typhoons is strong, but the sporadic presence of clouds may be slight for data analysis. Therefore, we directly removed the OLR raw data during typhoons to diminish the contributions by typhoons to OLR variations.

It is important to note that OLR raw data were acquired twice for each location and at the same time of day (daytime and nighttime) under the similar background conditions to reduce the variability of signals due to the daily variation of temperature and humidity and the vegetation and cloud coverage. The local grid value of the OLR is subtracted from the spatial variation of the 1-year mean value as the daily eddy. The current day value (the current daily eddy) is deducted from the average value of 16 days preceding the observation day as the OLR anomaly. A standardized anomaly, E_{Index}, can be determined, computed from the OLR anomaly divided by a standard deviation $\tau_{i,j}$. In this study, when E_{Index} is observed to have consecutive abnormal changes in some specific area in a short period, it may then be considered as a possible precursor for identifying seismic events. Seismic data are acquired from the earthquake catalogs of the Central Weather Bureau and United States Geological Survey. There are 35 seismic events with magnitudes

[1] http://www.cdc.noaa.gov/

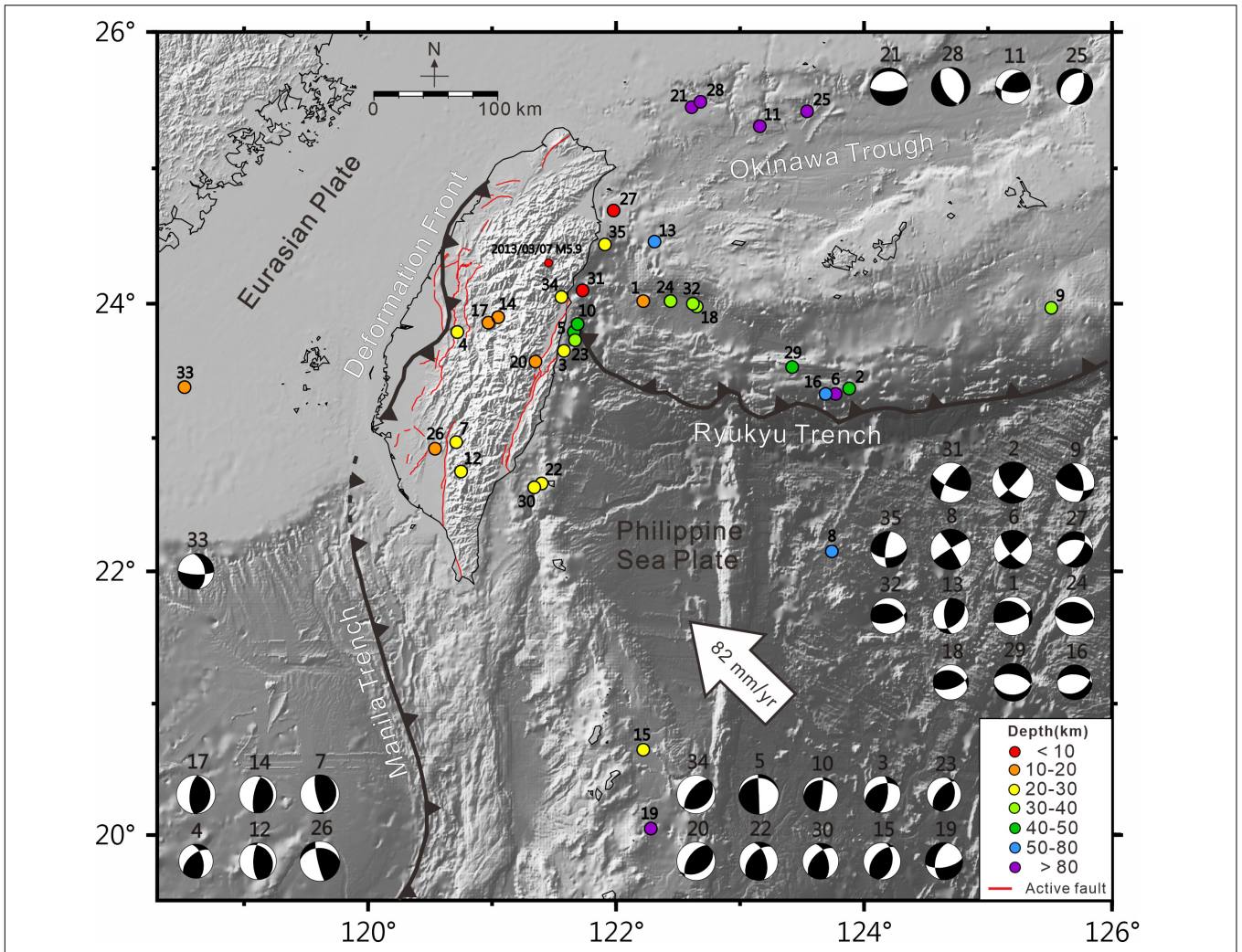

FIGURE 1 | A regional map and the principal tectonic structures around Taiwan showing the Philippine Sea Plate moving northwest at ~82 mm/yr toward the Eurasian Plate (Yu et al., 1997). The circles represent $M \geq 6$ earthquake epicenters from 2009 to 2019 with the colors corresponding to different focal depths. These earthquakes are labeled and listed in **Table 1**. The red lines indicate the active faults of Taiwan.

greater than 6.0 during 2009–2019 around the Taiwan area (**Figure 1**) and the variation in E_{Index} on the nearest grid-point adjacent to the epicenter of the earthquake was selected for further investigation.

The data processing method for extracting E_{Index} from daytime and nighttime OLR data connected with the earthquakes is summarized in **Figure 2**. The procedure of data analysis uses the following equations:

$$\overline{S_{i,j}} = \langle S_{i,j} \rangle_{one\ year} \tag{1}$$

$$S^*\left(X_{i,j}, t\right) = S_{i,j} - \sum W_{i,j}\overline{S_{i,j}} \tag{2}$$

where $S_{i,j}$ is the OLR value of the target grid-point, as defined in **Figure 2A**, $W_{i,j}$ is the number of the surrounding grid points around the target point, and $\overline{S_{i,j}}$ is the yearly average. By subtracting the weighted yearly average from the four surrounding grid points for removing the regional mean, $S^*\left(X_{i,j}, t\right)$ can be obtained as the daily eddy (shown in **Figure 2B**):

$$\bar{S}^* = S^*_{16days} \tag{3}$$

$$\text{OLR (t)}^{\text{A}} = S^*\left(x_{i,j}, t\right) - \bar{S}^*\left(x_{i,j}, t\right) \tag{4}$$

where $S^*\left(x_{i,j}, t\right)$ is the current daily eddy and $\bar{S}^*\left(x_{i,j}, t\right)$ is the 16-day average daily eddy fields excluding the current day. OLR (t)$^{\text{A}}$ indicates a residual value of the eddy as the OLR anomaly (**Figure 2C**) that can be determined as the difference between the current eddy and the average eddy of the 16 days preceding the observation day:

$$\text{E}_{\text{Index}(t)} = \left(S^*\left(x_{i,j}, t\right) - \bar{S}^*\left(x_{i,j}, t\right)\right) / \tau_{i,j} \tag{5}$$

where E_{Index} is defined by the OLR anomaly divided by the standard deviation of $\tau_{i,j}$. E_{Index} can then represent the maximum change in OLR values for specific spatial locations

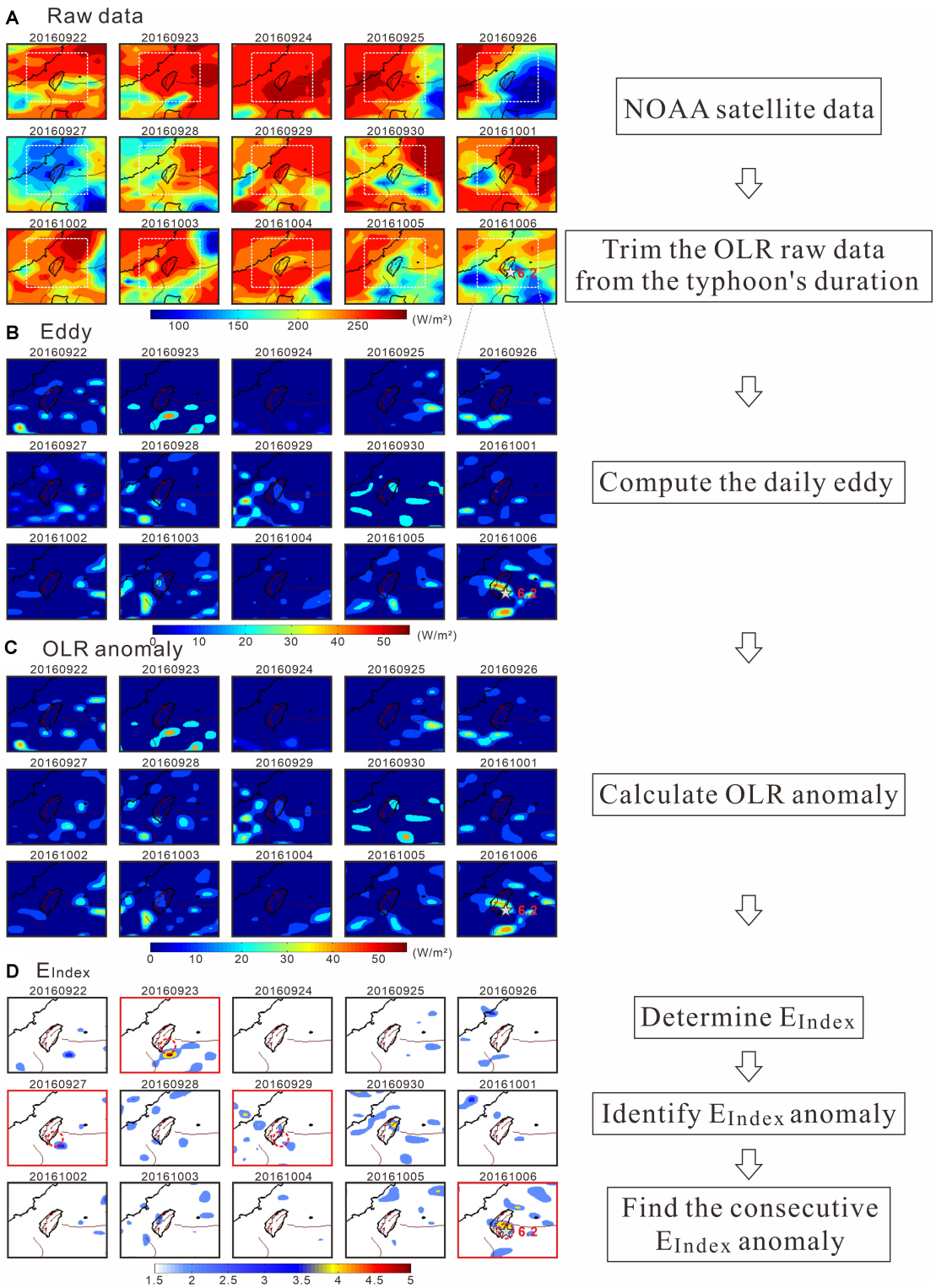

FIGURE 2 | Flowchart of the methodology and procedure for extracting E_{Index} from OLR daytime data observed by the NASA-18 satellite during the period from Sept. 22 to Oct. 6, 2016: **(A)** the raw data of the OLR, **(B)** eddy, **(C)** OLR anomaly, and **(D)** E_{Index}. The epicenter of the M6.0 2016/10/06 earthquake is marked with a gray star. This shows an example of the abnormal E_{Index} anomaly (EA) within the epicenter's vicinity with a red circle for September 23, 27, 29, and October 6 for Event 30 in southwest Taiwan.

and predefined times as an indicator of abnormality (shown in **Figure 2D**). This methodology follows a similar analysis process to that described in detail by Ouzounov et al. (2007) and Pulinets and Ouzounov (2011).

RESULTS

Figure 3 shows the daytime and nighttime variations of E_{Index} for each significant earthquake. The threshold values were determined to be when the E_{Index} value exceeded 2, which is called the E_{Index} anomaly (EA) to identify each seismic event's precursor (**Figure 1** and **Table 1**). The earthquake preparation is considered to be a continuous process, as shown in **Figure 2D**, and we propose that the consecutive appearances of EAs around the epicentral area are a precursor to an earthquake. Based on this scenario, the EQ-1 event in **Figure 3** shows an example of the temporal variations of precursory EAs. Here, red and blue dots are the daily variations in the daytime and nighttime EAs, respectively. In this study, we propose that at least three appearances of EAs found within 4 days over the epicentral area before significant seismic events ($M \geq 6$) be the criteria for earthquake precursory anomalies, and we refer to this as a pre-earthquake OLR E_{Index} anomaly (POEA). The EAs are observed on July 5, July 7, and July 8, 2009, in the daytime and nighttime results, respectively, which means there are a total of six EAs within 4 days (6, 7, and 9 days in the daytime and 6, 7, and 9 days in the nighttime before the 2009/07/14 M6.0 earthquake, respectively). Similarly, precursors in the OLR usually indicate significant and anomalous variability associated with significant earthquakes lasting more than 1 day and repeating at the same local time (Jing et al., 2013; Tramutoli et al., 2013; Genzano et al., 2015; Ouzounov et al., 2015, 2018).

DISCUSSION

Figure 3 presents the temporal evolution of the propagation characteristics of the EA to the earthquake, which may be related to the POEA. Comparing the rates of anomaly occurrences in the daytime and nighttime and 35 earthquakes with $M \geq 6$ during 2009–2019 shows that the POEA quite often occurred ∼2–15 days before the earthquakes, except for 11 of the 35 selected seismic events (EQ-2, EQ-3, EQ-6, EQ-8, EQ-9, EQ-19, EQ-21, EQ-25, EQ-28, EQ-31, and EQ-33 in **Figure 3** and **Table 1**). In other words, the progressive POEA accompanying the relevant earthquake can be termed as the precursory event (PE). It is worth noting that, for all of the cases, significant EAs are much weaker and fewer after the earthquake occurrence (**Figure 3**).

The Influence of Typhoons

The disturbance to OLR E_{Index} variations seems to be caused by the occurrence of a typhoon before but not after the earthquake. There is no frequent appearance of EA before the EQ-2, EQ-3, EQ-9, and EQ-19 events during the occurrence of a typhoon before the earthquake. Similarly, Liu et al. (2007) pointed out that high-temperature anomalies from a satellite observation could not be identified because of the influence of the typhoons. In contrast, a continuous anomalous E_{Index} is observed as the POEA before the EQ-1 event; in this case, a typhoon occurs later than the earthquake. This is because the OLR raw data for the typhoon period were already removed before the data analysis so that the anomaly cannot be recognized without the complete results. The anomalous E_{Index} signals might be present in the OLR raw data; however, the influence of the typhoon cannot entirely be eliminated by using the data processing method of this study. This example illustrates the potential of this methodology for finding a POEA during the occurrence of a typhoon over the earthquake period, as shown in **Figure 3**. When excluding four events during the occurrence of a typhoon before an earthquake, 24 out of 31 such earthquakes show the POEA (an ∼77% success rate).

Influence of the Focal Depth of the Earthquake

An earthquake's focal depth appears to be a significant parameter that affects E_{Index} variations. Earthquakes with a hypocenter depth greater than 70 km, such as EQ-6, EQ-8, EQ-19, EQ-21, EQ-25, and EQ-28, have no precursors of the abnormal E_{Index} anomaly, except for the EQ-11 event. It is worth noting that the POEA can be observed for EQ-11, but not for EQ-21, EQ-25, and EQ-28 in similar tectonic settings (**Figure 1**), which might be attributed to the different focal mechanism. However, no further discussion can be made as only one case of this has been observed.

Positive hole charge carriers are proposed as a physical mechanism for the buildup of surface charges over stressed rock to transport energy from the Earth's crust to the surface. This hypothesis is used to explain the pre-earthquake thermal anomalies, by generating electric fields strong enough to ionize the air (Ouzounov and Freund, 2004; Freund et al., 2007) and drive current flow upward in the atmosphere and into the ionosphere (Freund, 2007a,b; Kuo et al., 2011). Alternatively, gases (e.g., radon, carbon dioxide, and methane) emitted along the fault zones over the epicenter area is another hypothesized mechanism for the ionization of the near-surface air for increased air temperature and latent heat flux (Tronin, 2002; Pulinets et al., 2006; Ouzounov et al., 2007; Tramutoli et al., 2009, 2013; Pulinets and Ouzounov, 2011). Changes in gas emissions may be attributed to near- or far-field earthquakes and strain-induced changes in permeability within the earthquake's preparation zone (Walia et al., 2009, 2013; Fu et al., 2015, 2017b, 2019).

Earthquakes occurring at a focal depth of greater than 70 km are classified as intermediate-focus earthquakes, suggesting that they are located lower than the crust–mantle boundary of Taiwan (Ustaszewski et al., 2012). The strength of the rock in the upper mantle is ductile and decreases with depth as the temperature increases, and has no substantial brittle strengths to cause microfractures and activate p-hole charge carriers. Furthermore, above 700°C, the activated charge carriers may be consumed by a reaction with CH_4 from olivine crystal through oxidative coupling in the deep region (Chen and Molnar, 1983; Hadi et al., 2012). That might be why the POEA is rarely observed before earthquakes with large focal depths. Similarly,

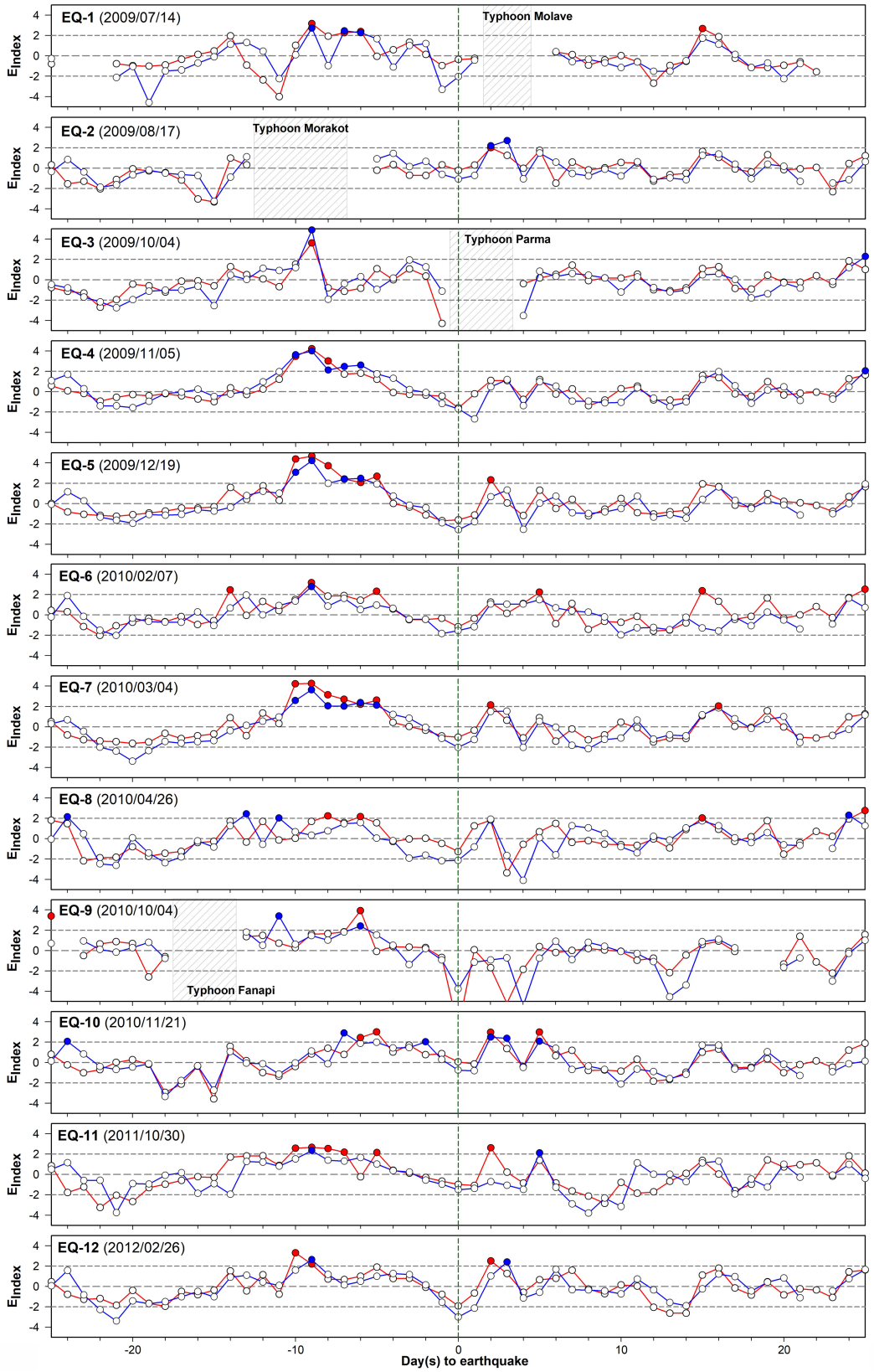

FIGURE 3 | Continued

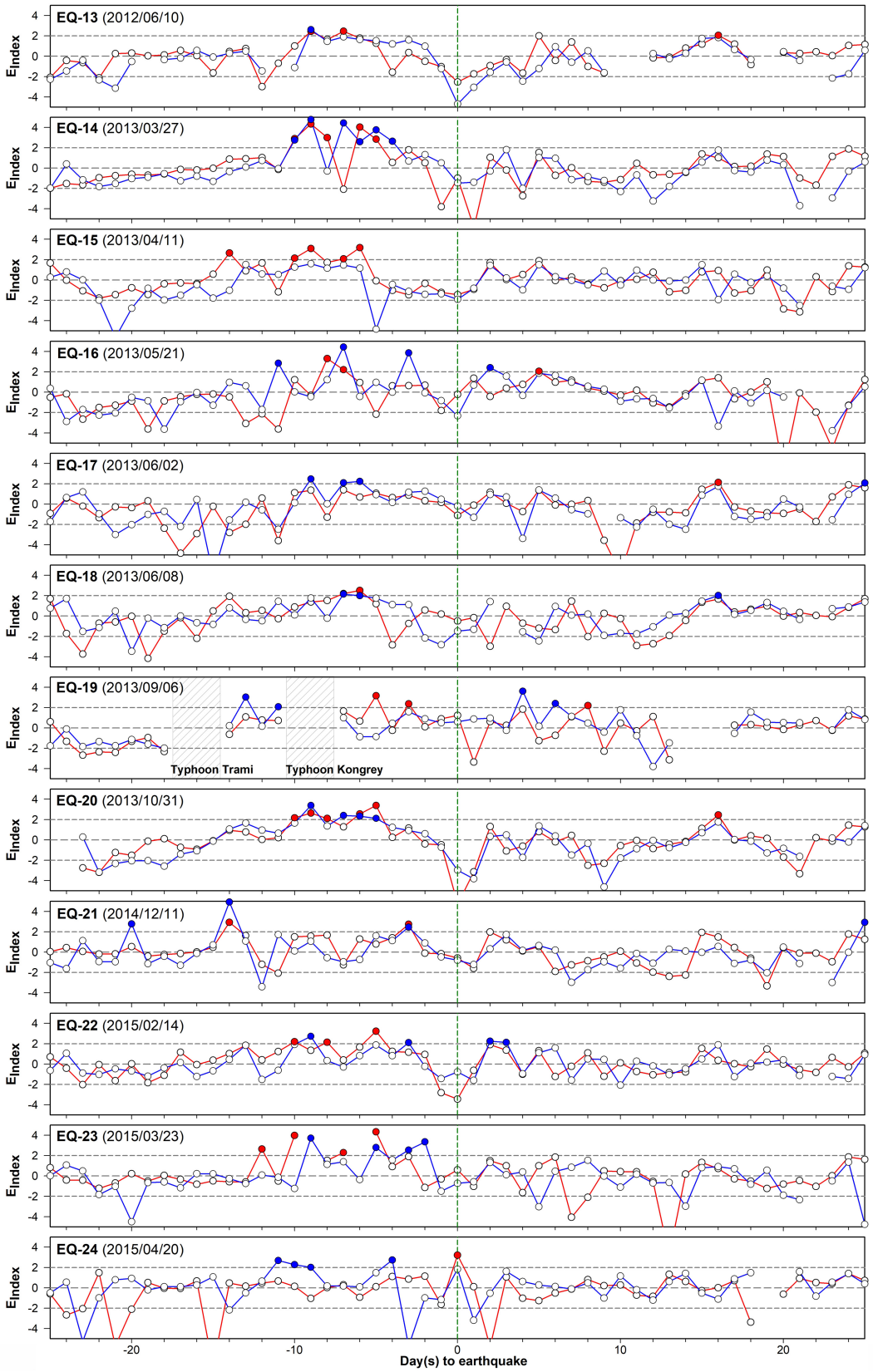

FIGURE 3 | Continued

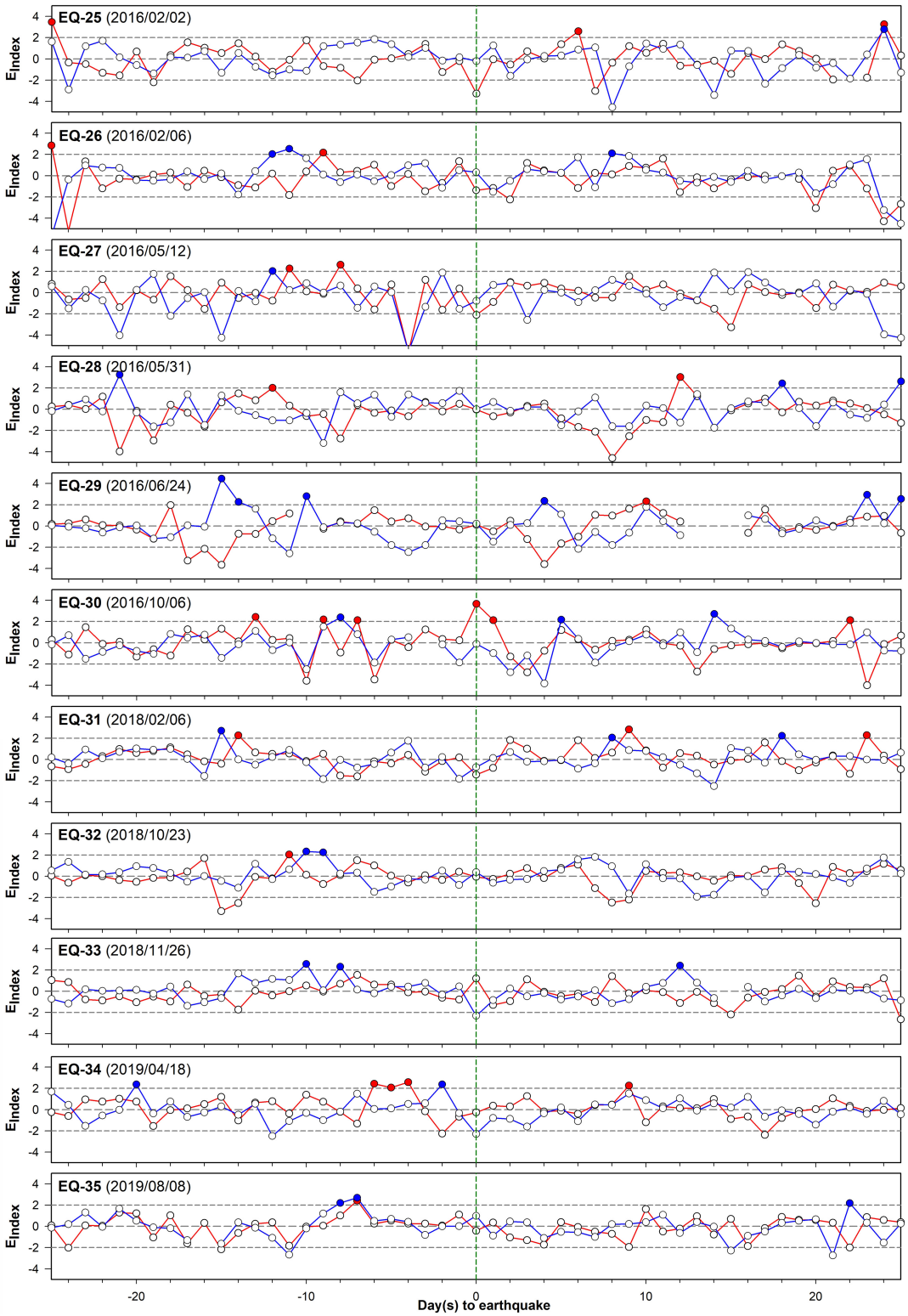

FIGURE 3 | Time-series of daily OLR E_{Index} values associated with $M \geq 6$ earthquakes over the epicenter area from 2009 to 2019 around Taiwan. The red and blue lines indicate the daily E_{Index} variations in the daytime and nighttime, respectively, within 25 days before and after the earthquake. The earthquake's anomalous days are considered to be when the increasing E_{Index} value is greater than the threshold value ($E_{Index} \geq 2$), as given by the red and blue dots. The occurrence of an earthquake is marked with the green dashed line. The shaded region indicates typhoon period. The relevant earthquakes are marked by the numbers shown in **Figure 1** and listed in **Table 1**.

TABLE 1 | Catalog of OLR E_{Index} anomalies (EA) and related earthquakes occurring around Taiwan from 2009 to 2019.

No.[a]	Date	Long.	Lat.	Mag.	Depth	Daytime EA[b]	Nighttime EA[b]	P[c]
		(°E)	(°N)	(M_L)	(km)	(Days before the EQ)		
1[d]	2009/07/14 02:05	122.22	24.02	6.0	18.1	6, 7, 9	6, 7, 9	Y
2[d]	2009/08/17 08:05	123.88	23.37	6.8	43.3			N
3[d]	2009/10/04 01:36	121.58	23.65	6.1	29.2	9	9	N
4	2009/11/05 17:32	120.72	23.79	6.2	24.1	8, 9, 10	6, 7, 8, 9, 10	Y
5	2009/12/19 21:02	121.66	23.79	6.9	43.8	5, 6, 7, 8, 9, 10	6, 7, 9, 10	Y
6	2010/02/07 14:10	123.77	23.33	6.6	88.0	5, 9, 14	9	N
7	2010/03/04 08:18	120.71	22.97	6.4	22.6	5, 6, 7, 8, 9, 10	5, 6, 7, 8, 9, 10	Y
8	2010/04/26 10:59	123.74	22.15	6.8	73.4	6, 8	11, 13	N
9[d]	2010/10/04 21:28	125.51	23.97	6.6	35.0	6	6, 11	N
10	2010/11/21 20:31	121.69	23.85	6.1	46.9	5, 6	2, 7, 24	Y
11	2011/10/30 11:23	123.16	25.31	6.3	215.8	5, 7, 8, 9, 10	9	Y
12	2012/02/26 10:35	120.75	22.75	6.4	26.3	9, 10	10	Y
13	2012/06/10 05:00	122.31	24.46	6.6	69.9	7, 9	9	Y
14	2013/03/27 10:03	121.05	23.90	6.2	19.4	5, 6, 8, 9, 10	4, 5, 6, 7, 9, 10	Y
15	2013/04/11 04:20	122.22	20.65	6.1	22.1	6, 7, 9, 10, 14		Y
16	2013/05/21 16:25	123.69	23.33	6.1	53.1	7, 8	3, 7, 11	Y
17	2013/06/02 13:43	120.97	23.86	6.5	14.5		6, 7, 9	Y
18	2013/06/08 00:38	122.65	23.98	6.2	35.3	6, 7	6, 7	Y
19[d]	2013/09/06 19:33	122.28	20.05	6.8	206.2	3, 5	11, 13	N
20	2013/10/31 20:02	121.35	23.57	6.4	15.0	5, 6, 8, 9, 10	5, 6, 7, 9	Y
21	2014/12/11 05:03	122.61	25.45	6.7	268.6	3, 13	3, 13, 20	N
22	2015/02/14 04:06	121.40	22.66	6.3	27.8	5, 8, 10	3, 9	Y
23	2015/03/23 18:13	121.67	23.73	6.2	38.4	5, 7, 9, 12	2, 3, 5, 9	Y
24	2015/04/20 09:42	122.44	24.02	6.4	30.6		4, 9, 10, 11	Y
25	2016/02/02 22:19	123.54	25.42	6.7	203.7			N
26	2016/02/06 03:57	120.54	22.92	6.6	14.6	9, 25	11, 12	Y
27	2016/05/12 11:17	121.98	24.69	6.1	8.9	8, 11	12	Y
28	2016/05/31 13:23	122.68	25.49	6.9	256.9	12	21	N
29	2016/06/24 05:05	123.42	23.53	6.1	47.0		10, 14, 15	Y
30	2016/10/06 23:52	121.34	22.63	6.2	23.7	7, 9, 13	8	Y
31	2018/02/06 23:50	121.73	24.10	6.2	6.3	14	15	N
32	2018/10/23 12:34	122.62	24.00	6.1	31.2	11	9, 10	Y
33	2018/11/26 07:57	118.52	23.38	6.2	12.3		8, 10	N
34	2019/04/18 13:01	121.56	24.05	6.3	20.3	4, 5, 6	2, 20	Y
35	2019/08/08 05:28	121.91	24.44	6.2	24.2	7	7, 8	Y

*[a]Numbers of the relevant earthquakes marked in **Figures 1**, **3**, **5**. [b]An E_{Index} value higher than 2 can be called the E_{Index} anomaly (EA), and only EAs observed before the EQ are listed. [C]"P" denotes "Precursor." [d]The number of the relevant earthquake denotes a typhoon occurring during 25 days before and after the EQ.*

Xiong and Shen (2017) pointed out that TIR anomalies are not easily observed during the earthquakes with depth larger than 60 km and Ho et al. (2018) reported that the precursory ion density and velocity anomalies associated with surface charges are small before and after earthquakes with a depth greater than 70 km. These observations correspond to the results of previous studies, indicating that the depth of earthquakes can play a significant role in earthquake-related effects (Rodger et al., 1999; Fu et al., 2017b).

Relationship Between OLR E_{Index} Variations and Seismicity

Presented here are a few examples of the abnormal POEA, along with different types of observations in Taiwan. The 2010/03/04 M6.4 Jiashian Earthquake (EQ-7) occurred in southern Taiwan. Significant changes in soil radon concentrations along the fault zones over the epicenter were observed ∼14 days before EQ-7, followed by the appearance of the POEA from satellite data and the crust with surface movement based on GPS residual displacement nearly 10 days before the event (Chen et al., 2013c; Fu and Lee, 2018). Similarly, the reoccurrence of a significant increase in soil radon concentrations was found ∼2 weeks before the 2020/02/06 M6.6 Meinong earthquake (EQ-26) in southern Taiwan, and a substantial POEA occurred following the radon anomalies 9–12 days before the EQ-26 event (Fu et al., 2017a). Furthermore, Chen et al. (2015a) reported that the high-conductivity materials were enhanced ∼12–13 days before the M6.2 2013/03/27 Nantou earthquake (EQ-14) and

were followed by significant changes in the POEA ∼4–10 days before the same event. In contrast to the anomalies observed in the lithosphere and atmosphere, the substantial precursory changes in the ionosphere often appear 1 day and 1–5 days before $M \geq 6.0$ and $M \geq 5.0$ earthquakes, respectively (Liu et al., 2000, 2006). Those observations would support a constant and positive relationship with the pre-earthquake generation process and be associated with the model for the LAIC (Pulinets and Ouzounov, 2011; Kuo et al., 2014).

Most precursory phenomena in previous studies of earthquake precursors in Taiwan have been fragmentary, especially for atmospheric OLR investigations using satellite techniques. The mechanism of the earthquake generation process and the reasons for the OLR anomalies are not well-understood. According to the mechanisms and previous results described above, we propose a possible mechanism based on the previous observations together with the results of this study (e.g., multi-precursors before EQ-7, EQ-14, and EQ-26). Gases spread out along the fault zones together with the positive hole charge carriers, generated by the amount of gases degassed from compressed rock and the magnetic enhancements of high-conductivity materials around the earthquake preparation zone emanating to the surface, which is caused by changes in rock permeability and conductivities due to pre-earthquake stress accumulation. The ionization of the near-surface air and latent heat exchange is related to gas emissions and the upward flow of current with the positive hole charge carriers, respectively, leading to an increase in air temperature and intensive outgoing longwave radiation. The time sequence of anomalous changes between the lithospheric and atmospheric observations explain

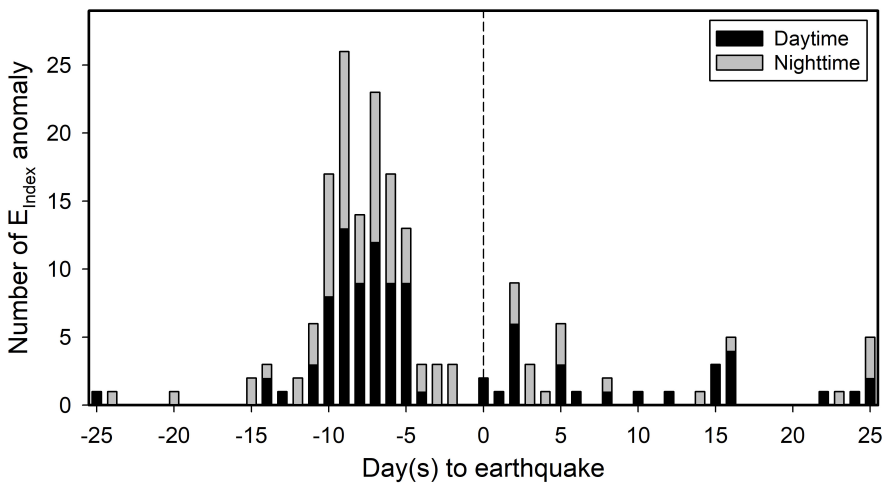

FIGURE 4 | Temporal profile of daily OLR E_{Index} anomalies (EA) associated with each precursory event within 25 days before and after the earthquake. The black and gray bars denote the EAs in the daytime and the nighttime, respectively.

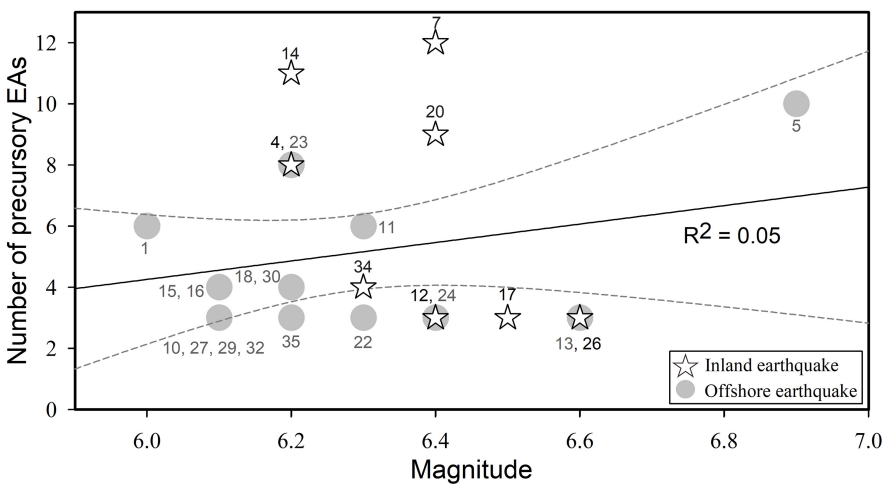

FIGURE 5 | Variation diagrams showing the relationship between earthquake magnitude and distribution of the number of total precursory E_{Index} anomalies. Solid and open symbols denote the inland and offshore earthquakes with the associated anomalous OLR E_{Index}. Dashed lines indicate the 95% confidence interval of the data set.

the appearances of the precursory OLR anomalies in the epicentral areas before earthquakes with $M \geq 6$ around the Taiwan area. Then, the influence on the total electron content (TEC) leads to substantial ionospheric perturbations, followed by the contributions of the lithosphere-atmosphere before the impending earthquake. Hence, the significant relationship between different types of observations between the lithosphere, atmosphere, and ionosphere can be validated in Taiwan. Similar models have also been proposed by Freund (2007a; 2007b), Pulinets and Ouzounov (2011), and Tramutoli et al. (2013). Multi-parameter monitoring data could reveal multiple pre-earthquake signals that could provide a possible explanation of the origin of thermal fluctuations before earthquakes and support the LAIC's theoretical mechanism.

When the EA occurrence is present within a specific day in the daytime and the nighttime before and after an earthquake, we count one for a certain day to the relevant PE. **Figure 4** shows all PEs to display the proportion of the number of total

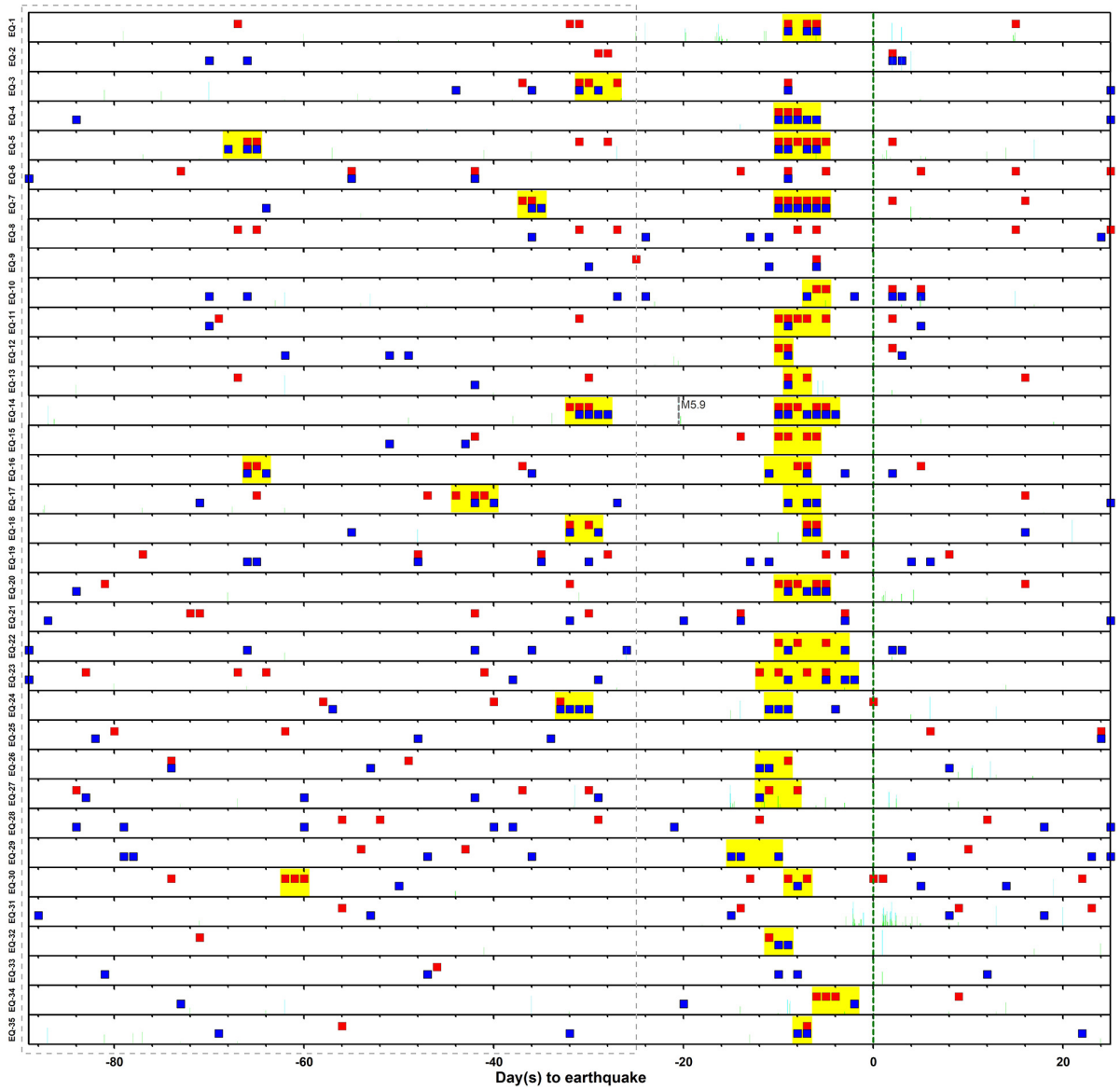

FIGURE 6 | Time-series of daily OLR E_{Index} anomalies (EA) associated with the $M \geq 6$ earthquakes from 2009 to 2019 around Taiwan for a confutation test over the same area. The red and blue squares indicate the daily EAs in the daytime and the nighttime, respectively, within 90 days before and 25 days after the earthquake. When at least three EAs are found within 4 days, this is referred to as a POEA (marked by the yellow highlighting). The occurrence of the strong earthquakes ($M \geq 6$) and the 2013/03/07 M5.9 earthquake are marked with the green and gray dashed lines, respectively. The occurrence of the earthquakes with the magnitude between 5–6 and 4–5 are denoted by light-blue line and light-green line, respectively. The unperturbed period without the strong earthquakes during 90–25 days before the event is marked by the gray dashed rectangle.

EAs during the observation period. It can be seen that the occurrence of EAs mainly appears from 5 to 10 days before the earthquake, regardless of being in the daytime or the nighttime. This provides a useful precursory index for OLR monitoring of the impending significant seismic activity, at least in the Taiwan area. The dependent relationship between the number of total precursory EAs and the magnitude of each PE is shown in **Figure 5**. A weak correlation (R^2 = 0.05) is obtained between these variables, suggesting that the number of precursory EAs does not reflect the magnitude of the earthquake. The amounts of EAs may not be used to estimate the magnitude of an earthquake for neither inland nor offshore earthquakes.

A confutation test was performed to verify the appearance or absence of the POEA before or after significant earthquakes over the same area (Di Bello et al., 2004; Genzano et al., 2009; Tramutoli et al., 2013; Xiong et al., 2013; Lisi et al., 2015; Khalili et al., 2019). As shown in **Figure 6**, most of the POEAs were only observed once within 90 days before and 25 days after the related earthquake, except for eight of the 35 selected seismic events (EQ-5, EQ-7, EQ-14, EQ-16, EQ-17, EQ-18, EQ-24, and EQ-30). However, only a few sporadic EAs appeared only in 1 day, which did not approach the anomalous criteria of this study. It is important to note that a POEA observed during the 2013/02/23-2/27 event may relate the 2013/03/07 M5.9 earthquake (marked by a black arrow) as a true positive occurring in the same grid of the EQ-14. The POEA occurring 27–31 days before EQ-3 may be considered as a false positive as opposed to most POEAs that appear 2–15 days prior to the significant earthquakes. Therefore, excluding a POEA related to the M5.9 event in the time series of the EQ-14, only a few false positives (∼23%) appear in the absence of the strong earthquake ($M \geq 6$), by considering the unperturbed period within 90–25 days before the event as shown by the dashed rectangle in **Figure 6**.

Based on the observations from the present study, the consecutive POEAs generally appear several days over the epicenter before a strong earthquake. This can be utilized to trace the appearance of EAs around Taiwan using the spatial-temporal monitoring of OLR observations. Currently, an automatic-process monitoring system has been established in Taiwan to routinely monitor variations in OLR. As mentioned above, substantial POEAs can be observed, followed by an increase in radon concentrations, before significant seismic activities in Taiwan. The appearance of the significant POEAs could be further compared with soil radon observations along fault zones around Taiwan (Walia et al., 2013; Fu et al., 2015, 2017a, 2019), which can be validated and used to evaluate the potential mechanism of the coupling processes between the lithosphere and atmosphere before significant earthquakes.

CONCLUSION

In the present study, we applied a satellite technique to outgoing longwave radiation (OLR) variations in order to search for the precursors of $M \geq 6.0$ earthquakes over 2009–2019. The major findings of this study are listed below:

(1) The results showed that most precursors, as shown by the pre-earthquake OLR E_{Index} anomaly, mainly appeared 5–10 days before significant earthquakes.
(2) There is a weak correlation between the number of E_{Index} anomalies and the earthquake's magnitude, indicating that the increasing intensity of OLR anomalies is not associated with increased magnitude.
(3) The effects of the focal depth and typhoon events are proposed as critical factors that affect OLR variations for earthquake precursor studies, as when an earthquake has a hypocenter depth greater than 70 km and a typhoon occurs before the earthquake, consecutive E_{Index} anomalies are rarely observed.
(4) A high percentage of earthquakes (∼77%) with pre-earthquake OLR anomalies are consistently observed when the possible factor of a typhoon's occurrence is removed.
(5) We proposed a potential mechanism to interpret the pre-earthquake generation process, suggesting the existence of multiple responses triggered by coupling processes between the lithosphere, atmosphere, and ionosphere through OLR anomalies by combining different types of observations.
(6) Therefore, our studies provide a useful indicator for exploring earthquake precursors, especially in the Taiwan region.

DATA AVAILABILITY STATEMENT

The datasets generated for this study are available on request from the corresponding author and from the NOAA Climate Prediction Center website (http://www.cdc.noaa.gov/).

AUTHOR CONTRIBUTIONS

C-CF organized and wrote the manuscript. L-CL provided the concepts of the manuscript. DO and J-CJ assisted in improving the data processing. All authors contributed to the article and approved the submitted version.

FUNDING

The research was supported by Grants MOST 108-2116-M-002-025 and MOST 108-2116-M-001-024 through the Ministry of Science and Technology (MOST) and MOTC-CWB-108-E-01 from the Central Weather Bureau of Taiwan.

ACKNOWLEDGMENTS

We thank Mr. Peng-Kang Wang and Kuo-Hang Chen for help with data collection and preliminary analysis. We would like to thank Uni-edit (www.uni-edit.net) for editing and proofreading this manuscript. The TEC contribution number for this article is 00163. We are also thankful to the editor and reviewers and the referee for their valuable comments and suggestions, which helped us to improve the manuscript.

REFERENCES

Aliano, C., Corrado, R., Filizzola, C., Genzano, N., Pergola, N., and Tramutoli, V. (2008a). Robust TIR satellite techniques for monitoring earthquake active regions: limits, main achievements and perspectives. *Ann. Geophys.* 51, 303–317.

Aliano, C., Corrado, R., Filizzola, C., Pergola, N., and Tramutoli, V. (2008b). Robust satellite techniques (RST) for the thermal monitoring of earthquake prone areas: the case of Umbria-Marche October, 1997 seismic events. *Ann. Geophys.* 51, 451–459.

Canitano, A., Hsu, Y. J., Lee, H. M., Linde, A. T., and Sacks, S. (2015). Near-field strain observations of the October 2013 Ruisui, Taiwan, earthquake: source parameters and limits of very-short term strain detection. *Earth Planets Space* 67:125. doi: 10.1186/s40623-015-0284-1

Canitano, A., Hsu, Y. J., Lee, H. M., Linde, A. T., and Sacks, S. (2017). A first modeling of dynamic and static crustal strain field from near-field dilatation measurements: example of the 2013 MwMw 6.2 Ruisui earthquake. *Taiwan. J. Geod.* 91, 1–8. doi: 10.1007/s00190-016-0933-6

Chan, H. P., and Chang, C. P. (2018). Exploring and monitoring geothermal and volcanic activity using satellite thermal infrared data in TVG, Taiwan. *Terr. Atmos. Ocean. Sci.* 29, 387–404. doi: 10.3319/TAO.2018.01.22.01

Chan, H. P., Chang, C. P., and Dao, P. D. (2018). Geothermal anomaly mapping using landsat ETM+ data in ilan plain, Northeastern Taiwan. *Pure Appl. Geophys.* 175, 303–323. doi: 10.1007/s00024-017-1690-z

Chan, H. P., Chang, C. P., Lin, T. H., Blackett, M., Kuo-Chen, H., and Lin, A. T. S. (2020). The potential of satellite remote sensing for monitoring the onset of volcanic activity on Taipei's doorstep. *Int. J. Remote Sens.* 41, 1372–1388. doi: 10.1080/01431161.2019.1667549

Chen, C. C., Rundle, J. B., Holliday, J. R., Nanjo, K. Z., Turcotte, D. L., Li, S. C., et al. (2005). The 1999 Chi-Chi, Taiwan earthquake as a typical example of seismic activation and quiescence. *Geophys. Res. Lett.* 32:L22315. doi: 10.1029/2005GL023991

Chen, C. C., Rundle, J. B., Li, H. C., Holliday, J. R., Nanjo, K. Z., Turcotte, D. L., et al. (2006). From tornadoes to earthquakes: forecast verification for binary events applied to the 1999 Chi-Chi, Taiwan, earthquake. *Terr. Atmos. Ocean. Sci.* 17, 503–516.

Chen, C. H., Hsu, H. L., Wen, S., Yeh, T. K., Chang, F. Y., Wang, C. H., et al. (2013a). Evaluation of seismo-electric anomalies using magnetic data in Taiwan. *Nat. Hazards Earth Syst. Sci.* 13, 1–8.

Chen, C. H., Wang, C. H., Wen, S., Yeh, T. K., Lin, C. H., Liu, J. Y., et al. (2013b). Anomalous frequency characteristics of groundwater level before major earthquakes in Taiwan. *Hydrol. Earth Syst. Sci.* 17, 1693–1703. doi: 10.5194/hess-17-1693-2013

Chen, C. H., Wen, S., Yeh, T. K., Wang, C. H., Yen, H. Y., Liu, J. Y., et al. (2013c). Observation of surface displacements from GPS analyses before and after the Jiashian earthquake (M = 6.4) in Taiwan. *J. Asian Earth Sci.* 62, 662–671. doi: 10.1016/j.jseaes.2012.11.016

Chen, C. H., Lin, C. H., Hsu, H. L., Wang, C. H., Lee, L. C., Han, P., et al. (2015a). Evaluating the March 27, 2013 M6.2 earthquake hypocenter using momentary high conductivity materials. *Terr. Atmos. Ocean Sci.* 26, 1–9.

Chen, C. H., Lin, C. H., Wang, C. H., Liu, J. Y., Yeh, T. K., Yen, H. Y., et al. (2015b). Potential relationships between seismo-deformation and seismo-conductivity anomalies. *J. Asian Earth Sci.* 114, 327–337. doi: 10.1016/j.jseaes.2015.03.023

Chen, C. H., Tang, C. C., Cheng, K. C., Wang, C. H., Wen, S., Lin, C. H., et al. (2015c). Groundwater-strain coupling before the 1999 Mw 7.6 Taiwan Chi-Chi earthquake. *J. Hydrol.* 524, 378–384. doi: 10.1016/j.jhydrol.2015.03.006

Chen, H. J., Chen, C. Y., Tseng, J. H., and Wang, J. H. (2012). Effect of tidal triggering on seismicity in Taiwan revealed by the empirical mode decomposition method. *Nat. Hazards Earth Syst. Sci.* 12, 2193–2202. doi: 10.5194/nhess-12-2193-2012

Chen, K. J., Chiu, B., Wang, J. S., Lee, C. Y., Lin, C. H., and Chao, K. (2011). Geomagnetic anomaly at Lunping before the 1999 Chi-Chi earthquake (Mw = 7.6) in Taiwan. *Nat. Hazards* 58, 1233–1252. doi: 10.1007/s11069-011-9726-7

Chen, W. P., and Molnar, P. (1983). Focal depths of intracontinental and intraplate earthquakes and their implications for the thermal and mechanical properties of the lithosphere. *J. Geophys. Res. Solid Earth* 88, 4183–4214. doi: 10.1029/JB088iB05p04183

Chen, Y. I., Liu, J. Y., Tsai, Y. B., and Chen, C. S. (2004). Statistical tests for pre-earthquake ionospheric anomaly. *Terr. Atmos. Ocean Sci.* 15, 385–396.

Chia, Y., Wang, Y. S., Chiu, J. J., and Lin, C. W. (2001). Changes of groundwater level due to the 1999 Chi-Chi earthquake in the Choshui River alluvial fan in Taiwan. *Bull. Seismol. Soc. Am.* 91, 1062–1068. doi: 10.1785/0120000726

Chyi, L. L., Quick, T. J., Yang, T. F., and Chen, C. H. (2005). Soil gas radon spectra and earthquakes. *Terr. Atmos. Ocean. Sci.* 16, 763–774.

Di Bello, G., Filizzola, C., Lacava, T., Marchese, F., Pergola, N., Pietrapertosa, C., et al. (2004). Robust satellite techniques for volcanic and seismic hazards monitoring. *Ann. Geophys.* 47, 49–64.

Freund, F. (2007a). Pre-earthquake signals – part I: deviatoric stresses turn rocks into a source of electric currents. *Nat. Hazards Earth Syst. Sci.* 7, 535–541. doi: 10.5194/nhess-7-535-2007

Freund, F. (2007b). Pre-earthquake signals – part II: flow of battery currents in the crust. *Nat. Hazards Earth Syst. Sci.* 7, 543–548. doi: 10.5194/nhess-7-543-2007

Freund, F., Takeuchi, A., Lau, B., Al-Manaseer, A., Fu, C., Bryant, N. A., et al. (2007). Stimulated infrared emission from rocks: assessing a stress indicator. *eEarth* 2, 7–16. doi: 10.5194/ee-2-7-2007

Fu, C. C., and Lee, L. C. (2018). "Continuous monitoring of fluid and gas geochemistry for seismic study in Taiwan," in *Pre-Earthquake Processes: A Multidisciplinary Approach to Earthquake Prediction Studies*, eds D. Ouzounov, S. Pulinets, K. Hattori, and P. Taylor, (Hoboken, NJ: John Wiley and Sons, Inc. Press), 199–218.

Fu, C. C., Lee, L. C., Yang, T. F., Lin, C. H., Chen, C. H., Walia, V., et al. (2019). Gamma ray and radon anomalies in northern Taiwan as a possible preearthquake indicator around the plate boundary. *Geofluids* 2019:14. doi: 10.1155/2019/4734513

Fu, C. C., Walia, V., Yang, T. F., Lee, L. C., Liu, T. K., Chen, C. H., et al. (2017a). Preseismic anomalies in soil-gas radon associated with 2016 M6.6 meinong earthquake, Southern Taiwan. *Terr. Atmos. Ocean. Sci.* 28, 787–798. doi: 10.3319/tao.2017.03.22.01

Fu, C. C., Yang, T. F., Chen, C. H., Lee, L. C., Wu, Y. M., Liu, T. K., et al. (2017b). Spatial and temporal anomalies of soil gas in northern Taiwan and its tectonic and seismic implications. *J. Asian Earth Sci.* 149, 64–77. doi: 10.1016/j.jseaes.2017.02.032

Fu, C. C., Yang, T. F., Tsai, M. C., Lee, L. C., Liu, T. K., Walia, V., et al. (2017c). Exploring the relationship between soil degassing and seismic activity by continuous radon monitoring in the Longitudinal Valley of eastern Taiwan. *Chem. Geol.* 469, 163–175. doi: 10.1016/j.chemgeo.2016.12.042

Fu, C. C., Wang, P. K., Lee, L. C., Lin, C. H., Chang, W. Y., Giuliani, G., et al. (2015). Temporal variation of gamma rays as a possible precursor of earthquake in the Longitudinal Valley of eastern Taiwan. *J. Asian Earth Sci.* 114, 362–372. doi: 10.1016/j.jseaes.2015.04.035

Fu, C. C., Yang, T. F., Du, J., Walia, V., Liu, T. K., Chen, Y. G., et al. (2008). Variations of helium and radon concentrations in soil gases from an active fault zone in southern Taiwan. *Radiat. Meas.* 43, 348–352.

Fu, C. C., Yang, T. F., Walia, V., and Chen, C. H. (2005). Reconnaissance of soil gas composition over the buried fault and fracture zone in southern Taiwan. *Geochem. J.* 39, 427–439. doi: 10.2343/geochemj.39.427

Fu, C. C., Yang, T. F., Walia, V., Liu, T. K., Lin, S. J., Chen, C.-H., et al. (2009). Variations of soil-gas composition around the active Chihshang Fault in a plate suture zone, eastern Taiwan. *Radiat. Meas.* 44, 940–944. doi: 10.1016/j.radmeas.2009.10.095

Genzano, N., Aliano, C., Corrado, R., Filizzola, C., Lisi, M., Mazzeo, G., et al. (2009). RST analysis of MSG-SEVIRI TIR radiances at the time of the Abruzzo 6 April 2009 earthquake. *Nat. Hazards Earth Syst. Sci.* 9, 2073–2084. doi: 10.5194/nhess-9-2073-2009

Genzano, N., Aliano, C., Filizzola, C., Pergola, N., and Tramutoli, V. (2007). Robust satellite technique for monitoring seismically active areas: the case of Bhuj-Gujarat earthquake. *Tectonophysics* 431, 197–210. doi: 10.1016/j.tecto.2006.04.024

Genzano, N., Corrado, R., Coviello, I., Grimaldi, C. S., Filizzola, C., Lacava, T., et al. (2010). "A multi-sensors analysis of RST-based thermal anomalies in the case of the Abruzzo earthquake," in *Proceedings of the 2010 IEEE Int. Geosci. Remote Sens. Symp.* (Piscataway, NJ: IEEE). 761–764.

Genzano, N., Filizzola, C., Paciello, R., Pergola, N., and Tramutoli, V. (2015). Robust Satellite Techniques (RST) for monitoring earthquake prone areas by

satellite TIR observations: the case of 1999 Chi-Chi earthquake (Taiwan). *J Asian Earth Sci.* 114, 289–298. doi: 10.1016/j.jseaes.2015.02.010

Gorny, V. I., Salman, A. G., Tronin, A. A., and Shilin, B. B. (1988). The Earth outgoing IR radiation as an indicator of seismic activity. *Proc. Acad. Sci. USSR* 301, 67–69.

Graham, E., Sarazin, M., and Matzler, C. (2011). Using re-analysis model data ("FriOWL") to analyse climate trends related to astroclimatology of Paranal and La Silla. *Rev. Mex. Astron. Astrofis. (Ser Conf).* 41, 12–15.

Hadi, N. I., Freund, M. M., and Freund, F. (2012). Electrical conductivity of rocks and dominant charge carriers: the paradox of thermally activated positive holes. *J. Earth Sci. Climate Change* 3:128. doi: 10.4172/2157-7617.1000128

Hatchett, B. J. (2018). Snow level characteristics and impacts of a spring typhoon-originating atmospheric river in the sierra nevada. *U S A. Atmosphere (Basel).* 9:233. doi: 10.3390/atmos9060233

Ho, Y.-Y., Jhuang, H.-K., Lee, L.-C., and Liu, J. Y. (2018). Ionospheric density and velocity anomalies before M≥6.5 earthquakes observed by DEMETER satellite. *J. Asian Earth Sci.* 166, 210–222. doi: 10.1016/j.jseaes.2018.07.022

Hsu, Y. J., Chang, Y. S., Liu, C. C., Lee, H. M., Linde, A. T., Sacks, S., et al. (2015). Revisiting borehole strain, typhoons, and slow earthquakes using quantitative estimates of precipitation-induced strain changes. *J. Geophys. Res.* 120, 4556–4571. doi: 10.1002/2014JB011807

Jing, F., Shen, X. H., Kang, C. L., and Xion, G. P. (2013). Variations of multi-parameter observed in atmosphere related to earthquake. *Nat. Hazards Earth Syst. Sci.* 13, 27–33. doi: 10.5194/nhess-13-27-2013

Jing, F., Shen, X. H., Kang, C. L., Xiong, P., and Sun, K. (2012). Variation of outgoing longwave radiation around the time of New Zealand Earthquake M7.1. *Adv. Earth Sci.* 27, 979–986.

Kane, R. P., and Buriti, R. A. (1997). Latitude and altitude dependence of the interannual variability and trends of atmospheric temperatures. *Pure Appl. Geophys.* 149, 775–792. doi: 10.1007/s000240050052

Kawamura, M., Chen, C. C., and Wu, Y. M. (2014). Seismicity change revealed by ETAS, PI, and Z-value methods: a case study of the 2013 Nantou, Taiwan earthquake. *Tectonophysics* 634, 139–155. doi: 10.1016/j.tecto.2014.07.028

Khalili, M., Abdollahi Eskandar, S. S., and Alavi Panah, S. K. (2020). Thermal anomalies detection before Saravan earthquake (April 16th, 2013, MW = 7.8) using time series method, satellite, and meteorological data. *J. Earth Syst. Sci.* 129:5. doi: 10.1007/s12040-019-1286-3

Khalili, M., Alavi Panah, S. K., and Abdollahi Eskandar, S. S. (2019). Using Robust Satellite Technique (RST) to determine thermal anomalies before a strong earthquake: a case study of the Saravan earthquake (April 16th, 2013. *M w = 7.8, Iran). J. Asian Earth Sci.* 173, 70–78. doi: 10.1016/j.jseaes.2019.01.009

Koll, D. D., and Cronin, T. W. (2018). Earth's outgoing longwave radiation linear due to H2O greenhouse effect. *Proc. Natl. Acad. Sci. U S A.* 115, 10293–10298. doi: 10.1073/pnas.1809868115

Kumar, A., Walia, V., Arora, B. R., Yang, T. F., Lin, S. J., Fu, C. C., et al. (2015). Identifications and removal of diurnal and semidiurnal variations in radon time series data of Hsinhua monitoring station in SW Taiwan using singular spectrum analysis. *Nat. Hazards* 79, 317–330. doi: 10.1007/s11069-015-1844-1

Kuo, C. L., Huba, J. D., Joyce, G., and Lee, L. C. (2011). Ionosphere plasma bubbles and density variations induced by pre-earthquake rock currents and associated surface charges. *J. Geophys. Res.* 116:A10317. doi: 10.1029/2011ja016628

Kuo, C. L., Lee, L. C., and Huba, J. D. (2014). An improved coupling model for the lithosphere-atmosphere-ionosphere system. *J. Geophys. Res. Space Physics.* 119, 3189–3205. doi: 10.1002/2013ja019392

Kuo, M. C. T., Fan, K., Kuochen, H., and Chen, W. (2006). A mechanism for anomalous decline in radon precursory to an earthquake. *Ground Water* 44, 642–647.

Kuo, T., Su, C., Chang, C., Lin, C., Cheng, W., Liang, H., et al. (2010). Application of recurrent radon precursors for forecasting large earthquakes (Mw > 6.0) near Antung. *Taiwan. Radiat. Meas.* 45, 1049–1054. doi: 10.1016/j.radmeas.2010.08.009

Lai, W. C., Hsu, K. C., Shieh, C. L., Lee, Y. P., Chung, K. C., Koizumi, N., et al. (2010). Evaluation of the effects of ground shaking and static volumetric strain change on earthquake-related groundwater level changes in Taiwan. *Earth Planets Space* 62, 391–400. doi: 10.5047/eps.2009.12.008

Lee, C. S., Lin, Y. L., and Cheung, K. K. W. (2006). Tropical cyclone formations in the South China Sea associated with the Mei-Yu front. *Mon. Wea. Rev.* 134, 2670–2687. doi: 10.1175/mwr3221.1

Liebmann, B., and Smith, C. A. (1996). Description of a complete (Interpolated) outgoing longwave radiation dataset. *Bull. Amer. Meteor. Soc.* 77, 1275–1277.

Lin, C. H. (2009). Foreshock characteristics in Taiwan: potential earthquake warning. *J. Asian Earth Sci.* 34, 655–662. doi: 10.1016/j.jseaes.2008.09.006

Lin, C. H., Chen, Y. I., Liu, J. Y., Chen, L. J., and Yeh, Y. H. (2003). Earthquake clustering relative to lunar phases in Taiwan. *Terr. Atmos. Ocean. Sci.* 14, 289–298.

Lisi, M., Filizzola, C., Genzano, N., Paciello, R., Pergola, N., and Tramutoli, V. (2015). Reducing atmospheric noise in RST analysis of TIR satellite radiances for earthquakes prone areas satellite monitoring. *Phys. Chem. Earth Sci.* 8, 87–97. doi: 10.1016/j.pce.2015.07.013

Liu, C. C., Linde, A. T., and Sacks, I. S. (2009). Slow earthquakes triggered by typhoons. *Nature* 459, 833–836. doi: 10.1038/nature08042

Liu, J. Y., Chen, Y. I., and Chuo, Y. J. (2006). A statistical investigation of pre-earthquake ionospheric anomaly. *J. Geophys. Res.* 111:A05304.

Liu, J. Y., Chen, Y. I., Chuo, Y. J., and Tsai, H. F. (2001). Variations of ionospheric total electron content during the Chi-Chi earthquake. *Geophys. Res. Lett.* 28, 1383–1386. doi: 10.1029/2000GL012511

Liu, J. Y., Chen, Y. I., Huang, C. H., Ho, Y. Y., and Chen, C. H. (2015). A statistical study of lightning activities and M = 5.0 earthquakes in Taiwan during 1993-2004. *Surv. Geophys.* 36, 851–859. doi: 10.1007/s10712-015-9342-2

Liu, J. Y., Chen, Y. I., Pulinets, S. A., Tsai, Y. B., and Chuo, Y. J. (2000). Seismo-ionospheric signatures prior to M = 6.0 Taiwan earthquakes. *Geophys. Res. Lett.* 27, 3113–3116. doi: 10.1029/2000GL011395

Liu, J. Y., Chuo, Y., Shan, S., Tsai, Y., Chen, Y., Pulinets, S., et al. (2004). Pre-earthquake ionospheric anomalies registered by continuous GPS TEC measurements. *Ann. Geophys.* 22, 1585–1593. doi: 10.5194/angeo-22-1585-2004

Liu, J. Y., Tsai, H. F., Lin, C. H., Kamogawa, M., Chen, Y. I., Huang, B. S., et al. (2010). Coseismic ionospheric disturbances triggered by the Chi-Chi earthquake. *J. Geophys. Res.* 115, A08303. doi: 10.1029/2009ja014943

Liu, K. K., Yui, T. F., Yeh, Y. H., Tsai, Y. B., and Teng, T. (1985). Variations of radon content in ground waters and possible correlation with seismic activities in northern Taiwan. *Pure Appl. Geophys.* 122, 231–244. doi: 10.1007/bf00874596

Liu, S., Yang, D., Ma, B., Wu, L., Li, J., and Dong, Y. (2007). "On the features and mechanism of satellite infrared anomaly before earthquakes in Taiwan region," in *Proceedings of the International Geoscience and Remote Sensing Symposium (IGARSS)*, (Barcelona: IEEE), 3719–3722.

Ouzounov, D., Bryant, N., Logan, T., Pulinets, S., and Taylor, P. (2006). Satellite thermal IR phenomena associated with some of the major earthquakes in 1999-2003. *Phys. Chem. Earth* 31, 154–163. doi: 10.1016/j.pce.2006.02.036

Ouzounov, D., and Freund, F. (2004). Mid-infrared emission prior to strong earthquakes analyzed by remote sensing data. *Adv. Space Res.* 33, 268–273. doi: 10.1016/s0273-1177(03)00486-1

Ouzounov, D., Liu, D., Kang, C. L., Cervone, G., Kafatos, M., and Taylor, P. (2007). Outgoing long wave radiation variability from IR satellite data prior to major earthquakes. *Tectonophysics* 431, 211–220. doi: 10.1016/j.tecto.2006.05.042

Ouzounov, D., Pulinets, S., and Davidenko, D. (2015). "Revealing pre-earthquake signatures in atmosphere and ionosphere associated with 2015 M7.8 and M7.3 events in Nepal: Preliminary results," in *Proceedings of the Conference: 2nd International Workshop on Earthquake Preparation Process: Observation, Validation, Modeling, Forecasting (IWEP2 2015*, (Chiba).

Ouzounov, D., Pulinets, S., Kafatos, M., and Taylor, P. (2018). "Thermal radiation anomalies associated with major earthquakes," in *Pre-Earthquake Processes: A Multidisciplinary Approach to Earthquake Prediction Studies*, eds D. Ouzounov, S. Pulinets, K. Hattori, and P. Taylor, (Hoboken, NJ: John Wiley and Sons, Inc. Press), 259–274. doi: 10.1002/9781119156949.ch15

Pergola, N., Aliano, C., Coviello, I., Filizzola, C., Genzano, N., Lacava, T., et al. (2010). Using RST approach and EOS-MODIS radiances for monitoring seismically active regions: a study on the 6 April 2009 Abruzzo earthquake. *Nat. Hazards Earth Syst. Sci.* 10, 239–249.

Pulinets, S., and Ouzounov, D. (2011). Lithosphere-Atmosphere-Ionosphere Coupling (LAIC) model-An unified concept for earthquake precursors validation. *J. Asian Earth Sci.* 41, 371–382. doi: 10.1016/j.jseaes.2010.03.005

Pulinets, S. A., and Dunajeck, M. A. (2007). Specific variations of air temperature and relative humidity around the time of Michoacan earthquake M8.1 September 19, 1985 as a possible indicator of interaction between tectonic plates. *Tectonophysics* 431, 221–230. doi: 10.1016/j.tecto.2006.05.044

Pulinets, S. A., Ouzounov, D., Karelin, A. V., Boyarchuk, K. A., and Pokhmelnykh, L. A. (2006). The physical nature of the thermal anomalies observed before strong earthquake. *Phys. Chem. Earth* 31, 143–153. doi: 10.1016/j.pce.2006.02.042

Rodger, C. J., Dowden, R. L., and Thomson, N. R. (1999). "Observations of electromagnetic activity associated with earthquakes by low-altitude satellites," in *Atmospheric and Ionospheric Electromagnetic Phenomena Associated with Earthquakes*, ed. M. Hayakawa, (Tokyo: Terra Sci. Publ), 697–710.

Song, S. R., Ku, W. Y., Chen, Y. L., Lin, Y. C., Liu, C. M., Kuo, L. W., et al. (2003). Groundwater chemical anomaly before and after the Chi-Chi earthquake in Taiwan. *Terr. Atmos. Oceanic Sci.* 14, 311–320.

Song, S. R., Ku, W. Y., Chen, Y. L., Liu, C. M., Chan, P. S., Chen, Y. G., et al. (2006). Hydrogeochemical anomalies in the springs of the Chiayi area in west-central Taiwan as likely precursors to earthquakes. *Pure Appl. Geophys.* 163, 675–691. doi: 10.1007/3-7643-7584-1_5

Susskind, J., Molnar, G., Iredell, L., and Loeb, N. (2012). Interannual variability of outgoing longwave radiation as observed by AIRS and CERES. *J. Geophys. Res.* 117:D23107. doi: 10.1029/2012JD017997

Tramutoli, V., Aliano, C., Corrado, R., Filizzola, C., Genoano, N., Lisi, M., et al. (2013). On the possible origin of thermal infrared radiation (TIR) anomalies in earthquake-prone areas observed using robust satellite techniques (RST). *Chem. Geol.* 339, 157–168. doi: 10.1016/j.chemgeo.2012.10.042

Tramutoli, V., Aliano, C., Corrado, R., Filizzola, C., Genzano, N., Lisi, M., et al. (2009). Abrupt change in greenhouse gases emission rate as a possible genetic model of TIR anomalies observed from satellite in Earthquake active regions. *Proc. ISRSE* 2009, 567–570.

Tramutoli, V., Cuomo, V., Filizzola, C., Pergola, N., and Pietrapertosa, C. (2005). Assessing the potential of thermal infrared satellite surveys for monitoring seismically active areas: the case of Kocaeli (Izmit) earthquake, August 17, 1999. *Remote Sens. Environ.* 96, 409–426. doi: 10.1016/j.rse.2005.04.006

Tramutoli, V., Di Bello, G., Pergola, N., and Piscitelli, S. (2001). Robust satellite techniques for remote sensing of seismically active areas. *Ann. Geofis.* 44, 295–312.

Tronin, A. A. (1996). Satellite thermal survey—a new tool for the study of seismoactive regions. *Int. J. Remote Sens.* 17, 1439–1455. doi: 10.1080/01431169608948716

Tronin, A. A. (2000). Thermal IR satellite sensor data application for earthquake research in China. *Int. J. Remote Sens.* 21, 3169–3177. doi: 10.1080/01431160050145054

Tronin, A. A. (2002). "Atmosphere-lithosphere coupling: thermal anomalies on the Earth surface in seismic processes", in *Seismo-Electromagnetics: Lithosphere-Atmosphere-Ionosphere Coupling*, eds M. Hayakawa, and O. A. Molchanov, (Tokyo: Terra Scientific Publ), 173–176.

Tsai, Y. B., Liu, J. Y., Ma, K. F., Yen, H. Y., Chen, K. S., Chen, Y. I., et al. (2004). Preliminary results of the iSTEP program on integrated search for Taiwan earthquake precursors. *Terr. Atmos. Ocean Sci.* 15, 545–562.

Tsai, Y. B., Liu, J. Y., Ma, K. F., Yen, H. Y., Chen, K. S., Chen, Y. I., et al. (2006). Precursory phenomena associated with the Chi-Chi earthquake in Taiwan as identified under the iSTEP program. *Phys. Chem. Earth* 31, 365–377. doi: 10.1016/j.pce.2006.02.035

Ustaszewski, K., Wu, Y. M., Suppe, J., Huang, H. H., Chang, C. H., and Carena, S. (2012). Crust-mantle boundaries in the Taiwan - Luzon arc-continent collision system determined from local earthquake tomography and 1D models: implications for the mode of subduction polarity reversal. *Tectonophysics* 578, 31–49. doi: 10.1016/j.tecto.2011.12.029

Walia, V., Lin, S. J., Hong, W. L., Fu, C. C., Yang, T. F., Wen, K. L., et al. (2009). Continuous temporal soil-gas composition variation for earthquake precursory studies along Hsincheng and Hsinhua faults in Taiwan. *Radiat. Meas.* 44, 934–939. doi: 10.1016/j.radmeas.2009.10.010

Walia, V., Yang, T. F., Lin, S. J., Kumar, A., Fu, C. C., Chiu, J. M., et al. (2013). Temporal variation of soil gas compositions for earthquake surveillance in Taiwan. *Radiat. Meas.* 50, 154–159. doi: 10.1016/j.radmeas.2012.11.007

Wang, C. Y., Cheng, I. H., Chin, C. V., and Yu, S. B. (2001). Coseismic hydrologic response of an alluvial fan to the 1999 Chi-Chi earthquake. *Taiwan. Geol.* 29, 831–834.

Wu, L., Liu, S., and Wu, Y. W. (2006). "The experiment evidences for tectonic earthquake forecasting based on anomaly analysis on satellite infrared image," in *Proceedings of the International Geoscience and Remote Sensing Symposium (IGARSS)*, (Denver, CO: IEEE), 2158–2162.

Wu, Y. M., and Chen, C. C. (2007). Seismic reversal pattern for the 1999 Chi-Chi, Taiwan, Mw7.6 earthquake. *Tectonophysics* 429, 125–132. doi: 10.1016/j.tecto.2006.09.015

Wu, Y. M., Chen, C. C., and Rundle, J. B. (2008). Detecting precursory earthquake migration patterns using the pattern informatics method. *Geophys. Res. Lett.* 35, L19304. doi: 10.1029/2008GL035215

Wu, Y. M., and Chiao, L. Y. (2006). Seismic quiescence before the 1999 Chi-Chi. Taiwan, Mw7.6 earthquake. *Bull. Seism. Soc. Am.* 96, 321–327. doi: 10.1785/0120050069

Xiong, P., Gu, X. F., Bi, Y. X., Shen, X. H., Meng, Q. Y., Zhao, L. M., et al. (2013). Detecting seismic IR anomalies in bi-angular advanced along-track scanning radiometer data. *Nat. Hazards Earth Syst. Sci.* 13, 2065–2074. doi: 10.5194/nhess-13-2065-2013

Xiong, P., and Shen, X. (2017). Outgoing longwave radiation anomalies analysis associated with different types of seismic activity. *Adv. Space Res.* 59, 1408–1415. doi: 10.1016/j.asr.2016.12.011

Xiong, P., Shen, X. H., Bi, Y. X., Kang, C. L., Chen, L. Z., Jing, F., et al. (2010). Study of outgoing longwave radiation anomalies associated with Haiti earthquake. *Nat. Hazards Earth Syst. Sci.* 10, 2169–2178. doi: 10.5194/nhess-10-2169-2010

Xiong, P., Shen, X. H., Gu, X. F., Meng, Q. Y., Zhao, L. M., Zhao, Y. H., et al. (2015). Seismic infrared anomalies detection in the case of the Wenchuan earthquake using bi-angular advanced along-track scanning radiometer data. *Ann. Geophys.* 58, S0217. doi: 10.4401/ag-6706

Yang, T. F., Fu, C. C., Walia, V., Chen, C. H., Chyi, L. L., Liu, T. K., et al. (2006). Seismo-geochemical variations in SW Taiwan: multi-parameter automatic gas monitoring results. *Pure Appl. Geophys.* 163, 693–709. doi: 10.1007/3-7643-7584-1_6

Yang, T. F., Walia, V., Chyi, L. L., Fu, C. C., Chen, C. H., Liu, T. K., et al. (2005). Variations of soil radon and thoron concentrations in a fault zone and prospective earthquakes in SW Taiwan. *Radiat. Meas.* 40, 496–502. doi: 10.1016/j.radmeas.2005.05.017

Yen, H. Y., Chen, C. H., Hsieh, H. H., Lin, C. R., Yeh, Y. H., Tsai, Y. B., et al. (2009). Magnetic survey of Taiwan and its preliminary interpretations. *Terr. Atmos. Ocean Sci.* 20, 309–314.

Yen, H. Y., Chen, C. H., Yeh, Y. H., Liu, J. Y., Lin, C. R., and Tsai, Y. B. (2004). Geomagnetic fluctuations during the 1999 Chi-Chi earthquake in Taiwan. *Earth Planets Space.* 56, 39–45. doi: 10.1186/bf03352489

Yu, S. B., Chen, H. Y., and Kuo, L. C. (1997). Velocity field of GPS stations in the Taiwan area. *Tectonophysics* 274, 41–59. doi: 10.1016/s0040-1951(96)00297-1

Conflict of Interest: The authors declare that the research was conducted in the absence of any commercial or financial relationships that could be construed as a potential conflict of interest.

Copyright © 2020 Fu, Lee, Ouzounov and Jan. This is an open-access article distributed under the terms of the Creative Commons Attribution License (CC BY). The use, distribution or reproduction in other forums is permitted, provided the original author(s) and the copyright owner(s) are credited and that the original publication in this journal is cited, in accordance with accepted academic practice. No use, distribution or reproduction is permitted which does not comply with these terms.

frontiers in Earth Science

ORIGINAL RESEARCH
published: 04 September 2020
doi: 10.3389/feart.2020.554924

Spatial Distribution of Rn, CO_2, Hg, and H_2 Concentrations in Soil Gas Across a Thrust Fault in Xinjiang, China

Yang Xiang[1,2], Xiaolong Sun[1]†, Dongying Liu[1], Long Yan[3], Bo Wang[4] and Xiaoqi Gao[1]*

[1] National Institute of Natural Hazards, MEMC, Beijing, China, [2] College of Geoscience and Surveying Engineering, China University of Mining and Technology, Beijing, China, [3] Earthquake Agency of the Xinjiang Uygur Autonomous Region, Ürümqi, China, [4] China Earthquake Networks Center, Beijing, China

OPEN ACCESS

Edited by:
Antonella Peresan, Istituto Nazionale di Oceanografia e di Geofisica Sperimentale (OGS), Italy

Reviewed by:
Iren Adelina Moldovan, Institutul National de Cercetare si Dezvoltare pentru Fizica Pamantului, Romania
Alessandra Sciarra, Istituto Nazionale di Geofisica e Vulcanologia (INGV), Italy
Giovanni Martinelli, National Institute of Geophysics and Volcanology, Section of Palermo, Italy

***Correspondence:**
Xiaolong Sun
xlsun04@163.com

†ORCID:
Xiaolong Sun
orcid.org/0000-0003-0807-3784

Specialty section:
This article was submitted to Solid Earth Geophysics, a section of the journal Frontiers in Earth Science

Received: *23 April 2020*
Accepted: *14 August 2020*
Published: *04 September 2020*

Citation:
Xiang Y, Sun X, Liu D, Yan L, Wang B and Gao X (2020) Spatial Distribution of Rn, CO_2, Hg, and H_2 Concentrations in Soil Gas Across a Thrust Fault in Xinjiang, China. Front. Earth Sci. 8:554924. doi: 10.3389/feart.2020.554924

Spatial distribution characteristics and origin of soil gasses were discussed in this study. We also examine the correlation between the spatial variation of soil gasses and fault activity, based on the measurements of Rn, Hg, H_2, and CO_2 concentrations in the eastern segment of the BLT fault zone in the southern Tianshan Mountains, Xinjiang, China. The results show that the Rn and CO_2 concentrations on the hanging wall were higher than those near the fault zone and on the footwall of the fault. Moreover, the Hg and H_2 concentrations on the footwall were also higher than those near the fault and on the hanging wall of the fault. The main factors affecting the variations in soil gas spatial distribution were gaseous origin structure of the crust, fault activity, fault fracture degree, stratigraphic lithology, and the cover layer. The results of active structural fault mapping show that the BLT fault has been active since the Late Quaternary and the thrust has broken the fault surface. Under the influence of tectonic compressive stress, the tension zone was formed on the hanging wall of the fault and fractures were developed. This result is consistent with the characteristics of soil gas concentrations measured in this study, indicating that the concentrations of Rn, Hg, H_2, and CO_2 are closely related to the fault activity. These findings can be applied to identify seismic precursors from gas monitoring data of the studied area.

Keywords: BLT fault, soil gas, spatial distribution, thrust fault, Xinjiang

INTRODUCTION

A fault zone is a channel for deflation of the crust, and the number of micro-cracks distributed in the fault zone randomly increases under the impact of the tectonic stress field. This accelerates the migration and release of deep gasses (Baubron et al., 2002; Pulinets and Dunajecka, 2007; Fu et al., 2017), and changes the concentration of chemical components near the fault (Wiersberg and Erzinger, 2008). General overviews of the geochemical, structural, and seismic features in tectonically active areas have shown some evidence of a correlation between soil gas geochemistry anomalies and tectonic activities. Evidence also shows that soil gas escaping through the fault and fractures in the active fault zones can be enhanced by fault and earthquake activity (Fu et al., 2008; Sciarra et al., 2017; Yuce et al., 2017). As such, analyzing the geochemical variations of soil gas near

fault zones has become an important method for investigating earthquake precursors, forecasting earthquakes, and evaluating fault activity (Li et al., 2013; Iovine et al., 2017).

Useful soil gasses include noble gasses, Rn, Hg, H_2, CO_2, and He, which play important roles in fault delineation and earthquake precursory studies (Chyi et al., 2005; Etiope et al., 2007; Caracausi and Paternoster, 2015; Camarda et al., 2016; Fu et al., 2017). Rn has been used by the scientific community as a tracer of natural phenomena related to outgassing from soil located along faults, fractures, and crustal discontinuities (King et al., 1996; Mazur et al., 1999). Rn concentration changes in soil gas and groundwater are commonly observed prior to earthquakes and volcanic eruptions; consequently, they have attracted considerable attention in studies of precursory geochemical signals (Morawska and Phillips, 1993; King et al., 1995; Giammanco et al., 2009; Walia et al., 2009; Iovine et al., 2017). Hg, H_2, He, CO_2, and CH_4 have also been utilized in revealing the relationship among fluid activities in fault zones (Ware et al., 1984; Sugisaki et al., 1996; Jones et al., 2010; Moore and Castro, 2012). Helium isotopes are of particular interest as they can provide unequivocal evidence for the presence in the crust of mantle-derived fluids; ^{3}He is essentially primordial and retained in the Earth's interior, whereas ^{4}He is mainly produced in the crust by the decay of U and Th. Hence, any ^{3}He/^{4}He ratio at the Earth's surface larger than the local and crustal production rates indicates the presence of mantle helium (Sano et al., 2016; Buttitta et al., 2020).

Active faults commonly exhibit anomalously high concentrations of various terrestrially generated gasses in groundwater and soil air (King, 1980, 1986; Sun et al., 2017b). Concentration abnormalities of soil gas were observed in the Tashkent earthquake area in Uzbek, San Andreas Fault in the United States, Hsinhua and Chaochou faults in southern Taiwan, and Longmenshan fault, Beichuan-Yingxiu fault, and Minjiang fault in China (Engle et al., 2001; Li et al., 2006; Fu et al., 2008; Walia et al., 2009; Zhou et al., 2010, 2015). These studies indicate that the application of soil gas concentrations near the fault zone is of great practical significance for studying the fault activity and capturing the precursory information of earthquakes.

In this study, the concentrations of Rn, Hg, H_2, and CO_2 in soil gas were measured in the field along the profiles approximately perpendicular to the BLT fault. The spatial distribution in the soil gas concentrations in the eastern segment of the BLT fault was analyzed. The BLT fault is a long-term successional active fault zone and has been active since the Late Quaternary. It controls the distribution of the Mesozoic and Cenozoic strata in the northern Tarim Basin (Yao et al., 2018). This study is the first to analyze the distribution characteristics of soil gas in the BLT fault.

OVERVIEW OF GEOLOGY AND SEISMOLOGY

The BLT fault is the boundary between the Tarim Basin and the South Tianshan, oriented along the NWW–EW direction. The length of the fault is approximately 300 km, and the fault plane is N-dipping with an inclination of 50–80° (**Figure 1**). The BLT fault cuts the Late Pleistocene and Holocene alluvial fans and has been active since the Late Quaternary. It forms clear large-scale paleoseismic deformation zones and fault scarps with different heights on the surface. According to the records, only M5.6 earthquakes in 1972 and M5.2 earthquakes in 1988 occurred along the BLT fault, and no large destructive earthquake has ever occurred. In the present study, we examine the Tiemenguan section of the eastern part of the BLT fault (hereinafter referred to as Tiemenguan). As shown in **Table 1**, since 1970, 12 earthquakes have occurred near the Tiemenguan section, including two earthquakes above M5 and M4 earthquakes. No earthquakes occurred during the study period, Only two earthquakes occurred after 2015, *M*4.6 on April 1, 2018, and *M*4.4 on May 9, 2020 (**Figure 1A**). However, these two earthquakes did not occur on the BLT fault. There are multiple terraces where the fault is faulted and the height of fault scarps varies between 2 and 20 m. According to the results of trench profile images, there have been more than two paleoseismic events in the fault segment since the late Pleistocene. The vertical displacement of the stratum caused by the latest paleoseismic event is 1.1 m (Yao et al., 2018). The surface strata near the fault are bent and flexed, forming a large number of bending faults, and the crustal shortening rate of SN is 1.43–1.81 mm/a. Large-scale earthquakes have not occurred in the BLT fault since the earliest recorded history. This indicates the potential for a large-scale earthquake to occur in the future. At the fault, the surface accumulation material is mainly gravel, primarily composed of granite, and also comprises limestone. The fault is exposed on the surface, and the overburden is mostly composed of fine sand or sandy sedimentary layers.

MEASUREMENT AND ANALYSIS METHODS

Figure 2 shows the schematic diagram for measuring Rn, Hg, CO_2, and H_2 concentrations. Before sampling, 0.8 m deep and 0.03 m wide holes were drilled in the soil at each sampling site. A pyramidal gas sampler was inserted into the hole after removing the drill bit. Before each measurement, the foreign gas in the samplers and in the rubber tube connecting the samplers and detector was removed prior to signal counting. The concentration of Rn in the soil gas was measured using AlphaGuard PQ 2000 PRO (AG) Radon Detector and the Hg concentrations were analyzed with portable RA-915+ Zeeman Mercury Analyzer. The error of measurement was 2 ng $\times$ m^{-3}. The concentration of CO_2 in the soil gas was measured using KG-3010E Portable Infrared CO_2 Analyzer, and the concentration of H_2 in the soil gas was measured by ATG-300H Portable Hydrogen Gauge with a detection limit of 0.01–10,000 ppm. In addition, five gas samples were collected following the drainage gas collection method at the fault zone for helium isotope (^{3}He/^{4}He) analysis. The container used for helium isotope detection was a 100 mL saline glass bottle. After the measurement of soil gas concentration, the gas in the sampler, connecting pipe, and air pump was removed using an air pump. The sampling container was cleaned with saturated saltwater three times, and then the gas was collected. The instrument used

TABLE 1 | Catalog of earthquakes occurring in the area near Tiemenguan from January 1, 1970 to May 31, 2020.

Date	Time (UTC)	Long (°E)	Lat (°N)	Mag (M)	Date	Time (UTC)	Long (°E)	Lat (°N)	Mag (M)
2020/5/9	12:11:19	85.640°	42.234°	4.4	1998/4/13	23:14:32	85.796°	41.995°	4
2018/4/1	1:18:36	85.580°	42.256°	4.6	1988/5/25	18:21:58	85.692°	42.010°	5.2
2014/9/9	12:04:57	85.196°	42.319°	4.4	1981/4/21	3:22:52	85.816°	41.988°	4.4
2013/8/28	12:57:41	85.776°	42.076°	4.5	1980/6/14	13:01:13	85.523°	41.954°	4.7
2013/7/9	14:51:55	85.276°	42.210°	4.3	1978/4/22	15:04:15	85.920°	42.004°	5.3
2005/6/3	19:11:23	85.770°	41.983°	4.1	1977/6/5	18:19:29	85.714°	42.004°	4.7

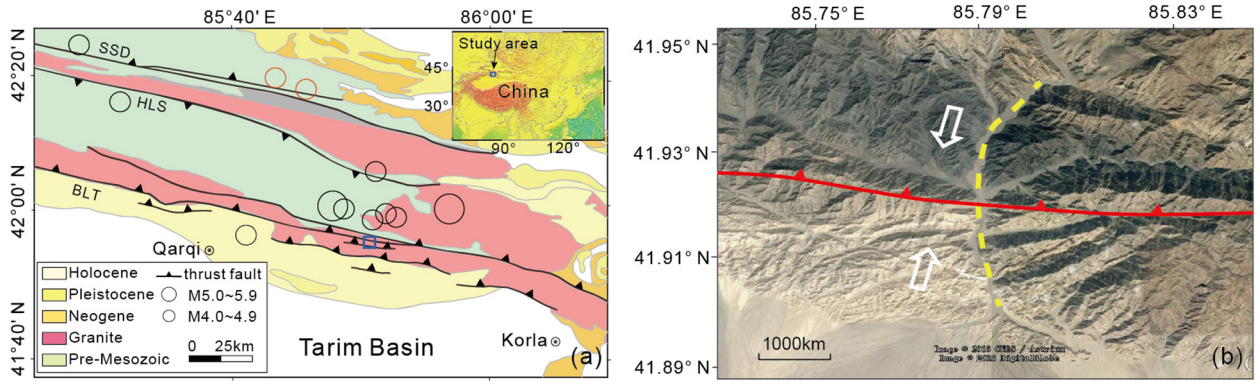

FIGURE 1 | Geologic structure map and seismic distribution of Tiemenguan section of BLT fault **(a)**, spatial distribution of soil gas survey lines **(b)**. The red circles indicate the earthquake that occurred after the measurement. SSD, Songshudaban fault; HLS, Huolashan fault; BLT, Beiluntai fault.

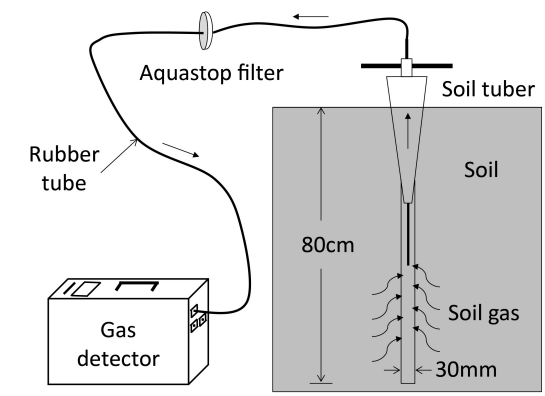

FIGURE 2 | Schematic diagram of soil gasses measurement.

was MM5400 mass spectrometer with a sensitivity greater than 1.5×10^{-6} a/PA. The gas samples were sent to the Lanzhou Center for Oil and Gas Resources Research, Institute of Geology and Geophysics, Chinese Academy of Sciences, immediately after the collection. Analysis of the samples was completed within 30 days of sampling.

Figure 3A shows that the measured values of Rn concentrations tended to stabilize after the second value of the initial measurement and there was a small amplitude of fluctuation. At each measurement time, 30 readings were taken and analyzed using the boxplot method, yielding a characteristic value of Rn concentration in each measurement site. The other three components, soil gas concentrations of CO_2, Hg, and H_2 were recorded based on the measurement time and their maximum values were taken. The concentration of soil gas CO_2 was relatively stable and the peaks were consistent with repeated measurements (**Figure 3B**). However, the concentrations of Hg and H_2 showed a gradual increase in the measured values and upon reaching the highest value, the concentrations tended to stabilize (**Figure 3C**) or rapidly decrease (**Figure 3D**).

RESULTS

In this study, soil gas measurements were obtained twice across the fault at Tiemenguan, the eastern segment of the BLT fault, Xinjiang. The results are shown in **Table 2**. During the first phase, the measurements of soil gas Rn and CO_2 concentrations were completed between April 20 and April 26, 2015. A total of 15 measuring points were identified from south to north. Measuring points 1–9 (P1–P9) were located at the footwall of the fault, and points 10 –15 (P10–P15) were located at the hanging wall of the fault. To determine whether there were similar changes in other gasses, we selected more measurement points at hanging wall (P13, P14, and P15), fault zone (P7, P8, and P10), and footwall (P2, P3, and P4) during the first phase from August 11–17, 2015, to conduct the second phase of soil gas measurements. The primary measurements recorded were the concentrations of Hg and H_2 in soil gas. As shown in **Figure 4**, due to the characteristics of H_2 (active) and Hg (adsorptive), such as the gas diffusion concentration that changes with time,

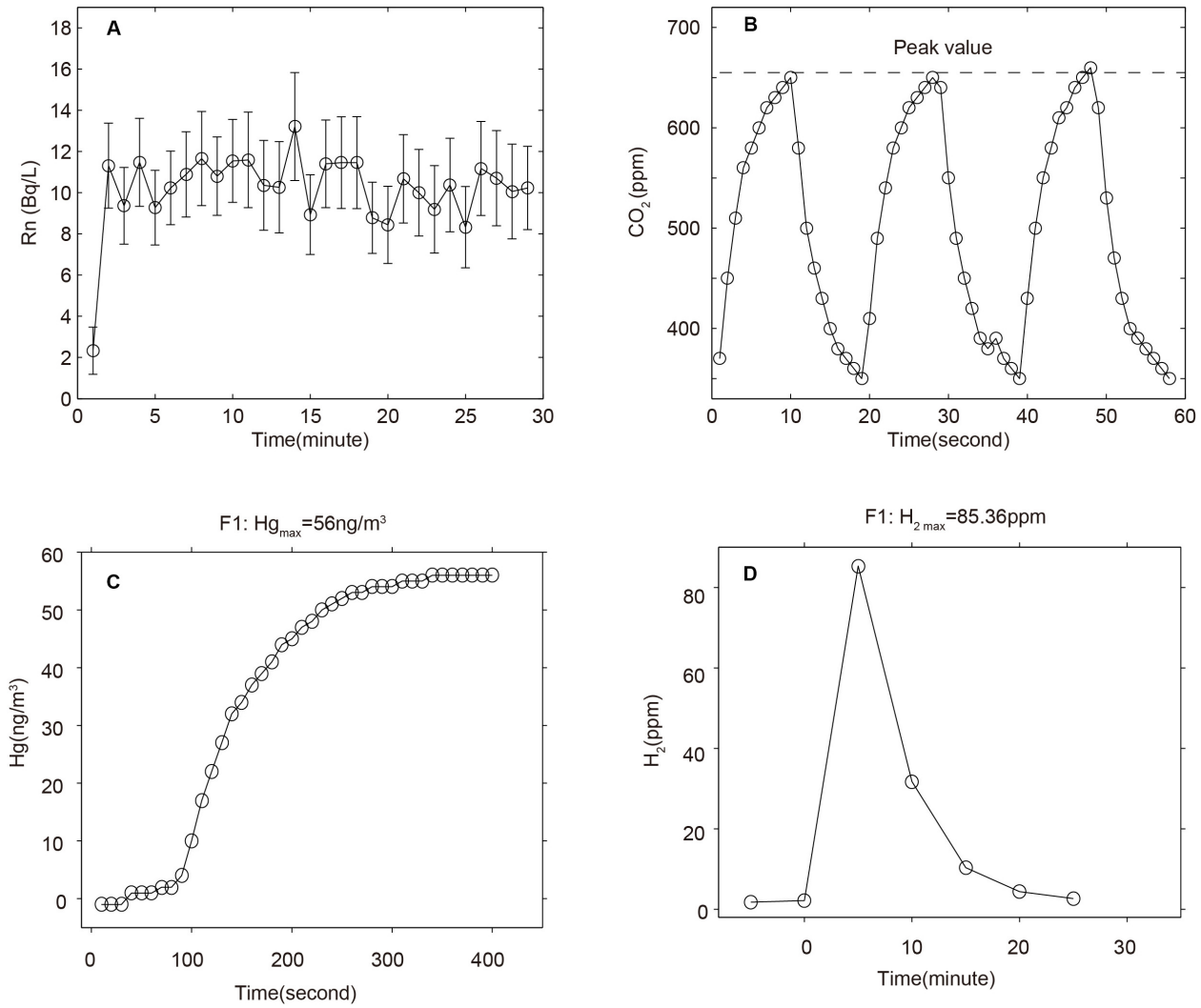

FIGURE 3 | The measurement curve of soil gas concentration in different components. The Rn concentration was determined according to the boxplot method to obtain the characteristics of Rn concentration at each site. A total of 30 measurements were acquired for each measurement point **(A)**. The other three components, soil gas concentration of CO_2, Hg and H_2 were recorded based on the measurement time, respectively. The peak of CO_2 concentration was the same after repeated measurements **(B)**, The Hg concentration value showed a steady change after rising to the highest value **(C)**, H_2 concentration characteristics showed a rapid decrease after rising to the highest value **(D)**. Therefore, the maximum value of the gas concentration curve of each component at sampling sites is analyzed.

the concentration of H_2 rapidly increased to the highest value and then decreased, while the concentration of Hg gradually increased to the highest value and then tended to stabilize. The maximum values of Hg and H_2 concentrations at each measuring point were obtained and the various characteristics of soil gas concentrations were analyzed.

As shown in **Figure 5E**, the terrain of the hanging wall of the fault is uplifted and that of the footwall is gentle. The survey line is vertical to the fault and extends approximately 2.5–3 km on both sides, with a total length of approximately 6 km. In addition, it should be noted that the study area is arid (i.e., precipitation and vegetation are not developed), with minimal soil moisture and stable temperature throughout the year, and the seasonal influence on soil gas concentrations is minimum in April and August.

The results show that in the footwall of the fault, the measured value of soil gas Rn concentration decreases toward the fault. It reaches the lowest value at the fault. However, in the hanging wall of the fault, the measured value increases toward the fault (**Figure 5A**). As shown in **Figure 5B**, the measured values of soil gas CO_2 concentration in the footwall of the fault (measuring points 1–9) are generally low, and the measured values decrease toward the exterior of the fault (measuring points 11 to 15). The concentrations of Rn and CO_2 are similar, and the measured values near the fault are high. The measured values gradually decrease with distance from the fault, and the concentration

TABLE 2 | Main statistic parameters of soil gas data in study area.

NO	Rn (Bq/L)	CO_2 (ppm)	Hg (ng/L)	H_2 (ppm)	$^3He/^4He$ R
P1	18.1686	520	–	–	–
P2	12.3266	910	59	85.36	–
P3	4.967	530	50	126.16	–
P4	10.1898	460	25	63.29	–
P5	4.1443	450	–	–	–
P6	2.3079	660	–	–	1.30×10^{-6}
P7	2.9054	470	10	37.04	1.21×10^{-6}
P8	7.6898	610	8	45.76	1.21×10^{-6}
P9	3.4503	480	–	–	1.38×10^{-6}
P10	17.6658	1510	7	48.64	1.23×10^{-6}
P11	13.6639	2110	–	–	–
P12	12.2356	1120	–	–	–
P13	8.2745	870	19	35.28	–
P14	8.2222	720	23	22.8	–
P15	6.883	360	16	47.84	–

measured in the hanging wall of the fault is higher than that in the footwall of the fault.

The Hg concentration of soil gas was the lowest near the fault (P7, P8, and P10) and was relatively high in the two walls of the fault. The concentrations in the footwall (P2–P4) were approximately twice as high as that in the hanging wall (P13–P15) (**Figure 5C**). The H_2 concentration of soil gas was higher in the footwall (P2–P4) and lower near the fault (P7, P8, and P10) and hanging wall (P13–P15) (**Figure 5D**).

In addition, helium isotope test results showed that the $^3He/^4He$ ratio ranges from 1.21×10^{-6} to 1.38×10^{-6}, which is lower than that of air (1.4×10^{-6}).

DISCUSSION

The measurement results show that the soil gas concentrations (Rn, CO_2, Hg, and H_2) in the Tiemenguan section in the BLT fault are different on either side of the fault zone. This may be closely related to the physical and chemical characteristics of the gas and its migration mechanism, the geological conditions of the measurement area, and the fracture development degree of the fracture zone.

Effect of Extent of Fracture Development on Soil Gas Concentration

The differences in soil gas concentrations are closely related to the distribution of fractures. The BLT fault is a thrust fault that is affected by the compressive force caused by regional tectonics. As shown in **Figure 1**, the bedrock type of BLT fault in the Tiemenguan section is primarily granite. Under regional tectonic compressive stress, a series of bending moment faults were formed in the hanging wall of the fault. Due to differences in the degrees of deformation in the hanging wall and footwall, their fractures exhibit different development degrees (**Figure 6**). As a result, the amount of deep gas escaping is different. In the hanging wall of the fault, under the regional tension stress environment, the surface at the top of the fault broke and formed a series of bending moment faults with many cracks. These bending moment faults are generally shallow fractures, allowing the gas in the soil to continuously escape to the atmosphere, which is not conducive to the enrichment of soil gas. On the other hand, the footwall topography, which is affected by compressive forces, is quite flat. The surface fractures are mainly closed or semi-closed, which is not suitable for the upward soil gas diffusion from the deep layers and its subsequent emission into the atmosphere. Thus, it is advantageous for the soil gas to be adsorbed on the particle surface of the rock. Then, it gradually accumulates in the soil. In the fault zone, the rock is highly fractured, and the fractures are further developed, which results in upward movement of the gas along the fracture.

Effect of Geological Conditions on Soil Gas Concentration

The spatial variation characteristics of soil gas concentration are not only related to the number of fractures on the fault, but also to the rock types and overburden properties. For

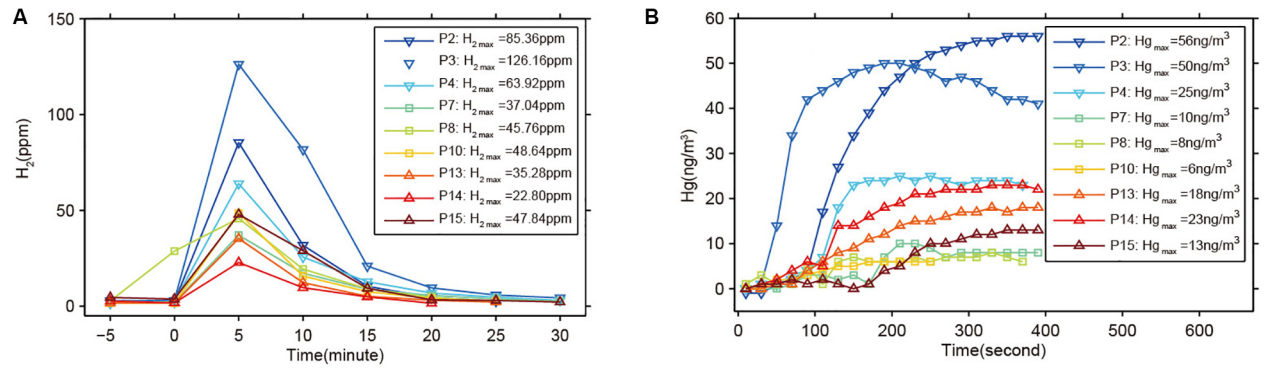

FIGURE 4 | Soil gas H_2 **(A)** and Hg **(B)** concentrations at nine sampling sites across the BLT fault zone at Tiemenguan. Different colors represent the variation cures of H_2 **(A)** and Hg **(B)** concentration of different measurement sites and the corresponding peaks.

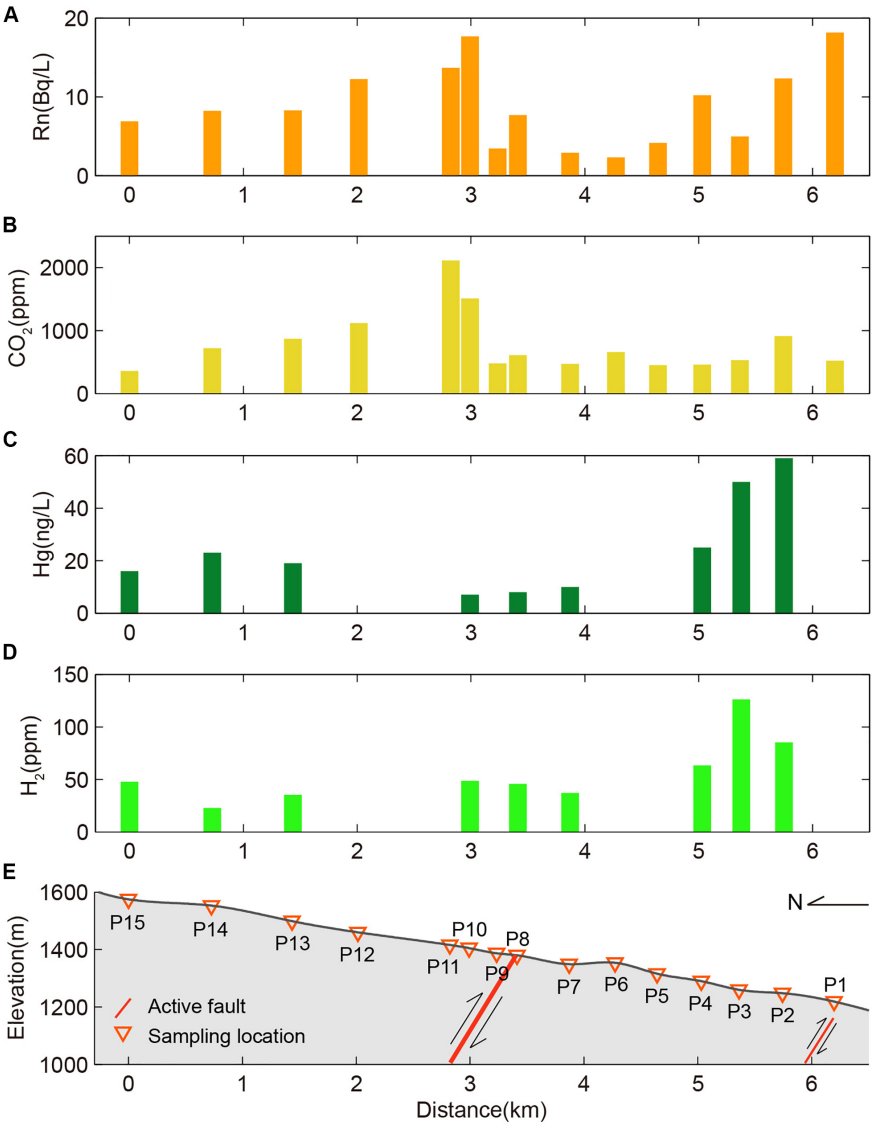

FIGURE 5 | Soil gas Concentrations of Rn **(A)**, CO_2 **(B)**, Hg **(C)**, and H2 **(D)** at Tiemenguan measuring point in BLT fault zone and distribution map of measuring points **(E)**. The north side is hanging wall, topographic uplift, south side is footwall, the terrain is gentle.

example, the surface sediments in the Tiemenguan section are primarily gravel and the rock types are mainly granite and limestone with high uranium and thorium content. This causes the soil gas Rn concentration in this section to be relatively high. Even if the rocks on either side of the fault are of the same type, different soil gas concentration characteristics will be formed if the overburden above the fault is different (Fu et al., 2005). As shown in **Figure 6**, there are differences in stratum type and overburden thickness between the two sides of the Tiemenguan fault. The hanging wall of the fault is covered with a thin layer of sandy soil; the fault is almost exposed to the surface, which results in the dilution of soil gas by air, and thus the soil gas concentration is low. The gravel layer in the footwall of the fault is comprised of weathered granite particles and medium coarse sand. The overburden layer is mainly sandy soil. It has strong gas sealing and adsorption properties. There are few channels available for the gas to escape and this results in a high gas concentration. This is reflected by the high concentrations of H_2 and Hg in the footwall of the fault.

Effects of Physical and Chemical Properties of Gasses

Hg is a heavy metal of great concern due to its extreme mobility and absorbability. Hg can be easily enriched in faults due to its special physical and chemical properties, and it can migrate from the interior to the surface along a fault or rock fracture due to fluid carrying or pressure gradient (Yangfen et al., 1989; Zhang et al., 2014; Sun et al., 2017a). H_2 is a relatively active

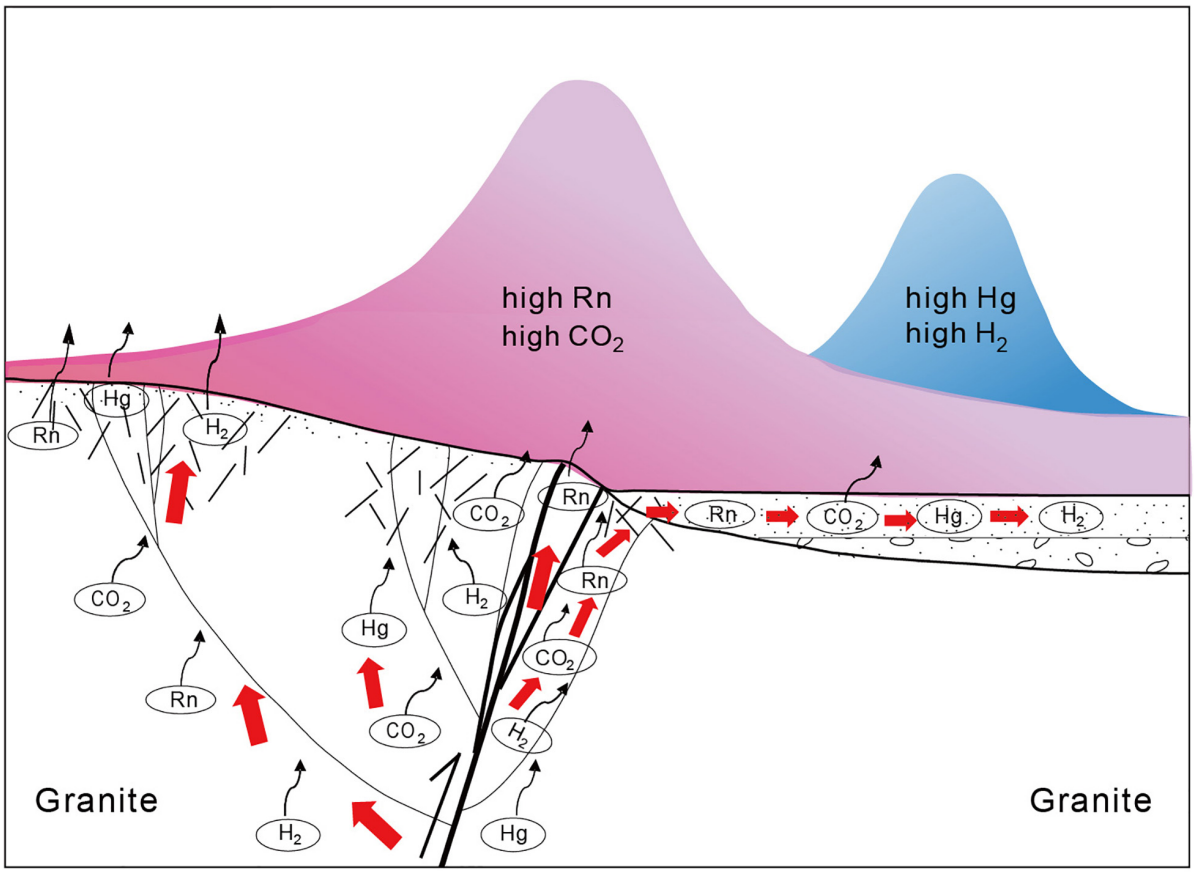

FIGURE 6 | Schematic diagram of thrust fault.

volatile substance and its diffusion speed is much higher than that of other gasses. It can easily migrate upward from the fault. The concentration of soil H_2 in the fault zone is closely related to the internal structure of the active fault and the development degree of fracture (Wakita et al., 1980). The sources of H_2 are as follows: microbial activity in shallow soil; deep water and abiogenic decomposition of CH_4 (King, 1986); and chemical reaction between fresh rock fracture surfaces and water (Sugisaki and Mizutani, 1983). CO_2 in the fault zone is usually a mixture of several source emissions. Surface biological activities or decomposition of organic matter may lead to increased CO_2 concentrations. However, active fault zones can directly produce a large amount of CO_2 and can also act as a channel to release deeply contained CO_2 (Ciotoli et al., 2007; Chiodini et al., 2008). Rn – a radioactive but chemically inert gas – is constantly generated all over the earth, normally in minute amount by radium in crustal materials (King et al., 1995). The short half-life of ^{222}Rn limits its diffusion in the soil; thus, the amount of radon measured at the ground surface cannot be released from a deep origin. Therefore, the concentration of Rn in soil gas is mainly affected by rocks containing radioactive elements U and Th. It also migrates from deep faults to the surface along with other carriers, such as CO_2, N_2, and CH_4 (Etiope and Martinelli, 2002; Yang et al., 2005; Chyi et al., 2010). The small carrier velocity can cause a large change in the concentration of the surface.

Changes in ^{3}He/^{4}He Isotope Ratio and Soil Gas Concentration

He is an inert gas with a small specific gravity and strong permeability. He in nature is mainly comes from the atmosphere, crust, and mantle. The helium in the atmosphere is mainly composed of ^{4}He, and the ^{3}He/^{4}He isotopic ratio is almost constant at 1.4×10^{-6}. The crust is dominated by radioactive atoms in rocks and minerals, such as radiogenic helium, with the ^{3}He/^{4}He value of 2.0×10^{-8} and the primary helium in the mantle, with the ^{3}He/^{4}He values ranging from 1.1×10^{-5} to 1.4×10^{-5}. R/Ra can represent the helium isotopic characteristics, where R is the ^{3}He/^{4}He ratio of the sample and Ra is the ^{3}He/^{4}He ratio of the atmosphere, i.e., 1.4×10^{-6}. When R/Ra <1, it represents the characteristic of shell source helium, while R/Ra > 1 represents the characteristic of mantle source helium. As shown in **Table 2**, the ^{3}He/^{4}He ratio of P6–P10 ranges from 1.21×10^{-6} to 1.38×10^{-6}. The calculation shows that R/Ra < 1 indicates that the helium in fault zone is formed from the crust; however, the ^{3}He/^{4}He ratio (1.21×10^{-6}–1.38×10^{-6}) at the fault zone is smaller than that in the

atmosphere (1.4×10^{-6}), which indicates that the helium from the crust has been diluted by atmospheric helium. The main causes of this effect are the U and Th contents in mineral rocks and the sealing characteristics of the system. The higher the content of U and Th in rocks, the more radioactive ^{4}He was that accumulated, and the sealing property of the system declined. The addition of helium outside the system changed the helium isotope ratio. The U and Th contents of the rocks are closely related to the Rn concentration, and the sealing property of the system is closely related to the ^{4}He. The addition of ^{4}He outside the system changes the helium isotope ratio. Therefore, the helium isotope results confirm the conjecture of this study.

Based on the above four aspects, we present the results of this paper. There may be two distinct reasons for the obvious difference in soil gas concentrations on either side of the fracture zone: one is the difference between the overburden layers and the other may be related to the fracture distribution in the fracture zone and its vicinity. As shown in **Figure 6**, the strain across the thrust faults is contractional. It causes the hanging wall to be highly deformed near the fault at the surface, resulting in local bending and extensional fractures that facilitate the upward escape of soil gas. It is not conducive to the enrichment of gas in shallow soil. Conversely, the surface fractures in the footwall are mostly closed, which is not suitable for the release of soil gas into the atmosphere, thus leading to the accumulation of gas in shallow soil. Therefore, the greater development of fractures in the hanging wall provides a good channel for gas escape, and the deep gas carriers, such as CO_2, can carry more Rn to the shallow surface and escape to the atmosphere. In the footwall, because there are fewer fractures, Rn in the deep soil layers cannot escape to the surface because of the short half-life period of 3.82 days and low migration rate; however, Hg and H_2 can reach the surface. Moreover, it is easy to enrich the surface of soil particles on the shallow surface with fewer fractures. In comparison, there are relatively high concentrations of Rn and CO_2 in the hanging wall (channel effect) and Hg and H_2 in the footwall (enrichment).

CONCLUSION

We obtained measurements of soil gas Rn, Hg, H_2, and CO_2 concentrations from the eastern section of the Beiluntai fault zone in the southern Tianshan Mountains, Xinjiang, China. The geochemical distribution characteristics of the soil gas along the eastern section of the Beiluntai fault were obtained and the possible reasons for the difference in concentrations of soil gas components in the fault were discussed. The following conclusions were drawn:

1. The concentration of the soil gas in the eastern segment of the Beiluntai fault zone in the southern Tianshan Mountains of Xinjiang showed a significant difference on either side of the fault. The concentration of Rn and CO_2 was higher on the hanging wall of the fault zone and the concentration of Hg and H_2 was higher on the footwall of the fault zone.
2. The soil gas Rn, Hg, H_2, and CO_2 concentrations of the fault zone are closely related to the physical and chemical characteristics, geological structure, and fracture distribution of the fault zone.

DATA AVAILABILITY STATEMENT

The raw data supporting the conclusions of this article will be made available by the authors, without undue reservation, to any qualified researcher.

AUTHOR CONTRIBUTIONS

YX and XS wrote the manuscript. All the authors participated in field measurements.

FUNDING

This research was supported by the research grants (ZDJ2019-06 and ZDJ2017-27) from National Institute of Natural Hazards, MEMC (former Institute of Crustal Dynamics, China Earthquake Administration) and National Natural Science Foundation of China (41972253).

REFERENCES

Baubron, J. C., Rigo, A., and Toutain, J. P. (2002). Soil gas profiles as a tool to characterise active tectonic areas: the Jaut Pass example (Pyrenees, France). *Earth Planet. Sci. Lett.* 196, 69–81. doi: 10.1016/s0012-821x(01)00596-9

Buttitta, D., Caracausi, A., Chiaraluce, L., Favara, R., and Sulli, A. (2020). Continental degassing of helium in an active tectonic setting (northern italy): the role of seismicity. *Sci. Rep.* 10:162.

Camarda, M., De Gregorio, S., Di Martino, R. M. R., and Favara, R. (2016). Temporal and spatial correlations between soil CO_2 flux and crustal stress. *J. Geophys. Res. Solid Earth* 121, 7071–7085. doi: 10.1002/2016jb013297

Caracausi, A., and Paternoster, M. (2015). Radiogenic helium degassing and rock fracturing: a case study of the southern Apennines active tectonic region. *J. Geophys. Res. Solid Earth* 120, 2200–2211. doi: 10.1002/2014jb011462

Chiodini, G., Caliro, S., Cardellini, C., Avino, R., Granieri, D., and Schmidt, A. (2008). Carbon isotopic composition of soil CO_2 efflux, a powerful method to discriminate different sources feeding soil CO_2 degassing in volcanic-hydrothermal areas. *Earth Planet. Scie. Lett.* 274, 372–379. doi: 10.1016/j.epsl.2008.07.051

Chyi, L. L., Quick, T. J., Yang, F. T., and Chen, C. H. (2005). Soil gas radon spectra and earthquakes. *Terrest., Atmosph. Oceanic Sci.* 16, 763–774. doi: 10.3319/TAO.2005.16.4.763(GIG)

Chyi, L. L., Quick, T. J., Yang, T. F., and Chen, C. H. (2010). The experimental investigation of soil gas radon migration mechanisms and its implication in earthquake forecast. *Geofluids* 10, 556–563. doi: 10.1111/j.1468-8123.2010.00308.x

Ciotoli, G., Lombardi, S., and Annunziatellis, A. (2007). Geostatistical analysis of soil gas data in a high seismic intermontane basin: fucino Plain central Italy. *J. Geophys. Res.* 112:B05407.

Engle, M. A., Gustin, M. S., and Zhang, H. (2001). Quantifying natural source mercury emissions from the Ivanhoe Mining District, north-central Nevada,USA. *Atmos. Environ.* 35, 3987–3997. doi: 10.1016/s1352-2310(01)00184-4

Etiope, G., and Martinelli, G. (2002). Migration of carrier and trace gases in the geosphere: an overview. *Phys. Earth Planet. Interiors* 129, 185–204. doi: 10.1016/s0031-9201(01)00292-8

Etiope, G., Martinelli, G., Caracausi, A., and Italiano, F. (2007). Methane seeps and mud volcanoes in Italy: gas origin, fractionation and emission to the atmosphere. *Geophys. Res. Lett.* 34:L14303.

Fu, C. C., Yang, T. F., Du, J., Walia, V., Chen, Y. G., Liu, T. K., et al. (2008). Variations of helium and radon concentrations in soil gases from an active fault zone in southern Taiwan. *Radiat. Measur.* 43, S348–S352.

Fu, C. C., Yang, T. F., Tsai, M. C., Lee, L. C., Liu, T. K., Walia, V., et al. (2017). Exploring the relationship between soil degassing and seismic activity by continuous radon monitoring in the Longitudinal Valley of eastern Taiwan. *Chem. Geol.* 469, 163–175. doi: 10.1016/j.chemgeo.2016.12.042

Fu, C. C., Yang, T. F., Walia, V., and Chen, C. H. (2005). Reconnaissance of soil gas composition over the buried fault and fracture zone in Southern Taiwan. *Geochem. J.* 39, 427–439. doi: 10.2343/geochemj.39.427

Giammanco, S., Immè, G., Mangano, G., Morelli, D., and Neri, M. (2009). Comparison between different methodologies for detecting radon in soil along an active fault: the case of the Pernicana fault system, Mt. Etna (Italy). *Appl. Radiat. Isot.* 67, 178–185. doi: 10.1016/j.apradiso.2008.09.007

Iovine, G., Guagliardi, I., Bruno, C., Greco, R., Tallarico, A., Falcone, G., et al. (2017). Soil-gas radon anomalies in three study areas of Central-Northern Calabria, (Southern Italy). *Nat. Hazards* 91, 193–219.

Jones, L. C., Rosenbauer, R., Goldsmith, J. I., and Oze, C. (2010). Carbonate control of H2 and CH4 production in serpentinization systems at elevated P-Ts. *Geophys. Res. Lett.* 37, 381–389.

King, C. Y. (1980). Episodic radon changes in subsurface soil gas along active faults and possible relation to earthquakes. *J. Geophys. Res. Solid Earth* 85, 3065–3078. doi: 10.1029/jb085ib06p03065

King, C. Y. (1986). Gas geochemistry applied to earthquake prediction: an overview. *J. Geophys. Res. Solid Earth* 91, 12269–12281. doi: 10.1029/jb091ib12p12269

King, C. Y., King, B. S., Evans, W. C., and Zhang, W. (1996). Spatial radon anomalies on active faults in California. *Appl. Geochem.* 11, 497–510. doi: 10.1016/0883-2927(96)00003-0

King, C. Y., Koizumi, N., and Kitagawa, Y. (1995). Hydrogeochemical anomalies and the 1995 Kobe earthquake. *Science* 269, 38–40. doi: 10.1126/science.269.5220.38

Li, Y., Du, J. G., Wang, X., Zhou, X. C., Xie, C., and Cui, Y. J. (2013). Spatial variations of soil gas geochemistry in the tangshan Area of Northern China. *Terrestr. Atmos. Ocean. Sci.* 24, 323–332. doi: 10.3319/tao.2012.11.26.01(tt)

Li, Y. G., Chen, P., Cochran, E. S., Vidale, J. E., and Burdette, T. (2006). Seismic evidence for rock damage and healing on the San Andreas Fault associated with the 2004 M6.0 *Parkfield earthquake*. *Bull. Seismol. Soc. Am.* 96, S349–S363.

Mazur, D., Janik, M., Łoskiewicz, J., Olko, P., and Swakoń, J. (1999). Measurements of radon concentration in soil gas by CR-39 detectors. *Radiat. Measur.* 31, 295–300. doi: 10.1016/s1350-4487(99)00135-3

Moore, C. W., and Castro, M. S. (2012). Investigation of factors affecting gaseous mercury concentrations in soils. *Sci. Total Environ.* 419, 136–143. doi: 10.1016/j.scitotenv.2011.12.068

Morawska, L., and Phillips, C. R. (1993). Dependence of the radon emanation coefficient on radium distribution and internal structure of the material. *Geochim. Cosmochim. Acta* 57, 1783–1797. doi: 10.1016/0016-7037(93)90113-b

Pulinets, S. A., and Dunajecka, M. A. (2007). Specific variations of air temperature and relative humidity around the time of Michoacan earthquake M8.1 Sept. 19,1985 as a possible indicator of interaction between tectonic plates. *Tectonophysics* 431, 221–230. doi: 10.1016/j.tecto.2006.05.044

Sano, Y., Takahata, N., Kagoshima, T., Shibata, T., Onoue, T., and Zhao, D. (2016). Groundwater helium anomaly reflects strain change during the 2016 Kumamoto earthquake in Southwest Japan. *Sci. Rep.* 6:37939.

Sciarra, A., Cantucci, B., and Coltorti, M. (2017). Learning from soil gas change and isotopic signatures during 2012 Emilia seismic sequence. *Sci. Rep.* 7:14187.

Sugisaki, R., Ito, T., Nagamine, K., and Kawabe, I. (1996). Gas geochemical changes at mineral springs associated with the 1995 southern Hyogo earthquake *(M* = 7.2) Japan. *Earth Planet. Sci. Lett.* 139, 239–249. doi: 10.1016/0012-821x(96)00007-6

Sugisaki, R., and Mizutani, Y. (1983). Origin of hydrogen and carbon dioxide in fault gases and its relation to fault activity. *J. Geol.* 91, 239–258. doi: 10.1086/628769

Sun, X., Si, X., Xiang, Y., and Liu, D. (2017a). Soil mercury spatial variations in the fault zone and corresponding influence factors. *Terrstr. Atmos. Ocean. Sci.* 28, 283–294. doi: 10.3319/tao.2016.09.29.02

Sun, X., Yang, P., Xiang, Y., Si, X., and Liu, D. (2017b). Across-fault distributions of radon concentrations in soil gas for different tectonic environments. *Geosci. J.* 22, 227–239. doi: 10.1007/s12303-017-0028-2

Wakita, H., Nakamura, Y., Kita, I., Fujii, N., and Notsu, K. (1980). Hydrogen release: new indicator of fault activity. *Science* 210, 188–190. doi: 10.1126/science.210.4466.188

Walia, V., Yang, T. F., Hong, W. L., Lin, S. J., Fu, C. C., Wen, K. L., et al. (2009). Geochemical variation of soil–gas composition for fault trace and earthquake precursory studies along the Hsincheng fault in NW Taiwan. *Appl. Radiat. Isot.* 67, 1855–1863. doi: 10.1016/j.apradiso.2009.07.004

Ware, R. H., Roecken, C., and Wyss, M. (1984). The detection and interpretation of hydrogen in fault gases. *Pure Appl. Geophys.* 122, 392–402. doi: 10.1007/bf00874607

Wiersberg, T., and Erzinger, J. (2008). Origin and spatial distribution of gas at seismogenic depths of the San Andreas fault from drill-mud gas analysis. *Appl. Geochem.* 23, 1675–1690. doi: 10.1016/j.apgeochem.2008.01.012

Yang, T. F., Walia, V., Chyi, L. L., Fu, C. C., Chen, C. H., Liu, T. K., et al. (2005). Variations of soil radon and thoron concentrations in a fault zone and prospective earthquakes in SW Taiwan. *Radiat. Measur.* 40, 496–502. doi: 10.1016/j.radmeas.2005.05.017

Yangfen, J., Zonghua, W., Chunsheng, S., Jiazhen, W., and Hongren, Z. (1989). Earthquake prediction through the observation and measurement of mercury content variation in water. *J. Geochem. Explorat.* 33, 195–202. doi: 10.1016/0375-6742(89)90029-0

Yao, Y., Song, H. P., Chen, J. B., Li, S., and Jia, H. L. (2018). Late quaternary crustal shortening rate of the Beiluntai fault in southern. *Seismol. Geol.* 40, 71–86.

Yuce, G., Fu, C. C., D'Alessandro, W., Gulbay, A. H., Lai, C. W., Bellomo, S., et al. (2017). Geochemical characteristics of soil radon and carbon dioxide within the Dead Sea fault and Karasu fault in the Amik basin, (Hatay), Turkey. *Chem. Geol.* 469, 129–146. doi: 10.1016/j.chemgeo.2017.01.003

Zhang, L., Liu, Y., Guo, L., Yang, D., Fang, Z., Chen, T., et al. (2014). Isotope geochemistry of mercury and its relation to earthquake in the Wenchuan Earthquake Fault Scientific drilling project hole-1. (WFSD-1). *Tectonophysics* 619–620, 79–85. doi: 10.1016/j.tecto.2013.08.025

Zhou, X., Wang, W., Chen, Z., Yi, L., Liu, L., Xie, C., et al. (2015). Hot spring gas geochemistry in western sichuan province, China after the wenchuan ms 8.0 earthquake. *Terr. Atmos. Ocean. Sci.* 26, 361–373. doi: 10.3319/tao.2015.01.05.01(tt)

Zhou, X. C., Du, J. G., Chen, Z., Cheng, J. W., Tang, Y., Yang, L. M., et al. (2010). Geochemistry of soil gas in the seismic fault zone produced by the Wenchuan Ms = 8.0 earthquake, southwestern China. *Geochem. Trans.* 11:5.

Conflict of Interest: The authors declare that the research was conducted in the absence of any commercial or financial relationships that could be construed as a potential conflict of interest.

Copyright © 2020 Xiang, Sun, Liu, Yan, Wang and Gao. This is an open-access article distributed under the terms of the Creative Commons Attribution License (CC BY). The use, distribution or reproduction in other forums is permitted, provided the original author(s) and the copyright owner(s) are credited and that the original publication in this journal is cited, in accordance with accepted academic practice. No use, distribution or reproduction is permitted which does not comply with these terms.

frontiers in Earth Science

ORIGINAL RESEARCH
published: 09 September 2020
doi: 10.3389/feart.2020.571700

Revealing Short-Term Precursors of the Strong $M > 7$ Earthquakes in Southern California From the Simulated Stress–Strain State Patterns Exploiting Geomechanical Model and Seismic Catalog Data

*Valery G. Bondur, Mikhail B. Gokhberg, Igor A. Garagash and Dmitry A. Alekseev**

Institute for Scientific Research of Aerospace Monitoring "AEROCOSMOS", Moscow, Russia

OPEN ACCESS

Edited by:
Giovanni Martinelli, National Institute of Geophysics and Volcanology, Italy

Reviewed by:
Marcello Viti, University of Siena, Italy
Ming-Ching T. Kuo, National Cheng Kung University, Taiwan

***Correspondence:**
Dmitry A. Alekseev
alexeevgeo@gmail.com

Specialty section:
This article was submitted to Solid Earth Geophysics, a section of the journal Frontiers in Earth Science

Received: *11 June 2020*
Accepted: *18 August 2020*
Published: *09 September 2020*

Citation:
Bondur VG, Gokhberg MB, Garagash IA and Alekseev DA (2020) Revealing Short-Term Precursors of the Strong M > 7 Earthquakes in Southern California From the Simulated Stress–Strain State Patterns Exploiting Geomechanical Model and Seismic Catalog Data. Front. Earth Sci. 8:571700. doi: 10.3389/feart.2020.571700

Since 2009, the stress–strain state (SS) of the earth's crust in Southern California region is being monitored through geomechanical modeling, taking into account the ongoing seismicity with magnitudes $M > 1$. Every new earthquake is assumed to cause a new defect in the earth's crust, leading to redistribution in the SS. With half-monthly SS updates, we found that the two strong earthquakes with $M \sim 7$ that occurred in the area in 2010 and 2019 had been preceded by anomalies in the strength parameter D (indicating how close the rock is to its ultimate strength), which had emerged a few weeks to months before the main shock at a distance of 10–30 km from the future epicenter. Over the course of monitoring (nearly a decade), this approach has neither produced false alarms nor missed events with $M > 7$ falling within the modeling area.

Keywords: geomechanical modeling, earth's crust, stress–strain state, seismic risk, earthquakes, precursors, monitoring, South California

INTRODUCTION

The development of seismic hazard monitoring and prediction methods is crucial for preventing and mitigating the fatalities and damage caused by strong earthquakes. The primary focus of research in this field is linked to identification of precursors, preceding high-energy seismic events (Mogi, 1985; Sobolev and Ponomarev, 2003; Viti et al., 2003; Molchan and Keilis-Borok, 2008; Paresan et al., 2015; Bondur et al., 2018; Rundle et al., 2018 and references therein). Some precursors may be recognized from the anomalous behavior of various geophysical fields, including ones rendered by the dynamics of lineament systems (Bondur and Zverev, 2005; Paresan et al., 2015), variations of the ionosphere parameters (Liu et al., 2004; Bondur and Smirnov, 2005; Bondur et al., 2007; Singh et al., 2009), and other phenomena exhibiting increased activity before earthquakes. It is understood that the most effective approach for predicting significant seismic events is a joint comprehensive analysis of precursors of various physical nature recorded by ground-based and space instrumentation systems (Cenni et al., 2015 and references therein). However, an extreme complexity of the coupled processes and interaction mechanisms relating the subsurface mechanics during the stress accumulation (earthquake preparation) stage to potentially observable (geophysical) precursors makes the forecast a highly challenging goal, with relatively few examples of successful prediction.

The solid foundation of earthquake prediction would be the stress–strain state (SS) analysis, allowing for the identification of areas of elevated seismic risk employing regional-scale geomechanical models (Bondur et al., 2007; Bondur et al., 2010; Bondur et al., 2016). Making such models relevant requires reliable seismological data. Among the territories with elevated seismic risk, Southern California is one of the most studied in terms of tectonics, with high-quality seismic catalog data available.

The southern part of the US Pacific coast, in particular the state of California, as well as the adjacent territories of Mexico, is characterized by a significant level of seismic activity caused by the interaction of the Pacific and North American lithospheric plates, having the boundary along the San Andreas Fault (Wallace, 1990) (**Figures 1** and **2**). Given the high-density population of the area and the existing risk of strong and catastrophic seismic events, considerable attention has been paid for many decades to seismic monitoring and earthquake forecast in the region (Hutton et al., 2010). A seismological network deployed in Southern California (Clayton et al., 2015) provides a stream of high-resolution data, being processed, cataloged, and published by a number of specialized seismological centers and the US Geological Survey (USGS) nearly in real time (https://earthquake.usgs.gov/data/comcat/).

The main efforts of researchers aimed at short-term and medium-term earthquake forecast are related to statistical analysis of seismological datasets, resulting in probability estimates of seismic risk (Field et al., 2009; Field and Members of the 2014 WGCEP, 2015; Field et al., 2015; Ross et al., 2019). Although the models used in such an approach may incorporate data for the fault-block structure of the region, these do not provide a detailed image of elastic energy accumulation and redistribution in the subsurface. Another approach deals with local models of soil motion around the epicentral region, as derived from the earthquake focus mechanism post-quake data (Brandenberg et al., 2020).

At the same time, it is obvious that the physical basis for seismic risk assessment and forecast on a regional scale should exploit geomechanical models that take into account the structure, its heterogeneity, and current tectonic stresses (Turcotte, 1994). Some elements of this approach applied to Southern California have been discussed in Gomberg (1991), Williams and Richardson (1991), and Toda and Stein (2019). For identification of seismically hazardous zones, a joint analysis of the strength, stress state, and elastic energy distribution in the earth's crust has been proposed (Garagash, 1991; Bondur et al., 2007).

To monitor the SS dynamics in relation to strong earthquakes in Southern California, back in 2009 we launched a numerical simulation study, employing both geomechanical modeling and actual seismological data (Bondur et al., 2010; Bondur et al., 2016; Bondur et al., 2017; Bondur et al., 2020). In our model, every new earthquake is treated as a new crustal defect, causing the stress–state redistribution and variation over time. By successive calculation of various SS attributes, the model makes it possible to trace the destruction and healing of the earth's crust, reveal the patterns of elastic energy accumulation and relaxation, and ultimately identify the seismic precursors through imaging of elevated stress regions prior to strong ($M > 7$) shocks occurring in this territory.

In this article, we illustrate the application of this approach to particular seismic events of 2010 and 2019, being the strongest shocks in the region with M exceeding 7.

MATERIALS AND METHODS

The results presented in this study have been obtained with a geomechanical modeling-based monitoring technique (Bondur et al., 2010; Bondur et al., 2016; Bondur et al., 2017; Bondur et al., 2020), allowing one to image and trace the SS evolution over the Southern California region during the period from 2009 to 2019, with the identification of SS precursor patterns preceding strong ($M > 7$) seismic events. At the core of this technique lies a three-dimensional (3D) geomechanical model simulating the crustal rock deformation within the latitudes between 31 and 36°N and longitudes between 114 and 121.2°W assuming the Mohr–Coulomb yield criterion.

The modeling domain with lateral dimensions of 645 km × 560 km is discretized by a 5-km × 5-km rectangular mesh. The earth's crust and lithosphere are represented by a 6-layer structure within 0–35 km depth; the model includes the surface topography and crustal layers' boundaries with realistic geometry specified according to available geological data. Each layer was assigned the specific values of Mohr–Coulomb model parameters, namely, the bulk modulus K, shear modulus G, cohesion c, and angle of internal friction φ (**Table 1**). The fault-block tectonics of a region was incorporated into the model using lineament analysis data by introducing a so-called crustal damage function $g(x, y, z)$ that is applied to reduce the values of certain mechanical properties (elastic moduli, cohesion, and friction) in the corresponding mesh cells, for imitation of distracted portions of the crust associated with fault zones in any given layer, as

$$P(x, y) = P_0\left(1 - \kappa\, g(x, y)\right), \tag{1}$$

where P_0 is the constant initial value of the model property for the intact rock and κ is the small term (see **Figure 2** and model properties maps in **Figures 3** and **4**). Damage function $g(x, y)$ represents the normalized spatial distribution of a dimensionless parameter (with values between 0 and 1), produced from fault maps, surface topography/bathymetry, and satellite imagery data (Bondur et al., 2010). At the earth's surface, the degree of crustal destruction is assumed to be equal to 1 on the fault axis and 0 outside the zone of its influence, while in between it is approximated by the 2D spline function. Initially, the map of the damage function was constructed for the upper layer (L1) only, and then the damage distributions were calculated sequentially for deeper layers through the smoothing of the maps for upper ones, with the smoothing window size increasing with depth, forming a volumetric array $g(x, y, z)$.

At the initial stage, the "stationary" stress state of the model, $\mathrm{SS}(x, y, z, t_0)$, is calculated under gravity load and the effect of regional tectonic forces assuming static approximation. Modeling

TABLE 1 | Values of the material properties (Mohr–Coulomb model parameters) assumed for six laterally homogenous model layers at the initial stage of model construction, followed by application of "damage function" to produce heterogeneous property patterns (see **Figures 3** and **4**).

Model layer (element)	Bulk modulus (GPa)	Shear modulus (GPa)	Angle of internal friction (°)	Cohesion (MPa)	Density (kg/m^3)
L1 upper crust	17.3	8	26	20	2,600
L2 upper crust	19.5	9	30	35	2,700
L3 middle crust	16.2	7.5	27	32	2,700
L4 middle crust	14.5	6.7	25	29	2,800
L5 middle crust	11.9	5.5	24	26	2,800
L6 lower crust	18.4	8.5	27	30	2,800

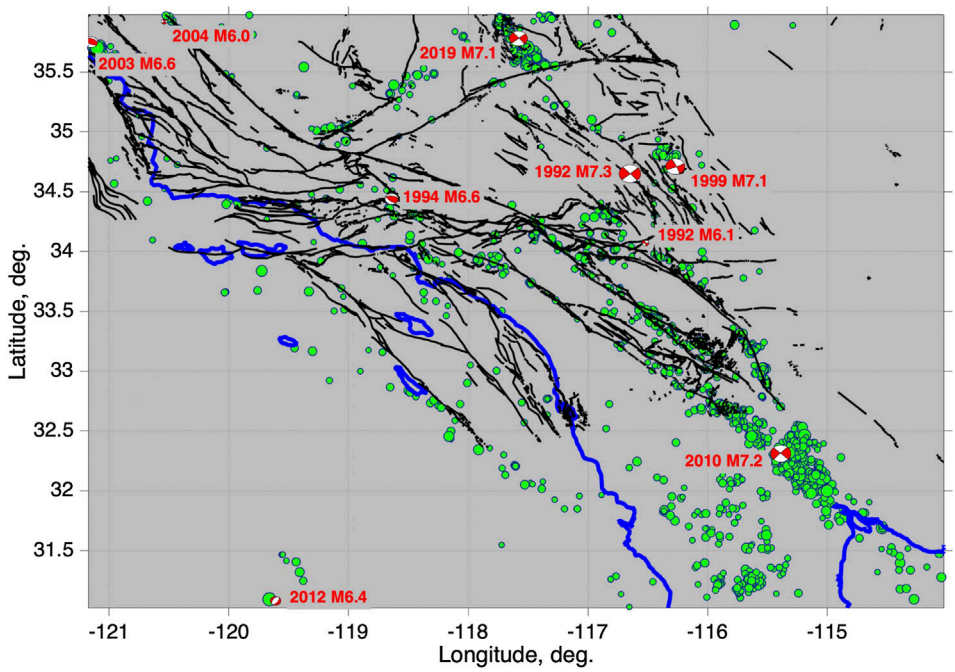

FIGURE 1 | Fault tectonics (black lines, USGS database) and seismicity (green circles, ComCat database) in the study area. Beach balls and red text labels indicate earthquake mechanisms, year, and magnitude of major shocks during the time interval from 1990 to 2020.

is performed using FLAC3D software code (Itasca Consulting Group, 2006), solving the continuum mechanics equations with the explicit finite-difference method.

The stationary (or initial) state modeled as described above reflects the initial damage corresponding to fault-block tectonics; however, at this stage, the current seismic activity is ignored (see **Figure 5**).

The left column in **Figure 5** presents the layered diagram of the Lode–Nadai coefficient, allowing one to classify the resulting stress distribution in terms of stress regime. This quantity is defined by the second and the third invariants of the stress tensors' deviatoric part, and falls between −1 and +1. It equals −1 under pure tension and 1 under pure compression, while zero value is associated with pure shear.

The right-hand-side layered diagram in **Figure 5** illustrates shear strain energy maps. Both quantities show elevated inhomogeneity in the upper layers compared to the lower ones and indicate complex overall patterns, defined by the interaction of Pacific and North American plates, complex geometry of crustal boundaries, and mosaic structure associated with fault tectonics in the study area.

The next (main) stage of calculation uses an iterative procedure to update the current state of the model:

$$\mathrm{SS}(x, y, z, t_0) \rightarrow \cdots \rightarrow \mathrm{SS}(x, y, z, t_i) \rightarrow \mathrm{SS}(x, y, z, t_{i+1}) \quad (2)$$

This is achieved through subsequent update of the model geomechanical parameters, such as the bulk and shear moduli, cohesion, and friction angle, of those mesh elements which had been affected by seismic events during a 3-month time interval preceding the time point of the calculation. To achieve this, the foci locations taken from the seismic catalog are projected onto the model grid, and the released energy values E are estimated from the magnitude data M as

$$\lg E = 4 + 1.8M \quad (3)$$

To evaluate the cumulative energy accommodated in each cell, the energies of all earthquakes falling within this cell are summed up over the 3-month period (about 4,000 individual shocks in

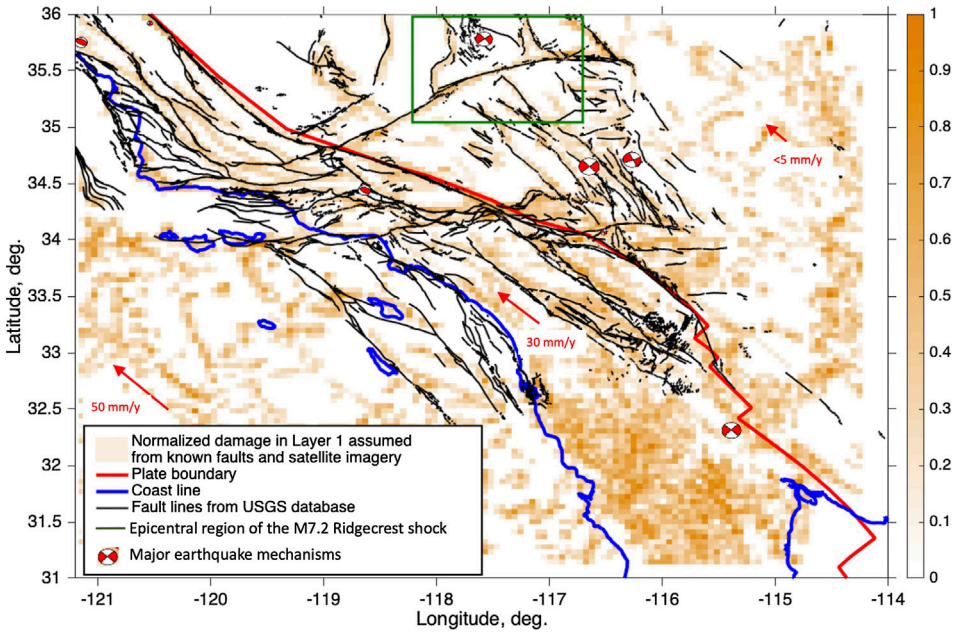

FIGURE 2 | Fault tectonics and crustal destruction pattern (damage function) for the upper model layer. Red arrows show characteristic GPS-measured plate velocities in different parts of the study area.

average). Then, the smoothing is applied to the resulting energy distributions $e(x, y, z, t_i)$, and the SS obtained at the previous iteration is used to calculate the updated damage function:

$$g(x, y, z, t_{i+1}) = f_{\mathrm{DM}}\left(\mathrm{SS}(x, y, z, t_i),\ e(x, y, z, t_{i+1})\right) \tag{4}$$

f_{DM} has the meaning of a transform converting energy array E at the current step into the updated damage function $g_{i+1} = g(x, y, z, t_{i+1})$. This is done with some algebra involving elements σ_{ij} of the stress tensor at the ith step. From those, the maximum shear stress is calculated:

$$\tau_{\max}(x, y, z, t_i) = \sqrt{\frac{1}{6}\left[\left(\sigma_{xx} - \sigma_{yy}\right)^2 + \left(\sigma_{yy} - \sigma_{zz}\right)^2 + \left(\sigma_{zz} - \sigma_{xx}\right)^2\right] + \sigma_{xy}^2 + \sigma_{yz}^2 + \sigma_{zx}^2}, \tag{5}$$

and then, shear energy E_S and updated damage function g are evaluated based on the previous-step SS and current seismic energy distribution E:

$$E_S(x, y, z, t_i) = \frac{\tau_{\max}^2}{G} \tag{6}$$

$$g(x, y, z, t_{i+1}) = \frac{E(x, y, z, t_{i+1})}{E(x, y, z, t_{i+1}) + E_s(x, y, z, t_i)} \tag{7}$$

In turn, g is applied to update the model parameters:

$$P(x, y, z, t_{i+1}) = f_{\mathrm{MD}}\left(P(x, y, z, t_i), g(x, y, z, t_{i+1})\right). \tag{8}$$

Specifically,

$$P_{i+1} = (P_i - \Delta P_i \cdot r)(1 - \kappa \cdot g_{i+1}). \tag{9}$$

Here, P stands for any model property (bulk modulus K, shear modulus G, cohesion, or angle of friction φ); $\Delta P_i = P_i - P_{i-1}$ indicates the damage-associated increment added to each property value at the previous step, while $\boldsymbol{r}$ =1/8 is the recovery factor applied to account for "rock healing" by 1/8 of every 2 weeks (which means if no new earthquakes occur within a particular mesh element, its properties' values return back to original values within 4 months), $\kappa = 0.3$ is a small factor, and $g_{i+1} = g(x, y, z, t_{i+1})$ is the normalized damage function given by Eq. 7.

Finally, the new SS is computed from the corrected model:

$$\mathrm{SS}(x, y, z, t_{i+1}) = f_{\mathrm{SS}}(P(x, y, z, t_{i+1})). \tag{10}$$

Unlike the above transforms, f_{SS} is essentially a numerical solution to the equation of motion obtained with the FLAC^{3D} program code returning the full set of elements of the stress and strain tensors.

Thus, running the model implies serial evaluation of f_{DM}, f_{MD}, and f_{SS} transforms, yielding the updated datasets at each time step, that is, repeated half-monthly:

$$t_{i+1} - t_i = 15 \text{ days}. \tag{11}$$

Once a new SS at the $(i + 1)$th step is calculated, the incremental part of the stresses is used to evaluate the strength parameter D, showing the proximity of the structure to its ultimate strength:

$$D = \frac{\Delta\sigma_1 - \Delta\sigma_3}{2} + \frac{\Delta\sigma_1 + \Delta\sigma_3}{2}\sin\varphi. \tag{12}$$

Here, σ_1, σ_3 stand for principal stresses and φ is the friction angle. The model regions with negative values of D at a given step are excluded from further analysis, since these indicate the stress relaxation with the crustal material state evolving in the opposite direction from strength limit (downgrading). At the same time,

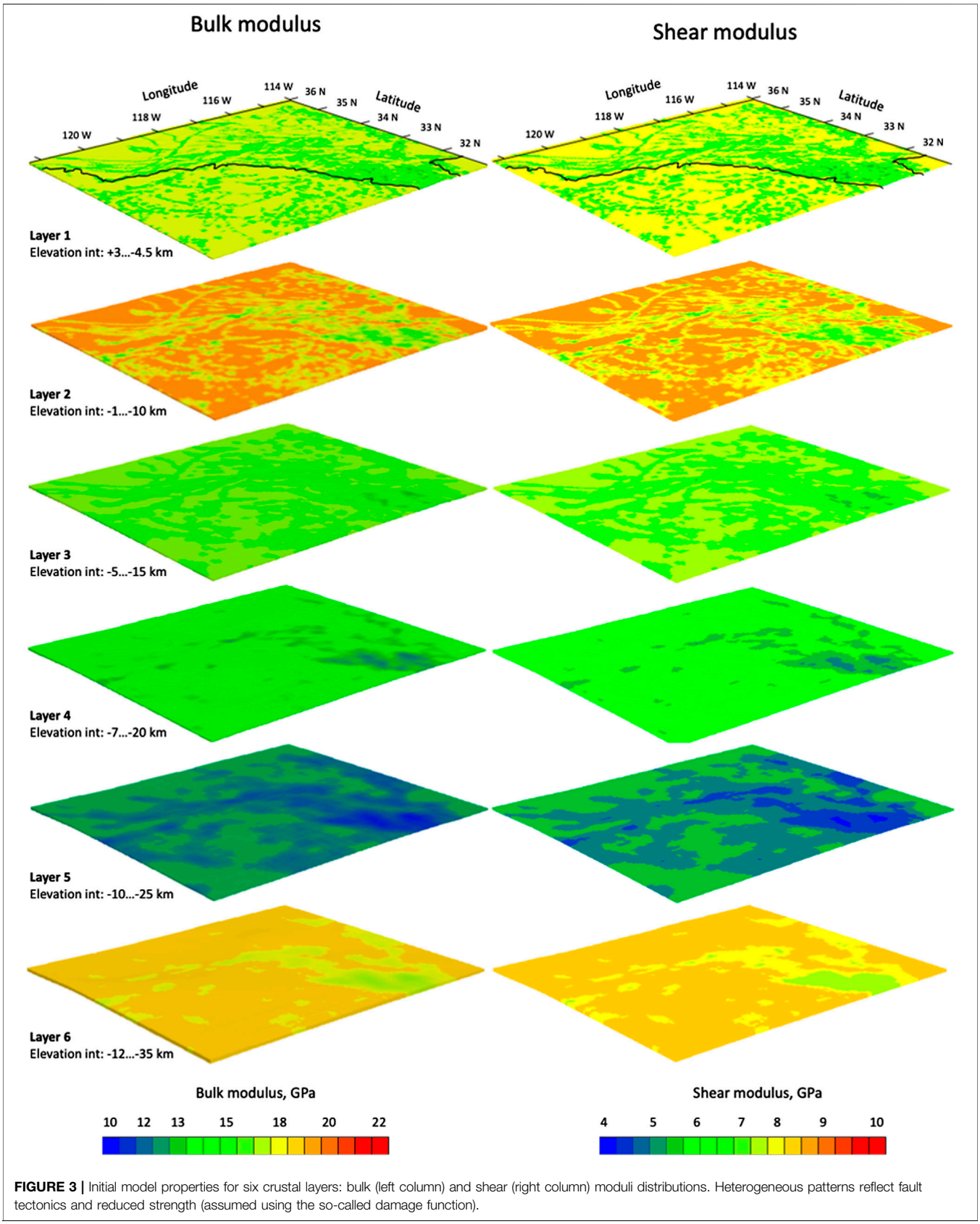

FIGURE 3 | Initial model properties for six crustal layers: bulk (left column) and shear (right column) moduli distributions. Heterogeneous patterns reflect fault tectonics and reduced strength (assumed using the so-called damage function).

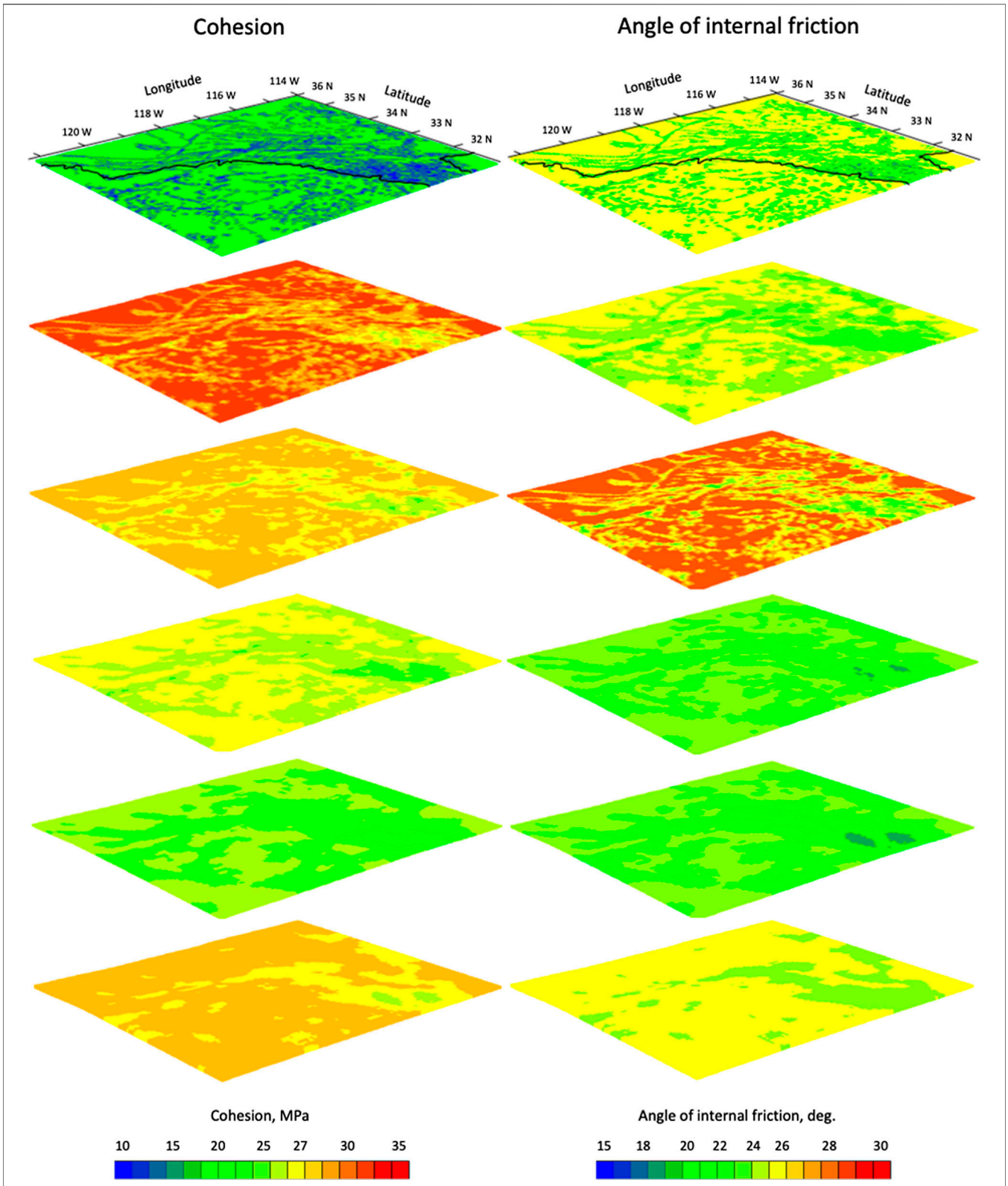

FIGURE 4 | Initial model properties for six crustal layers: cohesion (left column) and angle of internal friction (right column) distributions. Heterogeneous patterns reflect fault tectonics and reduced strength (assumed using the so-called damage function).

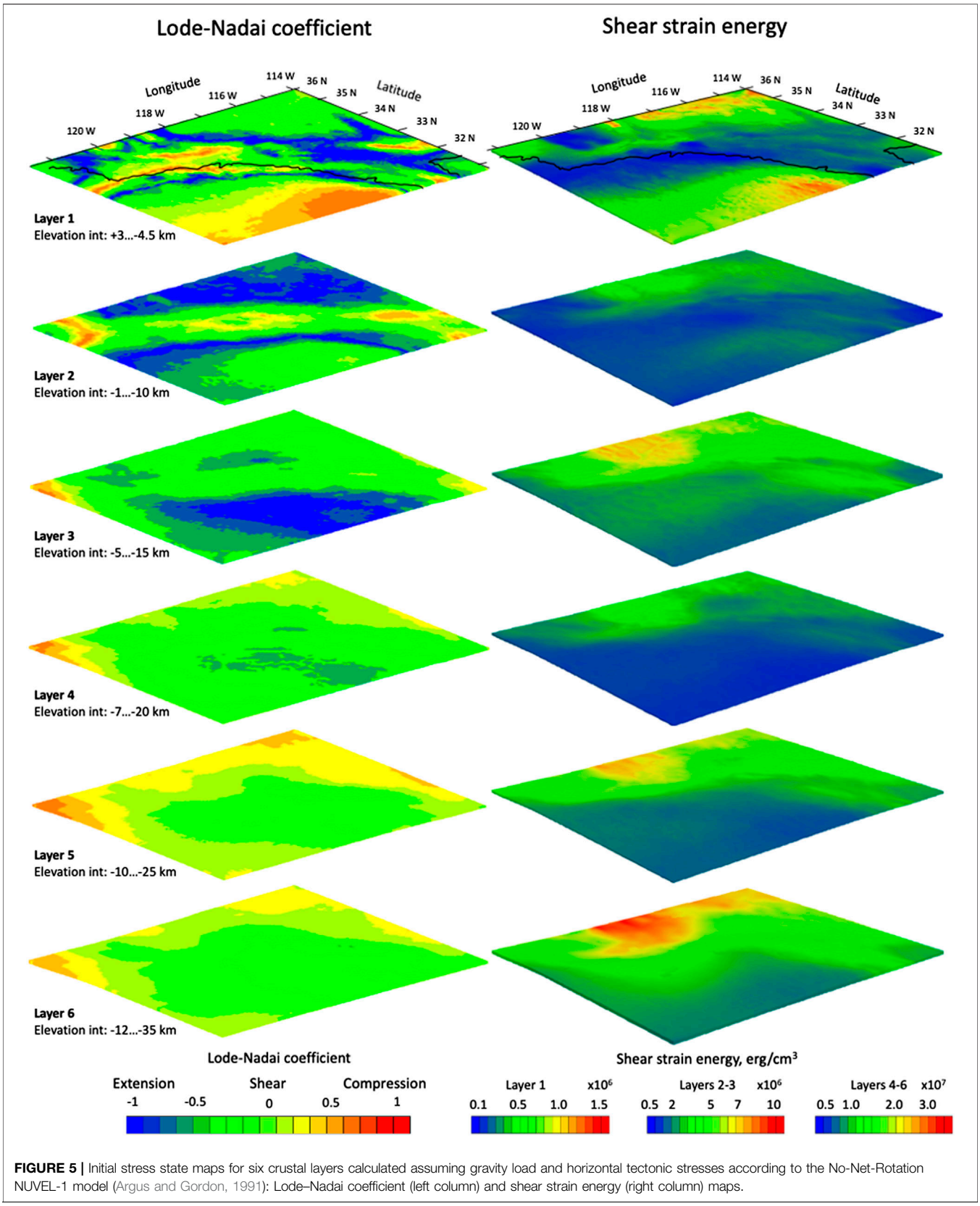

FIGURE 5 | Initial stress state maps for six crustal layers calculated assuming gravity load and horizontal tectonic stresses according to the No-Net-Rotation NUVEL-1 model (Argus and Gordon, 1991): Lode–Nadai coefficient (left column) and shear strain energy (right column) maps.

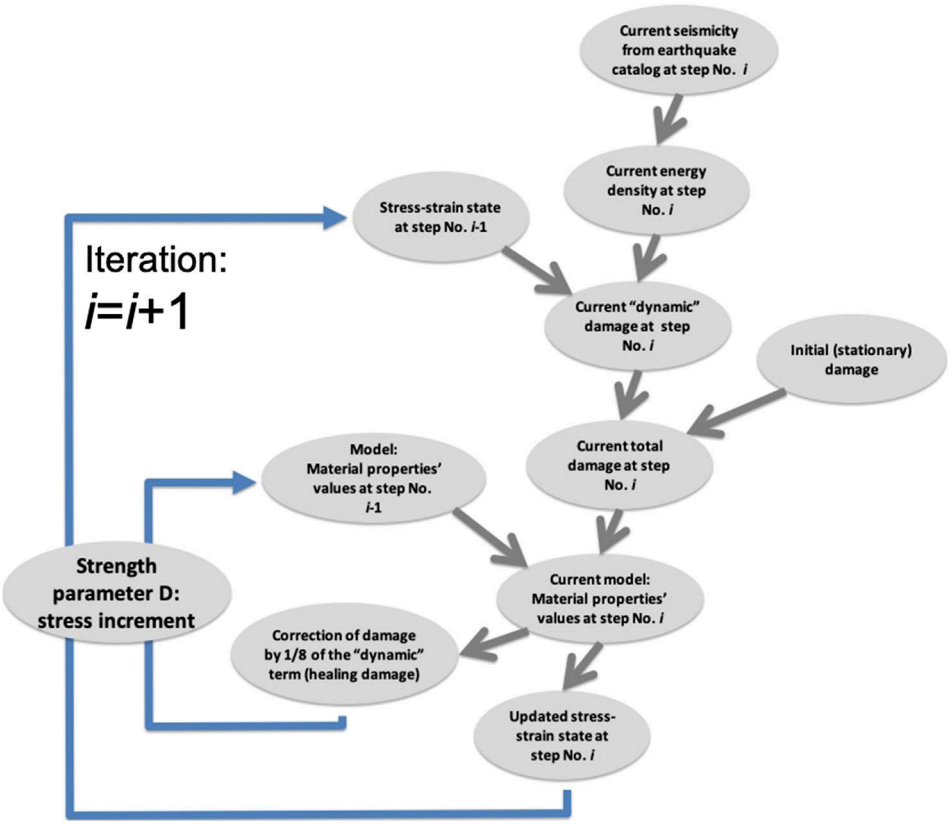

FIGURE 6 | Stress–strain state simulation cycle and strength parameter monitoring.

the patterns of positive values of D are visualized and analyzed in terms of absolute and relative (normalized by maximum value over a particular model layer or subdomain) distributions. Ultimately, all the above procedures are repeated for a new 3-month time-window, shifted by 1/2 month, forming a recursive loop (**Figure 6**).

Besides analysis of the strength parameter D, we also evaluate the time variation of maximum shear deformation in the upper and middle crust. Shear deformation is calculated as

$$\gamma = \sqrt{\frac{1}{6}\left[\left(\varepsilon_{xx}-\varepsilon_{yy}\right)^2+\left(\varepsilon_{yy}-\varepsilon_{zz}\right)^2+\left(\varepsilon_{zz}-\varepsilon_{xx}\right)^2\right]+\varepsilon_{xy}^2+\varepsilon_{yz}^2+\varepsilon_{zx}^2}, \quad (13)$$

where ε_{ij} are the strain tensor elements.

The main concept of such simulation-based monitoring consists in tracing the spatial migration of regions with abnormally high D and shear strain, and revealing of the correlation between migration patterns and seismic activity (here, we only include sufficiently strong shocks with $M >$ 5.2). Besides, the time variations of maximum D values for individual layers and/or model subdomains are of particular interest.

Since 2009, such geomechanical simulation has been run continuously, with seismic magnitude data for all relevant earthquakes ($M > 1$) taken from the USGS ComCat catalog (https://earthquake.usgs.gov/data/comcat/). The monitoring results reported in this article include the SS patterns preceding the April 2010 M7.2 and July 2019 M7.1 earthquakes.

RESULTS

To illustrate the approach described above, we focus on particular seismic events of 2010 and 2019, being the strongest shocks in the region with M exceeding 7.

Baja California 2010 Earthquake

Approximately 1 year after the start of our monitoring study, a strong M7.2. earthquake hit the Baja California region on April 4, 2010. This shock was preceded by elevation in strength parameter and specific pattern of its relocation during February–March 2010.

The spatial migration of the elevated-stress anomaly in terms of the strength parameter D within approximately 3 months before the event is given in **Figure 7A**. It can be seen that originally the anomaly emerges east of the future epicenter at a distance of $R \sim 20$ km. Then, it migrates closer to the epicenter ($R \sim 10$ km) and one extra anomaly arises northwest of the epicenter, where it follows the San Andreas fault ($R \sim 30$ km). Next, the anomaly goes north to $R \sim 50$ km, after which the high-stress region progressively moves toward the epicenter of the future M7.2 event.

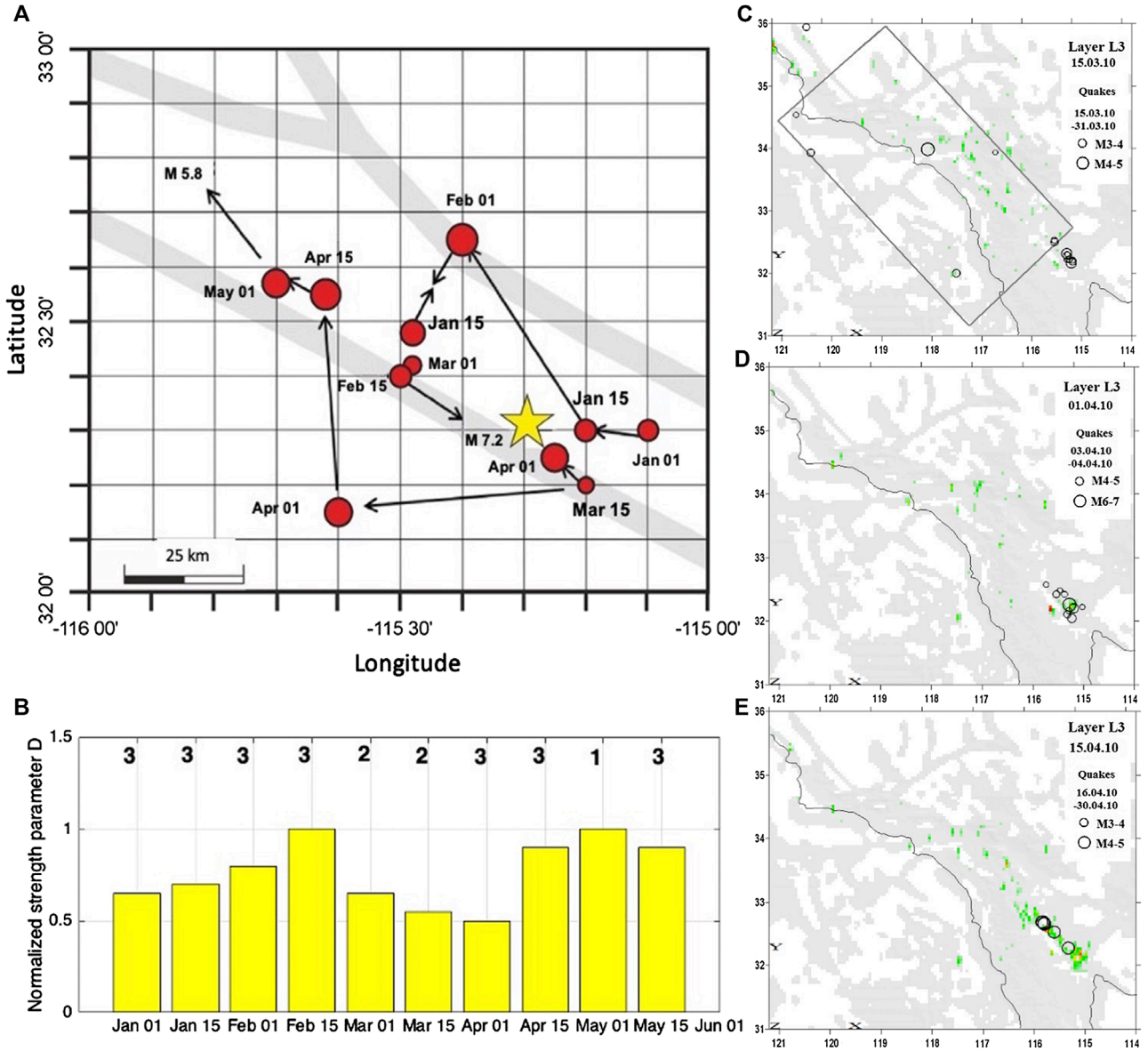

FIGURE 7 | (A) Migration path of the strength parameter *D* maximum (red circles), as it is approaching the future epicenter of the *M*7.2 earthquake (yellow star) during January–July 2010. Gray-colored regions indicate zones of elevated rock damage; **(B)** variation in normalized maximum strength parameter *D*, calculated over the model domain; numbers above the bars indicate the corresponding model layer. **(C)**–**(E)** Particular states of middle crustal layer 3 in terms of *D* for March 15, April 1, and April 15, 2010, with black circles showing the epicenters of main shocks, occurring during this period.

Figure 7B shows the variation of the maximum normalized strength parameter *D* (evaluated across layers 1–3) during January–May 2010. A visible increase in *D* is observed during February, some 40–50 days prior to the main shock. Afterward, elevated *D* levels had been observed in late April–May, while the anomaly position left the earthquake area and no longer emerged close to it (within 50 km).

From the maps showing anomalies in *D*, it is possible to figure out that 20 days prior to the earthquake, no significant anomalies were observed over the entire model domain (**Figure 7C**), while such an anomaly emerged 15 days later (red point near the future epicenter, **Figure 7D**) and spread after the earthquake, forming the fault-associated region of distracted crust, where it remained during a few subsequent 2-week calculation cycles (**Figure 7E**).

Figure 8 demonstrates the behavior of shear strain for the same time samples, also showing the presence of anomalous displacements close to the epicenter a few days prior to the shock.

We evaluated the stress regime for April 1, 2010, in terms of Lode–Nadai coefficient distribution in crustal layer 4 (**Figure 9**), in order to check whether it is consistent with the focal mechanism of the *M*7.2 Baja California earthquake, estimated from seismological data and known to be a strike-slip in the

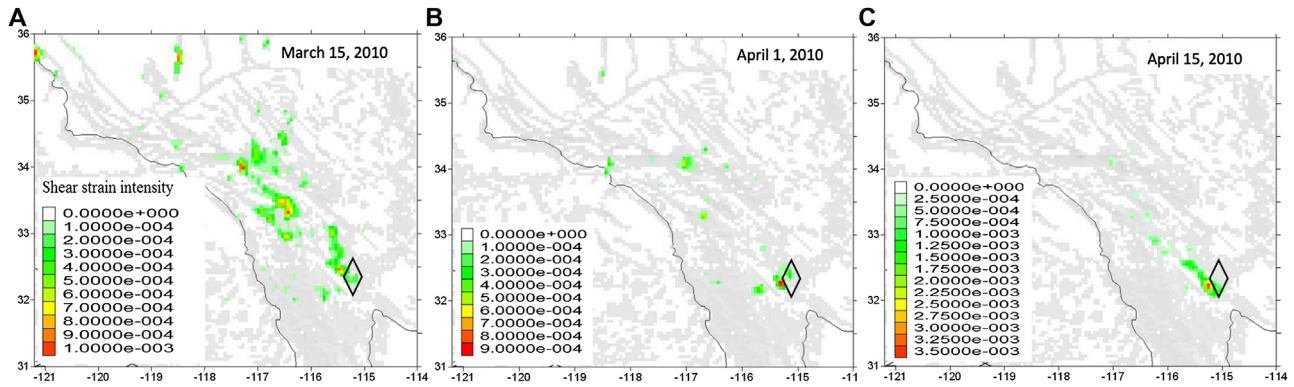

FIGURE 8 | Shear strain mapped in middle crustal layer 2 corresponding to March 15, April 1, and April 15, 2010. The elevated strain is given as colored image map, with individual colorscales shown in each panel. Underlying grayscale corresponds to initial normalized damage. Black diamond shows the epicenter of the Baja California M7.2 shock.

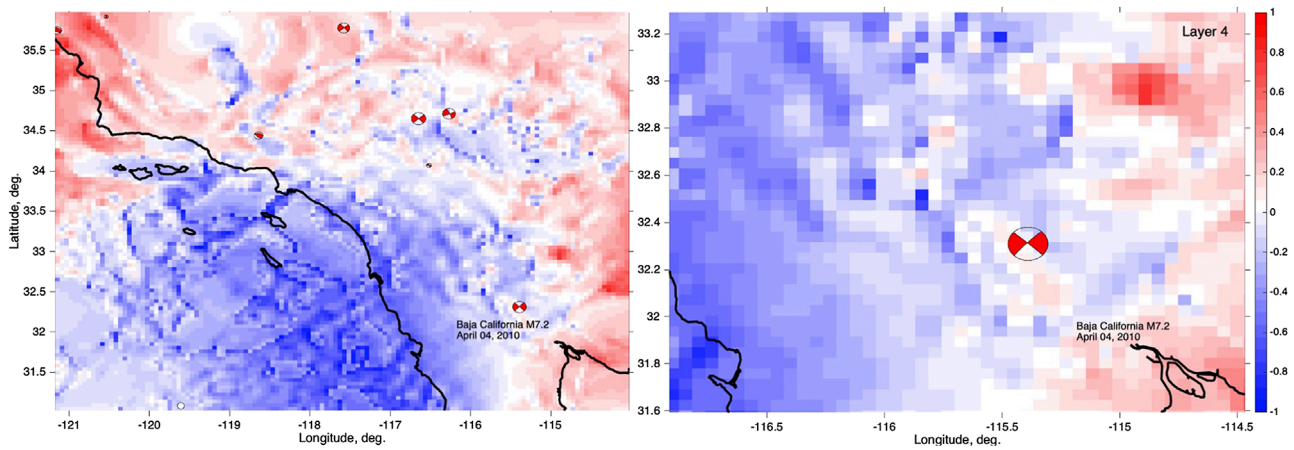

FIGURE 9 | Lode–Nadai coefficient maps in layer 4 as of April 1, 2010, before the *M*7.2 Baja California earthquake for the entire study area (left panel) and epicentral region (right panel). Reddish color indicates compression, bluish—extension, and whitish—shear stress setting.

northwest–east-south direction (https://www.globalcmt.org/CMTsearch.html). Notably, we found that the epicenter falls within the whitish-colored cell with nearly zero value, which corresponds to shear setting.

Ridgecrest July 2019 Earthquakes

In a similar way, we analyzed the computed stress–strain patterns for a few months prior to the 2019 Ridgecrest earthquakes, which had struck the region near the northern boundary of the study area. The main *M*7.1 shock occurred on July 5, 2019, and was preceded by an *M*6.4 foreshock on July 4, 2019 (Shelly, 2020). However, in this case, the spatial–temporal variation of the crustal strength parameter did not immediately reveal an isolated anomaly near the epicenter. Instead, a relatively faint anomaly was observed within the epicentral area (**Figure 10**) west of the epicenter starting from April 2019, accompanied by numerous higher-amplitude spots scattered all across the central part of the model domain. However, most of these spots displayed unstable behavior, changing their position chaotically or vanishing during model evolution. At the same time, the anomaly identified within the epicentral area remained steady with nearly no displacement during April, May, and June 2015, which attracted special attention to this region.

Figure 11A shows the path of migration sequence of the strength parameter anomaly for the period from January 1 to August 15, 2019. The epicenters of these two seismic events are shown by star symbols, while the gray-colored regions indicate the strength-reduced zones associated with tectonic faults. Tracing the anomaly migration, one can see that during January–March 2019, it was moving slowly in the southeastern corner of the epicentral subdomain and then jumped over to the northwest, approaching the epicenters of the July earthquakes. In May 2019 (i.e., 2 months before the seismic event), this anomaly reached its maximum value (**Figure 11B**), being located 30–35 km west of the epicenters.

The time variation of the strength parameter *D* (**Figure 11B**) indicates the maximum elevated stress in the upper part of the

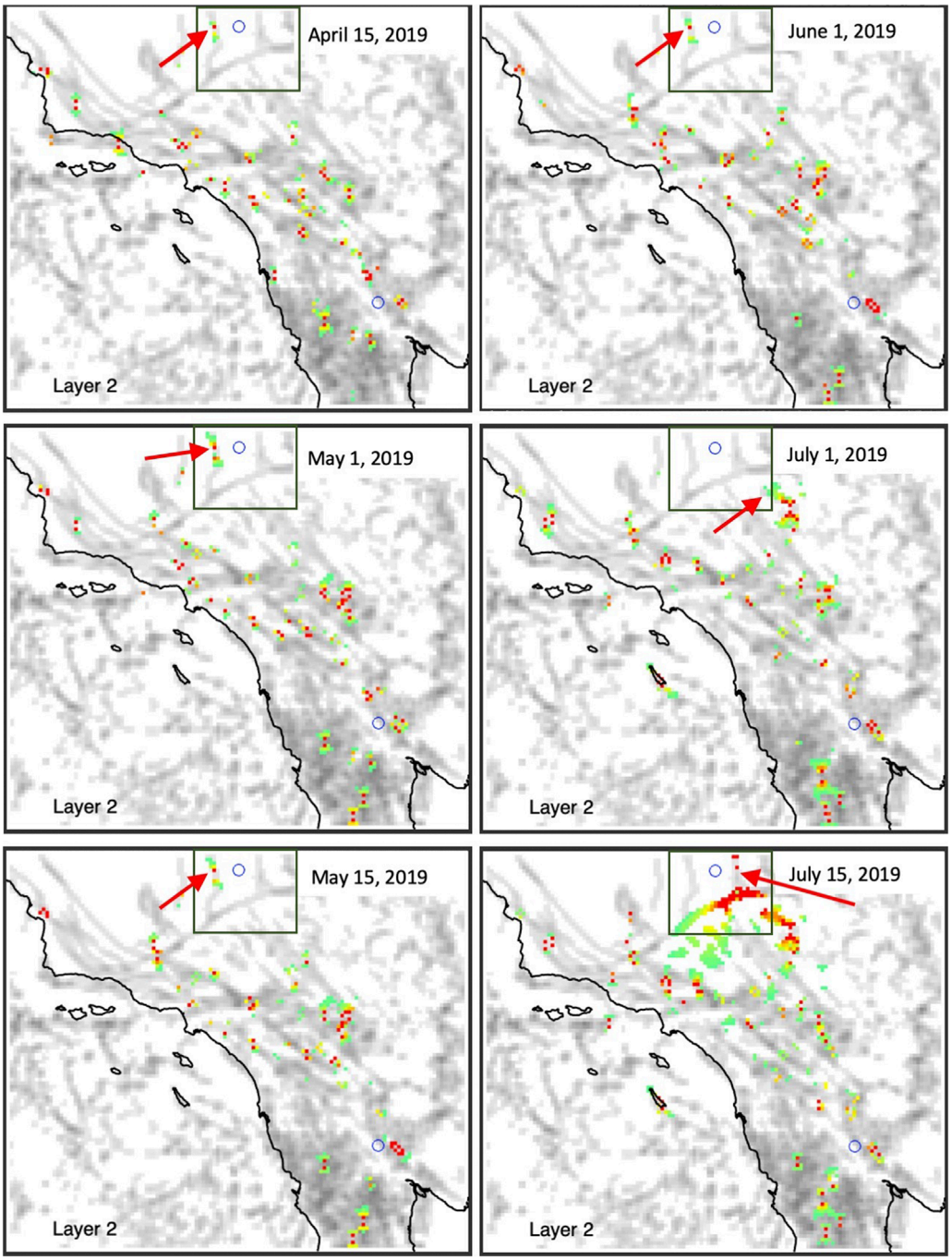

FIGURE 10 | Strength parameter patterns for layer 2, plotted for a series of instants from April to June 2019. Grayscale corresponds to initial normalized damage, while colored spots indicate anomalous model cells with elevated *D*. Red arrows point at anomaly locations within the epicentral area (shown by dark-green rectangle), traced in the subsequent analysis (as demonstrated in **Figure 11**).

earth's crust at depths of about 7 km on May 1, 2019, that is, a half-month before the earthquake, when it significantly exceeded the background values. Besides, the zone of the maximum stress was located within the same area for as long as 2.5 months (from April to June 2019). We interpret this behavior as a precursor indicating that a strong seismic event had been in preparation in that area during that time. The steady identification of strength parameter maximum in nearly the same place over a substantially long time followed by a strong shock is definitely in sharp contrast with a normal (background) migration pattern, which is pretty chaotic, with relatively large moves all over the model domain. The occurrence of the *M*7.1 earthquake followed by an aftershock series caused the *D* parameter maximum to rocket in the mid-July. By August, it was back to background values.

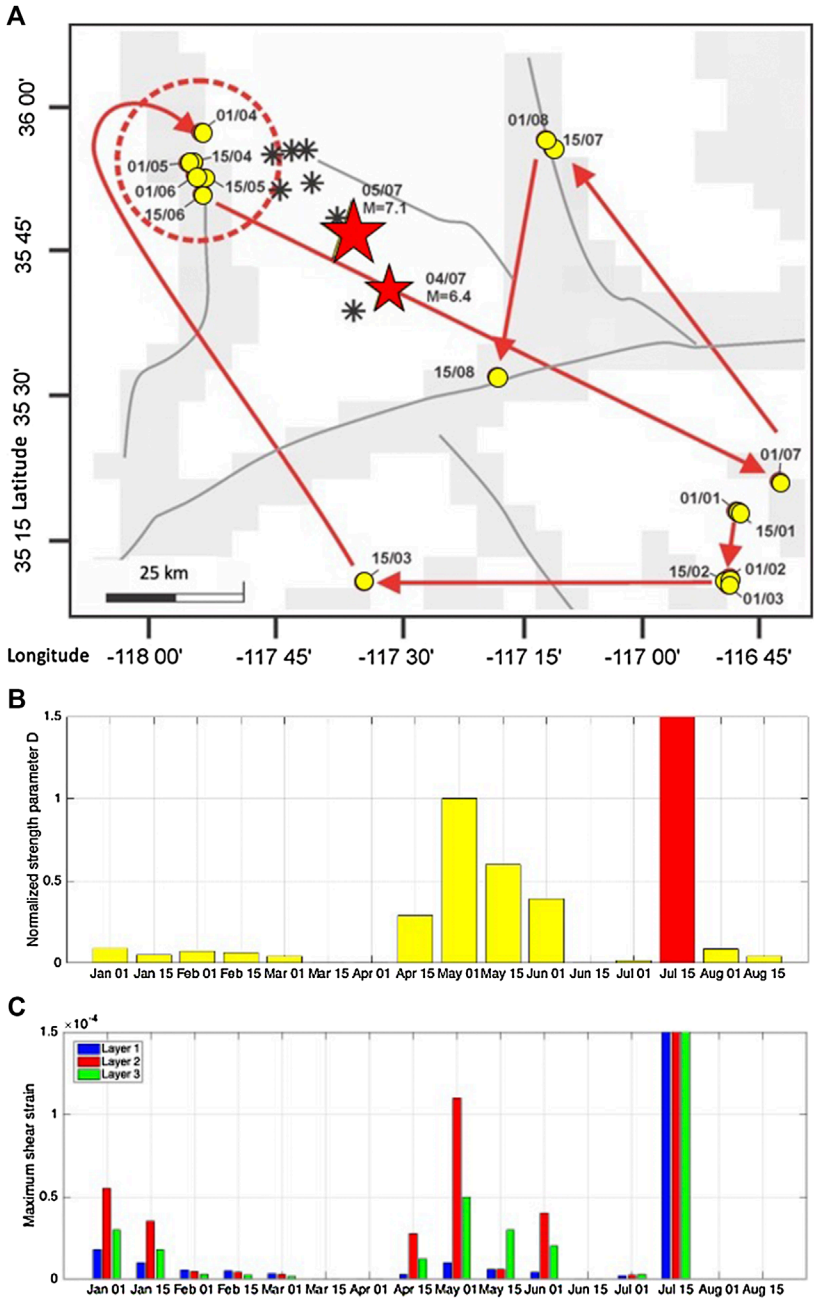

FIGURE 11 | (A) Migration path of the strength parameter *D* maximum (yellow circles), as it is approaching the future epicenters of the *M*6.4 and *M*7.2 Ridgecrest earthquakes (red stars) during January–July 2019. Gray-colored regions indicate zones of elevated rock damage. Red dashed circle indicates the region where the maximum stays for a significantly long period over 2 months, which is identified as a precursor; **(B)** variation in the normalized maximum strength parameter *D*, calculated over the epicentral subdomain during January–August 2019; **(C)** plots of the maximum shear strain absolute values calculated for the three upper layers of the earth's crust during January–July 2019, prior to the *M*7.1 Ridgecrest earthquake.

In addition to revealing the anomaly in terms of *D*, it was found that starting early April till mid-June 2019, the maximum shear strain exhibited elevated values, with spatial location of the anomaly being in close proximity to the northwestern flank of the future earthquake fault line (staying in the region confined by the dotted line in **Figure 11A**). **Figure 11C** shows time variations of the maximum shear deformation calculated separately for each of the three upper layers of the earth's crust during the period from February 1, 2019, to July 15, 2019. The maximum of the shear strain local anomaly is observed in May, 2 months before the *M*7.1 earthquake, which is similar to the behavior simulated strength parameter *D*. It is important to note that the deformation in layer

2, within a depth interval of nearly 3–7 km, exceeds the deformation in layer 3 (middle crust, 6–15 km depth). At the same time, in the upper part of the model (layer 1), deformation is of a lower level, which means the earthquake preparation process is not observable at the earth's surface directly. It should be noticed that the quantities plotted in the above figure reflect only the relative SS dynamics and may not take into account some stationary parts of the deformation. However, in the subsequent analysis, it is possible to "calibrate" the model and adjust the obtained strain values based on available estimates of coseismic deformation in the earthquake source region.

DISCUSSION

Having a decade-long series of SS distributions, with incremental parameters sampled half-monthly, we were to detect local anomalies months before the strong April 4, 2010, *M*7.2 earthquake and July 5, 2019, *M*7.1 earthquake. Both shocks are the only events with magnitude exceeding $M = 7$ that have occurred in the study area during the last decade. The revealed elevated-stress anomalies and the patterns of their migration prior to the shock can be considered as seismic precursors.

The described technique of SS monitoring in the Southern California region through geomechanical numerical simulation, launched in 2009, revealed some specific patterns of its behavior weeks and months prior to strong earthquakes. This provides substantial evidence for the efficiency of the approach based on the detailed geomechanical model updated continuously with current seismicity data. The earthquake foci parameters data, including even the weakest events ($M > 1$), characterize the process of crustal rupture and destruction and are critically important for the success of monitoring.

The core element of the modeling is the so-called damage parameter function, which determines the reduction in elastic constants of the crustal rocks due to destruction caused by earthquakes, which consists of the stationary part controlled by fault-block tectonics and the dynamic part associated with the ongoing seismic activity. Damage dynamics is estimated by summation of the impact of all earthquakes occurring over the 3-month interval, whose foci fall within a model. Each event is treated as a new crustal defect with dimensions determined by the Kasahara equation (Kasahara, 1981), and the entire simulation process allows for imaging and tracing the variations of elastic energy distribution. That reveals the patterns of its accumulation and dissipation, and enables identification of places where the rock state is of maximum proximity to ultimate strength, anomalies of strength parameter *D*.

Implementation of this quantity was proposed in our earlier research and seems to have a clear physical meaning, showing whether the stress state is getting closer to the strength limit (positive *D*) or farther from it (negative *D*). Although numerous other quantities describing the stress state might be employed to highlight areas of elevated stress, the stress elements alone are not indicative of possibility of failure. Analysis of *D* enables tracing the step-by-step variations of the model state, showing its evolution either toward failure or relaxation.

Since the SS includes both the stress (analyzed in terms of D) and strain parts (although related to each other via a constitutive model), we believe that some deformation-related quantity is useful for the analysis. As is known, strain accumulation may be considered as an earthquake precursor, and a significant amount of research has been focused on this subject. At the earth's surface, deformations can be measured directly, with GPS-based or laser interferometry systems as well as compact strainmeters, mostly used in trenches and mines (Savage et al., 1981; Lyons and Sandwell, 2003; Fialko, 2006; Segall, 2010; Mazzotti et al., 2011). In Southern California, borehole deformation monitoring is performed in the Parkfield area (Johnston et al., 2006). However, such observations do not provide information on the spatial strain patterns deep in the subsurface, which is necessary for monitoring the stress–strain dynamics in connection with the prediction of strong earthquakes.

For the purpose of deformation analysis, we have chosen the shear strain due to its relation to shear, since most of the seismic shocks in the area are associated with this particular mechanism. An important feature seen from the shear strain distribution across layers indicates that no significant deformation anomaly emerges in the surface layer, even in the case of a fairly strong earthquake ($M > 7$), occurring in deeper layers of the crust. This explains the limited success of the forecast based on direct strain measurements.

However, to some extent, the strain anomalies can be revealed through geomechanical model-based simulations accounting for ongoing seismic shock magnitude data. As a result, the SS patterns are calculated, showing the way the rocks are being deformed across the entire modeling domain. Besides, this approach enables discrimination and further analysis of only those shear deformations that are not associated with regional-scale tectonic forces, but are rather caused by the current seismicity alone; the process of destruction; and post-quake healing of the earth's crust.

Thus, by exemplifying two strong earthquakes in Southern California, namely, the *M*7.2 Baja California earthquake of April 4, 2010, and the Ridgecrest *M*7.1 main shock that occurred on July 5, 2019, we have shown that the proposed simulation-based method can be used for seismic hazard monitoring and prediction of strong shocks.

DATA AVAILABILITY STATEMENT

Publicly available datasets were analyzed in this study. These data can be found here: https://earthquake.usgs.gov/data/comcat.

AUTHOR CONTRIBUTIONS

VB initiated and guided the study and prepared the introductory part of the manuscript; MG proposed the concept of strength parameter tracing in application to Southern California and prepared the draft of the main body of the manuscript; IG

implemented geomechanical modeling, providing the code to control SS calculation with FLAC software; and DA contributed with stress–strain data numerical analysis and visualization, along with final editing of the manuscript. All authors have read and approved the final manuscript.

FUNDING

The study was supported by the Institute for Scientific Research of Aerospace Monitoring "AEROCOSMOS" (Project No. AAAA-A19-119081390037-2).

REFERENCES

Argus, D. F., and Gordon, R. G. (1991). No-net-rotation model of current plate velocities incorporating plate motion model NUVEL-1. *Geophys. Res. Lett.* 18, 2039–2042. doi:10.1029/91gl01532

Bondur, V. G., Garagash, I. A., and Gokhberg, M. B. (2017). The dynamics of the stress state in Southern California based on the geomechanical model and current seismicity: short term earthquake prediction. *Russ. J. Earth Sci.* 17, ES105. doi:10.2205/2017ES000596

Bondur, V. G., Gokhberg, M. B., Garagash, I. A., and Alekseev, D. A. (2020). A local anomaly of the stress state of the earth's crust before the strong earthquake (M = 7.1) of July 5, 2019, in the area of ridgecrest (Southern California). *Dokl. Earth Sci.* 490, 13–17. doi:10.1134/S1028334X20010018

Bondur, V. G., Garagash, I. A., Gokhberg, M. B., Lapshin, V. M., Nechaev, Yu. V., Steblov, G. M., et al. (2007). Geomechanical models and ionospheric variations related to strongest earthquakes and weak influence of atmospheric pressure gradients. *Dokl. Earth Sci.* 414 (4), 666–669. doi:10.1134/S1028334X07040381

Bondur, V. G., Garagash, I. A., Gokhber, M. B., Lapshin, V. M., and Nechaev, Y. V. (2010). Connection between variations of the stress–strain state of the Earth's crust and seismic activity: the example of Southern California. *Dokl. Earth Sci.* 430 (1), 147–150. doi:10.1134/S1028334X10010320

Bondur, V. G., Garagash, I. A., Gokhberg, M. B., and Rodkin, M. V. (2016). The evolution of the stress state in Southern California based on the geomechanical model and current seismicity. *Izv. Phys. Solid Earth* 52 (1), 117–128. doi:10.1134/S1069351316010043

Bondur, V. G., and Smirnov, V. M. (2005). Method for monitoring seismically hazardous territories by ionospheric variations recorded by satellite navigation systems. *Dokl. Earth Sci.* 403 (5), 736–740.

Bondur, V. G., Tsidilina, M. N., Gaponova, E. V., and Voronova, O. S. (2018). Systematization of ionospheric, geodynamic, and thermal precursors of strong (M ≥ 6) earthquakes detected from space. *Izv. Atmos. Ocean. Phys.* 54 (9), 1172–1185. doi:10.1134/S0001433818090475

Bondur, V. G., and Zverev, A. T. (2005) A method of earthquake forecast based on the lineament analysis of satellite images. *Dokl. Earth Sci.* 402 (4), 561–567.

Brandenberg, S. J., Stewart, J. P., Wang, P., Nweke, C. C., Hudson, K., Goulet, C. A., et al. (2020). Ground deformation data from GEER investigations of ridgecrest earthquake sequence. *Seismol. Res. Lett.* 91, 2024. doi:10.1785/0220190291

Cenni, N., Viti, M., and Mantovani, E. (2015). Space geodetic data (GPS) and earthquake forecasting: examples from the Italian geodetic network. *Boll. di Geofis. Teor. ed Appl.* 56 (2), 129–150. doi:10.4430/bgta0139

Clayton, R. W., Heaton, T., Kohler, M., Chandy, M., Guy, R., and Bunn, J. (2015). Community seismic network: a dense array to sense earthquake strong motion. *Seismol. Res. Lett.* 86, 1354–1363. doi:10.1785/0220150094

Fialko, Y. (2006). Interseismic strain accumulation and the earthquake potential on the southern San Andreas fault system. *Nature* 441, 968–971. doi:10.1038/nature04797

Field, E. H., Biasi, G. P., and Bird, P.; Working Group on California Earthquake Probabilities (2015). Long-term, time-dependent probabilities for the third uniform California earthquake rupture forecast (UCERF3). *Bull. Seismol. Soc. Am.* 105 (2A), 511–543. doi:10.3133/fs20153009

Field, E. H., Dawson, T. E., Felzer, K. R., Gupta, V. A. D., Jordan, T. H., Parsons, T., et al. (2009). Uniform California earthquake rupture forecast, version 2 (UCERF 2). *Bull. Seismol. Soc. Am.* 99, 2053–2107. doi:10.1785/0120080049

Field, E. H. and Members of the 2014 WGCEP. (2015). UCERF3: a new earthquake forecast for California's complex fault system. *U.S. Geological Survey*, 2015–3009. doi:10.3133/fs20153009

Garagash, I. A. (1991). Search of origination sites of strong earthquakes. *Dokl. Akad. Nauk SSSR* 318 (4), 862–867.

Gomberg, J. (1991). Seismicity and shear strain in the southern great basin of Nevada and California. *J. Geophys. Res.* 96 (B10), 16383–16399. doi:10.1029/91jb01576

Hutton, K., Woessner, J., and Hauksson, E. (2010). Earthquake monitoring in southern California for seventy-seven years (1932–2008). *Bull. Seismol. Soc. Am.* 100 (2), 423–446. doi:10.1785/0120090130

Itasca Consulting Group, Inc. (2006). *FLAC3D—fast Lagrangian analysis of continua in 3 dimensions, version 3.1. User's Manual*. Minneapolis, MN: Itasca.

Johnston, M. J. S., Borcherdt, R. D., Linde, A. T., and Gladwin, M. T. (2006). Continuous borehole strain and pore pressure in the near field of the 28 September 2004 M 6.0 Parkfield, California, earthquake: implications for nucleation, fault response, earthquake prediction, and tremor. *Bull. Seismol. Soc. Am.* 96 (4B), S56–S72. doi:10.1785/0120050822

Kasahara, K. (1981). *Earthquake mechanics*. Cambridge, United Kingdom: Cambridge University Press.

Liu, J. Y., Chuo, Y. J., Shan, S. J., Tsai, Y. B., Chen, Y. I., Pulinets, S. A., et al. (2004). Pre-earthquake ionospheric anomalies registered by continuous GPS TEC measurements. *Ann. Geophys.* 22, 1585–1593. doi:10.5194/angeo-22-1585-2004

Lyons, S., and Sandwell, D. (2003). Fault creep along the southern San Andreas from interferometric synthetic aperture radar, permanent scatterers, and stacking. *J. Geophys. Res.* 108, 2047. doi:10.1029/2002jb001831

Mazzotti, S., Lucinda, L., Cassidy, J., Rogers, G., and Halchuk, S. (2011). Seismic hazard in western Canada from GPS strain rates versus earthquake catalog. *J. Geophys. Res.* 116, 12310. doi:10.1029/2011JB008213

Mogi, K. (1985). *Earthquake prediction*. Tokyo, Japan: Academic Press.

Molchan, G., and Keilis-Borok, V. (2008). Earthquake prediction: probabilistic aspect. *Geophys. J. Int.* 173, 1012–1017. doi:10.1111/j.1365-246x.2008.03785.x

Peresan, A., Gorshkov, A., Soloviev, A., and Panza, G. F. (2015). The contribution of pattern recognition of seismic and morphostructural data to seismic hazard assessment. *Boll. Geofis. Teor. Appl.* 56 (2), 295–328. doi:10.4430/bgta0141

Ross, Z. E., Trugman, D. T., Hauksson, E., and Shearer, P. M. (2019). Searching for hidden earthquakes in Southern California. *Science* 364, 767–771. doi:10.1126/science.aaw6888

Rundle, J. B., Luginbuhl, M., Giguere, A., and Turcotte, D. L. (2018). Natural time, nowcasting and the physics of earthquakes: estimation of seismic risk to global megacities. *Pure Appl. Geophys.* 175, 647–660. doi:10.1007/s00024-017-1720-x

Savage, J. C., Prescott, W. H., Lisowski, M., and King, N. E. (1981). Strain accumulation in southern California, 1973–1980. *J. Geophys. Res.* 86 (B8), 6991–7001. doi:10.1029/JB086iB08p06991

Segall, P. (2010). *Earthquake and volcano deformation*. Princeton, NJ: Princeton University Press.

Shelly, D. R. (2020). A high-resolution seismic catalog for the initial 2019 ridgecrest earthquake sequence: foreshocks, aftershocks, and faulting complexity. *Seismol Res. Lett.* 91, 1971. doi:10.1785/0220190309

Singh, O. P., Chauhan, V., Singh, V., and Singh, B. (2009). Anomalous variation in total electron content (TEC) associated with earthquakes in India during September 2006–November 2007. *Phys. Chem. Earth Parts A/B/C* 34, 479–484. doi:10.1016/j.pce.2008.07.012

Sobolev, G. A., and Ponomarev, A. V. (2003). *Physics of the earthquakes and their precursors*. Moscow, Russia: Nauka [in Russian].

Toda, S., Stein, R., and Stein, R. (2019). Ridgecrest earthquake shut down cross-fault aftershocks. *Temblor*. doi:10.32858/temblor.043

Turcotte, D. L. (1994). "Crustal deformation and fractals, a review," in *Fractals and dynamic systems in geosciences*. Editor J. H. Kruhl (Berlin, Germany: Springer-Verlag), 7–23.

Viti, M., D'Onza, F., Mantovani, E., Albarello, D., and Cenni, N. (2003). Post-seismic relaxation and earthquake triggering in the southern Adriatic region. *Geophys. J. Int.* 153, 645–657. doi:10.1046/j.1365-246x.2003.01939.x

R. E. Wallace (Editor) (1990). *The San Andreas fault system*. California: U.S. Geological Survey. Professional Paper 1515. Available at: https://pubs.usgs.gov/pp/1990/1515/pp1515.pdf (Accessed August 31, 2020).

Williams, C. A., and Richardson, R. M. (1991). A rheologically layered three-dimensional model of the San Andreas Fault in central and southern California. *J. Geophys. Res.* 96 (B10), 16597–16623. doi:10.1029/91jb01484

Conflict of Interest: The authors declare that the research was conducted in the absence of any commercial or financial relationships that could be construed as a potential conflict of interest.

Copyright © 2020 Bondur, Gokhberg, Garagash and Alekseev. This is an open-access article distributed under the terms of the Creative Commons Attribution License (CC BY). The use, distribution or reproduction in other forums is permitted, provided the original author(s) and the copyright owner(s) are credited and that the original publication in this journal is cited, in accordance with accepted academic practice. No use, distribution or reproduction is permitted which does not comply with these terms.

frontiers in Earth Science

BRIEF RESEARCH REPORT
published: 29 September 2020
doi: 10.3389/feart.2020.00373

"Bristle-State" Friction: Modeling Slip Initiation and Transient Frictional Evolution From High-Velocity Earthquake Rupture Experiments

Seth Saltiel[1]*, *Tushar Mittal*[2†], *Jorge G. F. Crempien*[3,4] *and Jaime Campos*[5]

[1] *Lamont-Doherty Earth Observatory, The Earth Institute, Columbia University, New York, NY, United States,* [2] *Earth and Planetary Science Department, University of California, Berkeley, Berkeley, CA, United States,* [3] *Department of Structural and Geotechnical Engineering, Pontifica Universidad Católica de Chile, Santiago, Chile,* [4] *Research Center for Integrated Disaster Risk Management (CIGIDEN), Santiago, Chile,* [5] *Departmento de Geofísica, Universidad de Chile, Santiago, Chile*

OPEN ACCESS

Edited by:
Giovanni Martinelli, National Institute of Geophysics and Volcanology, Italy

Reviewed by:
Qi Li, Chinese Academy of Sciences (CAS), China
Ze'Ev Reches, University of Oklahoma, United States
Paolo Plescia, National Research Council (CNR), Italy

***Correspondence:**
Seth Saltiel
saltiel@ldeo.columbia.edu

†Present address:
Tushar Mittal, Department of Earth, Atmosphere and Planetary Sciences, Massachusetts Institute of Technology, Cambridge, MA, United States

Specialty section:
This article was submitted to Solid Earth Geophysics, a section of the journal Frontiers in Earth Science

Received: *06 July 2020*
Accepted: *10 August 2020*
Published: *29 September 2020*

Citation:
Saltiel S, Mittal T, Crempien JGF and Campos J (2020) "Bristle-State" Friction: Modeling Slip Initiation and Transient Frictional Evolution From High-Velocity Earthquake Rupture Experiments. Front. Earth Sci. 8:373. doi: 10.3389/feart.2020.00373

Fracture mechanics theory and seismological observations suggest that slip-rate is constantly changing during earthquake rupture, including dramatic acceleration from static conditions to high velocity sliding followed by deceleration and arrest. This slip history is partly determined by a complex frictional evolution, including overcoming peak friction, rapid weakening, and re-strengthening (or healing). Recent experimental developments have allowed friction evolution measurements under realistic slip histories reaching high co-seismic slip-rates of meters per second. Theoretical work has focused on describing the observed steady-state weakening at these high-velocities, but the transient behavior has only been fit by direct parameterizations without state variable dependence, needed to simulate arbitrary slip-histories. Commonly used forms of rate-state friction (RSF) are based on low-velocity, step-change experiments and have been shown to not fit the entire frictional evolution using a single set of realistic parameters. Their logarithmic form precludes zero fault slip-rate, assuming it is never truly static, thus does not capture slip initiation phenomena that might contribute to nucleation behavior. Inverting high slip-rate and friction data from different types of experiments, we show that RSF can work by using parameter ranges far from typical low-velocity values. In comparison, we introduce "bristle-state" friction (BSF) models, developed by control-system engineers to predict the transient frictional evolution during arbitrary stressing, especially reversals through static conditions. Although BSF models were also designed for low-velocities, we show that their form provides advantages for fitting frictional evolution measurements under high slip-rate, long-displacement, non-trivial slip histories, especially during the initial strengthening stage.

Keywords: earthquake nucleation, earthquake rupture dynamics, friction laws, transient evolution, high-velocity experiments, state-variable models, sliding regimes

INTRODUCTION: FRICTIONAL EVOLUTION STAGES AND SLIDING REGIMES DURING EARTHQUAKE RUPTURE

Earthquake nucleation and rupture models implement constitutive relations to represent the frictional response to transient slip pulses. However, these frictional models have been tested almost exclusively on steady-state measurements and simple velocity-step experiments of the transition between them (Scholz, 2019). In contrast, kinematic inversions of seismic and geodetic data (Wald, 1996) or fracture mechanics theory (Tinti et al., 2005) estimate fault slip histories during earthquakes that never reach steady-state, as the slip-rate is continuously changing—first accelerating dramatically from static to high-velocity unstable sliding, followed by deceleration and arrest—all within a short event duration. Frictional resistance to these changes in slip-rate follow a common set of stages. First, to undergo unstable sliding, shear stress must reach and overcome peak friction (Pennestrì et al., 2016), appearing as an initial strengthening. With accelerating slip, the fault then experiences significant weakening, potentially due to powder lubrication (Reches and Lockner, 2010), grain fragmentation to weaker phases (Hung et al., 2019; Rattez and Veveakis, 2019), acoustic fluidization (Van der Elst et al., 2012), flash-heating (Goldsby and Tullis, 2011; Kitajima et al., 2011), frictional melt (Niemeijer et al., 2011), and/or other chemical processes (Violay et al., 2013). As the slip deficit is used up, fault slip must decelerate and friction will re-strengthen or heal (Violay et al., 2019), allowing seismologically-inferred self-healing pulsed slip behavior (Heaton, 1990) and larger dynamic than static stress drops (Brune, 1970). Recent experimental developments (Di Toro et al., 2004; Hirose and Shimamoto, 2005; Reches and Lockner, 2010) have allowed measurement of friction evolution under these non-trivial slip histories, reaching co-seismic slip-rates of meters per second; **Figure 1** shows an example.

Of these stages, transient frictional evolution in the initial strengthening stage, during nucleation, is particularly understudied, because it is short-lived (Liao and Reches, 2019). Consequently, many fault friction models leave it out entirely (**Supplement 1**). Although long observed, recent high-velocity experiments suggest initial strengthening could be larger than previously thought (Sone and Shimamoto, 2009). This is partly

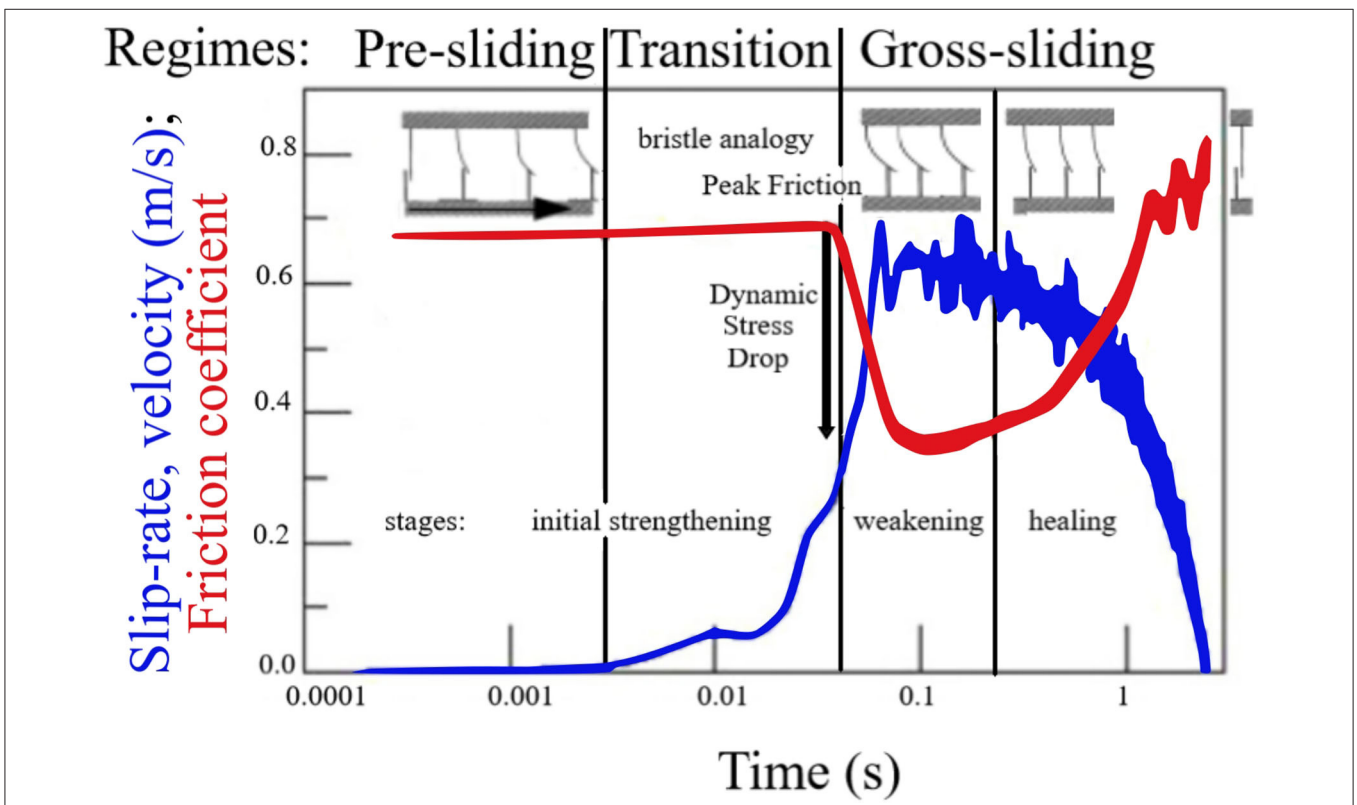

FIGURE 1 | Conceptual cartoon describing the bristle analogy for internal state variable evolution and different sliding regimes as applied to a conception of earthquake rupture process. Fault frictional evolution stages (initial strengthening, weakening, and healing) are labeled within the figure, while the corresponding sliding regimes are organized on top. Motivated by Figure 2E of Liao and Reches (2019), frictional data from a spinning flywheel impact experiment on a Sierra White granite sample [run 733 from Chang et al. (2012)]. The logarithmic time scale (x axis) enhances the evolution at early times and the initial strengthening stage, it also makes the initial acceleration look less dramatic in comparison to the deceleration. Motivating data are plotted with a linear time scale with inversions in the **Supplement**.

due to the special experimental attention needed to accurately measure static friction, where slip initiates, separate from the increase in applied shear stress during initial elastic loading. The initial increase in strength (friction) has been suggested to act as a barrier to rupture growth, playing a part in final earthquake magnitude and slip complexity (Lapusta, 2009). Recent geodetic observations suggest that stress increase due to slow, aseismic "preslip" occurring adjacent to the nucleation zone may be an important component of spontaneous earthquake generation (Roeloffs, 2006; Socquet et al., 2017). Further support for this "preslip" hypothesis comes from laboratory nucleation experiments (Latour et al., 2013; McLaskey et al., 2015; Passelègue et al., 2016; Svetlizky et al., 2018), where precursory slip has been observed proceeding "labquakes" of different scales, materials, and conditions. Understanding how friction evolves in the nucleation stage warrants revisiting friction models designed for slip initiation.

While the stages of frictional evolution summarize experimental rupture observations, they lack a framework for broader frictional phenomenon and parameterizations. In tribology, common behaviors from a wide-range of interfacial observations have been organized into different regimes: pre-sliding, gross-sliding, and the transition between them (Al-Bender et al., 2004). As shown in **Figure 1**, the regime organization focuses more on slip initiation, compared to fault models which commonly only address gross-sliding. During pre-sliding, slip fronts propagate along the interface, yet some elastically-coupled contacts remain stuck, holding back the entire fault segment from unstable sliding (Svetlizky et al., 2018). In gouge, force chains conceptually fit this role (Lyu et al., 2019). Also referred to as partial slip or incipient sliding, the friction force shows a nonlinear, hysteretic dependence on bulk displacement (Selvadurai et al., 2017). Hertz-Mindlin contacts (Mindlin, 1949) can capture this non-linearity and have been modeled in geomechanics and rock physics (Boitnott et al., 1992; Saltiel et al., 2017a), but not earthquake rupture. Although non-linear, the pre-sliding regime is still dominated by elastically stuck asperities; peak friction, or breakaway force, occurs after the interface starts to yield, failing though fracture (Chen et al., 2020) or other processes depending on conditions. Capturing this transition regime, also referred to as "stiction," is critical to modeling velocity reversals (as static conditions are reached each time before re-accelerating in the opposite direction) (Saltiel et al., 2017b). Fault slip is not commonly thought to reverse, except potentially from overshoot (Brodsky et al., 2020), but "stiction" is also relevant during initiation from static. Friction increases over a finite slip to a peak above the steady-state curve, then evolves to gross-sliding conditions (Al-Bender et al., 2004). The main gross-sliding observations, well-established in velocity-steps, are steady-state rate-dependence and frictional lag, the transition toward a new steady-state. In this regime asperities are constantly broken and remade, friction depends on slip-rate and contact history, often tracked through the evolution of an internal state variable (**Supplement 1.2**).

To the authors' knowledge this sliding regime framework is new to earthquake source physics, and common fault friction models lack mechanics of slip initiation. There are very few models that attempt to quantitatively fit the transient behavior during all three evolution stages (**Supplement 1.5**). In order to address these issues, we introduce to the geophysics community the bristle analogy for frictional state (Dahl, 1976) as well as a group of models we term "bristle-state," designed to capture all three sliding regimes. We then derive an analytical form for state evolution assuming no elastic coupling. Finally, we test the ability of these models to capture high-velocity measurements of frictional evolution during simulated earthquake rupture.

METHODS: FRICTION PARAMETERIZATIONS AND ANALYTICAL SOLUTION

"Bristle-State" Friction Formulation Development and Components

Given the challenges of modeling all the sliding regimes with current fault friction laws (reviewed in **Supplement 1**), we explore alternative parameterizations, from the control-systems engineering community, designed to predict friction during arbitrary driving stresses. A group of models have been used to capture all the sliding regime behaviors using the analogy of bristles on a brush which must bend elastically before the brush can begin gross-sliding (Aström and De Wit, 2008). As their nomenclature can be confusing, we introduce the name "bristle-state" friction (BSF), to refer to state-variable models that employ this bristle analogy, where state is the average deflection of asperity bristles (Pennestrì et al., 2016). It is not to be confused with other models based on this analogy, such as the Bristle Model (Haessig and Friedland, 1991) or the Compressed Bristle Model (Drincic and Bernstein, 2012), but use different mathematical forms to represent asperities as a population of elastic bristles with a range of stiffness. BSF models retain rate and state dependence, thus are straightforward to compare with standard rate-state friction (RSF) formulations (**Supplement 1.2**) for fault settings. Also like RSF, these models were proposed for purely empirical (i.e., curve fitting) reasons. We appreciate the need for physics-based models (**Supplement 1.3**), but argue for the importance of empirical parameterizations, especially given the complex and diverse relevant fault conditions and processes. BSF's conceptual attraction is its flexibility for attributing types of deformational processes (i.e., elastic, plastic) without trying to prescribe specific mechanisms (i.e., fracture, melt). In the following, we briefly discuss their historical and conceptual development, highlighting the origin of each term and what it was designed to capture.

Dahl Model

Observations of frictional lag first necessitated models of friction outside of steady-state. Dahl (1968) introduced the internal state variable dependence through a differential equation, which was later incorporated by Dieterich (1979) in what became the RSF model widely used to describe rock friction. While RSF was designed to describe experiments of step changes in velocity, Dahl's model was designed for transitioning through static conditions as a ball bearing rolls back and forth (Dahl, 1976). This

simulates pre-sliding and the associated hysteresis, equivalently described by a lag in the friction force when there is a change in the direction of motion. The Dahl model also introduces the bristle deflection analogy for the internal state variable—the load initially deforms the asperities elastically, like bristles, until gross-sliding brings permanent displacement. This analogy directly addresses the 'stiction' phase through the asperities' elastic range (Pennestrì et al., 2016). This linear elasticity is clear through the proportionality between the current friction coefficient (μ) and bristle deflection, or state, (θ):

$$\mu(\theta) = \alpha_0 \theta, \tag{1}$$

where α_0 is bristle stiffness. The state variable evolves according to the following equation:

$$\frac{d\theta}{dt} = v - \frac{\alpha_0 |v| \theta}{\mu_k}, \tag{2}$$

where v is the sliding velocity and μ_k is the constant kinetic friction coefficient. While the Dahl model introduces the internal state variable, its bristle analogy, and the differential equation form of state evolution, it is designed for the pre-sliding regime, so it has no steady-state velocity dependence. This can be easily seen by setting the state evolution equation to zero (as is the case for steady-state) and the velocity dependence drops out.

Stribeck Curve

The classic Stribeck curve is a steady-state velocity curve which includes the observation of increased static friction around zero velocity, then weakens with velocity before increasing again in velocity strengthening behavior at high velocity (Stribeck, 1902). This was observed in lubricated friction, where the weakening is attributed to building up hydrodynamic pressure (and thus lower effective normal stress), transitioning to strengthening as the lubricating film grows thicker and must be viscously sheared. Later observed in dry friction settings, the term "viscous friction" coefficient (α_3) has remained, for the proportionality between velocity (or strain-rate) and friction (Al-Bender et al., 2004). The Stribeck friction model gives steady-state friction (μ_{ss}):

$$\mu_{ss} = \left[\mu_c + (\mu_s - \mu_c)\, e^{-(\frac{v}{v_s})^2}\right] sgn\,(v) + \alpha_3 v, \tag{3}$$

where μ_c is the Coulomb friction coefficient, μ_s is the static friction coefficient, and v_s is the Stribeck velocity. It can be seen that the peak friction coefficient is μ_s, while the local minimum is μ_c, and v_s defines the velocities over which the first term dominates, while $\alpha_3 v$ takes over as velocity increases (Liu et al., 2015). A negative α_3 gives high-velocity rate-weakening behavior. The simple linear velocity dependence of steady-state friction at velocities $v >> v_s$ is retained in the BSF model described below, and is responsible for its shortcomings in fitting steady-state friction data (**Supplement 2**).

Stribeck is a single variable (velocity) dependent friction model, which describes the steady-state velocity weakening and strengthening curves as well as the stiction phase. Since it lacks state variable dependence it cannot describe frictional lag or hysteresis.

"Bristle-State" Friction

By adding the Stribeck curve to the Dahl model, de Wit et al. (1993) created a model that could capture the common observations of all three sliding regimes, including steady-state, hysteresis and lag, stiction, as well as stick-slip motion. They called it the modified Dahl model, and it is an example of an *integrated* friction model, incorporating a variety of frictional phenomena into a single formulation (Al-Bender et al., 2004). The functional form clearly combines aspects of the previous formulations:

$$\mu(v(t), \theta(t)) = a_3 v(t) + a_0 \theta(t) \tag{4}$$

$$\frac{d\theta(t)}{dt} = -\frac{|v(t)|\,\theta(t)}{L} + \frac{a_1 v(t)}{L} + \frac{a_2 v(t)}{L} e^{-(\frac{v(t)}{v_s})^2}, \tag{5}$$

where μ is the current friction coefficient; a_3 is now the viscous friction parameter with units of s/m, related to α_3 above; a_0 is the bristle stiffness, related to α_0, which we set to unity, absorbing it into the state variable, and thus drop for the rest of this study; L is a constant with dimensions of length, related to D in RSF (**Supplement 1.2**); v_s is the characteristic (Stribeck) velocity, described above; a_1 is the Coulomb friction parameter; related to μ_c; and a_2 is the Stribeck friction parameter, related to $\mu_s - \mu_c$, and defines the weight of the stiction effect. In this study, we only use positive velocities so $|v(t)|$ is replaced by $v(t)$. Although the state variable has the interpretation of the average deflection of the bristles, by absorbing the stiffness, a_0, into the state variable it takes on the units of friction coefficient or unit-less, ensuring that a_1 and a_2 are also unit-less.

We refer to this model as an example "bristle-state" model in an effort to define a group of similar models that vary slightly in form but use the same analogy for internal state variable and the *integrated* approach. The more common, but more complex, example (LuGre) is given in the **Supplement 1.4**. Modified Dahl was previously implemented to fit measurements of shear stress oscillations on rock fractures in the pre-sliding regime (Saltiel et al., 2017b), but to the authors' knowledge these models have not otherwise been applied to geophysical problems.

Analytical Solution of State Evolution Equations for Direct Velocity Forcing

To test the hypothesis that the BSF model can better capture the initiation and transient friction evolution during realistic rupture experiments, we quantitatively invert a range of high-velocity datasets. Following the interpretations of the original experimental papers, and in an effort to simplify our analysis and focus purely on the frictional evolution, we assume that the measurements give the slip-rate history on the interface. This allows us to apply the constitutive relations to a single slider block without a driving spring, eliminating the coupling between sliding velocity and friction from a spring's finite compliance. We can thus also neglect inertia in the force balance.

Our approach assumes that the experiments give the fault zone's effective frictional response to a realistic slip history, providing the opportunity to test which models can produce the observed frictional evolution for that specific slip history. In a way, the elastic aspects of the BSF model design allow

for an elastic response in the fault zone, which can be interpreted as the scale of the entire experimental apparatus, not the interface's asperity scale. We acknowledge that these assumptions and the friction laws do not explicitly represent the physical processes occurring during earthquake rupture, or even in the experiments. *Our empirical approach is to represent the phenomenon mathematically, not explain them physically. By finding a constitutive relation that captures the frictional evolution, it can be applied to finite rupture models to explore the importance of frictional changes within the context of the entire elastodynamic problem*.

These assumptions are useful because they simplify the inversion and minimize the number of free parameters, including stiffness and inertia would add under-constrained parameters. By applying the driving velocity directly to the interface as a sliding velocity, the differential equation for state evolution can be solved to give the state variable in the analytical function:

$$\theta(v(t)) = e^{\int_0^t -\frac{v(\xi)}{L}d\xi}\int_0^t \frac{v(\zeta)[a_1 e^{\int_0^\zeta \frac{v(\xi)}{L}d\xi} + a_2 e^{-\frac{v(\zeta)^2}{v_s^2}-\int_0^\zeta \frac{v(\xi)}{L}d\xi}]}{L} d\zeta + ce^{\int_0^t -\frac{v(\xi)}{L}d\xi}, \text{ or}$$

$$\mu(v(t)) = a_3 v(t) + e^{G(v(t))}\int_0^t \frac{v(\zeta)[a_1 e^{-H(v(t))} + a_2 e^{-\frac{v(\zeta)^2}{v_s^2}} e^{-H(v(t))}]}{L} d\zeta + ce^{G(v(t))}, \quad (6)$$

where the functions $G(v(t)) = \int_0^t -\frac{v(\xi)}{L}d\xi$ and $H(v(t)) = \int_0^\zeta -\frac{v(\xi)}{L}d\xi$, give the effect of the specific slip-rate history, and c is an integration constant that gives the initial friction at zero sliding velocity. Although the integrals require numerical calculation, this analytical form allows direct calculation of the friction force given a slip-rate history. In comparison, when using the fully coupled differential equations, including spring stiffness, the slip-rate needs to be solved for as well as friction.

This same analysis undertaken with the RSF aging law ($\frac{d\theta}{dt} = 1 - \frac{\theta(t)v(t)}{D}$) is illuminating, because it is equivalent to the state evolution for the BSF model ($\frac{d\theta}{dt} = -\frac{v(t)\theta(t)}{L} + \frac{a_1 v(t)}{L} + \frac{a_2 v(t)}{L} e^{-(\frac{v(t)}{v_s})^2}$) when the final two terms are equal to 1. Equivalent analysis gives the following analytical solution for state in the RSF aging law:

$$\theta(v(t)) = e^{\int_0^t -\frac{v(\xi)}{D}d\xi}\int_0^t e^{-\int_0^\zeta -\frac{v(\xi)}{D}d\xi} d\zeta + ce^{\int_0^t -\frac{v(\xi)}{D}d\xi}, \text{ or}$$

$$\mu(v(t)) = \mu_0 + a\ln\left(\frac{v}{v_0}\right) + b\, ln(\frac{v_0}{D}e^{G(v(t))}\int_0^t e^{-H(v(t))}d\zeta + ce^{G(v(t))}) \quad (7)$$

The mathematical steps taken to reach these forms, constant velocity solutions, further justification, and consequences of this assumption are discussed further in **Appendix A**.

RESULTS: FITTING NON-TRIVIAL, HIGH-VELOCITY EXPERIMENTS

In order to compare the ability of BSF and RSF for capturing the observed frictional response to realistic rupture, we performed a MCMC inversion (detailed in **Appendix B**) of the analytical equations above on two sets of high velocity experiments (a third is included in **Supplement 3**), each with its own benefits and issues representing earthquake rupture. For each study, we digitized the slip-rate and corresponding frictional evolution from published figures and found a best-fitting set of parameters for each model to minimize the misfit (χ^2) to the data.

Steady Acceleration/Deceleration From Sone and Shimamoto (2009)

Sone and Shimamoto (2009) utilized a high-velocity rotary-shear apparatus (Hirose and Shimamoto, 2005), to deform samples of recovered Chelungpu fault gouge from the location of the 1999 Chi Chi earthquake. They measured the applied shear stress evolution under a constant normal stress of 0.56 MPa, consistent with the depth of the sample, at constant and varying shear rates. The constant velocity experiments and their model are described and compared with BSF results in **Supplement 2**. To simulate the slip-rate history of the Chi Chi earthquake, they manually accelerated and decelerated the slip velocity to reproduce a kinematic waveform inversion solution for the approximate sample locality, where the fault accelerated to ∼1.9 m/s in 6 s, then decelerated back to stationary in 4 s (Ji et al., 2003). The experiments roughly follow this with constant acceleration/deceleration, except the acceleration increases for the final second to the deceleration rate (**Figure 2**). The experiment was run five times with slightly different velocity histories, Sone and Shimamoto (2009) provided a representative curve, which we digitized, along with one of the five equivalent measurements of friction evolution. The focus is on capturing the relative magnitude and evolution trends, so digitization errors are not a problem.

While Sone and Shimamoto (2009) found that RSF with the aging law was not able to capture both the weakening and healing trends of their data with a single set of parameters (their **Figure 4**), they did not perform a full inversion, but explored the range of behaviors by finding the parameters needed for each trend individually. If parameter values are restricted to the ranges found in low-velocity experiments, the inversion shows that RSF is not able to capture the full amplitude of frictional changes in the data, staying within a narrow range of friction coefficients (**Figure 2A**). If all the parameters are given a wide range of values except for v_0, which was restricted to values below 10^{-4} m/s, then RSF can fit the weakening or healing, but not both (**Figure 2B**). Both the RSF and BSF models with full flexibility in free parameters are able to capture all three frictional evolution stages (**Figure 3**). Given BSF's conceptual attention to initial strengthening, as described in section "Bristle-State" Friction Formulation Development and Components, it is better able to match the sharpness of the friction peak, whereas the best-fit RSF model broadens the peak significantly. Yet over

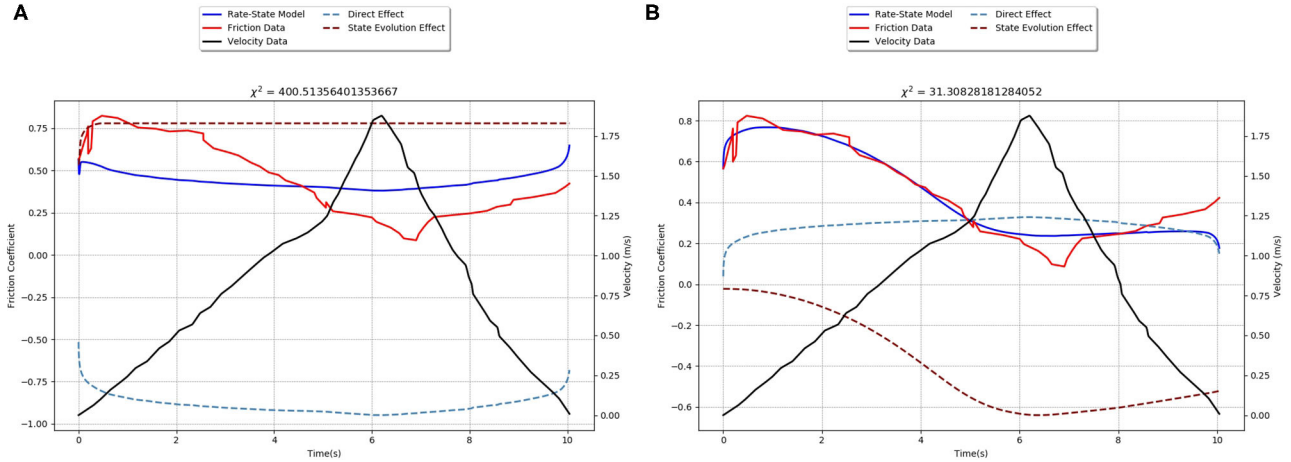

FIGURE 2 | Best-fitting models, with χ^2-values given on top of the plots, for the Sone and Shimamoto (2009) steady acceleration/deceleration experimental data. RSF with restricted parameter ranges: **(A)** a and b [−0.03 to 0.03], D [<1 mm], and v_0 [$<10^{-4}$ m/s] are restricted to values consistent with low-velocity measurements, while in **(B)** only v_0 is restricted to this range. The solid red line is the frictional data; the solid blue line shows the inversion fit for each model; the solid black line is the driving velocity data which the interface is forced at; the dotted blue line is the direct effect term of each friction model; while the dotted brown line is the state evolution term. In order to best fit both terms on the plot with minimal overlap, they are offset. In RSF, μ_0 provides a natural offset, since the friction coefficient is the sum of the two terms and μ_0 (thus the friction coefficient curve is a summation of the two terms, as they are plotted, plus this additional offset). As expected, commonly used RSF parameters cannot capture the dynamic friction evolution at high-velocities, but with the parameters outside of these common ranges, the model is able to reproduce more of the observed frictional evolution stages.

all, the two models follow the general trends and have similar goodness-of-fit χ^2-values.

The parameter v_0 is interesting because it is a relative value, set to be lower than experimental velocities, that is often assumed not to affect the behavior. Commonly set to order $\sim 10^{-6}$ m/s (the lowest experimental velocities), or even as low as background plate tectonic rates ($\sim 10^{-12}$ m/s), v_0 is the constant velocity at which a steady-state friction is measured. The steady-state friction relation for RSF is $\mu_{ss} = \mu_0 + (a - b)\ln\left(\frac{v}{v_0}\right)$, thus $\mu_{ss} = \mu_0$ when $v = v_0$. When v_0 is left as a free parameter (while the steady-state relationship defines μ_0), the inversion is able to fit the data (**Figure 3A**), but v_0 must be much higher, in this inversion ∼2.5 m/s. This higher v_0 makes the direct effect negative and thus varies its effect more dramatically to capture the initial peak. In many of our best-fit models, v crosses v_0 during the initial strengthening stage, so the direct effect goes from negative to positive and varies greatly compared to a low v_0 where velocity must change orders of magnitude to change the direct effect significantly. These behaviors are outside of the original RSF interpretation.

Although the steady-state friction relation for this form of BSF friction is not ideal (as discussed in Stribeck Curve), **Supplement 2** shows the same best-fit parameters were able to reproduce the peak friction of their constant velocity measurements, providing a relation between peak friction and velocity that fits their data much better than their relation. This further supports that the BSF inversion is capturing the underlying frictional behavior.

Spontaneously Developing Slip From Rubino et al. (2017)

Rubino et al. (2017) presents novel measurements of evolving local friction and velocity of dynamic ruptures at different normal stresses in an analog Homalite fault using ultrahigh speed full-field imaging techniques. Since their reported velocities are calculated by imaging the movement at the fault interface, our assumption of applying the actual slip velocity (not a driving velocity) to the model is accurate. The ruptures were induced by rapid expansion of an electrically charged wire filament, but the subsequent slip develops spontaneously. Since the sample has limited dimensions (∼200 mm), the entire fault ruptures, not terminating in a healing stage. Still, this dataset offers an opportunity to test each friction models' ability to match the initial strengthening and weakening stages at high slip velocities (up to ∼20 m/s), which are spontaneously developed, not prescribed experimentally. The paper shows that rupture propagates steadily along the fault (their **Supplementary Figures 3.2a, 3.3a, 3.4a**), so we use the data from a single location (showing no evidence of edge effects) at two different normal stress conditions (their **Figures 4A,B**). They also include data from an intermediate stress condition at a shallower fault angle, but the rupture has a very different slip-rate history, including a reflected super-shear crack, and the friction evolution is too complex, with friction peaking before velocity increase was measured, to model with our simple force balance.

Rubino et al. (2017) appeal to the combined model of RSF with flash-heating, Equation (1.5) in **Supplementary Material**, to explain the dramatic weakening at high velocities. They show that

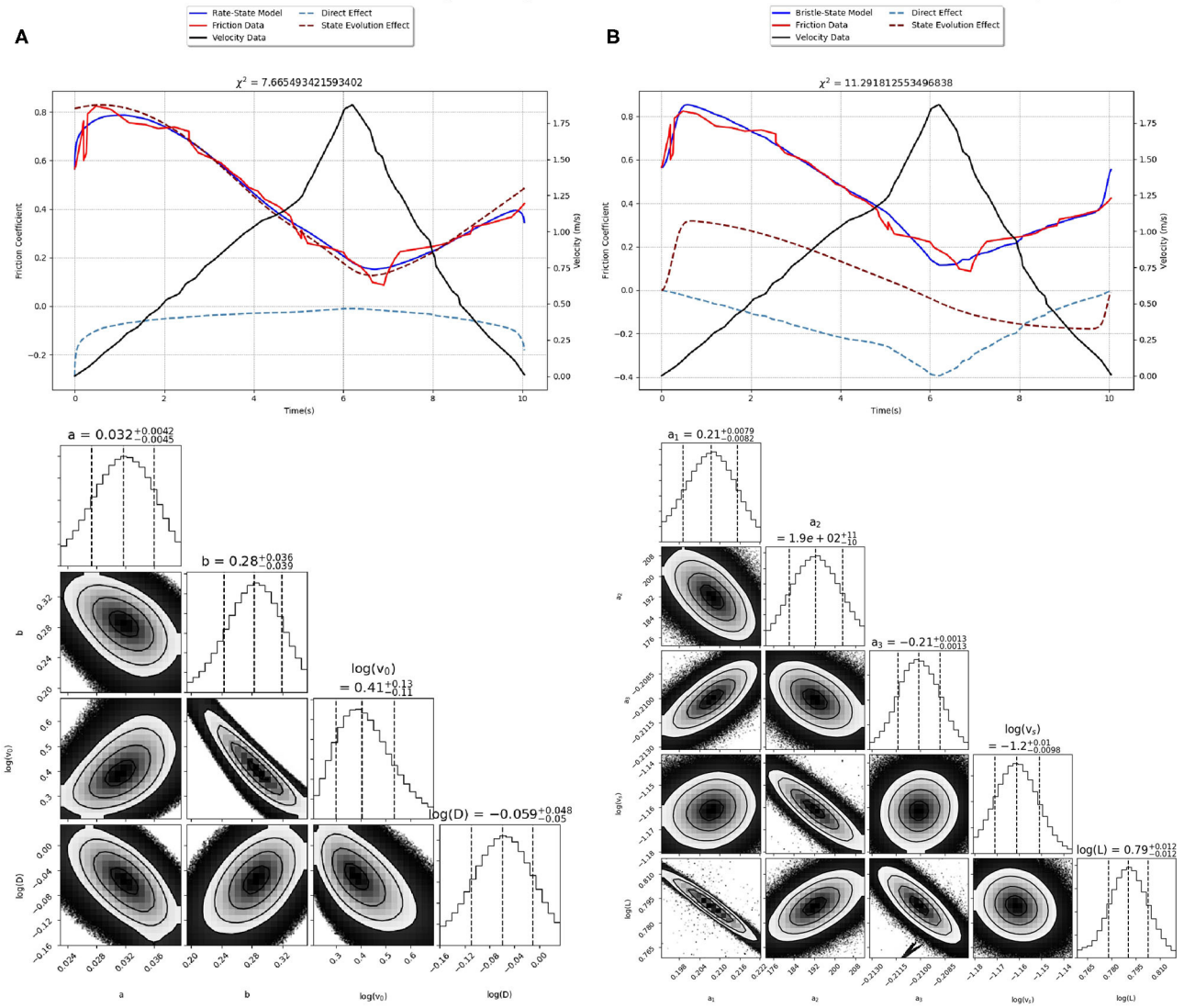

FIGURE 3 | Best-fitting models (same details as **Figure 2** above) and MCMC posterior probability distribution corner plots are shown for fully flexible inversions of **(A)** RSF and **(B)** BSF. In order to best fit both terms on the plot with minimal overlap, they are offset. RSF doesn't require an additional offset because μ_0 is part of the friction coefficient, but BSF the friction is only the sum of these two terms, so we use the initial friction coefficient (μ(t = 0)) such that the initial values for each term is zero (thus the friction coefficient curve is a summation of the two terms, as they are plotted, plus this additional offset). The triangle plot shows the 1D and 2D projections of the posterior probability distributions of our model parameters. In the 1D plots, the vertical lines show median and the 1-sigma values of the parameters while the 2D histograms show the contour intervals for the 0.5, 1, 1.5, and 2 sigma levels 11.7, 39.3, 67.5, and 86.4% confidence intervals. Although the fully flexible RSF model achieves a slightly lower χ^2, this includes digitization errors and visual inspection suggests BSF better fits the initial peak.

the final steady-state friction values for their three experiments fit the steady-state version of this friction law, providing best-fit parameter values (a-b, v_0, μ_w, v_w). They claim that the initial strengthening is quantitatively consistent with the RSF direct effect, but did not model their transient friction measurements. To test this hypothesis, we invert the frictional data for the experiments at normal stresses of 5.66 MPa (**Figure 4**) and 17.6 MPa (**Supplement**) using RSF combined with flash-heating (**Supplement Figure 4.1b**), as well as standard RSF (**Figure 4A**). We found that the combined model is not able to match the peak friction, given the provided parameter values for either normal stress experiment, offering no improvement to standard RSF. With all six free parameters left free, the inversion was able to find a set of parameters that could match the frictional peak for high normal stress data (**Supplement**), but not at the lower normal stress (**Figure 4A**). In comparison, the best-fit BSF model is able to fit the peak at both normal stresses (**Figure 4B** and **Supplement**).

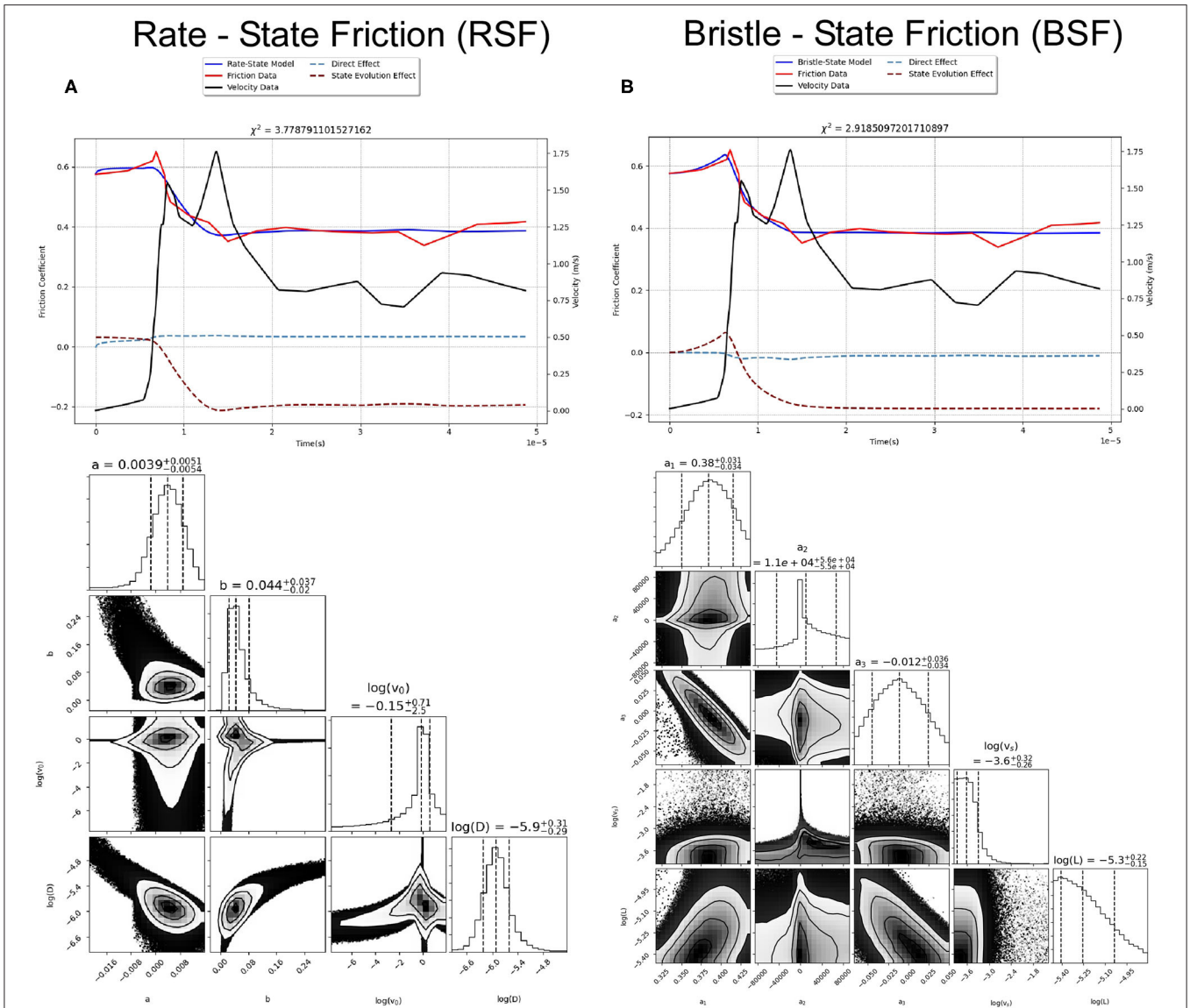

FIGURE 4 | Best-fits of **(A)** RSF and **(B)** BSF models to spontaneously developing slip experiment at 5.66 MPa normal stress from Rubino et al. (2017), details are the same as for **Figure 3** above.

DISCUSSION AND CONCLUSION: MODEL COMPARISON

The sliding regime framework and the bristle state variable analogy, from engineering and tribology literature, are conceptually useful for addressing slip initiation, as in earthquake nucleation, and transient frictional evolution, as co-seismic slip is never expected to reach steady-state. Although originally designed for low-velocity settings, we show that the BSF formulation is sufficiently flexible to describe the observed frictional evolution in high-velocity, realistic slip-history experiments, performing well relative to (various forms of) RSF. At the same time, we show that RSF can represent aspects of the experimental results, given parameter values outside of common use and interpretation. We do not endorse the use of these extreme parameter values, unrealistically high v_0 was found to be vital for fitting the data, but it should be noted that parameters from current RSF simulations are not consistent with these experiments. Although this inconsistency has been known for the magnitude of steady-state high-velocity weakening [motivating the development of new laws such as flash-heating (Rice, 1999)], we highlight that the transient evolution also requires modification. We acknowledge that since BSF is new to rock friction, there is little context to evaluate or interpret BSF parameter values; this will be undertaken in future work by exploring a wide range of rock friction experiments.

As expected, the BSF model shows clear benefits for fitting the initial strengthening stage, due to the attention to pre-sliding and transition processes. Although the overall χ^2-values are not always significantly different, visual inspection shows that BSF fits the rate and magnitude of peak friction better than RSF. In **Figure 3A** RSF smooths out the frictional peak significantly compared to the data and (b) BSF fit. **Figure 4A** shows a low RSF peak friction, earlier than the data and (b) BSF initial evolution. The supplementary examples show similar behavior, and in those cases that RSF can fit the frictional peak relatively well, the overall χ^2 is much poorer. These results suggest that BSF might prove a useful parameterization for friction during the initiation of slip and thus inform models of earthquake nucleation.

In this study, we are only representing the temporal evolution of friction in a single location undergoing realistic slip-rate histories, but applying these parameterizations to finite fault dynamic rupture models could help address the interplay between temporal frictional evolution and spatial heterogeneities, such as fluid pressure. Observations of preslip nucleation often appeal to spatially varying conditions to explain how aseismic slip grows into seismic events, but models that capture the friction evolution to peak could explore the possible contribution of temporally evolving friction on this behavior.

DATA AVAILABILITY STATEMENT

The digitized datasets, inversion code, and MCMC results used for the analysis are provided as Supplementary files at DOI: 10.6084/m9.figshare.11473530. The original authors should be contacted in order to obtain the non-digitized datasets.

AUTHOR CONTRIBUTIONS

SS was responsible for the writing, analysis, and formulation of the study. TM was responsible for the inversion, as well as contribution to the writing and analysis. JGFC contributed to the formulation and literature background. JC provided resources. All authors contributed to the article and approved the submitted version.

FUNDING

SS acknowledges the support of the Lamont-Doherty Fellowship in Earth and Environmental Sciences. TM acknowledges graduate funding support from the NSF grant EAR/#1615203. JGFC acknowledges the sponsorship of the National Research Center for Integrated Natural Disaster Management ANID/FONDAP/15110017, as well as grant no. 15090013 (Andean Geothermal Center of Excellence, CEGA).

ACKNOWLEDGMENTS

Many thanks to B. P. Bonner, B. Delbridge, P. Bhattacharya, A.M. Rubin, C. Marone, and R. Madariaga for fruitful discussions. Reviewer's comments also improved the manuscript.

SUPPLEMENTARY MATERIAL

The Supplementary Material for this article can be found online at: https://www.frontiersin.org/articles/10.3389/feart.2020.00373/full#supplementary-material

REFERENCES

Al-Bender, F., Lampaert, V., and Swevers, J. (2004). Modeling of dry sliding friction dynamics: from heuristic models to physically motivated models and back. *CHAOS* 14, 446–460. doi: 10.1063/1.1741752

Aström, K.. J., and De Wit, C. C. (2008). Revisting the LuGre friction model. *IEEE Control Systems Magazine.* 28, 101-114. doi: 10.1109/MCS.2008.929425

Boitnott, G. N., Biegel, R. L., and Scholz, C. H. (1992). Micromechanics of rock friction 2: quantitative modeling initial friction with contact theory. *J. Geophys. Res.* 97, 8965–8978. doi: 10.1029/92JB00019

Brodsky, E. E., Mori, J. J., Anderson, L., Chester, F. M., Conin, M., Dunham, E. M., et al. (2020). The state of stress before, during, and after a major earthquake. *Annu. Rev. Earth Planet. Sci.* 48, 2.1–2.26. doi: 10.1146/annurev-earth-053018-060507

Brune, J. N. (1970). Tectonic stress and the spectra of seismic shear waves from earthquakes. *J. Geophys. Res.* 75, 4997–5009. doi: 10.1029/JB075i026p04997

Chang, J. C., Lockner, D. A., and Reches, Z. (2012). Rapid acceleration leads to rapid weakening in earthquake-like laboratory experiments. *Science* 338, 101–105. doi: 10.1126/science.1221195

Chen, X., Carpenter, B. M., and Reches, Z. (2020). Asperity failure control of stick–slip along brittle faults. *Pure Appl. Geophys.* 117, 3225–3242. doi: 10.1007/s00024-020-02434-y

Dahl, P. R. (1968). *A Solid Friction Model. No. TOR-0158 (3107-18)-1.* El Segundo, CA: The Aerospace Corporation.

Dahl, P. R. (1976). Solid friction damping in mechanical vibrations. *AIAA J.* 14, 1675–1682. doi: 10.2514/3.61511

de Wit, C. C., Olsson, H., Astrom, K. J., and Lischinsky, P. (1993). "Dynamic friction models and control design," in *1993 American Control Conference* (San Francisco, CA: IEEE), 1920–1926.

Di Toro, G., Goldsby, D. L., and Tullis, T. E. (2004). Friction falls towards zero in quartz rock as slip velocity approaches seismic rates. *Nature* 427, 436–439. doi: 10.1038/nature02249

Dieterich, J. H. (1979). Modeling of rock friction: 1. Experimental results and constitutive equations. *J. Geophys. Res.* 84, 2161–2168. doi: 10.1029/JB084iB05p02161

Drincic, B., and Bernstein, D. S. (2012). A frictionless bristle-based friction model that exhibits hysteresis and stick-slip behavior. *J. Sound Vibrat.* doi: 10.1109/ACC.2011.5991180

Goldsby, D. L., and Tullis, T. (2011). Flash heating leads to low frictional strength of crustal rocks at earthquake slip rates. *Science* 334, 216–218. doi: 10.1126/science.1207902

Haessig, D. A., and Friedland, B. (1991). On the modeling and simulation of friction. *J. Dyn. Sys. Meas. Control.* 113, 354–362. doi: 10.1115/1.2896418

Heaton, T. H. (1990). Evidence for and implications of self-healing pulses of slip in earthquake rupture. *Phys. Earth Planet. Inter.* 64, 1–20. doi: 10.1016/0031-9201(90)90002-F

Hirose, T., and Shimamoto, T. (2005). Growth of a molten zone as a mechanism of slip weakening of simulated faults in gabbro during frictional melting. *J. Geophys. Res.* 110:B05202. doi: 10.1029/2004JB003207

Hung, C. C., Kuo, L. W., Spagnuolo, E., Wang, C. C., Di Toro, G., Wu, W. J., et al. (2019). Grain fragmentation and frictional melting during initial experimental deformation and implications for seismic slip at shallow depths. *J. Geophys. Res. Solid Earth* 124, 11150–11169. doi: 10.1029/2019JB017905

Ji, C., Helmberger, D. V., Wald, D. J., and Ma, K. F. (2003). Slip history and dynamic implications of the 1999 Chi-Chi, Taiwan, earthquake. *J. Geophys. Res.* 108:2412. doi: 10.1029/2002JB001764

Kitajima, H., Chester, F. M., and Chester, J. S. (2011). Dynamic weakening of gouge layers in high-speed shear experiments: Assessment of temperature-dependent friction, thermal pressurization, and flash heating. *J. Geophys. Res. Solid Earth* 116, 1–19. doi: 10.1029/2010JB007879

Lapusta, N. (2009). Seismology: the roller coaster of fault friction. *Nat. Geosci.* 2:676. doi: 10.1038/ngeo645

Latour, S., Schubnel, A., Nielsen, S., Madariaga, R., and Vinciguerra, S. (2013). Characterization of nucleation during laboratory earthquakes. *Geophys. Res. Lett.* 40, 5064–5069. doi: 10.1002/grl.50974

Liao, Z., and Reches, Z. E. (2019). An experimentally-based friction law for high-velocity, long-displacement slip-pulse events during earthquakes. *Earth Planet. Sci. Lett.* 515, 209–220. doi: 10.1016/j.epsl.2019.03.032

Liu, Y. F., Li, J., Zhang, Z. M., Hu, X. H., and Zhang, W. J. (2015). Experimental comparison of five friction models on the same test-bed of the micro stick-slip motion system. *Mech. Sci.* 6, 15–28. doi: 10.5194/ms-6-15-2015

Lyu, Z., Riviere, J., Yang, Q., and Marone, C. (2019). On the mechanics of granular shear: the effect of normal stress and layer thickness on stick-slip properties. *Tectonophysics* 763, 86–99. doi: 10.1016/j.tecto.2019.04.010

McLaskey, G. C., Kilgore, B. D., and Beeler, N. M. (2015). Slip-pulse rupture behavior on a 2 m granite fault. *Geophys. Res. Lett.* 42, 7039–7045. doi: 10.1002/2015GL065207

Mindlin, R. D. (1949). Compliance of elastic bodies in contact. *J. Appl. Mech.* 6, 259–268.

Niemeijer, A., Di Toro, G., Nielsen, S., and Di Felice, F. (2011). Frictional melting of gabbro under extreme experimental conditions of normal stress, acceleration, and sliding velocity. *J. Geophys. Res.* 116:B07404. doi: 10.1029/2010JB008181

Passelègue, F. X., Schubnel, A., Nielsen, S., Bhat, H. S., Deldicque, D., and Madariaga, R. (2016). Dynamic rupture processes inferred from laboratory microearthquakes. *J. Geophys. Res. Solid Earth* 121, 4343–4365. doi: 10.1002/2015JB012694

Pennestrì, E., Rossi, V., Salvini, P., and Valentini, P. P. (2016). Review and comparison of dry friction force models. *Nonlinear Dynam.* 83, 1785–1801. doi: 10.1007/s11071-015-2485-3

Rattez, H., and Veveakis, E. (2019). Weak phases production and heat generation controls fault friction during seismic slip. *Nat. Commun.* 11:350. doi: 10.31223/osf.io/xupr8

Reches, Z., and Lockner, D. A. (2010). Fault weakening and earthquake instability by powder lubrication *Nature* 467, 452–455. doi: 10.1038/nature09348

Rice, J. R. (1999). Flash heating at asperity contacts and rate-dependent friction. *Eos Trans. AGU Fall Meet. Suppl.* 80:F681.

Roeloffs, E. A. (2006). Evidence for aseismic deformation rate changes prior to earthquakes. *Annu. Rev. Earth Planet. Sci.* 34, 591–627. doi: 10.1146/annurev.earth.34.031405.124947

Rubino, V., Rosakis, A. J., and Lapusta, N. (2017). Understanding dynamic friction through spontaneously evolving laboratory earthquakes. *Nat. Commun.* 8:15991. doi: 10.1038/ncomms15991

Saltiel, S., Bonner, B. P., and Ajo-Franklin, J. B. (2017a). Strain-dependent partial slip on rock fractures under seismic-frequency torsion. *Geophys. Res. Lett.* 44, 4756–4764. doi: 10.1002/2017GL073108

Saltiel, S., Bonner, B. P., Mittal, T., Delbridge, B., and Ajo-Franklin, J. (2017b). Experimental evidence for dynamic friction on rock fractures from frequency-dependent nonlinear hysteresis and harmonic generation. *J. Geophys. Res. Solid Earth* 122, 4982–4999. doi: 10.1002/2017JB014219

Scholz, C. H. (2019). *The Mechanics of Earthquakes and Faulting, 3rd Edn.* Cambridge: Cambridge University Press.

Selvadurai, P. A., Parker, J. M., and Glaser, S. D. (2017). Numerical modeling describing the effects of heterogeneous distributions of asperities on the quasi-static evolution of frictional slip. *Rock Mech. Rock Eng.* 50, 3323–3335. doi: 10.1007/s00603-017-1333-9

Socquet, A., Valdes, J. P., Jara, J., Cotton, F., Walpersdorf, A., Cotte, N., et al. (2017). An 8 month slow slip event triggers progressive nucleation of the 2014 Chile megathrust. *Geophys. Res. Lett.* 44, 4046–4053. doi: 10.1002/2017GL073023

Sone, H., and Shimamoto, T. (2009). Frictional resistance of faults during accelerating and decelerating earthquake slip. *Nat. Geosci.* 2:705. doi: 10.1038/ngeo637

Stribeck, R. (1902). Die wesentlichen eigenschaften der gleit- und rollenlager – The key qualities of sliding and roller bearings. *Z. Vereines Seutscher Ing.* 48, 1342–1348, 1432–1437.

Svetlizky, I., Bayart, E., and Fineberg, J. (2018). Brittle fracture theory describes the onset of frictional motion. *Annu. Rev. Condens. Matter Phys.* 10, 253–273. doi: 10.1146/annurev-conmatphys-031218-013327

Tinti, E., Fukuyama, E., Piatanesi, A., and Cocco, M. (2005). A kinematic source-time function compatible with earthquake dynamics. *Bull. Seismol. Soc. Am.* 95, 1211–1223. doi: 10.1785/0120040177

Van der Elst, N. J., Brodsky, E. E., Le Bas, P. Y., and Johnson, P. A. (2012). Auto-acoustic compaction in steady shear flows: experimental evidence for suppression of shear dilatancy by internal acoustic vibration. *J. Geophys. Res. Solid Earth* 117:04. doi: 10.1029/2011JB008897

Violay, M., Nielsen, S., Spagnuolo, E., Cinti, D., Di Toro, G., and Di Stefano, G. (2013). Pore fluid in experimental calcite-bearing faults: abrupt weakening and geochemical signature of co-seismic processes. *Earth Planet. Sci. Lett.* 361, 74–84. doi: 10.1016/j.epsl.2012.11.021

Violay, M., Passelegue, F., Spagnuolo, E., Di Toro, G., and Cornelio, C. (2019). Effect of water and rock composition on re-strengthening of cohesive faults during the deceleration phase of seismic slip pulses. *Earth Planet. Sci. Lett.* 522, 55–64. doi: 10.1016/j.epsl.2019.06.027

Wald, D. J. (1996). Slip history of the 1995 Kobe, Japan, earthquake determined from strong motion, teleseismic, and geodetic data. *J. Phys. Earth* 44, 489–503. doi: 10.4294/jpe1952.44.489

Conflict of Interest: The authors declare that the research was conducted in the absence of any commercial or financial relationships that could be construed as a potential conflict of interest.

Copyright © 2020 Saltiel, Mittal, Crempien and Campos. This is an open-access article distributed under the terms of the Creative Commons Attribution License (CC BY). The use, distribution or reproduction in other forums is permitted, provided the original author(s) and the copyright owner(s) are credited and that the original publication in this journal is cited, in accordance with accepted academic practice. No use, distribution or reproduction is permitted which does not comply with these terms.

frontiers in Earth Science

PERSPECTIVE
published: 21 October 2020
doi: 10.3389/feart.2020.585733

Multi-Level Gas Monitoring: A New Approach in Earthquake Research

Heiko Woith[1], Kyriaki Daskalopoulou[1], Martin Zimmer[1], Tomáš Fischer[2], Josef Vlček[2], Jakub Trubač[2], Jan-Erik Rosberg[3], Tomáš Vylita[2] and Torsten Dahm[1]*

[1]GFZ German Research Centre for Geosciences, Potsdam, Germany, [2] Faculty of Science, Charles University, Prague, Czech Republic, [3] Lund University, Lund, Sweden

Fluid anomalies were often considered as possible precursors before earthquakes. However, fluid properties at the surface can change for a variety of reasons, including environmental changes near the surface, the response of the superficial fluid system to loads associated with the mechanical nucleation of earthquake fractures, or as a result of transients in fluid flow from the depths. A key problem is to understand the origin of the anomaly and to distinguish between different causes. We present a new approach to monitor geochemical and geophysical fluid properties along a vertical profile in a set of drillings from a depth of a few hundred meters to the surface. This setup can provide hints on the origin of temporal variations, as the migration direction and speed of properties can be measured. In addition, potential admixtures of fluids from a deep crustal or mantle origin with meteoric fluids can be better quantified. A prototype of a multi-level gas monitoring system comprising flow and pressure probes, as well as monitoring of fluid-geochemical properties and stable isotopes is being implemented in a mofette field with massive CO_2 (up to 97 tons per day) degassing. The mofette is believed a gas emission site where CO_2 ascends through crustal-scale conduits from as deep as the upper mantle, and may therefore provide a natural window to ongoing magmatic processes at mantle depth. Fluids from three adjacent boreholes—30, 70, and 230 m deep—will be continuously monitored at high sampling rates.

Keywords: mantle degassing, crustal fluids, gas monitoring, radon, swarm earthquakes, scientific drilling

OPEN ACCESS

Edited by:
Giovanni Martinelli, National Institute of Geophysics and Volcanology, Section of Palermo, Italy

Reviewed by:
Fuqiong Huang, China Earthquake Networks Center, China
Naoji Koizumi, University of Shiga Prefecture, Japan

****Correspondence:***
Heiko Woith
heiko.woith@gfz-potsdam.de

Specialty section:
This article was submitted to Solid Earth Geophysics, a section of the journal Frontiers in Earth Science

Received: *21 July 2020*
Accepted: *18 September 2020*
Published: *21 October 2020*

Citation:
Woith H, Daskalopoulou K, Zimmer M, Fischer T, Vlček J, Trubač J, Rosberg J-E, Vylita T and Dahm T (2020) Multi-Level Gas Monitoring: A New Approach in Earthquake Research. Front. Earth Sci. 8:585733. doi: 10.3389/feart.2020.585733

INTRODUCTION

The majority of earthquake precursor studies follow a simple scheme: identify an anomaly in a timeseries (often defined as values above 2, 3, or 4 standard deviations) and then relate it one-on-one to a selected earthquake (see anomaly-earthquake compilation in Cicerone et al. (2009)). The selection of the earthquake is often arbitrary. If a magnitude-distance relation is discussed at all, the precursory strain impact at the monitoring site is often calculated according to a formula presented by Dobrovolsky et al. (1979), which according to our present-day knowledge over-estimates the size of the earthquake preparation zone significantly (Woith et al., 2018). Only few studies were truly multi-disciplinary, which is fundamental to understand the physics of earthquakes. A positive example is the design of the "Alto Tiberina Near Fault Observatory" in the northern Appenines, Italy (Chiaraluce et al., 2014). Another key problem with potentially precursory anomalies in timeseries is the correct interpretation of their origin. An anomaly physically related to the build-up of strain and stress before an earthquake might look strikingly similar to an anomaly caused by external drivers like rainfall (Woith, 2015). A typical approach to eliminate external signals from a timeseries is to use

regressive models to predict the impact of environmental processes (like rainfall or groundwater changes) on the signal of interest. Zmazek et al. (2003) used decision trees to predict soil radon concentrations from meteorological parameters and then compared the predicted vs. the actually observed radon values. Sabbarese et al. (2020) applied a hybrid method—combining multiple linear regression, empirical mode decomposition, and support vector regression—to identify residuals and trends of radon timeseries from Campi Flegrei. A long-term increasing radon trend correlated with vertical displacement, increasing background seismicity, as well as the calculated increasing pressure and temperature of the hydrothermal system. The radon residuals correlated with tremors recorded at a fumarole. Unfortunately, such good examples of a process-oriented multi-disciplinary investigation are the exception rather than the rule. Furthermore, even after the most careful and thoroughly data correction, the evidence that a trend or an anomaly is physically related to a seismo-tectonic process remains an indirect one.

A totally new perspective of a vertical array of continuous multi-parameter fluid sampling is suggested. Japanese scientists implemented a similar borehole-based concept in their most modern earthquake research observatories, which consist of three observation wells drilled to depths of 30, 200, and 600 m (Matsumoto and Koizumi, 2013) tapping one shallow, unconfined as well as two confined aquifers. The wells are equipped with seismometers, groundwater level and temperature sensors at all three depth levels, plus tilt and strain meters usually at the deepest level. The idea is to identify strain transients in the crust, specifically to understand the groundwater response to crustal deformation related to episodic slow-slip events (Itaba et al., 2010). We adapt this idea, adding fluid geochemical composition and CO_2 isotopic signatures to the online monitoring of geophysical parameters. This will help to distinguish the different origins of anomalies and to separate down- and upward migrating transients in the fluid system analog to observations already made by Hatuda (1953). Hatuda measured the radon concentration of soil air from 0.6, 1, and 2 m depth once a day for more than 2 years and noted about an earthquake-related anomaly *"the deeper the sampling site was, the greater proportionately was the increase in concentration, an instance opposite to the case where meteorological influences are at work"*.

MULTI-LEVEL GAS MONITORING

Strategy

The strategy is to monitor the gas composition and its isotopic signature continuously at different depth levels. If the fluid composition changes at depth—e.g., due to the admixture of crustal components to an otherwise steady mantle degassing during swarm earthquakes as proposed by Weise et al. (2001) for our investigation area—it will take a certain amount of time until the changes can be detected at the Earth's surface. The time delay depends on the velocity of the rising fluids. In a comprehensive review, Etiope and Martinelli (2002) compared the effectiveness of gas migration processes in the geosphere. Neither diffusion (with average velocities below 10^{-2} m/day), nor groundwater advection can explain fast vertical gas migration. Instead, in permeable rocks with fracture apertures within the range between 0.01 and 10 mm, advective migration of gas with velocities between 1 and 1,000 m/day is feasible. At Mammoth Mountains, Sorey et al. (1998) suggested velocities of the order of 10–40 m/day for the transport of CO_2/helium from a depth of 2–4 km. Slightly higher values were obtained by Lewicki et al. (2014), who concluded that CO_2 migrated from a depth of about 20 km to the surface at Mammoth Mountains in less than a year, corresponding to a velocity of 50+ m/day. Six months before the eruption of Usu volcano the CO_2 flux increased significantly in the summit caldera (Hernandez et al., 2001). Seismic data indicated magma 4 km below the summit, which yields a migration velocity of about 20 m/day. A CO_2 increase was also observed 50 d before the El Hierro eruption (Peréz et al., 2012), indicating a fluid velocity of the order of 100 m/day. For the Cheb Basin, gas migration velocities are rather uncertain. While the estimates of Weise et al. (2001) and Bräuer et al. (2003) range between 50 and 400 m/day for fractured basement rocks (granites, phyllites), the fast and long-term postseismic gas flow increase in the Hartoušov mofette (Fischer et al., 2017) points to velocities more than 2 km/day. If we assume similar fluid transport velocities for the subsurface, the delay time between the deepest well (230 m) and the surface would be somewhere in the range between several days and few hours. Thus, with a measurement interval of fractions of an hour we should be able to detect transients coming from below. The same logic applies to changes coming from above, i.e. changes induced by rain, snowmelt, and water level changes in shallow aquifers.

Technical Setup

Hartoušov mofette field is located in the Cheb Basin (West Bohemia) and is known for intense mantle-CO_2 degassing and nearby recurring earthquake swarms (**Figure 1A**) (Fischer et al., 2014; Bräuer et al., 2018). Estimated daily CO_2 flux of up to 97 t over an area of about 350,000 m^2 (Nickschick et al., 2015) and long-term monitoring of gas flow in shallow borehole F1 made it a key site to study fluid-earthquake-interactions in the frame of ICDP Project: "Drilling the Eger Rift: Magmatic fluids driving the earthquake swarms and the deep biosphere" (Dahm et al., 2013). Three adjacent boreholes have been drilled about 90 m NW of a natural mofette (**Figure 1B**): F1, F2, and F3 to a depth of 28.2, 108.5, and 239.3 m, respectively. F1 was drilled in 2007 and taps a CO_2-rich shallow aquifer; a plastic casing of 115 mm is perforated between 20 and 28 m. Gas flow measurements started in 2009 (Fischer et al., 2020). F2 was drilled in 2016 to study geo-bio interactions in extreme environments (Bussert et al., 2017). At a depth of 78.5 m a CO_2 blowout occurred. Following a pumping test, which produced a mixture of gas and mineralized water, the well was closed and the wellhead pressure of about 500 kPa remained stable, except for two events of unknown origin in July 2016 when the pressure dropped to 50 kPa within hours before returning to the pre-event level after some days. In September 2019, a set of sensors was installed in F2 as shown

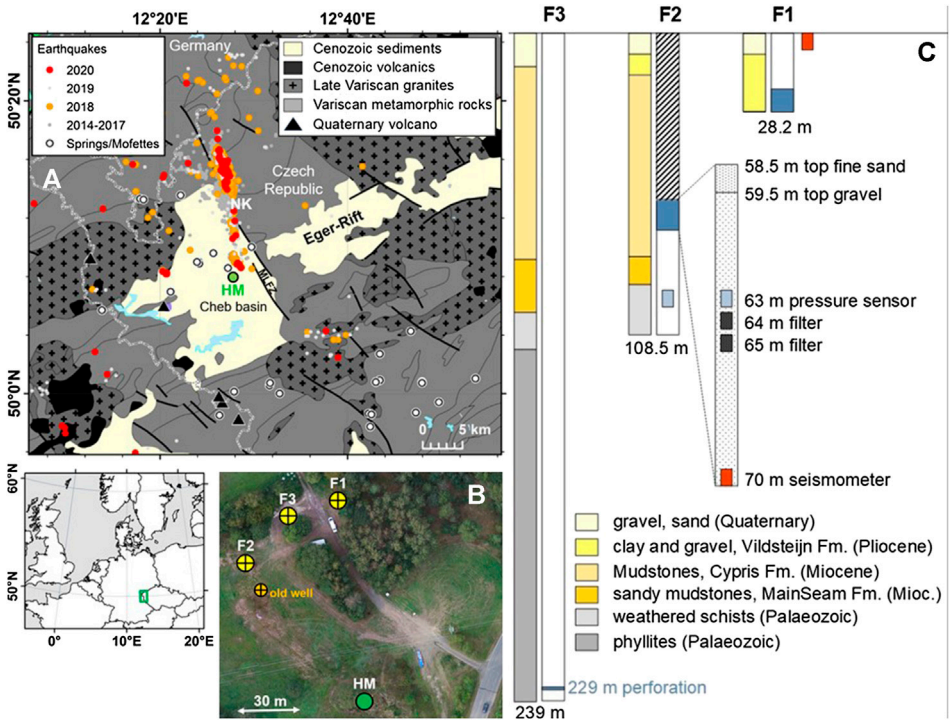

FIGURE 1 | Technical set-up of the multi-level gas monitoring system. **(A)** Geological map [simplified from the "Geological Map of Germany 1:1,000,000 (GK1000)", BGR] showing the position of the Hartoušov mofette (HM) in the Eger-Rift. White circles mark mofettes and springs with CO_2 > 1 g/L. Orange and red dots depict seismic activity during 2018 and 2020, respectively. NK – Nový Kostel focal zone **(B)** Bird's view of the boreholes and the natural Hartoušov mofette, **(C)** simplified lithological section of boreholes F1, F2, and F3. Sensor configuration of F2. Perforated sections of the wells are marked in blue.

in **Figure 1C**. Within 3 years after the drilling, the lowermost part of the borehole obviously filled up with sediments. Thus, a borehole seismometer (ASIR AFF1.005) was installed at the deepest possible position at 70 m. At 65 and 64 m two stainless-steel filters were fixed and connected to capillary tubes of 4 mm inner diameter. Finally, a pressure sensor (KELLER PAA36-XW) was placed at a depth of 63 m before the instrumented borehole section was filled with gravel and 1 m of fine sand on top. The uppermost part of the well was filled with cement. In August 2019, F3 was drilled half-way between F1 and F2 and various gas-bearing horizons have been encountered between 110 m and the final depth of 238 m.

Instrumentation for the on-site gas analysis is installed at F1 and comprises a QMS (Omnistar Quadrupole Mass Spectrometer by Pfeiffer Vacuum), an infrared gas analyser (DeltaRay by Thermo-Fischer), and three radon detectors (by GFZ)—one for each well. QMS measures the gas composition, i.e. H_2, He, CO_2, Ar, N_2, O_2, and CH_4, whereas the DeltaRay measures CO_2, $\delta^{13}C$, and $\delta^{18}O$. A multi-valve is connected to F1, F2, and F3 via capillary tubes and thus it is possible to measure all three wells with one set of instruments one after the other in a cycling mode. For details of the applied techniques the reader is referred to Zimmer et al. (2011 and 2018). Given CO_2 concentrations above 99.5%, small changes in the CO_2 concentration will be difficult, if not impossible, to detect. Hence, monitoring and recording the temporal variations of the other gas components found in minor abundances is crucial. Discrete fluid sampling complements the online monitoring program including noble gases, specifically the $^3He/^4He$ and $^4He/^{20}Ne$ ratios.

Additional to the gas monitoring equipment, the following instruments are installed:

- A weather station (Vaisala WXT536) records meteorological standard parameters.
- A broadband seismometer (Trillium Compact 120″) is installed outside of F1.
- At F1 the gas flow is recorded with a drum gas counter (RITTER), water temperature and water level/pressure is measured at three different depth levels. The gas pressure is measured in the wellhead. Details are given in Fischer et al. (2020).
- At F2 fluid pressure is measured at a depth of 92 and 63 m. A borehole seismometer was installed at 70 m.
- F3 instrumentation will be completed similar to F2, if technically feasible.

First Results

We present measurements obtained during the drilling phase of the deepest borehole F3. The most important aim of the F3 drilling was to find additional CO_2-bearing strata below 100 m. Drill-site selection was difficult despite various geophysical pre-site surveys. From the analysis of noise tremors using matched

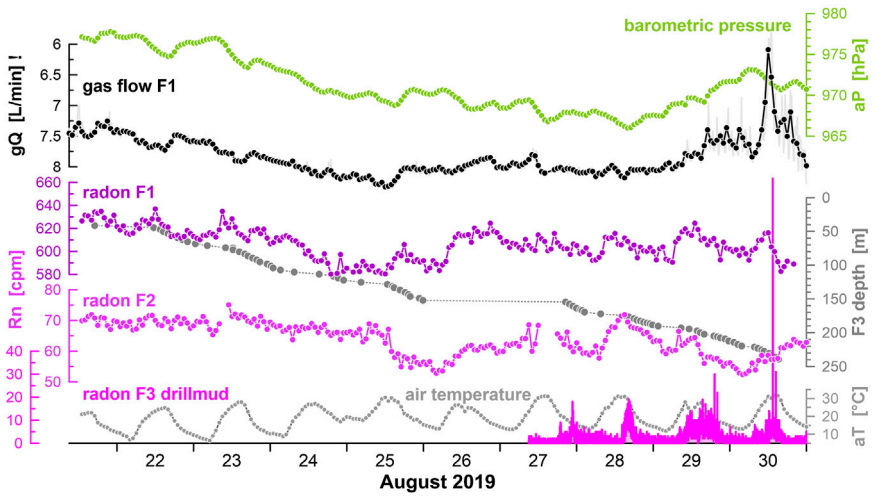

FIGURE 2 | Hourly averages of barometric pressure, gas flow rate of F1, radon concentration of F1 and F2 as well as in the drillmud of F3 (1-min raw data), and air temperature during the drilling phase. Note the inverted *Y*-axis of the gas flow. Drill depths estimated from core-on-deck times.

field processing techniques Umlauft and Korn (2019) postulated a northward dipping fluid channel down to a depth of 100 m. The center of the noise anomaly at a depth of 100 m was located slightly east of the old well (see **Figure 1B**). Extrapolating this trend to greater depth indicated that the fluid channel is hit at a depth of about 200 m at the location of F3 (see **Figure 1B**). Interestingly, the surface CO_2 flux measurements by Nickschick et al. (2015) observed only moderate values at the F3 borehole position. Drilling operations started in August 2019. At first, two anchor pipes were cemented down to a depth of 15 and 40 m. Between 21 and August 30, 2019 drilling continued until a final depth of 239.3 m was reached. During all drilling operations, a blowout-preventer was used. Due to a heavy drillmud (1.15 g/cm^3) no gas eruptions were encountered. Cores of 83 mm were obtained; sub-samples for microbiological studies were deep-frozen on site. The borehole was completely cased with steel rods (ID about 78 mm) and cemented.

A further challenge was the selection of the perforation depth. Significant degassing of the fresh cores started at a depth of 110 m and was observed until the final depth with varying intensities. To identify the most promising CO_2-horizon a combination of different methods was applied: visual inspection of core material, fluid sampling from cores, online gas monitoring of the drillmud, and finally borehole logging of the open hole after the drilling was completed. Pyrite occurred prominently at 175 and 230 m depth, preferentially on interfaces (divisional surface) within the mica schists and might be indicative for the circulation of CO_2-rich fluids under reducing conditions (personal communication Robert Bussert, 2020). The core section 226–234 m was heavily fractured. Another hint for permeable, fluid-filled fractures was obtained from the online radon measurements of the drillmud, which showed a clear spike at a depth of about 230 m (**Figure 2**). The perforation of the steel casing was performed on January 15, 2020 at a depth of 229 m. On February 6, 2020 the water level of F3 was lowered to 15 m below the surface. Thereafter the wellhead was closed and a pressure built-up of 60 kPa was observed within the next 3 h. The test was repeated on March 10, 2020. Lowering the water level to 80 m resulted in a pressure increase of 120 kPa within 6 h.

An important question immediately arises: Are the boreholes hydraulically connected? Online monitoring revealed i) a fluid pressure transient of 10 kPa in F2 between 24 and August 25, 2019. The anomaly started when F3 reached a depth of about 110 m, i.e. when the first significant degassing of the cores could be observed, ii) a drop in the gas flow at F1 on 30 August while the radon concentration in the drillmud showed its maximum (**Figure 2**). The latter event coincides with a conductivity increase and a decreased redox potential at the natural mofette located about 90 m SE of the drillsite, both indicating the admixture of a mineralized deep fluid component to the low-conductivity shallow water typically present at the Hartoušov mofette. The raw data presented in **Figure 2** indicate similarities between the F1 gas flow and the radon concentrations in F1 and F2, which are likely due temperature and barometric pressure effects. Barometric pressure and gas flow at F1 are clearly anti-correlated. For an in-depth discussion about the environmental effects on the gas flow the reader may refer to Fischer et al. (2020). Radon in the drillmud of F3 seems to be unrelated to barometric pressure and air temperature variations (radon spikes occur at 00:00, 18:00, 21:00, and 15:00 local time). There was no rainfall except two small events around noon on 26 and 29 August with 5 and 2 mm of rain, respectively. Seismic activity could be ruled out to explain the described transients. During the drilling operation maximum co-seismic strains remained below one nanostrain, i.e. smaller than the Earth's tidal strain. That may change in future, because earthquakes migrated further to the south toward our monitoring site in recent years. The southernmost cluster of the Nový Kostel (NK) seismic zone occurs only 2–3 km NNE from the Hartoušov mofette and demonstrates increasing seismicity rate. Its activity culminated during the 2018 swarm by a short sequence reaching the magnitude of 3.1 in a cluster located about 3 km north

of Hartoušov mofette (see orange dots in **Figure 1**). This may, along with the ongoing southward migration of hypocenters in 2020 (see red dots in **Figure 1**), generate strains capable of interfering the gas paths from the depth to the surface.

DISCUSSION AND OUTLOOK

A prototype of a multi-level gas monitoring system installed at three wells tapping CO_2-horizons at 20, 65, and 229 m has been set-up in a mofette site. Seismometers and a weather station were installed on-site in order to quantify the impact of earthquakes as well as environmental effects on the fluid regime. Continuous radon measurements while drilling revealed a promising CO_2-horizion, which was later chosen for the perforation of the steel casing. Further hydraulic tests at F3 are needed to confirm whether the perforation was successful. Ultimately, a borehole seismometer will be installed at the bottom of F3 as well as a capillary tube to collect "fresh" gases from the CO_2-horizon at depth. It is very important to collect the gas directly at the point where the fluids enter the borehole. Otherwise the measurements might be affected by external processes like "barometric pumping" inside the open well as described by Zafrir et al. (2016).

It is fair to note, that the complex geological underground at the Hartoušov mofette makes a proper measurement of a fluid gradient and thus a correct velocity estimate demanding. Fluid flow is assumed to preferentially occur along fractures or channels which may change in time. Miller and Nur (2000) noted that the local permeability can change instantaneously from extremely low to extremely high values. For the Hartoušov mofette field, evidences that the degassing pattern is highly dynamic in space and time were already provided by Nickschick et al. (2015), who found variations between 1 and 100 g/m^2 per day. Flores Estrella et al. (2016) revealed from repeated seismic array measurements changes in the flow pattern from 1 day to the next. What causes short-term pressure transients (in the order of days) observed in mofettes? Weinlich (2014) observed sharp CO_2 peaks in the Soos mofette—located less than 5 km WNW of Hartoušov—lasting less than 24 h. Either sudden fault permeability changes or pressure pulses induced by fault movements were discussed based on the short duration of the anomalies, but not finally proven. The seismic sequence of October 2008 and May 2014 triggered a fast and steady increase of CO_2 flow monitored at the F1 borehole in the Hartoušov mofette field (Fischer et al., 2017). Contrary, the same mofette did not respond either to the 2011 earthquake swarm or to the most recent swarms of 2017 and 2018. Is a threshold value needed to activate the postulated fault-valve mechanism? More data and experiments are needed to develop, constrain, and calibrate a hydro-mechanical model for the mofette system. Once our novel monitoring system is fully operational, fluid transients can be observed in great detail. We expect new insights into the physical processes that control the complex interplay between earthquakes, deep degassing, and permeability variations along the path to the surface.

DATA AVAILABILITY STATEMENT

The data analyzed in this study is subject to the following licenses/restrictions: Data related to the drilling operations are stored in the drilling information system (DIS) of the ICDP. After a short embargo time, the data will be made available at http://dataservices.gfz-potsdam.de/portal/. Requests to access these datasets should be directed to Heiko Woith, heiko.woith@gfz-potsdam.de.

AUTHOR CONTRIBUTIONS

HW, TF, and TD developed the conception and design of the study; JER was responsible for the scientific drilling of F3. TV provided valuable knowledge about the hydrogeology of the Cheb Basin and supervised the drilling process. KD and MZ setup the online measurements of the gas composition with a mass spectrometer, JV is responsible for gas flow and water level measurement, JT set-up the instrument for the onsite monitoring of the stable isotopes $\delta^{13}C$ and $\delta^{18}O$, while HW developed radon detectors used in this study; HW wrote the first draft of the manuscript. All authors contributed to manuscript revision, read and approved the submitted version.

FUNDING

Drilling operations have been funded by ICDP (International Continental Scientific Drilling Program) in the frame of the project "Drilling the Eger Rift: Magmatic fluids driving the earthquake swarms and the deep biosphere" and were partially supported also by GFZ. The infrared gas analyzer was obtained in the frame of the CzechGeo/EPOS-Sci infrastructure (CZ.02.1.01/0.0/0.0/16_013/0001800) co-funded by the EU Operational Program Research, Development and Education. This work is a part of MoRe—"Mofette Research"—project which was funded by the Deutsche Forschungsgemeinschaft (DFG, German Research Foundation)—419880416.

ACKNOWLEDGMENTS

We are grateful for constructive comments by two reviewers which helped to improve our manuscript. For technical guidance before and during the drilling we are grateful to Ulrich Harms, Thomas Wiersberg, Santiago Aldaz, and Jochem Kück of the operational support group of ICDP. Last, but not least we thank the international team of drillers from Protek Norr AB and PRUY KG, with special thanks to Danilo Pruy (Saxonia), Johan Kullenberg from Lund University/Riksriggen (Sweden), and Friðfinnur K Danielsson (Iceland).

REFERENCES

Bräuer, K., Kämpf, H., Niedermann, S., and Strauch, G. (2018). Monitoring of helium and carbon isotopes in the western Eger Rift area (Czech Republic): relationships with the 2014 seismic activity and indications for recent (2000-2016) magmatic unrest. *Chem. Geol.* 482, 131–145. doi:10.1016/j.chemgeo.2018.02.017.

Bräuer, K., Kämpf, H., Strauch, G., and Weise, S. M. (2003). Isotopic evidence (^{3}He/^{4}He, $^{13}C_{CO2}$) of fluid-triggered intraplate seismicity. *J. Geophys. Res., B* 108 (B2), 2070. doi:10.1029/2002JB002077.

Bussert, R., Kämpf, H., Flechsig, C., Hesse, K., Nickschick, T., Liu, Q., et al. (2017). Drilling into an active mofette: pilot-hole study of the impact of CO_2-rich mantle-derived fluids on the geo-bio interaction in the western Eger Rift (Czech Republic). *Sci. Dril.* 23, 13–27. doi:10.5194/sd-23-13-2017.

Chiaraluce, L., Amato, A., Carannante, S., Castelli, V., Cattaneo, M., Cocco, M., et al. (2014). The Alto Tiberina near fault observatory (northern Apennines, Italy). *Ann. Geophys.* 57 (3), 16. doi:10.4401/ag-6426.

Cicerone, R. D., Ebel, J. E., and Britton, J. (2009). A systematic compilation of earthquake precursors. *Tectonophysics* 476 (3–4), 371–396. doi:10.1016/j.tecto.2009.06.008.

Dahm, T., Hrubcová, P., Fischer, T., Horálek, J., Korn, M., Buske, S., et al. (2013). Eger Rift ICDP: an observatory for study of non-volcanic, mid-crustal earthquake swarms and accompanying phenomena. *Sci. Dril.* 16, 93–99. doi:10.5194/sd-16-93-2013.

Dobrovolsky, I. P., Zubkov, S. I., and Miachkin, V. I. (1979). Estimation of the size of earthquake preparation zones. *Pure Appl. Geophys.* 117 (5), 1025–1044. doi:10.1007/BF00876083.

Etiope, G., and Martinelli, G. (2002). Migration of carrier and trace gases in the geosphere: an overview. *Phys. Earth Planet. Inter.* 129 (3–4), 185–204. doi:10.1016/S0031-9201(01)00292-8.

Fischer, T., Horálek, J., Hrubcová, P., Vavryčuk, V., Bräuer, K., and Kämpf, H. (2014). Intra-continental earthquake swarms in West-Bohemia and Vogtland: a review. *Tectonophysics* 611, 1–27. doi:10.1016/j.tecto.2013.11.001.

Fischer, T., Matyska, C., and Heinicke, J. (2017). Earthquake-enhanced permeability—evidence from carbon dioxide release following the M L 3.5 earthquake in West Bohemia. *Earth Planet Sci. Lett.* 460, 60–67. doi:10.1016/j.epsl.2016.12.001

Fischer, T., Vlček, J., and Lanzendörfer, M. (2020). Monitoring crustal CO_2 flow: methods and their applications to the mofettes in West Bohemia. *Solid Earth.* 11, 983–998. doi:10.5194/se-11-983-2020.

Flores Estrella, H., Umlauft, J., Schmidt, A., and Korn, M. (2016). Locating mofettes using seismic noise records from small dense arrays and matched field processing analysis in the NW Bohemia/Vogtland Region, Czech Republic. *Near Surf. Geophys.* 14 (4), 327–335. doi:10.3997/1873-0604.2016024.

Hatuda, Z. (1953). Radon content and its change in soil air near the ground surface. *Mem. College Sci., Univ. Kyoto, Series B* 20 (4), 285–306.

Hernandez, P. A., Notsu, K., Salazar, J. M., Mori, T., Natale, G., Okada, H., et al. (2001). Carbon dioxide degassing by advective flow from Usu Volcano, Japan. *Science* 292 (5514), 83–86. doi:10.1126/science.1058450

Itaba, S., Koizumi, N., Matsumoto, N., and Ohtani, R. (2010). Continuous observation of groundwater and crustal deformation for forecasting Tonankai and Nankai earthquakes in Japan. *Pure Appl. Geophys.* 167 (8–9), 1105–1114. doi:10.1007/s00024-010-0095-z.

Lewicki, J. L., Hilley, G. E., Shelly, D. R., King, J. C., McGeehin, J. P., Mangan, M., et al. (2014). Crustal migration of CO2-rich magmatic fluids recorded by tree-ring radiocarbon and seismicity at Mammoth Mountain, CA, USA. *Earth Planet Sci. Lett.* 390, 52–58. doi:10.1016/j.epsl.2013.12.035.

Matsumoto, N., and Koizumi, N. (2013). Recent hydrological and geochemical research for earthquake prediction in Japan. *Nat. Hazards.* 69 (2), 1247–1260. doi:10.1007/s11069-011-9980-8.

Miller, S. A., and Nur, A. (2000). Permeability as a toggle switch in fluid-controlled crustal processes. *Earth Planet Sci. Lett.* 183 (1–2), 133–146. doi:10.1016/s0012-821x(00)00263-6

Nickschick, T., Kämpf, H., Flechsig, C., Mrlina, J., and Heinicke, J. (2015). CO_2 degassing in the Hartoušov mofette area, western Eger Rift, imaged by CO_2 mapping and geoelectrical and gravity surveys. *Int. J. Earth Sci.* 104 (8), 2107–2129. doi:10.1007/s00531-014-1140-4.

Pérez, N. M., Padilla, G. D., Padrón, E., Hernández, P. A., Melián, G. V., Barrancos, J., et al. (2012). Precursory diffuse CO_2 and H_2S emission signatures of the 2011–2012 El Hierro submarine eruption, Canary Islands. *Geophys. Res. Lett.* 39 (16), L16311. doi:10.1029/2012GL052410.

Sabbarese, C., Ambrosino, F., Chiodini, G., Giudicepietro, F., Macedonio, G., Caliro, S., et al. (2020). Continuous radon monitoring during seven years of volcanic unrest at Campi Flegrei caldera (Italy). *Sci. Rep.* 10 (1), 9551. doi:10.1038/s41598-020-66590-w.

Sorey, M. L., Evans, W. C., Kennedy, B. M., Farrar, C. D., Hainsworth, L. J., and Hausback, B. (1998). Carbon dioxide and helium emissions from a reservoir of magmatic gas beneath Mammoth Mountain, California. *J. Geophys. Res.* 103 (B7), 15303–15323. doi:10.1029/98jb01389

Umlauft, J., and Korn, M. (2019). 3-D fluid channel location from noise tremors using matched field processing. *Geophys. J. Int.* 219 (3), 1550–1561. doi:10.1093/gji/ggz385.

Weinlich, F. H. (2014). Carbon dioxide controlled earthquake distribution pattern in the NW Bohemian swarm earthquake region, western Eger Rift, Czech Republic—gas migration in the crystalline basement. *Geofluids* 14 (2), 143–159. doi:10.1111/gfl.12058.

Weise, S. M., Bräuer, K., Kämpf, H., Strauch, G., and Koch, U. (2001). Transport of mantle volatiles through the crust traced by seismically released fluids: a natural experiment in the earthquake swarm area Vogtland/NW Bohemia, Central Europe. *Tectonophysics* 336 (1–4), 137–150. doi:10.1016/s0040-1951(01)00098-1

Woith, H. (2015). Radon earthquake precursor: a short review. *Eur. Phys. J. Spec. Top.* 224 (4), 611–627. doi:10.1140/epjst/e2015-02395-9.

Woith, H., Petersen, G. M., Hainzl, S., and Dahm, T. (2018). Review: can animals predict earthquakes? *Bull. Seismol. Soc. Am.* 108 (3A), 1031–1045. doi:10.1785/0120170313.

Zafrir, H., Ben Horin, Y., Malik, U., Chemo, C., and Zalevsky, Z. (2016). Novel determination of radon-222 velocity in deep subsurface rocks and the feasibility to using radon as an earthquake precursor. *J. Geophys. Res. Solid Earth.* 121 (9), 6346–6364. doi:10.1002/2016jb013033.

Zimmer, M., Erzinger, J., and Kujawa, C., and CO2SINK-Group (2011). The gas membrane sensor (GMS): a new method for gas measurements in deep boreholes applied at the CO2SINK site. *Int. J. Greenhouse Gas Control.* 5 (4), 995–1001. doi:10.1016/j.ijggc.2010.11.007.

Zimmer, M., Szizybalski, A., Norden, B., Vieth-Hillebrand, A., and Liebscher, A., and the Ketzin Group (2018). Monitoring of the gas composition and stable carbon isotopes during side track drilling in Ktzi 203 at the Ketzin CO_2 storage pilot site, Germany. *Adv. Geosci.* 45, 7–11. doi:10.5194/adgeo-45-7-2018.

Zmazek, B., Todorovski, L., Džeroski, S., Vaupotič, J., and Kobal, I. (2003). Application of decision trees to the analysis of soil radon data for earthquake prediction. *Appl. Radiat. Isot.* 58 (6), 697–706. doi:10.1016/s0969-8043(03)00094-0

Conflict of Interest: The authors declare that the research was conducted in the absence of any commercial or financial relationships that could be construed as a potential conflict of interest.

Copyright © 2020 Woith, Daskalopoulou, Zimmer, Fischer, Vlček, Trubač, Rosberg, Vylita and Dahm. This is an open-access article distributed under the terms of the Creative Commons Attribution License (CC BY). The use, distribution or reproduction in other forums is permitted, provided the original author(s) and the copyright owner(s) are credited and that the original publication in this journal is cited, in accordance with accepted academic practice. No use, distribution or reproduction is permitted which does not comply with these terms.

frontiers in Earth Science

BRIEF RESEARCH REPORT
published: 29 October 2020
doi: 10.3389/feart.2020.595209

On the Long Range Clustering of Global Seismicity and its Correlation With Solar Activity: A New Perspective for Earthquake Forecasting

Vito Marchitelli[1,2], *Claudia Troise*[3,4], *Paolo Harabaglia*[1]*, *Barbara Valenzano*[2] and *Giuseppe De Natale*[3,4]

[1] Scuola di Ingegneria, Università Della Basilicata, Potenza, Italy, [2] Department of Mobility, Urban Quality, Public Works, Ecology and the Environment, Puglia Region Government, Bari, Italy, [3] Istituto Nazionale di Geofisica e Vulcanologia, Naples, Italy, [4] CNR-INO, Pozzuoli, Italy

Large earthquakes occurring worldwide have long been recognized to be non Poisson distributed, so involving some large scale correlation mechanism, which could be internal or external to the Earth. We have recently demonstrated this observation can be explained by the correlation of global seismicity with solar activity. We inferred such a clear correlation, highly statistically significant, analyzing the ISI-GEM catalog 1996–2016, as compared to the Solar and Heliospheric Observatory satellite data, reporting proton density and proton velocity in the same period. However, some questions could arise that the internal correlation of global seismicity could be mainly due to local earthquake clustering, which is a well-recognized process depending on physical mechanisms of local stress transfer. We then apply, to the ISI-GEM catalog, a simple and appropriate de-clustering procedure, meant to recognize and eliminate local clustering. As a result, we again obtain a non poissonian, internally correlated catalog, which shows the same, high level correlation with the proton density linked to solar activity. We can hence confirm that global seismicity contains a long-range correlation, not linked to local clustering processes, which is clearly linked to solar activity. Once we explain in some details the proposed mechanism for such correlation, we also give insight on how such mechanism could be used, in a near future, to help in earthquake forecasting.

Keywords: worldwide earthquakes, solar activity, long range correlation, solar and heliospheric observatory satellite, proton density

OPEN ACCESS

Edited by:
Giovanni Martinelli,
National Institute of Geophysics and Volcanology, Italy

Reviewed by:
Paolo Plescia,
National Research Council (CNR), Italy
Alexey Lyubushin,
Institute of Physics of the Earth (RAS), Russia

***Correspondence:**
Paolo Harabaglia
paolo.harabaglia@unibas.it

Specialty section:
This article was submitted to Solid Earth Geophysics, a section of the journal Frontiers in Earth Science

Received: *15 August 2020*
Accepted: *23 September 2020*
Published: *29 October 2020*

Citation:
Marchitelli V, Troise C, Harabaglia P, Valenzano B and De Natale G (2020) On the Long Range Clustering of Global Seismicity and its Correlation With Solar Activity: A New Perspective for Earthquake Forecasting. Front. Earth Sci. 8:595209. doi: 10.3389/feart.2020.595209

INTRODUCTION

Worldwide seismicity does not follow a Poisson distribution (e.g., Corral, 2005), but the character and cause of such internal correlation has not been explained till now. Recently, Marchitelli et al. (2020) found a clear correlation between the global seismicity and the proton density associated to the solar activity. This finding represents the first evidence allowing to propose an explanation for the internal correlation among worldwide earthquakes: it can be due to a triggering effect from high proton density. A mechanism has been proposed for such a triggering effect, in terms of an inverse piezoelectric effect, which would produce strain/stress pulses in the quartz crystals, abundant on large faults, as a response to huge current discharges from the ionosphere.

However, the character and properties of the internal correlation observed in global seismicity have never been analyzed before: it is not clear, for instance, if it only depends from local clustering, which could only be due to the very trivial and well known physical mechanisms of stress redistribution (Stein et al., 1992; Troise et al., 1998). In this case, any correlation found with large scale events (like the solar activity) would obviously be meaningless.

In this paper, after recalling the main results of Marchitelli et al. (2020), we first analyze the global earthquake catalog (ISI-GEM, from 1964 to 2016), by applying to it the most appropriate and "neutral" de-clustering able to eliminate local clustering. After such de-clustering procedure, we demonstrate the presence, in the catalog, of a long range internal correlation, which still correlates, at a very high statistical significance, with proton density generated by solar activity.

Once demonstrated the robustness, against any possible bias due to other local stress interaction effects, of the correlation between global seismicity and solar activity, we discuss more the proposed physical mechanism for the triggering effect.

Finally, we discuss how the new evidence could be, in future, used to improve earthquake forecast.

INTERNAL CORRELATION OF GLOBAL SEISMICITY

By interpreting the internal correlation of global seismic catalogs, an important concern would be to investigate the role played by local, short-range clustering, which mainly depends from well recognized physical mechanisms of stress interaction (Stein et al., 1992; Troise et al., 1998). Such an investigation is important, and at our knowledge never afforded, because it can enlighten if the internal correlation in the global catalog is due, besides to short range clustering, also to some long-range clustering which would be much more interesting to explain, with respect to such trivial effects of local stress interaction. Although it is almost impossible to distinguish, among such effects of stress interaction, foreshocks, main events, aftershocks and background seismicity (e.g., Bak et al., 2002), all of these effects have a common, well grounded physically, property to act only within relatively short distances (comparable to the fault size: see Wells and Coppersmith, 1994). As a consequence, in order to eliminate, from the earthquake catalog, such short-range effects, an appropriate de-clustering method should consider, as correlated events, all couples which occur within a given distance (on the order of the largest fault size between the two events) and within a suitable time window.

So, in order to obtain a declustered catalog we used the ISC-GEM catalog (Storchak et al., 2013; Storchak et al., 2015; Di Giacomo et al., 2018) that is complete from $M \geq 6.0$ for shallow events (depth up to 60 km) from early fifties. Epicentral locations however improve dramatically since 1964. We used therefore the time interval 1964–2016. In order to de-cluster it, we considered all the event pairs that were comprised in a time window of 6 months and that were spaced less than twice the fault length of the larger of the two events, according to the formula for a generic earthquake according to Wells and Coppersmith (1994). We anyway considered a minimum epicentral distance of 160 km, that is that any two events spaced less then 160 km within a time interval were anyway considered correlated, not depending from the fault size. If a pair satisfied this criteria, we discarded the smaller. Even discarded events were considered however as able to trigger other events. In this way we ended up with about 60% of the original earthquakes.

We used two data sets both based on the ISC-GEM catalog (Storchak et al., 2013).

The first data set, we applied such a de-clustering procedure, is relative to the shallow (depth < 60 km) $M \geq 8.00$ events that occurred since 1905. There are 83 of them. We manually de-clustered it so to discard even events, located within the mentined distance, occurring to within 3 years from another one. We remained with 76 events. Both data sets are available as **Supplementary Material**.

The second data set is relative to the shallow (depth < 60 km) $M \geq 6.00$ events that occurred since 1964. The choice of 1964 as lower bound is due to the fact that epicentral location quality dramatically increases starting from that date.

Once the new de-clustered catalog was obtained, we checked it for poissonianity. Then, we applied the algorithm devised by Harabaglia (2020) to verify poissonianity. This algorithm states that

$$\lambda(\Delta t_i) = -\log[SP(\Delta t_i)]/\Delta t_i$$

where $SP(\Delta t_i)$ is the Survival Probability Function at the Δt_i timing interval. If the data set where truly poissonian, $SP(\Delta t) = \exp(-\mu\Delta t)$ (where μ is the average value of Δt), so that λ should be constant over the entire Δt_i data set. This approach is even more powerful than that devised by Vecchio et al. (2008).

Figure 1 shows λ for the de-clustered data set with $M > 8$. Inter-event times are normalized to the average value of about 536.5 days. As far as the first six points are concerned, they refer to earthquake pairs that occurs at distances between 2,375 and 14,091 km with mean of 6,993 km and median of 6,479 km: hardly aftershocks. This is tantamount to say that long range (both temporally and spatially) internal correlation do exist.

In **Figure 2A** we show for each earthquake its relation, in terms of Δt vs. Δd, with every single event that follows it, up to the end of the catalog; that is, we show over 14×106 pairs of data. The left side of **Figure 2A** is the most interesting. The lower left corner is the area of foreshocks and aftershocks. The upper left corner represents the non poissonian distribution that will survive any de-clustering process. **Figure 2B** is the equivalent of **Figure 1** for the shallow (depth < 60 km) $M \geq 6.00$ data set after de-clustering according to the method used in appendix. It is obvious that for Δt_i of 20.000 s or less the non poissonianity is evident. In **Figure 2C** we show the Survival Probability Functions both in terms of Δt and Δd, relatively to the declustered $M \geq 6.00$ data set. It is clearly visible that Δt_i spans over more orders of magnitude with respect to Δd_i. This means that events are more clustered in time than in space, so that a kind of long range interaction, which is not destroyed by the local de-clustering, exists in the catalog. The obvious consequence of this finding is that a global process is affecting the seismicity.

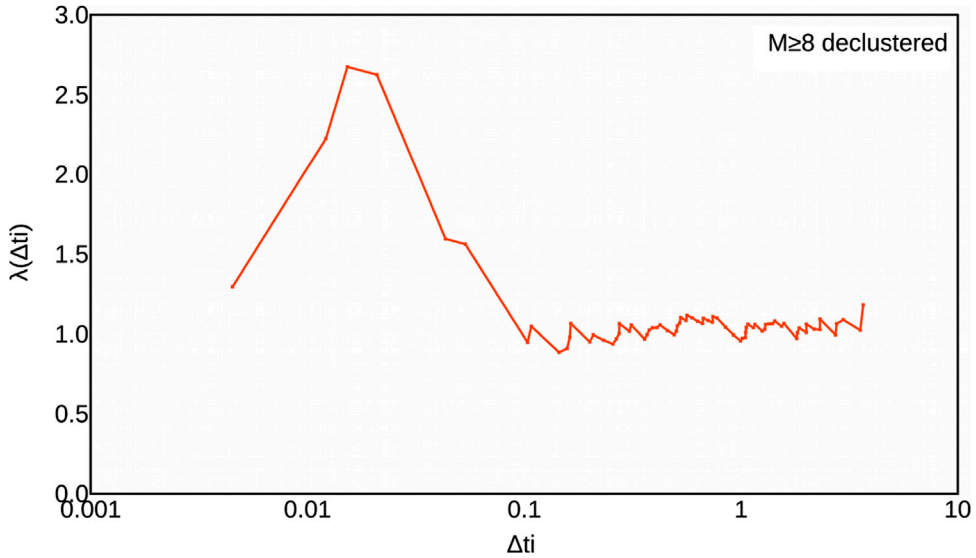

FIGURE 1 | Poisson's test according to Harabaglia (2020), for the declustered M ≥ 8, depth≤60 km worldwide ISC-GEM catalog in the period 1904–2016. The catalog is normalized. Perfect poissonianity would be represented by an horizontal line.

ANALYZING THE CORRELATION WITH SOLAR ACTIVITY

Once we stated the de-clustered seismic catalogs still are non poissonian, so evidencing a long range correlation among the worldwide earthquakes we want to specify its origin. Marchitelli et al. (2020) showed that the whole worldwide seismic catalog ISC-GEM, with threshold magnitude M > 5.6, is clearly correlated with the proton density as recorded by the SOHO (Solar and Helioscopic Observatory) satellite, at a confidence level as high as 99.999%. Here, we want to check if also the ISC-GEM catalog, de-clustered as explained in the former paragraph, is still correlated with the proton density. We have to consider the period 1996–2016, in order to compare it with the SOHO proton density data; so, we can use the whole ISC-GEM catalog (with earthquakes of any depth) down to the magnitude threshold of completeness M = 5.6. Using such a catalog, which is exactly the same used by Marchitelli et al. (2020) for our computations, will make easier the comparison with previous results.

We then apply the de-clustering method previously described to this catalog. Such a de-clustered catalog has only 3,241 events, instead of 6,612 of the original one analyzed by Marchitelli et al. (2020).

We used the conceptual Molchan (1990) method, as modified and adapted by Marchitelli et al. (2020) to test the correlation with the SOHO proton density catalog. We recall here the method. The procedure has been adapted from the concept of the Molchan diagram (Molchan, 1990). We start considering a time window whose length in days is 0.01 of the total catalog: 0.01 × 6,774 = 67.74, rounded to 68 days. We than consider all the parts of length 68 days in the catalog, by sliding progressively the 68 days windows of 1 day each step, until the 68th day corresponds to the ending day of the catalog. In this way, we obtain 6,774 − 68 = 6,706 time windows. For each time window, we compute if the Event Relative Rate R, for earthquakes occurring within 24 h from the end of a density peak, is higher or lower than the average number of events per day computed from the whole catalog (1,322/6,774 = 0.196 events/day): if it is higher, the prediction outcome is positive, otherwise it is negative. In case there is, in a given time window, no day occurring after the end of a density peak, that window is excluded from the count. On the *Y* axis, we indicated the fraction of the sliding time windows with a prediction failure. Then, we repeat the same procedure and computation for time windows progressively larger, from a fraction 0.01 to 1 of the total catalog time duration; for each fractional length of the sliding window, indicated on the *X* axis, we report on the *Y* axis the fraction of prediction failures. For a totally random outcome, the fraction of prediction failures is around 0.5; a number significantly smaller indicates a significant correlation, whereas a number significantly higher would indicate a significant anti-correlation.

In **Figure 3A** we show the results obtained, by the modified Molchan method applied to the de-clustered catalog, with the best fitting threshold of 16 counts cm^{-3} for the proton density. We want to stress that such a best fitting threshold is only slightly larger than the best one used for the original (non de-clustered) catalog in Marchitelli et al. (2020). However, how it can be seen from **Figure 3B**, which reports the values of the modified Molchan integral (fraction of prediction failures), the best fitting value of 16 counts cm^{-3} is another, almost equivalent, best fitting value also for the original catalog. We see that total fraction of failures amounts to 10% for the de-clustered catalog (it is 5.5% for the original catalog), so indicating the correlation is highly significant. In the next chapter, we will discuss anyway in more detail the results obtained, with different threshold values, for the original and the de-clustered catalog.

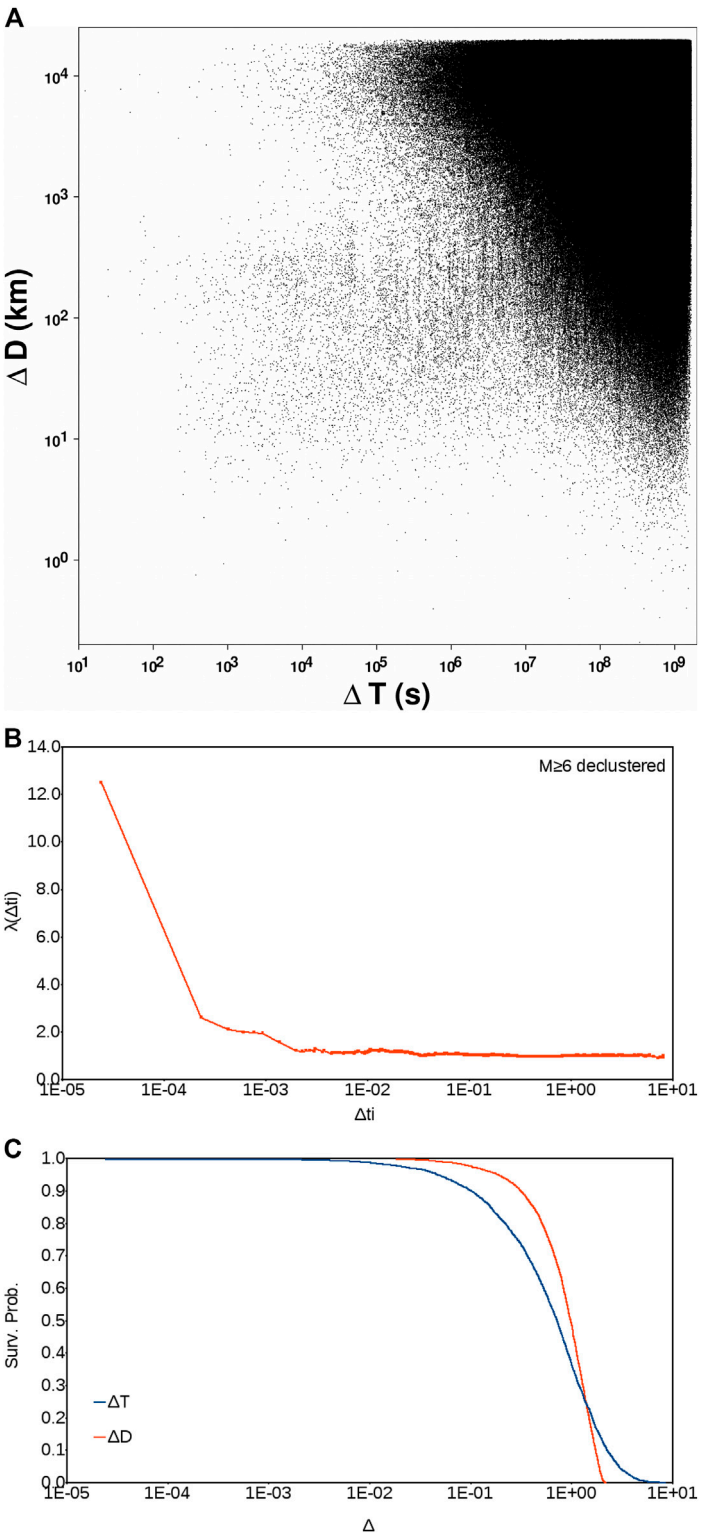

FIGURE 2 | (A) M ≥ 6, depth≤60 km, worldwide ISC-GEM catalog in the period 1964–2016. Each point represents ΔT vs. ΔD of every event with respect to all other earthquakes that occurred after it. There are over 14×10^6 pairs. **(B)** Poisson's test as in **Figure 1**) but relative to the declustered M ≥ 6, depth ≤ 60 km worldwide ISC-GEM catalog in the period 1964–2016. **(C)** Survival Probability functions both in time (blue) and in space (red) for the data set of **(B)**. Both temporal and spatial functions are normalized.

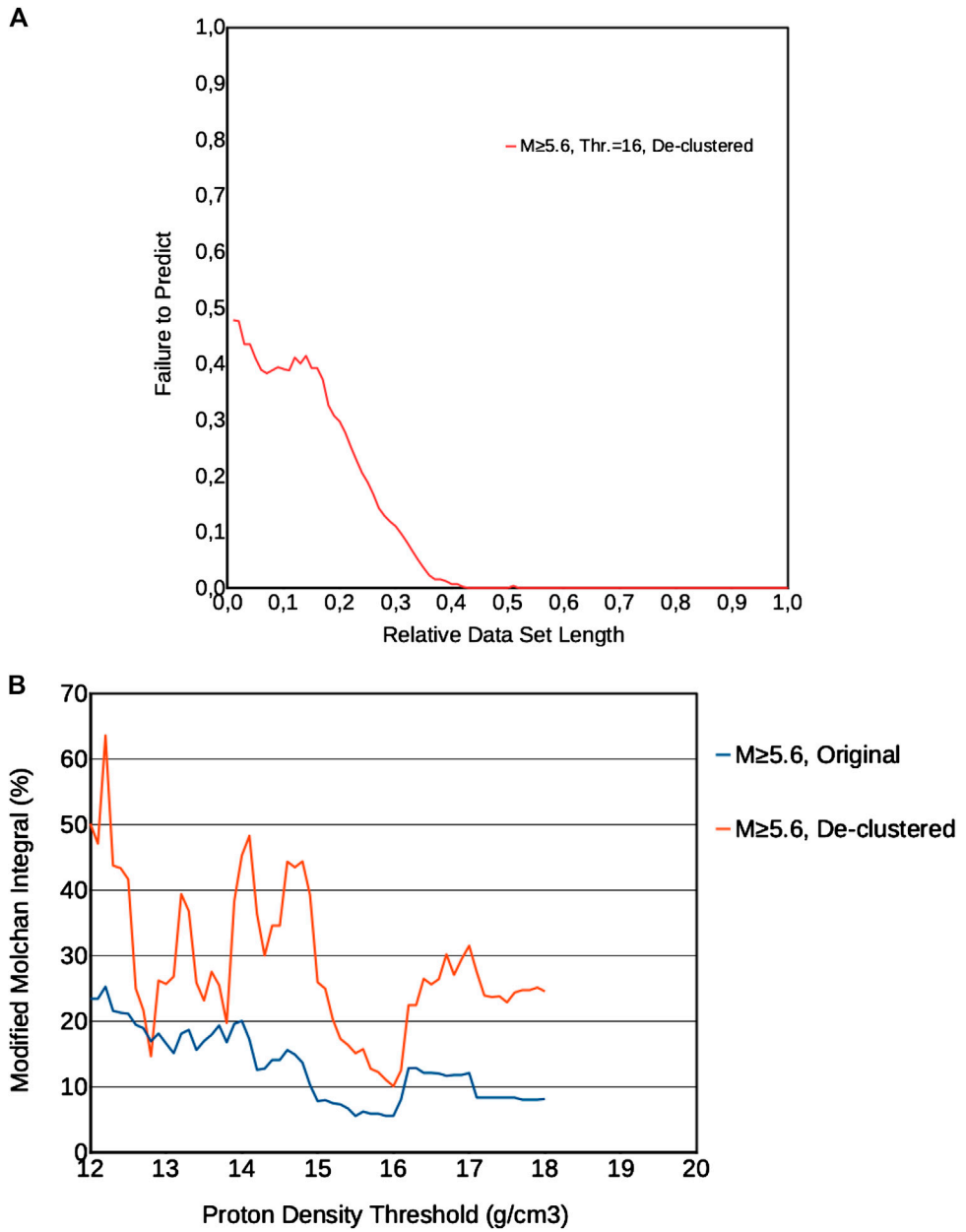

FIGURE 3 | (A) modified Molchan method, defined as in Marchitelli et al. (2020), applied to the de-clustered catalog with magnitude M > 5.6. **(B)** Values of the Molchan integrals (total fraction of prediction failure) for all the tested values of proton density threshold, for the original catalog with M > 5.6 (blue line) and for the de-clustered catalog with M > 5.6.

We have then demonstrated that also cutting from the catalog the local clustering, a long-range internal correlation remains, which is still significantly correlated with proton density due to solar activity.

DISCUSSION AND CONCLUSIONS

Although the non poissonian character of worldwide earthquake catalogs was a well recognized effect since more than half a century, we demonstrate here, for the first time in a clear way, that internal correlation among worldwide earthquakes is dominated by a long range clustering effect. Such effect is well distinct from local clustering, which is due to local stress interaction among the faults.

Once such long range effect has been identified, we have shown that correlation between solar activity and earthquakes still holds even for de-clustered data sets, after removing the local clustering effects. This means that the long range internal correlation of the worldwide catalog, which has not a simple

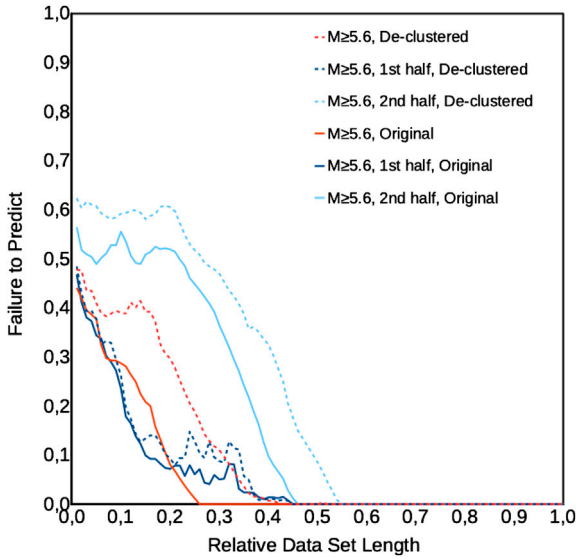

FIGURE 4 | Modified Molchan diagrams (Marchitelli et al., 2020) applied to the whole original catalog, first half (1996–2006) and second half (2006–2016), and to the corresponding de-clustered catalogs. Diagrams for the original catalog and its partitions are marked by continuous lines (colors are indicated in the figure); diagrams for the corresponding de-clustered catalogs are indicated by dashed lines (colors indicated in figure).

physical explanation, is certainly linked with proton density modulated by solar activity. We could also speculate if the short range clustering, which is generally interpreted in terms of local stress interaction, would also be affected by proton density. In principle, there would be no reason to neglect interaction with solar activity at all scales. In fact, the correlation inferred by Marchitelli et al. (2020) for the whole, not de-clustered catalog, i.e., including the local clustering, appears to be even more significant than the results obtained with the de-clustered catalog. Even the test with the modified Molchan-like method (Molchan, 1990; Marchitelli et al., 2020) indicates a total failure integral, for the de-clustered catalog, of 10%, compared with 5% obtained with the original catalog. This confirms that the proton density effect on seismicity is significant at all scales, and also adds to the common, local stress interaction effects, in order to increase short range clustering. It is important to stress that we hypothesize the influence of high proton density just represents a triggering effect, which adds up to the tectonic loading, which is by far the most important factor for earthquake generation. Such a triggering effect, able to anticipate earthquakes on faults already close to tectonic loading (De Natale et al., 2011) would obviously act at any scale (because there is no reason to believe the contrary), so being able to affect the foreshock-mainshock-aftershock sequences also at local scale.

However, besides we were able, by using an appropriate de-clustering technique, to isolate and put in evidence the long range internal correlation of the worldwide earthquake catalog, we are anyway convinced (and the results obtained here, even more clear using the whole catalog, represent a further confirmation) that any statistical analysis to infer the properties of an earthquake sequence should avoid de-clustering procedures. As an example, it is quite obvious that the generation mechanism in case of multiple events is still poorly understood. For instance in Italy, in 2016, we had 3 $M > 6$ events spaced apart few tenths of kilometers. The first occurred on August 24th, the second on October 26th and the third on October 30th. The latter being also the largest. Does it means that stress transfer induced the three events in sequence or does it imply that a larger slow process, such as that envisaged by Michel et al. (2019), was in place? In fact slow earthquakes have been recognized at least since Jordan (1991) and Ihmlé et al. (1993) but only recently it has been hypothesized that they could last for months (Michel et al., 2019). Moreover, Harabaglia (2020) showed that an event occurrence probability strongly depends on the timing interval of the two events that preceeded it. This dependence holds even at long timing intervals. Such an effect is so strong, that it can explain large Italian earthquakes ($M > 6$) where the occurrence rate is on the order of a few tenths per century.

The main reason however we are against declustering is that it certainly adds a high degree of subjectivity. There is in fact no commonly accepted method: declustering therefore would make any statistical finding about the catalog weaker.

We proceed now to discuss how our results correlate with the well known main cycles of solar activity. Some researchers had previously claimed the existence of some correlation between earthquake occurrence and the main period of solar activity, lasting 11 years (e.g., Mazzarella and Palumbo, 1989). Since our data catalogs last only 21 years, less than twice the period of 11 years, we could not see anyway such eventual periods. However, since in our hypothesis the influence of proton density is only a trigger, which can destabilize faults already close to a critical loading, what we should note in periods of low solar activity is just a decrease of correlation with seismicity. Marchitelli et al. (2020), applying their modified Molchan method to the original catalog (non declustered) noted in fact that, for the second half of the catalog (2006–2016), corresponding to considerably lower solar activity, the correlation with worldwide seismicity was less marked. Here, we show in detail the different results obtained, for the original and the de-clustered catalogs, in the whole period and in the two half periods (1996–2005 and 2006–2016) characterized by very different levels of solar activity.

Figure 1 shows the modified Molchan diagrams for the original and the de-clustered whole catalogs, as well as the same diagrams applied to the first and second halves of the original and of the de-clustered catalogs. We used, for such figure, a common value for the proton density threshold of 16.0 counts cm^{-3}, which appears to be a closely best fitting value for all the catalogs (the value of 15.5 counts cm^{-3} used by Marchitelli et al. for the original catalog gives an almost equivalent total prediction failure: 0.054 instead of 0.055). The total prediction failures for the original catalog are 0.05 for both the total catalog and the first half; whereas it is 0.17 for the second part, in the period of considerably lower solar activity. For the de-clustered catalog, the total prediction failure is 0.10 for the total

catalog, 0.07 for the first half and 0.23 for the second half. These results confirm the observation that, in periods of lower solar activity, the correlation between proton density and global earthquakes is lower.

Once the correlation between solar activity (proton density) and worldwide seismicity is assessed, as we demonstrate, beyond any reasonable doubt, what remains is to describe the mechanism producing such a correlation.

Marchitelli et al. (2020) postulated a mechanism of interaction involving electric discharges, caused by high electric potentials induced by large proton density. However, also magnetic effects (i.e., Duma and Ruzhin, 2003), should be considered, which could be even more effective for deep earthquakes. We anyway prefer the electric hypothesis since it would allow for a more extensive involvement of this rupture mechanism. We think that the charged particles interact with the magnetosphere and through a Coulomb effect they alter the electric circuit, which constantly crosses the entire planet. Since Quartz crystals are by far the most common elements in the crust, any increment of potential can cause the Quartz dilatation/contraction (depending from the current polarity) and favor the rupture nucleation. An inverse piezoelectric rupture nucleation could in fact occur even in absence of anomalous solar activity since electric currents flow throughout the entire planet constantly, as proven by the constant existence of lightning. This explanation could even allow for a feed-back mechanism. Recently, Martinelli et al. (2020a); Martinelli et al. (2020b) conducted a series of laboratory tests on Quartz crystals. In particular Martinelli et al. (2020b) showed that stressed Quartz crystals emit radiowaves. This means that nearby crystals could be in turn deformed and this could lead to a catastrophic process. Any alteration of the electric potential: external, due to the solar activity, or internal, caused by electric currents that flow through the crust, could add to this process.

Once the most appropriate mechanism will be precisely assessed for the solar-earthquake interactions, is could likely represent a powerful element to help in earthquake forecast. Actually, a large number of methods devoted to earthquake forecast have been implemented: an extensive review can be found, for example, in Martinelli (2020), as far as geofluid precursors are concerned. Among the most promising methods, anyway, there is the "pattern recognition" approach (Rotwain and Novikova, 1999; Kossobokov et al., 2002; Peresan et al., 2005). These pattern recognition algorithms, as well as any algorithm for probabilistic earthquake forecast, can in future include proton density as a key element. In addition, if the mechanism of proton density-earthquake interaction could be, in a near future, deeply understood, it could be used for short term forecasting (about 1 day in advance) in a more efficient way and in a completely different way, just detecting the preparatory processes we discussed above.

DATA AVAILABILITY STATEMENT

Publicly available datasets were analyzed in this study. This data can be found here: http://www.isc.ac.uk/iscgem/ http://umtof.umd.edu/pm/crn/.

AUTHOR CONTRIBUTIONS

PH elaborated statistical programs and analyses; VM worked the original idea; GN and CT wrote the core of the paper; all authors participated to the data analysis and interpretation, and contributed to write the final version.

ACKNOWLEDGMENTS

We gratefully acknowledge Paolo Plescia and Alexey Lyubushin, who reviewed the paper and greatly helped to improve it. This work has been partially supported by the project OT4CLIMA, funded by the Italian Ministry of Education, University and Research (*D.D. 2261 del 6.9.2018*, PON R&I 2014-2020 and FSC).

SUPPLEMENTARY MATERIAL

The Supplementary Material for this article can be found online at: https://www.frontiersin.org/articles/10.3389/feart.2020.595209/full#supplementary-material

REFERENCES

Bak, P., Christensen, K., Danon, L., and Scanlon, T. (2002). Unified scaling law for earthquakes. *Phys. Rev. Lett.* 88, 178501–178504. doi:10.1103/PhysRevLett.88.178501

Corral, A. (2005). Time-decreasing hazard and increasing time until the next earthquake. *Phys. Rev. E* 71, 017101. doi:10.1103/physreve.71.017101

De Natale, G., Crippa, B., Troise, C., and Pingue, F. (2011). Abruzzo, Italy, earthquakes of April 2009: heterogeneous fault-slip models and stress transfer from accurate inversion of ENVISAT-InSAR data. *Bull. Seismol. Soc. Am.* 101 (5), 2340–2354. doi:10.1785/0120100220

Di Giacomo, D., Engdahl, E. R., and Storchak, D. A. (2018). The ISC-GEM earthquake catalogue (1904-2014): status after the extension project. *Earth Syst. Sci. Data.* 10, 1877–1899. doi:10.5194/essd-10-1877-2018

Duma, G., and Ruzhin, Y. (2003). Diurnal changes of earthquake activity and geomagnetic Sq-variations. *Nat. Hazards Earth Syst. Sci.* 3, 171–177. doi:10.5194/nhess-3-171-2003

Harabaglia, P. (2020). Non-Poissonian earthquake occurrence probability through empirical survival functions. *Appl. Sci.* 10 838. doi:10.3390/app10030838

Ihmlé, P. F., Harabaglia, P., and Jordan, T. H. (1993). Teleseismic detection of a slow precursor to the great 1989 macquarie ridge earthquake. *Science* 261 (5118), 177–183. doi:10.1126/science.261.5118.177

Jordan, T. H. (1991). Far-field detection of slow precursors to fast seismic ruptures. *Geophys. Res. Lett.* 18 (11), 2019–2022. doi:10.1029/91GL02414

Kossobokov, V. G., Romashkova, L. L., Panza, G. F., and Peresan, A. (2002). Stabilizing intermediate-term medium-range earthquake predictions. *J Seismol Earthq Eng.* 8, 11–19.

Marchitelli, V., Harabaglia, P., Troise, C., and De Natale, G. (2020). On the correlation between solar activity and large earthquakes worldwide. *Sci. Rep.* 10, 11495. doi:10.1038/s41598-020-67860-3

Martinelli, G. (2020). Previous, current, and future trends in research into earthquake precursors in geofluids. *Geosciences* 10, 189. doi:10.3390/geosciences10050189

Martinelli, G., Plescia, P., and Tempesta, E. (2020a). "Pre-Earthquake" microstructural effects induced by shear stress on α-quartz in laboratory experiments. *Geosciences* 10, 155. doi:10.3390/geosciences10050155

Martinelli, G., Plescia, P., and Tempesta, E. (2020b). Electromagnetic emissions from quartz subjected to shear stress: spectral signatures and geophysical implications. *Geosciences* 10, 140. doi:10.3390/geosciences10040140

Mazzarella, A., and Palumbo, A. (1989). Does the solar cycle modulate seismic and volcanic activity?. *J. Volcanol. Geoth. Res.* 39 (1), 89–93. doi:10.1016/0377-0273(89)90023-1

Michel, S., Gualandi, A., and Avouac, J.-P. (2019). Similar scaling laws for earthquakes and Cascadia slow-slip events. *Nature* 574, 522–526. doi:10.1038/s41586-019-1673-6

Molchan, G. M. (1990). Strategies in strong earthquake prediction. *Phys. Earth Planet. In.* 61, 84–98. doi:10.1016/0031-9201(90)90097-H

Peresan, A., Kossobokov, V., Romashkova, L., and Panza, G. (2005). Intermediate-term middle-range earthquake predictions in Italy: a review. *Earth Sci. Rev.* 69 (1–2), 97–132. doi:10.1016/j.earscirev.2004.07.005

Rotwain, I., and Novikova, O. (1999). Performance of the earthquake prediction algorithm CN in 22 regions of the world. *Phys. Earth Planet. In.* 111, 207–213. doi:10.1016/s0031-9201(98)00161-7

Stein, R. S., King, G. C. P., and Lin, J. (1992). Change in failure stress on the southern san andreas fault system caused by the 1992 magnitude = 7.4 landers earthquake. *Science* 258, 1328–1332. doi:10.1126/science.258.5086.1328

Storchak, D. A., Di Giacomo, D., Bondár, I., Engdahl, E. R., Harris, J., Lee, W. H. K., et al. (2013). Public release of the ISC-GEM global instrumental earthquake catalogue (1900-2009). *Seismol Res. Lett.* 84, 810–815. doi:10.1785/0220130034

Storchak, D. A., Di Giacomo, D., Engdahl, E. R., Harris, J., Bondár, I., Lee, W. H. K., et al. (2015). The ISC-GEM global instrumental earthquake catalogue (1900-2009): introduction. *Phys. Earth Planet. In.* 239, 48–63. doi:10.1016/j.pepi.2014.06.009

Troise, C., De Natale, G., Pingue, F., and Petrazzuoli, S. M. (1998). Evidence for static stress interaction among earthquakes in the south-central Apennines (Italy). *Geophys. J. Int.* 134, 809–817. doi:10.1046/j.1365-246x.1998.00610.x

Vecchio, A., Carbone, V., Sorriso-Valvo, L., De Rose, C., Guerra, I., and Harabaglia, P. (2008). Statistical properties of earthquakes clustering. *Nonlin. Processes Geophys.* 15, 333–338. doi:10.5194/npg-15-333-2008

Wells, D., and Coppersmith, K. (1994). New empirical relationships among magnitude, rupture length, rupture width, rupture area, and surface displacement. *Bull. Seismol. Soc. Am.* 84, 974–1002.

Conflict of Interest: The authors declare that the research was conducted in the absence of any commercial or financial relationships that could be construed as a potential conflict of interest.

Copyright © 2020 Marchitelli, Troise, Harabaglia, Valenzano and De Natale. This is an open-access article distributed under the terms of the Creative Commons Attribution License (CC BY). The use, distribution or reproduction in other forums is permitted, provided the original author(s) and the copyright owner(s) are credited and that the original publication in this journal is cited, in accordance with accepted academic practice. No use, distribution or reproduction is permitted which does not comply with these terms.

frontiers in Earth Science

ORIGINAL RESEARCH
published: 30 October 2020
doi: 10.3389/feart.2020.536332

Electric and Magnetic Recordings by Chieti CIEN Station During the Intense 2016–2017 Seismic Swarms in Central Italy

Cristiano Fidani[1,2]*, *Massimo Orsini*[1,2], *Giovanni Iezzi*[2], *Noemi Vicentini*[2] and *Francesco Stoppa*[2]

[1]Central Italy Electromagnetic Network, Fermo, Italy, [2]DiSPUTer, University "G. d'Annunzio" of Chieti-Pescara, Chieti, Italy

We monitored electric and magnetic fields synchronously and continuously in an Italian area prone to moderate-to-high magnitude seismic activity. Identifying and monitoring of potential precursors may contribute to risk mitigation. A decade after the Central Italy Electromagnetic Network started, nine strong shakes with magnitudes between 5.0 and 6.6 occurred in Central Italy between August 2016 and January 2017. The events produced a fault offset of up to 2.8 m along a NNW–SSE normal fault system, 75 km long and located NW of the fault system, which generated the destructive L'Aquila 2009 earthquake sequence. This paper describes the electric and magnetic variations in the extremely low frequency band recorded at the Chieti Station of the network. Meteorological and geomagnetic data were compared to the recordings of these electric and magnetic activities by statistical correlations. We recorded several abrupt increases in electric and magnetic activities not simultaneous to the main seismic events and presumptively related to them. Electrical signals consist in discrete electric field oscillations between 50 and 200 Hz, with time lapses lasting between 3 and 45 min. In addition, magnetic signals consisting of magnetic field pulses with time lapses greater than 10 m were recorded in the same time interval. Similar signals occurred during the 2009 L'Aquila, Central Italy, sequence. Days before each strong earthquake, both electric and magnetic phenomena increased in intensity and number. Two physical models are proposed to describe and interpret electric and magnetic signal events. A number of hypotheses about the origin of recorded electric and magnetic signals may fit coherently with electromagnetic theory and are discussed in the light of a consistent dataset.

Keywords: earthquake forecasting, electrical oscillations, magnetic pulses, electric properties, electromagnetic models

OPEN ACCESS

Edited by:
Antonella Peresan, Istituto Nazionale di Oceanografia e di Geofisica Sperimentale (OGS), Italy

Reviewed by:
Dedalo Marchetti, Nanjing University of Information Science and Technology, China
Kaiguang Zhu, Jilin University, China

***Correspondence:**
Cristiano Fidani
c.fidani@virgilio.it

Specialty section:
This article was submitted to Solid Earth Geophysics, a section of the journal Frontiers in Earth Science

Received: *19 February 2020*
Accepted: *15 September 2020*
Published: *30 October 2020*

Citation:
Fidani C, Orsini M, Iezzi G, Vicentini N and Stoppa F (2020) Electric and Magnetic Recordings by Chieti CIEN Station During the Intense 2016–2017 Seismic Swarms in Central Italy. Front. Earth Sci. 8:536332. doi: 10.3389/feart.2020.536332

INTRODUCTION

On August 24, 2016, a Mw = 6.0 earthquake shake devastated Amatrice, Accumuli (Rieti, Latium) and Arquata del Tronto (Ascoli Piceno, Marche Region), reaching a maximum intensity of X (MCS) at Pescara del Tronto causing a total of about 300 casualties. The earthquake badly damaged many other villages at the junction between Lazio-Umbria-Marche and Abruzzi. The hypo-centre was located at the deep junction of Mt. Vettore and Mt. Gorzano faults, which were both activated and

ruptured during this first event. In the following 3 months a continuous sustained seismic activity persisted, the fracture propagated toward the north along the Mt. Vettore–Sibillini fault system, producing three significant events, one of Mw = 5.3 occurring 40′ after in Norcia, and two Mw = 5.4 and 5.9, both occurring on the evening of 26 October. Considering these events, the rupture area extended for over 25 km NNW from the epicentre of the 24 August event. On October 30, 2016 (Italian time 07:40), a Mw = 6.6 ± 0.2 shock followed, about 15 km NNW of the epicentre of the 24 August shock (Galli et al., 2017). On January 18, 2017 in the Campotosto area to the south of the mega-seismic area, further rupturing of the Mt. Gorzano fault produced other four significant events of Mw ~5.1, 5.5, 5.4 and 5.0 during a few hours. At this point, a NNW–SSE mega-seismic elliptic area ~75 km long, including several normal faults of high seismic potential, was affected by cumulative damage between IX and X MCS. There is some doubt about which faults took part in the event as consistent fault-rock breakage and noticeable offset and displacement were observed and related to each event. Notably, some fault sections were reactivated in several stages (Brozzetti et al., 2019). Continuous ground dislocations ranged several kilometres for the 24 August and 26 October events, but on 30 October the fracture was 30 km long with up to 200 cm of displacement in some places. This event extended from the fracture of August to those of October. As a whole, the Sibillini faults collapsed totally during the event of October 30, and the previous events must definitely be considered as foreshocks. Any stronger shocks was a main shock since there was a stronger one. At the same time, seismic swarms of moderate magnitude of up to Mw ~ 4 were triggered in other tectonic domains such as Tuscany, Piana Umbra and Marche foreland. The cumulative magnitude of the 2016–2017 sequence may be near to Mw ~ 6.8, which is in turn the maximum credible magnitude for each of the mentioned faults. The first significant event was in fact in the between of Mt. Vettore and Mt. Gorzano faults, which were activated according to a complex stress transmission which may be considered in continuity with the faults activated by the L'Aquila earthquake (Lavecchia et al., 2012; Lavecchia et al., 2016a,b). The 2016–2017 seismic sequence in central Italy filled a seismic gap between the 1997–1998 Umbria-Marche at NW and the 2009 L'Aquila-Campotosto at SE (Ferrarini et al., 2015), spanning a total extent of approximately 80 km (Calderoni et al., 2017). The seismicity of the area was depicted well in Baratta's book written in 1900 (Baratta, 1901), and even though only Gorzano fault has been associated with large historical earthquakes, the whole of the area is known for repeated destructive earthquakes.

Independent knowledge of the physical mechanisms driving seismic and volcanic activity can be obtained from observations of electric and magnetic fields generated by these complex processes (Johnston, 1997). A partial collection of electric and magnetic phenomena observed with strong earthquakes was first made by Mario Baratta at the end of the 19th century (Baratta, 1891), reporting many observations made in central Italy. Following this work, many experiments were executed in the 20th century attempting to do instrumental observations in Italy and everywhere in the world (Uyeda et al., 2009). However, the extremely interdisciplinary character of these researches tends to make their accomplishments difficult for the conventional earthquake community to understand (Uyeda et al., 2009). Even if it was clear that a variety of source processes generated the observed electric and magnetic field perturbations, several problems reflected on the credibility of this observations including (Johnston, 1997):

(1) missing constraints on the various physical mechanisms and models of various processes that are imposed by data from other disciplines,
(2) observations lacking self-consistency, an adequate signal-to-noise ratio, an adequate noise quantification, or consistency with other geophysical data obtained in the area,
(3) lack of the use of reference stations to quantify and remove common-mode noise generated in the ionosphere/magnetosphere and to isolate the most likely location of signal sources in the Earth's crust.

Specifically, extended research on electric field variations of the Earth were realized by measuring the potential difference between two ground dipoles (Varotsos and Alexopoulos, 1984a; Varotsos and Alexopoulos, 1984b; Varotsos and Alexopoulos, 1987; Varotsos and Lazaridou, 1991). This research culminated in the VAN method of earthquake prediction through seismic electric signals, which received extended discussion in a special issue of Tectonophysics (vol. 224, 1993) and criticism in a special issue of Geophysical Research Letters (vol. 23, 1996). Also based on coil magnetometer measurements, magnetic field variations were associated to electric field variations with one to 2 s of delay (Varotsos et al., 2003). Such electric and magnetic pulses were detected minutes before strong earthquakes (Varotsos et al., 2007). Vertical electrodes were also used for the detection of random pulse-like signals at Very Low Frequency (VLF) in Japan (Enomoto et al., 1991). Another trend of research concerned disturbances in VLF radio signals related to seismic activity (Molchanov and Hayakawa, 1999; Biagi et al., 2001). In these studies, wave propagation in sub-ionospheric channels of the Earth-ionosphere wave-guide covering epicentre areas showed recurrent driving-wave depletion on the occasions of strong earthquakes (Biagi et al., 2009; Hayakawa et al., 2010). Moreover, satellite studies of earthquakes detected changes in the ionospheric Extremely Low Frequency (ELF) and VLF emissions as well (Larkina et al., 1989). A statistical study of ELF and VLF emissions recorded from near-Earth space by the AUREOL-3 satellite around the epicentres of 325 earthquakes was described (Parrot, 1994). Finally, recent observations from low-orbit satellites evidenced quasi-static electric field perturbations above some strong earthquake epicentres (Nemek et al., 2009; Zhang et al., 2012). A large number of publications regarding electromagnetism and earthquakes concerned radiation and propagation in Ultra Low Frequency (ULF) band are not cited here, leaving their quote later if called into question. Despite fairly abundant circumstantial evidence, many of the problems of fundamental importance in seismo-electromagnetics remain unresolved (Uyeda et al., 2009).

Electrodynamics studies, in association with seismic activity, were suggested from past and present observations of earthquake lights during strong seismic events (Fidani, 2010). Given that strong earthquakes are rare events, continuous long-term instrumental monitoring is necessary to verify the usefulness of electrodynamics research so as to understand earthquake processes and to obtain reliable results regarding their mutual correlation (Uyeda et al., 2009). The Central Italy Electromagnetic Network (CIEN), which aims to verify the association between electrodynamics and seismicity, has been operating in Central Italy for more than ten years (Fidani, 2011). The network was composed of 10 active stations at the time of the intense seismic sequence in Central Italy, after a long and continual updating of observational locations and instruments. Stations of CIEN were initially equipped with electrical monitoring in Central Italy in 2006 as this region appeared to be the most probable area for future moderate earthquakes (Cinti et al., 2004). In particular, electric field oscillations recorded by CIEN concurred to strong earthquakes in Italy (Fidani, 2011; Fidani and Martinelli, 2015) have not been reported up to now. Also, the same type of detector has never been used by other researchers for earthquake studies, whereas other kinds of electric signals, like air ion concentrations (Bleir et al., 2009) and atmospheric electric fields (Kamogawa et al., 2004; Röder et al., 2002), have been used. Only on 2011, when an independent result focused on magnetic pulse recordings for the L'Aquila earthquake (Orsini, 2011), the network was extended to magnetic monitoring. A multi-parametric monitoring of CIEN started after 2011, when Chieti Station supported terrestrial currents and magnetic component recordings. Magnetic detectors have been widely used in every region of the world and recently they have been refined; for example, in the development of coil induction magnetometers (Grosz et al., 2011). Results from several studies have strongly suggested the possibility to detect ULF (Han et al., 2014) and ELF (Schekotov et al., 2015) magnetic signatures of earthquakes, as well as ELF magnetic pulses measured hours before moderate and strong seismic activity (Bleier et al., 2009; Scoville et al., 2015). The QuakeFinder network (www.quakefinder.com), consisting of 122 stations in California, mostly along the San Andreas Fault, and another 42 stations along fault zones in Greece, Taiwan, Peru, Chile and Indonesia have already recorded a confirmation of magnetic pulses preceding strong earthquakes (Kappler et al., 2019). Recordings of coupled ELF electric and magnetic fields from the Chieti Station are presented in this work for the first time, while measurements of VLF electric fields and terrestrial currents are still not considered together with the aforementioned.

Geotectonics and Seismic Data

The complex tectonic pattern of the fault activated in the period of 2009 and 2016–17 offers a field of argument about stratigraphic interpretation. Basically we have two main tectono-stratigraphic units. The lowermost is the crystalline basement made of gneiss and granite covered by a thick layer of anagenites (quartzite). Being the units formed by many thrust and fold systems cross-cut by extensional faults, there are no borehole data or robust direct evidence to establish their number of overlaps and crustal thickening before the extensional phase. Depending on the model adopted (e.g., Brozzetti and Lavecchia, 1994) the depth of the basement may be 4 km beneath Mt. Vettore and only 2 km in the western part of the fault system. Thus, all the main seismic shakes would be located in the crystalline basement. The uppermost unit is the Mesozoic sequence formed by 2,000 m of Triassic evaporates and a thicker cover of Mesozoic limestone. The terrains present in the western side of the Apennine chain and up to the coastal line are involved in a compression thrust and fold system which developed mostly in 6,000-m-thick Tertiary soft terrains such as sandstones, marls, and clays having a depocentre in the foredeep area (deformed). Below these sequences there is again the limestone-evaporites stratigraphic unit and then, much deeper, the crystalline basement, at a depth of about 7–8 km in the Chieti-Pescara area, which is near the limit of the Adriatic foreland (near the undeformed area).

Seismic events of Mw ≥ 4.0 recorded in this region of Central Italy between July 2015 and October 2017 are shown in **Table 1**. The Chieti Station is located at the Volcanology Laboratory in the Department of Psychology, Health and Territory Sciences (DiSPUTer) of the University of Chieti-Pescara "G. d'Annunzio" in Chieti Scalo (42° 22′ 05.09″ N; 14° 08′ 51.56″ E) with an altitude of 51 m amsl in the Abruzzo region. **Figure 1** shows the distance of the Chieti Station from the main areas of the central Apennines where the main shocks struck between Norcia, Amatrice, and Capitignano at distances of about 100, 80, and 70 km respectively.

Electromagnetic Data

Electrical detectors are made up of two principal parts: the outdoor sensor constituted by a pair of orthogonal electrodes with a couple of amplifiers (A1 in **Figure 2A**) and the indoor real time signal analysis with a recording system realized by a personal computer (IC1 in **Figure 2A**). The two electrodes oriented along the NNW and WSW directions at Chieti Station are located above the building of the Volcanology Laboratory. The resolution for this electric field detector is calculated to be around 50 μV/m between 10 and 1,000 Hz with a precision of around ±500 μV/m, see **Supplementary Appendix A**. The natural electric noise level at Chieti Station in the ELF band varied considerably depending on the meteorological conditions. Spectrum Lab measurements of it ranged from about −90 dB at around 10 Hz to −80 dB at around 100 Hz for fair weather conditions, which corresponds to an electric fields spectral density noise floor of about $10^{-4}\,Vm^{-1}\,Hz^{-½}$ (Boldyrev et al., 2016). Spectrum Lab measurements meanwhile around −60 dB with peaks of −40 dB for the whole of the ELF spectrum, corresponding to an electric field spectral density of about 10^{-3} to $10^{-2}\,Vm^{-1}\,Hz^{-½}$ (see **Supplementary Appendix A**), were made under perturbed meteorological conditions with thunderstorms above or around the station. Typical recordings for fair weather of ELF electric recording at Chieti Station are shown in **Figure 3A**. The picture displays the dynamic spectra on a color graph which corresponds to both the WSW and NNW direction electrodes, recorded on January 2, 2016 over a 70-min period. Moving along the time

TABLE 1 | List of the 29 earthquakes localized within a distance of 150 km from Chieti with M ≥ 4 shown in **Figures 5, 6, 9**. Seismic events with 4 ≤ M < 5 are omitted when occurred the same day of a seismic event with M ≥ 5, and only the major with 4 ≤ M < 5 is reported when more than one event occurred the same day. Official data are taken from the INGV website at http://terremoti.ingv.it.

Date	Time (l.t.)	Mw	Zone	Depth (km)	Lat.	Lon.
2015-12-06	17:24:38	4.4	Adriatic sea	12	42.40	15.24
2016-01-16	19:55:11	4.3	Baranello (CB)	10	41.53	14.60
2016-08-24	03:36:32	6.0	Accumoli (RI)	8	42.70	13.23
2016-08-24	04:33:28	5.3	Norcia (PG)	9	42.79	13.15
2016-08-25	14:36:05	4.4	Amatrice (RI)	8	42.60	13.28
2016-08-26	06:28:25	4.8	Amatrice (RI)	9	42.61	13.29
2016-08-27	04:50:59	4.0	Montegallo (AP)	8	42.84	13.24
2016-08-28	17:55:35	4.2	Arquata (AP)	9	42.82	13.23
2016-09-03	12:18:51	4.3	Castelsantangelo sul Nera (MC)	8	42.86	13.22
2016-10-16	11:32:35	4.0	Accumoli (RI)	9	42.75	13.18
2016-10-26	19:10:36	5.4	Castelsantangelo sul Nera (MC)	9	42.88	13.13
2016-10-26	21:18:05	5.9	Castelsantangelo sul Nera (MC)	8	42.91	13.13
2016-10-27	10:21:45	4.3	Preci (PG)	9	42.88	13.10
2016-10-29	18:24:33	4.1	Norcia(PG)	11	42.81	13.10
2016-10-30	07:40:17	6.5	Norcia (PG)	9	42.83	13.11
2016-10-31	04:27:40	4.0	Norcia (PG)	11	42.76	13.09
2016-11-01	08:56:40	4.8	Ussita (MC)	8	42.99	13.13
2016-11-03	01:35:01	4.7	Pieve Torina (MC)	8	43.03	13.05
2016-11-12	15:43:33	4.1	Accumoli (RI)	10	42.72	13.21
2016-11-14	02:33:43	4.1	Castelsantangelo sul Nera (MC)	11	42.86	13.16
2016-11-29	17:14:02	4.4	Capitignano (AQ)	11	42.53	13.28
2016-12-11	13:54:52	4.3	Castelsantangelo sul Nera (MC)	9	42.91	13.12
2017-01-18	10:25:40	5.1	Montereale (AQ)	9	42.55	13.26
2017-01-18	11:14:09	5.5	Capitignano (AQ)	10	42.53	13.28
2017-01-18	11:25:23	5.4	Capitignano (AQ)	9	42.49	13.31
2017-01-18	14:33:36	5.0	Cagnano Amiterno (AQ)	10	42.48	13.28
2017-02-03	05:10:05	4.2	Monte Cavallo (MC)	7	42.99	13.02
2017-04-27	23:16:58	4.0	Visso (MC)	8	42.96	13.05
2017-07-22	06:13:08	4.0	Campotosto (AQ)	13	42.57	13.33

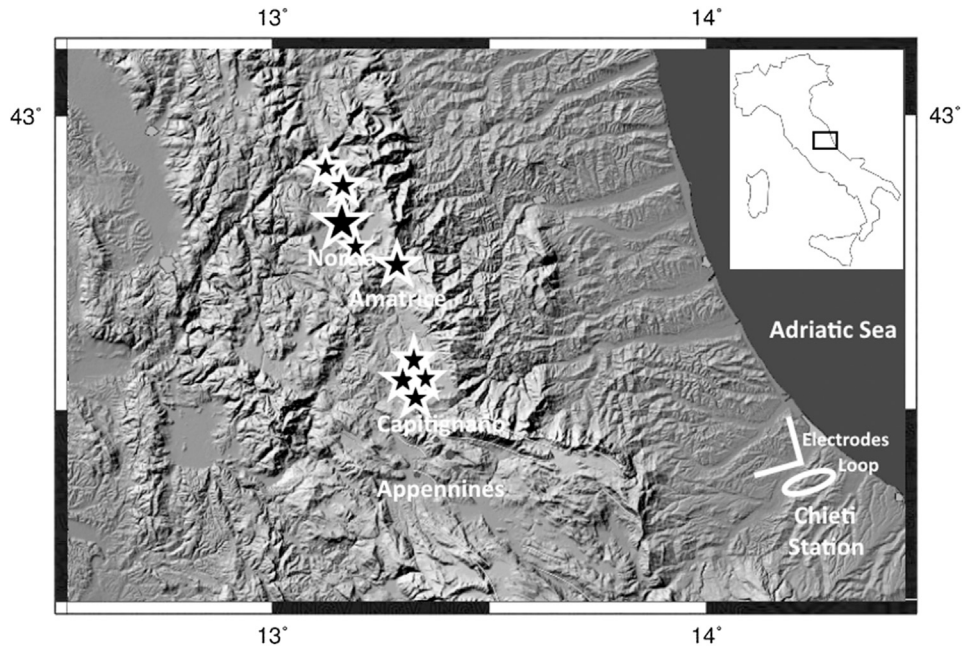

FIGURE 1 | The figure shows the azimuth of the magnetic antenna, which was oriented mainly to reduce the 50 Hz noise coming from the local electrical power line as far as possible. Furthermore, the directions of wire electrodes are indicated by white segments. They are located in Chieti, about 70–100 km from the areas of the main shocks (stars).

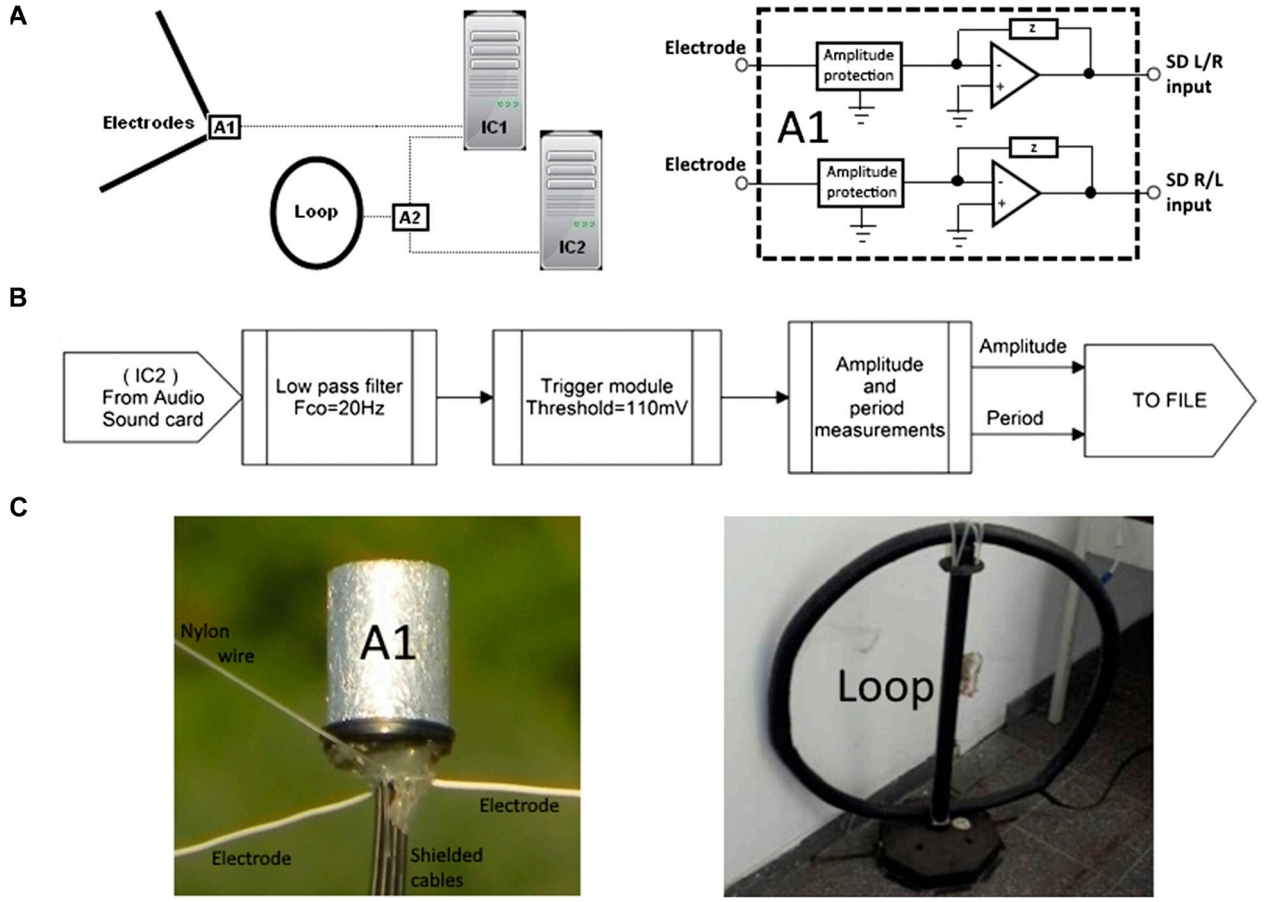

FIGURE 2 | A) Configuration of the connections of the electrodes and the loop antenna through the amplifiers A1 and A2 at computers IC1 and IC2, on the left, and the basic scheme of A1 on the right. **(B)** Simplified block diagram of the laboratory view data acquisition software at IC2 only, consisting of three main blocks starting from the first low-pass filter; the second block is the voltage threshold discriminator, the next block measure the amplitude and the period of the signals. **(C)** The electric detector made up of electrodes converging in the A1 double amplifier box in the photo on the left, and a particular of the loop in the photo on the right.

direction at constant frequencies which are integer multipliers of 50 Hz, continuous intense phenomena are described by marked horizontal thin lines; they represent the power supply network emission with the first harmonic intensity at about −50 dB. Other less well defined horizontal green/blue lines appear below 50 Hz; these are known as Schumann Resonances (Jackson, 1975) and occur at about 7.6, 14, 19, 24, 31, 37, and 43 Hz. The power intensity increased sporadically by around 10–20 dB, indicated by yellow and red spots above the green band in **Figure 3A** for frequencies between 50 and 150 Hz. These phenomena were observed during past years by other CIEN stations and the maximum daily intensity of the spots was observed to increase around major earthquake times (Fidani, 2011; Fidani and Martinelli, 2015). The maximum daily intensity of the spots was also observed at Chieti Station and was stored in the IC1 memory. If plotted with respect to the frequency corresponding to the maximum amplitude, the phenomena are circumscribed in a well defined area of the ELF band (see **Figure 3B**). Green spots with frequencies of around 300, 500 and 900 Hz, which appeared in other positions of **Figure 3A**, reflected variations in the power absorption of the power network line.

The magnetic detector is also made up of two principal parts: the sensor constituted by a loop antenna with an amplifier (A2 in **Figure 2A**) real-time signal analyser with two recording systems realized by two personal computers (IC1 and IC2 in **Figure 2A**), both indoors in the building basement. The apparatus receives radio waves in the audio frequency band by magnetic induction at the loop antenna. Then the amplified signal from the output of A2 is divided into two parts, which are connected to two different sound cards of the two different computers: IC1 was used for the comparison with the electrical signals and IC2 was completely dedicated to the magnetic pulse analysis (see **Figure 2A**). The resolution of this magnetic field detector is around 0.05 nT at 10 Hz with a precision of ±1 nT, see **Supplementary Appendix B**. The loop antenna is located in the underground floor of the building. It has been oriented with the axis of symmetry NNW to reduce the 50 Hz noise coming from the local electrical power line in order to turn down the voltage threshold, which is adjustable by software. Electric currents induced in the magnetic loop were amplified and divided into two equal signals to be analyzed by IC1, which was equipped with a supplementary sound card, and by IC2. Dynamic spectra obtained by IC1 analysis revealed a very stable and regular

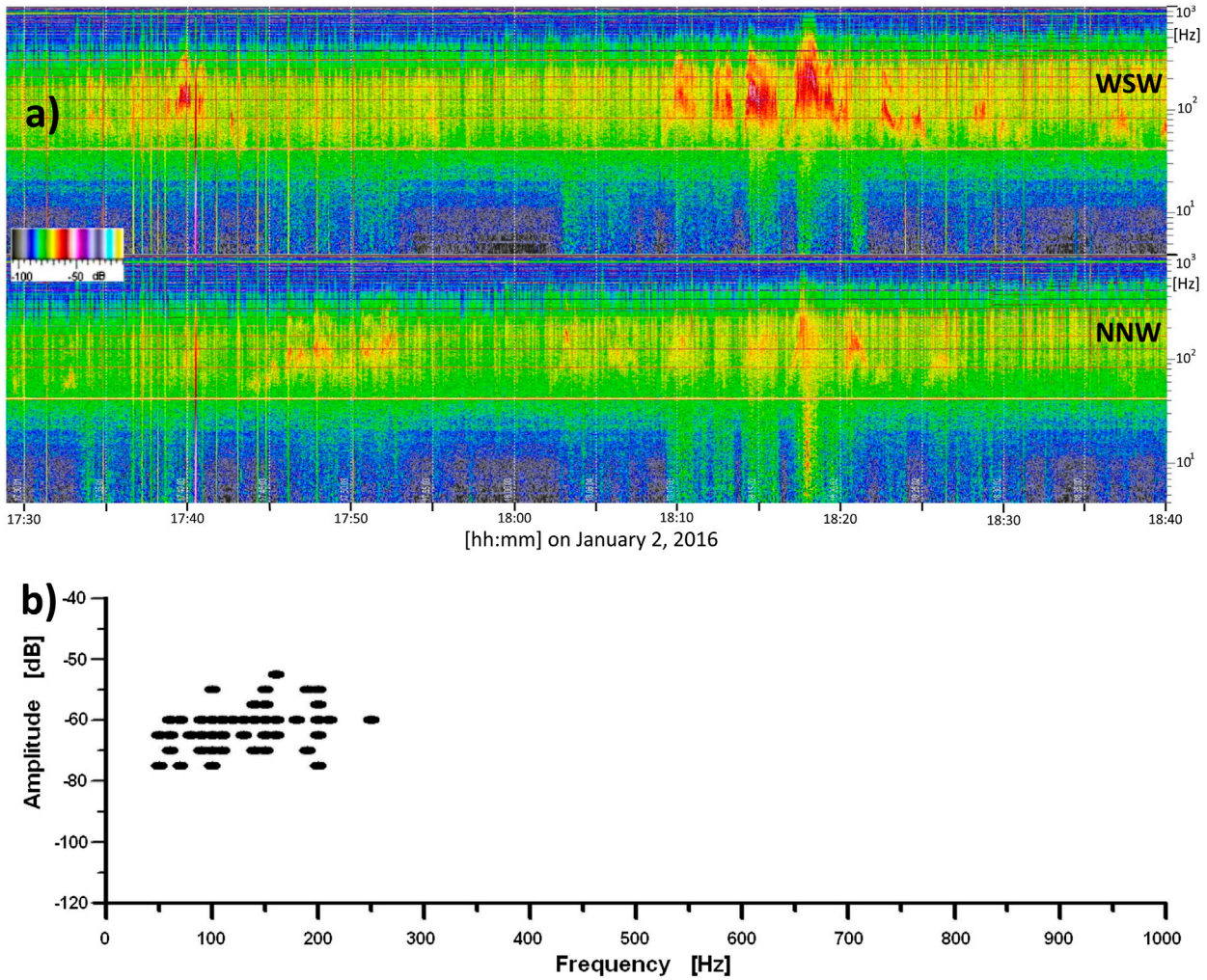

FIGURE 3 | A) Dynamic spectra of both WSW and NNW electrodes recorded on January 2, 2016 during the afternoon. Recordings lasted 70 min and show several electric phenomena of natural and anthropological origin. The evident vertical lines covering the entire frequency band and characterized by high intensity are EM waves produced by lightning bolts not too far from the station (Barr et al., 2000). The green band represents the numerous lightning strikes that occurred at distances of thousands of kilometres in the tropics. Red spots are the electrical oscillations. **(B)** A typical spectrum of maximum daily electric oscillations recorded at IC1 during several months by Spectrum Lab software before the main strike of Norcia. It consists of 81 events of electric oscillations, which are mainly above the noise threshold of –80 dB; all of them fall between 50 and 250 Hz.

behavior with a uniform noise level that reached −70 dB between 12 and 30 Hz, −80 dB above 30 Hz and −90 dB below 12 Hz. The uniform noise was interrupted almost exclusively by magnetic pulses which were rarely observed during either weak or strong meteorological phenomena and lightning bolt strikes which occurred near Chieti Station. Magnetic pulses appeared like vertical lines in the dynamic spectra, as expected. Power spectra of pulses covered nearly all the frequencies up to several hundreds of hertz, with a 5–10 dB power level greater than the noise level (see **Figure 4**). The Labview data acquisition software at IC2 allowed to test different settings of the threshold, as well as different filter configurations to evaluate the number of daily triggers. A search of the filter cut-off frequency was implemented, being so the 50 Hz influence coming from the electrical power line was almost completely excluded from data. The acquisition at IC2 had constant parameters between September 2, 2016 and June 28, 2017, when the voltage threshold defined by the Labview data acquisition software was set to 110 mV; corresponding to about 2.5 nT at 10 Hz (see **Supplementary Appendix B**), while the filter cut-off frequency was set to 20 Hz, and the data acquisition ran for 24 h per day. Computers IC1 and IC2 for the electrical and magnetic recordings and analysis are located in the underground floor of the building.

Chieti Station was also equipped with a subterranean electrodes system which was installed in September 2010. Electrodes were made up of three square boreholes, 2 m depth, and 1 m width each, aligned to the magnetic field in the NW-SE direction; the center of each borehole is distant 3 m from the other two. Because of the 20° dip in the field surface, the borehole tops are shifted by 1.20 m from the NE borehole to the SW

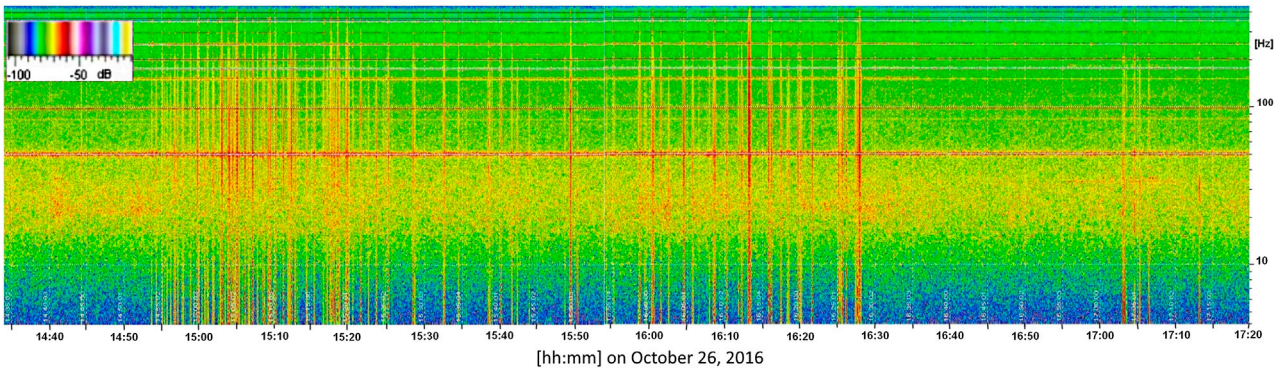

FIGURE 4 | Dynamic spectra recorded on 26 October in the afternoon. Recordings lasted 175 min and show a train of magnetic pulses that started at 14:55 LT, indicated by vertical lines; horizontal lines are the traces of 50-Hz power supply harmonics.

borehole. In the center of each borehole were placed four electrodes, constituted of Fe plates 50 × 50 × 0.5 cm, for a total of 12 electrodes. The first four are on the bottoms of the holes, the others separated by 50 cm of soil levels from each other and from the surface. The acquisition hardware was certified USB DAQ module E14–140 M by L-Card LLC (Bobrovsky et al., 2017). Analysis of the Chieti Station subterranean electrodes database showed impulse-like signals of ground electromagnetic field values measured up to 14 days before the strongest quakes in Central Italy. Furthermore, to compare micro-seismicity with electromagnetic acquisitions, an SR04 EDUGEO three-axis seismograph was recently installed at the same position.

DATA ANALYSIS

Spectrograms related to the electric fields were analyzed for a year and half from the beginning of January 2016 up to the end of June 2017. This period was characterized by a lot of gaps in the data, which were caused by power supply interruptions during several time intervals in 2016 and 2017. Gaps in the data occurred in intervals of one or more days, and they exactly corresponds to gaps in spectrograms being the sample frequency of kHz. The ELF bands of electric fields were collected in a time series of the maximum daily intensity of oscillations in both the NNW and the WSW direction. These series of data showed intensity variations with some correspondence with the recorded seismic activity from October 2016 to the beginning of January 2017, as shown below. In fact, electric ELF oscillations at Chieti Station increased in intensity from 10 to 20 dB above the noise level along WSW direction, when strong seismic activity occurred near the station, namely at the time of the Castelsantangelo sul Nera-Norcia (on October 26, 19:10 Mw = 5.4 and 21:18 Mw = 5.9, and on October 30, 07:40 Mw = 6.5, UTC) earthquakes in 2016. The same type of increase in ELF oscillations was detected at the time of the Emilia (Mw = 6.0, Mw = 5.8) earthquakes in 2012 (Fidani and Martinelli, 2015) and at the time of the L'Aquila (Mw = 6.3) earthquake in

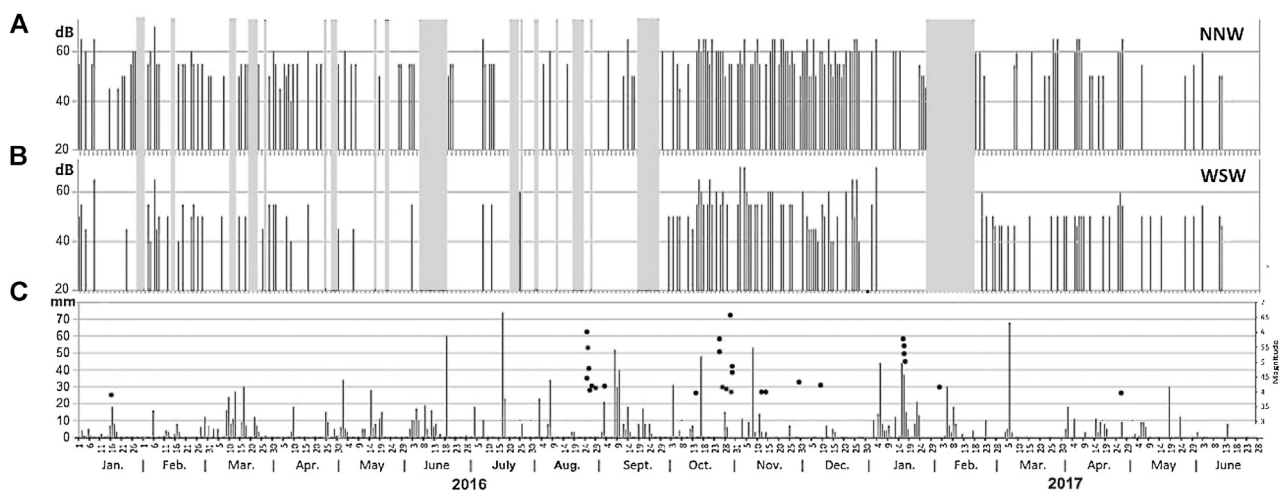

FIGURE 5 | The distribution of WSW electric oscillations **(A)** and the distribution of NNW electric oscillations **(B)** are indicated by black vertical lines. Rain is indicated by vertical lines in **(C)**, together with strong seismic events, indicated by black circles. Periods of lost data are indicated by gray shadows for both **(A,B)**.

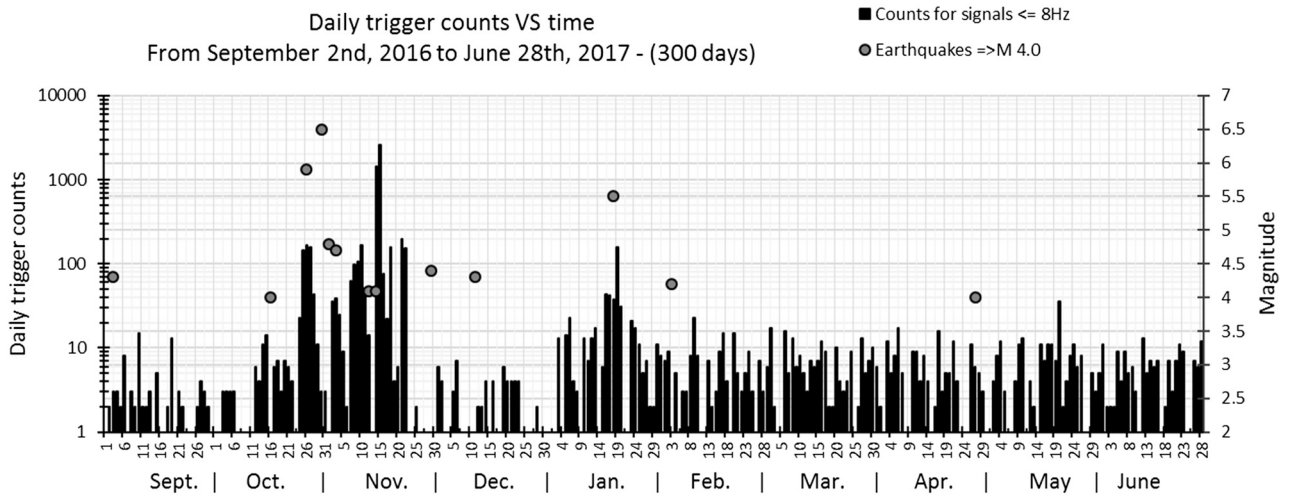

FIGURE 6 | Two significant increases of the daily counting rate below 8 Hz were recorded, the first from 25 October to 23 November and then another that appeared from 16 to 20 January. Notice that the plot reports only the biggest daily earthquakes listed in **Table 1**. The plot reports only the daily biggest earthquakes listed in **Table 1** by gray circles.

2009 (Fidani, 2011). At the same times, behaviors differed between the NNW and WSW components. Namely, a near constant behavior characterized the maximum intensity of ELF oscillations recorded by the NNW electrode. Detected ELF oscillations are indicated by vertical bars in **Figures 5A,B**. Recordings by the WSW electrode between January 2016 and June 2017 (see **Figure 5B**) shown a maximum intensity increased since mid-October 2016 and reached a peak a few days after the main shock in Norcia. The daily frequency of oscillations in both the NNW and the WSW direction increased to cover near all days from October to December 2016. Chieti Station data before and after the Amatrice earthquake that occurred on August 24, 2016 (Mw = 6.0), were partially lost because of the power supply shutdown at Chieti University during the vacation period. The Chieti Station has always recorded low ELF activity since 2011, even if less than1 every 3 days and with an average amplitude of around −65 dB for both the NNW and the WSW direction. Amplitudes of ELF oscillations reached about −50 dB around the maximum values; they correspond to induced electric potentials of 360 $\mu V\ Hz^{-½}$, see **Supplementary Appendix A**. Rainy days with elevated electrical activity are also shown in **Figure 5C** by vertical bars proportional to the daily amount of rain, whereas seismic events are indicated by black circles. No clear correspondence between rain and electric potential measurements is apparent at Chieti Station.

Starting from September 2, 2016, the Labview software saved data for 24 h. On October 25 the daily count below 8 Hz increased significantly above the total average of 29 pulses; then it returned to the typical daily rate on November 24 (**Figure 6**), which was characterized by an average of six pulses of at least 2.5 nT. A significant decrease in the daily count reached the average value of two when the frequency was below 8 Hz: this occurred between December 18, 2016, and January 10, 2017, when a very high rate of pulses above the threshold of 2.5 nT at 10 Hz (see **Supplementary Appendix B**) appeared eight days before the Capitignano earthquakes (Mw = 5.5) on January 18, 2017. From 24 October, several pulses with amplitudes much greater than 2.5 nT were recorded in the frequency band lower than 10 Hz, as shown by the daily spectrum in **Figure 7**. The same effect was recorded in terms of the daily trigger number, which first increased in the band below 10 Hz, where the detector is less sensitive, and then decreased progressively until it almost disappeared on the day of the mainshock in Norcia (October 30, 2016). It is important to point out that the detector even recorded some pulses with amplitudes greater than 10 nT below 10 Hz, where the typical voltage gain of the amplifier decreases for those frequencies. In fact, a first signal with the amplitude of 53 nT at 6.8 Hz was recorded on October 25, along with a few other pulses recorded at lower frequencies reaching amplitudes beyond 60 nT. Several other pulses with amplitudes greater than 60 nT under 4 Hz, were recorded on the 27, 28 and October 29, 2016, near 80 nT on 29. The number of pulses with amplitudes greater than 2.5 nT increased significantly on 10 and January 12, 2017, when the number of these signals was 3.4 and 2.1 times greater than usual, respectively. Around the average numbers of pulses were also detected on January 11, 13 and 15. During the days preceding the Capitignano earthquake on January 18, 2017, several signals greater than 2.5 nT appeared, mainly between 4 and 10 Hz, as shown in **Figure 8**. In the same figure, it is possible to see that sometimes several pulses were recorded even below 7 Hz and all were above the voltage threshold. In fact, the day preceding the quake, the antenna received a pulse with a frequency of 4.4 Hz with an amplitude of 45 nT, while at a greater frequency of 16.8 Hz had an amplitude of 10 nT. The day after the mainshock, the detector recorded two big pulses, the first with a frequency of 9.5 Hz and an amplitude of 20 nT, and the second with a frequency of 14 Hz and an amplitude of 31 nT.

Spectrograms of the magnetic loop signals obtained by IC1 were saved with frequencies between 4 and 450 Hz in a logarithmic scale, starting from July 21, 2015, to October 31,

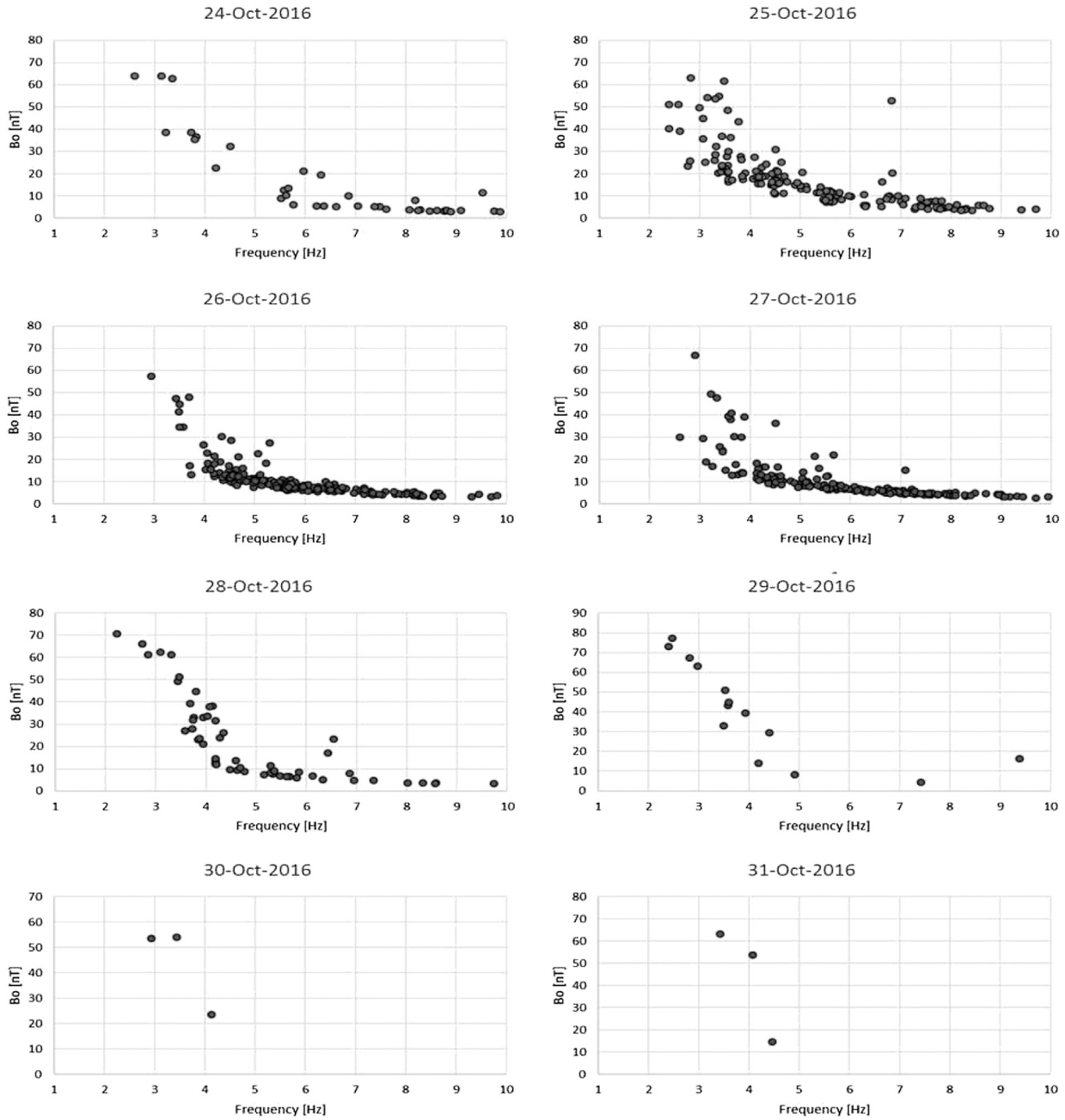

FIGURE 7 | The daily spectrum from 24 to October 31, 2016. From 24 October, the detector recorded an increase in the number of pulses below 10 Hz. The detector recorded some pulses with amplitudes near 80 nT between 2 and 3 Hz even though the gain of the preamplifier was lower at those frequencies. It is evident from the above graphs that the magnetic induction threshold is frequency dependent after that the limit of 110 mV was fixed.

2017. Spectrograms of magnetic components evidenced a regular pattern that was interrupted a few times every day by vertical lines; such lines represented the graphic markers of pulses. Magnetic pulses were selected with a 5-dB threshold above the noise level in this representation. The average number of pulses was around eight pulses for day. Daily pulse numbers typically did not increase during strong meteorological perturbations and thunderstorms. There was no evidence of increases in the daily pulse number around the Amatrice main event on August 24, 2016, when the detector was on. It increased slightly on 25 October and increased strongly on 26 October, reaching 45 pulses when two moderate earthquakes of Mw = 5.4 and Mw = 5.9 struck Central Italy about 100 km from the Chieti Station (see **Figure 9A**). Pulse rates increased about 4 h before the Castelsantangelo sul Nera quakes occurred (on October 26, 19: 10 Mw = 5.4 and 21:18 Mw = 5.9, UTC), as shown in **Figure 5**.

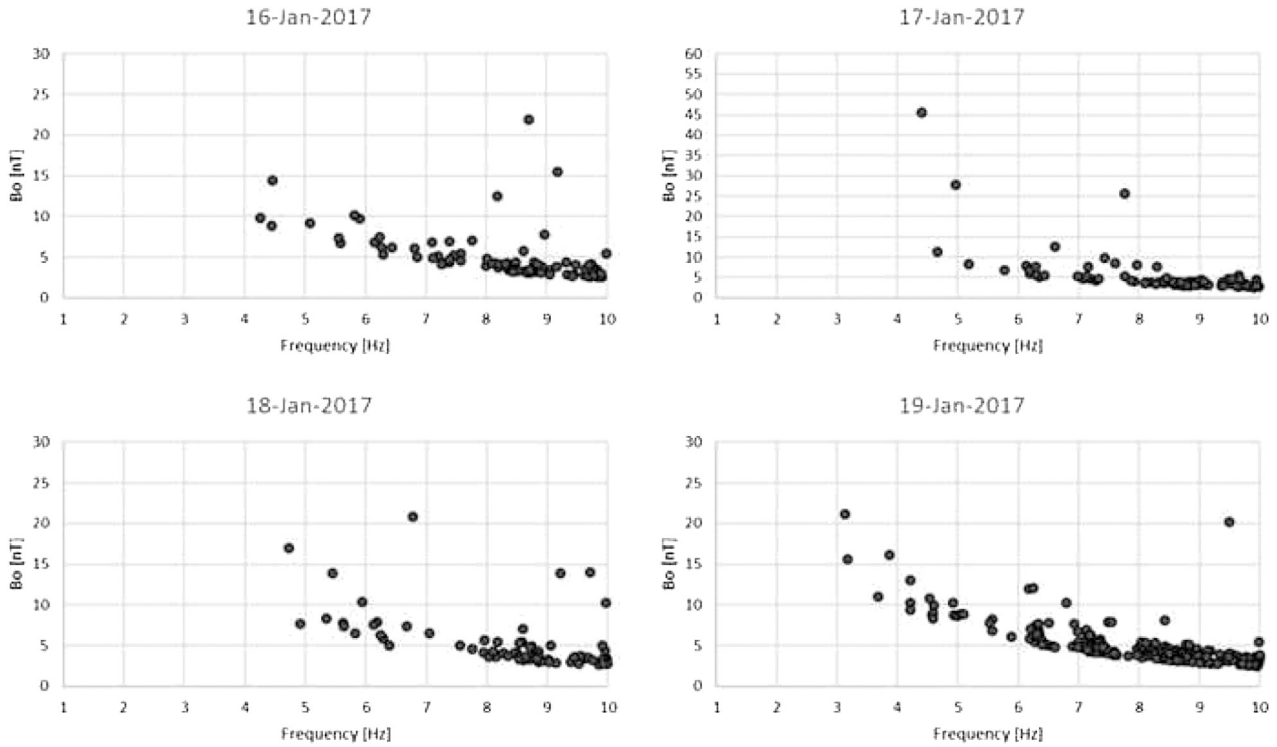

FIGURE 8 | The daily spectra from 16 to January 19, 2017. A day before the main shock in Capitignano (January 18, Mw = 5.5), three pulses with amplitudes greater than 20 nT appeared in the band between 4 and 8 Hz and even during the day of the main shock in Capitignano a pulse and the day after two pulses between 3 and 10 Hz.

The pulse rate increased to 88 on 27 October, decreased to 30 on 28 October, and increased again to 60 on October 29, 2016, the day before the main shock in Norcia (see **Figure 9A**). After this day, the pulse rate returned to the average value of eight pulses for day in the next days until November 3, 2016, when a new maximum of 92 was reached (see **Figure 9A**). For the next three weeks, pulse rate maxima appeared at intervals of exactly one week. Therefore, the entire process of weekly increases in pulse rate covered a four-week interval with a total of five maxima. The same pattern appears in **Figure 6** as was obtained by IC2 analysis. A new strong pulse rate was measured by IC1 on January 16, 2017, 2 days before the strong seismic swarm of Montereale, L'Aquila, about 70 km from Chieti Station, when 96 daily magnetic pulses were recorded by IC1. A similar peak was observed by IC2 analysis as well. The methodologies performed by IC1 and IC2 were essentially different, as the first was based on FFT with a threshold chosen from the signal power, whereas the other was based on a threshold chosen from the signal amplitude after filtering in signal periods. However, they produced identical results of significant variations in pulse rates. IC2 analysis revealed that the characteristic pulse frequencies reached the upper border of ULF band, where natural phenomena such as geomagnetic activity are able to generate disturbances. The majority of the ULF radiation have magnetospheric origin, thus, the geomagnetic activity of the same period was reported by means of the Ap (downloaded from ftp://ftp.ngdc.noaa.gov/STP/GEOMAGNETICDATA/APSTAR/apindex) and Dst (downloaded from http://wdc.kugi.kyoto-u.ac.jp/dst_final/index.html) indexes (see **Figures 9B,C** for comparisons with the magnetic pulse number). The Ap index is a measure of the general level of geomagnetic activity over the globe that is related to solar activity such as solar storms and the eleven-year cycle, which produces strong magnetospheric influences (Vassiliadis, 2008). Dst was also considered to take into account sub-storm activity, when geomagnetic perturbations can be of considerable intensity even if concentrated in the ULF band (Echer et al., 2004; Kozyreva et al., 2007). In particular, the sudden negative variations in Dst could be misinterpreted as magnetic pulses when intensity variations exceeded 100 nT. **Figures 9A,B** show that magnetic pulse maxima do not in general coincide with peaks of the Ap index or with stronger quakes. Even Dst variations are not related to the pulse number according to **Figures 9A,C**. Finally, statistical correlations were calculated between the magnetic pulses and the Ap index time series (see **Supplementary Material**), and between the magnetic pulses and the Dst index time series (see the **Supplementary Materials**). They are reported in **Figure 10** left, which show no significant statistical correlations.

DISCUSSION OF PHYSICAL MODELS

Electric and magnetic fields recorded by Chieti Station in 2016 and 2017 evidenced several excesses with respect to the average

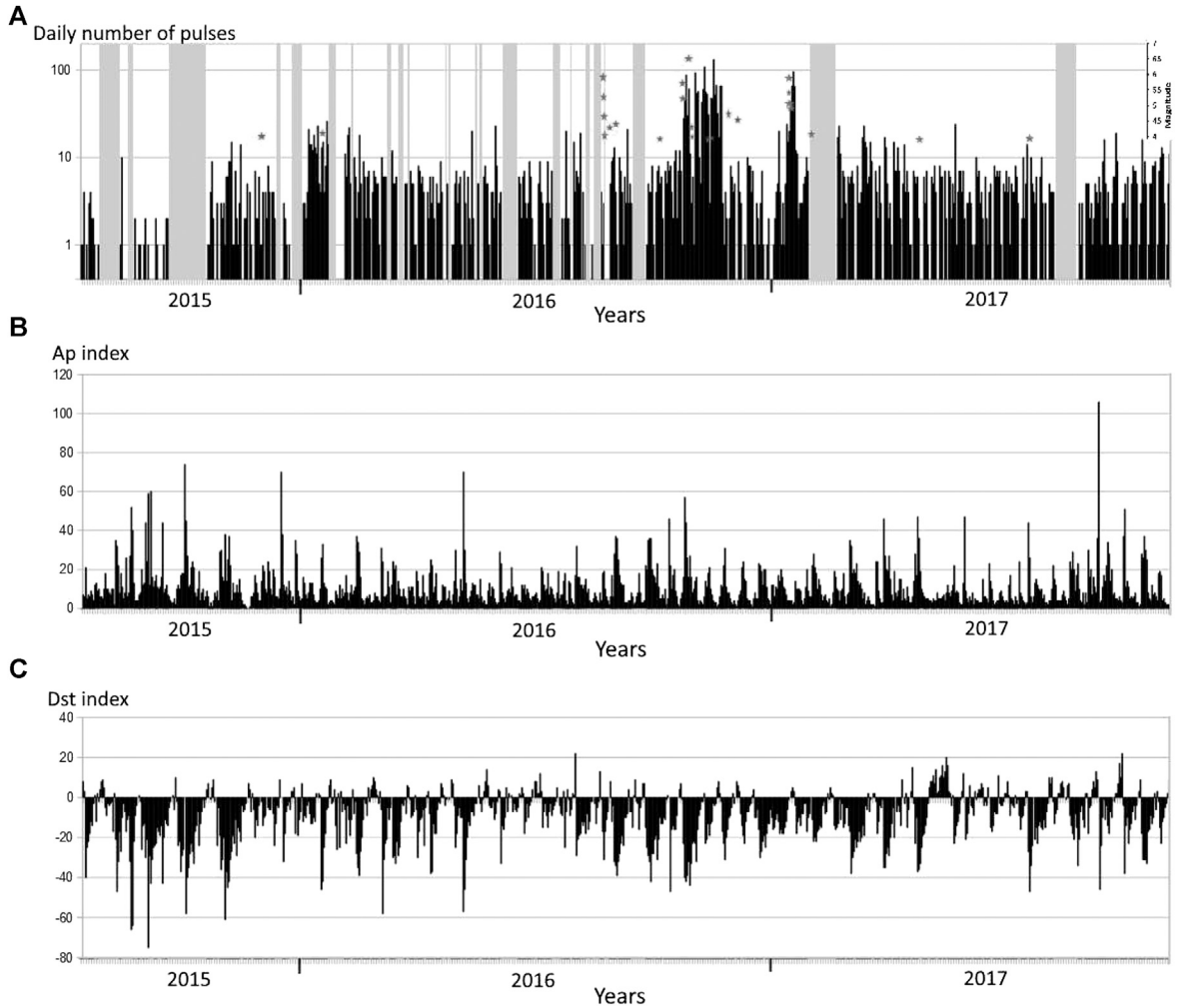

FIGURE 9 | The daily number of magnetic pulses recorded by IC1 for the time interval from the end of July 2015 to October 2017 is indicated by vertical lines in **(A)**. Vertical lines in **(B,C)** describe geomagnetic activity by means of Ap and Dst indexes, respectively. The occurrence of strong seismic events (M ≥ 4) is indicated by grey stars. Periods of lost data are indicated by gray shadows.

recordings which occurred around the major seismic events. Indeed, no excesses were recorded around the Amatrice earthquake of Mw = 6.0 on August 24, 2016 for electric or magnetic fields. Even though a significant loss of data occurred days and weeks before this event, first from 5 to 7 August and then from 13 to 21 August, during the 3 days preceding the "main shock" and even during the 6 days afterward, the data acquisition did not record any significant variations of electric or magnetic signals. Moreover, electric and magnetic excesses were recorded around the Castelsantangelo sul Nera earthquake on 26 October (Mw = 5.9), the Norcia earthquake on 30 October (Mw = 6.5), and the Montereale earthquake on 18 January (Mw = 5.5). However, such excesses were detected not exactly on the occurrence of these events but hours and days before and after the quake times. Thus, electromagnetic propagation is not able to justify such time differences, nor did the electric and magnetic recording times coincide with the passage of seismic waves (Yamazaki, 2012) at the position of Chieti Station. Therefore, it seems that any possible physical model connected with charge separation which occurs during rock fractures or seismo-electromagnetic generation must be discarded in this discussion.

Specifically, electric field excesses measured on the occasions of the L'Aquila and Modena earthquakes which occurred in 2009 and 2012, respectively, consisted in ELF oscillations whose intensities reached a maximum during the days around the main shocks (Fidani, 2011; Fidani and Martinelli, 2015). Electric field oscillations in the ELF band with the same spectral pattern as the cited cases were also recorded around Norcia and Capitignano earthquakes, as shown above. In all of the described cases, the intensity excesses of electric oscillations lasted weeks before and after the respective main shocks, with intensity distributions centered around the earthquake times. Therefore, even if some excesses in electric oscillations cannot be excluded around the Amatrice earthquake when loss of data occurred, the recordings show that a distribution centered around

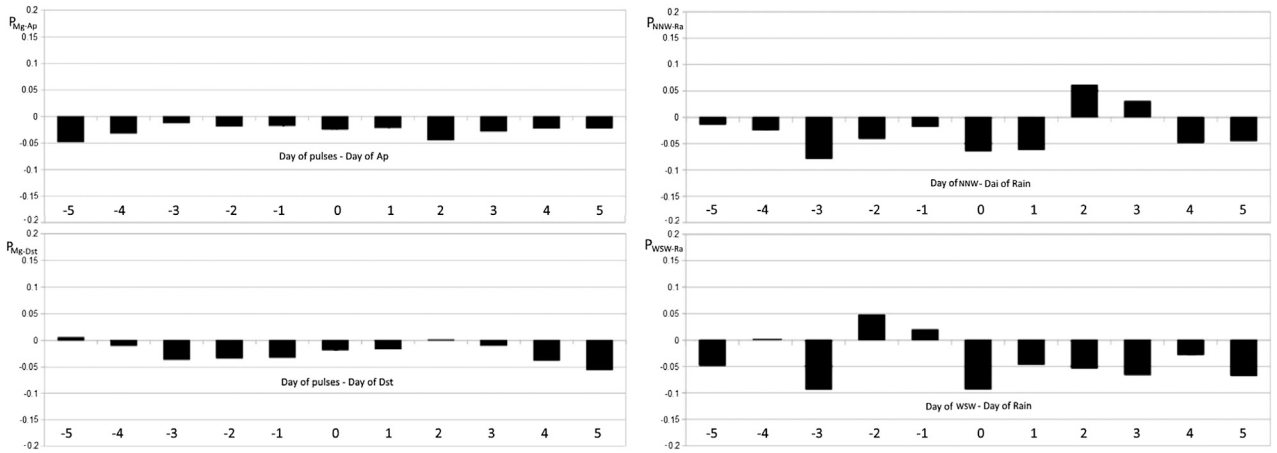

FIGURE 10 | Statistical correlations of ±5 days in time differences between magnetic pulses and Ap index time series, and between magnetic pulses and Dst index time series on the left, degree of freedom were 835; between NNW electrical oscillations and rain at Chieti Scalo time series, and between WSW electrical oscillations and rain at Chieti Scalo time series on the right, degree of freedom were 467.

the Amatrice earthquake time did not appear. Moreover, the increased density in daily detection of electric oscillations which was observed weeks before and after the L'Aquila 2009, Modena 2012, and Norcia 2016 earthquakes was also observed by the Chieti electric detector around the time of the Amatrice earthquake. Further properties are evidenced in this study concerning electric oscillations with respect to those observed for the L'Aquila and Modena earthquakes, as the intensity of electric oscillations was discriminated between the NNW and WSW directions in this work. Recordings evidenced that intensity variations increased significantly only in the WSW direction, while the density in daily detection increased for both the NNW and the WSW direction.

Regarding the magnetic field, excesses occurred in the number and intensities of magnetic pulses, which exceeded some thresholds. Such excesses were also observed for the L'Aquila earthquake in 2009, by means of a loop located near L'Aquila city (Orsini, 2011), and for the Modena earthquake in 2012 by means of an integrated semiconductor device near Modena [Curcio, 2012 (personal communication)]. Pulses were not observed for the Modena earthquake in 2012, probably because no loops were working at less than 300 km from the epicentre. Excesses in the number of magnetic field pulses were also recorded around Norcia and Capitignano earthquakes (see **Figures 6, 9A**), while they were not recorded around the Amatrice earthquake (see **Figure 9A**). Magnetic pulses were recorded with the same data gaps as the electric recordings. As for the electric signals, excesses in the number of magnetic pulse also showed a persistence of several days before and after the L'Aquila, Norcia, and Capitignano earthquakes. Such persistence was not observed around the Amatrice earthquake. Moreover, unlike past works, where magnetic pulses were recorded in the ULF band below 1 Hz (Johnston, 1997), here the harmonic content of pulses was concentrated in the ELF band, around 5 Hz. Finally, magnetic pulses in the ELF band were recently detected for moderate earthquakes reaching intensities of tens of nT, and in some cases beyond 100 nT (Scoville et al., 2015; Kappler et al., 2019).

The intensity and distribution of electric oscillations increased during the same weeks when the number of magnetic pulses increased around the Norcia earthquake, even though there were some differences. WSW electric oscillations increased around October 15, 2016, 11 days before the Castelsantangelo sul Nera events and 15 days before the Norcia event, reached a maximum intensity on 3 November, decreased in the next weeks, and then reached a new maximum on January 10, 2017. The number of magnetic pulses increased on October 25, 2016, reaching a maximum on 28 October and a minimum on November 2, 2016. The number of pulses continued to oscillate with a weekly period at least three more times, reaching an absolute maximum on November 16, 2016, then decreased, and then increased again on 17 January to reach a new maximum on January 19, 2017. Therefore, the ELF band electric activity started to increase about 10 days before the strong events of Castelsantangelo sul Nera and Capitignano, whereas the magnetic pulse activity started to increase about 1 day before strong shocks. A further comparison between electric and magnetic activity using IC1 evidenced the absence of magnetic pulses or oscillations corresponding to the electric oscillations, and the absence of electric oscillations and electric pulses also shifted in time corresponding to magnetic pulses, see Varotsos et al. (2003). More specifically, electric phenomena recorded around the earthquake time represent oscillations lasting from few minutes to tens of minutes with a frequency dispersion of several tens of hertz. Magnetic phenomena recorded around the earthquake time instead represent pulses lasting several tens of milliseconds with a frequency dispersion that is very large. Moreover, although they were both recorded in the ELF band, electric phenomena have a maximum power spectrum around 100 Hz while magnetic phenomena have a maximum power spectrum around and less than 10 Hz. Therefore, the two phenomena observed for the strong earthquakes of both

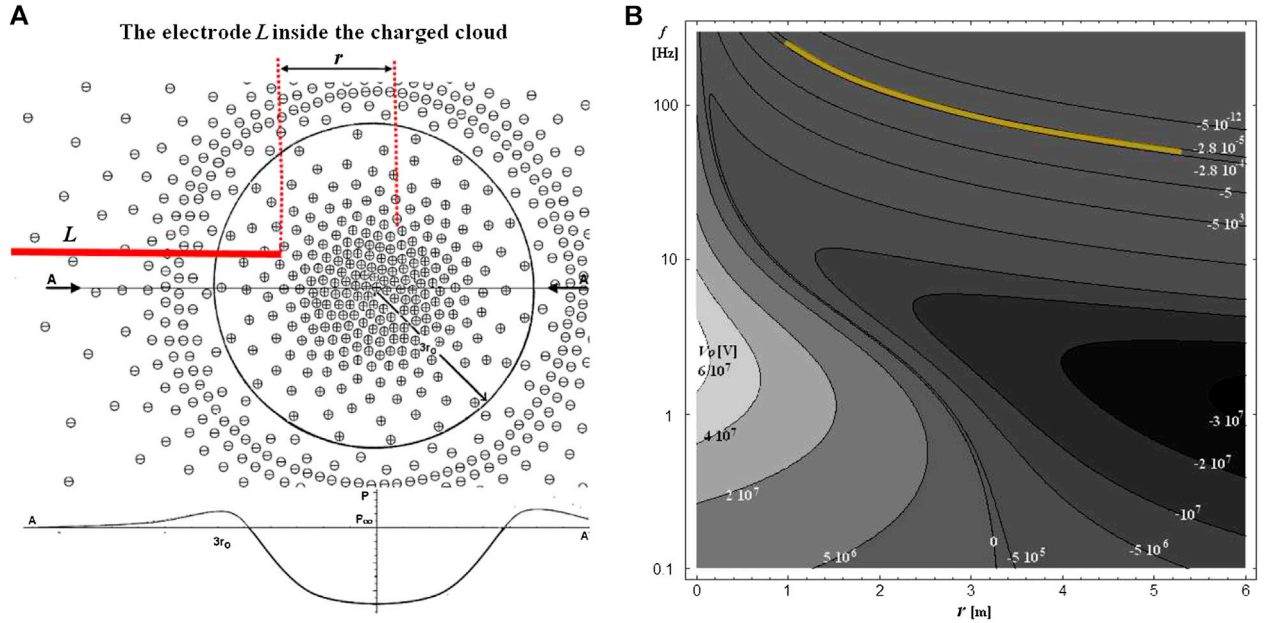

FIGURE 11 | The model of spherical charged clouds surrounding an electrode in **(A)**; the cloud radius separating opposite charges is $3r_o$, and the pressure P inside the section A-A of the cloud is depicted under it, where P_∞ is the pressure of 1 atmosphere. The retrieved induced potential V_o in the electrode L is shown with respect to the distance r and the oscillation frequencies f retrieved by **A6** and **A8**; the set of possible solutions for cloud distances and frequencies is evidenced on the contour plot of potentials **(B)**.

October 2016 and January 2017 did not seem to be directly related to one another. Consequently, the Maxwell equations can be used to verify failure of electric and magnetic recordings at Chieti Station together. They can be used to start with two different electrodynamics models describing observations, and then an attempt will be made to verify if a common cause can be found.

Starting with electric field measurements, the frequencies of electric field oscillations were very well defined in repeated electrical recordings with a persistent behavior of up to tens of minutes, which suggested some relatively stable source. Electric field oscillations were recorded only by one electrode at a time and one station at a time. Measurements suggested localized floating sources in the atmosphere of limited dimensions able to create a local electric field. For these reasons, the source of electric oscillations measured above the ground was thought to have been produced by charged clouds floating in the atmosphere. To evaluate the electric induction on the electrodes due to charged clouds, a comparison with the magnitude of Schumann Resonances phenomena was carried out. Intensities of Schumann Resonances are well defined, for the first at f = 7.4 Hz their induced potential can be estimated to be around 55 μV Hz$^{-½}$ (see **Supplementary Appendix A**). Potentials induced by charged clouds are evaluated by calculating the average potential along the electrode length as

$$V_o = 1/L \int_L^0 V(\mathbf{r}, x)\, dx, \qquad (1)$$

where the vector $\boldsymbol{r}$ is the distance between the tip of the wire and the center of the cloud. Mathematically, symmetric and dynamically stable charged clouds were proposed (Tennakone, 2011) by balancing electrostatic forces with air pressure, see **Figure 11A**. This model is attractive because it suggests that with high charge concentrations, corona discharges in the space between the separate charges can render the cloud luminous (Tennakone, 2011). Therefore, it is able to give a response for a class of observations of earthquake lights, ball lightning, which was one of the arguments (Fidani, 2010) that inspired the CIEN for electromagnetic monitoring. Finally, measurements obtained by CIEN allowed the possibility of estimating the electric field E in the atmosphere and its frequency, making it possible to roughly evaluate the dimensions of the charged clouds. Following **Supplementary Appendix A**, the cloud separation diameters of opposite charges are evaluated between 108 and 27 cm respectively with the corresponding positive charges ranging between 2.3 × 10^{-4} C, in a volume of 6.6 × 10^5 cm^3, and 1.4 × 10^{-5} C, in a volume of 7.6 × 10^4 cm^3, respectively. These give average ion concentrations inside the clouds of about 2.2 × 10^9 and 1.2 × 10^9 ions/cm^3, respectively. They are able to induce an emf along the electrodes which is calculated in **Supplementary Appendix A**, it resulted between 2.8 × 10^{-5} to 2.8 × 10^{-4} V Hz$^{-½}$, see **Figure 11B**. Based on this model and the ratio between induced potentials, it is demonstrated in **Supplementary Appendix A** that the electrodes are completely surrounded by negative charge density.

Electric activity observed during the L'Aquila seismic swarm in 2009 (Fidani, 2011) and during the Modena seismic swarm in 2012 (Fidani and Martinelli, 2015) evidenced that increases in electrical activity occurred in the spring and summer seasons. Meteorological activity also manifested itself more frequently

with thunderstorms in spring and summer (Camuffo et al., 2000; Poelman et al., 2014), so past works took into account the possibility that intensity excesses of electric oscillations could be produced by meteorological activity. However, this should be not the case for the 2016 and 2017 Central Italy earthquakes, when electric oscillation excesses appeared between October 2016 and January 2017 (see **Figure 6**). More specifically, electric oscillations recorded at less than 1 h from rainfall were excluded and a statistical correlation, between the remaining electric oscillations and rainfall at Chieti Station was studied by means of the Pearson product-moment correlation coefficient. The considered period of one and a half years, with 467 effectively recorded days, included 213 days of electric oscillations and 131 rainfall days. The result of the correlation calculation showed that a correlation between the electric oscillations and rainfall is not significantly different from zero (see **Figure 10** right). Furthermore, **Figures 5A,B** show equal density of daily electrical oscillations in the NNW and WSW directions between June 2016 and January 2017, but intensities sound different, with only intensities in the WSW direction having maxima around the Norcia and the Capitignano earthquakes. The difference, which was not evidenced for the L'Aquila and Modena earthquakes, could be linked to wind direction as wind is able to transport clouds of ions. In these pictures, WSW is the direction perpendicular to the Apennine chain.

The model can now be tested to explain magnetic measurements corresponding in time to electric field oscillations, which report no apparent signals emerging from the noise. To this end, it can be considered that in a perfectly spherical symmetric charge distribution, the only direction in which the electric, magnetic, and radiation fields can point is radially outward from the center of the sphere. Moreover, in a radiation field, the electric and magnetic fields must be transverse to the direction of motion, so even if this system is pulsating, it does not produce any radiation. In general, symmetric structures which oscillate radially do not radiate electromagnetic fields due to the symmetry (Heller et al., 2004). However, if a magnetic field detector is in the atmosphere and the charged cloud goes around it, surrounding and encasing it, then the instrument is able to see asymmetric charge movements and to measure variations in the electric and magnetic fields. In the case of Chieti Station, the electric detector can be reached by charged clouds while the magnetic one cannot because it is located underground, at about 20 m from the position of the electric detector. Therefore, it is clear that the Chieti magnetic detector is not able to measure the magnetic component of electric oscillations of charged clouds.

With regard to electric signatures of magnetic pulse recordings, pulses were characterized by a threshold fixed at the Chieti magnetic detector which corresponds to pulse amplitudes exceeding 2.5 nT at 10 Hz, with many recorded pulse amplitudes that reached several tens of nT. To have an initial estimate of the minimal electrical current flowing in the Earth's crust, a simple model using the Biot-Savart law which considers an infinitely long line conductor that is at some depth in the Earth's crust was used.

$$B_o = \mu_o I_o / (2\pi r). \tag{2}$$

Given that the loop has an axis oriented approximately NNW–SSE, the idealized current flowing parallel to the ground plane that can be induced in the loop will have an approximately WSW-ENE direction, which is perpendicular to the fault strike of Central Italy. This configuration required current variations from at least 1 kA for 2.5 nT to 30 kA for the 80 nT pulses measured before the Norcia earthquake, where the WSW-ENE line is about 75 km from Chieti, and 0.5–10 kA for the Capitignano earthquakes, where the WSW-ENE line is about 40 km from Chieti, in order to produce magnetic induction intensities of up to 50 nT. However, a localized infinitely long line conductor seems a very particular and unlikely condition to be verified in the Earth's crust to describe magnetic recordings at the Chieti station, as it is not possible to demonstrate that such long line conductors exist underground and currents are not dispersed much earlier. Then, a second model of a finite short horizontal dipole located at the hypo-centre was considered to model magnetic pulses measured at ground (Bortnik et al., 2010). The theoretical approach was developed for an antenna lying near a planar interface (King et al., 1981), which was placed underground in a simple homogeneous medium characterized by its magnetic permeability μ, electric permittivity ε, and electric conductivity σ. The generation of underground electrical currents that may account for the reported observations at large distances of many tens of km can thus be estimated for concentrated sources. The second Maxwell equation system which makes it possible to estimate the magnetic induction generated in a complex permittivity medium $\epsilon = \varepsilon + i\,\sigma/\omega$ can be written as

$$\begin{aligned} \nabla \times \mathbf{E} &= i \cdot \omega \cdot \mathbf{B}, \\ \nabla \times \mathbf{B} &= \mu\,(\mathbf{J} - i \cdot \omega \cdot \varepsilon \cdot \mathbf{E}), \end{aligned} \tag{3}$$

where the dipole current $\boldsymbol{J_y} = \delta(x)\,\delta(y)\,\delta(z - d)$ is located at a depth d in the half-space $z > 0$, oriented along the x-axis in the WSW-ENE direction at the position $x = 0$ and $y = 0$. Thus, the intensity of the radiating element $I\Delta l$ is a seismo-telluric current which can be constrained by **Eq. 3**. The system **3** can be solved by a two-dimensional spatial Fourier transform of the fields and imposition of the boundary conditions at the ground, between the atmosphere and soil. The results can be scaled as $\sim e^{-z/\delta}$ (Bortinik et al., 2010), where the skin depth is defined by

$$\delta = \left(\pi f \mu_o \sigma\right)^{-1/2}, \tag{4}$$

while the magnetic field intensity coupled with the loop B_y scales linearly with $I\Delta l$. Based on the reported typical pulse lengths, a frequency of f = 2–10 Hz was considered in the following. With regard to the conductivity of the Earth's crust in Central Italy, the Apennine chain is characterized by a 4 km thick top layer of quartzite with $\sigma = 5 \times 10^{-4}\ \Omega^{-1}\mathrm{m}^{-1}$ and underlying gneiss and granite basement with $\sigma = 2.2 \times 10^{-3}\ \Omega^{-1}\mathrm{m}^{-1}$, where μ is approximately $10\,\mu_o$ (Juhlin, 1999). These values were confirmed by magneto-telluric studies which obtained a three-strata model that also included superficial soft terrains not present on the Apennines, characterized by values of $0.2\ \Omega^{-1}\mathrm{m}^{-1}$ up to 2 km, $3.33 \times 10^{-4}\ \Omega^{-1}\mathrm{m}^{-1}$ for the next 3 km, and $2 \times 10^{-3}\ \Omega^{-1}\mathrm{m}^{-1}$ for the next 5 km, respectively (Di Lorenzo et al., 2011). A conductivity of $2.2 \times 10^{-3}\ \Omega^{-1}\mathrm{m}^{-1}$ is used for the

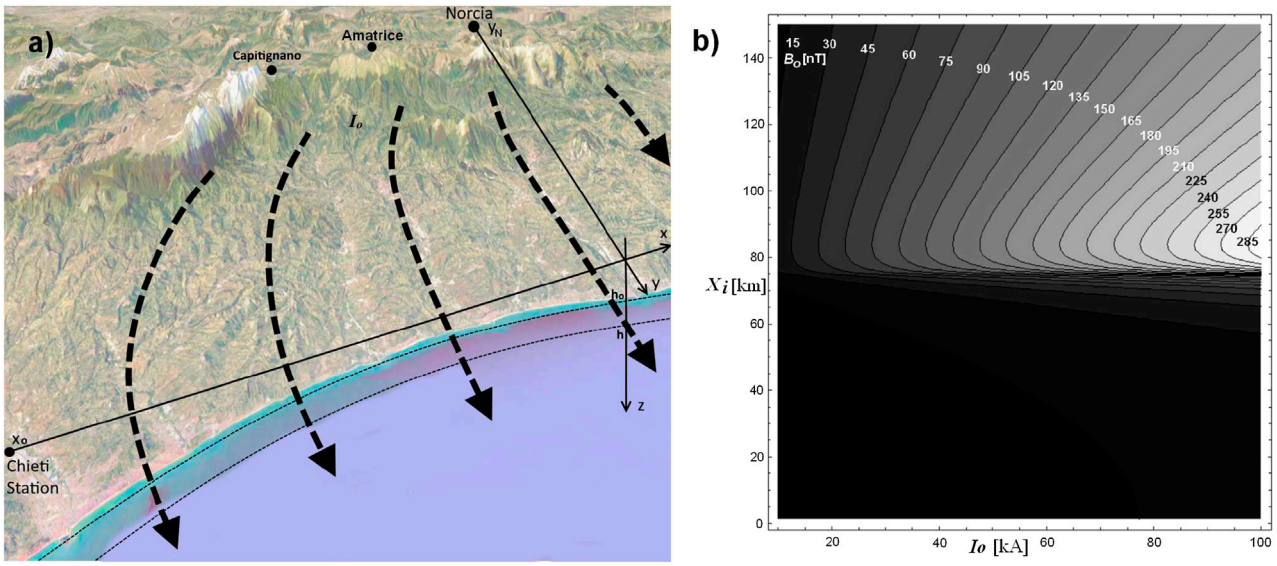

FIGURE 12 | The model of electrical currents flowing from the Apennines around the hypo-centre to the Adriatic Sea through the conductive clay layer with the system coordinates in **(A)**; the Chieti Station is at x_o = −75 km while Norcia is at y_N = −65 km. The retrieved magnetic field B_o in the position of Chieti due to the total current I_o, flowing through the conductive layer thickness h–h_o = 5.9 km of width between -x_i and x_i, in a contour plot **(B)**.

homogeneous model considered here as the basement with resulting skin depths δ = 1–2.2 km, depending on f. The top 4 km quartzite layer is characterized by skin depths δ = 2.2–5 km, depending on f. However, ulterior overlying 6 km soft terrains characterized by conductivity of 0.1 $\Omega^{-1}m^{-1}$ and $\mu = 6\,\mu_o$ (Juhlin, 1999), at places eastwards from Apennines such as Chieti, provide skin depths δ = 0.2–0.4 km, depending on f. Magnetic field intensities collected by means of the Chieti loop were calculated to be between 2.5 and 80 nT for the Castelsantangelo sul Nera and Norcia seismic events and between 2.5 and 50 nT for the Capitignano events. Following Bortnik's work (2010) which is to be used directly in calculating the minimal current necessary to produce magnetic perturbations, a minimum of B_o = 2.5 nT to be observed at Chieti Station was calculated. Taking into account the further estimated loss due to the 6 km soft terrain, it should have required at least $I\Delta l = 4.8 \times 10^{18}$ A·m at a distance of 70 km. That is, a 10-km-long radiating element requires a 4.8×10^{14} A telluric current at a source hypo-centre such as Capitignano. On the other hand, a minimum of B_o = 2.5 nT to be observed at Chieti Station should require $I\Delta l = 2.1 \times 10^{24}$ A·m at a distance of 100 km. That is, a 10-km-long radiating element requires a 2.1×10^{20} A telluric current at a source hypo-centre such as Norcia. Both values, being minimal values due to the nodes of magnetic distribution, are so elevated as to be unrealistic too. Even if the variable magnetic fields can enter into the atmosphere above the Apennines with intensity losses of 2.5×10^{-3} to 1.8×10^{-2}, depending on f, and considering only the geometric loss into the atmosphere, a minimum of 92 and 190 MA current variations would be required to induce signals above the threshold of the magnetometer at Chieti for Capitignano and Norcia, respectively.

Finally, a more realistic model of a distributed electrical current was considered starting from the geological settings of the eastern region in Central Italy. In fact, the Sibillini Mountains where the intense seismic sequence occurred are about 60 km WSW of the Adriatic Sea, which can behave like a very good electric mass, having $\sigma = 5\,\Omega^{-1}\,m^{-1}$, toward which any electric charge excess will converge. The geology of the region between mountains and sea is characterized by several kilometres of Laga's wet clay, which is a good conductor with a conductivity of 0.05–0.2 $\Omega^{-1}\,m^{-1}$. Thus, as Laga is a large area extending parallel to both the Adriatic sea and the Apennines, eventually electrical currents between them will be distributed over large sections of the clay deposits. This means that if a charge excess is generated inside the Apennines it will migrate preferentially eastwards, where the large clay area is parallel to the Adriatic coast, and it is thus able to reach lower latitudes equal to Chieti Station latitude (see **Figure 12A**). These geological considerations are sufficient to suggest a new physical model of a magnetic field created by electrical current density migrating perpendicular to the Adriatic coast. The calculation described in **Supplementary Appendix C** retrieves the magnetic induction B_o concatenated with the coil of the instrument and generated by an electrical current density going through a soil section east of the Apennines (see **Figure 12A**). A current source I_o is located at the earthquake epicentre (x_N,y_N), where x_N = 0 km and y_N = −65 km, while current lines go toward the Adriatic sea, partially passing below Chieti Station at (x_o,y_o), where x_o = −75 km and y_o = 0. The current density is supposed to extends in a section of $2x_i\,(h - h_o)$ and is coupled with the loop depending on distance of the idealized infinite line current, and loop reciprocal orientations (see **Supplementary Appendix C**). A contour plot of B_o is shown in **Figure 12B** with respect to x_i extension, using a total current

variation of I_o. Supposing I_o is able to extends under the Chieti Station, therefore $x_i = x_o$, about 40 kA of distributed current variations are sufficient to create variations of B_o = 80 nT, with h_o = 0.1 km and h = 6 km according to geological results for the conductive layer. About 1.3 kA of distributed current variations are necessary to create variations of B_o = 2.5 nT. The electric current density variations to create B_o = 2.5–80 nT can be calculated to about 1.5–44 μA m^{-2} at the position of Chieti and, considering the fault length of 20 km and the layer thickness of 6 km, as variations of about 0.011–0.3 mA m^{-2} around the epicentre position. The retrieved magnetic induction B_o was found to be little influenced by either h or h_o. The same calculation can be repeated for the Capitignano earthquakes located at $x_C = -35$ and $y_C = -55$ km, where the difference between the Chieti Station coordinate and the WSW-ENE line position of such earthquakes was about $x_o - x_C = -40$ km. In this case, considering $x_{oi} = x_C$, the distributed electric current variations can be calculated to create B_o = 2.5–50 nT as about I_o = 0.7–14 kA with 1.4–28 μA m^{-2} of current density variations at the position of Chieti.

Magnetic field pulses are thought of as sudden interruptions of current density in the hypo-centre region to produce current variations and magnetic field variations all around the current density layer. To compare corresponding electric field pulses to magnetic ones, it is necessary to consider that both magnetic and electric detectors are located near the conductor, the conductive layer. In this case, the emitted electromagnetic energy will be principally magnetic with a small electric component, which is due to the conductor's presence, which reduces the electric field inside it to zero by definition. Indeed, the conductive clay layer is characterized by a finite conductivity (0.1 Ω^{-1} m^{-1}) and its effect on the electric field can be calculated. Electric fields corresponding to the measured magnetic fields can be written as (Lifstis and Pitaevskij, 1986):

$$E_y \approx 2\pi\delta B_x / (\mu_o \lambda), \quad (5)$$

where δ is the skin depth and was evaluated above to be between 0.5 and 1.1 km and λ is the wavelength of the electromagnetic emission that is equal to 30,000 km at 10 Hz and 150,000 km at 2 Hz. Electric field pulse intensities are therefore calculated to be in the range between 2.5 and 4 μV m^{-1}, for greatest pulses of Capitignano and Norcia earthquakes, respectively, around 2–4 Hz. These values are well under the noise level of the electric field and should not be revealed by electric detectors used in this experiment in accordance with the results.

A possible common cause for both observed magnetic and electric measurements with strong earthquakes it is premature at this stage of research. However, some specific model of electrified CO_2 gases passing through the newly created fracture surface of the rock can be considered (Enemoto et al., 2017). Electrified gases are able to produce electric charge excesses in the crust and atmosphere and to generate pressure-impressed current/electric dipoles (Enemoto et al., 2012). Another possible model is the hypotheses of the Lithosphere-Atmosphere-Ionosphere Coupling (Pulinets, 2011; Pulinets and Ouzounov, 2011). It can unite the gaseous emissions before earthquake, charged clouds and thermal anomalies in the common chain, where the key role plays the process of ionization of atmospheric gases (Pulinets et al., 2015). This ionization is provided by α-active radon released over active tectonic faults and tectonic plates borders. Pulses of electrified gases could be responsible for electric charged clouds in the atmosphere and electrical current variations in the crust.

CONCLUSIONS

Continuous recordings of non stationary electric fields and magnetic fields with frequencies in the band (3–300 Hz) evidenced specific signals which were exceptional in number and intensity at Chieti Station between 2016 and 2017. Electric anomalies consisting of oscillations of up to a few hundred hertz did not correlate with meteorological lightning and rainfall. Magnetic anomalies consisting of pulses with characteristic frequencies up to 10 Hz did not correlate with Dst and Kp indexes. Nine strong earthquakes distributed in three main periods struck Central Italy in August 2016, October 2016, and January 2017. Events that occurred in October 2016 and January 2017 were preceded by increases in electric oscillations weeks beforehand and were preceded by increases in the number of magnetic pulses 1 day before. It was discussed that the duration of electric oscillations and magnetic pulses lasted for several days and weeks around the earthquake times. Therefore, the Amatrice earthquake in August 2016 seemed to be not accompanied by increased electric magnitude and pulse number even though the data from Chieti Station show gaps during the days around the time of that earthquake.

The electric field components along the WSW and NNW directions showed a gradually increasing number of horizontal electric oscillations. Specifically, the WSW component of the electric field perpendicular to the Apennine chain was characterized by an increase in intensity since mid-October 2016, a maximum in electric intensity occurred on November 2, 2016, and a second maximum of the same intensity on January 6, 2017, about 10 days before the Capitignano shocks. The number of days with electric oscillations also increased during the same period. In contrast, the NNW component of the electric field parallel to the Apennine chain was not characterized by intensity increases but only by the number of days on which electric oscillations increased, from middle of October to the end of December 2016. These results are in agreement with observations made on the occasions of the L'Aquila 2009 (Mw = 6.3) and the Emilia 2012 (Mw = 6.0) earthquakes, when increases of electric oscillations were recorded by Fermo and Zocca stations, respectively.

The magnetic data analysis at Chieti Station, performed through two independent sample systems of the same signal, and two different methods made by Labview and Spectrum Lab programs, shows that 6 days before the earthquake of Norcia and 1 day before the Castelsantangelo sul Nera earthquakes, a large number of pulses were recorded in the ELF band below 10 Hz with amplitudes mostly in the range of 2.5–80 nT, which almost disappeared on the day that the main shock (Mw = 6.5) occurred in Norcia, October 30, 2016. Furthermore, 1 day before the main shock occurred in Capitignano (Mw = 5.5) on January 18, 2017, a larger number of pulses started to be recorded with amplitudes

mostly in the range of 2.5–50 nT, and the number then decreased the day after the main shock. These kinds of magnetic signals were already recorded before the L'Aquila (Mw = 6.3) earthquake that occurred on April 6, 2009 (Orsini, 2011), and should be considered to verify their recurrence in sufficiently large number of strong earthquakes.

Physical models were developed to allow for an interpretation of the electric and the magnetic measurements. The model for electric oscillations consisted of charged clouds kept together by atmospheric pressure holes which yielded a stable structure able to oscillate. This model was able to describe the lack of corresponding magnetic components from the loop detector. It was not able to describe differences between WSW measurements and NNW measurements. Data recorded in the other CIEN stations was used up to now exclusively to verify that electric oscillations are not coincident in time and amplitude at different positions, confirming to be local phenomena. The model for magnetic pulses consisted of diffused underground electrical currents between the Apennines and the Adriatic Sea. Furthermore, following this model, the amplitudes and the increased trigger counts recorded before the earthquakes could even be related to the distance from the epicentres to the antenna, which was about 70 km for the Capitignano earthquake epicentre and about 100 km for the Norcia earthquake epicentre. In a model constrained by the geology of the area, a clay conductive layer was able to drive charge excess into the Adriatic Sea, and therein also underneath the Chieti station. The current required to induce detectable pulses is greater than 1 kA, and is greater than 40 kA for strongest pulses, which is of the same order than previous estimated (Bortnik et al., 2010).

The two models, of charged clouds and diffused currents, are self-consistent. Spherically symmetric charged clouds are unable to radiate electromagnetic energy, according with the lack of corresponding magnetic components from the coil magnetometer. Diffused electric currents in the crust are able to describe the lack of corresponding electrical components from the electric field detector as energy was principally concentrated in the magnetic field near the conductive layer. Signal to noise ratio limits of two instruments are consistent with measurements of natural signals such as Schumann Resonances. Common-mode noise generated in the ionosphere/magnetosphere was quantified and considered through geomagnetic indexes. The two different models used for electrical oscillations and magnetic pulses have not yet assigned a common cause, although upwards migrating fluids offer some well-founded answers.

DATA AVAILABILITY STATEMENT

The datasets generated for this study are available on request to the corresponding author.

AUTHOR CONTRIBUTIONS

CF is the coordinator of the work and he interpreted the data. MO is the acquisition data expert of the work and helped the first author to interpret the data. GI and NV monitored the acquisitions and the laboratory. FS helped the coordination of the work and revised it.

ACKNOWLEDGMENTS

The authors are grateful to Joerg Renner for his valuable comments.

SUPPLEMENTARY MATERIAL

The Supplementary Material for this article can be found online at: https://www.frontiersin.org/articles/10.3389/feart.2020.536332/full#supplementary-material

REFERENCES

Baratta, M. (1891). "Catalogo dei fenomeni elettrici e magnetici apparsi durante i principali terremoti,"in *Rendiconti della Società Italiana di Elettricità pel progresso degli studi e delle applicazioni*, Milano, Italy: Tip. Lamperti di G. Rozza, Vol. 1-anno XIII, 15.

Baratta, M. (1901). *I Terremoti d'Italia: saggio di storia, geografia e bibliografia sismica italiana con 136 sismocartogrammi*. Editor A. Forni (East Lansing, MI: Michigan State University), 950.

Barr, R., Jones, D. L., and Rodger, C. J. (2000). ELF and VLF radio waves. *J. Atmos. Sol. Terr. Phys.* 62 (17), 1689–1718. doi:10.1016/s1364-6826(00)00121-8

Biagi, P. F., Castellana, L., Maggipinto, T., Loiacono, D., Schiavulli, L., et al. (2009). A pre seismic radio anomaly revealed in the area where the Abruzzo earthquake (M = 6.3) occurred on 6 April 2009. *Nat. Hazards Earth Syst. Sci.* 9, 1551–1556. doi:10.5194/nhess-9-1551-2009

Biagi, P. F., Ermini, A., and Kingsley, S. P. (2001). Disturbances in LF radio signals and the Umbria-Marche (Italy) seismic sequence in 1997–1998. *Phys. Chem. Earth C* 26 (10–12), 755–759. doi:10.1016/s1464-1917(01)95021-4

Bleier, T., Dunson, C., Maniscalco, M., Bryant, N., Bambery, R., and Freund, F. (2009). Investigation of ULF magnetic pulsations, air conductivity changes and infra red signatures associated with the 30 October Alum Rock M5.4 earthquake. *Nat. Hazards Earth Syst. Sci.* 9 (2), 585–603. doi:10.5194/nhess-9-585-2009

Bobrovskiy, V. S., Stoppa, F., Nicoli, L., and Losyeva, Y. (2017). Nonstationary electrical activity in the tectonosphere-atmosphere interface retrieving by multielectrode sensors: case study of three major earthquakes in Central Italy with M > 6. *Earth Sci. India* 10, 269–285. doi:10.1007/s12145-017-0296-4.

Boldyrev, A. I., Vyazilov, A. E., Ivanov, V. N., Kemaev, R. V., Korovin, V. Y., Melyashinskii, A. V., et al. (2016). Registration of weak ULF/ELF oscillations of the surface electric field strength. *Geomagn. Aeron.* 56, 503–512. doi:10.1134/s0016793216040034

Bortnik, J., Bleier, T. E., Dunson, C., and Freund, F. (2010). Estimating the seismotelluric current required for observable electromagnetic ground signals. *Ann. Geophys.* 28, 1615–1624. doi:10.5194/angeo-28-1615-2010

Brozzetti, F., and Lavecchia, G. (1994). Seismicity and related extensional stress field: The case of the Norcia Seismic Zone (Italy). *Annales Tectonicae*, 8, 36–57.

Brozzetti, F., Boncio, P., Cirillo, D., Ferrarini, F., de Nardis, R., Testa, A., et al. (2019). High-resolution fieldmapping and analysis of the August-October 2016 coseismic surface faulting (central Italy earthquakes): Slip distri-bution, parameterization, and comparison with global earthquakes. *Tectonics* 38, 417–439. doi:10.1029/2018TC005305

Calderoni, G., Rovelli, A., and Di Giovambattista, R. (2017). Rupture directivity of the strongest 2016–2017 Central Italy earthquakes. *J. Geophys. Res. Solid Earth* 122, 9118–9131. doi:10.1002/2017JB014118

Camuffo, D., Cocheo, C., and Enzi, S. (2000). Seasonality of instability phenomena (hailstorms and thunderstorms) in Padova, northern Italy, from archive and instrumental sources since AD 1300. *Holocene* 10 (5), 635–642. doi:10.1191/095968300666845195

Cinti, F. R., Faenza, L., Marzocchi, W., and Montone, P. (2004). Probability map of the next M ≥ 5.5 earthquakes in Italy. *Geochem. Geophys. Geosyst.* 5 (11). doi:10.1029/2004gc000724

Di Lorenzo, C., Palangio, P., Santarato, G., Meloni, A., Villante, U., and Santarelli, L. (2011). Non-inductive components of electromagnetic signals associated with L'Aquila earthquake sequences estimated by means of inter-station impulse response functions. *Nat. Hazards Earth Syst. Sci.* 11, 1047–1055. doi:10.5194/nhess-11-1047-2011

Echer, E., Alves, M. V., and Gonzalez, W. D. (2004). Geoeffectiveness of interplanetary shocks during solar minimum (1995–1996) and solar maximum (2000). *Sol. Phys.* 221, 361–380. doi:10.1023/B:SOLA.0000035045.65224.f3

Enomoto, Y. (2012). Coupled interaction of earthquake nucleation with deep Earth gases: a possible mechanism for seismo-electromagnetic phenomena. *Geophys. J. Int.* 191 (3), 1210–1214. doi:10.1111/j.1365-246X.2012.05702.x

Enomoto, Y., Tsutsumi, A., Fujinawa, Y., Kasahara, M., and Hashimoto, H. (1991). Candidate precursors: pulse-like geoelectric signals possibly related to recent seismic activity in Japan. *Geophys. J. Int.* 131, 485–494. doi:10.1111/J.1365-246X.1997.TB06592.X

Enomoto, Y., Yamabe, T., and Okumura, N. (2017). Causal mechanisms of seismo-EM phenomena during the 1965–1967 Matsushiro earthquake swarm. *Sci. Rep.* 7, 44774. doi:10.1038/srep44774

Ferrarini, F., Lavecchia, G., de Nardis, R., and Brozzetti, F. (2015). Fault geometry and active stress from earthquakes and field geology data analysis: the Colfiorito 1997 and L'Aquila 2009 cases (Central Italy). *Pure Appl. Geophys.* 172 (5), 1079–1103. doi:10.1007/s00024-014-0931-7

Fidani, C., and Martinelli, G. (2015). A possible explanation for electric perturbations recorded by the Italian CIEN stations before the 2012 Emilia earthquakes. *Boll. Geofis. Teor. Appl.* 56, 211–226. doi:10.4430/bgta0145

Fidani, C. (2010). The earthquake lights (EQL) of the 6 April 2009 Aquila earthquake, in Central Italy. *Nat. Hazards Earth Syst. Sci.* 10, 967–978. doi:10.5194/nhess-10-967-2010

Fidani, C. (2011). The Central Italy electromagnetic network and the 2009 L'Aquila earthquake: observed electric activity. *Geosci. J.* 1 (1), 3–25. doi:10.3390/geosciences1010003

Galli, P., Castenetto, S., and Peronace, E. (2017). The macroseismic intensity distribution of the 30 October 2016 earthquake in Central Italy (M_w 6.6): seismotectonic implications. *Tectonics* 36, 2179–2191. doi:10.1002/2017TC004583

Gradshteyn, I. S., and Ryzhik, I. M. (2007). *Table of integrals, series, and products*. Editors A. Jeffrey and D. Zwillinger (Burlington, MA: Academic Press).

Grosz, A., Paperno, E., Amrusi, S., and Zadov, B. (2011). A three-axial search coil magnetometer optimized for small size, low power, and low frequencies. *IEEE Sens. J.* 11 (4), 1088–1094. doi:10.1109/jsen.2010.2079929

Han, P., Hattori, K., Hirokawa, M., Zhuang, J., Chen, C.-H., Febriani, F., et al. (2014). Statistical analysis of ULF seismomagnetic phenomena at Kakioka, Japan, during 2001–2010. *J. Geophys. Res. Space Phys.* 119 (6), 4998–5011. doi:10.1002/2014ja019789

Hayakawa, M., Kasahara, Y., Nakamura, T., Muto, F., Horie, T., et al. (2010). A statistical study on the correlation between lower ionospheric perturbations as seen by subionospheric VLF/LF propagation and earthquakes. *J. Geophys. Res.* 115, A09305. doi:10.1029/2009JA015143

Heller, L., Ranken, D., Best, E., Ranken, D., and Best, E. (2004). The magnetic field inside special conducting geometries due to internal current. *IEEE Trans. Biomed. Eng.* 51 (8), 1310–1318. doi:10.1109/tbme.2004.827554

Jackson, J. D. (1975). *Classical electrodynamics*. 1st Edn. Hoboken, NJ: Wiley and Sons Inc., 363.

Johnston, M. J. S. (1997). Review of electric and magnetic fields accompanying seismic and volcanic activity. *Surv. Geophys.* 18, 441–476. doi:10.1023/a:1006500408086

Juhlin, C. (1999). *Geotechnology: Geophysical Methods*.

Kamogawa, M., Liu, J.-Y., Fujiwara, H., Chuo, Y.-J., Tsai, Y.-B., Hattori, K., et al. (2004). Atmospheric field variations before the march 31, 2002 M6.8 earthquake in taiwan. *Terr. Atmos. Ocean Sci.* 15 (3), 397–412. doi:10.3319/tao.2004.15.3.397(ep)

Kappler, K. N., Schneider, D. D., MacLean, L. S., Bleier, T. E., and Lemon, J. J. (2019). An algorithmic framework for investigating the temporal relationship of magnetic field pulses and earthquakes applied to California. *Comput. Geosci.* 133, 104317. doi:10.1016/j.cageo.2019.104317

King, R. W. P., Smith, G. S., Owens, M., and Wu, T. T. (1981). *Antennas in Matter: Fundamentals, Theory and Applications*. Cambridge, MA: MIT Press.

Kozyreva, O., Pilipenko, V., Engebretson, M. J., Yumoto, K., Watermann, J., and Romanova, N. (2007). In search of a new ULF wave index: comparison of Pc5 power with dynamics of geostationary relativistic electrons. *Planet. Space Sci.* 55, 755–769. doi:10.1016/j.pss.2006.03.013

Kulak, A., Kubisz, J., Klucjasz, S., Michalec, A., Mlynarczyk, J., Nieckarz, Z., et al. (2014). Extremely low frequency electromagnetic field measurements at the hylaty station and methodology of signal analysis. *Radio Sci.* 49, 361–370. doi:10.1002/2014rs005400

Larkina, V. I., Migulin, V. V., Molchanov, O. A., Kharkov, I. P., Inchin, A. S., and Schvetcova, V. B. (1989). Some statistical results on very low frequency radiowave emissions in the upper ionosphere over earthquake zones. *Phys. Earth Planet. In.* 57 (1–2), 100–109. doi:10.1016/0031-9201(89)90219-7

Lavecchia, G., Adinolfi, G. M., de Nardis, R., Ferrarini, F., Cirillo, D., Brozzetti, F., et al. (2016a). Multidisciplinary inferences on a newly recognized active eastdipping extensional system in Central Italy. *Terra. Nova.* 29 (1) 77–89. doi:10.1111/ter.12251

Lavecchia, G., Castaldo, R., de Nardis, R., De Novellis, V., Ferrarini, F., Pepe, S., et al. (2016b). Ground deformation and source geometry of the 24 August 2016 Amatrice earthquake (Central Italy) investigated through analytical and numerical modeling of DInSAR measurements and structural-geological data. *Geophys. Res. Lett.* 43, 389. doi:10.1002/2016GL071723

Lavecchia, G., Ferrarini, F., Brozzetti, F., deNardis, R., Boncio, P., and Chiaraluce, L. (2012). From surface geology to aftershock analysis: constraints on the geometry of the L'Aquila 2009 seismogenic fault system. *Ital. J. Geosci.* 131 (3), 330–347. doi:10.3301/IJG.2012.24

Lifstis, E. M., and Pitaevskij, L. P. (1986). *Elettrodinamica dei Mezzi Continui*. Moscow, Russia: Mir, 655.

Molchanov, O. A., and Hayakawa, M. (1999). Subionospheric VLF signal perturbations possibly related to earthquakes. *J. Geophys. Res.* 103, 17489–17504. doi:10.1029/98JA00999

Němec, F., Santolík, O., and Parrot, M. (2009). Decrease of intensity of ELF/VLF waves observed in the upper ionosphere close to earthquakes: a statistical study. *J. Geophys. Res.* 114, A04303. doi:10.1029/2008JA013972

Orsini, M. (2011). Electromagnetic anomalies recorded before the earthquake of L'Aquila on April 6, 2009. *Bollettino di Geofisica Teorica e Applicata* 52 (1), 123–130.

Ouzounov, H., Büttner, R., and Zimanowski, B. (2002). Seismo-electrical effects: experiments and field measurements. *Appl. Phys. Lett.* 80, 334–336. doi:10.1063/1.1431693

Parrot, M. (1994). Statistical study of ELF/VLF emissions recorded by a low-altitude satellite during seismic events. *J. Geophys. Res.* 99, 23339–23347. doi:10.1029/94ja02072

Poelman, D. R., Schulz, W., Diendorfer, G., and Bernardi, M. (2014). "European cloud-to-ground lightning characteristics," in Proceedings of the International Conference on Lightning Protection (ICLP), Shanghai, China, October 11–18, 2014 (IEEE).

Pulinets, S. A., Ouzounov, D. P., Karelin, A. V., and Davidenko, D. V. (2015). Physical bases of the generation of short-term earthquake precursors: a complex model of ionization-induced geophysical processes in the lithosphere-atmosphere-ionosphere-magnetosphere system. *Geomagn. Aeron.* 55 (4), 521–538. doi:10.1134/s0016793215040131

Pulinets, S., and Ouzounov, D. (2011). Lithosphere-atmosphere-ionosphere coupling (LAIC) model-an unified concept for earthquake precursors validation. *J. Asian Earth Sci.* 41 (4–5), 371–382. doi:10.1016/j.jseaes.2010.03.005

Pulinets, S. (2011). The synergy of earthquake precursors. *Earthq. Sci.* 24 (6), 535–548. doi:10.1007/s11589-011-0815-1

Schekotov, A., Izutsu, J., and Hayakawa, M. (2015). On precursory ULF/ELF electromagnetic signatures for the Kobe earthquake on April 12, 2013. *J. Asian Earth Sci.* 114, 305–311. doi:10.1016/j.jseaes.2015.02.019

Scoville, J., Heraud, J., and Freund, F. (2015). Pre-earthquake magnetic pulses. *Nat. Hazards Earth Syst. Sci.* 15, 1873–1880. doi:10.5194/nhess-15-1873-2015

Tennakone, K. (2011). Stable spherically symmetric static charge separated configurations in the atmosphere: implications on ball lightning and earthquake lights. *J. Electrost.* 69, 638–640. doi:10.1016/j.elstat.2011.08.005

Uyeda, S., Nagao, T., and Kamogawa, M. (2009). Short-term earthquake prediction: current status of seismo-electromagnetics. *Tectonophysics* 470, 205–213. doi:10.1016/j.tecto.2008.07.019

Varotsos, P., and Alexopoulos, K. (1984a). Physical properties of the variations of the electric field of the earth preceding earthquakes, I. *Tectonophysics* 110, 73–98. doi:10.1016/0040-1951(84)90059-3

Varotsos, P., and Alexopoulos, K. (1984b). Physical properties of the variations of the electric field of the earth preceding earthquakes. II. determination of epicenter and magnitude. *Tectonophysics* 110, 99–125. doi:10.1016/0040-1951(84)90060-x

Varotsos, P., and Alexopoulos, K. (1987). Physical properties of the variations of the electric field of the Earth preceding earthquakes, III. *Tectonophysics* 188, 321–347. doi:10.1016/0040-1951(84)90060-X

Varotsos, P., and Lazaridou, M. (1991). Latest aspects of earthquake prediction in Greece based on seismic electric signals. *Tectonophysics* 136, 335–339. doi:10.1016/0040-1951(91)90462-2

Varotsos, P. A., Sarlis, N. V., and Skordas, E. S. (2003). Electric fields that "arrive" before the time derivative of the magnetic field prior to major earthquakes. *Phys. Rev. Lett.* 91 (14), 148501. doi:10.1103/physrevlett.91.148501

Varotsos, P. A., Sarlis, N. V., Skordas, E. S., and Lazaridou, M. S. (2007). Electric pulses some minutes before earthquake occurrences. *Appl. Phys. Lett.* 90, 064104. doi:10.1063/1.2450779

Vassiliadis, D. (2008). Response of the radiation belt electron flux to the solar wind velocity: parameterization by radial distance and energy. *J. Atmos. Sol. Terr. Phys.* 70 (14), 1810–1828. doi:10.1016/j.jastp.2008.05.019

Yamazaki, K. i. (2012). Estimation of temporal variations in the magnetic field arising from the motional induction that accompanies seismic waves at a large distance from the epicentre. *Geophys. J. Int.* 190, 1393–1403. doi:10.1111/j.1365-246x.2012.05586.x

Zhang, X., Shen, X., Parrot, M., Zeren, Z., Ouyang, X., Liu, J., et al. (2012). Phenomena of electrostatic perturbations before strong earthquakes (2005–2010) observed on DEMETER. *Nat. Hazards Earth Syst. Sci.* 12, 75–83. doi:10.5194/nhess-12-75-2012

Conflict of Interest: The authors declare that the research was conducted in the absence of any commercial or financial relationships that could be construed as a potential conflict of interest.

Copyright © 2020 Fidani, Orsini, Iezzi, Vicentini and Stoppa. This is an open-access article distributed under the terms of the Creative Commons Attribution License (CC BY). The use, distribution or reproduction in other forums is permitted, provided the original author(s) and the copyright owner(s) are credited and that the original publication in this journal is cited, in accordance with accepted academic practice. No use, distribution or reproduction is permitted which does not comply with these terms.

frontiers in Earth Science

ORIGINAL RESEARCH
published: 06 November 2020
doi: 10.3389/feart.2020.585317

The Method of the Minimum Area of Alarm for Earthquake Magnitude Prediction

*Valeri Gitis and Alexander Derendyaev**

The Institute for Information Transmission Problems, Moscow, Russia

An approach for the systematic forecasting of earthquake magnitudes is considered. To solve this problem, we use the minimum area of alarm method. Testing the approach for Kamchatka and the Aegean Region shows a satisfactory quality of the forecast of earthquakes and their magnitudes.

Keywords: machine learning, one class classification, earthquake forecasting, method of the minimum area of alarm, earthquake magnitude prediction

OPEN ACCESS

Edited by:
Giovanni Martinelli, National Institute of Geophysics and Volcanology, Italy

Reviewed by:
Filippos Vallianatos, Technological Educational Institute of Crete, Greece
Vladimir G. Kossobokov, Institute of Earthquake Prediction Theory and Mathematical Geophysics (RAS), Russia

****Correspondence:***
Alexander Derendyaev
wintsa@gmail.com

Specialty section:
This article was submitted to Solid Earth Geophysics, a section of the journal Frontiers in Earth Science

Received: *20 July 2020*
Accepted: *28 September 2020*
Published: *06 November 2020*

Citation:
Gitis V and Derendyaev A (2020) The Method of the Minimum Area of Alarm for Earthquake Magnitude Prediction. Front. Earth Sci. 11:585317. doi: 10.3389/feart.2020.585317

1. INTRODUCTION

Field observations show that before a strong earthquake, anomalous phenomena are observed in a number of natural processes: seismic regime, earth surface deformations, fluid chemistry, groundwater level, seismic wave travel times, electric and geomagnetic fields, etc. Usually, these precursors are detected locally near the source of a future earthquake (Mogi, 1979; Kanamori, 1981; Sobolev, 1993; Sobolev and Ponomarev, 2003). At the same time, it is known that with an increase in the energy of the expected earthquake, the epicenter distance to the area of the manifestation of precursors increases and can be more than 1,000 km (Dobrovolsky et al., 1979; Guomin and Zhaocheng, 1992). This introduces additional uncertainty in the estimation of the location of the expected earthquake.

Many aspects of earthquake prediction have been studied, including rock failure and earthquake precursor phenomena, mathematical models for earthquake prediction, machine learning methods, and earthquake prediction testing algorithms (Sobolev, 1993; Kossobokov, 1997; Sobolev and Ponomarev, 2003; Zavyalov, 2006; Rhoades, 2007; Marzocchi and Zechar, 2011; Amei et al., 2012; Keilis-Borok and Soloviev, 2013; Rhoades, 2013; Shebalin et al., 2014). At the same time, a number of works state that earthquakes cannot be predicted (Geller et al., 1997; Koronovsky and Naimark, 2009; Gufeld et al., 2015).

An earthquake forecast is an estimate of the location, time, and magnitude of an earthquake. Usually, forecasts involve estimating the spatial zone and the time interval in which an earthquake with a magnitude above a certain threshold is expected. Such a spatio-temporal region is often called an alarm zone, which is regularly built with a constant step in a systematic earthquake prediction. The forecast is successful if the epicenter of the target earthquake falls into the alarm zone.

Here, we consider the issue of earthquake magnitude prediction. Most studies have addressed the problem of predicting earthquake magnitudes for a limited area. A few successful studies are presented in Panakkat and Adeli (2007), Adeli and Panakkat (2009), and Asim et al. (2017). The authors solved the problem of predicting the maximum magnitude of a seismic event in a preselected location. For example, in the first two studies, the maximum magnitude per month was predicted in the Southern California region and in the 200 km zone surrounding San Francisco. The input data were eight time series calculated from catalogs of earthquakes that occurred in the forecast area. For training, neural network methods were used. Training was carried out for the interval 1950–1990,

and the 1991–2005 interval was used for testing. In Alexandridis et al. (2013), neural network methods were also used to estimate inter-event times between significant seismic events. The examples studied are from across California.

In our case, the forecast problem is solved not for the time series geographically localized at one point but the area presented by the spatio-temporal grid fields. The forecast for a particular geographical object can be considered a special case. Here, it is possible to use the time series of parameters tuned to the local place of the forecast, such as foreshock precursors of earthquakes (Boore, 2001), energy precursors (Wyss et al., 1990; Bufe and Varnes, 1993; Vallianatos and Chatzopoulos, 2018), precursors tuned to the frequency of strong earthquakes in a given area (Kagan and Jackson, 1991), and others. In our case, the forecast is not based on time series but on spatial and spatio-temporal grid fields. Fields of forecast features and training parameters cannot be configured to detect the process preceding a strong earthquake in a single predetermined geographical object. They should be universal for the entire area under analysis. Further, it is desirable that the grid fields used for the forecast contain patterns of anomalous behavior of seismic and geodynamic processes that are characteristic of the analyzed region and preceded by strong earthquakes.

We briefly consider the method of the minimum area of alarm and two ways to apply it to predict earthquake magnitudes in **Section 2**. In **Section 3.1**, we report the test results obtained to predict earthquakes and their magnitudes for Kamchatka and the Aegean Region. Testing was carried out on the GIS web-based platform for earthquake prediction (https://distcomp.ru/geo/prognosis/) and on the multifunctional web-GIS GeoTime 3 (http://geo.iitp.ru/GT3/).

2. METHODS

We have developed the method of the minimum area of alarm for the systematic forecast of strong earthquakes with a magnitude above a certain threshold (Gitis and Derendyaev, 2018; Gitis and Derendyaev, 2019). The system of systematic earthquake prediction regularly with a step Δt calculates the alarm zone, in which the epicenter of the target earthquake is expected at the interval Δt. A demo version of the system since 2018 is available at https://distcomp.ru/geo/prognosis/.

We assume that strong earthquakes are preceded by anomalous manifestations, which can be represented in the grid spatio-temporal fields of features. The method of the minimum area of alarm trained to calculate alarm zones based on retrospective observations consisting of a) the spatio-temporal fields of features, and b) a sample consisting of marked target anomalous objects and an unmarked mixture of target and normal objects. Anomalous objects here are vectors selected by the learning algorithm with field values at grid nodes that precede the epicenters of target earthquakes $q = 1, \ldots, Q$ with magnitudes $m \geq M$ (earthquake precursors). An unlabeled mixture of objects is represented by vectors with field values at all other grid nodes. This formulation in machine learning refers to one-class classification problems (Bishop, 2006; Kotsiantis et al., 2007; Khan and Madden, 2009).

The fields $\mathbf{F}_i$ are set in a unified coordinate grid. The values of the fields at the grid nodes $n = 1, \ldots, N$ correspond to the vectors of the I-dimensional feature $f(n) \in \mathbb{R}^{\mathbb{I}}$. During training, the spatio-temporal field $\Phi(\mathbf{F}_i)$, called the alarm field, is calculated. The values of the alarm field $\phi^{(n)} \geq \phi_0$ allocate a spatio-temporal region in it, called the alarm area. The temporal slice of the alarm area at the time of the forecast t^* is exactly *the alarm zone* in which the appearance of the epicenter of the target earthquake is predicted on the interval Δt.

During training, the algorithm detects target events. An event is detected if its epicenter falls into the alarm area during the training interval. A target earthquake is predicted at the step Δt if its epicenter falls into the alarm zone. The larger the product $S(t^*)\Delta t$, the more successful the forecast. However, it is obvious that the value of this spatio-temporal area should be reasonably limited. The indicators of the forecast quality are the estimations of the probability of a successful forecast of events (the forecast probability) and the size of the alarm area in the training interval. As a result of training, it is desirable to obtain a solution in which the maximum number of successful forecasts of target events is achieved for a given size of the alarm zone.

In a systematic forecast of earthquake magnitude, it is necessary to indicate the area in which the target event is expected and to evaluate its magnitude. We consider two ways to complete each forecast step t^*: 1) to predict an alarm zone $S(t^*)$ and to evaluate the magnitudes of the expected earthquakes in this zone; 2) to predict several alarm zones $S(m, t^*)$ in which earthquakes with magnitudes in predetermined small intervals are expected. Solving the problem in the first method requires restoring the dependence of earthquake magnitudes on feature fields. The indicators of the forecast quality here are the probability of successful detection of target events, the size of the alarm area in the training interval, and the RMS difference between the forecasts and the actual values of the predicted target events. The second method seems simpler; the accuracy of the estimation of the target earthquake magnitudes is determined by the given boundaries of the interval. Therefore, indicators of the quality of the forecast are only the probability of the successful detection of target events and the size of the alarm area in the training interval.

The solution to the problem of earthquake prediction is required for both approaches. Our method of the minimum area of alarm is trained to detect abnormal target objects from a sample consisting of labeled abnormal objects and a mixture consisting of unlabeled abnormal and normal objects. The data model contains two assumptions that allow us to introduce a measure of the abnormality of the analyzed objects.

(1) Abnormality condition: in feature space, the target earthquakes are preceded by vectors (earthquake precursors) for which the values of some components (the values of some feature fields) are unlikely and close to the maximum (or minimum). To simplify the explanation, we assume that the precursors refer only to the maximal values of the fields of features.
(2) Monotonicity condition: feature space vectors that are component-wise larger (or smaller) than the earthquake

precursor vector can also be precursors of similar target events.

For training, the earthquake prediction algorithm requires determining the precursor for each target event. Let the event q be preceded by a precursor $\mathbf{f}^{(q)} \in \mathbb{R}^I$. The precursor is associated with a feature space area whose vectors are component-wise greater than or equal to $\mathbf{f}^{(q)}$, i.e., the area $O^{(q)} = \{\mathbf{f}^{(n)} \in \mathbb{R}^I : f_i^{(n)} \geq f_i^{(q)}, i = 1, 2, \ldots, I\}$. We call this area the orthant $O^{(q)}$ with a vertex at $\mathbf{f}^{(q)}$, and the vectors $\mathbf{f}^{(n)} \in O^{(q)}$ are called the base vectors of the target event q. According to the monotonicity condition, base vectors are also precursors of events that are similar to the event q. In geographical coordinates, each base vector forms *a cylinder of alarm* with the radius R and the element T. The alarm cylinder of the base vector $\mathbf{f}^{(n)}$ has a circular base center at the grid node n with coordinates $(x^{(n)}, y^{(n)}, t^{(n)})$, a radius of the base R, and the element $[(x^{(n)}, y^{(n)}, t^{(n)}), (x^{(n)}, y^{(n)}, t^{(n)} + T)]$, where $t^{(n)} \in [t_0, t^*]$ and t_0 is the start time of training. An earthquake can only be predicted if its epicenter falls into one of the alarm cylinders. The union of alarm cylinders formed by the base vectors of the orthant $O^{(q)}$ selects a set of grid nodes $W^{(q)}$, $\left|W^{(q)}\right| = L^{(q)}$. From this, it follows that an earthquake q with the epicenter coordinates $(x^{(q)}, y^{(q)}, t^{(q)})$ can be predicted only if the cylinder with the center of the base $(x^{(q)}, y^{(q)}, t^{(q)})$, a radius R, and the element $[(x^{(q)}, y^{(q)}, t^{(q)} - T), (x^{(q)}, y^{(q)}, t^{(q)})]$ contains at least one base point. This cylinder is called *a precursor cylinder*. The precursor of event q is the vector $\mathbf{f}^{(q)} \in \mathbb{R}^{\mathbb{I}}$, which has the minimum value of the alarm volume $v^{(q)} = L^{(q)}/L$ among all vectors corresponding to the grid nodes of the precursor cylinder, where L is the number of all grid nodes of the spatio-temporal region of analysis. The quantity $v^{(q)}$ (volume of the precursor) defines the measure of abnormality for the precursor of event q. In the study by Gitis et al. (2020b), the measure of the abnormality for target events was determined by the likelihood ratio estimate.

The forecast quality is determined by two indicators: 1) *the probability of prediction* U, equal to the fraction of correctly forecast target events Q^* to all target Q events, $U = Q^*/Q$, and 2) *the volume of alarm* V, equal to the fraction of the number of grid nodes of the alarm field L^* with the values $\phi^{(n)} \geq \phi$ to the number of all grid nodes of the analyzed area L, $V = L^*/L$. It can be seen from the definition that the alarm volume V is equal to the probability of the detection of target events by random areas consisting of $V = L^*/L$ grid nodes.

In classification problems, the decision rule is found by minimizing the function of losses from target detection errors and false alarms. The training algorithm is optimal if it calculates an alarm area with the volume V_0, which, for any value $V \leq V_0$, provides the maximum value of U. In our case, this solution requires large calculations because the sets of base vectors associated with different precursors intersect. Therefore, we consider solutions that are close to optimal.

The algorithm for constructing the forecast field is nonparametric. It consists of two steps: (I) generating a training sample set $\{\mathbf{f}^{(q)}, v^{(q)}\}$ and (II) calculating the alarm field $\Phi(\mathbf{F}_i)$. Three versions of the learning algorithm are the most significant. The first version requires the least amount of computation and is selected for testing. The alarm field in this version is determined by the sequence wherein the values of alarm volumes of precursors increase: $v^{(1)} \leq v^{(2)} \leq \ldots \leq v^{(q)} \leq \ldots \leq v^{(Q)}$. The second version of the algorithm allows the alarm field to be optimized so that with each increase in the probability of detecting U by $1/Q$, the next point $\mathbf{f}^{(q)}$ is selected which provides the minimum increase in the alarm volume. The third version of the algorithm allows the forecast field to be optimized so that it detects the maximum number of target events with an alarm volume that does not exceed a given one.

Consider the first version of the algorithm.

(1) Generate a training sample set $\{\mathbf{f}^{(q)}, v^{(q)}\}$. Arrange the precedents $\mathbf{f}^{(q)}, q = 1, \ldots, Q$, in accordance with the increase in the alarm volume of the target events $v^{(1)} \leq v^{(2)} \leq \ldots \leq v^{(q)} \leq \ldots \leq v^{(Q)}$.
(2) Calculate the alarm field $\Phi(\mathbf{F}_i)$.

   a. Assign to the nodes of the grid of the alarm field Φ a value of 1.
   b. Replace the value of 1 of the field Φ with $V(1) = v^{(1)}$ in the set $W^{(1)}$ of grid nodes corresponding to the base points of the precedent $\mathbf{f}^{(1)}$; replace the value of 1 with $V(2) = \left|W^{(1)} \cup W^{(2)}\right|/L$ at the grid nodes related to the base points of the precedent $\mathbf{f}^{(2)}$; replace the value of 1 with $V(3) = \left|W^{(1)} \cup W^{(2)} \cup W^{(3)}\right|/L$ at the grid nodes related to the base points of the precedent $\mathbf{f}^{(3)}$ and then sequentially replace the values of 1 with the corresponding values of the alarm volumes. The resulting field Φ takes the values $V(1) \leq V(2) \leq \ldots \leq V(q) \leq \ldots \leq V(Q)$ or 1. The value $V(1)$ refers to grid nodes from the set $W^{(1)}$, $V(2)$ refers to grid nodes from the set $(W^{(2)} \backslash W^{(1)})$, $V(3)$ refers to grid nodes from the set $(W^{(3)} \backslash (W^{(1)} \cup W^{(2)}))$, etc.

The calculated field $\Phi(\mathbf{F}_i)$ determines the values of the alarm volumes for all alarm cylinders into which the target events fall. The grid nodes of the alarm field with values less than or equal to V_0 define the alarm area.

3. TEST RESULTS

3.1. Methodology

Testing simulates the operation mode of the forecast. As in the forecast, it is performed with a constant step Δt. The choice of the area of analysis is crucial to testing. We thus selected the analysis area in such a way that any circle with a radius of $R = 100$ km for an interval of 10 years before the test contains more than 300 earthquake epicenters. This condition makes it possible to distinguish a seismically active area of analysis in which the grid fields of the density of the epicenter and the average magnitude of earthquakes can be calculated with acceptable smoothing parameters. Earthquake catalogs were not cleared

of aftershocks. Earthquake prediction by the method of the minimum area of alarm based on complete earthquake catalogs and catalogs cleared of aftershocks is analyzed in Gitis et al. (2020a). The formal rule defines an unambiguous choice of the area of analysis, which allows us to compare the forecast results obtained by different methods and for different fields of features. In particular, we can compare the probabilities of predicting target events U obtained when constructing the alarm field using regular fields of features and a random field. Since the probability of a random forecast is equal to the volume of alarm, this action is equivalent to comparing U with the corresponding volume of alarm V.

A comparison of the success of regular and random forecasts cannot properly account for the heterogeneity of the spatial distribution of seismicity in the field of analysis. If the area where the target earthquakes occur is small, compared to the analysis area, then a trivial solution is possible because for a large area of analysis L, the announcement of a constant alarm in a relatively small area can lead to a high probability of a forecast with a small level of the alarm volume V. To avoid a trivial solution, the probability of a regular forecast is compared to that of a forecast based on stationary spatial data. The most common method is to compare the number of predicted earthquakes detected during a regular forecast with the number of events expected in the same place in the spatio-temporal alarm zones, which is estimated from a catalog of earthquakes with an interval of 20–30 years before testing (Molchan, 1997; Kossobokov et al., 1999).

The spatial heterogeneity of the seismic process can be controlled not only by the epicenters of earthquakes in a relatively short period but also by, for example, a spatial field of seismic activity or a field of maximum magnitudes Mmax of expected earthquakes (Bune and Gorshkov, 1980). Therefore, we use a different method for assessing the quality of the analysis area (Gitis and Derendyaev, 2018; Gitis and Derendyaev, 2019): for the same volume of alarm, we compare the probabilities of detecting target events obtained using the spatial field of the earthquake epicenter density and the fields of features selected for the regular forecast.

Our systematic earthquake prediction technology is universal with respect to input data types. All data types, including point fields, time series, and linear, polygonal, and raster fields, are converted to grid spatial and spatio-temporal fields. This provides versatility to the system for incoming data types. In this work, only forecasting methods were tested. For this, we used the most famous characteristics of earthquake catalogs:

- $\mathbf{F}_1$ is the 3D field of the density of earthquake epicenters.
- $\mathbf{F}_2$ is the 3D field of mean earthquake magnitudes.
- $\mathbf{F}_3$ is the 3D field of negative temporal anomalies of the density of earthquake epicenters.
- $\mathbf{F}_4$ is the 3D field of positive temporal anomalies of the density of earthquake epicenters.
- $\mathbf{F}_5$ is the 3D field of positive temporal anomalies of the mean earthquake magnitude.
- $\mathbf{F}_6$ is the 2D field of the density of earthquake epicenters: kernel smoothing with the parameter R = 50 km in the interval from the beginning of the analysis to the start of training.
- $\mathbf{F}_7$ is the 3D field of quantiles of the background density of earthquake epicenters, calculated on the interval from the beginning of the analysis to the start of training, which corresponds to the density values of earthquake epicenters at the current time.

The estimation of 3D fields of $\mathbf{F}_1$ and $\mathbf{F}_2$ is performed with the method of local kernel regression. The kernel function for the nth earthquake has the form $K_n = [cosh^2(r_n/\mathrm{R})^2 cosh^2(t_n/\mathrm{T})]^{-1}$, where $r_n < R\varepsilon$ and $t_n < T\varepsilon$ are the distance and time interval between the nth epicenter of the earthquake and the node of the 3D grid of the field, $\varepsilon = 2$, $R = 50$ km and $T = 100$ days for $\mathbf{F}_1$, and $R = 100$ km and $T = 730$ days for $\mathbf{F}_2$. The field $\mathbf{F}_6$ is calculated with the kernel function $Kn = [cosh^2(r_n/\mathrm{R})^2]^{-1}$. The parameters for evaluating the fields, the radii R and the intervals T, were chosen empirically, considering the step of the network of fields and the approximate number of events in the evaluation window. To calculate the fields of $\mathbf{F}_3$, $\mathbf{F}_4$, and $\mathbf{F}_5$, Student's t-test statistic is used, which is defined for each grid node as the ratio of the difference in average values of the current interval T_2 and background interval T_1 to the standard deviation of this difference. Positive values of the t-statistic correspond to an increase in the value on the test interval. The fields $\mathbf{F}_3$, $\mathbf{F}_4$, and $\mathbf{F}_5$ are calculated with different time intervals: T_1 = 3,500 days and T_2 = 200 days, T_1 = 1,500 days and T_2 = 1,500 days, T_1 = 1,000 days and T_2 = 1,000 days, T_1 = 1,000 days and T_2 = 500 days, and T_1 = 500 days and T_2 = 500 days. In addition, we analyzed the fields that are the functions of the original feature fields, such as $\mathbf{F}_1 \times \mathbf{F}_2$, $\mathbf{F}_2/\mathbf{F}_1$, $\mathbf{F}_2/\mathbf{F}_7$, $\mathbf{F}_1 \times \mathbf{F}_7$, $\mathbf{F}_2 \times \mathbf{F}_7$, and others.

There were two objectives for the tests: to verify the possibility of 1) predicting earthquake magnitudes using a linear approximation of the dependence of earthquake magnitudes on the fields of features in relatively large intervals of magnitudes and 2) using the method of the minimum area of alarm for the prediction of earthquakes in small magnitude intervals.

3.2. Testing the Forecast of Earthquakes and Their Magnitudes

Tests were performed in Kamchatka and the Aegean Region.

Initial data for Kamchatka contain the earthquake catalog of Kamchatka Branch, Geophysical Survey, Russian Academy of Sciences, for April 4, 1986–May 20, 2019, with the magnitudes $m \geq 3.5$ and the depths of hypocenters $H \leq 160$ km. The target earthquake depths of hypocenters are $H \leq 60$ km. The grid step is $\Delta x \times \Delta y \times \Delta t = 0.16^\circ \times 0.09^\circ \times 30$ days. The training interval is from January 1, 2000, to the next forecast after December 12, 2011, while the testing interval is December 12, 2011–May 20, 2019.

Initial data for the Aegean Region contain the earthquake catalog of the International Seismological Center (2020) (accessed June 11, 2020) for May 27, 1983–September 13, 2019, with the magnitudes $m \geq 2.7$ and the depths of hypocenters $H \leq 160$ km. The target earthquake hypocenter depths are $H \leq 60$ km. The grid step is $\Delta x \times \Delta y \times \Delta t = 0.11^\circ \times 0.08^\circ \times 40$ days. The training

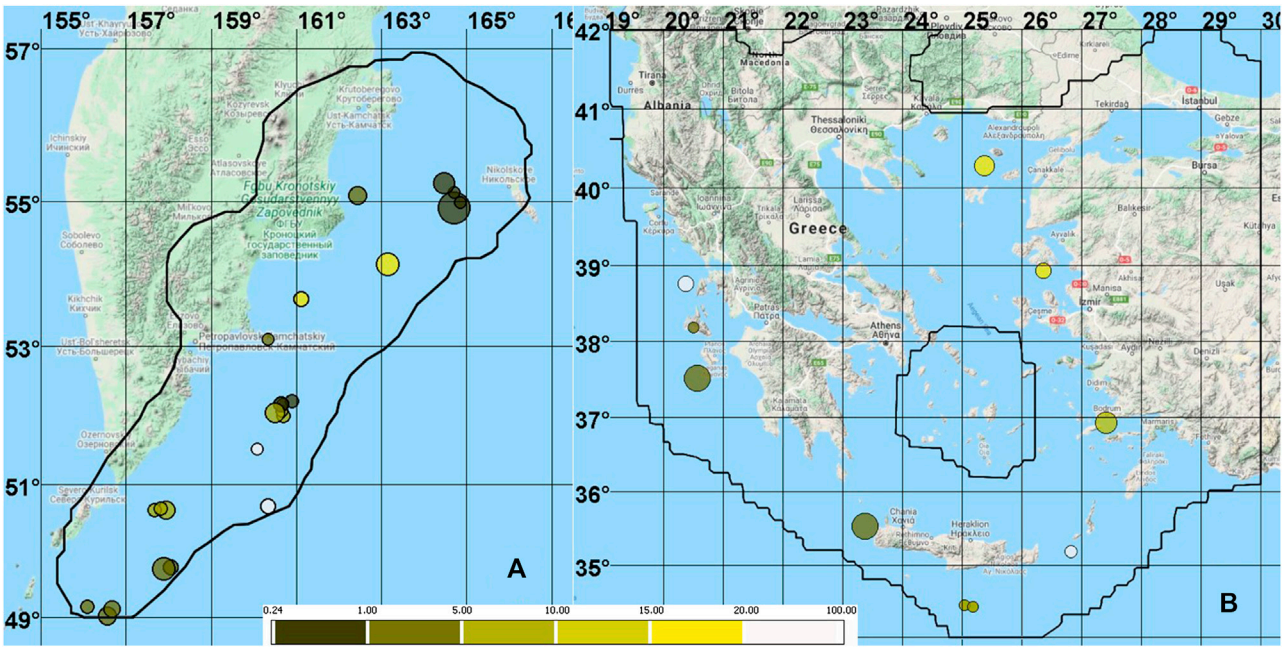

FIGURE 1 | The maps of epicenters of the target earthquakes in the test sample color-coded with respect to the volume of alarm required for its successful prediction: **(A)** 24 magnitude $m \geq 6.0$ earthquakes in Kamchatka and **(B)** 10 magnitude $m \geq 5.9$ earthquakes in the Aegean Region. The outline highlights areas of analysis. The circles show the epicenters of the test earthquakes. The size of the circles increases with the magnitude of the earthquake. The intensity of the shading of the epicenters decreases with an increase in the volume of alarm with which the epicenter is predicted: 1, 5, 10, 15, 20%. The white color indicates a forecast skipping error.

interval is from November 16, 1991, to the next forecast after December 12, 2011, while the testing interval is January 8, 2010–September 13, 2019.

The fields of features and the parameters of the algorithm were selected when testing the forecast of earthquakes with the magnitudes $m \geq 6.0$ (Kamchatka) and $m \geq 5.9$ (Aegean Region). All further testing results for both regions were obtained using these fields and parameters.

The fields of features $\mathbf{F}_8 = \mathbf{F}_1/(\mathbf{F}_7 + 0.001)$ and $\mathbf{F}_9 = \mathbf{F}_2 \times \mathbf{F}_7$ were selected for Kamchatka. Anomalous values of the $\mathbf{F}_8$ field correspond to areas of the seismic process in which the density values of earthquake epicenters are quite high but significantly less than the average values of the density of epicenters in the interval from the beginning of the analysis to the start of training. Anomalous values of the $\mathbf{F}_9$ field correspond to areas of the seismic process in which an increase in the density of earthquake epicenters (compared to the interval from the beginning of analysis to the start of training) occurs simultaneously with an increase in the average magnitude of earthquakes. Adding fields of features from the existing set does not provide a significant improvement in the quality of the forecast. The parameters of the learning algorithm are the radii of the forecast and precursor cylinders $R = 10$ km and their elements $T = 100$ days.

The fields of features $\mathbf{F}_8 = \mathbf{F}_1/(\mathbf{F}_7 + 0.001)$ and $\mathbf{F}_{10}$, negative anomalies of Student's t-test statistic with the intervals $T_1 =$ 1,000 days and $T_2 = 500$ days, were selected for the Aegean Region. The interpretation of the anomalous values of the field $\mathbf{F}_8$ is given above. The abnormal values of the $\mathbf{F}_{10}$ field correspond to areas of the seismic process in which the average density of earthquake epicenters for 500 days significantly decreases, compared to the previous average value for 1,000 days. Notably, adding other attribute fields to an existing set does not significantly improve the forecast quality. The parameters of the learning algorithm are the radius of the cylinder $R = 7$ km and its element $T = 202$ days.

Alarm zone maps are computed at each test step. The number of such maps for each of the selected regions is from 70 to 90. Alarm maps for three regions can be seen on a demo site (https://distcomp.ru/geo/prognosis/). The prediction accuracy for test data is determined by the value of the alarm area $V = 0.2$. It shows that in the interval from the beginning of training to the moment of forecasting, on average, each alarm zone occupies 20% of the analysis area.

Forecast maps for earthquakes with magnitudes $m \geq 6.0$ in Kamchatka and $m \geq 5.9$ in the Aegean Region are shown in **Figure 1**. The polygon and circles show the area of analysis and the epicenters of the target earthquakes with magnitudes of 6.0–7.3 for Kamchatka and 5.9–6.6 for the Aegean Region. The size of the circles increases with the strength of the earthquakes. The shading intensity of earthquake epicenters decreases with an increase in the alarm field with which the earthquake epicenter is predicted: 1, 5, 10, 15, and 20%. The white color indicates that an earthquake is predicted with an alarm volume of $V \geq 0.2$. Such a forecast is considered miscalculated.

Consider the results of testing the forecast of earthquakes in large magnitude intervals. For Kamchatka, the intervals

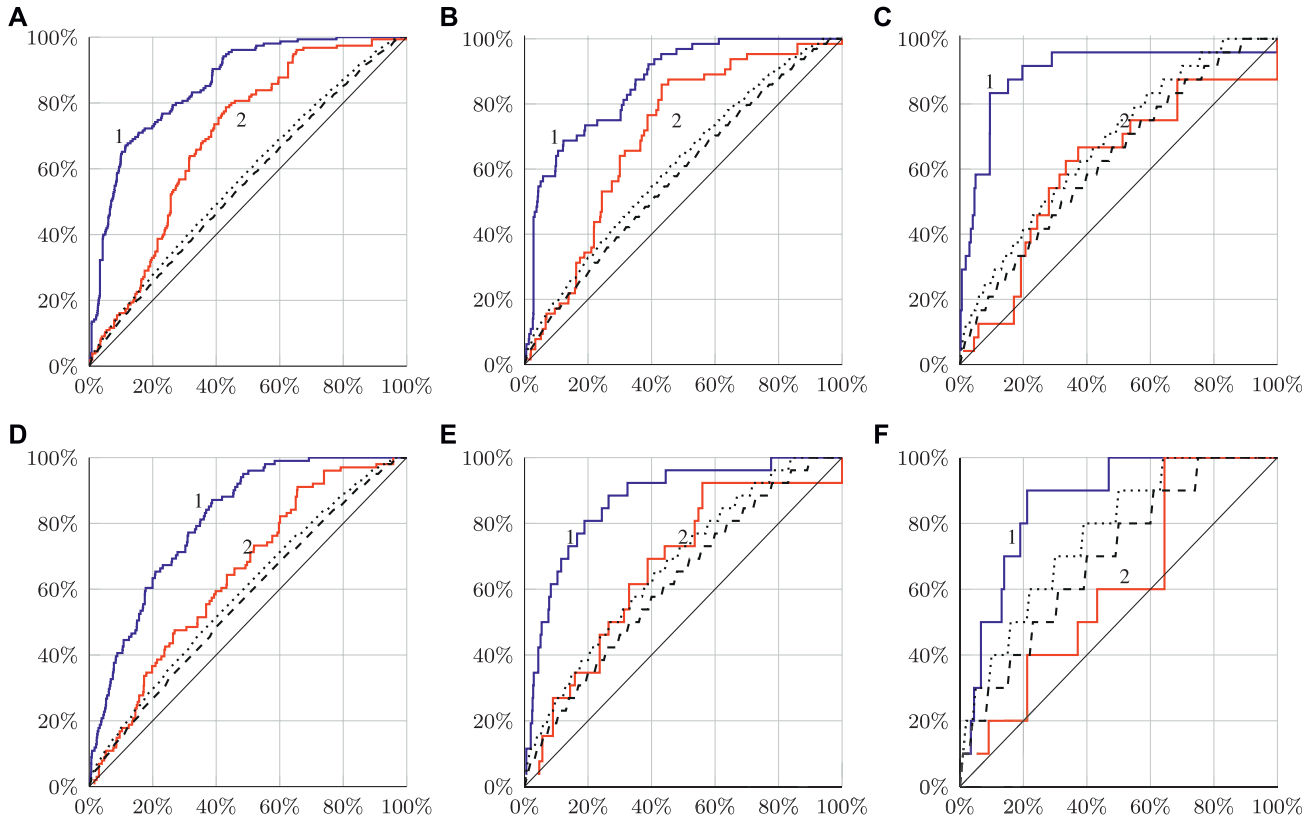

FIGURE 2 | Graphs of dependencies $U(V)$: **(A)–(C)** are the plots of $U(V)$ for the Kamchatka magnitude intervals $m \in [5.0, 5.4]$, $m \in [5.5, 5.9]$, $m \geq 6.0$; **(D)–(F)** are the plots of $U(V)$ for the Aegean Region magnitude intervals $m \in [5.0, 5.3]$, $m \in [5.5, 5.8]$, $m \geq 5.9$; 1 labels the plots obtained for regular forecasting; 2 labels the plots obtained using the spatial density field $\mathbf{F}_6$; dotted and dashed lines are associated with 99 and 95% confidence levels correspondingly.

TABLE 1 | Kamchatka: probabilities of forecasting the earthquakes in magnitude intervals $m \in [5.0, 5.4]$, $m \in [5.5, 5.9]$, $m \geq 6.0$ (earthquake magnitudes are accurate to tenths).

Magnitude interval and number of events	Volume of alarm	Fields F_8 and F_9		Fields F_6	
		Number of predicted events	Probability of forecast	Number of predicted events	Probability of forecast
$m \in [5.0, 5.4]$, $Q = 155$	0.01	21	0.14	6	0.04
	0.05	62	0.40	16	0.10
	0.10	99	0.64	25	0.16
	0.15	108	0.70	35	0.23
	0.20	113	0.73	51	0.33
$m \in [5.5, 5.9]$, $Q = 64$	0.01	4	0.06	1	0.02
	0.05	35	0.55	5	0.08
	0.10	41	0.64	11	0.17
	0.15	44	0.69	14	0.22
	0.20	47	0.73	22	0.35
$m \geq 6.0$,$Q = 24$	0.01	7	0.29	1	0.04
	0.05	14	0.58	2	0.08
	0.10	20	0.83	3	0.13
	0.15	20	0.83	3	0.13
	0.20	22	0.92	8	0.33

$m \in [5.0, 5.4]$, $m \in [5.5, 5.9]$, and $m \geq 6.0$ were selected (the magnitudes of the test earthquakes are given to the nearest tenth). For the Aegean Region, the intervals $m \in [5.0, 5.3]$, $m \in [5.5, 5.8]$, and $m \geq 5.9$ were selected. For each interval, we compare quality indicators calculated from the fields of features used for the regular forecast and the field of the spatial density earthquake epicenters $\mathbf{F}_6$. The earthquake forecast using regular feature fields considers spatial and temporal properties of the

TABLE 2 | The Aegean Region: probabilities of forecasting the earthquakes in the magnitude intervals $m \in [5.0, 5.3]$, $m \in [5.4, 5.8]$, $m \geq 5.9$.

Magnitude interval and number of events	Volume of alarm	Fields F_8 and F_{11}		Fields F_6	
		Number of predicted events	Probability of forecast	Number of predicted events	Probability of forecast
$m \in [5.0, 5.3]$, $Q = 101$	0.01	11	0.11	0	0.00
	0.05	24	0.24	9	0.09
	0.10	41	0.41	17	0.17
	0.15	49	0.49	25	0.25
	0.20	64	0.63	37	0.37
$m \in [5.4, 5.8]$, $Q = 26$	0.01	3	0.12	0	0.00
	0.05	11	0.42	2	0.08
	0.10	16	0.62	7	0.27
	0.15	19	0.73	8	0.31
	0.20	21	0.81	9	0.35
$m \geq 5.9$, $Q = 10$	0.01	0	0.00	0	0.00
	0.05	3	0.30	0	0.00
	0.10	5	0.50	2	0.20
	0.15	7	0.70	2	0.20
	0.20	8	0.80	2	0.20

TABLE 3 | Results of forecasting the earthquake magnitudes for Kamchatka.

Magnitude interval and number of events	Mean values of earthquake magnitudes	RMS of earthquake magnitudes	RMS of discrepancies of actual magnitudes with forecasts
$m \in [5.0, 5.4]$, $Q = 155$	5.18	0.143	0.145
$m \in [5.5, 5.9]$, $Q = 64$	5.65	0.133	0.136
$m \geq 6.0$, $Q = 24$	6.29	0.321	0.325

seismic process, while the one using the field $\mathbf{F}_6$ considers only the former. The results of these tests are presented in graphs of the dependencies $U(V)$ in **Figure 2** and are summarized in **Tables 1, 2**.

According to Molchan (2003) and Kossobokov (2006), we also provide two lines: the dotted one corresponds to the confidence levels of 95% and the dashed one corresponds to 99%. They are used to denote "significant" and "very significant" deviation from random guessing, denoted with a diagonal line.

Alarm zones in each region are limited to $V_0 = 0.2$. The probability of the forecast is estimated by the ratio of the number of predicted events and the number of all events. It can be seen that, in all cases, the probabilities of earthquake prediction obtained using the feature fields selected for regular forecasting are significantly higher than the probabilities obtained using the spatial density field. This indicates that the forecast results take into account both the spatial and temporal properties of the seismic process.

The results of testing the forecast of earthquake magnitudes in large intervals of magnitudes are presented in **Tables 3, 4**. For the forecast, the dependence of the earthquake magnitudes on the values of the feature fields is approximated by the linear function. The forecast results are calculated only for those earthquakes whose epicenters are in the alarm zone. It can be seen that in each interval, the standard error of approximation of the dependence of the earthquake magnitudes on the values of the feature fields practically coincides with the standard deviation of the magnitudes of the target earthquakes. There are two possible reasons for the poor approximation: the magnitude of the earthquake is independent of the values of the selected feature fields or this dependence is non-linear.

Tables 5, 6 present the results of earthquake prediction in small magnitude intervals. The following intervals of magnitudes were chosen: for Kamchatka, the intervals are $m \in [5.1, 5.2]$, $m \in [5.3, 5.4]$, $m \in [5.5, 5.6]$, $m \in [5.7, 5.9]$, $m \in [6.0, 6.1]$, and $m \geq 6.2$; for the Aegean Region, the intervals are $m \in [5.0, 5.1]$, $m \in [5.2, 5.3]$, $m \in [5.4, 5.5]$, $m \in [5.6, 5.8]$, and $m \geq 5$. For the alarm volume $V_0 = 0.2$, the probability of a successful forecast varies from 0.68 to 0.92 for Kamchatka and from 0.62 to 0.80 for the Aegean Region. The forecast of earthquakes in such small magnitude intervals is almost equivalent to the forecast of their magnitudes. The forecast can be represented by the maps of alarm zones, each of which contains an epicenter of an earthquake with a magnitude in the corresponding interval that is expected in the interval Δt. It is possible to present the result of the forecast in the form of a single map. To do this, it is necessary to identify zones with the same values of the alarm volume V_0 on the maps related to each of the magnitude intervals. Using the obtained alarm zones, it is possible to construct a single map with the maximum magnitudes of the expected earthquake epicenters.

The test results presented in **Tables 1, 2, 5, 6** indicate that the fields of features and parameters of our training algorithm, selected for the forecast of strong earthquakes with magnitudes $m \geq 5.9$, provide satisfactory learning results for the forecasts of earthquakes with smaller magnitudes. For many regions, the

TABLE 4 | Results of forecasting the earthquake magnitudes for the Aegean Region.

Magnitude interval and number of events	Mean values of earthquake magnitudes	RMS of earthquake magnitudes	RMS of discrepancies of actual magnitudes with forecasts
$m \in [5.0, 5.3]$, $Q = 101$	5.10	0.108	0.112
$m \in [5.4, 5.8]$, $Q = 26$	5.52	0.148	0.159
$m \geq 5.9$, $Q = 10$	6.19	0.275	0.382

TABLE 5 | Kamchatka: probabilities of earthquake forecasts for the magnitude intervals $m \in [5.1, 5.2]$, $m \in [5.3, 5.4]$, $m \in [5.5, 5.6]$, $m \in [5.7, 5.9]$, $m \in [6.0, 6.1]$, $m \geq 6.2$.

Volume of alarm	Magnitude intervals and number of events					
	$m \in [5.1, 5.2]$	$m \in [5.3, 5.4]$	$m \in [5.5, 5.6]$	$m \in [5.7, 5.9]$	$m \in [6.0, 6.1]$	$m \geq 6.2$
V	$Q = 61$	$Q = 56$	$Q = 35$	$Q = 22$	$Q = 11$	$Q = 13$
0.01	0.16	0.11	0.03	0.01	0.36	0.15
0.05	0.41	0.29	0.54	0.27	0.45	0.54
0.10	0.64	0.63	0.54	0.64	0.82	0.54
0.15	0.74	0.63	0.66	0.77	0.82	0.75
0.20	0.77	0.68	0.71	0.82	0.82	0.92

TABLE 6 | The Aegean Region: probabilities of earthquake forecasts for the magnitude intervals $m \in [5.0, 5.1]$, $m \in [5.2, 5.3]$, $m \in [5.4, 5.5]$, $m \in [5.5, 5.8]$, $m \geq 5.9$.

Volume of alarm	Magnitude intervals and number of events				
	$m \in [5.0, 5.1]$	$m \in [5.2, 5.3]$	$m \in [5.4, 5.5]$	$m \in [5.6, 5.8]$	$m \geq 5.9$
V	$Q = 71$	$Q = 30$	$Q = 17$	$Q = 9$	$Q = 10$
0.01	0.13	0.03	0.12	0.00	0.00
0.05	0.25	0.17	0.29	0.44	0.30
0.10	0.46	0.33	0.53	0.56	0.50
0.15	0.52	0.50	0.65	0.67	0.70
0.20	0.62	0.63	0.71	0.78	0.80

forecast of strong earthquakes is difficult because of the small number of examples of such events in the training sample. We tested the ability to use the method of the minimum area of alarm to strong event forecast from a sample supplemented by earthquakes with smaller magnitudes $m \geq 5.0$. For testing, we used the same feature fields and forecast parameters as those in previous experiments. The results are summarized in **Tables 7, 8**. It can be seen that for Kamchatka, the estimates of the probability of forecasting earthquakes with magnitudes of 5.9–6.1 and 6.2–7.3 turned out to be 0.78 and 0.85. A similar result was obtained for the Aegean Region: estimates of the probability of detecting earthquakes with magnitudes of 5.8–6.0 and 6.1–6.6 turned out to be 0.86 and 0.83. This indicates that when we learn to predict strong earthquakes, we can introduce examples of earthquakes of lesser magnitudes into the training set. During the training process, our algorithm calculates the orthants for all precursors and, using the measure of abnormality, selects precursors from them with the minimum values of the alarm volume (or with the maximum values of the likelihood ratio). The selected precursors provide a satisfactory probability of predicting strong earthquakes. **Tables 7, 8** show that the results of the forecast of earthquakes with magnitudes of 5.0–5.8 are also mostly satisfactory.

4. DISCUSSION

Some disciplines study complex processes and their relationships with simpler instrumentally measured properties. The purpose of one of these tasks is to predict the critical states of the process by the values of the properties. To do this, first, the connections of the process with each property are investigated separately to determine the values of the properties wherein the process does not pass into critical states. For example, in medicine for healthy people, the norms of indicators of functional diagnostics are established. In earthquake prediction for each localized area, the seismic regime parameters' long-term average values are taken as the norm. It can be assumed that the greater the deviation from the norm, the greater or equal (but not less) the deviation of the process from the normal state to the critical one, given that everything else is equal. This means that the value of the deviation from the norm is a monotonic non-decreasing function of the feature values.

The formulation of the method of minimum area of alarm is discussed as follows. Consider a set of objects. An object is described by a set of properties denoted in numerical form (a vector of features). The values of properties of the objects that are close to the highest possible value have a low probability. Among the set of objects, there are abnormal objects. They differ from other objects so that the values of some of their properties are close to the maximum possible value. Let there be a training sample from anomalous objects (precedents). It seems natural to classify an object as anomalous if its vector is greater or equal to one of the vectors corresponding to a precedent. However, the description of the object properties can be incomplete and some precedents lack properties that are close to the maximum values.

TABLE 7 | Kamchatka: probabilities of earthquake forecasts for the magnitudes $m \geq 5.0$ and the volume of alarm $V = 0.2$.

Magnitude of earthquakes m	Number of events Q	Number of predicted events Q^*	Probability of forecast U
5.0	38	28	0.74
5.1	30	24	0.80
5.2	31	23	0.74
5.3	29	18	0.62
5.4	27	19	0.70
5.5	20	17	0.85
5.6	15	10	0.67
5.7	12	9	0.75
5.8	10	8	0.80
5.9	7	4	0.78
6.0	6	5	
6.1	5	5	
6.2	4	3	0.85
6.3	1	1	
6.4	3	3	
6.5	1	1	
6.6	1	1	
6.7	2	1	
6.8	—	—	
6.9	—	—	
7.0	—	—	
7.1	—	—	
7.2	—	—	
7.3	1	1	

TABLE 8 | The Aegean Region: probabilities of earthquake forecasts for the magnitudes $m \geq 5.0$ and the volume of alarm $V = 0.2$.

Magnitude of earthquakes m	Number of events Q	Number of predicted events Q^*	Probability of forecast U
5.0	49	31	0.63
5.1	22	14	0.64
5.2	16	12	0.75
5.3	14	8	0.57
5.4	14	9	0.64
5.5	3	3	0.89
5.6	4	4	
5.7	2	1	
5.8	3	3	0.86
5.9	2	3	
6.0	1	0	
6.1	2	2	0.83
6.2	—	—	
6.3	1	0	
6.4	2	2	
6.5	—	—	
6.6	1	1	

For such precedents, the number of objects classified as anomalous by them can be vast and the objects themselves are very likely to be erroneously classified as abnormal. The task is to allocate the largest number of precedents for a given number of objects classified by them as anomalous.

The idea of the algorithm of the minimum area of alarm is described as follows. In the first step, the algorithm builds for each precedent a set of objects classified by it as abnormal. Next, for a given number N^*, the algorithm selects the maximal number of the precedents for which the cardinality of the union of these sets is equal to the predetermined number N^*. The decision rule classifies the objects using only the selected precedents. For other precedents, we should look for new distinctive properties and add them to the feature space. The algorithm is greatly simplified if it selects not the maximal number of precedents but close to it.

Earthquake magnitude forecasts can be made in two ways: first, by systematically calculating the alarm area of expected earthquakes with an interval Δt and with magnitudes from a sufficiently large interval, evaluating the dependence of earthquake magnitudes on the values of the feature fields, and

constructing a map of the magnitudes for expected earthquakes in this area; second, by systematically calculating the alarm areas in which earthquakes with magnitudes from predetermined small intervals are expected. The second approach seems simpler. The quality of the forecast is determined by the probabilities of predicting the target events in the selected intervals and the value of alarm. The accuracy of the magnitude assessment is determined by the value of the earthquake magnitude interval. The solution can be represented by maps of alarm zones for each magnitude interval. Using these alarm zones, we can build a map of the maximum magnitudes of expected earthquakes.

Figure 2 shows the $U(V)$ curves that are mirrored version of the error diagram along with the confidence levels of 95% and 99% of random guessing (Bradley, 1997; Molchan, 1997; Kossobokov, 2006; Molchan and Romashkova, 2010). It is possible to see that the method of the minimum area of alarm could forecast earthquakes better than randomly guessing with confidence level more than 99% and that the forecast based on the spatial density on the lower alarm volume (less than 20%) shows the worse result, at the level of confidence of 1%.

Our tests show that a linear approximation of the dependence of earthquake magnitudes on the values of feature fields does not provide satisfactory results. The use of the method of the minimum area of alarm for predicting earthquakes belonging to small intervals of magnitudes has been successful enough to predict earthquake magnitudes.

When forecasting earthquakes with large magnitudes, sometimes difficulties arise because of the small number of target events that can be used for training. Testing shows that the method of the minimum area of alarm provides a better result of the forecast of strong earthquakes than the stationary forecast for the case in which the training set of the target earthquakes with large magnitudes is supplemented by earthquakes with smaller magnitudes.

Testing of the application of the method of the minimum area of alarm was carried out according to the fields $\mathbf{F}_8$, $\mathbf{F}_9$, and $\mathbf{F}_{10}$, which were not used in our previous works (Gitis and Derendyaev, 2019; Gitis et al., 2020a). These fields turned out to be more informative than $\mathbf{F}_1 - \mathbf{F}_7$ fields. Fields $\mathbf{F}_8$ and $\mathbf{F}_9$ use the information of the field $\mathbf{F}_7$ of quantiles of the background density of earthquake epicenters. The quantile field was proposed by Vadim Saltykov and used for the system of online monitoring of seismic activity (https://distcomp.ru/geo/2, https://distcomp.ru/geo/3; Gitis et al., 2015). We assume that anomalous values of $\mathbf{F}_8$ correspond to areas of the seismic process in which the density values of earthquake epicenters are quite high but significantly less than the average values of the density of epicenters in the interval from the beginning of the analysis to the start of training. Anomalous values of the $\mathbf{F}_9$ field correspond to areas of the seismic process in which an increase in the density of earthquake epicenters (compared with the interval from the beginning of analysis to the start of training) occurs simultaneously with an increase in the average magnitude of earthquakes. The $\mathbf{F}_{10}$ field simulates the preparation process for a strong earthquake according to the AUF model in Mjachkin et al. (1975). Anomalously high values of the $\mathbf{F}_{10}$ field are confined to the regions in which, during the preparation of a strong earthquake, the density of epicenters in the interval of diffuse seismicity increases, and then, in the interval of fracture formation, the density of epicenters decreases.

DATA AVAILABILITY STATEMENT

The original contributions presented in the study are publicly available. These data can be found here: http://www.isc.ac.uk/iscbulletin/search/ for Aegean Region Centre (2020) (accessed June 11, 2020) and http://sdis.emsd.ru/info/earthquakes/catalogue.php for Kamchatka.

AUTHOR CONTRIBUTIONS

VG and AD contributed to conception and design of the study. AD wrote the software. VG and AD made the analyses. VG wrote the first draft of the manuscript. VG and AD reviewed and edited the manuscript. All authors contributed to the manuscript revision and read and approved the submitted version.

FUNDING

This research was funded by the Russian Foundation for Basic Research (grant number 20-07-00445).

REFERENCES

Adeli, H., and Panakkat, A. (2009). A probabilistic neural network for earthquake magnitude prediction. *Neural Netw.* 22, 1018–1024. doi:10.1016/j.neunet.2009.05.003

Alexandridis, A., Chondrodima, E., Efthimiou, E., Papadakis, G., Vallianatos, F., and Triantis, D. (2013). Large earthquake occurrence estimation based on radial basis function neural networks. *IEEE Trans. Geosci. Rem. Sens.* 52, 5443–5453. doi:10.1109/TGRS.2013.2288979

Amei, A., Fu, W., and Ho, C.-H. (2012). Time series analysis for predicting the occurrences of large scale earthquakes. *Int. J. Appl.* 2, 64, 2012 . Available at: http://www.ijastnet.com/journal/index/313 or https://www.ijastnet.com/journals/Vol_2_No_7_August_2012/8.pdf.

Asim, K. M., Martínez-Álvarez, F., Basit, A., and Iqbal, T. (2017). Earthquake magnitude prediction in Hindukush region using machine learning techniques. *Nat. Hazards* 85, 471–486. doi:10.1007/s11069-016-2579-3

Bishop, C. M. (2006). "Machine learning and pattern recognition," in *Information science and statistics*. Heidelberg: Springer.

Boore, D. M. (2001). Comparisons of ground motions from the 1999 chi-chi earthquake with empirical predictions largely based on data from California. *Bull. Seismol. Soc. Am.* 91, 1212–1217. 10.1785/0120000733

Bradley, A. P. (1997). The use of the area under the roc curve in the evaluation of machine learning algorithms. *Pattern Recognit.* 30, 1145–1159. doi:10.1016/s0031-3203(96)00142-2

Bufe, C. G., and Varnes, D. J. (1993). Predictive modeling of the seismic cycle of the greater san francisco bay region. *J. Geophys. Res.* 98, 9871–9883. doi:10.1029/93jb00357

Bune, V., and Gorshkov, G. (1980). *Seismic zonation of USSR*. Moscow, Russia: Nauka, 307.

Dobrovolsky, I. P., Zubkov, S. I., and Miachkin, V. I. (1979). Estimation of the size of earthquake preparation zones. *Pure Appl. Geophys.* 117, 1025–1044. doi:10.1007/bf00876083

Geller, R. J., Jackson, D. D., Kagan, Y. Y., and Mulargia, F. (1997). Earthquakes cannot be predicted. *Science* 275, 1616. doi:10.1126/science.275.5306.1616

Gitis, V. G., and Derendyaev, A. B. (2018). "Web-based gis platform for automatic prediction of earthquakes," in International conference on computational science and its applications, Melbourne, United States, July 2–5, 2018, 268–283.

Gitis, V. G., and Derendyaev, A. B. (2019). Machine learning methods for seismic hazards forecast. *Geosciences* 9, 308. doi:10.3390/geosciences9070308

Gitis, V., Derendyaev, A., and Saltykov, V. (2015). "Gis platform for monitoring and analysis of seismic activity fields (in Russian)," in Problems of complex geophysical monitoring of the Russian far east. Proceedings of the fifth scientific and technical conference, Petropavlovsk-Kamchatsky, October 1–7, 2017, Vol. 27, 47–50.

Gitis, V. G., Derendyaev, A. B., and Petrov, K. N. (2020a). Analysis of the impact of removal of aftershocks from catalogs on the effectiveness of systematic earthquake prediction. *J. Commun. Technol. Electron.* 65, 756–762. doi:10.1134/s106422692006011x

Gitis, V. G., Derendyaev, A. B., and Petrov, K. N. (2020b). A method of abnormal geological zone identification. *Information processes* 20, 79–94. Available at: http://www.jip.ru/2020/79-94-2020.htm or http://www.jip.ru/2020/79-94-2020.pdf.

Gufeld, I. L., Matveeva, M. I., and Novoselov, O. N. (2015). Why we cannot predict strong earthquakes in the earth's crust. *Geodyn. Tectonophys.* 2, 378–415. 10.5800/GT-2011-2-4-0051

Guomin, Z., and Zhaocheng, Z. (1992). The study of multidisciplinary earthquake prediction in China. *J. Earthq. Prediction Res.* 1, 71–85.

International Seismological Centre (2020). On-line Bulletin. Available at: http://www.isc.ac.uk/iscbulletin/search/ (Accessed June 11, 2020).

Kagan, Y. Y., and Jackson, D. D. (1991). Long-term earthquake clustering. *Geophys. J. Int.* 104, 117–134. doi:10.1111/j.1365-246x.1991.tb02498.x

Kanamori, H. (1981). "The nature of seismicity patterns before large earthquakes," in *Earthquake prediction*. Editors D. W. Simpson and P. G. Richards (Washington, DC: American Geophysical Union), 1–19.

Keilis-Borok, V., and Soloviev, A. A. (2013). *Nonlinear dynamics of the lithosphere and earthquake prediction*. Berlin, Germany: Springer.

Khan, S. S., and Madden, M. G. (2009). "A survey of recent trends in one class classification," in *Irish conference on artificial intelligence and cognitive science*. New York, NY: Springer, 188–197.

Koronovsky, N. V., and Naimark, A. A. (2009). Earthquake prediction: is it a practicable scientific perspective or a challenge to science? *Moscow Univ. Geol. Bull.* 64, 10–20. doi:10.3103/s0145875209010025

Kossobokov, V. (1997). "User manual for m8," in *Algorithms for earthquake statistics and prediction*. Editor J. H. Healy, V. I. Keilis-Borok, and W. H. K. Lee, Vol. 6, 167–222.

Kossobokov, V. G. (2006). Testing earthquake prediction methods: the west pacific short-term forecast of earthquakes with magnitude mwhrv $\geq$ 5.8. *Tectonophysics* 413, 25–31. doi:10.1016/j.tecto.2005.10.006

Kossobokov, V. G., Romashkova, L. L., Keilis-Borok, V. I., and Healy, J. H. (1999). Testing earthquake prediction algorithms: statistically significant advance prediction of the largest earthquakes in the Circum-Pacific, 1992-1997. *Phys. Earth Planet. Inter.* 111, 187–196. doi:10.1016/s0031-9201(98)00159-9

Kotsiantis, S. B., Zaharakis, I., and Pintelas, P. (2007). "Supervised machine learning: a review of classification techniques," in *Emerging artificial intelligence applications in computer engineering*. Amsterdam, Netherlands: IOS Press, 160, 3–24.

Marzocchi, W., and Zechar, J. D. (2011). Earthquake forecasting and earthquake prediction: different approaches for obtaining the best model. *Seismol Res. Lett.* 82, 442–448. doi:10.1785/gssrl.82.3.442

Mjachkin, V., Brace, W., Sobolev, G., and Dieterich, J. (1975). "Two models for earthquake forerunners," in *Earthquake prediction and rock mechanics*. New York, NY: Springer, 169–181.

Mogi, K. (1979). Two kinds of seismic gaps. *Pure Appl. Geophy.* 117, 1172–1186. doi:10.1007/bf00876213

Molchan, G., and Romashkova, L. (2010). Earthquake prediction analysis based on empirical seismic rate: the M8 algorithm. *Geophys. J. Int.* 183, 1525–1537. doi:10.1111/j.1365-246x.2010.04810.x

Molchan, G. (2003). "Earthquake prediction strategies: a theoretical analysis," in *Nonlinear dynamics of the lithosphere and earthquake prediction*. New York, NY: Springer, 209–237.

Molchan, G. M. (1997). Earthquake prediction as a decision-making problem. *Pure Appl. Geophy.* 149, 233–247. doi:10.1007/bf00945169

Panakkat, A., and Adeli, H. (2007). Neural network models for earthquake magnitude prediction using multiple seismicity indicators. *Int. J. Neural Syst.* 17, 13–33. doi:10.1142/s0129065707000890

Rhoades, D. A. (2007). Application of the eepas model to forecasting earthquakes of moderate magnitude in southern California. *Seismol Res. Lett.* 78, 110–115. doi:10.1785/gssrl.78.1.110

Rhoades, D. A. (2013). Mixture models for improved earthquake forecasting with short-to-medium time horizons. *Bull. Seismol. Soc. Am.* 103, 2203–2215. doi:10.1785/0120120233

Shebalin, P. N., Narteau, C., Zechar, J. D., and Holschneider, M. (2014). Combining earthquake forecasts using differential probability gains. *Earth Planets Space* 66, 37. doi:10.1186/1880-5981-66-37

Sobolev, G., and Ponomarev, A. (2003). *Earthquake physics and precursors*. Moscow, Russia: Nauka.

Sobolev, G. (1993). *Fundamentals of earthquake prediction (in Russian)*. Moscow, Russia: Nauka, 314.

Vallianatos, F., and Chatzopoulos, G. (2018). A complexity view into the physics of the accelerating seismic release hypothesis: theoretical principles. *Entropy* 20, 754. doi:10.3390/e20100754

Wyss, M., Bodin, P., and Habermann, R. E. (1990). Seismic quiescence at parkfield: an independent indication of an imminent earthquake. *Nature* 345, 426–428. doi:10.1038/345426a0

Zavyalov, A. (2006). *Intermediate term earthquake prediction*. Moscow, Russia: Nauka, 52, 641–646.

Conflict of Interest: The authors declare that the research was conducted in the absence of any commercial or financial relationships that could be construed as a potential conflict of interest.

Copyright © 2020 Gitis and Derendyaev. This is an open-access article distributed under the terms of the Creative Commons Attribution License (CC BY). The use, distribution or reproduction in other forums is permitted, provided the original author(s) and the copyright owner(s) are credited and that the original publication in this journal is cited, in accordance with accepted academic practice. No use, distribution or reproduction is permitted which does not comply with these terms.

frontiers in Earth Science

ORIGINAL RESEARCH
published: 10 November 2020
doi: 10.3389/feart.2020.592561

Influence of Lithosphere Rheology on Seismicity in an Intracontinental Rift: The Case of the Rhine Graben

Denis Anikiev[1]*, *Mauro Cacace*[1], *Judith Bott*[1], *Maria Laura Gomez Dacal*[1] and *Magdalena Scheck-Wenderoth*[1,2]

[1]Section 4.5: Basin Modelling, Department 4: Geosystems, GFZ German Research Centre for Geosciences, Potsdam, Germany, [2]Faculty of Georesources and Material Engineering, RWTH Aachen University, Aachen, Germany

The Upper Rhine Graben (URG), as a part of the wider European Cenozoic Rift System, is a tectonically active area that has been extensively investigated for its geothermal energy potential. In this study, we carry out a first investigation of the present-day thermo-mechanical stability of the area as based on a detailed 3D geological and thermal model. The overall goal is, therefore, to assess how the lithospheric strength varies within the URG in response to the natural tectonic setting as well as the internal thermal configuration, and how those variations can be related to the recorded seismicity. The results from the modeling indicate that there is a spatial correlation between the predictions for the graben-wide rheological configuration with both the deep thermal field and the configuration of the crystalline crust. We find that the regional characteristics of the long-term strength of the lithosphere match the spatial distribution of seismicity, indicating that the mechanical stability of the area is primarily controlled by resolved strength variations. By cross-plotting the modeled strength distribution with available seismicity catalogs, our results suggest that seismicity in the graben area is shallower and of lower intensity due to a hotter and weaker crust compared to its surrounding areas. In contrast, seismic energy release appears to occur at deeper levels and being of larger magnitudes east of the graben and in the adjacent Lower Rhine Graben to the north. These results demonstrate the relevance of a proper quantification of the lithospheric rheological configuration and its spatial variability in response to its tectonic inheritance as an asset to interpret the pattern and distribution of seismicity observed in the area.

Keywords: lithosphere rheology, seismicity, 3D thermal model, effective viscosity, integrated strength, intracontinental rift, upper rhine graben, lower rhine graben

OPEN ACCESS

Edited by:
Antonella Peresan, Istituto Nazionale di Oceanografia e di Geofisica Sperimentale (OGS), Italy

Reviewed by:
Piotr Åšroda, Institute of Geophysics (PAN), Poland
Enzo Mantovani, University of Siena, Italy

***Correspondence:**
Denis Anikiev
denis.anikiev@gfz-potsdam.de

Specialty section:
This article was submitted to Solid Earth Geophysics, a section of the journal Frontiers in Earth Science

Received: *07 August 2020*
Accepted: *30 September 2020*
Published: *10 November 2020*

Citation:
Anikiev D, Cacace M, Bott J, Gomez Dacal ML, Scheck-Wenderoth M (2020) Influence of Lithosphere Rheology on Seismicity in an Intracontinental Rift: The Case of the Rhine Graben. Front. Earth Sci. 8:592561. doi: 10.3389/feart.2020.592561

INTRODUCTION

The Upper Rhine Graben (URG) is a continental rift that extends for roughly 320 km in a NNE-SSW direction (Mayer et al., 1997; Lopes Cardozo and Granet, 2005; Barth et al., 2015) along the French-German border in Central Europe (**Figures 1A,B**). It formed as a part of European Cenozoic Rift System (Ziegler, 1992) on a heterogeneous crust which was consolidated during the Variscan orogeny in the Latest Paleozoic and subsequently affected by regional subsidence during the Mesozoic (Ziegler, 1990; Franke, 2000). Bounded by the Vosges and Black Forest mountain ranges in the south (**Figure 1B**), the URG has an average width of 36 km (Mayer et al., 1997). Extensional tectonics in the graben started in Eocene times and has evolved into a transtensional

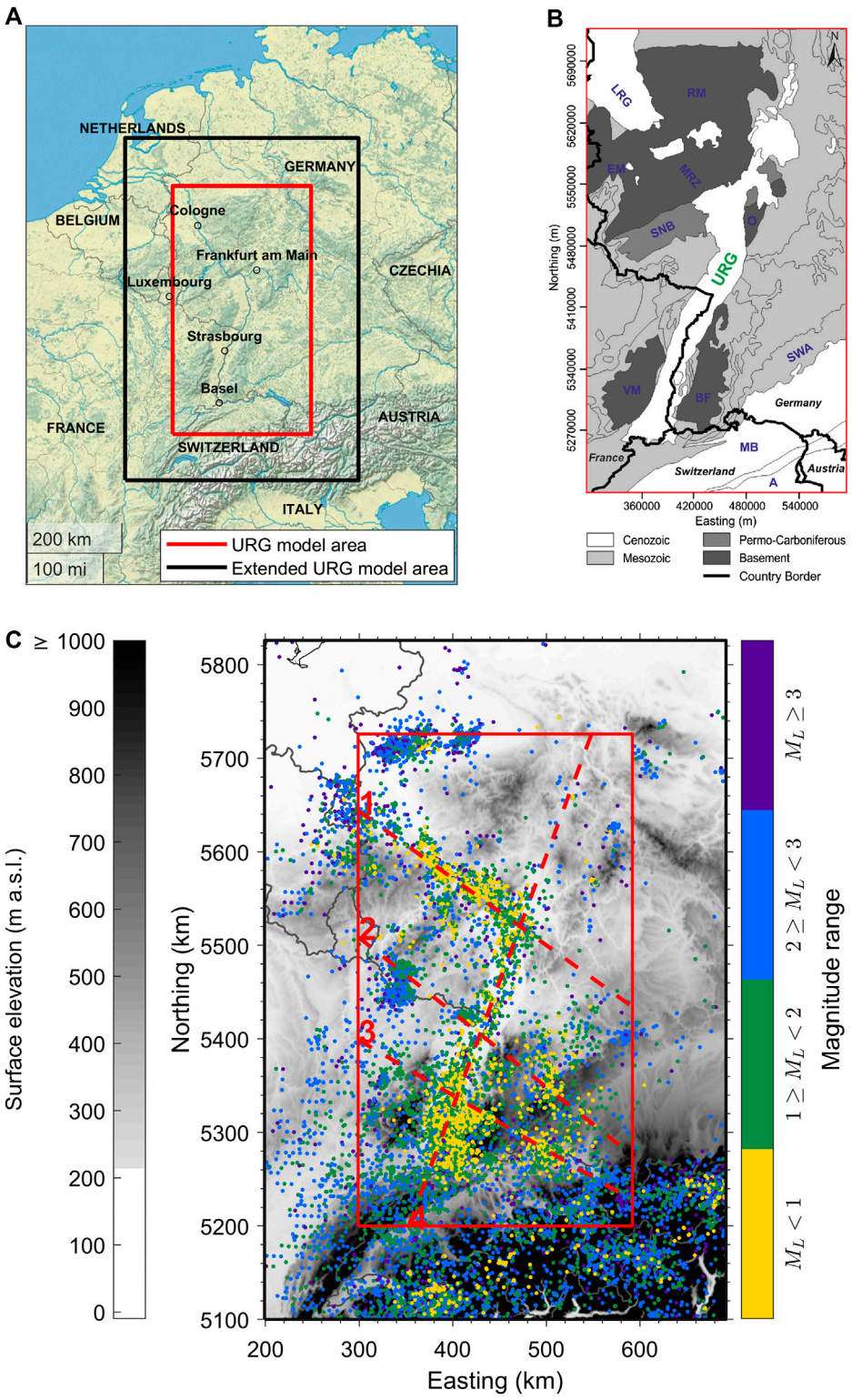

FIGURE 1 | (A) Geographical location of the area of interest: original 3D URG (Freymark et al., 2017; Freymark et al., 2020) area (inner red rectangle) and extended study area (outer black rectangle); **(B)** geological map of the URG model [modified from Freymark et al. (2017)], depicting the main tectonic domains: Upper Rhine Graben (URG), Lower Rhine Graben (LRG), Black Forest (BF), Eifel Mountains (EM), Vosges Mountains (VM), Molasse Basin (MB), Middle Rhine Zone (MRZ), Odenwald (O), Rhenish Massif (RM), Saar Nahe Basin (SNB), Swabian Alb (SWA) and Alps (A); **(C)** topography (ETOPO1, Amante and Eakins, 2009] of the extended study area in grayscale **(left color bar)** with recorded seismicity shown as dots color-coded according to their magnitudes **(right color bar);** the original 3D URG model area is limited by the red rectangle; red dashed lines display the four vertical profiles selected for a detailed study (see text for more details). Coordinates are given in UTM Zone 32 N.

regime at present with predominant sinistral-normal kinematics (Schumacher, 2002; Lopes Cardozo and Granet, 2005; Homuth et al., 2014; Bertrand et al., 2018). This makes the URG one of the seismically most active areas in Germany (Henrion et al., 2020; **Figure 1C**).

In the last decades, the URG has been the focus of a long list of exploration studies aiming at quantifying the distribution and availability of potential geothermal resources in the subsurface (e.g., Meixner et al., 2016; Vidal and Genter, 2018). Given its geological setting, all geothermal operations so far have considered its petrothermal potential (Cuenot et al., 2006; Baujard et al., 2017; Kushnir et al., 2018; Vallier et al., 2019), thereby relying on stimulation techniques to enhance the productivity of the *in-situ* reservoirs ("hot dry rock system"). These stimulation treatments have been shown to potentially increase the seismic hazard in the URG, thus posing safety concerns among the public (Egert et al., 2020). Different studies have investigated the mechanical response of specific targeted reservoirs during reservoir operations (Charléty et al., 2007; Calò et al., 2014; Maurer et al., 2020), though a regional investigation of the graben stability under the *in-situ* stress field is still lacking. Therefore, in this study, we investigate the thermo-mechanical configuration of the whole region with respect to the natural, that is, the tectonic and structural framework. We make use of a recently published 3D structural and thermal model of the URG (Freymark et al., 2017; Freymark et al., 2020) to derive spatial variations in lithospheric and crustal strength. The input 3D structural and thermal model integrate detailed information about the geology of the area, comprising a heterogeneous sedimentary sequence, upper and lower crustal domains and a lithospheric mantle. The model area also covers parts of the Alpine Orogen south of the URG as well as the western Molasse Basin and extends northward to the Lower Rhine Graben (LRG) and the Eifel region (**Figure 1B**). The model has originally been developed to assess the geothermal potential based on the variability in predicted temperatures, to overcome the lack of direct observables for the deeper crust and mantle. This structural and thermal model has been input into a rheological module (Cacace and Scheck-Wenderoth, 2016) to compute the steady strength distribution for the study area describing the long-term background rheological configuration.

The model outcomes are compared to the observed distribution of seismicity (**Figure 1C**) in the region (e.g., Homuth et al., 2014; Barth et al., 2015) in an attempt to understand if a causative relationship exists between the resolved variations in crustal rheology and the seismic activity in the area and to derive insights into the interaction of deformation controlling factors across the entire rift.

MATERIALS AND METHODS

Seismic Catalog

For the purpose of our study, we first derive a consistent seismic catalog as based on available sources. In total, we rely on eight different seismic catalogs: four catalogs are available from global earthquake web services: the GEOFON program of the GFZ German Research Centre for Geosciences using data from the GEVN partner networks (GEOFON Data Centre, 2020), USGS (U.S. Geological Survey, 2020), International Seismological Centre: ISC Bulletin (Storchak et al., 2017; International Seismological Centre, 2020b) and ISC-EHB Bulletin (Weston et al., 2018; International Seismological Centre, 2020a). These have been integrated both with earthquake catalogs of specific regions in the study area—the federal states of Baden-Württemberg (Seismisches Bulletins Baden-Württemberg, 1996–2019; LGRB, 2020) and Hessen (Seismischer Katalog des Landes Hessen, Version 2019, SKHe 2019; HLNUG, 2020) and with two combined earthquake catalogs published by Homuth et al. (2014) and Barth et al. (2015).

Based on these instrumental seismic records and harmonized data from modern and ancient sources dating back to the XI century (Grünthal et al., 2009; Barth et al., 2015), seismic activity in the URG has been constrained to occur preferentially within the graben area proper and, though minor, along its shoulders (**Figure 1C**). The largest known event in the area occurred near Basel in 1356 with an estimated MW of 6.9 ± 0.2 (Fäh et al., 2009; Barth et al., 2015).

The seismic catalogs were analyzed for their consistency and spatial reliability and finally merged into a unified catalog for our area of interest. In the following, we describe in some details the processing sequence followed [as also suggested by Barth et al. (2015)], which comprises the following steps:

- merging all available information to a single joint catalog of seismicity;
- limiting the data with respect to the spatial extent of the study area;
- evaluating the type of seismic events and restricting them to natural seismicity;
- limiting the data to a relevant time frame for the study;
- identifying and removing all double-listed events;
- evaluating the depth reliability/validity of events.

After merging the available information, we selected the spatial coverage of the seismicity data by extending by 100 km across each side the original 3D model of the URG (Freymark et al., 2017; Freymark et al., 2020; **Figure 1A**). This was done to include events that may affect the model boundaries. The final box for which seismic events are considered (**Figure 1A**) therefore covers an area of 493 km in W-E direction times 726 km in N-S direction (**Figure 1C**).

The catalog provided by Barth et al. (2015) contains information about the type of event (main shock, aftershock, foreshock, induced, single event) as described in the supplementary materials of Barth et al. (2015). For the sake of consistency, we have limited our catalog to single and main shock events only, thus dismissing all fore-/aftershocks and induced seismicity. Our choice stems from the fact that we are interested in correlating the first-order variations in the long-term crustal strength to the recorded seismic activity as occurring naturally from the background thermo-mechanical configuration of the

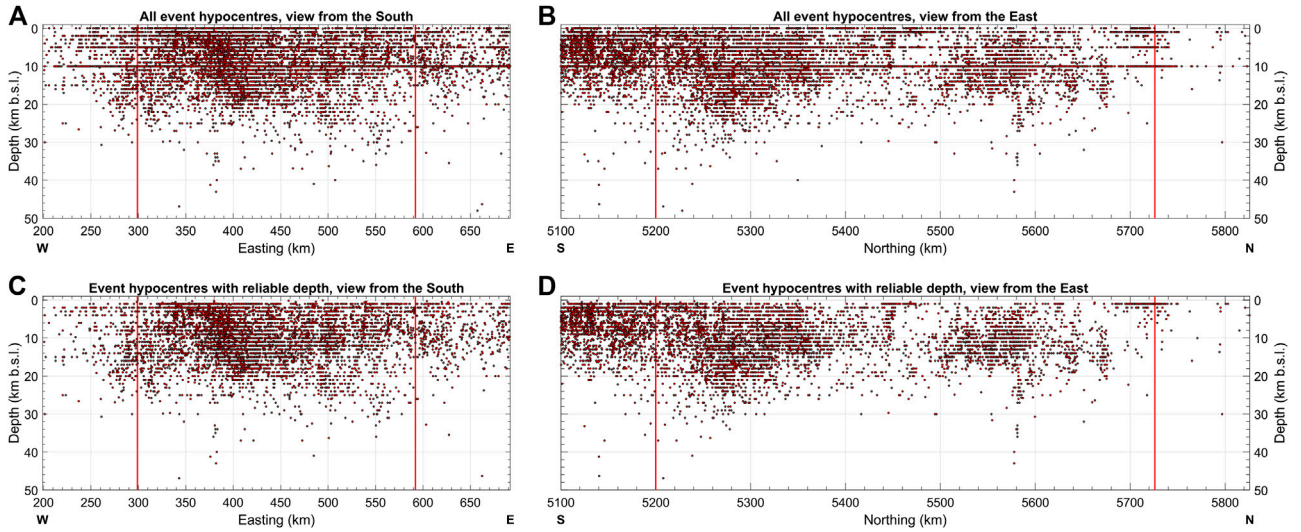

FIGURE 2 | Depths of hypocenters of seismic events bounded by the extended model rectangle: **(A)**–**(B)** all events; **(C)**–**(D)** events with reliable depths; **(A)** and **(C)** correspond to the view from the South; **(B)** and **(D)** shows the view from the East. Hypocenters are shown by red dots. The two red vertical lines depict the boundaries of the 3D URG model.

area and therefore not being overprinted by anthropogenic sources and or transients.

The Baden-Württemberg (LGRB, 2020) and the Hessen (HLNUG, 2020) earthquake catalogs are complete till the end of 2019. Therefore, we have limited the time frame of the joint catalog to the end of December 2019. The time frame starts from December 1080, when the first event described in the literature (CENEC; Grünthal and Wahlström; 2003; Grünthal et al., 2009; **Supplementary Material**) took place.

Double-listed events were sampled out from the joint catalog by following the procedure suggested by Barth et al. (2015): we assumed two events to represent the same earthquake, if their origin times differ by less than 5 s and their epicenters are closer than 15 km. This left us with 17,886 seismic events in the final catalog (**Figure 1C**; **Supplementary Material**).

The majority of magnitude values gathered in the joint catalog are local magnitudes M_L. However, some original catalogs included also body-wave magnitudes M_B and moment magnitudes M_W. In line with our research goals, we prioritized the reliability of the determined earthquake hypocenter depths over the magnitude of completeness, assuming all magnitude values to be consistent with local magnitudes M_L in the range from $M_L = 0.4$ to $M_L = 6.8$ (**Figure 1C**) and leaving any further magnitude distribution analysis out of the scope of this paper.

The source depth of an earthquake is the most difficult parameter to be determined. Its accuracy depends on the density and proximity of the seismic stations to the earthquake epicenter. It is quite often that the reported depth of an event hypocenter is not explicitly determined but is rather fixed (see, e.g., GEOFON Data Center, 2020; U.S. Geological Survey, 2020). Therefore, in the final processing step, we removed events with unreliable depths. At first, all events reported to have fixed and zero depths were excluded. Then, we removed all events with depth errors larger than 5 km from the USGS (U.S. Geological Survey, 2020) and the ISC-EHB Bulletin (Weston et al., 2018; International Seismological Centre, 2020a) catalogs. Finally, we excluded events with assigned constant depths of 5 and 10 km from the GEOFON catalog (GEOFON Data Centre, 2020), the ISC Bulletin (International Seismological Centre, 2020b) and the catalog from Barth et al. (2015). This was done because these data entered a significant and unrealistic bias to the trend, as seen from comparison of depth distributions between the full catalog and the resulting catalog of events with reliable depths (**Figure 2**).

Figures 2A,B portray the depths of all 17,886 events in the extended model area (**Figures 1A,C**; **Supplementary Material**) along a south and east perspective, whereas **Figures 2C,D** show a similar view though limited to events with reliable hypocenter depths (9,522 events; **Supplementary Material**). Although **Figure 2** represents only a cumulative view of the distribution of hypocenter depths, it already reveals the seismicity in the southern part of the URG to have a larger depth variability and density when compared to the central part of the graben (**Figure 2D**). In the south, the majority of events are shallower than 25 km b.s.l., whereas in its central part a gap of seismicity is evident at depths between 1 and 10 km b.s.l. In the northern part of the URG, the majority of events is above 20 km b.s.l. with a clear vertical trend of seismic events down to 45 km b.s.l. at the border of the URG with the Rhenish Massif (380 km Easting, 5,580 km Northing on **Figures 2C,D**; see also **Figure 1B**). The southern part of the URG, as well as the Alpine region, are the two areas that are more densely and accurately observed for seismic events which results in a higher accuracy of seismic events depths (reported depths for these areas often have extended accuracy beyond the usual rounded values, thus filling gaps between integer depth levels in **Figure 2**). In general, the Alpine region

reveals a denser and shallower (above 15 km b.s.l.) distribution of earthquakes.

Though the time frame for the full catalog starts from December 1080 (as mentioned above), the first event with sufficient reliability of depth occurred on August 1, 1956. Therefore, we finally restricted the time frame of the catalog of events with reliable depth to start on August 1956 and to end on December 2019 (see **Supplementary Material**).

To further explore the depth trends, we have selected four vertical profiles across the model based on their spatial proximity to seismicity clusters (**Figure 1C**). In order to associate seismicity with these selected profiles, we have picked seismic events with reliable depths (from **Figures 2C,D**) and epicenters within 5 km distance from each profile. **Figure 3** shows the four selected profiles where different colors are used to highlight events associated to each profile.

3D Geological and Thermal Model

The Cenozoic and Permo-Mesozoic sedimentary basins covering the area are located in the foreland of the Alps (**Figure 1B**) and were studied by integrating boreholes and seismic data

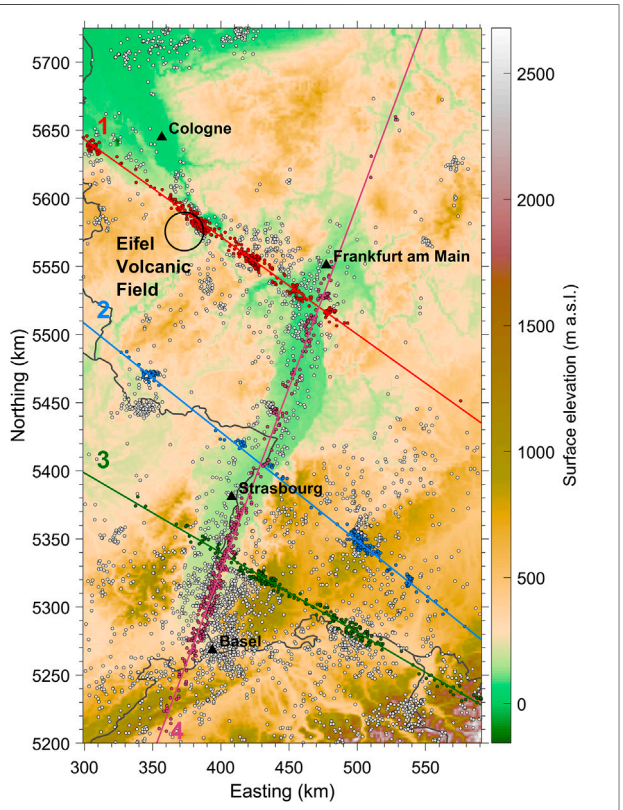

FIGURE 3 | Selected vertical profiles and associated seismic events with reliable depths and epicenters (within 5 km distance from each profile), shown with dots color-coded by profile colors and plotted on topography background (ETOPO1, Amante and Eakins, 2009). Profile 1 has 775 associated events, profile 2: 480 events, profile 3: 486 events; profile 4: 679 events. White dots represent remaining non-associated events. Deep-grey lines show country boundaries. Black circle shows the location of the Eifel Volcanic Field. Black triangles depict reference cities.

(Behrmann et al., 2005; GeORG-Projektteam, 2013; Freymark et al., 2017). The crystalline crust, imaged by deep seismic experiments (Lüschen et al., 1989; Blundell et al., 1992; Meissner and Bortfeld, 2014, among others), is differentiated into a "transparent" upper crust and a reflective lower crust. Furthermore, seismological models provided information about the variability in lithospheric mantle thickness across the region (Geissler et al., 2010). These different types of data have been integrated into a lithospheric-scale 3D density model by Freymark et al. (2017), which was further constrained against the observed gravity. The model covers a region extending 525 km in N-S direction and 290 km in E-W direction (**Figure 1C**).

According to differences in rock types, as constrained from outcropping sections and from geophysical data, the 3D model of Freymark et al. (2017) differentiates 24 units that altogether represent the sedimentary and volcanic cover, the crystalline upper and lower crust and the lithospheric mantle (**Table 1**). The first-order structural characteristics, as relevant for this study, are illustrated in **Figure 4**, where the maps of the upper and lower crustal thickness (**Figures 4A and 4B**, respectively) as well as the depth to the crust-mantle-boundary (Moho; **Figure 4C**) and to the Lithosphere-Asthenosphere Boundary (LAB; **Figure 4D**) are depicted. Also, the structural configuration is exemplary shown along the profile 4 (**Figure 4E**).

As a result of a comprehensive integration of existing 3D models [e.g., "Hessen 3D" of Arndt et al. (2011); "GeORG" of the GeORG-Projektteam (2013)] and various geological and geophysical observations, the 3D model of Freymark et al. (2017) is consistent with geological maps, borehole formation top data, reflection and refraction seismic profiles and major gravity anomalies (Freymark et al., 2017 and references therein). Furthermore, the 3D model resolves computed variations in the thermal field that have been validated against a set of available borehole temperatures. Hence, the model provides us with unit-specific information on the prevailing lithology, bulk density, and bulk rock thermal properties (**Table 1**) as well as computed temperatures under the assumption of steady-state heat conduction. These attributes are distributed on a grid of 1 km horizontal resolution and a vertical resolution corresponding to the variable thicknesses of the geological layers.

The modeled crystalline crust below the depositional cover is bi-parted with a homogeneous lower crust and a laterally differentiated upper crust representing crustal blocks of different tectonic origins (Freymark et al., 2017). The configuration of the crystalline upper crust traces back to the Variscan Orogeny when terranes of different composition collided and experienced intensive syn- and post-orogenic deformation and metamorphism (e.g., Franke, 2000). These developments find their expression in a lateral differentiation of the upper crust into seven sub-units considered as individual units with specific rock properties in the model of Freymark et al. (2017) (**Table 1**). At present day, the study area is part of the northern Alpine foreland where the Rhine graben developed as a part of the European Cenozoic Rift System through different tectonic phases dating back to the Eocene (e.g., Dèzes et al., 2004). As a result of rifting, the upper crust in the URG was thinned by several kilometers compared to the adjacent domains

TABLE 1 | Thermal and mechanical properties of model units.

3D structural and thermal model (Freymark et al., 2017)						Power-law dislocation creep parameters (from Ranalli and Murphy, 1987)			
		Prevailing lithology	**Density (kg m^{-3})**	**Bulk thermal conductivity (W m^{-1} K^{-1})**	**Radiogenic heat production (μW m^{-3})**	**Type rheology**	**Activation enthalpy, H (J mol^{-1})**	**Power law exponent, n**	**Strain rate, A (Pa^{-n} s^{-1})**
Sedimentary and volcanic cover		(various)[a]	2,600[b] (2,200–2,860)	2.4[b] (1.2–6.0)	1.0[b] (0.0–1.6)	(—)	(—)	(—)	(—)
Upper crust	Rhenohercynian	Slates	2,700	2.7	1.00	Quartzite	1.56E+05	2.4	2.51E-24
	Northern phyllite zone	Phyllites	2,710	2.7	3.00				
	Mid German crystalline high	Granitoids, gneisses	2,700	2.4	1.80				
	Odenwald	Granitoids, gneisses	2,650	3.0	1.80				
	Saxothuringian	Slates, granitoids	2,730	2.5	2.50				
	Moldanubian	Gneisses, granitoids	2,690	2.5	2.60				
	Alps	Granitoids	2,830	2.3	2.40				
Lower crust		(Unknown)	2,900	2.1	0.50	Diabase	2.60E+05	3.4	8.04E-25
Lithospheric mantle	Outside southern URG	(Peridotite)	3,300	3.95	0.03	Olivine	5.40E+05	3.0	4.00E-12

[a]*The model differentiates 14 sedimentary and volcanic cover units of diverse lithologies (clastics, carbonates, basalts, evaporites).*
[b]*Median (range).*

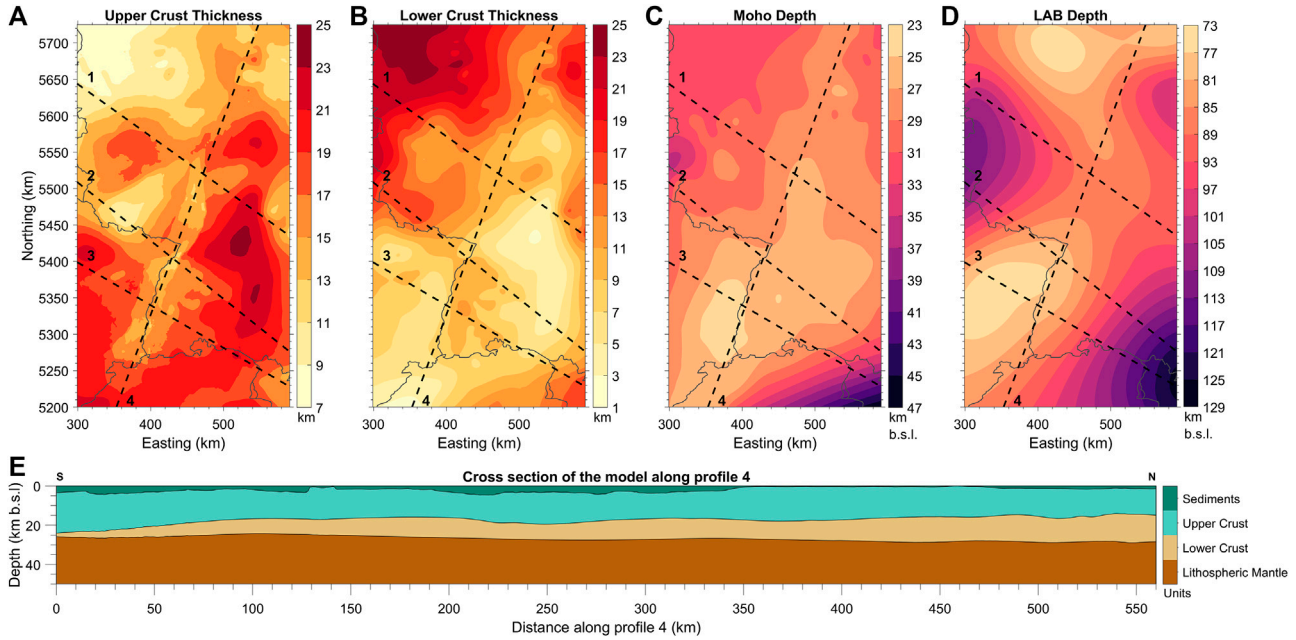

FIGURE 4 | Main characteristics of the 3D structural model after Freymark et al. (2017):**(A)** thickness of the Upper Crust; **(B)** thickness of the Lower Crust; **(C)** depth to the Moho crust-mantle boundary; **(D)** depth to the Lithosphere-Asthenosphere boundary; **(E)** geological units across profile 4 [simplified after Freymark et al. (2017)]. Deep-grey lines on **(A)**–**(C)** delineate country boundaries.

(**Figure 4A**). The upper/lower crustal interface (Freymark et al., 2017) has been derived based on 21 reflection and refraction seismic profiles (mainly originating from the DEKORP seismic program, e.g., Meissner and Bortfeld, 2014) and thus widely corresponds to the interface between the "transparent," seismically slower upper crust and the highly reflective, faster lower crust. Off the seismic profiles, the 3D depth configuration of this interface has been derived by relying on the best gravity response of the model considering observed gravity anomalies and density differences between the upper and the lower crust (**Table 1**). Based on seismic velocities and modeled densities, Freymark et al. (2017) interpreted the upper crust to be composed of felsic rocks, whereas the lower crust is interpreted to be of a mafic composition. Overall the work of Freymark et al. (2017) integrating seismic data with the observed gravity field, demonstrated that both the upper and the lower crust show large lateral thickness variations (**Figures 4A,B**) that in turn will influence the rheological characteristics of the lithosphere. In particular, the upper crust is thicker in the surroundings of the URG whereas the mafic lower crust severely thickens in the north-western part of the model area.

The depth to the crust-mantle-boundary (Moho; **Figure 4C**) is the result of an interpolation between the seismically constrained dataset derived from Mechie (2007) and NAGRA (Heidbach and Hergert, 2012). The Moho is shallowest (<25 km deep) below the URG, moderately deep in the NW domain (30–35 km) and deepest in the SE below the Alps (>40 km).

The deepest structural element of the 3D model is the seismological lithosphere-asthenosphere boundary (LAB) as derived from SP receiver functions (Geissler et al., 2010). The latter is assumed to coincide with an internal thermo-chemical boundary separating the rigid lithosphere from the underlying convective viscous mantle (1,300° isotherm). The most important features in the LAB topology are 1) a NE-SW elongated structural high in the SW, 2) a N-S striking high below the Eifel region, and 3) a structural low below the Alpine foothills in the SE (**Figure 4D**). The LAB is assumed to coincide with an isotherm (fixed lower boundary condition of T = 1,300°C), therefore variations in its topography (ca. 75–125 km) have important implications for the steady-state conductive thermal state of the whole plate, where a shallower LAB corresponds to a steeper geothermal gradient and vice versa.

The other boundary condition adopted in the thermal modeling is a fixed, though spatially varying temperature (range between 1 and 12°C) at the model surface [global Earth's surface elevation derived from Amante and Eakins (2009)], here adopted as representing an annual mean of surface temperature in the study area (Freymark et al., 2017 and references therein).

As the details of the thermal modeling study have been published elsewhere (Freymark et al., 2017), we here only outline the most important features, as relevant for the rheological study that follows. Therefore, we limit our discussion to the description of depth maps for two isotherms (450–600°C; **Figure 5**). These isotherms are considered representative for the thermal field at crustal and deeper levels. They also have important rheological implications as upper and lower bounds of the region of maximum dissipation potential for a viscous fluid-like plate parameterized in terms of commonly assumed minerals representative of crustal and mantle rocks,

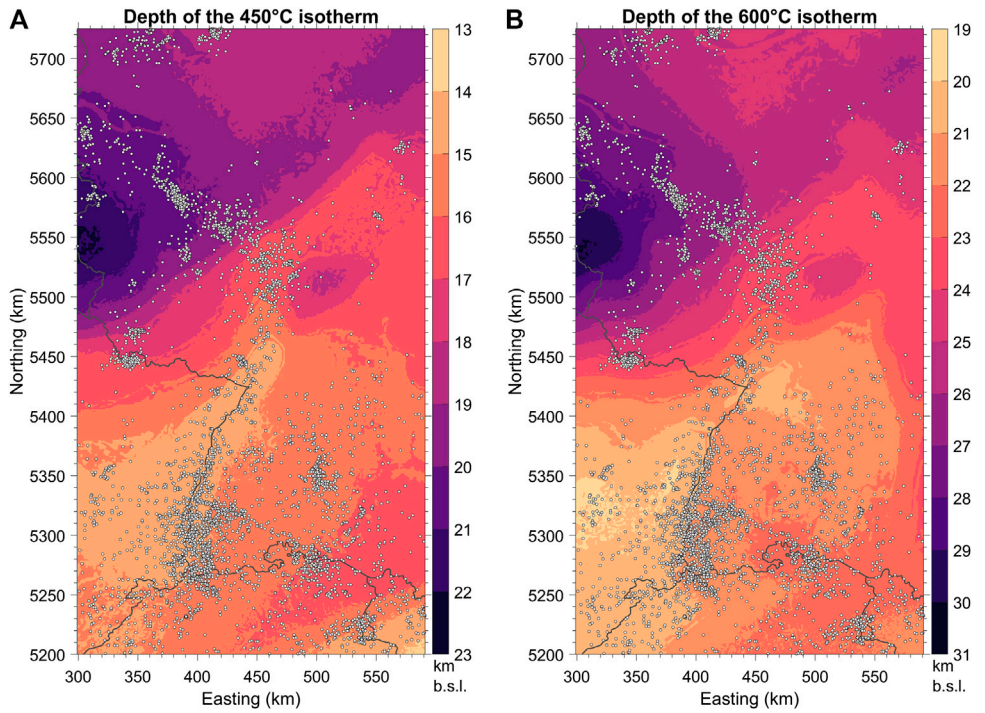

FIGURE 5 | Maps of depths of the **(A)** 450°C isotherm and **(B)** 650°C isotherm compared with seismicity. Light-grey dots show epicenters of seismic events with reliable depths. Deep-grey lines show country boundaries.

respectively (see also next paragraph). The 450°C isotherm (**Figure 5A**) is located within the upper crust in the SE parts of the study area and within the lower crust in the NW. The match between the domain where this isotherm attains greater depths in the NW and the extent of the thickened mafic lower crust (**Figure 4B**) is striking and we relate this finding to the fact that this model unit is depleted in radiogenic minerals (**Table 1**). Moreover, the parameterization of the different upper crustal blocks in terms of heat generation rates differentiates less radiogenic domains in the NW consistent with the main lithological trends outcropping at the surface (Freymark et al., 2017). The same authors demonstrated that such differentiation was indeed needed to fit observed borehole temperatures. The 450°C isotherm is shallowest in the domain of the URG proper and in the area adjacent to the URG in the SW, areas where a thick sedimentary cover is also present. Sediment thickness varies from 0 m in the NW part of the study area to locally >3.5 km in the URG (Freymark et al., 2017). Also, the Moho and the LAB are significantly elevated in this region (**Figures 4C,D**), the latter implying an overall steeper geothermal gradient in this area. Accordingly, the thermal influences of the thick radiogenic upper crust and the shallow LAB depth are superimposed in these domains by thermal blanketing from the sedimentary and volcanic units. The latter are characterized by lower thermal conductivities than the crystalline crustal rocks (**Table 1**), which results in heat storage in the shallow part of the crust.

The 600°C isotherm (**Figure 5B**) is located within the lower crystalline crust and in the upper lithospheric mantle. Overall the 600°C isotherm displays a similar pattern as the 450°C isotherm, indicating a colder NW half of the study area and a hotter SW domain with shallowest depths in the URG. The isotherm is deepest (up to 31 km b.s.l.) NW of the URG and S of the LRG. Northeast of the LRG, the isotherm rises again in the central part of the northern model boundary in response to a shallowing of the LAB in the Eifel region.

The distribution of seismicity (**Figure 1C**) indicates a clustering of earthquakes in the domains where the two isotherms are shallowest in the URG, an aspect that already suggests a first-order correlation between the regional tectono-thermal configuration of the study area and its mechanical stability. However, there are also clusters of seismicity in the colder NW part aligned along the 20 and 27 km depth isolines for the 450–600°C isotherms, respectively. These observations will be investigated in more details in the following.

Rheological Modeling Approach

As discussed in the introduction, the main goal of this study is to investigate whether a correlation between the seismicity distribution and the internal thermal and rheological configuration exists in the study area. We therefore assess its rheological state as based on the previously described data-constrained 3D structural and thermal model (Freymark et al., 2017). The model is the main input into a rheological module to compute the steady strength distribution following the approach as described in more details in Cacace and Scheck-Wenderoth (2016). The long-term mechanical behavior of the lithosphere (i.e., for time scales greater than the characteristic relaxation time of the considered plate) is usually modeled by relying on the

concept of a static (secondary creep) rheology. Under this assumption, at shallow depth levels rocks exhibit primarily static frictional behavior. Frictional rock behavior is considered to follow Byerlee's law, thereby being independent of the background temperature conditions, but only sensitive to the level of effective confining pressure (static friction) described by the following constitutive law (e.g., Ranalli, 1995):

$$\Delta\sigma^b = c_f \rho(T) g z (1 - \lambda) \quad (1)$$

In **Eq. 1**, c_f is the static friction coefficient, ρ is the density of the bulk rock, g is the gravity acceleration, z is the depth below sea level, and λ is the hydrostatic fluid factor given by the ratio of the pore pressure to the lithostatic pressure.

With increasing depths, rocks tend to deform as a viscous (non)Newtonian fluid, though experiments demonstrated the onset of low temperature crystal plasticity to occur at confining pressures higher than approximately 200 MPa (Katayama and Karato, 2008), which can be parameterized as:

$$\begin{cases} \left(\frac{\dot{\varepsilon}}{A}\right)^{\frac{1}{n}} e^{\left(\frac{H}{nRT}\right)} & \text{if} \quad \Delta\sigma^d < 200 \ \text{MPa} \\ \sigma_0 \left(1 - \left[\frac{-RT}{Q} ln \frac{\dot{\varepsilon}}{\dot{\varepsilon}_0}\right]^{\frac{1}{2}}\right) & \text{if} \quad \Delta\sigma^d > 200 \ \text{MPa} \end{cases}, \quad (2)$$

where $\dot{\varepsilon}$ is the strain rate, A the power law strain rate, n the power law exponent, H the activation enthalpy, R the gas constant, T the temperature, σ_0 the Peierls critical stress, Q the Dorn activation energy, and $\dot{\varepsilon}_0$ the Dorn critical strain rate.

This view of rock deformation leads to the overly famous Brace and Kohlstedt strength concept (Brace and Kohlstedt, 1980), where the envelope in a differential stress vs. depth diagram (minimum between $\Delta\sigma^b$ and $\Delta\sigma^d$) exemplifies the maximum strength of a rock under a given, though steady, state of loading (constant strain rate approximation). This definition is based on a dissipative fluid mechanics concept of rock deformation, where the transition from a brittle-like behavior to a ductile-like behavior coincides with maximum values in energy/entropy dissipation (Regenauer-Lieb and Yuen, 2008). Following this view, it is the efficiency of ductile creep to accommodate the stored deformation that provides the first-order control on the distribution of maximum dissipation with depth, thus resulting in a sharp brittle-to-ductile transition (BDT hereafter). The power law functional dependency of ductile creep on temperature, together with the assumption of a constant strain rate, permits to correlate the BDT to characteristic temperature values that only depend on the parameters adopted in the viscous flow laws (typically the 400/600°C and 800/900°C isotherms are taken for a pure quartz and an olivine rheology, respectively). This leads to two basic ingredients to fully characterize a static rheology, that is, the bulk rock mineralogical composition, and the background temperature.

The BDT is thought to provide a conservative estimate of the seismogenic zone, and therefore, of the depth distribution of seismicity within a lithospheric plate. The assumption at play is that stored elastic energy can be effectively dissipated by viscous creep below the BDT, thus limiting earthquake occurrence to the brittle realm (Burov, 2011). The efficiency of viscous creep can be parameterized in terms of an effective viscosity parameter that follows a thermally activated power-law flow law, as typical for dislocation creep as:

$$\eta_{\text{eff}} = \frac{2^{\frac{1-n}{n}}}{3^{\frac{1+n}{2n}}} A^{-\frac{1}{n}} \dot{\varepsilon}^{\frac{1}{n}-1} e^{\left(\frac{H}{nRT}\right)} \quad (3)$$

Given that the rate of viscous dissipation depends primarily upon background temperature conditions, it seems rather obvious to correlate the seismicity pattern beneath a specific area to the resolved thermal configuration of the plate. This approach has been extremely successful when applied to the study of the evolution of oceanic plates, though its direct use for the continental lithosphere has been hindered by the relative geological complexity of the latter (Burov, 2011).

The main assumption of our rheological approach stems from quasi-static loading conditions, i.e., a steady strain rate approximation. Though, strain rate values can be assigned as non-uniform across the model, we decided at this stage to make use of a constant and uniform strain rate value of $10^{-15}s^{-1}$. Our choice for the background strain rate is consistent with strain rates derived from GNSS analysis for the study area, recording maximum horizontal displacement rates of approximately 500 μm/yr (Fuhrmann et al., 2013; Henrion et al., 2020). These values are also consistent with previous studies suggesting horizontal extension rates in the URG below 1 mm/a (Rózsa et al., 2005; Tesauro et al., 2006). Taking these estimates as a representative extensional deformation rate for the whole URG, we compute a maximum strain rate value of approximately $8.9 \times 10^{-16}s^{-1}$ (considering the average width of the Tertiary Rhine Graben between Basel and Frankfurt of 36 ± 5 km; Mayer et al., 1997). Hence, the imposed strain rate used in our model should be considered as providing a maximum estimate.

To assign viscous creep parameters, we follow the main structural units of the 3D model, whereby each unit has been parameterized as uniform in terms of its prevalent lithology. In doing so, we opt for a quartzite upper crust, a diabase enriched lower crust, and a peridotitic upper mantle (**Table 1**). This differentiation accounts for an overall strength increase from felsic to mafic and to ultramafic composition (e.g., Ranalli and Murphy, 1987). **Table 1** lists the rheological parameters adopted in the study. Frictional brittle behavior has been parameterized consistent with the prevailing extensional-to-transtentional kinematics observed across the region (Heidbach et al., 2016) with additional constraints from the model by Freymark et al. (2017) (**Table 1**). In the present study, we did not attempt any further differentiation in the bulk rheological behavior of the different upper crustal sub-units since we consider that such a differentiation would lead to over-interpreting the geodynamic implications of the structural model. Instead, by assuming a constant rheology for all upper crustal sub-units, we are able to quantify the first-order effects of the resolved thermal configuration on the regional mechanical behavior, and, by direct comparison with the available seismic catalog, to the observed seismicity distribution in the area.

RESULTS

Figure 6 portrays the computed map of integrated strength [crust and total lithosphere in panels **(A)** and **(B)**, respectively] for the whole study area. A remarkable feature of the two maps is a heterogeneous strength distribution, with a clear minimum across the URG. The presence of lower than surrounding crustal (and lithospheric) strength values in this domain are structurally linked to the regional thermal configuration, with the URG being hotter than the surrounding domains (**Figure 5**). This is due to the concomitant presence of an elevated LAB underlying a thinned and mechanically decoupled upper crust (in response to transtentional tectonics).

The degree of mechanical decoupling inversely correlates with the local temperature conditions, where the presence of higher mid-crustal temperatures (shallower 450–600°C isotherms; **Figure 5**) leads to an internal decoupling as the hot crust is no longer able to sustain imposed stress but would rather accommodate stored deformation by ductile creep. Accordingly, higher than background temperatures in the graben proper imply a weak crust, an aspect that correlates with the clustering of, preferentially low-magnitude, earthquakes in the area (**Figure 1C**).

There is an overall spatial correlation between the distribution of hypocenters and lateral variations in the computed crustal strength, with the majority of events lying within the boundaries of the weakest crust (**Figure 6**). This clear correlation between earthquake distribution and crustal and lithosphere strength breaks down, however, when moving toward the NW domain, for example, along the Middle Rhine Zone (MRZ) which connects the URG with the LRG (compare with **Figure 1B**). Moving virtually from the northern parts of the URG toward the NW means entering a domain that is characterized by lower temperatures (larger depth of the 450–600°C-isotherms; **Figure 5**) as mostly controlled by the lower radiogenic heat production of the Rhenohercynian upper crust (**Table 1**) and a thicker lower crust (**Figure 4B**). As a consequence, our model predicts overall larger crustal and lithospheric strengths for this domain, which appears at odds with the presence of a second belt of seismicity striking NW-SE and connecting the URG with the LRG (**Figure 6**). Under a similar background stress field, we would expect few if not no earthquake activity to occur within a stronger and thicker crust. Comparing the crustal and lithospheric strength maps we note, however, that in this area the mantle contribution to the total strength is larger than in the other parts of the study area where the crustal and lithosphere strength maps display more consistent patterns. This configuration of a strong crust and a strong mantle indicates a mechanically coupled crustal-upper mantle lithosphere, i.e., a thicker elastic root in this part of the study area. Increasing the contribution of the lower crust and upper mantle to the total plate strength would therefore translate in an increase in the portion of the lithosphere that is able to sustain imposed stress, thus resulting in a deepening of higher in magnitudes seismic events in this area (**Figures 7A**, **1C**—see also the discussion that follows). Such a rheologically heterogeneous lithosphere is likely to control also the horizontal distribution of hypocenters, which in the MRZ are located within a domain of finite lateral

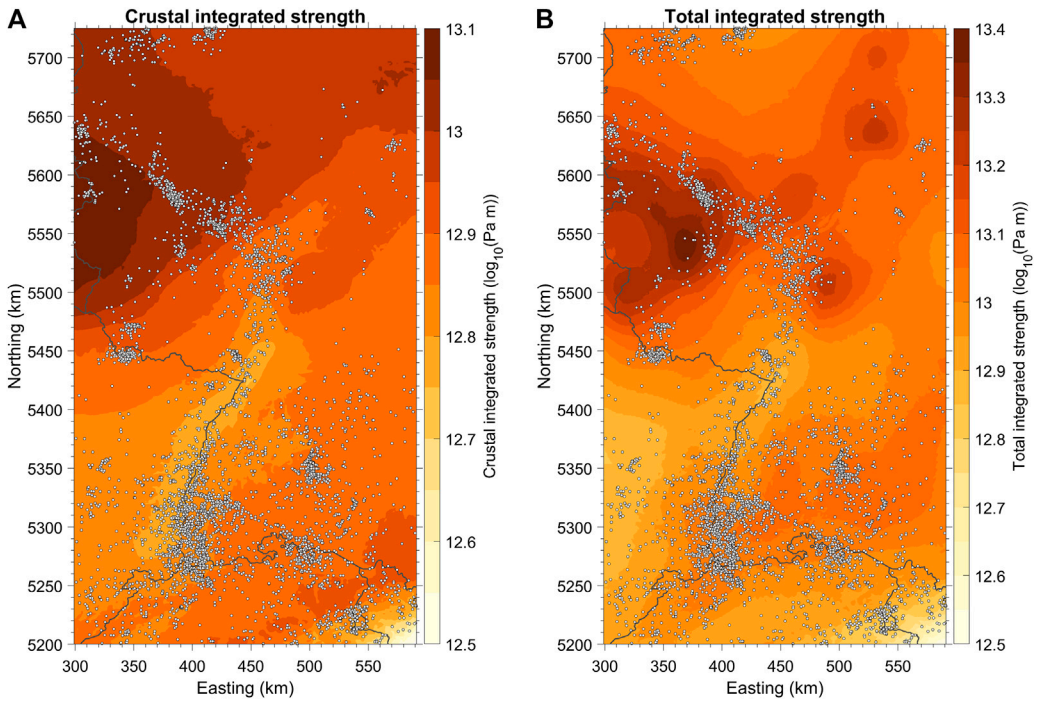

FIGURE 6 | Maps of the integrated **(A)** crustal and **(B)** total strength compared with seismicity. Light-grey dots show epicenters of seismic events with reliable depths. Deep-grey lines show country boundaries.

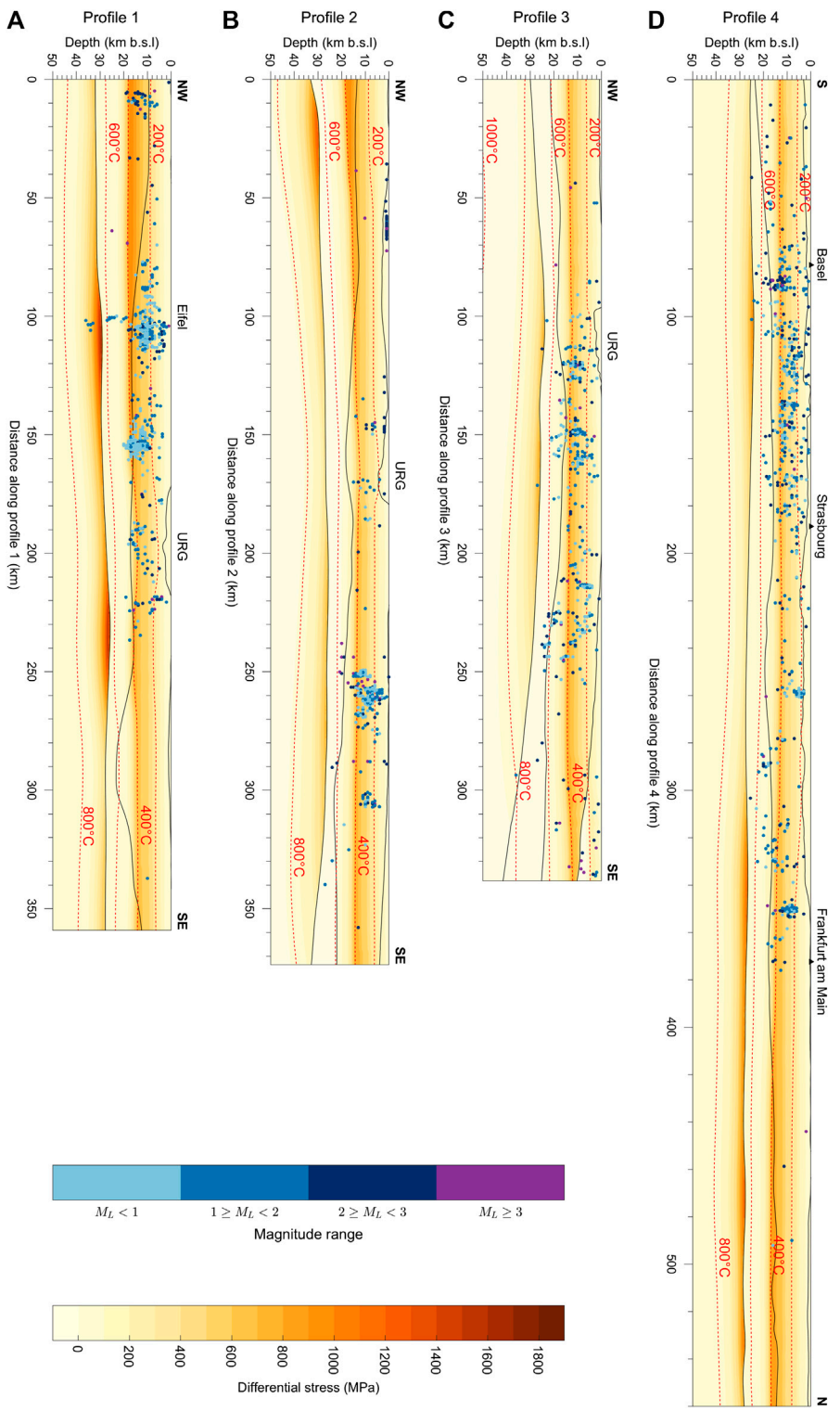

FIGURE 7 | Differential stress displayed along depth cross-sections for each profile: **(A)** profile 1; **(B)** profile 2; **(C)** profile 3; **(D)** profile 4. Dots indicate hypocenters of seismic events associated with the profile (see **Figure 3**) and are color-coded by their local magnitude (the upper color bar). The differential stress color legend is explained by the lower color bar. Dashed red lines depict isotherms derived from the thermal model, and gray lines mark the structural model units (see **Figure 4E**).

extent. This hypocenter cluster spatially correlates with transitional LAB depths (**Figure 4D**; deep south of the seismicity cluster and shallow north of it) and thus a gradient in the long-term strength of the plate. In addition, the localization of seismicity in the MRZ might be causally related with smaller-scale crustal features not resolved by our model. This includes, for example, 1) the NW-SE striking Lower Rhine Graben System of presently reactivated faults (Cloetingh et al., 2006) which tapers off toward the MRZ as it is increasingly outranged by NE-SW trending Variscan lineaments of the Rhenish Massif [e.g., compiled tectonic map in Grünthal et al. (2018)] or 2) the magmatic and tectonic structures related to the Eifel volcanic field (black circle in **Figure 3**).

So far, the discussion has mostly been limited to the regional characteristics of the modeling in terms of computed integrated strength maps (**Figure 6**). Despite the general agreement found between seismicity and first-order lateral rheological contrasts, no information has been derived on their depth distributions. An attempt is done in **Figure 7** where we plot the computed differential stress together with the depth locations of hypocenters across the four profiles introduced in the previous chapters.

In our modeling approach, the depth at which a maximum in the differential stress occurs marks the transition between the brittle frictional deformation regime and the ductile domain, i.e., the BDT. Therefore, we could consider this depth level, to a first order, as indicative of the lower boundary for the seismogenic zone. If we compare this depth level to the depth distribution as provided by the seismic catalog, we note an overall correlation between the rheological modeling results and the depth distribution of hypocenters. The majority of the recorded events are shallower than and limited by our computed BDT, despite the steady-state assumptions of our modeling approach. We can go that far in interpreting these results as to provide a causative mechanism explaining the observed variations in the depth distribution of hypocenters, characterized by shallower seismic events in the S than in the N(W). Accordingly, the observed northward increasing depth of hypocenters can be related to a northward thickening of the brittle crustal portion of the lithosphere and to a deepening of the BDT as evident in all profiles (**Figure 7**). Thus, a thicker and therefore stronger brittle crust would have the potential to produce deeper and larger in magnitude events. This is again in agreement with the distribution of the seismic magnitudes (**Figure 1C**). Thickening of the brittle crustal layer can also explain the deepening of hypocenters along profile 3 while moving from the URG proper to the east and the associated increase in earthquake magnitudes (**Figure 1C**). Based on these findings, we can conclude that, on a regional scale, first-order lithology contrasts in the crust within an overly diffusive lithosphere loaded by a background stress likely control the overall mechanical behavior of the plate.

Locally, also seismic events that are deeper than the modeled 450°C isotherm are observed as shown in profile 1 at the western graben margin or in profile 3 east of the URG. Also, along the graben axis (profile 4) such deeper events are evident. Most of these deeper events are within the mafic lower crust and their depth is mostly shallower than the 600°C isotherm. Given that the BDT is occurring at higher temperatures in mafic rocks (e.g., Ranalli and Murphy, 1987), the seismicity down to the depth of 600°C is therefore not surprising in these domains. Alternatively, the presence of hypocenters deeper than the resolved BDT could be related to secondary, transient and therefore other than conductive thermal effects associated with local structural heterogeneities (i.e., faults) and variations in rock properties, which could affect the location of the BDT in the modeling. Such transient effects are important, though locally, and were already evidenced in previous works (Freymark et al., 2017; Freymark et al., 2019), where the local mismatch between computed temperature and T-logs has been explained by active fluid circulation along major fault zones. This can explain the presence of hypocenters along the western portion in profile 1 reaching down to more than 30 km (lithospheric mantle) that appear to be aligned.

An important factor controlling the depth distribution of the brittle frictional domain is viscous relaxation by crustal and mantle creep. The ability of crustal and mantle rocks to efficiently accommodate accumulated stress can be parameterized in terms of an effective viscosity (see the previous paragraph). Based on experimental evidence, in the present study we have assumed dislocation creep to be the only active relaxation mechanism. Dislocation creep is characterized by a nonlinear relationship between stress and strain rate (**Eq. 2**), thus by a nonlinear effective viscosity that has a power-law dependence on the assumed strain rate (or stress) and an exponential dependence on temperature (**Eq. 3**). The profiles in **Figure 8** illustrate this non-linear behavior. Despite assuming a uniform and constant background strain rate and a constant uniform lithology for each major geological unit, the viscosity profiles are characterized by a marked viscosity gradient in each unit due to a heterogeneous thermal field. Average values of the calculated effective viscosity for the upper crust are in a range between $10e^{21}$ and $10e^{24}$ Pa*s, with a two to four orders of magnitude decrease in viscosity at lower crustal and upper mantle levels, respectively. A drastic jump in effective viscosity is indeed evident at the upper-lower crustal discontinuity, indicating that most of the relaxation takes place in the lower crust and upper mantle. Relatively low viscosity values in the lower crust and upper mantle promote stable aseismic creep, possibly enhanced by lower crustal flow, thus explaining the overall drop in seismic activity at these depths. As described above, we can correlate the depth location of recorded seismicity to the upper crustal configuration, with deeper events occurring within a thicker and stronger crust in the north and south-east of the URG, while being limited to shallower depths in the URG due to efficient lower crustal viscous relaxation in the presence of a thin brittle upper crust. Though we cannot rule out that there might be other active co-players, including transient creep processes or pore pressure mediated effects, the results of **Figure 9** provide additional evidence on the role of crustal rheological contrasts in controlling the overall strength and mode of lithospheric deformation in the study area.

To discuss in a more quantitative way the implications of the modeled crustal thermo-mechanical configuration and the potential seismic hazard in the study area, we present a map of spatial variations in the base of the seismogenic crust in

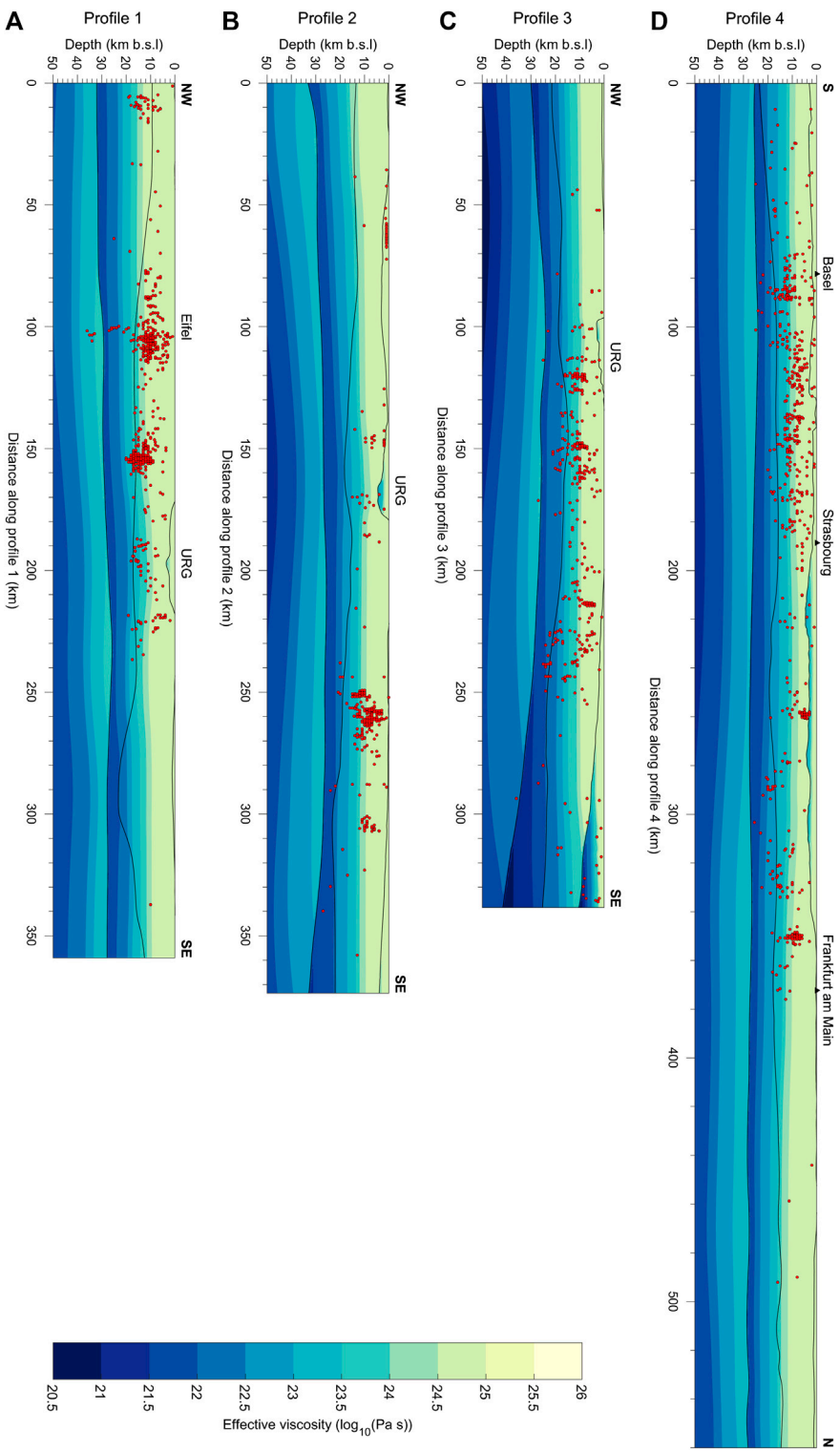

FIGURE 8 | Effective viscosity cross-sections along each profile: **(A)** profile 1; **(B)** profile 2; **(C)** profile 3; **(D)** profile 4. Red dots represent hypocenters of seismic events associated with the profile (see **Figure 3**). The color legend of effective viscosity is explained by the color bar. Gray lines mark the boundaries of the structural model units (see **Figure 4E**).

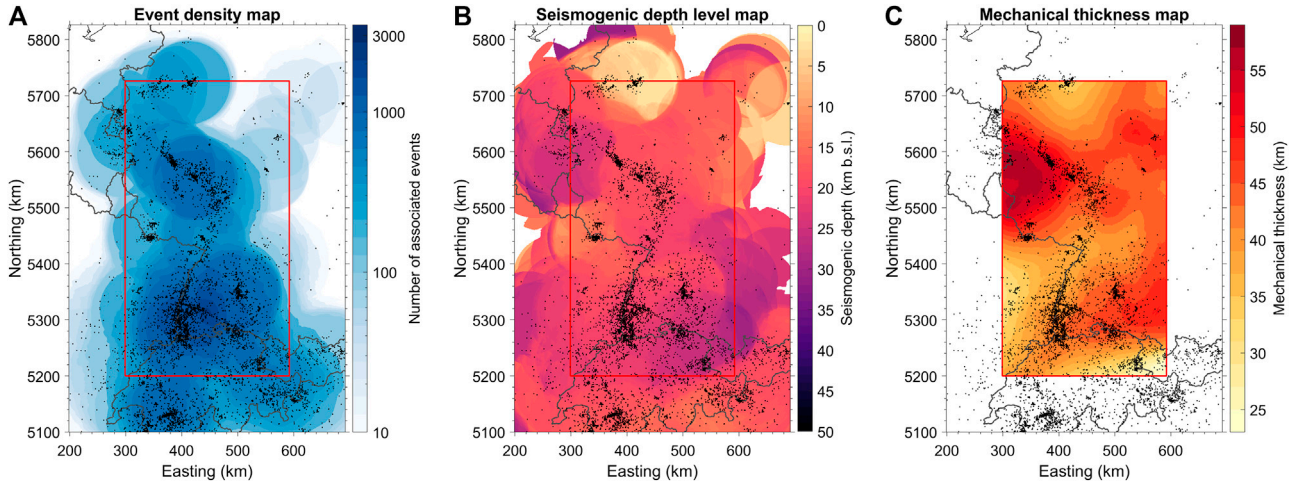

FIGURE 9 | Maps of **(A)** event density derived by considering circular bin of 75 km radius (logarithmic scale); **(B)** seismogenic depth level map derived as the depth above which 95% of events occur for each circular bin; **(C)** mechanical thickness derived from the rheological model of the area. Black dots mark the epicenters of seismic events with reliable depths.

Figure 9B. The seismogenic depth level has been calculated from the seismic dataset as the depth above which 95% of the total seismicity occurs. To derive the map, we have first subdivided the model area into a grid of equal radius bins by using an effective searching radius of 75 km. **Figure 9A** shows the density of events in terms of number of events associated with each grid point of the model. To compute the base map of the seismogenic zone, we considered for any given bin that seismicity is inactive below a depth level underlying the majority of hypocenters. We disregarded distributions with less than five events that are considered as statistically meaningless. The radius has been defined in order to ensure that a statistically significant number of epicenters could be located inside each of the grid bins. For the radius of 75 km, the minimum number of associated events in each bin turned out to be eight which ensures that no gaps exist in the seismogenic depth level map in **Figure 9B**.

Figure 9B displays a seismogenic depth that is highly variable across the study area, covering a range of less than 5 km below sea level up to 50 km below sea level. There is a systematic deepening in the seismogenic base at the northern boundary of the URG, toward the northwest and toward the east of the graben proper, which also correlates spatially with a change in the seismic energy released as evidenced by the catalog (**Figure 1C**). Events of higher magnitude occur in areas where the seismogenic depth is larger. These variations positively correlate with the topography of the 450°C isotherm in **Figure 5A**, which we have taken as representative of the maximum dissipation potential isosurface in the crust. This correlation suggests that, on a regional scale, the brittle portion of the crust in the area is controlled by the geothermal diffusive gradient and that first-order variations in the crustal configuration and their thermal consequences exert the primary control on the spatial distribution of the seismicity.

We have based our evaluation so far by relying on the hypothesis that the recorded seismicity distribution provides a direct observation-based constraint for the lithospheric strength. The rationale behind this assumption stems from the fact that a rock must be able to retain enough strength in order to nucleate an earthquake, though a finite strength does not necessarily imply seismicity to happen. This said, we can interpret the seismogenic depth level map described above as an observation-driven estimate of the depth levels in the plate that are able to retain enough strength so to store elastic strain energy under a given *in-situ* stress state. Therefore, the implications of our study can be further quantitatively tested by a direct comparison of the observation summarized in **Figure 9B** with the map depicting lateral variations in the computed mechanical thickness as derived from our rheological study (**Figure 9C**). The mechanical thickness, not to be confounded with the effective elastic thickness, is defined as an integrated value corresponding to the depth at which the strength of the rocks becomes negligible, that is smaller than a finite threshold level for which usually 20 MPa is considered (Ranalli, 1995). Therefore, the computed mechanical thickness is, like the effective viscosity introduced above, an effective parameter, rather than a rock property sensu stricto and it is used to represent the thickness of the stress bearing part of the plate (seismically active) in an integral sense. In other words, it provides an estimate for the strength of the plate itself, defined by the depth levels above which dissipation of stored elastic energy is negligible, thus being directly comparable to the seismogenic base map in **Figure 9B**.

The map in **Figure 9C** displays a mechanical thickness that is highly variable over the study area in a range from 24 to 57 km. In general, the spatial distribution of minima and maxima resembles variations in the lithospheric strength (**Figure 6**), with lower values within the URG area, the Eifel area in the central part, at the northern model boundary and across the Alps, that are bordered by maxima in mechanical thickness to the east and to the north-west of the URG. The range of variations in modeled mechanical thickness is in the same order of magnitude like the

one obtained for the seismogenic base derived from the seismicity data and the two maps also show a spatially similar pattern. The agreement between the two maps obtained with completely independent methods suggests that the bulk of the seismic activity in the study area is indeed controlled by the long-term thermo-mechanical configuration of the crust under a consistent *in-situ* stress field.

DISCUSSION

A major outcome of the modeling is the correlation between the regional seismicity observed in the study area and the crustal rheological configuration, the latter being, to a first order, controlled by resolved variations in the thermal configuration within a heterogeneous crust. We, therefore, open this paragraph by deepening the discussion of these implications. The seismicity in the study area shows a bimodal distribution in its spatial trend. A first cluster of seismic events, aligned NNE-SSW is found in the southern-central part of the area, that follows the outlines of the URG. To the north, at the northern end of the URG and up to the southern boundary of the LRG, a second cluster of seismic events displays a counter-clockwise rotation and higher local magnitudes. Another cluster is located in the south, between the eastern flank of the URG and the Black Forest region, that also features increased earthquake magnitudes (**Figure 1C**). This systematic variation in the spatial distribution and local magnitudes in the seismic catalog raises the question on the causative mechanisms to the observed distribution.

Cloetingh et al. (2005) found that zones of concentrated seismic activity correspond to areas of crustal contrast between the Cenozoic rifts and their surrounding platform areas, which is consistent with our findings. In our study we go one step further by comparing the depth distribution of seismicity in addition to a lateral distribution. An attempt to provide an answer to the aforementioned question is provided below where we correlate these observations with the results of our rheological modeling exercise.

The URG proper is a domain of a thin and hot upper crust and therefore of reduced crustal strength (see **Figures 4A, 5, 6A**). To the east of the URG, the model features a gradual increase in crustal thickness superposed to a deepening of the LAB, leading to overall lower deep temperatures and to a mechanically stronger crust. The presence of a heterogeneous crustal configuration across this area is indicative of an asymmetric strength configuration, which, in turn, can explain observed variations in the seismicity. That a causative relation exists between the distribution of earthquakes and the crustal structure is also evident when looking at the depth distribution of the hypocenters (). As also reported by previous studies (e.g., Faber et al., 1994; Mayer et al., 1997), seismicity reaches its maximum down to 25 km (approximately coinciding with the Moho boundary of our model) in the easternmost domain of the URG and toward the Black Forest, and it exhibits a pronounced peak between 12 and 18 km within the graben proper. If we take the 450° isotherm as indicative of a maximum crustal dissipation potential, it is striking how the majority of recorded seismic events are delimited by the topology of this isotherm that also marks the maximum strength level in the upper crust. The observed shallow seismicity in the URG aligns with a local minimum in the depth of the same isotherm at around 13–16 km. The observation that the majority of shallow hypocenters concentrate above and/or along this rheological boundary is indicative of an internal decoupling horizon at upper crustal depths that provides an effective limit to the depth distribution of earthquakes to the shallower brittle crust. The shallower this horizon is, the lower are the magnitudes of potential earthquakes. The observed eastward deepening in hypocenter locations (with maxima toward the Black Forest area) is also consistent with the modeled increase in integrated crustal strength due to a gradual crust-mantle coupling. This in turn provides additional evidence of the correlation between seismic activity and resolved variations in the crustal rheological configuration.

Following a similar reasoning, we can also explain the NNW-SSE trend in the seismicity pattern across the northern boundary of the URG (**Figure 1C**). This second cluster of seismic events spatially correlates with a region of increased crustal strength (**Figure 6A**) associated to a thicker mafic lower crust and a deepening in the LAB (**Figure 4**) that spatially correlates to a seismicity trend that features deeper sources of earthquakes (**Figures 7, 8**). Also, the seismic energy release in this area is found to vary more than an order of magnitude if compared to the values within the graben domain proper (**Figure 1C**). We can summarize these findings by stating that: earthquakes preferentially rupture with moderate magnitudes through a weaker crust within the URG and through a stronger crust to the east and in the north, thereby being accompanied by higher energy release as evidenced by the seismic catalog. Based on all these observations, we can therefore conclude that rapid accommodation of permanent deformation by thermally activated viscous-creep efficiently limits the deepening of seismic energy release in the graben area to the shallower portion of the upper crust, the latter being mechanically decoupled from the deeper crustal domain.

To explain the presence of, relatively few in number, hypocenters deeper than the modeled BDT in the URG (**Figure 7D**) requires a mechanism to either locally increase the strain rate or to lower the temperature with respect to the background values. Observations within the study area are indicative of a regional stress field (Heidbach et al., 2016) that shows an overall consistent pattern across the graben. This aspect makes it difficult to envisage any mechanism that could promote a local and systematic increase in the background strain rates without disturbing the regional stress field. It is, therefore, likely that the local deepening in the hypocenters could correlate with the presence of a preferential westward dipping plane of weakness or local faults which have not been included in the current input model. Such geological discontinuities would have the potential to cause local deviations from the average stress field in the near fault area as well as in the local temperature conditions, which, if also accompanied by fluid induced metamorphism, could be considered as a viable mechanism to explain the observed deepening in the seismicity. Though at a speculative level, we can conclude that the presence of major rupture planes might be

effective in promoting local changes in the rheological crustal configuration (frictional weakening) resulting in a locally mechanically coupled reflective crust, which would explain the deepening in the hypocenter locations with respect to an overall shallow crustal seismicity in the graben area.

Seismicity is a slip-pulse mechanism "sensu" (Scholz, 1998) and it therefore reflects a frictional coseismic instability along a certain fault patch in response of dynamic weakening, thereby leading to an overall reduction in the dynamic stress that could or could not affect the long-term stress state (Ohnaka, 2013). We have already pointed out current limitations of the study being confined to capture first-order indicators that could be useful to link seismicity to the lithospheric strength in the area. In doing so, we have been inspired by an increasing amount of experimental evidence demonstrating how coseismic dynamic weakening is limited by depth and temperature (Maggi et al., 2000; Ohnaka, 2013). This is mainly the result of ongoing (mostly off-fault) viscoplastic deformation leading to an overall increase in the fault frictional resistance. At upper crustal conditions, rocks might undergo time- and displacement-dependent changes in their frictional coefficient which could potentially lead to slip instabilities along fault surfaces (Marone and Scholz, 1988; Rice, 1993; Cowan, 1999). However, and most important to our study, independent to the local mechanism at play within the fault, for a slip instability to occur it requires a gradient in the mechanical strength among the fault-host rock system even at upper crustal pressure (equal to mean stress)-temperature conditions. In contrast, deeper in the crust and upper mantle, thermally activated viscous creep is velocity strengthening, preventing deformation from attaining seismic rates even upon localization (Scholz, 1989). This provides a direct link between the degree of velocity weakening on a seismogenic fault and the background shear stress required to trigger the seismic pulse. If based on studies of fault rocks in exhumed continental crust (Handy and Brun, 2004; Niemeijer and Spiers, 2007), it also becomes clear that faults in the upper crust are dominated by a low effective coefficient of friction due to the presence of a clay-rich fault gouge, and that they rapidly transition to higher effective coefficient of frictions at deeper depth levels (approximately at the BDT). The most important implication of these observations is that this change from brittle cataclastic deformation to a more ductile flow mode of deformation can still be captured and approximated to a first degree by the intercept point between Byerlee's law and ductile creep in a static long-term rheological profile.

A second point worth discussing is how to best reconcile observed earthquake magnitudes to the long-term strength of a plate. During an earthquake cycle the fault-host rock system will undergo an overall increase in its strength as a non-linear function of progressive deformation and temperature conditions (strain rates and temperature dependency of viscous creep). Upon reaching (or approaching) the system static strength, the stored internal energy would be released coseismically only within mechanically compliant domains. Following an earthquake, the system will be then reloaded interseismically and the lithosphere strength will gradually recover to its long-term profile. If we follow the established concept of an earthquake as a frictional dynamic instability (Ruina, 1983; Dieterich, 1994), we should also conclude that its magnitude does not only correlate to the peak strength of a specific rock, but must also scale with the gradient in stress drop resolved between the fault and host rock. This picture does entail a subtle, though important causal correlation between the static strength of the host crustal rock domain and the transient co-seismic strength. On the one hand, it suggests that earthquakes are likely to nucleate within strong and stress bearing layers of the lithosphere upon reaching their peak strength. The fact that the latter increases with depth thereby results in higher magnitudes events nucleating at larger depths. In contrast, weak areas would rather yield in an aseismic manner. Indeed, if the seismogenic portion of the plate would be completely dissected by weak faults, it will be unlikely to transmit any stress. This situation might change depending on local conditions where dynamic weakening processes like frictional melting, flash heating, thermal pressurization and endothermic fluid mediated reactions (Di Toro et al., 2011; Rice, 2017) might result in runaway instabilities even under near-adiabatic and lower than critical temperature conditions (though grain growth could lead to a (re)-stabilization of the system). On the other hand, the generally observed cut-off depth for coseismic slip (i.e., the thickness of the seismogenic zone defined as the depth below which earthquake frequencies and magnitudes rapidly decrease) can be taken as a quantitative indication of how the downward propagation of the velocity weakening domain is a function of the actual deformation and thereof of the geothermal gradient and overall strain rate. Viscous creep is, therefore, the process limiting the extent of downward coseismic rupture by preventing, via energy dissipation, stresses from attaining the fracture strength of the surrounding rock. This observation once again implies a causal correlation between the long-term lithosphere strength and frictional seismic instabilities and the usefulness of quantitative studies on the long-term rheological behavior of the plate.

CONCLUSION

Calculated 3D rheological characteristics, using a data-based lithosphere-scale 3D thermal model of the URG and adjacent areas, show remarkable consistency with independent data on seismicity distribution. Resolving the first-order lithological variations in the plate, consisting of a sedimentary cover, the upper and lower crystalline crust as well as the lithospheric mantle, we found that the computed 3D strength configuration and its major gradients correspond to the main characteristics of observed seismicity with respect to both seismogenic depth and magnitudes.

We find that, on a regional scale, the brittle portion of the crust is controlled by the geothermal diffusive gradient. As the latter is determined by the structural configuration of the crust and lithosphere, the depth level to which seismic activity may occur, varies significantly. For the URG area, first-order variations in the crustal configuration and in lithosphere thickness exert the primary control on the spatial distribution of the seismicity. The calculated variations in

strength, differential stress and effective viscosity show clear spatial correlations with observed seismicity in that:

- The URG is mainly characterized by a hotter and weaker crust than its surroundings with seismic events of moderate magnitude largely shallower than the depth to the 450°C isotherm. The brittle part of the crust is thinner in the URG compared to the surroundings and mechanically decoupled from the mantle, which leads to shallow and moderate in magnitudes seismic events. Deeper events are local and probably related to deep reaching faults. A similar rheological configuration is found for the Alps and the Eifel area.
- The areas north-west and east of the URG are characterized by a thicker, colder and stronger crust and are characterized by deeper seismic events of higher magnitudes.

In general, we find a correlation between the computed mechanical thickness and the data derived seismogenic base. The study demonstrates how the assessment of potential seismic hazards can profit if observation-based knowledge of the 3D thermal field is integrated with seismic catalogs.

DATA AVAILABILITY STATEMENT

All datasets presented in this study are included in the article/ **Supplementary Material**.

AUTHOR CONTRIBUTIONS

DA performed the seismic catalog processing and analysis, wrote the relevant parts in the manuscript and prepared all figures and the final manuscript for submission. MC performed the rheological modeling, investigated the results from the model and their comparison to the seismic catalogs and wrote the relevant parts in the manuscript. JB has been strongly involved in the development of the basic 3D structural and thermal model of the URG and thus contributed to the parameter selection for the rheological modeling and to the writing of the manuscript (in particular to chapters 2.2 and 2.3). MG contributed to preparation of the seismic catalog and rheological modeling setup, and helped with writing of the relevant chapters. MS leaded the research group and contributed to the structuring and writing of the manuscript, especially of discussion and conclusions parts.

FUNDING

The research is funded by the Helmholtz Centre Potsdam—GFZ German Research Centre for Geosciences.

ACKNOWLEDGMENTS

We would like to thank the Hessian Agency for Nature Conservation, Environment and Geology (HLNUG) who kindly provided us with data of the seismic catalog of Hessen.

SUPPLEMENTARY MATERIAL

The Supplementary Material for this article can be found online at: https://www.frontiersin.org/articles/10.3389/feart.2020.592561/full#supplementary-material

REFERENCES

Amante, C., and Eakins, B. W. (2009). "ETOPO1 arc-minute global relief model: procedures, data sources and analysis," in *NOAA Technical Memorandum NESDIS NGDC-24*. Boulder, CO: National Geophysical Data Center, NOAA).

Arndt, D., Bär, K., Fritsche, J.-G., Kracht, M., Sass, I., and Hoppe, A. (2011). 3D structural model of the federal state of Hesse (Germany) for geopotential evaluation [Geologisches 3D-Modell von Hessen zur Bestimmung von Geo-Potenzialen]. *Zeitschrift der Deutschen Gesellschaft für Geowissenschaften.* 162 (4), 353–369. doi:10.1127/1860-1804/2011/0162-0353

Barth, A., Ritter, J. R. R., and Wenzel, F. (2015). Spatial variations of earthquake occurrence and coseismic deformation in the upper rhine graben, central Europe. *Tectonophysics* 651-652, 172–185. doi:10.1016/j.tecto.2015.04.004

Baujard, C., Genter, A., Dalmais, E., Maurer, V., Hehn, R., Rosillette, R., et al. (2017). Hydrothermal characterization of wells GRT-1 and GRT-2 in Rittershoffen, France: implications on the understanding of natural flow systems in the rhine graben. *Geothermics* 65, 255–268. doi:10.1016/j.geothermics.2016.11.001

Behrmann, J. H., Ziegler, P. A., Schmid, S. M., Heck, B., and Granet, M. (2005). The eucor-urgent project. *Int. J. Earth Sci.* 94 (4), 505–506. doi:10.1007/s00531-005-0513-0

Bertrand, L., Jusseaume, J., Géraud, Y., Diraison, M., Damy, P.-C., Navelot, V., et al. (2018). Structural heritage, reactivation and distribution of fault and fracture network in a rifting context: case study of the western shoulder of the upper rhine graben. *J. Struct. Geol.* 108, 243–255. doi:10.1016/j.jsg.2017.09.006

Blundell, D. J., Freeman, R., and Mueller, S. (1992). *A continent revealed: the European geotraverse, structure and dynamic evolution*. Cambridge, United Kingdom: Cambridge University Press.

Brace, W. F., and Kohlstedt, D. L. (1980). Limits on lithospheric stress imposed by laboratory experiments. *J. Geophys. Res. Solid Earth.* 85 (B11), 6248–6252. doi:10.1029/JB085iB11p06248

Burov, E. B. (2011). Rheology and strength of the lithosphere. *Mar. Petrol. Geol.* 28 (8), 1402–1443. doi:10.1016/j.marpetgeo.2011.05.008

Cacace, M., and Scheck-Wenderoth, M. (2016). Why intracontinental basins subside longer: 3-D feedback effects of lithospheric cooling and sedimentation on the flexural strength of the lithosphere. *J. Geophys. Res. Solid Earth.* 121 (5), 3742–3761. doi:10.1002/2015jb012682

Calò, M., Dorbath, C., and Frogneux, M. (2014). Injection tests at the EGS reservoir of Soultz-sous-Forêts. Seismic response of the GPK4 stimulations. *Geothermics* 52, 50–58. doi:10.1016/j.geothermics.2013.10.007

Charléty, J., Cuenot, N., Dorbath, L., Dorbath, C., Haessler, H., and Frogneux, M. (2007). Large earthquakes during hydraulic stimulations at the geothermal site of Soultz-sous-Forêts. *Int. J. Rock Mech. Min. Sci.* 44 (8), 1091–1105. doi:10.1016/j.ijrmms.2007.06.003

Cloetingh, S., Ziegler, P. A., Beekman, F., Andriessen, P., Hardebol, N., and Dezes, P. (2005). Intraplate deformation and 3D rheological structure of the rhine rift system and adjacent areas of the northern Alpine foreland. *Int. J. Earth Sci.* 94 (4), 758–778. doi:10.1007/s00531-005-0502-3

Cloetingh, S., Cornu, T., Ziegler, P., and Beekman, F. (2006). Neotectonics and intraplate continental topography of the northern Alpine foreland. *Earth Sci. Rev.* 74 (3-4), 127–196. doi:10.1016/j.earscirev.2005.06.001

Cowan, D. S. (1999). Do faults preserve a record of seismic slip? A field geologist's opinion. *J. Struct. Geol.* 8 (21), 995–1001. doi:10.1016/S0191-8141(99)00046-2

Cuenot, N., Charléty, J., Dorbath, L., and Haessler, H. (2006). Faulting mechanisms and stress regime at the European HDR site of Soultz-sous-Forêts, France. *Geothermics* 35 (5), 561–575. doi:10.1016/j.geothermics.2006.11.007

Dèzes, P., Schmid, S. M., and Ziegler, P. A. (2004). Evolution of the European cenozoic rift system: interaction of the alpine and pyrenean orogens with their foreland lithosphere. *Tectonophysics* 389 (1), 1–33. doi:10.1016/j.tecto.2004.06.011

Di Toro, G., Han, R., Hirose, T., De Paola, N., Nielsen, S., Mizoguchi, K., et al. (2011). Fault lubrication during earthquakes. *Nature* 471 (7339), 494–498. doi:10.1038/nature09838

Dieterich, J. (1994). A constitutive law for rate of earthquake production and its application to earthquake clustering. *J. Geophys. Res.: Solid Earth.* 99 (B2), 2601–2618. doi:10.1029/93JB02581

Egert, R., Korzani, M. G., Held, S., and Kohl, T. (2020). Implications on large-scale flow of the fractured EGS reservoir Soultz inferred from hydraulic data and tracer experiments. *Geothermics* 84, 101749. doi:10.1016/j.geothermics.2019.101749

Faber, S., Bonjer, K.-P., Brüstle, W., and Deichmann, N. (1994). Seismicity and structural complexity of the Dinkelberg block, southern rhine graben. *Geophys. J. Int.* 116 (2), 393–408. doi:10.1111/j.1365-246X.1994.tb01805.x

Fäh, D., Gisler, M., Jaggi, B., Kästli, P., Lutz, T., Masciadri, V., et al. (2009). The 1356 basel earthquake: an interdisciplinary revision. *Geophys. J. Int.* 178 (1), 351–374. doi:10.1111/j.1365-246X.2009.04130.x

Franke, W. (2000). The mid-European segment of the variscides: tectonostratigraphic units, terrane boundaries and plate tectonic evolution. *Geol. Soc. Spec. Publ.* 179 (1), 35–61. doi:10.1144/gsl.sp.2000.179.01.05

Freymark, J., Sippel, J., Scheck-Wenderoth, M., Bär, K., Stiller, M., Fritsche, J.-G., et al. (2017). The deep thermal field of the upper rhine graben. *Tectonophysics* 694, 114–129. 10.1016/j.tecto.2016.11.013

Freymark, J., Bott, J., Cacace, M., Ziegler, M., and Scheck-Wenderoth, M. (2019). Influence of the main border faults on the 3D hydraulic field of the central upper rhine graben. *Geofluids* 2019, 1–21. doi:10.1155/2019/7520714

Freymark, J., Bott, J., Scheck-Wenderoth, M., Bär, K., Stiller, M., Fritsche, J.-G., et al. (2020). [Dataset] 3D-URG: 3D gravity constrained structural model of the upper rhine graben. GFZ Data Services.

Fuhrmann, T., Heck, B., Knöpfler, A., Masson, F., Mayer, M., Ulrich, P., et al. (2013). Recent surface displacements in the upper rhine graben—preliminary results from geodetic networks. *Tectonophysics* 602, 300–315. 10.1016/j.tecto.2012.10.012

Geissler, W. H., Sodoudi, F., and Kind, R. (2010). Thickness of the central and eastern European lithosphere as seen by S receiver functions. *Geophys. J. Int.* 181 (2), 604–634. doi:10.1111/j.1365-246X.2010.04548.x

GEOFON Data Centre (2020). [Online] GEOFON seismic network Deutsches GeoForschungsZentrum GFZ. Available at: https://geofon.gfz-potsdam.de/eqinfo/list.php (Accessed Jun 11, 2020).

GeORG-Projektteam (2013). GeORG FTA-2. Geopotenziale des tieferen Untergrundes im Oberrheingraben, Fachlich-Technischer Abschlussbericht des INTERREG-Projekts GeORG LGRB-Informationen. Available at: http://www.geopotenziale.eu (Accessed January, 2013).

Grünthal, G., and Wahlström, R. (2003). An Mw based earthquake catalogue for central, northern and northwestern Europe using a hierarchy of magnitude conversions. *J. Seismol.* 7 (4), 507–531. doi:10.1023/b:Jose.0000005715.87363.13

Grünthal, G., Stromeyer, D., and Wahlström, R. (2009). Harmonization check of M w within the central, northern, and northwestern European earthquake catalogue (CENEC). *J. Seismol.* 13 (4), 613–632. doi:10.1007/s10950-009-9154-2

Grünthal, G., Stromeyer, D., Bosse, C., Cotton, F., and Bindi, D. (2018). The probabilistic seismic hazard assessment of Germany—version 2016, considering the range of epistemic uncertainties and aleatory variability. *Bull. Earthq. Eng.* 16 (10), 4339–4395. doi:10.1007/s10518-018-0315-y

Handy, M. R., and Brun, J.-P. (2004). Seismicity, structure and strength of the continental lithosphere. *Earth Planet Sci. Lett.* 223 (3-4), 427–441. doi:10.1016/j.epsl.2004.04.021

Heidbach, O., and Hergert, T. (2012). NAGRA interner bericht NIB 12-007. Geomechanisch-numerische Modellierung des rezenten Spannungsfeldes der Nordschweiz. Available at: https://gfzpublic.gfz-potsdam.de/pubman/item/item_1529126 (Accessed 2012).

Heidbach, O., Rajabi, M., Reiter, K., Ziegler, M. O., and Team, W. (2016). [Dataset] Version 1.1. World stress map database release 2016. GFZ Data Services. doi:10.5880/WSM.2016.001 (Accessed May 25, 2020)

Henrion, E., Masson, F., Doubre, C., Ulrich, P., and Meghraoui, M. (2020). Present-day deformation in the upper rhine graben from GNSS data. *Geophys. J. Int.* 223, 599–611. doi:10.1093/gji/ggaa320

HLNUG (2020). [Online]. Version 2019 (SKHe2019). Seismischer Katalog des Landes Hessen, Hessisches Landesamt für Naturschutz, Umwelt und Geologie. Available at: https://www.hlnug.de/themen/geologie/erdbeben (Accessed Jun 11, 2020).

Homuth, B., Rümpker, G., Deckert, H., and Kracht, M. (2014). Seismicity of the northern upper rhine graben—constraints on the present-day stress field from focal mechanisms. *Tectonophysics* 632, 8–20. doi:10.1016/j.tecto.2014.05.037

International Seismological Centre (2020a). Dataset [Online]. ISC-EHB. Available at: https://doi.org/10.31905/PY08W6S3 (Accessed Jun 12, 2020).

International Seismological Centre (2020b). [Online]. On-line Bulletin. Available at: https://doi.org/10.31905/D808B830 (Accessed Jun 11, 2020).

Katayama, I., and Karato, S.-i. (2008). Low-temperature, high-stress deformation of olivine under water-saturated conditions. *Phys. Earth Planet. Inter.* 168 (3), 125–133. doi:10.1016/j.pepi.2008.05.019

Kushnir, A. R. L., Heap, M. J., and Baud, P. (2018). Assessing the role of fractures on the permeability of the Permo-Triassic sandstones at the Soultz-sous-Forêts (France) geothermal site. *Geothermics* 74, 181–189. doi:10.1016/j.geothermics.2018.03.009

LGRB (2020). [Online]. Seismisches Bulletins baden-württemberg 1996–2019 Landesamt für Geologie, Rohstoffe und Bergbau, Regierungspräsidium Freiburg, Baden-Württemberg. Available at: https://lgrb-bw.de/erdbeben/jahresbulletins (Accessed Jun 11, 2020).

Lopes Cardozo, G. G. O., and Granet, M. (2005). A multi-scale approach to study the lithospheric structure of the southern upper rhine graben: from seismic tomography through reflection seismics to surface geology. *Int. J. Earth Sci.* 94 (4), 615–620. doi:10.1007/s00531-005-0476-1

Lüschen, E., Wenzel, F., Sandmeier, K. J., Menges, D., Rühl, T., Stiller, M., et al. (1989). "Near-vertical and wide-angle seismic surveys in the schwarzwald," in *The German continental deep drilling program (KTB)*. Editors R. Emmermann and J. Wohlenberg (Berlin, Germany: Springer), 297–362.

Maggi, A., Jackson, J., McKenzie, D., and Priestley, K. (2000). Earthquake focal depths, effective elastic thickness, and the strength of the continental lithosphere. *Geology* 28 (6), 495–498. doi:10.1130/0091-7613(2000)28<495:EFDEET>2.0.CO;2

Marone, C., and Scholz, C. (1988). The depth of seismic faulting and the upper transition from stable to unstable slip regimes. *Geophys. Res. Lett.* 15 (6), 621–624. doi:10.1029/GL015i006p00621

Maurer, V., Gaucher, E., Grunberg, M., Koepke, R., Pestourie, R., and Cuenot, N. (2020). Seismicity induced during the development of the Rittershoffen geothermal field, France. *Geotherm. Energy.* 8 (1), 5. doi:10.1186/s40517-020-0155-2

Mayer, G., Mai, P. M., Plenefisch, T., Echtler, H., Lüschen, E., Wehrle, V., et al. (1997). The deep crust of the Southern rhine graben: reflectivity and seismicity as images of dynamic processes. *Tectonophysics* 275 (1), 15–40. doi:10.1016/S0040-1951(97)00014-0

Mechie, J. (2007). "A 3-D P-wave velocity crustal structure model for Germany derived from seismic refraction/wide-angle reflection data," in Proceedings of the 67th annual meeting of the German geophysical society (DGG). Aachen, Germany. March 26–29, 2007.

Meissner, R., and Bortfeld, R. K. (2014). *DEKORP-atlas, results of deutsches kontinentales reflexionsseismisches programm*. Berlin, Germany: Springer-Verlag.

Meixner, J., Schill, E., Grimmer, J. C., Gaucher, E., Kohl, T., and Klingler, P. (2016). Structural control of geothermal reservoirs in extensional tectonic settings: an example from the upper rhine graben. *J. Struct. Geol.* 82, 1–15. doi:10.1016/j.jsg.2015.11.003

Niemeijer, A. R., and Spiers, C. J. (2007). A microphysical model for strong velocity weakening in phyllosilicate-bearing fault gouges. *J. Geophys. Res. Solid Earth.* 112 (B10). doi:10.1029/2007JB005008

Ohnaka, M. (2013). *The physics of rock failure and earthquakes*. Cambridge,UnitedKingdom: Cambridge University Press.

Ranalli, G., and Murphy, D. C. (1987). Rheological stratification of the lithosphere. *Tectonophysics* 132 (4), 281–295. doi:10.1016/0040-1951(87)90348-9

Ranalli, G. (1995). *Rheology of the Earth*. Dordrecht, Netherlands: Springer Netherlands.

Regenauer-Lieb, K., and Yuen, D. A. (2008). Multiscale brittle-ductile coupling and genesis of slow earthquakes. *Pure Appl. Geophys.* 165 (3), 523–543. doi:10.1007/s00024-008-0326-8

Rice, J. R. (1993). Spatio-temporal complexity of slip on a fault. *J. Geophys. Res. Solid Earth.* 98 (B6), 9885–9907. doi:10.1029/93JB00191

Rice, J. R. (2017). Heating, weakening and shear localization in earthquake rupture. *Philos. Trans. A Math. Phys. Eng. Sci.* 375 (2103), 20160015. doi:10.1098/rsta.2016.0015

Rózsa, S., Mayer, M., Westerhaus, M., Seitz, K., and Heck, B. (2005). Towards the determination of displacements in the upper rhine graben area using GPS measurements and precise antenna modelling. *Quat. Sci. Rev.* 24 (3), 425–438. doi:10.1016/j.quascirev.2004.07.007

Ruina, A. (1983). Slip instability and state variable friction laws. *J. Geophys. Res. Solid Earth.* 88 (B12), 10359–10370. doi:10.1029/JB088iB12p10359

Scholz, C. H. (1989). Mechanics of faulting. *Annu. Rev. Earth Planet Sci.* 17(1), 309–334. doi:10.1146/annurev.ea.17.050189.001521

Scholz, C. H. (1998). Earthquakes and friction laws. *Nature* 391 (6662), 37–42. doi:10.1038/34097

Schumacher, M. E. (2002). Upper rhine graben: role of preexisting structures during rift evolution. *Tectonics* 21 (1), 1–17. doi:10.1029/2001tc900022

Storchak, D. A., Harris, J., Brown, L., Lieser, K., Shumba, B., Verney, R., et al. (2017). Rebuild of the bulletin of the international seismological centre (ISC), part 1: 1964–1979. *Geosci. Lett.* 4 (1), 32. doi:10.1186/s40562-017-0098-z

Tesauro, M., Hollenstein, C., Egli, R., Geiger, A., and Kahle, H.-G. (2006). Analysis of central western Europe deformation using GPS and seismic data. *J. Geodyn.* 42 (4), 194–209. doi:10.1016/j.jog.2006.08.001

U.S. Geological Survey (2020). [Online]. USGS earthquake catalog. Available at: https://earthquake.usgs.gov/earthquakes/search/ (Accessed Jun 11, 2020).

Vallier, B., Magnenet, V., Schmittbuhl, J., and Fond, C. (2019). Large scale hydro-thermal circulation in the deep geothermal reservoir of Soultz-sous-Forêts (France). *Geothermics* 78, 154–169. doi:10.1016/j.geothermics.2018.12.002

Vidal, J., and Genter, A. (2018). Overview of naturally permeable fractured reservoirs in the central and southern upper rhine graben: insights from geothermal wells. *Geothermics* 74, 57–73. https://doi.org/10.1016/j.geothermics.2018.02.003

Weston, J., Engdahl, E. R., Harris, J., Di Giacomo, D., and Storchak, D. A. (2018). ISC-EHB: reconstruction of a robust earthquake data set. *Geophys. J. Int.* 214 (1), 474–484. doi:10.1093/gji/ggy155

Ziegler, P. A. (1990). *Geological atlas of western and central Europe*. Bath, England: Geological Society Publishing House.

Ziegler, P. A. (1992). European cenozoic rift system. *Tectonophysics* 208 (1), 91–111. doi:10.1016/0040-1951(92)90338-7

Conflict of Interest: The authors declare that the research was conducted in the absence of any commercial or financial relationships that could be construed as a potential conflict of interest.

Copyright © 2020 Anikiev, Cacace, Bott, Gomez Dacal and Scheck-Wenderoth. This is an open-access article distributed under the terms of the Creative Commons Attribution License (CC BY). The use, distribution or reproduction in other forums is permitted, provided the original author(s) and the copyright owner(s) are credited and that the original publication in this journal is cited, in accordance with accepted academic practice. No use, distribution or reproduction is permitted which does not comply with these terms.

frontiers in Earth Science

BRIEF RESEARCH REPORT
published: 12 November 2020
doi: 10.3389/feart.2020.584716

Earthquake-Related Signals in Central Italy Detected by Hydrogeochemical and Satellite Techniques

Giovanni Martinelli[1,2,3], Gianluca Facca[4], Nicola Genzano[5], Fabrizio Gherardi[4], Mariano Lisi[6], Lisa Pierotti[4] and Valerio Tramutoli[5]*

[1]Istituto Nazionale di Geofisica e Vulcanologia, Palermo, Italy, [2]Northwest Institute of Eco-Environment and Resources, Chinese Academy of Sciences (CAS), Lanzhou, China, [3]Key Laboratory of Petroleum Resource Research, Lanzhou, China, [4]Consiglio Nazionale delle Ricerche (CNR), Istituto di Geoscienze e Georisorse (IGG), Pisa, Italy, [5]School of Engineering, University of Basilicata, Potenza, Italy, [6]Consiglio Nazionale delle Ricerche (CNR), Istituto di Metodologie per Analisi Ambientale (IMAA), Tito Scalo (Potenza), Italy

Central Apennines are one of the highest seismic risk regions in Italy. A number of energetic events (M_W > 5) struck the region during the period 2004–2017, killing several hundreds of people (e.g., 294 casualties associated with the August 24th, 2016, M_W 6.0 event of Amatrice). These earthquakes impacted piezometric levels, springs discharges, and groundwater chemistry across a large area, even at distances of dozens of kilometers from the epicenters. Here we present a multidisciplinary dataset based on hydrogeochemical and satellite observations associated with the seismic events that occurred in Central Italy during the period 2004–2017, which combines information derived from the application of groundwater monitoring and satellite techniques. Groundwater monitoring techniques allowed for the detection of hydrogeochemical anomalies in spring and well waters (14 water sampling points in total, with 22 variations larger than 2σ), while satellite techniques were applied to detect time-space variations in ground thermal emissions. We detected two significant, almost synchronous, anomalies in 2009 and 2016–2017 with both techniques, and we tentatively correlated them to crustal deformation processes. Part of the observed signals were detected before mainshocks, and they appear to be related to aseismic slip or to seismic slip eventually induced by minor fluctuations in seismicity. We argue that the combination of two factors, i.e., the shallow depth of local earthquakes and the concurrent deepening of groundwater circulation paths to several km depth, allow for the recording of variations in the stress field by geofluids released at the surface.

Keywords: groundwater chemistry, CO_2 degassing, CO_2 anomaly, satellite observation, thermal infrared anomaly, crustal deformation, earthquake forecasting, central Italy

OPEN ACCESS

Edited by:
Frédéric Frappart, UMR5566 Laboratoire d'études en géophysique et océanographie spatiales (LEGOS), France

Reviewed by:
Ahmed Kenawy, Mansoura University, Egypt
Pingping Luo, Chang'an University, China

****Correspondence:***
Fabrizio Gherardi
f.gherardi@igg.cnr.it

Specialty section:
This article was submitted to Hydrosphere, a section of the journal Frontiers in Earth Science

Received: *21 July 2020*
Accepted: *16 October 2020*
Published: *12 November 2020*

Citation:
Martinelli G, Facca G, Genzano N, Gherardi F, Lisi M, Pierotti L and Tramutoli V (2020) Earthquake-Related Signals in Central Italy Detected by Hydrogeochemical and Satellite Techniques. Front. Earth Sci. 8:584716. doi: 10.3389/feart.2020.584716

INTRODUCTION

Central Italy is affected by intense crustal deformation processes driven by the relative motion of the African and the Eurasian plates. In this region, active extension occurs along the axial and western zones of the Apennine mountainous belt (backarc extension area, characterized by crustal thinning and active volcanism toward the Tyrrhenian Sea). Conversely, compression mostly occurs along the frontal part of the belt, toward the Adriatic Sea (contraction area, associated with the eastward

propagation of the Apennine accretionary prism). Strain values of 1.5–2 cm/year are currently estimated all over the extensive belt. An array of northwest-striking (i.e., northeast- and southwest-dipping) normal and normal-oblique faults control regional seismicity, so that earthquake foci are prevalently distributed along the Apennines axis (e.g., Doglioni, 1991; Patacca and Scandone, 2001; Patacca et al., 2008; Montone and Mariucci, 2016).

Since the late 1970s, carbon dioxide emissions have been recognized to be associated on a global scale with areas of intense tectonic activity and/or extensive seismicity (e.g., Barnes et al., 1978; Irwin and Barnes, 1980; Tamburello et al., 2018). Large stresses associated with earthquakes and crustal deformations are known to cause measurable changes in the physical properties of rocks and significant hydrologic perturbations in the connected aquifers (e.g., Rojstaczer et al., 1995). Major hydrologic effects observed worldwide include spring and stream flow variations, groundwater level oscillations, triggered eruptions of mud volcanoes, gas emissions, modifications of the geochemical signature of spring and/or well waters (e.g., among many others, Wakita, 1975; King et al., 1981; Sato et al., 1986; Roeloffs, 1988; Roeloffs et al., 1989; Toutain and Baubron, 1999; King et al., 2006; Pierotti et al., 2015). Martinelli and Dadomo (2018) recently evidenced that a large part of possible geochemical precursory phenomena recorded worldwide have been found in areas characterized by i) shallow seismicity, ii) relatively high heat flux, and iii) significant crustal deformation rates. All these features are characteristics of the study area (e.g., Chiodini et al., 2004; Chiodini et al., 2011; Chiodini et al., 2020).

Moderate-magnitude earthquakes ($4.0 < M_W < 6.5$) have been frequently recorded in Central Italy during historical and instrumental time. The hypocenters of these earthquakes were recognized in the upper crust, mainly at depths <15 km (Pace et al., 2006). The western part of the Apennine belt is also affected by intense CO_2 degassing. It has been estimated that several tons of CO_2 per day are discharged into the atmosphere via cold gas venting and by exsolution from high-P_{CO_2} thermal springs. An overall discharge rate of more than 20 Mt-CO_2/year is associated to this area, roughly equivalent to one third of the total geological CO_2 degassed in Italy (e.g., Minissale, 1991; Chiodini et al., 2004; Minissale, 2004; Frezzotti et al., 2010; Chiodini et al., 2018).

Significant variations in the chemical composition of dissolved gases (e.g., Italiano et al., 2004), and in water level, temperature and chemical composition of water (Lapenna et al., 2004) were detected in thermal waters of Umbria region, Central Italy, during the 1997–1998 seismic sequence (Colfiorito M_W 5.4 to 5.9 earthquakes). On April 6, 2009, a M_W 6.3 earthquake rocked L'Aquila province. A seismic sequence including some $4 < M_W < 5$ events followed. Mainshock and aftershock effects upset deep fluids over a large area. Significant variations in the CO_2 degassing rate were detected in a gas vent located 80 km away from the epicenter (Heinicke et al., 2011). Other gas flow rate anomalies were detected on a regional scale by Bonfanti et al. (2012), and references therein) employing satellite-based techniques. Chiodini et al. (2011) reported an increase of deep originated CO_2 in local groundwater possibly connected with the L'Aquila seismic sequence. Nine more shocks characterized by $5 < M_W < 6.5$ occurred in Central Italy in 2016 and 2017 (Chiaraluce et al., 2017; Festa et al., 2017, and references therein). Barberio et al. (2017) and Boschetti et al. (2019) reported water level and chemical composition variations in local groundwater, while De Luca et al. (2018) reported about groundwater pressure variations in some wells in the Abruzzo region before and during the 2016 Amatrice seismic sequence. These authors claimed that such variations "could potentially represent earthquake precursors".

Variations of the geomagnetic field (from satellites and observatories), and of atmospheric climatological data recorded during the 2015–2016 period have been retrospectively investigated to search for possible lithosphere-atmosphere-ionosphere coupled effects during the preparatory phase of the Central Italy seismic sequence 2016–2017, and a few anomalies in electromagnetic parameters were identified over the year preceding the Amatrice earthquake of August 24th, 2016 (Marchetti et al., 2019). Satellite-based techniques (TIR index) captured possible intense and large scale degassing phenomena that occurred in concomitance with the 1997–1998 seismic sequence (Aliano et al., 2008). Further pieces of evidence of degassing during the 2009 seismic sequence were recorded by satellite techniques (TIR index; Genzano et al., 2009; Bonfanti et al., 2012; and references therein). Seismic sequences in Central Italy have been accompanied by crustal deformation processes (e.g., Cheloni et al., 2017). In some cases, the beginning of the crustal deformation processes was detected before the start of the sequences (Bella et al., 1995; Sgrigna and Malvezzi, 2003; Moro et al., 2017). Under these conditions, any geochemical precursor possibly detected by ground and/or satellite techniques, could be theoretically attributable to CO_2–driven crustal permeability variations able to induce volume and shape changes in CO_2 reservoirs. These flux variations have the potential to modify the chemical composition of fluids hosted in deep and shallow aquifers. This mechanism is particularly effective in areas where natural manifestations (mostly mofettes) with high-CO_2 discharge rate occur (e.g., Chiodini et al., 2008; **Figure 1**).

In order to better understand the possible relations between local seismicity, groundwater chemistry, and CO_2 degassing activity, geochemical data recorded by several Regional Agencies for the Environmental Protection (ARPA) located in Central Italy were analyzed (the geographic coordinates of the water points of the ARPA network are given in Table 1 of the Supplementary Material). Furthermore, Thermal InfraRed spectral range radiations (TIR) attributable to fluctuations in CO_2 degassing rate (e.g., Tramutoli et al., 2013) were recorded by satellite techniques, and compared with other fluid-related parameters (pH, chemical composition of major constituents, P_{CO_2}). The multidisciplinary dataset used for this study spans the period 2004–2017, for which hydrogeochemical and TIR data were simultaneously available. The combined analysis of TIR and geochemical signals proposed here to indirectly evaluate variations in the stress field, is intrinsically innovative, and partially fills a methodological gap in the multidisciplinary approach to the study of earthquake precursors.

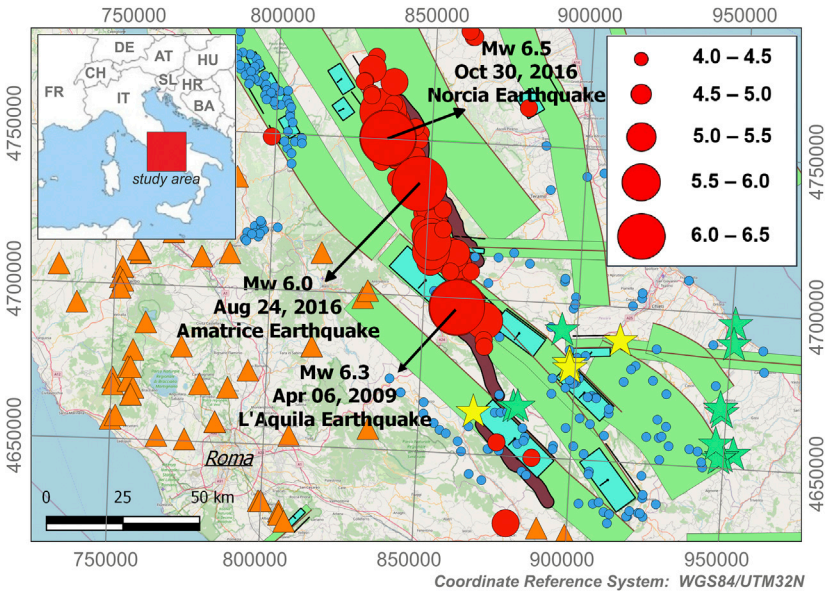

FIGURE 1 | Location of earthquakes with $M_w > 4$ (red dots) occurred in Central Italy in the period 2004–2017. Blue dots: water points of ARPA network; green stars: water points of ARPA network with geochemical anomalies in 2009; yellow stars: water points of ARPA network with geochemical anomalies in 2016; orange triangles: additional high-P_{CO2} emission points included in the MAGA project database (MAGA Project 2013–2018, 2018); blue rectangles: individual seismogenic sources; green rectangles: dipping planes of composites seismogenic sources; brown curves: top traces of composite seismogenic sources; brown rectangles: seismogenic sources still under discussion. All the data about seismogenic sources are from DISS Working Group (2018) website.

GEOLOGICAL AND SEISMOLOGICAL SETTING

The study area is located in the Central Apennines. The Apennine chain is the result of the opening of the Tyrrhenian sea that induced the eastward migration of a compressive front (e.g., Vai and Martini, 2001). Areas previously controlled by compressive tectonics were affected by back-arc extension due to the migration of the compressive front eastwards since the early Miocene. Crustal thinning due to extension in the Tyrrhenian area induced volcanic activities along the western margin of Italy. This region is characterized by high heat flow, positive gravity anomalies and shallow earthquakes due to the presence of a relatively thin crust (0–25 km). The eastern compressive Adriatic area is characterized by relatively low heat flow values, negative gravity anomalies and relatively high crustal thickness (30–35 km). Seismicity follows tectonic boundaries of distensive and compressive domains. All seismic sequences occurred in Central Apennines in past twenty years have been characterized by the occurrence of multiple events represented by $M_W > 5$ mainshocks activating southwest-dipping normal fault. Each Central Apennine sequence may last 1–12 months (Chiaraluce et al., 2017). The most relevant seismic sequences occurred in Central Italy during the last 15 years are the destructive mainshocks that struck the L'Aquila province in 2009 (L'Aquila earthquake; M_W 6.3) and the provinces of Rieti, Ascoli Piceno and Perugia in 2016 and 2017 (Amatrice earthquake; M_W 6.0; Norcia earthquake, M_W 6.5). Other minor seismic sequences characterized by lower magnitudes occurred in Umbria, Tuscany, Lazio and Marche regions during the same period (**Figure 1**).

The main shock of the L'Aquila seismic event was preceded by a foreshock sequence that lasted four months, and was followed by an aftershock sequence that lasted eight months (Valoroso et al., 2013). The hypocenter of this earthquake was found along the Paganica-San Demetrio fault, a southwestward dipping fault segment intermediate between the eastern and the western major fault systems recognized in the Abruzzo sector of Central Apennines. The L'Aquila earthquake broke a ~15–18 km long NW–SE trending fault, mainly confined to the upper 10 km of the crust (Serpelloni et al., 2012, and references therein). The area is characterized by a baseline heat flux of about 60 $mW \times m^{-2}$, and by the absence of exploitable geothermal reservoirs.

The Amatrice earthquake started on August 24th, 2016, with a M_W 6.0 mainshock apparently not preceded by foreshocks. Two months later, on October 26th, 2016, another M_W 5.9 mainshock occurred 25 km to the north, and four days later, on October 30th, 2016, a M_W 6.5 event (Norcia earthquake) hit the area in between the two previous quakes. Aftershocks sequence lasted about 1 year. Contrary to 2009 sequence, the 2016 seismic sequence apparently started without foreshock activity. A list of the major seismic events occurred in Central Italy during the observation period is given in Table 2 of the Supplementary Material.

METHODS

For the present study, we propose a novel approach (see Cicerone et al., 2009, for a review of previous monitoring techniques) that combines groundwater monitoring and satellite techniques to indirectly evaluate variations in the stress field, and possibly examine the effects due to the crustal deformation processes associated with such variations. Groundwater monitoring techniques were applied to detect hydrogeochemical anomalies (e.g., Gherardi and Pierotti, 2018; Martinelli and Dadomo, 2018), whereas satellite techniques were applied to detect time-space variations in thermal ground emissions (e.g., Tramutoli et al., 2013). The main advantage of the proposed approach is that it allows for i) identifying possible anomalies over large areas, thanks to the application of satellite techniques, and ii) for independently verifying these anomalies on a local scale, by ground-based inspection of the relevant geochemical parameters, with beneficial results for diagnostic accuracy.

Hydrogeochemical monitoring consisted of the discrete monitoring of dissolved CO_2 on a large number of water points belonging to the ARPA (Regional Environmental Protection Agency of Italy) network (see Table 1 of the Supplementary Material). In particular, we processed a subset of 114 chemical analyses collected from springs and wells roughly distributed within and around the area of greatest damage caused by the 2016 seismic events, in the Umbria and Abruzzo regions. Finally, the MSG-SEVIRI (Meteosat Second Generation - Spinning Enhanced Visible and Infrared Imager) night-time TIR images collected over the Italian region during the 2004–2017 period were analyzed with the RST (Robust Satellite Techniques) methodology (Tramutoli, 1998; Tramutoli, 2005).

Robust Satellite Techniques Methodology and Robust Estimator of Thermal InfraRed Anomalies Index

The Earth's thermally emitted radiation measured by satellite sensors operating in the Thermal InfraRed (8–14 μm) spectral range (TIR) was considered in its apparent relation with the seismic events. The most recent literature (e.g., Tramutoli et al., 2013) now supports the hypothesis that a relationship could exist between positive TIR anomalies, and the release of volatiles originally stored at depth in rocks, as a result of stress field variations. Along with Rn, optically active gases like CO_2 and CH_4 are considered the gases most likely involved in this process. The areal extension and the geometric distribution of the thermal anomalies detected by the satellite likely also depends on the relative density of the emitted gas: the larger the amount of heavier-than-air gases present, the smaller the effect of atmospheric dispersion, and the more focused the detected thermal anomaly. On the reverse, the predominant release of gases lighter than air would produce diffusion-like patterns of the thermal anomalies. The RST (Robust Satellite Techniques) approach proposed by Tramutoli (1998), Tramutoli (2005), and Tramutoli (2007) was adopted to isolate possible TIR anomalies from other signal variations related to natural and/or observational factors that can be responsible of "false" proliferations. The methodology was already used to study the different seismic phases of earthquakes with a wide range of magnitudes (from 4.0 to 7.9), and occurred in different geotectonic settings (compressive, extensional and transcurrent). More details can be found in Tramutoli et al. (2015); Tables 3 and 4 of the Supplementary Material).

The RST methodology identifies space-time anomalies with respect to a preliminarily defined "normal" (i.e., under unperturbed conditions) signal behaviour, which is achievable by the analysis of long-term series of satellite records. TIR transients normally affect areas of several thousand square kilometers and can be detected up to several hundred kilometers far from the epicenter zone, some days to almost one month prior to a seismic event, and can last for a few days after the seismic event.

For seismic monitoring prone areas, TIR anomalies are identified by using the specific index RETIRA (Robust Estimator of TIR Anomalies; Filizzola et al., 2004; Tramutoli et al., 2005). The RETIRA index is computed on the image at hand only over locations not affected by cloudiness[1], using the following equation:

$$\otimes_{\Delta T}(x,\ y,\ t) = \frac{\Delta T(x,y,t) - \mu_{\Delta T}(x,y)}{\sigma_{\Delta T}(x,y)} \quad (1)$$

where:

$\Delta T(x,y,t) = T(x,y,t) - T(t)$ is the value of the difference between the punctual value of TIR brightness temperature $T(x,y,t)$ measured at the location x,y and acquisition time t, and its spatial average $T(t)$ is computed on the investigated area by only considering cloud-free locations, all belonging to the same, land or sea, class;

$\mu_{\Delta T}(x,y)$ and $\Sigma_{\Delta T}(x,y)$ are the time average and standard deviation values of $\Delta T(x,y,t)$ computed for the location x,y using only cloud free records acquired under similar observational conditions (same month of the year, same hour of the day).

The RETIRA index is intrinsically not protected by the proliferation of signal outliers, and TIR anomalies are subject to a space-time persistence analysis (e.g., Tramutoli et al., 2015). Such analysis is devoted to discriminating significant anomalies from well-known spurious effects (e.g., local warming due to cloud passages, error in image navigation/co-location process; see Aliano et al., 2008; Eleftheriou et al., 2016; Genzano et al., 2015).

Finally, it should be noted that by using the RETIRA index, the effects of natural (e.g., topography and land cover) and observational (e.g., solar illumination and satellite view angle) conditions are minimized, and the occasional warming due to daily variations and/or season time-drifts (i.e., inter-annual changes) are also reduced (see Tramutoli et al., 2005, for more details).

[1]Cloudy pixels are identified by means the One channel Cloudy radiance detection Approach (OCA; Cuomo et al., 2004).

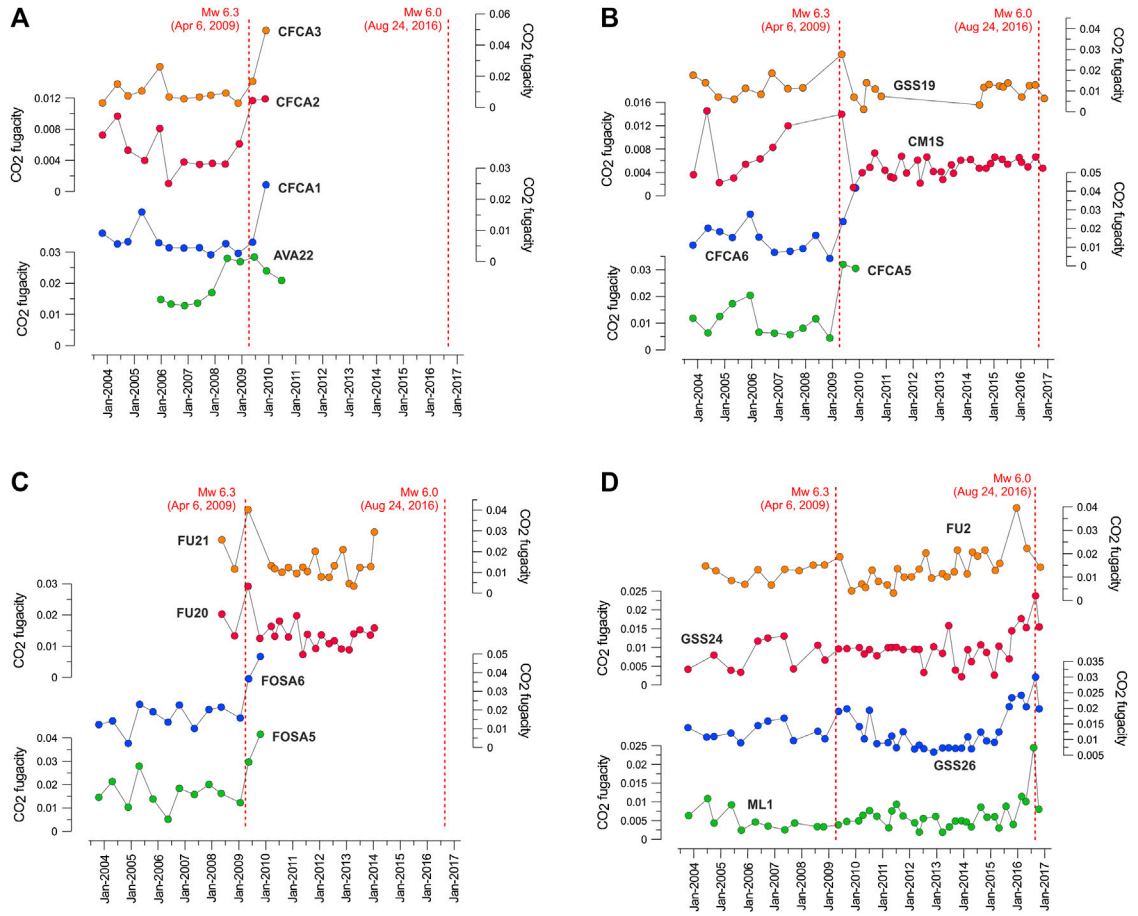

FIGURE 2 | Temporal trends (2004–2017) of P_{CO2} (fugacity) values for selected springs and wells from the ARPA network of Central Italy. From the upper left to the right bottom, **(A–C)**: manifestations responsive to 2009 seismic events; **(D)**: manifestations responsive to 2016 seismic events.

RESULTS AND DISCUSSION

Discrete Monitoring of CO_2 in Selected Cold Aquifers of Central Italy

Two major areas of CO_2 earth degassing have been identified in Central-Southern Italy (Chiodini et al., 2004): i) the Tyrrhenian hinterland, where CO_2 is directly released into the atmosphere predominantly by two degassing structures, the so-called Tuscan-Roman and Campanian degassing structure, respectively; ii) the Adriatic foreland, where CO_2 is predominantly dissolved into groundwaters circulating through major carbonate aquifers hosted along the Apennine mountainous range. The central-southern part of Apennines is a highly active seismic area, and some authors (e.g., Chiodini et al., 2004; Chiodini et al., 2018) have speculated that the existence of high-pressure, CO_2-rich fluid pockets at depth may play a major role in the generation of Apennine earthquakes. Groundwater circulation patterns in Central Italy have been described by Boni et al., (1986) and Petitta et al. (2018), and references therein), among others. From these studies, it emerged that groundwater hosted in the vadose zone is affected by fast vertical flow, while significant groundwater flow toward local springs with relatively high discharge values is generally driven by the relatively high thickness of the saturated zone.

A number of springs, and wells 100 to 200 m deep, are currently monitored for environmental purposes by the Regional Environmental Protection Agencies (ARPA) of Central Italy. These manifestations are sampled for chemical analyses two to four times per year, according to the needs of local governments. All the samples have a calcium-bicarbonate chemical composition, low salinity, and outlet temperatures close to the average annual air temperature. The goal of the survey was to quantify the contents of CO_2 dissolved in the waters, and to compare any possible anomaly in CO_2 contents with seismic activity over time. Carbon dioxide fugacity values were calculated with the PHREEQC code (Parkhurst and Appelo, 2013) from the analytical concentration of total inorganic dissolved carbon and pH values measured in the field. Noteworthy, a quite high $logP_{CO2}$ baseline value between -2 to -1.7 has been recognized all over the study area, and positive peaks of $logP_{CO2}$ were observed roughly in the same areas during the seismic events of 2009 and 2016 (Table 5 of the Supplementary Material).

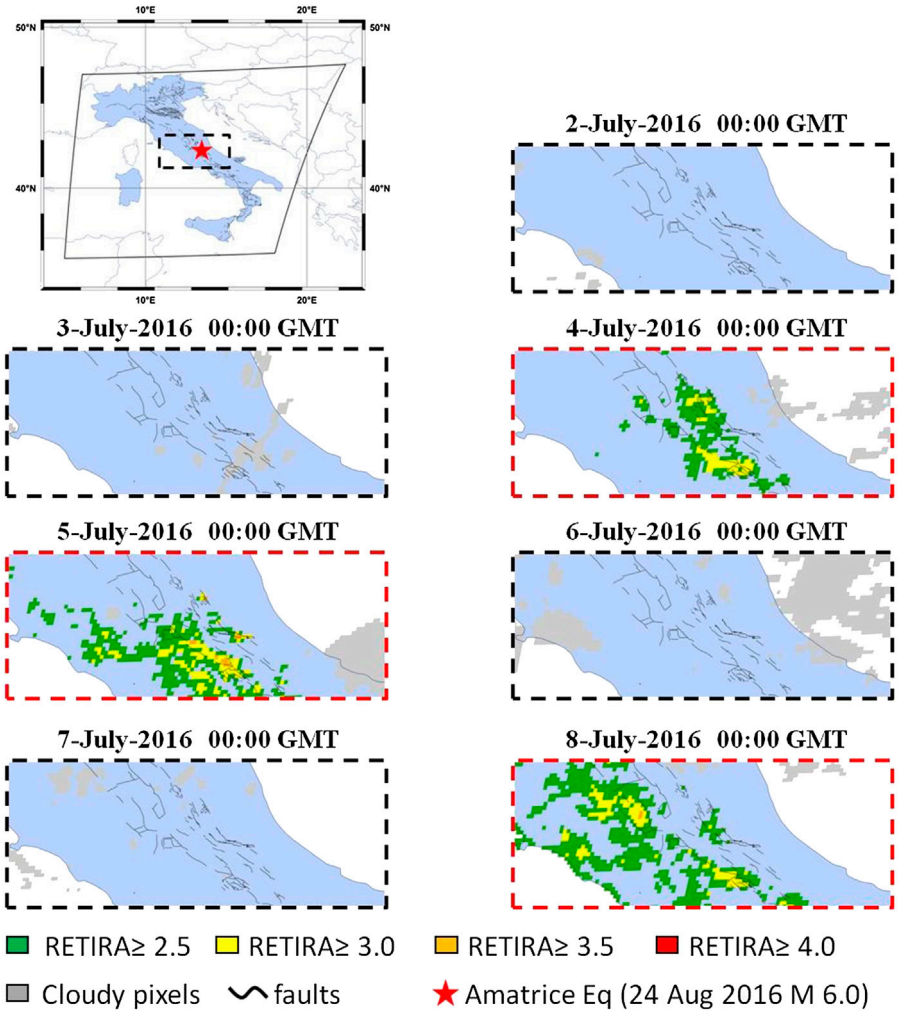

FIGURE 3 | Example of sequence of TIR anomalies. The RETIRA index over Central Italy at the time of Amatrice earthquake (August 24, 2016, M_W 6.0) (upper left box) was computed also considering low intensity anomalies (i.e., by considering pixels with $\otimes_{\Delta T}(x, y, t) > 2.5$). Generally, low intensity anomalies follow high intensity anomalies, noticeably enlarging the anomaly area and filling gaps in both space (among isolated anomalous pixels) and time domains.

Time series of recalculated $logP_{CO2}$ values were compared with regional major seismic events (**Figure 2**). Two main groups of water points were identified: i) manifestations that sensitively responded to the M_W 6.3 event of 2009 (largest in number); ii) manifestations that sensitively responded to the M_W 6.0 event of 2016. Both pre- and post-seismic anomalies were observed, reflecting the intrinsic difficulty of extracting earthquake-related signals unequivocally usable as seismic precursors from surface monitoring sites (Kumpel, 1992). Interestingly, the largest increases in CO_2 concentration were observed in the springs characterized by the highest P_{CO2} baseline values. Further to this, the largest anomalies associated with the seismic activity of Central Italy were observed in a well and a number of springs characterized by a large outflow of up to several hundred L/s. All these manifestations feed the Pescara river and drain the largest hydrostructure of the area, located in the Gran Sasso mountainous range. The occurrence of detectable CO_2 anomalies under such high water flow conditions was interpreted as additional, striking evidence concerning the large-scale increase in CO_2 degassing associated with the 2016 Amatrice earthquake. In the same area, similar phenomena were observed in different sampling points by Martini (2016) and by Chiodini et al. (2020).

Thermal InfraRed Anomalies

Daily TIR images collected at night-time[2] (time slot 00:00÷00:15 GMT) by MSG-SEVIRI satellite (sensor with spatial resolution of ~3.5 × 3.5 km) over the Italian region in the period 2004–2017 were analyzed by means RST methodology and RETIRA index, with the aim to discern TIR anomalies possibly related to seismic process (**Figures 3**, **4**).

[2]Night-time imagery is less influenced by effects related to soil-air temperature differences (normally higher during other hours of the day) and is less sensitive to local solar exposure.

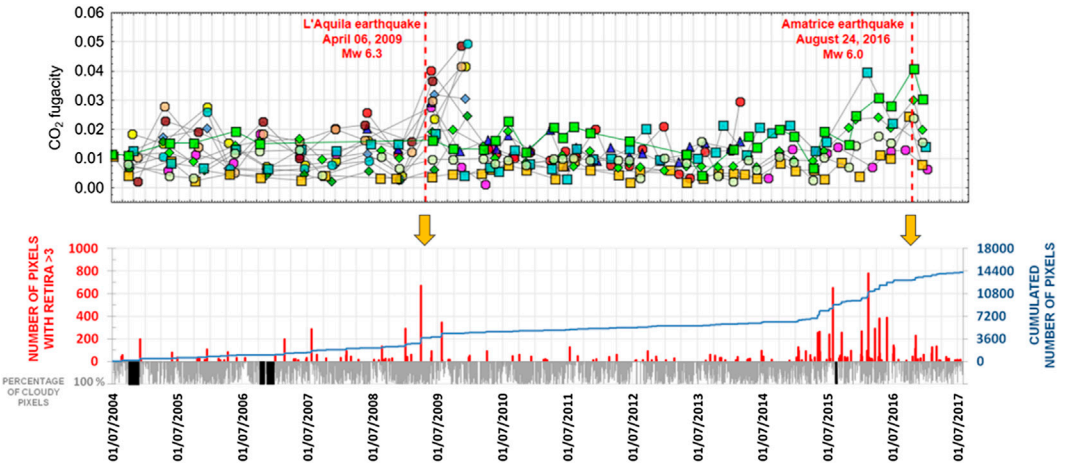

FIGURE 4 | Comparison between time variations of P_{CO2} (fugacity) values in water samples from ARPA network (upper box), and TIR anomalies (lower box). Red dotted lines and yellow arrows indicate the two major seismic events (2009 and 2016) occurred during the 2004–2017 observation period. In the lower box, red bars report the number of pixels with $\otimes_{\Delta T}(x, y, t) > 3.0$, and the blue line the cumulated number of anomalous pixels. Gray bars indicate the percentage of cloudy pixels over the investigated area, and black boxes periods of missing satellite data.

In order to discriminate significant anomalies from residual well-known spurious effects (outliers, geo-location errors, night-time warm cloud passages and asymmetric distribution over the scene; see Eleftheriou et al., 2016, and references therein), in this work we considered to be significant anomalies those with pixels with $\otimes_{\Delta T}(x, y, t) > 3$ that covered an appreciable spatial extension (at least 150 km^2), and that persistently appear in the study area (Central Italy). Two peaks of anomalous pixels with $\otimes_{\Delta T}(x, y, t) > 3$ were detected over Northern-Central Italy during the 2004–2017 period (**Figure 4**) at the time of the Abruzzo earthquake (April 6, 2009, Mw ≈ 6.3) and of the seismic swarms that occurred in Central Italy in 2016 and 2017 (a further nine shocks with $5 < M_W < 6.5$ were recorded during this period).

An additional example of TIR anomaly sequence in Central Italy is reported in **Figure 3**. Here, the RETIRA index at the time of the Amatrice earthquake (August 24, 2009, M_W 6.0) is shown based on low intensity TIR anomalies "anomalous" pixels with $\otimes_{\Delta T}(x, y, t) > 2.5$). In general, low intensity anomalies follow high intensity anomalies, noticeably enlarging the anomaly area and filling the gaps in both space and time domains (e.g., Tramutoli et al., 2015, and references therein).

Cross-Checking of Independent Signals

A qualitative cross-check of the different signals considered in this study was finally done in **Figure 4** by graphically superimposing geochemical (i.e., CO_2) patterns and TIR anomalies.

It emerged that a quite large number of springs/wells (14 water points in total, with 22 variations larger than 2σ; Table 6 of the Supplementary Material) from the ARPA network sensitively responded to both major seismic events that occurred in the Central Apennines during the 2004–2017 observation period (**Figure 3**). Associated with the main shock of the L'Aquila earthquake (2009), significant TIR anomalies were recorded almost concomitantly with P_{CO2} variations in groundwater samples from ARPA network.

Conversely, the Amatrice earthquake (2016) was largely anticipated by TIR anomalies observed up to several months before the event. In this case, the water points from the ARPA network registered an early increase in CO_2 concentration. The occurrence of possible precursory signals in Central Italy is not limited to degassing activity. Terakawa et al. (2017) reported that variations in local seismicity possibly induced by CO_2 pressure fluctuations at depth were observed before the 2009 L'Aquila mainshock, while crustal deformation processes were evidenced by GNSS before the 2016 mainshock (Panza et al., 2018). Furthermore, a possible precursory seismic pattern was observed in the same period and in the same area by Montuori et al. (2016) and by Gentili et al. (2017). Further possible precursory geophysical anomalies were also observed by Marchetti et al. (2019), Crespi et al. (2020) and Nardò et al. (2020).

The multidisciplinary approach presented in this manuscript has the potential to be applied to investigate seismic precursors outside the region considered here, in areas undergoing significant degassing, and characterized by the presence of surface water sampling points sensitive to crustal deformation processes (e.g., Martinelli and Albarello, 1997; Cioni et al., 2007; Gherardi and Pierotti, 2018). The key point to advance from a condition of mere *a posteriori* recognition of possible anomalies to the analysis of possible seismic precursors foresees the capability to detect the real temporal variability of the natural system under observation, and requires that relevant geochemical parameters should be strictly monitored continuously, as done elsewhere (e.g., in Tuscany, Italy; Pierotti et al., 2015; Pierotti et al., 2017).

CONCLUSION

Geochemical effects of crustal deformation processes on geofluids in Central Italy have been evidenced by ground and satellite techniques. Geochemical sampling in thermal springs and in gaseous emissions has allowed us to identify large-scale degassing phenomena in concomitance with the seismic sequence that occurred in Central Italy in 2009. The time series analysis of P_{CO2} values in groundwaters showed multiple degassing episodes in concomitance with seismic sequences that occurred in 2009 and 2016–2017. These large-scale CO_2 degassing phenomena have also been evidenced by satellite techniques capable of identifying transient temperature anomalies due to eventual temporary greenhouse gas emissions. Part of the anomalous signals were recorded by both techniques before the most relevant mainshocks. The contemporary observation and recording of geophysical and geochemical parameters emerged as an efficient method to gain a better understanding of seismogenic features of Central Italy. This approach has the potential to be successfully applied elsewhere, in areas of active crustal deformation, to possibly identify geophysical and geochemical signals before relevant seismic events. The continuous monitoring of relevant geochemical parameters from properly selected water manifestations is highly recommended to ensure the capability to detect signal variations occurring over short time intervals, and possibly improve the performance of the method in terms of earthquake forecasting.

DATA AVAILABILITY STATEMENT

The original contributions presented in the study are included in the article/Supplementary Materials, further inquiries can be directed to the corresponding author/s.

AUTHOR CONTRIBUTIONS

GM, FG, LP, and GF contributed to the collection and interpretation of the geochemical results. NG, ML, and VT contributed to the collection and interpretation of the geophysical results. All authors provided critical feedback and helped shape the research, analysis and manuscript.

FUNDING

Preliminary scientific communications related to present paper were done during the 14th and the 15th International Conference in Gas Geochemistry. This study benefited from funding provided by the Presidenza del Consiglio dei Ministri – Dipartimento della Protezione Civile (DPC), Project S3-2012. This paper does not necessarily represent official DPC opinion and policies. GM was partially supported by the Chinese Academy of Sciences Visiting Professorship for Senior International Scientists (2018VMA0007).

ACKNOWLEDGMENTS

The authors are indebted with Aeronautica Militare Italiana for their support and for granting the access to MS-SEVIRI satellite data, and with the Regional Agencies for Environmental Protection of Umbria, Lazio and Abruzzo Regions for sharing groundwater chemical data. The authors dearly thank two reviewers and Gaetano De Luca (INGV, L'Aquila) for their constructive comments, which have significantly contributed to improving the quality of the manuscript.

SUPPLEMENTARY MATERIAL

The Supplementary Material for this article can be found online at: https://www.frontiersin.org/articles/10.3389/feart.2020.584716/full#supplementary-material

REFERENCES

Aliano, C., Corrado, R., Filizzola, C., Genzano, N., Pergola, N., and Tramutoli, V. (2008). Robust TIR satellite techniques for monitoring earthquake active regions: limits, main achievements and perspectives. *Ann. Geophys.* 51 (1), 303–317. doi:10.4401/ag-3050

Barberio, M. D., Barbieri, M., Billi, A., Doglioni, C., and Petitta, M. (2017). Hydrogeochemical changes before and during the 2016 Amatrice-Norcia seismic sequence (central Italy). *Sci. Rep.* 7, 11735. doi:10.1038/s41598-017-11990-8

Barnes, I., Irwin, W. P., and White, D. E. (1978). Global distribution of carbon-dioxide discharges, and major zones of seismicity, scale 1:40000,000, in Water Resour. Invest., 78-39, open-file report, 11 pp., U.S. Geol. Surv., Washington, DC.

Bella, F., Biagi, P. F., Caputo, M., Della Monica, G., Ermini, A., Manjgaladze, et al. (1995). Possible creep-related tilt precursors obtained in the central Apennines (Italy) and in the southern Caucasus (Georgia). *Pure Appl. Geophys.* 144, 277–300. doi:10.1007/BF00878635

Bonfanti, P., Genzano, N., Heinicke, J., Italiano, F., Martinelli, G., Pergola, N., et al. (2012). Evidence of CO_2-gas emission variations in the central Apennines (Italy) during the L'Aquila seismic sequence (March-April 2009). *B. Geofis. Teor. Appl.* 53, 147–168. doi:10.4430/bgta0043

Boni, C. F., Bono, P., and Capelli, G. (1986). Schema idrogeologico dell'Italia centrale. *Memorie Società Geologica Italiana*, 35, 991–1012 [in Italian].

Boschetti, T., Barbieri, M., Barberio, M. D., Billi, A., Frondini, S., and Petitta, M. (2019). CO_2 inflow and elements desorption prior to a seismic sequence, Amatrice-Norcia 2016, *Italy. Geochem. Geophys.* 20, 2303–2317. doi:10.1029/2018GC008117

Cheloni, D., De Novellis, V., Albano, M., Antonioli, A., Anzidei, M., Atzori, S., et al. (2017). Geodetic model of the 2016 Central Italy earthquake sequence inferred from InSAR and GPS data. *Geophys. Res. Lett.* 44 (13), 6778–6787. doi:10.1002/2017GL073580

Chiaraluce, L., Di Stefano, R., Tinti, E., Scognamiglio, L., Michele, M., Casarotti, E., et al. (2017). The 2016 central Italy seismic sequence: a first look at the mainshocks, aftershocks and source models. *Seismol. Res. Lett.* 88, 757–771. doi:10.1785/0220160221

Chiodini, G., Caliro, S., Cardellini, C., Frondini, F., Inguaggiato, S., and Matteucci, F. (2011). Geochemical evidence for and characterization of CO_2 rich gas sources in the epicentral area of the Abruzzo 2009 earthquakes. *Earth Planet. Sci. Lett.* 304, 389–398. doi:10.1016/j.epsl.2011.02.016

Chiodini, G., Cardellini, C., Amato, A., Boschi, E., and Caliro, S. (2004). Carbon dioxide Earth degassing and seismogenesis in central and southern Italy. *Geophys. Res. Lett.* 31, L07615. doi:10.1029/2004GL019480

Chiodini, G., Cardellini, C., Di Luccio, F., Selva, G., Frondini, F., Caliro, S., et al. (2020). Correlation between tectonic CO_2 Earth degassing and seismicity is revealed by a 10-year record in the Apennines, *Italy. Sci. Adv.* 6, eabc2938. doi:10.1126/sciadv.abc2938

Chiodini, G., Frondini, F., Cardellini, C., Caliro, S., Beddini, G., and Rosiello, A. (2018). Measuring and interpreting CO_2 fluxes at regional scale: the case of Apennines, Italy. *J. Geol. Soc.* doi:10.1144/jgs2017-169.

Chiodini, G., Valenza, M., Cardellini, C., and Frigeri, A. (2008). A new web-based catalog of earth degassing sites in Italy. *EOS* 89, 341–342.

Cicerone, R. D., Ebel, J. E., and Britton, J. (2009). A systematic compilation of earthquake precursors. *Tectonophysics* 476, 371–396. doi:10.1016/j.tecto.2009.06.008

Cioni, R., Guidi, M., Pierotti, L., and Scozzari, A. (2007). An automatic monitoring network installed in Tuscany (Italy) for studying possible geochemical precursory phenomena. *Nat. Hazards Earth Syst. Sci.* 7, 405–416. doi:10.5194/nhess-7-405-2007

Crespi, M., Kossobokov, V., Panza, G. F., and Peresan, A. (2020). Space-time precursory features within ground velocities and seismicity in North-Central Italy. *Pure Appl. Geophys.* 177, 369–386. doi:10.1007/s00024-019-02297-y

Cuomo, V., Filizzola, C., Pergola, N., Pietrapertosa, C., and Tramutoli, V. (2004). A self-sufficient approach for GERB cloudy radiance detection. *Atmos. Res.*, 72, 39–56. doi:10.1016/j.atmosres.2004.03.030

De Luca, G., Di Carlo, G., and Tallini, M. (2018). A record of changes in the Gran Sasso groundwater before, during and after the 2016 Amatrice earthquake, central Italy. *Sci. Rep.* 8, 15982. doi:10.1038/s41598-018-34444-1

DISS Working Group (2018). Database of Individual Seismogenic Sources (DISS), Version 3.2.1: a compilation of potential sources for earthquakes larger than M 5.5 in Italy and surrounding areas. http://diss.rm.ingv.it/diss/ (Istituto Nazionale di Geofisica e Vulcanologia) (Accessed on July 16, 2020). doi:10.6092/INGV.IT-DISS3.2.1

Doglioni, C. (1991). A proposal for the kinematic modelling of W-dipping subductions-possible applications to the Tyrrhenian-Apennines system. *Terra. Nova* 3, 423–434.

Eleftheriou, A., Filizzola, C., Genzano, N., Lacava, T., Lisi, M., Paciello, R., et al. (2016). Long-term RST analysis of anomalous TIR sequences in relation with earthquakes occurred in Greece in the period 2004–2013. *Pure Appl. Geophys.* 173, 285–303. doi:10.1111/j.1365-3121.1991.tb00172.x

Festa, G., Picozzi, M., Caruso, A., Colombelli, S., Cattaneo, M., Chiaraluce, L., et al. (2017). Performance of earthquake early warning systems during the 2016–2017 Mw 5–6.5 Central Italy sequence. *Seismol. Res. Lett.* 89, 1–12. doi:10.1785/0220170150

Filizzola, C., Pergola, N., Pietrapertosa, C., and Tramutoli, V. (2004). Robust satellite techniques for seismically active areas monitoring: a sensitivity analysis on September 7, 1999 Athens's earthquake. *Phys. Chem. Earth* 29, 517–527. doi:10.1016/j.pce.2003.11.019

Frezzotti, M. L., Peccerillo, A., and Panza, G. (2010). "Earth's degassing in Italy. Journal of the virtual explorer," in *The geology of Italy: Tectonics and life along plate margins*. Editors C. Beltrando C. Peccerillo C. Mattei C. Conticelli and Doglioni, Vol. 36, paper 21. http://virtualexplorer.com.au/article/2010/227/earth-co-degassing.

Gentili, S., Di Giovambattista, R., and Peresan, A. (2017). Seismic quiescence preceding the 2016 central Italy earthquakes. *Phys. Earth Planet. In.* 272, 27–33. doi:10.1016/j.pepi.2017.09.004

Genzano, N., Aliano, C., Corrado, R., Filizzola, C., Lisi, M., Mazzeo, G., et al. (2009). RST analysis of MSG-SEVIRI TIR radiances at the time of the Abruzzo 6 April 2009 earthquake. *Nat. Hazard. Earth Sys.* 9 (6), 2073–2084. doi:10.5194/nhess-9-2073-2009

Genzano, N., Filizzola, C., Paciello, R., Pergola, N., and Tramutoli, V. (2015). Robust Satellite Techniques (RST) for monitoring earthquake prone areas by satellite TIR observations: the case of 1999 Chi-Chi earthquake (Taiwan). *J. Asian Earth Sci.* 114, 289–298. doi:10.1016/j.jseaes.2015.02.010

Gherardi, F., and Pierotti, L. (2018). The suitability of the Pieve Fosciana hydrothermal system (Italy) as a detection site for geochemical seismic precursors. *Appl. Geochem.* 92, 166–179. doi:10.1016/j.apgeochem.2018.03.009

Heinicke, J., Martinelli, G., and Telesca, L. (2011). Geodynamically induced variations in the emissions of CO_2 gas at San Faustino (Central Apennines, Italy). *Geofluids* 12, 123–132. doi:10.1111/j.1468-2011.00345.x

Irwin, W. P., and Barnes, I. (1980). Tectonic relations of carbon dioxide discharges and earthquake. *J. Geophys. Res.* 85 (B6), 3115–3121. doi:10.1029/jb085ib06p03115

Italiano, F., Martinelli, G., and Rizzo, A. (2004). Geochemical evidence of seismogenic-induced anomalies in the dissolved gases of thermal waters: a case study of Umbria (Central Apennines, Italy) both during and after the 1997-1998 seismic swarm. *Geochem. Geophys.* 5, Q11001. doi:10.1029/2004GC000720

King, C.-Y., Evans, W. C., Presser, T., and Husk, R. (1981). Anomalous chemical changes in well water and possible relation to earthquakes. *Geophys. Res. Lett.* 8, 425–428. doi:10.1029/GL008i005p00425

King, C.-Y., Zhang, W., and Zhang, Z. (2006). Earthquake-induced groundwater and gas changes. *Pageoph special issue hiroshi Wakita vol. I "Terrestrial fluids, earthquakes and volcanoes"* 163, 633–645. doi:10.1007/s00024-006-0049-7

Kumpel, H.-J. (1992). About the potential of wells to reflect stress variations within inhomogeneous crust. *Tectonophysics* 211, 317–336. doi:10.1016/0040-1951(92)90068-H

MAGA Project 2013-2018 (2018). Mapping gas emissions. http://www.magadb.net/ (Accessed July 16 2020).

Marchetti, D., De Santis, A., D'Arcangelo, S., Poggio, F., Piscini, A., Campuzano, S. A., et al. (2019). Pre-earthquake chain processes detected from ground to satellite altitude in preparation of the 2016–2017 seismic sequence in Central Italy. *Remote Sens. Environ.* 229, 93–99. doi:10.1016/j.rse.2019.04.033

Martinelli, G., and Albarello, D. (1997). Main constraints for siting monitoring networks devoted to the study of earthquake related phenomena in Italy. *Ann. Geophys.* 40, 1505–1522. doi:10.4401/ag-3827

Martinelli, G., and Dadomo, A. (2018). "Geochemical and fluid-related precursors of earthquakes: previous and ongoing research trends" in *Pre-earthquake processes, a multidisciplinary approach to earthquake studies*. Editors S. Ouzounov K. Pulinets P. Hattori Taylor (Washington D.C: AGU-Wiley), .219–228.

Martini, C. (2016). Signals in water- the deep originated CO2 in the Peschiera-Capone aqueduct in relation to monitoring of seismic activity in central Italy. *It. J. Groundwater*, 5, 7–20. doi:10.7343/as-2016-246

Minissale, A. (1991). Thermal springs in Italy and their relation to recent tectonics. *Appl. Geochem.* 6, 201–212. doi:10.1016/j.earscirev.2003.09.001

Minissale, A. (2004). Origin, transport and discharge of CO_2 in central Italy. *Earth Sci. Rev.* 66, 89–141.

Montone, P., and Mariucci, M. T. (2016). The new release of the Italian contemporary stress map. *Geophys. J. Int.* 205, 1525–1531. doi:10.1093/gji/ggw100

Montuori, C., Murru, M., and Falcone, G. (2016). Spatial variation of the b-value observed for the periods preceding and following the 24 August 2016, Amatrice earthquake (ML 6.0) (Central Italy). *Ann. Geophys.* 59, doi:10.4401/ag-7273.

Moro, M., Saroli, M., Stramondo, S., Bignami, C., Albano, M., Falcucci, E., et al. (2017). New insights into earthquake precursors from InSAR. *Sci. Rep.* 7, 12035. doi:10.1038/s41598-017-12058-3.

Nardò, S., Ascione, A., Mazzoli, S., Terranova, C., and Vilardo, G. (2020). InSAR data analysis: pre-seismic ground deformation in the 2009 L'Aquila earthquake region. *Boll. Geofis. Teor. Appl.*, 61, 41–56. doi:10.4430/bgta0251

Pace, B., Peruzza, L., Lavecchia, G., and Boncio, P. (2006). Layered seismogenic source model and probabilistic seismic hazard analyses in central Italy. *Bull. Seism. Soc. Am.* 96, 107–132. 10.1785/0120040231

Panza, G. F., Peresan, A., Sansò, F., Crespi, M., Mazzoni, M., and Nascetti, A. (2018). How geodesy can contribute to the understanding and prediction of earthquakes. *Rend. Lincei Sci. Fis. Nat.* 29, 81–93. doi:10.1007/s12210-017-0626-y

Parkhurst, D. L., and Appelo, C. A. J. (2013). "Description of input and examples for PHREEQC version 3–a computer program for speciation, batch-reaction, one-dimensional transport, and inverse geochemical calculations." (Denver, CO: U.S. Geological Survey techniques and methods), Book 6, Chapter A43.

Patacca, E., Scandone, P., Di Luzio, E., Cavinato, G. P., and Parotto, M. (2008). Structural architecture of the central Apennines: interpretation of the CROP 11 seismic profile from the Adriatic coast to the orographic divide: CROP 11 seismic profile. *Tectonics* 27, doi:10.1029/2005TC001917

Patacca, E., and Scandone, P. (2001). "Late thrust propagation and sedimentary response in the thrust-belt—foredeep system of the Southern Apennines

(Pliocene-Pleistocene)," in *Anatomy of an orogen: the Apennines and adjacent Mediterranean basins*. Editors G. B. Vai and I. P. Martini, 401–440.

Petitta, M., Mastrorillo, L., Preziosi, E., Banzato, F., Barberio, M. D., Billi, A., et al. (2018). Water-table and discharge changes associated with the 2016-2017 seismic sequence in central Italy: hydrogeological data and a conceptual model for fractured carbonate aquifers. *Hydrogeol. J.* 26, 1009–1026. doi:https://doi.org/10.1007/s10040-017-1717-7

Pierotti, L., Botti, F., D'Intinosante, V., Facca, G., and Gherardi, F. (2015). Anomalous CO_2 content in the Gallicano thermo-mineral spring (Serchio valley, Italy) before the 21 June 2013, Alpi Apuane earthquake (M = 5.2). *Phys. Chem. Earth* 85–86, 131–140. doi:10.1016/j.pce.2015.02.007

Pierotti, L., Gherardi, F., Facca, G., Piccardi, L., and Moratti, G. (2017). Detecting CO_2 anomalies in a spring on Mt.Amiata volcano (Italy). *Phys. Chem. Earth* 98, 161–172. doi:10.1016/j.pce.2017.01.008

Roeloffs, E. A., Burford, S. S., Riley, F. S., and Records, A. W. (1989). Hydrologic effects on water level changes associated with episodic fault creep near Parkfield, California. *J. Geophys. Res.*, 94, 12387–12402. doi:10.1029/JB094iB09p12387

Roeloffs, E. A. (1988). Hydrologic precursors to earthquakes: a review. *Pure Appl. Geophys.* 126, 177–209. doi:10.1007/BF00878996

Rojstaczer, S., Wolf, S., and Michel, R. (1995). Permeability enhancement in the shallow crust as a cause of earthquake-induced hydrological changes. *Nature* 373, 237–239. doi:10.1038/373237a0

Sato, M., Sutton, A. J., McGee, K. A., and Russel-Robinson, S. (1986). Monitoring of hydrogen along the san andreas and calaveras faults in central California in 1980–1984. *J. Geophys. Res.* 91, 12315–12326. doi:10.1029/JB091iB12p12315

Serpelloni, E., Anderlini, L., and Belardinelli, M. E. (2012). Fault geometry, coseismic-slip distribution and Coulomb stress change associated with the 2009 April 6, Mw 6.3, L'Aquila earthquake from inversion of GPS displacements. *Geophys. J. Int.* 188, 473–489. doi:10.1111/j.1365-246X.2011.05279.x

Sgrigna, V., and Malvezzi, V. (2003). Preseismic creep strains revealed by ground tilt measurements in central Italy on the occasion of the 1997 Umbria-Marche Apennines earthquake sequence. *Pure Appl. Geophys.* 160 (8), 1493–1515. doi:10.1007/s00024-003-2357-5

Tamburello, G., Pondrelli, S., Chiodini, G., and Rouwet, D. (2018). Global-scale control of extensional tectonics on CO_2 Earth degassing. *Nat. Commun.* 9, 4608. doi:10.1038/s41467-018-07087-z

Terakawa, T., Zoporowski, A., Galvan, B., and Miller, S. M. (2017). High-pressure fluid at hypocentral depths in the L'Aquila region inferred from earthquake focal mechanisms. *Geology* 38, 995–998. doi:10.1130/G31457.1

Toutain, J. P., and Baubron, J. C. (1999). Gas geochemistry and seismotectonics: a review. *Tectonophysics* 304 (1–2), 1–27. doi:10.1016/S0040-1951(98)00295-9

Tramutoli, V., Aliano, C., Corrado, R., Filizzola, C., Genzano, N., Lisi, M., et al. (2013). On the possible origin of thermal infrared radiation (TIR) anomalies in earthquake-prone areas observed using robust satellite techniques (RST). *Chem. Geol.* 339, 157–168. doi:10.1016/j.chemgeo.2012.10.042

Tramutoli, V., Corrado, R., Filizzola, C., Genzano, N., Lisi, M., and Pergola, N. (2015). From visual comparison to Robust satellite techniques: 30 years of thermal infrared satellite data analyses for the study of earthquake preparation phases. *Boll. Geof. Teor. Appl.* 56, 167–202. doi:10.4430/bgta0149

Tramutoli, V., Cuomo, V., Filizzola, C., Pergola, N., and Pietrapertosa, C. (2005). Assessing the potential of thermal infrared satellite surveys for monitoring seismically active areas. The case of Kocaeli (Izmit) earthquake, August 17th, 1999. *Remote Sens. Environ.* 96, 409–426. doi:10.1016/j.rse.2005.04.006

Tramutoli, V. (1998). "Robust AVHRR techniques (RAT) for environmental monitoring: theory and applications," in *Earth surface remote sensing II: SPIE*. Editors E. Cecchi and Zilioli. Vol. 3496, 101–113.

Tramutoli, V. (2005). "Robust satellite techniques (RST) for natural and environmental hazards monitoring and mitigation: ten years of successful applications," in Proceeding of the 9th international symposium on physical measurements and signatures. In remote sensing XXXVI, 792–795.

Tramutoli, V. (2007). "Robust satellite techniques (RST) for natural and environmental hazards monitoring and mitigation: theory and applications," in 2007 international workshop on the analysis of multi-temporal remote sensing images (IEEE), 1–6.

Vai, G. B., and Martini, I. P. (2001). *Anatomy of an orogen: the Apennines and adjacent Mediterranean basins*. Dordrecht: Springer-Science+Business Media, 633.

Valoroso, L., Chiaraluce, L., Piccinini, D., Di Stefano, R., Schaff, D., and Waldhauser, F. (2013). Radiography of a normal fault system by 64,000 high-precision earthquake locations: the 2009 L'Aquila (central Italy) case study. *J. Geophys. Res.* 118, 1–21. doi:10.1002/jgrb.50130

Wakita, H. (1975). Water wells as possible indicators of tectonic strain. *Science* 189, 553–555. doi:10.1126/science.189.4202.553

Conflict of Interest: The authors declare that the research was conducted in the absence of any commercial or financial relationships that could be construed as a potential conflict of interest.

Copyright © 2020 Martinelli, Facca, Genzano, Gherardi, Lisi, Pierotti and Tramutoli. This is an open-access article distributed under the terms of the Creative Commons Attribution License (CC BY). The use, distribution or reproduction in other forums is permitted, provided the original author(s) and the copyright owner(s) are credited and that the original publication in this journal is cited, in accordance with accepted academic practice. No use, distribution or reproduction is permitted which does not comply with these terms.

frontiers in Earth Science

ORIGINAL RESEARCH
published: 24 November 2020
doi: 10.3389/feart.2020.596283

Stress-Related Pre-Seismic Water Radon Concentration Variations in the Panjin Observation Well, China (1994–2020)

Zhihua Zhou[1], Lei Tian[1], Jing Zhao[1], Haiyan Wang[2] and Jianguang Liu[3]*

[1]Department of Earthquake Prediction, China Earthquake Networks Center, Beijing, China, [2]Liaoning Earthquake Station, Liaoning Earthquake Administration, Shenyang, China, [3]Panjin Earthquake Station of Liaoning Province, Panjin, China

Continuous observation data from a period of 26 years show that water radon concentrations in the Panjin observation well document pre-seismic anomalies prior to earthquakes of $4.8 \leq M \leq 7$ within a radius of 300 km. Among these earthquakes, two distinct groups with different water radon concentration anomalies and anomaly mechanisms are apparent. The abnormal characteristics of water radon concentrations clearly reflect the processes of stress change, while Cl^- concentration, Ca^{2+} concentration, Mg^{2+} concentration, and escaping gas flow only document part of these processes. According to Global Positioning System main strain rate fields and area strain rate fields, the change in anomalous behavior coincides with the 2011 Great Tohoku M 9.1 earthquake. This event caused the stress state of the study area, located in eastern China, to change from a relative compressive stress state to a tensile state, and may be the main reason for the change in the precursory characteristics of water radon concentrations (from increasing to decreasing prior to earthquakes). Regardless, water radon concentration in the well remains a good pre-seismic indicator for earthquakes of $M \geq 4.8$. In the near future (~50–100 years), water radon anomalies in the Panjin observation well prior to earthquakes of $M \geq 4.8$ will most likely manifest as a V-shaped concentration change. Helium and neon isotopic compositions of gas samples from the Panjin observation well show that the present relatively high levels of water radon concentrations are normal and not an earthquake precursor.

Keywords: water radon concentrations, seismic precursor, anomaly mechanisms, helium and neon isotopic compositions, Panjin observation well, regional geodynamics

OPEN ACCESS

Edited by:
Giovanni Martinelli, National Institute of Geophysics and Volcanology, Italy

Reviewed by:
Zheming Shi, China University of Geosciences, China
Carlo Sabbarese, University of Campania "Luigi Vanvitelli," Italy
Adnan Barkat, National Centre for Physics, Pakistan

****Correspondence:***
Zhihua Zhou
basalin@hotmail.com

Specialty section:
This article was submitted to Geochemistry, a section of the journal Frontiers in Earth Science

Received: *19 August 2020*
Accepted: *05 November 2020*
Published: *24 November 2020*

Citation:
Zhou Z, Tian L, Zhao J, Wang H and Liu J (2020) . Front. Earth Sci. 8:596283. doi: 10.3389/feart.2020.596283

INTRODUCTION

The half-life of radon (from here on referred to as ^{222}Rn) is short and constant (3.8 days); as a result, water radonconcentrations tend to be in equilibrium under the stable physical and chemical conditions of aquifers (Kuo et al., 2009; Ambrosino et al., 2020). Since a threefold radon increase in deep groundwater was observed before the Tashkent M 5.5 earthquake of April 26, 1966 (Woith, 2015), water radon has been widely studied as a potential seismic precursor. The stress-strain developed within Earth's crust during an earthquake changes the elastic properties of the rock, the local fracture system, and the compressibility of rock pores, causing fractures in the rock mass to open up pathways through which unusually high amounts of radon can be released (Thomas, 1988;

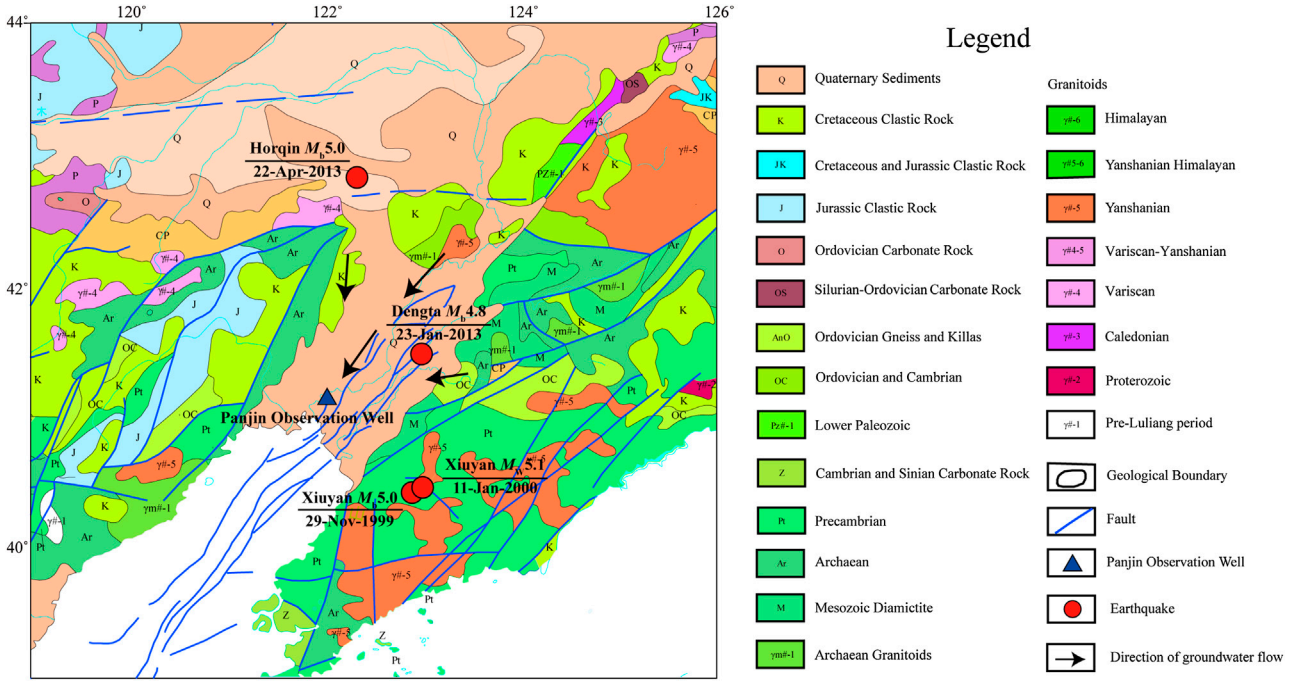

FIGURE 1 | Geographical location of Panjin observation well, Liaoning province, China. Red circles denote earthquakes of $M \geq 4.8$ within a radius of 300 km (1994–2020). The black arrows represent the groundwater flow direction of the Neogene Guantao formation.

Torgersen et al., 1990; Woith, 2015; Ambrosino et al., 2020). Most water radon observations indicate a radon increase prior to earthquakes (Hauksson, 1981; Liu et al., 1985; Igarashi and Wakita, 1990; Igarashi et al., 1995; Roeloffs, 1999; Zmazek et al., 2002; Ye et al., 2015; Kawabata et al., 2020); although, a few studies have observed decreases in water radon concentration before earthquakes (Wakita et al., 1980; Kuo et al., 2009; Namvaran and Negarestani, 2013). Regardless, it is generally believed that radon concentrations under similar geological conditions can be a sensitive indicator of strain changes in the crust preceding an earthquake and, as such, show similar precursory characteristics (Kuo et al., 2009). However, until now there have been no reports of two opposite precursory characteristics and mechanisms on one long-term continuous observation curve.

Earthquake precursors are complex processes. Time series of radon concentrations are affected by both exogenous and endogenous factors and show complex dynamics, including periodic and aperiodic oscillations on different time scales (Yan, 2018). The exogenous factors of radon concentration are common in dissolution and exchange, which are easily affected by rainfall and atmospheric pressure. Many studies have attempted to weaken the influence of exogenous factors through calculated statistical uncertainties (Asher-Bolinder et al., 1993; Heinicke et al., 2010), and to correlate anomalous increases/decreases in radon concentration with endogenous phenomena (Hauksson and Goddarard, 1981; Ambrosino et al., 2020), especially the influence of regional geodynamics on earthquake precursors. The consensus is that only long-term observation data can illustrate reliable radon precursory anomalies (Woith, 2015). In this study, we used 26 years of continuous water radon observation data, without the restriction of exogenous factors, to identify the characteristics and mechanisms of two opposite precursory anomalies observed before earthquakes. The relationship between radon precursory variations and regional geodynamics was analyzed to identify potential earthquake precursory characteristics.

GEOLOGICAL SETTINGS AND WELL BOREHOLE

The Liaohe depression is geologically located in a Cenozoic inland rift-type fault basin developed within the North China Craton, one of the world's oldest Archean cratons (Xu et al., 2014). It is at the northern extension of the Tan Lu fault zone, the main fault system of eastern China. Owing to fault activity, the Liaohe depression contains many depressions and uplifts. The study area experiences frequent earthquakes, including the 1975 Haicheng M_W 7.0 earthquake; there have been 31 earthquakes of M 5.0 or greater since 1800 (119–126°E, 39–44°N; http://www.csi.ac.cn/).

The Panjin observation well (122.02°E, 41.18°N) is located in the central, southern part of the Liaohe depression, within the middle of the second subsidence zone of the Neocathaysian structural system (**Figure 1**). The fault depression is divided

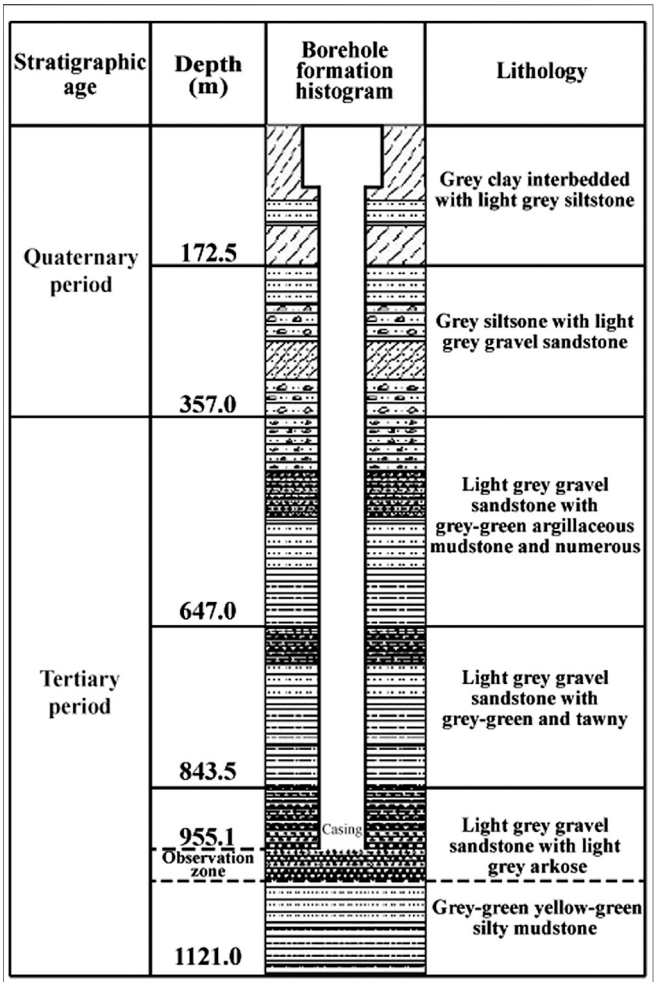

FIGURE 2 | Lithological cross-section of the Panjin observation borehole.

into six secondary structural zones by first-order major faults. The observation well is located on the Taian buried fault, a NE–SW trending normal active fault system (Lei et al., 2008). The drilling depth of the Panjin observation well is 2,892 m and the casing depth is 955.1 m. It is flowing well with confined aquifer. The base of the observed aquifer (955.1 m) is within gravel sandstone and arkose of the Neogene Guantao formation (**Figure 2**). The hydrochemical type of the observed aquifer is HCO_3-Na•Ca. The groundwater flow direction of Guantao formation is from the mountains on both sides to the middle depression, and then flows into southwest Liaodong Bay (**Figure 1**). The well is about 25 km away from the southwest coastline. In the deep aquifers of the study area, there are oil and gas exploitation layers and enriched chloride aquifers. Wang et al. (2012) showed that within the upper 360 m of depth, the shallow aquifer system has obvious vertical water circulation. Groundwater in the aquifer below 360 m constitutes an independent deep aquifer system. The vertical recharge capacity of the observation aquifer is poor; rainfall and surface water have little to no impact on the aquifer.

METHODOLOGY AND EARTHQUAKES

Monitoring Methods

Water radon concentration is measured using automatic continuous sampling once per day (1994–2020). Water is pumped out of the Panjin observation well into bubbling degassing equipment and transported into an ion chamber, where the radon concentration is measured by an ionization method using a FD-105K electrometer. When an alpha particle decays in the detector chamber, ionization of the air takes place leading to a change in the total charge on the electret. The change in the total charge results in the voltage drop over the measurement period and is used to quantify the ^{222}Rn concentration (Baskaran, 2016). The measurement precision is 0.1 Bq/L (Ye et al., 2007; Ren et al., 2012).

The Ca^{2+}, Mg^{2+}, and Cl^- concentrations and the escaping gas flow are manually sampled once a day (1994–2020). The Ca^{2+} concentration is titrated with an EDTA (ethylene diamine tetraacetic acid) standard solution at pH = 12 and the combined Ca^{2+} + Mg^{2+} concentration is titrated with an EDTA standard solution at pH = 10. The Mg^{2+} concentration is calculated using the subtraction method. The chloride concentration is obtained by titration with silver nitrate standard solution. Ion concentration precision is ~1%. Escaping gas flow is calculated by displacement water volume during the degassing process of saturated salt water; the measurement precision is 2%.

Bubbling gas samples were collected in 50-ml volume glass containers using the water displacement method; samples were taken in 2013, 2014, and 2016. He and Ne isotopes in the gas samples were measured using a MM5400 mass spectrometer. The minimum heat blanks are 1.1×10^{-14} (mol) for ^4He and 1.82×10^{-14} (mol) for ^{20}Ne, respectively. The measurements were normalized to standard atmospheric value (Ye et al., 2007; Zhou et al., 2017).

Earthquakes

Some reports show that radon anomalies can occur hundreds of kilometers from earthquake epicenters (Briestenský et al., 2014; Jilani et al., 2017; Nevinskya et al., 2018; Ambrosino et al., 2020). Jiang et al. (2019) pointed out that the distance between precursory wells and the epicenters of earthquake of $M_S < 7$ is generally less than 300 km, and that of $5 \leq M_S \leq 5.9$ is generally less than 200 km, based on a large number of earthquakes in China. Following this rules, we analyzed $5 \leq M_S < 7$ earthquakes data from 1994 to 2020 with a radius of 300km, and four eligible earthquakes were identified (http://www.csi.ac.cn/). The information they present on the USGS website is shown in **Table 1**.

Abnormal Extraction Method

We note that there are two significant changes in the measured concentration of radon in water (1999-2003 and 2011-2014) and three other less relevant changes (1994-1999, 2003-2011 and 2014-2020). Both the significant changes are found in correspondence with two groups of seismic events (**Table 1**). The occurrence of events led the background value of the

TABLE 1 | Earthquakes of $M \geq 4.8$ within 300 km of the Panjin observation well, Liaoning province (1994–2020).

Date	Location	Magnitude	Longitude (°E)	Latitude (°N)	Epicentral distance (km)
November 29, 1999	Xiuyan	M_b 5.0	122.889	40.459	108.5
January 11, 2000	Xiuyan	M_W 5.1	122.994	40.498	111.6
January 23, 2013	Dengta	M_b 4.8	122.984	41.526	89.2
April 22, 2013	Horqin	M_b 5.0	122.326	42.859	188.4

Data from https://earthquake.usgs.gov/.

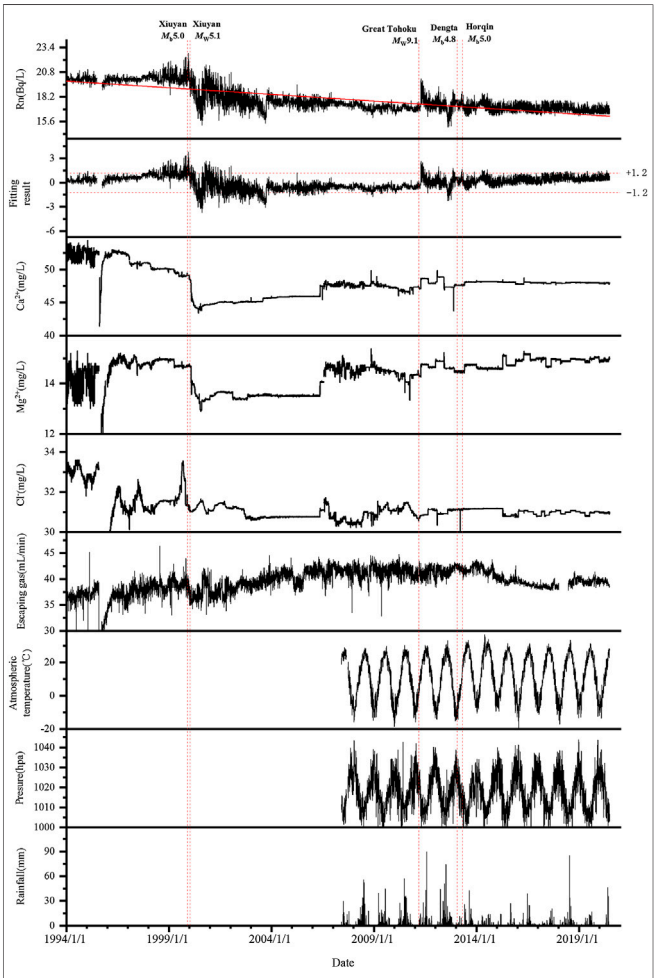

FIGURE 3 | Time series of water radon concentration, fitting result, Ca^{2+}, Mg^{2+}, and Cl^- concentrations, escaping gas flow, atmospheric temperature, pressure, and rainfall of the Panjin observation well for the period 1994–2020. The dates of earthquakes are marked by vertical red dashed lines. The red trend line is the linear fitting of the observed water radon concentration. The fitting result is calculated using the subtraction method between observed water radon concentration and the linear fitting; mean square error (MSE) is ±1.2.

observed radon concentration to decrease from 19.3 - 20.5 Bq/L (1994-1999) to 16.7-17.8 Bq/L (2003-2011), while the third observed water radon concentration change fluctuated in the range of 16.3-17.9 Bq/L (2014-2020). To compare the magnitude of these radon changes, we made a linear fit over the entire time series of the radon concentration. The result of the subtraction between the radon concentration in the measured water and that of the linear fit is shows in **Figure 3**. It was found that the amplitude of variations before the two groups of earthquakes was greater than ±1.2 of mean square error (MSE). The three other changes of water radon concentration was less than ±1.2 of MSE (**Figure 3**). The ±1.2 of MSE should be the threshold line of abnormal variation.

RESULTS

Data in the 1994–2020 times series of water radon concentrations at Panjing observation well are stable and reliable (**Figure 3**). The fitting result was calculated using the subtraction method between observed water radon concentration and the linear fitting; the mean square error (MSE) was ±1.2. Atmospheric temperature, pressure, and rainfall have been observed since June 2007 and show clear seasonal patterns. In contrast, there are no seasonal variations in the water radon concentrations or fitting results. Furthermore, August marks the rainy season, and the rainfall in August 2012 was not the historical maximum. However, the decrease in radon concentration prior to the Dengta and Horqin earthquakes was the only significant change in the time series (**Figure 3**); as such, rainfall is not responsible for the water radon changes. In summary, exogenous meteorological effects have a negligible influence on water radon in the well.

The 26 years of continuous observation data show three groups marked by significant large amplitude changes (MSE > 1.2), all of which are related to earthquakes (**Figure 3**). The first group is related to the Xiuyan M_b 5.0 and M_W 5.1 events, which occurred in 1999 and 2000, respectively. Water radon concentration increased before these earthquakes and decreased afterward. The second group is related to Great Tohoku M 9.1 earthquake of 2011. The water radon concentration increased sharply in the month following the earthquake. The third group is related to the Dengta M_b 4.8 and Horqin M_b 5.0 earthquakes in 2013. Here, there was a V-shaped progression before the earthquakes and initially low values after the earthquakes. However, the water radon concentration fluctuated for 2 years after the earthquakes, before gradually reaching a high threshold line of 1.2 times MSE.

Xiuyan M_b 5.0 and M_W 5.1 earthquakes occurred on the same fault (**Figure 1**), with a space distance of 9.9 km and a time interval of 43 days (**Table 1**). It was difficult to distinguish which earthquake caused the anomalies of observation items. Therefore,

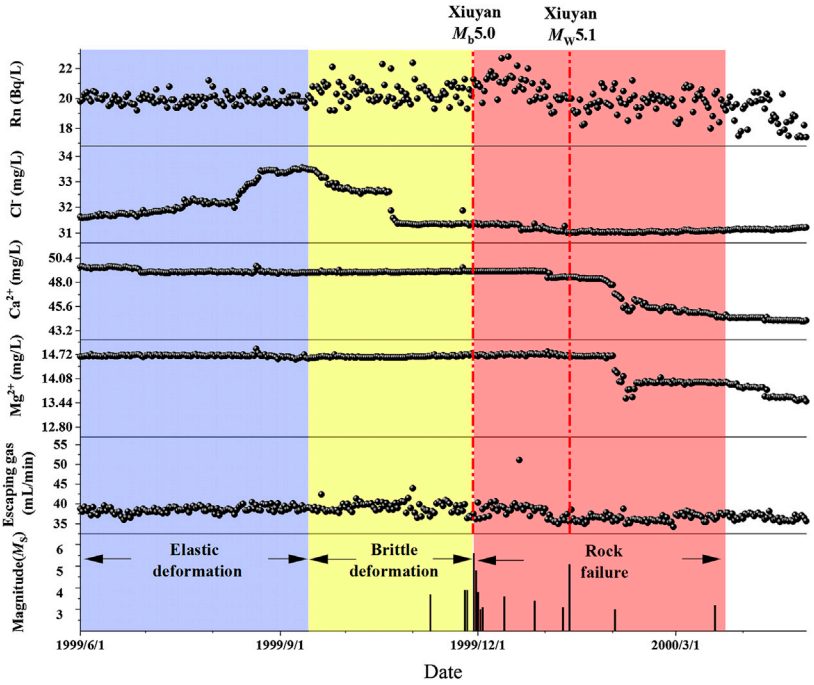

FIGURE 4 | Time series of water radon, Cl^-, Ca^{2+}, and Mg^{2+} concentrations and escaping gas flow at the Panjin observation well and their relationships to the 1999 Xiuyan M_b 5.0 and 2000 M_W 5.1 earthquakes (shown by red dashed lines). The bottom panel shows $M_S \geq 3$ foreshock and aftershock of Xiuyan earthquakes (http://www.csi.ac.cn/). Blue shading shows the elastic deformation stage; yellow shading shows the brittle deformation stage; and red shading shows the rock failure stage.

we analyzed the two earthquakes as a group. Radon concentrations around the 1999 Xiuyan earthquakes can be further split into three periods (**Figure 4**; **Table 2**). In the first stage, 80–180 days before the Xiuyan M_b 5.0 earthquake, there was no change in water radon concentration, Ca^{2+} and Mg^{2+} concentration, or escaping gas flow. The Cl^- concentration increased rapidly 110 days before the Xiuyan M_b 5.0 earthquake. The second stage was characterized by a significant increase in water radon concentration in the 80 days before the earthquake; this was accompanied by an increase in the escaping gas flow. The Cl^- concentration dropped suddenly 38 days before the earthquake. It is noteworthy that the increase in water radon concentration occurred earlier than it did for foreshocks ($M \geq 3$). In the third stage, the radon concentration decreased significantly after the Xiuyan earthquakes; the Ca^{2+} and Mg^{2+} concentrations also showed a sudden decline, but they did not change significantly before or during the earthquakes (**Table 2**).

Coincidentally, variations in the radon concentration related to the 2013 Dengta and Horqin earthquakes can also be explained by three stages; however, all occurred prior to the earthquakes (**Figure 5**; **Table 2**). In the first stage, 197 days before the Dengta earthquake, the radon concentration was stable. The Ca^{2+} and Mg^{2+} concentrations fluctuated and then dropped abruptly 237 days before the Dengta earthquake. In the second stage, 160–197 days before the earthquake, the radon concentration decreased to its lowest value (14 Bq/L). Near the third stage, the Cl^- concentration showed stepwise increases, while the radon concentration increased. The radon concentration increased to the background value 60 days before the Dengta earthquake. The change in water radon concentration had already occurred before the foreshock ($M \geq 3$). The escaping gas flow did not change significantly at any point. There was no significant change in radon concentration, Cl^- concentration, Ca^{2+} concentration, Mg^{2+} concentration, or escaping gas flow between the Dengta and Horqin earthquakes, but the radon concentration decreased significantly after the Horqin earthquake. Therefore, we analyzed the two earthquakes as a group (**Figure 5**).

DISCUSSION

Mechanism of Water Radon Anomaly in 1999

Analysis shows that pre-seismic water radon anomalies are often influenced by exogenous factors, which introduces significant uncertainty into the determination of endogenous factors (Nield and Bejan, 2006; Zafrir, 2008). Although no environmental records were recorded in 1999, significant seasonal variation can be inferred from the changes since 2007 (**Figure 3**). Seasonal changes in exogenous factors cannot explain the water radon variations before the Xiuyan M_b 5.0 and M_W 5.1 earthquakes (**Figure 3**). From the time series, the increase in radon concentrations occurred before the foreshocks of the Xiuyan earthquakes (**Figure 4**). Therefore, the anomalous changes only need to be considered in terms of the earthquake endogenous factors.

TABLE 2 | The precursory anomalies characteristics of radon and ion concentrations related to two groups of earthquakes.

Events	Processes	Time of processes	Anomaly	Rn (Bq/L)	Cl^- (mg/L)	Ca^{2+} (mg/L)	Mg^{2+} (mg/L)	Escaping gas (mL/min)
Xiuyan earthquakes	Elastic deformation	From June 1, 1999 to September 13, 1999	Start time	-	August 9, 1999	-	-	-
			Change	-	↑ 1.56	-	-	-
	Brittle deformation	From September 13, 1999 to November 29, 1999	Start time	September 13, 1999		-	-	September 20, 1999
			End time		October 21, 1999	-	-	
			Change		↓ 2.55	-	-	
	Rock failure	From November 29, 1999 to March 20, 2000	Start time		-	January 27, 2000	February 1, 2000	
			End time	December 15, 1999	-	February 12, 2000	February 12, 2000	December 15, 1999
			Change	↑ 3.00	-	↓ 6.24	↓ 1.30	↑ 17.30
Dengta and horqin earthquake	Buildup of elastic strain	From March 1, 2012 to July 10, 2012	Start time	-	-	June 1, 2012	June 1, 2012	-
			Change	-	-	↓ 1.96	↑↓ 0.68	-
	Development of cracks	From July 10, 2012 to August 13, 2012	Start time	July 10, 2012	August 8, 2012			-
			End time	August 13, 2012	August 13, 2012			-
			Change	↓ 3.2	↑ 0.31			-
	Influx of groundwater	From August 13, 2012 to April 22, 2013	Start time	August 13, 2012				-
			End time	December 18, 2012		November 29, 2012	November 29, 2012	-
			Change	↑ 4.1		↑ 0.34	↓ 0.14	-

"-" represents the normal value; The blank space represents keeping in an abnormal state.

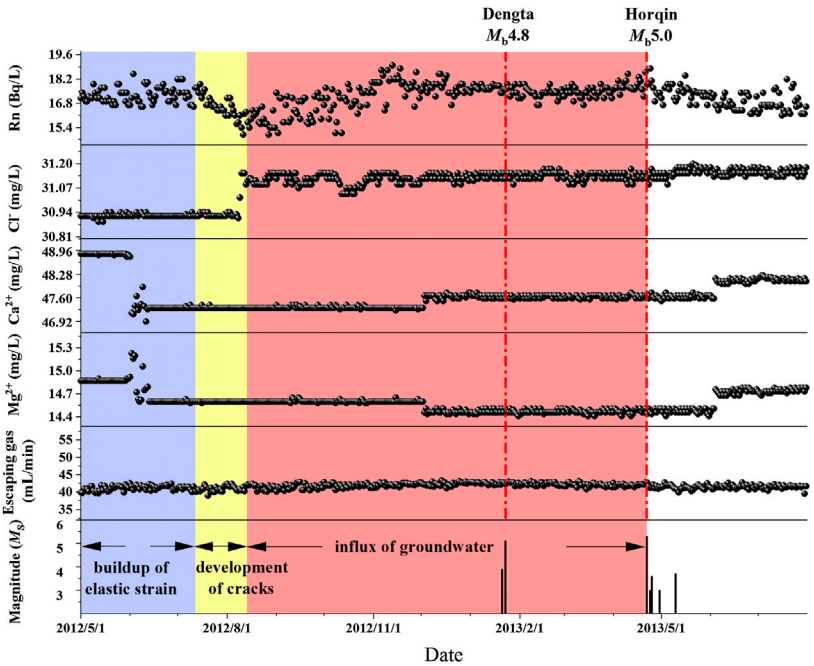

FIGURE 5 | Time series of water radon, Cl^-, Ca^{2+}, and Mg^{2+} concentrations and escaping gas flow at the Panjin observation well and their relationships to the 2013 Dengta Mb 4.8 and Horqin Mb 5.0 earthquakes (shown by red dashed lines). The bottom panel shows $M \geq 3$ foreshock and aftershock of the Dengta and Horqin earthquakes (http://www.csi.ac.cn/). Blue shading shows the buildup of elastic strain; yellow shading shows the development of cracks; and red shading shows the influx of groundwater.

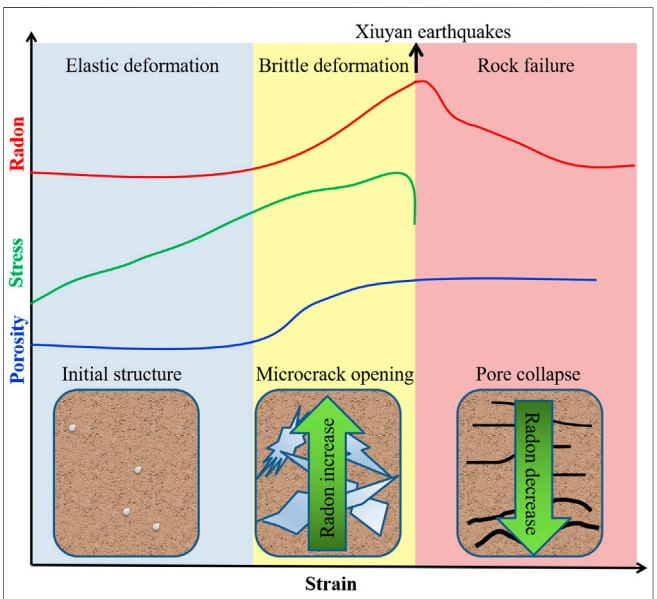

FIGURE 6 | Simplified sketch illustrating the model of radon concentration change caused by the Xiuyan earthquakes.

Gao and Zhong (2000) showed that the Xiuyan earthquakes occurred on NW trending faults under the same stress conditions (**Figure 1**). These faults are located within a new ascending NNW arched zone caused by strong crustal uplift, and the stress continued to increase before the earthquakes. The three-stage changes in radon concentration due to the earthquakes reflect three distinct processes: elastic deformation, brittle deformation, and rock failure (**Figure 4**).

Based on the pore collapse model (Schery and Gaeddert, 1982; Thomas, 1988; Toutain and Baubron, 1999), rock substrate is responsible for pore pressure changes (**Figure 6**). During the elastic deformation phase, the closure of internal pore spaces did not produce any variation in radon concentration or escaping gas flow (**Figure 4**). The rock substrate did not macroscopically fail until the end of elastic deformation, but it did cause significant irreversible microcrack damage (Mollo et al., 2018). However, this microcrack damage was not sufficient to increase radon emissions or aggravate water-rock reactions in the aquifer, as shown by the stable Ca^{2+} and Mg^{2+} concentrations. Among all the hydrochemical observations (**Figure 4**), the only one that can be proved to be in the stage of stress increase was the sudden increase of Cl^- concentration (**Figure 6**). Changing pressure in aquifer systems due to elastic compression can result in changes to Cl^- concentration (Tsunogai and Wakita, 1996). Sudden increases in Cl^- concentration can be attributed to an introduction of groundwater enriched in chloride, such as before the October 24, 1995 Wuding *M*6.5 earthquake in Yunnan (Yang, 1997) and before the September 21, 1999 Chi-Chi *M*7.3 earthquake in Taiwan (Song et al., 2005). The mixing of waters with different chemical compositions can occur quickly, and the chemical changes can also disappear rapidly (e.g., **Figure 4**; Song et al., 2006).

The brittle deformation stage conformed to the reactive surface area model (Thomas, 1988). Microcrack propagation

with increasing stress caused an increase in the surface area of the rock substrate (**Figure 6**); after which, pores ruptured and radon concentrations increased owing to the exposure of fresh rock surfaces, and escaping gas flow increased owing to the escape of trapped gas from the rock matrix (Teng, 1980; Igarashi et al., 1995; Cicerone et al., 2009). An increase in the reactive surface area should lead to more extensive water-rock interactions, and an increase in Ca^{2+} and Mg^{2+} concentrations (Claesson et al., 2007). However, there was no observed change in ion concentrations. The reason for this was that high stress can result in permeability changes within a well-aquifer system and this may break hydraulic barriers between the aquifer and other nearby small isolated reservoirs, thereby leading to mixing of chemically distinct waters (Domenico and Schwartz, 1990). However, as the volume of water added to the system is small, there would be no change in the major ions (Shi et al., 2020).

The occurrence of an earthquake marks an inflection point of stress, and this can result in radon concentration changes; that is, and increase prior to the earthquake and a decrease after (Tarakç et al., 2014). The Xiuyan earthquakes caused rock failure at a high stress level, while dike intrusions and hydrothermal fluid injections caused pervasive pore collapse at constant pressure; as a result, there was a sharp post-seismic decline in the radon concentration (Ye et al., 2015). Rock failure also caused changes in the physical and chemical properties of the observed aquifer, and this led to long-term changes in the Ca^{2+} and Mg^{2+} concentrations after earthquakes (**Figure 4**). According to the hydrochemical observations of the well in 1999 (**Figure 4**), it was found that the variations of water radon concentration could clearly show the regional geodynamic change processes, while the hydrochemical ion concentrations resulted from water-rock reactions or mixing, which led to more uncertainty.

Mechanism of the Water Radon Anomaly in 2012–2013

Decreases in radon concentration are often observed immediately after heavy rainfall (Ye et al., 2015); however, as shown in **Figure 3**, the largest rainfall in 2012 began in August, while the decline in water radon concentration began in July. In addition, August is the rainy season, and the rainfall in August 2012 was not the historical maximum, although the decrease in the radon concentration was the only significant change except for post-seismic effects. Therefore, there was no link between water radon concentration and rainfall in 2012. The Dengta M_b 4.8 earthquake was an isolated event with no foreshock and few aftershocks (Li et al., 2014). The foreshock of the Horqin M_b 5.0 earthquake occurred after the V-shaped change in the radon concentration (**Figure 5**). The stress state changes rapidly from extrusion to tension according to the aftershock information (Liu et al., 2014). It can be seen that the abnormal variation in water radon concentration in 2012 was entirely the result of endogenous factors.

Only a few other documented anomalies manifest as a decrease in pre-seismic water radon concentrations (Kuo et al., 2010; Ali Yalım et al., 2012). The process associated with this change before the Dengta earthquake can be divided into three

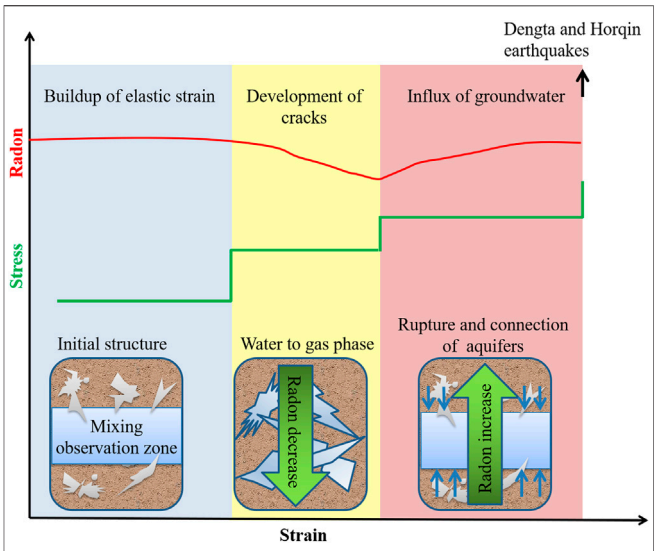

FIGURE 7 | Simplified sketch illustrating the model of radon concentration change caused by the Dengta and Horqin earthquakes.

stages (buildup of elastic strain, development of cracks, and influx of groundwater; **Figure 7**; Kuo et al., 2006), which mainly depend on the periodic changes in stress and water radon concentration. Changes in ion concentrations also reflect these stages.

During the buildup of elastic strain, the radon concentration in the groundwater was fairly stable, because the stress was relatively stable rather than gradually increasing (**Figure 7**). The stress is reflected by the sudden changes in Ca^{2+} and Mg^{2+} concentrations (**Figure 5**). According to the dilatancy-diffusion model (Scholz et al., 1973), such a change is not the result of water-rock reaction, but the result of aquifer mixing when the stress on the aquifers reaches a critical point; similar events occurred prior to the 2010 M_W 6.3 Jiasian and 2016 M_W 6.4 Meinong earthquakes (Kuo et al., 2018).

For the second stage, the stress increased suddenly, and the radon concentration decreased. Different scholars have different views on the reasons for this change. One is that the closure of cracks by small increases in compressive stress decreases radon emanation (Sultankhodzhayev et al., 1976; Fleischer and Mogrocampero, 1985), leading to reduced radon flux from crustal rocks (Einarsson et al., 2008). However, here, the escaping gas flow had no corresponding decline (**Figure 5**). The second view is that the development of new cracks in aquifer rocks can occur at a rate that is faster than the recharge of pore water (Brace et al., 1966; Scholz et al., 1973). In this scenario, dissolved radon in water is converted into a gas phase, leading to a decrease in the radon concentration of groundwater (Tsunomori and Kuo, 2010; Kuo et al., 2018). This is consistent with the decrease in radon concentration in this study, in which we also observed no change in the escaping gas flow. Additionally, because there was no pore water supply, the Ca^{2+}, Mg^{2+}, and Cl^- concentrations did not change significantly.

A further sudden increase in stress marked the third stage (**Figure 7**). The radon concentration increased owing to the

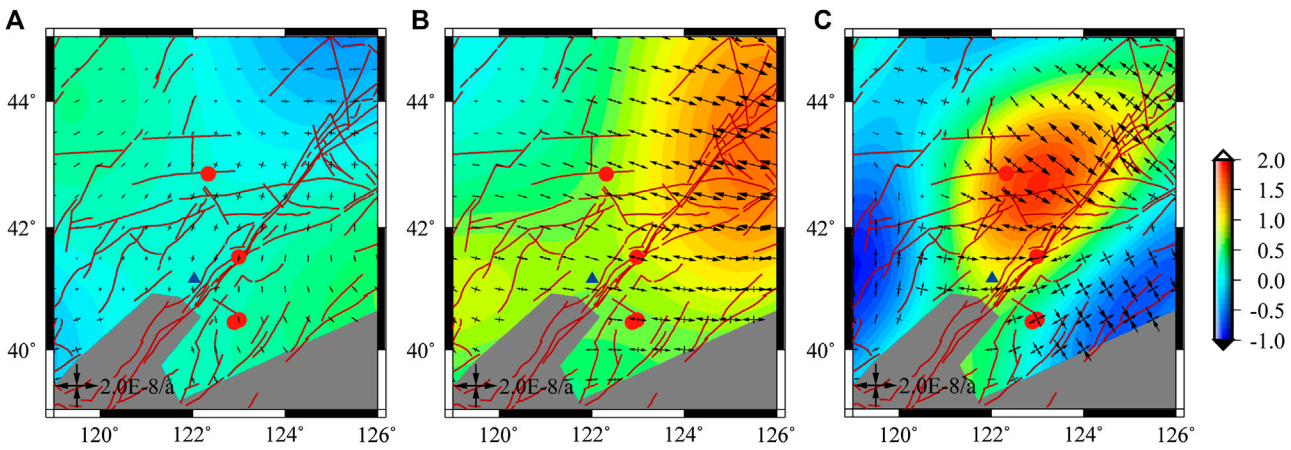

FIGURE 8 | Global Positioning System (GPS) main strain rate fields and area strain rate fields. Results for **(A)** 1999–2007, **(B)** 2011–2013, and **(C)** 2013–2016. Arrows denote the main strain rate fields and the color base map denotes the area strain rate fields. The blue triangle denotes the Panjing observation well; the red circles denote earthquake epicenters, as in **Figure 1**.

influx of groundwater, and recovered to the previous background level before the Dengta and Horqin earthquakes (**Figure 5**). The mechanism of this process was a slowing of the dilatancy rate, such that the rate of water diffusion was faster than the rate of rock dilatancy; water saturation increased and rock cracks became saturated again (Kuo et al., 2006; Kuo et al., 2010; Mollo et al., 2018). The mixing effect caused by groundwater influx, especially for groundwater enriched in chloride, can increase the chloride concentration suddenly. A continuous increase in stress results in the rupture and connection of aquifers; here, the physical and chemical properties of the aquifer changed as expected (**Figure 5**).

TABLE 3 | Chemical and isotopic compositions of gas from the Panjing observation well.

Sampling Data	$^3He/^4He$ ($\times10^{-8}$)	$^4He/^{20}Ne$	He_M[a] (%)	He_C[a] (%)	He_A[a] (%)
August 2013	165	30.88	13.62	86.38	0.00
April 2014	33	6.70	2.19	82.79	15.02
August 2016	36	13.65	2.62	90.84	6.54

[a]*He_M, He_C, and He_A denote the percentages of helium from the mantle, crust, and atmosphere, respectively.*

Explaining Two Opposing Mechanisms at Panjin Observation Well

We observed contrasting radon anomalies in the Panjin observation prior to two groups of earthquakes. Between these groups, a significant water radon anomaly occurred in 2011, a month after the Great Tohoku *M* 9.1 earthquake, for which the epicenter was 1,790 km away. We speculate that the reason for the change in water radon precursor characteristics reflects the influence of the Great Tohoku *M* 9.1 earthquake on eastern China, and particularly on regional post-seismic relaxation (Shao et al., 2015; Wang et al., 2015; Meng et al., 2019).

Endogenous factors that influence radon concentrations are primarily related to fault movement (Briestenský et al., 2014). According to Global Positioning System (GPS) main strain rate fields and area strain rate fields, there was no obvious tensile strain in the study area from 1999 to 2007 (**Figure 8A**); however, the study area experienced tensile strain after the Great Tohoku *M* 9.1 earthquake in 2011 (**Figures 8B**,C). Shao et al. (2015) also showed that the study area was in a state of compression before the Great Tohoku *M* 9.1 earthquake in 2011 and in a state of tension afterward. That is, under the condition of regional compressive strain, the stress was continuously increasing, and precursory radon anomalies in the Panjin observation well were characterized by increasing concentrations (**Figure 6**). In contrast, under a tensile strain state, the stress increased abruptly before earthquakes, and anomalies were characterized by V-shaped changes in radon concentrations (**Figure 7**). Wang et al. (2013) found that the Great Tohoku *M* 9.1 earthquake could continue to impact on the elastic relaxation of the study area for 50–100 years. Therefore, for the next ~50–100 years, precursory radon anomalies in the Panjin observation well will likely manifest as a V-shaped changes in concentration.

After the Horqin earthquake, from 2016 to 2020, the water radon concentration almost reached the upper limit of 1.2 times the MSE (**Figure 3**). To identify whether or not these high water radon concentrations represent a precursory anomaly, we carried out helium and neon isotopic compositional ($^3He/^4He$ and $^4He/^{20}Ne$) analysis of hydrothermal gas from the Panjin observation well (**Table 3**). The atmospheric $^3He/^4He$ (Ra) is 140×10^{-8}, and that of the mantle is 8 ± 1 Ra (Mamyrin and Tolstikhin, 1984). Therefore, $^3He/^4He$ is a powerful indicator for the source of volatiles entering the crust and mantle (Xu et al., 2014; Zhu et al., 2020). According to Duchkov et al. (2010), the portion of mantle helium (He_m) in the total helium of the sample (He_{meas}) can be estimated from **Equations 1**, **2**:

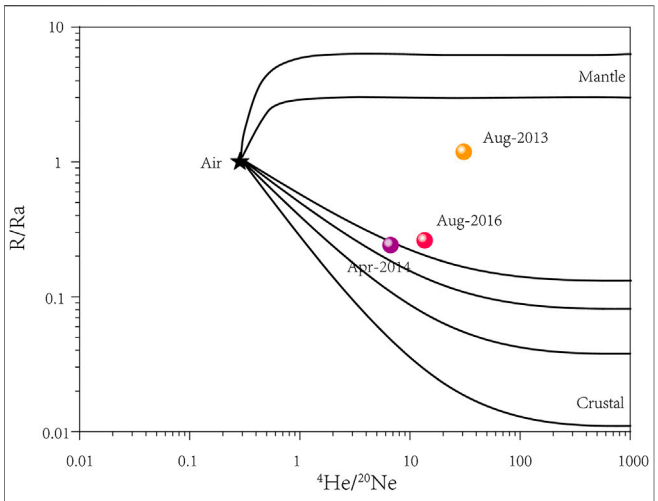

FIGURE 9 | Relationship between the R/Ra and $^4He/^{20}Ne$ ratios of hydrothermal gas in the Panjin observation well.

$$R_{cor} = \frac{R_{meas}\,(^4He/^{20}Ne)_{meas} - 42 \times 10^{-8}}{(^4He/^{20}Ne)_{meas} - 0.3} \quad (1)$$

$$\frac{He_m}{He_{meas}} \approx \frac{R_{cor} - R_c}{R_m} \approx \frac{R_{cor} - 2 \times 10^{-8}}{1,200 \times 10^{-8}}\%, \quad (2)$$

where R_{cor} is the corrected value by excluding the portion of atmospheric helium from the helium balance of the sample (Duchkov et al., 2010), R_{meas} is the $^3He/^4He$ isotopic composition of gas from the Panjing observation well, R_c is 2×10^{-8}, and R_m is $1{,}200 \times 10^{-8}$.

The atmospheric contribution to the total helium is calculated the same way, and the proportion of helium in the crust can be calculated from the difference. Calculated He_m, He_c, and He_a values are shown in **Table 3**. Mantle-derived $^3He/^4He$ represented 13.62% of the sample from mantle in 4 months after the Horqin earthquake, reflecting a post-seismic effect. Mantle-derived $^3He/^4He$ in 2014 and 2016 was ~2% (**Table 3**; **Figure 9**). The similar percentages of mantle-derived material suggest that the reaction area was under a relatively stable stress state. Furthermore, the relatively high water radon concentration in 2014–2016 occurred under a stable stress stage, and does not represent a pre-seismic anomaly.

From the analysis of GPS, $^3He/^4He$, and $^4He/^{20}Ne$, it can be concluded that the water radon concentration is relatively high owing to tensile stress in the study area. Therefore, in the future, more attention should be paid to sudden decreases in water radon concentrations, as these are more likely to be potential earthquake precursor anomalies.

CONCLUSIONS

Based on 26 years of continuous monitoring, water radon concentrations in the Panjin observation well show clear precursory responses prior to $4.8 \leq M \leq 7$ earthquakes within a distance of 300 km, suggesting that water radon in the Panjing observation well is sensitive to crustal strain within a radius of 300 km. The characteristics of the precursory response are related to the stress state, but have no relationship with the epicentral distance. Under a state of compressive stress, the observation well undergoes three stages (elastic deformation, brittle deformation, and rock failure), with water radon concentrations increasing before earthquakes (e.g., the 1999 and 2000 Xiuyan earthquakes). Under a tensile stress state, the observation well experiences three stages before earthquakes (buildup of elastic strain, development of cracks, and influx of ground water). Precursory water radon anomalies manifest as V-shaped changes in radon monitoring, such as those that occurred in 2012–2013. Changes in ion concentrations also reflected the stress change processes before both groups of earthquakes. GPS main strain rate fields and area strain rate fields suggest that the reason for the change in stress states, and as such the change in water radon precursory characteristics, is the continuing influence of the 2011 Great Tohoku M 9.1 earthquake, particularly in terms of regional post-seismic relaxation. Isotopic compositions show that the present relatively high water radon concentration is not an earthquake precursor. In the near future (~50–100 years), pre-seismic anomalies in the Panjin observation well will probably continue to manifest as V-shaped changes in water radon concentration.

DATA AVAILABILITY STATEMENT

The original contributions presented in the study are included in the article, further inquiries can be directed to the corresponding author.

AUTHOR CONTRIBUTIONS

ZZ designed the research and wrote the manuscript. LT and JZ collected data and created figures and illustrations. All authors performed the research, analyzed the results, and approved the manuscript.

FUNDING

This work was supported by the National Natural Science Foundation of China (grant number 41503114), and the China Earthquake Administration Earthquake Tracking Program (grant number 2020020302).

ACKNOWLEDGMENTS

We are grateful to Rui Yan of CENC and four reviewers for constructive comments and suggestions. We thank the First Monitoring and Application Center of China Earthquake Administration for providing the GPS velocity field datasets.

REFERENCES

Ali Yalım, H., Sandıkcıoğlu, A., Ertuğrul, O., and Yıldız, A. (2012). Determination of the relationship between radon anomalies and earthquakes in well waters on the Aksehir-Simav Fault System in Afyonkarahisar province, Turkey. *J. Environ. Radioact.* 110, 7–12. doi:10.1016/j.jenvrad.2012.01.015

Ambrosino, F., Thinová, L., Briestenskỳ, M., Guidicepietro, F., Roca, V., and Sabbarese, C. (2020). Analysis of geophysical and meteorological parameters influencing ^{222}Rn activity concentration in Mladeč caves (Czech Republic) and in soils of Phlegrean Fields caldera (Italy). *Appl. Radiat. Isot.* 160, 109140. doi:10.1016/j.apradiso.2020.109140

Asher-Bolinder, S., Owen, D. E., and Schumann, R. R. (1993). "A preliminary evaluation of environmental factors influencing day-to-day and seasonal soil-gas radon concentration," in *Field studies of radon in rocks, soils and water*. Editors L. C. S. Gundersen and R. B. Wanty (Reston, VA: U. S. Geological Survey), 23–31.

Baskaran, M. (2016). "Radon as a tracer for earthquake studies," in *Part of the Springer Geochemistry book series (SPRIGEO)*. Editor M. Baskaran, Cham: Springer, 205–228. doi:10.1007/978-3-319-21329-3

Brace, W. F., Paulding, B. W., Jr, and Scholz, C. (1966). Dilatancy in the fracture of crystalline rocks. *J. Geophys. Res.* 71, 3939–3953. doi:10.1029/jz071i016p03939

Briestenský, M., Thinová, L., Praksová, R., Stemberk, J., Rowberry, M. D., and Knejflová, Z. (2014). Radon, carbon dioxide and fault displacements in central Europe related to the Tōhoku earthquake. *Radiat. Rotect. Dosim.* 160 (1–3), 68–82. doi:10.1093/rpd/ncu090

Cicerone, R. D., Ebel, J. E., and Britton, J. (2009). A systematic compilation of earthquake precursors. *Tectonophysics* 476, 371–396. doi:10.1016/j.tecto.2009.06.008

Claesson, L., Skelton, A., Graham, C., and Mörth, C. M. (2007). The timescale and mechanisms of fault sealing and water-rock interaction after an earthquake. *Geofluids* 7 (4), 427–440. doi:10.1111/j.1468-8123.2007.00197.x

Domenico, P. A., and Schwartz, F. W. (1990). *Physical and chemical hydrogeology*. Singapore: John Wiley & Sons.

Duchkov, A. D., Rychkova, K. M., Lebedev, V. I., Kamenski, I. L., and Sokolova, L. S. (2010). Estimation of heat flow in Tuva from data on helium isotopes in thermal mineral springs. *Russ. Geol. Geophys.* 51, 209–219. doi:10.1016/j.rgg.2009.12.023

Einarsson, P., Theodórsson, P., Hjartardóttir, Á. R., and Guðjónsson, G. I. (2008). Radon changes associated with the earthquake sequence in June 2000 in the south Iceland seismic zone. *Pure Appl. Geophys.* 165, 63–74.

Fleischer, R. L., and Mogrocampero, A. (1985). Association of subsurface radon changes in Alaska and the northeastern United States with earthquakes. *Geochem. Cosmochim. Acta* 49, 1061–1071. doi:10.1016/0016-7037(85)90319-9

Gao, C. B., and Zhong, Y. Z. (2000). Geological background and seismogenic fault of the Haicheng-Xiuyan N5.6 earthquake of November 29, 1999. *Seismol. Geol.* 22 (4), 405–412 [in Chinese with English abstract]. doi:10.3969/j.issn.0253-4967.2000.04.009

Hauksson, E., and Goddard, J. G. (1981). Radon earthquake precursor studies in Iceland. *J. Geophys. Res.* 86 (B8), 7037–7054. doi:10.1029/jb086ib08p07037

Hauksson, E. (1981). Radon content of groundwater as an earthquake precursor: evaluation of worldwide data and physical basis. *J. Geophys. Res.* 86, 9397–9410. doi:10.1029/jb086ib10p09397

Heinicke, J., Italiano, F., Koch, U., Martinelli, G., and Telesca, L. (2010). Anomalous fluid emission of a deep borehole in a seismically active area of Northern Apennines (Italy). *Appl. Geochem.* 25 (4), 555–571. doi:10.1016/j.apgeochem.2010.01.012

Igarashi, G., Saeki, S., Takahata, N., Sumikawa, K., Tasaka, S., Sasaki, Y., et al. (1995). Groundwater radon anomaly before the Kobe earthquake in Japan. *Science* 269 (5220), 60–61. doi:10.1126/science.269.5220.60

Igarashi, G., and Wakita, H. (1990). Groundwater radon anomalies associated with earthquakes. *Tectonophysics* 180, 237–254. doi:10.1016/0040-1951(90)90311-u

Jiang, H. K., Yang, M. L., and Fu, H. (2019). *Earthquake cases in China (2013)*. Beijing, Seismol. Press.

Jilani, Z., Mehmood, T., Alam, A., Awais, M., and Iqbal, T. (2017). Monitoring and descriptive analysis of radon in relation to seismic activity of Northern Pakistan. *J. Environ. Radioact.* 172, 43–51. doi:10.1016/j.jenvrad.2017.03.010

Kawabata, K., Sato, T., Takahashi, H. A., Tsunomori, F., Hosono, T., Takahashi, M., et al. (2020). Changes in groundwater radon concentrations caused by the 2016 Kumamoto earthquake. *J. Hydrol.* 584, 124712. doi:10.1016/j.jhydrol.2020.124712

Kuo, M. C. T., Fan, K., Kuochen, H., and Chen, W. (2006). A Mechanism for anomalous decline in radon precursory to an earthquake. *Ground Water* 44 (5), 642–647. doi:10.1111/j.1745-6584.2006.00219.x

Kuo, T., Chen, W., and Ho, C. (2018). Anomalous decrease in groundwater radon before 2016 M_w 6.4 Meinong earthquake and its application in Taiwan. *Appl. Radiat. Isot.* 136, 68–72. doi:10.1016/j.apradiso.2018.02.015

Kuo, T., Lin, C., Fan, K., Chang, G., Lewis, C., Han, Y., et al. (2009). Radon anomalies precursory to the 2003 MW=6.8 hengkung and 2006 MW=6.1 Taitung earthquakes in Taiwan. *Radiat. Meas.* 44, 295–299. doi:10.1016/j.radmeas.2009.03.020

Kuo, T., Su, C., Chang, C., Lin, C., Cheng, W., Liang, H., et al. (2010). Application of recurrent radon precursors for forecasting large earthquakes (Mw > 6.0) near Antung, Taiwan. *Radiat. Meas.* 45, 1049–1054. doi:10.1016/j.radmeas.2010.08.009

Lei, Q. Q., Liao, X., Dong, X. Y., and Yang, S. C. (2008). Main active faults and their seismic activities in Liaoning Province. *Technol. Earthq. Disaster Prev.* 3 (2), 111–125 [in Chinese with English abstract]. doi:10.11899/zzfy20080202

Li, T. X., Chen, N., Wu, J. T., Wang, Y., Zhai, L. N., and Wang, L. (2014). A shallow study of Dengta M5.1 earthquake on January 23, 2013 in Liaoning Province. *J. Disast. Prevent. Reduc.* 30 (2), 27–30 [in Chinese with English abstract]. doi:10.13693/j.cnki.cn21-1573.2014.02.006

Liu, F., Diao, G. L., Han, X. M., Zhang, F., Jin, X. X., and Ji, B. R. (2014). Primarily discussion about the seismogenic structure of Horqin Left Back Banner *M* 5.3 earthquake on April 22, 2013. *Sesmol. Geomagn. Obs. Res.* 35 (5/6), 63–67 [in Chinese with English abstract]. doi:10.3969/j.issn.1003-3246.2014.05/06.011

Liu, K. K., Yui, T. F., Yeh, Y. H., Tsai, Y. B., and Teng, T. L. (1985). Variations of radon content in groundwaters and possible correlation with seismic activities in northern Taiwan. *Pure Appl. Geophys.* 122, 231–244. doi:10.1007/bf00874596

Mamyrin, B. A., and Tolstikhin, I. N. (1984). *Helium isotopes in nature*. Amsterdam, Netherlands: Elsevier, 273.

Meng, G. J., Su, X. N., Wu, W. W., Nikolay, S., Takahashi, H., Ohzono, M., et al. (2019). Crustal deformation of northeastern China following the 2011 Mw 9.0 Tohoku, Japan earthquake estimated from GPS observations: strain heterogeneity and seismicity. *Rem. Sens.* 11 (24), 3029. doi:10.3390/rs11243029

Mollo, S., Tuccimei, P., Soligo, M., and GalliScarlato, G. P. (2018). "Advancements in understanding the radon signal in volcanic areas: a laboratory approach based on rock physicochemical changes. Integrating disaster science and management," in *Integrating disaster science and management, global case studies in mitigation and recovery*. Editors P. Samui, D. Kim, and C. Ghosh (Amsterdam, Netherlands: Elsevier), Chap. 18, 309–328. doi:10.1016/B978-0-12-812056-9.00018-X

Namvaran, M., and Negarestani, A. (2013). Measuring the radon concentration and investigating the mechanism of decline prior an earthquake (Jooshan, SE of Iran). *J. Radioanal. Nucl. Chem.* 298, 1–8. doi:10.1007/s10967-012-2162-7

Nevinskya, I., Tsvetkovaa, T., Dogrub, M., Aksoyc, E., Inceozc, M., Baykarad, O., et al. (2018). Results of the simultaneous measurements of radon around the Black Sea for seismological applications. *J. Environ. Radioact.* 192, 48–66. doi:10.1016/j.jenvrad.2018.05.019

Nield, D. A., and Bejan, A. (2006). *Convection in porous media*. New York, NY: Springer.

Ren, H. W., Liu, Y. W., and Yang, D. Y. (2012). A preliminary study of post-seismic effects of radon following the Ms 8.0 Wenchuan earthquake. *Radiat. Meas.* 47, 82–88. doi:10.1016/j.radmeas.2011.10.005

Roeloffs, E. (1999). Radon and rock deformation. *Nature* 339, 104–105. doi:10.1038/20072

Schery, S. D., and Gaeddert, D. H. (1982). Measurements of the effect of cyclic atmospheric pressure variation on the flux of 222-Rn from the soil. *Geophys. Res. Lett.* 9, 835–838. doi:10.1029/gl009i008p00835

Scholz, C. H., Sykes, L. R., and Aggarwal, Y. P. (1973). Earthquake prediction: a physical basis. *Science* 181, 803–810. doi:10.1126/science.181.4102.803

Shao, Z. G., Zhan, W., Zhang, L. P., and Xu, J. (2015). Analysis of the far-field Co-seismic and post-seismic responses caused by the 2011 M W 9.0 Tohoku-Oki earthquake. *Pure Appl. Geophys.* 173 (2), 411–424. doi:10.1007/s00024-015-1131-9

Shi, Z. M., Zhang, H., and Wang, G. C. (2020). Groundwater trace elements change induced by M5.0 earthquake in Yunnan. *J. Hydrol.* 581, 124424. doi:10.1016/j.jhydrol.2019.124424

Song, S. R., Chen, Y. L., Liu, C. M., Ku, W. Y., Chen, H. F., Liu, Y. J., et al. (2005). Hydrochemical changes in spring waters in Taiwan: implications for evaluating sites for earthquake precursory monitoring. *Terr. Atmos. Ocean Sci.* 16, 745–762. doi:10.3319/tao.2005.16.4.745(gig)

Song, S. R., Ku, W. Y., Chen, Y. L., Liu, C. M., Chen, H. F., Chan, P. S., et al. (2006). Hydrogeochemical anomalies in the springs of the Chiayi area in west-central Taiwan as possible precusors to earthquakes. *Pure Appl. Geophys.* 163, 675–691. doi:10.1007/s00024-006-0046-x

Sultankhodzhayev, A. N., Chernov, I. G., and Zakirov, T. (1976). Hydroseismic precursors to the Gazli earthquake. *Acad. Sci. Rep. Uzbekistan* 7, 51–53.

Tarakç, M., Harman, C., Saç, M. M., and Içhedef, M. (2014). Investigation of the relationships between seismic activities and radon level in Western Turkey. *Appl. Radiat. Isot.* 83 (Part A), 12–17. doi:10.1016/j.apradiso.2013.10.008

Teng, T. L. (1980). Some recent studies on groundwater radon content as an earthquake precursor. *J. Geophys. Res.* 85 (B6), 3089–3099. doi:10.1029/jb085ib06p03089

Thomas, D. (1988). Geochemical precursors to seismic activity. *Pure Appl. Geophys.* 126, 241–265. doi:10.1007/bf00878998

Torgersen, T., Benoit, J., and Mackie, D. (1990). Controls on groundwater Rn-222 concentrations in fractured rock. *Geophys. Res. Lett.* 17, 845–848. doi:10.1029/gl017i006p00845

Toutain, J. P., and Baubron, J. C. (1999). Gas geochemistry and seismotectonics: a review. *Tectonophysics* 304 (1–2), 1–27. doi:10.1016/s0040-1951(98)00295-9

Tsunogai, U., and Wakita, H. (1996). Anomalous changes in groundwater chemistry—possible precursors of the 1995 Hyogo-ken Nanbu earthquake, Japan. *J. Phys. Earth* 44, 381–390. doi:10.4294/jpe1952.44.381

Tsunomori, F., and Kuo, T. (2010). A mechanism for radon decline prior to the 1978 Izu-Oshima-Kinkai earthquake in Japan. *Radiat. Meas.* 45 (1), 139–142. doi:10.1016/j.radmeas.2009.08.003

Wakita, H., Nakamura, Y., Notsu, K., Noguchi, M., and Asada, T. (1980). Radon anomaly: a possible precursor of the 1978 Izu-Oshima-kinkai earthquake. *Science* 207, 882–883. doi:10.1126/science.207.4433.882

Wang, L. F., Gao, Y. X., Zhang, Y. Z., and Zhang, B. (2012). Research on vertical hydrological cycle of different aquifers in piedmont plain of North China. South North Water Divers. *Water Sci. Technol.* 10 (5), 136–152 [in Chinese with English abstract]. doi:10.3969/j.issn.1672-1683.2012.05.030

Wang, L. F., Liu, J., and Zhao, J. G. (2013). Coseismic slip and post-seismic relaxation of the 2011 M9.0 Tohoku-oki earthquake and its influence on China Mainland. *Earthquake* 33 (4), 238–247. doi:10.3969/j.issn.1000-3274.2013.04.025

Wang, L. F., Liu, J., Zhao, J., and Zhao, J. (2015). Tempo-spatial impact of the 2011 M9 Tohoku-Oki earthquake on eastern China. *Pure Appl. Geophys.* 173 (1), 35–47. doi:10.1007/s00024-015-1121-y

Woith, H. (2015). Radon earthquake precursor: a short review. *Eur. Phys. J. Spec. Top.* 224, 611–627. doi:10.1140/epjst/e2015-02395-9

Xu, S., Zheng, G. D., Wang, X. B., Wang, H., Nakai, S., and Wakita, H. (2014). Helium and carbon isotope variations in Liaodong Peninsula, NE China. *J. Asian Earth Sci.* 90, 149–156. doi:10.1016/j.jseaes.2014.04.019

Yan, R. (2018). Study on the characteristics and mechanism of hydrological changes at Banglazhang hot spring site in Longling county, Yunnan province. Doctoral dissertation. Beijing (China): China university of geosciences [in Chinese with English abstract].

Yang, J. (1997). Hydrochemistry anomaly prior to Wuding M6.5 earthquake. *South China J. Seismol.* 17 (1), 30–37 [in Chinese with English abstract].

Ye, Q., Singh, R. P., He, A., Ji, S., and Liu, C. (2015). Characteristic behavior of water radon associated with Wenchuan and Lushan earthquakes along Longmengshan fault. *Radiat. Meas.* 76, 44–53. doi:10.1016/j.radmeas.2015.04.001

Ye, X., Tao, M., Yu, C., and Zhang, M. (2007). Helium and neon isotopic compositions in the ophiolites from the Yarlung Zangbo River, Southwestern China: the information from deep mantle. *Sci. China Earth Sci.* 50, 801–812. doi:10.1007/s11430-007-0017-9

Zafrir, H. (2008). The evolution, transportation and variation in time of Rn-222 within rocks in a desert 999 region. *Geophys. Res. Abstr.* 10, EGU2008-A-05386.

Zhou, X. C., Liu, L., Chen, Z., Cui, Y. J., and Du, J. G. (2017). Gas geochemistry of the hot spring in the Litang fault zone, Southeast Tibetan Plateau. *Appl. Geochem.* 79, 17–26. doi:10.1016/j.apgeochem.2017.01.022

Zhu, H. G., Li, X. F., and Xu, Y. K. (2020). A helium stratified and ingassed lower mantle: resolving the helium paradoxes. *Acta Geochimica* 39 (1), 4–10. doi:10.1007/s11631-019-00378-2

Zmazek, B., Italiano, F., Zivcic, M., Vaupotič, J., Kobal, I., and Martinelli, G. (2002). Geochemical monitoring of thermal waters in Slovenia: relationships to seismic activity. *Appl. Radiat. Isot.* 57, 919–930. doi:10.1016/s0969-8043(02)00200-2

Conflict of Interest: The authors declare that the research was conducted in the absence of any commercial or financial relationships that could be construed as a potential conflict of interest.

Copyright © 2020 Zhou, Tian, Zhao, Wang and Liu. This is an open-access article distributed under the terms of the Creative Commons Attribution License (CC BY). The use, distribution or reproduction in other forums is permitted, provided the original author(s) and the copyright owner(s) are credited and that the original publication in this journal is cited, in accordance with accepted academic practice. No use, distribution or reproduction is permitted which does not comply with these terms.

frontiers in Earth Science

ORIGINAL RESEARCH
published: 24 November 2020
doi: 10.3389/feart.2020.611663

Global Seismic Noise Entropy

Alexey Lyubushin *

Institute of Physics of the Earth, Russian Academy of Sciences, Moscow, Russia

Data of continuous records of low-frequency (periods from 2 to 1,000 min) seismic noise on a global network of 229 broadband stations located around the world for 23 years, 1997–2019, are analyzed. The daily values of the entropy of the distribution of the squares of the orthogonal wavelet coefficients are considered as an informative characteristic of noise. An auxiliary network of 50 reference points is introduced, the positions of which are determined from the clustering of station positions. For each reference point, a time series is calculated, consisting of 8,400 samples with a time step of 1 day, the values of which are determined as the medians of the entropy values at the five nearest stations that are operable during the given day. The introduction of a system of reference points makes it possible to estimate temporal and spatial changes in the correlation of noise entropy values around the world. Estimation in an annual sliding time window revealed a time interval from mid-2002 to mid-2003, when there was an abrupt change in the properties of global noise and an intensive increase in both average entropy correlations and spatial correlation scales began. This trend continues until the end of 2019, and it is interpreted as a feature of seismic noise which is connected with an increase in the intensity of the strongest earthquakes, which began with the Sumatran mega-earthquake of December 26, 2004 (M = 9.3). The values of the correlation function between the logarithm of the released seismic energy and the bursts of coherence between length of day and the entropy of seismic noise in the annual time window indicate the delay in the release of seismic energy relative to the coherence maxima. This lag is interpreted as a manifestation of the triggering effect of the irregular rotation of the Earth on the increase in global seismic hazard.

Keywords: entropy, seismic noise, correlation, length of day, wavelets, coherence

OPEN ACCESS

Edited by:
Giovanni Martinelli,
National Institute of Geophysics and Volcanology, Italy

Reviewed by:
Filippos Vallianatos,
Technological Educational Institute of Crete, Greece
Paolo Harabaglia,
University of Basilicata, Italy

***Correspondence:**
Alexey Lyubushin
lyubushin@yandex.ru

Specialty section:
This article was submitted to Solid Earth Geophysics, a section of the journal Frontiers in Earth Science

Received: *29 September 2020*
Accepted: *27 October 2020*
Published: *24 November 2020*

Citation:
Lyubushin A (2020) Global Seismic Noise Entropy. Front. Earth Sci. 8:611663. doi: 10.3389/feart.2020.611663

INTRODUCTION

The preparation processes for strong earthquakes are accompanied by changes in the statistical properties of seismic noise (Lyubushin, 2012, 2013, 2015, 2017, 2018, 2020c). As shown in (Berger et al., 2004, Fukao et al., 2010, Koper and de Foy, 2008, Koper et al., 2010; Ardhuin et al., 2011; Aster et al., 2008; Friedrich et al. 1998; Grevemeyer et al., 2000; Kobayashi, Nishida, 1998; Nishida et al., 2008, Nishida et al., 2009, Stehly et al., 2006; Rhie, Romanowicz 2004, 2006; Tanimoto, 2001, 2005), the main source of energy of seismic noise is ocean waves affecting the shelf and coast, as well as variations in atmospheric pressure on the Earth's surface arising from the movement of cyclones. In (Lyubushin, 2012; Lyubushin, 2013; Lyubushin, 2018; Lyubushin, 2020c), changes in the temporal and spatial structure of seismic noise in Japan and California, which are precursors of strong earthquakes, are identified. The article investigates the properties of seismic noise entropy from continuous records of the global network of broadband seismic stations for 23 years, 1997–2019. The main goal of the article is to evaluate the spatial and temporal correlations of entropy changes and the

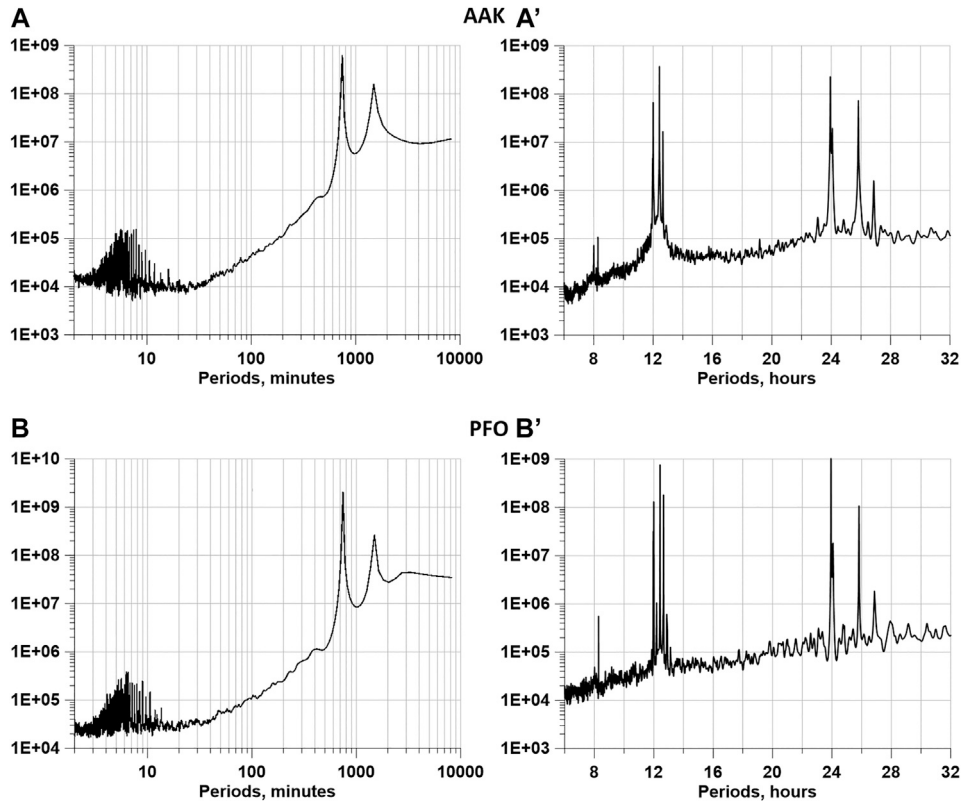

FIGURE 1 | Power spectra estimates for 2 seismic stations: AAK (**(a)** and **(a′)** - Ala Archa, Kyrgyzstan, Latitude = 42.639, Longitude = 74.494) and PFO (**(b)** and **(b′)** - Pinon Flat, California, USA, Latitude = 33.611, Longitude = −116.456). Plots **(a)** and **(b)** correspond to range of periods from 2 up to 10000 minutes, whereas **(b)** and **(b′)** - to range of periods from 6 up to 32 hours.

relationship between the entropy of seismic noise and the length of day (LOD) parameter (day length), which is a sequence of day length values and a characteristic of the Earth's irregularity of rotation, and to estimate the possible trigger effect of the irregularity of the Earth's rotation on the occurrence of the strongest earthquakes.

SEISMIC NOISE DATA

The used data present vertical components of continuous records of seismic noise with a sampling time interval of 1 s which were downloaded by request from the site of Incorporated Research Institutions for Seismology by the address http://www.iris.edu/forms/webrequest/ from 229 broadband seismic stations of the following three networks:

Global Seismographic Network: http://www.iris.edu/mda/_GSN.

GEOSCOPE: http://www.iris.edu/mda/G.

GEOFON: http://www.iris.edu/mda/GE.

Seismic noise records with a sampling rate of 1 Hz (LHZ records) were considered for 23 years of registration (from January 1, 1997, to December 31, 2019). These data were converted to a time series with a time step of 1 min by calculating averages for successive time slices of 60 s. Orthogonal wavelets were used to calculate daily entropy values for low-frequency seismic noise.

An important issue in the application of the technique used to study the properties of seismic noise is that, formally, the frequency range of signals recorded using seismic sensors does not include periods from two to about 1,000 min, which are actually investigated after the transition to a time step of 1 min at a time interval of 1 day length. The question arises about the legality of the transition to such a low-frequency region of the seismic signal records. We believe that when solving the problems of geophysical monitoring, there is a fundamental possibility of a wider application of broadband seismic equipment, which exceeds the formal limitations on the operating frequency band, which is traditionally used in the study of individual earthquakes. The basis for this assumption is the estimates of the power spectra of seismic signals after the transition to a time step of 1 min and even 1 h, shown in **Figure 1** for two seismic stations. In **Figures 1A,B**, it can be seen that the spectral estimates contain peaks corresponding to the excitation of natural oscillations of the Earth as a result of constantly occurring earthquakes of low and medium strength and peaks corresponding to the 12 and 24 h groups of tidal harmonics. From the graphs of the estimates of the power spectra after the transition to a time step of 1 h, presented in **Figures 1A',B'**, it can be seen that the 12 and 24 h spectral peaks in **Figures 1A,B** are

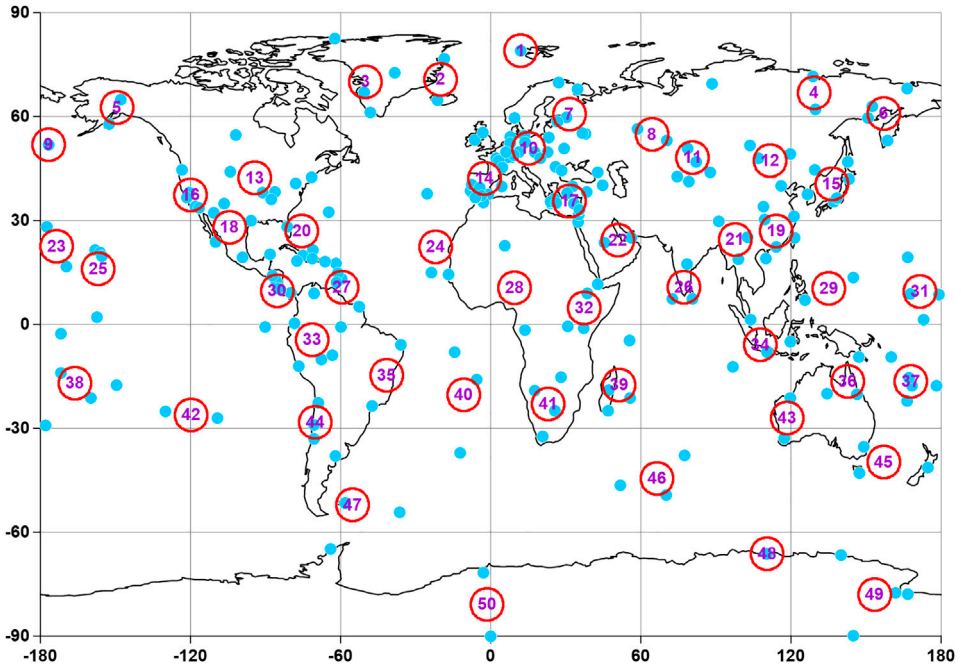

FIGURE 2 | Blue circles - positions of 229 broadband seismic stations; red numbered circles - 50 reference points.

additionally split into separate tidal harmonics. Thus, broadband seismometers have a sensitivity which allows investigating fine structure of tidal spectral peaks.

Let us consider an auxiliary network of 50 reference points, the positions of which will be determined using the hierarchical cluster analysis of the positions of 229 seismic stations by the "far neighbor" method. This method of cluster analysis has the ability to form compact clusters (Duda et al., 2000). The positions of both 229 seismic stations and 50 reference points are shown in **Figure 2**.

MINIMUM WAVELET-BASED NORMALIZED ENTROPY

Let $x(t)$ be the time series of a certain random signal, and let $t = 1,.,N$ be the index enumerating the successive data points (the discrete time). Normalized entropy of the finite sample is defined by the following formula:

$$E_n = -\sum_{k=1}^{N} p_k \cdot \log(p_k)/\log(N), \quad p_k = c_k^2 \Big/ \sum_{j=1}^{N} c_j^2, \quad 0 \le E_n \le 1 \quad (1)$$

Here, $c_k, \quad k = 1, N$ are the coefficients of decomposition by certain orthogonal wavelet basis. We used 17 orthogonal Daubechies wavelets: 10 ordinary bases with minimal support width with 1–10 vanishing moments and seven bases of the so-called Daubechies symlets (Mallat, 1999) with 4–10 vanishing moments. We defined an optimal basis providing minimum to entropy in **Eq. 1**.

It should be noted that the sum of squared coefficients is equal to the variance (energy) of the signal $x(t)$. It means that quantity in **Eq. 1** presents the entropy of energy distribution of the oscillations on the different frequencies and time scales.

The minimum normalized entropy E_n was suggested in (Lyubushin, 2012) and was used for investigating seismic noise properties in (Lyubushin, 2013; Lyubushin, 2014; Lyubushin 2020a; Lyubushin 2020b; Lyubushin 2020c). The used entropy in **Eq. 1** could be considered as multiscale and has some common features with entropy which was introduced in (Costa et al., 2003; Costa et al., 2005) for analysis of time series. The multiscale property follows from the use of orthogonal wavelet transform of the signal which allows decomposition into discrete dyadic time-frequency "atoms" with energy equal to c_k^2. In the natural time approach (Varotsos et al., 2011; Sarlis et al., 2018), the related entropy construction was proposed for data analysis. Application of Tsallis non-extensive entropy to investigating properties of ambient seismic noise was performed in (Koutalonis and Vallianatos, 2017; Vallianatos et al., 2019).

Our choice of wavelet-based entropy in **Eq. 1** is due to the fact that it has the property to take into account the variety of vibration energy distribution over a system of independent time-frequency scale atoms, due to the use of a discrete orthogonal basis of functions with a finite support. In addition, the value in **Eq. 1** is very simple and fast to calculate (because of using fast discrete wavelet transform), which is important when processing large amounts of data.

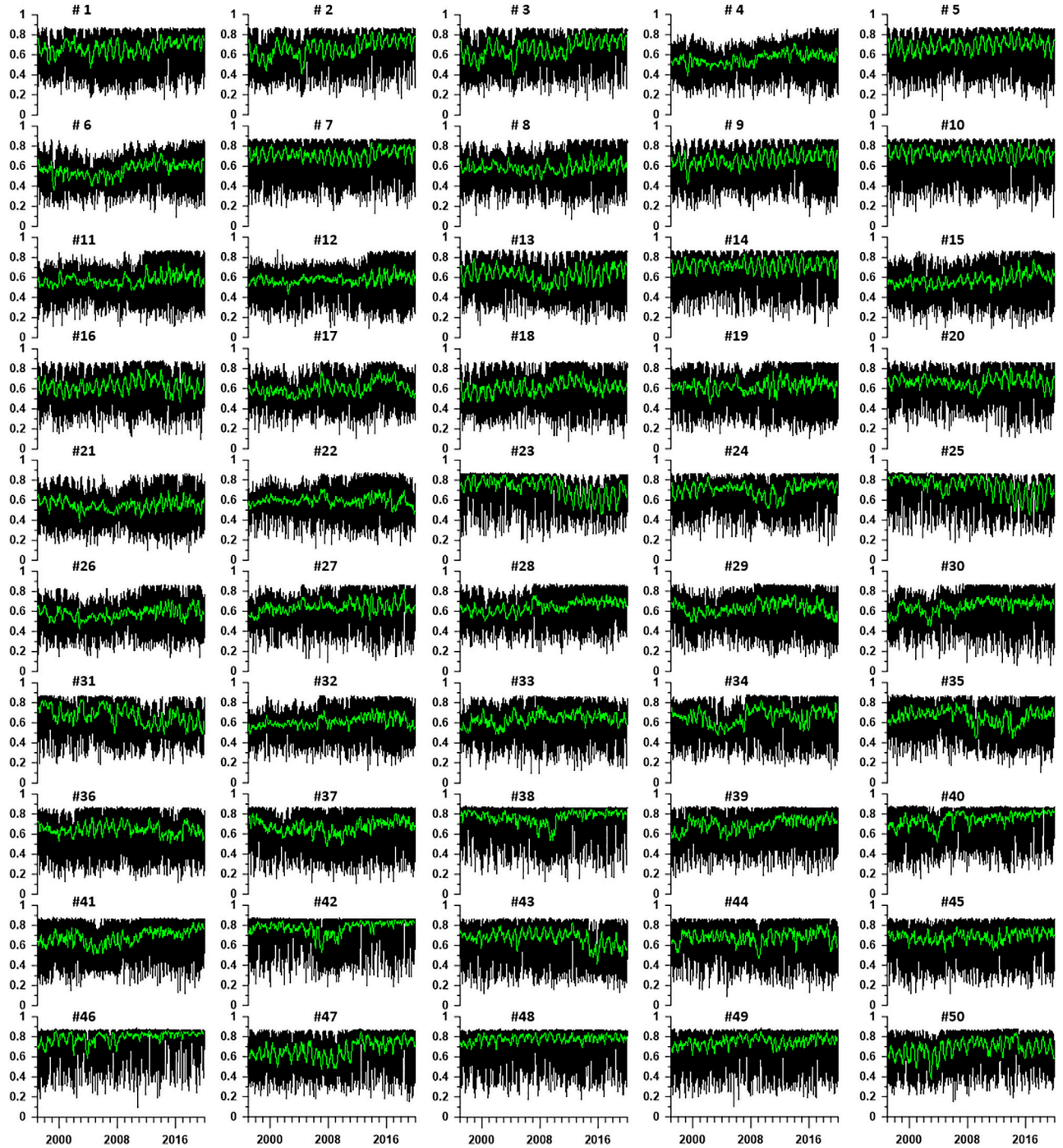

FIGURE 3 | Graphs of daily values of the minimum normalized seismic noise entropy for each of the 50 reference points. The values are obtained as median values from the five nearest operational stations. The green lines represent the moving averages in a 57-day window.

Figure 3 shows graphs of values of entropy at 50 reference points, calculated daily as medians of values at the five nearest operational stations. In order to get rid of the influence of tidal and thermal deformations of the Earth's crust and to proceed to the study of noise characteristics, before calculating the normalized entropy in **Eq. 1**, an operation was performed to eliminate the trend by an 8th order polynomial within each daily time window. The values presented in **Figure 3** can be considered as samples of typical entropy behavior in the vicinity of reference points, covering the entire world. These 50 time series with a sampling time step of 1 day, having 8,400 samples, will be the object of investigation further on in the article.

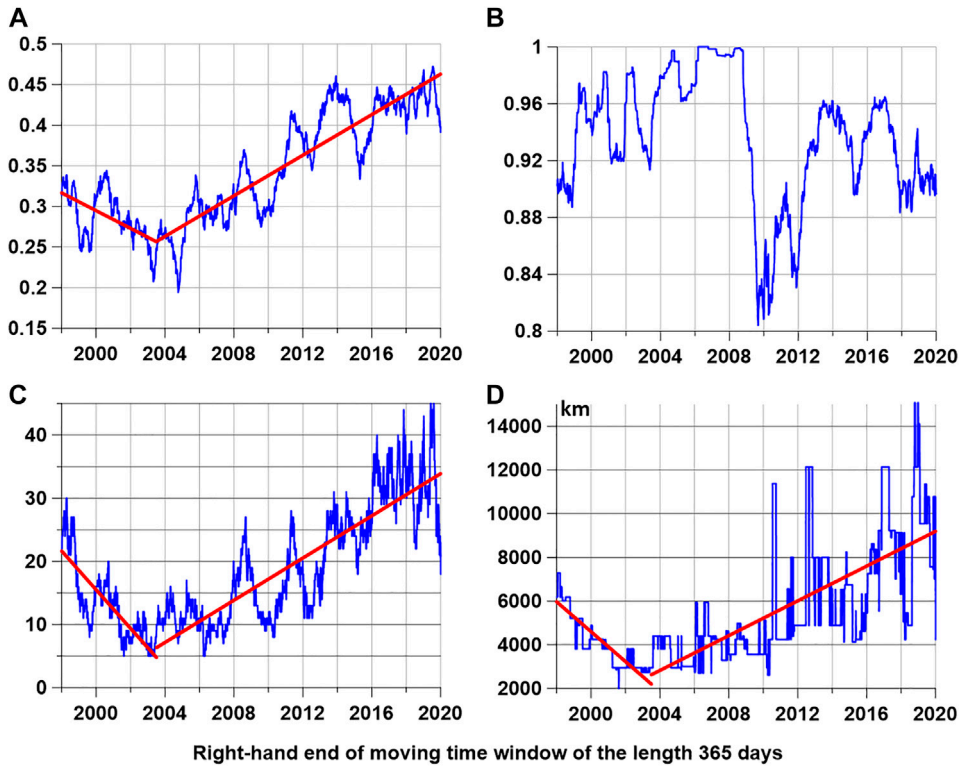

FIGURE 4 | (A,B) Mean and maximum values of pairwise correlation coefficients of entropy values at 50 reference points. **(C)** The number of pairs of 50 reference points, between which in the current time window, there is a correlation exceeding the threshold of 0.7 in absolute value. **(D)** The maximum distance between pairs of reference points, between which a correlation has arisen in the current time window, exceeding the threshold of 0.7 in magnitude. The red lines represent piecewise linear trends with a corner point in 2003.5.

SPATIAL CORRELATIONS OF ENTROPY

Let us consider a sequence of time windows of 365 days in length taken with an offset of 3 days. In each such window, we calculate the correlation coefficients between the entropy values in all pairs of reference points (for 50 points, the number of such pairs is 1,225) and take the average value of their modules. In addition, we will separately consider strong correlations, the values of which exceed the threshold of 0.7.

Figure 4 shows the results of estimates of the temporal and spatial correlations of the entropy values at the reference points, obtained in a moving time window of 365 days in length, taken with a mutual shift of 3 days. The graphs are plotted depending on the position of the right end of the time window. **Figure 4A** represents the average values of all pairwise correlation coefficients, and **Figure 4B** represents maximum values of the correlation coefficient in each window. **Figure 4C** represents a graph of the number of strong pairwise correlations between entropy values at 50 reference points exceeding the 0.7 threshold. **Figure 4D** shows the maximum distances between pairs of reference points that have strong correlations.

First of all, a common feature of the graphs in **Figures 4A,C,D** could be noticed, the presence of a time point 2003.5 of the position of the right end of the time window, for which the downward linear trend is abruptly replaced by an upward one and its growth continues until the end of 2019. This feature is highlighted in **Figure 4** by graphs of piecewise linear trends depicted by red lines. Taking into account that the window length is 365 days, this means that the temporal and spatial dynamics of the global seismic noise entropy underwent rapid changes during the year time interval from mid-2002 to mid-2003. For the average value of the correlations (**Figure 4A**), this feature was previously identified in (Lyubushin, 2020a), where it was associated with the peculiarities of the uneven rotation of the Earth. The rapid increase in the number of strong correlations and their spatial scale since 2004, as seen in **Figures 4C,D**, is a new result.

Also, note the unusual behavior of the maximum correlation coefficient in **Figure 4B**—a sharp drop for the timestamp of the right end of the window at the end of 2009. After this drop, outliers began in the values of the maximum distances between the reference points with strong entropy correlations (**Figure 4D**).

Figure 5 shows the results of identifying strong correlations between the control points. In each 365-day time window, we connect with a straight line those pairs of reference points for which the calculated correlation coefficient in absolute value exceeded the threshold of 0.7. **Figure 5A** presents correlation connectivity for a time window with low number of strong correlations (2003 years, 10 correlations), whereas **Figure 5A′**

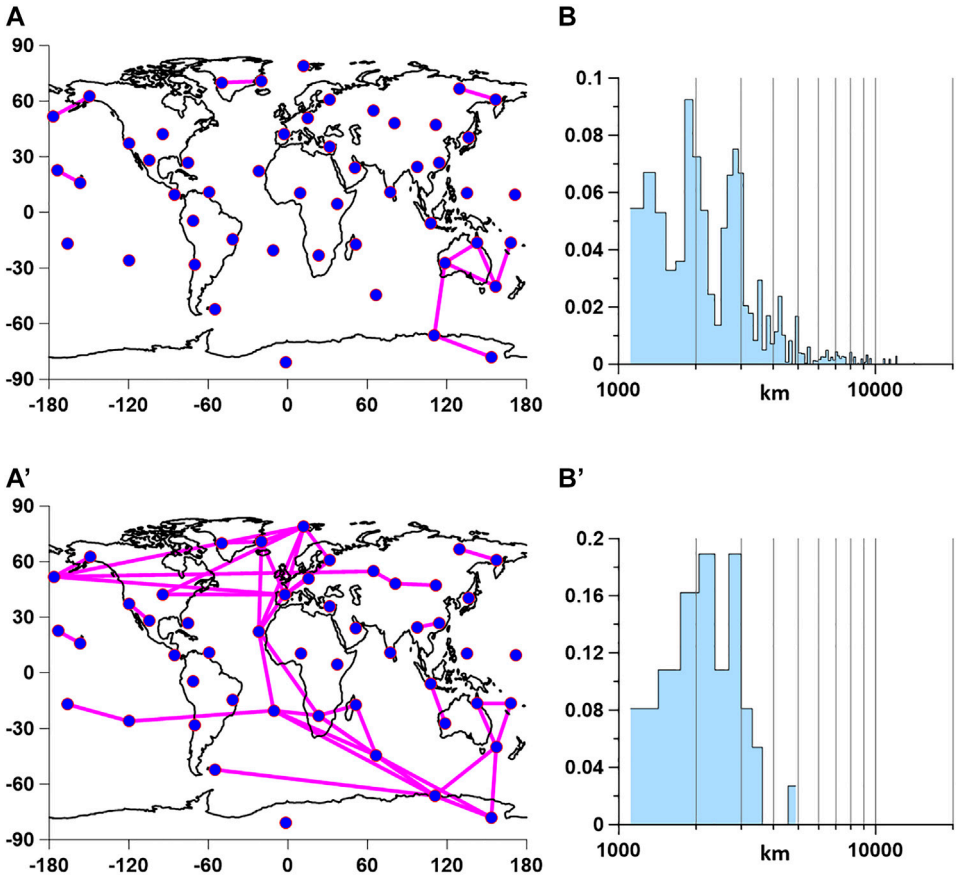

FIGURE 5 | (A,A') Red lines show pairs of reference points, between which correlations of seismic noise entropy values that exceed the threshold of 0.7 arose in two time windows of 365 days in length with a small [**(A)**, 2003-10 correlations] and a large number of strong correlations [**(A')**, 2018.5–2019.5-43 correlations]. **(B)** Histogram of distances between pairs of reference points, between which a correlation arose exceeding the threshold of 0.7, for all time windows of 365 days in length, taken with an offset of 3 days. **(B')** A histogram of the values of the nearest distances between all pairs of reference points.

corresponds to the time window with a large number of strong correlations (from mid-2018 to mid-2019, 43 correlations). The whole number of time windows of 365 days in length taken with a mutual shift of 3 days within 23 years of observations (1997–2019) equals 2,679. **Figure 5B** presents a histogram with 100 bins for the set of distances between reference points with strong entropy correlations for all time windows. This histogram has three intervals of maximum: 1,250–1,400 km, 1,810–1,950 km, and 2,790–2,630 km. A question arises whether these most frequent intervals of strong correlation distances could occur because they are most frequent for the nearest distances between reference points. The whole number of nearest distances between reference points equals 37 varying from 1,111 km up to 4,880 km. **Figure 5B′** presents histogram with 12 bins for this set of nearest distances. The histogram in **Figure 5B′** has two intervals of maximum with distances 2,054–2,368 km and 2,682–2,996 km. Taking into account the roughness of the histogram in **Figure 5B′**, we can propose that maximum in a histogram of strong correlation distances could occur due to most frequent nearest distances between reference points. After comparing histograms in **Figure 5B,B′** we can conclude that strong correlation distances which exceed 4,000 km reflect important changes in the global seismic noise spatial structure which could be connected with activation of global seismic process after 2004. These changes are illustrated by a broken linear trend in **Figure 4D**.

Temporal dynamics of strong correlations could be presented as the graphs of the number of strong correlations for each of the reference points that arose in all moving time windows. The graphs of these numbers are shown in **Figure 6**.

Figure 6 shows that the reference points differ greatly from each other in the number of strong correlations and in the time of their occurrence. Reference points with a large number of strong correlations can be called "sensitive" points on the Earth's surface. It is interesting to represent graphically the distribution of the "intensity" of strong correlations and the change of this intensity over time in the form of maps. For each time window and for each reference point, you can specify the number of strong correlations, which, according to the graphs in **Figure 6**, can vary from 0 to 9. For each time

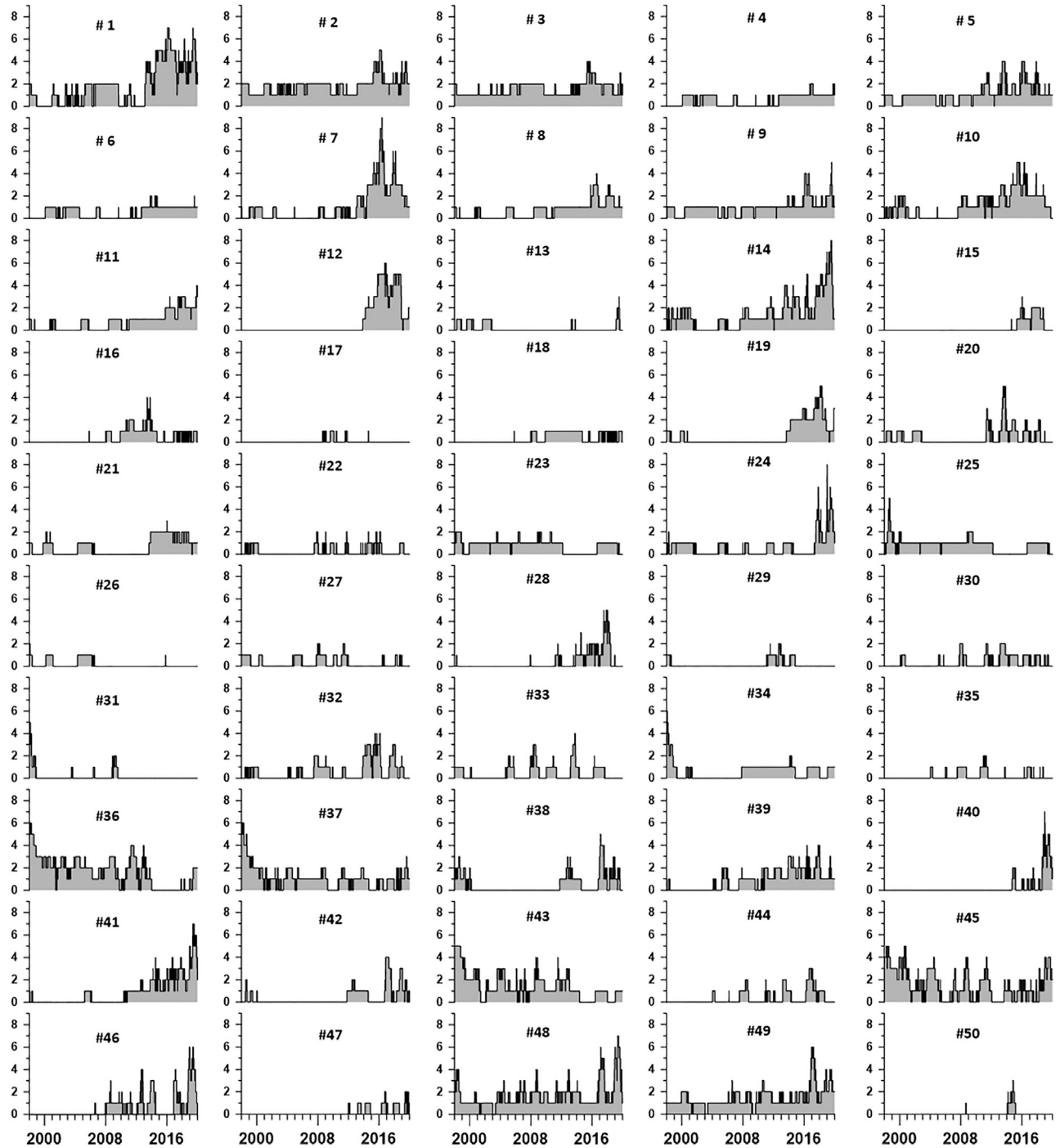

FIGURE 6 | Graphs of the numbers of strong correlations that arose for each of 50 reference points with some other reference point in a sliding window of 365 days in length with an offset of 3 days. Graphs are plotted in dependence on position of the right end of the moving time window.

window, we construct a spatial distribution map of the number of strong correlations by extrapolating the number of strong correlations from the reference points to the nodes with a regular grid of 100 nodes in longitude and 50 nodes in latitude using a Gaussian smoothing kernel (Duda et al., 2000):

$$\widehat{Z}(r) = \sum_{k=1}^{m} Z_k \exp\left(-d^2(\zeta_k, r)/h^2\right) \Big/ \sum_{k=1}^{m} \exp\left(-d^2(\zeta_k, r)/h^2\right) \quad (2)$$

Here ζ_k, $k = 1, ., m$, are the coordinates of reference points, in our case, $m = 50$; are the number of strong correlations in the reference point $\#k$, r represents coordinates of nodes of

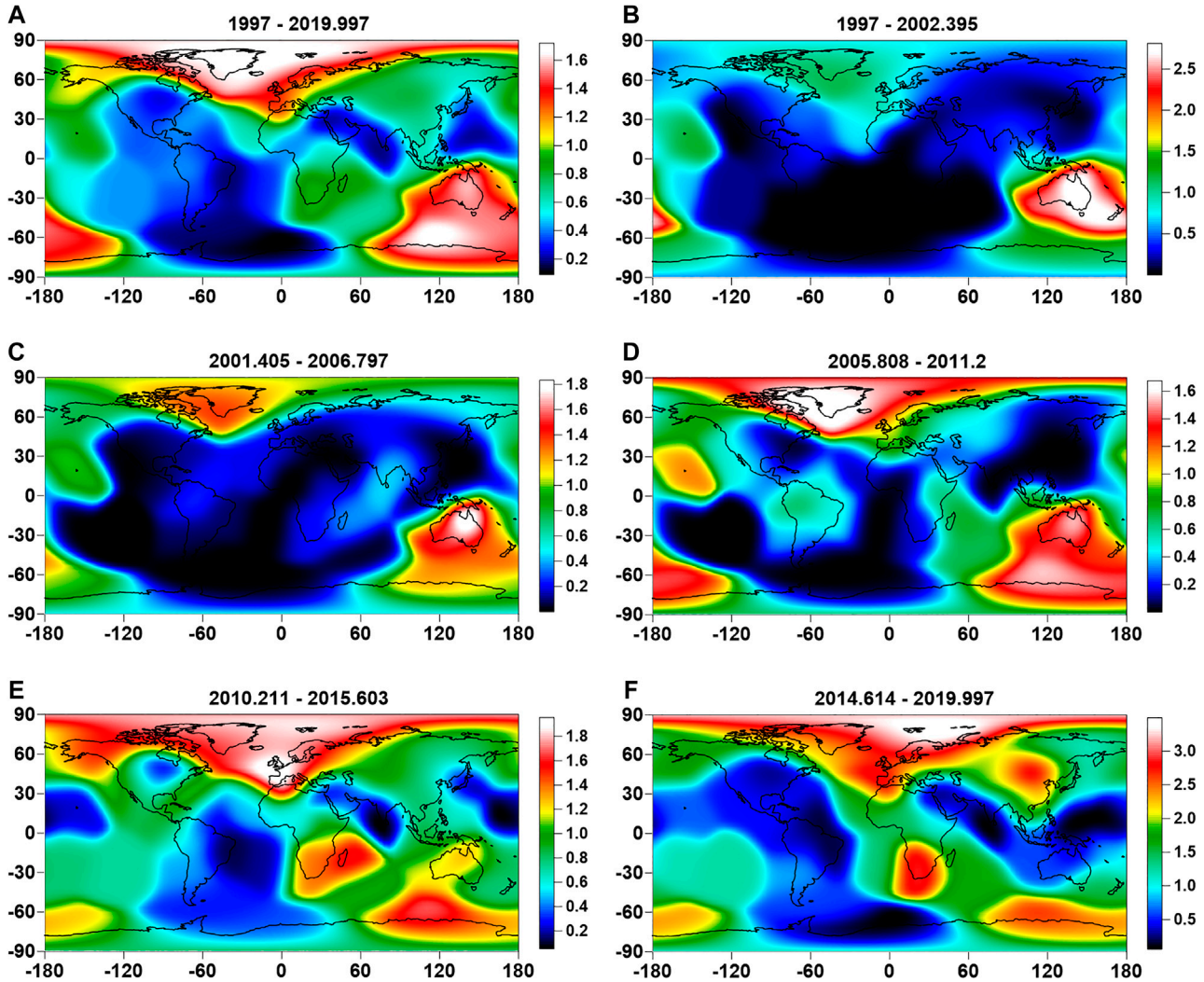

FIGURE 7 | Averaged maps of intensity of correlation links which were obtained by spatial smoothing and extrapolating numbers of strong correlations within time windows of the length 365 days with a mutual shift of 3 days in 50 reference points (Figure 6) by using Gaussian kernel with smoothing radius 15°. Each map has time marks of most left and most right ends of time windows laying between two dates, given in fractional year format. Map **(A)** is obtained by averaging elementary maps from all time windows. Maps **(B–F)** correspond to averaging of equal successive number of elementary 365-day maps.

regular grid, $d(\zeta_k, r)$ is the distance from the surface of spherical Earth between points ζ_k and r, and h is a smoothing parameter (bandwidth). We take the bandwidth $h = 15^\circ$ which corresponds to the distance ≈1,700 km from the surface of the spherical Earth. The value $\widehat{Z}(r)$ is extrapolated and the number of strong correlations from reference points to the nodes of regular grid is smoothed. We will call $\widehat{Z}(r)$ as the intensity of strong correlations for the node with coordinates r.

After calculating the values (**Eq. 2**) in all nodes of regular grid of the size for some time windows, we will have the map of correlation intensities corresponding to this window. Let us call such maps as "elementary" ones. For the sequence of time windows of the length 365 days taken with a mutual shift of 3 days covering interval 1997–2019, the number of elementary maps equals 2679. By averaging all elementary maps, we will have a mean map of strong correlation intensity which is presented in **Figure 7A**. According to this map, the most "sensitive" regions of the Earth are sub-Arctic including Greenland in the northern hemisphere and Australia and west Antarctica in the southern hemisphere. Equatorial latitudes and most of temperate latitudes are not "sensitive."

Other maps in **Figure 7** present the temporal dynamics of correlation intensity as the sequence of maps which are obtained by averaging equal successive parts: 536 elementary maps in **Figures 7B–E** and 535 elementary maps in **Figure 7F**. From the sequence of maps in **Figures 7B–F**, it can be seen that the correlation intensity at the beginning of the considered time interval was maximum in the south, but then moved to the north.

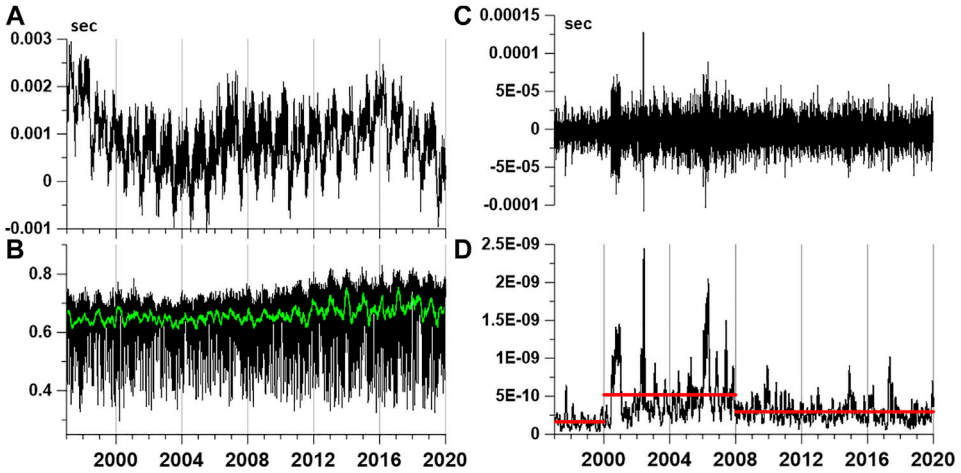

FIGURE 8 | (A) Values of the length of the day [time series length of day (LOD)]. **(B)** Mean values of the minimum normalized seismic noise entropy for all 50 control points in **Figure 3**; green line presents the moving average in a 57-day window. **(C)** High-frequency component of LOD with periods less than 6 days. **(D)** Variance of high-frequency LOD component within a moving time window of 28 days in length; red lines present mean values of variance in three successive time fragments: 1997–2000.106, 2000.106–2007.926, and 2007.926–2020.

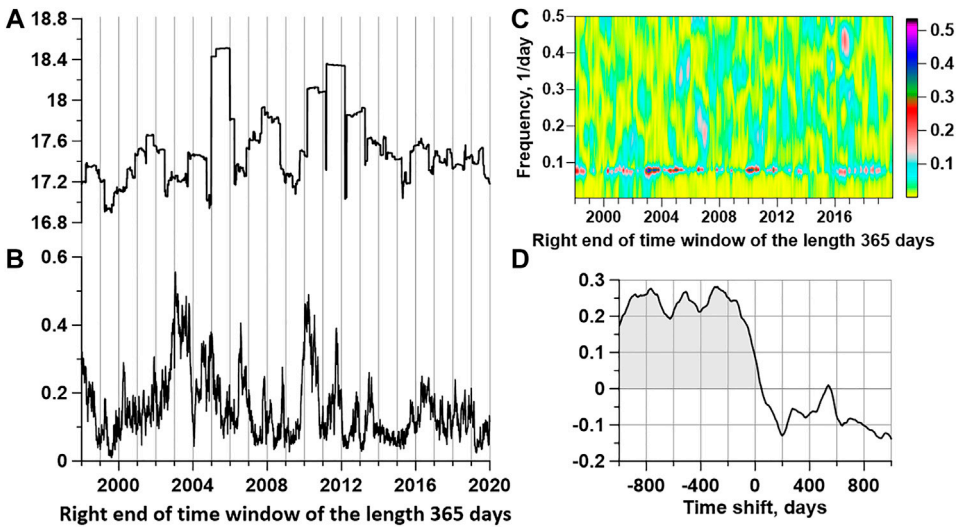

FIGURE 9 | (A) A plot of the decimal logarithm of the released seismic energy (Joules) in a sliding time window of 365 days. **(B)** The maximum values with respect to the frequencies of the quadratic coherence between length of day (LOD) and the average value of the entropy in a moving time window of 365 days. **(C)** A time-frequency diagram of the change in the quadratic coherence between the LOD time series and the average entropy value (see panel 8B) in a sliding window of 365 days long with an offset of 3 days. **(D)** The correlation function between the values of the logarithm of the released seismic energy and the maximum of coherence between the day length and the average value of entropy. Negative values of time shifts correspond to the lag in the release of seismic energy relative to bursts of coherence between LOD and noise entropy.

CONNECTION OF SEISMIC NOISE ENTROPY TO IRREGULARITY OF EARTH'S ROTATION

The influence of the irregularity of the Earth's rotation on the sequence of strong earthquakes has been studied in many works, for example, in (Shanker et al., 2001; Bendick and Bilham, 2017). This article continues the study of the relationship between the irregularity of rotation with the synchronization of the properties of seismic noise and the possible triggering effect of the irregular rotation of the planet on the seismic process, begun in (Lyubushin, 2020a; Lyubushin, 2020b).

Figures 8A,B present graphs of LOD) and mean noise entropy which is obtained by averaging all values from reference points (**Figure 3**). The data on the length of the day are taken from the International Earth Rotation and Reference Systems Service

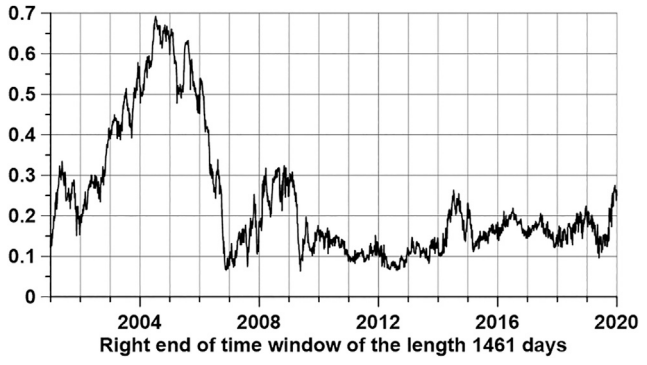

FIGURE 10 | Maximum values of the quadratic coherence between length of day and the average value of the entropy in a moving time window of 1,461 days (4 years).

(IERS) database from the address https://hpiers.obspm.fr/iers/eop/eopc04/eopc04.62-now.

Figure 8C is a graph of high-frequency LOD component with periods less than 6 days, and **Figure 8D** presents an estimate of variance of high-frequency LOD variations within moving time window of the length 28 days. We can notice that evolution of high-frequency LOD component variance could be split into three time intervals, 1997–2000.106, 2000.106–2007.926, and 2007.926–2020, with different mean values which are drawn by horizontal red lines. Bounds of three time intervals in fractional years were found automatically from minimum of variance of deflections from local mean values. The time interval 2000.106–2007.926 corresponds to high power of high-frequency LOD variations. This time interval is interpreted as the reason of abrupt changes in temporal and spatial correlations of global seismic noise properties which are presented in **Figure 4** (Lyubushin, 2020a; Lyubushin, 2020b).

Figure 9A shows the graphs of the logarithm of energy (Joules) released as a result of seismic events in the whole world in a moving time window of length 365 days with a 3-day shift, whereas **Figure 9B** is the parallel graph of bursts maxima of squared coherence between LOD and daily mean entropy in the same time windows. Information about global seismicity is taken from the USGS site from the address https://earthquake.usgs.gov/earthquakes/search/. The coherence estimation was performed using a 5th-order vector autoregressive model (Marple, 1987) with preliminary removal of linear trends and transition to increments. **Figure 9C** presents the time-frequency diagram of squared coherence evolution, and we can notice that bursts of coherence are mainly concentrated within narrow frequency band with periods from 11 up to 14 days. Estimates of maxima of squared coherence were already used in (Lyubushin, 2020a; Lyubushin, 2020b) when analyzing trends in the properties of global seismic noise and their relationships with the uneven rotation of the Earth.

From **Figures 9A,B**, it is visually noticeable that the curve of the logarithm of the released energy often lags after the curve of the maxima of the coherence spectrum when it is calculated in a moving time window.

Let us quantitatively estimate this shift by calculating their cross-correlation function for time shifts ± 1,000 days, the graph of which is shown in **Figure 9D**. From the estimate of the correlation function in **Figure 9D**, it can be seen that its values for negative time shifts significantly exceed the values for positive shifts, which confirms the fact that the release of seismic energy is delayed, relative to bursts of the coherence measure. As for the lag time, it is not determined unambiguously, since the values of the correlation function for negative shifts actually reach a certain plateau, which contains three local maximums for shifts of -280, -510, and -720 days.

The estimation of the coherence maxima between LOD and average entropy in a 4-year window deserves special attention. Since 1 year out of four consecutive years is a leap year, the length of the 4-year time window is 1,461 days. **Figure 10** shows a graph of estimates of the maxima of the quadratic coherence in a sliding time window with a length of 1,461 days with an offset of 3 days. Since the window length is four times larger than the previously used 365-day window, a model of the order 20 was used to estimate the coherence spectrum instead of the 5th-order autoregressive model.

The coherence estimate in **Figure 10** is interesting because before the Sumatran mega-earthquake at the end of 2004, after which the global seismic process began to activate, the coherence estimate reaches a very significant maximum, reaching almost 0.7. We interpret this peak of coherence as a manifestation of the triggering effect of the anomaly of the uneven rotation of the Earth, previously considered in (Lyubushin, 2020a; Lyubushin, 2020b).

CONCLUSION

Software tools have been developed to study the global low-frequency seismic noise recorded continuously from the beginning of 1997 to the end of 2019 on a network of 229 broadband seismic stations located around the world. The analyzed value is determined daily at the nodes of the auxiliary network of 50 reference points as the median of the Shannon information entropy of the distribution of the squares of the orthogonal wavelet coefficients of the seismic noise waveforms at the five nearest operable stations. The time interval from mid-2002 to mid-2003 was determined, when the downward trend of the average correlation of the noise entropy changed abruptly to an upward trend, which persists until the end of 2019. Along with the growth of the average correlation, an increase in the radius of spatial correlations of the noise entropy is observed, and the increasing trend of spatial correlations persists until the end of 2019 as well.

At the same time, with an increase in the average correlation, an increase in the radius of spatial correlations of the entropy of noise is observed, and after 2010, bursts of maximum distances between the reference points with strong pairwise entropy correlations, reaching 10–15 thousand km, began to appear.

These features of the behavior of global seismic noise are interpreted as a result of the triggering effect of the unevenness of the Earth's rotation on an increase in noise correlation and, at the same time, on an increase in the intensity of the strongest seismic events in the world after the Sumatran mega-earthquake of December 26, 2004, M = 9.3. This interpretation is confirmed by a correlation estimate of the seismic energy release lag in relation to bursts of coherence between the average entropy value and the length of the day when estimated in a sliding time window of 365 days.

The emergence of sharp bursts of an increase in the maximum distance between the reference points with a strong entropy correlation after 2010 can be associated with the destabilization of the global seismic noise field after two mega-earthquakes close in time: February 27, 2010, M = 8.8, in Chile and March 11, 2011, M = 9.1, in Japan. The persistence of an increasing trend of increasing average correlations of noise entropy and distances at which maximum correlations occur is interpreted as persistence of a high global seismic hazard that arose after 2004. A spatial measure of entropy correlations was introduced by extrapolating and averaging the numbers of strong correlations at each reference point in an annual sliding time window using a Gaussian smoothing kernel function. It turned out that areas of strong correlation are adjacent to the polar regions of the Earth, and for the period 1997–2019, the region of strong entropy correlation gradually moved from the south to the north.

DATA AVAILABILITY STATEMENT

Publicly available datasets were analyzed in this study. These data can be found as follows: http://www.iris.edu/mda/_GSN, http://www.iris.edu/mda/G, http://www.iris.edu/mda/GE, https://hpiers.obspm.fr/iers/eop/eopc04/eopc04.62-now, https://earthquake.usgs.gov/earthquakes/search/.

AUTHOR CONTRIBUTIONS

The author is the developer and programmer of all algorithms used in the article.

FUNDING

The research was supported by the Russian Foundation for Basic Research, Grant No. 18-05-00133, project "Estimation of fluctuations of seismic hazard on the basis of complex analysis of the Earth's ambient noise."

REFERENCES

Ardhuin, F., Stutzmann, E., Schimmel, M., and Mangeney, A. (2011). Ocean wave sources of seismic noise. *J. Geophys. Res.* 116, C09004. doi:10.1029/2011jc006952

Aster, R. C., McNamara, D. E., and Bromirski, P. D. (2008). Multidecadal climate-induced variability in microseisms. *Seismol Res. Lett.* 79, 194–202. doi:10.1785/gssrl.79.2.194

Bendick, R., and Bilham, R. (2017). Do weak global stresses synchronize earthquakes?. *Geophys. Res. Lett.* 44, 8320–8327. doi:10.1002/2017GL074934

Berger, J., Davis, P., and Ekström, G. (2004). Ambient earth noise: a survey of the global seismographic network. *J. Geophys. Res.* 109, B11307. doi:10.1029/2004jb003408

Costa, M., Goldberger, A. L., and Peng, C.-K. (2005). Multiscale entropy analysis of biological signals. *Phys. Rev. E* 71 021906. doi:10.1103/physreve.71.021906

Costa, M., Peng, C.-K., Goldberger, A. L., and Hausdorff, J. M. (2003). Multiscale entropy analysis of human gait dynamics. *Physica A* 330, 53–60. doi:10.1016/j.physa.2003.08.022

Duda, R. O., Hart, P. E., and Stork, D. G. (2000). *Pattern classification*. New York, Chichester, Brisbane, Singapore, Toronto: Wiley-Interscience Publication

Friedrich, A., Krüger, F., and Klinge, K. (1998). Ocean-generated microseismic noise located with the Gräfenberg array. *J. Seismol.* 2 (1), 47–64. doi:10.1023/a:1009788904007

Fukao, Y., Nishida, K., and Kobayashi, N. (2010). Seafloor topography, ocean infragravity waves, and background love and rayleigh waves. *J. Geophys. Res.* 115, B04302. doi:10.1029/2009jb006678

Grevemeyer, I., Herber, R., and Essen, H.-H. (2000). Microseismological evidence for a changing wave climate in the northeast Atlantic Ocean. *Nature* 408, 349–352. doi:10.1038/35042558

Kobayashi, N., and Nishida, K. (1998). Continuous excitation of planetary free oscillations by atmospheric disturbances. *Nature* 395, 357–360. doi:10.1038/26427

Koper, K. D., and de Foy, B. (2008). Seasonal anisotropy in short-period seismic noise recorded in South Asia. *Bull. Seismol. Soc. Am.* 98, 3033–3045. doi:10.1785/0120080082

Koper, K. D., Seats, K., and Benz, H. (2010). On the composition of Earth's short-period seismic noise field. *Bull. Seismol. Soc. Am.* 100 (2), 606–617. doi:10.1785/0120090120

Koutalonis, I., and Vallianatos, F. (2017). Evidence of non-extensivity in earth's ambient noise. *Pure Appl. Geophys.* 174, 4369–4378. doi:10.1007/s00024s-017-1669-9

Lyubushin, A. (2012). Prognostic properties of low-frequency seismic noise. *Nat. Sci.* 4, 659–666. doi:10.4236/ns.2012.428087

Lyubushin, A. (2013). How soon would the next mega-earthquake occur in Japan? *Nat. Sci.* 5, 1–7. doi:10.4236/ns.2013.58A1001

Lyubushin, A. (2018). "Synchronization of geophysical fields fluctuations -," in *Complexity of seismic time series: measurement and applications*. Editors T. Chelidze, L. Telesca, and F. Vallianatos (Amsterdam, Oxford, Cambridge: Elsevier 2018), Chap. 6, 161–197.

Lyubushin, A. (2020a). Trends of global seismic noise properties in connection to irregularity of Earth's rotation. *Pure Appl. Geophys.* 177 (2), 621–636. doi:10.1007/s00024-019-02331-z

Lyubushin, A. A. (2014). Analysis of coherence in global seismic noise for 1997–2012. *Izvestiya Phys. Solid Earth.* 50 (3), 325–333. doi:10.1134/s1069351314030069

Lyubushin, A. A. (2015). Wavelet-based coherence measures of global seismic noise properties. *J. Seismol.* 19 (2), 329–340. doi:10.1007/s10950-014-9468-6

Lyubushin, A. A. (2017). Long-range coherence between seismic noise properties in Japan and California before and after Tohoku mega-earthquake. *Acta Geod. Geophys.* 52, 467–478. doi:10.1007/s40328-016-0181-5

Lyubushin, A. A. (2020c). Seismic noise wavelet-based entropy in southern California. *J. Seismol.* doi:10.1007/s10950-020-09950-3

Lyubushin, A. (2020b). Connection of seismic noise properties in Japan and California with irregularity of Earth's rotation. *Pure Appl. Geophys.* 177, 4677–4689. 10.1007/s00024-020-02526-9

Mallat, S. A. (1999). *Wavelet tour of signal processing*. 2nd Edn. San Diego, London, Boston, New York, Sydney, Tokyo, Toronto: Academic Press

Marple, S. L., and Jr (1987). Digital spectral analysis with applications. Englewood Cliffs, NJ: Prentice-Hall, Inc.

Nishida, K., Kawakatsu, H., Fukao, Y., and Obara, K. (2008). Background love and rayleigh waves simultaneously generated at the Pacific Ocean floors. *Geophys. Res. Lett.* 35, L16307. doi:10.1029/2008gl034753

Nishida, K., Montagner, J.-P., and Kawakatsu, H. (2009). Global surface wave tomography using seismic hum. *Science* 326 (5949), 112. doi:10.1126/science.1176389

Rhie, J., and Romanowicz, B. (2004). Excitation of Earth's continuous free oscillations by atmosphere-ocean-seafloor coupling. *Nature* 431, 552–554. doi:10.1038/nature02942

Rhie, J., and Romanowicz, B. (2006). A study of the relation between ocean storms and the Earth's hum. *Geochem. Geophys. Geosyst.* 7 (10). doi:10.1029/2006gc001274

Sarlis, N. V., Skordas, E. S., Mintzelas, A., and Papadopoulou, K. A. (2018). Micro-scale, mid-scale, and macro-scale in global seismicity identified by empirical mode decomposition and their multifractal characteristics. *Sci. Rep.* 8, 9206. doi:10.1038/s41598-018-27567-y

Shanker, D., Kapur, N., and Singh, V. P. (2001). On the spatio temporal distribution of global seismicity and rotation of the earth - a review. *Acta Geod. Geophys. Hung.* 36, 175. doi:10.1556/ageod.36.2001.2.5

Stehly, L., Campillo, M., and Shapiro, N. M. (2006). A study of the seismic noise from its long-range correlation properties. *J. Geophys. Res.* 111, B10306. doi:10.1029/2005jb004237

Tanimoto, T. (2001). Continuous free oscillations: atmosphere-solid earth coupling. *Annu. Rev. Earth Planet. Sci.* 29, 563–584. doi:10.1146/annurev.earth.29.1.563

Tanimoto, T. (2005). The oceanic excitation hypothesis for the continuous oscillations of the Earth. *Geophys. J. Int.* 160, 276–288. doi:10.1111/j.1365-246X.2004.02484.x

Vallianatos, F., Koutalonis, I., and Chatzopoulos, G. (2019). Evidence of Tsallis entropy signature on medicane induced ambient seismic signals. *Physica A* 520, 35–43. doi:10.1016/j.physa.2018.12.045

Varotsos, P. A., Sarlis, N. V., and Skordas, E. S. (2011). "Precursory seismic electric signals, earthquakes and other complex time series," in *Natural time analysis: the new view of time*. Berlin, Heidelberg: Springer-Verlag, 449.

Conflict of Interest: The authors declare that the research was conducted in the absence of any commercial or financial relationships that could be construed as a potential conflict of interest.

Copyright © 2020 Lyubushin. This is an open-access article distributed under the terms of the Creative Commons Attribution License (CC BY). The use, distribution or reproduction in other forums is permitted, provided the original author(s) and the copyright owner(s) are credited and that the original publication in this journal is cited, in accordance with accepted academic practice. No use, distribution or reproduction is permitted which does not comply with these terms.

frontiers in Earth Science

ORIGINAL RESEARCH
published: 24 November 2020
doi: 10.3389/feart.2020.540398

A Multiparametric Approach to Study the Preparation Phase of the 2019 M7.1 Ridgecrest (California, United States) Earthquake

Angelo De Santis[1], Gianfranco Cianchini[1], Dedalo Marchetti[1,2], Alessandro Piscini[1], Dario Sabbagh[1], Loredana Perrone[1], Saioa Arquero Campuzano[1†] and Sedat Inan[1†]*

[1]Istituto Nazionale di Geofisica e Vulcanologia, Roma, Italy, [2]School of Remote Sensing and Geomatics Engineering, Nanjing University of Information Science and Technology, Nanjing, China

The 2019 M7.1 Ridgecrest earthquake was the strongest one in the last 20 years in California (United States). In a multiparametric fashion, we collected data from the lithosphere (seismicity), atmosphere (temperature, water vapor, aerosol, and methane), and ionosphere (ionospheric parameters from ionosonde, electron density, and magnetic field data from satellites). We analyzed the data in order to identify possible anomalies that cannot be explained by the typical physics of each domain of study and can be likely attributed to the lithosphere-atmosphere-ionosphere coupling (LAIC), due to the preparation phase of the Ridgecrest earthquake. The results are encouraging showing a chain of processes that connect the different geolayers before the earthquake, with the cumulative number of foreshocks and of all other (atmospheric and ionospheric) anomalies both accelerating in the same way as the mainshock is approaching.

Keywords: earthquake, lithosphere-atmosphere-ionosphere coupling, multiparametric approach, earthquake precursor anomalies, earthquake preparation process

OPEN ACCESS

Edited by:
Giovanni Martinelli, National Institute of Geophysics and Volcanology, Italy

Reviewed by:
Michael Emmanuel Contadakis, Aristotle University of Thessaloniki, Greece
Jing Liu, China Earthquake Administration, China

****Correspondence:***
Angelo De Santis
angelo.desantis@ingv.it

†Present address:
Saioa Arquero Campuzano, Instituto de Geociencias IGEO (CSIC-UCM), Madrid, Spain
Sedat Inan, Faculty of Mines, Department of Geological Engineering, Istanbul Technical University, Istanbul, Turkey

Specialty section:
This article was submitted to Solid Earth Geophysics, a section of the journal Frontiers in Earth Science

Received: *04 March 2020*
Accepted: *25 September 2020*
Published: *24 November 2020*

Citation:
De Santis A, Cianchini G, Marchetti D, Piscini A, Sabbagh D, Perrone L, Campuzano SA and Inan S (2020) A Multiparametric Approach to Study the Preparation Phase of the 2019 M7.1 Ridgecrest (California, United States) Earthquake. Front. Earth Sci. 8:540398. doi: 10.3389/feart.2020.540398

INTRODUCTION

The 2019 Ridgecrest seismic sequence started on July 4, 2019: many small magnitude events (Ml ~ 0) preceded by 2 h the major earthquake with a 6.4 magnitude (Ross et al., 2019), occurred at 17:33 UTC on 4 July and now considered as the largest foreshock. The sequence of foreshocks continued with numerous events with magnitude from intermediate to large (e.g., an M5.4 about 16 h, and an M5.0 almost 3 min before the mainshock) culminating with the M7.1, which struck on 6 July at 03:19 UTC. This earthquake was the most powerful event occurring in California in the last 20 years (after the M7.1 1999 Hector Mine earthquake, e.g., Rymer et al., 2002). These major shocks occurred north and northeast of the town of Ridgecrest, California (about 200 km north-northeast of Los Angeles). After 21 days, they were followed by more than 111,000 aftershocks (M > 0.5, Ross et al., 2019), mainly within the area of the Naval Air Weapons Station China Lake (California).

Recent works on the Ridgecrest seismic sequence revealed much of the complexity of the seismic source of the major ruptures and relative mechanisms (e.g., Barnhart et al., 2019; Ross et al., 2019; Chen et al., 2020), but nothing was investigated about the preparation phase of the seismic sequence and its possible coupling with the above geolayers, such as the atmosphere and ionosphere. This article intends to fill the gap.

We know how much difficult the study of what happens before a large earthquake is and how controversial the concept of preparation phase of an earthquake is within the scientific community.

Nevertheless, it is rather difficult to think that a so large energetic phenomenon such as a strong earthquake cannot provide any sign of its preparation (e.g., Sobolev et al., 2002; Bulut 2015). With this work, we want to give a fundamental contribution to the study of the preparation phase of earthquakes, considering the case study of the 2019 Ridgecrest seismic sequence.

The idea of an interconnected planet where all its parts interact each other is known as geosystemics (De Santis, 2009; De Santis, 2014) and it is a very interesting concept to apply to the study of earthquakes (De Santis et al., 2019a). This idea suggests that the best way to study Earth's physical phenomena is a multiparametric analysis. This means that, in order to understand how some processes work, we need to analyze different parameters from the area of interest, originating from different sources. In the particular case of earthquakes, the lithosphere-atmosphere-ionosphere coupling (LAIC) proposes a relation between events occurred in lithosphere, atmosphere, and ionosphere that could precede the occurrence of large earthquakes. Therefore, the study of the preparation phase of large earthquakes, as this one in California, can be especially useful to identify possible precursors. There exist different models to explain how these three layers could be linked to each other. A model predicts at fault level the existence of p-holes (positive holes) that, once released at the surface, are able to ionize the atmosphere (Freund, 2011; Freund, 2013) and finally reach the ionosphere. Another model is based on a gas or fluid (such as radon) that can be released by the lithosphere during the preparation phase of earthquake (Pulinets and Ouzounov, 2011; Hayakawa et al., 2018). Both models foresee the creation of a chain of processes that connects the lithosphere to the atmosphere and then to the ionosphere.

In this work, we analyze data from the lithosphere (earthquakes), atmosphere (temperature, water vapor, aerosol, and methane), and ionosphere (e.g., electron density, magnetic field, and other ionospheric parameters) in order to possibly identify the chain of processes preceding the seismic sequence of concern. Limited ground-based observations have been also incorporated. Such an approach demonstrated its powerful capability also in some previous case studies (e.g., Akhoondzadeh et al., 2018; Akhoondzadeh et al., 2019; Marchetti et al., 2019a; Marchetti et al., 2019b; Marchetti et al., 2020), when the view of the earthquake is wider (geosystemic view) and includes all the geolayers involved in the processes (De Santis et al., 2019a; De Santis et al., 2019b).

Being a multiparametric approach, the statistics we applied in this article depends on the parameter and its historical availability (e.g., while atmospheric data have a long history of about 40 years, the satellite data are rather short, about 6 years, so we had to resort to another approach). For the single parameters and their methodology of analysis, we already conducted some statistical validations in our previous works, i.e., skin temperature and total column water vapor analyzed by Climatological Analysis for seismic PRecursor Identification (CAPRI) algorithm have been statistically demonstrated to be successfully related as EQ-precursors in Central Italy in the last 25 years (with 73–74% of overall accuracy; Piscini et al., 2017). The accelerated moment release (AMR) seismic methodology has been successfully validated on 14 medium-large earthquakes (M6.1–M8.3), providing statistical evidence on this set of events that the technique is able to detect a seismic acceleration (Cianchini et al., 2020).

DATA ANALYSES

A seismic characterization of the sequence was conducted by inspecting data collected by the Southern California Earthquake Data Center (SCEDC): we downloaded its catalog from January 1, 2000, to November 13, 2019 (last visit November 14, 2019).

Then, we restricted the events in time (t), depth (z), and magnitude (M) by setting the threshold values to $2000.0 \leq t < 2019.51$ (this latter being the mainshock origin time in decimal year), $z \leq 50$ km and $M \geq 2$, respectively: from now on, this is the complete catalog considered for our analyses. **Figure 1** represents the seismicity of South California as emerged by the imposed limits. The epicenter and the focal mechanism of the M7.1 mainshock are shown. The thick white line shows approximately (more detailed in **Figure 2** by Ross et al., 2019) the projection on the surface of the rupture plane as is depicted by the sequence of the aftershocks. In evidence, a green star shows the strongest foreshock (M6.4), which preceded by almost 34 h the main event, indicated by a red star.

The Ridgecrest sequence occurred in a region with a prevailing NW-SE faulting trend, almost parallel to the more famous San Andreas Fault. The double-couple solution obtained by the U.S. Geological Survey (USGS) indicates that it could have been due to either a right NW-SE or a left NE-SW slip, the former being the more reasonable, if we consider that this fault lays approximately 150 km NE of San Andreas Fault and that the Pacific Plate moves to the NW with respect to the North America Plate (USGS, https://earthquake.usgs.gov/earthquakes/eventpage/ci38457511/executive, last visit January 08, 2020): a confirmation of that is offered by the GPS data analysis conducted by Ross et al. (2019) (please see their Supplementary Figure S13). The "pervasive orthogonal faulting" (Ross et al., 2019) of the area is the origin of a certain degree of geometric complexity: indeed, the largest foreshock was expression of the NE-SW trending fault, orthogonal to that of the M7.1 event.

In the past, around 2002, a former seismic sequence occurred almost in the same area of Ridgecrest, where the recent M7.1 seismic event has been localized (Ross et al., 2019). In order to better analyze the recent Ridgecrest seismicity, we further restricted the time and spatial intervals to those events, which occurred starting from January 1, 2000, confined by a circular area whose radius is 100 km and centered in the epicenter. The obtained catalog of the events in this circular area shows some interesting features: the plot on top of **Figure 2** represents the time-magnitude distribution of the selected events where, in particular, the red color identifies all the events, which fall onto the superficial projection of the fault plane (thick white line in **Figure 1**); on the bottom, the cumulative number of the events is reported: it increments earthquake by earthquake, i.e., as a new earthquake occurs. It is evident that around the first half of 2001, the Ridgecrest fault area was hit by a sequence whose maximum magnitude was a

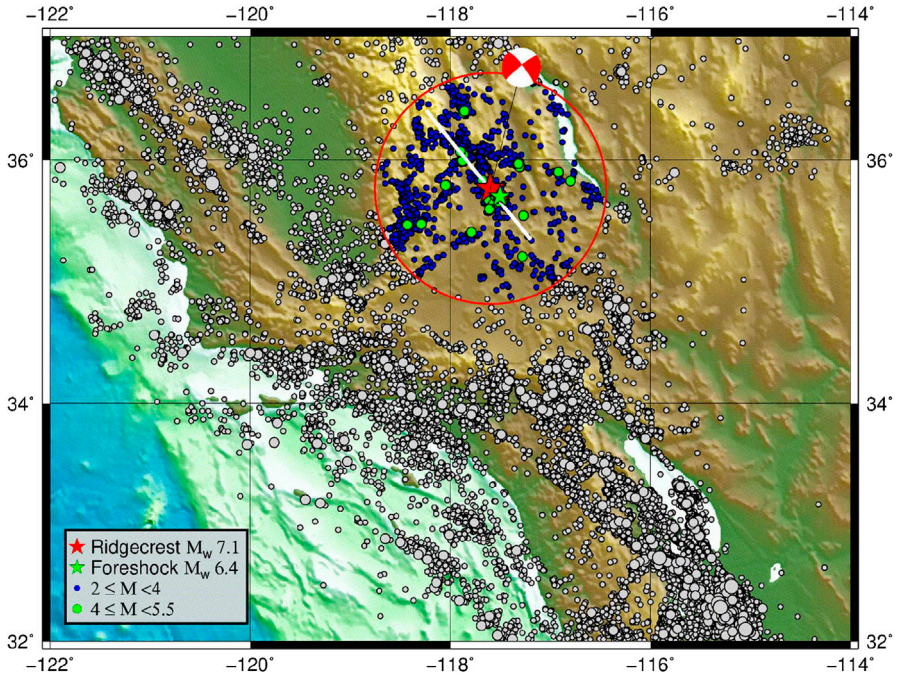

FIGURE 1 | Spatial distribution of earthquake epicenters from 2000 to 2019.5. The thick white line at the central top represents approximately the projection on the surface of the rupture plane, which has been depicted by the aftershocks of the Ridgecrest main event (realized by the GMT Tool). The red circle has a radius of 100 km and is explained in the text. The earthquakes outside the circular areas are presented without colors, but the size corresponds to the range of magnitudes.

bit larger than 5. Although many other events followed this sequence and rarely exceeded magnitude 4, it was only around 2010 that another shorter sequence took place: even in that case, the maximum magnitude did not exceed M4. Please note the steep accumulation of events at the end of the figure. When focusing on approximately the previous month before the mainshock to better inspect the distribution of the earthquakes (**Figure 2**), we can check that no significant event occurred on the fault, except for the earlier 2 days when many earthquakes, several M4+, hit the area, starting from (triggered by) the M6.4 foreshock.

One of the features of the seismic sequences is its accelerating character, i.e., the increase in the rate of earthquake occurrence, which can appear in a region before a large earthquake: this is called AMR, whose physical model promoted by Bowman et al. (1998) is based on the hypothesis that stress changes in the lithosphere lead to an increase in the rate of smaller sized earthquakes before a mainshock. Here, for clarity purpose, we give only the formulation of the quantities involved in the analysis: for a complete discussion of this topic, please refer to De Santis et al. (2015).

To take into account the cumulative effect of a series of N earthquakes at the time t of the last N-th earthquake on a fault, Benioff (1949) introduced the quantity $s(t)$, now called cumulative Benioff strain:

$$s(t) = \sum_i \sqrt{E_i} = \sum_{i=1}^{N(t)} 10^{2.4} 10^{0.75 \cdot M_i}, \quad (1)$$

where the energy in Joule $E_i = (10^{1.5M_i+4.8})$ of the i-th event as a function of its magnitude is involved (De Santis et al., 2015). The AMR can be estimated by looking at the power-law behavior with time of $s(t)$, as given by the following form:

$$s(t) = A + B \cdot \left(t_f - t\right)^m, \quad (2)$$

where $A > 0$, $B < 0$, $t_f > 0$, and $0 < m < 1$ are sequence-dependent "constant" parameters to be determined through a fit to $s(t)$ (**Figure 3**). In theory, t_f would represent the time of failure of the earthquake fault.

A measure of presence for acceleration is the so-called *C-factor* (Bowman et al., 1998) defined as the ratio between the root mean square errors for the power law and the linear fit: when $C < 1$ significantly, then acceleration is meant to be present.

The initial time and the threshold in the minimum magnitude of earthquakes for the AMR analysis are usually a subjective choice: we preferred to be conservative and decided that 5 years of M4+ data were sufficient to detect any possible acceleration in the data. **Figure 3** shows the AMR analysis applied to the events with M4+ occurred in the selected region from 2013.0 to the M7.1 origin time (excluded): blue dots represent the cumulative Benioff strain $s(t)$; the black lines and the red curve are their linear and power-law fits, respectively. We note that the power-law curve fits better data as even *C-factor* confirms, being well below 1 (C = 0.46). However, the most impressive fact is that the acceleration is driven by the rapid sequence of earthquakes happening just after the M6.4 foreshock, i.e., 2 days before the large event, and that

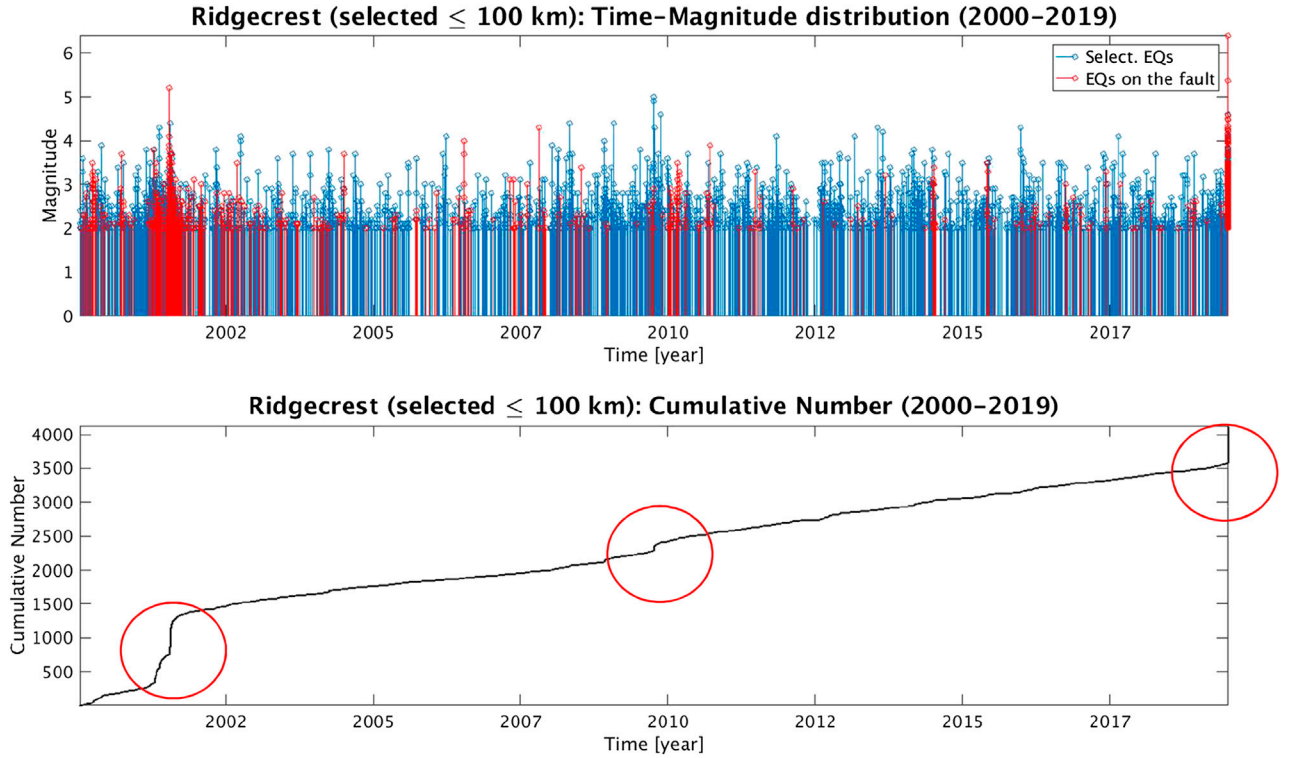

FIGURE 2 | (Top) Time-magnitude distribution of the seismicity in the circular area of 100 km radius around the epicenter of the M7.1 mainshock since January 1, 2000. The earthquakes which are on the fault are indicated with red lines. **(Bottom)** The cumulative number of earthquakes in the same area. At least three sequences can be recognized (as evidenced by red circles): the first, a long lasting one, in 2001, where the largest magnitude exceeded M5; the second, shorter, around the beginning of 2010, whose largest magnitude slightly went beyond M4 and the last concentrated within just 2 days before the 2019 mainshock.

most of the events occurred on the mainshock fault plane, as evidenced by the use of the red color for them.

Atmosphere

Regarding the atmosphere and how it is possibly affected by the preparation phase of the earthquake, we analyze four different parameters, i.e., skin temperature (skt), total column water vapor (tcwv), aerosol optical thickness (AOT), and methane (CH4) concentration, in an adequate region around the mainshock epicenter. Each parameter is taken at some epoch (day, year) as spatial mean of the considered region. In addition to the typical parameters that we already analyzed in previous works, such as skt and tcwv (Piscini et al., 2017) and AOT (Marchetti et al., 2019a; Marchetti et al., 2019b; Piscini et al., 2019), we also considered CH_4 since it seems a potential precursor of seismic activity from recent studies (e.g., Cui et al., 2019).

With regard to the land data, skt and tcwv have been collected from European Centre for Medium-Range Weather Forecasts (ECMWF), the meteorological European center that provides meteo-climatological observations and forecasts. The real time observations are provided in a global model called "operational archive" that is the base for the forecast. The elaboration of the measurements for long-term studies is constantly inserted in another climatological model called "Era-Interim" (ECMWF is now updating to Era-5). The year of interest has been compared to ERA-Interim historical time series. This dataset is a global atmospheric reanalysis project that uses satellite data (European remote sensing satellite, EUMETSAT, and others), input observations prepared for ERA-40, and data from ECMWF's operational archive. Starting from January 1, 1979, it is continuously updated in real time (Dee et al., 2011). The data have been extracted with a spatial resolution of 0.5° corresponding to a resolution of around 50 km.

The AOT has been retrieved from climatological physical-chemical model MERRA-2 (Modern-Era Retrospective Analysis for Research and Applications, version 2, Gelaro et al., 2017) provided by NOAA in the sub-dataset M2T1NXAER version 5.12.4. The data have a spatial resolution of 0.625° longitude and 0.5° latitude and a temporal resolution of 1 h. For this study, the values of skt, tcwv, and AOT closer to the local midnight have been considered to avoid disturbances induced by the daily solar variability. Moreover, the data from 1980 to 2019 have been analyzed, using the data from 1980 to 2018 to construct the historical time series and 2019 to investigate the earthquake preparation phase.

The square area selected for the above three parameters is centered on the mainshock epicenter and the size is selected inside the Dobrovolsky strain radius of $10^{0.43 \cdot M}$ = 1,130 km (Dobrovolsky et al., 1979), which approximates the large-scale

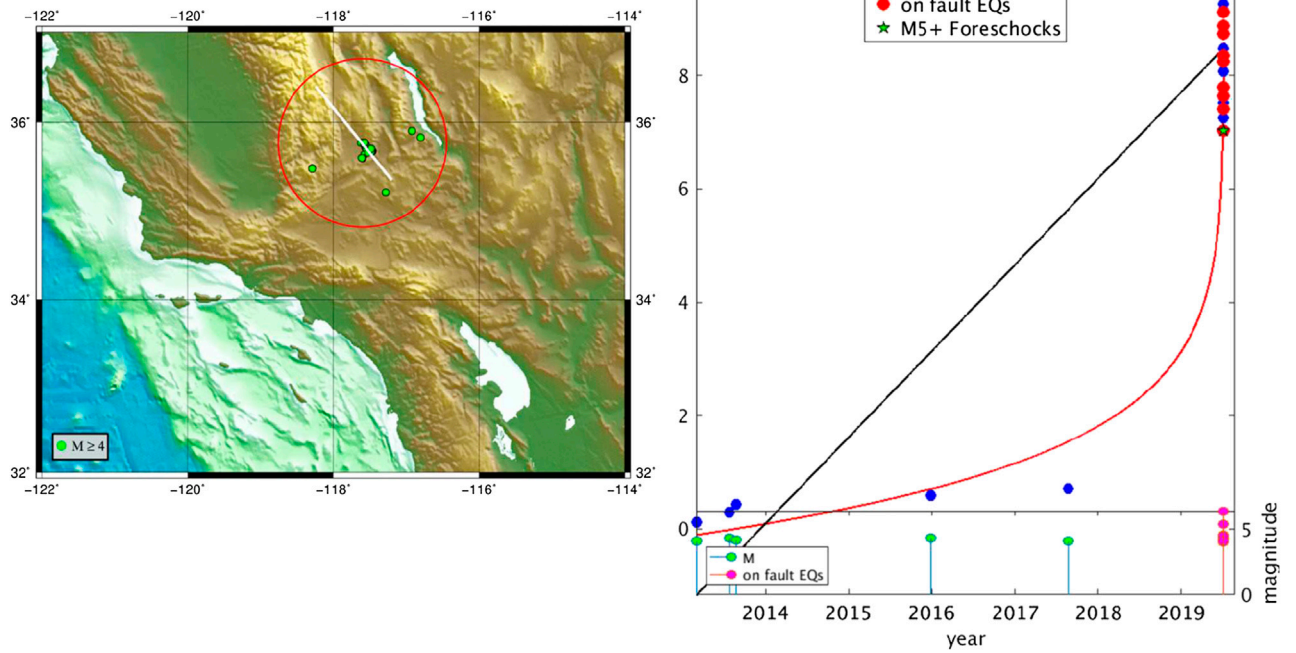

FIGURE 3 | (Left) Geographical map with the M4+ earthquakes, selected since 2013.0 until the mainshock origin time, inside the 100 km radius circle for the accelerated moment release (AMR) analysis. **(Right)** The results of the AMR technique applied together with the temporal sequence of earthquake magnitudes. We notice an acceleration mostly occurring in the few days preceding the mainshock. Two green stars show the largest foreshocks, i.e., the M6.4 and M5.4.

region where seismic precursors are usually expected around the impending faults.

The methane measurements are given as a daily product extracted from atmospheric infrared sounder (AIRS) instrument onboard NASA Earth observation system satellite Aqua provided separately for ascending and descending orbits, so the first one corresponds to daytime (1:30 PM local time at the equator) and the second one to the nighttime (1:30 AM local time at the equator). The satellite was launched into Earth's orbit on May 4, 2002, and it is still in orbit. The instrument is based on a multispectral microwave detector (2,378 channels) that permits to monitor the atmosphere determining the surface temperature, water vapor, cloud, and overall the greenhouse gases concentrations such as ozone, carbon monoxide, carbon dioxide, and methane (Fetzer et al., 2003). In this study, we analyzed the methane volume mixing ratio data (variable CH4_VMR_D) retrieved from level 3 dataset version 6.0.9.0 from 2002 until the 2019 California earthquake only descending orbits, i.e., nighttime at about 1:30 AM. These measurements come directly from the instrument, so differently from investigated data of skt, tcwv, and AOT, the coverage depends on the orbit and so not the whole world is covered for each day. To have some data for every day, we selected an area sufficiently large, but this means to mediate different parts of the same region. For methane data, the area is smaller than the Dobrovolsky area, because it is very sensitive to anthropic activity (e.g., Le Mer and Roger, 2001). In fact, this quantity has been selected in a circle (distance of the center of the pixel from epicenter not greater than 2.0°). As methane is a powerful greenhouse gas, we applied the "global warming" correction (see next paragraph for details).

For all parameters, we essentially applied the method CAPRI or MEANS ("MErra-2 ANalysis to search Seismic precursors" that does not include the "global warming"; see below), already introduced by Piscini et al. (2017) and Piscini et al. (2019) and applied both to seismic and volcanic hazards. These methods compare the present values of the parameter of interest with the corresponding historical time series, i.e., the background, in terms of mean and standard deviation (σ).

The CAPRI algorithm searches for anomalies in the time series of climatological parameters by a statistical analysis. Before being processed, the data are spatially averaged day-by-day selecting those over the land only by applying a land-sea mask because the sea tends to stabilize most of the atmospheric parameters (especially temperature), attenuating all eventual anomalies. Then, the algorithm removes the long-term trend over the whole day-by-day dataset mainly to remove a possible "global warming" effect, which is particularly important in skt and

methane. For analogy, we removed the "global warming" effect also to tcwv data, but of course not to AOT because this parameter cannot be affected by a global warming. The data of the time series are averaged over all the years, thus obtaining the average value of a particular day over the past 40 years. Then, to make the comparison feasible, we impose the (operational archive) average value in the period analyzed to coincide with the average of the historical (ERA-Interim) time series, by a simple subtraction. Finally, an anomaly is defined when the present value overcomes the historical mean by two standard deviations. Since with both CAPRI and MEANS approaches there is an uncertainty of 1–2 days in the background, the detected anomaly should also emerge clearly such as a shift by 2–3 days (to be conservative) does not cover the data by the background.

Skin Temperature

This parameter shows three anomalies (**Figure 4**). We exclude the first two (blue circles) because there is not a clear emergence from the historical time series: shifting the peaks by a few days, they could be covered by the typical signal and its variations. On the other hand, the red circle indicates an evident anomaly around 25 days before the mainshock, clearly emerging by more than 2σ the historical time series. In addition, it is also characterized by a two-day persistence. The negative anomaly on around 16 March is not considered because a LAIC model expects only positive increments of temperature due to the earthquake preparation (e.g., Pulinets and Ouzounov, 2011).

Total Column Water Vapor

For the water vapor, we can see one anomaly, which does not clearly emerge from the historical time series (**Figure 5**) and, in addition, it is not persistent. Hence, we consider this anomaly unlikely associated to the earthquake preparation phase.

Aerosol Optical Thickness

AOT is more irregular in time with respect to the two previous parameters. For this reason, we prefer to estimate the mean and standard deviation for a longer time period (6 months instead of 4). The analysis of AOT (**Figure 6**) shows two possible anomalies but only that one around two months before the mainshock looks more reliable: although not persistent, it clearly emerges from the overall background. In this case, the historical time series starts in 1980, because no data are available before this year. MEANS algorithm automatically excluded the 1982 and 2009 datasets because some of their values are particularly anomalous (i.e., greater than 10σ with respect to a preliminary estimation of the historical mean).

Methane

As for AOT, we extended the analysis to 6 months before the mainshock also for methane because it is more irregular than skt and tcwv: **Figure 7** shows the analysis. Please note that the historical time series of CH_4 concentration is computed over a time interval (2002–2018) much shorter than that of the previous climatological quantities (1979–2018 for both historical skt and tcwv time series; 1980–2018 for AOT), because the methane parameter is temporally limited by the AQUA satellite availability. The first apparent CH_4 anomaly (blue circle) is not considered, because there is a close peak (by a few days) in the historical time series, so it could be within 2σ if we shift this point by 2–3 days. The second anomaly, at around 70 days from the mainshock (red circle), is considered significant instead, being clearly emerging from the 2σ band. The negative anomaly on around 15 January is not considered because a reliable LAIC model

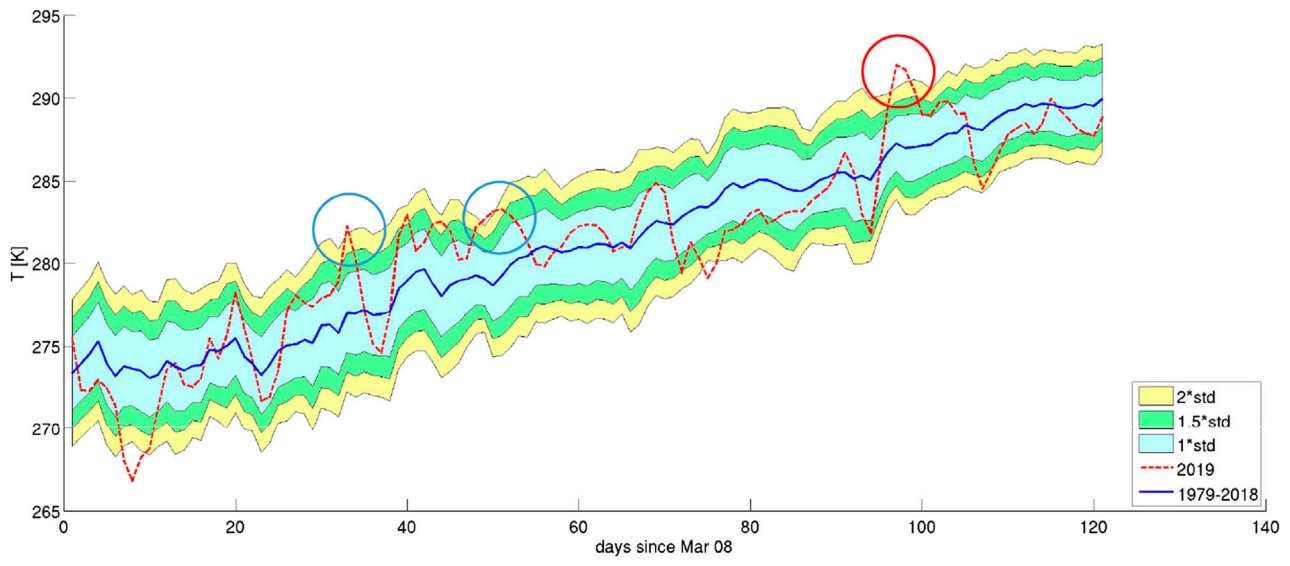

FIGURE 4 | Skin temperature (skt) in the 4 months before the mainshock compared with the historical time series of the previous 40 years. The blue line is the historical mean, while the colored bands present the 1 (light blue), 1.5 (green), and 2 (yellow) standard deviations. Blue circles are anomalies that do not emerge clearly from the 2σ background, while the red circle shows a clear anomaly.

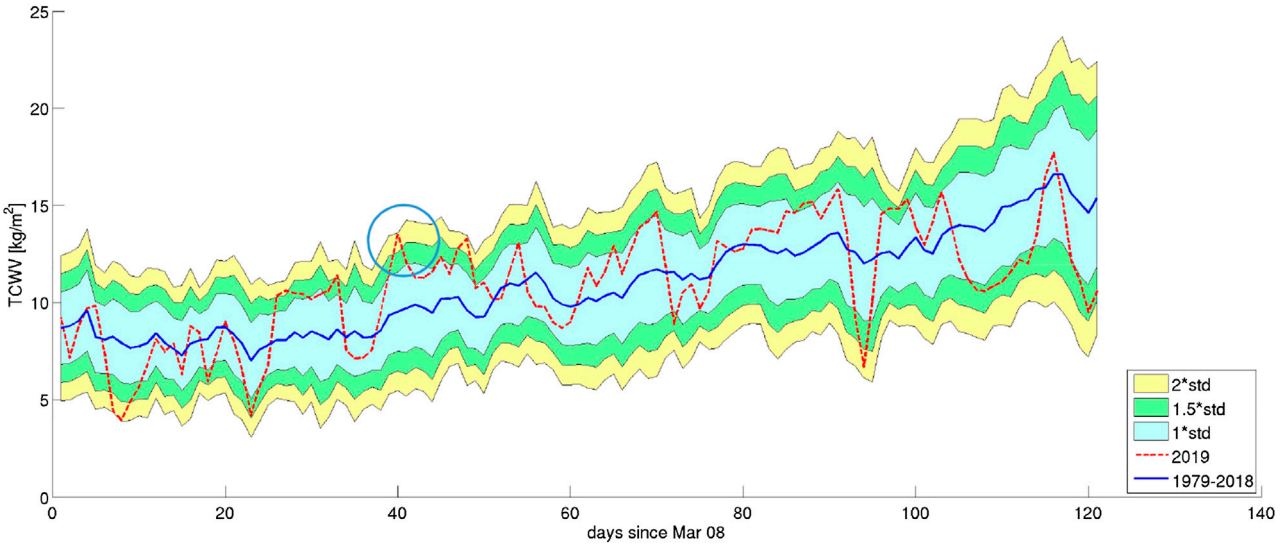

FIGURE 5 | Total column water vapor (tcwv) in the 4 months before the mainshock compared with the historical time series of the previous 40 years. The blue line is the historical mean, while the colored bands present the 1 (light blue), 1.5 (green), and 2 (yellow) standard deviations. The blue circle indicates an anomaly that does not emerge clearly from the 2σ background.

expects a release from underground sources, i.e., a positive increment due to the earthquake preparation.

Ionosphere

Ionosonde

In order to search for possible pre-earthquake ionospheric anomalies, the method proposed by Korsunova and Khegai (2006) and Korsunova and Khegai (2008) and successively developed by Perrone et al. (2010), Perrone et al.(2018), and Ippolito et al. (2020) for ionosonde data was applied here. A peculiar feature of this method is the multi-ionospheric parameter approach, which takes into account the variations of sporadic E (Es) and regular F2 layers occurred simultaneously during magnetically quiet conditions (Perrone et al., 2010; Perrone et al. 2018; Ippolito et al., 2020). The occurrence of the abnormally high Es layer with $\Delta h'$Es ≥ 10 km is considered followed by an increase over 20% in f_oEs (maximum frequency of the ionogram trace associated to the Es layer) and over 10% in f_oF2 (critical frequency of the F2 layer) within

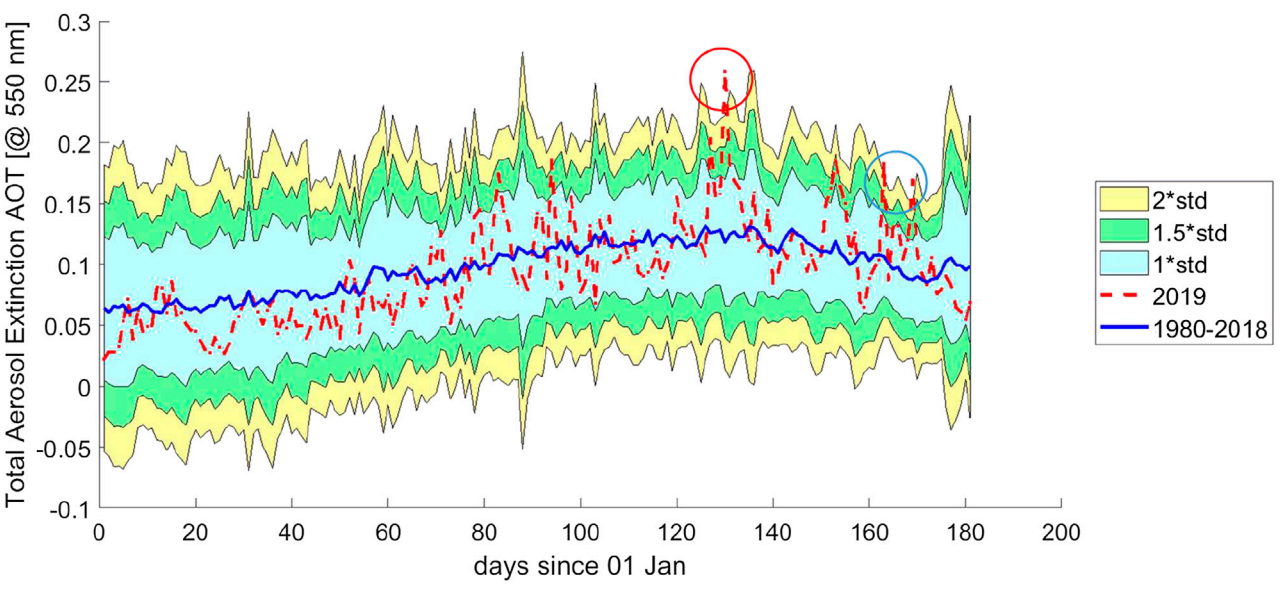

FIGURE 6 | Aerosol optical thickness (AOT) in the 6 months before the mainshock, compared with the historical time series of the previous almost 40 years. The blue line is the historical mean, while the colored bands present the 1 (light blue), 1.5 (green), and 2 (yellow) standard deviations. The blue circle indicates two distinct anomalies that do not emerge clearly from the 2σ background, while the red circle shows a clear anomaly.

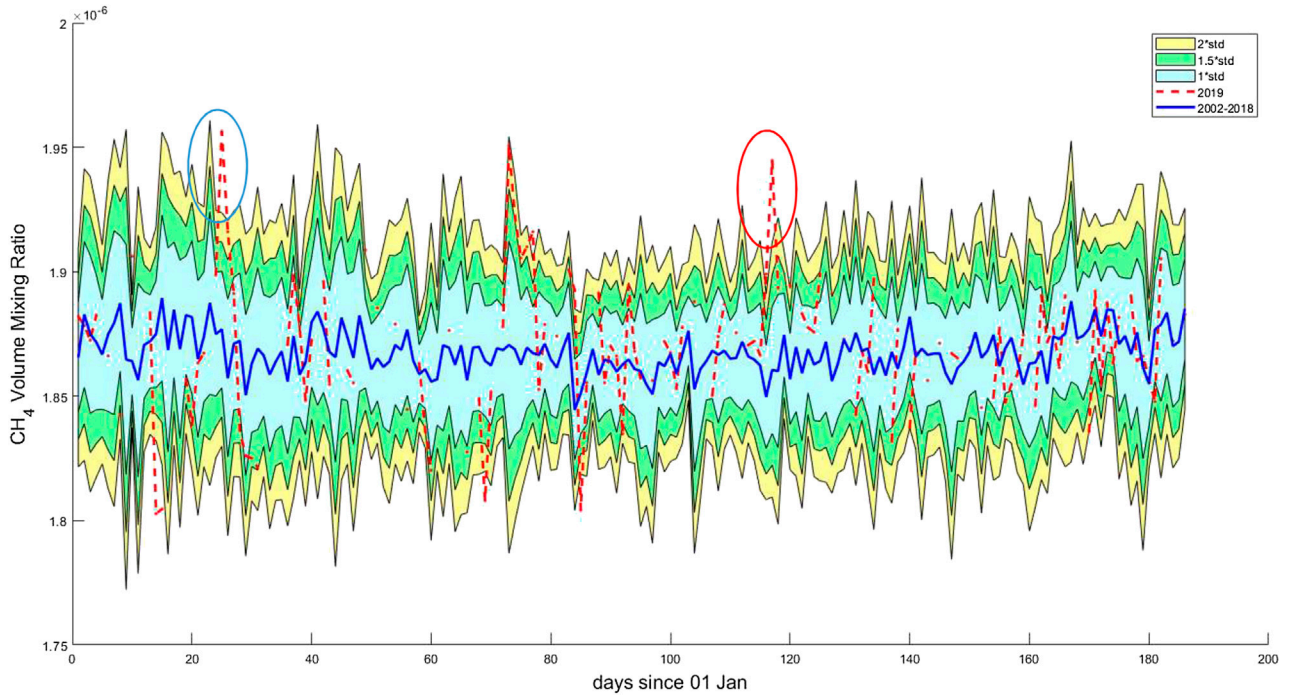

FIGURE 7 | Methane (CH4) concentration in the 6 months before the mainshock compared with the historical time series of the previous almost 20 years. The blue line is the historical mean, while the colored bands present the 1 (light blue), 1.5 (green), and 2 (yellow) standard deviations. The blue circle indicates an anomaly that does not emerge clearly from the 2σ background, while the red circle shows a clear anomaly.

one day for 2–3 h, where the variations are computed w.r.t. 27-days running medians.

Applying the method to the hourly data from the ionosonde of Point Arguello (34.7°N, 239.4°E; distant around 264 km from the epicenter), we recognize a possible pre-earthquake ionospheric anomaly from 22:00 UT on 2 June to 04:00 UT on 3 June (see **Figure 8**), with a significant increasing in f_oF2 at 03:00 UT on 3 June. According to the time of its occurrence, this anomaly anticipates by 5–10 h a magnetic field anomaly found by the Swarm Alpha satellite (see below and **Figure 9**).

Electron Density and Magnetic Field From Satellite

For the electron density (*Ne*), we considered a background based on median values from ionosonde data of hmF2 (peak true height of the F2 layer). The satellite data have been scaled at the F2 altitude by a simple proportion using the International Reference Ionosphere, IRI-2016, model (Bilitza et al., 2017) computed for both altitudes. This background was associated to a geographic cell of 5° longitude and 3° latitude centered in the ionosonde location, used to select the satellite data and compare them with the ionosonde background. For the comparison of *Ne*, we resorted to Swam satellite data. The Swarm mission by ESA is composed of three identical quasi-polar satellites, Alpha, Bravo, and Charlie launched on November 22, 2013, with a multisensor payload: among them, magnetometers and Langmuir probes (Friis-Christensen et al., 2006). Alpha and Charlie fly almost in parallel at around 460 km of altitude, while Bravo flies at around 510 km (in an almost 90° phase orbit in longitude at the epoch of Ridgecrest earthquake). One of the most interesting results was obtained during the comparison of the background *Ne* value of the ionosonde with that measured by the Swarm Alpha satellite (**Figure 9**). During the satellite passage over the same cell of the ground ionosonde on 3 June at 09:14 UT (i.e., around 01 LT), we obtained a relative variation of 1.94, i.e., the *Ne* value measured by the satellite is almost double w.r.t. the background (the latter has been represented in **Figure 9** as a green dashed line extended in latitude for 5° around Pt. Arguello ionosonde location).

Following recent works (e.g., De Santis et al., 2017), a magnetic anomaly from the satellite can be defined from first differences, comparing the root mean square (rms) over a 3°-latitude window with respect to the analogous RMS of the whole satellite track within ±50° geomagnetic latitude. An interesting result is shown in **Figure 9** (in this case rms>2.5 RMS for the window highlighted by red circle). During the same orbit when we detected the *Ne* anomaly, a clear anomaly in Y (East) component of the magnetic field (actually first differences in nT/s are shown) was recorded by the Swarm Alpha satellite on 3 June at 09:14 UT, when the external magnetic field was negligible (magnetic indices Dst = 4 nT and a_p = 2 nT). We notice that the track is almost along the epicenter longitude and the anomaly is located northward in latitude with respect to the epicenter. The anomaly has been recorded in nighttime, and in the same moment, the absolute value of *Ne* was about the double of the typical one (as shown by the green dashed line in **Figure 9**). The anomalous features of the magnetic and plasma measurements of Swarm for this track cannot be

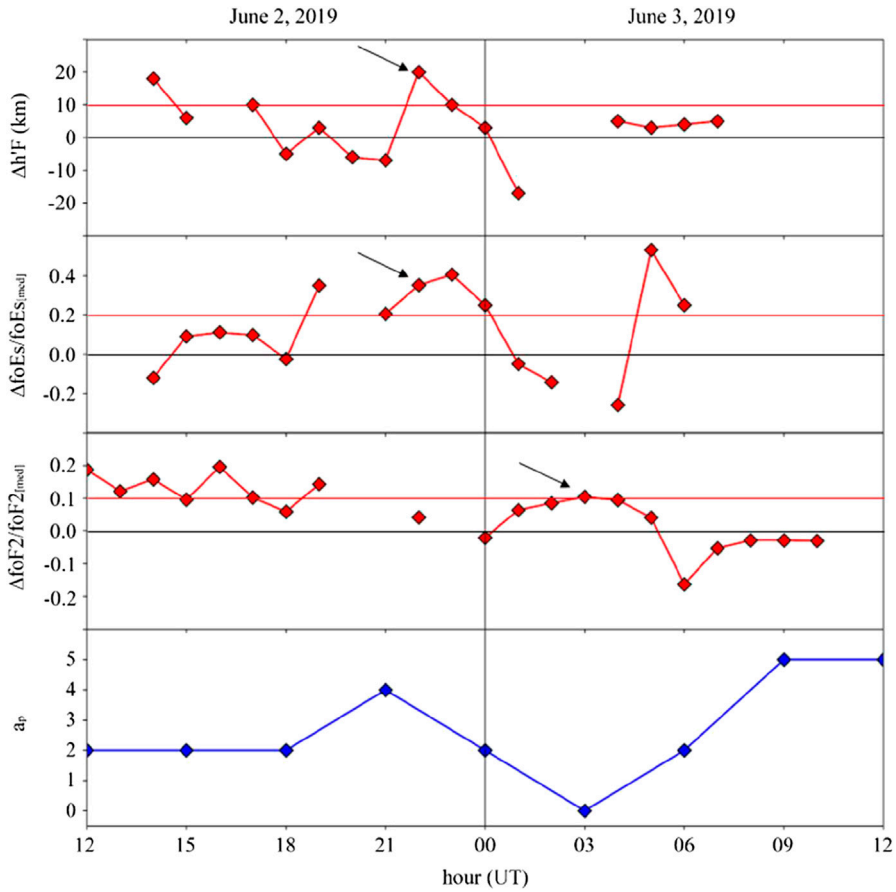

FIGURE 8 | Anomaly taken from ionosonde of Point Arguello (34.7°N, 239.4°E) using observed Δh'Es, δfoEs, and δfoF2 variations (arrows). Three-hour ap geomagnetic index values are given in a lower panel. Black arrows point to possible anomalies.

simply explained by typical ionospheric disturbances. Therefore, we suggest the preparation of the seismic event as a possible source for these phenomena.

As an alternative technique for magnetic field anomaly detection, the residual values, with respect to the recently updated international geomagnetic reference model IGRF-13 (https://www.ngdc.noaa.gov/IAGA/vmod/), have been calculated. Y (East) component of geomagnetic field measured by Swarm Alpha, Bravo, and Charlie satellites has been systematically inspected over the 6 months before the mainshock (this time interval is useful to have sufficiently robust statistics). A three-degree polynomial has been also further subtracted after the removal of the model in order to clean the time series from the seasonal or magnetospheric variations, not predicted by the model.

As in Akhoondzadeh et al. (2018) and Akhoondzadeh et al. (2019), we estimate a median over the 6 months before the mainshock together with the corresponding interquartile (IQR). We then define an anomaly when the residual overcomes the median by more than 1.25 IQR, by at least 1 nT, and the possible effect of the external magnetic fields can be neglected (i.e., the magnetic indices are very low: $|Dst| \leq 20$ nT and $a_p \leq 10$ nT). We prefer to use IQR instead of standard deviation because ionospheric magnetic signals are expected non-Gaussian. However, by analogy, the choice of this threshold would correspond for a Gaussian signal to the largest threshold of 2σ applied in the previous analyses.

Although the threshold is constant for the analyzed 6 months, please note that, before computing it, we removed the daily variation by daily median and the seasonal trend by a polynomial fit. So, after this data processing, the residuals are not anymore affected by daily or seasonal variations.

The disturbed days are automatically excluded from the graph. Three days are particularly anomalous (**Figure 10**): January 31, 2019 (+3.1 nT more than the upper threshold), April 26, 2019 (+2.8 nT above the upper threshold), and June 12, 2019 (−3.3 nT down the lower threshold). Another anomalous day is April 29, 2019 (+1.0 nT).

The same time series analysis has been also applied to the scalar intensity of magnetic field F measured by Swarm (**Figure 11**). The residuals depict some days as clearly anomalous (also here at least 1 nT larger than the adopted threshold): June 3, 2019 (+6.2 nT), June 5, 2019 (−7.3 nT), June 12, 2019 (+1.4 nT), June 16, 2019 (−13.7 nT), June 22,

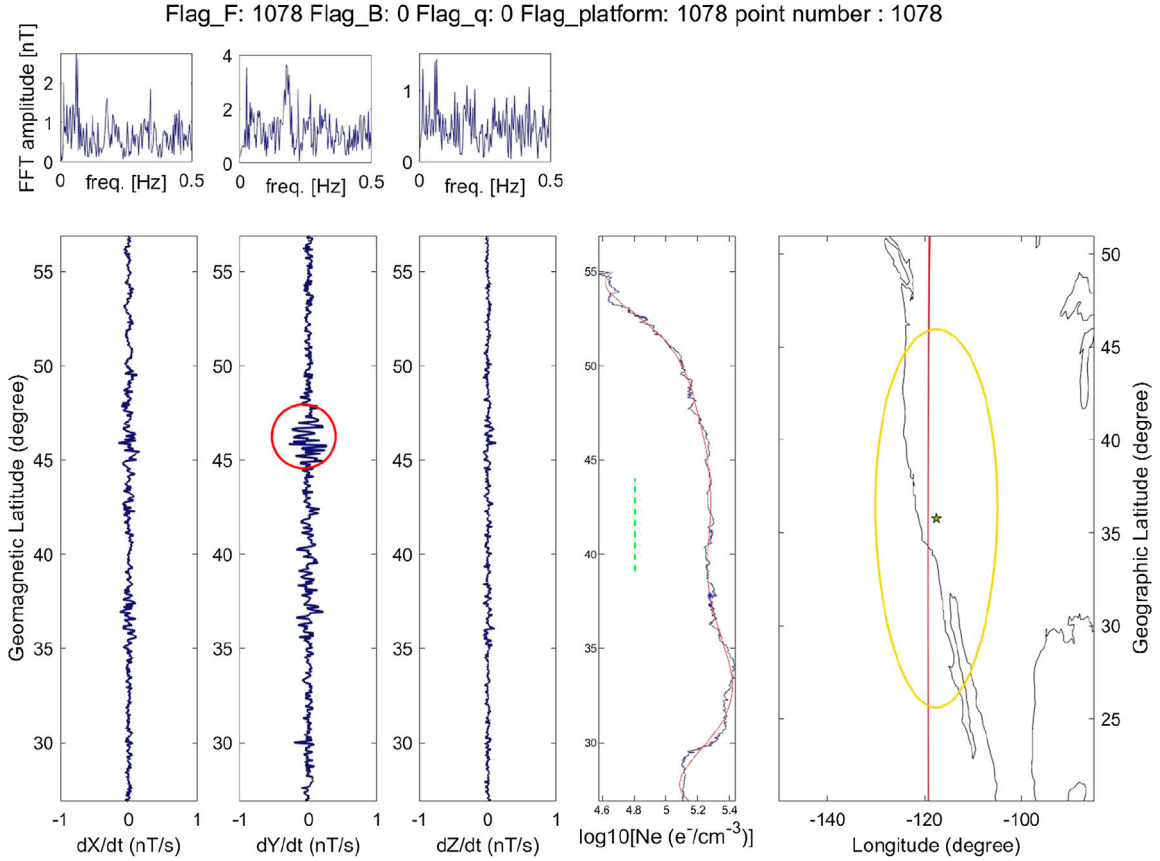

FIGURE 9 | Magnetic anomaly (red circle in Y magnetic field component) taken from the Swarm Alpha satellite on June 3, 2019, at 9:14 UT (around 01 LT). From left, we show plots of dX/dt, dY/dt, and dZ/dt (i.e., the first differences of X, Y, and Z magnetic field components), the logarithm of the electron density Ne along with a green dashed line that is the Ne background level expected from the ionosonde, and finally the geographic map of the region, where the central star represents the earthquake epicenter, the yellow oval is the Dobrovolsky region, and the south-north red line indicated the satellite track projection at the Earth's surface. Top small pictures show the FFT amplitudes for the magnetic components. First line of the heading reports the most important information about the analysis (i.e., type of satellite, date, track number, mean LT and UT, Dst, and ap magnetic indices); second line reports information about the status of satellite data flags that can reveal any problem in the satellite operations or sensor functioning.

2019 (+1.7 nT), June 24, 2019 (−9.1 nT), June 27, 2019 (−8.9 nT), June 30, 2019 (+2.6 nT), and July 3, 2019 (+2.8 nT). We notice that June 12, 2019, is extracted as anomalous by both Y and F analyses. It is interesting to note that in the last period (around one month) approaching the earthquake, the residuals of the magnetic field intensity present more anomalies (highlighted by large red ovals in the figure).

DISCUSSION AND CONCLUSION

Table 1 summarizes the occurrence of all anomalies (dubious anomalies are within a square bracket). It is interesting to highlight that our found precursor times are much longer than those identified by many other papers on earthquake precursors, especially ionospheric precursors, which seem to occur only a few hours to days before large earthquakes (e.g., Heki, 2011; He and Heki, 2017; Yan et al., 2017). Indeed, our recent works highlight a preparation time much longer than few days (e.g., Liu et al., 2020; Marchetti et al., 2019a; Marchetti et al., 2019b). These longer precursor times could be attributed to the long-term process of earthquake preparation (Sugan et al., 2014; Di Giovambattista and Tyupkin, 2004). Moreover, our recent results turned out to be in agreement with the empirical Rikitake (1987) law, recently confirmed for ionospheric precursors from the satellite by De Santis et al. (2019c), which also provide a reasonable physical explanation for the law itself. In accordance to this law, where the precursor time depends on the earthquake magnitude (i.e., the greater the magnitude, the longer the precursor time), Rikitake (1987) estimated an anticipation time from 32 days (radon) to some years for the seismicity precursor of a M7.1 earthquake. It should also be considered that the distance of the monitoring site to the earthquake epicenter could also be important for land-based observations. In fact, it is expected that with a shorter distance, the precursory time is usually longer (Sulthankhodaev, 1984). Therefore, precursory anomalies of only hours to days are

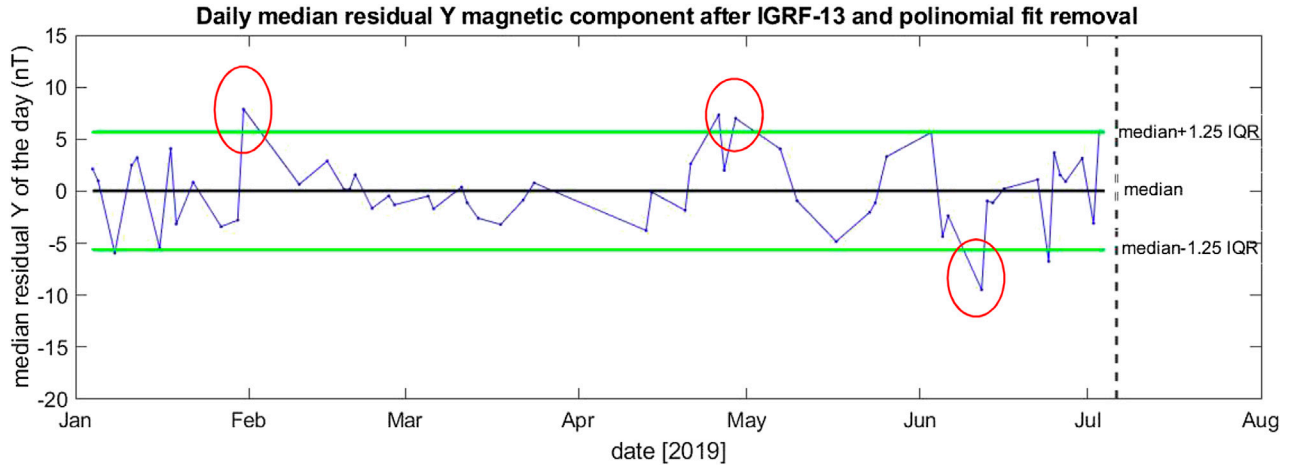

FIGURE 10 | Daily median anomaly taken from Y magnetic field of all Swarm satellites with respect to IGRF-13 model predictions. We underline only the most significant anomalies with red circles. The vertical dashed line represents the mainshock occurrence.

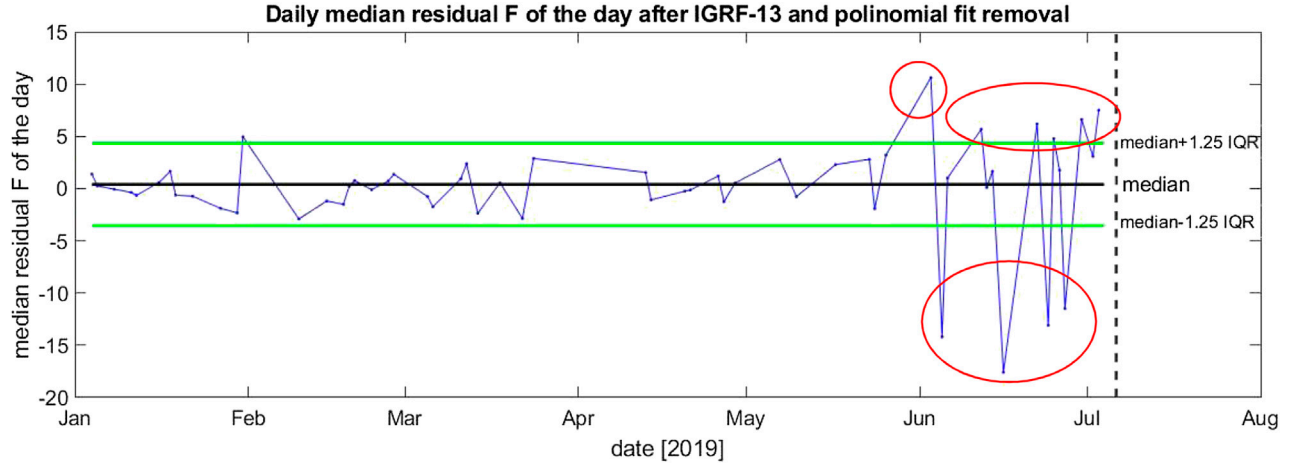

FIGURE 11 | Daily median anomaly taken from total intensity F of all Swarm satellites with respect to IGRF-13 model predictions. Periods of anomalies are evidenced by red circles. The vertical dashed line represents the mainshock occurrence.

TABLE 1 | Type of precursor and corresponding advance time(s).

Type of precursor		Advance time
Lithosphere (increase of seismicity)		−17 years, −9 years, quick acceleration a few days before
Atmosphere	Skin temperature (skt)	[−90–75 days] −25 days
	Total column water vapor (tcwv)	[−85 days]
	Aerosol optical thickness (AOT)	−60 days
	Methane (CH_4)	−70 days
Ionosphere	Ionosonde	−34 days
	Swarm satellite (individual tracks)	−33 days
	(Daily median anomalies)	
	Y	−150 days, −70–65 days, −25 days
	F	−35 days > −25 days

We highlight synchronicity in some precursors. The dubious anomalies (blue circles in the previous figures) are shown within square brackets.

not frequent. Inan et al. (2010) mention precursory hydrogeochemical anomalies in Western Turkey lasting for more than a month before an earthquake magnitude 4.8; the epicenter was within few tens of kilometers to the observation site. The ground water level data we provide from a borehole located some 200 km distant from the epicenter (**Figure 12**) also show a precursory anomaly lasting almost a year (between September 2018 and July 2019). Another important point is to check whether previous researches investigated or not a long time in advance with respect to the seismic event. For example, DEMETER data investigation (e.g., Yan et al., 2017, which is the last statistic study on EQs-DEMETER) has explored only from 15 days before each earthquake. In De Santis et al. (2019c), published by most of the authors of this article, the DEMETER results with anticipation time around 6 days were confirmed, also giving evidences of the existence of possible longer time precursors, for example, 80 days before the seismic event or even some hundred days before for higher magnitude seismic events, which is in accordance to the Rikitake law. On the other hand, some ionospheric precursors have been also registered up to some months in advance (middle-term precursors) (Sidorin, 1979; Korsunova and Khegai, 2006; Korsunova and Khegai, 2008; Hao et al., 2000; Perrone et al., 2010; Perrone et al., 2018), confirming our present results.

From the overall results of our study, the atmosphere looks very sensitive to the preparation of the impending earthquake and the anomalies tend to concentrate in a few occasions, from three months to almost one before the mainshock. The ionosphere (from ionosonde and Swarm satellite data analysis) provides anomalous signals from five months before the mainshock and then at around 2 months before. It then clearly depicts 2–3 June 2019 as a disturbed period in both ionosonde and satellite, during very quiet geomagnetic conditions. The high compatibility of the anticipation time and distance of the ionosonde with respect to the future epicenter of the earthquake using the Korsunova and Khegai (2006) and Korsunova and Khegai (2008) method can strongly support the hypothesis that this feature is induced by the earthquake preparation processes, e.g., release of ionized particles from the lithosphere (see Freund, 2011; Pulinets and Ouzounov, 2011; Hayakawa et al., 2018), before the Ridgecrest major earthquakes.

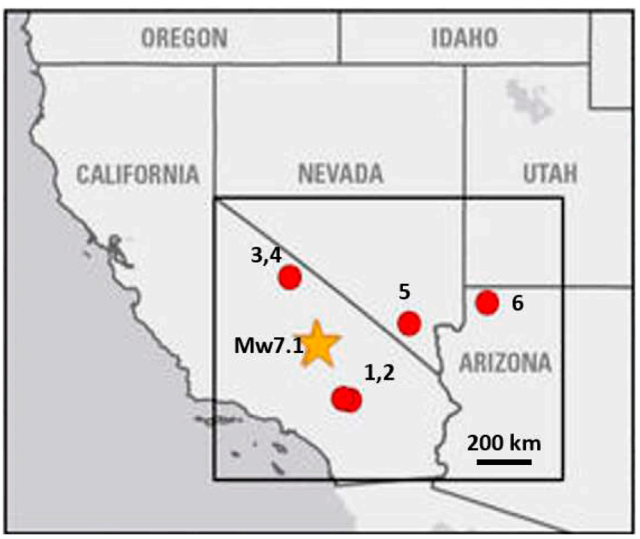

FIGURE 12 | Locations of the epicenter of the July 6, 2019, M7.1 Ridgecrest earthquake and six USGS groundwater-monitoring sites. The monitoring sites shown are California 1) 002S002W02F002S, 2) 002S002W12H001S, 3) 003S027E25N001M, and 4) 003S029E30E002M; Nevada 5) 212 S19 E61 19BC 1 CNLV Deer Springs; and, Arizona 6) B-40-04 06AAC1 [Kaibab-Paiute Well] (USGS 2019).

We can now attempt to consider all anomalies in a unique framework. Particularly powerful is to estimate a cumulative curve of all anomalies together (actually excluding the seismic ones, already included in the AMR fit). When we plot the cumulative number of anomalies (**Figure 13**), we find that a power-law fits the data points very well, much better than a straight line (we fixed the m-exponent of the power law as that typical of a critical system, i.e., m = 0.25). This can be measured by the analogous C-factor, already introduced for AMR, i.e., the ratio between the root mean square of the power-law fit w.r.t. the same of the straight line (Bowman et al., 1998). We estimate for this latter cumulate C = 0.49, which means a clear acceleration of all the anomalies: by the way, it is interesting that the value of this latter C-factor is almost the same as the one calculated for the AMR, producing a similar conclusion obtained for the M7.8 Nepal 2015 case study comparing seismic and magnetic anomaly patterns by De Santis et al. (2017). Therefore, from **Figure 13,** we can affirm that the anomalies tend to accelerate as the earthquake is approaching, pointing to the time of occurrence with a small uncertainty of only few days (±3 days). Inclusion of the few dubious anomalies (blue circles in the figures of analyses) does not change the overall result significantly. Ground-based precursory anomaly, for verification of our results, was sought and only borehole water level data have been found available from the USGS open access database. USGS reported in October 2019 (USGS, 2019) that oscillatory changes were recorded in short-term water levels of some boreholes varying in distance to the epicenter of the M7.1 earthquake from about 200 to 400 km (**Figure 12**). We downloaded the data for all six borehole locations for a time interval of 4 years (from January 1, 2016, to January 1, 2020) in order to assess the background level and evaluate pre-seismic anomalies, if any. Time series of the water level recorded in one borehole (#2) located about 200 km to the south of the epicenter is given in **Figure 14**. Data from other five boreholes did not enable robust evaluation with respect to seismicity (these can be viewed from USGS, (2019)): we explain this fact because one station (#6) is too far from the epicentral region, while the others (#1, #3, #4, and #5) do not show any pre-earthquake anomaly because of the stress anisotropy and/or block boundaries hindering stress transfer to localities of these stations (similar effects are discussed by Inan et al., 2012). In **Figure 14**, gradual shallowing trend in the water level is apparent until about September 2018 (about 9 months before the mainshock) when disturbance in the data started and the water level started to gradually decrease until July 6, 2019.

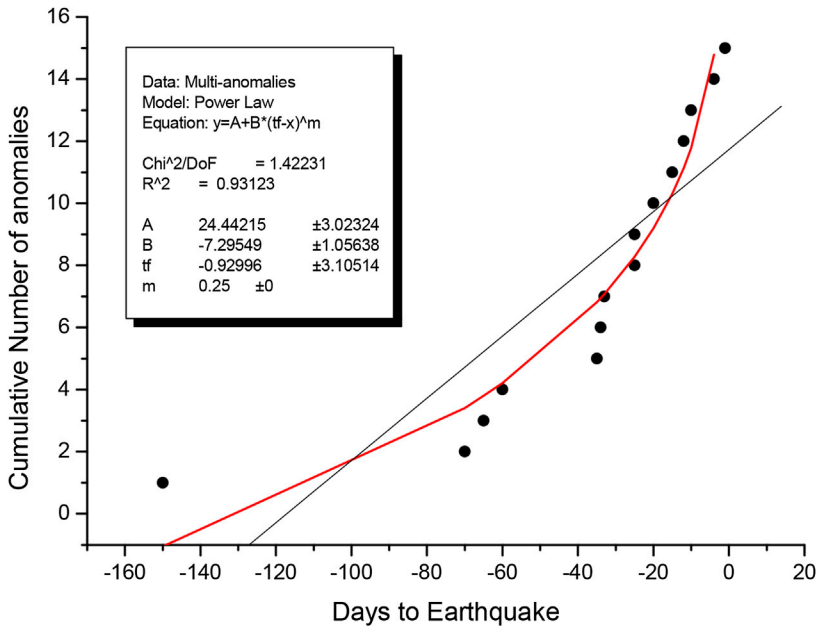

FIGURE 13 | Cumulative number of all clear anomalies (indicated here as black circles; here, we do not consider the lithospheric anomalies of seismicity, already counted in AMR). Time origin t = 0 is the mainshock occurrence. Red fit is a power law while the black is a straight line. As for AMR, also here can be estimated the C-factor, C = 0.49, which confirms a strong acceleration as the mainshock is approaching.

After that, the water level has gradually increased again. An anomaly at 270 days before the mainshock is suggested by the data. Using Sultankhodhaev's (1984) empirical formula, relating the time T (in days) of the anomaly, the distance D (in km) of its location w.r.t. the mainshock epicenter, and the earthquake magnitude M:

$$\log(\mathrm{DT}) = 0.63 \cdot \mathrm{M} - 0.15, \quad (3)$$

we calculated an expected anomaly anticipation time of 105 days as in this case D = 200 km and M = 7.1. The apparent anomaly anticipation time (270 days) from **Figure 14** and theoretical expected anticipation time (105 days) from the empirical approach correlate well with anomalies detected based on magnetic and ionospheric data as listed in **Table 1**.

From different analyses of seismic, atmospheric, and ionospheric data, as well as limited ground-based observations,

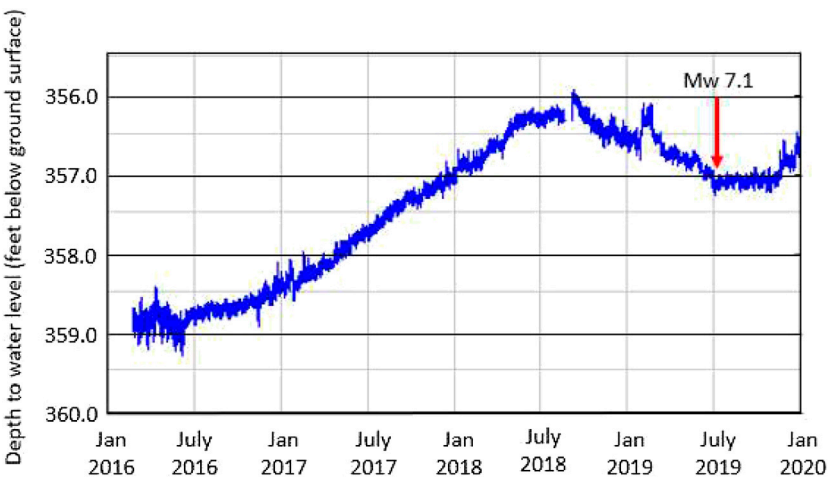

FIGURE 14 | Water level for about 4 years (3.5 years before and half year after the Ridgecrest mainshock) at location #2 (see **Figure 12** for location) (USGS report of October 2019). Disturbance of the water level in September 2018 is followed by gradual decrease of cumulative of about one foot (30.5 cm) until the day of the Ridgecrest mainshock. A peak representing a few weeks in February 2019 (about 5 months) prior to earthquake is also noteworthy.

we find a chain of processes from the ground to atmosphere and ionosphere. We can safely conclude that this series of anomalous events in the different geolayers (lithosphere where the earthquake occurs, atmosphere, and ionosphere) is probably activated by the preparation phase of the Ridgecrest earthquake.

DATA AVAILABILITY STATEMENT

Publicly available datasets were analyzed in this study. These data can be found in USGS Seismic Catalogue, ESA Swarm, ECMWF, and MERRA-2, data Portals.

AUTHOR CONTRIBUTIONS

ADS was responsible for the design and organization of the work, bibliography search, some data analyses and drawing of a few figures, writing the first draft of the article, and editing the final version. GC was involved in the bibliography search, data analyses and preparation of some figures, and editing for the final version. DM, AP, DS, LP, SAC, and SI were involved in the data analyses and preparation of a few figures, and editing the final version.

FUNDING

This work was undertaken in the framework of the European Space Agency (ESA)-funded project SAFE (Swarm for earthquake study) 4000116832/15/NL/MP, while Agenzia Spaziale Italiana (ASI) funded project LIMADOU-Scienza n. 2016-16-H0. Part of the work has been made also under the project ISSI-BJ "The electromagnetic data validation and scientific application research based on CSES satellite."

REFERENCES

Akhoondzadeh, M., De Santis, A., Marchetti, D., Piscini, A., and Cianchini, G. (2018). Multi precursors analysis associated with the powerful Ecuador (MW = 7.8) earthquake of 16 April 2016 using Swarm satellites data in conjunction with other multi-platform satellite and ground data, *Adv. Space Res.* 61, 248–263. doi:10.1016/j.asr.2017.07.014

Akhoondzadeh, M., De Santis, A., Marchetti, D., Piscini, A., and Jin, S. (2019). Anomalous seismo-LAI variations potentially associated with the 2017 Mw = 7.3 Sarpol-e Zahab (Iran) earthquake from Swarm satellites, GPS-TEC and climatological data. *Adv. Space Res.* 64, 143–158. doi:10.1016/j.asr.2019.03.020

Barnhart, W. D., Hayes, G. P., and Gold, R. D. (2019). The July 2019 Ridgecrest, California, earthquake sequence: kinematics of slip and stressing in cross-fault ruptures. *Geophys. Res. Lett.* 46, 11859–11867. doi:10.1029/2019gl084741

Bilitza, D., Altadill, D., Truhlik, V., Shubin, V., Galkin, I., Reinisch, B., et al. (2017). International Reference Ionosphere 2016: from ionospheric climate to real-time weather predictions. *Space Weather* 15, 418–429. doi:10.1002/2016SW001593

Bowman, D. D., Ouillon, G., Sammis, C. G., Sornette, A., and Sornette, D. (1998). An observational test of the critical earthquake concept. *J. Geophys. Res.* 103, 24359–24372. doi:10.1029/98jb00792

Bulut, F. (2015). Different phases of the earthquake cycle captured by seismicity along the North Anatolian Fault. *Geophys. Res. Lett.* 42, 2219–2227. doi:10.1002/2015gl063721

Chen, K., Avouac, J.-P., Aati, S., Milliner, C., Zheng, F., and Shi, C. (2020). Cascading and pulse-like ruptures during the 2019 ridgecrest earthquakes in the Eastern California shear zone. *Nat. Commun.* 11, 22. doi:10.1038/s41467-019-13750-w

Cianchini, G., De Santis, A., Giovambattista, R. D., Abbattista, C., Amoruso, L., Campuzano, S. A., et al. (2020). Revised accelerated moment release under test: fourteen worldwide real case studies in 2014–2018 and simulations. *Pure Appl. Geophys.* 177, 4057–4087. doi:10.1007/s00024-020-02461-9

Cui, J., Shen, X., Zhang, J., Ma, W., and Chu, W. (2019). Analysis of spatiotemporal variations in middle-tropospheric to upper-tropospheric methane during the Wenchuan Ms = 8.0 earthquake by three indices. *Nat. Hazards Earth Syst. Sci.* 19, 2841–2854. doi:10.5194/nhess-19-2841-2019

De Santis, A. (2009). "Geosystemics," in *Proceedings of the 3rd IASME/WSEAS international conference on geology and seismology (GES'09)*, Cambridge, UK, 21–26 February 2009, 36–40.

De Santis, A. (2014). "Geosystemics, Entropy and criticality of earthquakes: a vision of our planet and a key of access," in *Addressing global environmental security through innovative educational curricula*. (Basingstoke, United Kingdom: Springer Nature), 3–20.

De Santis, A., Cianchini, G., and Di Giovambattista, R. (2015). Accelerating moment release revisited: examples of application to Italian seismic sequences. *Tectonophysics* 639, 82–98. doi:10.1016/j.tecto.2014.11.015

De Santis, A., Balasis, G., Pavón-Carrasco, F. J., Cianchini, G., and Mandea, M. (2017). Potential earthquake precursory pattern from space: the 2015 Nepal event as seen by magnetic Swarm satellites. *Earth Planet Sci. Lett.* 461, 119–126. doi:10.1016/j.epsl.2016.12.037

De Santis, A., Abbattista, C., Alfonsi, L., Amoruso, L., Campuzano, S. A., Carbone, M., et al. (2019a). Geosystemics view of earthquakes. *Entropy* 21 (4), 412. doi:10.3390/e21040412

De Santis, A., Marchetti, D., Spogli, L, Cianchini, G., Pavón-Carrasco, F. J., Franceschi, G. D., et al. (2019b). Magnetic field and electron density data analysis from Swarm satellites searching for ionospheric effects by great earthquakes: 12 case studies from 2014 to 2016. *Atmosphere* 10, 371. doi:10.3390/atmos10070371

De Santis, A., Marchetti, D., Pavón-Carrasco, F. J., Cianchini, G., Perrone, L., Abbattista, C., et al. (2019c). Haagmans, Precursory worldwide signatures of earthquake occurrences on Swarm satellite data. *Sci. Rep.* 9, 20287. doi:10.1038/s41598-019-56599-1

Dee, D. P., Uppala, S. M., Simmons, A. J., Berrisford, P., Poli, P., Kobayashi, S., et al. (2011). The ERA-Interim reanalysis: configuration and performance of the data assimilation system. *Q. J. R. Meteorol. Soc.* 137, 553–597. doi:10.1002/qj.828

Di Giovambattista, R., and Tyupkin, Y. S. (2004). Seismicity patterns before the M=5.8 2002, Palermo (Italy) earthquake: seismic quiescence and accelerating seismicity. *Tectonophysics* 384 (1-4), 243–255. doi:10.1016/j.tecto.2004.04.001

Dobrovolsky, I. P., Zubkov, S. I., and Miachkin, V. I. (1979). Estimation of the size of earthquake preparation zones. *PAGE*, 117, 1025–1044. doi:10.1007/bf00876083

Fetzer, E., McMillin, L. M., Tobin, D., Aumann, H. H., Gunson, M. R., McMillan, W. W., et al. (2003). Airs/amsu/hsb validation, geoscience and Remote sensing. *IEEE Transactions* 41 (2), 418–431. doi:10.1109/tgrs.2002.808293

Freund, F. (2011). Pre-earthquake signals: underlying physical processes. *J. Asian Earth Sci.* 41, 383–400. doi:10.1016/j.jseaes.2010.03.009

Freund, F. (2013). Earthquake forewarning—a multidisciplinary challenge from the ground up to space. *Acta Geophysica* 61 (4), 775–807. doi:10.2478/s11600-013-0130-4

Friis-Christensen, E., Luhr, H., and Hulot, G. (2006). Swarm: a constellation to study the Earth's magnetic field. *Earth Planet. Space* 58, 351–358. doi:10.1186/bf03351933

Gelaro, R., McCarty, W., Suárez, M. J., Todling, R., Molod, A., Takacs, L., et al. (2017). The Modern-Era retrospective analysis for research and applications, version 2 (MERRA-2), American meteorological society - modern-Era retrospective analysis for research and applications version 2 (MERRA-2) special collection. *J. Climate* 30 (14), 5419–5454. doi:10.1175/JCLI-D-16-0758.1

Hao, J., Tianming, T., and Li, D. (2000). Progress in the research of atmospheric electric field anomaly as an index for short-impending prediction of earthquakes. *J. Earthquake Prediction Res.* 8, 241–255. doi:10.1007/BF02650462

Hayakawa, M., Asano, T., Rozhnoi, A., and Solovieva, M. (2018). "Very-low- and low-frequency sounding of ionospheric perturbations and possible association with earthquakes," in *Pre-earthquake Processes: a multidisciplinary approach to earthquake prediction studies*. Editors D. Ouzounov, et al. (New York, NY: AGU Book, Wiley), 277–304.

He, L., and Heki, K. (2017). Ionospheric anomalies immediately before Mw7.0–8.0 earthquakes. *J. Geophys. Res. Space Phys.* 122, 8659–8678. doi:10.1002/2017ja024012

Heki, K. (2011). Ionospheric electron Enhancement preceding the 2011 tohoku-oki earthquake. *Geophys. Res. Lett.* 38 (17), 1–5. doi:10.1029/2011gl047908

Ippolito, A., Perrone, L., De Santis, A., and Sabbagh, D. (2020). Ionosonde data analysis in relation to the 2016 central Italian earthquakes. *Geosciences* 10, 354. doi:10.3390/geosciences10090354

İnan, S., Ertekin, K., Seyis, C., Şimşek, Ş., Kulak, F., Dikbaş, A., et al. (2010). Multi-disciplinary earthquake researches in Western Turkey: hints to select sites to study geochemical transients associated to seismicity. *Acta Geophysica* 58, 767–813. doi:10.2478/s11600-010-0016-7

İnan, S., Pabuccu, Z., Kulak, F., Ergintav, S., Tatar, O., Altunel, E., et al. (2012). Microplate boundaries as obstacles to pre-earthquake strain transfer in Western Turkey: inferences from continuous geochemical monitoring. *J. As. Earth Sc.* 48, 56–71. doi:10.1016/j.jseaes.2011.12.016

Korsunova, L. P., and Khegai, V. V. (2006). Medium-term ionospheric precursors to strong earthquakes. *Int. J. Geomagn. Aeron.* 6, GI3005, doi:10.1029/2005gi000122

Korsunova, L. P., and Khegai, V. V. (2008). Analysis of seismo-ionospheric disturbances at the chain of Japanese stations for vertical sounding of the ionosphere. *Geomagn. Aeron.* 48, 392–399. doi:10.1134/s0016793208030134

Le Mer, J., and Roger, P. (2001). Production, oxidation, emission and consumption of methane by soils: a review. *Eur. J. Soil Biol.* 37, 25–50. doi:10.1016/s1164-5563(01)01067-6

Liu, Q., De Santis, A., Piscini, A., Cianchini, G., Ventura, G., and Shen, X. (2020). Multi-parametric climatological analysis reveals the involvement of fluids in the preparation phase of the 2008 Ms 8.0 wenchuan and 2013 Ms 7.0 lushan earthquakes. *Rem. Sens.* 12, 1663. doi:10.3390/rs12101663

Marchetti, D., De Santis, A., D'Arcangelo, S., Poggio, F., Piscini, A., Campuzano, A., et al. (2019a). Pre-earthquake chain processes detected from ground to satellite altitude in preparation of the 2016–2017 seismic sequence in Central Italy. *Remote Sens. Environ.* 229, 93–99. doi:10.1016/j.rse.2019.04.033

Marchetti, D., De Santis, A., Shen, X., Campuzano, S. A., Perrone, L., Piscini, A., et al. (2019b). Possible Lithosphere-Atmosphere-Ionosphere Coupling effects prior to the 2018 Mw=7.5 Indonesia earthquake from seismic, atmospheric and ionospheric data. *J. Asian Earth Sci.* 188, 104097. doi:10.1016/j.jseaes.2019.104097

Marchetti, D., De Santis, A., D'Arcangelo, S., Poggio, F., Jin, S., Piscini, A., et al. (2020). Magnetic field and electron density anomalies from Swarm satellites preceding the major earthquakes of the 2016–2017 Amatrice-Norcia (Central Italy) seismic sequence. *Pure Appl. Geophys.* 177, 305–319. doi:10.1007/s00024-019-02138-y

Perrone, L., Korsunova, L. P., and Mikhailov, A. V. (2010). Ionospheric precursors for crustal earthquakes in Italy. *Ann. Geophys.* 28, 941–950. doi:10.5194/angeo-28-941-2010

Perrone, L., De Santis, A., Abbattista, C., Alfonsi, L., Amoruso, L., Carbone, M., et al. (2018). Ionospheric anomalies detected by ionosonde and possibly related to crustal earthquakes in Greece. *Ann. Geophys.* 36, 361–371. doi:10.5194/angeo-36-361-2018

Piscini, A., De Santis, A., Marchetti, D., and Cianchini, G. (2017). A multi-parametric climatological approach to study the 2016 Amatrice-Norcia (Central Italy) earthquake preparatory phase. *Pure Appl. Geophys.* 174 (10), 3673–3688. doi:10.1007/s00024-017-1597-8

Piscini, A., Marchetti, D., and De Santis, A. (2019). Multi-parametric climatological analysis associated with global significant volcanic eruptions during 2002–2017. *Pure Appl. Geophys.* 176, 3629–3647. doi:10.1007/s00024-019-02147-x

Pulinets, S., and Ouzounov, D. (2011). Lithosphere–atmosphere–ionosphere coupling (LAIC) model—an unified concept for earthquake precursors validation. *J. Asian Earth Sci.* 41 (4–5), 371–382. doi:10.1016/j.jseaes.2010.03.005

Rikitake, T. (1987). Earthquake precursors in Japan: precursor time and detectability. *Tectonophysics* 136, 265–282. doi:10.1016/0040-1951(87)90029-1

Ross, Z. E., Idini, B., Jia, Z., Stephenson, O. L., Zhong, M., Wang, X., et al. (2019). Hierarchical interlocked orthogonal faulting in the 2019 Ridgecrest earthquake sequence. *Science* 366, 346–351. doi:10.1126/science.aaz0109

Rymer, M. J., Langenheim, V. E., and Hauksson, E. (2002). The hector mine, California, earthquake of 16 october 1999: introduction to the special issue. *Bull. Seismol. Soc. Am.* 92 (4), 1147–1153. doi:10.1785/0120000900

Sidorin, A. Y. (1979). The dependence of the time of appearance of earthquake precursors on the epicenter distance. *Proc. Acad. Sci. USSR* 25 (4), 825, 1979 [in Russian].

Sobolev, G. A., Huang, Q., and Nagao, T. (2002). Phases of earthquake's preparation and by chance test of seismic quiescence anomaly. *J. Geodyn.* 33, 413–424. doi:10.1016/s0264-3707(02)00007-8

Sugan, M., Kato, A., Miyake, H., Nakagawa, S., and Vuan, A. (2014). The preparatory phase of the 2009 Mw 6.3 L'Aquila earthquake by improving the detection capability of low-magnitude foreshocks. *Geophys. Res. Lett.* 41, 6137–6144. doi:10.1002/2014GL061199

Sultankhodhaev, G. A. (1984). *Earthquake prediction*. Paris: UNESCO, 181–191.

USGS (2019). The ups and downs of groundwater levels after the july 2019 ridgecrest, CA earthquakes. Available at: https://www.usgs.gov/center-news/ups-and-downs-groundwater-levels-after-july-2019-ridgecrest-ca-earthquakes. (Accessed October, 2019).

Yan, R., Parrot, M., and Pinçon, J.-L. (2017). Statistical study on variations of the ionospheric ion density observed by DEMETER and related to seismic activities. *J. Geophys. Res. Space Phys.* 122, 12421–12429. doi:10.1002/2017ja024623

Conflict of Interest: The authors declare that the research was conducted in the absence of any commercial or financial relationships that could be construed as a potential conflict of interest.

Copyright © 2020 De Santis, Cianchini, Marchetti, Piscini, Sabbagh, Perrone, Campuzano and Inan. This is an open-access article distributed under the terms of the Creative Commons Attribution License (CC BY). The use, distribution or reproduction in other forums is permitted, provided the original author(s) and the copyright owner(s) are credited and that the original publication in this journal is cited, in accordance with accepted academic practice. No use, distribution or reproduction is permitted which does not comply with these terms.

frontiers in Earth Science

MINI REVIEW
published: 26 November 2020
doi: 10.3389/feart.2020.576017

Hydrogeological Earthquake Precursors: A Case Study From the Kamchatka Peninsula

Galina Kopylova and Svetlana Boldina*

Geophysical Survey of the Russian Academy of Sciences, Kamchatka Branch, Petropavlovsk-Kamchatsky, Russia

The relevance of hydrogeological precursors (HGPs) study is justified by the need to obtain reliable information about the spatio-temporal manifestations and the relationships of HGPs with the parameters of subsequent earthquakes for seismic forecasting. In the review the data on repeated manifestations of HGPs before strong earthquakes obtained from long-term observations in five deep wells on the Kamchatka Peninsula (Far East of Russia) are presented. The analysis of the correlation of HGPs occurring in several wells is carried out in comparison with earthquake parameters characterizing both earthquake sources (magnitude, linear size of the source) and the impact of earthquakes in the area of wells (specific energy density in wave, intensity of shaking). It is shown that the manifestation of HGPs in several wells is observed before earthquakes with M_w = 6.6–7.8 at epicentral distances up to the first hundreds of km to observation wells in the near and intermediate zones of the sources with the ratio of the epicentral distances and the source sizes no more than 1–5. A feature of our study was the use of certain types of HGPs in water-level changes for predictive assessments of the strong earthquakes in the Kamchatka Peninsula. The review presents precursors in water-level changes detected in real time and the corresponding earthquake forecasts, which were recognized as successful according to the conclusions of the expert council on earthquake prediction.

Keywords: precursor, earthquake, seismic forecast, observational well, water-level, Kamchatka Peninsula, groundwater chemical composition

OPEN ACCESS

Edited by:
Giovanni Martinelli, National Institute of Geophysics and Volcanology, Italy

Reviewed by:
Jens Heinicke, Freiberg University of Mining and Technology, Germany
Ching-Chou Fu, Institute of Earth Sciences, Academia Sinica, Taiwan

****Correspondence:***
Galina Kopylova
gala@emsd.ru

Specialty section:
This article was submitted to Solid Earth Geophysics, a section of the journal Frontiers in Earth Science

Received: *24 June 2020*
Accepted: *27 October 2020*
Published: *26 November 2020*

Citation:
Kopylova G and Boldina S (2020) Hydrogeological Earthquake Precursors: A Case Study From the Kamchatka Peninsula. Front. Earth Sci. 8:576017. doi: 10.3389/feart.2020.576017

INTRODUCTION

Studies of hydrogeological precursors of earthquakes, manifested in changes in physical and chemical parameters of groundwater HGPs have been carried for decades (Roeloffs, 1988; Thomas, 1988; Wang and Manga, 2010; King, 2018; King and Manga, 2018; Skelton et al., 2019). The relevance of studying such phenomena is justified by the need to obtain reliable information about the spatio-temporal manifestations and the relationships of HGPs with the parameters of subsequent earthquakes for seismic forecasting. The basis for studying the HGPs for predicting earthquakes is the systematization of their recurring manifestations according to the data of long-term observations in individual wells. Unfortunately, there are few such reliable data on HGPs. In the above-mentioned works, it is reported mainly about "supposed" precursors in the parameters of groundwater. The lack of a sufficient number of such "supposed" precursors does not

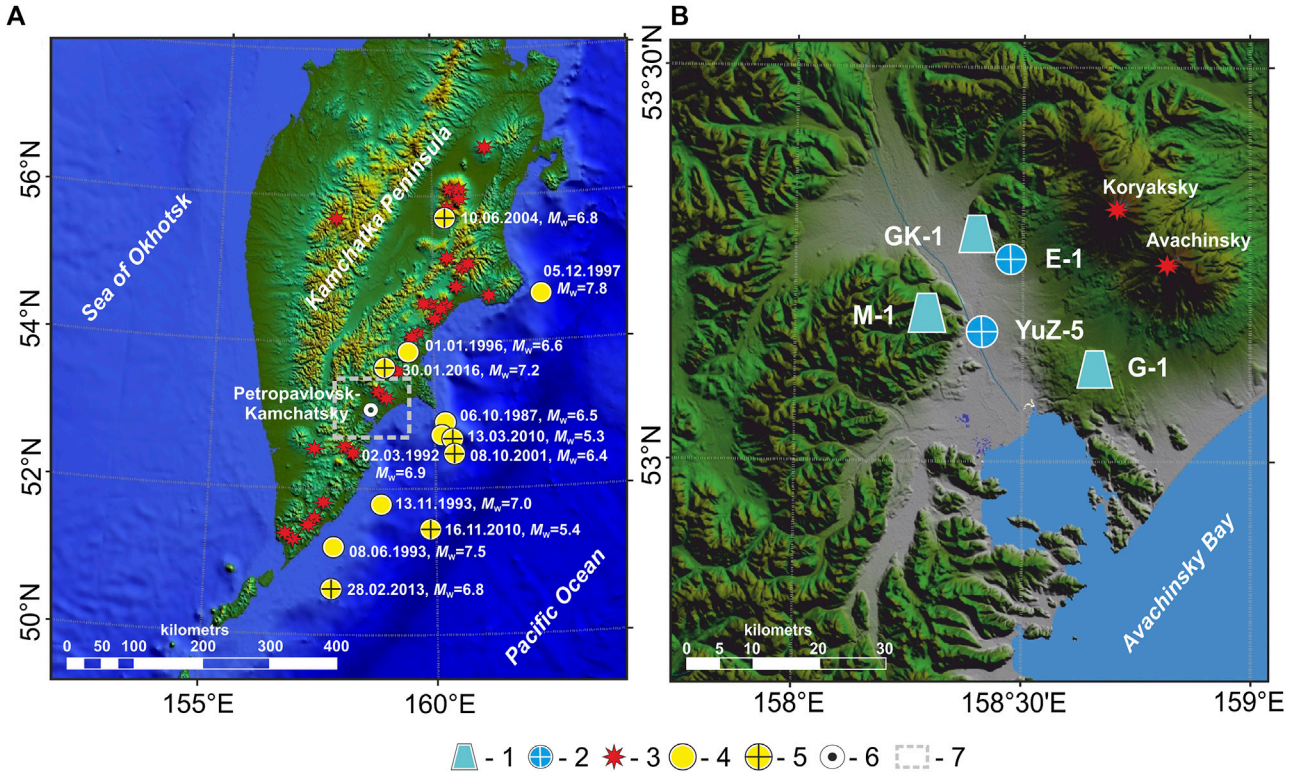

FIGURE 1 | The layout of the observation wells and earthquake epicenters in the Kamchatka Peninsula: **(A)** earthquakes preceded by hydrogeological precursors; **(B)** observation wells at the Petropavlovsk-Kamchatsky test site. Designations: 1, flowing wells; 2, piezometric wells; 3, active volcanoes; 4, 5, earthquake epicenters: 4, hydrogeological precursors revealed retrospectively; 5, hydrogeological precursors detected in water-level changes in the E-1 well in real time; 6, Petropavlovsk-Kamchatsky city; 7, Petropavlovsk-Kamchatsky test site in **Figure 1A**.

allow them to be used for seismic forecasting and obtaining of such new data is the primary task of further research.

The review presents data on HGPs obtained from long-term hydrogeochemical and level observations in five wells on the Kamchatka Peninsula. These data are poorly known, because most of the previous publications about HGPs in wells of Kamchatka were in Russian. Brief information on hydrogeochemical observations in the Kamchatka Peninsula is given in (Wang and Manga, 2010). In Biagi et al. (2000a) and Biagi et al. (2000b) some anomalies in the chemical composition of groundwater and gas before the Kamchatka earthquakes of the 1990s were described.

Our review is aimed to a description at both of data on HGPs in the Kamchatka wells, and an experiment for predicting earthquakes in real time using some types of HGPs. The data on HGPs in previously works of authors and other researchers along with the graphical presentation of the HGPs (see **Supplementary Materials S1**) provide detailed information on the observation wells, methods of observations and the features of HGPs manifestations in the individual wells. These materials form the basis of generalization about the relationship of the considered HGPs with parameters of the subsequent earthquakes.

An important feature of our long-term study of HGPs in water-level changes is the combination of observations in wells with an experiment on the use of certain types of HGPs for predictive assessments of the strong earthquakes in the Kamchatka Peninsula. This review presents examples of the precursors in water-level changes detected in real time, and forecasts of strong earthquakes recognized as successful according to conclusions of the expert council on earthquake prediction working in the Kamchatka Krai.

OBSERVATIONAL DATA, PRECURSORS, COOPERATION WITH THE EXPERT COUNCIL

The Kamchatka Peninsula (**Figure 1A**) is part of the Kamchatka Krai in the Russian Far East. It is located at the junction of the Pacific oceanic plate with the Eurasian and North American continental plates. This region is prone to frequent strong earthquakes which cause damaging ground motion and devastating tsunami. The strategies for reducing negative impacts from the earthquakes include, inter alia, the monitoring studies aimed at establishing the precursors and forecasting the time of the strong earthquakes.

Kamchatka Branch of the Geophysical Survey of the Russian Academy of Sciences (KB GS RAS) conducts long-term

groundwater-level and chemical composition monitoring at a network of wells in the Petropavlovsk-Kamchatsky testing site (**Figure 1B**) in order to search for hydrogeological precursors of earthquakes and other effects of seismicity in groundwater parameters (Kopylova and Boldina, 2019). The data on the wells with repeated HGPs occurrences are presented in **Supplementary Materials Table S1 and Figure S1**. In all considered wells, water is not pumped out, as well as other man-made activities do not affect their natural state.

During the visits to the flowing wells GK-1, M-1, and G-1, the employees of the Laboratory of hydroseismology carried out flow rate measurements and water sampling every three days in 1986–1999. Free gas sampling was conducted from the GK-1 well. Water samples were tested for pH as well as for the anion and cation concentrations. The gas content was analyzed chromatographically. Water and gas parameters were determined with an accuracy of 2–10% (Khatkevich and Ryabinin, 2006). After 1999, the system of hydrogeochemical observations had changed due to an increase in the observation interval, a decrease in the set of determined parameters of the groundwater composition and experiments with the installation of equipment into wellbores that violate the natural hydrodynamic and hydrogeochemical regime of wells. Therefore, we consider the hydrogeochemical data only for the period 1986–1998, for which uniform time series were obtained under the conditions of the natural regime of observation wells.

In piezometric wells E-1 and YuZ-5 the instruments installed in 1996 provide highly sensitive water-level and atmospheric pressure recording up to ±0.1 cm and ±0.1 hPa, respectively, with a frequency of 5–10 min (Kopylova et al., 2017). In 1987–1994, water-level measurements in the E-1 well were carried out daily with an accuracy of ±0.5 cm, variations in atmospheric pressure were recorded by a barograph with an accuracy of 1 hPa (Kopylova, 2001). The seismic effects in water-level changes are identified with due regard of the influence of atmospheric pressure, precipitation, Earth's tides, seasonal trend, and other factors (Kopylova et al., 2019).

The primary outcome of long-term observations is that it was revealed hydrogeochemical and hydrogeodynamic phenomena preceding strong local earthquakes (**Figure 1A**). The data on earthquakes preceded by HGPs manifested in two to four observation wells are presented in **Supplementary Materials Table S2**.

In this paper, we consider the following effects as HGPs originally detected retrospectively:

i) visually distinguishable and statistically confirmed anomalies in the ionic and dissolved gas composition of the groundwater in the flowing wells GK-1, M-1 and G-1 (Kopylova et al., 1994; Biagi et al., 2000a; Biagi et al., 2000b; Khatkevich and Ryabinin, 2006; Kopylova and Taranova, 2013);

ii) higher-rate water-level decreases repeatedly manifested before earthquakes with $M \geq 5.0$ in the E-1 well which were identified as the precursors PS1 and PS2 (Kopylova, 2001; Kopylova and Boldina, 2012; Kopylova and Boldina, 2019);

iii) substantial deviation in water-level behavior from seasonal average pattern in the YuZ-5 well (Boldina and Kopylova, 2017; Kopylova and Boldina, 2019; **Supplementary Materials Figure S4**).

Hydrogeological precursors in the groundwater ion and gas composition in three wells are presented in **Supplementary Materials Figure S3**.

In the GK-1 well, a decline in chloride ion concentration was observed within one to nine months before six earthquakes (**Supplementary Materials Table S2 and Figure S3A**, left diagram). In the cases of the earthquakes of January 1, 1996 and December 5, 1997, the decreases in chloride ion concentration were changed into the sharp increases lasting 4–5 months. The increase in the variance and the change in the average concentrations of free gases were observed during 2 months before the earthquake of March 2, 1992 (**Supplementary Materials Figure S3A**, right diagram).

In the M-1 well, the concentration of bicarbonate ion decreased before five earthquakes (**Supplementary Materials Table S2 and Figure S3B**). In four cases, simultaneous increases were detected in the concentrations of sulfate ion, calcium, and sodium. Within one month before the earthquake of March 2, 1992, water mineralization increased by 25%, and the hydrogeochemical type of water has changed due to the increase in the concentration of sulfate ion and the decrease in the concentration of bicarbonate ion (Kopylova et al., 1994).

The changes in the concentrations of chloride ion, sulfate ion, bicarbonate ion as well as sodium and calcium were observed in the G-1 well before the earthquakes of January 1, 1996 and December 5, 1997 (**Supplementary Materials Figure S3C**) (Khatkevich and Ryabinin, 2006).

The maximum durations of hydrogeochemical anomalies (T_1) and lead times before earthquakes (T_2) in individual wells are presented in **Supplementary Materials Table S2**. The T_1 and T_2 values coincide for wells GK-1 and G-1. At the same time, the M-1 well is characterized by the appearance of relatively short-term hydrogeochemical anomalies (T_1 = 4 weeks) during 4–21.5 weeks before earthquakes. This feature of the well is associated with a high rate of water exchange in the wellbore due to the high water discharge (q = 1.5 dm^3/s) compared to wells GK-1 and G-1 (q = 0.1 and <0.001 dm^3/s).

Examples of hydrogeological precursors in water-level changes in wells E-1 and YuZ-5 are given in (Kopylova, 2001; Kopylova, 2006; Boldina and Kopylova, 2017; Kopylova and Boldina, 2019; **Supplementary Materials Figures S4–S7**).

According to digital observations 1996–2016 at well E-1, two types of the pre-seismic signals are identified in daily rate of water-level decreases: PS1 developing weeks prior to the earthquakes (**Supplementary Materials Figures S4,S6**) and PS2 with a manifestation time of 5–6 years (**Supplementary Materials Figure S7**). The PS1 signal manifests itself in a more rapid water-level decline with increased daily rate before the earthquakes with $M \geq 5.0$ at epicentral distances $d_e \leq 350$ km. It was found that an expected earthquake can occur within a time of about one month after the end of the PS1 (in 90% of the cases) or during the PS1 development (in 10% of the cases).

According to the manual level measurements in 1987–1994, seven cases of a water-level decreases with amplitudes 4–47.4 cm were revealed during 3–36 weeks before earthquakes with M_w = 5.6–7.5 considered as hydrogeodynamic precursors (Kopylova, 2001).

The PS2 signal appears as a more rapid long-term water-level decline with increased daily rate preceding and accompanying the groups of the Kamchatka strong earthquakes (Kopylova and Boldina, 2019). This type of HGP was observed in 1991–1997 (six 1992–1997 earthquakes with M_w = 6.9–7.8 at epicentral distances up to 300 km) (Kopylova, 2001) and in 2012–2016 (four 2013–2016 earthquakes with magnitudes M_w = 6.6–8.3 (**Supplementary Materials Figure S7**).

In the YuZ-5 well, we have revealed retrospectively two cases of the anomalous changes in the water-level before the earthquakes of December 5, 1997 with M_w = 7.8 and January 30, 2016 with M_w = 7.2 (Kopylova and Boldina, 2019; **Supplementary Materials Figure S5**).

The durations of hydrogeological precursors in different wells prior to individual earthquakes (T_1) ranged from 4 to 39 weeks, i.e., from about 1 to 9 months, and do not show any relationship with earthquake magnitudes (**Supplementary Materials Figure S2A**). For the M-1 well, there is an increase in the lead time of the hydrogeochemical anomaly (T_2) in the range 1–5 months with an increase in the magnitude of subsequent earthquake (**Supplementary Materials Figure S2B**).

The hypothetical mechanisms of the hydrogeochemical and hydrogeodynamic precursors in observation wells of the Kamchatka Peninsula were considered in previous publications and briefly presented in **Supplementary Materials S2**.

The expert councils for earthquake prediction have been working in Kamchatka Krai for many years providing official seismic forecasts based on seismological, geophysical, hydrogeological, and other types of observations (Chebrov et al., 2011; Chebrov et al., 2013). Observation data at the wells of the Petropavlovsk-Kamchatsky test site are also used in the practice of such expert councils. Our collaboration with the Kamchatka branch of the Russian Expert Council for Earthquake Forecasting and Seismic Hazard and Risk Assessment (KB REC) which determines the correspondence between the released forecasts and the occurrence of the actual earthquakes provides the unique possibility to demonstrate practical significance of the some types of HGPs for real-time forecasting of the Kamchatka earthquakes.

Long-term data were obtained on the occurrences of the precursory signal PS1 in water-level changes in the E-1 well. The retrospective forecasting 1996–2012 earthquakes on the base of PS1 according the approach (Gusev, 1974; Kopylova, 2001; Chebrov et al., 2011; Chebrov et al., 2013) is presented in **Supplementary Materials Table S3**.

When PS1 is detected in real time, the forecast is made for 1–2 months (**Supplementary Materials Figure S8**). The observational data and the timing of the forecast are shown in **Supplementary Materials Figure S6**.

In accordance with the KB REC assessments our forecasts made on base of PS1 in 2004–2016 were true in terms of the time, location, and magnitude of the six events with M_w = 5.3–7.2 (**Figure 1A**).

RELATIONSHIP BETWEEN HYDROGEOLOGICAL PRECURSORS AND EARTHQUAKE PARAMETERS

When using HGP in individual well to predict earthquakes, it is necessary to know about the relationship between the HGP in that well and the parameters of subsequent earthquakes (magnitude, epicentral distance), as well as to estimate the expected seismic impact in the observation area.

We have analyzed the relationship between considered HGPs in individual wells and the parameters of the subsequent earthquakes (**Figure 2**). As the parameters characterizing the earthquakes, we considered the ratio between magnitude M_w and epicentral distance to the well (d_e). The value of the specific density of seismic energy in the wave (e) was used as a parameter of the earthquake impact in the area of the observation well. The e value is proportional to the square of the seismic wave velocity and can be applied as a metric for some co- and post-seismic processes such as soil liquefaction and undrained consolidation of sedimentary deposits (Wang and Chia, 2008; Wang and Manga, 2010). The e values were estimated by the formula $\log d_e = 0.48M_w - 0.33\log e - 1.4$ (Wang, 2007; Wang and Chia, 2008) and used to evaluate the range of e variations for the earthquakes preceded by the HGPs in the wells of the Kamchatka Peninsula. Previously in (Wang, 2007; Wang and Chia, 2008; Wang and Manga, 2010; Kopylova and Boldina, 2020), the e values were applied to assess co- and postseismic phenomena in ground- and surface waters. In this work, the e values are used to assess the possible seismic impact of earthquake in the observation area with manifestations of hydrogeological precursors.

The earthquakes with M_w = 6.5–7.8 before which there have been precursory anomalies in the groundwater chemical composition in two to three wells occurred at the epicentral distances d_e = 95–308 km, or 2.1–3.7 maximum linear sizes of earthquake sources according to (Riznichenko, 1976) (**Figure 2A**). During these earthquakes which were accompanied by the ground shaking with intensity I = 4.5–5.5 on MSK-64 scale (**Supplementary Materials Table S2**) the e values were 0.1–0.3 J/m^3. Close values of e were obtained for the two earthquakes, before which a precursor appeared in water-level changes in the YuZ-5 well (**Figure 2B**).

As mentioned above, long-term data were obtained on the occurrences of the precursory signal PS1 in the E-1 well before earthquakes with $M \geq 5.0$, $d_e \leq 350$ km highlighted retrospectively (**Figure 2B**, **Supplementary Materials Table S3**). **Figure 2B** also shows 1996–2012 earthquakes with $M \geq 5.0$, $d_e \leq 350$ km before which PS1 did not appear for the period of retrospective analysis (red crosses). In the range of magnitudes M = 5.0–6.5, the PS1 signal appears in 44% of cases (blue crosses), whereas before earthquakes with M_w = 6.6–7.8, PS1 manifested itself almost always.

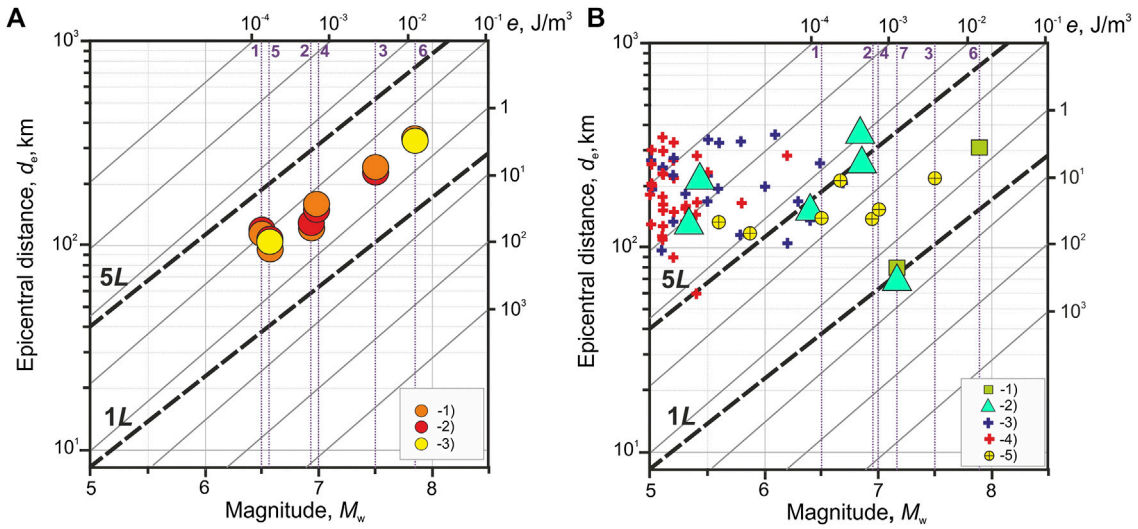

FIGURE 2 | Distribution of earthquake hydrogeological precursors in the observation wells as function of the parameters of the subsequent earthquakes: magnitude M_w, epicentral distance d_e, and specific density of seismic energy e: **(A)** hydrogeological precursors in chemical composition of water in flowing wells (1) GK-1, (2) M-1, (3) G-1 (**Supplementary Materials Table S2**); **(B)** hydrogeological precursors in water-level changes in wells (1) YuZ-5, (2)–(5) E-1: (2) PS1, determined in real time with the issuance of a conclusion on a possible earthquake for KB REC; (3) 1996–2012 earthquakes with $M \geq 5.0$, $d_e \leq 350$ km preceded by retrospectively identified PS1 (**Supplementary Materials Table S3**); (4) 1996–2012 earthquakes with $M \geq 5.0$, $d_e \leq 350$ km not preceded by PS1, and (5) water-level decreases at an increased rate preceded the 1987–1996 earthquakes (Table 3 in Kopylova, 2001). Thin vertical dotted lines on the magnitude scale indicate earthquakes preceded by hydrogeological precursors in two to four wells, the earthquake numbers correspond to the numbers in **Supplementary Materials Table S2**. The lines 1*L*, 5*L* show one and five maximal linear sizes of the source.

Before the six 2004–2016 earthquakes, PS1 was identified in real time and advanced forecasts were issued (**Figures 1A**, **2B**). We believe that with pronounced manifestations of PS2 and PS1 in water-level changes in the E-1 well, as well as other types of considered HGPs, a seismic forecast is possible for the strongest earthquakes in the adjacent segment of the Kamchatka seismic focal zone. Such earthquakes can be characterized by the magnitudes $M_w \geq 6.6$, the d_e/L ratio below 5, and the e value above 0.1 J/m^3 (**Figure 2**).

CONCLUSION

(1) Hydrogeological precursors manifesting themselves in the changes of chemical composition and pressure of groundwater at depths from hundreds of meters to a few first km are demonstrated on the case study from the Kamchatka Peninsula with a low population density and lack of industrial enterprises. The wells where hydrogeological precursors were detected are characterized by the absence of the influence of groundwater development and other anthropogenic factors which can disrupt the natural state of groundwater during the preparation of earthquakes. Unfortunately, in many cases when studying hydrogeological effects before earthquakes, an important aspect of the technogenic impact on the regime of observation wells is not sufficiently taken into account (King, 2018; King and Manga, 2018; Wang et al., 2018). When discussing the relatively long-term manifestations of hydrogeological precursors from urbanized and densely populated countries, it is necessary to consider technogenic factors in more detail, as well as climatic factors and their influence on the processes of groundwater filtration. Otherwise, ideas about the forms of hydrogeological precursors and their connections with the parameters of subsequent earthquakes may be distorted.

(2) A correlation was detected between the manifestations of hydrogeological precursors in considered wells and the parameters of the subsequent earthquakes (**Figure 2**). In the Kamchatka Peninsula, the hydrogeological precursors were mainly observed before the earthquakes with M_w = 6.6–7.8 at the epicentral distances of 80–300 km from the wells. These earthquakes caused ground shaking with intensity four to six on MSK-64 scale; seismic energy density during these events in the regions of the wells ranged from 0.1 to 4.5 J/m^3. The HGPs were mainly observed in the near and intermediate field zones of the earthquake sources (d_e/L = 0.9–3.7). The data obtained on the HGPs manifestations can be useful in the study of the phenomena in the groundwater preceding strong earthquakes of other seismically active regions and other geophysical fields associated with changes in water pressure and physical properties of water-saturated rocks.

(3) In the case of the E-1 well, we revealed the increased sensitivity of fluid pressure during the preparation of the strong earthquakes which manifested itself in the more rapid water-level falls at an increased rate both before separate earthquakes (PS1 precursory signal) and before groups of the

strong earthquakes (PS2 precursory signal). This indicates that during the preparation of strong ($M_w \geq 6.6$) earthquakes, a decrease of water pressure in gas-saturated groundwater occurs over a period of time from weeks to several years. Such a process can occur with an increase in the capacity of water-bearing rocks, as well as due to phase transitions of gas and an increase in the density of groundwater in water-bearing rocks and in the wellbore.

(4) The retrospective analysis of the PS1 manifestations has shown that with the increase in the magnitudes of the predicted earthquakes from $M \geq 5.0$ to $M_w \geq 5.8$, the efficiency of PS1 for the seismic forecast increases from J = 1.4 to J = 2.4 (**Supplementary Materials Table S3**). This indicates that PS1 is a useful precursor of the strong earthquakes which may improve the forecasts of such earthquakes by a factor of 1.4–2.4 compared to random guessing. At the same time, the relatively low statistical estimates of the correlation between the PS1 and the subsequent earthquakes make the PS1 applicable for seismic forecasting only if combined with the other observation data and other precursors. The correlations between the other precursors and the subsequent earthquakes in Kamchatka are also low and not exceeding the values obtained for the PS1 (Serafimova and Kopylova, 2010; Chebrov et al., 2011; Chebrov et al., 2013). This highlights the need for developing new methods for analyzing of the prognostic data for increase the accuracy and reliability of earthquake forecasting. The data on the joint occurrence of different precursors before earthquakes from the archives of the expert councils may help much in providing more objective estimates of the efficiency of the precursors for seismic forecasting.

(5) Since 2001, an experiment has been conducted on the use of the PS1 precursor, and since 2012, together with the PS2 precursor, to predict earthquakes in real time by submitting forecasts to the KB REC. According to the KB REC conclusions, successful predictions of the location, time, and magnitude were made for six 2004–2016 earthquakes with M_w = 5.3–7.2 (**Figures 1A**, **2B**).

We believe that progress in the study of hydrogeological and other types of earthquake precursors for seismic forecasting can be achieved with closer collaboration of specialists observing precursors with expert councils for earthquake prediction.

AUTHOR CONTRIBUTIONS

All authors listed have made a substantial, direct, and intellectual contribution to the work and approved it for publication.

FUNDING

The study was funded by the Kamchatka branch of the Geophysical Survey of the Russian Academy of Sciences (KB GS RAS) with the partial participation of the Russian Foundation for Basic Research, grant 18-05-00337.

ACKNOWLEDGMENTS

The work was supported by Ministry of Science and Higher Education of the Russian Federation (№ 075-01304-20) and the Russian Foundation for Basic Research under project 18-05-00337 "Typification and models of hydrogeoseismic effects of the earthquakes from water-level measurements in wells: case study of Kamchatka region."

SUPPLEMENTARY MATERIALS

The Supplementary Material for this article can be found online at: https://www.frontiersin.org/articles/10.3389/feart.2020.576017/full#supplementary-material

REFERENCES

Biagi, P. F., Ermini, A., Cozzi, E., Khatkevich, Y. M., and Gordeev, E. I. (2000a). Hydrochemical precursors in Kamchatka (Russia) related to the strongest earthquakes in 1988–1997. *Nat. Hazards* 21, 263. doi:10.1023/A:1008178104003

Biagi, P. F., Ermini, A., Kingsley, S. P., Khatkevich, Y. M., and Gordeev, E. I. (2000b). Groundwater ion content precursors of strong earthquakes in Kamchatka (Russia). *Pure Appl. Geophys.* 157, 1359. doi:10.1007/PL00001123

Boldina, S. V., and Kopylova, G. N. (2017). Effects of the January 30, 2016, M_w = 7.2 Zhupanovsky earthquake on the water level variations in wells Yuz-5 and E-1 in Kamchatka. *Geodin. Tektonofiz.* 8 (4), 863–880. doi:10.5800/GT-2017-8-4-0321

Chebrov, V. N., Saltykov, V. A., and Serafimova, Y. K. (2013). Identifying the precursors of large (M ≥ 6.0) earthquakes in Kamchatka based on data from the Kamchatka Branch of the Russian expert council on earthquake prediction: 1998-2011. *J. Volcanolog. Seismol.* 7 (1), 76–85. doi:10.1134/S074204631301003X

Chebrov, V. N., Saltykov, V. A., and Serafimova, Y. K. (2011). *Prognozirovaniye zemletryaseniy na Kamchatke. Po materialam raboty Kamchatskogo filiala Rossiyskogo ekspertnogo soveta po prognozu zemletryaseniy, otsenke seysmicheskoy opasnosti i riska v 1998–2009 gg. (Forecasting earthquakes in Kamchatka. Based on the work of the Kamchatka branch of the Russian Expert Council on earthquake forecasting, seismic hazard and risk assessment in 1998–2009)*. Moskva: Svetoch Plyus. [in Russian].

Gusev, A. A. (1974). "Earthquake prediction based on seismicity statistics," in *Seismichnost' i seismicheskii prognoz, svoistva verkhnei mantii i ikh svyaz' s vulkanizmom na Kamchatke (Seismicity and Earthquake Prediction, Upper Mantle Properties and Their Relationship to Volcanism in Kamchatka)*. (Novosibirsk: Nauka), 109–119. [in Russian].

Khatkevich, Y. M., and Ryabinin, G. V. (2006). Geochemical and ground water studies in Kamchatka in the search for earthquake precursors. *Volkanologiya i seysmologiya* 4, 34–42. [in Russian].

King, C.-Y. (2018). Characteristics of a sensitive well showing pre-earthquake water-level changes. *Pure Appl. Geophys.* 175, 2411–2424. doi:10.1007/s00024-018-1855-4

King, C.-Y., and Manga, M. (2018). Hydrological, geochemical and geophysical changes related to earthquakes and slow-slip events: introduction. *Pure Appl. Geophys.* 175, 2407–2409. doi:10.1007/s00024-018-1923-9

Kopylova, G. N., and Boldina, S. V. (2020). Effects of seismic waves in water level changes in a well: empirical data and models. *Izvestiya Phys. Solid Earth* 56 (4), 530–549. doi:10.1134/S1069351320030039

Kopylova, G. N., and Boldina, S. V. (2019). Hydrogeoseismological research in Kamchatka: 1977-2017. *J. Volcanolog. Seismol.* 13 (2), 71–84. doi:10.1134/S0742046319020040

Kopylova, G. N., and Boldina, S. V. (2012). On the relationships of water-level variations in the E-1 well, Kamchatka to the 2008-2009 resumption of activity on Koryakskii volcano and to large (M ≥ 5) earthquakes. *J. Volcanolog. Seismol.* 6 (5), 316–328. doi:10.1134/S074204631205003X

Kopylova, G. N., Boldina, S. V., Smirnov, A. A., and Chubarova, E. G. (2017). Experience in registration of variations caused by strong earthquakes in the level and physicochemical parameters of ground waters in the piezometric wells: the case of Kamchatka. *Seism. Instr.* 53 (4), 286–295. doi:10.3103/S0747923917040065

Kopylova, G. N. (2006). Earthquake-induced water level changes in the YuZ-5 well Kamchatka. *Volkanologiya i seysmologiya* 6, 52–64. [in Russian].

Kopylova, G. N., Lyubushin, A. A., and Boldina, S. V. (2019). Statistical analysis of precision water level data from observations in a seismoactive region: case study of the YuZ-5 well, Kamchatka. *Seism. Instr.* 55 (5), 507–523. doi:10.3103/S0747923919050086

Kopylova, G. N., Sugrobov, V. M., and Khatkevich, Y. M. (1994). Variations in the regime of springs and hydrogeological boreholes in the Petropavlovsk polygon (Kamchatka) related to earthquakes. *Volkanologiya i seysmologiya*. 2, 53–70. [in Russian].

Kopylova, G. N., and Taranova, L. N. (2013). Synchronization signals in the variations of groundwater chemical composition in Kamchatka in relation to the strong (M W ≥ 6.6) earthquakes. *Izvestiya Phys. Solid Earth* 49 (4), 577–586. doi:10.1134/S106935131304006X

Kopylova, G. N. (2001). Variations of water level elizovskaya 1 well, Kamchatka due to large earthquakes: 1987–1998 observations. *Volkanologiya i seysmologiya.* 2, 39–52. [in Russian].

Riznichenko, Y. V. (1976). "The source dimensions of the crustal earthquakes and the seismic moment," in *Issledovaniya po fizike zemletryasenii (studies in earthquake physics).* (Moscow: Nauka), 9–27. [in Russian].

Roeloffs, E. A. (1988). Hydrologic precursors to earthquakes: a review. *Pageoph* 126, 177–209. doi:10.1007/bf00878996

Serafimova, Y. K., and Kopylova, G. N. (2010). Intermediate-term precursors of large (M ≥ 6.6) Kamchatka earthquakes for the period from 1987 to 2004: a retrospective assessment of their information content for prediction. *J. Volcanolog. Seismol.* 4 (4), 223–231. doi:10.1134/S0742046310040019

Skelton, A., Liljedahl-Claesson, L., Wästeby, N., Andrén, M., Stockmann, G., Sturkell, E., et al. (2019). Hydrochemical changes before and after earthquakes based on long-term measurements of multiple parameters at two sites in northern Iceland–a review. *J. Geophys. Res. Solid Earth* 124 (3), 2702. doi:10.1029/2018JB016757

Thomas, D. (1988). Geochemical precursors to seismic activity. *Pageoph* 126 (2–4), 241–266. doi:10.1007/bf00878998

Wang, B., Liu, Y., Sun, X., Ma, Y., Zhang, L., Ren, H., et al. (2018). Hydrogeological and geochemical observations for earthquake prediction research in China: a brief overview. *Pure Appl. Geophys.* 175, 2541–2555. doi:10.1007/s00024-018-1885-y

Wang, C.-Y., and Chia, Y. (2008). Mechanism of water level changes during earthquakes: near field versus intermediate field. *Geophys. Res. Lett.* 35, L12402. doi:10.1029/2008GL034227

Wang, C.-Y. (2007). Liquefaction beyond the near field. *Seismol Res. Lett.* 78, 512–517. doi:10.1785/gssrl.78.5.512

Wang, C.-Y., and Manga, M. (2010). *Earthquakes and water. Lecture notes in Earth Sciences*. Berlin: Springer. doi:10.1007/978-3-642-00810-8

Conflict of Interest: The authors declare that the research was conducted in the absence of any commercial or financial relationships that could be construed as a potential conflict of interest.

Copyright © 2020 Kopylova and Boldina. This is an open-access article distributed under the terms of the Creative Commons Attribution License (CC BY). The use, distribution or reproduction in other forums is permitted, provided the original author(s) and the copyright owner(s) are credited and that the original publication in this journal is cited, in accordance with accepted academic practice. No use, distribution or reproduction is permitted which does not comply with these terms.

frontiers in Earth Science

ORIGINAL RESEARCH
published: 21 December 2020
doi: 10.3389/feart.2020.559624

Aftershock Rate Changes at Different Ocean Tide Heights

*P. N. Shebalin and A. A. Baranov**

Institute of Earthquake Prediction Theory and Mathematical Geophysics, Russian Academy of Sciences, Moscow, Russia

The differential probability gain approach is used to estimate quantitatively the change in aftershock rate at various levels of ocean tides relative to the average rate model. An aftershock sequences are analyzed from two regions with high ocean tides, Kamchatka and New Zealand. The Omori-Utsu law is used to model the decay over time, hypothesizing an invariable spatial distribution. Ocean tide heights are considered rather than phases. A total of 16 sequences of M ≥6 aftershocks off Kamchatka and 15 sequences of M ≥6 aftershocks off New Zealand are examined. The heights of the ocean tides at various locations were modeled using FES 2004. Vertical stress changes due to ocean tides are here about 10–20 kPa, that is, at least several times greater than the effect due to Earth tides. An increase in aftershock rate is observed by more than two times at high water after main M ≥6 shocks in Kamchatka, with slightly less pronounced effect for the earthquakes of M = 7.8, December 15, 1971 and M = 7.8, December 5, 1997. For those two earthquakes, the maximum of the differential probability gain function is also observed at low water. For New Zealand, we also observed an increase in aftershock rate at high water after thrust type main shocks with M ≥6. After normal-faulting main shocks there was the tendency of the rate increasing at low water. For the aftershocks of the strike-slip main shocks we observed a less evident impact of the ocean tides on their rate. This suggests two main mechanisms of the impact of ocean tides on seismicity rate, an increase in pore pressure at high water, or a decrease in normal stress at low water, both resulting in a decrease of the effective friction in the fault zone.

Keywords: ocean tides, Kamchatka, New Zealand, FES 2004, Omori-Utsu law, differential probability gain, pore pressure, effective friction

OPEN ACCESS

Edited by:
Antonella Peresan, Istituto Nazionale di Oceanografia e di Geofisica Sperimentale (OGS), Italy

Reviewed by:
Cataldo Godano, University of Campania Luigi Vanvitelli, Italy
Prosanta Kumar Khan, Indian Institute of Technology Dhanbad, India

****Correspondence:***
A. A. Baranov
baranov@ifz.ru

Specialty section:
This article was submitted to Solid Earth Geophysics, a section of the journal Frontiers in Earth Science

Received: *06 May 2020*
Accepted: *26 October 2020*
Published: *21 December 2020*

Citation:
Shebalin PN and Baranov AA (2020) Aftershock Rate Changes at Different Ocean Tide Heights. Front. Earth Sci. 8:559624. doi: 10.3389/feart.2020.559624

INTRODUCTION

During last decades, the question of the effect of ocean tides on seismicity has been widely investigated. The issue of whether tidal forces really affect seismicity has been raised many times in the literature. Most of the studies established a connection between tides and seismicity, mainly on a regional scale (Klein, 1976a; Klein, 1976b; Souriau et al., 1982; Wilcock, 2001; Lin et al., 2003; Tanaka et al., 2004; Crockett et al., 2006; Stroup et al., 2007; Tanaka, 2010; Chen et al., 2012a; Datta and Kamal, 2012; Tanaka, 2012; Ide and Tanaka, 2014; Saltykov, 2014; Vergos et al., 2015; Arabelos et al., 2016; Baranov et al., 2019; Scholz et al., 2019) and others. There are also many studies linking seismicity and tides using global catalogues (Heaton, 1975; Nikolaev, 1994; Tsuruoka, et al., 1995; Tanaka et al., 2002; Cochran et al., 2004; Yurkov and Gitis, 2005; Métivier, et al., 2009; Chen et al., 2012b; Ide et al., 2016). However, many studies do not find such a correlation (Schuster, 1897; Morgan et al., 1961; Knopoff, 1964; Simpson, 1967; Shudde and Barr, 1977; Heaton, 1982; Rydelek et al., 1992; Vidale et al., 1998). A detailed review of the influence of tides on seismicity was given, for example, in (Emter, 1997).

Laboratory experiments were also conducted to study the effect of tides on seismicity (Lockner and Beeler, 1999; Beeler and Lockner, 2003). A strong correlation was found to exist between periodic stress (tides) and the occurrence of failure (earthquake) at shear stress amplitudes above approximately 0.3 MPa. Shear stress variations between 10 kPa (1 m of ocean tide load) and 0.1 MPa represent a transition region in which correlation with earthquake occurrence may occur. For amplitudes below 10 kPa (the order of the vertical component of the Earth tide), little or no correlation can be detected. These results are consistent with observations. This suggested that tidal stress amplitudes of about 3–10 kPa are required to trigger earthquakes (Hardebeck et al., 1998; Cochran et al., 2004). For example, it was shown that aftershocks after the M = 7.4 Landers event were triggered by stress increases greater than 10 kPa (Stein, 1999).

Largely since (Schuster, 1897), the tidal phases, mainly the semidiurnal phase, were studied. The amplitude-frequency properties of tides are very complex, and it is necessary to take into account the change in the amplitudes of various components of the tides. However, some studies such as (Klein, 1976a; Klein, 1976b; Souriau et al., 1982; Vidale et al., 1998; Lockner and Beeler, 1999; Wilcock, 2001; Beeler and Lockner, 2003; Stroup et al., 2007) and more recent ones (Ide and Tanaka, 2014; Ide et al., 2016; Baranov et al., 2019) analyzed tidal heights rather than tidal phases. The present study is concerned with aftershock rates after large earthquakes. This gives us high rates and high rate changes on the time scale of hours and days, compatible with the time scale of tides. In this time scale, tide height analysis seems more appropriate due to the complex tide phase structure. Actually, researchers studied the effect of Earth tides (Morgan et al., 1961; Heaton, 1975; Klein, 1976a; Klein, 1976b; Heaton, 1982; Burton, 1986; Rydelek et al., 1992; Lin et al., 2003; Métivier et al., 2009; Chen et al., 2012a; Chen et al., 2012b; Datta and Kamal, 2012; Saltykov, 2014) or the combined effect of Earth and ocean tides on seismicity (Souriau et al., 1982; Vidale et al., 1998; Tsuruoka, et al., 1995; Wilcock, 2001; Tanaka et al., 2002; Tanaka et al., 2004; Cochran et al., 2004; Stroup et al., 2007; Tanaka, 2010; Tanaka, 2012; Ide et al., 2016).

There are relatively few studies where the connection between seismicity and ocean tides was analyzed. This is due to the complexity of numerical calculations of ocean tides. Only in recent years computer programs for the numerical modeling of ocean tides have been developed. These programs were used to study the connection between ocean tides and seismicity (Crockett et al., 2006; Ide and Tanaka, 2014; Baranov et al., 2019). The result was to detect a clear connection between seismicity and ocean tides. Despite a large number of comparative studies of seismicity and tides, the relationship between aftershock rates and tides was studied in few papers (Souriau et al., 1982; Chen et al., 2012b; Datta and Kamal, 2012; Saltykov, 2014; Baranov et al., 2019). A partial dependence of aftershock rate on tidal heights (ocean and Earth tides) for normal-fault and thrust-fault earthquakes was found for the Pyrenees (Souriau et al., 1982). But for strike-slip earthquakes no statistical connection was found. The M >7 earthquakes worldwide since 1900 are more likely to occur during the 0°, 90°, 180° or 2,70° phases (i.e., earthquake-prone phases) of the semidiurnal solid Earth (M_2) tidal curve (Chen et al., 2012b). Diurnal and semi-diurnal periodicities in aftershock rate ($M \geq 4$) were found for the aftershock sequence of the Tohoku M = 9.1 earthquake of March 11, 2011 in Japan with an apparent weakening of the tidal triggering effect over time (Datta and Kamal, 2012). This suggests that large aftershocks in the fault zone of the Japan 2011 earthquake were strongly influenced by Earth tides.

Partial dependence of aftershock rates on Earth tides was also found for aftershocks of the M = 6.8 earthquake of June 21, 1996 off Kamchatka (Saltykov, 2014), and an alternative trigger mechanism was proposed for tidal effects based on an amplitude-dependent dissipation model. Another study of aftershock sequences following Kamchatka earthquakes using the method of differential probability gain, DPG (Baranov et al., 2019), demonstrated a considerable increase in the aftershock rate (by factors of two and more) at low or at high water. An increase in aftershock rate at low water corresponds to unloading of the seafloor, while high water may result in an increase of pore pressure in the fracture zone and therefore decreasing friction forces. The correlation between seismicity and tides in relation to focal mechanisms was studied by several authors. Correlation was mainly found for normal and partly for thrust slip types (Heaton, 1975; Souriau et al., 1982; Tsuruoka, et al., 1995; Tanaka et al., 2002; Cochran et al., 2004). The connection between seismicity and tides at ocean ridges were studied extensively (Wilcock, 2001; Tolstoy et al., 2002; Stroup et al., 2007; Scholz et al., 2019). A correlation between tides and seismicity was found along the Juan de Fuca Ridge (Wilcock, 2001; Tolstoy et al., 2002) and for East Pacific Rise (Stroup et al., 2007). Scholz et al. (2019) suggested pulsation of magma chambers due to vertical stress changes as a mechanism responsible for the tidal triggering of earthquakes for mid-ocean ridges.

The impact of tides on earthquakes is often explained by changes in the stress field in the fault using the Coulomb criterion (Stein, 1999; Cochran et al., 2004). Coulomb failure stress change $\Delta\tau_c = \Delta\tau + \mu(\Delta\sigma_n - \Delta P)$, where τ and σ_n are the shear stress change on the fault (assumed to be positive in the direction of slip) and the normal stress change on the fault (positive if the fault is unclamped), respectively, P is the pore pressure change in the fault, and μ is the coefficient of friction (with range 0–1). Failure is encouraged if $\Delta\tau_c$ is positive and discouraged if negative; both increased shear and unclamping of faults facilitate failure. Thus friction threshold can be exceeded either when the normal stress is decreased or when pore pressure is increased (Klein, 1976a; Klein, 1976b; Wilcock, 2001; Tolstoy et al., 2002; Cochran et al., 2004; Stroup et al., 2007; Métivier et al., 2009). This can reflect earthquake initiation (Stein, 2004). Some authors suggested alternative mechanisms to explain the effect of tides on seismicity: nonlinear dilatancy-diffusion model (Heaton, 1982), seismic modulation by combination of different tidal waves, impacts of tidal waves occurring in resonance with the self-oscillating system of the focal zone under the influence of tidal waves (Nikolaev, 1996) or an amplitude-dependent dissipation model taking into account tidal variations in physical properties

TABLE 1 | A review of studies of the impact of tides on seismicity.

№	Paper	Earth tides	Ocean tides	Tidal phase	Connection with seismicity	Tidal amplitude	Influence mechanism, methods	Object of investigations
1	(Morgan et al., 1961)	+	–	–	–	–	No definite evidence for effects due to earth tides	1933 earthquakes from different regions
2	(Heaton, 1975)	+	–	+	+ Partly. Oblique slip and dip-slip earthquakes are triggered by tidal stresses, M > 5, depth <30 km	–	Tidal triggering is discussed from the viewpoint of the dilatancy-diffusion model. The earthquake frequency is highest with tidal phase from –90° to 90°	107 earthquakes from different regions
3	(Klein, 1976a)	+	–	+	+ Partly	+ Through vertical stress	Three conceivable triggering mechanisms: Maximum shear stress, least compressive normal stress and maximum pore pressure	Mainshocks and aftershocks (M > 5), mid-atlantic ridge and Iceland region
4	(Klein, 1976b)	+	–	+	+ Partly	+ Through vertical stress	Tidal stresses are oriented to enhance the tectonic stress. No preference between elastic loading and pore pressure as the mechanism of reservoir-induced seismicity. The time of primary earthquake occurrence is mostly during the quarter of the tidal cycle in which tidal shear stress most enhances fault slip	Eight reservoirs, 10–20 mainshocks for each reservoir
5	(Heaton, 1982)	+	–	+	–	–	Dilatancy-diffusion model for tidal triggering	328 earthquakes from different regions
6	(Souriau et al., 1982)	+	+	+	+ Partly, for normal and thrust fault types	+	Statistical test using binomial distribution. Model takes into account both phase and amplitude variations of the tidal stresses	Aftershock sequence in the pyrenees (515 events)
7	(Burton, 1986)	+	–	–	+ Partly	–		An overview
8	(Rydelek et al., 1992)	+	–	+	– The results of the schuster test indicate lack of tidal triggering	–	Tidal stress may trigger an earthquake by increasing the shear stress, by decreasing the effective normal stress, or by some combination of these factors	Earthquake swarms, Pozzuoli catalogue, Italy
9	(Nikolaev, 1994)	+	–	+	+ Partly for some areas	–	No mechanism	Hadson`s catalogue from 1962 to 1988, M > 5
10	(Tsuruoka, et al., 1995)	+	+	+	+ Partly for normal fault, maximum seismicity for tidal phase from 0° to 60° –For strike-slip or thrust	–	Normal-fault-type earthquakes tend to occur at the time when the cubic tidal stress takes a maximum tensile value or a little bit later	988 globally distributed earthquakes with magnitude of 6.0 or larger from CMT from 1977 to 1992
11	(Nikolaev, 1996)	+	–	+	+ Partly, for some areas	–	Two possible mechanisms: Seismic modulation by combination of different tidal waves or hit in resonance of the self-oscillating system of the focal zone under the influence of tidal waves	8,985 events for caucasus, 3 < M < 5.5, 1962–1989; Hadson`s catalogue, 8,500 events, 1962–1988 without aftershocks
12	(Hardebeck et al., 1998)	–	–	–	+ Partly	–	Static stress change triggering model is useful in explaining the landers aftershocks particularly those which are not too close to (d < 5 km or [ACS> 0.5–1 MPa]) or too far from (d > 75 km or [ACS <0.01 MPa]) the mainshock fault plane	California, 2 aftershock sequences from landers and northridge earthquakes
13	(Vidale et al., 1998)	+	+	+	–	+ Through vertical stress	Probability distribution of tidal stress. Binomial model of triggering	13,042 earthquakes near San-Andreas fault (1969–1994)

(Continued on following page)

TABLE 1 | (*Continued*) A review of studies of the impact of tides on seismicity.

№	Paper	Earth tides	Ocean tides	Tidal phase	Connection with seismicity	Tidal amplitude	Influence mechanism, methods	Object of investigations
14	(Lockner and Beeler, 1999)	–	–	–	–	+ Through vertical stress	Strong correlation between the periodic stress and the occurrence of failure at shear stress amplitudes above approximately 0.3 MPa. Little or no correlation at amplitudes below 0.01 MPa	Laboratory experiments. Samples were deformed in a triaxial loading frame at constant confining pressure 50 MPa. Earth's crust permits delayed failure
15	(Wilcock, 2001)	+	+	+	+ The earthquake frequency nearly doubles at the lowest tides	+ Frequency of events as a function of tidal height	The earthquake frequency is lowest at high water and highest at low water and in the quadrant following low water	1899 microearthquakes recorded during a 55 days experiment on the endeavor segment of the Juan de Fuca ridge
16	(Tanaka et al., 2002)	+	+	+	+ Partly	–	Correlation is found for reverse fault type and normal fault type. Earthquakes tend to occur when the tidal stress accelerates the fault slip. There is no correlation for strike-slip type	9,350 global events from CMT, M > 5.5
17	(Tolstoy et al., 2002)	+	+	–	+ Maximum at low water	+	Reduction in normal stress, which causes faults already very close to their failure point to slip, increasing of pore pressure. Schuster`s test	402 earthquakes near the summit caldera of axial volcano on the Juan de Fuca ridge
18	(Lin et al., 2003)	+	–	+	+ Partly, correlation only for 2.5 < M < 5	–	No mechanisms	1973–1991 local Taiwan catalogue
19	(Beeler and Lockner, 2003)	–	–	–	+ Partly for earth tides, minimum 13,000 earthquakes are needed	+ Through vertical stress	Delayed failure is key to understanding why earthquake occurrence correlates weakly with small stress changes such as the solid earth tides	Laboratory experiments. The degree of correlation between failure time and the phase of the driving stress depends on the amplitude and frequency of the stress oscillation and on the stressing rate
20	(Saltykov et al., 2004)	+	–	+	+ Before mainshock in focal area	–	No mechanism, maximum of seismicity for positive values of the decreasing tidal height with a delay to a quarter of the period concerning a maximum	Catalogue of Kamchatka, M > 2.6, only mainshocks
21	(Tanaka et al., 2004)	+	+	+	+ Partly	–	Earthquakes preferentially occur when the tidal compressional stress is near the dominant direction of P-axes of focal mechanisms obtained in the corresponding regions	Japan meteorological agency for the period from October 1997 to May 2002, they use the origin times and hypolefts of shallow earthquakes (focal depth ≤70 km, M ≥ 2.0) occurring in Japan
22	(Cochran et al., 2004)	+	+	+	+ Partly	–	Earthquake triggering correlation is found for coefficient of friction between 0.2 and 0.6, using binomial and Schuster`s tests	Only main events (2027) from CMT, depth 0–40 km, M > 5.5
23	(Yurkov and Gitis, 2005)	+	–	+	+	–	Only lunar forces investigated, standard statistical test only	National Earthquake Information Center (NEIC) catalogue 161,060 earthquakes, M > 4, 1973–1999
24	(Crockett et al., 2006)	–	+	+	+	–	December 26, 2004 sumatra earthquake and its principal aftershocks (20–30 km depth) occurred in close relation to new and full moons	December 26, 2004 sumatra earthquake and its aftershocks. Advanced national seismic system database (www.ncedc.org/anss). 5,807 earthquakes of m_b = 3.5 and greater. Ocean tides were calculated using JTides program
25	(Stroup et al., 2007)	+	+	+	+ Maximum at low water	+ Tidal height	The modulation of 9°50′N microearthquakes by small-amplitude periodic stresses is consistent with earthquake nucleation within a high stressing rate environment that is maintained near a critical state of failure by on-axis magmatic and hydrothermal processes	Microearthquakes at 9°50′N East pacific rise

(Continued on following page)

TABLE 1 | (*Continued*) A review of studies of the impact of tides on seismicity.

№	Paper	Earth tides	Ocean tides	Tidal phase	Connection with seismicity	Tidal amplitude	Influence mechanism, methods	Object of investigations
26	(Métivier et al., 2009)	+	–	+	+ Clear correlation (with ~99% confidence) between the phase of the solid earth tide and the timing of seismic events	–	Earthquakes occur slightly more often at the time of ground uplift by the earth tide. No evidence for a focal mechanism dependence on earthquake triggering. Tidal stresses trigger up to about 0.2–0.3% of all the earthquakes. Shallow earthquakes are more easily triggered, because tidal dilations become relatively smaller	The NEIC catalogue with 442,412 events 1973–2007, M > 2.5
27	(Tanaka, 2010)	+	+	+	+	-	The frequency distribution of tidal phase angles in the prevent period before mainshock exhibited a peak near the angle where the tidal shear stress is at its maximum to accelerate the fault slip	Tidal triggering of earthquakes precursory to the three giant earthquakes (December 26, 2004, M = 9.0, March 28, 2005 M = 8.6, and September 12, 2007, M = 8.5). Global CMT catalogue, depth<70, 1976–2008, M > 5
28	(Chen et al., 2012a)	+	–	+	+ Maximum at low water	–	No mechanism, EMD statistical method, tidal triggering effect in both the non-declustered and declustered catalogues	Taiwan Telemetered Seismic Network catalogue earthquakes that occurred near Taiwan between 1973 and 2008
29	(Chen et al., 2012b)	+	–	+	+	–	M > 7 earthquakes are more likely to occur during the 0°, 90°, 180° or 270° phases of the semidiurnal solid earth tidal curve (M2)	420,747 M > 4 global earthquakes, aftershock sequence of the M = 6.2 Christchurch, New Zealand
30	(Datta and Kamal, 2012)	+	–	+	+	–	No mechanism	1,370 aftershocks (M > 4) during 1 month in the fault area of Japan earthquake of March 2011
31	(Tanaka, 2012)	+	+	+	+ Maximum seismicity for tidal phase from –90° to 90° before mainshock for focal area	–	Tidal phase distribution of earthquakes exhibits a peak where the shear stress is at its maximum to promote failure.No significant tidal correlation is found after the Tohoku-Oki mainshock	Focal area of Tohoku-Oki earthquake before main event (ten years) shallow earthquakes (depths less than 70 km) in the global CMT catalogue from 1976 to 2011, M > 5
32	(Ide and Tanaka, 2014)	–	+	+	+ Maximum seismicity at low water	+ Through shear stress	Strong correlation, most of events occur at low water from minimum to increasing of lithostatic pressure. A low water results in increased shear stress and decreased normal stress unclamping, resulting in an enhancement of plate subduction	Deep Tremor, western Japan, ocean tides were calculated using JTides program
33	(Saltykov, 2014)	+	–	+	+ Partly	–	An alternative trigger mechanism based on an amplitude-dependent dissipation model, taking into account tidal variations of the physical properties of a medium	147 aftershocks for (June 21, 1996, M = 6.8) event, Kamchatka
34	(Vergos et al., 2015)	+	+	+	+ Seismicity corresponds with the diurnal luni-solar (K1) and semidiurnal solar (S2) tidal variations	–	No mechanism, Schuster`s test	Catalogue of Geodynamic institute of the National Observatory of Athens (http://www.gein.noa.gr/services/cat.html), 16,137 shallow and 1,482 deep earthquakes with M < 6.2 occurred from 1964, to 2012, around the Hellenic Arch
35	(Arabelos et al., 2016)	+	+	+	+ Seismicity corresponds with the diurnal luni-solar (K1) and semidiurnal solar (S2) tidal variations	+	No mechanism, Schuster`s test	National Observatory of Athens catalogue, 33,281 shallow and 769 of intermediate depth earthquakes, Greece, 0.2 < M < 6.3, from January 1964 to December 2013, in an area bounded by $38^\circ \le f \le 39^\circ$ and $21^\circ \le \lambda \le 23^\circ$

(Continued on following page)

TABLE 1 | (*Continued*) A review of studies of the impact of tides on seismicity.

№	Paper	Earth tides	Ocean tides	Tidal phase	Connection with seismicity	Tidal amplitude	Influence mechanism, methods	Object of investigations
36	(Ide et al., 2016)	+	+	+	+ Partly, large earthquakes tend to occur near the time of maximum tidal stress amplitude	+ Through shear stress	Estimation of b-values and Utsu's test. The *b*-value decreases as the amplitude of tidal shear stress increases. The probability of a tiny rock failure expanding to a gigantic rupture increases with increasing tidal stress levels. Large earthquakes are more probable during periods of high tidal stress	CMT catalogue with M > 5.5 (>10,000 events, 1976–2015); National Research Institute for Earth Science and Disaster Resilience F-net moment tensor catalogue for earthquakes in northeastern Japan of Mw > 4.5, from 1997 to 2015; and the refined earthquake focal mechanism catalogue for southern California for earthquakes in southern California with M > 2.5
37	(Varga and Grafarend, 2017)	+	+	–	–	–	Triggering effect of earth tides is different in case of zonal, tesseral, and sectorial tides and also significantly depends on the latitude. Only the horizontal shear stresses produced by earth tides are most likely to influence the outbreak of an earthquake. The influence of load tides (ocean tides) is limited to the loaded area and its immediate vicinity	Theoretical model
38	(Baranov et al., 2019)	–	+	–	+	+ Tidal height	Mechanisms: Friction reduction in a fault due to vertical stress decreasing at low waters and increased pore pressure at high waters	16 aftershock sequences of earthquakes near Kamchatka with M > 6, depth<50 km from regional catalogue produced by the Geophysical survey of the Russian academy of sciences
39	(Scholz et al., 2019)	+	+	+	+	+	Tidal triggering of mid-ocean ridge seismicity, earthquakes occur preferentially during low water	Axial volcano on the Juan de Fuca ridge, ~60,000 earthquakes located between January 22nd and April 23rd, 2015

of the medium (Saltykov, 2014). The researchers used different methods to study the effect of tides on seismicity from simple visual comparison between time series of seismicity and tides to more or less sophisticated statistical methods as binomial distribution test, random distribution test, method of Chapman-Miller (Malin and Chapman, 1970), and Schuster's test using a statistical method of Rayleigh (Schuster, 1897). Schuster's test was described in detail in many papers (e.g., Heaton, 1975; Rydelek et al., 1992). **Table 1** summarized studies of tides on seismicity using several key parameters: type of tides (Earth tides, ocean tides), tidal phases, connection with seismicity, tidal amplitude, the mechanism responsible, and the object of study.

Why do we study the impact of ocean tides on aftershock rate using a model of tide heights?

(1) Time scales of tides and aftershock occurrence are comparable. The time-dependent distribution of aftershocks without impact of tides can be modeled.
(2) The impact of ocean tides on aftershock rates still remains a challenge (Cochran et al., 2004; Tanaka, 2012; Baranov et al., 2019).
(3) The well-known Schuster test using tide phases requires a correct catalogue declustering. Aftershocks that remain in the catalogue may alter the statistics.
(4) The impact of ocean tides on seismicity is often related to instabilities or a compliance of fault zones (Cochran et al., 2004). The aftershock zones marked by high stress perturbations perfectly fit those conditions.
(5) We concentrate here on ocean tides in areas where the amplitudes are 2 m or more (Kamchatka and New Zealand). The corresponding stress changes (10–20 kPa) are larger compared with Earth tides (Varga and Grafarend, 2017).
(6) We study ocean tide heights, not phases. Triggering of earthquakes is caused by stress changes depending on the level of tides. The frequency structure of the ocean tides is complex, and the prevailing periods may vary in time (Lyard et al., 2006).

The purpose of this publication is to assess the quantitative effect of ocean tidal heights on seismic activity and to compare these estimates for different types of faults.

METHODS

Selection of Aftershock Sequences

The aftershock sequences for analysis were found using the "nearest neighbor" algorithm of Zaliapin and Ben-Zion (Zaliapin and Ben-Zion, 2013). Aftershock sequences of large earthquakes may have complex structure, with significant "splashes" of secondary aftershocks caused by large primary aftershocks. Another component of seismicity is background seismicity, which is often referred to as seismic noise. Using the "nearest neighbor" algorithm, we selected only the direct "offspring" (Zaliapin and Ben-Zion, 2013) of the considered large earthquakes, thus minimizing the presence of secondary aftershocks and background seismicity in the selected sequences. This allowed us to model the aftershocks sequences using Omori's law. One alternative that we used in a previous analysis (Baranov et al., 2019) is the Molchan-Dmitrieva algorithm (Molchan and Dmitrieva, 1992), which selects aftershock sequences together with secondary aftershock subsequences. Large aftershocks often trigger a temporary increase of activity. In such cases the Omori model may be significantly altered by this temporary activation. Direct aftershocks found using the nearest neighbor approach do not contain the secondary aftershock sequences, and thus are correctly modeled by the Omori law. Another alternative could be a stochastic declustering of the earthquake catalogue with much deeper complexity and non-uniqueness of the clusters (Varini et al., 2020). Another disadvantage of the stochastic declustering methods is their basic hypothesis that the number of aftershocks

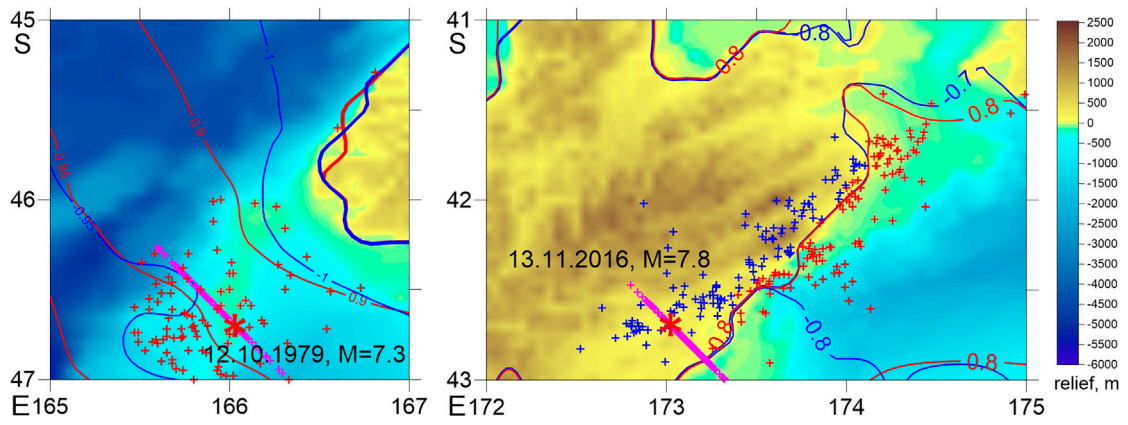

FIGURE 1 | Maps of tidal heights and examples of aftershock sequences in the interval (t_c, 720 h) of M = 7.3 earthquake of October 12, 1979, New Zealand **(A)** and M = 7.8 earthquake of November 13, 2016, New Zealand **(B)**. Crosses mark aftershock epicenters: red in the ocean, blue on land. Red contours show maximum ocean levels, whereas blue contours show minimum levels. Colour scale shows the relief (m) with respect to sea level.

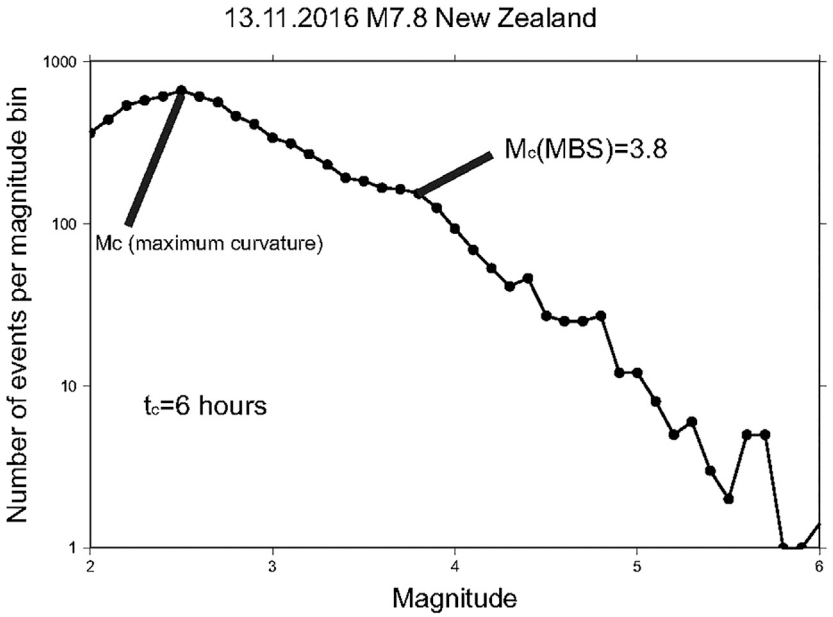

FIGURE 2 | Diagram of the magnitude of completeness M_c using data in the interval (t_c, 1 month) after the main shock (New Zealand, M = 7.8, November 13, 2016).

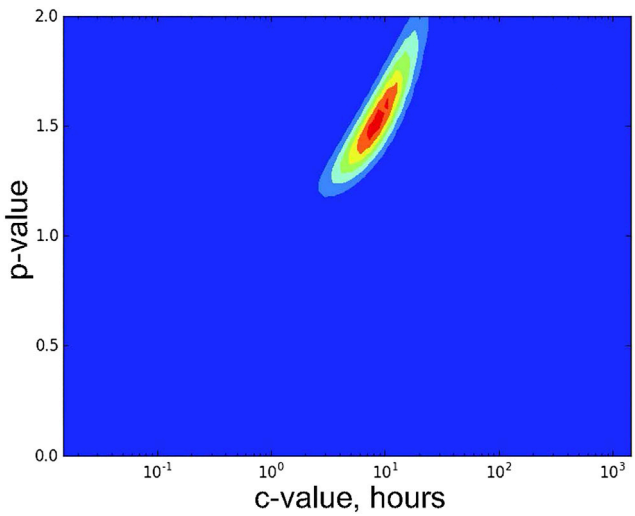

FIGURE 3 | The posterior distribution of the c and *p* values for Bayesian estimates (Holschneider et al., 2012) for aftershocks of the M = 7.8 earthquake of December 5, 1997 in Kamchatka. Light-blue area corresponds to the 95% quantile.

is a function of the magnitude of the corresponding main shock. This hypothesis, as was recently found, is not true (Shebalin et al., 2020).

We selected M ≥6 main shocks in the Kamchatka region, and M ≥6 events in the New Zealand region, which have offshore aftershocks. **Figures 1A,B** show a map of the maximum ocean tide amplitude with resolution 0.125° together with examples of offshore aftershocks for M = 7.5 (Kamchatka, June 08, 1993) and M = 7.8 (New Zealand, November 13, 2016) earthquakes. All aftershocks (as described above, we consider only direct aftershocks of the large earthquakes considered using the nearest neighbor approach), both onshore and offshore ones, were used to estimate the parameters of the Omori–Utsu law (Utsu, 1961), but only the offshore aftershocks were used to calculate the effects of ocean tides on seismicity. For selection of direct aftershocks in Kamchatka and New Zealand we used the parameters listed in **Supplementaty Table S1** of (Shebalin et al., 2020).

The Magnitude of Completeness Magnitude M_c and Time of Completeness t_c

The catalogue completeness usually decreases after large earthquakes (Helmstetter et al., 2006; Hainzl, 2016; Shebalin and Baranov, 2017). For each aftershock sequence we began by estimating the magnitude of completeness M_c using data in the interval (t_c, 1 month) after the main shock by the MBS method (Cao and Gao, 2002; Wossner and Wiemer, 2005) and t_c = 1 h. At this stage we disregarded data within first 6 h after the main shocks, where which the catalogue usually remains incomplete even for relatively large magnitudes. The MBS method allows one to detect the frequently observed effect of the lack of low-magnitude aftershocks during the first few hours and sometimes days after a large earthquake, not detectable by the Maximum Curvature technique (Wiemer and Wyss, 2000), see the example in **Figure 2**. Then, with the preliminary value of M_c, we found t_c using the equation (Helmstetter et al., 2006) $M_c = M_m - 4.5 - 0.75 \log_{10}(t_c)$, where M_m is the mainshock magnitude. The next step was to find the final value M_c using the same MBS technique, but with the new value of t_c. In the

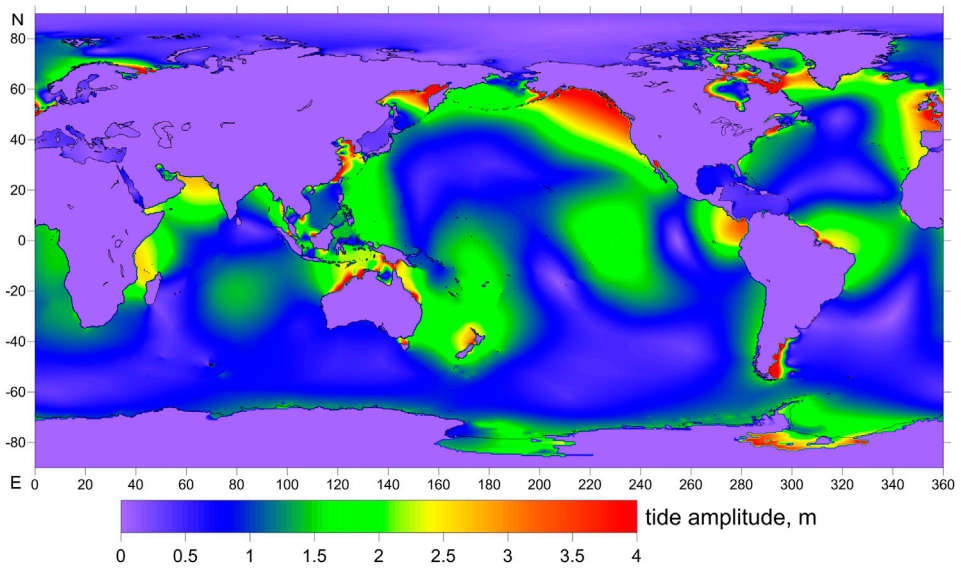

FIGURE 4 | A global map of ocean tide amplitude. The colour scale shows the maximum amplitude of the ocean tide, m.

following analysis we omit the interval $(0, t_c)$ after the main shocks.

Modelling the Aftershock Rates

We model aftershock rates $\lambda(t)$ using the Omori-Utsu model (Utsu, 1961)

$$\lambda(t) = \frac{K}{(t+c)^p}$$

where t is the time after the main shock, and c, p, and K are parameters. We estimated the parameters using aftershocks with $M \geq M_c$ in an interval (t_c, 720 h) with the Bayesian approach (Holschneider et al., 2012), assuming that c and p are homogeneous. **Figure 3** shows an example of the posterior distribution of (c, p) Bayesian estimates. We subdivide the aftershock zone into 0.2° × 0.2°boxes. The interval (t_c, 720 h) is divided in subintervals of 0.2 h. Supposing the c-value and the p-value are equal in all boxes, we calculated the modeled rates of

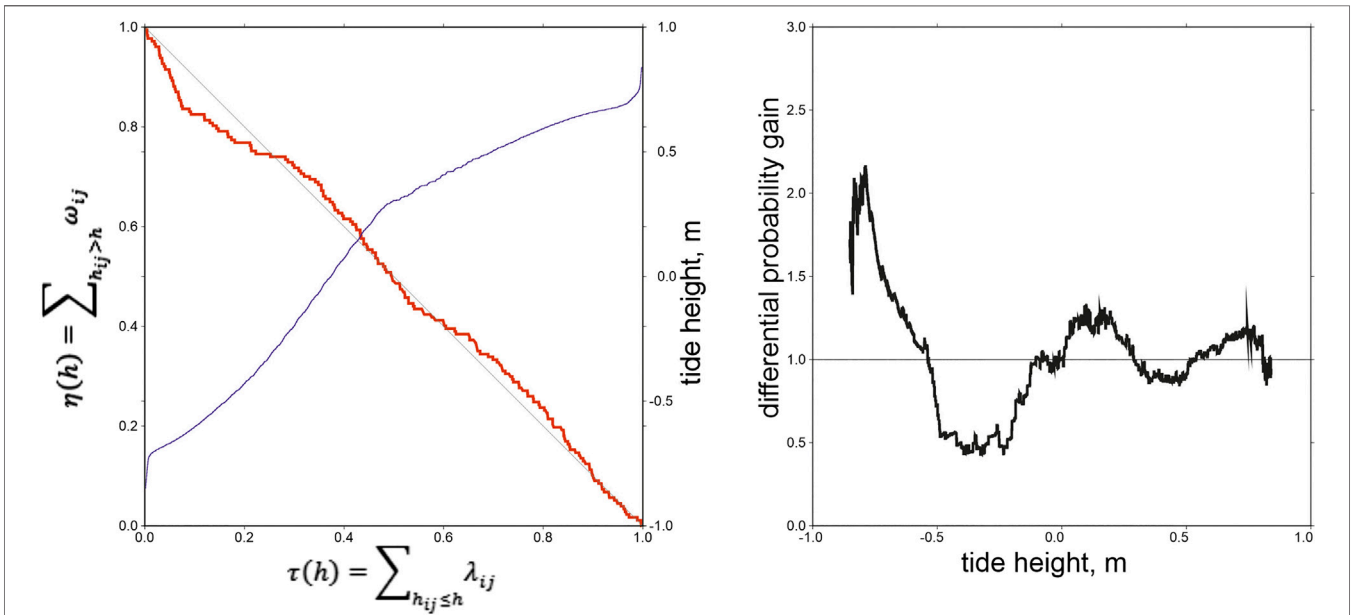

FIGURE 5 | An example of the differential probability gain function. Aftershocks of the M = 6.3 earthquake of June 21, 1992 in New Zealand. **A)** Error diagram (red line), $\eta(h) = \eta(\tau(h))$, with $\tau(h) = \sum_{h_{ij} \leq h} \lambda_{ij}$, $\eta(h) = \sum_{h_{ij} > h} \omega_{ij}$. The diagonal line $\eta = 1 - \tau$ corresponds to no impact ($\omega_{ij} = \lambda_{ij}$), blue line shows inverse function $h(\tau)$. **(B)** Differential probability gain function. Its values correspond to the slope of the error diagram as a function of h as given by **Eq. 2**.

TABLE 2 | The main parameters of the aftershock sequences for Kamchatka region. *H* denotes the main shock depth of focus; *M* is the mainshock magnitude; *N* denotes the number of $M \geq Mc$ aftershocks in the interval (t_c, 720 h) measured from the main shock time; the maximum amplitude of ocean tide in the interval (t_c, 720 h) measured from main shock time was converted to pressure, kPa; ocean depth at the epicentre of main event, m; type indicates the focal mechanism of the main event.

№	Date of main shock	*H*, km	*M*	M_c	t_c, *hour*	*N*	p	c, hour	Max amplitude of ocean tide, kPa	Ocean depth, m	Type
1	December 15, 1971	20	7.8	3.5	12	114	1.02	32.5	19	1,740	?
2	February 28, 1973	59	7.5	4.0	1	54	0.98	1.63	13	1,500	?
3	December 28, 1984	19	6.7	4.0	1	31	0.98	0.33	16	215	Normal fault
4	July 10, 1987	49	6.3	3.5	1	55	0.70	0.40	19	6,000	Strike-slip
5	March 02, 1992	20	6.8	3.3	1	65	1.14	0.89	14	1,075	Thrust
6	June 08, 1993	40	7.5	3.5	3	176	1.23	8.04	15	160	Thrust
7	November 13, 1993	40	7.0	3.5	0.1	69	0.89	0.73	16	1,370	Thrust
8	December 05, 1997	10	7.8	3.3	2	273	0.70	2.42	16	3,060	Thrust
9	December 05, 1997	24	6.4	3.3	1	78	0.63	0.05	16	3,190	Thrust
10	March 08, 1999	7	6.9	3.2	1	94	1.11	0.89	10	3,260	Thrust
11	October 08, 2001	24	6.3	3.4	2	100	1.36	2.43	13	1,360	Thrust
12	March 15, 2003	5	6.0	3.2	1	74	1.02	0.49	14	4,170	Normal fault
13	December 05, 2003	29	6.6	3.3	2	102	1.11	2.96	17	3,120	Thrust
14	July 30, 2010	38	6.3	3.4	1	37	1.14	0.33	13	3,200	Thrust
15	February 28, 2013	61	6.8	3.5	1	39	0.79	0.27	13	650	Thrust
16	March 24, 2013	48	6.0	3.4	1	26	1.01	0.07	12	5,650	Normal fault

the aftershocks λ_{ij}, where i is the index of spatial box, and j the time subinterval:

$$\lambda_{ij} = A_i \int_{t_c+0.2j}^{t_c+0.2j+0.2} \frac{1}{(t+c)^p}\,dt \qquad (1)$$

where $A_i = \frac{N_i}{\int_{t_c}^{720} \frac{1}{(t+c)^p}\,dt}$, N_i is the actual number of aftershocks in the ith bin within the interval (t_c, 720 h). We calculated the actual number of aftershocks λ_{ij} in each spatio-temporal volume. **Figure 3** shows an example of the *p*-value diagram for the M = 7.8, Kamchatka, December 05, 1997 earthquake.

Modeling Tide Heights

Real ocean tides can be as high as 12–18 m in some bays. The tidal amplitudes can reach 2 m near the Pacific coast of Kamchatka and the coast of New Zealand, producing a pressure contrast of approximately 20 kPa. The elastic response of the solid Earth to the ocean load is obtained by convolution of seawater mass distribution using FES 2004 program (http://www.aviso.altimetry.fr/). FES 2004 gives tide height at a specified point at a specified time instant (Lyard et al., 2006). The program is based on the solution of tidal barotropic equations by finite elements (triangles) on a global element grid (~1 million elements). It uses numerical models of ocean bottom topography and shoreline (Le Provost et al., 1994; Le Provost et al., 1998). The program can compute 15 main tidal components on a 1/8° grid (amplitudes and phases), as well as 28 additional tidal components. The presence of ice is incorporated for polar regions. The accuracy is within a few centimeters for open ocean and within 10 cm for offshore areas. The grid is not uniform, being denser near the shore and less detailed in the open ocean, according to Le Provost's criterion (Le Provost and Vincent, 1986). The program requires an input file that contains site coordinates and times in hours as measured from January 1, 1985. The program uses the sites as specified in the input file to yield tide heights at a required time instant. If a point is on land, the value is −9999. Using the FES 2004 software we modelled the heights h_{ij} of the ocean tides in each spatio-temporal volume. Next, we built a map of maximum amplitudes of ocean tides for the entire world. This map was calculated using a program of our own, *Amplitude*. The program iterates over the coordinates of latitude and longitude at steps of 0.125°. For each point of the mesh, the program generates a time series for a year with time step 1 min. Then, for each time series, the FES 2004 program is launched, which calculates the tide height at a given point for the annual interval and finds the maximum tide amplitude at the point. Thus, a grid is obtained where for each point the maximum amplitude of ocean tide is found. **Figure 4** shows the map of the maximum ocean tide amplitude with resolution 0.125° for the entire world. New Zealand and Kamchatka that we deal with here are regions with large ocean tide amplitudes.

Differential Probability Gains

The ocean tide height can be considered as a parameter controlling the relative changes of seismicity rates. If a correlation between ocean tides and seismicity rates exists, then it is possible to calculate what is the average change of the rates relative to an average model, at specific values of the control parameter (**Figure 5A**). The differential probability gain (DPG) function (Shebalin et al., 2012; Shebalin et al., 2014) is defined as the ratio of the actual number of seismic events to the number expected on the average model. It is a function of the control parameter. Here we estimate a smoothed differential probability gain function g(h) using ranges of the control parameter with constant width *dh*:

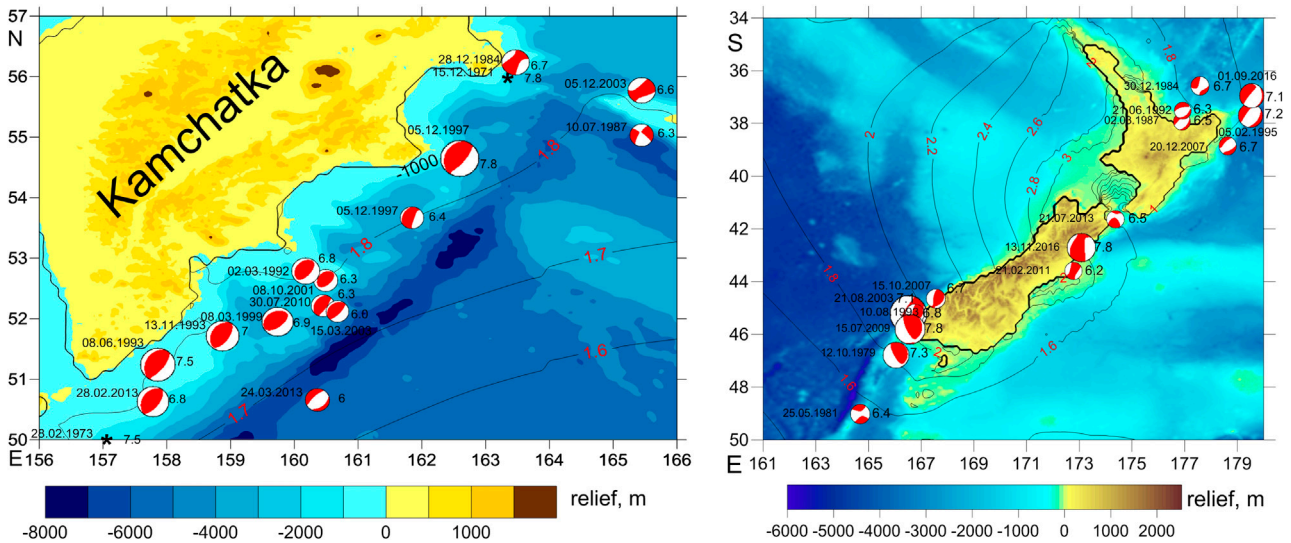

FIGURE 6 | Maps of $M \geq 6$ main shocks for Kamchatka, 1971–2013 **(A)** and New Zealand, 1979–2016 **(B)**. The colour scale shows the relief (m) with respect to sea level; black contours with red labels show maximum amplitude of the ocean tide, m. The mainshock fault-plane solutions were taken from the Global Centroid-Moment-Tensor catalogue (Ekström et al., 2012); epicentres prior to 1976 are not reported in Global Centroid-Moment-Tensor, and they are marked by asterisks.

TABLE 3 | The main parameters of the aftershock sequences for New Zealand. *H* denotes the mainshock depth of focus; *M* is the mainshock magnitude (magnitude M_L as converted from energy class in **Table 2**); *N* denotes the number of $M \geq M_C$ aftershocks in the interval (t_c, 720 h) measured from the mainshock time; the maximum amplitude of ocean tide in the interval (t_c, 720 h) measured from mainshock time was converted to pressure, kPa; relief at the epicentre of main event (m) with respect to sea level; type indicates the focal mechanism of the main event.

№	Date of main shock	*H*, km	*M*	M_c	t_c, *hour*	*N*	p	c, hour	Max amplitude of ocean tide, kPa	Relief (m) with respect to sea level	Type
1	October 12, 1979	12	7.3	3.8	1	81	0.92	0.33	18	−900	Thrust
2	May 25, 1981	33	6.4	4.2	0.1	55	1.20	1.99	15	−2,540	Strike-slip
3	December 30, 1984	12	6.7	4.0	1	76	0.92	0.60	18	−2,460	Strike-slip
4	March 02, 1987	10	6.5	3.3	2	125	1.30	1.89	19	20	Normal fault
5	June 21, 1992	5	6.3	3.2	1	133	1.49	2.09	20	−470	Normal fault
6	August 10, 1993	5	6.8	3.1	2	632	1.11	1.98	22	−2,200	Thrust
7	February 05, 1995	12	7.2	3.9	2	356	1.17	2.96	16	−2,500	Normal fault
8	August 21, 2003	24	7.1	3.5	2	375	1.14	1.63	21	−4,070	Thrust
9	ctober 15, 2007	5	6.7	3.3	6	89	1.36	6.58	22	−1,350	Thrust
10	December 20, 2007	33	6.7	3.5	1	29	0.82	0.60	16	−1,040	Normal fault
11	July 15, 2009	12	7.8	3.8	0.1	359	1.14	1.33	22	500	Thrust
12	February 21, 2011	5	6.2	3.2	1	295	0.98	0.49	20	60	Normal fault
13	July 21, 2013	16	6.5	3.2	2	184	1.20	2.09	18	−90	Strike-slip
14	September 01, 2016	22	7.1	3.2	3	323	1.17	5.39	20	−2,350	Normal fault
15	November 13, 2016	15	7.8	3.8	5	188	1.14	8.79	17	230	Thrust

$$g(h) = \frac{\sum_{i,j;h-dh<h_{ij}\leq h+dh}\omega_{ij}}{\sum_{i,j;h-dh<h_{ij}\leq h+dh}\lambda_{ij}} \quad (2)$$

Here, ω_{ij} and λ_{ij} denote, respectively, the actual numbers of seismic events and the numbers that are expected on the average model in spatial box i and time span j. The ocean tide height h may also be considered as an alarm function of a forecasting model. The error diagram (Molchan, 1991) evaluates retrospectively the performance of the model with respect to the reference model. With the error diagram (**Figure 5A**), the differential probability gains are defined as the local slope (derivative) of the diagram (**Figure 5B**). Thus we assume that at each point of the considered area and at any moment, a specific tide height corresponds to an increase or a decrease of the aftershock rate with respect to the local rate that would have been observed without the impact of tides. We model this

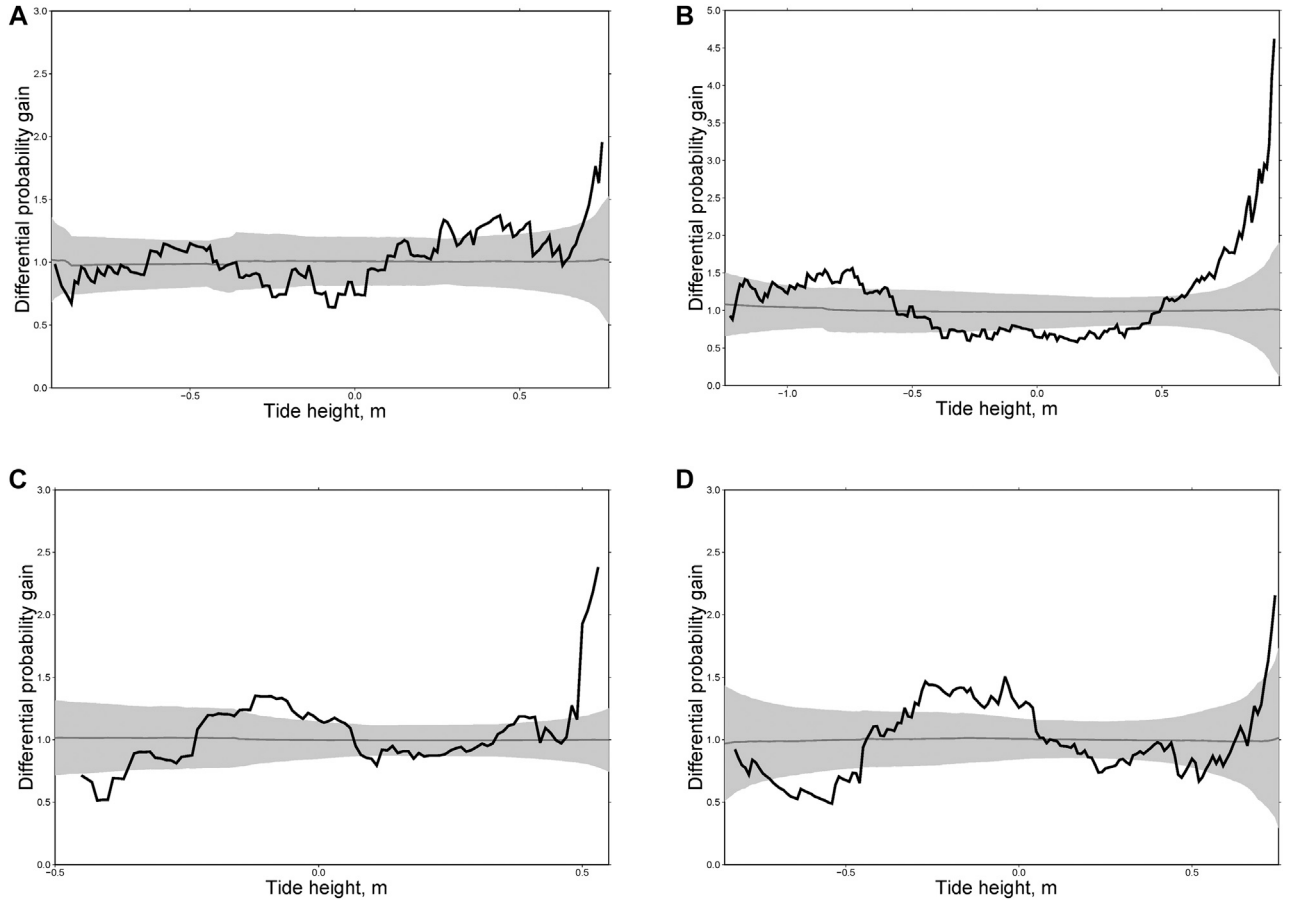

FIGURE 7 | Differential probability gain functions for four aftershock sequences for Kamchatka following the earthquakes of M = 6.7, December 28, 1984 **(A)**; M = 6.3, July 10, 1987 **(B)**; M = 6.8, March 2, 1992 **(C)**; M = 6.8, February 28, 2013 **(D)**. Solid line shows values of g, the straight line marks the level 1.0.

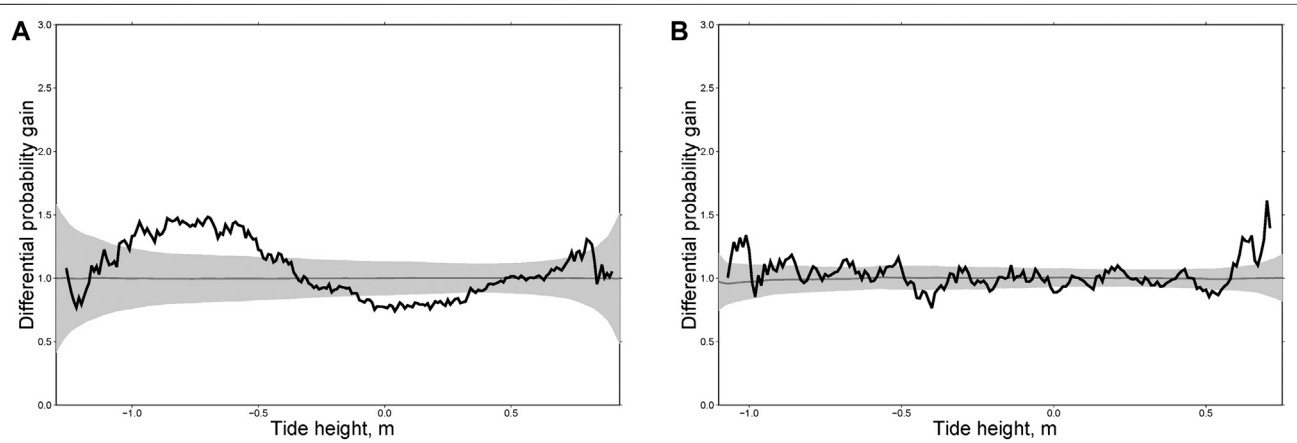

FIGURE 8 | Differential probability gain functions for two aftershock sequences in Kamchatka following the earthquakes of M = 7.8, December 15, 1971 **(A)** and M = 7.8, December 5, 1997 **(B)**.

expected tide-independent aftershock rate by the Omori-Utsu law in time with a spatial distribution obtained by averaging over two months, as defined by **Eq. 1**. The function g(h) is the corresponding indicator of influence. The larger the difference between *g(h)* and 1, the more significant is this impact at corresponding values of the ocean tide height *h*.

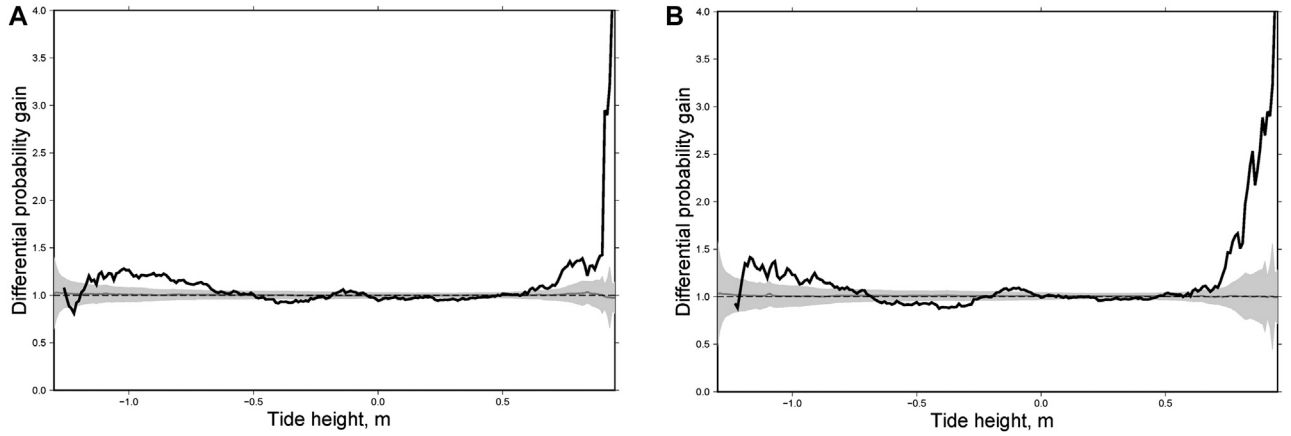

FIGURE 9 | Integral differential probability gain function for Kamchatka: all 16 aftershock sequences **(A)** and 14 sequences without those for the M = 7.8, December 15, 1971 and M = 7.8, December 5, 1997 earthquakes **(B)**.

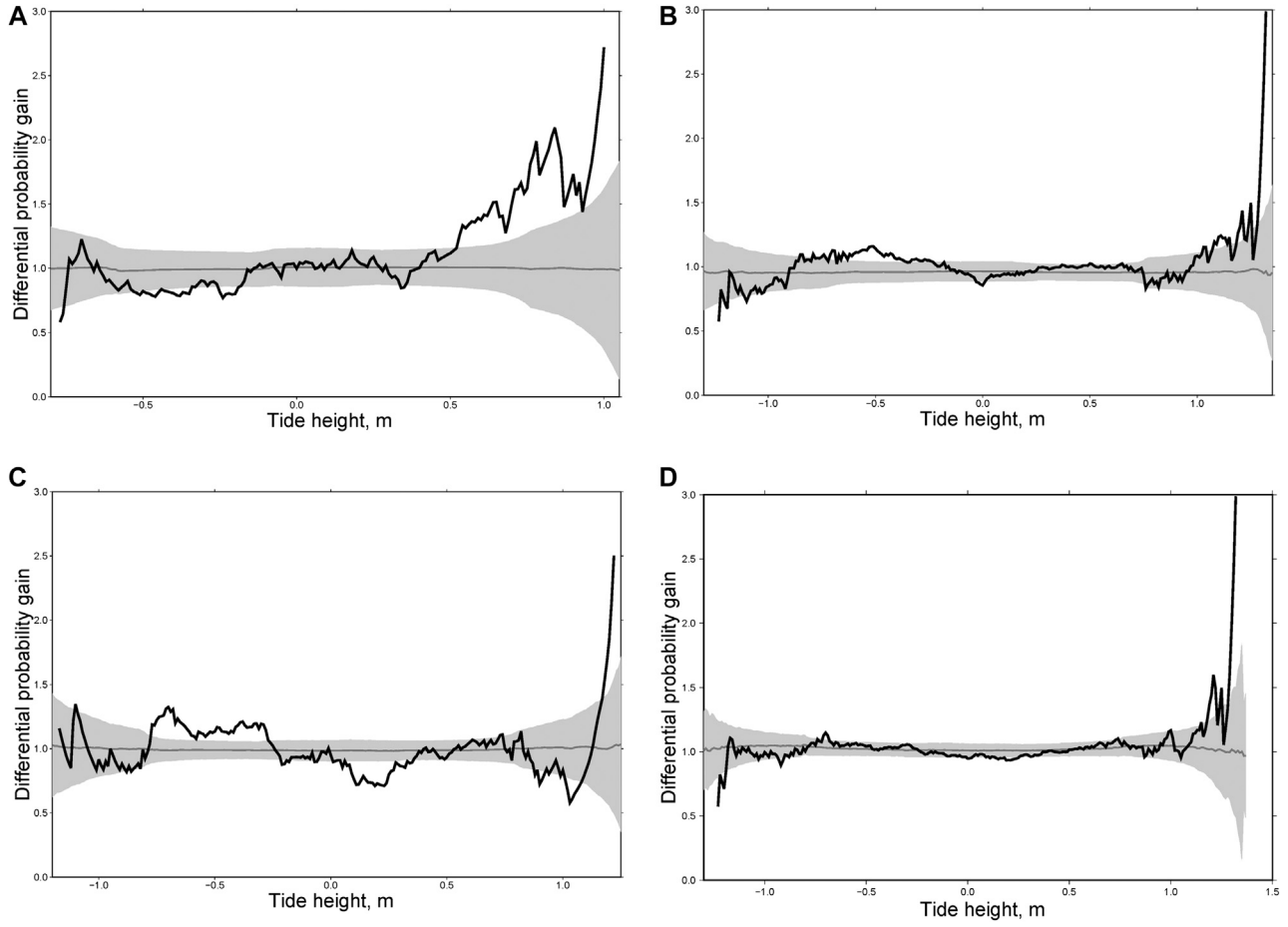

FIGURE 10 | Differential probability gain functions for three aftershock sequences in New Zealand following the earthquakes of M = 7.3, October 12, 1979 **(A)**; M = 6.8, August 10, 1993 **(B)**; M = 7.8, July 15, 2009 **(C)** and the integral differential probability gain function for five aftershock sequences of thrust type earthquakes **(D)**.

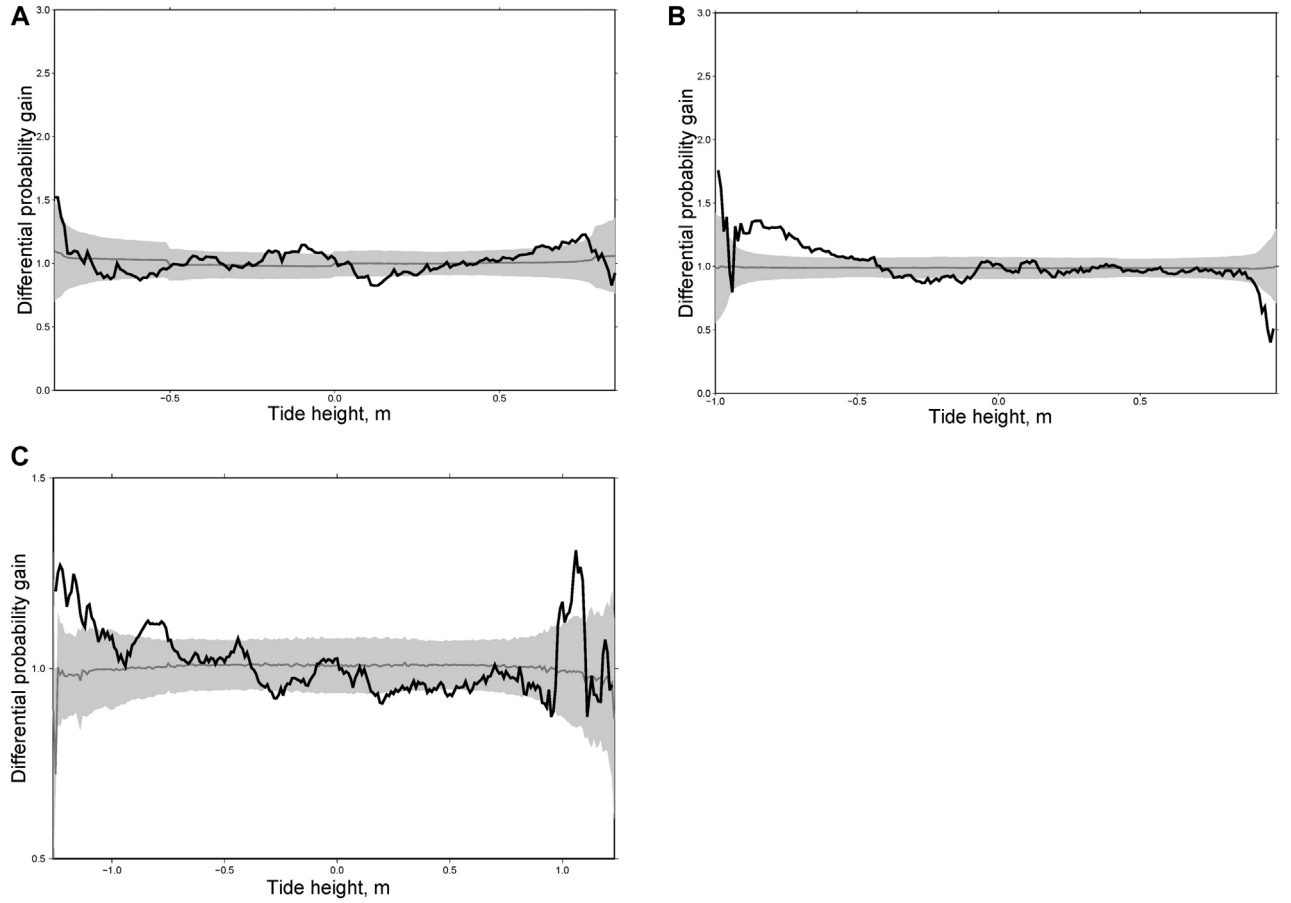

FIGURE 11 | Differential probability gain functions for two aftershock sequences in New Zealand following the earthquakes of M = 6.3, June 21, 1992 **(A)**; M = 7.8, November 13, 2016 **(B)**; and the integral differential probability gain function for six sequences with normal slip of main shocks **(C)**.

In order to check if our results could have been obtained by chance, we estimated the confidence interval of the DPG estimates. For each aftershock sequence we generated 10,000 random synthetic catalogues that satisfy the Omori-Utsu law with parameters determined from the real catalogue, and repeated the procedure for determining the DPG with each synthetic catalogue. Synthetic catalogues were constructed in a standard way for a non-stationary Poisson point process with successive times found using a random number generator:

$$t_{i+1} = t_i - \frac{\log(\xi)}{\lambda(t_i)}$$

where ξ is a random number uniformly distributed in (0,1), and intensity $\lambda(t)$ is given by the Omori-Utsu formula. We started at $t_0 = t_c/100$ and did not take into account events with $t_0 < t_c$, similarly to the analysis of the real catalogue. To each event we assigned the epicenter coordinates of the j-th event from the real aftershock sequence, randomly choosing an integer j uniformly distributed in (**1**, N), where N is the number of events in the real sequence. Finally, for each interval ($h–dh$, $h + dh$) of the tide height, we determined the mean and standard deviation of DPG from 10,000 values. If the value of the DPG falls outside the limits of the confidence interval determined in this way, the deviation of the DPG based on real data from 1.0 can be considered significant.

SEISMIC DATA

We investigated 16 aftershocks sequences of shallow earthquakes off Kamchatka, 1971–2013 (**Table 2**, **Figure 6A**). We used seismic data from the earthquake catalogue produced by the Kamchatka Branch of the Geophysical Survey of the Russian Academy of Sciences (Chebrov et al., 2016) for the period between 1962 and 2016 (http://www.emsd.ru/sdis/earthquake/catalogue/catalogue.php). Most of the main shocks are thrust events (**Figure 6A**; **Table 2**). For New Zealand we considered aftershock sequences of 15 large (M ≥ 6) earthquakes that had at least 100 aftershocks, near New Zealand, 1979–2016 (aftershocks hypocenter data of GeoNet, Earthquake Commission and GNS Science of New Zealand, available at: http://quakesearch.geonet.org.nz; **Table 3**, **Figure 6B**). **Tables 2**,**3** show the main parameters of these aftershock sequences.

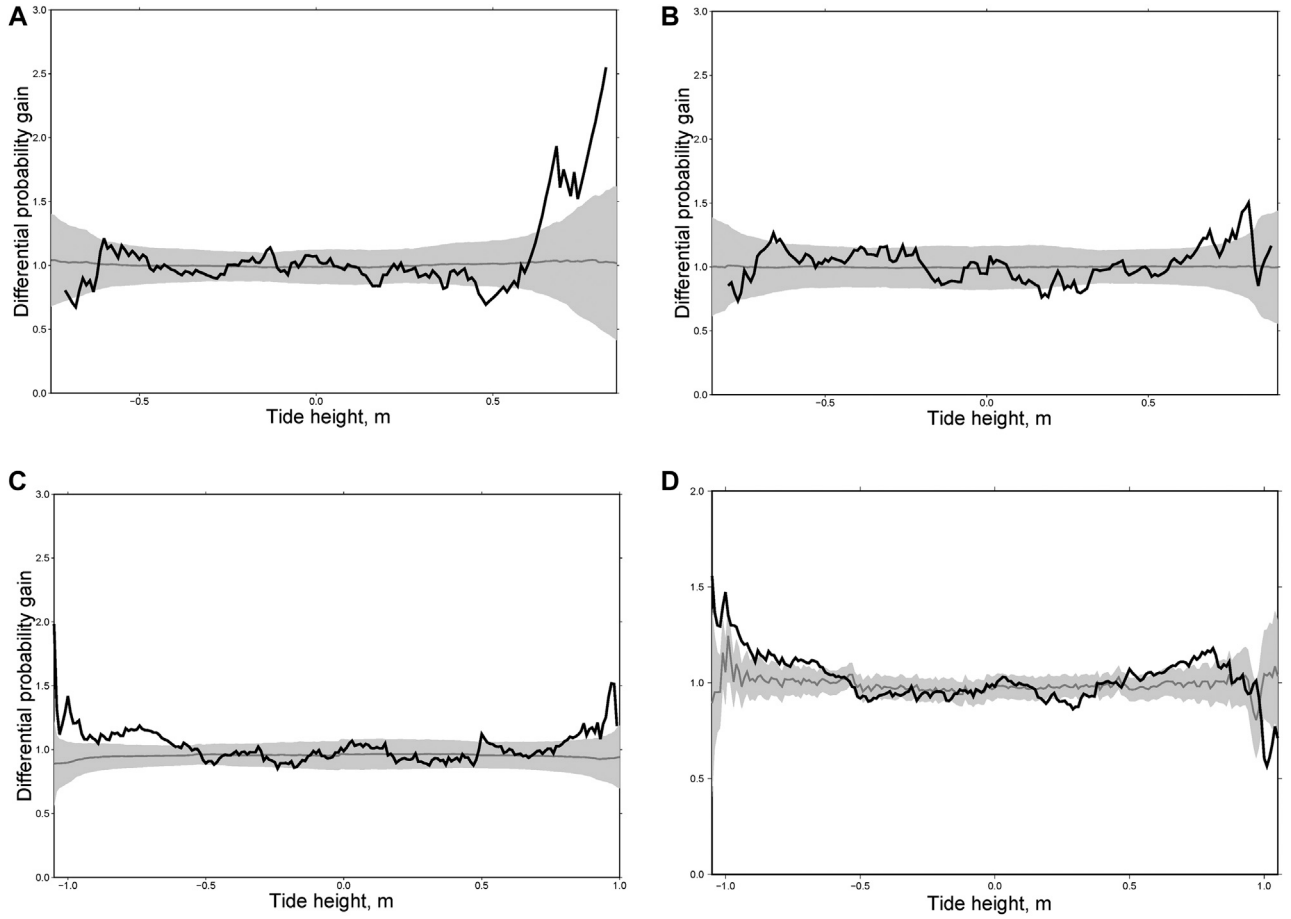

FIGURE 12 | The differential probability gain functions for three aftershock sequences in New Zealand following the strike-slip earthquakes of M = 6.4, May 25, 1981 **(A)**; M = 6.7, December 30, 1984 **(B)**; M = 6.5, July 21, 2013 **(C)**; and integral differential probability gain function for four sequences from strike-slip earthquakes **(D)**.

Figures 6A,B show a map of maximum ocean tide amplitude with resolution 0.125°. For Kamchatka near the coast, the amplitude of the ocean tides reaches 2 m, whereas for New Zealand it varies between 1.4 and 3 m, occasionally more. In Kamchatka all mainshock epicenters lie in the ocean, while for New Zealand some of the main shocks are on land, having a sufficient number of aftershocks in the ocean. Next, the quality of the catalogue for New Zealand is better, the magnitude of completeness M_c is generally smaller, and this generally results in a larger number of aftershocks to study and produces a better statistical significance of results compared with Kamchatka. The quality of hypocenter location in the catalogues is not important for our analysis. The spatial variation of the tide heights in all considered aftershock areas do not exceed 0.01 m in Kamchatka, and 0.02 m except earthquakes of 1993 and November 2016 in New Zealand; for those two earthquakes the spatial variation is about 0.07 m (**Figure 1**). The accuracy of the determinations of times of events (s) is very high when considered in relation to the time scale of tides (h).

RESULTS

Aftershock sequences have been identified for 16 (M ≥6) events with epicenters near Kamchatka (see **Figure 6A**; **Table 2**) and 15 (M ≥6) events with epicenters near New Zealand (see **Figure 6B**; **Table 3**) using the methods described above. For these sequences we estimated M_c and t_c as described in Section "Magnitude of completeness M_c and time of completeness t_c", and used these parameters to estimate c and p in 1 as described in Section "Modelling the aftershock rates" using data during the first month after the main shocks (**Tables 2**, **3**). Then for rectangular 0.2° × 0.2° boxes in the ocean we estimated the modeled aftershock rates λ_{ij} in (t_c, 720 h) within the aftershock areas and time intervals of 0.2 h assuming no impact of tides (**Eq. 1**), counted the actual aftershock numbers ω_{ij}, and used the FES 2004 program to find ocean tide heights h_{ij}. Finally, using **Eq. 2**, for all sequences we calculated the differential probability gain as a function of tide height. Everywhere we used the value dh = 0.15 m. We estimate also the confidence intervals

for DPG using random catalogues as described in *Differential Probability Gains*.

The Kamchatka Region

Figure 7 shows differential probability gain functions for four large earthquakes (M = 6.7, December 28, 1984; M = 6.3, July 10, 1987; M = 6.8, March 2, 1992; M = 6.8, February 28, 2013). Although the differential probability gain function shape may vary from one sequence to another, all examples demonstrate a clear increase of the function at high water (>0.5 m). A similar effect is observed for all sequences, with slightly less pronounced effect for the earthquakes of M = 7.8, December 15, 1971 and M = 7.8, December 5, 1997 (**Figure 8**). For those two earthquakes, the maximum of the DPG function is also observed at low water (near −1 m). We have constructed also the integral differential probability gain function for Kamchatka (**Figure 9**). **Eq. 2** was applied to all spatial boxes and time spans corresponding to several earthquakes. This analysis shows a clear maximum impact of the ocean tides at high water (>0.5 m).

New Zealand

Focal mechanisms of large earthquakes in New Zealand are different: mostly normal events in the north, thrusts in the south, and strike-slip earthquakes in the middle. Accordingly, we divided the main shocks into three groups: thrust faults (**Figure 10**), normal faults (**Figure 11**) and strike-slip faults (**Figure 12**). For each group we calculated individual and integral differential probability gain functions as we did for the Kamchatka sequences. As can be seen from **Figures 10**, for thrust faults the most general phenomenon consists in an increasing rate of aftershocks at high water (>0.5 m). A similar effect was found for Kamchatka (**Figures 7–9**) where almost all large earthquakes considered here were of the thrust type. For normal fault type earthquakes there is no effect at high water. In contrast, we observed a maximum of DPG at low water (<−0.5 m, **Figure 11**). A similar effect was observed for aftershocks following the earthquakes of M = 7.8, December 15, 1971 and M = 7.8, December 5, 1997 in Kamchatka (**Figure 8**). For strike-slip earthquakes the maximum of DPG functions is reached at high water for all sequences (>0.5 m). At low water, high DPG values were clearly observed for aftershocks of the M = 6.5 earthquake of July 21, 2013 (<−0.5 m, **Figure 12C**). These results demonstrate an impact of ocean tides on seismicity in the zones of large earthquakes within a period of 30 days after them. This highlights certain limitations to the analysis. The rupture zone of a large earthquake is in an excited state, so the impact of relatively weak disturbances, such as tides, may be stronger there than in the entire region.

LIMITATIONS OF THE ANALYSIS

In the analysis we used a model of ocean tides. The actual tide heights may be slightly different. However, continuous direct measurements do not exist at the moment. Another shortcoming of our analysis is that we could not ascertain the role of aftershock depth. This was mostly due to lack of data below the magnitude of completeness. An unreliable depth determination for offshore earthquakes is another factor. Accordingly, the physical model of the relationships found is very preliminary.

DISCUSSION AND CONCLUSION

In the present study we used the differential probability gain approach (Shebalin et al., 2012; Shebalin et al., 2014) to estimate quantitatively the change in aftershock rate at various levels of ocean tides, relative to an average Omori-Utsu model that supposes no dependence on tides. The differential probability gain function is a numeric factor indicating how much the rate of aftershocks is increased or decreased on average at specific values of the tide heights. The value one indicates no impact. We consider the impact of ocean tides only, because their effect is several times larger than the effect of solid Earth tides in the regions under consideration. Variations of vertical stresses of 10–20 kPa due to ocean tides for the coast of Kamchatka and New Zealand fall within the range of the effect of stresses on seismicity according to laboratory experiments (Lockner and Beeler, 1999). Similar variations due to Earth tides at shallow depths (<50 km) are only approximately 1 kPa, i.e., one order of magnitude less (Varga and Grafarend, 2017).

We considered aftershock sequences of large (M ≥6) earthquakes off Kamchatka, 1971–2013 (16 sequences) and New Zealand, 1979–2016 (15 sequences). For all sequences we disregarded data within a few first minutes or hours after main shocks, in which the catalogue usually remains incomplete even for relatively large magnitudes. Only aftershocks with epicenters in the ocean were used. In these regions, the amplitudes of ocean tides are large, and their influence is a few times or tens of times larger than the effects of Earth tides. The observed increase in the rate of aftershocks at high and/or low water demonstrated a significant effect of ocean tides on seismicity. One important feature that distinguishes this study from most others is that we studied the heights rather than the phases of ocean tides. Moreover, the goal of this study was to find quantitative estimates of the increase in seismicity rate at specific heights of the ocean tides. The effect varies from place to place and for different focal mechanisms. The main result consists in finding a significant change in seismicity rates at tide heights more than 0.5 m relative to the baseline, positive or negative. For normal fault earthquakes the effect is stronger at low water, for thrust events mostly at high water, and for strike-slip earthquakes at high and/or low water.

Although the differential probability gains function shape may vary from one sequence to another, we observed a clear tendency of increasing aftershock rate by about two times at either low or high water. As an explanation of this effect, we can suggest friction reduction on a fault due to vertical stress decreasing at low waters and due to increased pore pressure at high waters. For normal faults an increase in aftershock rate was observed at low water, and thus the friction reduction mechanism due to the unloading of vertical stress is more likely. For thrust earthquakes, an increase in aftershock rate was observed at high water, and in that case

increased pore pressure is the preferable mechanism. For strike-slip events with intermediate stresses both mechanisms can operate.

The main practical result of this study is a quantitative assessment of the effect of ocean tides on earthquake rate. Although the results were obtained for aftershocks, we may suppose that similar dependences are valid for all seismic events. Of course, this needs additional validation, but potentially opens a way to take into account ocean tides for time-dependent seismic hazard assessment.

DATA AVAILABILITY STATEMENT

The raw data supporting the conclusions of this article will be made available by the authors, without undue reservation.

AUTHOR CONTRIBUTIONS

PS provided the design and application of the differential probability gain tests. AB designed and performed calculations of the ocean tide heights.

FUNDING

We acknowledge the support from Russian Science Foundation Grant No. 20-17-00180.

ACKNOWLEDGMENTS

We acknowledge the New Zealand GeoNet project and its sponsors EQC, GNS Science and LINZ, and Kamchatka Branch of the Geophysical Survey of Russian Academy of Sciences for providing data used in this study. We are grateful to the authors of the FES 2004 for letting us use this software. We thank the reviewers for constructive comments which helped to improve the manuscript significantly.

SUPPLEMENTARY MATERIAL

The Supplementary Material for this article can be found online at: https://www.frontiersin.org/articles/10.3389/feart.2020.559624/full#supplementary-material.

REFERENCES

Arabelos, D. N., Contadakis, M. E., Vergos, G., and Spatalas, S. (2016). Variation of the Earth tide-seismicity compliance parameter during the recent seismic activity in Fthiotida, central Greece. *Ann. Geophys.* 59 (1), 102. doi:10.4401/ag-6795

Baranov, A. A., Baranov, S. V., and Shebalin, P. N. (2019). A quantitative estimate of the effects of sea tides on aftershock activity: Kamchatka. *J. Volcanol. Seismol.* 13 (1), 56–69. doi:10.1134/S0742046319010020

Beeler, N. M., and Lockner, D. A. (2003). Why earthquakes correlate weakly with the solid Earth tides: effects of periodic stress on the rate and probability of earthquake occurrence. *J. Geophys. Res. Solid Earth* 108 (B8), 2156–2202. doi:10.1029/2001JB001518

Burton, P. (1986). Geophysics: is there coherence between Earth tides and earthquakes? *Nature* 321 (6066), 115. doi:10.1038/321115a0

Cao, A. M., and Gao, S. S. (2002). Temporal variations of seismic b-values beneath northeastern Japan Island Arc. *Geophys. Res. Lett.* 29, 481–482. doi:10.1029/2001GL013775

Chebrov, V. N., Droznina, S. Ya., and Senyukov, S. L. (2016). *Kamchatka and the commander islands in Zemletryaseniya v Rossii v 2014 godu (Earthquakes in Russia in 2014)*. Obninsk, Russia: GS RAN, 60–66.

Chen, H.-J., Chen, C.-Y., Tseng, J.-H., and Wang, J.-H. (2012a). Effect of tidal triggering on seismicity in Taiwan revealed by the empirical mode decomposition method. *Nat. Hazards Earth Syst. Sci.* 12, 2193–2202. doi:10.5194/nhess-12-2193-2012

Chen, L., Chen, J. G., and Xu, Q. H. (2012b). Correlation between solid tides and worldwide earthquakes M C 7 since 1900. *Nat. Hazards Earth Syst. Sci.* 12, 587–590. doi:10.5194/nhess-12-587-2012

Cochran, E. S., Vidale, J. E., and Tanaka, S. (2004). Earth tides can trigger shallow thrust fault earthquakes. *Science* 306, 1164–1166. doi:10.1126/science.1103961

Crockett, R. G., Gillmore, M. G. K., Phillips, P. S., and Gilbertson, D. D. (2006). Tidal synchronicity of the December 26, 2004 Sumatran earthquake and its aftershocks. *Geophys. Res. Lett.* 33, L19302. doi:10.1029/2006GL027074

Datta, A., and Kamal, K. (2012). Triggering of aftershocks of the Japan 2011 earthquake by Earth tides. *Curr. Sci.* 102 (5), 792–796. doi:10.2307/24084467

Ekström, G., Nettles, M., and Dziewonski, A. M. (2012). The global CMT project 2004–2010: Centroid-moment tensors for 13,017 earthquakes. *Phys. Earth Planet. In.* 200–201, 1–9. doi:10.1016/j.pepi.2012.04.002

Emter, D. (1997). Tidal triggering of earthquakes and volcanic events. *Tidal Phenomena* 66, 293–309. doi:10.1007/BFb0011468

Hainzl, S. (2016). Rate-dependent incompleteness of earthquake catalogs. *Seismol Res. Lett.* 96 (2A), 337–344. doi:10.1785/0220150211

Hardebeck, J. L., Nazareth, J. J., and Hauksson, J. (1998). The static stress change triggering model: constraints from two southern California aftershock sequences. *J. Geophys. Res. Solid Earth* 103, 24427–24437. doi:10.1029/98JB00573

Heaton, T. H. (1975). Tidal triggering of earthquakes. *Geophys. J. Roy. Astron. Soc.* 43, 307–326. doi:10.1111/j.1365-246X.1975.tb00637.x

Heaton, T. H. (1982). Tidal triggering of earthquakes. *Bull. Seismol. Soc. Am.* 72, 2181–2200. doi:10.1111/j.1365-246X.1975.tb00637.x

Helmstetter, A., Kagan, Y. Y., and Jackson, D. (2006). Comparison of short-term and time-independent earthquake forecast models for southern California. *Bull. Seismol. Soc. Am.* 96 (1), 90–106. doi:10.1785/0120050067

Holschneider, M., Narteau, C., Shebalin, P., Peng, Z., and Schorlemmer, D. (2012). Bayesian analysis of the modified Omori law. *J. Geophys. Res.* 117, B05317. doi:10.1029/2011JB009054

Ide, S., and Tanaka, Y. (2014). Controls on plate motion by oscillating tidal stress: evidence from deep tremors in western Japan. *Geophys. Res. Lett.* 41, 3842–3850. doi:10.1002/2014GL060035

Ide, S., Yabe, S., and Tanaka, Y. (2016). Earthquake potential revealed by tidal influence on earthquake size–frequency statistics. *Nat. Geosci.* 9, 834–837. doi:10.1038/ngeo2796

Klein, F. W. (1976a). Earthquake swarms and the semidiurnal solid earth tide. *Geophys. J. Int.* 45, 245–295. doi:10.1111/j.1365-246X.1976.tb00326.x

Klein, F. W. (1976b). Tidal triggering of reservoir-associated earthquakes. *Eng. Geol.* 10, 197–210. doi:10.1016/0013-7952(76)90020-x

Knopoff, L. (1964). Earth tides as a triggering mechanism of earthquakes. *Bull. Seismol. Soc. Am.* 54, 1865–1870.

Le Provost, C., Lyard, F., Molines, J. M., Genco, M. L., and Rabilloud, F. (1998). A hydrodynamic ocean tide model improved by assimilating a satellite altimeter-derived data set. *J. Geophys. Res.* 103, 5513–5529. doi:10.1029/97JC01733

Le Provost, C., Genco, M. L., Lyard, F., Vincent, P., and Canceil, P. (1994). Spectroscopy of the world ocean tides from a finite element hydrodynamic model. *J. Geophys. Res.* 99, 777–797. doi:10.1029/94JC01381

Le Provost, C., and Vincent, P. (1986). Some tests of precision for a finite element model of ocean tides. *J. Comput. Phys.* 65, 273–291. doi:10.1016/0021-9991(86)90209-3

Lin, C. H., Yeh, Y. H., Chen, Y. I., Liu, J. Y., and Chen, K. J. (2003). Earthquake clustering relative to lunar phases in Taiwan. *Terr. Atmos. Ocean Sci.* 14, 289–298. doi:10.3319/TAO.2003.14.3.289(T)

Lockner, D. A., and Beeler, N. M. (1999). Premonitory slip and tidal triggering of earthquakes. *J. Geophys. Res.* 104 (B9), 20133–20151. doi:10.1029/1999JB900205

Lyard, F., Lefèvre, F., Letellier, T., and Francis, O. (2006). Modelling the global ocean tides: a modern insight from FES 2004. *Ocean Dynam.* 56, 394–415. doi:10.1007/s10236-006-0086-x

Malin, S. R. C., and Chapman, S. (1970). The determination of lunar daily geophysical variations by the Chapman-Miller method. *Geophys. J. Roy. Astron. Soc.* 19, 15–35. doi:10.1111/j.1365-246X.1970.tb06738.x

Metivier, L., de Viron, O., Conrad, C. P., Renault, S., Diament, M., and Patau, G. (2009). Evidence of earthquake triggering by the solid earth tides. *Earth Planet Sci. Lett.* 278, 370–375. doi:10.1016/j.epsl.2008.12.024

Molchan, G. M., and Dmitrieva, O. E. (1992). Aftershock identification: methods and new approaches. *Geophys. J. Int.* 109, 501–516. doi:10.1111/j.1365-246X.1992.tb00113.x

Molchan, G. M. (1991). Structure of optimal strategies in earthquake prediction. *Tectonophysics* 193, 267–276. doi:10.1016/0040-1951(91)90336-Q

Morgan, W. J., Stoner, J. O., and Dicke, R. H. (1961). Periodicity of earthquakes and the invariance of the gravitational constant. *J. Geophys. Res.* 66 (11), 3831–3843. doi:10.1029/JZ066i011p03831

Nikolaev, V. A. (1996). Relationships between seismicity and the phases of multiple and difference tidal waves. *Dokl. Akad. Nauk.* 349 (3), 389–394.

Nikolaev, V. A. (1994). The response of large earthquakes to the phases of earth tides. *Izvestiya Phys. Solid Earth* 11, 49–55.

Rydelek, P. A., Sacks, I. S., and Scarpa, R. (1992). On tidal triggering of earthquakes at Campi Flegrei. *Italy. Geophys. J. Int.* 109, 125–137. doi:10.1111/j.1365-246X.1992.tb00083.x

Saltykov, V. A., Ivanov, V. V., and Kugaenko, Y. A. (2004). The action of earth tides on seismicity prior to the Mw 7.0 November 13, 1993, Kamchatka earthquake. *Izvestiya Phys. Solid Earth* 7, 25–34.

Saltykov, V. A. (2014). Tidal effects and amplitude-dependent dissipation in seismicity. *Fizicheskaya Mezomekhanika* 17, 103–110.

Scholz, C. H., Tan, Y. J., and Albino, F. (2019). The mechanism of tidal triggering of earthquakes at mid-ocean ridges. *Nat. Commun.* 10, 2526. doi:10.1038/s41467-019-10605-2

Schuster, A. (1897). On lunar and solar periodicities of earthquakes. *Proc. Roy. Soc. Lond.* 61, 455. doi:10.1098/rspl.1897.0060

Shebalin, P., and Baranov, S. (2017). Long-delayed aftershocks in New Zealand and the 2016 M 7.8 Kaikoura earthquake. *Pure Appl. Geophys.* 174 (10), 3751–3764. doi:10.1007/s00024-017-1608-9

Shebalin, P. N., Narteau, C., and Baranov, S. V. (2020). Earthquake productivity law. *Geophys. J. Int.* 222 (2), 1264–1269. doi:10.1093/gji/ggaa252

Shebalin, P. N., Narteau, C., and Holschneider, M. (2012). From alarm-based to rate-based earthquake forecast models. *Bull. Seismol. Soc. Am.* 102, 64–72. doi:10.1785/0120110126

Shebalin, P. N., Narteau, C., Zechar, J. D., and Holschneider, M. (2014). Combining earthquake forecasts using differential probability gains. *Earth Planets Space* 66, 37. doi:10.1186/1880-5981-66-37

Shudde, R. H., and Barr, D. R. (1977). An analysis of earthquake frequency data. *Bull. Seismol. Soc. Am.* 67, 1379–1386.

Simpson, J. F. (1967). Earth tides as a triggering mechanism for earthquakes. *Earth Planet Sci. Lett.* 2, 473–478. doi:10.1016/0012-821X(67)90192-6

Souriau, M., Souriau, A., and Gagnepain, J. (1982). Modeling and detecting interactions between Earth tides and earthquakes with application to an aftershock sequence in the Pyrenees. *Bull. Seismol. Soc. Am.* 72, 165–180.

Stein, R. S. (1999). The role of stress transfer in earthquake occurrence. *Nature* 402, 605–609. doi:10.1038/45144

Stein, R. S. (2004). Tidal triggering caught in the act. *Science* 305 (5688), 1248–1249. doi:10.1126/sciencee.1100726

Stroup, D. F., Bohnenstiehl, D. R., Tolstoy, M., Waldhauser, F., and Weekly, R. T. (2007). Pulse of the seafloor: tidal triggering of microearthquakes at 9°50′N East Pacific Rise. *Geophys. Res. Lett.* 34, L15301. doi:10.1029/2007GL030088

Tanaka, S., Ohtake, M., and Sato, H. (2002). Evidence for tidal triggering of earthquakes as revealed from statistical analysis of global data. *J. Geophys. Res.* 107 (B10), 2211. doi:10.1029/2001JB001577

Tanaka, S., Ohtake, M., and Sato, H. (2004). Tidal triggering of earthquakes in Japan related to the regional tectonic stress. *Earth Planets Space* 56, 511–515. doi:10.1186/BF03352510

Tanaka, S. (2010). Tidal triggering of earthquakes precursory to the recent sumatra megathrust earthquakes of December 26, 2004 (Mw 9.0), March 28, 2005 (Mw 8.6), and September 12, 2007 (Mw 8.5). *Geophys. Res. Lett.* 37, L02301. doi:10.1029/2009GL041581

Tanaka, S. (2012). Tidal triggering of earthquakes prior to the 2011 Tohoku-Oki earthquake (Mw 9.1). *Geophys. Res. Lett.* 39, L00G26. doi:10.1029/2012GL051179

Tolstoy, M., Vernon, F. L., Orcutt, J. A., and Wyatt, F. K. (2002). Breathing of the seafloor: tidal correlations of seismicity at Axial volcano. *Geology* 30, 503–506. doi:10.1130/0091-7613(2002)030<0503:BOTSTC>2.0.CO;2

Tsuruoka, H., Ohtake, M., and Sato, H. (1995). Statistical test of the tidal triggering of earthquakes: contribution of the ocean tide loading effect. *Geophys. J. Int.* 122, 183–194. doi:10.1111/j.1365-246X.1995.tb03546.x

Utsu, T. A. (1961). Statistical study on the occurrence of aftershocks. *Geophys. Mag.* 30, 521–605.

Varga, P., and Grafarend, E. (2017). Influence of tidal forces on the triggering of seismic events. *Pure Appl. Geophys.* 175, 1–9. doi:10.1007/s00024-017-1563-5

Varini, E., Peresan, A., and Zhuang, J. (2020). Topological comparison between the stochastic and the nearest-neighbor earthquake declustering methods through network analysis. *J. Geophys. Res. Solid Earth* 125, e2020JB019718. doi:10.1029/2020JB019718

Vergos, G. S., Arabelos, D., and Contadakis, M. E. (2015). Evidence for tidal triggering on the earthquakes of the Hellenic Arc, Greece. *Phys. Chem. Earth* 85–86, 210–215. doi:10.1016/j.pce.2015.02.004

Vidale, J. E., Agnew, D. C., Johnston, M. J. S., and Oppenheimer, D. H. (1998). Absence of earthquake correlation with Earth tides: an indication of high preseismic fault stress rate. *J. Geophys. Res.* 103 (B10), 24567–24572. doi:10.1029/98JB00594

Wiemer, S., and Wyss, M. (2000). Minimum magnitude of completeness in earthquake catalogs: examples from Alaska, the western United States, and Japan. *Bull. Seismol. Soc. Am.* 90, 859–869. doi:10.1785/0119990114

Wilcock, W. S. (2001). Tidal triggering of microearthquakes on the Juan de Fuca ridge. *Geophys. Res. Lett.* 28, 3999–4002. doi:10.1029/2001GL013370

Woessner, J., and Wiemer, S. (2005). Assessing the quality of earthquake catalogues: estimating the magnitude of completeness and its uncertainty. *Bull. Seismol. Soc. Am.* 95, 684–698. doi:10.1785/0120040007

Yurkov, E. F., and Gitis, V. G. (2005). On relationships between seismicity and the phases of tidal waves. *Izvestiya Phys. Solid Earth* 4, 4–15.

Zaliapin, I., and Ben-Zion, Y. (2013). Earthquake clusters in southern California I: identification and stability. *J. Geophys. Res.* 118 (6), 2847–2864. doi:10.1002/jgrb.50179

Conflict of Interest: The authors declare that the research was conducted in the absence of any commercial or financial relationships that could be construed as a potential conflict of interest.

Copyright © 2020 Shebalin and Baranov. This is an open-access article distributed under the terms of the Creative Commons Attribution License (CC BY). The use, distribution or reproduction in other forums is permitted, provided the original author(s) and the copyright owner(s) are credited and that the original publication in this journal is cited, in accordance with accepted academic practice. No use, distribution or reproduction is permitted which does not comply with these terms.

frontiers in Earth Science

ORIGINAL RESEARCH
published: 21 December 2020
doi: 10.3389/feart.2020.584659

Characterizing the Foreshock, Main Shock, and Aftershock Sequences of the Recent Major Earthquakes in Southern Alaska, 2016–2018

B. G. Bukchin[1], *A. S. Fomochkina*[1,2], *V. G. Kossobokov*[1,3,4]* *and A. K. Nekrasova*[1]

[1]Institute of Earthquake Prediction Theory and Mathematical Geophysics, RAS, Moscow, Russia, [2]Gubkin Russian State University of Oil and Gas, Moscow, Russia, [3]Institut de Physique du Globe de Paris, Paris, France, [4]International Seismic Safety Organization, Arsita, Italy

For each of three major M ≥ 7.0 earthquakes (i.e., the January 24, 2016, M7.1 earthquake 86 km E of Old Iliamna; the January 23, 2018, M7.9 earthquake 280 km SE of Kodiak; and the November 30, 2018, M7.1 earthquake 14 km NNW of Anchorage, Alaska), the study considers characterization of the foreshock and aftershock sequences in terms of their variations and scaling properties, including the behavior of the control parameter η of the unified scaling law for earthquakes (USLE), along with a detailed analysis of the surface wave records for reconstruction of the source in the approximation of the second moments of the stress glut tensor to obtain integral estimation of its length, orientation, and development over time. The three major earthquakes at 600 km around Anchorage are, in fact, very different due to apparent complexity of earthquake flow dynamics in the orogenic corner of the Pacific and North America plate boundary. The USLE generalizes the classic Gutenberg-Richter relationship taking into account the self-similar scaling of the empirical distribution of earthquake epicenters. The study confirms the existence of the long-term periods of regional stability of the USLE control parameter that are interrupted by mid- or even short-term bursts of activity associated with major catastrophic events.

Keywords: earthquake sequences, earthquake source, Pacific and North America plate boundary, unified scaling law for earthquakes, control parameter analysis

OPEN ACCESS

Edited by:
Giovanni Martinelli, National Institute of Geophysics and Volcanology, Italy

Reviewed by:
Nguyen Huu Tuyen, Vietnam Academy of Science and Technology, Vietnam
Boyko Ranguelov, University of Mining and Geology "Saint Ivan Rilski," Bulgaria

***Correspondence:**
V. G. Kossobokov
volodya@mitp.ru

Specialty section:
This article was submitted to Solid Earth Geophysics, a section of the journal Frontiers in Earth Science

Received: *17 July 2020*
Accepted: *07 October 2020*
Published: *21 December 2020*

Citation:
Bukchin BG, Fomochkina AS, Kossobokov VG and Nekrasova AK (2020) Characterizing the Foreshock, Main Shock, and Aftershock Sequences of the Recent Major Earthquakes in Southern Alaska, 2016–2018. Front. Earth Sci. 8:584659. doi: 10.3389/feart.2020.584659

INTRODUCTION

The territories around Anchorage have recently experienced four major earthquakes (**Figure 1**) and associated seismic sequences which illustrate the complexity of the tectonic environment at the orogenic corner of the boundary between the Pacific and North America plates where an Eulerian plate model is not expected to be accurate (Bird, 2003). The January 24, 2016 and the November 30, 2018 earthquakes, both of M7.1, occurred under the North American plate at the south and north edges of the Cook Inlet, respectively. The largest of the four, the January 23, 2018, M7.9 earthquakes ruptured the Pacific plate in front of the continental crust of Alaska. The July 22, 2020, M7.8 Alaska Peninsula earthquake (July 22, 2020 06:12:44.719 UTC, 55.0683°N and 158.5543°W, 28 km, M_{ww}7.83) ruptured a 200-km segment of the Aleutian megathrust fault in the study area after the manuscript submittal. All four appear to rupture the subducting Pacific plate right at the border of or within the extended source region of the March 27, 1964 Great Alaska, M9.3 mega-earthquake (Press and Jackson, 1965; Wyss and Brune, 1967;

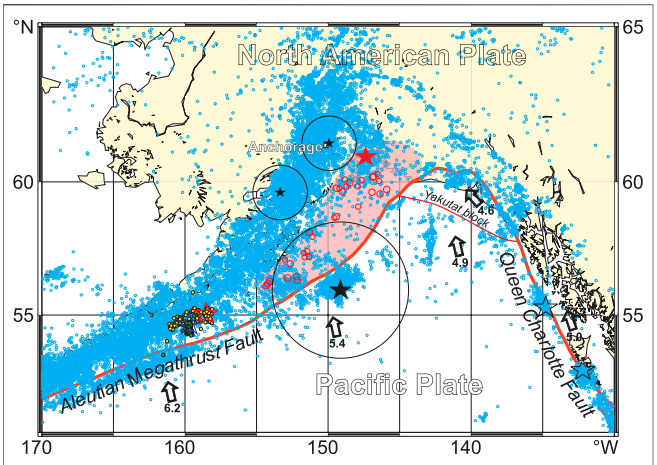

FIGURE 1 | Epicenters of the M ≥ 2.5 earthquakes (ANSS, 2006–2019; small blue circles) and the three major earthquakes (black stars) in Southern Alaska. Note: The two major earthquakes of M_W7.1 and the one of M_W7.9 under study are encircled with R = 1° and 2.5° circles, respectively. Red line marks the boundary of the North American and the Pacific plates. The epicenters of the 1964 Great Alaskan earthquake (big red star) and its first aftershocks (red circles) are given on top the subsurface rupture zone (shaded pink). The epicenters of the 22 July 2020, M_W7.8 (red outline star) and its first day M ≥ 2.5 aftershocks (small yellow circles) at 105 km SSE of Perryville, Alaska and the 19 October 2020, M_W7.6 earthquake at 97 km SSE of Sand Point, Alaska (blue outline star) and its first day aftershocks (small green circles) occurred after the manuscript submittal and acceptance, correspondingly. The directions and rates (in cm/year) of Pacific plate convergence are indicated by the arrows.

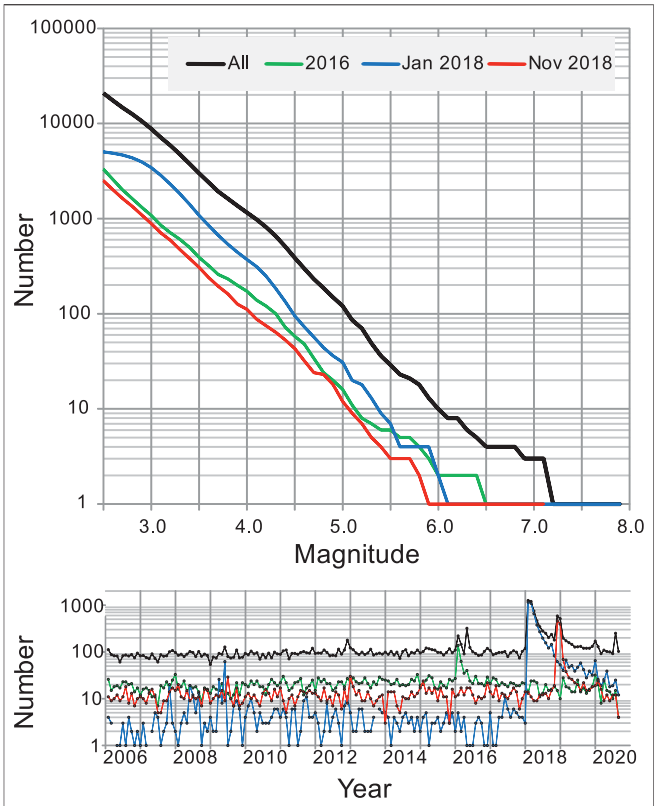

FIGURE 2 | The Gutenberg–Richter plot of the cumulative number of earthquakes (above) and the monthly number of the M ≥ 2.5 earthquakes (below) in the study region (black) and around each of the three major earthquakes: the January 24, 2016, M7.1 (green), January 23, 2018, M7.9 (blue), and November 30, 2018, M7.1 (red) earthquakes.

Kanamori, 1970; Christensen and Beck, 1994). The complexity of the megathrust is characterized with a multiple rupture of several segments of subducting Pacific plate, including the lateral transition faulting along the Yakutat block at the corner of the Pacific–North America plate boundary. The apparent reactivation of this region at the level of the M ≥ 7 earthquakes deserves special attention of seismologists. Therefore, in the following sections, we provide integral characterization of the fore- and aftershock sequences for each of the three earthquakes in terms of their magnitude–space–time distributions and the control parameter of the unified scaling law for earthquakes (Kossobokov and Mazhkenov, 1994; Bak et al., 2002; Kossobokov and Nekrasova, 2019), as well as the average estimates of the rupture extent, duration, and velocity, making use of the low-degree moments of the stress glut rate (Backus, 1977a; Backus, 1977b). Nowadays, when large earthquakes occur in sensible areas, including the Alaska's most populous city of Anchorage, numerous studies provide source tomographies (e.g., Ohta et al., 2006; Wei et al., 2012; Li et al., 2016; Grapenthin et al., 2018; Krabbenhoeft et al., 2018; Lay et al., 2018; Ruppert et al., 2018; Liu et al., 2019; Mann and Abers 2020; Ruppert et al., 2020; West et al., 2020). A large amount of work on the Alaskan earthquakes is based on different types of data and/or different methodological approaches. Therefore, some inconsistency and contradictions in the results obtained by different authors are inevitable, so that rupture process models are often different. That is why simple methods should be used to produce robust constrains to improve resolution of authoritative comprehensive determinations.

DATA

Seismicity of the region around Anchorage from January 01, 2006 through May 2019 is considered within 54°–64°N and 140°–160°W. The online search of the U.S. Geological Survey Advanced National Seismic System (ANSS) database provides a reasonably complete record of magnitude 2.5 or above earthquakes in the study area (**Figure 2**); in particular, the catalog is complete in the circles around the two M7.1 epicenters, while has an apparent deficiency of earthquakes below magnitude 3.0 in the larger circle around the M7.9 epicenter in front of the continental Alaska. The graphs of the monthly number of the M ≥ 2.5 earthquakes confirm the stability of hypocenters' determinations in the ANSS catalog in advance of the major events.

For each of the total 20,803 earthquakes considered, the catalog reports the ANSS preferred magnitude M. The Gutenberg–Richter plot (Gutenberg and Richter, 1944) of the cumulative number of earthquakes in magnitude range from 2.5 to 7.9 (**Figure 2**) follows the exponential best-fit trend line with the b-value of 0.868 (R^2 = 0.993). The plot is below its trend line in the magnitude range from below 5 up to 6.8, and then rises above due to the three major earthquakes on January 24, 2016, January 23, 2018, and November 30, 2018, whose parameters are listed in

TABLE 1 | Characteristics of the three major earthquake series in Southern Alaska, 2016–2018. Coefficients of the Unified Scaling Law for Earthquakes (USLE) are from the global map determinations (Nekrasova and Kossobokov, 2002) available from the ISC Dataset Repository.

Characteristic	January 24, 2016	January 23, 2018	November 11, 2018
Main shock origin time (UTC)	January 24, 2016 10:30:30	January 23, 2018 09:31:41	November 11, 2018 17:29:29
Main shock latitude, °N	59.6363	56.0039	61.3464
Main shock longitude, °W	153.4051	149.1658	149.9552
Main shock depth, km	129	14	47
Main shock magnitude M_{ANSS}	7.1	7.9	7.1
The USLE coefficient A at epicenter	–0.34	–0.19	–0.52
The USLE coefficient B at epicenter	0.89	0.90	0.87
The USLE coefficient C at epicenter	1.33	1.29	1.42
Number of M ≥ 2.5 (M ≥ 4) foreshocks	101 (2)	21 (1)	60 (2)
Number of M ≥ 2.5 (M ≥ 4) aftershocks	281 (16)	3,489 (262)	998 (42)
Magnitude of the last M ≥ 2.5 (M ≥ 4) foreshock	2.6 (4.0)	3.4 (4.1)	3.1 (4.5)
Time since the last M ≥ 2.5 (M ≥ 4) foreshock, days	2.50 (61.3)	4.98 (85.3)	0.28 (46.5)
Distance to the last M ≥ 2.5 (M ≥ 4) foreshock, km	23.2 (25.6)	181.31 (6.8)	72.57 (31.0)

Table 1. **Figure 3** displays the 4-D distribution of earthquakes in plots of magnitude, latitude, and longitude vs. time. The determination of depth is naturally biased by preset constants; therefore, to avoid potentially misleading conclusions, the depth vs. time distribution is not shown. Earthquakes with data points on pale yellow are not considered in the study.

Figure 4 provides the map of the coefficients of unified scaling law for earthquakes, USLE, which generalizes the Gutenberg–Richter relationship as follows (Nekrasova and Kossobokov, 2005; Kossobokov, 2020):

$$\log_{10} N(M, L) = A + B \times (5 - \mathrm{M}) + C \times \log_{10} L, \qquad (1)$$

where $N(M, L)$ is the number of earthquakes of a certain magnitude M expected in a year within an earthquake-prone area of diameter L; A and B are constants characterizing the annual rate of magnitude 5 events and the magnitude exponent analogous to a- and b-values of the Gutenberg–Richter relationship; and C estimates the fractal dimension of the epicenter loci at the given site. As evident from **Figure 4C**, the values of fractal dimension about 1.4 or larger highlight the highly fractured zone where subduction interacts with slippage along the Queen Charlotte transform fault. One can see that the highest values of C spread around the city of Anchorage accompanied with relatively low values of the logarithm of the seismic rate (A about −0.6). In contrast the area of Alaska–Aleutian trench is characterized by the highest level of earthquake rate (A about 0) and the lowest estimates of seismic locus dimension (C down to about 1). A, B, and C values at the epicenters of the three major earthquakes are listed in **Table 1**.

METHODOLOGY

Characterizing Earthquake Sequences

As clearly noted by Bak et al. (2002), in essence, the USLE states that the distribution of inter-event times between earthquakes depends only on the value of the variable control parameter

$$\eta = \tau \times 10^{B \times (5-M)} \times \mathrm{L}^{C}, \qquad (2)$$

where τ is the time between the two successive earthquakes, M is the magnitude of the second one, and L is the distance between the two. Recent studies of seismic sequences associated with strong M ≥ 6 earthquakes in Central Italy (Kossobokov and Nekrasova, 2017) and major M ≥ 7 earthquakes in New Zealand confirmed the existence of steady levels of the USLE control parameter η, called "*periods of stability*," which, apparently, may change at the shorter times of critical transitions of a seismic regime, including those associated with regional or local catastrophic events, that is, major or strong earthquakes. To characterize seismic dynamics around each of the three major earthquakes, we use the same choices of the space–time limits as in Kossobokov and Nekrasova (2019). In particular, we apply the 50-point moving averages to control parameter η evaluated at an angular distance of 1° (or 2.5°) from the epicenter of the M ≥ 7 (or M ≥ 7.5) main shock for 128 days before and 128 days after its origin time (**Figure 5**). (The choice of time interval allows for a sevenfold doubling of the 1-day period which is appropriate in analyzing either acceleration or deceleration of a daily time series.)

Characterizing an Earthquake Source

We analyze surface wave amplitude spectra at periods much longer than the earthquake duration to determine its source parameters derived from the moments of the stress glut rate. A detailed description of this methodology is given in Bukchin (1995). These techniques have been successfully applied in a number of studies of earthquake rupture processes (e.g., Aoudia et al., 2000; Lasserre et al., 2001; Clévédé et al., 2004).

Considering the source of an earthquake in approximation of an instant point, we determine the source depth and focal mechanism (in terms of strike, dip, and slip angles) by systematic exploration of 4D parametric space, as well as seismic moment by minimizing the residual between the observed and calculated long period surface wave amplitude spectra. To improve the resolution of surface wave inversion, we performed joint inversion of surface waves and first arrival polarities. We calculate amplitude spectra using the model of weak lateral inhomogeneity for the Earth structure (Babich et al., 1976; Woodhouse, 1974). As is well known, the focal mechanism

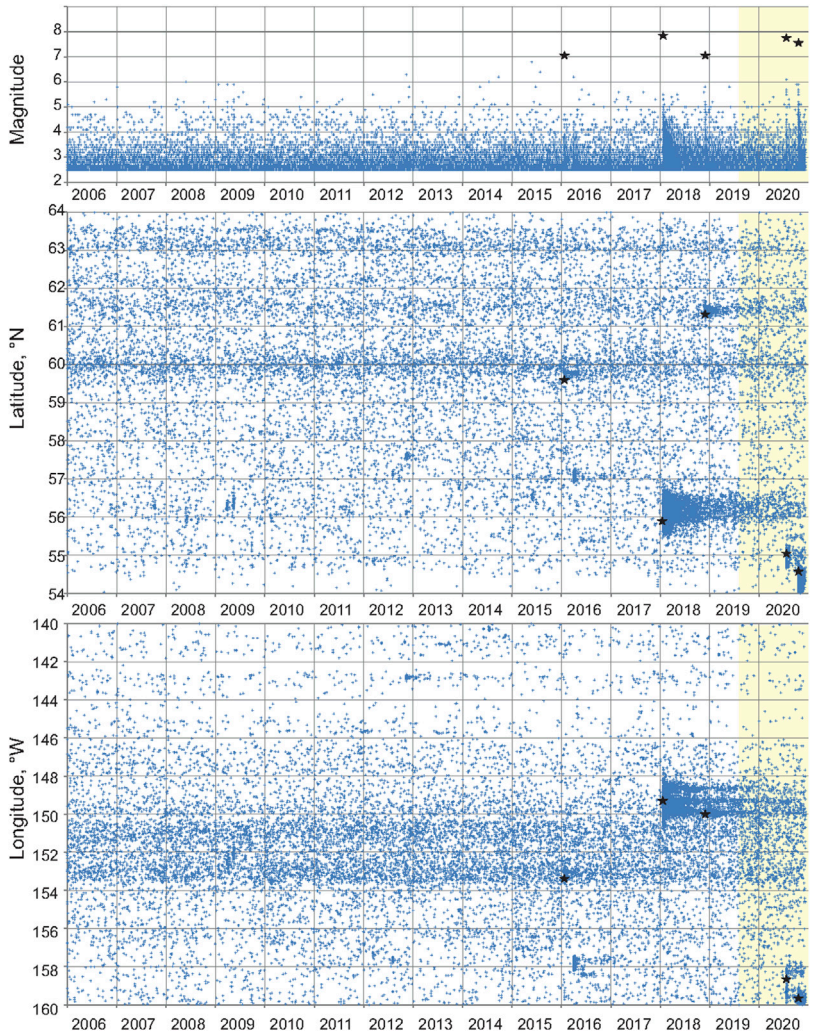

FIGURE 3 | Magnitude–latitude–longitude vs. time distribution of earthquakes in Southern Alaska, 2006–2020. The 4-D display of seismic activity shows the variable space–time intensity of earthquake energy release in the region, in particular, the irregular shapes of aftershock clusters including those of the three major earthquakes (black stars).

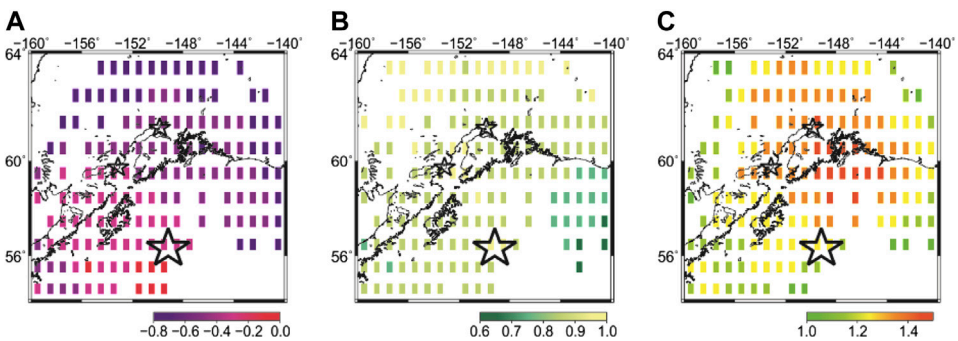

FIGURE 4 | The Unified Scaling Law for Earthquakes (USLE) coefficients in Southern Alaska (Nekrasova and Kossobokov, 2002; Nekrasova and Kossobokov, 2019). Note: stars mark the epicenters of the three major earthquakes.

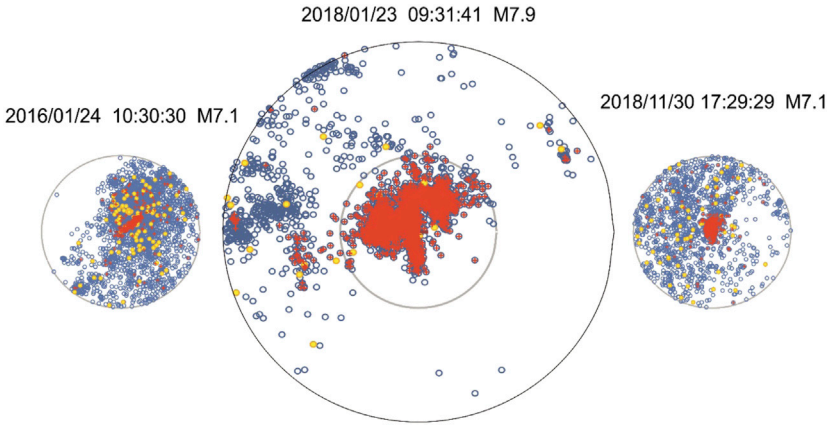

FIGURE 5 | Epicenters of the M ≥ 2.5 earthquakes at angular distance of 1° and 2.5° from the epicenter of each of the three major earthquakes in Southern Alaska. Note: open blue circles are epicenters of earthquakes in January 24, 2006–January 24, 2019, January 23, 2008–May 27, 2019, and November 30, 2008–May 27, 2019, correspondingly; yellow circles and small red crosses are those events occurring within 128 days before and 128 days after the origin time of a major event, respectively.

cannot be uniquely determined from the surface waves' amplitude spectra. We use P-wave first arrival polarities to select the optimal solution, which in detail description and constrains are given in Lasserre et al. (2001). Before inversion, we apply a smoothing procedure to the observed polarities, then use the frequency–time analysis program (FTAN) (Lander 1989a; Lander 1989b; Levshin et al., 1989) to isolate the Love and Rayleigh fundamental modes recorded by selected stations of the IRIS, GEOSCOPE, and GEOFON networks (Institut de physique du globe de paris, & ecole et observatoire des sciences de La terre de strasbourg, 1982; Scripps Institution of Oceanography, 1986; GEOFON, 1993). We simulated separately Love and Rayleigh fundamental modes, and compared them with observed records located by FTAN. The observed surface wave records were corrected for attenuation using PREM model and instrumental response. Analyzing the surface wave spectra at shorter periods, we describe the source as an approximation of the stress glut second moments (Backus, 1977a; Backus, 1977b). Using these moments, we determine integral estimates of the length of the source major and minor axes, l_{max} and l_{min}, its duration Δt, modulus of the axis average value of the instant centroid velocity $|v|$, and two angles: the angle between the strike axis and major axis, φ_l, and the angle between the strike axis and instant centroid velocity axis, φ_v.

Source dimension and spatial extent depend on the distribution of the stress glut rate in time and along the fault. In assumption of Gaussian distributions and 99% confidence levels, duration and length are set 2.5 and 3 times larger than their integral estimations, respectively.

To measure the effect of directivity, we consider a 1-D bilateral fault model with uniform slip from the nucleation point in two directions and define the modulus of uniform rupture velocity $|v|$ and the ratio $\alpha = \beta/\lambda$, where β is the shorter length to the source edge from the nucleation point and λ is the total source length. These two parameters can be expressed through the second moments of the stress glut rate. The vector v is directed along the vector of the average instant centroid velocity.

Identification of the fault plane based on the source description in terms of the second moment of stress glut rate approximation is impossible, if the major axis of the source is much larger than the minor one and rupture propagation is directed along the line of nodal planes' intersection. In the case of a frequently encountered type of earthquake in which the major axis and the average instantaneous centroid velocity are directed along the strike axis, the fault plane can be reliably identified for a strike-slip event ($\lambda = 0^\circ$ or $\lambda = 180^\circ$), and cannot be reliably identified for a dip-slip event ($\lambda = 90^\circ$ or $\lambda = 270^\circ$). If the earthquake considered is not of the type mentioned above, then its fault plane identification must be resolved with other available evidence (Bukchin, 2017).

RESULTS

Figure 5 shows epicenters of the M ≥ 2.5 earthquakes at angular distance of 1° and 2.5° from the epicenter of each of the three major earthquakes around Anchorage sampled in the time interval from 10 years before to 3 years after the origin time of the main shock or to the end of the available catalog. We specify those events occurring 128 days before (yellow circles) and after the main shock (red circles) and report a few related characteristics in the last rows of **Table 1**. The numbers of fore- and aftershocks differ dramatically; the ratio between them is 1:8, 1:262, and 1:21 for M ≥ 4.0 events around the January 2016, January 2018, and November 2018 main shocks, respectively. The delay time from the last foreshock differs from less than 7 h to about 5 days for the M ≥ 2.5 foreshocks and rises to a few months when M ≥ 4.0 foreshocks are considered. It is notable that the corresponding distances are much shorter for M ≥ 4.0 foreshocks (in particular, for both 2018 major earthquakes).

The sizes and shapes of aftershocks' time series are also very different in **Figure 5**: for the 2016, M7.1 event, we observe a nearly straight line extending for about 50 km; for the January 20518, M7.9 event, the pattern of epicenters looks like a butterfly,

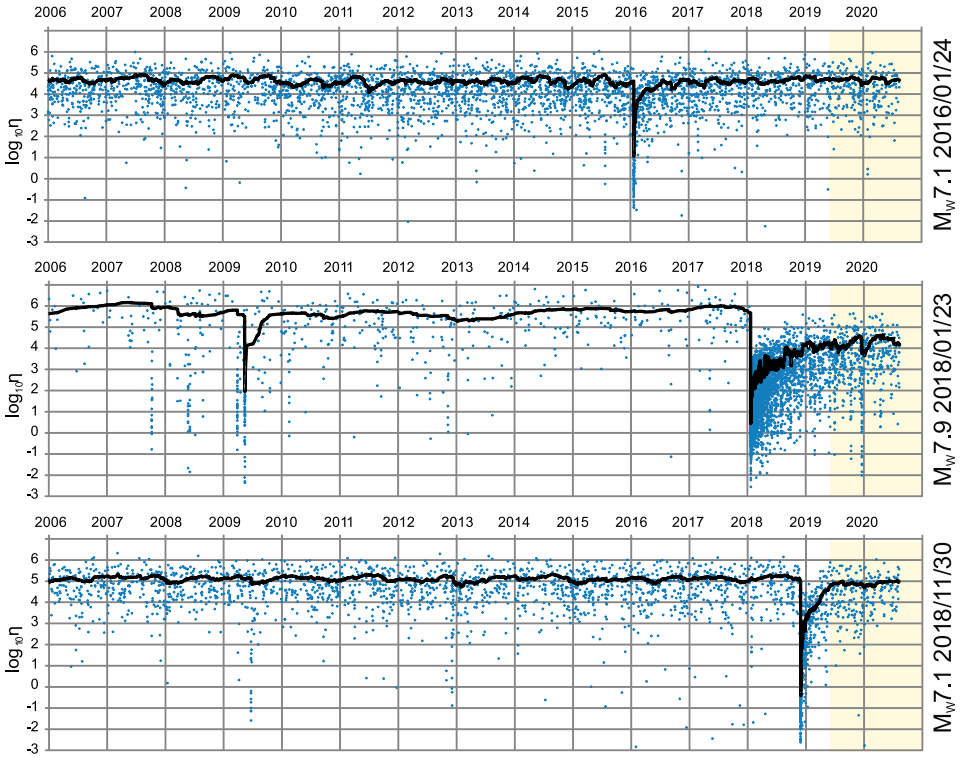

FIGURE 6 | Values of the USLE control parameter η (little crosses) vs. earthquake origin time within angular distance of 1° from the epicenters of M_W7.1 January 24, 2016 (top) and November 30, 2018 (bottom) and within 2.5° from the epicenter of M_W7.9 January 23, 2018 (middle) main shocks and their averages per 50 events (lines). An apparent rise and drop of $<\eta>$ by a factor of 2 in amplitude is observed in about a year preceding the two 2018 main shocks and not before the January 24, 2016, M7.1 event.

with the sub-meridian narrow body extending for about 130 km and the two wings with a span of about 150 km, which appears consistent with the Coulomb stress transfer pattern; for the November 2018, M7.1 Anchorage earthquake, aftershocks are concentrated within a 40 × 20-km area.

The individual values of the USLE control parameter η from 2006 to 2019, along with their 50-point moving average $<\eta>$, are shown in **Figure 6**. The single *period of stability* of $<\eta>$ for the entire interval of time (within a decimal order of their values $10^4 \leq <\eta> < 10^5$) was interrupted just for a few months after the January 24, 2016, M7.1 earthquake. In case of earthquake series around the January 23, 2018, M7.9 epicenter, the period of stability with $2 \times 10^5 \leq <\eta> < 2 \times 10^6$ was violated by a burst of activity from the end of March to the middle of May 2009 when seven earthquakes in magnitude range M5.0–5.9 occurred and then after the major shock. By the end of May 2019, the values of $<\eta>$ increased to about 10^4 and may remain at this level as characterized by more intensive seismic activity in the area (confirmed by $4 \times 10^3 \leq <\eta> < 4 \times 10^4$ in June 2019–July 2020). Among the three series, the period in advance of the November 30, 2018, M7.1 Anchorage earthquake, characterized with $5 \times 10^4 \leq <\eta> < 2 \times 10^5$, is the most stable in regard to the variance of the USLE control parameter. Moreover, by the end of May 2019, the values of $<\eta>$ have increased above 2×10^4, which indicates reaching the same decimal order of values as those in advance of the main major shock (confirmed by $5 \times 10^4 \leq <\eta> < 10^5$ in June 2019–July 2020).

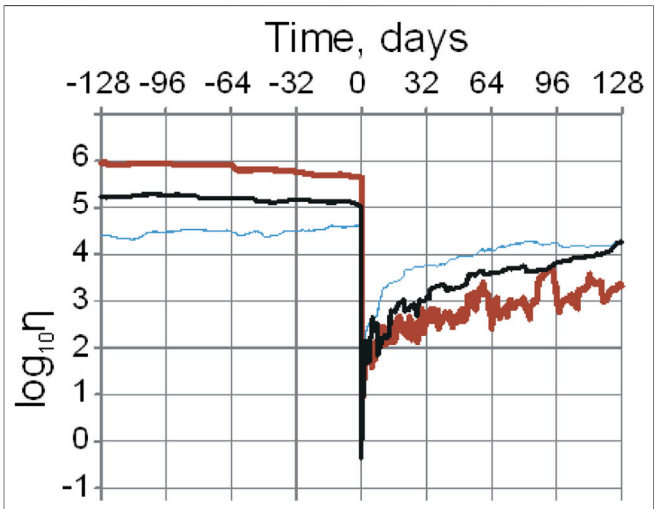

FIGURE 7 | Averages of the USLE control parameter η per 50 events vs. time to the main shock for the M_W7.1 January 24, 2016 (thin blue line), M_W7.9 January 23, 2018 (heavy red line), and M_W7.1 November 30, 2018 (black line) major earthquakes.

TABLE 2 | Characteristics of the three major earthquake sources in Southern Alaska, 2016–2018. The earthquake source parameters are given for each of the two nodal planes.

Characteristic	January 24, 2016		January 23, 2018		November 11, 2018	
Nodal planes (strike, dip, slip)	60°, 65°, 40°	310°, 4°,149°	165°,71°,164°	260°,75°,20°	189°,57°,−90°	9°, 33°, −90°
Length of major axis l_{max}, km	120	120	180	75	105	105
Length of minor axis l_{min}, km	37	37	23	23	18	18
Duration Δt, s	25	25	37.5	37.5	15	15
Modulus of velocity $\|v\|$, km/s	3.5	3.5	3	3	4.5	4.5
Angle φ_l,°	80	120	15	165	160	0
Angle φ_v,°	80	300	195	165	160	180
Residual	0.320	0.312	0.248	0.290	0.363	0.374

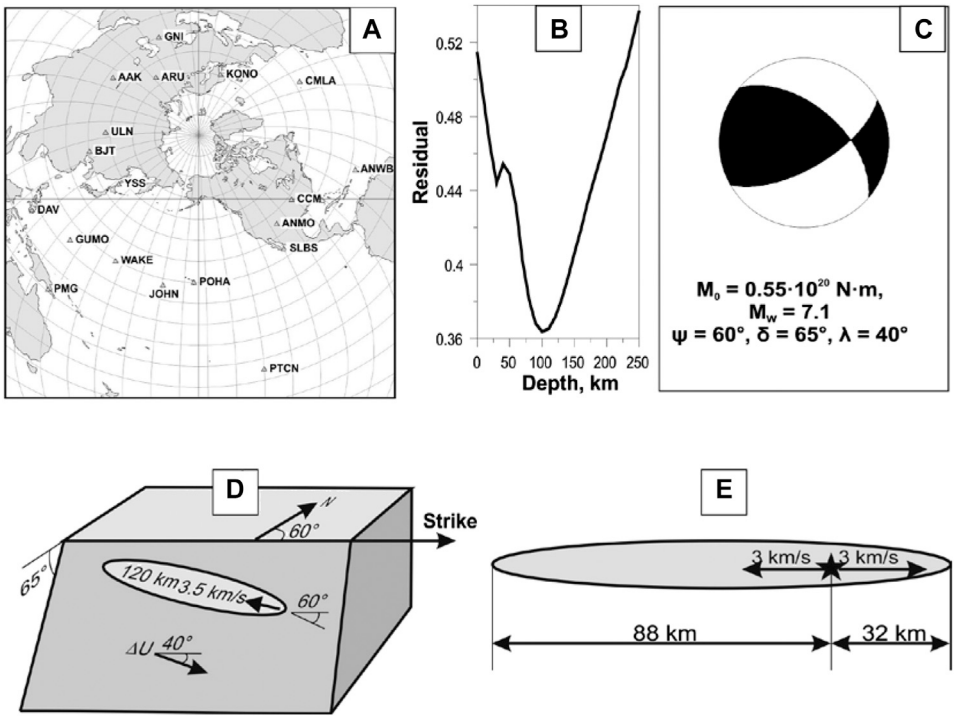

FIGURE 8 | Modeling the January 24, 2016, M_W7.1 earthquake: **(A)** stations used to determine parameters of the earthquake in the double couple approximation, **(B)** source depth residual function, **(C)** focal mechanism, **(D)** the earthquake focal model, **(E)** one-dimensional bilateral model of faulting oriented along the centroid velocity. Notes: the map **(A)** is centered at the epicenter of the major earthquake; M_0, M_W, ψ, δ, λ, and ΔU are seismic moment, moment magnitude, strike, dip, slip, and vector of slip direction, respectively.

Let us zoom in to the 128-day intervals in advance and after the three major earthquakes. In the expanded view of $<\eta>$ shown in **Figure 7**, we notice an apparent increase of $<\eta>$ by a factor of 2 in advance of the January 24, 2016, M7.1 event, as well as a drop of $<\eta>$ by a factor of 2 in advance of the other two major earthquakes, which does not appear to offer a method for short-term earthquake forecasting. The decay of the aftershock series is also rather diverse: the best fit of the 50-point moving average $<\eta>$ in the three aftershock series of the January 2016, January 2018, and November 2018, as a function of time after the main shock, t, is the power law equal to $80.8 \times t^{1.18}$ ($R^2 = 0.988$), $22.6 \times t^{1.18}$ ($R^2 = 0.949$), and $19.9 \times t^{0.88}$ ($R^2 = 0.932$), respectively.

To determine the source parameters of the three major earthquakes at 600 km around Anchorage as derived from the moments of stress glut rate (Bukchin, 1995), we selected the following spectral bands (spectral bands in brackets correspond to the second moment approximation): 70–250 s (40–60 s) for the two M7.1 major earthquakes in 2016 and 2018 and 150–250 s (40–60 s) for the M7.9 earthquake in 2018. **Table 2** shows for each of the three major earthquakes, the two nodal planes (first row) and, for each nodal plane, the six integral source parameters derived from the second stress glut moments (rows 2–7) along with the values of total residuals in the optimal solution (row 8). The six parameters characterize the earthquake model size, orientation, duration, and rupture propagation. The characteristics were obtained from making use of 36, 42, and 40 fundamental Love and Rayleigh mode records of the January 24, 2016, January 23, 2018, and November 30, 2018 earthquakes,

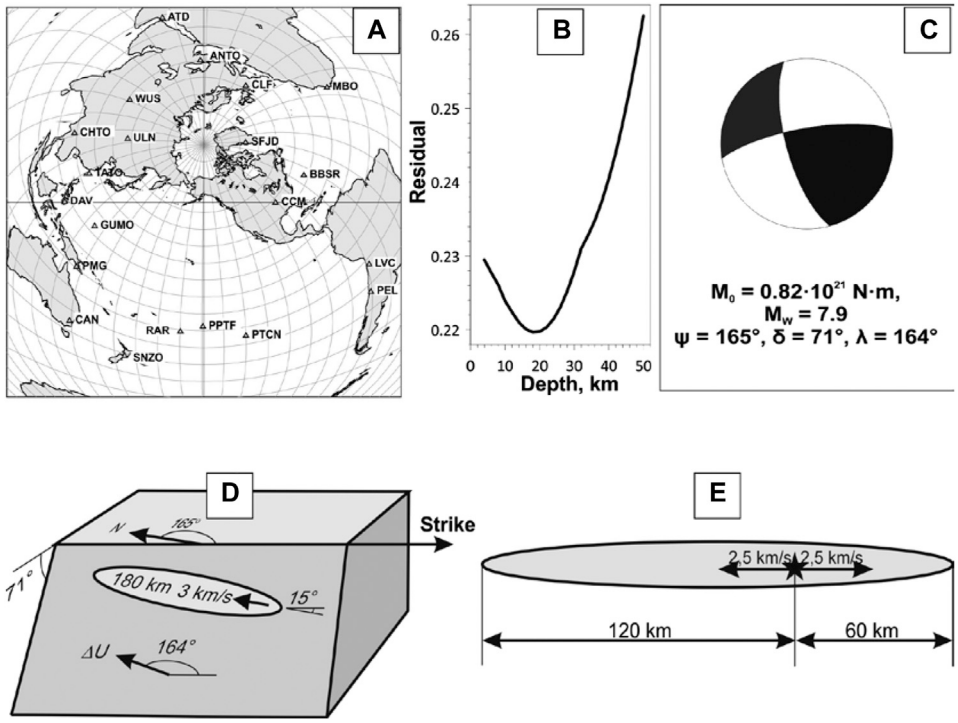

FIGURE 9 | Modeling the January 23, 2018, M_W7.9 earthquake: **(A)** stations used to determine parameters of the earthquake in the double couple approximation, **(B)** source depth residual function, **(C)** focal mechanism, **(D)** the earthquake focal model, e) one-dimensional bilateral model of faulting oriented along the centroid velocity. Notes: the same as in **Figure 8**.

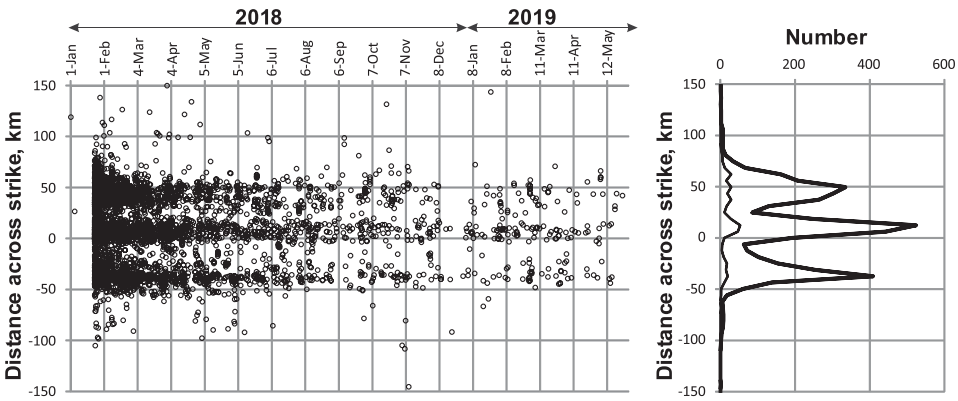

FIGURE 10 | Distribution of M ≥ 2.5 earthquakes across strike of the M_W7.9, January 23, 2018 main shock in time (left) and in number (right). The sub-meridian cluster dominates both in the first day of aftershocks (thin line) and to the end of May 2019 (heavy line); its width is much smaller than its length along the main shock strike (ψ = 165°).

respectively. Selecting the records, we did our best to satisfy the following conditions: i) signal quality, characterized by the value of the polarization anomaly, should be less than 15°, and ii) the azimuthal distribution of stations should be rather homogeneous.

Figure 8 summarizes modeling of the January 24, 2016, M_W7.1 earthquake source by displaying the location of stations used in the determination a), the residual function which minimum defines the depth of the instant point source b), the double couple beach ball solution c), the focal mechanism modeled by three angles d), and the 1-D bilateral model of faulting e). The solution is not a pure dip slip, which complicates identification the fault plane. The residuals for the nodal planes of this earthquake (**Table 2**, last row) are about the same and do not allow for a confident choice of the fault plane; however, the abovementioned shape of the distribution of its

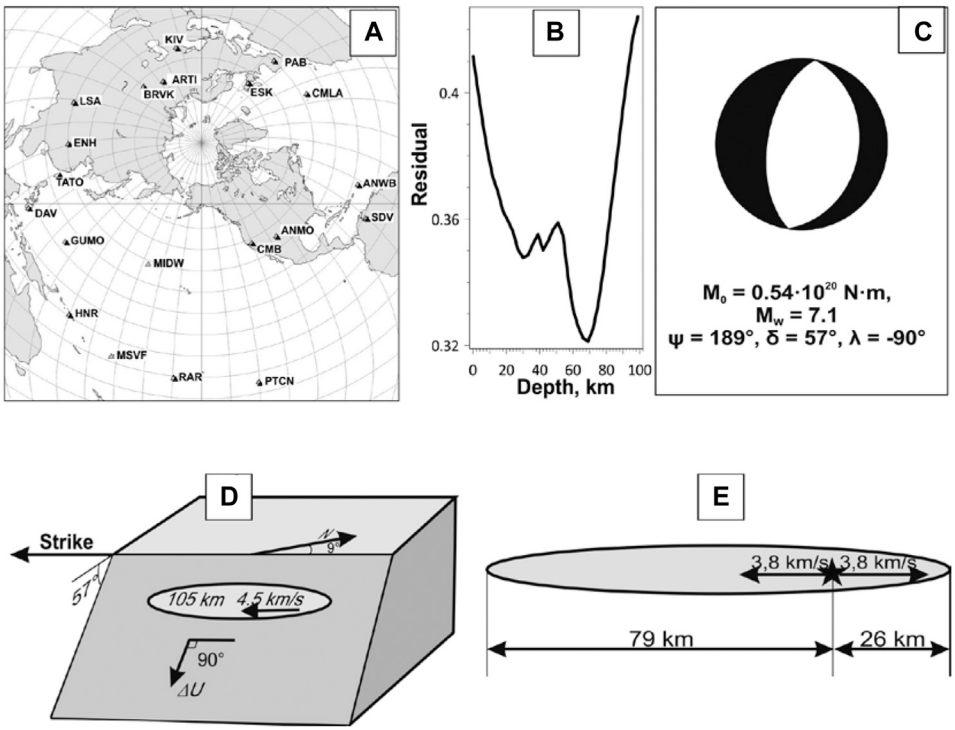

FIGURE 11 | Modeling the November 30, 2018, M_W7.1 earthquake: **(A)** stations used to determine parameters of the earthquake in the double couple approximation, **(B)** source depth residual function, **(C)** focal mechanism, **(D)** the earthquake focal model, **(E)** one-dimensional bilateral model of faulting oriented along the centroid velocity. Notes: the same as in **Figure 8**.

aftershocks in **Figure 5** favors the mechanism presented in **Figure 8D**.

By analogy, **Figure 9** summarizes modeling of the January 23, 2018, M_W7.9 earthquake source. In this case, the focal mechanism is practically pure strike-slip motion. The residuals, that differ by about 17%, favor the slippage along the near meridian strike of the narrow "butterfly body" of the aftershock distribution in **Figure 5**. As evident from **Figures 3**, **5**, **10**, the aftershocks of this earthquake split into three clusters with the narrow middle one associated with the largest number of aftershocks (**Figure 10**).

Figure 11 is analogous to **Figures 8**, **9**. The November 30, 2019, M_W7.1 earthquake is modeled as a pure dip slip. In this case, there is no evidence for a confident choice of the fault plane, so that the optimal choice based on nearly the same residuals (which differ by a negligible 3% of their value, **Table 2**) remains rather uncertain; an option of both nodal planes involved in the normal faulting at a depth of about 70 km (**Figure 11B**) cannot be dismissed (the apparently bimodal shape of the graph may explain different determinations reported by other agencies).

It is worth mentioning that there are no significant differences in focal mechanisms from the parameters provided by USGS, Global CMT, and ESMC. However, the depths of the three major earthquakes provided by these agencies differ from our determination (e.g., compare 100, 20, and 70 km with 129, 14.7, and 46.7 km by USGS, respectively). A significant difference is the choice of a nodal plane representing the fault plane for the January 23, 2018 event; the USGS determination favor E-W plane, while our analysis of the complex aftershock data (**Figures 3**, **5**, **10**) strongly suggests the orthogonal one as the correct representative of the fault plane.

DISCUSSION AND CONCLUSION

The determination of the spatial and temporal distribution of slip over the fault area of large earthquakes is essential for better comprehension of the mechanics of the seismic rupture and its environmental impact (e.g., Yagi and Kikuchi, 2000; Bouchon et al., 2001; Clevede et al., 2012). We use the integral source parameters given by the stress glut rate moments of total degree 2 for constraining the models of the three major earthquakes at 600 km around Anchorage, Southern Alaska. Beyond point source moment tensor and hypocenter determinations, we provide average estimates of the rupture length and width, duration, and velocity, making use of the low degree moments of stress glut rate (Backus, 1977a; Backus, 1977b). To our knowledge, a few earthquakes have been studied from this point of view (Gusev and Pavlov, 1988; Bukchin, 1995; Gomez et al., 1997a; Gomez et al., 1997b; Aoudia et al., 2000; McGuire et al., 2000; McGuire et al., 2001; McGuire et al., 2002; Clévédé et al., 2004).

Our analysis of the source models for the three earthquakes yields similar results to other moment tensor solutions. However, for the 2018 Kodiak earthquake, we infer that the conjugate plane

in the final USGS NEIC solutions is the fault plane. This is similar to the findings presented in the comprehensive study by Lay et al. (2018) based on seismic, GPS, and tsunami data. They conclude a multiple fault rupture dominated by right-lateral slip on an SSE trending, Specifically, their "primary faulting with $\phi = 155^{\circ}$ and $\delta = 72^{\circ}$, with slip of up to 15.6 m in the crust and uppermost mantle," is confirmed and complimented by our robust estimates based on the low-degree moments of the stress glut rate (**Table 2**; **Figure 9**).

In general, major earthquakes of Mw ≥ 7 are complex. The geometry, timing, and slip distribution of the complex nonlinear system of the lithospheric blocks and faults (Keilis-Borok, 1990) involved are usually not well resolved. Their rupture may propagate both upward into the crust and downward into the mantle (Liu et al., 2019; Ruppert et al., 2020). As a result, the expected ground shaking could be under- or over-predicted by an order of magnitude (Grapenthin et al., 2018; Mann and Abers 2020), causing unexpected societal impacts and errors in seismic hazard assessment (Wyss et al., 2012; West et al., 2020).

Seismic energy accumulation, release, and redistribution in the lithosphere are not yet well studied. It appears that seismic diversity is a cornerstone of understanding complex dynamics of a system of blocks and faults in advance and after catastrophic events, the main contributors to energy release (Ben-Zion, 2008; Zaliapin et al., 2008). Characterization of the fore- and aftershock sequences of the recent major earthquakes in Southern Alaska confirms the existence of the long-term periods of seismic stability defined by the averages $<\eta>$ of the USLE control parameter that are interrupted by mid- or even short-term bursts of activity associated with catastrophic events. However, at this time, neither of the two M7.1 events considered in this study showed a change in the level of $<\eta>$ observed in advance of their origin times; the January 23, 2018, M7.9 earthquake may become an exception, if the level of $<\eta>$ reached by the end of May 2019 persists. It seems premature to discuss if the variability of $<\eta>$ can be useful in operational earthquake forecasting (Kossobokov et al., 2015) of seismic catastrophes, due to the yet rather small number of case studies: five cases in Central Italy (Kossobokov and Nekrasova, 2017), nine in New Zealand (Kossobokov and Nekrasova, 2019), and three in Southern Alaska. Nevertheless, the apparent major seismic activity, in particular, the one associated with the M7.9 strike-slip earthquake 280 km SE of Kodiak and the most recent M7.8 Alaska Peninsula thrust faulting, right at the borders of the rupture zone of the 1964 Great Alaska, M9.3 mega-earthquake (**Figure 1**), deserves special attention, with continued further studies and monitoring of this region.

DATA AVAILABILITY STATEMENT

Datasets related to this article can be found at **https://doi.org/10.5066/F7MS3QZH**, hosted at U.S. Geological Survey, Earthquake Hazards Program (U.S. Geological Survey, Earthquake Hazards Program 2017), accessed June 1, 2019; **http://ds.iris.edu/wilber3/find_event**, hosted at Incorporated Research Institutions for Seismology (Institut de Physique du Globe de Paris & Ecole et Observatoire des Sciences de la Terre de Strasbourg, 1982; Scripps Institution of Oceanography, 1986; GEOFON, 1993); **https://doi.org/10.31905/XT753V44**, hosted at the International Seismological Centre (ISC) Dataset Repository (Nekrasova and Kossobokov, 2019).

AUTHOR CONTRIBUTIONS

BB and AF contributed the solutions and interpretation of the three major earthquake sources; VK and AN contributed presentation of seismic flow dynamics in advance and after the three major earthquakes.

FUNDING

This study was carried out as part of the RF state task of Scientific Research Works on "Development of methods of seismic data analysis in order to study the source, environment, seismic hazard" (No. 0143-2019-0007). No other funding received.

REFERENCES

Aoudia, A., Saraó, A., Bukchin, B., and Suhadolc, P. (2000). The 1976 Friuli (NE Italy) thrust faulting earthquake: a reappraisal 23 years later. *Geophys. Res. Lett.* 27, 573–576. doi:10.1029/1999GL011071

Babich, V. M., Chikachev, B. A., and Yanovskaya, T. B. (1976). Surface waves in a vertically inhomogeneous elastic half-space with weak horizontal inhomogeneity. *Izv. Akad. Nauk. SSSR - Fiz. Zemli* 4, 24–31.

Backus, G. E. (1977a). Interpreting the seismic glut moments of total degree two or less. *Geophys. J. Int.* 51, 1–25. doi:10.1111/j.1365-246x.1977.tb04187.x

Backus, G. E. (1977b). Seismic sources with observable glut moments of spatial degree two, *Geophys. J. Int.* 51, 27–45. doi:10.1111/j.1365-246x.1977.tb04188.x

Bak, P., Christensen, K., Danon, L., and Scanlon, T. (2002). Unified scaling law for earthquakes. *Phys. Rev. Lett.* 88, 178501–178504. doi:10.1103/physrevlett.88.178501

Ben-Zion, Y. (2008). Collective behavior of earthquakes and faults: continuum-discrete transitions, progressive evolutionary changes, and different dynamic regimes. *Rev. Geophys.* 46, RG4006. doi:10.1029/2008RG000260

Bird, P. (2003). An updated digital model of plate boundaries. *Geochem. Geophys. Geosyst.* 4. 1027–1078. doi:10.1029/2001GC000252

Bouchon, M., Bouin, M.-P., Karabulut, H., Toksöz, M. N., Dietrich, M., and Rosakis, A. J. (2001). How fast is rupture during an earthquake? New insights from the 1999 Turkey earthquakes. *Geophys. Res. Lett.* 28, 2723–2726. doi:10.1029/2001gl013112

Bukchin, B. G. (1995). Determination of stress glut moments of total degree 2 from teleseismic surface wave amplitude spectra. *Tectonophysics* 248, 185–191. doi:10.1016/0040-1951(94)00271-A

Bukchin, B. G. (2017). Second-moment approximation of the earthquake source and fault plane identification. *Izv. Phys. Solid Earth* 53, 243–249. doi:10.1134/s1069351317020045

Christensen, D. H., and Beck, S. L. (1994). The rupture process and tectonic implications of the great 1964 Prince William Sound earthquake. *Pageoph* 142, 29–53. doi:10.1007/BF00875967

Clévédé, E., Bouin, M.-P., Bukchin, B., Mostinskiy, A., and Patau, G. (2004). New constraints on the rupture process of the 1999 August 17 Izmit earthquake deduced from estimates of stress glut rate moments. *Geophys. J. Int.* 159, 931–942. doi:10.1111/j.1365-246X.2004.02304.x

Clevede, E., Bukchin, B., Favreau, P., Mostinskiy, A., Aoudia, A., and Panza, G. F. (2012). Long-period spectral features of the Sumatra-Andaman 2004 earthquake rupture process. *Geophys. J. Int.* 191, 1215–1225. 10.1111/j.1365-246X.2012.05482.x

GEOFON (1993). GEOFON seismic network. *Deutsches GeoForschungsZentrum GFZ*. Other/Seismic Network. doi:10.14470/TR560404

Gómez, J. M., Bukchin, B., Madariaga, R., Rogozhin, E. A., and Bogachkin, B. (1997a). Rupture process of the 19 August 1992 susamyr, Kyrgyzstan, earthquake. *J. Seismol.* 1, 219–235. doi:10.1023/a:1009780226399

Gómez, J. M., Bukchin, B., Madariaga, R., and Rogozhin, E. A. (1997b). A study of the Barisakho, Georgia, earthquake of 1992 October 23 from broad-band surface and body waves. *Geophys. J. Int.* 129, 613–623. doi:10.1111/j.1365-246x.1997.tb04497.x

Grapenthin, R., West, M., Tape, C., Gardine, M., and Freymueller, J. (2018). Single-frequency instantaneous GNSS velocities resolve dynamic ground motion of the 2016 Mw 7.1 iniskin, Alaska, earthquake. *Seismol Res. Lett.* 89, 1040–1048. doi:10.1785/0220170235

Gusev, A. A., and Pavlov, V. M. (1988). Determination of space-time structure of a deep earthquake source by means of power moments. *Tectonophysics* 152, 319–334. doi:10.1016/0040-1951(88)90057-1

Gutenberg, R., and Richter, C. F. (1944). Frequency of earthquakes in California. *Bull. Seism. Soc. Am.* 34, 185–188.

Institut de Physique du Globe de Paris & Ecole et Observatoire des Sciences de la Terre de Strasbourg (1982). GEOSCOPE, French global network of broad band seismic stations. *Institut de Physique du Globe de Paris*. doi:10.18715/GEOSCOPE

Kanamori, H. (1970). The Alaska earthquake of 1964: radiation of long-period surface waves and source mechanism. *J. Geophys. Res.* 75, 5029–5040. doi:10.1029/jb075i026p05029

Keilis-Borok, V. I. (1990). The lithosphere of the Earth as a nonlinear system with implications for earthquake prediction. *Rev. Geophys.* 28, 19–34. doi:10.1029/rg028i001p00019

Kossobokov, V. (2020). "Unified scaling law for earthquakes that generalizes the fundamental gutenberg-richter relationship," in *Encyclopedia of solid Earth geophysics. Encyclopedia of Earth sciences series*. Editor H. Gupta, Springer.

Kossobokov, V. G., and Mazhkenov, S. A. (1994). "On similarity in the spatial distribution of seismicity," in *Computational Seismology and geodynamics*, Editors D. K. Chowdhury, Washington DC: Am. Geophys. Union, 6–15.

Kossobokov, V. G., and Nekrasova, A. K. (2017). Characterizing aftershock sequences of the recent strong earthquakes in central Italy. *Pure Appl. Geophys.* 174, 3713–3723. doi:10.1007/s00024-017-1624-9

Kossobokov, V. G., and Nekrasova, A. K. (2019). Aftershock sequences of the recent major earthquakes in New Zealand. *Pure Appl. Geophys.* 176, 1–23. doi:10.1007/s00024-018-2071-y

Kossobokov, V. G., Peresan, A., and Panza, G. F. (2015). On operational earthquake forecast and prediction problems. *Seismol Res. Lett.* 86, 287–290. doi:10.1785/0220140202

Krabbenhoeft, A., von Huene, R., Miller, J. J., Lange, D., and Vera, F. (2018). Strike-slip 23 January 2018 MW 7.9 Gulf of Alaska rare intraplate earthquake: complex rupture of a fracture zone system. *Nat. Sci. Rep.* 8, 13706. doi:10.1038/s41598-018-32071-4

Lander, A. (1989a). "Frequency-time analysis," in *Seismic surface waves in laterally inhomogeneous Earth*, Editor V. Keilis-Borok, Dordrecht, Netherlands: Kluwer Academic Publishers, 153–163.

Lander, A. (1989b). "Linear-polarization analysis," in *Seismic surface waves in laterally inhomogeneous Earth*, Editor V. Keilis-Borok, Dordrecht, Netherlands: Kluwer Academic Publishers, 164–178.

Lasserre, C., Bukchin, B., Bernard, P., Tapponnier, P., Gaudemer, Y., Mostinsky, A., et al. (2001). Source parameters and tectonic origin of the 1996 June 1 tianzhu (Mw=5.2) and 1995 July 21 yongden (Mw=5.6) earthquakes near the haiyuan fault (gansu, China). *Geophys. J. Int.* 144, 206–220. doi:10.1046/j.1365-246x.2001.00313.x.

Lay, T., Ye, L., Bai, Y., Cheung, K. F., and Kanamori, H. (2018). The 2018 M W 7.9 gulf of Alaska earthquake: multiple Fault rupture in the Pacific plate. *Geophys. Res. Lett.* 45, 9542–9551. doi:10.1029/2018GL079813

Levshin, A. L., Yanovskaya, T. B., Lander, A. V., Bukchin, B. G., Barmin, M. P., Ratnikova, L. I., et al. (1989). "Recording, identification and measurement of surface wave parameters," in *Seismic surface waves in laterally inhomogeneous Earth*, Editor V. Keilis-Borok, Dordrecht, Netherlands: Kluwer Academic Publishers, 131–182.

Li, S., Freymueller, J., and McCaffrey, R. (2016). Slow slip events and time-dependent variations in locking beneath lower cook inlet of the Alaska-Aleutian subduction zone. *J. Geophys. Res. Solid Earth* 121. 1060–1079. doi:10.1002/2015jb012491

Liu, C., Lay, T., Xie, Z., and Xiong, X. (2019). Intraslab deformation in the 30 november 2018 Anchorage, Alaska, M W 7.1 earthquake. *Geophys. Res. Lett.* 46, 2449–2457. doi:10.1029/2019GL082041

Mann, M. E., and Abers, G. A. (2020). First-order mantle subduction-zone structure effects on ground motion: the 2016 Mw 7.1 iniskin and 2018 Mw 7.1 Anchorage earthquakes. *Seismol Res. Lett.* 91, 85–93. doi:10.1785/0220190197

McGuire, J. J., Zhao, L., and Jordan, T. H. (2002). Predominance of unilateral rupture for a global catalog of large earthquakes. *Bull. Seismol. Soc. Am.* 92, 3309–3317. doi:10.1785/0120010293

McGuire, J. J., Zhao, L., and Jordan, T. H. (2000). Rupture dimensions of the 1998 Antarctic Earthquake from low-frequency waves, *Geophys. Res. Lett.* 27, 2305–2308. doi:10.1029/1999gl011186

McGuire, J. J., Zhao, L., and Jordan, T. H. (2001). Teleseismic inversion for the second-degree moments of earthquake space-time distributions. *Geophys. J. Int.* 145, 661–678. doi:10.1046/j.1365-246x.2001.01414.x

Nekrasova, A., and Kossobokov, V. (2002). Generalizing the Gutenberg-Richter scaling law. Fall Meeting Suppl., Am. Geophys. Union. Abstract NG62B-0958.

Nekrasova, A. K., and Kossobokov, V. G. (2005). Temporal variations in the parameters of the unified scaling law for earthquakes in the eastern part of honshu island (Japan). *Dokl. Earth Sci.* 405, 1352–1356.

Nekrasova, A. K., and Kossobokov, V. G. (2019). *Unified scaling law for earthquakes: global map of parameters*, ISC's Seismological Dataset Repository. doi:10.31905/XT753V44

Ohta, Y., Freymueller, J., Hreinsdottir, S., and Suito, H. (2006). A large slow slip event and the depth of the seismogenic zone in the south central Alaska subduction zone. *Earth Planet Sci. Lett.* 247, 108–116. doi:10.1016/j.epsl.2006.05.013

Press, F., and Jackson, D. (1965). Alaskan Earthquake, 27 March 1964: vertical extent of faulting and elastic strain energy release. *Science* 147, 867–868. doi:10.1126/science.147.3660.867

Ruppert, N. A., Nayak, A., Thurber, C., and Richards, C. (2020). Aftershock analysis of the 2018 Mw 7.1 Anchorage, Alaska, earthquake: relocations and regional moment tensors. *Seism. Res. Lett.* 91, 114–125. doi:10.1785/0220190199

Ruppert, N. A., Rollins, C., Zhang, A., Meng, L., Holtkamp, S. G., West, M. E., et al. (2018). Complex faulting and triggered rupture during the 2018 MW7.9 offshore Kodiak, Alaska, earthquake. *Geophys. Res. Lett.* 45, 7533–7541. doi:10.1029/2018GL078931

Scripps Institution of Oceanography (1986). Global seismograph network - IRIS/IDA. *International federation of digital seismograph networks*. Available at: https://doi.org/10.7914/SN/II.

U.S. Geological Survey, Earthquake hazards program (2017). *Advanced national seismic system (ANSS) comprehensive catalog of earthquake events and products: various*, Available at: https://doi.org/10.5066/F7MS3QZH.

Wei, M., McGuire, J. J., and Richardson, E. (2012). A slow slip event in the south central Alaska subduction zone and related seismicity anomaly. *Geophys. Res. Lett.* 39, L15309. doi:10.1029/2012GL052351

West, M. E., Bender, A., Gardine, M., Gardine, L., Gately, K., Haeussler, P., et al. (2020). The 30 november 2018 Mw 7.1 anchorage earthquake. *Seism Res. Lett.* 91, 66–84. doi:10.1785/0220190176

Woodhouse, J. H. (1974). Surface waves in the laterally varying structure. *Geophys. J. R. Astr. Soc.* 90, 713–728. 10.1111/j.1365-246X.1974.tb04098.x

Wyss, M., Nekrasova, A., and Kossobokov, V. (2012). Errors in expected human losses due to incorrect seismic hazard estimates. *Nat. Hazards* 62, 927–935. doi:10.1007/s11069-012-0125-5

Wyss, M., and Brune, J. (1967). The Alaska earthquake of 27 March 1964: a complex multiple rupture. *Bull. Seism. Soc. Am.* 57. 1017–1023.

Yagi, Y., and Kikuchi, M. (2000). Source rupture process of the Kocaeli, Turkey, earthquake of August 17, 1999, obtained by joint inversion of near-field data and teleseismic data. *Geophys. Res. Lett.* 27, 1969–1972. doi:10.1029/1999gl011208

Zaliapin, I., Gabrielov, A., Keilis-Borok, V., and Wong, H. (2008). Clustering analysis of seismicity and aftershock identification. *Phys. Rev. Lett.* 101, 018501. doi:10.1103/PhysRevLett.101.018501

Conflict of Interest: The authors declare that the research was conducted in the absence of any commercial or financial relationships that could be construed as a potential conflict of interest.

Copyright © 2020 Kossobokov, Bukchin, Fomochkina and Nekrasova. This is an open-access article distributed under the terms of the Creative Commons Attribution License (CC BY). The use, distribution or reproduction in other forums is permitted, provided the original author(s) and the copyright owner(s) are credited and that the original publication in this journal is cited, in accordance with accepted academic practice. No use, distribution or reproduction is permitted which does not comply with these terms.

frontiers in Earth Science

ORIGINAL RESEARCH
published: 08 January 2021
doi: 10.3389/feart.2020.590724

Unified Scaling Law for Earthquakes: Space-Time Dependent Assessment in Friuli-Venezia Giulia Region

Anastasia Nekrasova[1]* *and Antonella Peresan*[2]

[1]*Institute of Earthquake Prediction Theory and Mathematical Geophysics, Moscow, Russia,* [2]*National Institute of Oceanography and Applied Geophysics - OGS, Udine, Italy*

The concept of the Unified Scaling Law for Earthquakes (USLE), which generalizes the Gutenberg-Richter relationship making use of the fractal distribution of earthquake sources in a seismic region, is applied to seismicity in the Friuli-Venezia Giulia region, FVG (Northeastern Italy) and its surroundings. In particular, the temporal variations of USLE coefficients are investigated, with the aim to get new insights in the evolving dynamics of seismicity within different tectonic domains of FVG. To this purpose, we consider all magnitude 2.0 or larger earthquakes that occurred in 1995–2019, as reported in the catalog compiled at the National Institute of Oceanography and Applied Geophysics (OGS catalog), within the territory of its homogeneous completeness. The observed variability of seismic dynamics for three sub-regions of the territory under investigation, delimited based on main geological and tectonic features, is characterized in terms of several moving averages, including: the inter-event time, τ; the cumulative Benioff strain release, Σ; the USLE coefficients estimated for moving six-years time intervals, and the USLE control parameter, η. We found that: 1) the USLE coefficients in FVG region are time-dependent and show up correlated; 2) the dynamical changes of τ, Σ, and η in the three sub-regions highlight a number of different seismic regimes; 3) seismic dynamics, prior and after the occurrence of the 1998 and 2004 Kobarid (Slovenia) strong main shocks, is characterized by different parameters in the related sub-region. The results obtained for the FVG region confirm similar analysis performed on a global scale, in advance and after the largest earthquakes worldwide. Moreover, our analysis highlights the spatially heterogeneous and non-stationary features of seismicity in the investigated territory, thus suggesting the opportunity of resorting to time-dependent estimates for improving local seismic hazard assessment. The applied methods and obtained parameters provide quantitative basis for developing suitable models and forecasting tools, toward a better characterization of future seismic hazard in the region.

Keywords: earthquake sequences, unified scaling law for earthquakes, seismic dynamics, control parameter, Benioff strain release, seismic hazard assessment, earthquake forecast/prediction

OPEN ACCESS

Edited by:
Joanna Faure Walker, University College London, United Kingdom

Reviewed by:
Filippos Vallianatos, Technological Educational Institute of Crete, Greece
R/ B. S. Yadav, Kurukshetra University, India

***Correspondence:**
Anastasia Nekrasova
nastia@mitp.ru

Specialty section:
This article was submitted to Geohazards and Georisks, a section of the journal Frontiers in Earth Science

Received: *02 August 2020*
Accepted: *17 November 2020*
Published: *08 January 2021*

Citation:
Nekrasova A and Peresan A (2021) Unified Scaling Law for Earthquakes: Space-Time Dependent Assessment in Friuli-Venezia Giulia Region. Front. Earth Sci. 8:590724. doi: 10.3389/feart.2020.590724

INTRODUCTION

Capturing the main features of seismicity in a region is not an easy task. While average properties of earthquakes occurrence over large areas can be defined in pretty robust way, when zooming to a smaller territory, the specific features from limited data sets may prevail, and space and time regularities may be lost. Due to heuristic limitations, the smaller is the region and data time span, the less representative (and verifiable) is the resulting seismicity "portrait," with obvious consequences on earthquake hazard assessments and forecasting. Therefore in this study we aim to analyze, within the Friuli Venezia Giulia region (Northeastern Italy) and surrounding areas, a set of quantitative measures of seismic activity, which have been investigated also in other regions worldwide, so as to verify their possible similarity/generality and identify their peculiar features.

The study region is located at the Alps-Dinarides transition, along the compressional belt that marks the northern edge of Adria micro-plate; earthquakes in the region are shallow, mostly up to 10–15 km depth, and are prevalently of thrust type to the west and strike-slip to the east (Bressan et al., 2018 and references therein). Northeastern Italy is prone to large earthquakes occurrence (e.g., Gorshkov et al., 2009); the rather high seismic hazard in the region is testified by the several destructive events with occurred in the past, the most recent one being the M6.4 1976 Friuli earthquake (Slejko et al., 1999). However, the instrumental seismic activity recorded since then prevalently consists of low to moderate earthquakes, only sporadically exceeding magnitude 4.0, and with the largest recorded event having magnitude 5.6.

Several efforts have been already devoted to explore the different components of seismicity in the study region, namely the clustering properties (Peresan and Gentili, 2018, 2020; Varini et al., 2020) as well as the temporal variability of background seismicity component (Benali et al., 2020). Here we investigate changes in seismicity as a whole, without differentiating between clustered and background components. At the same time, the proposed analysis aims to account for the main geological and tectonic features of the territory under investigation, by assessing and cross-comparing the temporal variability of seismic dynamics within sub-regions sharing a common tectonic setting, based on seismic districts defined by Bressan et al. (2019).

In order to quantify the changes of observed seismicity in the time-space-energy domain, we make use of different parameters, including classical inter-event times and Benioff strain release (Benioff, 1951). To capture both variability and scaling properties of seismic energy release, we resort to the Unified Scaling Law for Earthquakes (USLE), which generalizes the Gutenberg-Richter (GR) relationship making use of the fractal distribution of earthquake sources in a seismic region (Kossobokov and Mazhkenov, 1988, 1989; Bak et al., 2002; Kossobokov, 2020). In particular, besides the space-time variability of seismicity rate (A), earthquake magnitude exponent (B), and fractal dimension of epicenter loci (C), we consider the time series of the USLE control parameter, η (Kossobokov and Nekrasova, 2017; Kossobokov and Nekrasova, 2019).

An estimation of USLE coefficients for seismic hazard assessment at different space scales, namely from the local scale of FVG region and up to the national scale of Italy, was already performed by Nekrasova et al. (2011). This study, instead, focuses on the temporal variations of USLE parameters, rather than on their average time-independent estimates, with the aim to get new insights in the evolving dynamics of seismicity in different areas of FVG. Based on time-dependent estimates of USLE parameters, as well as on classical inter-event times and Benioff strain release, the time intervals of rather uniform seismic activity are identified for each of the investigated sub-regions; the features of seismicity, for different sub-regions and time windows, are then compared and their statistical significance is assessed by the Kolmogorov-Smirnov test. We anticipate that our analysis highlights significant differences and a number of changes in seismic regimes within the three outlined areas. Specifically, the long-term trend of seismic energy release is found to be different prior and after the occurrence of the largest main shocks within the related sub-region, evidencing non-stationary features of seismic activity that should be factored in seismic hazard assessment. Moreover the USLE coefficients in FVG sub-regions are found to be time-dependent and correlated, displaying interesting patterns in the dynamics of seismicity, which could be related with major earthquakes, as illustrated in some detail in **Supplementary Material**. Thus, the identified regions and time intervals, with homogeneous features of seismic activity, may provide valuable information for time-dependent seismic hazard assessment and may guide areas selection for earthquake forecasting.

METHODS

The seismic dynamics of the territory under investigation is characterized in terms of several moving averages, including 1) the inter-event time, τ, dual to seismic rate; 2) the Benioff strain release, Σ (Benioff, 1951) (i.e., the sum of square root of energy, thus, proportional to $10^{0.75M}$) 3) the Unified Scaling Law for Earthquake (USLE) control parameter, η and 4) the USLE parameters values estimated for the moving sexennial time intervals.

In agreement with earlier studies (e.g., Bak et al., 2002; Christensen et al., 2002) on the waiting times T between earthquakes with magnitude greater than M, occurring within a range L, the USLE generalizes the Gutenberg–Richter law (Gutenberg and Richter, 1944), and it provides the rate of occurrence $N(M,L)$ defined as:

$$\log_{10} N(M, L) = A + B(3.5 - M) + C \times \log_{10} L, \qquad (1)$$

where $N(M,L)$ is the expected annual number of earthquakes of magnitude M within an earthquake prone area of diameter L; A, B, and C are constants. A and B characterize the annual rate of magnitude 3.5 events and the magnitude exponent respectively, which are analogous to the a- and b-values in the Gutenberg–Richter relationship (GR), while C estimates the fractal dimension df of the epicenters' loci at the site (Nekrasova and Kossobokov, 2005).

The accumulated data on hypocenters provides enough evidence for assuming that locally seismic locus generating earthquakes might have a self-similar structure of fractures of different size (e.g., Kossobokov and Mazhkenov, 1988; Bak et al., 2002). The multiscale analysis involved in evaluation of the USLE coefficients at a given site, where the count of events is performed in a set of cascading squares (i.e., a "telescope"), combines recurrences for earthquakes obtained from enveloping areas of different size, so as to get enough statistics on larger magnitude shocks from larger territories around, for a reliable confident estimation of scaling.

The results of global and regional studies (Kossobokov and Mazhkenov, 1989; Bak et al., 2002; Nekrasova and Kossobokov, 2002; Nekrosova and Kossobokov, 2003; Nekrosova and Kossobokov, 2005; Nekrasova et al., 2011; Parvez et al., 2014; Nekrasova et al., 2016; Nekrasova et al., 2015) confirm the validity of the USLE at different scales of analysis. The definition of the scales based on the preliminary analysis of the quality of data, the research goal, length dimensions of the regions under investigation and the objects of the investigation in the regions.

We can characterize the seismic rate in terms of USLE used the control parameter η:

$$\eta = \tau \times 10^{B\times(3.5-M)} \times L^{C}, \quad (2)$$

where τ is the time between two successive earthquakes, M is the magnitude of the second one, L is the distance between them, B and C the Global USLE values. Bak et al. (2002) provide a physical viewpoint on USLE: "To understand the Unified Law for Earthquakes, it is essential to see what the value of x represents. The quantity $L^{df} \cdot S^{-b}$ in the scaling function represents the average number of earthquakes per unit time, with seismic moment greater than S occurring in the area size $L \times L$. Therefore, x is a measure of the number of earthquakes happening within a time interval T. The Unified Law states that the distribution of waiting times between earthquakes depends only on this value." Here x is equivalent to the control parameter η, and the USLE states that the distribution of inter-event times depends only on the value of the variable η.

The Scaling coefficient estimation (SCE) algorithm (Nekrasova et al., 2015) is used to obtain the values of USLE coefficients. For a fine scale analysis, timely fit to the latest and best data registration period, from 1995 up to now, the OGS catalog permits calculation of the USLE parameters making use of the five bisecting steps of the spatial hierarchy, from the linear size $L_0 = 1/2^{\circ}$ down to $L_4 = 1/32^{\circ}$. In addition, we also consider the global values of USLE (ABC_{GV}) parameters estimated by Nekrasova and Kossobokov (2019) to characterize the seismicity rate over the long time interval.

DATA

Earthquake data used in this study are published as monthly OGS bulletins (OGS, 2019), which are available via the following website http://www.crs.inogs.it/bollettino/RSFVG/. A general overview of data made available by the Friuli-Venezia Giulia (FVG) seismometric network, including the network characteristics, main changes related to network geometry and space-time completeness of the OGS catalog, is provided by Peruzza et al. (2015). A detailed analysis of data completeness in space and time is carried out in Peresan and Gentili (2018); based on their data analysis, we have selected the space-time and magnitude interval where data uniformly complete. Specifically, in our study, we used all earthquakes with duration magnitude $M_d \geq 2.0$, recorded during the time interval 1995/1/1–2019/3/21, and located within one of the three FVG sub-regions – Area 1 (A1), Area 2 (A2) and Area 3 (A3), outlined accounting for the tectonic setting of the study region, as shown in **Figure 1**.

The A1, A2 and A3 sub-regions are formed as combinations of 10 out of 11 FVG seismic districts as defined in Bressan et al. (2018; 2019). The map of the 11 seismic districts of the Friuli Venezia Giulia Region is provided as **Supplementary Material S1**. Specifically: area A1 is the combination of ALP, CL, AMP and FOA districts; area A2 is the combination of MN, TOC and GE districts and area A3 is the combination of TAR, BOV and BA districts. The PL district is not considered in our analysis, due to its very low level of seismic activity (less than one event per year with magnitude above 2.0). The coordinates of the three sub-regions are provided in **Supplementary Table S1**.

OGS catalog reports 6640 earthquakes with duration magnitude $M_d \geq 2.0$ in the time span from 1995/1/1 to 2019/03/21. The epicenters of 3,011 seismic events fall within the selected sub-regions and 3,629 out of them (**Figure 1B**). **Table 1** lists the OGS catalog earthquake statistics information for the three selected FVG sub-regions and the b-value of the sub-regions earthquakes sets. The time series of earthquakes magnitude, latitude and longitude vs. time, within each of the three Friuli-Venezia Giulia sub-regions, are provided in **Supplementary Figure S2.1**, along with the Gutenberg-Richter plots of the cumulative number of earthquakes in the different sub-regions (**Supplementary Figures S2.2 and S2.3**), which allow to verify the magnitude completeness of the data (e.g., according to Mignan and Woessner, 2012).

The spatial data distribution of events from OGS catalog and the borders of the three selected sub-regions are mapped in **Figure 1B**, while **Figure 1C** shows the empirical density distribution ρ of the OGS catalog data obtained from the regular geographic grid cells with size $1/16^{\circ} \times 1/16^{\circ}$. The temporal variability of seismicity rate parameters is compared with the occurrence of the largest earthquakes reported in the considered catalog. Although the FVG region and its surroundings experienced several destructive earthquakes in the past, including the 1976 Friuli earthquake; however, recent seismicity is characterized only by low to moderate magnitude events. The principal earthquakes occurred since 1977 are the 1998 April 12 (M_d 5.6) earthquake and the 2004 July 12 (M_d 5.1). **Table 2** lists the information about these principal earthquakes. These events are marked as red stars in **Figure 1B**.

RESULTS

We investigate the changes in seismic regime during the time period from 1995 to 2019 for the three sub-regions (A1, A2 and A3) of the FVG territory (**Figure 1A**). To quantify the temporal

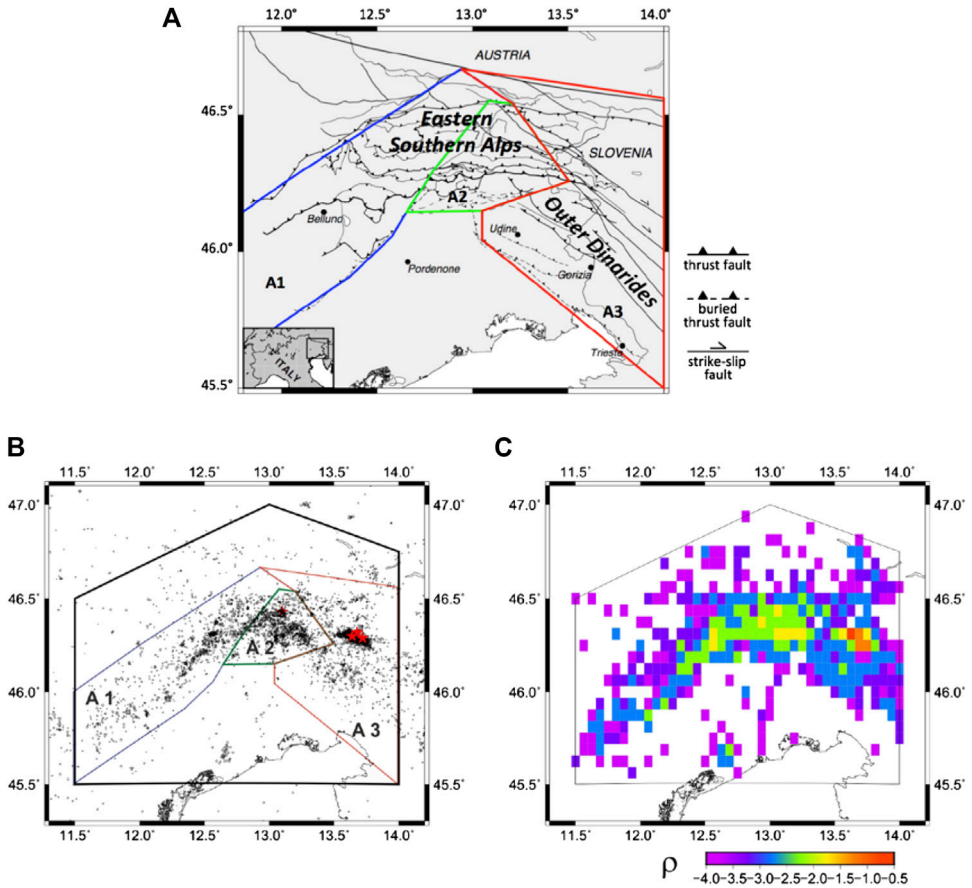

FIGURE 1 | The spatial data distribution based on OGS catalog, 1/1/1995–21/03/2019 **(A)** Map of tectonic lineaments after Bressan et al. (2018) and A1, A2 and A3 sub-regions borders (blue, green and red polygons); **(B)** $M_d \geq 2.0$ earthquakes, the area of uniform completeness (black polygon) and the epicenters of the two largest ($M_d \geq 5.0$) earthquakes from the considered catalog (red stars); **(C)** the empirical density distribution function of seismic activity, cells size 1/16° × 1/16°.

TABLE 1 | The three selected Friuli-Venezia Giulia sub-regions data.

Sub-region	OGS catalog estimates 1995/1/1–2019/3/21				Global values (Nekrasova and Kossobokov, 2019)				
	N_{eq}, $M \geq 2.0$	%, N_{eq}	b-value	Fine scale cells, N_{cells}	Lat	Lon	A	B	C
A1	815	27.07	1.06	58	45.5	11.5	-0.69	1.06	1.22
A2	732	24.31	1.19	40	46.5	13.5	-0.68	0.97	1.21
A3	1,464	48.62	1.17	52	46.5	13.5	-0.68	0.97	1.21

TABLE 2 | The two largest earthquakes in Friuli-Venezia Giulia region from 1995 to 2019.

Origin time	Latitude	Longitude	Depth	M_d	Place
1998/04/12 10:55:32.90	46.324	13.678	15.2	5.6	Kobarid (Slovenia)
2004/07/12 13:04:06.34	46.301	13.635	9.1	5.1	Kobarid (Slovenia)

variation of seismicity within each sub-region, we consider the following parameters as a function of time: the inter-event times τ, the cumulative strain release Σ, the coefficients *A, B, C* of the USLE and USLE control parameter η. The empirical cumulative distribution functions of inter-event time τ and Benioff strain release Σ for the entire FVG Region and its three sub-regions are presented in **Figure 2**. Each distribution can be characterized by the γ-values of the best fit trend. Specifically, the γ-values of the natural exponential trend fit for τ $p(>t) = \alpha\exp(-\gamma\tau)$ are estimated as 0.48 ($R^2 = 0.96$), 0.064 ($R^2 = 0.98$), 0.048 ($R^2 = 0.88$), and 0.065 ($R^2 = 0.83$) in FVG, A1, A2, and A3, respectively. Actually, the best trend fit of τ in A3 sub-region appears to be logarithmic: $p(>t) = -0.091\ln(\tau) + 0.41$ ($R^2 = 0.98$). The γ-values for the best power law trend fit for Σ, $p(>\Sigma) = \alpha\Sigma^{-\gamma}$, are estimated as 1.23, 1.598, 1.407, 1.586 in FVG, A1, A2, and A3, respectively ($R^2 = 0.98$ for all the four cases). LogΣ is a linear function of magnitude M, therefore the distribution of Benioff strain release (**Figure 2B**) differs from Gutenberg-Richter relation in the abscissa scale only. As is evident from Σ definition, which is proportional to $10^{0.75M}$, the γ-values for Σ are well in agreement with the Gutenberg-Richter the b-values (**Table 1**).

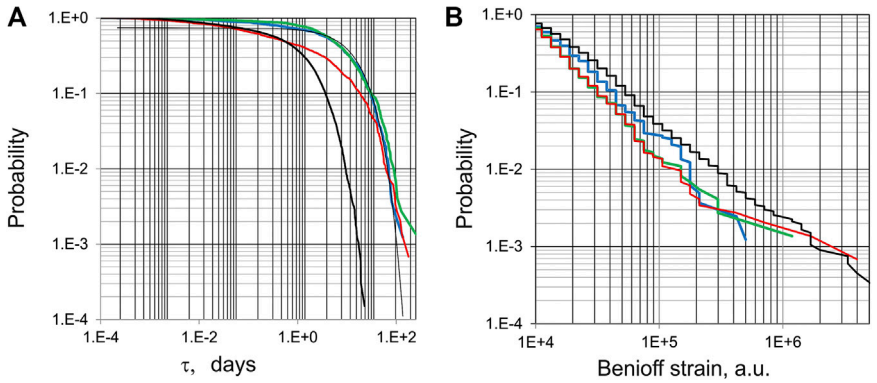

FIGURE 2 | Empirical cumulative distribution functions of **(A)** inter-event time (τ, in days), **(B)** Benioff strain release (Σ, in arbitrary units, a. u.), for $M_d \geq 2.0$ events, over the entire FVG territory (1995–2019) and the three sub-regions. Notes: FVG – black line, A1 sub-region – blue line, A2 sub-region – green line; A3 sub-region – red line.

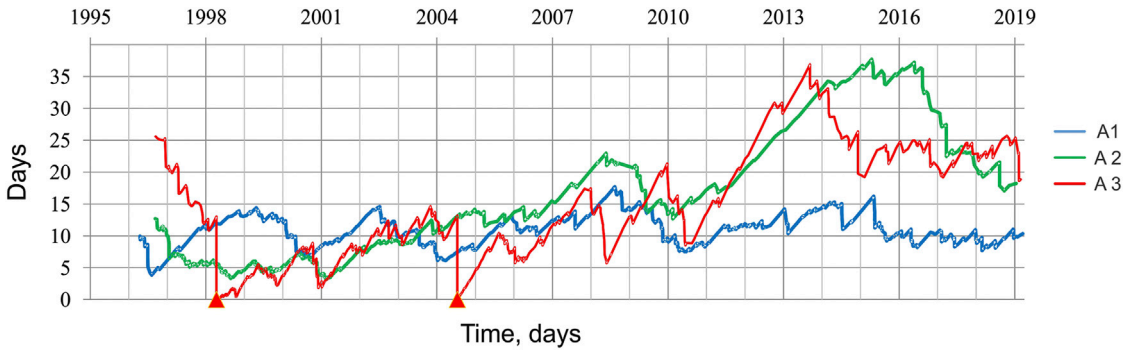

FIGURE 3 | Inter-event time (τ, in days) vs. earthquake origin time, for the three sub-regions of FVG territory (1995–2019). A1 – blue line, moving average for 50 earthquakes; A2 – green line, moving average for 50 events; A3 – red line, moving average for 25 earthquakes. The origin time of the two principal earthquakes (**Table 2**) are marked with red triangles on the origin time scale.

TABLE 3 | The moving average interevent time ⟨τ⟩ trend lines stable intervals for the three FVG sub-regions (1995–2019).

Sub-region	Start time	End time	Duration, years	⟨τ⟩ per year	R^2
A1			No trends		
A2	1998/06/08 12:51	2017/03/24 17:47	18.81	1.64	0.91
	2017/03/24 17:47	2019/01/15 00:00	1.81	-3.50	0.72
A3	1998/08/25 18:58	2004/07/12 13:31	5.88	1.97	0.80
	2004/07/12 20:44	2014/12/07 09:48	10.41	2.81	0.86

The sample size of the four regions considered may allow further comparison of the γ-values with "q-exponential" or "q-logarithmic" functions of Non-Extensive Statistical Physics (Tsallis, 1988), as is done by (Chochlaki et al., 2018) for most of the 50 regions of the Globe. However, at this time the high R-squared values of the trend fits presented here make us to believe that in case of FVG Region and its sub-regions the Boltzmann–Gibbs theory of additivity might apply, an aspect to be further investigated in the future.

Inter-Event Time τ Temporal Variability

Figure 3 shows the moving averages of inter-event time ⟨τ⟩ vs. the original event time for A1 (blue line), for A2 (green line) and for A3 (red line) sub-regions. The red trend-line for seismic events in A3 displays two dropping connected with aftershocks of M_d = 5.6 1998 and M_d = 5.1 2004 Kobarid (Slovenia) events.

Table 3 lists the linear fit intervals of ⟨τ⟩ values shown in **Figure 3**, for each of the three FVG sub-regions; the inspection of linear fit intervals, in fact, may reveal clustered irregularity of the

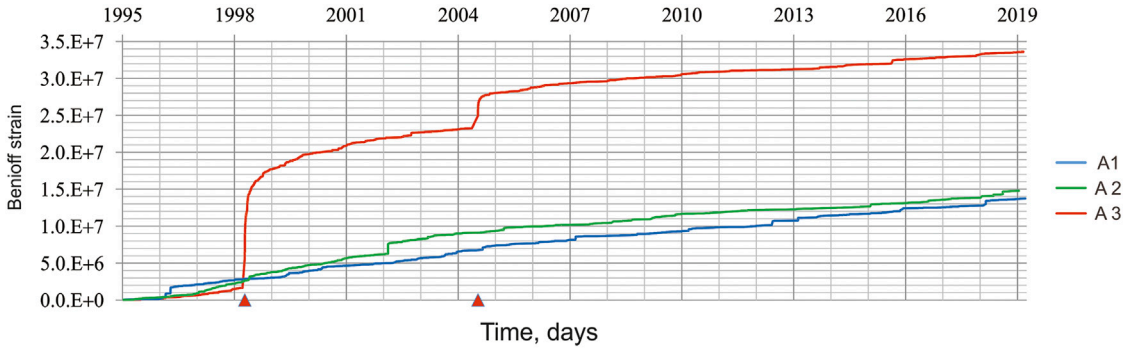

FIGURE 4 | The cumulative Benioff strain release Σ vs. earthquake origin time for three FVG sub-regions (1995–2019). The color code is the same as in **Figure 3**: area A1 – blue line, A2 – green line, A3 – red line. The origin time of the two principal earthquakes (**Table 2**) are marked with red triangles on the origin time scale.

TABLE 4 | The cumulative Benioff strain release Σ(t) function linear fit intervals for three FVG sub-regions.

Sub-region	Start time	End time	Duration, years	Benioff strain per day	R^2
A1	1997/03/05 23:59	2019/03/19 13:38	22.05	2.03 E+03	1.00
A2	1997/03/08 03:27	2001/08/18 21:09	4.45	3.14 E+03	0.98
	2003/05/01 22:28	2019/01/15 18:31	15.72	9.02 E+02	0.98
A3	1999/11/01 17:56	2004/04/04 18:48	4.43	2.28 E+03	0.97
	2006/04/01 19:08	2019/02/28 19:32	12.92	9.06 E+02	0.99

seismic dynamics in the study area. The time intervals for linear fit are determined in a iterative way, namely changing the beginning/ending times until the best fit is obtained (by least squares); the start/end times listed in **Table 3** correspond to the occurrence of the specific seismic events that bound the time interval with the best linear fit. Specifically, no evident linear trends can be identified for ⟨τ⟩ time variations in A1 sub-region. On the other side, within the A2 sub-region, ⟨τ⟩ time variations display different trends: a decreasing linear trend from June 08, 1998 to March 24, 2017, with the rate of decay of the seismic rate about −1.64 per year and the coefficient of determination R^2 = 0.91; a rising linear trend of seismic rate from March 24, 2017 to January 15, 2019 (i.e. up to the end OGS catalog), with the rate of 3.5 per year (R^2 = 0.72). Similarly, within the A3 sub-region the ⟨τ⟩ time function displays two seismic rate decays: one form August 25, 1998 to July 12, 2004, and another from July 12, 2004 to December 07, 2014, with rates -1.97 per year (R^2 = 0.80) and -2.81 per year (R^2 = 0.86) respectively; in A3 there is no evident trend of ⟨τ⟩ since 2015.

Benioff Strain Release Σ Time Changes

Figure 4 shows the cumulative Benioff strain release vs. earthquake origin time, Σ(*t*), for the three FVG sub-regions. As in **Figure 3** the origin time of the principal earthquakes is marked by red triangles. We may observe that, while the curve associated with A1 (blue) and A2 (green) sub-regions increase steadily, the red curve associated to the A3 sub-region displays evident jumps corresponding to both principal shocks, mostly reflecting the increased seismicity during aftershocks sequences.

Table 4 lists the linear fit intervals of Σ(*t*) function for the three FVG sub-regions, shown in **Figure 4**. The time intervals listed in **Table 4** are determined following the same procedure applied for ⟨τ⟩; the start/end times correspond to the first/last earthquakes that bound the intervals providing the best linear fit for Σ(*t*). Specifically, the sub-region A1 could be characterized by a uniform trend during the interval from 1997/03/05 to 2019/03/19 (i.e., up to the last event reported in sub-region), with Σ-value rate change (expressed in dimensionless arbitrary units, a. u.) of 2.027×10^3 a. u. *per day* (R^2 = 0.997). The A2 sub-region could be characterized by two intervals with uniform trend, from 1997/03/08 to 2001/08/18 and from 2003/05/01 to 2019/01/15 (last event in sub-region), which are characterized by Σ–value rate changes equal to 3.144×10^3 a. u. *per day* and R^2 = 0.984, and 0.902×10^3 a. u. *per day* and R^2 = 0.983 respectively. Similarly, for the A3 sub-region two intervals could be identified, from 1999/11/01 to 2004/04/04 and from 2006/04/01 to 2019/02/28 (i.e., up to the last event reported within the sub-region), with Σ–value rate changes equal to 2.204×10^3 a. u. *per day* and R^2 = 0.967 and 0.905×10^3 a. u. *per day* and R^2 = 0.992 respectively.

One can see that a stable rate of Σ–value over the observed time interval is obtained when no large event occurs (A1 sub-region), while in case of a relatively large event, the rate before and after it displays essential differences. Specifically, the M4.9 Sernio earthquake (2002/02/14; Lat: 46.426°N Lon: 13.100°E) eventually marks the separation between the two linear seismic rate intervals for A2 sub-region; the ratio of the Σ(*t*) slope coefficients is 3.5 for A2 two intervals. In a similar way, the 2004 Kobarid event separates two linear seismic rate intervals for A3 sub-region;

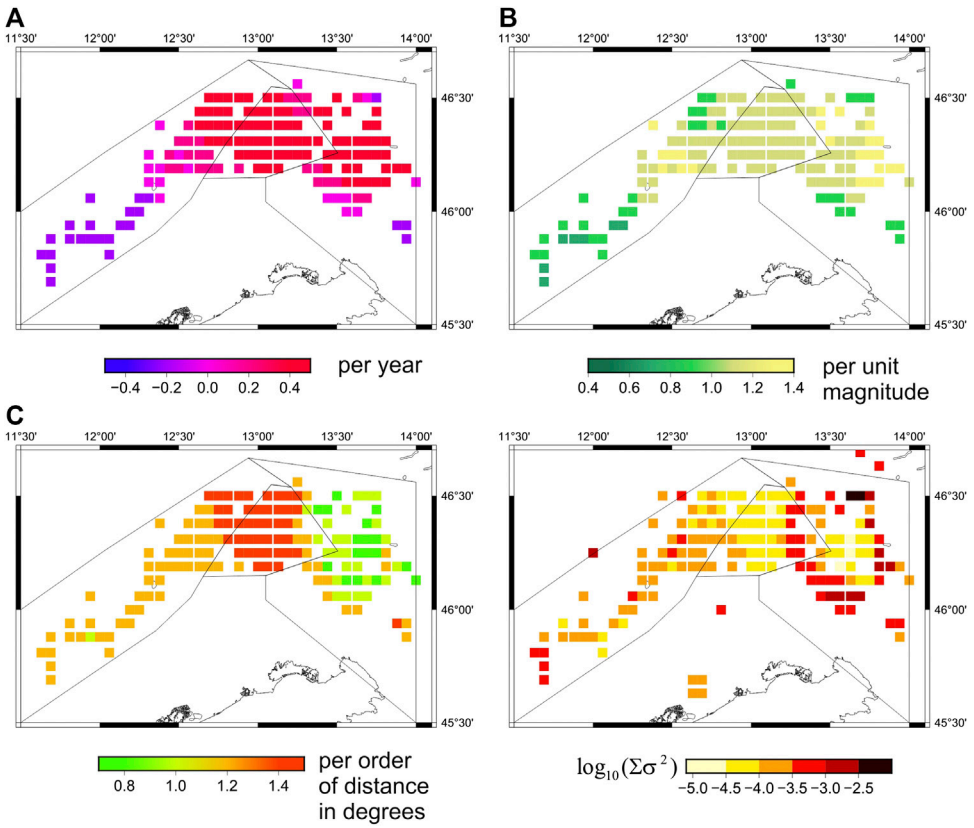

FIGURE 5 | The regional maps of A, B, and C coefficients (top panels) and spatial distribution of the sum of standard errors $\sum\sigma^2 = \sigma_A^2 + \sigma_B^2 + \sigma_C^2$. Color code symbols correspond to estimates associated with cells of size 1/16° × 1/16°.

the ratio of the $\Sigma(t)$ slope coefficients is 2.5 for A3 two time intervals.

Given that $\Sigma(t)$ function within sub-region A1 is characterized by a uniform trend during the whole investigated time span, we compare its slope coefficient with those of the other two regions, A2 and A3, for the different time intervals. Specifically, the ratios of A1 slope coefficient vs. slope A2 and A3 in advance of large events are 1.6 and 1.1, respectively, while after the large events they are both equal to 0.45 (i.e. the slope in A2 and A3 is 2.2 times lower than the slope in A1). Thus, after the large events, the increase of seismic rates in A2 and A3 sub-regions slows down, compared to the steady seismic rate in A1 sub-region.

In this analysis, the slope of $\Sigma(t)$ linear fits essentially characterize the long-term steady trend of seismicity within each area, excluding pre-shock and aftershock related changes. Following Vallianatos and Chatzopoulos (2018), the generalized Benioff strain evolution (which here corresponds to the well-known cumulative Benioff strain, with exponent = 1/2), during the initial part of a main shock preparation process is linear; then, as the time of the earthquake approaches, it deviates from linearity due to the beginning of an accelerating deformation stage. Our analysis shows that the slope of the linear part of cumulative Benioff strain release in areas A2 and A3 changes significantly after the occurrence of the largest earthquakes. According to a non-extensive statistical physics view (Vallianatos and Chatzopoulos, 2018), this observation suggests that the common exponent m associated with the steady (normal) time variation of the generalized Benioff strain within an area, may change after large events.

Unified Scaling Law for Earthquakes Coefficients Space-Time Variability

The available OGS catalog data allowed us to obtain 150 reliable estimates of the medium-term (24.2 years) USLE parameters. Specifically, we considered the hierarchy of square boxes, with linear size equal to 1/2°, 1/4°, 1/8°, 1/16° and 1/32°, respectively, centered at the nodes of a regular grid with 1/16° spacing, which include at least eight earthquakes from the OGS catalog in their 1/16° × 1/16° vicinity. The obtained A, B, and C coefficients are mapped in **Figure 5**, along with the squared sum of their standard errors σ_A, σ_B, and σ_C. The error of determination of the USLE coefficients does not exceed 0.05, which confirms a rather high quality of the mapped values for the FVG territory. Specifically, there are 58 cells located within sub-region A1, 40 cells within sub-region A2, and 52 cells within A3, while 10 cells are out of three selected sub-regions (**Table 1**).

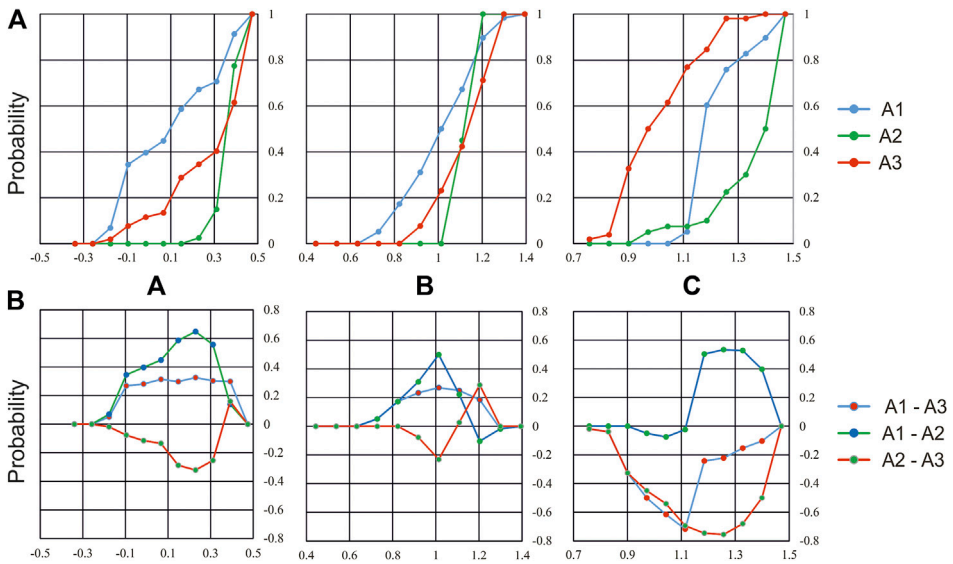

FIGURE 6 | Distribution of the USLE coefficients A, B and C, estimated for the fine scale grid in the three sub-regions A1, A2, A3: **(A)** the cumulative empirical probability functions F_i; **(B)** the pairwise differences F_m (*coef*) and F_n (*coef*), *coef* = A, B, C.

TABLE 5 | The Kolmogorov-Smirnov two-sample statistic λ_{K-S} applied to F(coef), the Sample size are in **Table 1**.

	F(A)	A2	A3	F(B)	A2	A3	F(C)	A2	A3
D	A1	0.647	0.326	A1	0.500	0.269	A1	0.534	0.718
	A2	—	0.321	A2	—	0.288	A2	—	0.756
λ_{K-S}	A1	3.150 (100)	**1.708 (99.42)**	A1	2.433 (99.99)	1.410 (96.25)	A1	2.596 (99.99)	3.757 (100)
	A2	—	1.527 (98.11)	A2	—	1.372 (95.37)	A2	—	3.594 (100)

Note: Probability values for Kolmogorov-Smirnov test are given in brackets. Values associated with probabilities larger than 99% are marked in bold, those with probabilities more than 99.9% are marked in red.

The seismic activity distribution (coefficient A), normalized to recurrence of a magnitude 3.5 earthquake, in a unit area of $1^\circ \times 1^\circ$ and in a unit time of one year, varies mainly in the interval [−0.25; 0.45] for A1 sub-region, [0.22; 0.42] for A2 sub-region, and [−0.10; 0.45] for A3 sub-region, with median values 0.10, 0.36 and 0.33 for A1, A2 and A3, respectively. The B values, which characterize the slope of the frequency–magnitude graph, for A1 sub-region vary from 0.8 to 1.2, without any dominant value. For A2 sub-region B-values are well focused: they are equal to 1.1 in 45% cases, and to 1.2 in 55% cases. Within A3 sub-region B-values spread from 0.9 to 1.3.

The fractal dimension of spatial distribution of epicentres C in A1 sub-region has a sharp peak (55% of cells) around the value C = 1.19; within A2 sub-region C varies from 0.90 to 1.47 (50% of cells), with the median value 1.40; in the A3 sub-region C displays a large variability, from below 0.9 to above 1.25.

Figure 6A compares the empirical cumulative distributions functions $F_i(coef)$ of A, B and C coefficients, estimated over the fine scale grid for the three FVG sub-regions. **Figure 6B** shows the plots of the pairwise difference curves $F_m(coef) - F_n(coef)$ for each USLE coefficient, and allows better understanding the differences in seismic activity in the three sub-regions. For instance, we may observe the remarkable differences between the distributions of C parameter obtained for A1, A2 and A3 sub-regions. Specifically the C-value distributions for A1 corresponds to a (fault) zone with a common dominant Alpine trend, while in A3 it corresponds to linear set of clusters, aligned with a Dinaric trend; finally it characterizes A2 as a highly complex, fractured (fault) zone, located at the Junction of the Alpine and Dinaric (fault) systems.

The maximum absolute difference between the empirical distributions is commonly used in the Kolmogorov–Smirnov two-sample criterion to distinguish whether or not the values from the two samples are drawn from the same statistical distribution of independent variables. Here the two sample Kolmogorov–Smirnov statistic (Smirnov, 1948) λ_{K-S} is applied to pairwise sets of USLE coefficients distributions, as estimated for each of the different FVG sub-regions. λ_{K-S} is defined as: $\lambda_{K-S}(D, n, m) = [n \times m/(n + m)]^{1/2} \times D$, where $D = \max |F_m(coef) - F_n(coef)|$ is the maximum value of the absolute difference between the empirical distributions $F_m(coef)$ and $F_n(coef)$, *coef* = A, B, C, whose sample sizes are *n* and *m* respectively. **Table 5** summarizes the results of comparison for each pairwise set of coefficients, in terms of D and λ_{K-S}. It is possible to observe that, with 95%

probability, the three sub-regions are different in terms of USLE coefficients. The λ_{K-S} statistic for F(A) allows us to conclude that the distributions of coefficient A for A1 and A2 sub-regions, as well as those for A1 and A3 sub-regions, are significantly different, with probability larger than 99.9%, The A coefficient distributions for A2 vs. A3 can also be marked as different, with probability larger than 95%. The pairwise comparison with λ_{K-S} statistic for F(B) distributions provides similar results. Specifically the F(B) distributions difference for A1 vs. A2, A1 vs. A3 and A2 vs. A3 confirm that they are all significantly different, with more than 99.9% probability for A1 vs. A2, and 95% probability for the others. For the C-coefficient distributions, the two samples statistics for three pairwise differences allows us rejecting the assumption that coefficients follow the same statistical distribution with more than 99.999% probability.

Besides the medium-term average estimates described so far, the time-variable estimates of USLE coefficients have been performed for the fine grid, considering moving six-years time intervals with one year shift. As a results 19 sets (with ending time from 2001 to 2019 years) of A, B and C coefficients values have been obtained for each of the A1, A2 and A3 sub-regions. It is worth noting that, for each six-years times interval (namely 1995/01/01–2001/01/01, . . . , 2014/01/01–2019/01/01), the number of cells with reliable data for SCE algorithm calculation may be different, which may influence the reliability of coefficients estimation.

The analysis of the pairwise 2D correlation plots of the A-values, B-values and C-values, computed for each six-years time interval (see **Supplementary Material S3**), allows us to observe that the coefficients and their correlation change significantly over time, in all of the three considered sub-regions (**Supplementary Figures S3.1–S3.3**). To facilitate the analysis of such variations, three time periods have been considered: 1) four time windows (six-years long, with ending time from 2001 to 2004), where USLE parameters are apparently affected by 1998/04/12 M = 5.6 Kobarid earthquake and related aftershocks; 2) six time windows (six-years long, with ending time from 2005 to 2010), with USLE parameters apparently affected by the 2004/07/12 M = 5.1 Kobarid earthquake aftershocks; 3) nine time windows (six-years long, with ending time from 2011 to 2019) without any principal (M ≥ 5.0) earthquake, and thus providing presumably independent (background) USLE parameters values. The A-values display relatively stable values in all three FVG sub-regions, except for the high variability of A-values within A3 sub-region starting from 2011. During the period from 2011 to 2019 the B-values decrease progressively in each of the three FVG sub-regions (**Supplementary Figures S3.1c,S3.3c**), while the A-value slightly increases in sub-region A1. Accordingly, the number of low magnitude earthquakes decreases during the 2011–2019 all over the FVG territory, in A3 sub-region especially. C-values in the three sub-regions vary from one to less than 1.4 and, from 2000 to 2010 years, take relatively low values in A2 and A3 sub-regions due to the aftershocks effect; in addition, an interesting decreasing trend of C-values, down to 0.8, characterizes the A1 region from 2013 to 2019 years.

Finally, to investigate in more detail the space-time variations of USLE coefficients, the medians of A-values, B-values and C-values have been computed, for six-years time intervals with shift of one year, within each of nine out of 10 seismic districts of Friuli-Venezia Giulia Region (**Supplementary Figure S1**), as defined by Bressan et al. (2018; 2019). The PL and FOA districts are not considered, because they do not include enough events for reliable estimation of USLE parameters. The values of the medians obtained for each of the nine seismic districts (**Supplementary Figure S3.4**) support the grouping into the three sub-regions used in this study: the districts that compose A3 sub-region (TAR, BA, BOV) display temporal trends of the A-B- and C-values much different that the other districts.

Control Parameter η Temporal Variability

The main parameter, which allows characterizing the seismic rate in terms of USLE, is the control parameter η defined in **Eq. 2**. In order to compute the η-values, necessary to investigate the temporal variability of this parameter within A1, A2 and A3 sub-regions, we used the global values of USLE coefficients listed in **Table 1**. Accordingly, the A, B and C coefficients used in **Eq. 2** correspond to long-term robust estimates of USLE, which account for the moderate-large M > 4.0 earthquakes that are reported in USGS Global Hypocenter Data base system, 1964–2001, (Nekrasova and Kossobokov, 2019). Note that for the purpose of this analysis we have extended the time window, including an additional time interval from 1988 to 1994, so as to be able and analyze seismicity changes before the principal 1998 Kobarid earthquake; according to Peruzza et al. (2015) this time interval is characterized by uniform OGS network conditions, and thus can be used for our analysis.

Figure 7 shows the plots of the 50-events moving average of $\langle\eta\rangle$ vs. origin time, for the earthquakes located within the A1, A2 and A3 sub-regions, which occurred during the time interval from January 1988 to April 2019. It is possible to observe some nearly-flat portions of the graphs, where the moving averages vary within one decimal order; these periods of stability are characterized by a low rate of seismicity. To quantify this feature, let us define the periods of stability by the condition that {t: $\langle\eta\rangle$(t) is larger than $\langle\eta\rangle_{max}/10$}, where $\langle\eta\rangle_{max}$ is the maximal value of $\langle\eta\rangle$ over the entire considered time interval. **Table 6** lists the periods of $\langle\eta\rangle$ stability identified for the three FVG sub-regions. For the A3 sub-region we identified three periods of stability of $\langle\eta\rangle$ interrupted by bursts of activity, associated with the origin times of principal earthquakes and their aftershocks. Namely, before the Kobarid April 12, 1998 event, a 5.8 years time interval with very low seismic rate $\langle\eta\rangle$ = 10.02 ± 0.39 is detected from 1992/07/13 to 1998/04/12; between the two principal events, precisely from 2001/10/26 to 2004/07/13, a 2.8 years interval with much larger seismic rate $\langle\eta\rangle$ = 3.59 ± 0.11 has been identified; during the last 13.4 years interval, from 2005/10/02 to the end of the OGS catalog, an intermediate level

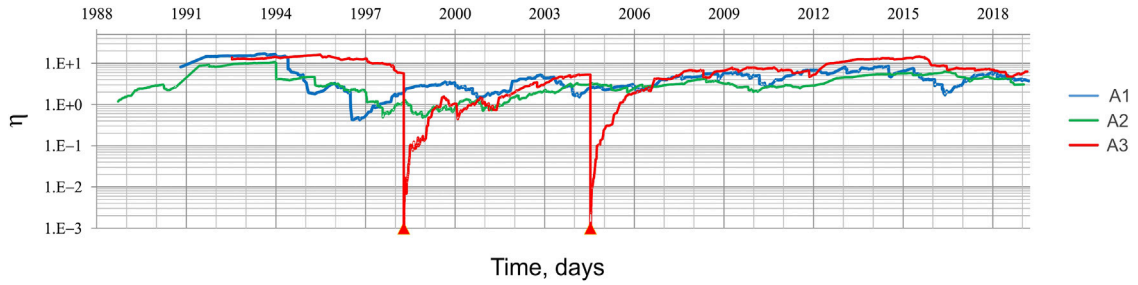

FIGURE 7 | USLE control parameter η (1988–2019) moving average per 50 events in three FVG sub-regions vs. earthquake origin time (A1 – blue line, A2-green line, A3 – red line). Note: the origin times of the two principal earthquakes (**Table 2**) are marked with red triangles on the origin time scale.

TABLE 6 | Periods of stability of the USLE control parameter ⟨η⟩ for three Friuli-Venezia Giulia sub-regions.

Sub-region	Start time	End time	Duration, years	⟨η⟩± err (⟨η⟩)
A1	1990/09/03 07:06	1996/06/29 11:52	5.8	7.87 ± 0.49
	1998/02/07 14:42	2000/09/19 06:46	2.6	2.71 ± 0.05
	2001/03/18 23:17	2003/12/27 21:11	2.8	3.31 ± 0.11
	2004/03/24 08:35	2019/03/19 13:38	15.0	4.71 ± 0.08
A2	1988/09/18 12:44	2019/01/15 18:31	30.3	2.51 ± 0.05
A3	1992/07/13 09:34	1998/04/12 11:38	5.8	10.02 ± 0.39
	2001/10/26 12:14	2004/07/13 05:33	2.7	3.59 ± 0.11
	2005/10/02 03:51	2019/02/28 19:32	13.4	6.92 ± 0.20

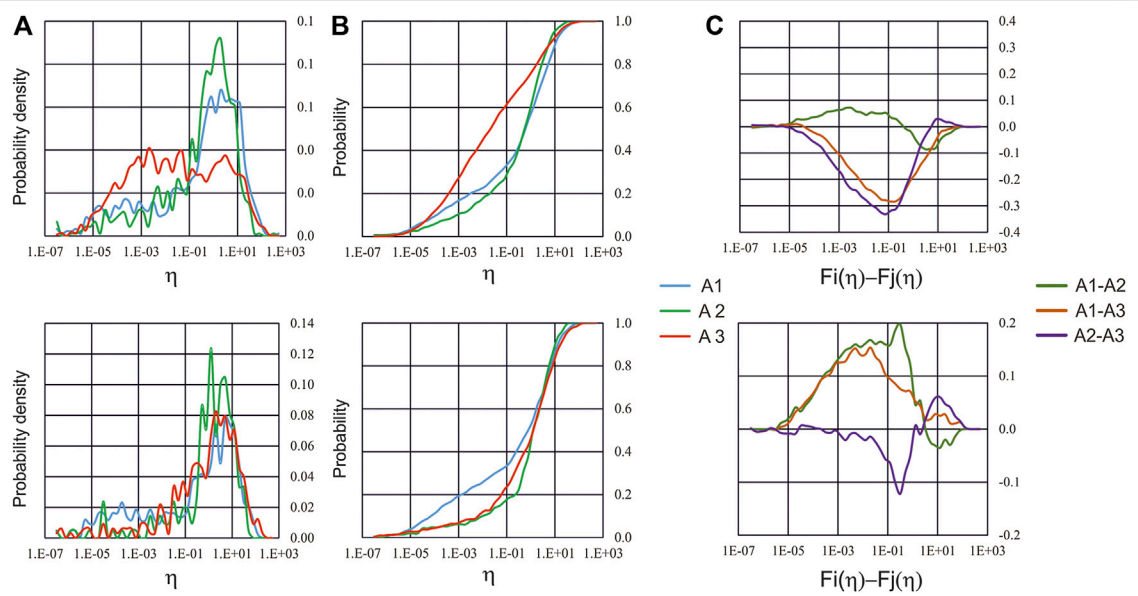

FIGURE 8 | Empirical density **(A)** and cumulative **(B)** distribution functions of USLE control parameter η and **(C)** pairwise difference $F_i(\eta) - F_j(\eta)$ for A1, A2 and A3 FVG sub-regions in 1988–2019 time interval (top panels) and in 2005/10/2–2019 time interval (bottom panels).

seismic rate, with ⟨η⟩ = 6.92 ± 0.20, is quantified. For A1 sub-region we determined four periods of ⟨η⟩ stability: a low seismic rate interval with ⟨η⟩ = 7.87 ± 0.49 in 1990/09/03–1996/06/29; two comparatively higher rate intervals in 1998/02/07–2000/09/19 and 2001/03/18–2003/12/27, with ⟨η⟩ equal 2.71 ± 0.05 and 3.31 ± 0.11 respectively; a 15 years interval of moderate seismic rate, with ⟨η⟩ value 4.71 ± 0.08, from 2004/03/24 to the end of catalog. Finally, according to η control parameter, a single ⟨η⟩ stable interval can be identified for A2 sub-region, from 1988/09/18 to 2019/01/15 (30.3 years), with ⟨η⟩ value 2.51 ± 0.05, which apparently characterizes the relatively high and constant seismic rate of this area.

TABLE 7 | The Kolmogorov-Smirnov two-sample statistic λ_{K-S} applied to distribution functions of USLE control parameter η.

	F(η)	1988–2019		2005/10/02–2019	
		A2	A3	A2	A3
D	A1	0.085	0.284	0.197	0.154
	A2	—	0.332	—	0.122
λ_{K-S}	A1	**1.841 (99.77)**	6.857 (100)	2.348 (99.99)	**2.100 (99.97)**
	A2	—	7.951 (100)	—	1.377 (95.49)

Note: Probability values for Kolmogorov-Smirnov test are given in brackets. Values associated with probabilities larger than 99% are marked in bold, those with probabilities more than 99.9% are marked in red.

The discrete and cumulative empirical distribution functions of η for each of three sub-regions are compared (left top panel, **Figure 8** and central top panel, **Figure 8**), confirming a broad spread over about six or more decimal orders of the bulk density distribution of η. According to the nonparametric two-sample Kolmogorov–Smirnov statistic λ_{K-S}, applied to the pairwise differences of η distribution functions η(A3), η(A2) and η(A3) for the three sub-regions, all of them have different probability distribution, with probability above 99% (**Tabure 7**). Finally, the comparison is restricted to the most recent time interval, from 2005/10/02 to the end of OGS catalog, when according to **Table 6**, stable intervals of ⟨η⟩ are obtained in all FVG sub-regions (**Figure 8**, bottom panels). The pairwise differences of η distribution functions for 2005–2019 time interval (**Figure 8**, right bottom panel) and the λ_{K-S} values for pairwise differences of η distributions (**Tab. 7**), confirm that even for the time period without principal earthquakes η(A3), η(A2) and η(A3) do not come from the same distribution, with probability above 99% in almost all cases (except for η(A2) vs. η(A3), for which probability is still above 95%).

DISCUSSION AND CONCLUSIONS

In order to get new insights in the evolving dynamics of seismicity, which controls its temporal variations within different areas of FVG territory, a multi-parametric analysis was performed. Different parameters, including inter-event times τ, Benioff strain release Σ, and the control parameter η of the USLE, were used to assess heterogeneity in spatial and temporal patterns of earthquakes occurrence, as reported in OGS catalog for Northeastern Italy and its surroundings.

As a preliminary step, the space variability of the USLE coefficients, namely the seismicity rate (A), the earthquake magnitude exponent (B), and the fractal dimension of epicenter loci (C), was examined in some detail, comparing the values obtained within three sub-regions defined grouping seismic districts with similar tectonic features (Bressan et al., 2019). Different tectonic domains, in fact, can be identified within the study region, which is located at the junction between the E-W oriented Alpine and the NW-SE oriented Dinaric fault systems (**Figure 1A**). According to Bressan et al. (2018), the superposition of different tectonic phases caused high fragmentation and heterogeneity of the upper crust in this area, which is characterized by sharp lateral heterogeneities of the elastic moduli in the upper crustal structure (down to 10 km depth). The analysis performed in this study confirms that the features of seismic energy release, including their temporal variations, are statistically different within the three outlined sub-regions A1, A2 and A3. The spatial distribution of USLE coefficients is shown in **Figure 5**, while their empirical probability functions are given in **Figure 6**. Specifically, the coefficient of magnitude balance B, which is analogous to the b-value of the Gutenberg-Richter law and quantifies the relative proportion between small and large earthquakes, is characterized by well focused B values within [1.1–1.2], in the central zone (area A2); this area hosted the M6.4 1976 Friuli earthquake, but since then instrumental seismicity has been characterized only by moderate size events. At the same time, the western zone (area A1), corresponding to the Carnie Pre-Alps, is characterized by higher variability, which indicates higher spatial heterogeneity in the seismic energy release, and by low-intermediate B values, within the range [0.8–1.2], and thus by a comparatively low ratio of small-moderate magnitude events. Instead, the Dinaric eastern zone (area A3) is associated with relatively higher B values, in the range [0.9–1.3], evidencing the occurrence of a comparatively large number small to moderate seismic events, mostly related with aftershocks occurrence. Significant differences have been observed between the distributions of the fractal dimension of earthquake epicenters C (**Figure 5**), obtained for A1, A2 and A3 sub-regions (**Figure 1A**). Specifically, within area A3, C appears characterized by quite low values, mostly up to 1.0, which can be related with a linear set of clusters, aligned with a Dinaric trend. This is possibly due to the occurrence, within area A3 of the two largest magnitude events reported in the considered data set (the 1998 and 2004 Kobarid earthquakes) that, along with their highly clustered aftershocks, dominate seismicity in the area. The western area (area A1) displays prevailing intermediate values, corresponding to a (fault) zone with a common dominant Alpine trend and associated with rather complex swarm-like earthquake sequences (Peresan and Gentili, 2018). Finally, the central zone (area A2) is characterized by higher fractal values, corresponding to a highly complex, fractured (fault) zone, located at the junction of the Alpine and Dinaric (fault) systems (**Figure 1A**).

In the long-term of the considered dataset (i.e., from 1988 to 2019) we found different intervals of rather steady seismic activity, which are characterized by a near constant value of η, with switches at times of transition associated with the relatively large $M_d > 5.0$ events. As long as the temporal features of seismicity are concerned, a time interval of rather stable seismic activity could be determined according to the different parameters; during such interval, starting on 2005 and up 2019 (i.e., up to the end of available data) no major earthquakes (i.e., $M_d > 5.0$) are reported in the catalog, thus providing presumably independent (background) parameters values. Although the temporal pattern of activity rate changes identified in this study reflects trends at the sub-regions scale, this result appears compatible with the observation of a period of rather low background seismicity rate (i.e. for the declustered catalog) ongoing since more than a decade, detected by Benali et al. (2020) for the whole FVG region.

The results obtained for Northeastern Italy and surrounding areas confirm similar analysis performed on a global scale, in advance and after the largest earthquakes worldwide. Specifically,

we found that: 1) the dynamical changes of τ, Σ, and η in the three sub-regions highlight a number of different seismic regimes; 2) the seismic activity prior and after the occurrence of strong main shocks (e.g., the 1998 and 2004 Kobarid earthquakes) is characterized by significantly different parameters within the related sub-region; 3) the USLE coefficients in FVG region are time-dependent (as observed in Nekrasova and Kossobokov, 2005; Nekrasova, 2007; Nekrasova et al., 2011) and show up correlated, displaying interesting features in dynamics of seismicity that can be related with major earthquakes (see **Supplementary Figures S3.1–S3.3**).

The temporal changes of the USLE coefficients estimated for three FVG sub-regions exposed correlated, though complex behaviors in dynamics of the Earth crust hierarchical system of blocks-and-faults. In addition, the analysis of time variations of the cumulative Benioff strain release, $\Sigma(t)$, evidenced that the slope of its linear long-term trend may change significantly after the occurrence of a major earthquake. Although the number of the moderate earthquakes in the FVG region is too small for contributing to "the hypothesis that many large earthquakes are preceded by accelerating-decelerating seismic release rates which are described by a power law time to failure relation" (Vallianatos and Chatzopoulos, 2018), according to a non-extensive statistical physics view, our observations suggest that the steady (normal) state of the system (as described by the common exponent m associated with the time variation of the Benioff strain within an area), may change after the occurrence of a large earthquake.

The obtained results highlight non-stationarity of seismic activity, at a time-scale of several years and up to decades, in agreement with earlier findings by Benali et al. (2020), an element that should be taken into account for improving local seismic hazard assessment. The regions and time intervals identified in this study, which display homogeneous features of seismic activity, may supply valuable information toward time-dependent seismic hazard assessment (e.g., Kossobokov et al., 2015 and references therein), while providing new constraints for earthquakes forecasting in Northeastern Italy.

DATA AVAILABILITY STATEMENT

Publicly available datasets were analyzed in this study. The earthquake datasets used in this study are published as yearly and monthly bulletins by the National Institute of Oceanography and Applied Geophysics (OGS) and are publicly available via the OGS website (http://www.crs.inogs.it/bollettino/RSFVG/).

AUTHOR CONTRIBUTIONS

AN performed time series computations, and ABC coefficients analysis, while AP provided the data, performed preliminary data analysis and defined the setting and regions for investigation. Both AN and AP collaborated at data interpretation and manuscript write up.

FUNDING

The IEPT RAS researcher part of this study is supported by grant of the *Russian Science Foundation* (project No. 20–17–00180). The research also benefited from financial support by Protezione Civile della Regione Autonoma Friuli-Venezia Giulia (Italy) in the framework of the cooperation with OGS ("Collaborazione nell'ambito del monitoraggio sismico e meteomarino di interesse Regionale e per il supporto tecnico-scientifico nella prevenzione e gestione di emergenze sismiche, meteomarine e ambientali sul territorio e lungo le coste della Regione Friuli Venezia Giulia").

ACKNOWLEDGMENTS

The authors are grateful to V. G. Kossobokov (IEPT RAS) for valuable comments and to C. Barnaba (OGS) for useful discussions. Earthquake data used in this study are published by the National Institute of Oceanography and Applied Geophysics (OGS) and are publicly available at www.crs.inogs.it/bollettino/RSFVG/. The data are collected in the framework of the cooperation between OGS and Regione Autonoma Friuli Venezia Giulia Civil Protection.

SUPPLEMENTARY MATERIAL

The Supplementary Material for this article can be found online at: https://www.frontiersin.org/articles/10.3389/feart.2020.590724/full#supplementary-material.

REFERENCES

Bak, P., Christensen, K., Danon, L., and Scanlon, T. (2002). Unified scaling law for earthquakes. *Phys. Rev. Lett.* 88, 178501–178504. doi:10.1103/PhysRevLett.88.178501

Benali, A., Peresan, A., Varini, E., and Talbi, A. (2020). Modelling background seismicity components identified by nearest neighbour and stochastic declustering approaches: the case of Northeastern Italy. *Stoch. Environ. Res. Risk Assess.* 34 (6), 775–791.

Benioff, H. (1951). Global strain accumulation and release as related by great earthquakes. *Bull. Geol. Soc. Am.* 62, 331–338.

Bressan, G., Barnaba, C., Bragato, P. L., Peresan, A., Rossi, G., and Urban, S. (2019). Distretti sismici del Friuli Venezia Giulia, Bollettino di Geofisica Teorica. *Applicata* 60, S1–S74. doi:10.4430/bgta0300

Bressan, G., Barnaba, C., Bragato, P., Ponton, M., and Restivo, A. (2018). Revised seismotectonic model of NE Italy and W Slovenia based on focal mechanism inversion. *J. Seismol.* 22 (6), 1563–1578. doi:10.1007/s10950-018-9785-2

Chochlaki, K., Vallianatos, F., and Michas, G. (2018). Global regionalized seismicity in view of non-extensive statistical physics. *Phys. Stat. Mech. Appl.* 493, 276–285. doi:10.1016/j.physa.2017.10.020

Christensen, K., Danon, L., Scanlon, T., and Bak, P. (2002). Unified scaling law for earthquakes. *Proc. Natl. Acad. Sci. U.S.A.* 99 (Suppl. 1), 2509–2513. doi:10.1073/pnas.012581099

Gorshkov, A., Panza, G. F., SolovievAoudia, A. A., and Peresan, A. (2009). Delineation of the geometry of nodes in the Alps-Dinarides hinge zone and recognition of seismogenic nodes ($M \geq 6$). *Terra. Nova.* 21 (4), 257–264. doi:10.1111/j.1365-3121.2009.00879.x

Gutenberg, R., and Richter, C. F. (1944). Frequency of earthquakes in California. *Bull. Seismol. Soc. Am.* 34, 185–188.

Kossobokov, V. G., and Mazhkenov, S. A. (1989). "On similarity in the spatial distribution of seismicity," in *Computational seismology and geodynamics*. Editor D. K. Chowdhury (Washington DC: AGU), 1, 6–15.

Kossobokov, V. G., and Mazhkenov, S. A. (1988). "Spatial characteristics of similarity for earthquake sequences: fractality of seismicity," in *Lecture notes of the workshop on global geophysical informatics with applications to research in earthquake prediction and reduction of seismic risk [15 Nov–16 Dec., 1988]*. Trieste: ICTP, 15.

Kossobokov, V. G., and Nekrasova, A. K. (2019). Aftershock sequences of the recent major earthquakes in New Zealand. *Pure Appl. Geophys.* 176, 1–23. doi:10.1007/s00024-018-2071-y

Kossobokov, V. G., and Nekrasova, A. K. (2017). Characterizing aftershock sequences of the recent strong earthquakes in Central Italy (2017). *Pure Appl. Geophys.* 174 (10), 3713–3723. doi:10.1007/s00024-017-1624-9

Kossobokov, V. G., Peresan, A., and Panza, G. F. (2015). On operational earthquake forecast and prediction problems. *Seismol Res. Lett.* 86 (2A), 287–290. doi:10.1785/0220140202

Kossobokov, V. (2020). "Unified scaling law for earthquakes that generalizes the fundamental Gutenberg-Richter relationship," in *Encyclopedia of solid Earth Geophysics, encyclopedia of Earth sciences series*. 2nd Edition. Editor H. K. Gupta doi:10.1007/978-3-030-10475-7_257-1/Ed.H

Mignan, A., and Woessner, J. (2012). Estimating the magnitude of completeness in earthquake catalogs, community online resource for statistical seismicity analysis. Available at: http://www.corssa.org (Accessed October 20, 2020). doi:10.5078/corssa-00180805

Nekrasova, A. (2007). "Part 4: earthquake Hazard in the Alps - 4.1 - unified scaling law for earthquakes in the Alps: a multiscale application," in *Final report of the ALPS-GPSQuakenet project, Interreg III B Alpine Space programme*. Muenchen: Bayerische akademie der Wissenschaften. 63–85.

Nekrasova, A. K., and Kossobokov, V. G. (2019). Unified scaling law for earthquakes: global map of parameters. *ISC Seismolog. Dataset Rep.* doi:10.31905/XT753V44

Nekrasova, A., and Kossobokov, V. (2003). Generalized Gutenberg-Richter recurrence law: global map of parameters. *Geophys. Res. Abst.* 5. Abstract EAE03-A-03801.

Nekrasova, A., and Kossobokov, V. (2002). Generalizing the Gutenberg-Richter scaling law. *EOS Trans. AGU.* 83 (47). Fall Meet. Suppl., Abstract NG62B-0958.

Nekrasova, A., Kossobokov, V., Parvez, I. A., and Tao, X. (2015). Seismic hazard and risk assessment based on the unified scaling law for earthquakes. *Acta Geod. Geophys.* 50 (1), 21–37. doi:10.1007/s40328-014-0082-4

Nekrasova, A., Kossobokov, V., Peresan, A., Aoudia, A., and Panza, G. F. (2011). A multiscale Application of the unified scaling law for earthquakes in the central mediterranean area and alpine region. *Pure Appl. Geophy.* 168 (1–2). doi:10.1007/s00024-010-0163-4

Nekrasova, A., and Kossobokov, V. (2005). Temporal variation of the coefficients of Unified scaling law for earthquakes on the east of Honshu Island (Japan). *Dokl. Earth Sci.* 405A (No. 9), 1352–1355.

Nekrasova, A., Peresan, A., Magrin, A., and Kossobokov, V. (2016). The unified scaling law for earthquakes in the Friuli -Venezia Giulia region. *Geophys. Res. Abstr.* 18, EGU2016–17706.

OGS (2019). OGS Bulletin, Centro di Ricerche Sismologiche (CRS), Istituto Nazionale di Oceanografia e di Geofisica Sperimentale (OGS), Udine, Italy. Available at: http://www.crs.inogs.it (Accessed May 30, 2019).

Parvez, I. A., Nekrasova, A., and Kossobokov, V. (2014). Estimation of seismic hazard and risks for the Himalayas and surrounding regions based on Unified Scaling Law for Earthquakes. *Nat. Hazards.* 71 (1), 549–562. doi:10.1007/s11069-0130926-1

Peresan, A., and Gentili, S. (2020). Identification and characterization of earthquake clusters: a comparative analysis for selected sequences in Italy and adjacent regions. *Boll. Geof. Teor. Appl.* 61 (1), 57–80. doi:10.4430/bgta0249

Peresan, A., and Gentili, S. (2018). Seismic clusters analysis in Northeastern Italy by the nearest-neighbor approach. *PEPI* 274, 87–104. doi:10.1016/j.pepi.2017.11.007

Peruzza, L., Garbin, M., Snidarcig, A., Sugan, M., Urban, S., Renner, G., et al. (2015). Quarry blasts, underwater explosions and other dubious seismic events in NE Italy from 1977 till 2013. *Boll. Geof. Teor. Appl.* 56 (4), 437–459.

Slejko, D., Neri, G., Orozova, I., Renner, G., and Wyss, M. (1999). Stress field in Friuli (NE Italy) from fault plane solutions of activity following the 1976 main shock. *Bull. Seism. Soc. Am.* 89, 1037–1052.

Smirnov, N. (1948). Table for estimating the goodness of fit of empirical distributions. *Ann. Math. Stat.* 19, 279–281. doi:10.1214/aoms/1177730256

Tsallis, C. (1988). Possible generalization of Boltzmann–Gibbs statistics. *J. Stat. Phys.* 52, 479–487. doi:10.1007/BF01016429

Vallianatos, F., and Chatzopoulos, G. (2018). A complexity view into the physics of the accelerating seismic release hypothesis: theoretical principles. *Entropy* 20 (10), 754. doi:10.3390/e20100754

Varini, E., Peresan, A., and Zhuang, J. (2020). Topological comparison between the stochastic and the nearest-neighbour earthquake declustering methods through network analysis. *J. Geophys. Res.: Solid Earth.* 125. doi:10.1029/2020JB019718

Conflict of Interest: The authors declare that the research was conducted in the absence of any commercial or financial relationships that could be construed as a potential conflict of interest.

Copyright © 2021 Nekrasova and Peresan. This is an open-access article distributed under the terms of the Creative Commons Attribution License (CC BY). The use, distribution or reproduction in other forums is permitted, provided the original author(s) and the copyright owner(s) are credited and that the original publication in this journal is cited, in accordance with accepted academic practice. No use, distribution or reproduction is permitted which does not comply with these terms.

frontiers in Earth Science

PERSPECTIVE
published: 15 January 2021
doi: 10.3389/feart.2020.548398

Precursor-Based Earthquake Prediction Research: Proposal for a Paradigm-Shifting Strategy

Alexandru Szakács *

Department of Endogene Processes, Natural Hazard and Risk, Romanian Academy, Institute of Geodynamics, Bucharest, Romania

The article discusses the controversial topic of the precursor-based earthquake prediction, based on a personal perspective intending to stir the current still waters of the issue after twenty years have passed since the influential debate on earthquake prediction hosted by Nature in 1999. The article challenges the currently dominant pessimistic view on precursor-based earthquake prediction resting on the "impossible in principle" paradigm. Instead, it suggests that a concept-based innovative research strategy is the key to obtain significant results, i.e., a possible paradigm shift, in this domain. The basic concept underlying such a possible strategy is the "precursory fingerprint" of individual seismic structures derived from the uniqueness of the structures themselves. The aim is to find as many unique fingerprints as possible for different seismic structures worldwide, covering all earthquake typologies. To achieve this, a multiparameter approach involving all possible sensor types (physical, chemical, and biological) of the highest available sensitivity and artificial intelligence could be used. The findings would then be extrapolated to other similar structures. One key issue is the emplacement location of the sensor array in privileged "sensitive" Earth surface sites (such as volcanic conduits) where the signal-to-noise ratio is maximized, as suggested in the article. The strategy envisages three stages: experimental phase, validation, and implementation. It inherently could be a costly, multidisciplinary, international, and long-term (i.e., multidecade) endeavor with no guaranteed success, but less adventurous and societally more significant to the currently running and well-funded SETI Project.

Keywords: earthquake prediction, precursor signal, paradigm shift, strategy, sensors, experiment

OPEN ACCESS

Edited by:
Ying Li,
China Earthquake Administration, China

Reviewed by:
Joern Lauterjung,
Helmholtz Centre Potsdam, Germany
Giovanni Martinelli,
National Institute of Geophysics and Volcanology, Italy

***Correspondence:**
Alexandru Szakács
szakacs@sapientia.ro

Specialty section:
This article was submitted to Geohazards and Georisks, a section of the journal Frontiers in Earth Science

Received: *02 April 2020*
Accepted: *03 December 2020*
Published: *15 January 2021*

Citation:
Szakács A (2021) Precursor-Based Earthquake Prediction Research: Proposal for a Paradigm-Shifting Strategy. Front. Earth Sci. 8:548398. doi: 10.3389/feart.2020.548398

INTRODUCTION

"Short-term earthquake prediction is the only useful and meaningful form for protecting human lives and social infrastructures" from the effects of disastrous seismic events (Hayakawa, 2018).

More than twenty years have passed since the *Nature* debate on earthquake prediction (introduced and concluded by Main, 1999a; Main, 1999b). The time passed since then apparently seems to justify the most "pessimistic (or skeptical) party" of that debate according to which earthquake prediction based on precursory signals is "impossible in principle" because of the chaotic and nonlinear nature of the seismic phenomenon (e.g., Geller et al., 1996; Matthews, 1997) or because "it is likely that an earthquake has no preparatory stage" (Kagan, 1997). As Uyeda and Nagao (2018) put it recently, "...because they could not identify reliable precursors, seismologists maintained a negative attitude toward earthquake prediction." This style of

reasoning penetrated the consciousness of the scientific community so profoundly that it is explicitly expressed in *Predicting the Unpredictable*—the title of a book (Hough, 2010). Meanwhile, a number of large-magnitude earthquakes struck worldwide without being "predicted" and causing numerous victims and incommensurable economic losses such as the 2004 Sumatra earthquake (227, 898 victims and US$15 billion total damage; Telford and Cosgrave, 2006), the 2010 Haiti earthquake (>100,000 death toll and USD 7.8–8.5 billion economic loss; U.S. Geological Survey, 2013), and the 2011 Tohoku earthquake (15,900 victims and USD 360 billion economic loss; Bachev, 2014) that apparently confirmed the pessimistic view on earthquake prediction reinforced by a number of post-1999 papers. This pessimism has essentially lasted until today (Uyeda and Nagao, 2018).

However, there are still a few alternative expert views around (e.g., "there are increased amounts of data, new theories and powerful computer programs and scientists are using those to explore ways that earthquakes might be predicted in the future.", Blanpied, 2008). Developments in the domain of earthquake prediction research during the last few decades prompted by the occurrence of devastating seismic events worldwide seem to confirm such an optimistic view as mentioned by Uyeda and Nagao (2018) referring to "the recent remarkable revival of seismology in earthquake prediction research (. . .) emerged from the shadows of electromagnetic research." Martinelli (2020) also noted that "some recent projects on earthquake precursors have produced interesting data recognized by the whole scientific community." Likewise, Hayakawa (2018) feels himself "very optimistic about the future of earthquake prediction."

On the other hand, one may question why all attempts in "predicting" earthquakes have failed so far or were not validated by the international scientific community: is it just because earthquake prediction is "impossible in principle" as most pessimists claim? Or, is "impossible in principle" the final and unquestionable answer to the precursor-based earthquake prediction problem? If not, then how an alternative solution may look like?

This article intends to discuss such questions and proposes a radically new approach to the issue of precursor-based earthquake prediction research strategy.

A SHORT SUMMARY OF THE STATE OF THE ART IN EARTHQUAKE PREDICTION RESEARCH

Jordan et al. (2011) evaluated the known "diagnostic precursors" (i.e., strain-rate changes, seismic velocity changes, electrical conductivity changes, radon emission, hydrogeological changes, electromagnetic signals, thermal anomalies, anomalous animal behavior, seismic patterns, and proxies for accelerating strain) individually, one-by-one, and found that none of them is universally valid concluding that "the search for diagnostic precursors has thus far been unsuccessful."

Crampin (2012) claimed that "in one case when seismic data from Iceland was being monitored online, the time, magnitude, and fault break of a M = 5 earthquake in Iceland was successfully stress-forecast three days before it occurred." However, this claimed prediction success "in one case," based on a single monitoring method, cannot be generalized as a universally valid solution applicable to all types of seismic events and all geodynamic environments.

As a consequence, the need for multiparameter monitoring of potential earthquake precursors emerged. It was increasingly invoked in the last 2 decades and researchers started coupling two or more monitored parameters in order to gain better confidence in their prediction efforts. Ryabinin et al. (2011), for example, studied together chlorine-ion concentration variations and geoacoustic emission in Kamchatka peninsula in boreholes within the same seismic zone claiming that they obtained significant anomalies "70 to 50 days before the earthquake for the hydrogeochemical data and at 29 and 6 days in advance for the geoacoustic data."

A recently (2018) published book (Pre-Earthquake Processes. A Multidisciplinary Approach to Earthquake Prediction Studies) edited by Dimitar Ouzounov, Sergey Pulinets, Katsumi Hattori, and Patrick Taylor resumes excellently the encouraging progress achieved in the research domain of earthquake prediction. However, the invoked positive results were rather disparate reflecting research efforts of individuals, small groups of researchers or, in the best case, national programs, such as those in China (Wang et al., 2018) or Taiwan (the iSTEP-1, two and three programs following the 1999 Chi-Chi earthquake, Tsai et al., 2018; Fu and Lee, 2018); they are essentially based on the most common approach of looking for the identification of universally valid precursors and considering only a small number of premonitory phenomena (different from country to country) in their respective multiparameter monitoring systems. Symptomatically, for instance, although biological sensors are mentioned as potential recorders of preseismic signals (e.g., Ouzounov et al., 2018a; Tramutoli et al., 2018b), none of the invoked monitoring systems considers them in their research programs. A common global research strategy concept is clearly lacking because, among other reasons, governmental opinions are different and changing over time. For instance, Iceland, Taiwan, China, Russian Federation, and Japan support researches oriented to possible earthquake forecasting, whereas the USA appears contradictory and Europe does not have a unique research policy.

Despite the encouraging results obtained in the last few decades in the field of earthquake prediction research, including a few alleged successful a priori predictions (e.g., using the CN seismicity pattern prediction algorithm, Peresan et al., 2012, Peresan, 2018, or using atmospheric-ionospheric precursors, Ouzounov et al., 2018b), no fully credible, validated, and generally accepted method emerged, as Jordan et al. (2011) put it: "the search for diagnostic precursors has not yet produced a successful short-term prediction scheme." Reviewing geofluid monitoring results, Martinelli (2020) also concluded that "earthquake prediction research based on parameters believed to be precursors of earthquakes is still controversial and still

appear to be premature for the practical purposes demanded by governmental standards."

Most reported "successes" were "a posteriori" statements (i.e., "postpredictions") based on the post-factum recognition or retrospective tests of precursory signals related to particular seismic events (e.g., Shebalin et al., 2006; Papadopoulos et al., 2018; Fu and Lee, 2018; Zafrir et al. (2020), including some of the most devastating recent ones, e.g., Peresan, 2018; Tramutoli et al., 2018b).

Ouzounov et al. (2018b) presented noticeable results in devising a sound methodology to check the predictive potential of preearthquake signals based on a sensor web of several physical and environmental parameters (satellite thermal infrared radiation, electron concentration in the ionosphere, air temperature, and relative humidity). They claim success in the validation of different anomalous preearthquake signals in both retrospective (3 M > 6 events in the US, Taiwan, and Japan) and prospective (22 M > 5.5 events in Japan) modes with a success rate of 21 out of 22 for the latter mode. However, one may question whether this methodology using just a small number of parameters registered by a few ground-based and satellite-held instruments can be generalized and considered valid for all types of earthquakes and all regional or local geodynamic environments.

Taking into consideration the above state of the art, this perspective article does not propose to review the burgeoning literature exhaustively on the subject of earthquake prediction. A number of recently published review articles (e.g., Martinelli, 2020) and books (e.g., Dimitar Ouzounov, Sergey Pulinets, Katsumi Hattori, and Patrick Taylor, eds, 2018) did that successfully. Rather, it focuses on the presentation of a possible strategic research approach based on a novel concept.

CHALLENGING THE PESSIMISTIC VIEW ON THE EARTHQUAKE PREDICTION PROBLEM

Science is about discovery. Discovering unknown features of nature is the foremost task of the natural sciences. Most scientific endeavors start by identifying unsolved problems. The scientists enrolled in such an adventure are interested, at least by genuine curiosity, to understand the unknown or unexplained. A lot of unknowns addressed by science were not solved and understood for a long time or during the lifetime of the generation that identified the problem. However, they remained in the collective scientific consciousness as something to be solved in the future, a challenge.

The history of science is rife with examples of universally accepted paradigms, equivalent with the "impossible in principle" statement, challenged by individuals and later recognized as viable. In Earth sciences, Wegener's hypothesis on the migration of continents was considered as "impossible in principle" (although not formulated with the same words). Likewise, flying with objects denser than air was explicitly declared "impossible in principle" just one hundred years ago even by leading scientists of the epoch.

The pessimists always argue that effort and money should not be spent for precursor-based earthquake prediction, given that all such efforts were unsuccessful in the past and, more importantly, because this is "impossible in principle"; rather, money should be spent for hazard mitigation programs. Leaving aside the fact that the two approaches are not mutually exclusive, one may wonder how other large-scale and costly research programs with uncertainties about their outcome comparable with possible earthquake prediction research programs were accepted for funding and are still ongoing for decades with no positive results. The NASA's SETI Program (run by the SETI Institute since 1994), for example, has spent more than USD 110 M in the 1980–2005 time period (https://phys.org/news/2015-08-seti-unprecedented.html) and is currently spending USD 2.5 M yearly (https://geeknewscentral.com/2011/05/02/the-real-cost-of-seti/) with no relevant results. One may wonder, for good reasons, whether the chances of identifying extraterrestrial intelligence are higher than devising a reliable precursor-based earthquake prediction methodology. And, what is the relevance of both of them to society?

I conclude that precursor-based earthquake prediction should be viewed as a challenge rather than an insolvable (in principle) problem. Wyss (2001) expressed a similar view: "as a physical phenomenon, earthquakes must be predictable to a certain degree." Addressing the earthquake prediction problem as a challenge for science is mobilizing (intelligence, effort, time, and money), whereas looking at it as an "impossible in principle" task is demobilizing. As so, "perhaps, now is the time to discard the long-held pessimism and combine all our forces to venture toward transforming precursor information into practical earthquake prediction" (Uyeda and Nagao, 2018).

WHY WAS PRECURSOR-BASED EARTHQUAKE PREDICTION UNSUCCESSFUL SO FAR?

Despite a large number of (mostly post-factum) claims of successful earthquake prediction based on precursory phenomena such as radon anomalies (e.g., Crockett et al., 2006) or anomalous behavior of living creatures (e.g., Polyakov et al., 2015), the scientific community did not validate them so far. A classic example of claimed but not validated success is the 1975 Haicheng earthquake in China claimed by the Chinese scientists (Wang et al., 2006) as a successful prediction saving many lives. However, the prediction was just in the following year questioned by the devastating Tangshan earthquake (>240,000 victims, USGS, 2013). The major lesson to be drawn is that no two earthquakes are alike. Therefore, the most frequently undertaken approach to predict earthquakes based on precursory signals by looking at, or monitoring, one single (or a few) parameter(s) of the presupposed precursory phenomenon, such as VAN, using merely electromagnetic parameters (Varotsos et al., 1986) does not work. There is no Holy Grail of a single, or a few, universally valid prediction signal to be surveyed at least because "it is practically impossible (. . .) to collect the large set of

data for all parameters in real-time globally" (Pulinets et al., 2018).

Another reason is that individuals or small groups of researchers addressed the challenge of precursor-based earthquake prediction on their own, detached from a broader, national or international, systemic approach. As Wyss (2001) puts it, "no real program for earthquake prediction research exists in the United States (. . .) but motivated individuals are active". Also, "research connected with earthquake prediction has been characterized by the absence of great projects" (Martinelli, 2018). And this is, in my opinion, the cornerstone of the failure: the lack of a long-term strategy. Long ago, Frank Press (1968) complained that there is no research strategy in the US in the domain of earthquake prediction. Japan's investigation strategy, given as an example, was short-lived (10 years, Press, 1968), far less than what would have been necessary to obtain significant results. More recent successive short-term programs in Japan following the 1995 Kobe earthquake ended in remarkable results by retrospectively identifying electromagnetic precursors associated with ground movements (e.g., in the case of the 2011 M 9 Tōhoku megaearthquake); however, no currently running long-term program is founded (Hayakawa, 2018).

It is true that multisensor-/multiparameter-based research strategies are currently implemented in a number of earthquake disaster-prone countries, such as Turkey (Yuce et al., 2010), Russia (Pulinets et al., 2016), Japan (Hayakawa, 2018), China (Wang et al., 2018), Taiwan (Tsai et al., 2018), and Italy (Peresan, 2018); however, they are 1) part of local national programs, 2) unconnected to each other, hence lacking a common strategic concept, and 3) partial, i.e., considering only a few or a limited number of precursor types and corresponding parameters and sensors. The spectrum of "preearthquake phenomena" considered in China for its current multidisciplinary earthquake monitoring system, for instance, includes crustal deformation, seismicity, geoelectricity and geomagnetism and the behavior of crustal fluids (Wang et al., 2018), but no biological response. In Taiwan, the components of the multidisciplinary research on earthquake prediction include monitoring of microearthquake activities, crustal deformation, microgravity, geomagnetic total intensity, and geothermal water changes complemented with ionospheric data and statistical studies (Fu and Lee, 2018; Tsai et al., 2018). Pulinets et al. (2018) considered using only two groups of precursors, thermal and ionospheric "in order to simplify" the investigations.

Some limited-participation international projects were also initiated recently, such as the PRE-EARTHQUAKES project (EU-FP7cordis.europa.eu/result/rcn/57410_en.html) involving research institutions from Italy, Germany, Turkey, and Russia (Ouzounov et al., 2018b).

All of the research initiatives and strategies mentioned above are, however, different—in breath, philosophy, underlying concept, and international significance—from the strategic approach proposed in this article.

To summarize, despite some notable recent advancements, the precursor-based earthquake prediction research, as a whole, is generally considered unsuccessful so far (e.g., Wang et al., 2006; Uyeda and Nagao, 2018). This is, in my opinion, due to 1) the lack of long-term research strategy and related funding 2), the lack of large-scale international cooperation, 3) individualism of researchers/groups, aiming at finding the Holy Grail of earthquake prediction based on a single (or a few) signal of a single (or a few) precursory phenomenon, and, perhaps 4) the lack of high-level technical prerequisites (e.g., computing facilities and sensor technology). Therefore, any further approach to the problem has to be based on a strategy. A strategy, in turn, has to be based on a concept. A possible shift of paradigm from today's dominant pessimistic "impossible in principle" to an optimistic "yes, we can" needs a new concept.

OUTLINES OF A POSSIBLE PARADIGM SHIFT IN PRECURSORY-BASED EARTHQUAKE PREDICTION RESEARCH

Conceptual Framework

The basic principle of a possible new paradigm is the uniqueness of seismogenic structures. This trivial statement needs some explanations. Seismogenic structures are most commonly defined as active faults or fault segments. However, there are other structures that cannot be equated with faults, such as the Vrancea seismic zone in Romania (e.g., Radulian et al., 2000) that is rather a seismogenic volume of rocks of ca. 280,000 km^3 having a surface-projected area of 70 × 40 km. Some "diffuse" seismogenic structures, such as those located in deep intraplate settings, are difficult to be defined, in the sense that their geometrical parameters (volume and outline) cannot be determined.

Irrespective of their nature, well-defined or not, those geological structures are "seismogenic" because they produce earthquakes. And they are unique. Each of them has its own particular geotectonic setting, unique mutual relationships with neighboring structures, unique internal composition and structure, unique seismic history, and a particular stress field.

As a consequence of their uniqueness, the seismogenic structures produce particular seismic events with typical features and parameters. Moreover, reequilibration after major events will cause modifications of the structure itself, so that the next events will take place in somewhat modified local conditions. However, one may suppose that seismogenic structures are stable enough in time (at least on the scale of human history) and that their basic features do not change and their general behavior is preserved.

Another consequence of the seismogenic structures' uniqueness and their consistent behavior in time is that any precursory phenomenology to be expected is also unique. Therefore, one should not expect the same precursory signal to be received from different seismogenic structures, not to mention any universally valid signals.

Although questioned, the concept of precursory phenomena is generally considered valid in the scientific community (e.g., Geller, 1991; Wyss, 2001). Theoretically, the sudden rupture/slide produced by/in the seismogenic structure is preceded by stress accumulation and escalation, which, in turn, triggers modifications of the physical fields and chemical components

(e.g., fluids) in the neighboring medium that propagate out from the critical zone in the form of geophysical and/or geochemical signals of various kinds. Those signals are, in principle, receivable at Earth's surface by adequately designed, tuned, and located sensors. Moreover, those propagating changes may trigger, by induction, modifications in other fields, with which they interact, hence generating secondary signals, for instance, in the atmosphere, ionosphere, and even the magnetosphere, through a complex coupling mechanism with the lithosphere, as Pulinets et al. (2018) and Hayakawa et al. (2018) convincingly demonstrated. As a consequence, an impending major seismic event may be preceded by a number of precursory signals of various kinds (physical, chemical, and biological), primary or induced.

Indeed, current research in China on "preearthquake phenomena" resulted in important findings (Wang et al., 2018). However, the use of those findings for actual preevent prediction (as opposed to postprediction) and warning meets enormous challenges, because of the complexity of the precursory phenomenology, since event location, time, and magnitude are to be "predicted", as Wang et al. (2018) put it, "this complexity may be due to differences in the tectonic environments around seismogenic zones". And, even more significantly, "the characteristics of the preearthquake phenomena preceding each event [of those monitored] differed," and "different geological structures and crustal environments are likely to produce different spatiotemporal patterns of pre-earthquake phenomena" (Wang et al., 2018). In other words, according to the terminology used in this article, this complexity and these differences arise because of the uniqueness of the seismogenic structures. Martinelli and Dadomo (2018) also arrived to the idea that not all seismogenic structures behave in the same manner as reflected in the fluid-related precursors: "Not all earthquakes seem to be preceded by detectable crustal strain changes in the epicentral area and this could explain the lack of fluid -related precursors." Hayakawa et al. (2018), searching for preseismic ionospheric perturbations found that "with earthquake depths of > 40 km (. . .) there is no clear precursory signal evident." Parrot and Li (2018) also emphasized that "it cannot be excluded that a [precursory] mechanism could be efficient in a given seismic area and not in another one." Ouzounov et al. (2018a) explicitly recognized that "no solitary existing method (. . .) can provide successful and consistent short-term forecasting on a global scale. This is most likely because of the local geology. . .." Furthermore, "it is difficult to determine the location of the epicenter of a major event based only on recorded observations of pre-earthquake phenomena" (Wang et al., 2018). Considering the concept proposed here (i.e., addressing "preearthquake phenomena" at/for particular individual seismogenic structures), this latter type of shortcomings is automatically eliminated.

The common sense statements, and the copiously cited examples, presented above, all converge toward the acceptance of the uniqueness of seismogenic structures, which, in turn leads to the derived concept of precursory fingerprint. Each seismogenic structure, in particular those well-defined (in terms of nature, stress field, and size/volume), might have its unique assemblage of precursory phenomena, each of them being associated with a particular type of signal propagating through the surrounding medium. As a consequence, an earthquake prediction researcher may consider a particular assemblage of precursory signals for every particular seismogenic structure, which is the unique precursory fingerprint of that unique seismogenic structure. The task is to find that precursory fingerprint of the studied seismogenic structure. How would a strategy that takes this task seriously look like?

Outlines of a Possible Internationally Coordinated Research Strategy

The conceptual framework of the envisaged strategy involves two postulates: 1) precursory signals do exist and they are detectable in principle; 2) the concept of precursory fingerprint of individual seismic structures is valid. Instead of looking for universally valid precursors, the strategy targets a less ambitious goal: identifying the precursory fingerprint of individual seismic structures, hence having a merely local validity (as a starting assumption). The precursory fingerprint has to be found at as many individual seismic structures as possible, ideally covering all types of tectonic regimes and stress field. This is achievable by monitoring selected well-known structures worldwide at purposefully designed and adequately equipped observatories hosting a wide range of sensors of the highest-resolution currently available covering all possible types of precursory signals (seismic, physical, chemical, and biological) in order to assure a multisensor/multiparameter monitoring system. It is worth noting that because "a majority of the reported earthquake precursor data found during the past few decades have been proven to be nonseismological (mainly electromagnetic)" (Hayakawa, 2018), the electromagnetic component of that part of the monitoring system considers that physical precursors must be adequately represented in the research programs including ground-based and satellite-held instruments (e.g., those on-board the currently active French DEMETER satellite, Parrot and Li, 2018) in order to understand the effects of lithosphere-atmosphere-ionosphere-magnetosphere coupling (e.g., Hattori and Han, 2018; Hayakawa, 2018; Hayakawa et al., 2018; Pulinets et al., 2018) at the local scale. Preseismic atmospheric thermal anomalies are among those signals able to be effectively detected by satellite-held instruments (Ouzounov et al., 2018a; Tramutoli et al., 2018a). Fu and Lee (2018) also advocate for a "systematic characterization of all possible precursors" that "may help us." Tramutoli et al., 2018b, based on a reach literature, listed a large number of precursors, identified (mostly post-factum!) at various locations as preceding strong earthquakes, during the many-decade-long modern history of earthquake prediction research: deformation, geochemical, thermal infrared, latent head, earthquake clouds and lights, air temperature and humidity, atmospheric pressure, VHF and VLF signals, and GPS-associated total electron content; interestingly, biological precursors are missing from that list. The potential benefits of "geofluid monitoring" (including hydrogeologic measurements and geochemical analyses) of earthquake-prone areas were recently discussed in great detail by Martinelli (2020) as part

of the research arsenal in the quest for diagnostic precursors. Ongoing geofluid monitoring research is mentioned by the same author at test sites located in China, Iceland, Japan, the Russian Federation, Taiwan, and the USA. However, he warns about the inherent limitations of that type of research: "in principle, all earthquakes occurring in compressional tectonic regimes cannot be forecasted by geofluid monitoring."

Therefore, there is an extremely rich "offer" of virtual preearthquake phenomena, and related parameters, to be observed/measured and monitored, of which an n-sized sensor matrix can be completed.

Once installed, a matrix of *n* (say, 50) different sensors, measuring many more (say 80) parameters, will monitor each selected structure trying to capture precursory signals preceding a potentially destructive earthquake. One may suppose that only a few (say, four of the 50) sensors will be activated with eight measured parameters before imminent seismic events and only above a certain magnitude threshold (also characteristic of the monitored structure) depending on the sensors' sensitivity. The number and type of activated sensors and above-the-threshold parameters would provide the precursory fingerprint of the individual seismic structure. Experts of each precursory phenomenon may establish the significant threshold values of the monitored parameters (e.g., following Shebalin et al., 2006) to distinguish signal from noise and anomalous behavior from background activity. Artificial intelligence and machine learning involving pattern-recognizing algorithms (Shebalin et al., 2006, and references within) can also be implemented to evaluate sensor activity. Such extremely powerful modern computing tools are able not only to process and evaluate the response of certain sensors but also to point out complex correlation patterns of sensor responses. Boxberger et al. (2017), for instance, concluded that the innovative "multi-Parameter Wireless Sensing system allows different sensor types to be combined with h-high-performance computing and communication components."

Such an endeavor involves large-scale international effort, leadership, coordination, and funding of decades-long observations (Wyss, 1997: *"long-term data sets are needed to make progress in earthquake prediction research"*), measurements, and experiments, as Wyss (2001) envisaged that "leadership is necessary to raise the funding to an adequate level and to involve the best minds in this promising, potentially extremely rewarding, but controversial research topic."

The leadership can be assumed by IUGG's IASPEI Commission that already had some sparse initiatives in this sense, as follows.

Resolution 1 of IASPEI RESOLUTIONS adopted at the closing plenary meeting in Santiago, Chile (October 2005), on an International Active-Monitoring Network expressed the need for international cooperation in this domain with the following words: "IASPEI encourages the formation of an International Network of Active Monitoring Test Sites in order to facilitate collaborative seismic and geoelectrical studies of crustal deformation; active monitoring of seismically active zones, and exchange of technical information, data and personnel" (IASPEI, 2020).

Of the 14 IASPEI Resolutions and Statements in the period 1991–2017 (IASPEI, 2020), two explicitly address earthquake prediction issues by recommending the "establishment of a global network of Test Areas for Earthquake Prediction corresponding to the major types of geotectonic settings: Kamchatka (plate-subduction), Iceland (plate spreading), Yunnan, China (intercontinental strike-slip), Gulf of Corinth, Greece (continental rifting) and Beijing (intra-continental) and it "urges all nations to collaborate to extend coverage to the full globe, and recommends its Commissions and Committees to pursue the task in the years ahead" (ftp://ftp.iaspei.org/pub/resolutions/resolutions_1997_thessaloniki.pdf).

Likewise, of the 14 ESC (European Seismological Commission) business meetings (1996–2015) (http://www.esc-web.org/minutes-of-esc-meetings.html), a few (http://www.esc-web.org/minutes-of-esc-meetings/79-european-seismological-commission/88-esc-buisness-meeting-reykjavik-iceland-september-12-1996.html; Reykjavik, 1996; http://www.esc-web.org/minutes-of-esc-meetings/79-european-seismological-commission/88-esc-buisness-meeting-reykjavik-iceland-september-12-1996.html; Tel Aviv, 1998) (http://www.esc-web.org/minutes-of-esc-meetings/79-european-seismological-commission/90-esc-buisness-meeting-tel-aviv-1998.html) addressed explicitly earthquake prediction issues expressing the need for international cooperation.

Although disparate so far and without being based on a unique strategic concept, such initiatives are valuable precedents worthy of being followed and enhanced in a much consequent manner to assure international professional guidance and leadership for the implementation of a global earthquake precursor research strategy such as that proposed here.

The long-term strategy involves three phases: 1) experimental, 2) validation/extension, and 3) implementation.

The experimental phase (or "learning stage," acc. to Peresan, 2018) aims at checking the validity of the precursory fingerprint concept by setting up a small number of observatories at/near the best-studied seismic structures worldwide, each equipped with a matrix of as many kinds of sensors as possible in consensus with Birkhäuser's (2004) statement: "progress in earthquake science and prediction over the next few decades will require increased monitoring in several active areas." Sensors designed to capture primary and/or induced precursory signals will measure a high number of parameters, combined with an array of seismographs detecting changes in background seismicity (Sammis and Sornette, 2002; Shebalin et al., 2006; Peresan, 2018) to recognize foreshock activity (Papadopoulos et al., 2018). Other sensors are destined to point out subtle changes of the physical parameters (e.g., temperature, mass-flux, and gas flow rate fluctuations) and composition of fluids (dissolved ions, dissolved gases, soil gas, CO_2, CH_4, He, H, radon, and thoron) (Zoran et al., 2012; Oh and Kim, 2015; Martinelli, 2020) circulating in the crust (e.g., Tsunogai and Wakita, 1995; Claesson et al., 2004; Hartman et al., 2005; Fu and Lee, 2018; Martinelli and Dadomo, 2018). Ground deformation and other space-monitorable atmospheric and ionospheric signals (e.g., Sgrigna et al., 2007; Hayakawa et al., 2018; Tramutoli et al., 2018a) might be considered to complete the ground-based monitoring system. Still other sensors will monitor the

behavior of living creatures under stress conditions induced by changes in their physical and chemical environment due to an impending megaseismic event. Biological sensors may include all levels of organization across the biosphere, from bacteria to the human sensor (e.g., Polyakov et al., 2015), including vegetal life.

In the experimental phase, laboratory investigations are also needed in specialized high-performance labs in order to devise and check adequate sensors, i.e., to check the capability of various instruments and methods to be used as seismic sensors, including living organisms as potential biological sensors. Innovative approaches are welcome. A worldwide network of laboratories performing experimental work on precursor-sensitive instruments and methods would be required. New enhanced-sensitivity sensors resulting from the lab investigations will be implemented and tested at the monitoring observatories.

Another set of experiments aims at identifying the most suitable sensor emplacement sites for certain types of parameters to be monitored. It might be based on the recognition that not all Earth surface points are equivalent in terms of signal-receiver capability. In other words, certain types of sensors have to be emplaced at locations where the signal/noise ratio is the highest in the vicinity of the targeted seismogenic structure. One may speculate that those most "sensitive sites" are located at the endpoints of signal transmission trajectories along which the energy/information loss of the precursory signal is minimal. For instance, crust-crossing volcanic conduits with no intervening magma-chambers may serve as upside-down antennas (waveguides) for signal transmission (Szakács, 2011), given that any possible geophysical signal will travel faster and with less loss of information energy along such a more homogenous medium than along any other crustal trajectory. Likewise, deep crustal fractures are privileged transmission paths for fluids-carrying geochemical signals. For example, in recent years, several multiparameter continuous soil gas and gamma-ray monitoring stations have been deployed in Taiwan, "strategically located near active faults" (Tsai et al., 2018). Likewise, Fu and Lee (2018) found that "the Rn precursory anomalies were not observed at all the stations because the crust was not homogeneous" (i.e., some of the stations are located in "sensitive" sites, whereas others are not). Martinelli and Dadamo (2018) also state, citing a number of previous works, that "possible geochemical and hydrogeologic precursors have been observed hours to months before some strong earthquakes in 'sensitive' monitoring sites among many insensitive sites." Martinelli (2020) reiterated the idea of monitoring location sensitivity in his review article: "sensitive locations [for geofluid monitoring] are generally found along active faults, in thermal springs, or in deep wells that reach confined reservoirs capable of acting as natural strain meters."

Therefore, in the experimental phase, purpose-oriented and interdisciplinary investigations are also needed to identify and map the most suitable sensor emplacement sites.

The duration of the experimental phase depends on the seismic activity of the monitored structures: at least one high-magnitude event has to occur in order to evaluate the effectiveness of the monitoring system and to find out whether the observed structure produced significant precursory signals detected by the sensor matrix or not. In other words, can that particular seismic structure be characterized by a specific precursory fingerprint or not?

In the most optimistic scenario, the expected outcome of the experimental phase would be the emergence of a reliable methodology to identify the precursory fingerprint of at least part of the monitored structures. In the case no such result is obtained for none of the observed structures, one has to evaluate whether the precursory fingerprint project has to be abandoned or continued at least until the next megaseismic event occurs.

In the validation/extension phase—following the experimental phase only if considered successful or, at least, meaningful—the experience gained during the first phase will be extended to more seismic structures worldwide in order to 1) validate the results at other structures similar to those where the experiments were successful and 2) enhance and refine the multiparameter sensor matrix for those structures where negative results were obtained in the experimental phase maintaining the monitoring observatories instead of being dismantled. Again, this phase's duration depends on the occurrence of major earthquakes.

The implementation stage will consider only those seismic structures where the first two stages provided positive results (where the characteristic precursory fingerprint was readily identified). As a result, a worldwide network of multiparameter monitoring stations will be operational at a number of well-known seismic structures, including part of those of the highest hazard and risk. The multiparameter monitoring system will be rationalized and optimized by eliminating the inert (i.e., nonresponsive) infrastructure from the sensor matrix. Instead, the sensitivity of the remaining sensors will be continuously improved through further onsite experimental work and the results shared with all active monitoring stations worldwide.

DISCUSSION

Attempts of setting up monitoring systems in order to detect seismic precursory signals are not without precedents as Martinelli (2020) has shown. However, they were territorially limited to particular countries, such the Soviet Union and China, and to a particular time, e.g., 1970–1990 in the Soviet Union (Martinelli, 2020), all prompted by the occurrence of damaging earthquakes in the surveyed area. Such efforts were basically national endeavors uncoordinated internationally or not based on an underlying strategic concept other than the desire to identify universally valid individual, or a group of "key" (i.e., diagnostic, acc. to Jordan et al., 2011) precursors.

It is possible that the final outcome of the multidecadal research effort based on the strategy sketched above will result in a small number of seismogenic structures whose precursory fingerprints are readily identified and where a reliable monitoring system is implemented based on an optimized sensor matrix. The worst scenario implies that no such case will be found. In that case, the whole project will be abandoned and no more money will be invested in it. In the most optimistic scenario, the precursory fingerprint of a significant number of seismogenic

structures will be found. Moreover, one may envisage that some kind of regularity of the identified precursory fingerprints will be revealed. For instance, it would turn out that a particular kind of stress regime or a particular genetic type of earthquakes manifests itself via a particular and recognizable type of precursory fingerprint, allowing the generalization of the findings over other structures belonging to the same class. Pattern-recognizing artificial intelligence would help in sorting and evaluating the results in the most optimistic outcome scenario. More innovative approaches, such as machine learning, as Rouet-Leduc et al. (2017) reported for laboratory earthquakes, using time-series datasets gathered at monitoring stations, might be implemented for information evaluation.

The final outcome of the proposed scientific endeavor, its benefits in terms of new knowledge and research methodology, is comparable with other large-scale scientific adventures of humankind (such as the SETI program) at a similar or lower cost and with a similar, if not higher, chance of success. In contrast, the pessimistic approach to the earthquake prediction puzzle (i.e., the "impossible in principle" postulate, which posits that any effort to solve it is futile) is of no benefit for science.

These conclusions are fully consistent with those of Wyss (2001) who stated that "earthquake prediction is difficult but not impossible," "we must exercise patience and not expect spectacular success quickly," and any expectations are unrealistic "unless the field of prediction research is reformed and well-funded."

DATA AVAILABILITY STATEMENT

The original contributions presented in the study are included in the article/Supplementary Material, further inquiries can be directed to the corresponding author.

AUTHOR CONTRIBUTIONS

The author confirms being the sole contributor of this work and has approved it for publication.

ACKNOWLEDGMENTS

Ágnes Gál is thanked for her help in acquiring up-to-date literature on the subject. Simona Szakács helped to improve the English expression of the text. Two reviewers are acknowledged for their thoughtful comments on the early version of the manuscript. Giovanni Martinelli, Antonella Peresan, and Ying Li contributed to improving the final version of the manuscript with their valuable comments and recommendations.

REFERENCES

Bachev, H. (2014). Impacts of March 2011 earthquake, tsunami and Fukushima nuclear accident in Japan. *SSRN Electron. J.* 125. doi:10.2139/ssrn.2538949

Birkhäuser, B. (2004). Rethinking earthquake prediction. *Pure Appl. Geophys*. 155 (2–4), 207–232. doi:10.1007/978-1-4020-4399-4_106

Blanpied, M. (2008). Can we predict earthquakes? USGS CoreCast. Available at: http://www.usgs.gov/corecast/details.asp?ID=76 (Accessed May 20, 2008).

Boxberger, T., Fleming, K., Pittore, M., Parolai, S., Pilz, M., and Mikulla, S. (2017). The multi-parameter wireless sensing system (MPwise): its description and application to earthquake risk mitigation. *Sensors*. 17, 10. doi:10.3390/s17102400

Claesson, L., Skelton, A., Graham, C., Dietl, C., Mörth, M., Torssander, P., et al. (2004). Hydrogeochemical changes before and after a major earthquake. *Geology*. 32 (8), 641–644. doi:10.1130/G20542.1

Crampin, S. (2012). Comment on the report "operational earthquake forecasting" by the international commission on earthquake forecasting for civil protection. *Ann. Geophys*. 55, 1. doi:10.4401/ag-5516

Crockett, R. G., Gillmore, G. K., Phillips, P. S., Denman, A. R., and Groves-Kirkby, C. J. (2006). Radon anomalies preceding earthquakes which occurred in the UK, in summer and autumn 2002. *Sci. Total Environ*. 364 (1–3), 138–148. doi:10.1016/j.scitotenv.2005.08.003

Fu, Ch.-Ch., and Lee, L.-Ch. (2018). "Continuous monitoring of fluid and gas geochemistry for seismic study in taiwan," in *Pre-earthquake Processes. a multidisciplinary approach to earthquake prediction studies.*. Editors D. Ouzounov, S. Pulinets, K. Hattori, and P. Taylor (John Wiley & Sons), 199–218.

Geller, R. J. (1991). Unpredictable earthquakes. *Nature*. 353, 612.

Geller, R. J., Jackson, D. D., Kagan, Y. Y., and Mulargia, F. (1996). Earthquakes cannot be predicted. *Science*. 275, 5306, 1616. doi:10.1126/science.275.5306.1616

Hartmann, J., Berner, Z., Stüben, D., and Henze, N. (2005). A statistical procedure for the analysis of seismotectonically induced hydrochemical signals: a case study from the Eastern Carpathians, Romania. *Tectonophysics*. 405, 77–98. doi:10.1016/j.tecto.2005.05.014

Hattori, K., and Han, P. (2018). "Statistical analysis and assessment of ultralow frequency magnetic signals in Japan as potential earthquake precursors," in *Pre-earthquake processes. a multidisciplinary approach to earthquake prediction studies*. Editors D. Ouzounov, S. Pulinets, K. Hattori, and P. Taylor (John Wiley & Sons), 229–240.

Hayakawa, M., Asano, T., Rozhnoi, A., and Solovieva, M. (2018). "Very-low- to low-frequency sounding of ionospheric perturbations and possible association with earthquakes," in *Pre-earthquake processes. a multidisciplinary approach to earthquake prediction studies*. Editors D. Ouzounov, S. Pulinets, K. Hattori, and P. Taylor (John Wiley & Sons), 277–304.

Hayakawa, M. (2018). "Earthquake precursor studies in Japan," in *Pre-earthquake processes. a multidisciplinary approach to earthquake prediction studies*. Editors D. Ouzounov, S. Pulinets, K. Hattori, and P. Taylor (John Wiley & Sons), 7–18.

Hough, S. (2010). *Predicting the unpredictable. The tumultuous science of earthquake prediction*. Princeton: Princeton University Press, 280.

IASPEI (2020). Resolutions & statements. Available at: http://www.iaspei.org/documents/resolutions-statements (Accessed October 2020).

Jordan, T. H., ChenGasparini, Y.-T. P., Madariaga, R., Main, I., Marzocchi, W., Papadopoulos, G., et al. (2011). Operational Earthquake forecasting. state of knowledge and guidelines for utilization. Report by the International Commission on earthquake forecasting for civil protection. Istituto Nazionale di Geofisica e Vulcanologia. *Ann. Geophys*. 54 (4), 391.

Kagan, Y. Y. (1997). Are earthquakes predictable?. *Geophys. J. Int*. 131 (3), 505–525. doi:10.1111/j.1365-246X.1997.tb06595.x

Kelman, I. (2019). Axioms and actions for preventing disasters. *Prog. Disaster Sci*. 2, 100008. doi:10.1016/j.pdisas.2019.100008.

Main, I. (1999a). Is the reliable prediction of individual earthquakes a realistic scientific goal? *Nature*. doi:10.1038/nature28107

Main, I. (1999b). Earthquake prediction: concluding remarks. *Nature*. doi:10.1038/nature28133

Martinelli, G. (2020). Previous, current, and future trends in research into earthquake precursors in geofluids. *Geosciences*. 10, 189. doi:10.3390/geosciences10050189

Martinelli, G. (2018). "Contributions to a history of earthquake prediction research," in *Pre-earthquake processes. a multidisciplinary approach to earthquake prediction studies*. Editors D. Ouzounov, S. Pulinets, K. Hattori, and P. Taylor (John Wiley & Sons), 67–76.

Martinelli, G., and Dadomo, A. (2018). "Geochemical and fluid-related precursors of earthquakes: previous and ongoing research trends," in *Pre-earthquake processes. a multidisciplinary approach to earthquake prediction studies*. Editors D. Ouzounov, S. Pulinets, K. Hattori, and P. Taylor (John Wiley & Sons), 219–228.

Matthews, R. A. J. (1997). Decision-theoretic limits on earthquake prediction. *Geophys. J. Int*. 131 (3), 526–529. doi:10.1111/j.1365-246X.1997.tb06596.x.

Oh, H. Y., and Kim, G. (2015). A radon-thoron isotope pair as a reliable earthquake precursor. *Sci. Rep*. 5, 13084. doi:10.1038/srep13084

Ouzounov, D., Pulinets, S., Kafatos, M. C., and Taylor, P. (2018a). "Thermal radiation anomalies associated with major earthquakes," in *Pre-earthquake processes: a multidisciplinary approach to earthquake prediction studies*. Editors D. Ouzounov, S. Pulinets, K. Hattori, and P. Taylor (John Wiley & Sons), 259–274.

Ouzounov, D., Pulinets, S., Liu, J.-Y., Hattori, K., and Han, P. (2018b). "Multiparameter assessment of pre-earthquake atmospheric signals," in *Pre-earthquake processes: a multidisciplinary approach to earthquake prediction studies*. Editors D. Ouzounov, S. Pulinets, K. Hattori, and P. Taylor (John Wiley & Sons), 339–359.

Papadopoulos, G., Minadakis, G., and Orfanogiannaki, K. (2018). "Short-term foreshocks and earthquake prediction," in *Pre-earthquake processes: a multidisciplinary approach to earthquake prediction studies*. Editors D. Ouzounov, S. Pulinets, K. Hattori, and P. Taylor (John Wiley & Sons), 127–147.

Parrot, M., and Li, M. (2018). "Statistical analysis of the ionospheric density recorded by the DEMETER satellite during seismic activity," in *Pre-earthquake processes: a multidisciplinary approach to earthquake prediction studies*. Editors D. Ouzounov, S. Pulinets, K. Hattori, and P. Taylor (John Wiley & Sons), 319–328.

Peresan, A., Kossobokov, V., and Panza, G. F. (2012). Operational earthquake forecast/prediction. *Rend. Fis. Acc. Lincei*. 23, 131–138. doi:10.1007/s12210-012-0171-7

Peresan, A. (2018). "Recent developments in the detection of seismicity patterns for the Italian region," in *Pre-earthquake processes. a multidisciplinary approach to earthquake prediction studies*. Editors D. Ouzounov, S. Pulinets, K. Hattori, and P. Taylor (John Wiley & Sons), 149–171.

Polyakov, Y. S., Ryabinin, G. V., Solovyeva, A. B., and Timashev, S. F. (2015). Is it possible to predict strong earthquakes? *Pure Appl. Geophys*. 172 (7), 1945–1957.

Press, F. (1968). A strategy for an earthquake prediction research program. *Tectonophysics*. 6 (1), 11–15. doi:10.1016/0040-1951(68)90022-X

Pulinets, S., Ouzounov, D., Karelin, A., and Davidenko, D. (2018). "Lithosphere–atmosphere–ionosphere–magnetosphere coupling—a concept for pre-earthquake signals generation," in *Pre-earthquake processes: a multidisciplinary approach to earthquake prediction studies*. Editors D. Ouzounov, S. Pulinets, K. Hattori, and P. Taylor (John Wiley & Sons), 79–98.

Pulinets, S., Ouzounov, D., and Petrukhin, A. (2016). Multiparameter monitoring of short-term earthquake precursors and its physical basis. implementation in the Kamchatka region. *E3S Web Conf*. 11, 00019. 10.1051/e3sconf/20161100019

Radulian, M., Mandrescu, N., Panza, G. F., Popescu, E., and Utale, A. (2000). Characterization of seismogenic zones of Romania. *Pure Appl. Geophys*. 157, 57–77. doi:10.1007/PL00001100.

Rouet-Leduc, B., Hulbert, C., Lubbers, N., Barros, K., Humphreys, C. J., and Johnson, P. A. (2017). Machine learning predicts laboratory earthquakes. *Geophys. Res. Lett*. 44, 9276–9282. doi:10.1002/2017GL074677.

Ryabinin, G. V., Polyakov, Yu. S., Gavrilov, V. A., and Timashev, S. F. (2011). Identification of earthquake precursors in the hydrogeochemical and geoacoustic data for the Kamchatka peninsula by flicker-noise spectroscopy. *Nat. Hazards Earth Syst. Sci*. 11, 541–548. doi:10.5194/nhess-11-541-2011

Sammis, C. G., and Sornette, D. (2002). Positive feedback, memory, and the predictability of earthquakes. *Proc. Natl. Acad. Sci. U.S.A*. 99 (Suppl. 1), 2501–2508. doi:10.1073/pnas.012580999

Sgrigna, V., Buzzi, A., Conti, L., Picozza, P., Stagni, C., and Zilpimiani, D. (2007). Seismo-induced effects in the near-earth space: combined ground and space investigations as a contribution to earthquake prediction. *Tectonophysics*. 431 (1–4), 153–171. doi:10.1016/j.tecto.2006.05.034

Shebalin, P., Keilis-Borok, V., Gabrielov, A., Zaliapin, I., and Turcotte, D. (2006). Short-term earthquake prediction by reverse analysis of lithosphere dynamics. *Tectonophysics*. 413, 63–75. doi:10.1016/j.tecto.2005.10.033

Szakács, A. (2011). Earthquake prediction using extinct monogenetic volcanoes: a possible new research strategy. *J. Volcanol. Geotherm. Res*. 201, 404–411. doi:10.1016/j.jvolgeores.2010.06.015.

Telford, J., and Cosgrave, J. (2006). Tsunami evaluation coalition: synthesis report. London: TEC. Available at: https://www.sida.se/contentassets/f3e0fbc0f97c461c92a60f850a35dadb/joint-evaluation-of-the-international-response-to-the-indian-ocean-tsunami_3141.pdf (Accessed March 2020).

Tramutoli, V., Filizzola, C., Genzano, N., and Lisi, M. (2018a). "Robust satellite techniques for detecting preseismic thermal anomalies," in *Pre-earthquake processes: a multidisciplinary approach to earthquake prediction studies*. Editors D. Ouzounov, S. Pulinets, K. Hattori, and P. Taylor (John Wiley & Sons), 243–258.

Tramutoli, V., Genzano, N., Lisi, M., and Pergola, N. (2018b). "Significant cases of preseismic thermal infrared anomalies," in *Pre-earthquake processes. a multidisciplinary approach to earthquake prediction studies*. Editors D. Ouzounov, S. Pulinets, K. Hattori, and P. Taylor (John Wiley & Sons), 331–338.

Tsai, Y-B., Liu, J. Y., Shin, T.-C., Yen, H.-Y., and Chen, C.-H. (2018). "Multidisciplinary earthquake precursor studies in taiwan: a review and future prospects," in *Pre-earthquake processes. a multidisciplinary approach to earthquake prediction studies*. Editors D. Ouzounov, S. Pulinets, K. Hattori, and P. Taylor (John Wiley & Sons), 41–65.

Tsunogai, U., and Wakita, H. (1995). Precursory chemical changes in ground water: Kobe earthquake, Japan. *Science*. 269, 61–63. doi:10.1126/science.269.5220.61

U.S. Geological Survey (2013). *Earthquakes with 50,000 or more deaths*. Archive. Available at: http://earthquake.usgs.gov/earthquakes/world/most_destructive.php (Accessed March 2013).

Uyeda, S., and Nagao, T. (2018). "International cooperation in pre-earthquake studies: history and new directions," in *Pre-earthquake processes. a multidisciplinary approach to earthquake prediction studies*. Editors D. Ouzounov, S. Pulinets, K. Hattori, and P. Taylor (John Wiley & Sons), 3–6.

Varotsos, P., Alexopoulos, K., Nomicos, K., and Lazaridou, M. (1986). Earthquake prediction and electric signals. *Nature*. 322, 120. doi:10.1038/322120a0

Wang, H., Zhang, Y., Liu, J., Shen, X., Yu, H., Jiang, Z., et al. (2018). "Pre-earthquake observations and their application in earthquake prediction in China: a review of historical and recent progress," in *Pre-earthquake processes. a multidisciplinary approach to earthquake prediction studies*. Editors D. Ouzounov, S. Pulinets, K. Hattori, and P. Taylor (John Wiley & Sons), 19–39.

Wang, K., Chen, Q. F., Shihong, S., and Wang, A. (2006). Predicting the 1975 Haicheng earthquake. *Bull. Seismol. Soc. Am*. 96 (3), 757–795. doi:10.1785/0120050191.

Wyss, M. (1997). Second round of evaluations of proposed earthquake precursors. *Pure Appl. Geophys*. 149, 3–16. doi:10.1007/BF00945158.

Wyss, M. (2001). Why is earthquake prediction research not progressing faster? *Tectonophysics*. 338 (3–4), 217–223. doi:10.1016/S0040-1951(01)00077-4

Yuce, G., Ugurluoglu, D., Adar, N., and Oeser, V. (2010). Monitoring of earthquake precursors by multi-parameter stations in Eskisehir region (Turkey). *Appl. Geochem*. 25 (4), 572–579. doi:10.1016/j.apgeochem.2010.01.013

Zafrir, H., Barbosa, S., Levintal, E., Weisbrod, N., Horin5, Y. B., and Zalevsky, Z. (2020). The impact of atmospheric and tectonic constraints on radon-222 and carbon dioxide flow in geological porous media—a dozen-year research summary. *Front. Earth Sci*. 8, 433. doi:10.3389/feart.2020.559298

Zoran, M., Savastru, R., Savastru, D., Chitaru, C., Baschir, L., and Tautan, M. (2012). Monitoring of radon anomalies in South-Eastern part of Romania for earthquake surveillance. *J. Radioanal. Nucl. Chem*. 293, 769–781. 10.1007/s10967-012-1780-4.

Conflict of Interest: The author declares that the research was conducted in the absence of any commercial or financial relationships that could be construed as a potential conflict of interest.

Copyright © 2021 Szakács. This is an open-access article distributed under the terms of the Creative Commons Attribution License (CC BY). The use, distribution or reproduction in other forums is permitted, provided the original author(s) and the copyright owner(s) are credited and that the original publication in this journal is cited, in accordance with accepted academic practice. No use, distribution or reproduction is permitted which does not comply with these terms.

frontiers in Earth Science

ORIGINAL RESEARCH
published: 29 January 2021
doi: 10.3389/feart.2020.586279

Short-Term Seismic Precursor Anomalies of Hydrogen Concentration in Luojishan Hot Spring Bubbling Gas, Eastern Tibetan Plateau

Xiaocheng Zhou, Yucong Yan, Wenya Fang, Wanli Wang, Hongyu Shi and Pengfei Li*

Institute of Earthquake Forecasting, China Earthquake Administration, Beijing, China

The gas compositions (He, H_2, CO_2, CH_4, Ar and N_2) and isotope ratios ($^3He/^4He$ and $\delta^{13}C$) were yearly investigated from April 2010 to April 2019 at the Luojishan spring located in the proximity of the Zemuhe Fault, eastern Tibetan Plateau. The continuous automatic monitoring of hydrogen concentrations in Luojishan hot spring bubbling gas for the purpose of earthquake prediction requires the discrimination of seismic precursor anomalies. Helium isotope ratios ($^3He/^4He$) in the bubbling gas of hot springs varied from 0.05 to 0.18 Ra (Ra = $^3He/^4He = 1.39 \times 10^{-6}$ in the air), with a maximum mantle-derived He up to 2.2% of the total He measured in the Luojishan hot spring (assuming R/Ra = 8.0 for mantle). This suggests that Zemuhe Fault might act as a conduit for crustal-derived fluid. N_2 concentrations in the majority of the hot spring was ≥80 vol%, and $\delta^{13}C_{CO2}$ values varied from −13.2 to −9.3‰ (vs.PDB). Hydrogen concentration time series display a complex temporal pattern reflecting a wide range of different physical processes. There were short-term (5–60 h) seismic precursor anomalies of hydrogen concentration before natural earthquake. The anthropogenically-induced earthquakes provoke only post-earthquake responses. The concentration of hydrogen in bubbling gas of the Luojishan hot spring is sensitive to increase of stress in the Xianshuihe-Xiaojiang fault system. Monitoring the hydrogen concentrations with automatic gas stations may be promising tool for unraveling earthquake mechanisms and for predicting earthquakes.

Keywords: hydrogen, hot spring, zemuhe fault, earthquake forecasting, seismic precursor

OPEN ACCESS

Edited by:
Giovanni Martinelli,
National Institute of Geophysics and Volcanology, Italy

Reviewed by:
Zheming Shi,
China University of Geosciences, China
Selin Süer,
Middle East Technical University, Turkey

****Correspondence:***
Xiaocheng Zhou
zhouxiaocheng188@163.com

Specialty section:
This article was submitted to Geochemistry, a section of the journal Frontiers in Earth Science

Received: *22 July 2020*
Accepted: *23 December 2020*
Published: *29 January 2021*

Citation:
Zhou X, Yan Y, Fang W, Wang W, Shi H and Li P (2021) Short-Term Seismic Precursor Anomalies of Hydrogen Concentration in Luojishan Hot Spring Bubbling Gas, Eastern Tibetan Plateau. Front. Earth Sci. 8:586279. doi: 10.3389/feart.2020.586279

INTRODUCTION

Earthquake precursors are elusive, and this elusiveness has hampered earthquake prediction (Donald, 1988; Cicerone et al., 2009; Gherardi et al., 2017). The high uncertainty and low predictability of earthquakes during forecasting make earthquakes one of the worst natural disasters, which may lead to the instant loss of lives and properties (Gupta, 2001; Wen et al., 2008). The anomalously high concentration of helium, hydrogen, carbon dioxide and radon in hot spring bubbling gas have been widely studied in seismically active faults in recent years, especially in Japan, China, Italy and United States, in hunt of changes that might be premonitory of for earthquake prediction (King, 1986; Sugisaki and Sugiura, 1986; Nagamine, 1994; Cicerone et al., 2009; Babuška et al., 2016; Weinlich et al., 2016; Fischer et al., 2017; Huang et al., 2017). Temporal abnormal variations of gas (He, H_2, CO_2, Rn, CH_4) concentration have been observed with durations of a few hours to several days before and after a lot of large earthquakes at some gas monitoring stations at the

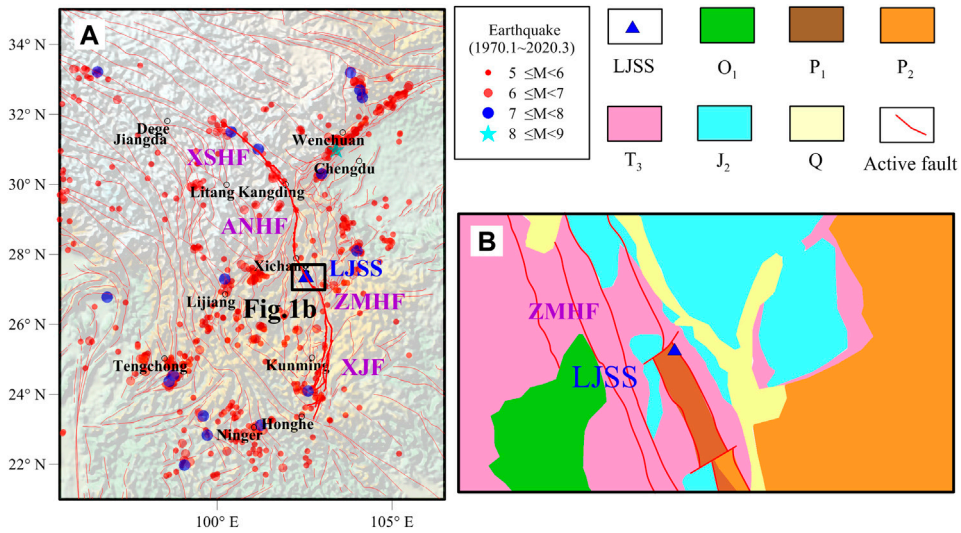

FIGURE 1 | Location of the Luojishan station (LJSS) **(A)** Topographic map of the east Tibetan Plateau. **(B)** Geological map of the Luojishan station and around are shown in **(A)**. Abbreviations: LMSF, Longmenshan Fault; ANHF, Anninghe Fault; XSHF, Xianshuihe Fault; ZMHF, Zemuhe Fault; XJF, Xiaojiang Fault.

epicentral distances of up to several hundreds of kilometers, which are usually related to the chemical and physical changes occurring in the active faults as enhanced/reduced water–rock interaction, crustal stress/strain, permeability structure, etc. before and after earthquakes (Sugisaki et al., 1983, 1996; Cicerone et al., 2009; Umeda et al., 2013; Weinlich et al., 2016). The large change of gas geochemical anomalies as regards shape, duration, delay/anticipation time and parameters-association with respect to foreshocks, main-shock and aftershocks are considered to be highly site specific (King, 1986; Sugisaki et al., 1996).

Noble gas and their isotopes are very good natural tracers for exploring crust-mantle interaction in different geologic background because they are chemically inert and thus their isotopic signature is conservative with respect to the source of gas/fluid in crustal water-rock interactions (Sano and Wakita., 1985; Hilton, 1996). The helium isotopes can provide clear evidence for the existence of mantle-derived fluids in the crust, ^{3}He is retained in the Earth's interior and essentially primordial, whereas ^{4}He is mainly produced in the crust by the decay of U and Th (Hilton, 1996; Hilton, 2007). The isotopic signatures of He showed some correlations with seismic activities (Sano and Marty, 1995; Kissin, 2007).

Hydrogen could play a very important role in mechanisms of process taking place in both the shallow and deep reservoirs (Zgonnik, 2020). Hydrogen in hot spring bubbling gas in active faults may be used in monitoring of earthquakes (Wakita et al., 1980; Sato et al., 1986). The increase of H_2 concentration may be correlated with 11 $M \geq 5$ earthquakes at some sites in the San Andreas Fault between July 1982 and November 1983 (Sato et al., 1986). The premonitory increases of the H_2 concentration in the bubbling gas of hot spring are geochemical signals of the earthquake nucleation process of stress-corrosion mechanism. In other words, aseismic slips before earthquakes might have enhanced H_2 production in pre-existing active fault planes by mechanochemical reaction of newly formed surface from fractured rock surface with water (Ito et al., 1999).

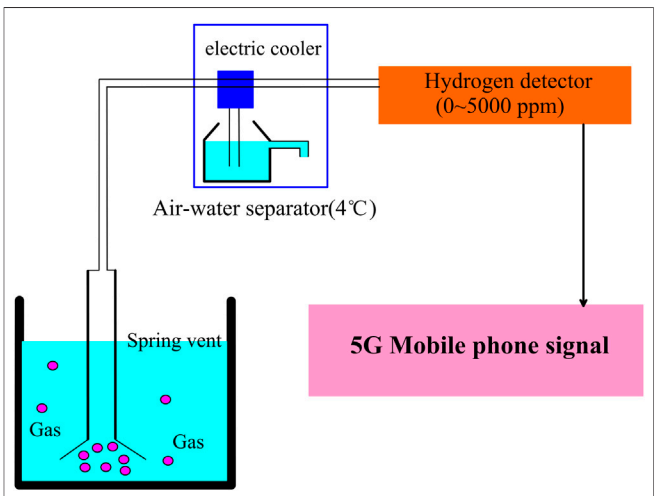

FIGURE 2 | Schematic diagram of H_2 concentration monitoring station.

The aim of this research was to 1) monitor the variations of gas and isotope composition at the Luojishan hot spring before, during and after seismic events, and 2) characterize the short-term seismic precursor anomalies of hydrogen concentration, 3) distinguish between the anomalies of hydrogen concentration induced by natural earthquake from the anomalies induced by anthropogenically-induced earthquakes.

Geological Setting

A huge left-lateral strike-slip active fault system in the eastern boundary of the Sichuan-Yunnan rhombus block in southwestern China contains four major faults named Anninghe Fault (ANHF), Zemuhe Fault (ZMHF), Xianshuihe Fault (XSHF), and Xiaojiang Fault (XJF), where the strongest seismicity in continental China occurs (Wen et al., 2008; Zhang, 2013). The ZMHF strikes

TABLE 1 | Gas and isotopic compositions of the Luojishan hot spring.

NO	Date		He	H_2	CO_2	CH_4	N_2	O_2	Ar	$^3He/^4He$	$^3He/^4He$		$\delta^{13}C_{CO2}$	$He_{mantle\text{-}derived}$
	(yyyy/mm/dd)		(ppm)	(ppm)	(%)	(%)	(%)	(%)	(%)	(R/Ra)	(Rc/Ra)	$^4He/^{20}Ne$	(‰)	(%)
1[a]	2008/6/20	T	1810.0		11.32		83.50	4.09	0.99	0.22			−11.2	
2[a]	2008/10/29	(℃)	1650.0		11.28		85.25	2.47	1.00	0.04	0.04	102.6	−12.2	0.47
3[a]	2009/6/22	43.8	1720.0		10.14	0.28	84.56	3.93	0.98	0.07	0.06	117.4	−10.8	0.80
4	2010/4/25	43.6	1540.0		10.44	0.00	86.15	2.30	0.99	0.05	0.05	99.1	−10.8	0.63
5	2010/6/16	44.0	1371.0		12.58	0.00	82.53	3.80	0.94	0.18	0.17	74.9	−10.8	2.16
6	2013/5/11	43.0	632.6	1.00	13.28		81.42	1.97	1.13	0.08	0.07	112.2	−9.3	0.91
7	2014/9/2	44.8	1800.0	0.00	7.42	0.04	90.69	0.37	1.23	0.05	0.05	83.6	−9.5	0.58
8	2015/7/18	44.5	1124.6	1.30	11.47	0.00	87.47	1.10	0.22	0.07	0.07	111.6	−10.6	0.85
9	2016/1/17	44.5	1279.5	1.00	12.66		83.51	1.35	1.26	0.06	0.05	37.3	−9.3	0.67
10	2017/1/8	44.5	1305.9	2.00	9.26	0.01	87.81	0.22	0.24	0.06	0.06	60.4	−11.8	0.69
11	2018/3/7	44.8	1483.0	1.00	13.06		83.45	0.16	0.93	0.06	0.06	96.7	−9.7	0.71
12	2019/4/19	43.3	1532.0	1.00	10.84	0.02	85.16	0.49	0.93	0.07	0.07	104.0	−13.2	0.84

[a]*Data come from Zhou et al. (2015).*

NNW–SSE and extends for about 120 km, which intersects the N–S-trending ANHF and XJF at an acute angle (**Figure 1**). The strain energy were released by the form of repeated large earthquakes in the ZMHF, which are caused by the southeastwards motion of the Tibetan Plateau (Ren et al., 2010).

Quaternary alluvial deposits are composed mainly of fine sand, sandy gravel, silt, and clay, and are widely distributed in the Luojishan hot spring. Cenozoic strata (Late Tertiary to Early Quaternary) consist mainly of interbedded sandstones and mudstones with thin layers of coal. The basement rock along the ZMHF consists mainly of metamorphic rocks including Pre-Cambrian rhyolite and granite, and Permian basalt and Triassic granite (He and Oguchi, 2008; Ren et al., 2010).

Historical earthquake records show there are three strong earthquakes over the last millennium in the ZMHF: the 814AD *M* 7.0 earthquake, and the 1536 *M* 7.5 earthquakes, and 1850 *M*7.5 Xichang earthquake (Wen et al., 2008). The historical seismicity indicates that the ZMHF is still active and the probability of a strong earthquake in the future is high (Wen et al., 2008; Ren et al., 2010).

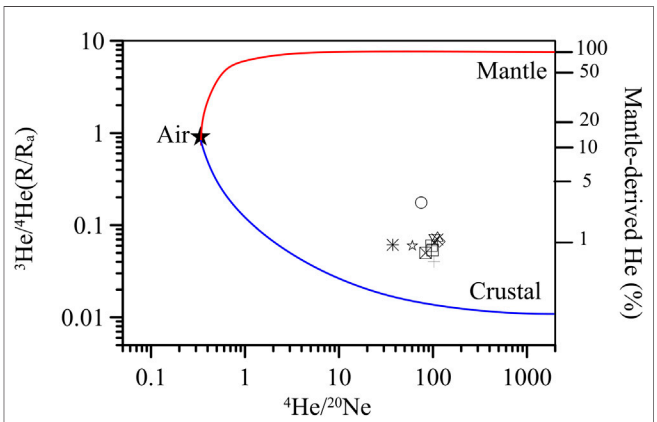

FIGURE 3 | Diagram of $^4He/^{20}Ne$ vs. $^3He/^4He$ (R/Ra) ratios. Mixing lines between the upper mantle and atmosphere , and the crust and atmosphere were calculated using the end members:upper mantle ($^4He/^{20}Ne$ = 100,000, $^3He/^4He = 12 \times 10^{-6}$) (Graham 2002), air ($^4He/^{20}Ne$ = 0.318, $^3He/^4He = 1.4 \times 10^{-6}$) (Ozima and Podosek, 1983), continental crust ($^4He/^{20}Ne$ = 100,000, $^3He/^4He = 0.02 \times 10^{-6}$) (Ballentine et al., 2005).

METHOD

Hot Spring Gas Sampling

Gas samples were nine times collected in Luojishan hot spring, using cylindroid bottles (500 ml) made of soda-lime glass from April 25, 2010 to April 19, 2019 (Zhou et al., 2017). The bubbling gas samples were immediately sent to the Key Laboratory of Petroleum Resources Research, Northwest Institute of Eco-Environment and Resources. The measurement of all samples was finished in 30 days.

The temperatures of Luojishan hot spring water were measured with a thermometer having an accuracy of 0.1°C. The composition of gas samples from Luojishan hot spring were analyzed with a Agilent Macro 3000 gas chromatography (Zhou et al., 2015; Zhou et al., 2020). Helium and Neon isotopes in the gas samples were measured using the Noblesse noble gas mass spectrometer. $^3He/^4He$ (R) > 1×10^{-7}, with a precision of ±10%, $1 \times 10^{-8} < {}^3He/^4He$ (R) < 1×10^{-7}, with a precision of ±15% (Cao et al., 2018). The measurements were normalized to standard atmospheric value. Carbon dioxide isotopic compositions in the bubbling gas samples were analyzed by the stable isotope ratio mass spectrometer (Thermo-Fisher Scientific Delta Plus XP) and the GC-IRMS analytical system gas chromatography (Agilent 6890) (Li et al., 2014). The values of $\delta^{13}C$ had a precision of ±0.5‰, and are reported relative to PDB in per mill (Li et al., 2014) .

Hydrogen Concentration of Hot Spring Gas

The continuous hydrogen monitoring was conducted in the Luojishan station at the middle of the XSHF-XJF system (**Figure 2**), which could monitor more earthquakes. The monitor environment is very stable. There is no industrial activity and mining around the monitor station. The depth of the hot spring pool is 1 m. The bubbling gas was collected by a

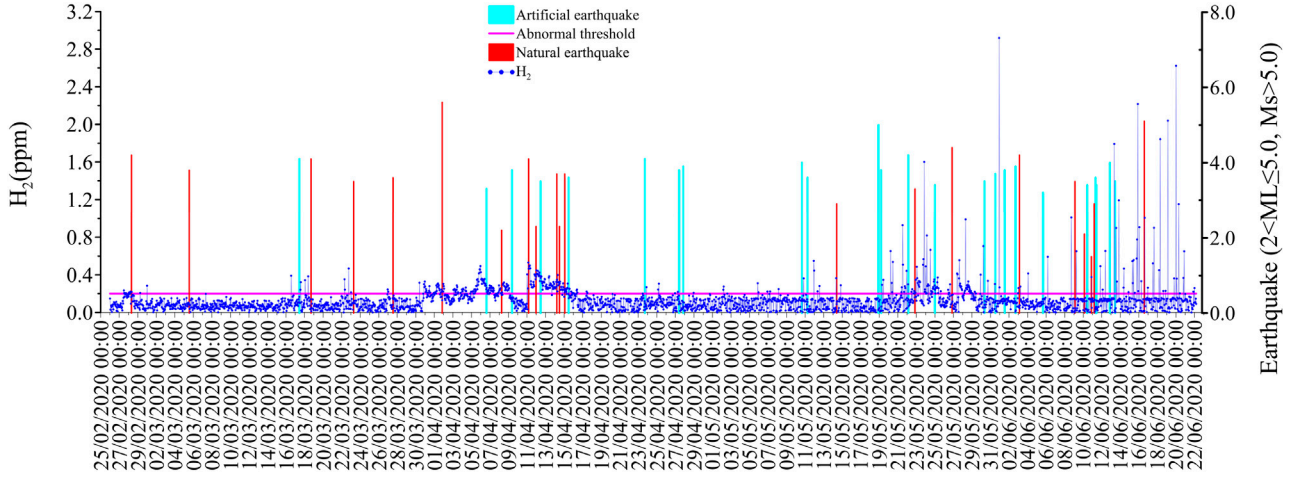

FIGURE 4 | Temporal variations of H_2 concentration in bubbling gas.

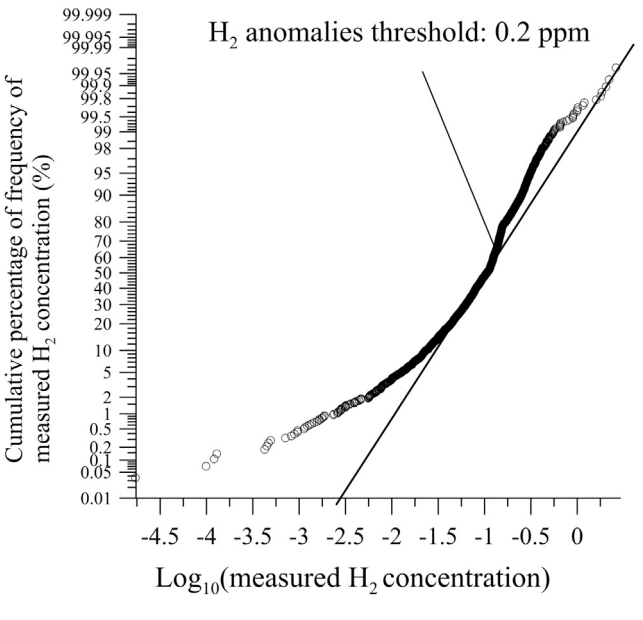

FIGURE 5 | Q–Q plot of H_2 concentration.

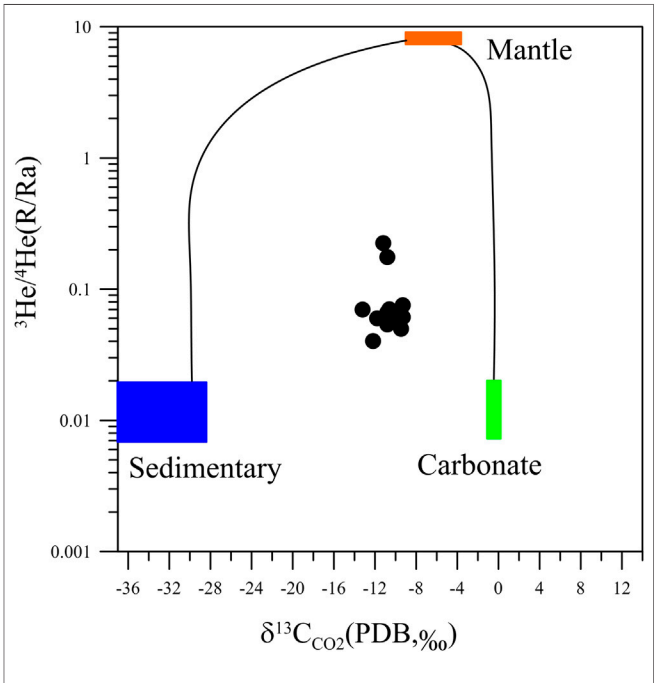

FIGURE 6 | Diagram of $^3He/^4He$ (R/Ra) vs. $\delta^{13}C_{CO2}$(PDB,‰) ratios.

funnel submerged at a depth of 1 m underwater (**Figure 2**). The bubbling gas was accumulated by a polytetrafluoroethylene (PTFE) pipe (length, $2m \times Ø_{outer\ diameter}$, $8cm \times Ø_{inner\ diameter}$, 6 cm). The humidity in the collected gas was reduced by an electric cooler in the unit. The hydrogen concentration is hourly monitored by the ATG-6118H automatic analyzer from 0.01 to 1000 ppm with precision of ±5%, which was calibrated and maintained by the instrument manufacturing company (Wen et al., 2018; NOA certification, 2019). All of the gas pipeline was well sealed, which wasn't affected by the air temperature, air humidity and rainfall. The data obtained by this system are sent to the laboratory located at Beijing via 5G mobile phone signal once an hour.

RESULTS

Chemical Composition of the Hot Spring Bubbling Gas

Gas collected at the Luojishan hot spring from the bubbling pools was characterized from April 25, 2010 to April 19, 2019 in detail (isotope ratios of CO_2, He and Ne and gas composition) (**Table 1**). The temperatures of Luojishan hot spring water ranged from 43°C to 44.8°C. The N_2 concentrations of hot spring gas samples were ≥80 vol%. Gas had relatively low concentrations of H_2 (≤2 ppm) and low to the detection limit

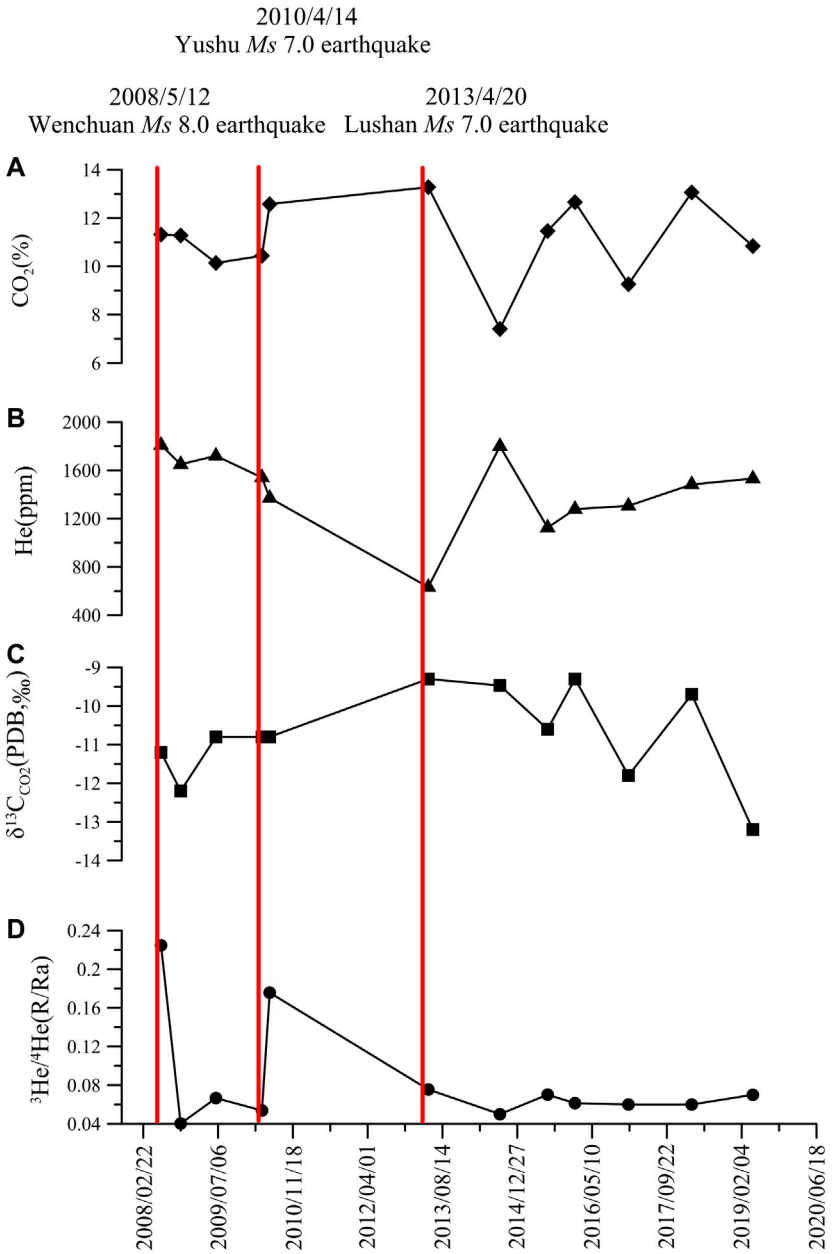

FIGURE 7 | Temporal variations of CO_2 concentration **(A)**, He concentration **(B)**, $\delta^{13}C_{CO2}$ (‰,PDB) values **(C)**, $^3He/^4He$ (R/Ra) **(D)** values in the spring gas samples.

of Macro 3000 gas chromatography. The gas samples had very higher concentrations of He (up to 1810 ppm). The concentration range of Ar in the bubbling gas was from 0.93 to 1.26%. The concentration of O_2 in the majority of bubbling gas samples was lower than 5%. Methane concentrations were lower than 1%.

He and Ne Isotopic Ratios

The $^3He/^4He$ ratios of the bubbling gas samples ranged from 0.04 to 0.22 Ra and were independent of the concentration of helium in each gas sample. **Figure 3** shows the relationships between the measured $^3He/^4He$ (R/Ra) and $^4He/^{20}Ne$ ratios. The $^4He/^{20}Ne$ and $^3He/^4He$ ratios suggest that all samples were from a mixing region with three end members: crustal-derived helium, mantle-derived helium and atmospheric helium dissolved in water. $^4He/^{20}Ne$ ratios ranged from 37.3 to 117.4, above the atmospheric background ($^4He/^{20}Ne = 0.318$, Ozima and Podosek, 1983). The $^4He/^{20}Ne$ ratios indicated that the gas samples had minimal atmospheric contamination (**Figure 3**). The Rc/Ra values are the corrected $^3He/^4He$ ratios (R/Ra) for air contamination (Jenkins, 1982; Sano and Wakita, 1985). The Rc/Ra values ranged from 0.04 to 0.17 (**Table 1**) in the bubbling gas of Luojishan hot spring.

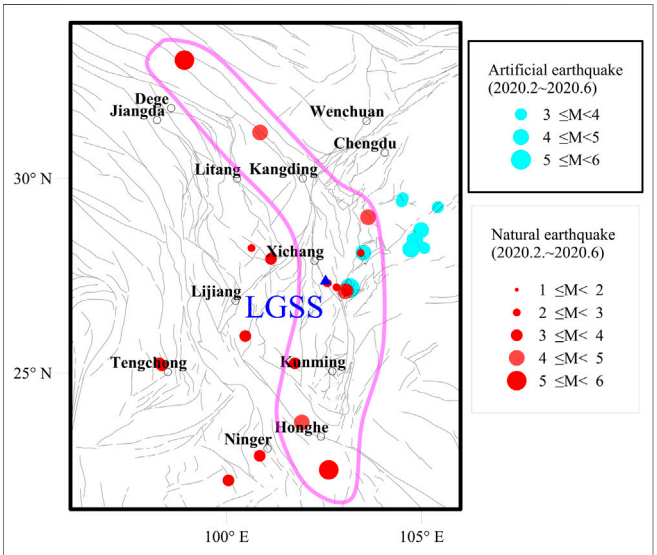

FIGURE 8 | Location of natural and artificial earthquake during the period of monitoring.

H_2 Concentration in Hot Spring Gas

There were 2813 observed values of H_2 concentration from 26 February to June 22, 2020 (**Figure 4**). The H_2 concentration ranged from 0.01 to 2.91 ppm (**Figure 4**), with average H_2 concentration, 0.13 ppm. The anomalous threshold was 0.2 ppm (**Figure 5**), which was determined by the Q-Q plot, which is a method of determining threshold values between background and anomalous geochemical data, based on partitioning a cumulative probability plot of the data (Sinclair, 1991).

DISCUSSION

Origin of He, CO_2, and H_2

He

The mixing proportion of mantle-derived He and crustal-derived He was estimated by using the Sano and Wakita (1985) equation's system (**Figure 3**). The proportion of mantle-derivd He varies from 0.47 to 2.16% at the Luojishan hot spring (**Table 1**). The radiogenic crustal-derived He was dominant in most of the bubbling gas samples in the Luojishan hot spring.

The majority of bubbling gas samples from the Luojishan hot spring have significantly lower $^3He/^4He$ signatures with $^3He/^4He$ < 0.1 Ra (mantle-derived He < 1%), (**Figure 3**, **Table 1**), indicative of crustal-derived ^4He production, with no resolvable mantle-derived contribution. The bubbling gas of Luojishan hot springs also have the highest concentrations of ^4He (**Table 1**), up to two orders of magnitude (1810 ppm) greater than the Longtougou hot springs (~5 ppm) in the Kangding city (Zhou et al., 2015).

CO_2

The end-member compositions for mantle carbon (M), sedimentary organic carbon (S) and lime stones (L) are $\delta^{13}C_{CO2}$ = −30, −6.5, and 0‰; and $^3He/^4He$ (R/Ra) = 0.02 and 8, respectively (Sano and Marty 1995). The trajectories for binary mixing between M and S, M and L, and L and S are shown in the diagram.

Combination of helium and carbon isotopes can provide more information of the carbon sources (Hilton, 1996). The main sources of carbon include the marine limestones, upper-mantle degassing, and the oxidation of organic carbon from sedimentary rocks. These main carbon sources have distinct $\delta^{13}C$ end-members, whereby upper-mantle degassing ranges between −9 and −4‰, sedimentary organic matter has $\delta^{13}C$ close to −30‰ and marine limestone has $\delta^{13}C$ close to 0‰ (Sano and Marty, 1995). **Figure 6** shows the analytical results of Luojishan hot spring gas. It is then clear that all Luojishan hot spring gas are plotted within the two mixing lines.This feature strongly suggests that CO_2 in Luojishan hot spring gases is released from three different sources: crustal metamorphic, mantle and organic components.

H_2

The origins of the hydrogen are most likely attributed to: **(A)** hydrogen generation from water-rock reactions. The abiotic H_2 is generated by the reaction of water with ultrabasic rocks or serpentinization under near-surface conditions and migration from the deep reservoirs (Lollar et al., 2014; Parnell and Blamey, 2017; Irfan et al., 2019; Wang et al., 2019; Wang et al., 2020), **(B)** the interaction of water with freshly exposed rock surfaces (Hirose et al., 2011), **(C)** mixing with the considerable amount of microbial H_2 from the biological activity and decomposition of organic matter (Prinzhofer et al., 2019; Myagkiy et al., 2020).

Temporal Variations of $^3He/^4He$ and $\delta^{13}C$ Values

The $\delta^{13}C_{CO2}$ values evidently increased from 2008 to 2016 in the Luojishan hot spring, whereas afterward, they showed an opposite trend from 2016 to 2019. These indicated that the proportion of CO_2 derived from limestone increased in the bubbling gas of Luojishan hot springs, which were related with the enhanced degassing of the triggering of the Wenchuan *Ms* 8.0 earthquake, Yushu *Ms* 7.0 earthquake and Lushan *Ms* 7.0 earthquake (**Figure 7**). The clear decrease of the $\delta^{13}C_{CO2}$ values measured from 2016 to 2019 would imply decrease of CO_2 derived from limestone and the relative increase of CO_2 from sedimentary organic, which is back to background level before Wenchuan *Ms* 8.0 earthquake. Due to the higher content of helium in the Luojishan hot spring gas, the $^3He/^4He$ ratios drop from 0.22 Ra down to 0.07 Ra from June 20, 2008 to June 22, 2009 at the Luojishan hot spring was observed after the Wenchuan *Ms* 8.0 earthquake due to the release of crustal-derived components. The $^3He/^4He$ ratios increased on June 16, 2010 after Yushu *Ms* 7.0 earthquake (April 14, 2010) in Luojishan hot spring, but He, CO_2 concentration and $\delta^{13}C_{CO2}$ isotope changed weakly. This is attributable to distance of epicenter 800 km. Yushu *Ms* 7.0 earthquake could trigger limitedly crustal-derived ^4He and CO_2, and

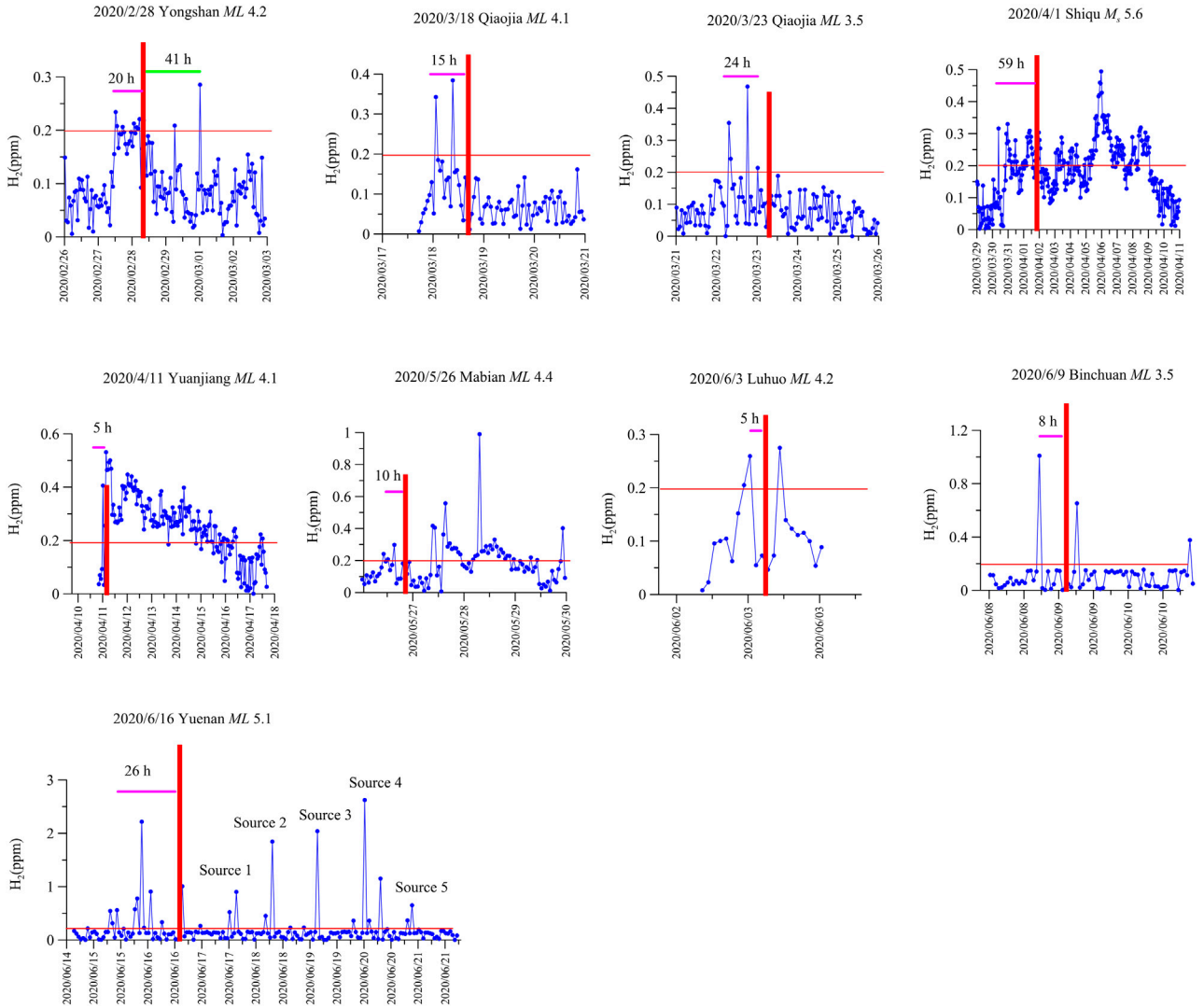

FIGURE 9 | Precursor anomalies induced by natural earthquake.

$\delta^{13}C_{CO2}$ isotope. The mantle-derived He was sensitive to Yushu *Ms* 7.0 earthquake. The $^{3}He/^{4}He$ ratios weakly increased after Lushan *Ms* 7.0 earthquake. The mantle-derived helium in the bubbling gas of hots springs was estimated that up to 62% in the Kangding region in June 2008 after Wenchuan *Ms* 8.0 earthquake. Over time, the proportion of the mantle-derived fluid contribution to the bubbling gas gradually decreased, but the crustal-derived gas components: CO_2 and CH_4 derived from organic matter and radiogenic He increased (Zhou et al., 2015). The Longtougou and Luojishan hot spring are in same strain field (XSHF, ANHF, ZMHF, XJF), which is a huge left-lateral strike-slip active fault system. A maximum shear strain rate of 40–60 nanostrain/yr is found along the XSHF-XJF system, which delineates the north and east boundaries of the crustal materials undergoing large-scale clockwise rotation around the eastern Himalaya syntaxis (Wang and Shen, 2020). The earthquake may play a very important role in He degassing in bubbling gas of hot spring from the active faults (Sano et al., 1998).

Temporal Variations of Hydrogen Concentration

Natural Earthquake Induced Precursor Anomalies

There were obvious short-term (5–60 h) seismic precursor anomalies of H_2 concentration of the Luojishan hot spring gas before some natural earthquakes from 26 February to June 21, 2020 (**Figures 8**, **9**, **Table 2**). When the stress increase up to sub-instability stress state of the faults in the XSHF-XJF system, earthquakes were occurred (Ma, 2016). The concentration of hydrogen in bubbling gas is sensitive to increase of stress in the XSHF-XJF system, which could enhance the opening of microfractures under the Luojishan

TABLE 2 | Seismic data is related to natural and artificial earthquakes recorded during the course of monitoring.

Time	Artificial earthquake	Natural earthquake	Location	Epicentral distance	Longitude	Latitude	Focal depth	Duration of preseismic precursor (h)	Types of earthquake	
(YYYY/MM/DD HH:mm)	Magnitude	Magnitude			(km)	(°)	(°)	(km)	(h)	
2020/2/28 7:56		4.2	ML	Yongshan	122.6	103.510	28.090	12	20	N
2020/3/5 13:23		3.8	ML	Muli	150.0	101.140	27.930	11		N
2020/3/17 10:30	4.1		ML	Changning	279.0	104.990	28.670	10		I
2020/3/18 16:43		4.1	ML	Qiaojia	60.3	103.050	27.100	8	15	N
2020/3/23 7:10		3.5	ML	Qiaojia	61.7	103.080	27.120	8	24	N
2020/3/27 13:07		3.6	ML	Simao	531.4	100.850	22.870	13	15	N
2020/4/1 20:23		5.6	Ms	Shiqu	717.2	98.920	33.040	10	59	N
2020/4/6 15:01	3.3		ML	Xingwen	264.7	105.070	28.210	8		I
2020/4/8 6:06		2.3	ML	Puge	6.3	102.540	27.341	8		N
2020/4/9 9:14	3.8		ML	Junlian	229.8	104.720	28.140	8		I
2020/4/11 4:03		4.1	ML	Yuanjiang	412.4	101.930	23.730	9	5	N
2020/4/11 23:19		2.3	ML	Puge	11.1	102.594	27.310	16		N
2020/4/12 11:06	3.5		ML	Rongxian	294.0	104.490	29.410	8	15	I
2020/4/14 5:10		3.7	ML	Lancang	626.1	100.050	22.240	11		N
2020/4/14 12:00		2.3	ML	Puge	11.7	102.598	27.306	14		N
2020/4/14 12:01		2.1	ML	Puge	10.0	102.565	27.311	15		N
2020/4/15 1:39		3.7	ML	Tengchong	484.7	98.340	25.200	13		N
2020/4/15 1:46		3.6	ML	Tengchong	487.1	98.280	25.250	12		N
2020/4/15 11:35	3.6		ML	Luxian	349.8	105.420	29.260	8		I
2020/4/23 17:04	4.1		ML	Changning	253.0	104.840	28.420	8		I
2020/4/27 9:37	3.8		ML	Gongxian	236.9	104.780	28.180	9		I
2020/4/27 20:19	3.9		ML	Qiaojia	65.0	103.150	27.180	11		I
2020/5/10 15:42	4		ML	Gongxian	232.8	104.740	28.170	11		I
2020/5/11 6:09	3.6		ML	Changning	247.9	104.770	28.440	10		I
2020/5/14 9:41		2.9	ML	Leibo	116.6	103.440	28.080	117		N
2020/5/18 21:47	5		Ms	Qiaojia	65.9	103.160	27.180	8		R
2020/5/19 4:35	3.8		ML	Qiaojia	65.9	103.160	27.180	8		R
2020/5/22 3:12	4.2		ML	Gongxian	230.5	104.710	28.180	8		I
2020/5/22 20:32		3.3	ML	Lufeng	251.5	101.750	25.250	15		N
2020/5/25 0:01	3.4		ML	Gongxian	234.4	104.770	28.140	8		I
2020/5/26 20:34		4.4	ML	Muchuan	207.7	103.630	29.000	14	10	N
2020/5/30 8:30	3.5		ML	Yongshan	122.7	103.520	28.080	11		N
2020/5/31 12:25	3.7		ML	Gongxian	234.5	104.740	28.210	8		I
2020/6/1 12:42	3.8		ML	Junlian	229.8	104.720	28.140	8		I
2020/6/2 16:39	3.9		ML	Gongxian	231.8	104.720	28.190	13		I
2020/6/3 2:57		4.2	ML	Luhuo	451.0	100.860	31.180	14	5	N
2020/6/5 15:49	3.2		ML	Gongxian	234.7	104.760	28.170	7		I
2020/6/9 2:39		3.5	ML	Binchuan	260.4	100.480	25.950	9	8	N
2020/6/10 3:03		2.1	ML	Ningnan	35.3	102.820	27.200	17		N
2020/6/10 10:20	3.4		ML	Gongxian	238.0	104.760	28.250	9		I
2020/6/10 21:08		1.5	ML	Puge	2.2	102.530	27.380	4		N
2020/6/11 4:29		2.9	ML	Muli	207.5	100.640	28.210	16		N
2020/6/11 7:47	3.6		ML	Rongxian	302.6	104.520	29.490	9		I
2020/6/11 10:25	3.4		ML	Gongxian	232.4	104.740	28.160	7		I
2020/6/12 21:03	4		ML	Gongxian	232.7	104.730	28.190	8		I
2020/6/13 10:32	3.5		ML	Gongxian	237.7	104.780	28.200	9		I
2020/6/16 14:12		5.1	ML	Vietnam	543.6	102.620	22.510	8	26	N

N, natural earthquake; I, injection-induced seismicity; R, reservoir-induced earthquake.

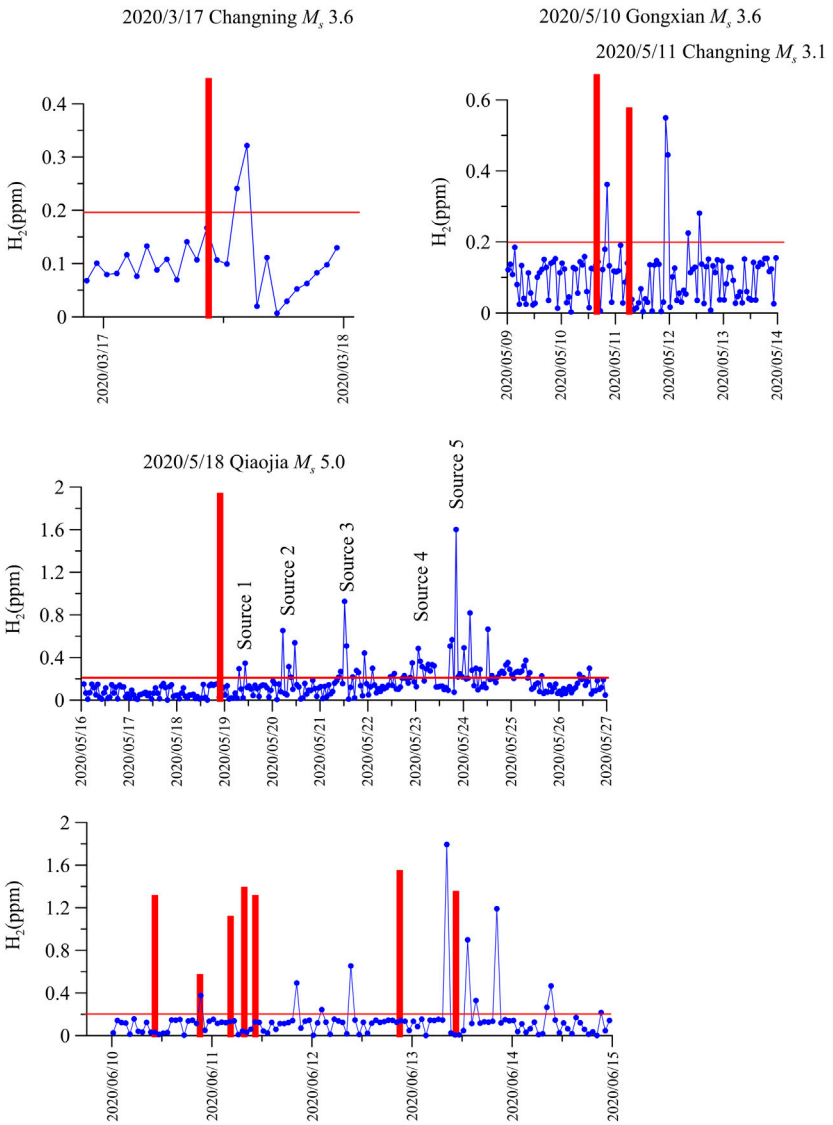

FIGURE 10 | Precursor anomalies induced by artificial earthquakes.

hot spring. According to the variation characteristics of the stress and strain, the anomalies of H_2 concentration have different characteristics. It exhibits a persistent stress increase most probably caused by a persistent contribution of the different depths and gas caused by the strain release before the natural seismic events (Cicerone et al., 2009; Crampin et al., 2015). Anomalous precursory (anomalous threshold was 0.2 ppm) changes in the diffuse emission of H_2 in hot spring have been observed before some of the micro-seismicity of the April 11, 2020 Puger earthquakes with distance of epicenter, 6.3 km. A significant increase (up to 0.32 ppm) in H_2 concentration was detected 60 h before a Shiqu *Ms* 5.6 earthquake on April 1, 2020, 717 km away from the Liojishan station. The anomalies of H_2 concentration are just one or two points of data before earthquake, which could be induced by pulsed stress increases in the XSHF-XJF system. In addition, pre- and post-seismic variations of H_2 concentration have also been observed related to the occurrence of a seismic swarm beneath ZMHF (**Figures 8**, **9**, **Table 2**).

It is suggested that observed preseismic precursor of H_2 concentration are geochemical signals of the earthquake preparation process due to stress-corrosion (Ito et al., 1999). Dynamic disturbances of frictional contacts in the fault planes by seismic waves may also account for co-and post-seismic increases in H_2 (Kita et al., 1982). Seismicity may induce permeability enhancement of fault fractures (Hirose et al., 2011). The Luojishan gas monitoring system is sensitive enough to quantify emission during periods of intense seismic activities. According to characteristic of short term precursors of H_2 concentration in Luojishan hot spring from February 23, 2020 to March 31, 2020, a day before the Shiqu *Ms* 5.6 earthquake on

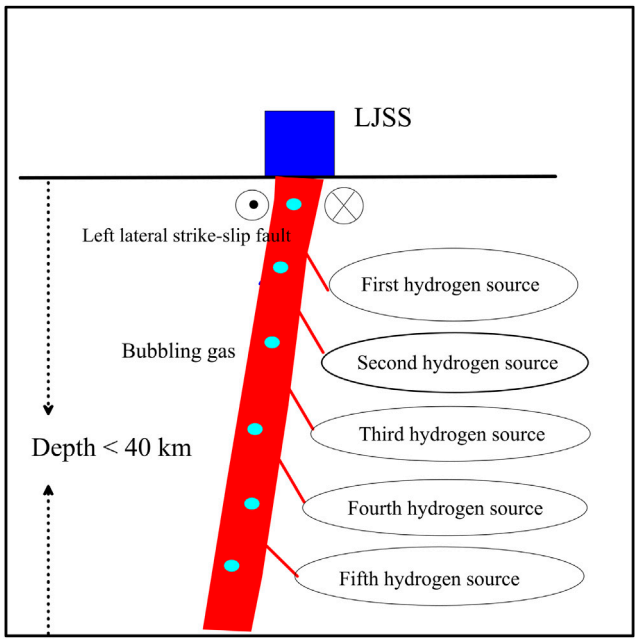

FIGURE 11 | Schematic diagram of hydrogen sources in Luojishan hot spring bubbling gas.

April 1, 2020 and Vietnam *ML*5.1 earthquake on June 16, 2020, forecasting informations (in the coming 24 h, in the eastern Tibetan Plateau, around *Ms* 5.0) were suggested to department of forcasting, institute of earthquake forcasting, China Earthquake administration. There were obvious persistent precursor anomalies of H_2 concentration of the Luojishan hot spring gas before the Shiqu *Ms* 5.6 earthquake and Vietnam M_L5.1 earthquake. The mechanism of precursor anomalies may be persistent stress increase before the natural seismic events in the XSHF-XJF system.

Hydrologic responses to earthquakes depend on earthquake magnitudes and distances from epicenters (Wang and Manga, 2010; Cox et al., 2015). Therefore it is difficult to identify short-term seismic precursory anomaly systematically by some criterias on the basis of several earthquakes (M > 5.0). After hundreds of natural earthquake (M > 5.0) were collected and analyzed, the formula about precursor anomalies and earthquake magnitude, epicentral distance may be summarized and some criterias may be provided.

Artificial Earthquake Trigger Anomalies

The earthquakes may trigger anomalies over great (>300 km) distances from the epicenter, but a robust relationship between post-seismic anomalies and seismic activity remains elusive. The relationship between a hot spring response and dynamic stresses propagated by surface waves, were demonstrated by changes in H_2 emissions measured by the gas monitoring station. The positive hot spring gas responses with the spike-like anomalies are identified if the post-earthquake H_2 mass was larger than the anomalies threshold of H_2 concentration. Micro-seismicity induced by injection in shale gas exploration in Changning (Liu et al., 2020) occurred repeatedly during the monitoring period. Qiaojia *Ms* 5.0 earthquake on May 18, 2020 was induced by Xiluodu reservoir filling (Liao et al., 2020). Artificial earthquakes (ML ≥ 3.0) triggered geochemical post-seismic anomalies were repeatedly observed (**Figure 10**, **Table 2**). The minimum artificial earthquakes, which may triggered geochemical post-seismic anomalies, can be estimated by a lot of seismic data in future.

Modeling of Migration of H_2 in Hot Spring Gas in the Zemuhe Fault

The positive post-earthquake H_2 anomalies responses with the five spike-like anomalies were observed from 18 to 25 May after Qiaojia *Ms* 5.0 earthquake on May 18, 2020 (**Figure 9**). This phenomenon were repeatedly observed after Vietnam *ML* 5.1 earthquake on June 16, 2020 (**Figure 10**). A model is developed to explain the observations of the changed mixing ratio among five hydrogen sources systems (**Figure 11**) as a result of a pressure disturbance triggered by seismic waves passing the Luojishan monitoring station. This model requires the existence of i) a mixed gas system with a high H_2 concentration contrast among the five sources with different depth in fault, ii) Five confined, stress sensitive fractures where five fluid components circulate along macro-fractures and where the gas components enter the ZMHF by diffusion through micro-fractures, iii) Five free bubbling gas phase in the fractures, and iv) a chance for free gas bubbles to rise toward the earth's surface before being trapped under an impermeable cover, which collects gas. The passing seismic waves may enhance the local pore pressure. Increased pressure changes in the mixing ratio in favor of the gas components which circulates through the macro-fractures (Kissin, 2007). Five hydrogen sources systems were simultaneously triggered by seismic waves. Hydrogen of five sources entered simultaneously into the main fracture of ZMHF. Since the depth of five hydrogen sources were different, the time of arrival of Hydrogen of five sources were diferent. The model provides a plausible physical and chemical explanations for the anomalies triggered by earthquake. There are a lot of free parameters in the model which are poorly resolved. Because helium isotope ratios (R/Ra) of the gas samples was 0.07 Ra on April 19, 2019, the ZMHF was a conduit for dominant crustal-derived fluid. The depth of Moho surface is ~40 km (Teng et al., 2014). The H_2 coming from fifth source migrated upward monitoring station during five days. The ascending velocity of H_2 is difficultly estimated. The depth of the fifth source of H_2 is shallower than 40 km.

CONCLUSION

1) Helium isotope ratios in Luojishan hot springs gas varied from 0.05 to 0.18 Ra, with mantle-derived He up to 2.2% in the Luojishan hot spring indicated the radiogenic crustal-derived He was dominant in most of the bubbling gas samples in the Luojishan hot spring. N_2 concentrations were ≥80 vol% and O_2 contents were lower than 5% in the majority of hot spring gas samples.

2) The time series of hydrogen concentration display a complex temporal pattern reflecting a wide range of different physical processes. There were clear short-term (5–60 h) seismic precursor anomalies of hydrogen concentration related with the epicentral distance and magnitude of earthquake before natural earthquake, with post-seismic response. The artificial earthquake only induced the post-seismic responses.
3) Monitoring the hydrogen concentrations with automatic gas stations may be promising tool for unraveling earthquake mechanisms and for predicting earthquakes. More parameters (He, CO_2, water temperature) may be monitored in the future studies to get a better insight into the possible relationships between earthquakes and gas geochemistry.

DATA AVAILABILITY STATEMENT

The raw data supporting the conclusions of this article will be made available by the authors, without undue reservation.

AUTHOR CONTRIBUTIONS

All authors have made a substantial, direct, and intellectual contribution to the work and approved it for publication.

FUNDING

This research was supported by National Key Research and Development Project (2017YFC1500501) and, the National Natural Science Foundation of China (41673106), The Special Fund of the Institute of Earthquake Forecasting, China Earthquake Administration (2017IES010205, 2016IES010304, 2018IEF010104, 2020IEF0604, 2020IEF0703).

ACKNOWLEDGMENTS

The authors are grateful to Prof. Fang Du and Prof. Hong Fu for her assistance with field work.

REFERENCES

Babuška, V., Růžek, B., and Dolejš, D. (2016). Origin of earthquakes warms in the western Bohemian Massif:Is the mantle CO_2 degassing, followed by the Cheb Basin subsidence, an essential driving force?. *Tectonophysics* 668–669, 42–51. doi:10.1016/j.tecto.2015.12.008

Ballentine, C. J., Marty, B., Sherwood Lollar, B., and Cassidy, M. (2005). Neon isotopes constrain convection and volatile origin in the Earth's mantle. *Nature* 433, 33–38. doi:10.1038/nature03182

Cao, C. H., Zhang, M. J., Tang, Q. Y., Yang, Y., Lv, Z. G., Zhang, T. W., et al. (2018). Noble gas isotopic variations and geological implication of Longmaxi shale gas in Sichuan Basin, China. *Mar. Petrol. Geol.* 89, 38–46. doi:10.1016/j.marpetgeo.2017.01.022

Cicerone, R. D., Ebel, J. E., and Britton, J. (2009). A systematic compilation of earthquake precursors. *Tectonophysics* 476 (3–4), 371–396. doi:10.1016/j.tecto.2009.06.008

Cox, S. C., Menzies, C. D., Sutherland, R., Denys, P. H., Chamberlain, C., and Teagle, D. A. H. (2015). Changes in hot spring temperature and hydrogeology of the Alpine Fault hanging wall, New Zealand, induced by distal South Island earthquakes. *Geofluids* 15, 216–239. doi:10.1111/gfl.12093

Crampin, S., Gao, Y., and Bukits, J. (2015). A review of retrospective stress-forecasts of earthquakes and eruptions. *Phys. Earth Planet. In.* 24, 76–87. doi:10.1016/j.pepi.2015.05.008

Donald, T. (1988). Geochemical precursors to seismic activity. *Pure Appl. Geophys* 126 (2-4), 241–266.

Fischer, T., Matyska, C., and Heinicke, J. (2017). Earthquake-enhanced permeability-evidence from carbon dioxide release following the M_L 3.5 earthquake in West Bohemia. *Earth Planet Sci. Lett.* 460, 60–67. doi:10.1016/j.epsl.2016.12.001

Gherardi, F., Pierotti, L., and Vista, A. D. (2017). Water-rock interactions in a site investigated for geochemical precursors of earthquakes: the pieve fosciana spring (Italy). *Earth Planet Sci. Lett.* 17, 360–363. doi:10.1016/j.proeps.2016.12.091

Graham, D. W. (2002). "Noble gas isotope geochemistry of mid-ocean ridge and ocean island basalts: characterization of mantle source reservoirs," in *Noble gases in geochemistry and cosmochemistry, reviews in mineralogy and geochemistry* (Washington), Vol. 47(1), 247–317. doi:10.2138/rmg.2002.47.8

Gupta, H. K. (2001). Short-term earthquake forecasting may be feasible at Koyna, India. *Tectonophysics* 338 (3–4), 353–357. doi:10.1016/s0040-1951(01)00083-x

He, H., and Oguchi, T. (2008). Late Quaternary activity of the Zemuhe and Xiaojiang faults in southwest China from geomorphological mapping. *Geomorphology* 96, 62–85. doi:10.1016/j.geomorph.2007.07.009

Hilton, D. R. (1996). The helium and carbon isotope systematics of a continental geothermal system: results from monitoring studies at Long Valley Caldera (California, U.S.A). *Chem. Geol.* 127, 269–295. doi:10.1016/0009-2541(95)00134-4

Hilton, D. R. (2007). Geochemistry. The leaking mantle. *Science* 318, 1389–1390. doi:10.1126/science.1151983

Hirose, T., Kawagucci, S., and Suzuki, K. (2011). Mechanoradical H_2 generation during simulated faulting: Implications for an earthquake-driven subsurface biosphere. *Geophys. Res. Lett.* 38, L17303. doi:10.1029/2011gl048850

Huang, F., Li, M., Ma, Y., Han, Y., Tian, L., Yan, W., et al. (2017). Studies on earthquake precursors in China: A review for recent 50 years. *Geod Geodyn.* 8 (1), 1–12. doi:10.1016/j.geog.2016.12.002

Irfan, M., Zhou, L., Bai, Y., Yuan, S., Liang, T. T., Liu, Y. F., et al. (2019). Insights into the hydrogen generation from water-iron rock reactions at low temperature and the key limiting factors in the process. *Int. J. Hydrogen Energy* 44 (33), 18007–18018. doi:10.1016/j.ijhydene.2019.05.086

Ito, T., Nagamine, K., Yamamoto, K., Adachi, M., and Kawabe, I. (1999). Preseismic hydrogen gas anomalies caused by stress-corrosion process preceding earthquakes. *Geophys. Res. Lett.* 26 (13), 2009–2012. doi:10.1029/1999gl900407

Jenkins, W. J. (1982). Tritium and ^{3}He in the Sargasso Sea. *J. Mar. Res.* 40, 533–569

King, C. Y. (1986). Gas geochemistry applied to earthquake prediction: an overview. *J. Geophys. Res.* 91, 12269–12281. doi:10.1029/jb091ib12p12269

Kissin, I. G. (2007). New data on crustal sensitive zones and formation of precursors and postseismic responses to earthquakes. *Russ. Geol. Geophys.* 48 (5), 429–441. doi:10.1016/j.rgg.2005.12.001

Kita, I., Matuo, S., and Wakita, H. (1982). H_2 generation by reactionbetween H_2O and crushed rock:An experimental study on H_2 degassing from the active fault zone. *J. Geophys. Res.* 87 (B13), 10789–10795. doi:10.1029/jb087ib13p10789

Li, Z. P., Wang, X. B., Li, L. W., Zhang, M. J., Tao, M. X., Xing, L. T., et al. (2014). Development of new method of δ^{13}C measurement for trace hydrocarbons in natural gas using solid phase micro-extraction coupled to gas chromatography isotope ratio mass spectrometry. *J. Chromatogr. A* 1372, 228–235. doi:10.1016/j.chroma.2014.10.089

Liao, L., Li, P., Yang, J., and Feng, J. (2020). The simulation of rupture dynamics from potential earthquakes around XiLuoDu reservoir dam, China. *Phys. Earth Planet. In.* 302, 106488. doi:10.1016/j.pepi.2020.106488

Liu, J., and Zahradník, J. (2020). The 2019 MW 5.7 changning earthquake, China: a shallow doublet with different faulting styles. Geophys. *Res. Lett*. 47. doi:10.1029/2019GL085408

Lollar, B. S., Onstott, T. C., Lacrampe-Couloume, G., and Ballentine, C. J. (2014). The contribution of the Precambrian continental lithosphere to global H2 production. *Nature* 516, 379–382. doi:10.1038/nature14017

Ma, J. (2016). On "whether earthquake precursors help for prediction do exist". *Chin. Sci. Bull.* 61, 409–414 [in Chinese]. doi:10.1360/n972015-01239

Myagkiy, A., Brunet, F., Popov, C., Krüger, R., Guimarães, H., Sousa, R. S., et al. (2020). H_2 dynamics in the soil of a H_2-emitting zone (São Francisco Basin, Brazil): Microbial uptake quantification and reactive transport modelling. *Appl. Geochem.* 112, 104474. doi:10.1016/j.apgeochem.2019.104474

Nagamine, K. (1994). Origin and coseismic behavior of mineral spring gas at Byakko, Japan, studied by automated gas chromatographic analyses. *Chem. Geol.* 114 (1–2), 3–17. doi:10.1016/0009-2541(94)90038-8

NOA certification (2019). Validity of the certificate:2019/7/25~2020/7/25. Certificate Number:NOA1994077. Available at: http://www.noagroup.org/certificate, http://cx.cnca.cn/CertECloud/result/skipResultList

Ozima, M., and Podosek, F. A. (1983). *Noble gas geochemistry*. Cambridge: Cambridge University Press, 367.

Parnell, J., and Blamey, N. (2017). Global hydrogen reservoirs in basement and basins. *Geochem. Trans.* 18, 2. doi:10.1186/s12932-017-0041-4

Prinzhofer, A., Moretti, I., Françolin, J., Pacheco, C., D'Agostino, A., Werly, J., et al. (2019). Natural hydrogen continuous emission from sedimentary basins: The example of a Brazilian H_2-emitting structure. *Int. J. Hydrogen Energy* 44 (12), 5676–5685. doi:10.1016/j.ijhydene.2019.01.119

Ren, Z., Lin, A., and Rao, G. (2010). Late Pleistocene–Holocene activity of the Zemuhe Fault on the southeastern margin of the Tibetan Plateau. *Tectonophysics* 495 (3–4), 324–336. doi:10.1016/j.tecto.2010.09.039

Sano, Y., and Marty, B. (1995). Origin of carbon in fumarolic gas from island arcs. *Chem. Geol.* 119 (1-4), 265–274. doi:10.1016/0009-2541(94)00097-r

Sano, Y., Takahata, N., Igarashi, G., Koizumi, N., and Sturchio, N. (1998). Helium degassing related to the Kobe earthquake. *Chem. Geol.* 150 (1-2), 171–179. doi:10.1016/s0009-2541(98)00055-2

Sano, Y., and Wakita, H. (1985). Geographical distribution of $^3He/^4He$ ratios in Japan: implications for arc tectonics and incipient magmatism. *J. Geophys. Res.* 90 (B10), 8729–8741. doi:10.1029/jb090ib10p08729

Sato, M., Sutton, A. J., McGee, K. A., and Russell-Robinson, S. (1986). Monitoring of hydrogen along the San Andreas and Calaveras faults in central Californiain 1980-1984. *J. Geophys. Res.* 91 (B12), 12315–12326. doi:10.1029/jb091ib12p12315

Sinclair, A. J. (1991). A fundamental approach to threshold estimation in exploration geochemistry: Probability plots revisited. *J. Geochem. Explor.* 41 (1-2), 1–22. doi:10.1016/0375-6742(91)90071-2

Sugisaki, R., Ido, M., Takeda, H., Isobe, Y., Hayashi, Y., Nakamura, N., et al. (1983). Origin of hydrogen and carbon dioxide in fault gases and its relation to fault activity. *J. Geol.* 91 (3), 239–258. doi:10.1086/628769

Sugisaki, R., Ito, T., Nagamine, K., and Kawabe, I. (1996). Gas geochemical changes at mineral springs associated with the 1995 southern Hyogo earthquake (M = 7.2), Japan. *Earth Planet Sci. Lett.* 139 (1-2), 239–249. doi:10.1016/0012-821x(96)00007-6

Sugisaki, R., and Sugiura, T. (1986). Gas anomalies at three mineral springs and a fumarole before an inland earthquake, central Japan. *J. Geophys. Res.* 91 (B12), 12296–12304. doi:10.1029/jb091ib12p12296

Teng, J., Deng, Y., Badal, J., and Zhang, Y. (2014). Moho depth, seismicity and seismogenic strcture in China mainland. *Tectonphysics* 627, 108–121. doi:10.1016/j.tecto.2013.11.008

Umeda, K., Asamori, K., and Kusano, T. (2013). Release of mantle and crustal helium from a fault following an inland earthquake. *Appl. Geochem.* 37, 134–141. doi:10.1016/j.apgeochem.2013.07.018

Wakita, H., Nakamura, Y., Kita, I., Fujii, N., and Notsu, K. (1980). Hydrogen release: New indicator of fault activity. *Science* 210, 188–190. doi:10.1126/science.210.4466.188

Wang, C. Y., and Manga, M. (2010). Hydrologic responses to earthquakes and a general metric. *Geofluids* 10, 206–216. doi:10.1111/j.1468-8123.2009.00270.x

Wang, J., Watanabe, N., Okamoto, A., Nakamura, K., and Komai, T. (2019). Acceleration of hydrogen production during water-olivine-CO_2 reactions via high-temperature-facilitated Fe(II) release. *Int. J. Hydrogen Energy* 44 (23), 11514–11524. doi:10.1016/j.ijhydene.2019.03.119

Wang, J., Watanabe, N., Okamoto, A., Nakamura, K., and Komai, T. (2020). Characteristics of hydrogen production with carbon storage by CO_2-rich hydrothermal alteration of olivine in the presence of Mg–Al spinel. *Int. J. Hydrogen Energy* 45 (24), 13163–13175. doi:10.1016/j.ijhydene.2020.03.032

Wang, M., and Shen, Z. K. (2020). Present-day crustal deformation of continental China derived from GPS and its tectonic implications. *J. Geophys. Res.: Solid Earth* 125, e2019JB018774. doi:10.1029/2019JB018774

Weinlich, F. H., Gaždová, R., Teschner, M., and Poggenburg, J. (2016). The October 2008 Nový Kostel earthquake swarm and its gas geochemical precursor. *Geofluids* 16 (5), 826–840. doi:10.1111/gfl.12187

Wen, L., He, L., Feng, E., Lian, K., Chen, Q., Zhang, L., et al. (2018). Calibration, Performance Testing and Their Results of the Automatic Trace Hydrogen Analyzer ATG-6118H. *Earthq. Res. China* 34 (3), 571–579 [in Chinese with English abstract].

Wen, X., Ma, S., Xu, X., and He, Y. (2008). Historical pattern and behavior of earthquake ruptures along the eastern boundary of the Sichuan-Yunnan faulted-block, southwestern China. *Phys. Earth Planet. In.* 168 (1-2), 16–36. doi:10.1016/j.pepi.2008.04.013

Zgonnik, V. (2020). The occurrence and geoscience of natural hydrogen: A comprehensive review. *Earth Sci. Rev.* 203, 103–140. doi:10.1016/j.earscirev.2020.103140

Zhang, P. (2013). A review on active tectonics and deep crustal processes of the Western Sichuan region, eastern margin of the Tibetan Plateau. *Tectonophysics* 584, 7–22. doi:10.1016/j.tecto.2012.02.021

Zhou, X., Wang, W., Chen, Z., Yi, L., Liu, L., Xie, C., et al. (2015). Hot spring gas geochemistry in western Sichuan Province, China after the Wenchuan *Ms* 8.0 earthquake. *Terr. Atmos. Oceanic Sci.* 26 (4), 361–373. doi:10.3319/tao.2015.01.05.01(tt)

Zhou, X., Liu, L., Chen, Z., Cui, Y., and Du, J. (2017). Gas geochemistry of the hot spring in the Litang fault zone, Southeast Tibetan Plateau. *Appl. Geochem.* 79, 17–26. doi:10.1016/j.apgeochem.2017.01.022

Zhou, X., Wang, W., Li, L., Hou, J., Xing, L., Li, Z., et al. (2020). Geochemical features of hot spring gases in the Jinshajiang-Red River fault zone, Southeast Tibetan Plateau. *Acta Petrol. Sin*. 36 (7), 2197–2214 [in Chinese with English abstract]. doi:10.18654/1000-0569/2020.07.18

Conflict of Interest: The authors declare that the research was conducted in the absence of any commercial or financial relationships that could be construed as a potential conflict of interest.

Copyright © 2021 Zhou, Yan, Fang, Wang, Shi and Li. This is an open-access article distributed under the terms of the Creative Commons Attribution License (CC BY). The use, distribution or reproduction in other forums is permitted, provided the original author(s) and the copyright owner(s) are credited and that the original publication in this journal is cited, in accordance with accepted academic practice. No use, distribution or reproduction is permitted which does not comply with these terms.

frontiers in Earth Science

BRIEF RESEARCH REPORT
published: 05 February 2021
doi: 10.3389/feart.2020.586283

New Possible Earthquake Precursor and Initial Area for Satellite Monitoring

Atanas Vasilev[1], Milen Tsekov[2], Petar Petsinski[1], Konstantin Gerilowski[3], Violeta Slabakova[1], Dimitar Trukhchev[4], Emil Botev[5], Orlin Dimitrov[1], Nikolai Dobrev[6] and Dimitar Parlichev[1]*

[1]Institute of Oceanology, Bulgarian Academy of Sciences, Varna, Bulgaria, [2]Department of Meteorology and Geophysics, Faculty of Physics, Sofia University "St. Kliment Ohridski", Sofia, Bulgaria, [3]Institute of Environmental Physics, University of Bremen, Bremen, Germany, [4]Institute of Metal Science, equipment, and technologies with Center for Hydro- and -Aerodynamics "Acad. A. Balevski", Bulgarian Academy of Sciences, Varna, Bulgaria, [5]National Institute of Geophysics, Geodesy and Geography, Bulgarian Academy of Sciences, Sofia, Bulgaria, [6]Geological Institute, Bulgarian Academy of Sciences, Sofia, Bulgaria

We propose a new possible earthquake precursor, a coastal water jet originating from shallow water gas seeps and colored by sediments, lifted from increased gas seeps emissions, preceding some earthquakes with offshore epicenters along the Bulgarian Black Sea coast and M ≥ 3. The new possible earthquake precursor is site specific and may be observed in shallow coastal water regions where active faults are accompanied by hydrocarbon gas seeps. We point out to a region where it can be easily detected by direct observation and satellite remote sensing, Zelenka methane seeps (ZMS), near the Bulgarian Black Sea coast. The ZMS activation is related to the tectonic stress and fracturing preceding and accompanying the earthquakes in the Shabla-Kaliakra-Balchik region along the northern part of the Bulgarian Black Sea coast. We also propose an earthquake forecasting experiment, based on the following four hypotheses: 1) The change of the methane emission of shallow horizons is related to crustal strain changes preceding earthquakes in the region; 2) extreme change of the activity of underwater methane seepages appears immediately before nearby earthquakes; 3) shallow water methane seepages activity can be monitored by remote sensing; 4) satellites can register effects from an extreme increase in their emissions. The proposed earthquake forecasting experiment is based on the monitoring of methane seepages activity in the ZMS area by direct observation and remote sensing which may provide indication for preparatory earthquake activity preceding offshore earthquakes in the region.

Keywords: earthquake precursor, methane, seeps, active faults, satellite images, Black Sea

OPEN ACCESS

Edited by:
Giovanni Martinelli, National Institute of Geophysics and Volcanology, Italy

Reviewed by:
Boyko Ranguelov, University of Mining and Geology "Saint Ivan Rilski," Bulgaria
Luca Piroddi, University of Cagliari, Italy

****Correspondence:***
Atanas Vasilev
gasberg@mail.bg

Specialty section:
This article was submitted to Solid Earth Geophysics, a section of the journal Frontiers in Earth Science

Received: *23 July 2020*
Accepted: *28 December 2020*
Published: *05 February 2021*

Citation:
Vasilev A, Tsekov M, Petsinski P, Gerilowski K, Slabakova V, Trukhchev D, Botev E, Dimitrov O, Dobrev N and Parlichev D (2021) New Possible Earthquake Precursor and Initial Area for Satellite Monitoring. Front. Earth Sci. 8:586283. doi: 10.3389/feart.2020.586283

INTRODUCTION

Paradoxically, no one seismologist denies that possible earthquake precursors exist, but not everyone believes that short-term forecast is possible based on their study (Ouzounov et al., 2018). Recently, increasingly complex methods are proposed in earthquake prediction research. Unique and high-precision equipment is used to study precursory variations of radon (Sabbarese et al., 2020), groundwater level (Nakagawa et al., 2019), tilt (Zhou et al., 2019), electromagnetic field (Florios et al., 2020), thermal radiation (Wei et al., 2019), outgoing long waves (Xiong and Shen, 2017), electron content in the ionosphere (Kelley et al., 2017), etc. Despite these efforts reliable short-term earthquake prediction methods are still elusive and searching for new earthquake precursors continues.

Recently, several studies demonstrated relationships between earthquake occurrences and underwater gas seepages (Nikonov, 2002; Gasperini et al., 2012; Fischer et al., 2013; Geersen et al., 2016; Géli et al., 2018; Bonini, 2019). It has been found that the great Maule earthquake in 2010 had caused new gas seepage off the coast of Chile (Geersen et al., 2016). Fischer et al. (2013) demonstrate an increase in the upward flux of gas-hydrate-derived methane after the strong 1945 Makran earthquake. Gasperini et al. (2012) demonstrate the correlation between tectonic structures and gas seepages at the seafloor along the North Anatolian Fault in the eastern Sea of Marmara and suggest that it is an interesting region for searching fluid exhalations as an earthquake precursor. Géli et al. (2018) find that aftershocks following the M 5.1 earthquake of July 25th, 2011, in the western Sea of Marmara, occur within a zone of gas overpressuring, further demonstrating relationships between seismic activity and gas dynamics along the North Anatolian Fault. Nikonov (2002) provides evidence for fire columns observed off the coast during the 1927 Crimea earthquakes probably related to self-ignition of underwater methane seepages. All these studies present evidence for coseismic and postseismic methane seepage changes or a correlation between tectonic faults and methane seepage sources. There are some papers relating gas seepage related precursory phenomena to seismic activity. Soter (1999) presents evidence for a number of precursory phenomena, including bubbling of the sea, observed prior to the M 6.2 Aigion, Greece earthquake, some of which may be considered as symptoms of gas venting. Khilyuk et al. (2000) also point out that prior to the Northridge, California earthquake of 1994 significant increase in the offshore hydrocarbon seepage has been observed but was attributed to a malfunction of the measuring device. To our knowledge, observed gas seepage related precursory phenomena have not been used as a testable tool for earthquake forecasting.

Here we propose a new possible site specific earthquake precursor (a coastal water jet originating from shallow water gas seeps and colored by sediments, lifted from increased gas seeps' emissions) and we point out a monitoring area, Zelenka methane seeps (ZMS), near the Bulgarian Black Sea coast where the new possible precursor is easily observed. We find an extreme increase in both the seeps' area and discharge 4 days before the strongest offshore earthquake near the Bulgarian Black Sea coast in recent decades (Md 4.7, August 5, 2009; Tsekov et al., 2019) occurring in a close proximity to the ZMS. We also find that the precursory jet with a diameter of ~8 km is observed on a sequence of satellite images with a resolution of 250 m (NASA Earth Data, 2020). We further document and discuss the relation between methane seeps activity and seismic activity in the highly seismic offshore Black Sea region near cape Kaliakra by finding evidence for increased methane seepage activity preceding some $M \geq 3$ earthquakes in the same region.

The new possible precursor is related to the common cause of earthquake precursors, the tectonic stress and the fluids properties in the Earth's crust. It is specific to coastal regions and may be important for earthquake prediction in such often densely populated regions where the population and infrastructure are threatened by both earthquakes (Géli et al., 2018) and tsunamis (Bryant, 2018).

We discuss the suitability of the Zelenka methane seeps area as an observation point to study the new possible earthquake precursor and the possibility to organize regular observations in the region providing information on the methane seeps activity not only as a possible earthquake precursor but also as a viable source of information on environmental change processes.

MATERIALS AND METHODS

Black Sea: Properties and Seismic Activity

The Black Sea is a semienclosed basin, characterized by strong stratification, the presence of oxygen-free water layer, mud volcanoes, freshwater springs, methane sources and gas hydrates (GH), etc. The Black Sea deep water is the biggest anoxic methane and hydrogen sulfide reservoir of the world (Reeburgh et al., 1991) (87% of the water volume). It is known that the first sample with natural GH was recovered in 1972 by a gravity corer in the Danube Fan (Yefremova and Zhizhchenko, 1974). A circum-Black Sea belt of gas flares marks the lateral boundary of the GH stability zone (Vassilev, 2006). The basin is almost aseismic during the last century. Seismic activity is restricted to the periphery of the basin. Seismic activity of the region may trigger earthquake tsunamis (Bryant, 2018), mud volcano eruptions, and coastal land and underwater landslides. There is a close geophysical and hydrodynamic connection between many of these processes. Some of them may be dangerous or even catastrophic, while others may have important practical applications.

The seismicity of the Black Sea increases toward the margins of the basin. The most active regions are offshore Bulgaria, Crimea, Georgia, and Turkey. The depths of the earthquake hypocenters are up to about 35 km. Only few earthquakes are registered in the abyssal part of the basin. An unexpected result from CRIMEA project was that areas with mud volcanoes are completely aseismic (Vassilev et al., 2006), in contrast to the strong time and space correlations between mud volcanoes and earthquake epicenters in the Caspian Sea.

The focal mechanisms show primarily N-S compression. The westward motion of the Anatolian Plate and N-S deformation of the Caucasus take up most of the motion of the Arabian Plate and only ~1 mm year^{-1} is transmitted through the Pontides to compress the Black Sea in N-S direction (Kalafat, 2017). The two strongest earthquakes in our area are an exception with focal mechanisms with primarily E-W compression with some N-S component and oblique strike-slip faulting (Kalafat, 2017).

The available information on the Black Sea tsunami can be divided into two types: historical (which is descriptive) and a limited number of modern data records from tide gauge measurements. A summary analysis can be found in Dotsenko and Ingerov (2007). According to sea level measurements, the highest recorded Black Sea tsunami height is 0.52 m, while visual estimates of tsunami height ~1–2 m exist (Dotsenko and Ivanov, 2010).

Bulgarian Coastal Gas Seeps

About 50 areas with underwater gas seeps are identified near the Bulgarian Black Sea coast (Dimitrov, 2002). The gas is mainly methane (Dimitrov et al., 1979). The first documented underwater gas seeps are observed (Palii et al., 1951) at

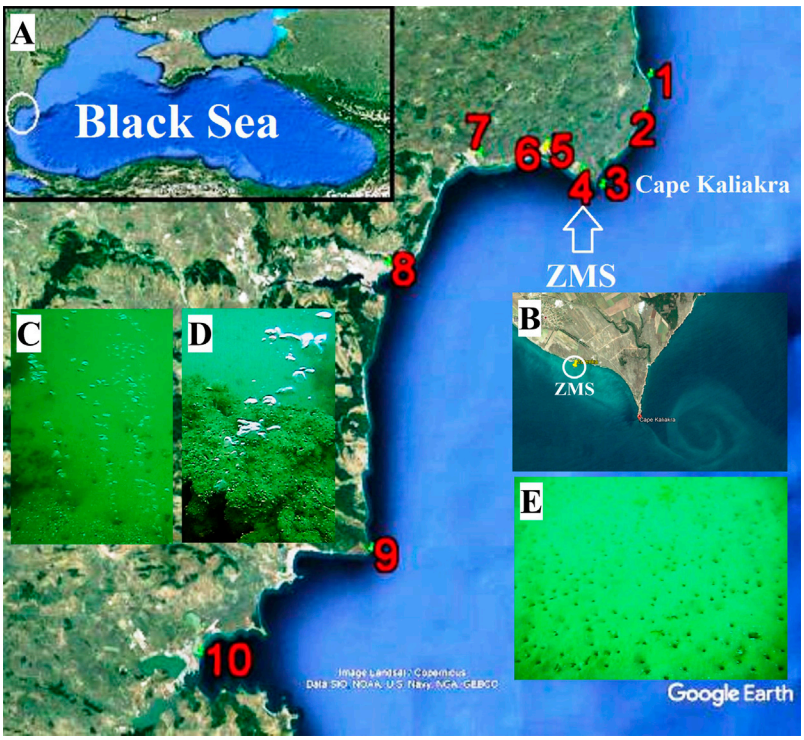

FIGURE 1 | (A) Black Sea (in the upper left corner) and the area of interest (enlarged). Numbers designate geographical locations discussed in the text: 1) cape Shabla, 2) Tyulenovo, 3) cape Kaliakra, 4) Zelenka, 5) cape Chirakman, 6) Town of Kavarna, 7) Town of Balchik, 8) City of Varna, 9) Cape Emine, 10) City of Bourgas (Google Earth™); **(B)** cape Kaliakra and ZMS (Google Earth™); **(C)** methane seeps from the seafloor covered by sand and clay aleurites; **(D)** ZMS outcrops of Sarmatian limestone; **(E)** photo of the ZMS seafloor with inactive microcraters at water depth ~9 m from Sep. 10, 2009, obtained 36 days after the Md = 4.7 earthquake (underwater photos K. Gerilowski).

Aladja Bank (between Varna and Balchik, see **Figure 1**). Later, underwater gas seeps areas along the Bulgarian coast zone are observed at Tsarevo, Rosen (Mandev et al., 1978), Kamchia, Rusalka, Shabla, and Tulenovo (Dimitrov et al., 1979).

Zelenka Methane Seeps

Intensive gas seeps from the seafloor are observed at least from a century in the area of the fisherman hut "Zelenka." The area, known as Zelenka methane seeps, is located 3 km to the west of cape Kaliakra (**Figures 1A,B**). According to the first investigations (Dimitrov et al., 1979): 1) the seepage area of ~29,000 m^2 is located 170–270 m of the coast and its size is 550× (25–100) m; 2) most of the seeps are at water depths 5–10 m; 3) sand and clay aleurites with outcrops of Sarmatian limestones cover the seafloor (**Figures 1C,D**); 4) the gas is mainly methane (93–96%) and nitrogen (4–5%) and the rest is divided between O_2, CO_2, and C_2H_6; 5) the discharge of a seep is ≤4 $lmin^{-1}$ and the ZMS annual discharge is ~0.04 km^3year^{-1} (37.5 × 10^6 m^3year^{-1}).

Historical Earthquakes and Tsunamis in the Shabla-Kaliakra-Balchik Region

Shabla-Kaliakra-Balchik region (43.0N-44.3N; 27.75E-30.0E) (Tsekov et al., 2019) where the methane seeps zone Zelenka is located is characterized by moderate seismic activity in recent decades. It is distributed on a multitude of intersecting onshore and offshore faults. In the past, several strong earthquakes hit the region. According to historical records, the settlements in the region suffered damage from earthquakes and even tsunamis (Papadopoulos et al., 2011; Oaie et al., 2016). In the first century BC, Strabo mentioned that the ancient Bizone (modern Kavarna, see **Figure 1A**) was destroyed in 64 BC–19 AD and the lobe part of cape Chirakman with the houses of the richest citizens sunk in the sea (Papadopoulos et al., 2011; Peev, 2016). Two strong historical earthquakes with not well-defined epicenters but possibly related to the Shabla-Kaliakra-Balchik zone occurred in 543 AD and 1444 AD (Guidoboni et al., 1994; Ranguelov, 2008; Oaie et al., 2016).

The strongest regional earthquake in recent times occurred on March 31, 1901, 07:12:24 with an epicenter on an offshore fault near Port Balchik, 22 km west from Zelenka. The estimated parameters of the quake are Mw 7.2, MMI X, and depth 14 km. The quake generated widespread landslides and rockfalls along the shore.

The quality of the information about the seismic activity in the region improved significantly after 1986, several years after starting of operation of the Bulgarian National Seismic Network in 1980 (Botev et al., 2013; Tsekov et al., 2019). In the recent decades, information on the weak seismicity in the Shabla-Kaliakra-Balchik region is also available, with a magnitude of completeness Mc = 2,2 (Tsekov et al., 2019).

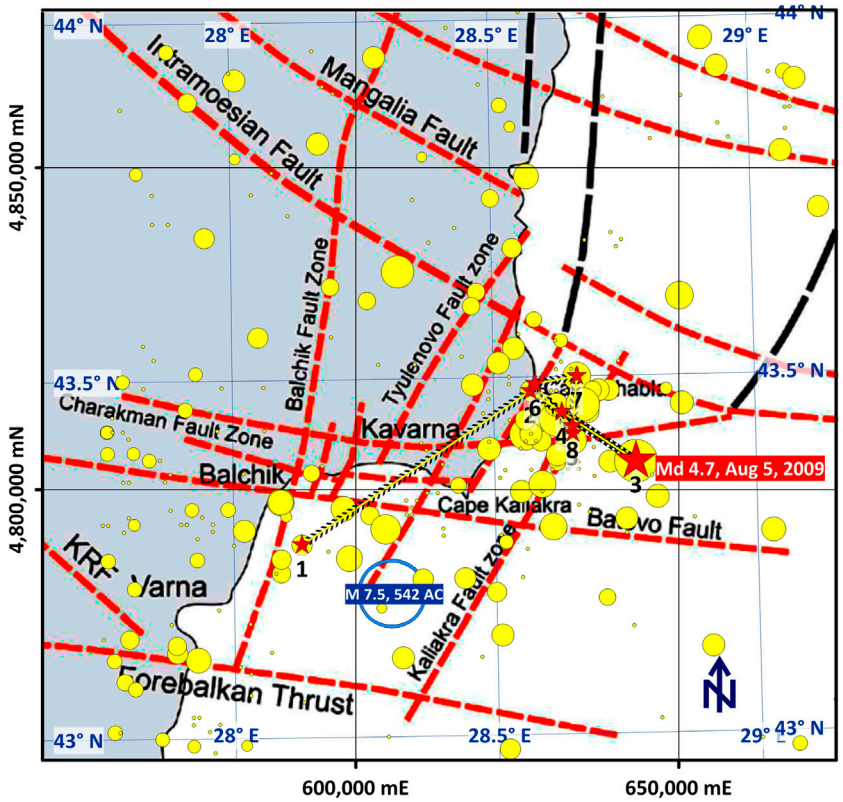

FIGURE 2 | The Shabla-Kaliakra-Balchik seismic region: main faults and registered earthquakes over the period 1986–2014 (after Oaie et al., 2016 and Tsekov et al., 2019). Yellow dots represent earthquake epicenters. With a red star is represented the strongest earthquake in the region over the period 1986–2014, occurring on 5 August, 2009, with Md 4.7. Numbers indicate this earthquake and its foreshocks and aftershocks in a chronological order.

Data

We use the following data in our analysis (provided as a supplement to this paper): 1) Data from the Bulgarian National Seismic Network about 198 seismic events occurring over the period 1986–2014 in the Shabla-Kaliakra-Balchik region (**Supplementary Table S1**), located in the NE part of Bulgaria and the adjacent part of the Black Sea (43.0°–44.3°N, 27.75°–30.0°E). The strongest earthquake in the region over the considered period: Western Black Sea; 27.5 km east of Zelenka; 43.38°N, 28.77°E; depth 8 km; Md 4.7; August 5, 2009, 07:49:00.3 (M4.7); 2) Global CMT (https://www.globalcmt.org; errors are from CMT inversion): 43.42 ± 0.02°N, 28.60 ± 0.02°E; depth = 19. 9 ± 1.6; half duration = 0.7; centroid time minus hypocenter time: 1.5; moment tensor: Expo = 23, 0.169, 2.850, −3.020, −1.650, 0. 354, 1.230; Mw = 5.0, Mb = 4.7, Ms = 0.0, scalar moment = 3. 59e+23; fault plane 1: strike = 211, dip = 65, slip = 171; fault plane 2: strike = 305, dip = 82, slip = 26 (200908050749A BLACK SEA); 3) geophysical and geochemical data from the offshore methane seepages area Zelenka (43.381°–43.383°N, 28.426°–28.431°E; ~350 × 200 m) including: (3.1) echosounder bathymetry and seafloor mosaic image from 800 kHz side-scan sonar (**Supplementary Images S1–S3**); (3.2) main onshore and offshore faults locations: Zelenka is in the Charakman Fault Zone (**Figure 2**); (3.3) locations of 102 most active seepage groups providing evidence for migration pathways (**Supplementary Image S1**); (3.4) underwater videos and photos, starting at depths 9.4, 8.9, and 6.8 m showing the seafloor with the most active seepages and wide areas around them showing microcraters but without gas bubbles, indicating recent strong gas seepage activity (10 September 2009); **Figure 1E** (3.5) images obtained by the infrared camera for thermal analysis FLIR from the cliff, showing seepages registered on the sea surface as thermal anomalies (**Supplementary Image S4**); (3.6) results from gas content and sediment samples analyses; 4) Aqua EOS satellite images with resolution 250 m from sensor MODIS true color R (700 nm), G (546.1 nm), B (435.8 nm) over the period 01.08.2009–04.08.2009, showing the development of a light colored jet originating from Zelenka (**Figure 3**); 5) 16 Aqua EOS satellite images with resolution 250 m from sensor MODIS true color R (700 nm), G (546.1 nm), B (435.8 nm) for days with M ≥ 3 earthquakes in the Shabla-Kaliakra-Balchik region, as well as some preceding and following days (**Supplementary Data Sheet S1**); 6) Copernicus data "Black Sea high-resolution L4 sea surface temperature" (30.07–11.08.2009) and satellite data for sea surface temperature from NOAA 15, 17, 18, 19 and MetOp 2 for the period from 30 July to 13 August 2009 (MHPHI-RAS Marine Portal, 2020).

METHODS

To identify possible methane seepage precursors the following analyses have been done: 1) ZMS area is surveyed with an echosounder and side-scan sonar as well as underwater video recording and infrared imaging of the sea surface with an infrared camera for thermal analysis from the cliff to obtain the temperature of the surface water: 1) lengths of the jets axes are determined from geo-referenced satellite images; 2) time of appearance of the jets is estimated. These results are supported by underwater visual observation of the sea floor and infrared observation of sea surface temperature changes above the active methane seeps region.

RESULTS

We find precursory changes in the activity of the shallow water Zelenka methane seeps (Black Sea, Bulgaria, Cape Kaliakra) related to the strongest earthquake in the Shabla-Kaliakra-Balchik region for recent decades (Tsekov et al., 2019) (Md 4.7, 5 August 2009, with an epicenter ~27.5 km east from Zelenka).

Eight earthquakes with Md 2.3–4.7 and depths 8–20 km are registered during the period 2–8 August 2009 in the Shabla-Kaliakra-Balchik region as a foreshocks, mainshock, aftershocks series. Five of the quakes occurred on 5 August (7:49–15:56), starting with the mainshock with Md 4.7, which has been followed by four aftershocks later on the same day (**Figure 3**).

To obtain satellite imaging information about the region of interest during the foreshocks, main shock, aftershock series from 2 to 13 August 2009, we search the NASA archives (https://ladsweb.modaps.eosdis.nasa.gov). In the period 1–14 August 2009 15 satellite images of the ZMS area are available. Four of these satellite images registered brightly colored jets in the area of ZMS during the 4 days preceding the 5 August 2009 mainshock. **Figure 3** shows the three images with highest quality. **Table 1** summarizes the times of the satellite images and the lengths of the jet axes. Unfortunately, due to the poor quality of the images the errors in the axes length determination are significant (**Figure 3**; **Table 1**).

Four days before the offshore M4.7 earthquake from 5 August 2009, the area with active methane seepages, located 27.5 km from the epicenter, increases 3–5 times. This estimation is based on the size of the area with microcraters but without seeps on the seafloor observed by the diver Dr. K. Gerilowski 36 days after the earthquake (**Figure 1E**). It indicates an extreme increase of methane emissions from the ZMS, which is further confirmed by the observed contrast jets in the satellite images (**Figure 3**).

Our working hypothesis is that upward gas flow lifts sediments from the sea floor, which may create observable sea surface temperature anomalies. Infrared camera observations show a temperature anomaly on the sea surface ≤0.5°C on a background temperature of 6.5°C in calm weather above the active seeps area, thus further confirming the extreme methane seepage activation.

The M4.7 offshore earthquake is preceded by two probable foreshocks (2 and 4 August 2009) and followed by several aftershocks, five of them in the period 5–8 August 2009. August 4th, 2009 Md = 2.3 earthquake is identified as a foreshock according to the Gardner and Knopoff (1974) window criteria (Tsekov et al., 2019). August 2nd, 2009 Md = 2.3 earthquake is just outside Gardner and Knopoff (1974) space-time window and formally it is not a foreshock according to their criteria. However, it occurs offshore, on the Batovo fault, which intersects the Kaliakra fault where the mainshock occurred and probably is part of the preparation process and thus may be considered as a distant foreshock. The proposed new possible precursor appears just a day before the first earthquake of the series (the distant foreshock). The epicenter of the second foreshock is near the coast, south of cape Shabla. It is followed by the 5 August Md4.7 main earthquake in the series, occurring offshore on the Kaliakra fault. It is interesting that the ZMS area is just in the line which connects the foreshocks epicenters and almost in its middle. The coincidence between the increased methane seeps activity and the occurrence of foreshocks is a strong suggestion that the methane seeps activity reflects the preparation process of the following earthquake and thus it may be considered as a possible earthquake precursor.

To study further the possible relation between surge in methane seepage activity and the seismic activity in the Shabla-Kaliakra-Balchik region we search satellite images for evidence of precursory or coseismic methane seepage activation prior to all regional earthquakes with $M \geq 3$. There are 11 such quakes over the period 1986–2014, excluding the $M \geq 3$ foreshocks and aftershocks as well as the already considered Md 4.7 earthquake of 5 August 2009. The epicenters of 3 of these 11 quakes are close to the shore but inland. No precursory or coseismic methane seeps activation is identified on satellite images for these 3 quakes. The remaining 8 earthquakes have offshore epicenters. Four of these are preceded by methane seepage surge identified on satellite images. Four days prior to the Md 3.8 earthquake of 30 November 2009 wide low-contrast colored jet indicating methane seepage activation is observed. A day prior to the Md 3.1 earthquake of 22 April 2011 contrast colored jet is observed. The jet enlarges the following day, hours before the quake. The proposed new possible earthquake precursor is also identified hours prior to the Md 3.7 earthquake of 3 December 2012 and a day prior to the Md 3.2 earthquake of 6 February 2013.

We also checked for the new possible precursor 33 Google Earth images of the study area for periods without earthquakes and we found none, which suggests that the new possible precursor is not a common event. Thus, the probability that it occurs by chance hours/days before the corresponding earthquakes is low.

DISCUSSION

The area of ZMS is appropriate for organizing an observation experiment and monitoring of the new possible precursor,

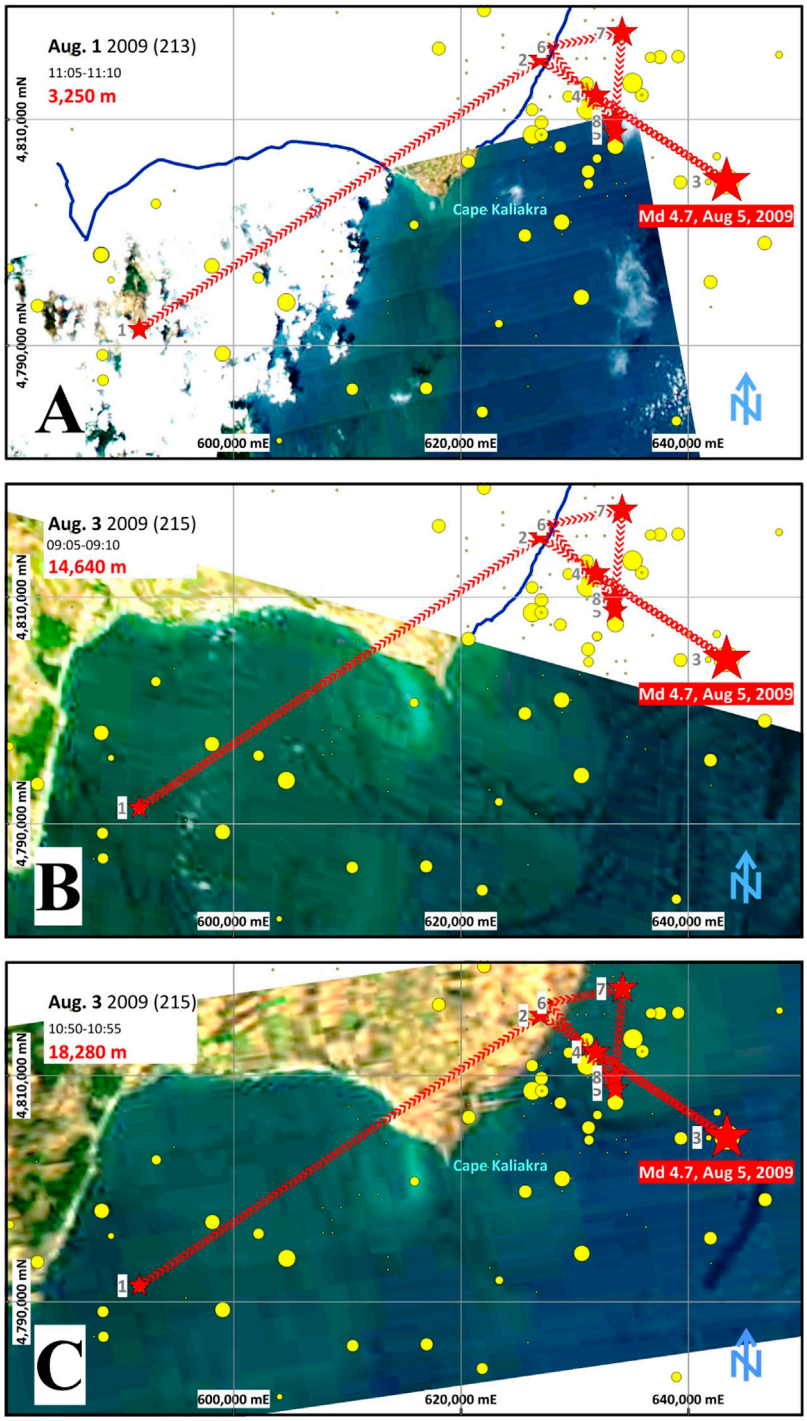

FIGURE 3 | Satellite images from the period 1 to 3 August with superimposed earthquake epicenters. Indicated are the dates of image generation and the lengths of the new possible precursor, the colored jets.

because of the following: 1) the area is easily observable, being close to the coast. The water is shallow which allows gas bubbles to reach the sea surface making it easy to monitor seeps activity observing the surface; 2) fine-grained almost white sediments cover the seafloor and strong methane emission could lift them to the surface creating contrast colored jets. Thus, identification of extreme methane emissions is relatively easy; 3) there is proximity to active seismic zone which potentially influences

TABLE 1 | Satellite images data.

Image	Date/Time UTC	Cloud length (m)	Diff.	Current (m/s)	Note
(A)	August 1, 2009 (213) 11:05–11:10	3,520			Cloud in the air
(B)	August 3, 2009 (215) 09:05–09:09:59	14,640	11,120 m 165,600 s	0.067	GeoRef problem: Rotation
(C)	August 3, 2009 (215) 10:50–10:55	18,280	3,640 m 6,300 s	0.578	Small rotation, 2 scans not pasted
(D)	August 4, 2009 (216) 09:50–09:55	22,620	4,340 m 82,800 s	0.052	Bad image quality, Unreliable value

methane seepage activity in the ZMS area. According to our database for the period 1986–2014, 198 earthquakes are registered by the Bulgarian National Seismic Network (Tsekov et al., 2019) or the average number of earthquakes per year is about 7. Also, a large number of active faults have been found offshore, along the Bulgarian Black Sea coast (Genov, Dimitrov, 2003; Dimitrov and Genov, 2004; Dimitrov and Vasilev, 2016), close to the ZMS area. Most active is the Kaliakra deep fault zone, the eastern wing of which sinks relative to the western. It is a bundle of subparallel faults, well expressed in the relief of the bottom, which can be traced to the cape Emine, and perhaps even on the land southwest of the city of Bourgas (see **Figure 1A**). The earthquake hypocenters in this area are relatively shallow, with depths up to 15–30 km.

Unfortunately, the proposed new possible precursor depends strongly on weather conditions. Storms could erase the microcraters on the seafloor produced by extreme methane emissions. Clouds and wind waves could mask the underwater jets and make their satellite registration impossible. To avoid the clouds dependence a drone may be used for remote monitoring in cloudy days.

On the other hand, studying the seismic activity in the Shabla-Kaliakra-Balchik region and possibly predicting some of the stronger regional earthquakes is of great importance. Earthquakes in the region pose significant hazard to the near coastal settlements (Ranguelov et al., 2011). Moreover, some regional earthquakes may trigger gravitational processes along the coast (landslides, rockfalls) increasing the earthquake risk.

We propose to organize monitoring of the activity of Zelenka methane seeps (ZMS) which may include 1) regular check of satellite images for possible detection of the new possible precursor; 2) drone observation with thermo- and 4K cameras; 3) geophysical survey with a small motorboat, ROV, USV, and/or AUV for estimation of the emissions area and discharge. Survey equipment may include GPS, underwater camera, side-scan sonar, multibeam, and profiler and sampling devices for gas, water, and seabed sediments; 4) setup of an online observation system with underwater video and gas discharge measurements and observations with a thermocamera from the cliff.

We also note that shallow water seeps with effects on water surface could be not so shallow. The critical depth is proportional to the gas discharge. A result from CRIMEA project shows that bubbles from natural gas seeps in the north-western part of the Black Sea reach the atmosphere if originating from depths shallower than 70 m. The rest of the deeper seeps are consumed from biological and chemical processes in the water volume.

CONCLUSION

This work proposes a new possible earthquake precursor, colored jets from lifted sea floor sediments triggered by extreme emissions of shallow water gas seeps. The new possible precursor is detected by satellite images with a resolution 250 m before a moderate offshore earthquake along the Bulgarian Black Sea coast. The precursor is observed ~24 hours before the first foreshock at a distance of 26.5 km from its epicenter and ~4 days before the main earthquake on 5 August 2009 at a distance of 27.5 km from its epicenter. It results from the abrupt increase of the emitting area of ZMS (3–5 times) and the gas discharge from the seeps. We find similar behavior prior to several $3 \leq M < 4$ earthquakes in the same region, with less pronounced colored jets detected by satellite images.

We note that this work provides only an initial case history in support of the proposed new possible earthquake precursor. To meet the strict IASPEI criteria for "significant" earthquake precursors (Wyss, 1991; Wyss, 1997; Wyss and Booth, 1997) it is necessary to have simultaneous long-term data on methane seeps activity and seismic activity in a given region, which is still not available. We also note that the time coincidence between the observed increase methane seeps activity and occurrence of foreshocks, which are one of the recognized "significant" earthquake precursors (Wyss, 1991; Wyss, 1997), suggests that the observed phenomenon may indeed be used as an earthquake precursor.

The new possible precursor is site specific. It may be used for predicting offshore seismic activity in shallow water coastal regions. Our results demonstrate the uncommonly suitable conditions for monitoring the possible earthquake related changes in methane seeps activity in the Zelenka methane seeps area, located ~3 km western from cape Kaliakra, Black Sea. The shallow water column allows bubbles and temperature anomalies to be easily registered at the sea surface.

One of the main strengths of the proposed new possible earthquake precursor is that it can be detected and observed relatively easily by remote sensing methods. We demonstrated it for the ZMS area, along the Bulgarian Black Sea coast, but it is probably applicable to other shallow water offshore seismic active regions. Thus, it is suitable for organizing regular monitoring. We discussed possible organization of regular observations searching for the proposed new earthquake precursor.

In parallel with monitoring for the precursor, the observation instruments may provide information on the budget of greenhouse gases and their impact on climate change, bioproductivity, and biodiversity, as well as to carry out an inventory of coastal gas seeps areas providing additional opportunities for energy development of coastal communities.

DATA AVAILABILITY STATEMENT

The raw data supporting the conclusions of this article will be made available by the authors, without undue reservation.

AUTHOR CONTRIBUTIONS

AV, EB, MT, and ND designed the research projects. AV wrote the first variant of the manuscript. AV, PP, and KG acquired survey data. VS collected and interpreted the satellite images. DT analyzed sea currents. EB, MT, and AV analyzed earthquake data provided by EB. OD, ND, and DP collected information for sections "*Introduction*" and "*Materials and Methods*" All authors contributed to the article and approved the submitted version.

FUNDING

This work was partially supported by Bulgarian Fund "Scientific Investigation" contracts: 1) KP-06-OPR04/7, 18.12.2018 GEOHydrate: Geothermal evolution of marine gas hydrate deposits, Danube paleodelta, Black Sea; 2) DN14/1, 11.12.2017 GEOAPREQ: Geophysical fields' anomalies preceding earthquakes in Balkan region and National Science Program "Environmental Protection and Reduction of Risks of Adverse Events and Natural Disasters," approved by the Resolution of the Council of Ministers No. 577/17.08.2018 and supported by the Ministry of Education and Science (MES) of Bulgaria (Agreement No. D01-322/18.12.2019).

ACKNOWLEDGMENTS

The authors would like to thank all the reviewers for their help in improving the paper.

SUPPLEMENTARY MATERIAL

The Supplementary Material for this article can be found online at: https://www.frontiersin.org/articles/10.3389/feart.2020.586283/full#supplementary-material.

REFERENCES

Bonini, M. (2019). Seismic loading of fault-controlled fluid seepage systems by great subduction earthquakes. *Sci. Rep.* 9 (1), 11332. doi:10.1038/s41598-019-47686-4

Botev, E., Solakov, D., and Christoskov, L. (2013). On the monitoring of the seismic activity in the territory of Bulgaria and surroundings. *Bulg. Geophys. J.* 39, 59–69.

Bryant, E. (2018). *Tsunami: the underrated hazard*. Berlin, Heidelberg: Springer.

Dimitrov, L. (2002). Contribution to atmospheric methane by natural seepages on the Bulgarian continental shelf. *Continent. Shelf Res.* 22, 2429–2442. doi:10.1016/s0278-4343(02)00055-9

Dimitrov, O., and Genov, I. (2004). Active faults in the south-eastern part of the moesian Plate and the lower-kamchia drop, C. R. Acad. *Bulg. Sci.* 57 (6), 83–88

Dimitrov, O., and Vassilev, A. (2016). Comprehensive analysis of data from geophysical studies in the western Black Sea. *C. R. Acad. Bulg. Sci.* 69 (10), 1333–1340.

Dimitrov, P., Dachev, V., Niklov, H., and Parlichev, D. (1979). Natural gas seepages in the offshore area of Balchik Bay. *Oceanology BAS.* 4, 43–49. (in Bulgarian)

Dotsenko, S., and Ingerov, A. (2007). Characteristics of tsunami waves in the Black Sea according to the data of measurements. *J. Phys. Oceanogr.* 17, 17–28. doi:10.1007/s11110-007-0002-z

Dotsenko, S., and Ivanov, V. (2010). *Natural disasters in the Azov-Black Sea region*. Sevastopol: MHI. in Russian.

Fischer, D., Mogollon, J. M., Strasser, M., Pape, T., Bohrmann, G., Fekete, N., et al. (2013). Subduction zone earthquake as potential trigger of submarine hydrocarbon seepage. *Nat. Geosci.* 6, 647–651. doi:10.1038/ngeo1886

Florios, K., Contopoulos, I., and Christofilakis, V. (2020). Pre-seismic electromagnetic perturbations in two earthquakes in northern Greece. *Pure Appl. Geophys.* 177, 787–799. doi:10.1007/s00024-019-02362-6

Géli, L., Henry, P., Grall, C., Tary, J. B., Lomax, A., and Batsi, E. E. (2018). Gas and seismicity within the Istanbul seismic gap. *Sci. Rep.* 8, 6819–6911. doi:10.1038/s41598-018-23536-7

Gardner, J. K., and Knopoff, L. (1974). Is the sequence of earthquakes in Southern California, with aftershocks removed, Poissonian?. *Bull. Seismol. Soc. Am.* 64, 1363–1367.

Gasperini, L., Polonia, A., Del Bianco, F., Etiope, G., Marinaro, G., Favali, P., et al. (2012). Gas seepage and seismogenic structures along the north Anatolian Fault in the eastern Sea of Marmara. *G-cubed* 13, 1–19. doi:10.1029/2012GC004190

Geersen, J., Scholz, F., Linke, P., Schmidt, M., Lange, D., Behrmann, J., et al. (2016). Fault zone controlled seafloor methane seepage in the rupture area of the 2010 Maule Earthquake, Central Chile. *Geochem. Geophys. Geosyst.* 17, 4802–4813. doi:10.1002/2016GC006498

Genov, I., and Dimitrov, O. (2003). Faults and fault activity determined on the basis of seismic stratigraphy in the region east from the west Ahtopol Rise - southern Bulgarian Black Sea shelf. *C. R. Acad. Bulg. Sci.* 56, 71–76.

Guidoboni, E., Comastri, A., and Traina, G. (1994). *Catalogue of ancient earthquakes in the mediterranean area up to the 10th century*. Rome: Pub. Ist. Naz. Geofis. Vulcanol.

Kalafat, D. (2017). Seismicity and tectonics of the Black Sea. *Int. J. Earth Sci. Geophys.* 3, 011. doi:10.35840/2631-5033/1811

Kelley, M. C., Swartz, W. E., and Heki, K. (2017). Apparent ionospheric total electron content variations prior to major earthquakes due to electric fields created by tectonic stresses. *J. Geophys. Res. Space Phys.* 122, 6689–6695. doi:10.1002/2016ja023601

Khilyuk, L. F., Chillingar, G. V., Robertson, J. O, Jr., and Endres, B. (2000). *Gas migration. Events preceding earthquakes*. Houston, TX: Gulf Publishing Company.

Mandev, P., Markova, K., and Kakacheva, V. (1978). Oil and gas manifestations along the Black Sea coast in the Burgas region. *J. Petrol. Coal Geol.* 8, 3–23.(in Bulgarian)

MHPHI-RAS Marine Portal. Black Sea archive (2020). (in Russian) Available at: https://ladsweb.modaps.eosdis.nasa.gov (Accessed July 22, 2020).

Nakagawa, K., Yu, Z.-Q., Berndtsson, R., and Kagabu, M. (2019). Analysis of earthquake-induced groundwater level change using self-organizing maps. *Env. Earth Sci.* 78, 445–455. doi:10.1007/s12665-019-8473-z

NASA Earth Data (2020). Available at: https://ladsweb.modaps.eosdis.nasa.gov (Accessed July 22, 2020).

Nikonov, A. A. (2002). Crimean earthquake in 1927. Unknown phenomena at sea. *Priroda* 9, 13–20.(in Russian)

Oaie, G., Seghedi, A., and Radulescu, V. (2016). Natural marine hazards in the Black Sea and the system of their monitoring and real-time warning. *Geo-Eco-Marina* 22, 5–28. doi:10.5281/zenodo.889593

Ouzounov, D., Pulinets, S., Hattori, K., and Taylor, P. (2018). *Pre-earthquake processes: a multi-disciplinary approach to earthquake prediction studies*. Hoboken, NJ: Wiley(AGU).

Palii, A., Gelev, S., and Yankov, K. (1951). *Geological framework and oil and gas perspectives of the Varna region: Open field work report*. Sofia: National Geofond

Papadopoulos, G., Diakogianni, G., Fokaefs, A., and Ranguelov, B. (2011). Tsunami hazard in the Black Sea and the azov sea: a new tsunami catalogue. *Nat. Hazards Earth Syst. Sci.* 11, 945–963. doi:10.5194/nhess-11-945-2011

Peev, P. (2016). Using archaeological data to infer past relative sea-level positions along the Bulgarian coast of the Black Sea. *Méditerranée* 126, 17–24. doi:10.4000/mediterranee.8171

Ranguelov, B., Radichev, R., Dimovsky, S., Oaie, G., Dimitriu, R., and Diaconescu, M. (2011). Marinegeohazards project—key core elements of the early warning system in the Black Sea. *Ann. Mc&G University, Part I, Geol. Geophys.* 54, 177–182.

Ranguelov, B. (2008). *Tsunamis in the Black Sea and some recent investigations: natural hazards in the marine area*. Bucharest, Romania: International Symopsium, 21–23.

Reeburgh, W. S., Ward, B. B., Whalen, S. C., Sandbeck, K. A., Kilpatrickt, K. A., and Kerkhof, L. J. (1991). Black Sea methane geochemistry. *Deep Sea Res. Part A. Oceanographic Research Papers.* 38, S1189–S1210. doi:10.1016/s0198-0149(10)80030-5

Roca, S. (1999). Macroscopic seismic anomalies and submarine pockmarks in the Corinth Patras rift, Greece. *Tectonophysics* 308, 275–290. doi:10.1016/S0040-1951(99)00090-6

Sabbarese, C., Ambrosino, F., Chiodini, G., Giudicepietro, F., and Macedonio, G. (2020). Continuous radon monitoring during seven years of volcanic unrest at Campi Flegrei caldera (Italy). *Sci. Rep.* 10, 9551–9610. doi:10.1038/s41598-020-66590-w

Tsekov, M., Botev, E., Dimova, L., and Raykova, R. (2019). Seismicity of the Shabla-Kaliakra-Balchik region over the period 1986–2014. *Balkan Geoph. Soc.* 2019, 1–5. doi:10.3997/2214-4609.201902652

Vassilev, A., Botev, E., and Hristova, R. (2006). Dvurechenskii mud volcano, Black Sea: long term activity from sedimentation, seismicity and tsunami data. *C. R. Acad. Bulg. Sci.* 59, 1181–1186.

Vassilev, A. (2006). Optimistic and pessimistic model assessments of the Black Sea gas hydrates. *C. R. Acad. Bulg. Sci.* 59, 543–550.

Wei, C., Lu, X., Zhang, Y., Guo, Y., and Wang, Y. (2019). A time-frequency analysis of the thermal radiation background anomalies caused by large earthquakes: a case study of the wenchuan 8.0 earthquake. *Adv. Space Res.* 65, 435–445. doi:10.1016/j.asr.2019.09.019

Wyss, M., and Booth, D. (1997). The IASPEI procedure for the evaluation of earthquake precursors. *Geophys. J. Int.* 131, 423–424. doi:10.1111/j.1365-246X.1997.tb06587.x

Wyss, M. (1991). *Evaluation of proposed earthquake precursors*. Washington, DC: American Geophysical Union.

Wyss, M. (1997). Second round of evaluation of proposed earthquake precursors. *Pure Appl. Geophys.* 149, 3–16. doi:10.1007/BF00945158

Xiong, P., and Shen, X. (2017). Outgoing longwave radiation anomalies analysis associated with different types of seismic activity. *Adv. Space Res.* 59, 1408–1415. doi:10.1016/j.asr.2016.12.011

Yefremova, A. G., and Zhizhchenko, B. P. (1974). Occurrence of crystal hydrates of gases in sediments of modern marine basins. *Dokl. Akad. Nauk SSSR, Earth Sci. Sect.* 214, 1179–1181.

Zhou, C., Zeng, X., Wang, Q., Liu, W., and Wang, C. (2019). Rotational motions of the Ms 7.0 Jiuzhaigou earthquake with ground tilt data. *Sci. China Earth Sci.* 62, 832–842. doi:10.1007/s11430-018-9320-3

Conflict of Interest: The authors declare that the research was conducted in the absence of any commercial or financial relationships that could be construed as a potential conflict of interest.

Copyright © 2021 Vasilev, Tsekov, Petsinski, Gerilowski, Slabakova, Trukhchev, Botev, Dimitrov, Dobrev and Parlichev. This is an open-access article distributed under the terms of the Creative Commons Attribution License (CC BY). The use, distribution or reproduction in other forums is permitted, provided the original author(s) and the copyright owner(s) are credited and that the original publication in this journal is cited, in accordance with accepted academic practice. No use, distribution or reproduction is permitted which does not comply with these terms.

frontiers in Earth Science

ORIGINAL RESEARCH
published: 23 February 2021
doi: 10.3389/feart.2021.579390

The Seismotectonic Significance of Geofluids in Italy

Paola Vannoli[1], *Giovanni Martinelli*[2,3,4] *and Gianluca Valensise*[1]*

[1]Istituto Nazionale di Geofisica e Vulcanologia, Sezione Roma 1, Rome, Italy, [2]Istituto Nazionale di Geofisica e Vulcanologia, Sezione di Palermo, Palermo, Italy, [3]Institute of Eco-Environment and Resources, Chinese Academy of Sciences, Lanzhou, China, [4]Key Laboratory of Petroleum Resources, Gansu Province/Key Laboratory of Petroleum Resources Research, Institute of Geology and Geophysics, Chinese Academy of Sciences, Lanzhou, China

There is growing interest in how geofluid emissions are released in the atmosphere by the planet's geodynamic activity, and how much they contribute to the global budget of greenhouse gases. Many workers are addressing this issue with studies conducted at global scale, so as to get the required global-scale answers. The data available at the global scale on geofluids, faults, earthquakes and volcanoes, however, are generally too coarse to provide these answers. We investigate the relationships between geofluid emissions and tectonics at a more detailed scale. Building on over a century of data on geofluid emissions and on an extensive knowledge of the region's tectonics and seismicity, we focused on Italy, one of the areas of the globe that experience the largest release of natural CO_2 and CH_4. We systematically overlaid and compared data collected by a number of workers into 13 published countrywide databases concerning geofluid emissions, carbon-bearing deposits, seismogenic faults, historical and instrumentally documented earthquakes, and heat flow observations. Our results indicate that 1) thermal springs and CO_2 emissions dominate in areas of mantle upwelling and crustal stretching, but also that 2) some of them occur in the extending inner Apennines, generally along major lithospheric chain-perpendicular lineaments that bound the largest normal faults. Conversely, 3) CH_4 emissions and mud volcanoes dominate in areas undergoing active contraction, where no CO_2 emissions are observed; in particular, we find 4) that mud volcanoes concentrate where the crests of active anticlines intersect major lithospheric chain-perpendicular lineaments. An overarching conclusion is that, in Italy, the release of geofluids is primarily controlled by deep crustal discontinuities that developed over the course of 5–10 My, and is only mildly affected by ongoing crustal strains. Geofluid emissions bring information on processes that occur primarily in the lower crust, marking the surface projection of generally hidden discontinuities that control the geometry and modes of seismic release. As such they may also provide valuable insight for improving the assessment of seismic hazard in hard-to-investigate seismically active regions, such as Italy.

Keywords: geofluid, thermal spring, CO_2 emission, mud volcano, CH_4 seep, fault, slab tear, transverse lineament

OPEN ACCESS

Edited by:
Max Rudolph,
University of California, Davis,
Unites States

Reviewed by:
Marco Bonini,
National Research Council of Italy (CNR), Italy
Steven Ingebritsen,
U.S. Geological Survey, Alaska, United States

****Correspondence:***
Gianluca Valensise
gianluca.valensise@ingv.it

Specialty section:
This article was submitted to Solid Earth Geophysics, a section of the journal Frontiers in Earth Science

Received: *02 July 2020*
Accepted: *11 January 2021*
Published: *23 February 2021*

Citation:
Vannoli P, Martinelli G and Valensise G (2021) The Seismotectonic Significance of Geofluids in Italy. Front. Earth Sci. 9:579390. doi: 10.3389/feart.2021.579390

INTRODUCTION: HOW DO GEOFLUID EMISSIONS RELATE TO TECTONICS AND EARTHQUAKES?

It is well established that pressure gradients existing in the Earth's crust can expel geofluids from deep geological formations toward the atmosphere. The intensity and duration of the expulsion processes depend mostly on crustal permeability (Gleeson and Ingebritsen, 2017) and on the forces that create pressure gradients. Heat from various sources in the core, in the mantle and in the crust generates fundamental tectonic forces at the Earth surface, but additional forces are supplied by topographic relief, diagenetic processes and circulating fluids (Bredehoeft et al., 1990).

Italy lies in the middle of the Mediterranean basin, one of the most active areas of the planet where all these primary forces act simultaneously, generating a large variety of tectonic environments, and hence geofluid assemblages. For many years Earth scientists have attempted to explore and understand the relationships that exist between the location and the characteristics of geofluid emissions and tectonic activity. More specifically, several workers focused on how the occurrence of significant earthquakes is related to the occurrence of anomalous fluids (Irwin and Barnes, 1980; Gold and Soter, 1984; Manga et al., 2012; Chiodini et al., 2020).

The focus was initially on time-domain relationships, and particularly on the detection of possible changes in the chemico-physical characteristics of known thermal springs or gas emissions following a large earthquake (for a worldwide review of the early works see Cicerone, et al., 2009; Wang and Manga, 2010; Martinelli and Dadomo, 2017; Girault et al., 2018; among others). Later, the availability of the first worldwide systematic georeferenced compilations of thermal springs (Waring, 1965), carbon dioxide emissions (Irwin and Barnes, 1980), methane seepages (Etiope, 2015) and other phenomena occurring in specific geological domains, shifted the attention of many workers to the space-domain. Along with the inception of computerized seismicity and active-fault catalogues, starting in the 1990s these data allowed the geofluids community to explore also the spatial relationships between the location of anomalous fluid emissions and the distribution of major faults and large earthquakes (e.g., Kuz'mina and Novopashina, 2018; Tamburello et at., 2018; Ciotoli et al., 2020).

Italy has often been the object of investigations on the origin and characteristics of geofluids in relation with ongoing geodynamic processes. This is due to the combination of its geological diversity and frequent seismicity with its multicentury tradition of field observation and data-keeping. This long tradition relied on the density of historical cities and villages, and hence on the number of potential "casual observers" of geofluid emissions.

Some early investigations are due to Barbier and Fanelli (1976), Minissale (1991) and De Rubeis et al. (1992), all of whom adopted independent research strategies. Barbier and Fanelli (1976: **Figure 1**) used a *point-to-point* or *point-to-line* approach to correlate qualitatively the presence of thermal springs with the location of Italian earthquakes and with "long lineations" derived from ERTS-A satellite imagery. They concluded that no clear spatial correlation could be established between thermal springs and earthquakes epicenters, and proposed that many such springs are aligned with large lineaments, possibly related to faults described generically as "active".

Fifteen years later, Minissale (1991) considered a point-to-area or point-to-line approach to correlate the presence of thermal springs with the most significant CO_2 degassing areas and Quaternary faults. He concluded that a significant part of CO_2 originates in the mantle, and that the main peri-Tyrrhenian fault systems release large amounts of CO_2 which is then dissolved into large carbonate aquifers.

De Rubeis et al. (1992) proposed an area-to-area geostatistical approach to the problem, searching for significant correlations between several geophysical parameters represented on a regular grid laid over Italy. Among other parameters, they correlated the density of Quaternary faults and the historical seismic release with the heat flow, concluding that "*...underground temperature and quantity of faults do not present significant areas of correlation....*"

TACKLING AN OLD QUESTION THROUGH A NEW APPROACH AND NEWLY ORGANIZED OBSERVATIONS

Exploring the relationships between geofluid emissions and active tectonics has fascinated a large number of geoscientists worldwide over at least the past 50 years, not to mention the important systematization efforts that were made around the end of the XX century. We would like to make a further step forward; to this end we propose a strategy that differs from those used in previous works for three fundamental reasons (**Figure 2**):

(1) we correlate seismogenic faults, seen as 3D sources projected onto the topographic surface, with point-like occurrences that include thermal springs, CO_2 emissions, gas seeps and mud volcanoes; that is to say, we use an *area-to-point* approach that allows for a better characterization of the processes leading to the observed emissions;
(2) our approach is geographically extensive, as it encompasses the main geodynamic domains of the whole Italian peninsula, but the grain of geofluid emission data is on the order of 1 km;
(3) most importantly, our approach is systematic, as it relies on carefully collected computer databases developed at national scale by independent research groups and unavailable to previous workers (**Supplementary Table S1**). Our paper represents the first occasion for looking at them simultaneously, taking advantage of the enormous recent progress in dealing with georeferenced information.

Over the past few years various workers have explored the relations between fluid emissions and tectonic activity, mostly in the framework of investigations aimed at estimating the total budget of greenhouse gases such as CO_2 and CH_4. Tamburello

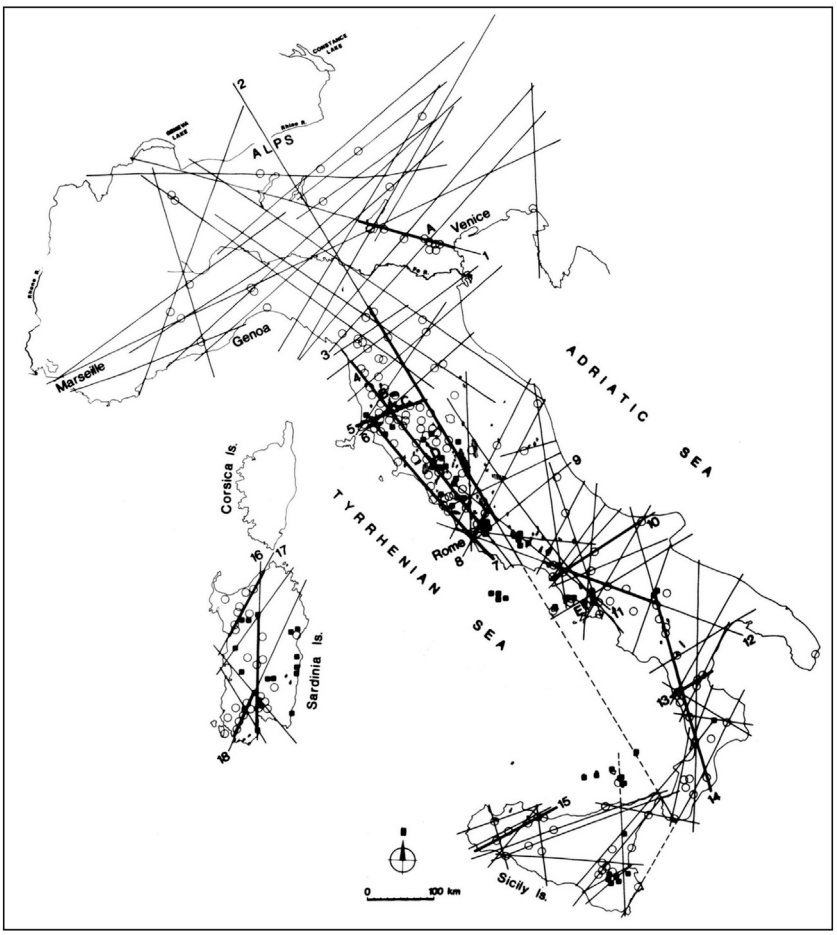

FIGURE 1 | Long lineations detected from ERTS-A satellite imagery compared with the location of thermal springs, shown by empty circles (from Barbier and Fanelli, 1976, modified). Thicker lines are defined as "hot lineaments" as they connect multiple springs. According to the authors of this pioneering study, about 80% of the springs lie on one or more lineaments.

et al. (2018), for instance, focused on how the permeability of the crust in areas undergoing active extension allows significant degassing of CO_2-rich fluids, whereas Ciotoli et al. (2020) explored the amount of CH_4 and other hydrocarbons that is released to the atmosphere by faulting in convergent basins. These workers used worldwide compilations of fluids, hydrocarbons and faults.

We share their general conclusions on the geodynamic processes that give rise to geofluid emissions, and trust their quantification of such emissions, but the scale of their analyses makes it impossible to explore how the emissions relate to the relevant tectonic structures three-dimensionally. Achieving this goal requires that all analyses be conducted at a more detailed scale, similar to that of the tectonic domains that are responsible for the emissions themselves.

This is exactly what we do in this paper. We hope that our conclusions will provide details that may be of practical use in the investigation of regional seismotectonics. We maintain that geofluid emissions can be used to set firm constraints on the location and extent of major seismogenic sources by highlighting the existence of permanent lithospheric discontinuities; hence they may contribute valuable data for the assessment of seismic hazard in hard-to-investigate active regions, such as Italy.

Our work followed a path that is mirrored in the structure of this paper.

In the **Input Data I: Available Databases of Geofluid Emissions**, **Input Data II: Discriminatory Data** and **Input Data III: Tectonic and Seismological Observations and Databases** sections we describe in detail the data and databases we used, concerning known geofluid emissions, heat flow estimates, the distribution of coal, lignite and peat deposits, and the tectonic and seismological framework: all adopted databases are all freely available (**Supplementary Tables S1, S2, S3**). We do not discuss the composition of individual emissions, but trust their original classification by the authors of the relevant databases.

In **Selecting the Terms of Comparison** Section we discuss how we elaborated these databases to suit our specific needs. We focused on emissions occurring in mid-to low-heat-flow areas, that are apparently controlled by the deeper crustal circulation; as

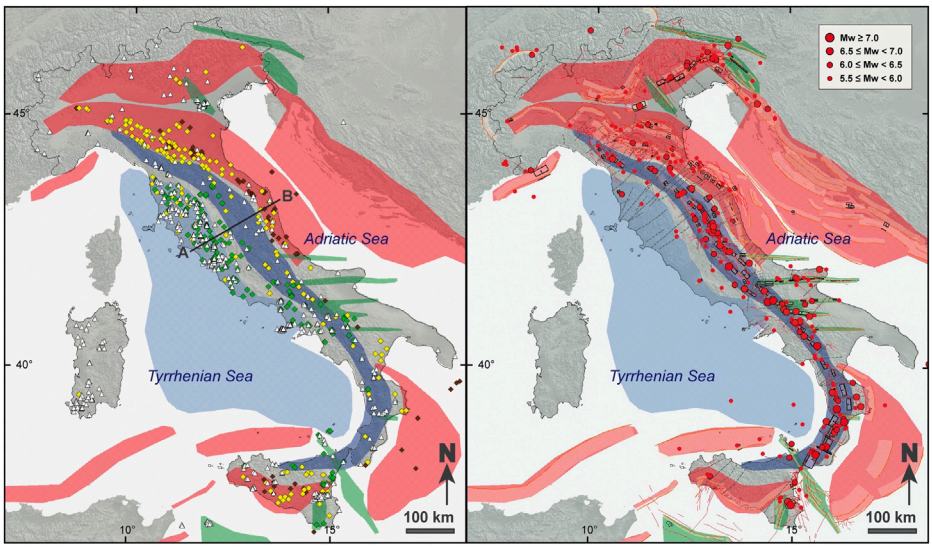

FIGURE 2 | Study area and summary of data used in this work. In both figures the shaded areas indicate active tectonic domains. Key: light blue, areas of rifting and mantle upwelling; blue, post-orogenic extension; red, active contraction; green, active strike-slip. Left: Geofluid emissions. Key: white triangles, thermal springs having $T > 20°C$; green diamonds, natural CO_2 emissions; yellow diamonds, gas seeps; brown diamonds, mud volcanoes. A-B: trace of the topographic profile of **Figure 14**. Right: Seismological and tectonic information. Key: black boxes and red ribbons, surface projection of Individual and Composite Seismogenic Sources, respectively (ISSs and CSSs) from the DISS 3.2.1 database; red lines, capable faults from the ITHACA database; black dashed lines, transverse lineaments from the DISS 2.0 database; red symbols, earthquakes of M_w 5.5 and larger from the CPTI15 catalogue.

such they illuminate processes that occur in the uppermost 10–15 km of the crust, where faults exhibit fully brittle behavior and most large earthquakes nucleate.

The Thermal Springs and **CO_2 Emissions** Sections illustrate the criteria we used to select our thermal spring and CO_2 data to minimize the "noise" arising from high-heat-flow conditions. Similarly, the **CH_4 Emissions and Mud Volcanoes** Section describes how we selected our CH_4 and mud-volcano data, discarding biogenic-methane emissions that would bring information only on very shallow-seated processes. Finally, the **Earthquake-Induced Geofluid Emissions** Section describes how we selected relevant earthquake-induced effects from the CFTI5Med.

In the **Correlations and Anticorrelations** Section we discuss the correlations, anticorrelations and non-correlations that arise from the superposition of the selected fluid emissions, or earthquake-induced effects, over the available tectonic and seismological information.

Lastly, in the **Discussion** and **Conclusion** Sections we combine all data into a global overview, highlighting 1) whether and how the different types of emissions overlap, or are mutually exclusive, and 2) what can be learned from them, both in terms of their geodynamic significance and of the constraints they set on seismogenic processes.

Input Data I: Available Databases of Geofluid Emissions

Thermal Springs

Strictly speaking, any spring (or water well: but for simplicity, in the rest of the paper we will refer only to springs) whose average temperature is noticeably above the local mean annual air temperature may be regarded as "thermal" (Waring, 1965). A more accurate definition of "thermal spring" is given in Pentecost et al. (2003): see their Table 1 and their Recommendations section).

Section S1 of the Supplementary Materials provides an overview of the available knowledge on Italian thermal springs. For this work we decided to refer to the *Database of Thermal Springs* by Martinelli and Albarello (1997), available for consultation and download as **Supplementary Table S2**, for two main reasons: 1) to increase the resolution of our analysis, mostly concerned with mildly but positively anomalous springs occurring in areas of moderate to low heat flow, and 2) because for these specific areas the most recent database (Trumpy and Manzella, 2017) reports only a fraction of the datapoints listed in the *Database of Thermal Springs*, although it does provide many new data for the peri-Tyrrhenian area.

CO_2 Emissions

CO_2 emissions are less widespread than thermal springs, as their existence depends on the occurrence of mantle degassing phenomena or of thermometamorphic/mechanochemical processes (Kerrick, 2001; Chiodini et al., 2004; Minissale, 2004; Italiano et al., 2008).

A database of volcanic and non-volcanic CO_2 emissions in Italy was compiled in the framework of project INGV-DPCV5, funded by the Italian Department of Civil Defense (Chiodini et al., 2008). Its aim was to locate, characterize and inventory all Italian gaseous emissions (http://googas.ov.ingv.it). The database has been subsequently updated by Cardellini et al. (2014) in the framework of the MaGa Project (**Supplementary Table S1**). It

currently holds 1,870 natural gas emission measurements from 877 locations distributed worldwide, although the majority of them fall in the Italian territory.

Gas Seeps and Mud Volcanoes

Onshore methane seepages in Italy exhibit a flow rate in the range 0.1–600 t y^{-1} (Burrato et al., 2013). Available data on gas seeps in Italy were collected and organized by Martinelli et al. (2012). Most of these emissions are dominated by CH_4. These investigators merged previous historical catalogues (Camerana et al., 1926; Zuber, 1940) and individual observations from the recent literature (e.g., Etiope et al., 2007). We will refer to gas seeps as "CH4 emissions".

It is widely accepted that CH_4 may be generated by methanogenic micro-organisms, in which case it is referred to as 'biogenic', or by the thermally-driven breakdown of larger molecules, in which case it is referred to as 'thermogenic'. It is also established that biogenic CH_4 generally originates at very shallow depth (<1 km), whereas thermogenic CH_4 generally rises from much deeper rock horizons. Hence, similarly to thermal springs, CH_4 emissions must be carefully selected to remove those dominated by biogenic gas, as they are insensitive to the deep-seated tectonic processes that are the object of our investigation.

Mud volcanoes comprise a distinct sub-category of gas seeps. Martinelli and Judd (2004) investigated the Italian mud volcanoes and collected all the available evidence, later turned into a catalogue by Martinelli et al. (2012). A significant part of these data have been used by Burrato et al. (2013) to set up a web site devoted to hydrocarbon seepages in Italy (http://hydrocarbonseeps.blogspot.com/p/hysed.html).

Input Data II: Discriminatory Data

As we stated earlier, all our geofluid emissions need to be carefully selected to minimize the masking effect of shallow-seated processes and emphasize the role of phenomena occurring at seismogenic depth. This section includes "discriminatory data", i.e., observations that are required only for achieving this goal and will not be used "per se".

Heat Flow Measurements

A number of workers discussed the distribution of heat flow in Italy, including Cataldi et al. (1995), Della Vedova et al. (2001), Pasquale et al. (1997), Pasquale et al. (2010), Pasquale et al. (2014) and Verdoya et al. (2019). We used the surface heat flux density map elaborated and published by Cataldi et al. (1995) and Della Vedova et al. (2001), and made available online as the Italian National Geothermal Database, the largest collection of Italian geothermal data through the 1980s (CNR-IGG, 2012; Trumpy and Manzella, 2017).

The Alps, the Po Plain, the Adriatic and Bradanic foretroughs are characterized by relatively low heat flow values in the range 40–70 mW/m^2 (**Figure 3**). A major regional anomaly affects large parts of Tuscany and Latium, where the average heat flow is 80 mW/m^2 but it may locally rise up to 200–400 mW/m^2. Similarly high values are observed in the Campanian volcanoes (Vesuvius, Phlegrean Fields and Ischia Island). According to the literature, springs occur in areas of peninsular Italy where the heat flow is >70 mW/m^2 are representative of hot waters or steam sources originating in high-enthalpy geothermal fields (e.g., Pauselli et al., 2019). Fluid circulation in such areas is strongly affected by magma intrusions at shallow depth (3–5 km), therefore the characteristics of thermal springs cannot be used to make robust inferences about the evolution and the structure of the upper crust.

Distribution of Coal, Lignite and Peat Deposits

Biogenic CH_4 chiefly originates from peats or from lignite/coal layers. In principle, geochemical and isotopic data can distinguish peat-originated methane from thermogenic methane (e.g. Stolper et al., 2015), but, unfortunately, not all Italian methane seepages have been sampled or analyzed over the past few decades. We used a national database of occurrence of fossil carbon recently developed by Martinelli et al. (2015) as a proxy for a first-order separation of biogenic and thermogenic seepages and mud volcanoes.

Input Data III: Tectonic and Seismological Observations and Databases

Data on Active and Seismogenic Faulting

The location, geometry and size of crustal faults, and particularly their length, dip and down-dip width, necessarily affects the nature and distribution of geofluid emissions at the Earth surface. Unfortunately, data on the location and characteristics of active faults carry at least three categories of inherent ambiguities that must be identified and understood prior to attempting the interpretation of a specific geofluid emission:

(1) is the fault currently active, and if so, is it also seismogenic? Or does it slip aseismically? There is no consensus in the current literature as to whether the emission of geofluids requires a network of active faults, or whether even inactive faults may allow geofluids to rise up from shallow-to mid-crustal depth (i.e., from the depth of the brittle-ductile transition at any given site);
(2) is the fault positively surface-breaking, i.e. does it reach the topographic surface? Or else, is it blind, meaning that it does not extend to the surface, but its upper tip occurs at a depth ranging from a few to 10–15 km? Notice that blind faults are themselves ambiguous, as they may still reach the surface through secondary, potentially multiple upward-propagating splays; in this case they may give rise to distributed emissions, that are inevitably more difficult to pinpoint;
(3) what is the hierarchy of any given fault with respect to all the faults that lie in the same area? In any seismotectonic application it is crucial to assess whether a certain fault extends to seismogenic depth, or whether it is only a subsidiary to some larger fault beneath it, which is hence the main player in the area. Fluid emissions associated with a secondary fault are likely to be representative of very shallow-seated processes only, unless that fault belongs to a larger and deeper fault system.

Choosing an appropriate fault dataset is therefore crucial in the correct interpretation of geofluid emission and in the

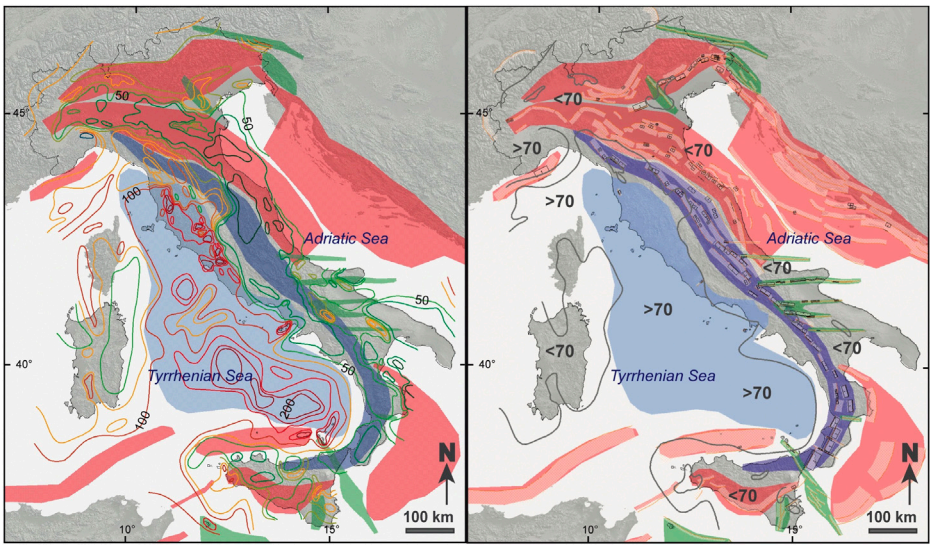

FIGURE 3 | Heat flow map of Italy from CNR-IGG (see text for details). Shaded areas indicate active tectonic domains (same as in **Figure 2**). Left - Complete model, showing high/medium heat flow areas in the peri-Tyrrhenian belt (contours in red/orange). Contour spacing is necessarily variable as it reflects the original elaborations. Right - Outline of the 70 mW/m^2 isoline (shown in dark grey), used in this work for separating areas were thermally anomalous fluids and CO_2 emissions are mostly related to high heat flow, to the west, from areas where they may represent the outcome of fluid circulation in upper crustal rocks, to the east.

investigation of preferred pathways. Italy has two main faults datasets, both of which were conceived around the end of the 1990s: ITHACA (ITaly HAzard from CApable faults, **Supplementary Figure S2**, left), developed by ISPRA (Michetti et al., 2000; ITHACA Working Group, 2019), and DISS (**Supplementary Figure S2**, right), developed by INGV (Valensise and Pantosti, 2000, Valensise and Pantosti, 2001; Basili et al., 2008; DISS Working Group, 2018). Their characteristics and contents are described in **Section S2 of the Supplementary Materials**.

In addition to potential earthquake sources, the earlier versions of DISS (v. 2.0: http://diss.rm.ingv.it/diss/index.php/component/chronoforms5/?chronoform=DISS200) listed over 140 "transverse lineaments", a category of large, chain-perpendicular structural features inherited from previous tectonic regimes. It must be recalled that the Cenozoic compressional architecture of the Italian peninsula largely reflects the inherited Mesozoic palaeogeographic setting of its foreland, i.e. the Adriatic plate. There is ample evidence that inherited structures control the foreland monocline panels that lie below the basal detachment of the accretionary prisms and exhibit variable dip (Mariotti and Doglioni, 2000). These are commonly interpreted as evidence for the existence of slab tears (e.g., Rosenbaum et al., 2008; Rosenbaum and Piana Agostinetti, 2015), whose crustal expression could be strike-slip or transpressional transfer zones (Vannoli et al., 2015): pseudo-linear features resulting from the rectification of potentially complex elements but usually perpendicular to the thrust fronts, and hence "transverse" because they form an angle of 45–90° with respect to the dominant local structural trend. The role of such lineaments in the present geodynamic setting of Italy and their potential for substantial earthquakes are fully open to scientific debate, although there is growing evidence that they do generate both frequent background seismicity and relatively large earthquakes.

The Individual Seismogenic Sources (hereinafter ISSs) and Composite Seismogenic Sources (hereinafter CSSs) of the DISS database (introduced in Section S2) include also a number of seismogenic sources that, similarly to the transverse lineaments, form an angle with the main structural trends, but whose seismogenic capability is testified by several large pre-instrumental earthquakes and confirmed by a handful of instrumentally investigated earthquakes. Most of these sources are believed to indicate the reactivation of older and deeper strike-slip faults that crisscross the foreland areas of both the Alps and the Apennines, although the principal ones concentrate between northern Apulia and eastern Sicily (Di Bucci et al., 2010). Two examples of the seismogenic potential of such deeper faults are the May 5, 1990, Potenza earthquake (M_w 5.8) and the 31 October-1 November 2002, San Giuliano di Puglia earthquakes (both of M_w 5.7), all of which were generated by dextral motion on E–W striking strike-slip faults at 15–25 km depth. We postulate that these deeper faults may act as pathways for the rise of thermally anomalous fluids and CO_2, even in areas of low heat flow. Their potential role in controlling the distribution of geofluid emissions will be discussed in **Correlations and Anticorrelations** Section.

Inevitably, the use of these two databases in our investigation is subject to uncertainties and limitations. For instance, lacking a 3D characterization and hierarchization, only some of the faults listed in ITHACA may reach a significant depth and hence be considered as viable pathways for upper crustal geofluids. Conversely, DISS lists only primary faults, i.e. faults extending to seismogenic depth, and describes them in 3D, but the accuracy

of their location may not always be sufficient to explore their relationships with fluid emissions. In Nevertheless, in the following discussion we will rely primarily on the faults described in the DISS database, as they are more likely to be relevant for the scopes of this work.

Earthquake Catalogues

We rely on two major, regularly updated earthquake compilations available for Italy and its surroundings: the *Catalogue of Strong Italian Earthquakes* (Guidoboni et al., 2018, 2019), a large compilation that summarizes the knowledge acquired through nearly 4 decades of modern research in historical seismology, and the *Database Macrosismico Italiano*, or DBMI (Locati et al., 2019), whose current version (2.0) provides macroseismic intensity datasets relating to Italian earthquakes in the time window 1,000–2017.

In some instances we plotted also instrumental seismicity recorded by the INGV national network and by other local networks over the past 35+ years (from ISIDe-Italian Seismological Instrumental and Parametric Database: ISIDE Working Group, 2007).

The characteristics and contents of these compilations are described in **Section S3 of the Supplementary Materials**.

SELECTING THE TERMS OF COMPARISON

The tectonic and seismological significance of the databases upon which our analysis is based may differ with the geographical area concerned, the local predominance of subcrustal geodynamic processes, and fracturing that may have been inherited from older tectonic regimes. In this section we discuss how the geofluids observations have been selected from their respective databases to remove potential noise and emphasize their relationships with deep-seated seismotectonic processes. But first we develop a simplified scheme of the dominant strain regime acting in the mid-upper crust over the Italian peninsula and its surrounding areas and seas.

In conjunction with seismicity (Guidoboni et al., 2018; Guidoboni et al., 2019; Rovida et al., 2019; Rovida et al., 2020) and tectonic stress data (Montone and Mariucci, 2016; Mariucci and Montone, 2020), the availability of orderly fault databases allows the most active portions of the Italian peninsula to be separated into four distinct tectonic domains. The resulting model is shown in **Figure 2** and is replicated in **Figures 3–8** to serve as context.

We first subdivided the study area into a dominantly extensional and a dominantly contractional domains. The former was further subdivided into a peri-Tyrrhenian belt of Plio-Quaternary rifting and mantle upwelling (e.g. Peccerillo, 2005: shown in light blue in **Figure 2**), and an elongated region of post-orogenic extension running along the axis of the Apennines (DISS Working Group, 2018: shown in blue), where large shallow normal faults cause most of the largest earthquakes of the Italian peninsula. This latter region has also undergone continuous regional uplift over the past 1–2 My; a very effective process in causing erosional denudation and promoting the visibility of the geofluid emissions. The purely contractional domain extends along the frontal portions of the Alps and of the Apennines (frontal with respect to the direction of orogenic transport), i.e. in the Po Plain, in the peri-Adriatic and peri-Ionian regions, and in much of the corresponding offshore area (DISS Working Group, 2018: shown in red).

The Italian peninsula is also surrounded by foreland areas that extend along the Adriatic microplate, i.e. from the central and eastern Po Plain to the Adriatic and Ionian offshore, in southern Sicily and in the Sicily Channel. These foreland areas are subjected to NW–SE compression exerted by the northwestward motion of the African plate: the resulting contraction is primarily accommodated by deeper strike-slip faults that are known to exist in the central and southern Apennines (already mentions in **Data on Active and Seismogenic Faulting** Section), where they strike nearly E–W, and in southern Sicily, where they strike NNE-SSW (e.g., Di Bucci et al., 2010: all shown in green in **Figure 2**). Notice that the "post orogenic extension" and "deeper strike-slip" domains overlap in limited areas of the southern Apennines.

In the following, for all databases, we will refer to the selected and removed data as the "selected dataset" and "removed dataset", respectively. In our figures each emission type is shown with a specific color, but all removed data are shown in grey, whereas red is used to indicate specific emissions that are referenced in the discussion.

Thermal Springs

The average annual temperature in mountain and plain areas of Italy is in the range 5–20°C, thus for this work we decided to focus only on springs whose mean temperature falls in the range 20–150°C (see **Figure 4**). The most common temperature range for the springs reported in the *Database of Thermal Springs* (see **Thermal Springs** Section) is 25–40°C. Springs in this temperature range are widespread all throughout the Italian peninsula, providing evidence for ongoing tectonic activity: as recently discussed in a worldwide overview by Bense et al. (2013), a high density of thermal springs is always associated with ongoing tectonic activity, whereas thermal springs tend to be very sparse or absent in tectonically quiescent areas.

The recent tectonic history of Italy, and the goals of our study, required that all thermal springs falling in the geothermal or volcanic areas along the Italian peninsula be removed prior to the beginning of our analysis. As mentioned earlier, springs associated with high heat flow carry information only on shallow-seated processes, hence they are useless or even misleading if one is to explore processes driven by forces acting on the full thickness of the seismogenic layer.

It is known that the "excess heat" observed in high heat flow areas (e.g., Tuscany) is large enough to mask more localized thermal contrasts between warm and cold springs. For instance, Celati et al. (1990) demonstrated that when the heat flow reaches 100–200 mW/m^2, no faulting due to tectonic activity—that is to say, no contribution from deep-seated fluid circulation—is needed to justify the occurrence of thermally anomalous springs.

Pauselli et al. (2019) stated that "*Five crustal geotherms (extending to the Moho) and the corresponding rheological*

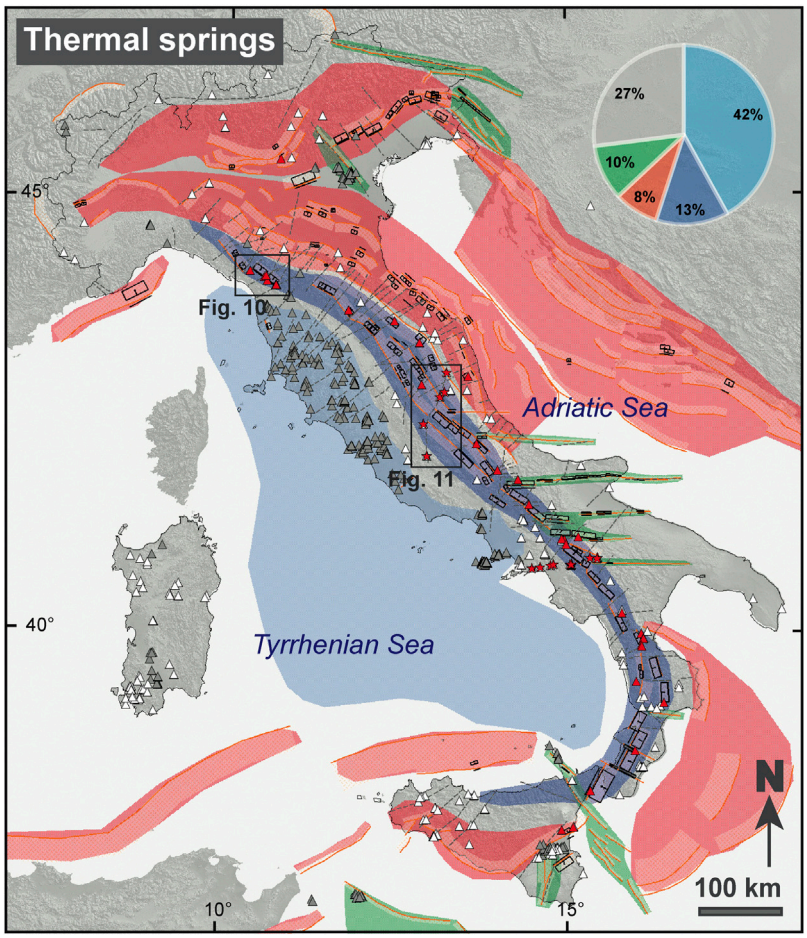

FIGURE 4 | Distribution of thermal springs (see **Thermal Springs**, **Thermal Springs** and **Thermal Springs: Potential Evidence for Lithospheric Discontinuities**). Tectonic domains, seismogenic sources and transverse lineaments are shown as in **Figure 2**. Removed datapoints are shown in grey. Selected datapoints are shown in red if they fall within 5 km of the edge of the surface projection of an Individual Seismogenic Source, otherwise in white. Red stars indicate additional critical datapoints discussed in the text. Two rectangles indicate the area discussed in **Test Case 1: The Garfagnana Region, Northern Apennines** and **Test Case 2: The Olevano–Antrodoco–Sibillini Line, Central Apennines** Sections. The pie chart shows the distribution of thermal springs in the different active tectonic domains (see **Table 1**). Notice that 42% of the springs fall in the area of rifting and mantle upwelling.

profiles confirm that the 70 mW/m^2 isoline corresponds to a major tectonic boundary, across which the thermal, structural, and seismic properties of the lithosphere go through a significant change". In the framework of a large worldwide compilation of heat flow data, Lucazeau (2019) found that 70 mW/m^2 is a global average. We hence postulate that warm or hot springs falling in areas where the heat flow is <70 mW/m^2 are likely representative of thermally anomalous fluids reaching the ground surface by means of geological structures due to sustained tectonic activity at scales of ~100,000 years.

In summary, prior to analyzing the data we removed all thermal springs falling in areas where the heat flow is >70±5 mW/m^2 (to account for uncertainties in the heat flow estimates, particularly in northern Tuscany and Campania: see **Figure 3**). **Table 1** shows the distribution of data into the four seismotectonic domains described earlier, before and after the selection process.

CO_2 Emissions

CO_2 emissions listed by Cardellini et al. (2014) consist of *mofete* characterized by flow rates in the range 1–2,000 t d^{-1}, and can be considered unaffected by non-geological contributions. Nevertheless, and similarly to the case of the thermal springs, our interpretations require that CO_2 emissions originating in volcanic and geothermal areas be removed (see **Figure 5**).

CO_2 emissions originate at different depths and by at least two different primary processes: 1) the anatexis of carbonate rocks at relatively shallow depth (3–5 km), which dominates in areas of mantle upwelling due to high heat flow, and 2) degassing from the mantle lithosphere, which is virtually ubiquitous in geodynamically active areas such as the Italian peninsula. According to Chiodini et al. (2004), the discharge of CO_2 in Italy reflects a combination of these two sources, with the upper crustal component dominating in high-heat-flow areas and the mantle component prevailing elsewhere. The "shallow" and

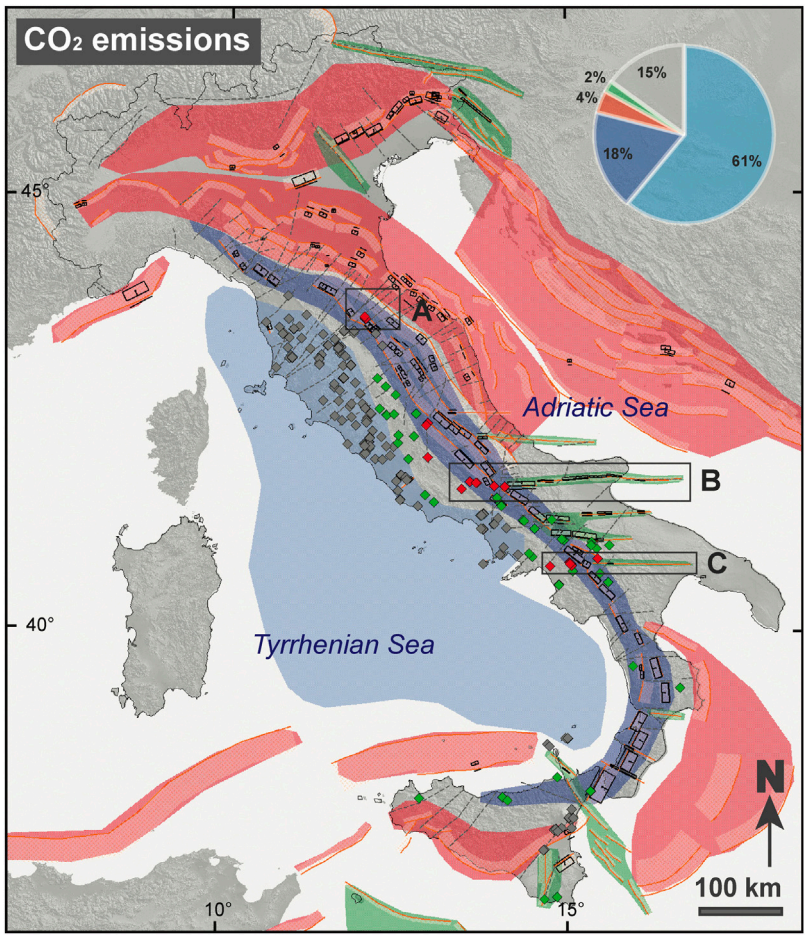

FIGURE 5 | Distribution of CO_2 emissions (see **CO_2 Emissions**, **CO_2 Emissions** and **CO_2 Emissions: Combined Evidence for Carbonate Dissolution and Mantle Degassing** Sections). Tectonic domains, seismogenic sources and transverse lineaments are shown as in **Figure 2**. Removed datapoints are shown in grey. Selected datapoints are shown in red if they are individually discussed in the text, otherwise in white. The areas marked with A, B and C are discussed in **Test Case 1: Central-Northern Apennines**, **Test Case 2: Central-Southern Apennines** and **Test Case 3: Southern Apennines** Sections, respectively. The pie chart shows the distribution of CO_2 emissions in the different active tectonic domains (see **Table 1**). Notice that as many as 61% of the CO_2 emissions fall in the area of rifting and mantle upwelling.

"deep" CO_2 emissions have a distinct $\delta^{13}C$ signature, but analytical results are available only for a minority of cases. We used the heat flow as a proxy to discriminate between "possibly shallow" and "positively deep" CO_2 (**Figure 5**), using the same threshold adopted for discriminating "shallow" and "deep" thermal springs (70 mW/m^2).

CH_4 Emissions and Mud Volcanoes

As we discussed in **Distribution of Coal, Lignite and Peat Deposits** Section, CH_4 emissions must be selected to remove those dominated by biogenic gas, whose shallow origin is incompatible with the goals of this paper. To this end we removed all CH_4 seepages falling within 5 km of any occurrence of fossil carbon as shown in the database compiled by Martinelli et al. (2015: see **Distribution of Coal, Lignite and Peat Deposits** Section and **Figure 6**). In principle, all seepages left should be of thermogenic, i.e. of deeper origin.

In consideration of their genetic similarities, in parallel with the CH_4 seepage dataset we also examined all mud volcanoes listed in Martinelli et al. (2012). These data were also interpreted after removal of occurrences that fall close to a known fossil carbon reservoir (**Figure 7**).

Earthquake-Induced Geofluid Emissions

Earthquake-induced effects on the environment were one of the main innovations of CFTI5Med (see **Earthquake Catalogues** Section). Its authors systematically analyzed, geo-referenced observations and filed testimonies describing 2,337 such effects. Notwithstanding the difficulties involved in translating historical testimonies into corresponding natural phenomena as we know them today, these effects were classified into 32 categories belonging to five macro-groups. One of these groups is named "Gas emissions/Others" and contains two subcategories that are relevant to the scopes of this paper:

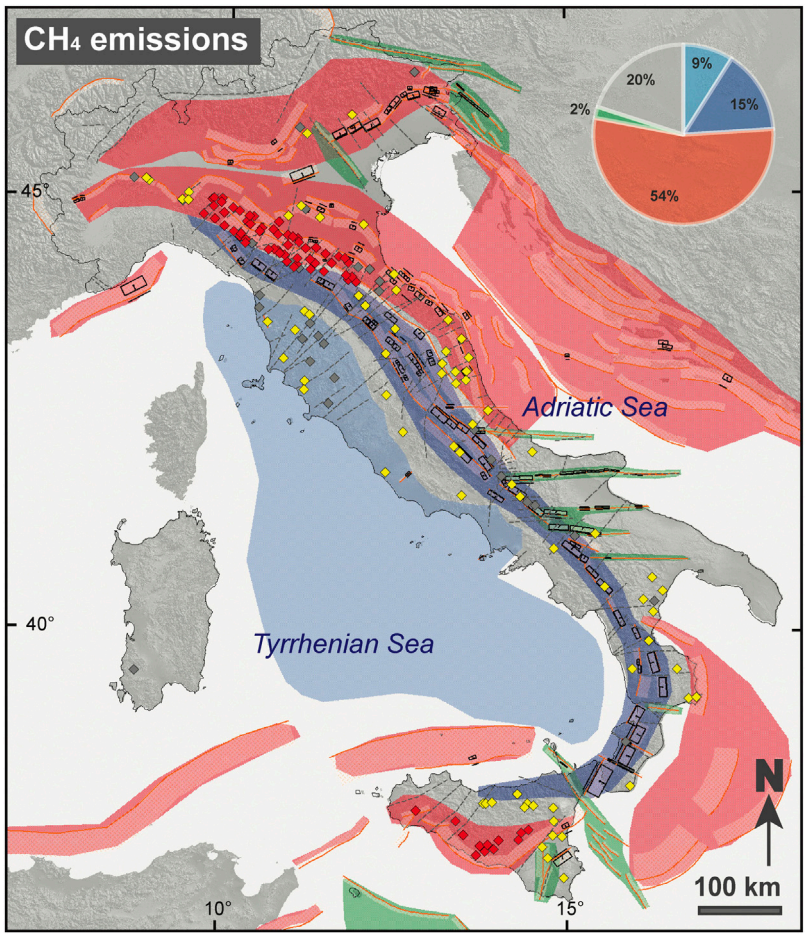

FIGURE 6 | Distribution of CH_4 emissions (see **Gas Seeps and Mud Volcanoes**, **CH_4 Emissions and Mud Volcanoes** and **CH_4 Emissions and Mud Volcanoes: The Signature of Contractional Domains** Sections). Tectonic domains, seismogenic sources and transverse lineaments are shown as in **Figure 2**. Removed datapoints are shown in grey. Selected datapoints are shown in red if they are discussed in the text, otherwise in yellow. The pie chart shows the distribution of CH_4 emissions in the different active tectonic domains (see **Table 1**). Notice that 54% of these emissions fall in areas of active contraction.

1) Gas emissions and mud-cone eruptions, containing 79 testimonies, the oldest from the great December 5, 1456 southern Italy earthquake sequence; and 2) H_2S emissions, containing 60 testimonies, the oldest from the October 3, 1624 earthquake in southeastern Sicily.

These testimonies are plotted in **Figure 8** and will be discussed in subsequent sections.

CORRELATIONS AND ANTICORRELATIONS

In this section we discuss what can be learned about the seismotectonics of Italy by overlaying all geofluid observations selected in **Selecting the Terms of Comparison** Section over the countrywide distribution of large earthquakes, seismogenic faults and other major tectonic lineaments. In the process, we plan to learn also how the distribution of thermal springs, CO_2 emissions and CH_4 emissions relates to the recent geodynamic evolution of the Italian peninsula.

Thermal Springs: Potential Evidence for Lithospheric Discontinuities

Figure 4 shows the distribution of our "selected" and "removed" datasets of thermal springs (see **Thermal Springs** Section). A first notable feature is that they tend to occur rather regularly along the axis of the Apennines. To investigate this circumstance more quantitatively we calculated a variogram, i.e. a description of the spatial continuity of the data, using the classical methodology described and supplied by Pannatier (1996). **Figure 9** shows variograms calculated for any azimuth and for a 135°N trend; this corresponds to the average strike of the Apennines, from their northern boundary, near the Tuscany–Liguria border (~44.0°N), to the Pollino Massif (~40.0°N), near the Basilicata–Calabria border, over a distance of about 700 km. Comparison between the two trends shows that the most significant peak is found along the Apennines trend at a distance of about 30 km. In other words, the dominant feature of the spatial distribution of all springs is a ~30 km spacing in the NW–SE direction. This distance is slightly larger than the average length of the largest

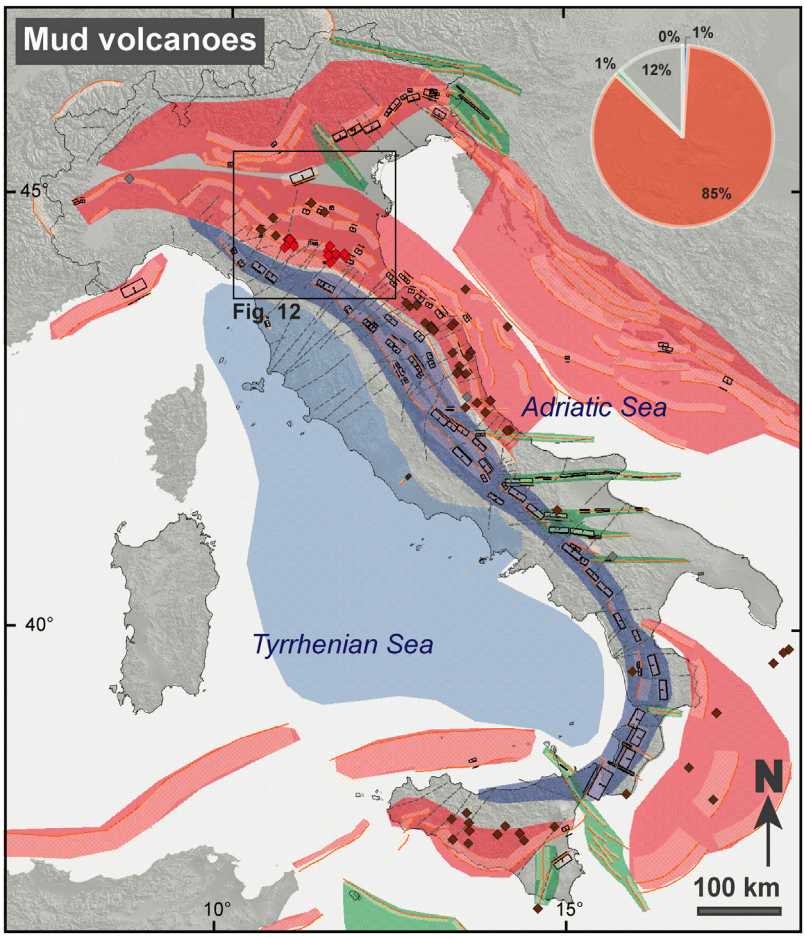

FIGURE 7 | Distribution of mud volcanoes (see **Gas Seeps and Mud Volcanoes**, **CH_4 Emissions and Mud Volcanoes** and **CH_4 Emissions and Mud Volcanoes: The Signature of Contractional Domains** Sections). Tectonic domains, seismogenic sources and transverse lineaments are shown as in **Figure 2**. Removed datapoints are shown in grey. Selected datapoints are shown in red if they are discussed in the text, otherwise in dark brown. The area shown with a rectangle is discussed in **CH_4 Emissions and Mud Volcanoes: The Signature of Contractional Domains** Section. The pie chart shows the distribution of mud volcanoes in different active tectonic domains (see **Table 1**). Notice that as many as 85% of these peculiar phenomena fall in areas of active contraction.

Individual Seismogenic Sources (see **Data on Active and Seismogenic Faulting** Section) that are encountered along the crest of the Apennines. Current empirical relationships show that in a typical normal-faulting environment, such as that dominating the current tectonics of the Apennines, a 30 km-long fault typically generates a M_w 6.8 earthquake: this estimate matches the range of the largest observed M_w of Apennines earthquakes (6.5–7.0).

The spacing between thermal springs tends to decrease in geothermal areas (e.g., McNitt, 1978; Minissale, 2018), and to increase in cooler, tectonically stable areas. These features were qualitatively described over 50 years ago by Waring (1965), who compiled a rather complete worldwide catalogue of thermally anomalous springs.

We then overlaid the "selected dataset" onto the seismogenic sources (ISSs and CSSs) and the "transverse lineaments" introduced in **Data on Active and Seismogenic Faulting** Section. This procedure reveals a rather systematic anticorrelation between earthquake sources and the distribution of thermally anomalous springs all along the Apennines. A closer inspection shows that

(1) thermal springs appear to be anticorrelated with the surface projection of major seismogenic sources, implying that the relevant crustal volumes are less permeable than adjacent areas. This phenomenon has also been inferred by Micklethwaite et al. (2010) from the distribution of ore deposits, which occur mainly along transverse features located at fault tips, rather than along large, well-developed faults;
(2) conversely, many thermal springs cluster at the edges of the best defined sources, as suggested over 2 decades ago by Curewitz and Karson (1997). More precisely, in many instances where well-identified sources define a clear segmentation pattern, the springs seem to occur along tectonic lineaments that mark the transition from one segment to the other. The evidence from the DISS database suggests that these discontinuities act as segment

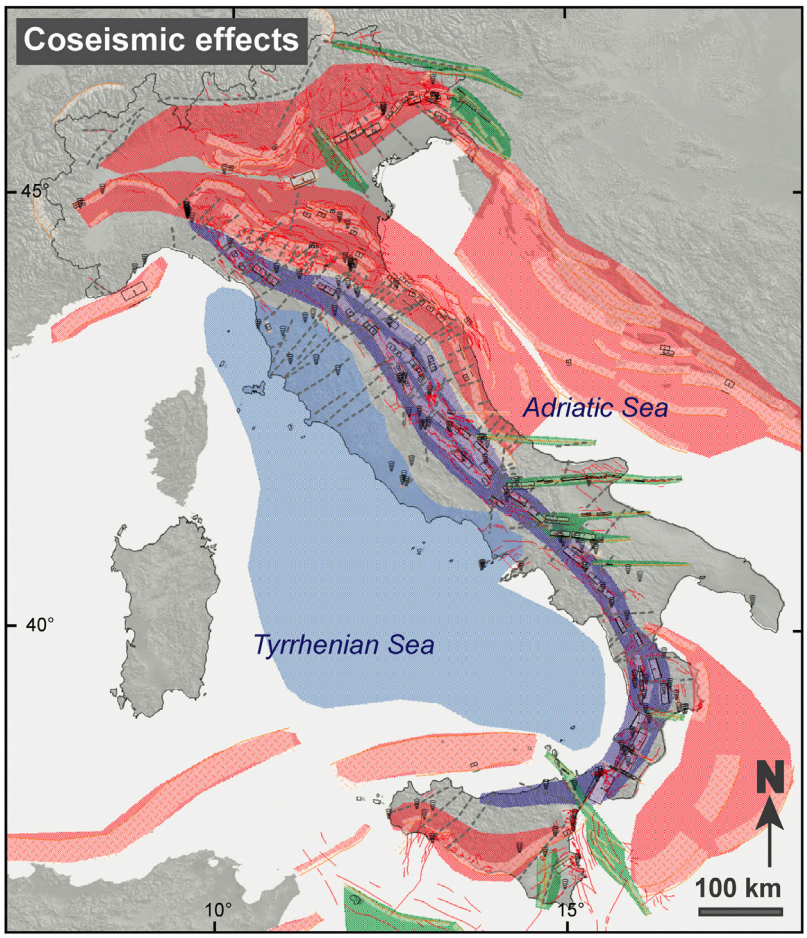

FIGURE 8 | Summary of the testimonies filed under "Gas emissions and mud-cone eruptions" (79 data) and "H_2S emissions" (60 data) from the CFTI5Med catalogue. All data are shown with a 3D spiral symbol.

boundaries for earthquake strain accumulation, whereas the evidence from our selected thermal springs is that they also allow deep fluid circulation to reach the surface. **Test Case 1: The Garfagnana Region, Northern Apennines** Section discusses a significant example from the Garfagnana region (northern Tuscany);and

(3) some thermal springs (and CO_2 emissions) line up along major lithospheric lines of weakness that cross the Apennines; these lines may hold significant seismogenic potential, particularly in the southern Apennines, or be only mildly seismogenic as a result of passive reactivation by regional tectonic forces. **Test Case 2: The Olevano–Antrodoco–Sibillini Line, Central Apennines** Section discusses the example of the Olevano–Antrodoco–Sibillini Line.

The postulated correlation between thermally anomalous springs and transverse lineaments is supported by recent experience during the search for exploitation of natural geofluids (hydrocarbons, steam etc.). Important physical constraints were reviewed by Hickman et al. (1995), Caine et al. (1996), Holness (1997), Manning and Ingebritsen (1999), Sibson (2000), Kennedy and van Soest (2007), Faulkner et al. (2010), Ingebritsen and Manning (2010), Micklethwaite et al. (2010), Bense et al. (2013), and Jang et al. (2018), among several others. These investigators have shown that fluid flow through fractured rock masses depends on their permeability, and specifically 1) on the hydraulic conductivity of fractures, and 2) on the degree to which fractures form continuous pathways or barriers through the rock volume.

In the next two subsections we discuss at a higher spatial resolution the interplay of tectonics and thermal springs in two selected test areas of the northern and central Apennines, respectively.

Test Case 1: The Garfagnana Region, Northern Apennines

The area referred to as Garfagnana (**Figure 10**) coincides with the upper and middle reach of the Serchio River valley at the northwestern edge of Tuscany. Garfagnana is located between the axis of the Apennines and the smaller Apuan Alps, which separate it from the Tyrrhenian coastline. According to the DISS database, the Upper Serchio Valley was the locus of the September 7, 1920 catastrophic earthquake (M_w 6.5). The

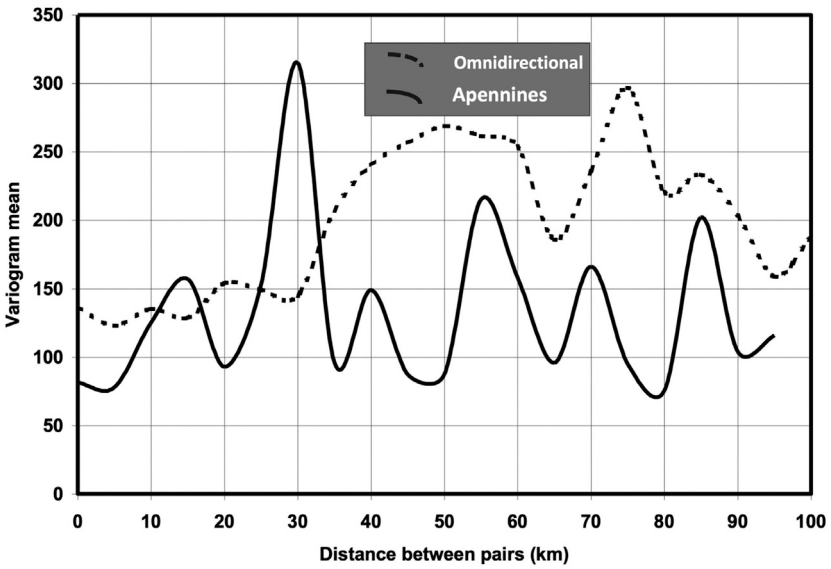

FIGURE 9 | Variogram of our selected thermal springs occurring in the latitude range 44.0°N to 40.0°N (see text and **Supplementary Material** for details). The continuous and dashed lines represent the result of an analysis performed along the strike of the Apennines and along the average of all possible directions, respectively. The *X* axis reports the distance between pairs of springs, whereas the *Y* axis shows the value of the variogram function. The most significant peak is found along the function calculated along the Apennines trend at slightly less than 30 km distance.

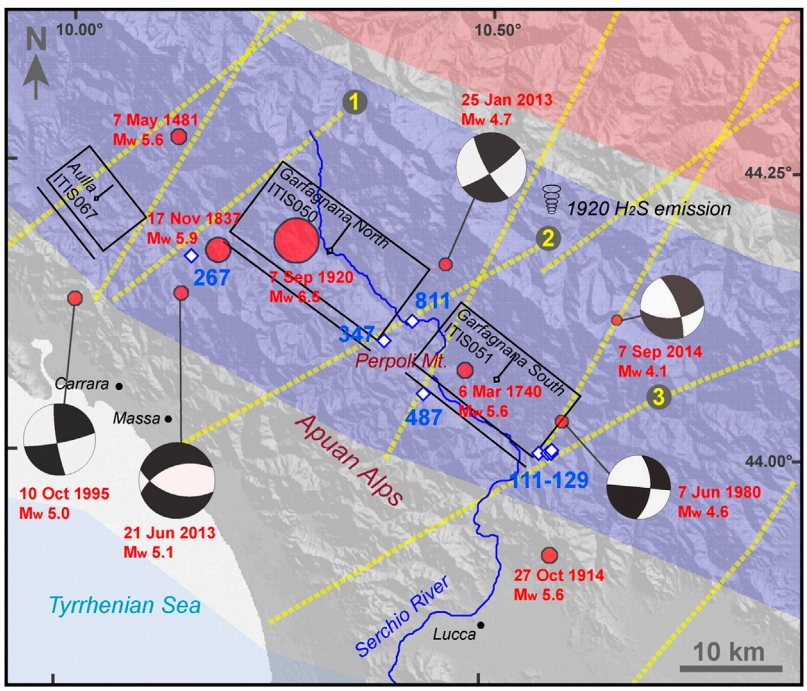

FIGURE 10 | Seismogenic faults, transverse lineaments and thermal springs in the Garfagnana area, northern Tuscany (see **Figure 4** for location). The black boxes are the surface projections of Individual Seismogenic Sources from the DISS database: source ITIS050 is assumed to have caused the September 9, 1920, M_w 6.5 earthquake, while source ITIS051 is assumed to be quiescent and capable of generating a M_w 6.1 earthquake. The transverse lineaments are shown with yellow dashed lines and identified by a number (see text). The springs are shown by diamonds and are labeled with their ID from the *Database of Thermal Springs*. The 3D spiral symbol locates a H_2S emission that was activated following the 1920 earthquake (Casoni site, from CFTI5Med; see **Earthquake-Induced Geofluid Emissions** Section). Notice that the most recent earthquakes fall near the edges of the largest seismogenic normal faults, that their faulting mechanism is consistently strike-slip.

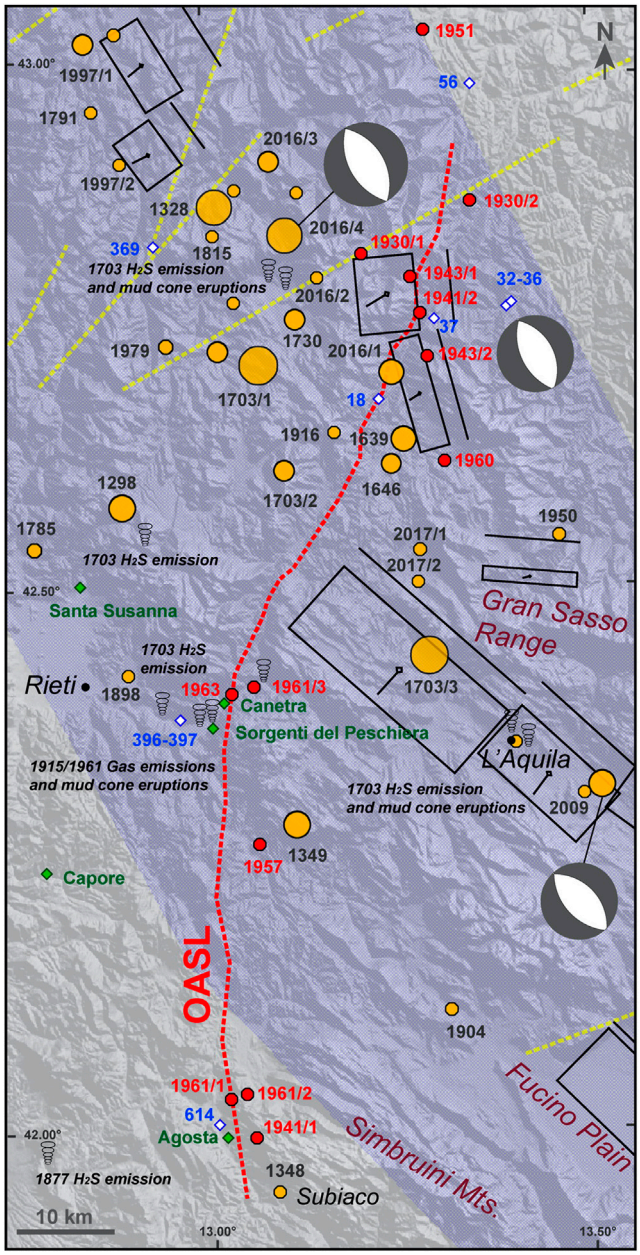

FIGURE 11 | Seismogenic faults, transverse lineaments, thermal springs and CO_2 emissions in the central Apennines (see **Figure 4** for location). The black boxes are the surface projections of Individual Seismogenic Sources from the DISS database: they are assumed to have caused—from north to South—the September 26, 1997 (M_w 6.0), the October 14, 1997 (M_w 5.6), the August 24, 2016, M_w 6.2, Amatrice (sources from Valensise et al., 2016), the February 2, 1703, M_w 6.7, and the April 6, 2009, M_w 6.3, L'Aquila earthquakes. Transverse lineaments are shown by yellow dashed lines, and the OASL is highlighted in red. Thermal springs are shown by blue diamonds along with their ID from the *Database of Thermal Springs*. CO_2 emissions are shown by green diamonds and labeled with their name from the database available at http://googas.ov.ingv.it. The 3D spiral symbols locate gas emissions, mud cone eruptions and H_2S emissions that were activated following the 1703 earthquake sequence and the 1877, 1915 and 1961 earthquakes

(*Continued*)

same database shows that the Lower Serchio Valley hosts a seismogenic source similar to that responsible for the 1920 earthquake, but which has not been active historically over its entire length of 15–18 km. These two Individual Seismogenic Sources are labeled in **Figure 10** (ITIS050-Garfagnana North and ITIS051-Garfagnana South, respectively).

The entire region is crisscrossed by a number of pre-existing tectonic structures referred to as "tectonic lineaments" (see **Data on Active and Seismogenic Faulting** Section), which seem to control the location and length of the two mentioned seismogenic sources, effectively acting as segment boundaries.

The three most notable lineaments are (from north to south, labeled 1, 2, 3 in **Figure 10**) the Sarzana–Equi Terme Line (Bartolini and Bortolotti, 1971; Boccaletti et al., 1977), the Massa-Monte Cervarola Line (Boccaletti et al., 1977; Puccinelli, 1987), and the Viareggio–Val di Lima–Bologna Line (Boccaletti et al., 1977; Bemporad et al., 1986; Sorgi et al., 1998).

Several significant thermal springs and earthquakes fall along all three of these lineaments, again suggesting that they are not shallow-rooted features generated during the latest compressional tectonic phase, but rather mark the surface expression of important lithospheric discontinuities, as highlighted in the geological literature (e.g., Fazzuoli et al., 1985; Puccinelli et al., 2015). In detail (each spring is identified with its name, ID and reported temperature):

Sarzana-Equi Terme Line (#1)—Spring: Equi Terme, ID 267 (24°C). This lineament bounds the Apuan Alps to the north and coincides with a seismogenic relay ramp discussed in Stramondo et al. (2014), following the June 21, 2013, M_w 5.1, Lunigiana earthquake. This event was caused by oblique slip on a dominantly normal fault striking perpendicular to the main Apennines trend, and may represent a smaller repeat of the April 11, 1837, M_w 5.9, Equi Terme earthquake. The lineament is supposed to have hosted the October 10, 1995, M_w 5.0 earthquake, that is assigned a pure strike-slip mechanism (Frepoli and Amato, 1997).

Massa-Monte Cervarola Line (#2)—Springs: Turrite Secca, ID 347 (34°C) and Pieve Fosciana, ID 811 (39°C), both reported as falling on recent surface faults in the geological literature (Puccinelli et al., 2015). This lineament marks the Monte Perpoli threshold, a physiographic and structural discontinuity the separates the Garfagnana basin into two halves. It was the locus of the January 25, 2013, M_w 4.7, strike-slip earthquake. According to CFTI5Med, the September 7, 1920 event triggered a H_2S emission near Casoni, about 15 km east of the causative fault.

FIGURE 11 | (see **Earthquake-Induced Geofluid Emissions** and **Test Case 2: The Olevano–Antrodoco–Sibillini Line, Central Apennines** Sections; from CFTI5Med). Earthquakes of M_w 5.5 and larger are shown by yellow symbols, while those mentioned in the text are shown in red (from CPTI15). The largest instrumental earthquakes locate along the crest of the Apennines and are caused by normal faulting along planes dipping 35°–50° to the southwest (e.g., http://terremoti.ingv.it/tdmt, Scognamiglio et al., 2006, and periodical updates). Notice that the two fault patches that experienced the largest slip during the August 24, 2016 earthquake (black boxes) occurred on either side of the OASL.

Viareggio-Val di Lima-Bologna Line (#3)—Springs: Bagni di Lucca cluster, ID 111-129, formed by 19 independent springs known and exploited for at least two millennia (34–55°C). This lineament transects the southern Apuan Alps, mirroring Lineament #1. It was the locus of two pure strike-slip earthquakes on June 7, 1980, M_w 4.6 (Eva and Solarino, 1992) and September 7, 2014, M_w 4.1 (http://terremoti.ingv.it/tdmt; Scognamiglio et al., 2006), and of the October 27, 1914, M_w 5.6 earthquake, which has recently been assigned a focal depth of 24 km (Sbarra et al., 2019).

Additional springs are reported in the official geological map of Italy (Puccinelli et al., 2015) as falling on the surface projection of the Garfagnana South source near its intersection with the Massa-Monte Cervarola Line. The most important is the Gallicano spring, ID 487 (23°C).

Test Case 2: The Olevano–Antrodoco–Sibillini Line, Central Apennines

The NNE-SSW Olevano–Antrodoco–Sibillini Line (OASL, formerly known as Ancona–Anzio Line: Parotto and Praturlon, 1975; Castellarin et al., 1978, Castellarin et al., 1982; Patacca et al., 1990; Calamita et al., 2012; Di Domenica et al., 2014, with references) marks the contact between units overlain onto the Latium–Abruzzi carbonate platforms and units belonging to the Umbro–Marchean Apennines (see **Figure 11**). It is interpreted as the surface trace of a regional paleogeographic feature that may also have acted as a lateral ramp or transpressional fault during the buildup of the Apennines, and its deeper portion may coincide with a large inherited Mesozoic fault.

The OASL is easily recognized only in the portion of the Apennines chain that is currently undergoing uplift and extension (in dark blue in **Figures 4–8**): nevertheless, according to the literature (e.g., Castellarin et al., 1978), and as suggested by thermal springs and CO_2 emissions (see **Figure 11**), and even by an align-ment of travertine deposits (Minissale, 2004: see his Figure 4), the OASL may well extend beyond the boundaries of this domain, beneath the volcanic deposits of the peri-Tyrrhenian area and the young terrigenous deposits of the peri-Adriatic area.

The OASL appears as a distinctive feature in the topography and in the geology of the central Apennines, and hosts a number of significant geofluid occurrences, including:

- At least 11 thermal springs (from north to south: Amandola, ID 56 (38°C); Acquasanta Terme, ID 32–36 (26–38°C); Acquasanta Terme-Venamartello, ID 37 (25°C); Accumoli, ID 18 (21°C); Ceciri and Bonafaccia, near Cittaducale, ID 396–397 (25–26°C); and Marano Equo, ID 614 (24°C);
- At least three CO_2 emissions (from north to south: Canetra, Sorgenti del Peschiera, Agosta);
- Gas emissions, H_2S emissions and mud volcanoes observed near Cittaducale following the large 14 Jan–2 Feb 1703 earthquake sequence, when two M_w 6.7–6.9 earthquakes occurred just to the NW and to the SE of the site, and following the catastrophic January 15, 1915 earthquake (M_w 7.1), located 50–80 km SE of the site;
- The large Peschiera springs, feeding the city of Rome.

Furthermore, the OASL is the locus of several minor earthquakes, all seemingly shallow-seated (focal depth <10 km), that occur spatially and temporally clustered along its entire length of about 130 km. For instance, 13 clearly felt earthquakes are reported over a period of 33 years (Apr 7, 1930, M_w 4.5; Nov 9, 1930, M_w 4.3; Sep 8, 1941, M_w 4.4; Dec 19, 1941, M_w 5.0; Jan 16, 1943, M_w 5.0; Jan 29, 1943, M_w 4.9; Sep 1, 1951, M_w 5.3; Apr 11, 1957, M_w 4.9; Mar 16, 1960, M_w 4.4; Apr 10, 1961, M_w 4.6; Apr 12, 1961, M_w 4.6; Oct 31, 1961, M_w 5.1, the only event to cause sizable damage in Antrodoco and its surroundings; and Feb 2, 1963, M_w 4.6; see **Figure 11**).

The OASL acted as a major segment boundary during the mentioned 14 January–2 February 1703 earthquake sequence, when two M_w 6.9 and 6.7 shocks occurred just to the NW and to the SE of the lineament and a M_w 6.0 occurred on 16 January very close to the OASL itself (from CFTI5Med). The OASL is suspected to have played a similar role during other earthquake sequences, such as the August–October 2016 events in the Amatrice–Norcia–Visso area (Bonini et al., 2016; Bonini et al., 2019). The OASL falls between the two fault patches that experienced the largest slip during the August 24, 2016, M_w 6.0, Amatrice earthquake, although this is commonly considered a single event (shown by two black boxes and red labels in **Figure 11**).

In summary, a distinct alignment of thermal springs and CO_2 emissions in a low-heat-flow inner portion of the peninsula highlights the presence of the OASL, a major tectonic lineament that played–and still plays–an important role 1) in the geological evolution of the central Apennines, and 2) in controlling the segmentation of seismogenic faults in central Italy, while 3) releasing its own low-level but continuous seismicity.

CO_2 Emissions: Combined Evidence for Carbonate Dissolution and Mantle Degassing

Natural CO_2 emissions are characteristic of areas undergoing extension. A recent paper by Tamburello et al. (2018) explored the relationships between CO_2 degassing and active faulting on a global scale, concluding that this process is greatly favored by the presence of surface-breaking normal faults. This is one of the first papers that focused explicitly on the relationships between CO_2 emissions and active faulting: some of its conclusions, however, are disproved by our observations on central Italy, one of the areas of the globe where this process has been best investigated.

Figures 2, **5** show that Italian CO_2 emissions occur dominantly in the peri-Tyrrhenian domain (light blue band in both figures; see pie chart in **Figure 5** and **Table 1**). Very few are seen along the main axis of the central and southern Apennines, and none are reported for the northern Apennines, except for the Pieve di Santo Stefano–Caprese Michelangelo area (discussed in **Test Case 1: The Garfagnana Region, Northern Apennines** Section), and for some CO_2 associated with gas seeps, which were demonstrated by Capozzi and Picotti (2010) to be not of deep

origin. Furthermore, no CO_2 is generally reported in the composition of fluids rising from several wells drilled along the axis of the Apennines, mostly in the early phases of the hydrocarbon exploitation in Italy (see VIDEPI Project: https://www.videpi.com/videpi/videpi.asp). Finally, CO_2 emissions are virtually absent in areas where large reverse and thrust faults accommodate ongoing contraction (red bands in **Figure 5**).

Most importantly, CO_2 emissions are largely anticorrelated with the occurrence of large seismogenic normal faults (blue band in **Figure 5**), and in particular with the Individual Seismogenic Sources. In fact, the Italian case suggests that the control by extensional tectonics invoked by Tamburello et al. (2018) is restricted to areas of ongoing crustal rifting and mantle upwelling, such as the peri-Tyrrhenian volcanic belt of Tuscany, Latium and northern Campania. Therefore, their conclusion that there exists a "*...positive spatial correlation between gas discharges and extensional tectonic regimes...*" must be partially reconsidered, at least for Italy and for areas that share a similar setting worldwide. As discussed earlier, there is a useful distinction between extension generated by crustal thinning, that dominates in the peri-Tyrrhenian domain, and post-orogenic extension, the engine of nearly all seismicity in central Italy (and of most large earthquakes countrywide: e.g., Basili et al., 2008; Meletti et al., 2008; Carafa et al., 2015, all with references: see **Figure 2**, right). Similarly, the "*...concordance between CO_2 discharge, seismic activity, and major faults...*" is a primary characteristic of the rift area the authors use to support this statement (the East African Rift), but is not observed in Italy, as shown by our data.

Our observations have two main implications. The first is that generic tectonic extension alone is not sufficient to promote a significant discharge of CO_2. The second is that, at least in Italy, CO_2 discharge is abundant almost exclusively where the heat flow is rather high (>100 mW/m^2), implying that most emissions may originate from carbon dissolution at relatively shallow depth. The ascent of CO_2 may be favored by a network of small-scale normal faults and extensional joints, but in high-heat-flow areas the rheology of the relevant crustal volumes prevents the generation of larger faults, and hence of significant earthquakes. In fact, the occurrence of significant earthquakes is largely anticorrelated with the existence of abundant CO_2 emissions, as clearly seen over the entire peri-Tyrrhenian extensional domain and specifically in central and western Tuscany (see **Figures 2**, **5**).

Tamburello et al. (2018) also contend that CO_2 degassing is favored by the subvertical attitude of normal faults, whereas in contractional domains the rise of mantle fluids would be prevented by the low-dip of thrust faults and by the stacking of multiple thrust sheets. The evidence available for the Italian peninsula, however, does not support this statement. For a combination of reasons that we will not discuss here [the reader may refer to Doglioni et al. (1999), and Tiberti et al. (2017), for a discussion of this topic], the attitude of normal faults generated by post-orogenic extension is generally rather low. One of the principal extensional structures of central Italy, commonly referred to as the Etrurian Fault System (e.g., Boncio et al., 2000, among several others), dips consistently less than 45°, the opposite of what would be expected for a typical Andersonian normal fault, and often less than 30°. In fact, many well investigated Italian seismogenic normal faults are positively assigned a low dip, including the causative faults of the September 26, 1997, April 6, 2009 (see Table 5 in Vannoli et al., 2012), August 24, 2016 (Bonini et al., 2016) and October 30, 2016 (see Tables 1, 2 in Bonini et al., 2019) earthquakes.

Nevertheless, there are significant departures from the above rules, and substantial CO_2 degassing may take place even in the innermost portions of the Apennines. In **Data on Active and Seismogenic Faulting** Section we discussed the existence and role of the "transverse lineaments", most of which straddle the crest of the Apennines. In **Test Case 1: The Garfagnana Region, Northern Apennines** and **Test Case 2: The Olevano–Antrodoco–Sibillini Line, Central Apennines** Sections we showed examples of how these discontinuities affect both the location of geofluid emissions, and particularly of thermal springs, and the geometry and extent of the seismogenic sources. In the next three subsections we discuss at a higher spatial resolution the interplay of tectonics, CO_2 emissions and thermal springs in three selected test areas of the central-northern, central-southern and southern Apennines, respectively.

Test Case 1: Central-Northern Apennines

A spectacular case of CO_2 degassing is found in the area of Pieve di Santo Stefano–Caprese Michelangelo (shown with A in **Figure 5**), near the boundary of Tuscany, Umbria, Marche and Romagna. Degassing is so abundant that the CO_2 has long been exploited by the bottled beverage industry (e.g., Chiodini et al., 2004). Here a 20 km-wide, NE-SW trending discontinuity appears to break and displace both the main extensional trend running along the crest of the Apennines, and the trend of compressional structures running along their eastern (Adriatic) flank (see **Figure 2**, right). It is generally interpreted as a long-lived lithospheric tectonic lineament cross-cutting the chain from the Tyrrhenian to the Adriatic Sea (e.g., Nirta et al., 2007 and reference therein). As such, it experienced different kinematics through time, accommodating the differential motion between different portions of the Apennines during the Miocene rotation of the chain and the subsequent opening of the Tyrrhenian Sea (Nirta et al., 2007).

Bonini (2009) investigated the structural control of the abundant release of CO_2-rich fluids at Pieve Santo Stefano. Based on a detailed fault-pattern analysis, he recognized that CO_2 emissions locate along steep NE-trending faults associated with the Val Marecchia Line, perhaps the most important of all the transverse lineaments crossing this portion of peninsular Italy. According to Nirta et al. (2007) and Bonini (2009), the Val Marecchia Line corresponds to a set of overstepping, NE-SW major transverse lineaments described in the geological literature for over 50 years (starting with Ghelardoni, 1965), and also with a distinct promontory of the heat flow pattern (Pauselli et al., 2019: see **Figure 3**). Surprisingly, this corridor marks also a substantial gap in seismic moment release along the crest of the Apennines, in terms of both major earthquakes and background seismicity;

perhaps the most significant gap of the entire northern and central Apennines.

Test Case 2: Central-Southern Apennines

A roughly E–W, 55 km-long alignment of six CO_2-rich emissions is found west of the Apennines regional divide at an average latitude of 41.65°N, near the Lazio–Molise administrative boundary (from west to east: Fontana Liri, Lago Fibreno, Polla Monticchio, Casa Ianni, Capo Volturno, and Isernia–Castel Romano; shown with B in **Figure 5**). It falls along the westward extension of a well-known, ~180 km-long, ~20 km-wide, E–W-trending major shear zone that affects (from west to east) portions of the Adriatic crust beneath the external Apennines thrust belt, the Apulian foreland and the Molise–Mattinata–Gondola shear zone (see Di Bucci et al., 2010; Kastelic et al., 2013 and references therein). This large discontinuity is the locus of recent, instrumentally investigated earthquakes, such as the Oct 31–Nov 1 2002 Molise events (both with M_w 5.7), and of a number of large historical earthquakes, such as the July 30, 1627, M_w 6.7 event.

The DISS database represents this important seismogenic area with a large CSS and eight ISSs, one of which is assumed to be the source of one of the main shocks of the M_w 7.2, December 5, 1456 earthquake, the largest—or second largest—Italian earthquake of all times (Fracassi and Valensise, 2007). Available focal mechanisms consistently show right-lateral strike-slip over the entire structure, which is commonly interpreted as an inverted, left-lateral Mesozoic shear zone (Di Bucci et al., 2010).

The identified alignment of CO_2 emissions appears to continue this large shear zone westward, suggesting its possible extension to the west beneath the Apennines foothills of southern Latium, and may shed light on the origin of damaging historical earthquakes that occurred further to the west, between Sora and Frosinone.

Test Case 3: Southern Apennines

A further E–W alignment of at least 11 CO_2 emissions and 24 thermal springs is seen west of the Apennines drainage divide around the latitude of 40.70°N. From west to east the CO_2 emissions are found at San Benedetto, near Polla and Contursi (cluster of nine emissions), and at Terme di San Cataldo (shown with C in **Figure 5**), whereas the thermal springs are Solfurea della Grotta (Maiori), ID 605 (24°C), Acque Grecole di Salerno, ID1046 (25°C), All'Ovest di Salerno, ID 1047 (22°C), Montecorvino Pugliano, ID 691 (22°C), a cluster of 14 springs around Contursi Terme, ID 422–434 (21–43°C), Oliveto Citra, ID 763 (32°C), Bella, ID 178 (38°C), and Terme di San Cataldo, ID 174–177 (25–53°C).

Similarly, to the previous case, this discontinuity follows a well-known, though much shorter, E-W-trending, deep shear zone that has been the locus of instrumentally-investigated strike-slip earthquakes, such as the May 5, 1990, Potenza event (M_w 5.8). The same shear zone could be the source of the July 31, 1561, M_w 6.3, and August 19, 1561, M_w 6.7 earthquakes, the two largest shocks of a sequence that affected the Basilicata-Campania border in historical times.

CH_4 Emissions and Mud Volcanoes: The Signature of Contractional Domains

The occurrence of CH_4 emissions and mud volcanoes exhibits a spatial pattern that is complementary to that of the thermal springs and CO_2 emissions. Ciotoli et al. (2020) recently explored the modes and rates of CH_4 seepage, concluding that this process is chiefly associated with convergent, hydrocarbon-bearing sedimentary basins. They added that the details of the interplay between seepage and tectonics are generally unknown except for a few local studies. We maintain that in this respect Italy makes a perfect case study, due to the combination of good-quality data on tectonics and active faulting, an extensive dataset of CH_4 seepages, data from carbon-bearing deposits, and data from several hundred wells drilled for hydrocarbon exploration starting in the 1950s (see the **Gas Seeps and Mud Volcanoes** and **CH_4 Emissions and Mud Volcanoes** Sections).

CH_4 Emissions and Mud Volcanoes: Distribution

A simple inspection of our dataset (**Figures 6**, **7**, **Table 1**) shows that the vast majority of mud volcanoes (85%) occur in regions currently undergoing compression and shortening, whereas gas seeps are more sparse: 54% fall in areas currently undergoing contraction, but 20% of them are 'undefined' and 15% occur in areas of post-orogenic extension. Most likely this different behavior has to do with the construction of the Apennines range, which proceeded as a propagating wave causing compression at the front and extension in the back. Under these circumstances, a significant number of gas seeps occur in areas that were undergoing contraction until recently, but that are no longer recording any shortening. For instance, in the northern Apennines (Bonini, 2013: see his Figure 3) documented the existence of number of fossil gas seeps aligned near the boundary between currently active extension, to the SW, and currently active contraction, to the NE.

The actively contracting areas correspond with the hydrocarbon-bearing basins of the northern and central Apennines, of eastern Calabria and southern Sicily, along with their associated Adriatic and Ionian foredeeps; an association that agrees with observations in other productive basins worldwide (Etiope and Klusman, 2002; Van der Meer et al., 2002). It is also expected that many gas seeps and mud volcanoes exist in the Adriatic and Ionian offshore; in fact, some have already been reported in the recent literature (e.g. Donda, et al., 2019), but they are still too sparse to allow statistically significant inferences.

Perhaps surprisingly, the gas seeps and mud volcanoes are not uniformly distributed, but over 80% of them concentrate in two specific regions that are—or used to be, prior to heavy industrial exploitation over the past 70 years–the two largest onshore CH_4 fields countrywide (see red symbols in **Figure 6** and **Figure 7**): a relatively small (~18,000 km^2, about 6% of the entire country) rectangular area encompassing the northeastern flank of the northern Apennines and part of the adjacent southern Po Plain, and an even smaller area (~8,000 km^2) of central-southern Sicily.

More specifically, gas seeps and mud volcanoes occur almost exclusively where the pre-Pliocene bedrock—a set comprising variably deformed rocks—is exposed, and are very sparse or absent in the main present-day alluvial basins, e.g., the Po Plain, where the CH_4 reservoir rocks are buried beneath a thick blanket (100 m to over 8 km) of Plio-Pleistocene and Holocene deposits (e.g., Vannoli et al., 2015, with references). This circumstance causes truncation and sealing of potential ascending pathways, but may not prevent CH_4 from being dispersed into the atmosphere through pervasive microseepage. In fact, slow degassing from reservoirs located beneath the southern side of the Po Plain is very likely, as these reservoirs are the largest of the entire hydrocarbon province (e.g., Etiope et al., 2007).

A significant aspect of the distribution of gas seeps is their apparent anticorrelation with the largest earthquakes. Following a statistical study of the distribution of CH_4 fields in the southeastern Po Plain, Mucciarelli et al. (2015) proposed that their productivity is anti-correlated with the presence of seismogenic faults capable of M 5.5+ earthquakes. A visual inspection of **Figure 6** shows that the concentration of gas seeps is very low along a ~110 km stretch of coastal Romagna and Marche, between Cesena and Ancona. The same area shows a concentration of seismogenic faults and of significant earthquakes (**Figure 2**), and public data from the hydrocarbon industry show that it is devoid of deep wells—and presumably of productive CH_4 fields—whereas they are numerous to the northwest and southeast (https://www.arcgis.com/home/user.html?user=DGSUNMIG). The absence of gas seeps can hence be interpreted in terms of lack of CH_4 in the deep reservoirs, and both lines of evidence would be indicative of a larger seismogenic potential of the area under investigation.

CH_4 Emissions and Mud Volcanoes: Structural Control

According to the literature (e.g., Jakubov et al., 1971; Etiope et al., 2007; Bonini, 2012; Etiope et al., 2014; Mazzini and Etiope, 2017; Maestrelli et al., 2019), the reservoir of a mud volcano is generally located over the crest of a growing anticline, provided that the fluids are properly trapped by a sealing rock unit. This configuration is in agreement with the setting of the main fields of mud volcanoes in Italy—Regnano, Montegibbio, Nirano, and Ospitaletto—all of which occur in the hangingwall of the Pedeapenninic Thrust Front, a seismogenic system running along the foothills of the northern Apennines (PTF; DISS Working Group, 2018; **Figure 12**), and specifically near the crest of the anticlines associated with it. It is also well known that fault intersections act as preferential pathways for deep fluids, ultimately allowing them to easily reach the surface (see Mazzini and Etiope, 2017 and references therein). With specific reference to Italy we remark that:

(1) The reservoir-anticlines are usually generated by relatively shallow thrusts. **Figure 12** shows that these are concentrated near the nearly emergent PTF, or where the Pliocene deposits are thin or absent, or where the thrusts are very shallow; and

(2) A seal-bypass system is required to allow fluids to reach the surface. An efficient superficial path may be provided by extrados fracture arrays developed at the fold crest, i.e. parallel to the anticline axis (e.g., Bonini, 2012; Maestrelli et al., 2019). Nevertheless, we maintain that most mud volcanoes ultimately owe their existence to a deeper path that may be provided by some of the transverse structures described in **Data on Active and Seismogenic Faulting** Section: well-established, long-lived subvertical lineaments whose activity is testified by frequent background seismicity (see **Figure12A**) and that may represent the main pathways for fluid expulsion.

In fact, many Italian mud volcano fields are geographically coincident with zones where the dip of the regional monocline changes more drastically (Mariotti and Doglioni, 2000), likely indicating the presence of deep slab tears (Rosenbaum et al., 2008; Rosenbaum and Piana Agostinetti, 2015), which in turn correspond to major chain-orthogonal transverse faults in the upper crust (e.g., Vannoli et al., 2015 for the Po Plain). The adjacent fields of Nirano, Montegibbio, and Ospitaletto are located where the foreland monocline plunges beneath the northern Apennines thrust belt, with a dip that varies laterally between 8° and 23° (see cluster #1 in **Figure 12B**). This area appears to be a crucial crossroad that controls the extent of forward propagation of the PTF, that advanced further to the east of it and less to the west. Furthermore, this area of deformation locates near a major transverse structure generally known as the Secchia Line (Castaldini et al., 1979; Castellarin et al., 1985), whose role is testified by the sharp western termination of aftershocks following the 2012 Emilia earthquake sequence (**Figure 12A**). In turn, the Nirano mud volcanoes fall near a chain-orthogonal fault cutting an anticline that has deformed Plio-Pleistocene clayey sediments (Gasperi et al., 1987; Bonini, 2012).

The mud volcanoes located south of Bologna (San Martino in Pedriolo, San Clemente, Casa Bubano etc.: see cluster #2 in **Figure 12B**) also concentrate where the PTF intersects the Prato-Sillaro Line (**Figure 12A**), another transverse lineament identified as the possible surface of a slab tear (Rosenbaum and Piana Agostinetti, 2015). The Prato-Sillaro Line plays both an active and a passive role, because it is also the locus of earthquakes swarms and occasional moderate-size earthquakes (see Vannoli et al., 2015: **Figure 12A**).

In summary, the data suggest that most of the largest Italian mud volcanoes locate where an actively growing anticline intersects a primary transverse lineament. Therefore, we propose a systematic, genetic relationship between the existence and location of mud volcanoes and changes in dip of the foreland monocline (see **Figure 12C**).

DISCUSSION

In this work we investigated in detail the relationships among geofluid emissions, tectonics and seismogenic sources in Italy

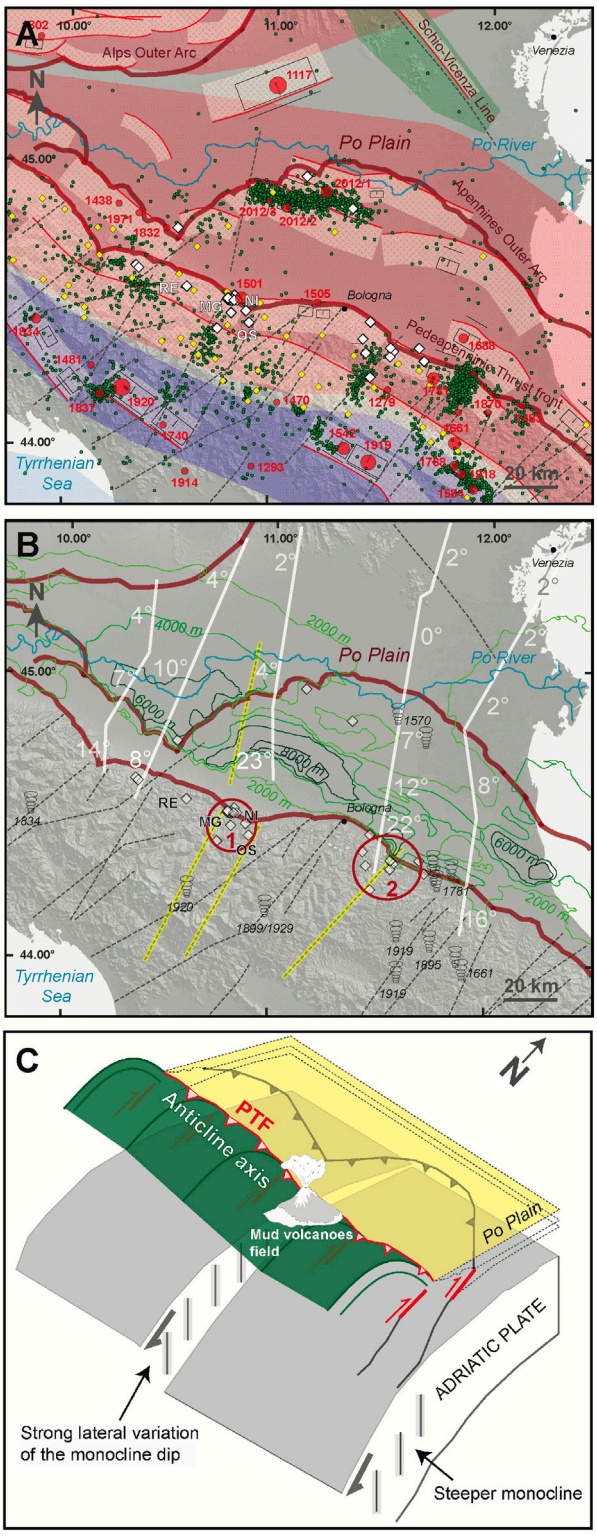

FIGURE 12 | Panel A- Seismogenic faults (black boxes and red ribbons), transverse lineaments (black dashed lines), main structural elements (brown lines; from Bigi et al., 1992), gas seeps (yellow diamonds) and mud volcanoes (white diamonds) in the northern Apennines (see **Figure 7** for location). Active tectonic domains as in **Figure 2**. Earthquakes of $M_w \geq 5.5$ are

(*Continued*)

(refer to **Figures 13**, **14** for a summary of methods, approaches and results). Our work has the threefold goal of improving the understanding of the relationships between fluid emissions and tectonics in Italy, improving seismic hazard estimates by constraining the location of poorly visible faults, and contributing to the ongoing efforts to calculate the global budget of greenhouse gases.

Some of our findings and interpretations challenge those arising from global compilations of geofluids and tectonics, as they stem from relatively high-resolution evidence gathered on Italy: a rather small country, but one endowed with a wealth of geophysical, geochemical and geological data. Over the course of our investigation we have come to realize that the high resolution of Italian data is in fact crucial for discriminating between alternative processes leading to apparently similar outcomes, and hence to possible misinterpretations. It is also crucial for describing the fine geographic grain of the observed phenomena, down to a resolution of less than 1 km: for example, the data show a consistently different behavior between the nature, number and distribution of geofluid emissions in peninsular Italy, which is globally affected by younger and faster tectonic activity, with respect to the more slowly deforming Alps, the Apulian foreland and Sardinia (**Figure 2**). For this reason, this discussion will refer mostly to the Apennines chain, including its foredeep and foreland areas beneath the Po Plain and the Adriatic and Ionian Seas.

Given the good spatial resolution of Italian data, the nature of the relationships between the different types of geofluid emissions and the ongoing tectonic strains can be analyzed in great detail (refer to **Figure 14**). First of all, our data and analyses confirm the substantial distinction between the location, behavior and motivations of thermal springs (**Figure 4**) and CO_2 emissions (**Figure 5**) on the one hand, and gas seeps (**Figure 6**) and mud volcanoes (**Figure 7**) on the other hand. With few exceptions, all geofluid emissions may be assigned to one of these two large geofluid families, and occur in areas currently undergoing extension and shortening, respectively.

FIGURE 12 | shown by red symbols and labeled with the year of occurrence (from CPTI15). Background earthquakes ($M_w \geq 2.5$) that occurred in the interval January 2000–May 2020 are shown by green dots (https://doi.org/10.13127/ISIDE; ISIDE Working Group, 2007). Key to mud volcanoes: NI: Nirano, MG: Montegibbio, OS: Ospitaletto, and RE: Regnano mud volcanoes fields. **Panel B**- Mud volcanoes (enclosed in a brown circle if mentioned in the text), transverse lineaments (highlighted in yellow if mentioned in the text), and main structural elements. The 3D spiral symbols locate gas emissions, mud cone eruptions and H_2S emissions that were activated following the earthquakes whose year of occurrence is indicated in italics (from CFTI5Med). Sections of the northern Apennines foreland monocline are shown by white lines; numbers indicate its inferred dip (from Mariotti and Doglioni, 2000). The green lines are isopachs of the Pliocene-Pleistocene marine and continental deposits (from Bigi et al., 1992). **Panel C** - Sketch illustrating the structural position of the mud volcanoes discussed in this work. The largest northern Apennines mud volcanoes locate where the anticline axis of the Pedeapenninic Thrust Front (PTF) intersects the surface manifestation of a lithospheric slab tear (see the **CH_4 Emissions and Mud Volcanoes: Distribution** and **CH_4 Emissions and Mud Volcanoes: Structural Control** Sections).

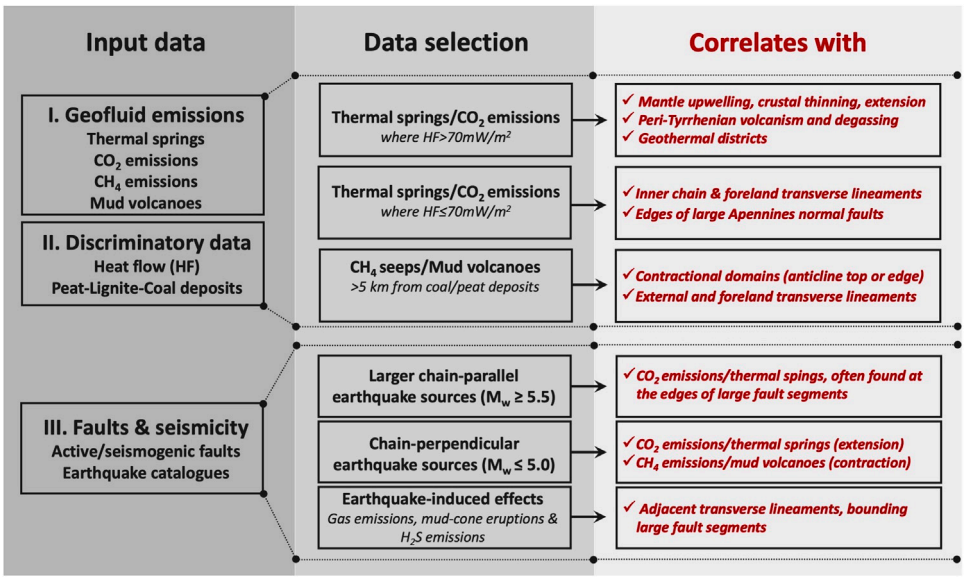

FIGURE 13 | Synthetic workflow of this study; from the input data, to data selection, to the final inferences. See text for further details (refer to the **Tackling an Old Question Through a New Approach and Newly Organized Observations**, **Selecting the Terms of Comparison** and **Correlations and Anticorrelations** Sections, respectively from the leftmost to the rightmost panel).

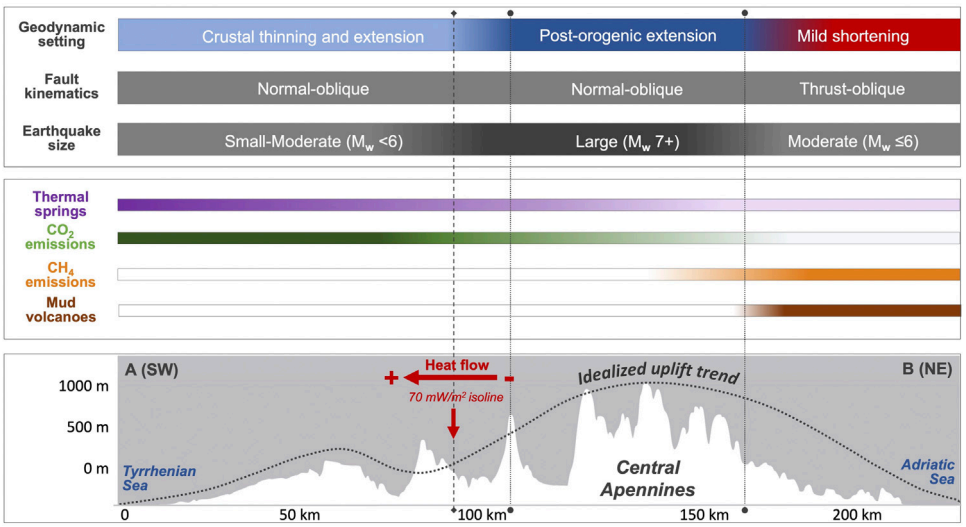

FIGURE 14 | Interpretative section across the central Apennines (see **Figure 2** for location), summarizing our main findings. The upper panel summarizes the geodynamic, tectonic and seismological characteristics of the three domains crossed by the section. The central panel summarizes the distribution of all geofluid emissions (i.e., prior to the selection described in the **Selecting the Terms of Comparison** Section) across the same domains. The lower panel show the topography encountered along the section, and an idealized trend of its Early Pleistocene-to-Present uplift (the southwestern and northeastern maxima reflect the uplift observed in the area of the peri-Tyrrhenian volcanism and along the crestal portion of the Apennines respectively).

More specifically, our results indicate that thermal springs and CO_2 emissions dominate in areas of mantle upwelling and crustal stretching, where only minor seismicity is expected owing to the limited thickness of the seismogenic layer; they are found also in the inner Apennines, a region currently undergoing uplift and extension, and specifically along major lithospheric, chain-perpendicular lineaments bounding large normal faults capable of M_w 7+ earthquakes. In contrast, CH_4 emissions and mud volcanoes dominate in areas undergoing active or recently active contraction, where no CO_2 emissions are observed and where earthquakes generally do not exceed M_w 6.0; in particular, the main mud volcano fields appear to fall where the crests of active anticlines intersect major chain-perpendicular lineaments.

An overarching—and largely unexpected—conclusion arising from our elaborations is that the geographic pattern and the nature of most geofluid emissions does not depend on the current geodynamic regime and on its spatial variability, but rather on the deeper architecture of the crust that results from mostly pre-Pliocene tectonic events. There is no doubt that the large-scale geographic pattern of most geofluid emissions is controlled by Italy's current tectonic setting; its fine-grain, however, exhibits little concordance with ongoing surface processes, being rather controlled by paleogeography and by the existence of buried weaknesses extending to lower crustal or even lithospheric depth. In other words, what is crucial for determining the geographic pattern and the nature of geofluid emissions is not only the nature of the current tectonic strains, but rather their integral over a 5–10 My-long geodynamic history. The only exception to this rule is the peri-Tyrrhenian volcanic and geothermal district (**Figure 2**), which includes most of coastal and central Tuscany and Latium, plus selected portions of coastal Campania: a region that has experienced crustal stretching and mantle upwelling in Pliocene and Quaternary times.

More specifically, most of our selected geofluid emissions (see **Selecting the Terms of Comparison** Section for a discussion of selection criteria) take advantage of the existence of transverse lineaments discussed earlier (e.g., **Data on Active and Seismogenic Faulting** Section). All of these lineaments predate the onset of the current extensional regime active over most of the Apennines, but are coeval with the initial phases of the Miocene–Pliocene buildup of the chain. Many of them are parallel to the current trend of extension, or form a small angle to it, and therefore should be only mildly active or totally inactive under the extensional tectonic regime that currently dominates in the core of the Apennines. But the existence of thermal springs and CO_2 emissions in the inner chain suggests that the transverse lineaments are continuously kept alive by one—or more likely, by a combination—of the following ongoing processes:

(1) the response of the upper crust to the activity of the slab tears, which dominates in the northern Apennines and is reflected in occurrences such as those described in the test cases of Garfagnana (**Test Case 1: The Garfagnana Region, Northern Apennines** Section: **Figure 10**), central-northern Apennines (**Test Case 1: Central-Northern Apennines** Section: area marked with A in **Figure 5**), and northern Apennines (**CH_4 Emissions and Mud Volcanoes: Structural Control** Section: **Figure 12C**);
(2) the progressive regional uplift of the Apennines chain, which takes place with a bell-shaped pattern peaking at nearly 2.0 mm/y near the crest and slowly tapering to zero toward the Tyrrhenian and Adriatic coasts (e.g., Bordoni and Valensise, 1998; Mancini et al., 2007: **Figure 14**). It is generally accepted that the regional-scale uplift of the Apennines is closely related with the ongoing extension, and hence with the occurrence of large earthquakes near the chain crest, but also that the rate of uplift may be different in adjacent portions of the chain, possibly as a result of changes in the geometry of the Apennines subduction caused by slab tears. The Olevano–Antrodoco–Sibillini Line (OASL) test case (**Test Case 2: the Olevano–Antrodoco–Sibillini Line, central Apennines** Section and **Figure 11**) provides an example of a regional structure that forms an angle of 45–60° with the current direction of extension in the central Apennines, and consequently should not be active in the current stress regime. Yet, the frequent low-to mid-level seismicity associated with the OASL and other similar lineaments suggests that differential regional uplift is likely responsible for their progressive rejuvenation—albeit in an indirect fashion—and hence for the rejuvenation of the pathways feeding geofluid emissions. This process, which certainly dominates in the central Apennines, most likely contributes to rejuvenating transverse lineaments throughout the chain as far as Liguria, to the north, and Sicily, to the south, and may also account for the limited number of thermal springs and CO_2 emissions found in the core of the Alps;
(3) the ongoing activity of transverse lineaments segmenting the Adriatic side of the northern Apennines accompanies the residual activity of both the thrust fronts expressed at the surface and of those buried beneath the Po Plain (Panels B and C in **Figure 12**);
(4) the right-lateral reactivation of deep E–W lineaments beneath the central and southern Apennines and in the Apulian foreland, and of left-lateral NNW–SSE lineaments in the Hyblean foreland; a primary effect of the residual NNW-oriented push of the African Plate with respect to stable Eurasia (areas marked with B, C in **Figure 5**).

In summary, tectonic stretching is not the primary reason for the existence of emissions belonging to the 'extensional geofluid family' in the core of the Apennines, although it is the indeed the reason for the generation of large normal-faulting earthquakes. We suggest that the ongoing extension, the seismicity and the release of geofluids are simultaneous but independent outcomes of the ongoing regional uplift of the chain: a process ultimately caused by the buoyancy of the orogen following the retreat of the underlying subducting slab and laterally modulated by the existence of slab tears. This finding may require revision of previous hypotheses (e.g., Chiodini et al., 2004; Chiodini et al., 2020) regarding the relationships between CO_2 degassing and seismicity in the central Apennines.

The close spatial correlation between CO_2 emissions belonging to the 'extensional geofluid family' and deep discontinuities suggests processes originating at depth, possibly below the brittle-ductile transition (e.g., Frezzotti et al., 2009, and references therein), and hence that the CO_2 is at least partly mantle-derived. This finding is further supported by the spatial anticorrelation between these emissions and the footprint (i.e., the projection onto the topographic surface) of the largest extensional faults that exist in peninsular Italy, which generate large earthquakes along the main axis of the Apennines. Extensional geofluid emissions almost never occur within the surface projection of the largest active extensional faults: rather, they concentrate at their edges, hence in the gaps between one fault and the next one in the same system, generally referred to as "segment boundaries" in the seismotectonic literature. Such boundaries are assumed to be permanent properties of the Earth's crust, at

TABLE 1 | Summary of the distribution of geofluid emissions collected for this paper in the four tectonic districts discussed in **Selecting the Terms of Comparison** Section. For each emission type the first line reports all available data, whereas the second line (in italics) reports only the data left following the selection discussed in the **Selecting the Terms of Comparison** Section. Numbers in parentheses indicate the % of each type of emissions falling in each tectonic district, relative to the total (last column to the right). Notice that some datapoints were deliberately double-counted as they fall in overlapping regions.

Tectonic style	Extension		Contraction		Style unassigned	Total
Geofluid type	Rifting/mantle upwelling	Post-orogenic extension	Thrusting	Strike-slip		
Thermal springs	409 (42%)	127 (13%)	74 (8%)	96 (10%)	267 (27%)	973 (970)[a]
(All/*selected*)	*1 (0%)*	*118 (27%)*	*66 (15%)*	*16 (4%)*	*244(55%)*	*445 (442)*[a]
CO_2 emissions	165 (61%)	49 (18%)	10 (4%)	5 (2%)	42 (15%)	271 (270)[b]
(All/*selected*)	*2 (2%)*	*46 (57%)*	*0 (0%)*	*5 (6%)*	*29 (36%)*	*82 (81)*[b]
Gas seeps	16 (9%)	25 (15%)	92 (54%)	3 (2%)	33 (20%)	169
(All/*selected*)	*8 (6%)*	*17 (12%)*	*82 (59%)*	*3 (2%)*	*29 (21%)*	*139*
Mud volcanoes	0 (0%)	1 (1%)	70 (85%)	1 (1%)	10 (12%)	82
(All/*selected*)	*0 (0%)*	*1 (1%)*	*68 (86%)*	*1 (1%)*	*9 (11%)*	*79*
Total	590	202	246	105	352	1,491
(All/*selected*)	*11*	*182*	*219*	*40*	*290*	*740*

[a]*Includes one datapoint falling into the region of overlap between thrusting and strike-slip, and two datapoints falling into the region of overlap between post-orogenic extension and strike-slip.*

[b]*Includes one datapoint falling into the region of overlap between post-orogenic extension and strike-slip.*

least at the scale of one to a few My, ultimately leading to the *characteristic earthquake concept* (e.g., Schwartz and Coppersmith, 1984) and to its implications for the location and size of future earthquakes.

A further finding is that most gas seeps—even those fed by thermogenic methane—originate at shallow (1–10 km) or even very shallow depth (1–3 km). Our observations confirm that the presence of gas seeps is a direct indication of underlying hydrocarbon reservoirs, combined with limited permeability of the overlying crust. Conversely, their absence may indicate that they gas reservoirs never developed, or that the gas has already been lost to the atmosphere due to enhanced faulting and fracturing.

CONCLUSION

Earthquakes causing significant shaking and permanents strains in a large rock volume allow the generation of new, episodic fluid-flow regimes, which may become permanent when rocks having limited permeability are pervasively fractured by the upward propagation of seismogenic faults. Such geophysical conditions are easily attained near the edges of seismogenic faults, where transverse lineaments are known to occur from independent lines of evidence (e.g., Curewitz and karson, 1997).

Our Italy-based hypotheses have important implications for the understanding of deep fluid circulation in active regions and for improving the quantification of natural CO_2 and CH_4 emissions. We have shown that the location of CO_2 emissions in the inner portions of the Apennines is not controlled by ongoing continental extension, but rather by other large-scale processes that are responsible "also" for rather localized extension. In contrast, the extrados faults that allow the development of gas seeps and mud volcanoes should imply ongoing activity of the underlying thrusts; alternatively, fluids might accumulate also at the core of inactive anticlines, where they may escape to the atmosphere through cross-fold joints.

The demonstrated interplay between large Apennines normal faults and transverse lineaments may also help constraining the location and geometry of blind and hidden seismogenic sources that remain undetected in the Italian territory. The relatively small earthquakes (generally $\leq M_w$ 5.0) that are spatially coincident with geofluid emissions in the core of the Apennines may be interpreted as generated by passive reactivation of the transverse lineaments under the current stress/train regime: a circumstance that acts as an upper boundary to their size, and allows for a more confident identification of the actual extent of the main chain-parallel seismogenic sources.

Our work provides also a detailed framework for exploring the preparation of large earthquakes based on geofluid emissions, potentially contributing to the identification of sites that are most promising for earthquake prediction investigations (e.g., Martinelli, 2020).

All the observations and hypotheses made in this paper were made possible by the systematization of knowledge concerning widely separated manifestations of the activity of the Earth. Although the databases we relied on are continuously improved, we maintain that they already form and exceptional body of information, probably unique worldwide, making our inferences reasonably robust.

DATA AVAILABILITY STATEMENT

This article was made possible by a great deal of published data, that actually represent the paper's main strength. The vast majority of these data are made available through Web-GIS databases, listed in **Supplementary Table S1** along with the corresponding URL. All these databases were fully functioning on the date of submission of the second version of this article. Since the most relevant of these databases (database of Thermal Springs, by Martinelli and Albarello, 1997) is also the oldest and the most difficult to access, we reported it in the **Supplementary Material** section for the convenience of all readers, after correcting a few typos the existed in the original version.

AUTHOR CONTRIBUTIONS

PV laid out the project, managed the manuscript organization, processed the data within the GIS and drafted most of the figures. GM contributed data on geofluid emissions, and discussed with the coauthors how the data should be filtered and what are the geophysical implications of the detected correlations and anticorrelations. GV contributed data on seismicity and seismogenic sources, and participated in the discussion on the implications of the distribution of geofluids in relation with local-scale and regional tectonics. All three authors contributed to the bibliographic search and to the writing of the submitted version of the paper.

ACKNOWLEDGMENTS

This work is dedicated to Marco Mucciarelli, who passed away prematurely in 2016. Marco was a curious investigator and an outstanding scientist who loved "wandering off the beaten path". He started research on the subject of this paper with two of us (GM and GV) nearly 20 years ago, and contributed to the further development of this research with all three of us in 2014–2015. We are deeply indebted with him for his intuitions and his rigorous approach to characterizing natural geofluid emissions. We are also indebted with with Marco Bonini and with Steven Ingebritsen for their constructive criticism and helpful suggestions.

SUPPLEMENTARY MATERIAL

The Supplementary Material for this article can be found online at: https://www.frontiersin.org/articles/10.3389/feart.2021.579390/full#supplementary-material.

REFERENCES

Barbier, E., and Fanelli, M. (1976). "Main fractures of Italy from ERTS satellite images and correlations with thermal springs, volcanoes and earthquakes," in *Volcanoes and Tectonosphere*. Editors H. Aoki and S. Iizuka. (Tokai: Tokai University Press), 321–331.

Bartolini, C., and Bortolotti, V. (1971). Studi di geomorfologia e neotettonica. I depositi continentali dell'Alta Garfagnana in relazione alla tettonica plio-pleistocenica. *Mem. Soc. Geol. It.* 10, 203–245.

Basili, R., Valensise, G., Vannoli, P., Burrato, P., Fracassi, U., Mariano, S., et al. (2008). The Database of Individual Seismogenic Sources (DISS), version 3: summarizing 20 years of research on Italy's earthquake geology. *Tectonophysics* 453, 20–43. doi:10.1016/j.tecto.2007.04.014

Bemporad, S., Conedera, C., Dainelli, P., Ercoli, A., and Facibeni, P. (1986). Landsat imagery: a valuable tool for regional and structural geology. *Mem. Soc. Geol. It.* 31, 287–298.

Bense, V. F., Gleeson, T., Loveless, S. E., Bour, O., and Scibek, J. (2013). Fault zone hydrogeology. *Earth Sci. Rev.* 127, 171–192. doi:10.1016/j.earscirev.2013.09.008

Bigi, G., Bonardi, G., Catalano, R., Cosentino, D., Lentini, F., and Parotto, M. (1992). *Structural model of Italy 1:500,000*. New York: CNR Progetto Finalizzato Geodinamica.

Boccaletti, M., Coli, M., and Napoleone, G. (1977). Nuovi allineamenti strutturali da immagini Landsat e rapporti con l'attività sismica negli Appennini. *Boll. Soc. Geol. It.* 96, 679–694.

Boncio, P., Brozzetti, F., and Lavecchia, G. (2000). Architecture and seismotectonic of a regional low-angle normal fault zone in central Italy. *Tectonics* 19 (6), 1038–1055. doi:10.1029/2000TC900023

Bonini, L., Basili, R., Burrato, P., Cannelli, V., Fracassi, U., Maesano, F. M., et al. (2019). Testing different tectonic models for the source of the Mw 6.5, 30 October 2016, Norcia earthquake (central Italy): a youthful normal fault, or negative inversion of an old thrust? *Tectonics* 38. doi:10.1029/2018TC005185

Bonini, L., Maesano, F. E., Basili, R., Burrato, P., Carafa, M. M. C., Fracassi, U., et al. (2016). Imaging the tectonic framework of the 24 August 2016, Amatrice (central Italy) earthquake sequence: new roles for old players?. *Ann. Geophys.* 59, 5. doi:10.4401/ag-7229

Bonini, M. (2013). Fluid seepage variability across the external Northern Apennines (Italy): structural controls with seismotectonic and geodynamic implications. *Tectonophysics* 590, 151–174. doi:10.1016/j.tecto.2013.01.020

Bonini, M. (2012). Mud volcanoes: indicators of stress orientation and tectonic controls. *Earth Sci. Rev.* 115, 121–152. doi:10.1016/j.earscirev.2012.09.002

Bonini, M. (2009). Structural controls on a carbon dioxide-driven mud volcano field in the Northern Apennines (Pieve Santo Stefano, Italy): relations with pre-existing steep discontinuities and seismicity. *J. Struct. Geol.* 31, 44–54. doi:10.1016/j.jsg.2008.10.003

Bordoni, P., and Valensise, G. (1998). "Deformation of the 125 ka marine terrace in Italy: tectonic implications,". *Coastal Tectonics* Editors I. S. Stewart and C. Vita-Finzi (London, UK: Special Publication-Geological Society of London), 146, 71–110. doi:10.1144/GSL.SP.1999.146.01.05

Bredehoeft, J. D., Norton, D., Engelder, T., Nur, A., Oliver, J. E., Taylor, H. P., Jr., et al. (1990). "Overview and recommendations," in *The role of fluids in crustal processes*. Editors J. D. Bredehoeft, D. Norton, T. Engelder, A. Nur, J. E. Oliver, H. P. Taylor Jr., et al. (New York: National Academic Press), 3–23.

Burrato, P., Etiope, G., Vannoli, P., Ionescu, A., and Martinelli, G. (2013). *HYSED-IT: a database of hydrocarbon seeps in Italy. Results from MIUR/PRIN2009 projectHydrocarbon emissions from geological sources to the atmosphere in Italy* http://hydrocarbonseeps.blogspot.it/p/hysed.html.

Caine, J. S., Evans, J. P., and Forster, C. B. (1996). Fault zone architecture and permeability structure. *Geology* 24, 1025–1028.

Calamita, F., Pace, P., and Satolli, S. (2012). Coexistence of fault-propagation and fault-bend folding in curve-shaped foreland fold-and-thrust belts: examples from the Northern Apennines (Italy). *Terra Nova* 24, 396–406. doi:10.1111/j.1365-3121.2012.01079.x

Camerana, E., Cortese, E., Crema, C., De Stefani, C., Fossa-Mancini, E., Lotti, B., et al. (1926). Studi geologic per la ricercar del petrolio in Italia. *Mem. Descr. della Carta Geol. Italia.* 20, 1–288.

Capozzi, R., and Picotti, V. (2010). Spontaneous fluid emissions in the Northern Apennines: geochemistry, structures and implications for the petroleum system. *Geol. Soc. Lond. Spec. Publ.* 348, 115–135. doi:10.1144/SP348.7

Carafa, M. M. C., Barba, S., and Bird, P. (2015). Neotectonics and long-term seismicity in Europe and the Mediterranean region. *J. Geophys. Res. Solid Earth* 120 (7), 311–315. doi:10.1002/2014JB011751

Cardellini, C., Chiodini, G., Frigeri, A., Bagnato, E., Aiuppa, A., and McCormick, B. (2014). *MAGA, a new database of gas natural emissions: a collaborative web environment for collecting data*. Vienna: EGU 2014 (Abstract).

Castaldini, D., Gasperi, G., Panizza, M., Pellegrini, M., and McCormick, B. (1979). *e 75 (Mirandola) nell'intervallo da 18.000 B.P. all'Attuale (interv. V), C.N.R., Nuovi contributi alla realizzazione della Carta Neotettonica di Italia, publ. n. 251 of Progetto Finalizzato Geodinamica*, 317–332. (Reggio nell'Emilia: Neotettonica dei Fogli 74 (Reggio nell'Emilia))

Castellarin, A., Colacicchi, M., Praturlon, A., and Cantelli, C. (1982). The jurassic-lower Pliocene history of the ancona-anzio line (Central Italy). *Mem. Soc. Geol. It.* 24, 325–336.

Castellarin, A., Colacicchi, R., and Praturlon, A. (1978). Fasi distensive, trascorrenze e sovrascorrimenti lungo la "linea Ancona-Anzio" dal Lias medio al Pliocene. *Geol. Rom.* 27, 161–189.

Castellarin, A., Eva, C., Giglia, G., and Vai, G. B. (1985). Analisi structural del Fronte Appenninico Padang. *Giorn. Geol.* 47, 47–75.

Cataldi, R., Mongelli, F., Squarci, P., Taffi, L., Zito, G., and Calore, C. (1995). Geothermal ranking of Italian territory. *Geothermics* 24 (1), 115–129. doi:10.1016/0375-6505(94)00026-9

Celati, R., Grassi, S., and Calore, C. (1990). Overflow thermal springs of Tuscany (Italy). *J. Hydrol.* 118, 191–207. doi:10.1016/0022-1694(90)90258-Y

Chiodini, G., Cardellini, C., Amato, A., Boschi, E., Caliro, S., Frondini, F., et al. (2004). Carbon dioxide Earth degassing and seismogenesis in central and southern Italy. *Geophys. Res. Lett.* 31. doi:10.1029/2004GL019480

Chiodini, G., Cardellini, C., Di Luccio, F., Selva, J., Frondini, F., Caliro, S., et al. (2020). Correlation between tectonic CO_2 earth degassing and seismicity is revealed by a 10-year record in the Apennines, Italy. *Sci. Adv.* 6, 35. doi:10.1126/sciadv.abc2938

Chiodini, G., Valenza, M., Cardellini, C., and Frigeri, A. (2008). A new web-based catalog of earth degassing sites in Italy. *Eos Trans. Am. Geophys. Union*. 89 (37), 341. doi:10.1029/2008EO370001

Cicerone, R. D., Ebel, J. E., and Britton, J. (2009). A systematic compilation of earthquake precursors. *Tectonophysics* 476, 371–396. doi:10.1016/j.tecto.2009.06.008

CNR-IGG (2012). *Italian National Geothermal Database [online]*. http://geothopica.igg.cnr.it/.

Ciotoli, G., Procesi, M., Etiope, G., Fracassi, U., and Ventura, G. (2020). Influence of tectonics on global scale distribution of geological methane emissions. *Nat. Commun.* 11, 1–19. 10.1038/s41467-020-16229-1

Curewitz, D., and Karson, J. A. (1997). Structural settings of hydrothermal outflow: fracture permeability maintained by fault propagation and interaction. *J. Volcanol. Geoth. Res.* 79, 149–168. doi:10.1016/S0377-0273(97)00027-9

De Rubeis, V., Gasparini, C., Solipaca, A., and Tosi, P. (1992). Seismotectonic characterization of Italy using statistical analysis of geophysical variables. *J. Geodyn.* 16, 103–122. doi:10.1016/0264-3707(92)90021-J

Della Vedova, B., Bellani, S., Pellis, G., and Squarci, P. (2001). Deep temperatures andsurface heat flow distribution. In: *Anatomy of an orogeny: the Apennines and adjacent mediterranean basins*. The Netherlands: Springer, 65–76. doi:10.1007/978-94-015-9829-3

Di Bucci, D., Burrato, P., Vannoli, P., and Valensise, G. (2010). Tectonic evidence for the ongoing Africa-Eurasia convergence in central Mediterranean foreland areas: a journey among long-lived shear zones, large earthquakes, and elusive fault motions. *J. Geophys. Res.* 115, B12404. doi:10.1029/2009JB006480

Di Domenica, A., Petricca, P., Trippetta, F., Carminati, E., and Calamita, F. (2014). Investigating fault reactivation during multiple tectonic inversions through mechanical and numerical modeling: an application to the Central Apennines of Italy. *J. Struct. Geol.* 67, 167–185. doi:10.1016/j.jsg.2014.07.018

DISS Working Group (2018). *Database of Individual Seismogenic Sources (DISS), Version 3.2.1: a compilation of potential sources for earthquakes larger than M 5.5 in Italy and surrounding areas. Istituto Nazionale di Geofisica e Vulcanologia*. http://diss.rm.ingv.it/diss/

Doglioni, C., Harabaglia, P., Merlini, S., Mongelli, F., Peccerillo, A., and Piromallo, C. (1999). Orogens and slabs vs. their direction of subduction. *Earth Sci. Rev.* 45, 167–208. doi:10.1016/S0012-8252(98)00045-2

Donda, F., Tinivella, U., Gordini, E., Panieri, G., Volpi, V., Civile, D., et al. (2019). The origin of gas seeps in the Northern Adriatic Sea. *Ital. J. Geosci.* 138 (2), 171–183. doi:10.3301/IJG.2018.34

Etiope, G., and Klusman, R. W. (2002). Geologic emissions of methane to the atmosphere. *Chemosphere* 49, 777–789. doi:10.1016/s0045-6535(02)00380-6

Etiope, G., Martinelli, G., Caracausi, A., and Italiano, F. (2007). Methane seeps and mud volcanoes in Italy: gas origin, fractionation and emission to the atmosphere. *Geophys. Res. Lett.* 34, L14303. doi:10.1029/2007GL030341

Etiope, G., Panieri, G., Fattorini, D., Regoli, F., Vannoli, P., Italiano, F., Locritani, M., and Carmisciano, C. (2014). A thermogenic hydrocarbon seep in shallow Adriatic Sea (Italy): gas origin, sediment contamination and benthic foraminifera. *Marine and Petroleum Geology* 57, 283–293. doi:10.1016/j.marpetgeo.2014.06.006

Etiope, G. (2015). *Natural gas seepage. The Earth's hydrocarbon degassing*. (Switzerland: Springer International Publishing), p. 199. doi:10.1007/978-3-319-14601-0.319-14601-0

Eva, E., and Solarino, S. (1992). Aucune considerazioni sulla simotettonica dell'Appennino nord-occidentale ricavate dall'analisi si meccanismi focaliStudi Geologic Camerti Spec 1992/2. *Appendice CROP.* 1, 75–83.

Faulkner, D. R., Jackson, C. A. L., Lunn, R. J., Schlische, R. W., Shipton, Z. K., Wibberley, C. A. J., et al. (2010). A review of recent developments concerning the structure, mechanics and fluid flow properties of fault zones. *J. Struct. Geol.* 32, 1557–1575. doi:10.1016/j.jsg.2010.06.009

Fazzuoli, G., Ferrini, G., Pandeli, E., and Sguazzoni, G. (1985). Le formazioni giurassico-mioceniche della falda toscana a nord dell'Arno: considerazioni sull'evoluzione sedimentaria. *Mem. Soc. Geol. It.* 30, 159–201.

Fracassi, U., and Valensise, G. (2007). Unveiling the sources of the catastrophic 1456 multiple earthquake: hints to an unexplored tectonic mechanism in southern Italy. *Bull. Seismol. Soc. Am.* 97 (3), 725–748. doi:10.1785/0120050250

Frepoli, A., and Amato, A. (1997). Contemporaneous extension and compression in the northern Apennines from earthquake fault-plane solutions. *Geophys. J. Int.* 129, 368–388. doi:10.1111/j.1365-246X.1997.tb01589.x

Frezzotti, M. L., Peccerillo, A., and Panza, G. (2009). Carbonate metasomatism and CO_2 lithosphere–asthenosphere degassing beneath the Western Mediterranean: an integrated model arising from petrological and geophysical data. *Chem. Geol.* 262, 108–120. doi:10.1016/j.chemgeo.2009.02.015

Gasperi, G., Cremaschi, M., Mantovani Uguzzoni, M. P., Cardarelli, A., Cattani, M., and Labate, D. (1987). Evoluzione plio-quaternaria del margine appenninico modenese e dell'antistante pianura. Note illustrative alla Carta Geologica (with geological map scale 1:25,000). *Memorie Società Geologica Italiana* 39, 375–431.

Ghelardoni, R. (1965). Osservazioni sulla tettonica transversale dell'Appennino Septentrional. *Boll. Soc. Geol. It.* 84, 277–290.

Girault, F., Adhikari, L. B., and France-Lanord, C. (2018). Persistent CO_2 emissions and hydrothermal unrest following the 2015 earthquake in Nepal. *Nat. Commun.* 9, 2956. 10.1038/s41467-018-05138-z

Gleeson, T., and Ingebritsen, S. (2017). *Crustal permeability*. Chichester. Wiley-Blackwell, 472.

Gold, T., and Soter, S. (1984). Fluid ascent through the solid lithosphere and its relation to earthquakes. *Pure Appl. Geophys.* 122, 492–530. doi:10.1007/BF00874614

Guidoboni, E., Ferrari, G., Mariotti, D., Comastri, A., Tarabusi, G., Sgattoni, G., et al. (2018). *CFTI5Med, Catalogo dei Forti Terremoti in Italia (461 A.C.-1997) e nell'area Mediterranea (760 A.C.-1500)* Istituto Nazionale di Geofisica e Vulcanologia (INGV). http://storing.ingv.it/cfti/cfti5/# (September, 2018). doi:10.6092/ingv.it-cfti5

Guidoboni, E., Ferrari, G., Tarabusi, G., Sgattoni, G., Comastri, A., Mariotti, D., et al. (2019). CFTI5Med, the new release of the catalogue of strong earthquakes in Italy and in the Mediterranean area. *Sci. Data* 6, 80. doi:10.1038/s41597-019-0091-9

Hickman, S., Sibson, R., and Bruhn, R. (1995). Introduction to special section: mechanical involvement of fluids in faulting. *J. Geophys. Res.* 100 (12), 831–912. doi:10.1029/95JB01121

Holness, M. B. (1997). *Deformation-enhanced fluid transport in the Earth's crust and mantle*. London: Chapman and Hall.

Ingebritsen, S. E., and Manning, C. E. (2010). Permeability of the continental crust: dynamic variations inferred from seismicity and metamorphism. *Geofluids* 10, 193–205. doi:10.1111/j.1468-8123.2010.00278.x

Irwin, W. P., and Barnes, I. (1980). Tectonic relations of carbon dioxide discharges and earthquakes. *J. Geophys. Res.* 85 (3), 115–123.

ISIDE Working Group. (2007). *Italian seismological instrumental and parametric database (ISIDe)*. Italy: Istituto Nazionale di Geofisica e Vulcanologia (INGV). doi:10.13127/ISIDE

Italiano, F., Martinelli, G., and Plescia, P. (2008). "*CO2 degassing over seismic areas: the role of mechanochemical production at the study case of Central Apennines*," in *Terrestrial fluids, earthquakes and volcanoes: the hiroshi wakita volume III. Pageoph topical volumes*. Editors N. M. Pérez, S. Gurrieri, C. Y. King, and Y. Taran (Basel: Birkhäuser), 75–94.

ITHACA Working Group (2019). *ITHACA (Italy HAzard from CApable faulting), a database of active capable faults of the Italian territory, ISPRA Geological Survey of Italy, WebPorta.* http://sgi2.isprambiente.it/ithacaweb/Mappatura.aspx.

Jakubov, A. A., Ali-Zade, A. A., and Zeinalov, M. M. (1971). *Mud volcanoes of the Azerbaijan SSR. Atlas (in Russian)*. Baku: Azerbaijan Academy of Sciences.

Jang, Z., Xu, T., and Mariethoz, G. (2018). Numerical investigation on the implications of spring temperature and discharge. *Hydrogeol. J.* 26, 2121–2132. doi:10.1007/s10040-018-1769-3

Kastelic, V., Vannoli, P., Burrato, P., Fracassi, U., Tiberti, M., and Valensise, G. (2013). Seismogenic sources in the adriatic domain. *Mar. Petrol. Geol.* 42, 191–213. doi:10.1016/j.marpetgeo.2012.08.002

Kennedy, B. M., and van Soest, M. C. (2007). Flow of mantle fluids through the ductile lower crust: helium isotope trends. *Science* 318 (1), 433–441. doi:10.1126/science.1147537

Kerrick, D. M. (2001). Present and past nonanthropogenic CO_2 degassing from the solid earth. *Rev. Geophys.* 39, 565–585. doi:10.1029/2001RG000105

Kuz'mina, E. A., and Novopashina, A. V. (2018). Groundwater outflows and fault density spatial relation in the Baikal rift system (Russia). *Acque Sotterranee It. J. Groundwater* 317, 19–27. doi:10.7343/as-2018-317

Locati, M., Camassi, R., Rovida, A., Ercolani, E., Bernardini, F., Castelli, V., et al. (2019). *Database Macrosismico Italiano (DBMI15), version 2.0*. Italy: Istituto Nazionale di Geofisica e Vulcanologia (INGV). doi:10.13127/DBMI/DBMI15.2

Lucazeau, F. (2019). Analysis and mapping of an updated terrestrial heat flow data set. *G-cubed.* 20 (4), 001–004. doi:10.1029/2019GC008389

Maestrelli, D., Bonini, M., and Sani, F. (2019). Linking structures with the genesis and activity of mud volcanoes: examples from Emilia and Marche (Northern Apennines, Italy). *Int. J. Earth Sci.* 108, 1683–1703. doi:10.1007/s00531-019-01730-w

Mancini, M., D'Anastasio, E., Barbieri, M., and De Martini, P. M. (2007). Geomorphological, paleontological and $^{87}Sr/8^{6}Sr$ isotope analyses of early Pleistocene paleoshorelines to define the uplift of Central Apennines (Italy). *Quat. Res.* 67, 487–501. doi:10.1016/j.yqres.2007.01.005

Manga, M., Beresnev, I., Brodsky, E. E., Elkhoury, J. E., Elsworth, D., Ingebritsen, S. E., et al. (2012). Changes in permeability caused by transient stresses: field observations, experiments, and mechanics. *Rev. Geophys.* 50. doi:10.1029/2011RG000382

Manning, C. E., and Ingebritsen, S. E. (1999). Permeability of the continental crust: implications of geothermal data and metamorphic systems. *Rev. Geophys.* 37, 127–150. doi:10.1029/1998RG900002

Mariotti, G., and Doglioni, C. (2000). The dip of the foreland monocline in the Alps and Apennines, earth planet. *Sci. Lett.* 181, 191–202. doi:10.1016/S0012-821X(00)00192-8

Mariucci, M. T., and Montone, P. (2020). *IPSI 1.4, database of Italian present-day stress indicators*. Italy: INGV. doi:10.13127/IPSI.1.4

Martinelli, G., and Albarello, D. (1997). Main constraints for siting monitoring networks devoted to the studies of earthquake related hydrogeochemical phenomena in Italy. *Ann. Geofis.* 40 (6), 505–511. doi:10.4401/ag-3827

Martinelli, G., Cremonini, S., and Samonati, E. (2012). "*Geological and geochemical setting of natural hydrocarbon emissions in Italy*," in *Advances in natural gas technology*. Editor H. Al-Megren (Rijeka: INTECH Europe), 79–120.

Martinelli, G., Cremonini, S., and Samonati, E. (2015). "*Italian peat and coal fires*," in *Coal and Peat Fires: a global perspective. Volume 4: peat-Geology, combustion and case studies*. Editors G. Stracher, A. Prakash, and G. Rein, (New York: Elsevier Science (Publ.)), 39–73. 9780444595102.

Martinelli, G., and Dadomo, A. (2017). Factors constraining the geographic distribution of earthquake geochemical and fluid-related precursors. *Chem. Geol.* 469, 176–184. doi:10.1016/j.chemgeo.2017.01.006

Martinelli, G., and Judd, A. (2004). Mud volcanoes of Italy. *Geol. J.* 39, 49–61. doi:10.1002/gj.943

Martinelli, G. (2020). Previous, current, and future trends in research into earthquake precursors in geofluids. *Geosciences* 10, 189. doi:10.3390/geosciences10050189

Mazzini, A., and Etiope, G. (2017). Mud volcanism: an updated review. *Earth Sci. Rev.* 168, 81–112. doi:10.1016/j.earscirev.2017.03.001

McNitt, J. R. (1978). The United Nations approach to geothermal resource assessment. *Geothermics* 7, 231–242. doi:10.1016/0375-6505(78)90013-5

Meletti, C., Galadini, F., Valensise, G., Stucchi, M., Basili, R., Barba, S., et al. (2008). A seismic source zone model for the seismic hazard assessment of the Italian territory. *Tectonophysics* 450, 85–108. doi:10.1016/j.tecto.2008.01.003

Michetti, A. M., Serva, L., and Vittori, E. (2000). *Ithaca - Italy Hazard from Capable Faults: a database of active faults of the Italian onshore territory. CD-ROM and explanatory notes*. Rome: APAT.

Micklethwaite, S., Sheldon, H. A., and Baker, T. (2010). Active fault and shear processes and their implications for mineral deposit formation and discovery. *J. Struct. Geol.* 32, 151–165. doi:10.1016/j.jsg.2009.10.009

Minissale, A. (2018). A simple geochemical prospecting method for geothermal resources in flat areas. *Geothermics* 72, 258–267. doi:10.1016/j.geothermics.2017.12.001

Minissale, A. (2004). Origin, transport and discharge of CO2 in central Italy. *Earth Sci. Rev.* 66, 89–141. doi:10.1016/j.earscirev.2003.09.001

Minissale, A. (1991). Thermal springs in Italy: their relation to recent tectonics. *Appl. Geochem.* 6, 201–212. doi:10.1016/0883-2927(91)90030-S

Montone, P., and Mariucci, M. T. (2016). The new release of the Italian contemporary stress map. *Geophys. J. Int.* 205 (3), 1525–1531. doi:10.1093/gji/ggw100

Mucciarelli, M., Donda, F., and Valensise, G. (2015). Earthquakes and depleted gas reservoirs: which comes first?. *Nat. Hazards Earth Syst. Sci.* 15 (10), 201–202. doi:10.5194/nhess-15-2201-2015

Nirta, G., Principi, G., and Vannucchi, P. (2007). The Ligurian Units of Western Tuscany (Northern Apennines): insight on the influence of pre-existing weakness zones during ocean closure. *Geodin. Acta.* 20, 71–97. doi:10.3166/ga.20.71-97

Pannatier, Y. (1996). *VARIOWIN: software for spatial data analysis in 2D*. New York, NY. Springer, 91.

Parotto, M., and Praturlon, A. (1975). "*Geological summary of the central Apennines*," in *Structural Model of Italy. Maps explanatory notes. CNR, Quad.* Editors L. Ogniben, M. Parotto, and A. Praturlon, p. 257–311.

Pasquale, V., Chiozzi, P., and Verdoya, M. (2010). Tectonothermal processes and mechanical strength in a recent orogenic belt: northern Apennines. *J. Geophys. Res.* 115, B03301. doi:10.1029/2009JB006631

Pasquale, V., Verdoya, M., and Chiozzi, P. (2014). Heat flow and geothermal resources in northern Italy. *Renew. Sustain. Energy Rev.* 36, 277–285. doi:10.1016/j.rser.2014.04.075

Pasquale, V., Verdoya, M., Chiozzi, P., and Ranalli, G. (1997). Rheology and seismotectonic regime in the northern central Mediterranean. *Tectonophysics* 270, 239–257. doi:10.1016/S0040-1951(96)00211-9

Patacca, E., Sartori, R., and Scandone, P. (1990). Tyrrhenian basin and apenninic arcs: kinematic relations since late tortonian time. *Mem. Soc. Geol. It.* 45, 425–451. doi:10.1007/978-94-011-2016-6_7

Pauselli, C., Gola, G., Mancinelli, P., Trumpy, E., Saccone, M., Manzella, A., et al. (2019). A new surface heat flow map of the Northern Apennines between latitudes 42.5 and 44.5 N. *Geothermics* 81, 39–52. doi:10.1016/j.geothermics.2019.04.002

Peccerillo, A. (2005). *Polio-quaternary volcanism in Italy - petrology, geochemistry, geodynamics*. New York: Springer, 365. doi:10.1007/3-540-29092-3

Pentecost, A., Jones, B., and Renaut, R. W. (2003). What is a hot spring?. *Can. J. Earth Sci.* 40, 1443–1446.

Puccinelli, A., D'Amato Avanzi, G, Perilli, N., and Verani, M. (2015). *Foglio 262-pistoia. Note illustrative alla carta geologica d'Italia alla scala 1:50.000*. New York: ISPRA

Puccinelli, A. (1987). Un esempio di tettonica recente nella Val di Serchio: il sollevamento di Monte Perpoli. *Atti Soc. Tosc. Sci. Nat. Mem. Ser. B.* 94, 105–117.

Rosenbaum, G., Gasparon, M., Lucente, F. P., Peccerillo, A., and Miller, M. S. (2008). Kinematics of slab tear faults during subduction segmentation and implications for Italian magmatism. *Tectonics* 27, TC2008. doi:10.1029/2007TC002143

Rosenbaum, G., and Piana Agostinetti, N. (2015). Crustal and upper mantle responses to lithospheric segmentation in the northern Apennines. *Tectonics* 34, 648–661. doi:10.1002/2013TC003498

Rovida, A., Locati, M., Camassi, R., Lolli, B., and Gasperini, P. (2019). *Catalogo Parametric dei Terremoti Italiani (CPTI15), version 2.0*. Italy: Istituto Nazionale di Geofisica e Vulcanologia (INGV). doi:10.13127/CPTI/CPTI15.2

Rovida, A., Locati, M., Camassi, R., Lolli, B., and Gasperini, P. (2020). The Italian earthquake catalogue CPTI15. *Bull. Earthq. Eng.* 18, 1–2. doi:10.1007/s10518-020-00818-y

Sbarra, P., Burrato, P., Tosi, P., Vannoli, P., De Rubeis, V., and Valensise, G. (2019). Inferring the depth of historical earthquakes from macroseismic intensity data: a case history from Northern Italy. *Sci. Rep.* 9, 15583. doi:10.1038/s41598-019-51966-4

Schwartz, D. P., and Coppersmith, K. J. (1984). Fault behavior and characteristic earthquakes examples from the Wasatch and San Andreas fault zones. *J. Geophys. Res.* 89 (B7), 5681–5698. 10.1029/JB089iB07p05681

Scognamiglio, L., Tinti, E., and Quintiliani, M. (2006). Time domain moment tensor [data set]. *Istituto Nazionale di Geofisica e Vulcanologia (INGV)*. doi:10.13127/TDMT

Sibson, R. H. (2000). Fluid involvement in normal faulting. *J. Geodyn.* 29, 469–499. doi:10.1016/S0264-3707(99)00042-3

Sorgi, C., Deffontaines, B., Hippolyte, J. C., and Cadet, J. P. (1998). An integrated analysis of transverse structures in the northern Apennines, Italy. *Geomorphology* 25, 193–206. doi:10.1016/S0169-555X(98)00041-5

Stolper, D. A., Martini, A. M., Clog, M., Douglas, P. M., Shusta, S. S., Valentine, D. L., et al. (2015). Distinguishing and understanding thermogenic and biogenic sources of methane using multiply substituted isotopologues. *Geochem. Cosmochim. Acta* 161, 219–247. doi:10.1016/j.gca.2015.04.015

Stramondo, S., Vannoli, P., Cannelli, V., Polcari, M., Melini, D., Samsonov, S., et al. (2014). X- and C-Band SAR Surface Displacement for the 2013 Lunigiana earthquake (Northern Italy): a breached relay ramp?. *IEEE J-STARS.* 7 (7), 746–752. doi:10.1109/JSTARS.2014.2313640

Tamburello, G., Pondrelli, S., Chiodini, G., and Rouwet, D. (2018). Global-scale control of extensional tectonics on CO_2 earth degassing. *Nat. Commun.* 9, 4608. doi:10.1038/s41467-018-07087-z

Tiberti, M. M., Vannoli, P., Fracassi, U., Burrato, P., Kastelic, V., and Valensise, G. (2017). Understanding seismogenic processes in the Southern Calabrian Arc: a geodynamic perspective. *It. J. Geosci.* 136 (3), 365–388. doi:10.3301/IJG.2016.12

Trumpy, E., and Manzella, A. (2017). Geotropic and the interactive analysis and visualization of the updated Italian National Geothermal Database. *Int. J. Appl. Earth Obs. Geoinf.* 54, 28–37. doi:10.1016/j.jag.2016.09.004

Valensise, G., and Pantosti, D. (2000). *Database of individual source for earthquake larger than M 5.5 in Italy (DISS 2.0). Prototype version distributed on a CD-Rom and website open for consultation until 2005.*

Valensise, G., and Pantosti, D. (2001). Database of potential sources for earthquakes larger than 5.5 in Italy, version 2.0. *Annali di Geofisica*, 44, 797–964.

Valensise, G., Vannoli, P., Basili, R., Bonini, L., Burrato, P., Carafa, M. M. C., et al. (2016). Fossil landscapes and youthful seismogenic sources in the central Apennines: excerpts from the 24 August 2016, Amatrice earthquake and seismic hazard implications. *Ann. Geophys.* 59, 5. doi:10.4401/ag-7215

Van der Meer, F., van Dijik, P., van der Werff, H., and Yang, H. (2002). Remote sensing and petroleum seepage: a review and case study. *Terra Nova* 14, 1–17. 10.1046/j.1365-3121.2002.00390.x

Vannoli, P., Burrato, P., Fracassi, U., and Valensise, G. (2012). A fresh look at the seismotectonic of the abruzzi (central Apennines) following the 6 April 2009 L'aquila earthquake (Mw 6.3). *It. J. Geosci.* 131 (3), 309–329. doi:10.3301/IJG.2012.03

Vannoli, P., Burrato, P., and Valensise, G. (2015). The seismotectonic of the Po Plain (Northern Italy): tectonic diversity in a blind faulting domain. *Pure Appl. Geophys.* 172, 1105–1142. doi:10.1007/s00024-014-0873-0

Verdoya, M., Chiozzi, P., Gola, G., and Jbeily, E. E. (2019). Conductive heat flow pattern of the central-northern Apennines, Italy. *Int. J. Terrestr. Heat Flow Appl. Geotherm.* 2 (1), 37–45. doi:10.31214/ijthfa.v2i1.33

Wang, C-Y., and Manga, M. (2010). *Geofluids* 10, 206–216. doi:10.1111/j.1468-8123.2009.00270.x

Waring, G. A. (1965). *Thermal springs of the United States and other countries of the world: a summary*. New York: U.S. Geological Survey Professional Paper, p. 383–492.

Zuber, S. (1940). *Manifestazioni e prospettive petrolifere dell'Italia alla luce degli accertamenti dell'ultimo trentennio (Pubblicato col cortese concorso della presidenza dell'Azienda Generale Italiana Petroli AGIP)*. Roma: Italgraf, p. 135.

Conflict of Interest: The authors declare that the research was conducted in the absence of any commercial or financial relationships that could be construed as a potential conflict of interest.

Copyright © 2021 Vannoli, Martinelli and Valensise. This is an open-access article distributed under the terms of the Creative Commons Attribution License (CC BY). The use, distribution or reproduction in other forums is permitted, provided the original author(s) and the copyright owner(s) are credited and that the original publication in this journal is cited, in accordance with accepted academic practice. No use, distribution or reproduction is permitted which does not comply with these terms.

frontiers in Earth Science

ORIGINAL RESEARCH
published: 25 February 2021
doi: 10.3389/feart.2021.598784

Earthquake Shocks Around Delhi-NCR and the Adjoining Himalayan Front: A Seismotectonic Perspective

Prosanta Kumar Khan[1]*, *Sarada P. Mohanty*[2], *Partha P. Chakraborty*[3] and *Rashmi Singh*[1]

[1]Department of Applied Geophysics, Indian Institute of Technology (ISM), Dhanbad, India, [2]Department of Applied Geology, Indian Institute of Technology (ISM), Dhanbad, India, [3]Department of Geology, University of Delhi, Delhi, India

An increase in the number of earthquakes and subsequent clustering in northwest India, particularly around the Delhi-National Capital Region (NCR) and adjacent NW Himalayan front, provides a good opportunity to understand the underpinning tectonic controls and the likelihood of any large earthquake in the future. The 2001 M_w 7.7 Bhuj, 2011 M_w 6.9 Sikkim and 2015 M_w 7.8 and 7.3 Nepal earthquakes (and 2004 M_w 9.2 Sumatra event) are important in this context. We analyzed the seismicity around the Delhi-NCR and the adjoining Himalayan front, including event clustering and the spatio-temporal distribution of b-values, in the context of kinematics and the regional geodynamics. The overall moderate-to-low b-values, both in time and space, since 2016, provide information regarding an increase and subsequent stabilization of the stress field in the study area. The analysis led to the identification of (1) a structurally guided stress field in the region between the Kachchh and the NW Himalaya that coincides with the direction of Indian plate convergence and (2) frequent occurrences of earthquakes particularly in the Delhi, Kangra and Uttarkashi areas. We propose that faults in western Peninsular India, which pass through the margins of the Aravalli Range, the Marwar basin, and the isostatically over-compensated Indo-Gangetic Plains beneath the under-plated Indian lithosphere, act as stress guides; concentrating and increasing stress in regions of lithospheric flexure. This enhanced stress may trigger a large earthquake.

Keywords: Delhi-NCR, Kangra, Bhuj, clustering of seismicity, seismic b-value

OPEN ACCESS

Edited by:
Antonella Peresan, National Institute of Oceanography and Applied Geophysics (Italy), Italy

Reviewed by:
Pallabee Choudhury, Institute of Seismological Research, India
Denis Anikiev, German Research Centre for Geosciences, Helmholtz Centre Potsdam, Germany

***Correspondence:**
Prosanta Kumar Khan
khanprosanta1966@iitism.ac.in
khanprosanta1966@gmail.com

Specialty section:
This article was submitted to Solid Earth Geophysics, a section of the journal Frontiers in Earth Science

Received: *25 August 2020*
Accepted: *25 January 2021*
Published: *25 February 2021*

Citation:
Khan PK, Mohanty SP, Chakraborty PP and Singh R (2021) Earthquake Shocks Around Delhi-NCR and the Adjoining Himalayan Front: A Seismotectonic Perspective. Front. Earth Sci. 9:598784. doi: 10.3389/feart.2021.598784

INTRODUCTION

An increase in clustering of seismic shocks of magnitudes (M_L) ranging from 2.0 to 5.2 around the Delhi-NCR and in the adjacent region surrounding large historical damaging events (**Figures 1A,B**), has raised alarm in the society and scientific community. The seismicity record between January 2016 and June 2020 includes 414 events of $M_L \geq 2.0$, of which 135 shocks ($M_L \geq 2.0$) took place in the first six months of 2020 in the Delhi-NCR and adjacent Himalayan front. The fallout news coverage, claims and counter claims in electronic and print media raised some pertinent scientific questions, e.g., (1) possibility of any great event in the Delhi and adjoining areas in the future, (2) triggering of the recent shocks, and (3) possible role of pre-Himalayan heterogeneities behind the along-strike seismic behaviour of the Himalayan front including the Delhi-NCR region. It is interesting to note that majority of the shocks are

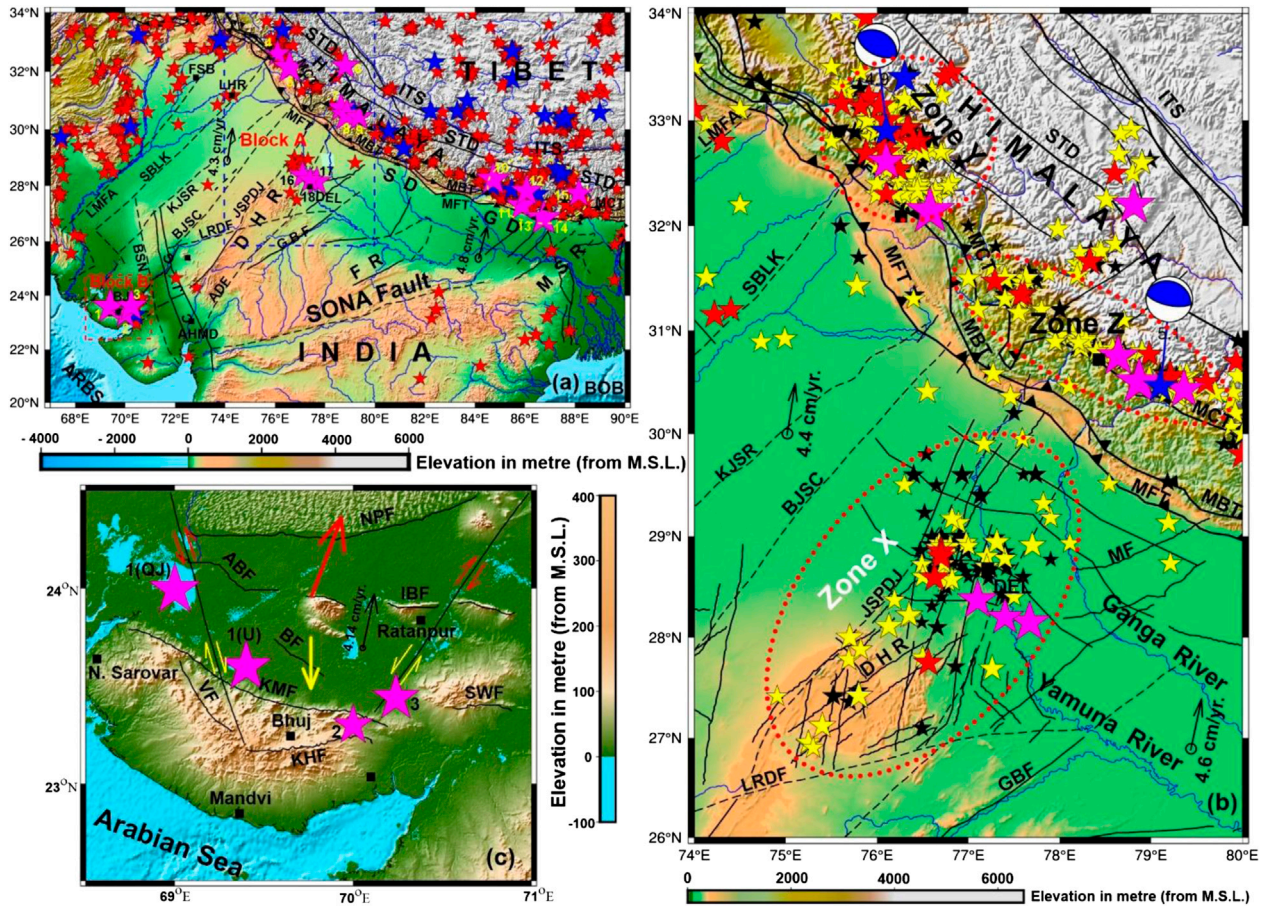

FIGURE 1 | (a) Map showing the distributions of earthquake events in northern India including Delhi-NCR area and adjoining mountain front. **(b)** The enlarged portion of block A (of a) of Delhi and adjoining showing epicentres of earthquakes during 2016–2020. **(c)** The enlarged portion of block B (of a), the Bhuj area, showing epicentres of historical earthquakes, Magenta stars: the epicenters of historical damaging earthquakes. Yellow arrow represents the compression direction during the 2001 event and associated slip patterns (yellow half arrows) along two regional transverse faults (after Sinha and Mohanty, 2012; Khan et al., 2016). Red arrow along NNE directions represents the predominant stress field (after Aggarwal et al., 2016). Periodic release of stress along the transverse faults results in opposite slip patterns marked by red half arrows (cf. Sinha and Mohanty, 2012). 1: 1819 M 8.3 Kutch (QJ after Quittmeyer and Jacob, 1979; U after Chandra, 1977), 2: 1956 M 6.5 Anjar, 3: 2001 M 7.6 Bhuj, 4: 1945 M 6.27 Chamba, 5: 1905 M 7.8 Kangra 6: 1975 M 6.8 Kinnaur, 7: 1991 M 6.8 Uttarkashi, 8: 1803 M 7.7 Garhwal, 9: 1999 M 6.5 Chamoli, 10: 2015 M 7.9 Nepal, 11: 1833 M 7.6 Nepal, 12: 2015 M 7.3 Nepal, 13: 1988 M 6.8 Nepal-Bihar border, 14: 1934 M 8.1 Nepal–Bihar border, 15: 2011 M 6.9 Sikkim, 16: 1720 M 6.5 Delhi, 17: 1803 M 6.8 Mathura, 18: 1960 M 6.0 Near Faridabad). Black stars in **(c)**: earthquakes with magnitude $2.0 \leq M_L < 3.0$, yellow stars: $3.0 \leq M_L < 4.0$, red stars: $4.0 \leq M_L < 5.0$, and blue stars: earthquakes with magnitude between 5.0 and 5.2. Size of the star in each domain varies with magnitude of earthquake. Solid arrow represents the convergence velocity of the Indian Plate against the Eurasian Plate (after DeMets et al., 1994). Positions of faults are reconstructed after Godin and Harris (2014) and Khan et al. (2014), Khan et al. (2017). Abbreviations: FSB, Faisalabad; LHR, Lahore; MFT, Main Frontal Thrust; MBT, Main Boundary Thrust; MCT, Main Central Thrust; STD, South Tibetan Detachment; ITS: Indus–Tsangpo Suture; DEL, Delhi; BJ, Bhuj; AHMD, Ahmedabad; DHR, Delhi–Hardwar Ridge; FR, Faizabad Ridge; MSR, Monghyr–Saharsha Ridge; LMFA, Larkana–Multan–Faisalabad–Akhnoor lineament; SBLK, Sukkur–Bahawalpur–Lahore–Kathua Lineament; KJSR, Kori Creek–Jaisalmer–Suratgarh–Ropar Lineament; BJSC, Bhachau–Jodhpur–Saddarshahar–Chandigarh Lineament; JSPDJ, Jamnagar–Sirohi–Phulad–Degana–Jamuna Lineament; ADF, Agucha–Dariba fault; GBF, Great Boundary Fault; LRDF, Luni–Rupnagar–Dausa–FatehpurSikri lineament; BSN, Bhavnagar–Surendranagar–Nagar Parker Fault; CJG, Cambay–Jaisalmer graben; SONA, Son–Narmada; SD, Sarada Depression; GD, Gandak Depression, ARBS, Arabian Sea; BOB, Bay of Bengal; ABF, Allahbund Fault; BF, Banni Fault; IBF, Island Belt Fault; KHF, Katrol Hill Fault; KMF, Kachchh Mainland Fault; NPF, Nagar Parkar Fault; SWF, South Wagad Fault; VF, Vigodi Fault.

concentrated around the regions of historical seismicity in the northern Indian plains, including the Delhi-NCR. Indeed, the catastrophic events of the 2001 M_w 7.7 Bhuj (**Figure 1C**), 2011 M_w 6.9 Sikkim and the 2015 M_w 7.8 Nepal (**Figure 1A**) earthquakes are still alive in the minds of population. The fault-bound 2001 Bhuj earthquake occurred at the shallow-level of the lower crust caused widespread damage with a toll of ~20,000 human lives. Small-to-moderate magnitude aftershocks were recorded in different parts of northern Gujarat till the end of 2014 (Khan et al., 2016; Aggarwal et al., 2016). In addition, the incidences of historical major earthquakes (1819 M_w 7.8 Allahbund and 1956 M_w 6.0 Anjar, **Figure 1C**) in the Bhuj region had rattled

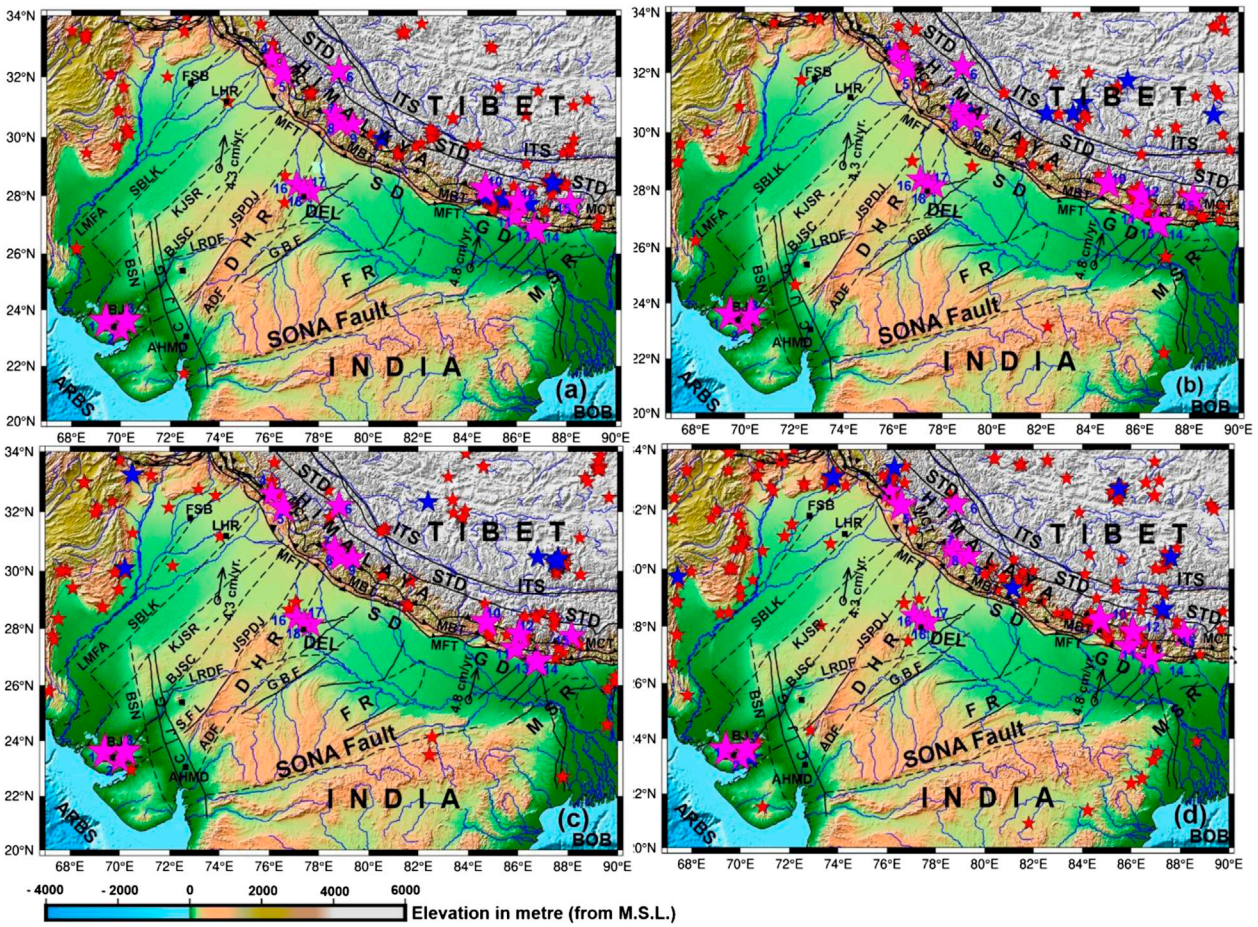

FIGURE 2 | Maps showing the distributions of earthquake events in northern India and adjoining regions during 2016–2020: **(a)** 2016; **(b)** 2017, **(c)** 2018, and **(d)** 2019–2020. Red stars: the epicentres of earthquakes with magnitude 4.0 ≤ M < 5.0. Blue stars: earthquakes with magnitude between 5.0 and 5.8. Size of the star in each domain varies with magnitude of earthquake. Solid black lines represent faults, and black dashed lines represent lineaments. Blue solid lines show the positions of various perennial rivers. Solid black squares represent locations of few important towns. Other abbreviations are similar with **Figure 1**.

the basic tenet of intraplate origin of damaging earthquakes (Chung and Gao, 1995). Copley et al. (2011) linked the Bhuj event with the subduction and collisional dynamics in the western segment of the Himalayas. It is suggested that the seismogenic Indian crust, extending from Gujarat to the Himalayas, supports the compressive stress linked with the subduction of the Indian plate in the region south of Tibet, and is actively involved in triggering moderate-to-great magnitude earthquakes in these areas. In this backdrop, we have investigated the possible reasons behind the recent incidents of small-to-moderate magnitude earthquakes around the Delhi-NCR and the adjoining Himalayas.

The ~2500 km long Himalayan orogeny is structurally and tectonically segmented by the trench-orthogonal ridges (Delhi–Hardwar, Faizabad and Monghyr–Saharsa) and depressions (Sarada and Gandak) in the underthrusted Indian plate (Valdiya, 1976; Gahalaut and Kundu, 2012; Hetényi et al., 2016). The segmented orogeny accommodates stress, which triggered several damaging earthquakes (e.g. 1803 M 7.7 Garhwal, 1833 M 7.6 Nepal–Bihar, 1897 M 8.1 Shillong, 1905 M 7.8 Kangra, 1945 M 6.3 Chamba, 1950 M 8.6 Assam, 1975 M 6.8 Kinnaur, 1988 M 6.8 North Bihar, 1991 M 6.8 Uttarkashi, 1999 M 6.5 Chamoli, 2011 M 6.9 Sikkim, 2015 M 7.8 Nepal and 2015 M 7.3 Nepal, **Figures 1**, **2**). The Delhi-NCR region, close to the foothills of the Himalayas, also experienced a few damaging earthquakes (e.g. 1720 M 6.5, 1956 M 6.7, 1960 M 6.0) in the past (**Figures 1**–**3**). Our aim is to document the trends of concentrated seismic activities that have been occurring since 2016, and identify the causative factors, selecting the area encompassing the Delhi-NCR and the adjoining mountain front in western India (**Figure 1A**). We attempt our study with the analysis of seismic b-values in space-time domains. Seismic b-value has been used in a variety of seismological studies, including earthquake forecasting, prediction, and seismic hazard analysis (Kagan and Knopoff, 1987; Rydelek and Sacks, 1989; Geller, 1997; Wiemer and Wyss, 2000; Beauval and Scotti, 2004; Woessner and Wiemer, 2005; Ogata and Zhuang 2006; Khan and Chakraborty, 2007; Felzer, 2008; Khan et al., 2011; Sobolev, 2011; Cheng and Sun, 2018; Peresan and Gentili, 2018). Special emphasis was given to simulate the distribution and the confinement of seismicity around the Delhi-

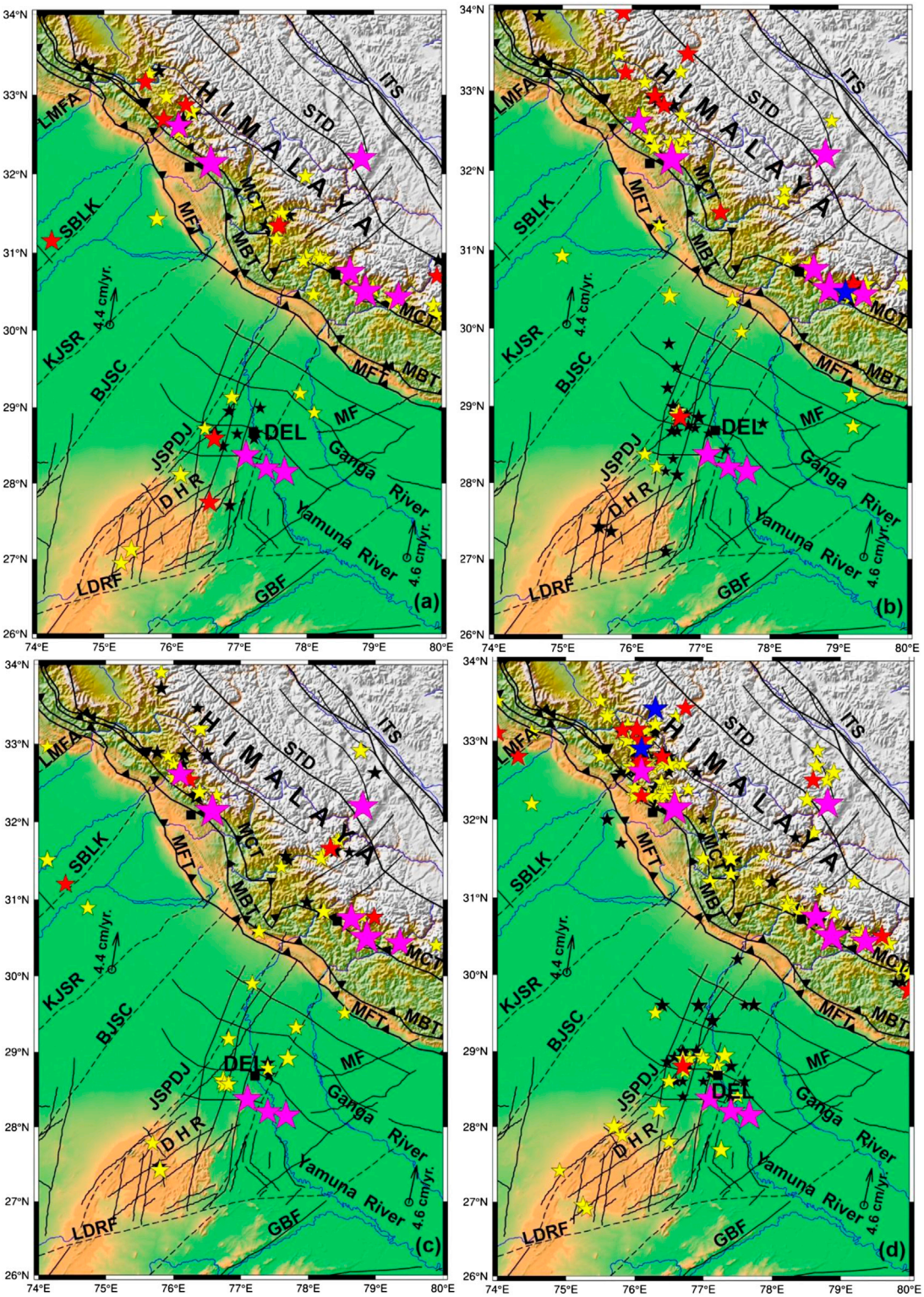

FIGURE 3 | Maps showing the distributions of earthquake events in Delhi and adjoining Himalayas: **(a)** 2016, **(b)** 2017, **(c)** 2018, and **(d)** 2019–20. Stars indicate epicentres of earthquakes (Black stars: magnitude $2.0 \leq M_L < 3.0$; yellow stars: $3.0 \leq M_L < 4.0$; red stars: $4.0 \leq M_L < 5.0$; blue stars: magnitude between 5.0 and 5.2). Size of the star in each domain varies with magnitude of earthquake. Solid black lines represent faults, and black dashed lines represent lineaments. Blue solid lines show the positions of various perennial rivers. Solid black squares represent locations of important places. Other abbreviations are similar with **Figure 1**.

NCR, the adjoining Himalayas, in general, and for three main tectonic domains of interest, i.e., Delhi (Zone X), Kangra (Zone Y) and Uttarkashi (Zone Z) regions, in particular (**Figure 1B**). We finally integrate all the observations into a holistic seismic model that may account for interpretation of signatures obtained from structurally complicated western Indian plain and the adjoining Himalayan front.

REGIONAL TECTONIC SETUP

The Late Mesozoic subduction of the Neotethyan oceanic crust at the leading edge of the Indian Plate below the Eurasian plate and the southward migration of the convergence zone in the Cenozoic gave rise to the evolution of the Himalayas (Patriat and Achache, 1984; Copley et al., 2010). The suturing migrated eastward along the Indus-Tsangpo zone, with concomitant oroclinal bending of the Himalayas (Klootwijck et al., 1985). The Paleozoic–Mesozoic Tethyan sedimentary cover on the subducting Indian plate got mobilized in the Himalayan orogenic front. The deformation, thus initiated, migrated southwards in the form of a series of crustal-scale thrust systems (Chakraborty et al., 2019). From north to south, these include the Main Central Thrust (MCT, between Tehyan Himalayas and Lesser Himalayas), Main Boundary Thrust (MBT, between Lesser Himalayas and Sub-Himalayas) and Main Frontal Thrust (MFT, between Sub-Himalayas and Indo–Gangetic Plains) (Le Fort, 1986). It is presumed that the Main Frontal Thrust (MFT) accommodates the maximum deformation of the southward verging orogeny (Lavé and Avouac, 2000). The MFT, MBT, and MCT are merged in a northward dipping decollement, i.e., the Main Himalayan Thrust (MHT) (Makovsky et al., 1996; Hauck et al., 1998; Bollinger et al., 2006), which is modeled as a duplex with two north-dipping sub-horizontal planes connected by a system of thrust faults (Mendoza et al., 2019), act as an impediment to the plate convergence.

The convergence rate of the Indian plate near the Himalayan front varies significantly between ~5.4 cm/yr and 4.2 cm/yr along the east–west direction (DeMets et al., 1994). The hard collision of the Indian plate during the Late Miocene caused the maximum upliftment of the Himalayas and the Tibet (Royer and Gordon, 1997). The enormity of deformation of the orogenic process has resulted in the development of unconformity in the floor of the Bay of Bengal, folding and faulting in the equatorial Indian Ocean, and the evolution of basins and ridges near the foothills of the Himalayas—all in response to tectonic processes in the orogen that evolved during Miocene–Pliocene time (Cochran, 1990; Curray, 2005; Gordon, 2009). Thus, the active resistance to the under thrusting distributes and perturbs the stress fields up to the Indian Ocean, and accounts for occasional incidents of great intraplate earthquakes (Khan et al., 2014; Aggarwal et al., 2016; Khan et al., 2016; Khan et al., 2020). Further, the excess weight of the orogeny is supported in parts by the strength of the Indian plate, which distributes the load by flexing down along the ~1000 km laterally extended and isostatically over-compensated Indo–Gangetic Plains (e.g., Lyon-Caen and Molnar, 1983; Tandon et al., 2014).

Experiments on deformation and numerical modeling involving tectonic units along collisional boundaries have revealed a complex geometry for sheared suture zone (Beaumont et al., 1996; Selzer et al., 2008). Continental plates, involving collision, get stacked and show the presence of double Moho below the overriding plate (Beaumont et al., 1996; Selzer et al., 2008). In these models, the curved geometry of the crustal elements in plan and cross-section act as the sites for stress accumulation and deformation leading to seismicity. The deformation scenario becomes more complex when the subducting plate inherits tectonic elements at high angles to the regional trend of the mountain belt. Converging plate, containing pre-orogenic anisotropies (e.g., ridge, fault systems, lineaments, etc.), leads to lateral variation of crustal thickness during subduction. The processes may further lead to segmentation of the mountain belt having variable stress-strain patterns (Khan et al., 2014; Hetényi et al., 2016). The northward continuation of the Pre-Himalayan heterogeneities within the converging Indian plate [e.g. the Aravalli Mountain belt as the Delhi-Haridwar ridge (DHR), the Bundelkhand massif as the Faizabad ridge (FR), the Satpura Mountain belt as the Monghyr–Saharsa ridge (MSR)] and the clustering of criss-cross fault systems are the examples of such heterogeneity (Valdiya, 1976; Karunakaran and Ranga Rao, 1979; Valdiya, 2003; Goswami, 2012; Godin and Harris, 2014). Many regional faults and lineaments, viz. the SONA Fault, the Great Boundary Fault (GBF), Bachau–Jodhpur–Saddarshahar–Chandigarh lineament (BJSC), Kori Creek–Jaisalmer–Suratgarh–Ropar lineament (KJSR) and Sukkur–Bahawalpur–Lahore–Kathua lineament (SBLK) parallel to these ridge systems (**Figure 1A**) define large-scale horsts, grabens and sedimentary basins with crystalline basement and sedimentary fills of variable thickness. Understandably, such heterogeneities cause segmentation in the subducting Indian Plate (**Figure 1**).

EARTHQUAKE DATA AND ANALYSIS

The present analysis has been carried out using the earthquake data recorded by local network of the National Centre of Seismology (NCS), Government of India, New Delhi (Srivastav et al., 2005; Dattatrayam et al., 2014; Prakash et al., 2020). The seismic network in Delhi NCR and the surrounding region has more than 30 broadband stations (**Figure 3** of Prakash et al., 2020), and the earthquake catalogue contains information on origin time/date, latitude and longitude of the epicentre, focal depth and magnitude. The network has a detection and location capabilities down to a magnitude 2.0 (M_L) earthquake. Also, the earthquake data in the catalogue have an accuracy of ±2 km in the epicentre. Despite upgradation of basic seismic network in recent time with addition of state-of-the-art broadband sensor having VSAT connectivity (Prakash et al., 2020), the accuracy in focal depth determination is not improved further because of limitation in recording station distribution. This has restricted any analysis based on hypocentre-information available in the

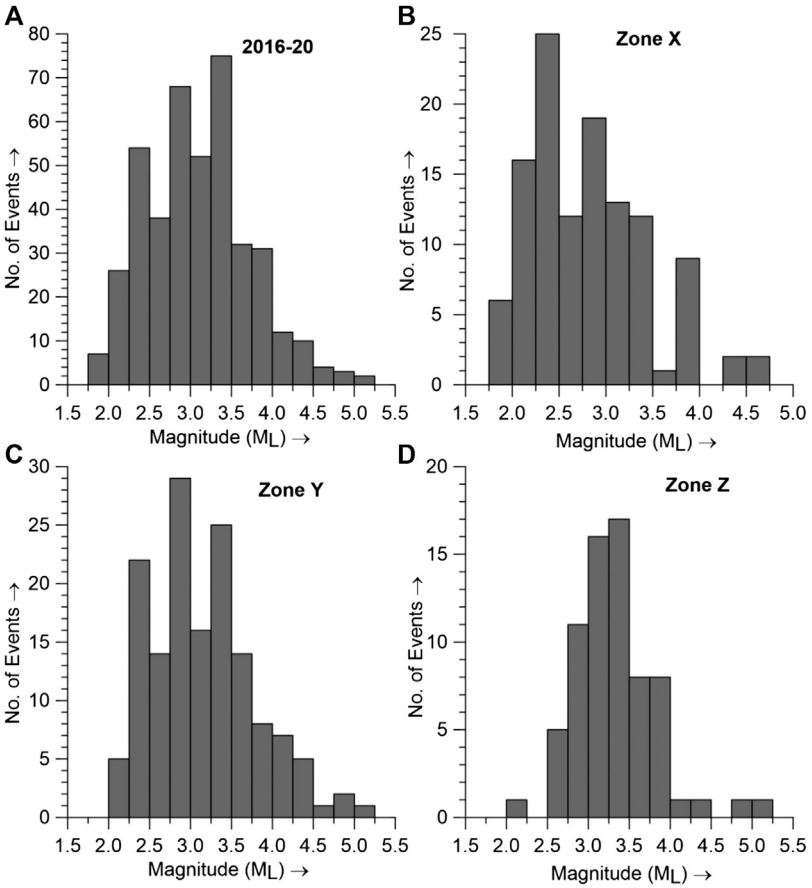

FIGURE 4 | Histogram illustrating the level of seismicity in Delhi and adjoining regions. **(A)** during 2016–2020, **(B)** Zones X, **(C)** Zone Y, and **(D)** Zone Z (**Figure 1B**). Note the occurrences of maximum magnitude earthquakes in different Zones.

catalogue. Taking into consideration the accuracy of locations and magnitudes of the events available in the NCS catalogue, a total of 414 events of $M_L \geq 2.0$ have been considered (**Figure 4B**) for detailed analysis of the earthquakes in the present study. Further, regional clustering of events ($M_L \geq 4.0$) has also been investigated in view of the major damaging earthquakes in different segments of the Himalayas and the Delhi region (**Figure 2**). We have compiled 441 such events for the duration 2016–19 from the catalogue of International Seismological Centre (ISC), and 84 events for the first 6 months of 2020 from NCS catalogue based on the coverage of recording stations.

Regional Seismicity Analysis

The elliptical segment of the Nepal–Bihar–Sikkim, a zone of interaction of MSR with the foothills of the Himalayas (shown in **Figure 1A**), covers the region of past six major earthquakes. Along with the MSR, many regional transcurrent faults (e.g., east and west Patna faults, Pingla fault and many others, Godin and Harris, 2014; Hetényi et al., 2016) passing through this region, have been accommodating the plate movements since the Holocene times (Valdiya, 1976, Valdiya, 2003). These are particularly involved in concentrating and raising the stress field (Sibson, 1980; Marshak and Paulsen, 1997), and occasionally trigger major earthquakes in this part of the Himalayas (Dasgupta et al., 2000; Paul et al., 2015; Singh et al., 2020). The spatially clustered seismic activities in this area (**Figure 1A**) are caused by occasional release of strain energy through occurrences of aftershocks and other main shocks subsequent to 2015 M_w 7.8 and 7.3 Nepal events.

The great 2001 M_w 7.7 Bhuj earthquake occurred along the Kachchh Mainland Fault (KMF), where another two major earthquakes occurred in 1819 and 1956 (block B, **Figures 1A,C**), and the aftershocks continued for a period of long-time (Aggarwal et al., 2016; Khan et al., 2017). The strain energy, released in form of earthquakes, apparently has migrated toward the western part, particularly in the northwest Himalaya and adjoining regions. Concentrated activities are noticed in the region with epicentres of major historical earthquake events near Kangra (no. 4, 5) and Delhi (no. 16–18) (**Figure 1A**).

The regional seismicity has been investigated in some details over four time-domains, viz., 2016 (**Figure 2A**), 2017 (**Figure 2B**), 2018 (**Figure 2C**), and 2019–2020 (**Figure 2D**).

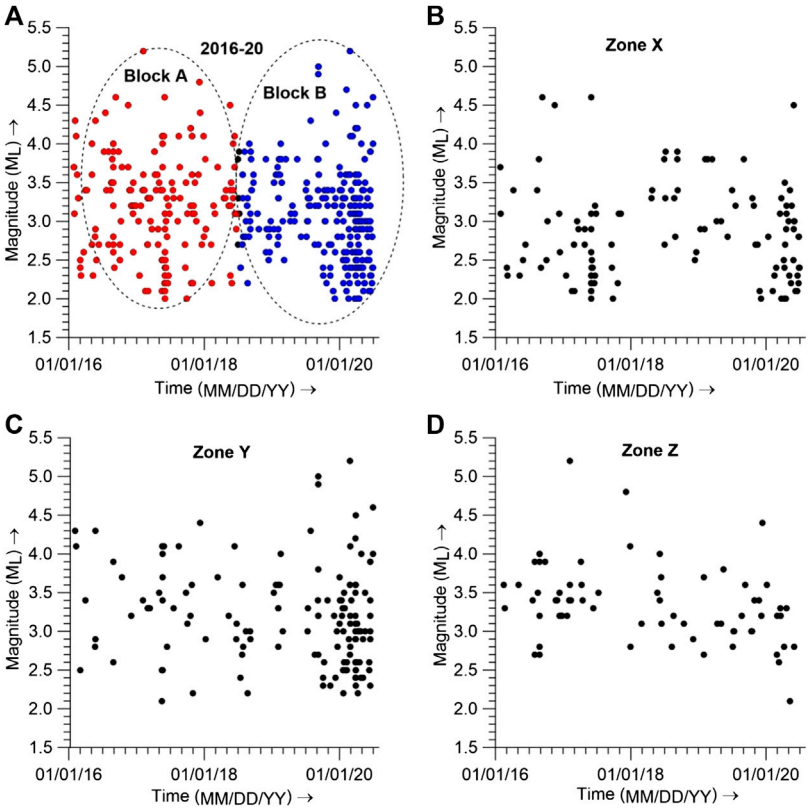

FIGURE 5 | Plots illustrating the seismicity in Delhi and adjoining regions. **(A)** during 2016–2020, **(B)** Zone X, **(C)** Zone Y, and **(D)** Zone Z (**Figure 1B**). The clustering is also apparent in the three Zones (X, Y and Z). Note the clustered seismicity in blocks A and B, and significant increase in frequency of occurrences in 2019–20.

Enhanced clustering of seismicity, few with magnitude more than 5.0, are noticed around the Nepal-Bihar zone, where the 2015 great Nepal event took place (**Figure 2**). Gradually, the seismic activities shifted toward west, and in 2019–20 maximum activity was recorded around the Delhi-NCR (**Figures 1**, **2**). Even earthquakes of magnitudes one blank> 5.0 are recorded in the western and central segments of the Himalaya including one in Bhuj (14 June, 2020 M_w 5.3 Bhuj) and near the Suleiman Range (March 16, 2019 M_w 5.0 and September 24, 2019 M_w 5.4).

Local Seismicity Analysis

Figure 1B displays the distribution of seismicity ($M_L \geq 2.0$) for the duration January 01, 2016 to June 30, 2020 (414 events, altogether) in the Delhi and adjoining mountain front (**Figures 4A**, **5A**). Seismicity is found to concentrate within specific areas, namely surrounding the Delhi (120 events, Zone X), Kangra (151 events, Zone Y) and Uttarkashi (87 events, Zone Z) regions (**Figures 1**, **4**, **5**). Spatial zone-specific distribution of seismicity, within the Delhi and adjoining Himalayas region, has been further investigated for different time intervals 2016 (59 events, **Figure 3A**), 2017 (89 events, **Figure 3B**), 2018 (57 events, **Figure 3C**), and 2019–2020 (209 events, **Figure 3D**). The concentration of seismicity in these domains has changed considerably with maximum of 209 in 2019–20; and this number has increased more sharply in 2020 (134 events over first six months). Significant number of events with magnitudes $M_L \geq 4.0$ has also been recorded in each time-domain. In particular, the Zone Y surrounding the Kangra area records significant number of events with magnitude $M_L \geq 4.0$ (**Figure 4**). Although, low-magnitude earthquakes are recorded in high numbers near the Delhi (Zone X) and Uttarkashi area (Zone Z), events with $M_L \geq 4.0$ are not rare in these areas. **Figure 5A** shows that the seismic activities are distinctly divided into two time-domains; one over 2016–18 and another over 2019–20, and apparently the energy release is explained to be discontinuous in nature. More or less similar oscillations are also found in Zones X and Y (**Figures 5B,C**). A distinct cluster of seismic activities with two events of magnitudes $M_L \geq 5.0$ was associated with the Kangra area since 2019 (**Figure 5C**). However, such distinct signature of clustering is apparently less prominent in Zone Z (**Figure 5D**).

Seismic b-Value Analysis

Earthquake magnitude-frequency domain is approximated by a power-law distribution as observed for other similar self-organized non-equilibrium systems. Gutenberg and Richter (1954) proposed an empirical relationship (the GR law) between frequencies of occurrence of earthquakes as a function of magnitude, which is expressed mathematically as:

$$\mathrm{Log}_{10}\mathrm{N}(\mathrm{M}) = \mathrm{a} - \mathrm{b}\,\mathrm{M} \quad (1)$$

where N(M) is the cumulative number of shocks with magnitude M ≥ 0, and 'a' is a measure of the background level of seismic activity/efficiency of the concerned area. It depends on the areal extent of the study-region and duration. The seismic b-value is computed from the slope of the Log_{10}(N) vs. M regression line. It accounts for large-magnitude earthquakes over the number of small-magnitude shocks (Khan and Chakraborty, 2007; Cheng and Sun, 2018), and is inversely related with the differential stress-level ($\sigma_1-\sigma_3$) and/or shear strength of the materials (Wyss, 1973; Urbancic et al., 1992; Schorlemmer et al., 2005; Spada et al., 2013; Scholz, 2015). It also determines the decay in the rate of occurrences of earthquake events with increasing magnitude. In natural situations, b-values are found to lie between 0.5 and 1.5, depending on the tectonics of a region (Khan et al., 2011).

The temporal and spatial heterogeneity in crust may break the power-law scaling for distribution of earthquakes (Rydelek and Sacks, 2003; Woessner and Wiemer, 2005), and result in anomalous b-value distribution owing to anomalous stress distribution at high and low levels. However, the self-organized and self-similar non-equilibrium condition in the subsurface medium, may still remain valid for earthquake generations (Rydelek and Sacks, 1989; Woessner and Wiemer, 2005; Sobolev, 2011), and stable for eqn. 1 over a definite time-window (Wiemer and Wyss, 2000). The plot systematically deviates from linearity because of rare incidents of large magnitude events at upper bound, and is constrained by the incompleteness of catalogue at lower bound (Rydelek and Sacks, 1989; Taylor et al., 1990; Wesnousky, 1994; Naylor et al., 2010). The latter may be caused by missing a large number of small magnitude earthquakes due to: detection threshold; aftershock (or other shocks) occurrence within the tail of larger events; aseismic slip during nucleation along a creeping fault (Heimpel and Malin, 1998; Vorobieva et al., 2016), or lack of enough stations to record very small magnitude events (Pacheco et al., 1992). Wiemer and Wyss (2000) and Woessner and Wiemer (2005) have examined such limitations, and advocated the essential requirement of minimum magnitudes of completeness (Mc) for seismicity analysis. Although, the Mc varies with time in most of the catalogues for several regions, namely it decreases with increase in the number of recording stations and advancement in the methodology of analysis, it is widely used for b-value estimation over high seismic areas (Rydelek and Sacks, 1989; Wiemer and Wyss, 2000). Further, the GR law needs to be estimated for different segments over the study area in view of self-similar seismotectonic character (Molchan et al., 1997), or distinct locations of geological units (Peresan and Gentili, 2018). Thus, the zonation in the region of present concern is constrained mainly by the self-similar seismotectonic behaviour, and a specific Mc value is determined for each zone.

With all discussed constraints, we carried out the analysis of seismic b-values following frequency-magnitude distribution (FMD, **Eq. 1**) of Gutenberg and Richter (1954) for understanding the possibilities of major earthquakes in any of the three zones (X, Y and Z, **Figure 1A**). The technique is being used ubiquitously in different tectonic settings at different levels of depths for several decades considering earthquake catalogues covering from few months to several years. This makes the GR law very effective for analysis of earthquake hazards and also attractive for its theoretical significance. Assuming the self-similarity in the GR law (Mignan and Woessner, 2012), we have performed the analysis for the entire study area and for the three demarcated zones in different time-domains between 2016 and June 30, 2020 (cf. **Figures 3**, **5A**,**6**). On the basis of spatial clustering of earthquakes epicentres in different time windows, the b-values are clubbed under two blocks A and B (**Figure 5A**). The uncertainties in the calculations of b-values are based on the model proposed by Shi and Bolt (1982), which can be written as

$$\sigma(b) = 2.30b^2\sigma(\overline{M}) \quad (2)$$

$$\sigma(\overline{M}) = \left\{ \sum_{i=1}^{n} \frac{(M_i - \overline{M})^2}{n(n-1)} \right\}^{\frac{1}{2}} \quad (3)$$

where σ(b) represents the standard error of b-value calculation, N and $\overline{M}$ are the number and the average value of the magnitude distribution ($\mathrm{M_i}$) of the events used for computation of b-values for magnitude $\mathrm{M_c}$ and above. We found few events of larger magnitudes in each domains fall little away from the best-fit line at its upper bound. These few events have been excluded from the analysis of b-values in view of scarcity of such events at the higher magnitude range. This also has improved the value of coefficient of determination (i.e. R^2) in this statistical regression analysis.

Selection of completeness magnitude ($\mathrm{M_c}$) of a sequence of natural shocks is crucial for any statistical analysis (Mignan and Woessner, 2012 and the references therein). The selection of lower value of Mc will normally contaminate the analysis, largely by threshold characteristics of the instruments as well the detection of events, whereas the high value results in under-sampling of the sequence of dataset beyond the Mc value. In the present study, attempt was made for Mc's selection for different zones with critical examination by visual inspection of departure of linearity (apparent break in the gradient) in the log-linear plot of cumulative FMD of earthquake events. However, the gradual change in the curvature of the plots made the selection of Mc difficult (Mignan and Woessner, 2012), particularly when resorting to maximum curvature method for Mc detection. This typical trend in the cumulative FMD is usually caused by the spatio-temporal heterogeneities in the Mc (Wiemer and Wyss, 2000; Mignan, 2011). Thus, to verify deviations from log-linearity of the FMD distribution, the Mc for each dataset has been computed on the basis on non-cumulative (i.e. computed $\log_{10}$ value of number of events for each magnitude increment) log-linear plot of events (Woessner and Wiemer, 2005; Mignan, 2012; Mignan and Woessner, 2012). The exercise was carried out to avoid the limitation in the selection of Mc threshold from the cumulative log-linear plot of FMD, and to provide a rather conservative specific Mc for each zone (**Table 1**).

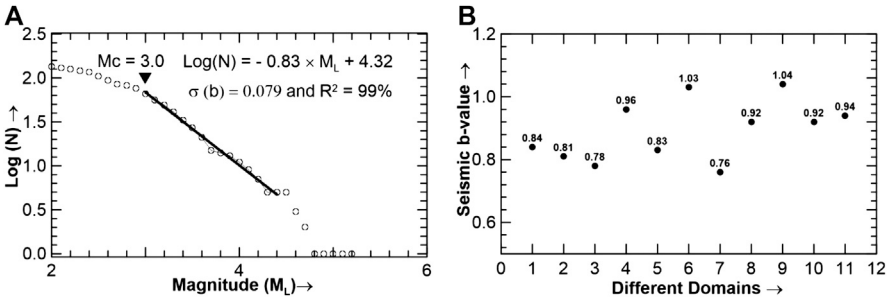

FIGURE 6 | Plots illustrating **(A)** the computation of seismic b-value (after Gutenberg and Richter, 1954) for earthquakes of 2020 and **(B)** the variation of seismic b-values for seismic zones (X, Y and Z) during different time domains. Index for time domains along the *x*-axis: 1—2016 (entire area); 2—2017 (entire area); 3—2018 (entire area); 4—2019 (entire area); 5—2020 (entire area); 6—2016–2020 (entire area); 7—Zone X; 8—Zone Y; 9—Zone Z; 10—Block A of **Figure 5A**; and 11—Block B of **Figure 5A**. Mc: Completeness magnitude, $\sigma_{(b)}$: Standard error (after Shi and Bolt, 1982), R^2: Coefficient of determination.

TABLE 1 | Details of the earthquake events used for computation of seismic b-values and the corresponding errors.

Sl. no	Time domain/Zone	Total no. of earthquake event	No. of earthquake event used	Seismic b value	M_c	σ(b) (Standard error of b)	R^2 (%)
1	2016	59	35	0.84	3.2	0.09	97
2	2017	89	45	0.81	3.1	0.09	98
3	2018	57	37	0.78	2.9	0.06	99
4	2019	75	52	0.96	3.0	0.10	98
5	2020	134	61	0.83	3.0	0.08	99
6	2016–20	414	169	1.03	3.3	0.08	99
7	Zone X	120	48	0.76	2.9	0.06	96
8	Zone Y	151	59	0.92	3.3	0.09	98
9	Zone Z	87	54	1.04	3.2	0.11	99
10	Block A	173	76	0.92	3.3	0.07	98
11	Block B	241	104	0.94	3.2	0.08	99

RESULTS

The maximum computed b-value of 1.04 is recorded in Zone Z (i.e., the Uttarkashi area; **Figure 1**), and the next low b-value of 1.03 is found for the entire region for the data ranging from 2016 to June 30, 2020 (**Figure 6B**; **Table 1**). The minimum b value of 0.76 is found for Zone X (i.e., Delhi-NCR), and the next higher one of 0.78 is noted during 2018. Other b-values lie at moderate-to-low-level with a maximum of 0.96 during 2019 (**Figure 6B**; **Table 1**).

We found clustered seismicity in Delhi (Zone X, **Figure 5B**) and Kangra (Zone Y, **Figure 5C**) areas but not so strongly at the Uttarkashi area (Zone Z, **Figure 5D**). Maximum number of events were found in the Kangra region in 2019–20, with the close next at Delhi. **Figure 6B** and **Table 1** illustrate the variations of seismic b-values in different time and space domains. Except a little higher b-value of about 1.0 during 2016–2020 for the entire region and the Uttarkashi area, other b-values in 2016, 2017, 2018, and 2020 are found to be around 0.8, with a minimum of 0.78 in 2018. Different zones such as X, Y and Z (Delhi-NCR, Kangra, Uttarkashi, **Figure 1B**) also record low to moderate b-values between 0.76 and 1.04 (**Table 1**). The overall two clustered seismicity in block A and B during 2016–2020 (**Figure 5A**) also shows moderate b-values of 0.92 and 0.94, respectively (**Table 1**).

Although we found a little high standard errors (≥0.09) for 2016, 2017, 2019, and Zone Y and Z, all the estimates are well compatible within the range of errors. The large uncertainties for some domains might have been found due to limited available observations and heterogeneities in the dataset; the b-value estimate for zone X, in particular, though being characterized by a pretty low standard error (~0.06), it has a lower value of coefficient of determination (96%) compared to other zones. The robustness of b-values estimates was also tested with other methods (i.e., maximum likelihood, Aki, 1965) and was found to be compatible within the errors limits; also it was found that such analysis is less sensitive to magnitude upper bound, although producing lower values of coefficient of determination R^2.

The persistent moderate (~1.0) to low b-values (~0.8–0.76) in all the Zones X,Y and Z, and blocks A and B (**Table 1**; **Figure 6B**) invariably account for higher stress accumulation in the entire study-area (cf. Tormann et al., 2012; Spada et al., 2013; Khan et al., 2018). The low b-values, over time and space domains, usually indicate high-strength homogeneous rock-mass, whereas high b-values are found for a large number of small earthquakes expected in regions of low strength and large heterogeneity (Tsapanos, 1990). Low b-value in a region is indicative of high stress accumulation and release of high seismic moment (Scholz, 1968; Wyss, 1973; Cao and Gao, 2002). From stable and unstable friction experiment, Rivière et al. (2018) have shown that the

reduction of b-value occurs when shear stress systematically rises before stick-slip failure, and results in large events when faults become highly stressed. Incidences of large number of foreshocks are also reported in such situation (Scholz, 1968; Goebel et al., 2013, Goebel et al., 2015). Scholz (1968) and Wyss (1973) suggested the low b-values to be compatible with release of higher seismic moment energy in an active seismic zone. Scholz (1968) also suggested that the b-value decreases with increasing differential crustal stress (Schorlemmer et al., 2005; Spada et al., 2013; Scholz, 2015; Khan et al., 2018), and the declining b-value accounts for an impending main shock. The increased number of events in 2019–20 (block B, **Figure 5A**) and an overall moderate-to-low b-value indicate the possibility of increasing stress accumulation in the study area and a future great earthquake.

We also found a cluster of seismic events near the regions where ridges (horsts) and basins (grabens) interact with the Himalayan orogenic front. This observation indicates stress concentrations at the intersection points (Sibson, 1980; Marshak and Paulsen, 1997; Khan et al., 2014). Indeed, concentration of most of the events in the re-entrants (e.g. 1803 M 7.7 Garhwal, 1905 M 7.8 Kangra, 1945 M 6.3 Chamba, 1975 M 6.8 Kinnaur, 1991 M 6.8 Uttarkashi, and 1999 M 6.5 Chamoli), and historical earthquakes along the margins of the regional faults in the Western India (e.g. 1720 M 6.5 Delhi, 1956 M 6.7 Delhi, 1960 M 6.0 Delhi, 1966 M 5.8 Delhi-NCR, 1819 M_w 7.8 Allahbund, 1956 M_w 6.0 Anjar, 1969 M_w 5.3 Mt Abu, 2001 M_w 7.6 Bhuj, 2009 M_w 5.1 Barmer) indicate a link between the seismic events with regional faults striking NNE-SSW and cross-faults forming horsts and grabens in the subducting Indian plate and their interaction with the MHT.

We have also noticed increased frequency of earthquakes of magnitudes $M_L \geq 4.0$ along the western part of India, particularly in 2019–20 (**Figures 1A**, **2**), with many events associated with the NNE directed lineaments transcend the Himalayan mountain front in the area. The 2012 M_w 5.1 Dholavira and 2020 Mw 5.3 Bhachau earthquakes with five other earthquakes of magnitudes 5.0 and above along the western part of India (**Figure 1A**) are indicators for increasing stress fields in Delhi and the adjoining regions. The fluctuation and multi-fractality in the sequence of aftershocks of 2001 Bhuj earthquakes (Aggarwal et al., 2015, Aggarwal et al., 2017) bear testimony for the oscillating nature of seismic energy release, and support the chaotic nature of shocks in Delhi and the adjoining regions (**Figure 6**). Further, the occurrences of earthquakes in a region follow the non-linear, chaotic and scale-invariant pattern, and the non-constraint of self-similarity in the earthquake sequence limits the predictability of large future earthquake (Sykes et al., 1999).

DISCUSSION

The analysis of regional seismicity indicates that the stress-strain patterns in the Himalayas, generating major earthquakes, are apparently linked with the regional structural patterns of the converging Indian plate. It is noted that the crustal heterogeneities are responsible for the lateral segmentation of the 2500 km long orogen into distinct tectonic domains (Valdiya, 1096; Gahalaut and Kundu, 2012; Godin and Harris, 2014; Hetényi et al., 2016). To resolve specific-controls, we have attempted tracking of regional structures in the study area to find their continuity, if any, from Indian plate interior through the foredeep to the Himalayas and the link between these structures and seismicity in the area. Transfer of stress into the Indian plate interior by the regional fault systems is documented and identified as an earthquake trigger in selected domains of the Peninsular India (Copley et al., 2011). One such zone of high seismicity is found in the western part of India, i.e. the Kachchh region. The 2001 M_w 7.6 Bhuj earthquake was considered to be the result of stress propagation from the Himalayas (Copley et al., 2011) or the Suleiman Range (Stein et al., 2002; Khan et al., 2016). The analysis of Khan et al. (2016) indicates that the far-field stress generated by the collision resistance between the Indian and Eurasian plates and anticlockwise rotation of the Indian plate are the main factors behind the stress accumulation in the western India and its periodic release through earthquakes. In addition to the earthquakes in the Kachchh region, two other events (1969 M_w 5.3 Mt. Abu and 2009 M_w 5.1 Barmer at 15 and 39 km depth, respectively) were also reported along regional fault systems demarcating the area (Khan et al., 2016).

With this understanding, we have further attempted an analysis of regional geotectonic backdrop that may have been causing the stress accumulation. Definitely, the northwestern margin of the Indian plate has a crucial role in this. It includes the Aravalli craton, the Indo–Gangetic Plains and the Kachchh–Saurashtra blocks. The eastern boundary of the block is demarcated by the Great Boundary Fault (GBF), and the western margin is defined by the Suleiman Range–Jacobabad Ridge (**Figures 1**–**3**). The intervening region is divided into five blocks (from west to east): the Indus basin, Pokhran–Bahawalpur ridge, Jodhpur–Marwar basin, the Aravalli Mountain Range and the Eastern Plains (Mahi–Banas–Chambal basin). The regional faults demarcating the boundaries between the morphotectonic units extend from the Arabian Sea to the Himalayas, and have surface expressions of: Sukkur–Bahawalpur–Lahore–Narowal–Kathua (–Dalhousie) lineament (SBLK; Ravi lineament), Kori Creek–Umarkot–Jaisalmer–Suratgarh–Ropar (–Bilaspur–Mandi) lineament (KJSR), Bhachau–Nagar Parker–Luni–Umednagar (Jodhpur)–Nokha (Nagaur)–Sadarshahar–Sirsa–Pachkula (Chandigarh)–(Kalka–Kufri) lineament (BJSC), Jamnagar–Sirohi–Phulad–Degana–Sikar–Rohtak–Karnal–Jamuna–Khairi lineament (JSPDJ) and East Aravalli dislocation zone (Agucha–Dariba Fault). Though major parts of the region to the west of the Aravalli Mountains is occupied by the eolian sands of Rajasthan desert, the faults and lineaments have been tracked and mapped from surface geomorphic features and shallow surface geophysical signals, viz., straight courses of river systems, regional gravity anomalies and distribution of sedimentary basins on the surface (cf. Balakrishnan, 1997; Sinha-Roy et al., 1998).

In the tectonic map of India by Merh (1995), the SBLK lineament is displayed as the "foredeep zone" and the combined block of the KJSR and BJSC as the "hinge zone", bordering the "shelf zone" to the west of the areas of the Aravalli–Delhi Fold Mountains. The interaction of alternate ridge (horst) and basins (grabens) with the MHT has led to the development of re-entrants over the ridges (horsts) and salient over the basins (grabens) in the frontal part of the Himalayas (**Figure 7**), which are manifested as the Dehra Dun re-entrant over the Delhi-Hardwar ridge, Kangra re-entrant over the Pokhran–Bhawalpur ridge and the Nahan salient against the Jodhpur–Marwar basin (graben). Over an area, delimited by the Rann of Kachchh in the west and fault system at the Shillong plateau margin in the east, the undeformed Indian lithosphere records signatures of breaking, in association with its flexure and underplating below the Eurasian plate along the MHT. The interactions between MHT and seismically active fault systems bounding the horsts and grabens present in the flexed Indian lithosphere are acting as zones of stress concentration in this highly dynamic, seismically active terrain. Since, it is argued that the fault systems, with effective coefficient of friction of ~0.8 in the seismogenic Indian crust, supports the compressive force that transpires through the Indian lithosphere due to subduction process (Copley et al., 2011), it may be logical to think that concentration of additional stress in these stress-equilibrated fault systems is the reason behind recent shallow-focus, low-magnitude events recorded around Delhi-NCR and the adjoining Himalayan front.

Additionally, when hypocentres of major damaging earthquakes are plotted on the reconstructed subduction profile of the Indian plate (**Figure 7**), they are found to fall in both Upper and Lower Crustal domains, invariably around the flexing zone. This observation raised question on triggering behind high-magnitude deep-focus earthquakes in the area; those, more often than not, are extremely damaging. Crustal heterogeneities including the fault systems may continue up to deep crustal level in the lithosphere, however the role behind generation of great events is still not fully understood (Schulte-Pelkum et al., 2019). Alternatively maximum strength is found to be associated with the bending zone (Kohlstedt et al., 1996; Conrad and Hager, 1999), and can trigger great to mega-shocks along subduction margin (Khan and Chakraborty, 2009; Khan et al., 2012). Using joint inversion of seismic and geodetic data sets, Copley et al. (2011) described the source model of 2001 M_w 7.7 Bhuj earthquake and suggested that the stress associated with event was possibly related to the flexural effects of down-going Indian lithosphere

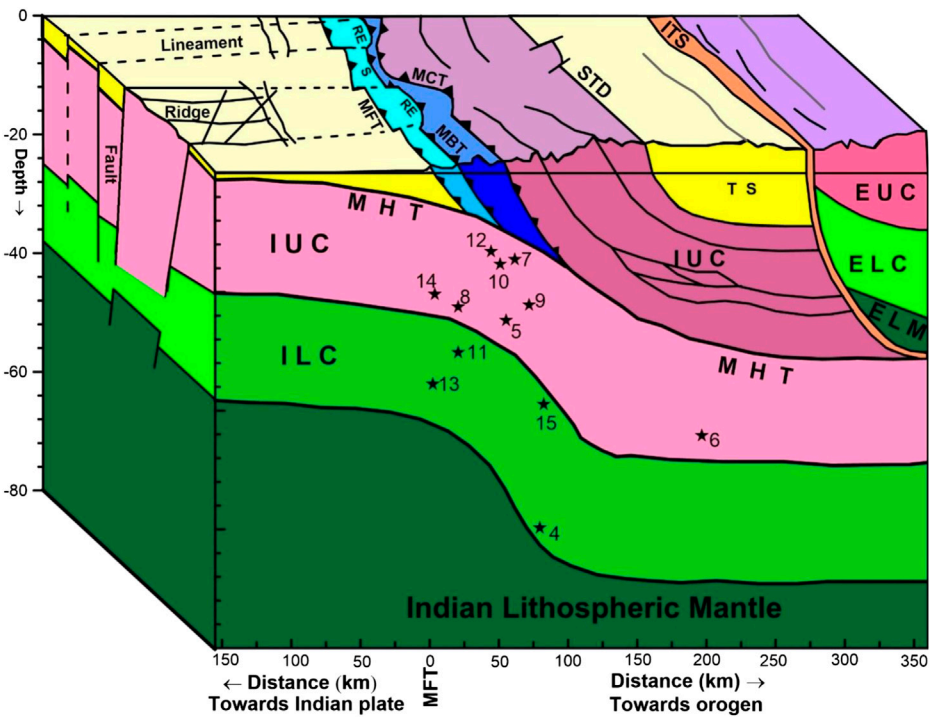

FIGURE 7 | Block diagram illustrating the distribution of hypocentres (★) of 12 great damaging earthquakes within the reconstructed subduction profile of the Indian lithosphere (after Ansari et al., 2014). 4: 1945 M 6.27 Chamba, 5: 1905 M 7.8 Kangra 6: 1975 M 6.8 Kinnaur, 7: 1991 M 6.8 Uttarkashi, 8: 1803 M 7.7 Garhwal, 9: 1999 M 6.5 Chamoli, 10: 2015 M 7.9 Nepal, 11: 1833 M 7.6 Nepal, 12: 2015 M 7.3 Nepal, 13: 1988 M 6.8 Nepal–Bihar border, 14: 1934 M 8.1 Nepal–Bihar border, 15: 2011 M 6.9 Sikkim. Abbreviations: MFT—Main Frontal Thrust, MBT—Main Boundary Thrust, MCT—Main Central Thrust, MHT—Main Himalayan Thrust, STD—South Tibetan Detachment, ITS—Indus-Tsangpo Suture, TS—Tethyan Sediment basin, IUC—Indian Upper Crust, ILC—Indian Lower Crust, ELC—Eurasian Lower Crust, EUC—Eurasian Upper Crust. ELM—Eurasian Lithospheric mantle; RE—Re-entrant; S—Salient. Note: The front panel of the diagram is true to the scale, but the topographic-structural variations in the plan are schematic.

beneath the Himalaya. Buckling of the Indian lithosphere due to the curved geometry, resulting from the underthrust below the Eurasian plate in the Himalayan Mountain Range–Tibetan Plateau, has been identified as the causative factor for the extension of the upper crust and compression in the lower crust; the finite neutral surface of the buckled layer was estimated to be at a depth of 25 ± 5 km (cf. Figure 1 in Copley et al., 2011).

Two alternative possibilities were suggested for the deeper depth of the high-magnitude compressional earthquake events in the Indian lithosphere: (a) increase in strain rate, and/or (b) geometrical hardening of the Indian lithosphere due to along-strike and across-strike curvature related to subduction. Analysis of the distribution of earthquakes in the Indian plate interior is also attributed to the enhanced strain rate, causing a deeper brittle-ductile transition (Mohanty, 2011). Mohanty (2011) has further shown that some of the critically oriented faults (shear zones) in the Indian plate interior are associated with periodic accumulation of high stress/shortening and release of stress/extension. These observations regarding strain-hardening due to high strain rate (~266×10^{-9} per year along N013°) and alternating sinistral and dextral slip (compression and extension) along the same fault has been corroborated by the field mapping and data analysis of the Bhuj area (Sinha and Mohanty, 2012). The critical fault passes through the epicentres of the 1956 Anjar event and 2001 Bhuj event and continues up to the Himalayas (BJHC in **Figure 1A**; see also F7.12 in Balakrishnan, 1997).

From above discussion it may be understood that the recent events around Delhi-NCR area cannot be analyzed in isolation without taking into consideration of events in entire northwestern India and associated Himalayan front. Khan et al. (2016) analyzed the frequency of occurrences of aftershocks following the 2001 Bhuj main shock and found it to be decreasing after 2014. The predominant stress direction of the aftershock activities were operative along the NNE direction towards the Himalayan front, passing through the Delhi region (**Figure 1C**). The self-organized criticality (SOC) behaviour is occasionally persistent over a chaotic nature of sequence of shocks because of gradual restoration of stresses by tectonic loading. Our integrated study involving b-values and operative crustal-scale kinematics and geodynamics, might be accounting for a process-based phenomenon that indicates an impending earthquake in the seismic cycle (**Figure 6**). Indeed, moderate-to-low 'b' values over the study-area and frequent incidents of small-magnitude earthquakes bear indication for a large failure by triggering a great event. The regional crustal-scale heterogeneities including fractures forming the boundaries between NNE–SSW aligned horst and graben structures are found to be the sites for stress-concentration; their interaction with the MHT is enhancing the stress in the bending zone of the subducting Indian lithosphere. Failure is inevitable when the accumulated stress exceeds the yield strength of the materials. Past failures in the bent portion were recorded in 12 disastrous seismic events in the Himalayan region (**Figure 7**). However, the conjecture drawn from this study can be more robust if results obtained from analysis of b-value clusters are backed with the 3D modeling of a rheological state, taking into account all major structural features involved in the complex structural heterogeneity in the region.

CONCLUSION

Frequent occurrences of earthquake shocks in Delhi-NCR, adjoining areas and in the immediate Himalayan front pose a serious alarm for population. Although no models are available to predict the impending earthquake in any region, statistical analysis backed by regional kinematics and overall geodynamic understanding can give insights into the details of recent seismic activities. We found that the west -northwestern part of India has been activated by triggering 134 earthquakes of $M_L \geq 2.0$ over only first half of 2020. The compilation and analysis of well-constrained dataset lead towards understanding of clustering and stabilization of the general moderate-to-low seismic b-values in the study area. The regional structural trends, tectonics in the western India, the operative stress field and seismicity, extended from the Kachchh region, are apparently found to be compatible up to the northwest Himalaya (**Figure 1B**). The present study, thus, is summarized under the following concluding points:

- Large number of events of magnitude $M_L \geq 2.0$ with occasional incidents of earthquakes of magnitudes reaching up to more than 5.0 (**Figure 4**) indicate high-level stress transmission, accumulation and release in the study area.
- Spatially clustered seismicity (**Figure 1**) is cyclic in time as well as in space domains (**Figure 5**). The incidents of large number of events of $M_L \geq 4.0$ in the western India are related to the general regional kinematics and tectonics.
- Moderate-to-low seismic b-values over time and space (**Figure 6**) indicate stable high stress field, which may lead to fracturing and trigger a large earthquake in the future.
- The fracture system in the down-flexing, over-compensated Indian lithosphere below the Indo–Gangetic Plains is equally accommodating the stress field, and may initiate nucleation for large earthquake.
- Insufficient coverage of stations/network for the recorded events under the present study limits the determination of accurate focal depths of the earthquake events within reliable limit of uncertainties. Reliable focal depths of the events would have been more impressive for analysis of stress regime through a 3D structural analysis involving rheological understanding of the area.
- The heterogeneities appear in the log-linear plots of FMD might be related to the complex structural setup of the study area. The used earthquake catalog seems to be incomplete because of poor coverage of recording stations.
- The homogeneity of the catalogue could have been achieved by recording more number of low magnitude events and the present study would have been more convincing for forecasting the moderate-to-great earthquakes in this part of the Himalaya based on b-value analysis.

DATA AVAILABILITY STATEMENT

The raw data supporting the conclusion of this article will be made available by the authors, without reservation.

AUTHOR CONTRIBUTIONS

Seismotectonics of the study area and its in-depth analysis were done by PK. Geology and modeling were done by SM and PC. Data compilation and map reconstruction were done by RS.

ACKNOWLEDGMENTS

First author is thankful to the University Grant Commission, Government of India, New Delhi for financial support to complete the present work. Authors are also thankful to the National Center of Seismology (NCS), Government of India, New Delhi and International Seismological Center (ISC), United Kingdom. for disseminating the earthquake data to all researchers. Authors are thankful to both the reviewers and Editor for their comments, which have improved the manuscript to a large extent.

REFERENCES

Aggarwal, S. K., Khan, P. K., Mohanty, S. P., and Roumelioti, Z. (2016). Moment tensors, state of stress and their relation to faulting processes in Gujarat, western India. *Phys. Chem. Earth.* 95, 19–35. doi:10.1016/j.pce.2016.01.004

Aggarwal, S. K., Lovallo, M., Khan, P. K., Rastogi, B. K., and Telesca, L. (2015). Multifractal detrended fluctuation analysis of magnitude series of seismicity of Kachchh region, Western India. *Physica A* 426, 56–62. doi:10.1016/j.physa.2015.01.049

Aggarwal, S. K., Pastén, D., and Khan, P. K. (2017). Multifractal analysis of 2001 Mw7.7 Bhuj earthquake sequence in Gujarat, Western India. *Physica A* 488, 177–186. doi:10.1016/j.physa.2017.06.022

Aki, K. (1965). Maximum likelihood estimate of b in the formula log N=a-bM and its confidence limits. *Bull. Earthquake. Res. Inst. Univ. Tokyo.* 43, 237–239.

Ansari, M. A., Khan, P. K., Tiwari, V. M., and Banerjee, J. (2014). Gravity anomalies, flexure, and deformation of the converging Indian lithosphere in Nepal and Sikkim–Darjeeling Himalayas. *Int. J. Earth Sci.* 103 (6), 1681–1697. doi:10.1007/s00531-014-1039-0

Balakrishnan, T. S. (1997). *Major tectonic elements of the Indian subcontinent and contiguous areas: a geophysical view. Geological Society of India Memoir, no 38.* Bangalore: Geological Society of India, 1–155.

Beaumont, C., Ellis, S., Hamilton, J., and Fullsack, P. (1996). Mechanical model for subduction-collision tectonics of Alpine-type compressional orogens. *Geology* 24 (8), 675–678. doi:10.1130/0091-7613(1996)024<0675:mmfsct>2.3.co;2

Beauval, C., and Scotti, O. (2004). Quantifying sensitivities of PSHA for France to earthquake catalog uncertainties, truncation of ground motion variability, and magnitude limits. *Bull. Seismol. Soc. Am.* 94 (5), 1579–1594. doi:10.1785/012003246

Bollinger, L., Henry, P., and Avouac, J. P. (2006). Mountain building in the Nepal Himalaya: thermal and kinematic model. *Earth Planet. Sci. Lett.* 244 (1–2), 58–71. doi:10.1016/j.epsl.2006.01.045

Cao, A., and Gao, S. (2002). Temporal variations of seismic b-values beneath northeastern japan island arc. *Geophys. Res. Lett.* 29, 1334. doi:10.1029/2001GL013775

Chakraborty, P. P., Tandon, S. K., and Saha, S. (2019). Development of Phanerozoic sedimentary basins of India. *J. Asian Earth Sci.* 184, 103391. doi:10.1016/j.jseaes.2019.103991

Chandra, U. (1977). Earthquakes of peninsular India—a seismotectonic study. *Bull. Seismol. Soc. Am.* 67 (5), 1387–1413.

Cheng, Q.-M., and Sun, H.-Y. (2018). Variation of singularity of earthquake-size distribution with respect to tectonic regime. *Geosci. Front.* 9 (2), 453–458. doi:10.1016/j.gsf.2017.04.006

Chung, W. Y., and Gao, H. (1995). Source parameters of the Anjar earthquake of July 21, 1956, India and its seismotectonic implications for the Kutch rift basin. *Tectonophysics* 242 (3, 4), 281–292. doi:10.1016/0040-1951(94)00203-l

Cochran, J. (1990). "Himalayan uplift, sea level, and the record of Bengal fan sedimentation at the ODP leg 116 sites S1," in Proceedings of the ocean drilling program: scientific results. J. R. Cochran D. A. V. Stow, et al. (Texas: Texas A & M University), 116, 397–414.

Conrad, C. P., and Hager, B. H. (1999). Effects of plate bending and fault strength at subduction zones on plate dynamics. *J. Geophys. Res.* 104 (B8), 17551–17571. doi:10.1029/1999jb900149

Copley, A., Avouac, J.P., Hollingsworth, J., and Leprince, S. (2011). The 2001 M_w 7.6 Bhuj earthquake, low fault friction, and the crustal support of plate driving forces in India. *J. Geophys. Res.* 116 (B8), B08405. doi:10.1029/2010jb008137

Copley, A., Avouac, J. P., and Royer, J. Y. (2010). India-Asia collision and the Cenozoic slowdown of the Indian plate: implications for the forces driving plate motions. *J. Geophys. Res.* 115 (B03410), 1–14. doi:10.1029/2009jb006634

Curray, J. R. (2005). Tectonics and history of the andaman sea region. *J. Asian Earth Sci.* 25 (1), 187–232. doi:10.1016/j.jseaes.2004.09.001

Dasgupta, S., Pande, P., Ganguly, D., Iqbal, Z., Sanyal, K., Venkataraman, N. V., et al. (2000). *Seismotectonic atlas of India and its environs*. Special Publication Series 59. Kolkata: Geological Survey of India, 87p.

Dattatrayam, R. S., Suresh, G., Baidya, P. R., Prakash, R., Gautam, J. L., Shukla, H. P., et al. (2014). Standards and methodologies of seismological data generation, processing and archival and guidelines for data sharing and supply. *Proc. Indian Nat. Sci. Acad.* 80 (3), 679. doi:10.16943/ptinsa/2014/v80i3/55143

DeMets, C., Gordon, R. G., Argus, D. F., and Stein, S. (1994). Effect of recent revisions to the geomagnetic reversal time scale on estimates of current plate motions. *Geophy. Res. Lett.* 21 (20), 2191–2194. doi:10.1029/94gl02118

Felzer, K. R. (2008). Simulated aftershock sequences for a M 7.8 earthquake on the southern San Andreas fault. *Seismol. Res. Lett.* 80 (1), 21–25. doi:10.1785/gssrl.80.1.21

Gahalaut, V. K., and Kundu, B. (2012). Possible influence of subduction ridges on the Himalayan arc and on the ruptures of great and major Himalayan earthquakes. *Gondwana Res.* 21 (4), 1080–1088. doi:10.1016/j.gr.2011.07.021

Geller, R. J. (1997). Earthquake prediction: a critical review. *Geophys. J. Int.* 131 (3), 425–450. doi:10.1111/j.1365-246x.1997.tb06588.x

Godin, L., and Harris, L. B. (2014). Tracking basement cross-strike discontinuities in the Indian crust beneath the Himalayan orogen using gravity data – relationship to upper crustal faults. *Geophys. J. Int.* 198 (1), 198–215. doi:10.1093/gji/ggu131

Goebel, T. H. W., Sammis, C. G., Becker, T. W., Dresen, G., and Schorlemmer, D. (2015). A comparison of seismicity characteristics and fault structure between stick–slip experiments and nature. *Pure Appl. Geophys.* 172 (8), 2247–2264. doi:10.1007/s00024-013-0713-7

Goebel, T. H. W., Schorlemmer, D., Becker, T. W., Dresen, G., and Sammis, C. G. (2013). Acoustic emissions document stress changes over many seismic cycles in stick–slip experiments. *Geophys. Res. Lett.* 40 (10), 2049–2054. doi:10.1002/grl.50507

Gordon, R. G. (2009). Lithospheric deformation in the equatorial Indian ocean: timing and Tibet. *Geology* 37 (3), 287–288. doi:10.1130/focus032009.1

Goswami, P. K. (2012). Geomorphic evidences of active faulting in the northwestern Ganga Plain, India: implications for the impact of basement structures. *Geosci. J.* 16 (3), 289–299. doi:10.1007/s12303-012-0030-7

Gutenberg, B., and Richter, C. F. (1954). *Seismicity of the earth and associated phenomenon*. Princeton, New Jersey: Princeton University Press.

Hauck, M. L., Nelson, K. D., Brown, L. D., Zhao, W., and Ross, A. R. (1998). Crustal structure of the Himalaya orogen at ~90° east longitude from INDEPTH deep reflection profiles. *Tectonics* 17 (4), 481–500. doi:10.1029/98tc01314

Heimpel, M., and Malin, P. (1998). Aseismic slip in earthquake nucleation and self-similarity: evidence from Parkfield, California. *Earth Planet. Sci.Lett.* 157 (3-4), 249–254. doi:10.1016/s0012-821x(98)00035-1

Hetényi, G., Cattin, R., Berthet, T., Moigne, N. L., Chophel, J., Lechmann, S., et al. (2016). Segmentation of the Himalayas as revealed by arc-parallel gravity anomalies. *Sci. Rep.* 6 (1), 33866. doi:10.1038/srep33866

Kagan, Y. Y., and Knopoff, L. (1987). Statistical short-term earthquake prediction. *Science* 236 (4808), 1563–1567. doi:10.1126/science.236.4808.1563

Karunakaran, C., and Ranga Rao, A. (1979). Status of exploration for hydrocarbons in the Himalayan region—contribution to stratigraphy and structure. *Geol. Sur. India Pub.* 41, 1–66.

Khan, P. K., Ansari, M. A., and Mohanty, S. (2014). Earthquake source characteristics along the arcuate Himalayan belt: geodynamic implications. *J. Earth Sys. Sci.* 123 (5), 1013–1030. doi:10.1007/s12040-014-0456-6

Khan, P. K., Ansari, A., and Singh, D. (2017). Insights into the great Mw 7.9 april 25, 2015 Nepal earthquake. *Curr. Sci.* 113 (10), 2014. doi:10.18520/cs/v113/i10/2014-2020

Khan, P. K., Banerjee, J., Shamim, Sk., and Mohanty, M. (2018). Long-term seismic observations along Myanmar–Sunda subduction margin: insights for 2004 $M_w > 9.0$ earthquake. *Int. J. Earth Sci.* 107 (7), 2383–2392. doi:10.1007/s00531-018-1603-0

Khan, P. K., and Chakraborty, P. P. (2009). Bearing of plate geometry and rheology on shallow-focus mega thrust seismicity with special reference to 26 December 2004 Sumatra event. *J. Asian Earth Sci.* 34 (3), 480–491. doi:10.1016/j.jseaes.2008.07.006

Khan, P. K., Chakraborty, P. P., Tarafder, G., and Mohanty, S. (2012). Testing the intraplate origin of mega-earthquakes at subduction margins. *Geosci. Front.* 3 (4), 473–481. doi:10.1016/j.gsf.2011.11.012

Khan, P. K., and Chakraborty, P. P. (2007). The seismic b value and its correlation with Bouguer gravity anomaly over the Shillong plateau area: a new insight for tectonic implication. *J. Asian Earth Sci.* 29 (1), 136–147. doi:10.1016/j.jseaes.2006.02.007

Khan, P. K., Ghosh, M., Chakraborty, P. P., and Mukherjee, D. (2011). Seismic b-value and the assessment of ambient stress in Northeast India. *Pure Appl. Geophys.* 168 (10), 1693–1706. doi:10.1007/s00024-010-0194-x

Khan, P. K., Mohanty, S. P., Sinha, S., and Singh, S. (2016). Occurrences of large-magnitude earthquakes in the Kachchh region, Gujarat, western India: tectonic implications. *Tectonophysics* 679, 102–116. doi:10.1016/j.tecto.2016.04.044

Khan, P. K., Shamim, S., Mohanty, S. P., and Aggarwal, S. K. (2020). Change of stress patterns during 2004 MW 9.3 off-Sumatra mega-event: insights from ridge–trench interaction for plate margin deformation. *Geol. J.* 55 (1), 372–389. doi:10.1002/gj.3419

Klootwijk, C. T., Conaghan, P. J., and Powell, C. M. (1985). The Himalayan arc: large-scale continental subduction, oroclinal bending, and back-arc spreading. *Earth Planet. Sci. Lett.* 75 (2, 3), 316–319. doi:10.1016/0012-821x(85)90099-8

Kohlstedt, D. L., Keppler, H., and Rubie, D. C. (1996). Solubility of water in the α, β and γ phases of $(Mg,Fe)_2SiO_4$. *Contri. Mineral. Pet.* 123, 345–357. doi:10.1007/s004100050161

Lavé, J., and Avouac, J. P. (2000). Active folding of fluvial terraces across the siwaliks hills, Himalayas of central Nepal. *J. Geophys. Res.* 105 (B3), 5735–5770. doi:10.1029/1999jb900292

Le Fort, P. (1986). "Metamorphism and magmatism during the Himalayan collision," in *Collision tectonics*. Editors M. P. Coward and A. C. Ries (London: Geol. Soc., Special Publication), 19, 159–172.

Lyon-Caen, H., and Molnar, P. (1983). Constraints on the structure of the Himalaya from an analysis of gravity anomalies and a flexural model of the lithosphere. *J. Geophys. Res.* 88 (B10), 8171–8191. doi:10.1029/jb088ib10p08171

Makovsky, Y., Klemperer, S. L., Huang, L., and Lu, D.Project INDEPTH Team (1996). Structural elements of the southern Tethyan Himalaya crust from wide-angle seismic data. *Tectonics* 15 (5), 997–1005. doi:10.1029/96tc00310

Marshak, S., and Paulsen, T. (1997). Structural style, regional distribution, and seismic implications of midcontinent fault-and-fold zones, United States. *Seismol. Res. Lett.* 68 (4), 511–520. doi:10.1785/gssrl.68.4.511

Mendoza, M. M., Ghosh, A., Karplus, M. S., Klemperer, S. L., Sapkota, S. N., Adhikari, L. B., et al. (2019). Duplex in the main himalayan thrust illuminated by aftershocks of the 2015 M_w 7.8 gorkha earthquake. *Nat. Geosci.* 12 (12), 1018–1022. doi:10.1038/s41561-019-0474-8

Merh, S. S. (1995). *Geology of Gujarat*. Bangalore: Geological Society of India, 222.

Mignan, A. (2012). Functional shape of the earthquake frequency-magnitude distribution and completeness magnitude. *J. Geophys. Res. Solid Earth.* 117 (B8), B08302. doi:10.1029/2012jb009347

Mignan, A. (2011). Retrospective on the accelerating seismic release (ASR) hypothesis: controversy and new horizons. *Tectonophysics* 505 (1-4), 1–16. doi:10.1016/j.tecto.2011.03.010

Mignan, A., and Woessner, J. (2012). Estimating the magnitude of completeness in earthquake catalogs. *Community Online Resour. Statistical Seism. Anal.* 4, 1–45. doi:10.5078/corssa-00180805

Mohanty, S. (2011). Crustal stress and strain patterns in the Indian plate interior: implications for the deformation behaviour of a stable continent and its seismicity. *Terra Nova.* 23 (6), 407–415. doi:10.1111/j.1365-3121.2011.01027.x

Molchan, G. M. (1997). Earthquake prediction as a decision-making problem. *Pure Appl. Geophys.* 149 (1), 233–247. doi:10.1007/bf00945169

Naylor, M., Orfanogiannaki, K., and Harte, D. (2010). Exploratory data analysis: magnitude, space, and time. *Community Online Resour. Stat. Seism. Anal.* 3, 5, 7, 37. Available at: http://www.corssa.org. doi:10.5078/corssa-92330203

Ogata, Y., and Zhuang, J. (2006). Space-time ETAS models and an improved extension. *Tectonophysics* 413 (1, 2), 13–23. doi:10.1016/j.tecto.2005.10.016

Pacheco, J. F., Scholz, C. H., and Sykes, L. R. (1992). Changes in frequency–size relationship from small to large earthquakes. *Nature* 355 (6355), 71–73. doi:10.1038/355071a0

Patriat, P., and Achache, J. (1984). India-Eurasia collision chronology has implications for crustal shortening and driving mechanism for plates. *Nature* 311 (5987), 615–621. doi:10.1038/311615a0

Paul, H., Mitra, S., Bhattacharya, S. N., and Suresh, G. (2015). Active transverse faulting within underthrust Indian crust beneath the Sikkim Himalaya. *Geophys. J. Int.* 201 (2), 1070–1081. doi:10.1093/gji/ggv058

Peresan, A., and Gentili, S. (2018). Seismic clusters analysis in Northeastern Italy by the nearest-neighbor approach. *Phys. Earth. Planet. Int.* 274, 87–104. doi:10.1016/j.pepi.2017.11.007

Prakash, R., Suresh, G., and Gahalaut, V. K. (2020). Earthquake monitoring in India. *Proc. Indian Natl. Sci. Acad.* 86, 631–642. doi:10.16943/ptinsa/2020/49819

Quittmeyer, R. C., and Jacob, K. H. (1979). Historical and modern seismicity of Pakistan, Afghanistan, northern India, and southern Iran. *Bull. Seismol. Soc. Am.* 69 (3), 773–823.

Rivière, J., Lv, Z., Johnson, P. A., and Marone, C. (2018). Evolution of b-value during the seismic cycle: insights from laboratory experiments on simulated faults. *Earth Planet. Sci. Lett.* 482, 407–413. doi:10.1016/j.epsl.2017.11.036

Royer, J. Y., and Gordon, R. G. (1997). The motion and boundary between the Capricorn and Australian plates. *Science* 277 (5330), 1268–1274. doi:10.1126/science.277.5330.1268

Rydelek, P. A., and Sacks, I. S. (2003). Comment on "Minimum magnitude of completeness in earthquake catalogs: examples from Alaska, the Western United States, and Japan," by Stefan Wiemer and Max Wyss. *Bull. Seismol. Soc. Am.* 93 (4), 1862–1867. doi:10.1785/0120020035

Rydelek, P. A., and Sacks, I. S. (1989). Testing the completeness of earthquake catalogs and the hypothesis of self-similarity. *Nature* 337, 251–253. doi:10.1038/337251a0

Scholz, C. H. (2015). On the stress dependence of the earthquake b value. *Geophys. Res. Lett.* 42 (5), 1399–1402. doi:10.1002/2014gl062863

Scholz, C. H. (1968). The frequency-magnitude relation of microfracturing in rock and its relation to earthquakes. *Bull. Seismol. Soc. Am.* 58 (1), 399–415.

Schorlemmer, D., Wiemer, S., and Wyss, M. (2005). Variations in earthquake-size distribution across different stress regimes. *Nature* 437 (7058), 539–542. doi:10.1038/nature04094

Schulte-Pelkum, V., Monsalve, G., Sheehan, A. F., Shearer, P., Wu, F., and Rajaure, S. (2019). Mantle earthquakes in the Himalayan collision zone. *Geology* 47 (9), 815–819. doi:10.1130/g46378.1

Selzer, C., Buiter, S. J. H., and Pfiffner, O. A. (2008). Numerical modeling of frontal and basal accretion at collisional margins. *Tectonics* 27 (3), TC3001. doi:10.1029/2007tc002169

Ghosh, S., Nandy, D. R., et al. (1991). Geothermal atlas of India. *Geol. Surv. India, Spec. Publ.* 19, 1–144.

Shi, Y., and Bolt, B. A. (1982). The standard error of the magnitude-frequency b-value. *Bull Seismol. Soc. Am.* 72 (5), 1677–1687.

Singh, R., Khan, P. K., and Singh, A. P. (2020). Earthquake source dynamics and kinematics of the EIS and adjoining regions. *Acta Geophys.* 68 (2), 337–355. doi:10.1007/s11600-020-00418-z

Sinha, S., and Mohanty, S. (2012). Spatial variation of crustal strain in the Kachchh region, India: implication on the Bhuj earthquake of 2001. *J. Geodyn.* 61 (1), 1–11. doi:10.1016/j.jog.2012.07.003

Sinha-Roy, S., Malhotra, G., and Mohanty, M. (1998). *Geology of Rajasthan*. Bangalore: Geol. Soc. India, 278.

Sobolev, G. A. (2011). Seismicity dynamics and earthquake predictability. *Nat. Haz. Earth Sys. Sci.* 11 (2), 445–458. doi:10.5194/nhess-11-445-2011

Spada, M., Tormann, T., Wiemer, S., and Enescu, B. (2013). Generic dependence of the frequency-size distribution of earthquakes on depth and its relation to the strength profile of the crust. *Geophys. Res. Lett.* 40 (4), 709–714. doi:10.1029/2012gl054198

Srivastav, S. K., Prakash, R., Dattatrayam, R. S., Arora, S. K., Bansal, B. K., and Bhattacharya, S. N. (2005). Configuration of an optimum seismological network for India. *Mausam* 56, 465–472.

Stein, S., Sella, G. F., and Okal, E. A. (2002). "The january 26, 2001 Bhuj earthquake and the diffuse western boundary of the Indian plate," in *Plate boundary zones. Geodynamics Series*. Editors S. Stein and R. Freymneller (Washington: American Geophysical Union), 30, 243–254.

Sykes, L. R., Shaw, B. E., and Scholz, C. H. (1999). Rethinking earthquake prediction. *Pure Appl. Geophys.* 155, 207–232. doi:10.1007/s000240050263

Tandon, S. K., Chakraborty, P. P., and Singh, V. (2014). "Geological and Tectonic framework of India: providing context to geomorphologic development," in *Landscapes and landforms of India*. Editor V. S. Kale (Netherlands: Springer), 1–14.

Taylor, D. W. A., Snoke, J. A., Sacks, I. S., and Takanami, T. (1990). Nonlinear frequency magnitude relationships for the Hokkaido Corner, Japan. *Bull. Seismol. Soc. Am.* 80 (2), 340–353.

Tormann, T., Wiemer, S., and Hardebeck, J. (2012). Earthquake recurrence models fail when earthquakes fail to reset the stress field. *Geophys. Res. Lett.* 39 (18), L18310. doi:10.1029/2012gl052913

Tsapanos, T. M. (1990). b-values of two tectonic parts in the circum-Pacific belt. *Pure App. Geophys.* 134, 229–242. doi:10.1007/bf00876999

Urbancic, T. I., Trifu, C. I., Long, J. M., and Young, R. P. (1992). Space-time correlations of b values with stress release. *Pure Appl. Geophys.* 139, 449–462. doi:10.1007/bf00879946

Valdiya, K. S. (1976). Himalaya transverse faults and their parallelism with subsurface structures of North Indian planes. *Tectonophys* 32 (3), 353–386. doi:10.1016/0040-1951(76)90069-x

Valdiya, K. S. (2003). Reactivation of himalayan frontal fault: implications. *Curr. Sci.* 85(7), 1031–1040.

Vorobieva, I., Shebalin, P., and Narteau, C. (2016). Break of slope in earthquake size distribution and creep rate along the San Andreas Fault system. *Geophs. Res. Lett.* 43 (13), 6869–6875. doi:10.1002/2016gl069636

Wesnousky, S. G. (1994). The Gutenberg-Richter or characteristic earthquake distribution, Which is it?. *Bull. Seismol. Soc. Am.* 84, 1940–1959.

Wiemer, S., and Wyss, M. (2000). Minimum magnitude of complete reporting in earthquake catalogs: examples from Alaska, the Western United States, and Japan. *Bull. Seismol. Soc. Am.* 90 (4), 859–869. doi:10.1785/0119990114

Woessner, J., and Wiemer, S. (2005). Assessing the quality of earthquake catalogues: estimating the magnitude of completeness and its uncertainty. *Bull. Seismol. Soc. Am.* 95 (2), 684–698. doi:10.1785/0120040007

Wyss, M. (1973). Towards a physical understanding of the earthquake frequency distribution. *Geophys. J. Int.* 31 (4), 341–359. doi:10.1111/j.1365-246x.1973.tb06506.x

Conflict of Interest: The authors declare that the research was conducted in the absence of any commercial or financial relationships that could be construed as a potential conflict of interest.

Copyright © 2021 Khan, Mohanty, Chakraborty and Singh. This is an open-access article distributed under the terms of the Creative Commons Attribution License (CC BY). The use, distribution or reproduction in other forums is permitted, provided the original author(s) and the copyright owner(s) are credited and that the original publication in this journal is cited, in accordance with accepted academic practice. No use, distribution or reproduction is permitted which does not comply with these terms.

frontiers in Earth Science

ORIGINAL RESEARCH
published: 05 April 2021
doi: 10.3389/feart.2021.563649

Long Memory in Earthquake Time Series: The Case Study of the Geysers Geothermal Field

S. Barani[1]*, *L. Cristofaro*[2], *M. Taroni*[3], *L. A. Gil-Alaña*[4,5] *and G. Ferretti*[1]

[1]DISTAV, University of Genoa, Genoa, Italy, [2]Department of Statistical Sciences, Sapienza University of Rome, Rome, Italy, [3]Istituto Nazionale Di Geofisica e Vulcanologia, Rome, Italy, [4]University of Navarra, Faculty of Economics and ICS-NCID, Pamplona, Spain, [5]University Francisco de Vitoria, Department of Business Administration, Madrid, Spain

The present study aims at proving the existence of long memory (or long-range dependence) in the earthquake process through the analysis of time series of induced seismicity. Specifically, we apply alternative statistical techniques borrowed from econometrics to the seismic catalog of The Geysers geothermal field (California), the world's largest geothermal field. The choice of the study area is essentially guided by the completeness of the seismic catalog at smaller magnitudes (a drawback of conventional catalogs of natural seismicity). Contrary to previous studies, where the long-memory property was examined by using non-parametric approaches (e.g., rescaled range analysis), we assume a fractional integration model for which the degree of memory is defined by a real parameter d, which is related to the best known Hurst exponent. In particular, long-memory behavior is observed for $d > 0$. We estimate and test the value of d (i.e., the hypothesis of long memory) by applying parametric, semi-parametric, and non-parametric approaches to time series describing the daily number of earthquakes and the logarithm of the (total) seismic moment released per day. Attention is also paid to examining the sensitivity of the results to the uncertainty in the completeness magnitude of the catalog, and to investigating to what extent temporal fluctuations in seismic activity induced by injection operations affect the value of d. Temporal variations in the values of d are analyzed together with those of the b-value of the Gutenberg and Richter law. Our results indicate strong evidence of long memory, with d mostly constrained between 0 and 0.5. We observe that the value of d tends to decrease with increasing the magnitude completeness threshold, and therefore appears to be influenced by the number of information in the chain of intervening related events. Moreover, we find a moderate but significant negative correlation between d and the b-value. A negative, albeit weaker correlation is found between d and the fluid injection, as well as between d and the annual number of earthquakes.

Keywords: long memory process, earthquake dependence, induced seismicity, geysers geothermal field, fractional integration, hurst index, b-value

OPEN ACCESS

Edited by:
Ying Li,
China Earthquake Administration, China

Reviewed by:
OlaOluwa S. Yaya,
University of Ibadan, Nigeria
Grzegorz Kwiatek,
German Research Centre for Geosciences, Germany

***Correspondence:**
S. Barani
simone.barani@unige.it

Specialty section:
This article was submitted to Solid Earth Geophysics, a section of the journal Frontiers in Earth Science

Received: *19 May 2020*
Accepted: *04 February 2021*
Published: *05 April 2021*

Citation:
Barani S, Cristofaro L, Taroni M, Gil-Alaña LA and Ferretti G (2021) Long Memory in Earthquake Time Series: The Case Study of the Geysers Geothermal Field. Front. Earth Sci. 9:563649. doi: 10.3389/feart.2021.563649

INTRODUCTION

The concept of long memory in the seismic process has a relatively long history. Most research on this topic dates back to the 80s, when Mandelbrot interpreted earthquakes as self-similar "objects" (Mandelbrot, 1983) and Bak et al. (1987) introduced the notion of self-organized criticality (SOC). According to this latter study and Bak and Tang (1989), earthquakes are interpreted as the result of interactive dissipative dynamical systems that evolve spontaneously toward critical (i.e., at the edge of collapsing), stationary states that can collapse in events of any size, forming self-similar fractal patterns. Systems that show significant statistical correlations across large time scales are said to be long-memory processes or processes with long-range dependence (LRD) (Karagiannis et al., 2004). The word "memory" is related to the connections between certain observations and those occurring after an amount of time has passed. The word "long" indicates that observations are correlated across widely separated times (i.e., the dependence among observations is significant, even across large time shifts). Interested readers on this topic may refer to the exhaustive dissertation of Samorodnitsky (2006).

Since then, many studies interpreted seismicity and tectonic deformations as the results of a dynamical process exhibiting a self-organized critical behavior (e.g., Sornette and Sornette, 1989; Ito and Matsuzaki, 1990; Sornette, 1991; Turcotte, 1999). In particular, Scholz (1991) used data from artificially induced seismicity to assert that the continental crust is virtually everywhere in a state close to seismic failure. Concurrently, Kagan and Jackson (1991) observed that earthquake clustering is a major long-term manifestation of the seismic process. In particular, it was observed that regions of recent high seismic activity have a larger than usual chance of producing new strong earthquakes (e.g., Lomnitz, 1994; Kagan and Jackson, 1999; Kagan and Jackson, 2013). In other words, periods of high release of seismic deformation will most likely be followed by years of higher-than-average seismic strain release. Conversely, seismically quiet periods will tend to be followed by quiet years. This implies that the process of accumulation and release of seismic strain is governed by long memory and presents a persistent behavior (e.g., Barani et al., 2018).

These findings have important consequences on the reliability of most earthquake forecasting models. Specifically, long-term clustering and self-organized criticality invalidate three important assumptions that are widely used in probabilistic seismic hazard analysis (PSHA), a key element of earthquake-resistant design, and long-term forecasting (e.g., Bak, 1991; Kagan et al., 2012): 1) seismicity as a Poisson process; 2) quasi-periodic or recurrent behavior; 3) characteristic earthquake model. A first attempt to incorporate long-term earthquake interactions into a forecasting model is the double-branching model of Marzocchi and Lombardi (2008). In this model, the first-step branching accounts for the short-term clustering, in which the occurrence of triggered events is modeled according to the modified Omori law (Utsu, 1961), while the second-step branching models the long-term triggering associated with post-seismic stress transfer produced by stronger events. The long-term evolution is essentially modeled according to an inverse exponential distribution of the form $e^{-\frac{t}{\tau}}$, where t is the elapsed time from the occurrence of the earthquake that generates stress variations, and τ is the characteristic time of the interaction.

Attempts to detect long memory in the earthquake process in a statistical robust way, were made by analyzing time series of earthquake frequency (Ogata and Abe, 1991; Li and Chen 2001; Jimenez et al., 2006), released energy (Jimenez et al., 2006), seismic moment (Cisternas et al., 2004; Barani et al., 2018; Mukhopadhyay and Sengupta, 2018), and time series of b-value (Chen, 1997). Gkarlaouni et al. (2017) searched for persistency in time series of magnitudes, inter-event times, and inter-event epicentral distances of successive events. Series of inter-event periods were also analyzed by Liu et al. (1995) and Alvarez-Ramirez et al. (2012). Most of these studies examine the long-memory feature through the rescaled range analysis (R/S analysis), which was originally proposed by Hurst (1951) and described rigorously by Mandelbrot and Wallis (1968). This technique estimates the Hurst exponent (H), a parameter that measures the level of correlation in time series. It takes values between 0 and 1 and indicates long memory for values different from 0.5. A value close to 0.5 indicates a stochastic process whose values have no dependence or mutual correlation (e.g., white noise). Most recently, in order to determine H, Peng et al. (1994) proposed the Detrended Fluctuation Analysis (DFA). The DFA was used in seismological studies by Lennartz et al. (2008), Telesca et al. (2004), and Shadkhoo et al. (2009). Shadkhoo and Jafari (2009) used a generalization of DFA, known as multifractal-DFA (Kandelhardt et al., 2002).

Although the majority of the previous studies give $H > 0.5$ (indicating a persistent, long-memory process), no general agreement about the presence of long memory in seismicity seems to emerge. Hence, this issue can be considered still open, and motivates the need of spending further efforts in this field of research with the aim of filling the lack of robust statistical evidence of this hypothesis.

In the present work, we apply for the first time techniques borrowed from econometrics to investigate the long-memory feature in seismicity. We analyze time series of earthquakes (i.e., daily number of earthquakes versus time and logarithm of seismic moment released per day versus time) associated with the industrial activity of The Geysers geothermal field (northern California), a dry-steam field in a natural greywacke sandstone reservoir at around 1.5–3 km depth. In this area, part of the seismic activity is induced by injection of fluids, but also present is triggered seismicity that includes aftershock sequences, swarms, and earthquake clusters (e.g., Johnson and Majer, 2017). The choice of the study area is essentially guided by the completeness of the seismic catalog at smaller magnitudes, which is a major drawback of conventional catalogs of natural seismicity. This allows examining the sensitivity of the results to the uncertainty in the completeness magnitude of the catalog. Moreover, since it has been shown that both seismic activity and clustering properties vary according to injection operations (e.g., Martínez-Garzón et al., 2013; Martínez-Garzón et al., 2014; Martínez-Garzón et al., 20s18; Trugman et al., 2016; Langenbruch and Zoback 2016), The Geysers field is an ideal

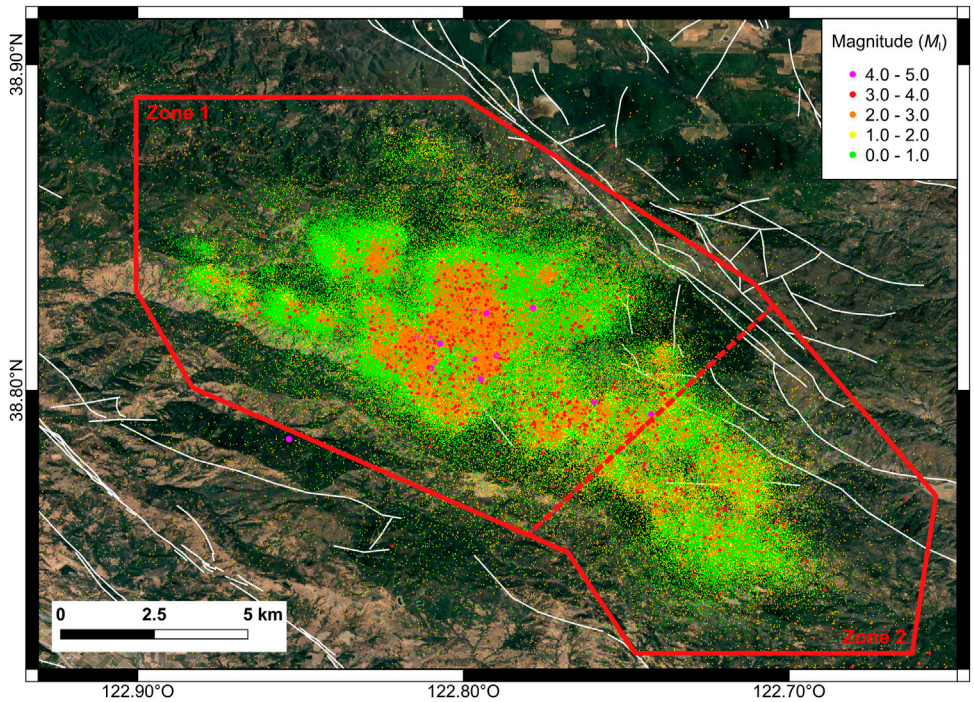

FIGURE 1 | Seismicity distribution in The Geysers geothermal field (from the Berkeley-Geysers catalog (NCEDC, 2014)). The polygon in red delimits the study area: the dashed line separates the northwestern sector (Zone 1) from the southeastern one (Zone 2). Faults are displayed by white lines (see acknowledgments).

area for investigating temporal variations of the long-memory property in seismicity time series. Such variations are examined in relation to those of the *b*-value of the Gutenberg and Richter relation.

Contrary to the studies mentioned above, which investigate the property of long memory in a non-parametric way (i.e., they do not assume any specific parametric model for the time series of interest), we consider a parametric model based on the concept of fractional integration that imposes a pole or singularity in the spectrum of the time series at zero frequency (see "*Methodology*" section). The level of correlations among observations in the time series is expressed by a real parameter *d*, which is related to the Hurst exponent. Long memory behavior is observed for $d > 0$. The results obtained by using the parametric approach are compared to those resulting from semi-parametric (i.e., the "local" Whittle approach of Robinson (1995)) and non-parametric (i.e., modified R/S analysis) methods applied to the same time series.

DATA

The data set considered in this study is the Berkeley-Geysers (BG) catalog, made available by the Northern California Earthquake Data Center (NCEDC, 2014). It collects 458,459 earthquakes with local magnitude (M_L) from 0 to 4.7 recorded between April 2003 and June 2016 in the area of The Geysers geothermal field (**Figure 1**). As stated above, the catalog includes earthquakes induced by injection of fluids, but also present is triggered seismicity (i.e., aftershock sequences, swarms, and earthquake clusters). Johnson and Majer (2017) found no basic differences between the source mechanisms of these different types of earthquakes.

In the subsequent analyses, we consider the events located within the red polygon in **Figure 1**. Specifically, first we analyze the property of long memory in the entire The Geysers field by comparing and contrasting alternative statistical techniques. Then, we analyze how temporal fluctuations in seismic activity induced by injection operations affect the value of *d*. This latter analysis is presented for the entire data set and northwestern sector (Zone 1 in **Figure 1**). Many authors (Stark, 2003; Beall et al., 2010; Beall and Wright, 2010) have observed that this part of The Geysers field is more active seismically than the southeastern part (Zone 2), following the expansion of the field in that sector. Following Beall and Wright (2010) and Convertito et al. (2012), the northwestern area includes all earthquakes with magnitude greater than 4, whereas the southeastern one is characterized by smaller magnitude events. Moreover, in Zone 1, earthquake hypocenters reach greater depths, reflecting the migration of fluids deeper into the reservoir (Johnson et al., 2016).

In order to compute the completeness magnitude (M_c) of the data set (i.e., the minimum magnitude value above which a data set can be assumed representative of the seismic productivity of an area), we apply the maximum curvature approach (Wiemer and Wyss, 2000), which defines M_c as the magnitude value corresponding to the maximum of the

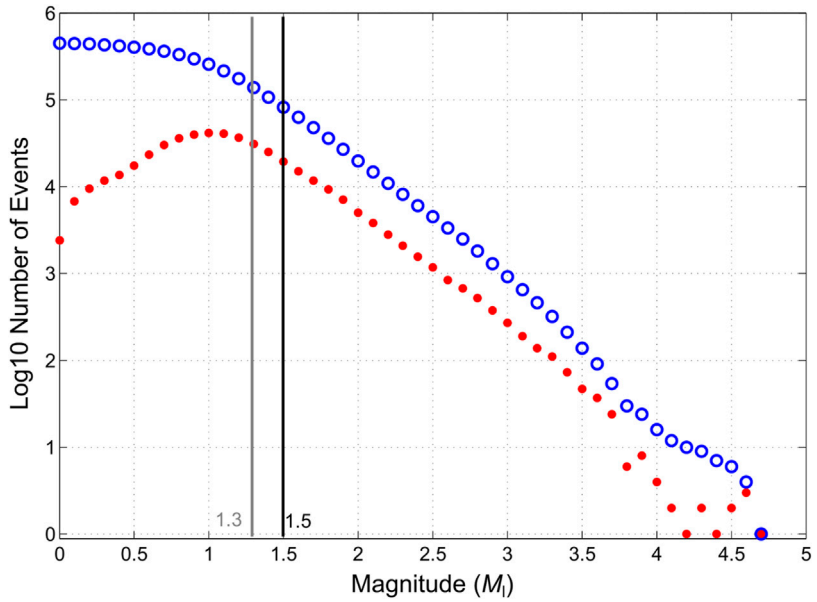

FIGURE 2 | Incremental (red dots) and cumulative (blue circles) magnitude-frequency distribution. The gray and black lines indicate alternative magnitude completeness thresholds: M_c = 1.3 (gray line) and M_c = 1.5 (black line). Bins of 0.1 magnitude units are used.

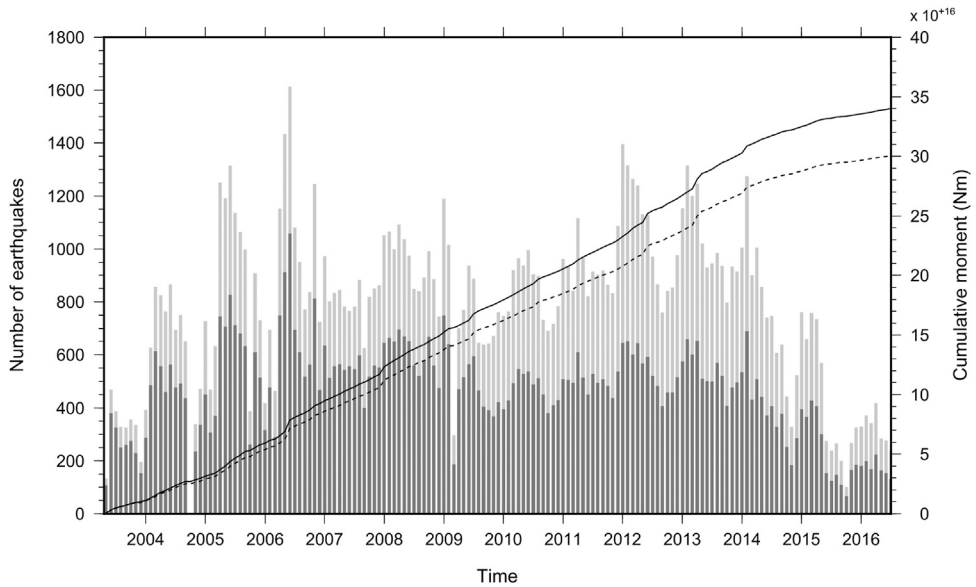

FIGURE 3 | Variability of the number of earthquakes in the period covered by the Berkeley-Geysers earthquake catalog (NCEDC, 2014) (April 2003–June 2016). Light and dark gray bars indicate the monthly number of events above the completeness thresholds M_c = 1.3 and M_c = 1.5, respectively. Curves of cumulative seismic moment are superimposed. The solid line is for M_c = 1.3, while the dashed one is for M_c = 1.5.

incremental magnitude-frequency distribution. In our catalog, the maximum curvature of the distribution corresponds to M_l = 1.0 (see **Figure 2**). Following Woessner and Wiemer (2005), a correction term is added to this value in order to avoid possible underestimation. We consider two alternative correction values, equal to 0.3 and 0.5 magnitude units, which lead to values of M_c of 1.3 and 1.5, respectively. Note that these correction values are both greater than 0.2, a standard value in such kind of applications (e.g., Tormann et al., 2015). Thus, both M_c values considered in the present study can be interpreted as conservative estimates of the completeness of the catalog. For both these values, **Figure 3** displays bar graphs showing the variability of the monthly number of earthquakes in the period covered by the

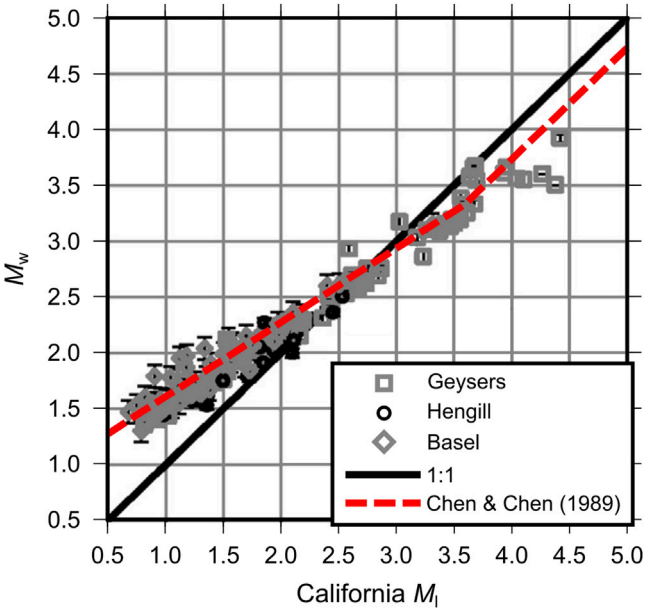

FIGURE 4 | Relation between local and moment magnitude for induced earthquakes in Hengill (Iceland), Basel (Switzerland), and Geysers (California) geothermal areas (modified from Edwards and Douglas (2014)). The Chen and Chen (1989) scaling relation is superimposed.

catalog along with the (cumulative) seismic moment (M_0) released over time. The seismic moment (in Nm) was calculated by applying the M_l-M_0 relations of Chen and Chen (1989) for California:

$$\log M_0 = M_l + 10.5 \quad (M_l \le 3.6) \tag{1}$$

$$\log M_0 = 1.5M_l + 8.7 \quad (3.6 < M_l \le 5.0) \tag{2}$$

$$\log M_0 = 3M_l + 1.2 \quad (5.0 < M_l \le 6.3) \tag{3}$$

The reliability of these relations when applied to induced seismicity is checked by comparison with the M_l-M_w data set of induced earthquakes of Edwards and Douglas (2014), which also includes data relevant to The Geysers geothermal field (**Figure 4**). Moment magnitude (M_w) values were calculated from M_0 by using the well-known Hanks and Kanamori (1979) relation.

Besides fluctuations of seismic activity, which can be related to injection operations, **Figure 3** shows relatively long periods of much milder (or absent) seismicity (e.g., October 2004, March 2009, November 2014; October 2015) that can be attributed to temporary issues in seismic monitoring operations rather than to actual periods of seismic inactivity. Such "instabilities" in the seismic catalog, along with short-period ones, are also discernible from the time series analyzed in the following (**Figure 5**). We indicate the time series of the daily number of earthquakes with N13+ and N15+ (where N stands for 'number', while '13+' and '15+' recall the values of the completeness magnitude M_c). Likewise, the time series of M_0 are labeled as M13+ and M15+.

METHODOLOGY

As mentioned in the earlier parts of the manuscript, we use alternative techniques to examine the long-memory property. We start by providing two definitions of this concept, one in the time domain and the other one in the frequency domain.

According to the time domain definition, a covariance stationary process $\{x_t, t = 1, 2, \ldots, T\}$ with autocovariance function $E[(x_t - E[x_t])(x_{t+u} - E[x_{t+u}])] = \gamma_u$ (with the usual notation E for the expectation operator) displays long memory if the infinite sum of the absolute value of its autocovariances is infinite, namely:

$$\lim_{T\to\infty} \sum_{u=-T}^{T} |\gamma_u| = \infty \tag{4}$$

Now, assuming that x_t has a spectral density function $f(\lambda)$, defined as the Fourier transform of the autocovariance function

$$f(\lambda) = \frac{1}{2\pi} \sum_{u=-\infty}^{\infty} \gamma_u \cos(\lambda u) \quad -\pi < \lambda \le \pi \tag{5}$$

the frequency domain definition of long memory states that the spectral density function must display a pole or singularity at least at one frequency in the interval $[0, \pi)$, namely:

$$f(\lambda) \to \infty, \quad \text{as } \lambda \to \lambda^*, \quad \text{for } \lambda^* \in [0, \pi) \tag{6}$$

In simple words, **Eq. 6** states that, in the context of long-memory processes (i.e., $d > 0$), the spectral density function is unbounded at a specific frequency λ, typically the zero frequency. The periodogram of the data[1], which is an estimator of the spectral density function of the series, should reproduce that behavior, with a large value at the smallest frequency. This can be observed in **Figure 6A**, which displays the first 200 values of the periodograms of the time series considered in this study for the completeness threshold $M_c = 1.3$. However, taking the first differences of the data (i.e., $y_t = x_t - x_{t-1}$), the periodograms (**Figure 6B**) display values close to zero at the zero frequency, which is clearly an indication of over-differentiation. This is indicative of $d < 1$ in the original time series. This was precisely the issue mentioned in Granger (1980) for the motivation of fractional integration with order of integration d in the range (0, 1). For further readings, see Granger (1980), Granger (1981), Granger and Joyeux (1980), and Hosking (1981).

In this article, we claim that the time series under investigation satisfy the two properties above, and we will test the hypothesis of long memory by using alternative methods based on parametric, semi-parametric, and non-parametric approaches.

Among the many methods to test the hypothesis of long memory, we focus on the fractional integration or $I(d)$ approach, which was originally developed by Granger (1980),

[1]The periodogram of a time series of length T $\{x_t, t = 1, 2, \ldots, T\}$, is defined as:

$$I(\lambda) = \frac{1}{2\pi T} \sum_{t=1}^{T} \sum_{s=1}^{T} x_t x_s e^{\lambda i(t-s)}$$

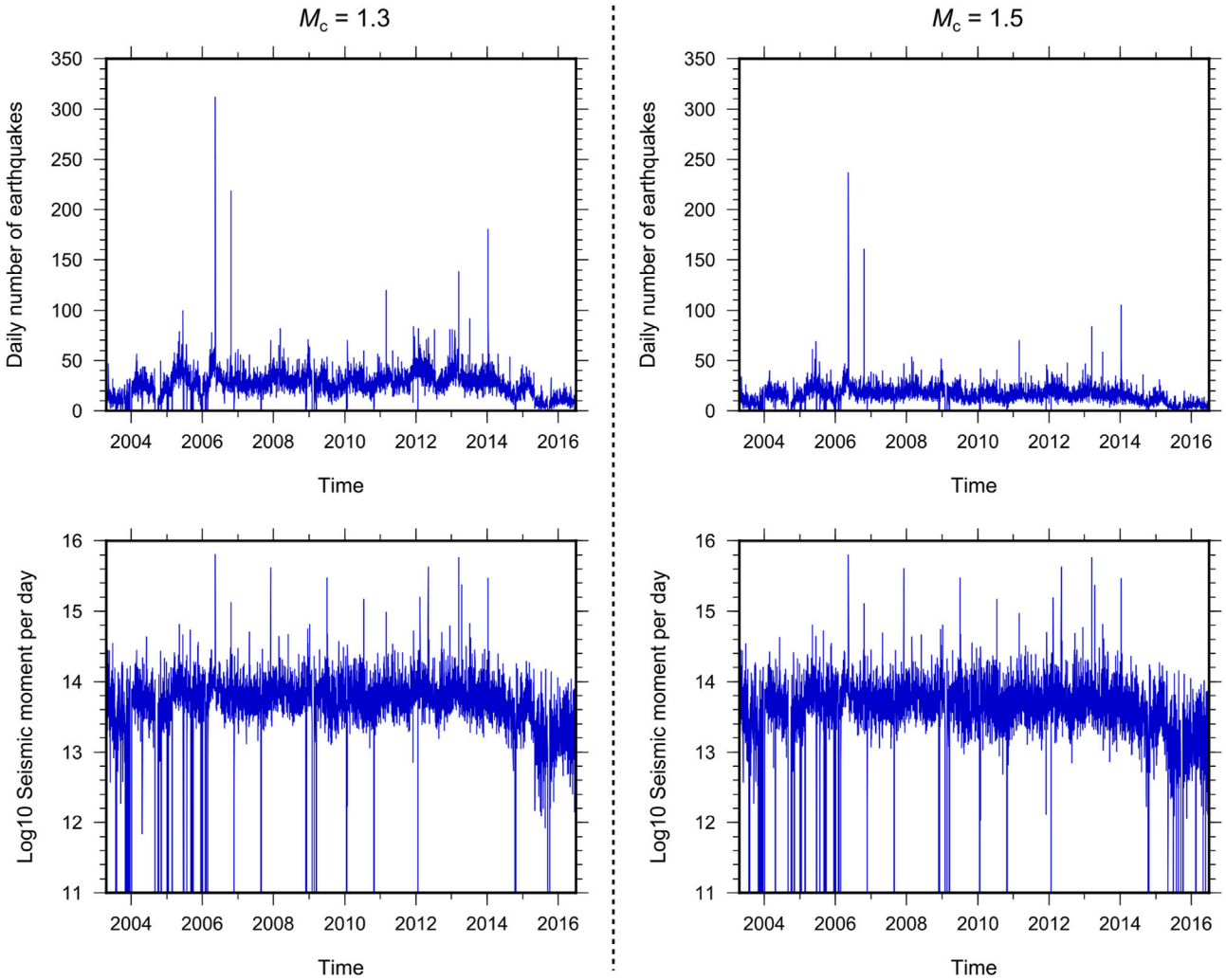

FIGURE 5 | Time series plots. Time series in the left column consider earthquakes with magnitudes above the completeness threshold M_c = 1.3, while time series in the right column are for M_c = 1.5. Top panels: time series of the daily number of earthquakes (N13+ and N15+). Bottom panels: time series of the (logarithmic) seismic moment M_0 released per day (M13+ and M15+). Time series go to zero when no data are reported in the catalog.

Granger (1981), Granger and Joyeux (1980), and Hosking (1981), and was widely used in the last twenty years in different fields (interested readers may refer Gil-Alana and Hualde (2009) for a review of applications involving fractional integration). In particular, assuming a generic time series $\{x_t, t = 1, 2, \ldots, T\}$, the fractional integration approach is based on the following equation:

$$(1 - L)^d x_t = u_t, \quad t = 1, 2, \ldots, T \tag{7}$$

where L is the lag operator (i.e., $L^k x_t = x_{t-k}$), d is a real value, and u_t is assumed to be a short memory or $I(0)$ time series, defined as a covariance stationary process satisfying

$$\lim_{T \to \infty} \sum_{u=-T}^{T} |\gamma_u| < \infty \tag{8}$$

or, in the frequency domain,

$$0 < f(\lambda) < \infty, \quad \text{for } \lambda \in [0, \pi) \tag{9}$$

In this framework, x_t is said to be integrated of order d, or $I(d)$, in the sense that "d differences" (i.e., the operator $(1 - L)$ is applied d times on x_t as expressed in **Eq. 7**) are required to remove the long memory from x_t, thus leading to a new time series u_t characterized by short memory (i.e., integrated of zero order, $I(0)$). Applying the Binomial expansion to the left-hand side of **Eq. 7** leads to:

$$(1 - L)^d x_t = \sum_{k=0}^{t-1} \binom{d}{k} (-1)^k L^k x_t \tag{10}$$

Thus, if d is a positive, non-integer value, then x_t depends on all its past history (i.e., the dependence among observations is significant, even across large time shifts), and the higher the value of d is, the greater the level of dependence between the

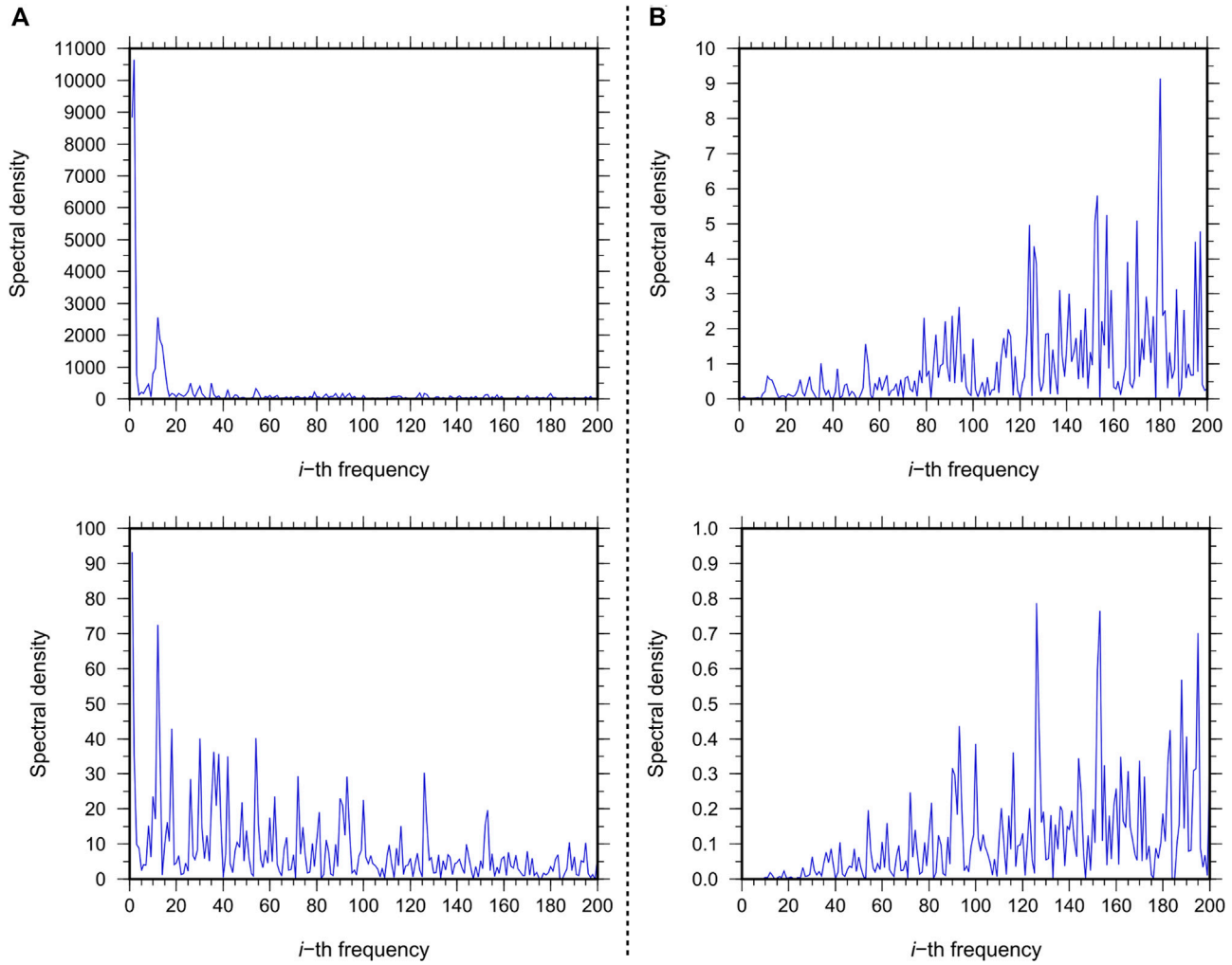

FIGURE 6 | First 200 values of the periodograms relative to the N13+ and M13+ time series (top and bottom panels of **(A)**, respectively) and relative to the time series of the first differences of N13+ and M13+ (top and bottom panel of **(B)**, respectively). The horizontal axis refers to the index i of the frequency $\lambda_i = 2\pi i/T$, where $i = 1, 2, \ldots, 200$.

observations is. Therefore, d can be interpreted as an indicator of the degree of dependence in the data.

In the context of $I(d)$ models, three values of d assume an important meaning. The first, $d = 0$, implies that the series is $I(0)$ or short memory. The second, $d = 0.5$, allows distinction between covariance stationary processes (i.e., $d < 0.5$) and nonstationary processes (i.e., $d \geq 0.5$)[2]. Finally, $d = 1$ is another turning value, as separates series that display the property of mean reversion (i.e., $d < 1$), for which any random shock will have a transitory effect disappearing in the long run, and series (with $d \geq 1$) for which the effect of the shocks become permanent and increases as d increases above 1. Thus, the fractional integration approach is a very flexible method because it allows considering different categories of $I(d)$ processes, with the following properties:

a. $d < 0$: anti-persistence (i.e., a time series switches between high and low values in adjacent pairs);
b. $d = 0$: $I(0)$ or short-memory behavior
c. $0 < d < 0.5$: covariance stationary, long-memory behavior with mean reversion;
d. $0.5 \leq d < 1$: nonstationary though mean-reverting long-memory behavior, with long-lasting effects of shocks (i.e., any random shock in the series will disappear in the long run though taking longer time than in the previous case);
e. $d = 1$: nonstationary $I(1)$ behavior with shocks having permanent effects in the series (i.e., lack of mean reversion);
f. $d > 1$: explosive behavior with lack of mean reversion.

Note that u_t in **Eq. 7** can also display some type short memory structure like the one produced by the stationary and invertible Auto Regressive Moving Average (ARMA)-type of models. Thus, for example, if u_t follows an ARMA (p, q) model (where p and q

[2]It is nonstationary in the sense that the variance of the partial sums increases with d.

are respectively the orders of the AR and MA components), we say that x_t is a fractionally integrated ARMA (i.e., ARFIMA (p, d, q)) model (Sowell, 1992; Beran, 1993).

There are several methods for estimating the value of the parameter d (or testing the hypothesis of long memory) in time series. The subsections below describe those applied in the present work.

Robinson Tests for Fractional Differentiation

The tests of Robinson (1994) are a number of parametric tests in the frequency domain that allow verifying the hypothesis of long-memory in time series assuming a fractional integration model. They consist in disproving the null hypothesis $H_O : d = d_O$ for different real values d_O. Such tests are widely used in many disciplines, including climatology (Gil-Alana, 2005; Gil-Alana, 2008; Gil-Alana and Sauci, 2019), economics (Gil-Alana and Robinson, 1997), finance (Gil-Alana and Moreno, 2012; Abbritti et al., 2016), and environmental sciences (Solarin and Bello, 2018; Gil-Alana and Trani, 2019).

In the present study, we use two tests. The first one (RBWN hereinafter) imposes a linear trend to the data, and uses the residuals to compute u_t (**Eq. 7**) for different values d_0 in order to find the value leading to a white noise series. Specifically, the regression model fitted through the data is expressed by:

$$x_t = \beta_0 + \beta_1 t + \xi_t \tag{11}$$

where β_0 and β_1 are regression coefficients, and ξ_t indicates the residual. In the present study, we consider three standard cases: 1) $\beta_0 = \beta_1 = 0$ (Model 1), 2) $\beta_1 = 0$ and β_0 determined from the data (Model 2), and 3) both β_0 and β_1 estimated from the data (Model 3).

The residuals are then used to compute u_t by applying **Eq. 7**:

$$(1 - L)^{d_0} \xi_t = u_t \tag{12}$$

The value d_0 that leads to a white noise series u_t is assumed the best value for d (i.e., the null hypothesis $H_0 : d = d_0$ is accepted if d_0 leads to a white noise series).

The second test (RBBL hereinafter), which is based on the original approach of Bloomfield (1973), is similar to the previous one but assumes short-memory as autocorrelation feature for u_t. The best value for d is chosen as the value d_0 that generates a time series u_t with spectral density function of the form of:

$$f(\lambda) = \frac{\sigma^2}{2\pi} e^{\left(2\sum_{j=1}^{p} \tau_j \cos(\lambda j)\right)} \tag{13}$$

where $p = 1$ in the present study (this means that any value in the series is correlated to the previous one only), and τ_j indicates the autocorrelation coefficients (see Robinson (1994) for details).

Bloomfield (1973) showed that the logarithm of $f(\lambda)$ approximates very well the logarithm of the spectrum of autoregressive (AR) processes. Thus, **Eq. 13** is used here to express the autocorrelation in u_t, which also accommodates very well in the context of fractional integration (see also Gil-Alana (2004)).

Robinson Test Based on the "Local" Whittle Approach

The Robinson test based on the "local" Whittle approach is a semi-parametric test originally proposed by Robinson (1995) (RB95 hereinafter). The word "local" is used to indicate that the method only considers a band of frequencies close to zero. The estimate of d ($\widehat{d}$) is calculated as:

$$\widehat{d} = \underset{-0.5 \le d \le 0.5}{\arg\min} \left(\log C(d)^* - 2d \frac{1}{m} \sum_{i=1}^{m} \log \lambda_i \right) \tag{14}$$

where $m = T^{\delta}$ (in this study, we assume $\delta = 0.40, 0.45, \ldots, 0.70$ with step of 0.05) is the bandwidth parameter, $\lambda_i = 2\pi i/T$, and

$$C(d)^* = \frac{1}{m} \sum_{i=1}^{m} I(\lambda_i) \lambda_i^{2d} \tag{15}$$

Although this method was extended and improved by many authors (e.g., Velasco, 1999; Shimotsu and Phillips, 2006; Abadir et al., 2007), we use the Robinson (1995) one due to its simplicity. In particular, unlike other methods that require additional user-chosen parameters and the results are typically very sensitive to them, it only requires the bandwidth parameter m.

Modified Rescaled Range Analysis

The rescaled range analysis (R/S analysis) is a non-parametric method that allows computation of the so-called Hurst exponent, H (Hurst, 1951). As with d, H measures the level of correlation in time series. It takes values between 0 and 1, and indicates anti-persistence if $H < 0.5$ and persistent behavior if $H > 0.5$. A value close to 0.5 indicates no correlation within the series. In the case of covariance stationary processes, the Hurst exponent is related to d through the following relationship (e.g., Beran, 1993):

$$H = d + 0.5 \tag{16}$$

In the present work, we apply the modified R/S procedure proposed by Lo (1991). Given a stationary time series x_t of length T, sample mean $\overline{x}$, sample variance $\widehat{\sigma}_x^2$, and sample autocovariance at lag u given by $\widehat{\gamma}_u$, the modified R/S statistic is:

$$Q_T(q) = \frac{1}{\widehat{\sigma}_T(q)} \left(\max_{1 \le k \le T} \sum_{t=1}^{k} (x_t - \overline{x}) - \min_{1 \le k \le T} \sum_{t=1}^{k} (x_t - \overline{x}) \right) \tag{17}$$

where

$$\widehat{\sigma}_T^2(q) = \widehat{\sigma}_x^2 + 2 \sum_{u=1}^{q} \omega_u(q) \widehat{\gamma}_u \tag{18}$$

and

$$\omega_u(q) = 1 - \frac{u}{q+1} \quad 1 \le u \le q < T \tag{19}$$

The parameter q in the previous equations is known as the bandwidth number. In this study, we assume $q = 0, 1, 3, 5, 10, 30, 50$.

An advantage of the modified R/S statistic is that it allows us to obtain a simple formula to estimate the value of the fractional differencing parameter d, namely:

TABLE 1 | Values of *d* (and relative 95% confidence interval) resulting from the two parametric approaches of Robinson (1994): a) RBWN; b) RBBL. Results are presented for three standard cases: $\beta_0 = \beta_1 = 0$ (Model 1), $\beta_1 = 0$ and β_0 determined from the data (Model 2), and both β_0 and β_1 estimated from the data (Model 3). In bold is the model accepted according to the *t*-values associated with the estimates of β_0 and β_1 for the three cases (see **Table 2**).

Series	Model 1	Model 2	Model 3
N13+	0.36 (0.34, 0.38)	**0.36 (0.34, 0.38)**	0.36 (0.34, 0.38)
N15+	0.33 (0.31, 0.35)	**0.32 (0.30, 0.34)**	0.31 (0.29, 0.33)
M13+	0.74 (0.71, 0.77)	**0.73 (0.69, 0.76)**	0.73 (0.69, 0.76)
M15+	0.67 (0.64, 0.70)	**0.66 (0.63, 0.69)**	0.66 (0.63, 0.69)

Series	Model 1	Model 2	Model 3
N13+	0.40 (0.37, 0.42)	**0.39 (0.36, 0.41)**	0.39 (0.36, 0.41)
N15+	0.34 (0.32, 0.37)	**0.33 (0.31, 0.36)**	0.33 (0.30, 0.36)
M13+	0.60 (0.56, 0.65)	**0.55 (0.50, 0.61)**	0.55 (0.50, 0.61)
M15+	0.58 (0.54, 0.63)	**0.54 (0.50, 0.58**)	0.54 (0.50, 0.58)

$$\widehat{d} = \frac{\log Q_T(q)}{\log T} - 0.5 \tag{20}$$

In the previous formulation, assuming $q = 0$ leads to the classic Hurst R/S analysis (Hurst, 1951).

The estimates of d are considered acceptable for values of the parameter $V_T(q)$ above 1.862 or less than 0.809 (corresponding to a 5% level of significance) (Lo, 1991), being $V_T(q)$ defined as:

$$V_T(q) = \frac{Q_T(q)}{\sqrt{T}} \tag{21}$$

The limit distribution of $V_T(q)$ is derived in Lo (1991), and the 95% confidence interval with equal probabilities in both tails is [0.809, 1.862].

Monte Carlo experiments conducted, for example, by Teverovsky et al. (1999) showed that the modified R/S analysis is biased in favor of accepting the null hypothesis of no long memory as q increases. Thus, using Lo's modified method alone is not recommended as it can distort the results.

RESULTS

We first present the results obtained by using the two parametric approaches of Robinson (1994). **Table 1** summarizes the estimates of d (and the relative 95% confidence band) obtained by using RBWN (**Table 1**) and RBBL (**Table 1**). As stated in the foregoing, we show the results for three standard cases: $\beta_0 = \beta_1 = 0$ (Model 1), $\beta_1 = 0$ and β_0 determined from the data (Model 2), and both β_0 and β_1 estimated from the data (Model 3). We have marked in bold the most significant model according to the statistical significance (i.e., *t*-value) of the values of β_0 and β_1 for the three cases considered (see **Table 2**).

Analyzing the values of d in **Table 1** reveals that all time series present the long-memory feature ($d > 0$), thus confirming the results from a number of previous studies showing that seismicity is a long-memory process (see the "*Introduction*" for a list of references about this issue). Model 2 has always been resulted the most significant model based on *t*-values (**Table 2**). Specifically, both **Table 1** show that the values of d corresponding to the time series of the daily number of earthquakes (N13+ and N15+) are in the range (0, 0.5), while those relative to the time series of M_0 (M13+ and M15+) are in the range (0.5, 1). Precisely, concerning these latter series, the values of d indicate a nonstationary, mean-reverting behavior with long-lasting effects of shocks. For these series, the values obtained by using RBBL are significantly lower (up to ≈25%) than those resulting from RBWN. This may be explained by recalling that RBBL assumes short-memory as autocorrelation feature for u_t (**Eq. 13**) while RBWN assumes that u_t is white noise. Roughly speaking, this means that if the data presents some short memory (which is reflected in ξ_t in **Eq. 11**), RBBL takes it into consideration (as a feature of u_t) while RBWN does not. Hence, in the case of RBWN, the values of d may be biased by the short memory in the data. Thus, the higher level of nonstationarity indicated by the values of d resulting from the application of RBWN to M13+ and M15 + may be attributed to some short memory in ξ_t. Comparing the estimates of d obtained by applying RBWN and RBBL to N13+ and N15 + shows that the latter approach provides greater values. However, in this case, the difference is negligible, as it is less than 10%. Finally, for both types of time series, we can observe that the value of d tends to decrease with increasing the magnitude completeness threshold M_c.

Table 3 summarizes the results obtained by applying the RB95 semi-parametric approach for different values of the bandwidth parameter $m = T^{\delta}$ (i.e., δ = 0.40, 0.45, 0.50, 0.55, 0.60, 0.65, and 0.70). We observe that, for the N13+ and N15 + series, the values of d reach around 0.5, which is the highest value allowed (see **Eq. 14**). This indicates an effect of saturation of d at lower m values (see also **Figure 7**, top panels). To overcome such an effect, we take the first differences of the data and apply RB95 to them. The final value of d is then obtained by adding 1 to the value resulting from the application of RB95 to the series of the first differences of the original data. The d values calculated this

TABLE 2 | Values of β_0 and β_1 (**Eq. 11**) for the three models in **Table 1**: a) RBWN; b) RBBL. The *t*-values computed for each coefficient are reported in brackets. A model has to be rejected if at least one of its coefficients presents a *t*-value less than 1.95.

Series	Model 1 β_0, β_1	Model 2 β_0, β_1	Model 3 β_0, β_1
N13+	0, 0	21.6 (9.0), 0	21.5 (7.0), 3.6E-5 (3.2E-2)
N15+	0, 0	13.3 (9.5), 0	15.9 (9.6), –9.5E-4 (–1.6)
M13+	0, 0	14.0 (10.9), 0	13.3 (9.4), –9.0E-7 (–3.5E-4)
M15+	0, 0	13.2 (9.4), 0	13.2 (9.3), –3.1E-5 (–2E-2)

Series	Model 1 β_0, β_1	Model 2 β_0, β_1	Model 3 β_0, β_1
N13+	0, 0	20.8 (7.1), 0	20.5 (5.7), 1.4E-4 (0.1)
N15+	0, 0	13.2 (13.6), 0	15.6 (8.4), –9E-4 (–1.4)
M13+	0, 0	13.9 (10.1), 0	13.1 (12.9), –4.8E-5 (7.7E-2)
M15+	0, 0	13.1 (12.8), 0	13.1 (12.0), 1.0E-5 (1.6E-2)

TABLE 3 | Values of d obtained by applying the Robinson test based on the "local" Whittle approach (RB95) for different values of the bandwidth parameter $m = T^{\delta}$.

Series	$T^{0.40}$	$T^{0.45}$	$T^{0.50}$	$T^{0.55}$	$T^{0.60}$	$T^{0.65}$	$T^{0.70}$
N13+	0.50	0.50	0.50	0.50	0.50	0.48	0.44
N15+	0.50	0.50	0.50	0.50	0.48	0.44	0.39
M13+	0.19	0.14	0.18	0.18	0.23	0.34	0.39
M15+	0.19	0.14	0.18	0.19	0.23	0.34	0.38

way are shown in **Figure 7** (red lines) in comparison with those obtained from the original data series (blue lines). Note that repeating the analysis on the series of the first differences produces a saturation of d as m increases. Saturated values have to be obviously discarded. Such a saturation effect along with the high variability of d, which is particularly evident for smaller values of m, could be indicative of "spurious" long memory due to regime change (e.g., short memory) or smoothly varying trend (Qu, 2011). This is confirmed by the results (not shown here for the sake of brevity) of test statistic proposed by Qu (2011) (which uses the local Whittle estimate of d for m frequency components) for the null hypothesis that a given time series is a "pure" stationary long-memory process. The saturation is not observed for the d values obtained for the M13+ and M15 + series (**Figure 7**, bottom panels), which range between about 0.1 and 0.4, thus indicating a covariance stationary, long-memory behavior with mean reversion. As opposed to the values of d obtained for N13+ and N15+ (**Figure 7**, top panels), for these

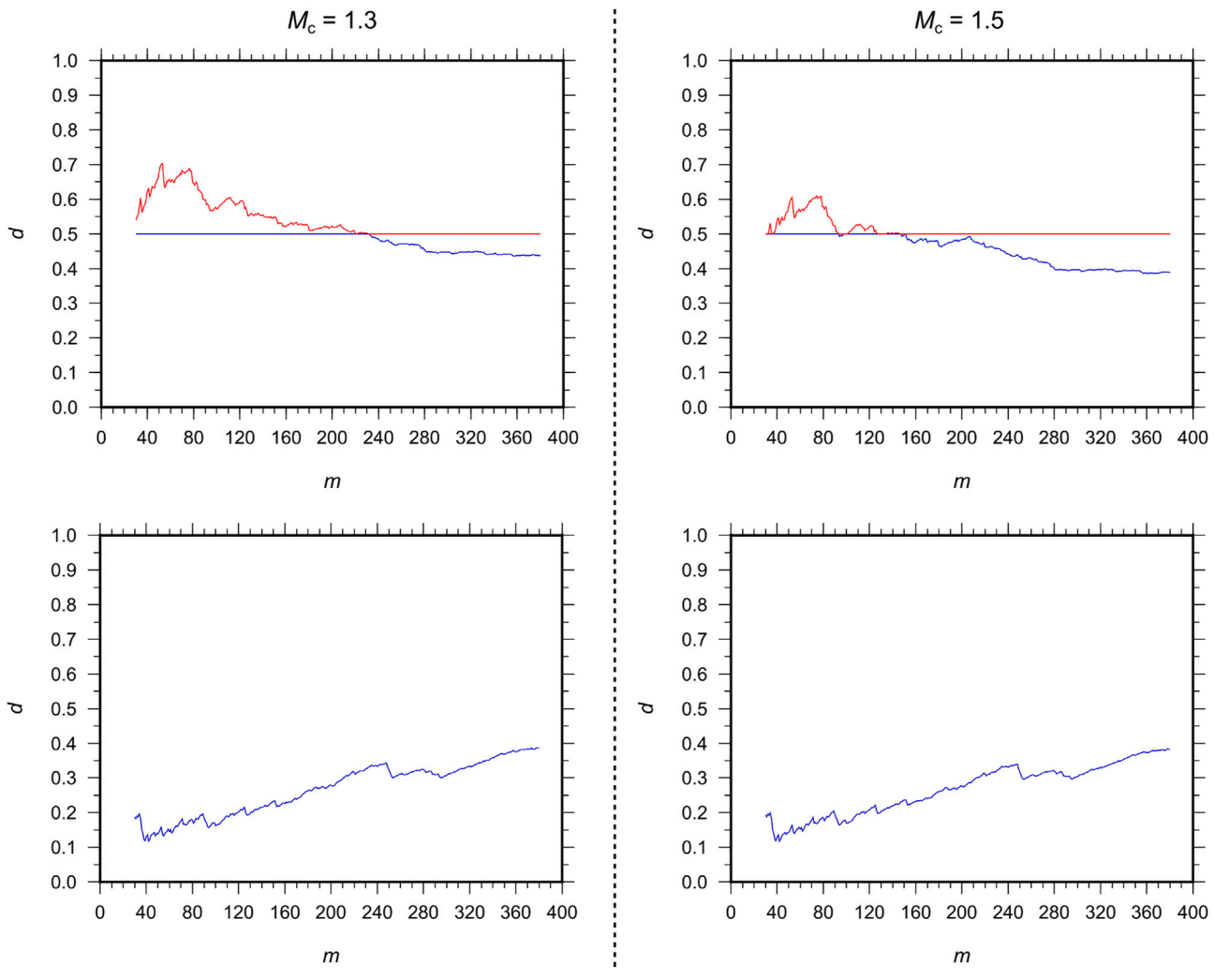

FIGURE 7 | Values of d obtained by applying the Robinson test based on the "local" Whittle approach (RB95) versus the bandwidth parameter $m = T^{\delta}$. Charts in the left column refer to the magnitude completeness threshold M_c = 1.3, while those in the right column are for M_c = 1.5. Top panels: d values computed from the time series of the daily number of earthquakes (N13+ and N15+). Bottom panels: d values computed from the time series of the (logarithmic) seismic moment M_0 released per day (M13+ and M15+). Blue and red lines display the d values resulting from the original data series and by taking the first differences of the data, respectively (see the main text for details).

TABLE 4 | Values of d determined through the application of the modified R/S analysis for different values of the bandwidth number q. The number in brackets are the values of $V_T(q)$ in **Eq. 21**.

Series	$q = 0$	$q = 1$	$q = 3$	$q = 5$	$q = 10$	$q = 30$	$q = 50$
N13+	0.32 (15.45)	0.29 (12.17)	0.26 (9.41)	0.25 (8.03)	0.22 (6.27)	0.16 (4.05)	0.14 (3.28)
N15+	0.30 (13.25)	0.28 (10.75)	0.25 (8.56)	0.24 (7.41)	0.21 (5.90)	0.16 (3.89)	0.14 (3.18)
M13+	0.24 (7.51)	0.20 (5.56)	0.17 (4.19)	0.15 (3.59)	0.13 (2.94)	0.09 (2.27)	0.09 (2.08)
M15+	0.24 (7.73)	0.21 (5.78)	0.17 (4.37)	0.16 (3.76)	0.13 (3.08)	0.10 (2.37)	0.09 (2.17)

series d tends to increase markedly with m. This leads of the observation that the values of d computed through the application of RB95 tend to converge toward those resulting from RBWN and, above all, RBBL as m increases. Finally, note that increasing the magnitude completeness threshold yields lower values of d only in the case of the time series of the daily number of earthquakes (i.e., N13+ and N15+). Conversely, the values of d obtained for the time series of M_0 are insensitive to M_c.

Table 4 lists the values of d determined through the modified R/S analysis for a selected number of q values. Evidence of long memory is once again found in all cases, with the values of d constrained between 0 and 0.5 for all series. On average, the values of d are lower than those discussed previously, with a better agreement for lower values of q. This seems in agreement with the observations of Teverovsky et al. (1999) showing that the modified R/S analysis is biased in favor of accepting the null hypothesis of no long memory as q increases. Again, increasing the magnitude completeness threshold yields lower values of d. As with RB95, this is observed only for the time series of the daily number of earthquakes.

DISCUSSION

As is widely known and remarked in the introduction, the rate of seismicity in geothermal areas is strongly related to fluid injection operations. Fluid injection induces perturbation in the crust that affect the local stress field and may lead to fault failure. Therefore, changes in the injection can induce changes in earthquake productivity (i.e., number of earthquakes), clustering properties, and known seismological parameters such as the b-value of the Gutenberg and Richter relation. Temporal variations in seismic activity at The Geysers geothermal field were studied by different authors (e.g., Eberhart-Phillips and Oppenheimer, 1984; Martínez-Garzón et al., 2013; Martínez-Garzón et al., 2014; Martínez-Garzón et al., 2018; Kwiatek et al., 2015; Johnson et al., 2016; Trugman et al., 2016), as well as changes in the b-value (Convertito et al., 2012; Martínez-Garzón et al., 2014; Kwiatek et al., 2015; Trugman et al., 2016). This section discusses how temporal fluctuations in fluid injection affect seismic activity and, consequently, the degree of memory in seismicity time series. To this end, time series of the daily number of earthquakes were analyzed in order to examine temporal variations in the value of d since 2005 both in the entire The Geysers area and in the northwestern sector (Zone 1 in **Figure 1**)[3]. For both cases, we divided the catalog into sections, each covering 1 year[4], and, for each of them, we computed the value of the completeness magnitude M_c. Specifically, we used a moving window approach with a 1-month shift between consecutive annual time series. Given the substantial fluctuation of the M_c value with time ($1.0 \leq M_c \leq 1.5$, not shown here), which may bias the results, we chose to consider only events with $M_c \geq 1.5$. Then, we applied the RBBL, RBWN (following the results in **Table 1**, the regression coefficients in **Eq. 11** were determined according to Model 2), and standard R/S (i.e., assuming $\underline{q} = 0$ in **Eq. 17**) techniques to determine the value of d for each section of the catalog. The RB95 method was not used because of the sensitivity of the results to the choice of the amplitude of the bandwidth parameter m (i.e., because of the subjectivity in the choice of the m value). Contextually, we computed the b-value of the Gutenberg and Richter relation through the maximum likelihood approach (Aki 1965) in the search of a possible relation between it and d.

For the entire The Geysers field, the charts in **Figure 8** present the temporal variation of fluid injection (we aggregated monthly injection data provided by the Department of Conservation State of California to obtain values of yearly fluid injection), annual number of earthquakes above $M_c = 1.5$ ($N(M_c)$), b-value, and d. On average, the value of d ranges between 0.15 and 0.35, thus indicating again a stationary long-memory process. However, temporal fluctuations are evident, suggesting that the value of d is modulated to some extent by the hydraulic operations in the study area. A visual examination of the trend of d in conjunction with that of the fluid injection seems to indicate a negative correlation, with d that tends to assume smaller values during periods of increased fluid injection. However, the level of correlation between these variables, which is quantified here by the well-known Pearson correlation coefficient (r), is weak (and not always significant), as r varies between −0.08 and −0.34

[3]Although the analysis was also carried out for Zone 2, results are not presented because of their instability, which possibly reflects the combined effect of catalog instabilities related to monitoring issues and the milder seismic activity of this zone. Both these factors contribute to the incompleteness of the catalog at smaller magnitudes and, consequently, to a significant proportion of zeroes in the time series analyzed.

[4]The length of the series was chosen in order to avoid instabilities in the results due to too short time series and short-term instabilities in the seismic catalog. The use of series with less than 300 samples is generally not recommended in this type of applications as leading to excessively wide confidence intervals.

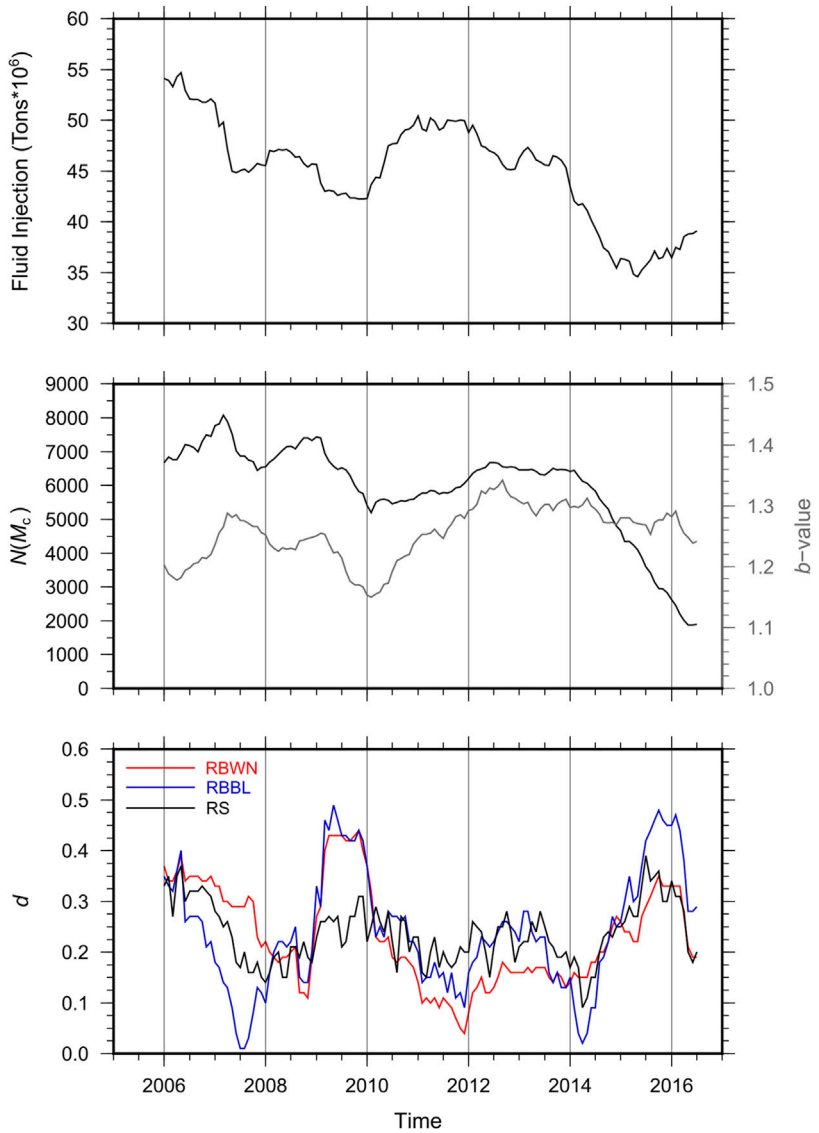

FIGURE 8 | Temporal variation of yearly fluid injection (top panel), annual number of earthquakes above M_c = 1.5 (N (M_c)) (mid panel, black line), b-value (mid panel, gray line), and d (bottom panel) in the entire The Geysers field (Zone 1 + Zone 2 in **Figure 1**). Data points are plotted at the end of each time interval considered in the moving window analysis.

depending on the method used to compute d (the values of r are summarized in **Table 5** along with the associated p-values). Similarly, a weak negative correlation is found between d and N (M_c) ($-0.05 \leq r \leq -0.46$), with this latter variable which, as expected, is positively correlated to the fluid injection ($r = 0.69$). Such a positive correlation is consistent with the results of Martínez-Garzón et al. (2018), showing that periods of higher seismicity coincide with periods of higher fluid injection. During these periods, the b-value tends to decrease slightly, in agreement with the study of Martínez-Garzón et al. (2014). Following Martínez-Garzón et al. (2018), Eberhart-Phillips and Oppenheimer (1984), and Johnson et al. (2016), such an increase of N (M_c), and the concurrent decrease of both d- and b-values, may be related to increased stress in the reservoir, mainly accommodated by strike-slip and thrust faults (Martínez-Garzón et al., 2014). Hence, fluid injection is considered the major factor driving the seismicity at The Geysers. Finally, moderate but significant negative correlation ($-0.53 \leq r \leq -0.31$) is observed between d and the b-value of the Gutenberg and Richter law. This finding is consistent with the results of Lee et al. (2009) and Lee et al. (2012), showing a negative correlation between the Hurst exponent and the b-value, both using a sandpile model and analyzing real seismicity in Taiwan. According to the explanations of Lee et al. (2009), the decreasing b-value during periods of high fluid injection, which reflects the

TABLE 5 | Values of the Pearson correlation coefficient (r) and associated p-values for the pairs of variables specified in the first column. $N(M_c)$ indicates the annual number of earthquakes above $M_c = 1.5$; the subscript of d_{RBWN}, d_{RBBL}, and d_{RS} indicates the technique used to compute d. Bold text indicates significant p-values (i.e., $p < 0.05/17 = 0.0029$ where 17 is the number of correlations tested according to the Bonferroni correction for multiple tests (Kato, 2019)). The correlation with fluid injection is not quantified for Zone 1, as specific injection data are not available.

	The geysers (whole)		Zone 1	
	r	p-value	r	p-value
$N(M_c)$ versus fluid injection	0.69	$\mathbf{3.4 \times 10^{-19}}$	-	-
b-value versus fluid injection	–0.26	0.005	-	-
d_{RBWN} versus fluid injection	–0.17	0.06	-	-
d_{RBBL} versus fluid injection	–0.34	$\mathbf{1.0 \times 10^{-4}}$	-	-
d_{RS} versus fluid injection	–0.08	0.39	-	-
d_{RBWN} versus $N(M_c)$	–0.05	0.61	–0.08	0.39
d_{RBBL} versus $N(M_c)$	–0.46	$\mathbf{7.5 \times 10^{-8}}$	–0.47	$\mathbf{2.3 \times 10^{-8}}$
d_{RS} versus $N(M_c)$	–0.24	0.006	–0.19	0.04
d_{RBWN} versus b-value	–0.53	$\mathbf{1.2 \times 10^{-10}}$	–0.56	$\mathbf{9.9 \times 10^{-12}}$
d_{RBBL} versus b-value	–0.37	$\mathbf{2.4 \times 10^{-5}}$	–0.28	**0.002**
d_{RS} versus b-value	–0.31	$\mathbf{3.5 \times 10^{-4}}$	–0.31	$\mathbf{3.3 \times 10^{-4}}$

increased number of events with larger magnitude, indicates that the system is in a critical state or is approaching it (see also De Santis et al., 2011). This is in agreement with the observations of Martínez-Garzón et al. (2018), showing an increase of main shock magnitude along with increased foreshock activity during these periods. The concurrent increase of d-value may be interpreted as an increase of the degree of the persistence of larger and larger events in the system. Conversely, the system is moving away from the critical state during periods of increased b-values, presenting an energy deficit. During these periods, the value of d tends to decrease, thus indicating a decrease of persistence.

Similar observations can be done by analyzing the moving window results for Zone 1 (**Figure 9** and **Table 5**). According to the findings of Martínez-Garzón et al. (2018), the similarity between the results obtained for this zone and the entire field suggests that the northwestern sector provides a fair representation of the processes that govern earthquake clustering in the whole field.

SUMMARY AND CONCLUSIONS

Our study has analyzed the long-memory feature in seismicity through a comprehensive statistical analysis of a set of earthquake time series associated with the activity in The Geysers geothermal field. In particular, we have applied different statistical techniques to time series of the daily number of earthquakes and seismic moment for different magnitude completeness thresholds. We have focused on the seismicity recorded in The Geysers geothermal field because of the high level of completeness of the seismic catalog.

Unlike to previous studies, which investigated the property of long memory in a non-parametric way, we have considered a parametric model based on the concept of fractional integration. The level of correlations among observations in the time series is expressed by a real parameter d, which is indicative of long memory for values greater than zero. The results obtained by using the parametric approach have been compared to those resulting from semi-parametric and non-parametric methods.

Our results have pointed out the presence of long memory for all the time series and methods considered, showing that seismicity is a process characterized by long memory. In particular, the estimates of the differencing parameter d obtained by applying the parametric RBWN and RBBL approaches have shown that the time series of the daily number of earthquakes present long memory with stationary behavior. Indeed, d ranges between around 0.3 and 0.4. The short memory does not affect the results, as the values of d resulting from RBWN are close to those estimated by RBBL. The long-memory feature has also been observed in the time series of seismic moment. However, nonstationary behavior has been shown in this case, as d resulted between 0.5 and 1. We have observed that the estimates obtained by using RBWN could be biased toward higher values (up to around 0.75) due to short-memory autocorrelation, which affects the values of d computed via RBBL to a lower extent ($d \approx 0.55$).

Similar results have been obtained by applying the semi-parametric RB95 approach and the non-parametric R/S analysis, although they were shown to be rather sensitive to the choice of the value of the bandwidth parameter. In particular, as regards RB95, we have shown that the values of d tend to converge to those resulting from RBBL at increasing values of the bandwidth parameter m. The opposite occurs considering the results of the modified R/S analysis. This would confirm the bias due to short-memory in the results obtained by applying RBWN to the seismic moment time series.

Finally, albeit moderately, our results have pointed out that the value of d is influenced by the number of information in the chain of intervening related events. In particular, d tends to decrease with increasing the magnitude completeness threshold M_c. This is more evident for the time series of the number of earthquakes. Indeed, the value of M_c is controlled by small events and therefore significantly affects the daily number of earthquakes in the series. Conversely, the total seismic moment released daily is controlled by stronger events and, therefore, the time series are less influenced by M_c. Nevertheless, according to the results obtained by applying RBWN to the seismic moment time series, small magnitude earthquakes with short memory effects would affect nonstationarity. Indeed, we have observed that d increases significantly above 0.5 as M_c decreases. Therefore, catalog completeness assessments may play a fundamental role on the reliability of d estimates.

The analysis of the temporal variation of d, besides corroborating the previous considerations about the long memory in the seismic process, has revealed a certain degree of correlation with hydraulic operations. Specifically, our results indicate a moderate but significant negative correlation between d and the b-value of the Gutenberg and Richter relation. A negative, albeit weaker

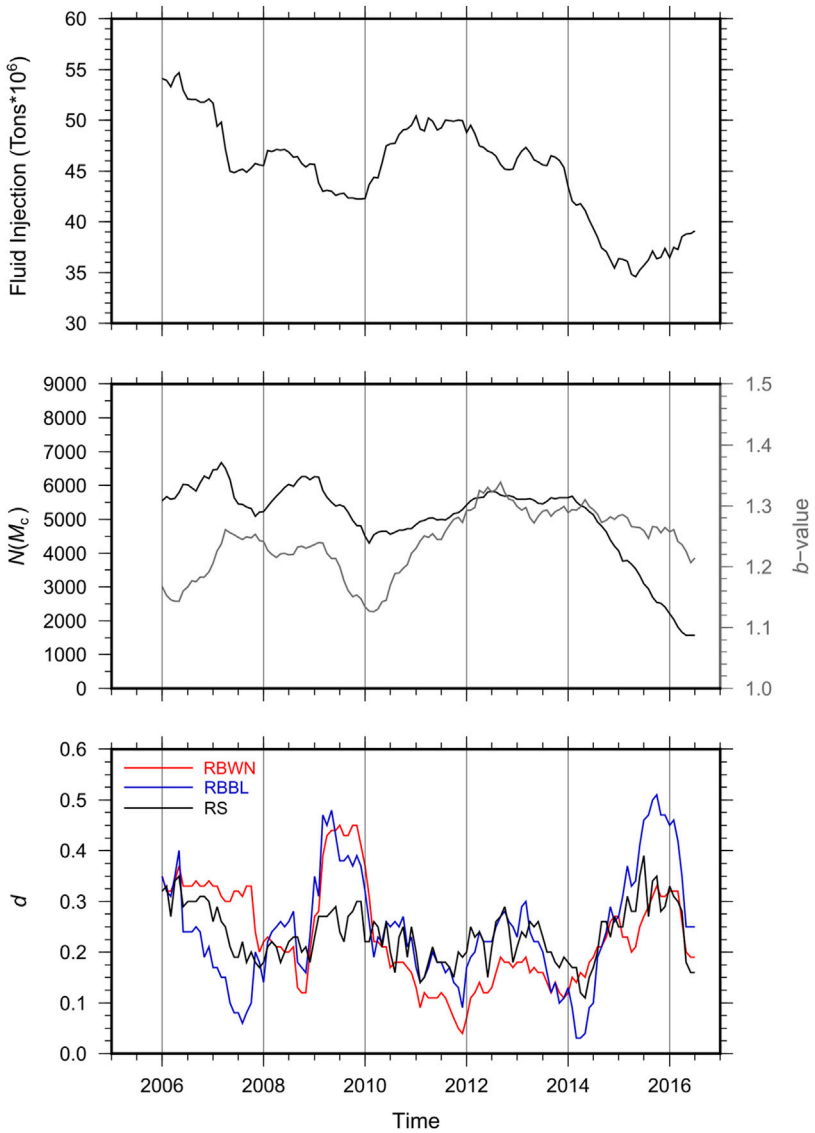

FIGURE 9 | Same as **Figure 8** but for the northerwestern sector of The Geysers area (Zone 1 in **Figure 1**). The fluid injection variation shown in the top panel refers to the entire The Geysers field.

correlation, which deserves further investigation in the future, is found between d and the fluid injection, as well as between d and the annual number of earthquakes.

Besides proving long memory in seismicity, our study has pointed out the importance of using multiple approaches to obtain reliable estimates of the parameters capturing the long-memory behavior in the earthquake process. The augmented possibility of computing reliable values of such parameters, along with the increasing availability of earthquake data, can strengthen the awareness of scientists on the importance of developing and using earthquake forecasting models based on stochastic processes that allow for long-memory dynamics (e.g., Garra and Polito, 2011).

DATA AVAILABILITY STATEMENT

Publicly available datasets were analyzed in this study. This data can be found here: http://ncedc.org/egs/catalog-search.html.

AUTHOR CONTRIBUTIONS

This study started from an original idea of all authors. SB and MT provided the time series that were subsequently analyzed by LC, SB, LG-A, and MT. MT also calculated the completeness of the data set. SB and LG-A wrote the main body of the manuscript in collaboration with LC. GF supervised the work since the early stages and

contributed to the choice of the magnitude conversion equations. SB, LC, and MT reviewed the manuscript and contributed to the interpretation of the results. Figures and Tables were prepared by SB and LC except for Figure 2 and Table 5 that were provided by MT.

ACKNOWLEDGMENTS

We are grateful to two anonymous reviewers for their valuable comments and suggestions that have significantly improved the manuscript. SB is thankful to Benjamin Edwards and Matteo Picozzi for the fruitful discussions about magnitude conversion. LC kindly acknowledges prof. Elvira Di Nardo (Università degli Studi di Torino) for her support and suggestions during the preparation of the article. LG-A gratefully acknowledges financial support from the MINEIC-AEI-FEDER ECO 2017–85503-R project from 'Ministerio de Economía, Industria y Competitividad' (MINEIC), 'Agencia Estatal de Investigación' (AEI) Spain and 'Fondo Europeo de Desarrollo Regional' (FEDER). Waveform data, metadata, or data products for this study were accessed through the Northern California Earthquake Data Center (NCEDC), doi:10.7932/NCEDC (https://ncedc.org/egs/catalog-search.html). Aggregated monthly injection data for the Geysers field were accessed through the Department of Conservation State of California T(https://www.conservation.ca.gov/calgem/geothermal/manual/Pages/production.aspx). Faults in **Figure 1** were accessed through the United States Geological Survey (United States Geological Survey and California Geological survey, Quaternary fault and fold database for the United States, accessed May 10, 2020, at: https://www.usgs.gov/natural-hazards/earthquake-hazards/faults).

REFERENCES

Abadir, K. M., Distaso, W., and Giraitis, L. (2007). Nonstationarity-extended local Whittle estimation. *J. Econom.* 141, 1353–1384. doi:10.1016/j.jeconom.2007.01.020

Abbritti, M., Gil-Alana, L. A., Lovcha, Y., and Moreno, A. (2016). Term structure persistence. *J. Financial Econom.* 14, 331–352. doi:10.1093/jjfinec/nbv003

Aki, K. (1965). Maximum likelihood estimate of b in the formula logN=a-bM and its confidence limits. *Bull. Earthq. Res. Inst. Tokyo Univ.* 43, 237–239.

Alvarez-Ramirez, J., Echeverria, J. C., Ortiz-Cruz, A., and Hernandez, E. (2012). Temporal and spatial variations of seismicity scaling behavior in Southern México. *J. Geodynamics* 54, 1–12. doi:10.1016/j.jog.2011.09.001

Bak, P., Tang, C., and Wiesenfeld, K. (1987). Self-organized criticality: an explanation of the 1/f noise. *Phys. Rev. Lett.* 59, 381–384. doi:10.1103/PhysRevLett.59.381

Bak, P. (1991). "Self-organized criticality and the perception of large events,". in *Spontaneous formation of space-time structures and criticality NATO ASI Series (Series C: Mathematical and Physical Sciences)*. Editors T. Riste and D. Sherrington (Dordrecht: Springer), Vol. 349.

Bak, P., and Tang, C. (1989). Earthquakes as a self-organized critical phenomenon. *J. Geophys. Res.* 94, 635–637. doi:10.1029/jb094ib11p15635

Barani, S., Mascandola, C., Riccomagno, E., Spallarossa, D., Albarello, D., Ferretti, G., et al. (2018). Long-range dependence in earthquake-moment release and implications for earthquake occurrence probability. *Sci. Rep.* 8, 5326. doi:10.1038/s41598-018-23709-4

Beall, J. J., Wright, M. C., Pingol, A. S., and Atkinson, P. (2010). Effect of high injection rate on seismicity in the Geysers. *Trans. Geotherm. Resour. Counc.* 34, 47–52.

Beall, J. J., and Wright, M. C. (2010). Southern extent of the Geysers high temperature reservoir based on seismic and geochemical evidence. *Trans. Geotherm. Resour. Counc.* 34, 53–56.

Beran, J. (1993). *Statistics for long memory processes*. Boca Raton, Florida, US: Chapman & Hall/CRC.

Bloomfield, P. (1973). An exponential model for the spectrum of a scalar time series. *Biometrika* 60, 217–226. doi:10.1093/biomet/60.2.217

Chen, P.-Y. (1997). Application of the value of nonlinear parameters H and ΔH in strong earthquake prediction. *Acta Seimol. Sin.* 10, 181–191. doi:10.1007/s11589-997-0087-y

Chen, P., and Chen, H. (1989). Scaling law and its applications to earthquake statistical relations. *Tectonophysics* 166, 53–72. doi:10.1016/0040-1951(89)90205-9

Cisternas, A., Polat, O., and Rivera, L. (2004). The Marmara Sea region: seismic behaviour in time and the likelihood of another large earthquake near Istanbul (Turkey). *J. Seismology* 8, 427–437. doi:10.1023/b:jose.0000038451.04626.18

Convertito, V., Maercklin, N., Sharma, N., and Zollo, A. (2012). From induced seismicity to direct time-dependent seismic hazard. *Bull. Seismological Soc. America* 102, 2563–2573. doi:10.1785/0120120036

De Santis, A., Cianchini, G., Favali, P., Beranzoli, L., and Boschi, E. (2011). The gutenberg-richter law and entropy of earthquakes: two case studies in Central Italy. *Bull. Seismological Soc. America* 101, 1386–1395. doi:10.1785/0120090390

Eberhart-Phillips, D., and Oppenheimer, D. H. (1984). Induced seismicity in the Geysers geothermal area, California. *J. Geophys. Res.* 89 (B2), 1191–1207. doi:10.1029/jb089ib02p01191

Edwards, B., and Douglas, J. (2014). Magnitude scaling of induced earthquakes. *Geothermics* 52, 132–139. doi:10.1016/j.geothermics.2013.09.012

Garra, R., and Polito, F. (2011). A note on fractional linear pure birth and pure death processes in epidemic models. *Physica A: Stat. Mech. its Appl.* 390, 3704–3709. doi:10.1016/j.physa.2011.06.005

Gil-Alana, L. A., and Hualde, J. (2009). "Fractional integration and cointegration: an overview and an empirical application," in *Palgrave handbook of econometrics 2*. Editors T. C. Mills and K. Patterson (Springer), 434–469.

Gil-Alana, L. A., and Moreno, A. (2012). Uncovering the U.S. term premium. An alternative route. *J. Bank. Financ.* 36, 1184–1193. doi:10.1016/j.jbankfin.2011.11.013

Gil-Alaña, L. A., and Robinson, P. M. (1997). Testing of unit root and other nonstationary hypotheses in macroeconomic time series. *J. Econom.* 80, 241–268. doi:10.1016/s0304-4076(97)00038-9

Gil-Alana, L. A., and Sauci, L. (2019). US temperatures: time trends and persistence. *Int. J. Clim.* 39, 5091–5103.

Gil-Alana, L. A. (2005). Statistical modeling of the temperatures in the northern hemisphere using fractional integration techniques. *J. Clim.* 18, 5357–5369. doi:10.1175/jcli3543.1

Gil-Alana, L. A. (2004). The use of the Bloomfield model as an approximation to ARMA processes in the context of fractional integration. *Math. Computer Model.* 39, 429–436. doi:10.1016/s0895-7177(04)90515-8

Gil-Alana, L. A. (2008). Time trend estimation with breaks in temperature time series. *Climatic Change* 89, 325–337. doi:10.1007/s10584-008-9407-z

Gil-Alana, L. A., and Trani, T. (2019). Time trends and persistence in the global CO2 emissions across Europe. *Environ. Resource Econ.* 73, 213–228. doi:10.1007/s10640-018-0257-5

Gkarlaouni, C., Lasocki, S., Papadimitriou, E., and George, T. (2017). Hurst analysis of seismicity in Corinth rift and Mygdonia graben (Greece). *Chaos, Solitons & Fractals* 96, 30–42. doi:10.1016/j.chaos.2017.01.001

Granger, C. W. J., and Joyeux, R. (1980). An introduction to long-memory time series models and fractional differencing. *J. Time Ser. Anal.* 1, 15–29. doi:10.1111/j.1467-9892.1980.tb00297.x

Granger, C. W. J. (1980). Long memory relationships and the aggregation of dynamic models. *J. Econom.* 14, 227–238. doi:10.1016/0304-4076(80)90092-5

Granger, C. W. J. (1981). Some properties of time series data and their use in econometric model specification. *J. Econom.* 16, 121–130. doi:10.1016/0304-4076(81)90079-8

Hanks, T. C., and Kanamori, H. (1979). A moment magnitude scale. *J. Geophys. Res.* 84, 2348–2350. doi:10.1029/jb084ib05p02348

Hosking, J. R. M. (1981). Fractional differencing. *Biometrika* 68, 165–176. doi:10.1093/biomet/68.1.165

Hurst, H. E. (1951). Long-term storage capacity of reservoirs. *T. Am. Soc. Civ. Eng.* 116, 770–799. doi:10.1061/taceat.0006518

Ito, K., and Matsuzaki, M. (1990). Earthquakes as self-organized critical phenomena. *J. Geophys. Res.* 95, 6853–6860. doi:10.1029/jb095ib05p06853

Jiménez, A., Tiampo, K. F., Levin, S., and Posadas, A. M. (2006). Testing the persistence in earthquake catalogs: the Iberian Peninsula. *Europhys. Lett.* 73, 171–177. doi:10.1209/epl/i2005-10383-8

Johnson, C. W., Totten, E. J., and Bürgmann, R. (2016). Depth migration of seasonally induced seismicity at the Geysers geothermal field. *Geophys. Res. Lett.* 43, 6196–6204. doi:10.1002/2016gl069546

Johnson, L. R., and Majer, E. L. (2017). Induced and triggered earthquakes at the Geysers geothermal reservoir. *Geophys. J. Int.* 209, 1221–1238. doi:10.1093/gji/ggx082

Kagan, Y. Y., Jackson, D. D., and Geller, R. J. (2012). Characteristic earthquake model, 1884-2011, R.I.P. *Seismological Res. Lett.* 83, 951–953. doi:10.1785/0220120107

Kagan, Y. Y., and Jackson, D. D. (1991). Long-term earthquake clustering. *J. Int.* 104, 117–134. doi:10.1111/j.1365-246x.1991.tb02498.x

Kagan, Y. Y., and Jackson, D. D. (2013). Tohoku earthquake: a surprise?. *Bull. Seismological Soc. America* 103, 1181–1194. doi:10.1785/0120120110

Kagan, Y. Y., and Jackson, D. D. (1999). Worldwide doublets of large shallow earthquakes. *Bull. Seismol. Soc. Amer.* 89, 1147–1155.

Kandelhardt, J. W., Zschiegner, S. A., Koscielny-Bunde, E., Havlin, S., Bunde, A., and Stanley, H. E. (2002). Multifractal detrended fluctuation analysis of nonstationary time series. *Physica A* 316, 87–114.

Karagiannis, T., Molle, M., and Faloutsos, M. (2004). Long-range dependence ten years of Internet traffic modeling. *IEEE Internet Comput.* 8, 57–64. doi:10.1109/mic.2004.46

Kato, M. (2019). On the apparently inappropriate use of multiple hypothesis testing in earthquake prediction studies. *Seismol. Res. Lett.* 90, 1330–1334. doi:10.1785/0220180378

Kwiatek, G., Martínez-Garzón, P., Dresen, G., Bohnhoff, M., Sone, H., and Hartline, C. (2015). Effects of long-term fluid injection on induced seismicity parameters and maximum magnitude in northwestern part of the Geysers geothermal field. *J. Geophys. Res. Solid Earth* 120, 7085–7101. doi:10.1002/2015jb012362

Langenbruch, C., and Zoback, M. D. (2016). How will induced seismicity in Oklahoma respond to decreased saltwater injection rates?. *Sci. Adv.* 2, e1601542, e1601542. doi:10.1126/sciadv.1601542

Lee, Y.-T., Chen, C.-c., Hasumi, T., and Hsu, H.-L. (2009). Precursory phenomena associated with large avalanches in the long-range connective sandpile model II: an implication to the relation between theb-value and the Hurst exponent in seismicity. *Geophys. Res. Lett.* 36, a. doi:10.1029/2008GL036548

Lee, Y.-T., Chen, C.-c., Lin, C.-Y., and Chi, S.-C. (2012). Negative correlation between power-law scaling and Hurst exponents in long-range connective sandpile models and real seismicity. *Chaos, Solitons & Fractals* 45, 125–130. doi:10.1016/j.chaos.2011.10.009

Lennartz, S., Livina, V. N., Bunde, A., and Havlin, S. (2008). Long-term memory in earthquakes and the distribution of interoccurrence times. *Europhys. Lett.* 81, 69001. doi:10.1209/0295-5075/81/69001

Li, J., and Chen, Y. (2001). Rescaled range (R/S) analysis on seismic activity parameters. *Acta Seimol. Sin.* 14, 148–155. doi:10.1007/s11589-001-0145-9

Liu, C.-H., Liu, Y.-G., and Zhang, J. (1995). R/S analysis of earthquake time interval. *Acta Seismologica Sinica* 8, 481–485. doi:10.1007/bf02650577

Lo, A. W. (1991). Long-term memory in stock market prices. *Econometrica* 59, 1279–1313. doi:10.2307/2938368

Lomnitz, C. (1994). *Fundamentals of earthquake prediction*. Hoboken, New Jersey, US: Wiley.

Mandelbrot, B. B. (1983). *The fractal geometry of nature*. New York, NY: W. H. Freeman.

Mandelbrot, B. B., and Wallis, J. R. (1968). Noah, Joseph, and operational hydrology. *Water Resour. Res.* 4, 909–918. doi:10.1029/wr004i005p00909

Martínez-Garzón, P., Bohnhoff, M., Kwiatek, G., and Dresen, G. (2013). Stress tensor changes related to fluid injection at the Geysers geothermal field, Californiafluid injection at the Geysers geothermal field, California. *Geophys. Res. Lett.* 40, 2596–2601. doi:10.1002/grl.50438

Martínez-Garzón, P., Kwiatek, G., Sone, H., Bohnhoff, M., Dresen, G., and Hartline, C. (2014). Spatiotemporal changes, faulting regimes, and source parameters of induced seismicity: a case study from the Geysers geothermal fieldeld. *J. Geophys. Res. Solid Earth* 119, 8378–8396. doi:10.1002/2014jb011385

Martínez-Garzón, P., Zaliapin, I., Ben-Zion, Y., Kwiatek, G., and Bohnhoff, M. (2018). Comparative study of earthquake clustering in relation to hydraulic activities at geothermal fields in California. *J. Geophys. Res. Solid Earth* 123. doi:10.1029/2017JB014972

Marzocchi, W., and Lombardi, A. M. (2008). A double branching model for earthquake occurrence. *J. Geophys. Res.* 113, B08317. doi:10.1029/2007JB005472

Mukhopadhyay, B., and Sengupta, D. (2018). Seismic moment release data in earthquake catalogue: application of Hurst statistics in delineating temporal clustering and seismic vulnerability. *J. Geol. Soc. India* 91, 15–24. doi:10.1007/s12594-018-0815-z

NCEDC (2014). *Northern California earthquake data center*. Dataset: UC Berkeley Seismological Laboratory. doi:10.7932/NCEDC

Ogata, Y., and Abe, K. (1991). Some statistical features of the long-term variation of the global and regional seismic activity. *Int. Stat. Rev./Revue Internationale de Statistique* 59, 139–161. doi:10.2307/1403440

Peng, C. K., Buldyrev, S. V., Havlin, S., Simons, M., Stanley, H. E., and Goldberger, A. L. (1994). Mosaic organization of DNA nucleotides. *Phys. Rev. E Stat. Phys. Plasmas Fluids Relat. Interdiscip. Top.* 49, 1685–1689. doi:10.1103/physreve.49.1685

Qu, Z. (2011). A test against spurious long memory. *J. Business Econ. Stat.* 29, 423–438. doi:10.1198/jbes.2010.09153

Robinson, P. M. (1994). Efficient tests of nonstationary hypotheses. *J. Am. Stat. Assoc.* 89, 1420–1437. doi:10.1080/01621459.1994.10476881

Robinson, P. M. (1995). Gaussian semiparametric estimation of long range dependence. *Ann. Statist.* 23, 1630–1661. doi:10.1214/aos/1176324317

Samorodnitsky, G. (2006). Long range dependence. *FNT Stochastic Syst.* 1, 163–257. doi:10.1561/0900000004

Scholz, C. H. (1991). "Earthquakes and faulting: self-organized critical phenomena with a characteristic dimension,". in *Spontaneous formation of space-time structures and criticality NATO ASI Series (Series C: Mathematical and Physical Sciences)*. Editors T. Riste and D. Sherrington (Dordrecht: Springer), Vol. 349.

Shadkhoo, S., Ghanbarnejad, F., Jafari, G. R., and Tabar, M. (2009). Scaling behavior of earthquakes' inter-events time series. *Cent. Eur. J. Phys.* 7, 620–623. doi:10.2478/s11534-009-0058-0

Shadkhoo, S., and Jafari, G. R. (2009). Multifractal detrended cross-correlation analysis of temporal and spatial seismic data. *Eur. Phys. J. B* 72, 679–683. doi:10.1140/epjb/e2009-00402-2

Shimotsu, K., and Phillips, P. C. B. (2006). Local Whittle estimation of fractional integration and some of its variants. *J. Econom.* 130, 209–233. doi:10.1016/j.jeconom.2004.09.014

Solarin, S. A., and Bello, M. O. (2018). Persistence of policy shocks to an environmental degradation index: the case of ecological footprint in 128 developed and developing countries. *Ecol. Indicators* 89, 35–44. doi:10.1016/j.ecolind.2018.01.064

Sornette, A., and Sornette, D. (1989). Self-organized criticality and earthquakes. *Europhys. Lett.* 9, 197–202. doi:10.1209/0295-5075/9/3/002

Sornette, D. (1991). "Self-organized criticality in plate tectonics". in *Spontaneous formation of space-time structures and criticality NATO ASI Series (Series C: Mathematical and Physical Sciences)*. Editors T. Riste and D. Sherrington (Dordrecht: Springer), Vol. 349.

Sowell, F. (1992). Modeling long-run behavior with the fractional ARIMA model. *J. Monetary Econ.* 29, 277–302. doi:10.1016/0304-3932(92)90016-u

Stark, M. (2003). Seismic evidence for a long-lived enhanced geothermal system (EGS) in the northern Geysers reservoir. *Trans. Geotherm. Resour. Counc.* 27, 727–731.

Telesca, L., Cuomo, V., Lapenna, V., and Macchiato, M. (2004). Detrended fluctuation analysis of the spatial variability of the temporal distribution of Southern California seismicity. *Chaos, Solitons & Fractals* 21, 335–342. doi:10.1016/j.chaos.2003.10.021

Teverovsky, V., Taqqu, M. S., and Willinger, W. (1999). A critical look at Lo's modified R/S statistic. *J. Stat. Plann. Inference* 80, 211–227. doi:10.1016/s0378-3758(98)00250-x

Tormann, T., Enescu, B., Woessner, J., and Wiemer, S. (2015). Randomness of megathrust earthquakes implied by rapid stress recovery after the Japan earthquake. *Nat. Geosci* 8, 152–158. doi:10.1038/ngeo2343

Trugman, D. T., Shearer, P. M., Borsa, A. A., and Fialko, Y. (2016). A comparison of long-term changes in seismicity at the Geysers, Salton Sea, and Coso geothermal fields. *J. Geophys. Res. Solid Earth* 121, 225–247. doi:10.1002/2015jb012510

Turcotte, D. L. (1999). Seismicity and self-organized criticality. *Phys. Earth Planet. Interiors* 111, 275–293. doi:10.1016/s0031-9201(98)00167-8

Utsu, T. (1961). A statistical study on the occurrence of aftershocks. *Geophys. Mag.* 30, 521–605.

Velasco, C. (1999). Gaussian semiparametric estimation of non-stationary time series. *J. Time Ser. Anal.* 20, 87–127. doi:10.1111/1467-9892.00127

Wiemer, S., and Wyss, M. (2000). Minimum magnitude of completeness in earthquake catalogs: examples from Alaska, the western United States, and Japan. *Bull. Seismological Soc. America* 90, 859–869. doi:10.1785/0119990114

Woessner, J., and Wiemer, S. (2005). Assessing the quality of earthquake catalogues: estimating the magnitude of completeness and its uncertainty. *Bull. Seismological Soc. America* 95, 684–698. doi:10.1785/0120040007

Conflict of Interest: The authors declare that the research was conducted in the absence of any commercial or financial relationships that could be construed as a potential conflict of interest.

Copyright © 2021 Barani, Cristofaro, Taroni, Gil-Alaña and Ferretti. This is an open-access article distributed under the terms of the Creative Commons Attribution License (CC BY). The use, distribution or reproduction in other forums is permitted, provided the original author(s) and the copyright owner(s) are credited and that the original publication in this journal is cited, in accordance with accepted academic practice. No use, distribution or reproduction is permitted which does not comply with these terms.

Advantages of publishing in Frontiers

OPEN ACCESS
Articles are free to read for greatest visibility and readership

FAST PUBLICATION
Around 90 days from submission to decision

HIGH QUALITY PEER-REVIEW
Rigorous, collaborative, and constructive peer-review

TRANSPARENT PEER-REVIEW
Editors and reviewers acknowledged by name on published articles

Frontiers
Avenue du Tribunal-Fédéral 34
1005 Lausanne | Switzerland

Visit us: www.frontiersin.org
Contact us: frontiersin.org/about/contact

REPRODUCIBILITY OF RESEARCH
Support open data and methods to enhance research reproducibility

DIGITAL PUBLISHING
Articles designed for optimal readership across devices

FOLLOW US
@frontiersin

IMPACT METRICS
Advanced article metrics track visibility across digital media

EXTENSIVE PROMOTION
Marketing and promotion of impactful research

LOOP RESEARCH NETWORK
Our network increases your article's readership